De interactie van complex harmonische elastische golven met periodiek ruwe oppervlakken en met anisotrope visco-elastische en/of piëzo-elektrische gelaagde media.

The interaction of complex harmonic elastic waves with periodically corrugated surfaces and with anisotropic viscoelastic and/or piezoelectric layered media.

Nico F. Declercq

Promotoren Prof. dr. ir. Joris Degrieck, Em. Prof. dr. dr.h.c. Oswald Leroy
Proefschrift ingediend tot het behalen van de graad van
Doctor in de Toegepaste Wetenschappen: Natuurkunde

Vakgroep Mechanische Constructie en Productie
Voorzitter: Prof. dr. ir. Joris Degrieck
Faculteit Toegepaste Wetenschappen
Academiejaar 2004 – 2005

UNIVERSITEIT GENT

ISBN 90-8578-014-4
NUR 924
Wettelijk depot: D/2005/10.500/14

Onderzoeksinstelling – *Research Institute*

Universiteit Gent
Vakgroep Mechanische Constructie en Productie – Laboratorium Soete
Faculteit Toegepaste Wetenschappen
Universiteit Gent
Sint Pietersnieuwstraat 41
B-9000 Gent
-
Soete Laboratory
Department of Mechanical Construction and Production
Faculty of Engineering
Ghent University
Sint Pietersnieuwstraat 41
B-9000 Ghent
Belgium

Beursverlenende instantie – *Research Grant offered by*

IWT-Vlaanderen: Instituut voor de aanmoediging van Innovatie door Wetenschap en Technologie in Vlaanderen
Bischoffsheimlaan 25, B-1000 Brussel, Tel. 32-02/209 09 00, Fax 32-02/223 11 81
Website : http://www.iwt.be, Email : info@iwt.be
-
IWT-Flanders: Institute for the Promotion of Innovation through Science and Technology in Flanders
Bischoffsheimlaan 25, B-1000 Brussels, Belgium, Tel. 32-02/209 09 00, Fax 32-02/223 11 81
Website : http://www.iwt.be, Email : info@iwt.be

The PhD examination Jury:

- **Prof. dr. ir. Ronny Verhoeven (chairman)**, Vakgroep Civiele Techniek (TW15), Sint Pietersnieuwstraat 41, B-9000 Gent. Logistieke dienst onderwijs Faculteit Toegepaste Wetenschappen (TW53), Jozef Plateaustraat 22, B-9000 Gent. Email: Ronny.Verhoeven@UGent.be

- **Prof. dr. ir. Joris Degrieck (promoter),** Vakgroep Mechanische Constructie en Productie (TW04), Sint Pietersnieuwstraat 41, B-9000 Gent. Email: Joris.Degrieck@UGent.be

- **Em. Prof. dr. dr.h.c. Oswald Leroy (promoter),** Faculteit Wetenschappen, Katholieke Universiteit Leuven Campus Kortrijk. Correspondentieadres: Meensesteenweg 453, 8501 Bissegem. Email: Oswald.Leroy@kulak.ac.be

- **Prof. dr. Rudy Briers,** Faculteit Geneeskunde, Katholieke Universiteit Leuven Campus Kortrijk, E. Sabbelaan 53, B-8500 Kortrijk. Email: Rudy.Briers@kulak.ac.be

- **Em. Prof. dr. Mack A. Breazeale,** National Center of Physical Acoustics, University of Mississipy, coliseum drive, Oxford, MS 38677, USA. Email: breazeal@sunset.backbone.olemiss.edu

- **Em. Prof. dr. Laszlo Adler,** Adler Consultants Inc., Columbus, Ohio, USA. Correspondence address: 301 Harbor Drive, Belleair Beach, FL 33786, USA. Email: LADLER1@aol.com

- **Prof. dr. Gennady Shkerdin,** Institute of Radio Engineering and Electronics, Russian Academy of Sciences, Moscow, Russia; Correspondence address: ul. Molostovykh, h. 4, app. 64, 111555, Moscow, Russian Federation. Email: shkerdin@yahoo.com

- **Prof. dr. Christ Glorieux,** Afdeling Akoestiek en Thermische fysica, Kuleuven, Celestijnenlaan 200D, B-3001 Heverlee. Email: Christ.Glorieux@fys.kuleuven.ac.be

- **Prof. dr. ir. Dick Botteldooren,** Vakgroep Informatietechnologie (TW05), Kuiperskaai 55, B-9000 Gent. Email: Dick.Botteldooren@UGent.be

- **Prof. dr. ir. Roger Van Keer,** Vakgroep Wiskundige Analyse (TW16), Galglaan 2, 9000 Gent. Email: Roger.VanKeer@UGent.be

- **Prof. dr. ir. Wim Van Paepegem (secretary),** Vakgroep Mechanische Constructie en Productie (TW04), Sint Pietersnieuwstraat 41, B-9000 Gent. Email: Wim.VanPaepegen@Ugent.be

The flow of time makes the road ahead unknown and the path behind withdrawn, what's left is the present joy,
the adjacent's bliss and the right choice of course.

Nico F. Declercq

This work is sincerely dedicated to my beloved wife Shirani,
to our son Benjamin and to our newborn daughter Anna-Laura.

The Beauty of Science is only Enlightened by the Purity of Nature…Darkness is Nature's Reply to Vanity.

Nico F. Declercq

Acknowledgements

Research funded by a PhD grant of the Institute for the Promotion of Innovation through Science and Technology in Flanders (IWT-Vlaanderen)

Partial sponsorship through travel grants by the Fund for Scientific Research Flanders-Belgium, by the International Commission for Acoustics, by the Acoustical Society of America and through a collaborative linkage grant offered by NATO, are highly appreciated.

Words of Gratitude

I would like to thank all my colleagues in Ghent and all my former colleagues in Kortrijk, for their presence during the last couple of years. Special thanks are also dedicated to Joris Degrieck, to Oswald Leroy and to Rudy Briers for their trust in me and for their professional guidance.

In addition, I would like to thank everybody with whom I have collaborated.

Furthermore, I thank my family and friends for their support.

Last but not least I would like to thank the members of the PhD Examination Jury for their preparedness to read this work, to pose questions and to make themselves available during the private and public defense.

Nico F. Declercq

Scientific output of the presented 3 years' work

Work reported by *Nature*

(Imp. Fact 30.979, SCI-index, 'Multidisciplinary Science's, rank: 1 /46)

- Mystery of 'chirping' pyramid decoded, **Nature News** 14 December 2004 (doi : 10.1038 / news 041213-5)

Publications in journals of Thomson's Science Citation Index

1. **Nico F. Declercq**, Rudy Briers, Joris Degrieck, Oswald Leroy, "The History and Properties of Ultrasonic Inhomogeneous Waves", accepted for publication in **IEEE Transactions on Ultrasonics, Ferroelectrics, and Frequency Control** *(Imp. Fact. 1.595 ;SCI-index, Engineering – electrical & electronic, rank:46/205)*
2. **Nico F. Declercq**, Joris Degrieck, Oswald Leroy, "Focal length control of complex harmonic and complex pulsed ultrasonic bounded beams", **J. Appl. Phys.** 97(5), 054904 1-8, 2005 *(Imp. Fact. 2.281; SCI-index, Physics-Applied, rank:13/76)*
3. A. Teklu, M. A. Breazeale, **Nico F. Declercq**, Roger D. Hasse, Michael S. McPherson, "Backward Displacement of Ultrasonic Waves Reflected from a Periodically Corrugated Interface", **J. Appl. Phys.** 97, 084904 1-4, 2005. *(Imp. Fact. 2.281; SCI-index, Physics-Applied, rank:13/76)*
4. **Nico F. Declercq**, Joris Degrieck, Oswald Leroy, "Simulations of Harmonic and Pulsed Ultrasonic Polar Scans", accepted for publication in **NDT & E International** *(Imp. Fact. 0.752; SCI-index, Materials Science – Characterization & Testing, rank:3/23)*
5. **Nico F. Declercq**, Joris Degrieck, Oswald Leroy, "Bounded beam interaction with plate-edge at Lamb angle", **Acta Acustica United with Acustica** 91, 326-332, 2005 *(Imp. Fact. 0.346; SCI-index, Acoustics, rank:21 /28)*
6. **Nico F. Declercq**, Joris Degrieck, Oswald Leroy, "Schlieren photography to study sound interaction with highly absorbing materials", accepted for publication in **Ultrasonics**. *(Imp. Fact. 0.844; SCI-index, Acoustics, rank:11 /28)*
7. **Nico F. Declercq,** A. Teklu, M. A. Breazeale, Roger D. Hasse, Joris Degrieck, Oswald Leroy, "Detection of fiber direction in composites by means of high frequency wide bounded ultrasonic beam and schlieren photography", accepted for publication in **Research in Nondestructive Evaluation** *(Imp. Fact 0.935; SCI-index, Materials Science – Characterization & Testing, rank:2/23)*
8. **Nico F. Declercq**, Rudy Briers, Oswald Leroy, Gennady Shkerdin, Joris Degrieck, "The radiation mode theory in ultrasonics", accepted for publication in **IEEE Transactions on Ultrasonics, Ferroelectrics, and Frequency Control** *(Imp. Fact. 1.595 ;SCI-index, Engineering – electrical & electronic, rank:46/205)*
9. **Nico F. Declercq**, Joris Degrieck, Oswald Leroy, "A useful analytical description of the coefficients in an Inhomogeneous Wave Decomposition of a symmetrical bounded beam", **Ultrasonics** 43(4), 279-282, 2005 *(Imp. Fact. 0.844; SCI-index, Acoustics, rank:11 /28)*
10. **Nico F. Declercq**, Joris Degrieck, Rudy Briers, Oswald Leroy, "A theoretical study of special acoustics effects caused by the staircase of the El Castillo pyramid at the Maya ruins of Chichen-Itza in Mexico", **J. Acoust. Soc. Am.** 116(6), 3328-3335, 2004 *(Imp. Fact. 1.310; SCI-index, Acoustics, rank:7 /28)*| Also published in **Nature News** 14 December 2004 (doi : 10.1038 / news 041213-5)

11. **Nico F. Declercq**, Joris Degrieck, Rudy Briers, Oswald Leroy, "Theory of the backward beam displacement on periodically corrugated surfaces and its relation to leaky Scholte-Stoneley waves", **J. Appl. Phys.** 96(11), 6869-6877, 2004 *(Imp. Fact. 2.281; SCI-index, Physics-Applied, rank:13/76)*
12. **Nico F. Declercq**, A. Teklu, M. A. Breazeale, Rudy Briers, Oswald Leroy, Joris Degrieck, Gennady N. Shkerdin, "Study of the scattering of leaky Rayleigh waves at the extremity of a fluid loaded thick plate", **J. Appl. Phys** 96(10),5836-5840, 2004 *(Imp. Fact. 2.281; SCI-index, Physics-Applied, rank:13/76)*
13. **Nico F. Declercq**, Joris Degrieck, Oswald Leroy, "The Double Sided Ultrasonic Beam Displacement", **Appl. Phys. let.** 85(18), 4234-4236, 2004 *(Imp. Fact. 4.207; SCI-index, Physics-Applied, rank:3/76)*
14. **Nico F. Declercq**, Oswald Leroy, Joris Degrieck, Jeroen Vandeputte "The interaction of inhomogeneous waves and Gaussian beams with mud in between a hard solid and an ideal liquid", **Acta Acustica United with Acustica** 90, 819-829, 2004 *(Imp. Fact. 0.346; SCI-index, Acoustics, rank:21 /28)*
15. **Nico F. Declercq,** Filip Van den Abeele, Joris Degrieck, Oswald Leroy, "The Schoch effect to distinguish between different liquids in closed containers", **IEEE Transactions on Ultrasonics, Ferroelectrics, and Frequency Control** 51(10), 1354-1357, 2004. *(Imp. Fact. 1.595 ;SCI-index, Engineering – electrical & electronic, rank:46/205)*
16. **Nico F. Declercq**, Joris Degrieck, Oswald Leroy, "Frequency bandgap for Rayleigh waves on coated surfaces", **Appl. Phys Let.** 85(1), 148-150, 2004. *(Imp. Fact. 4.207; SCI-index, Physics-Applied, rank:3/76)*
17. **Nico F. Declercq**, Joris Degrieck, Oswald Leroy, "The Laplace transform to describe bounded inhomogeneous waves", **J. Acoust. Soc. Am.** 116(1), 51-60, 2004. *(Imp. Fact. 1.310; SCI-index, Acoustics, rank:7 /28)*
18. **Nico F. Declercq**, Joris Degrieck, Oswald Leroy, "On the generalized Snell's law and its possible relation to coherent backscattering of ultrasonic waves", **Appl. Phys. let. ,** 4245-4247, 84(21), 2004. *(Imp. Fact. 4.207; SCI-index, Physics-Applied, rank:3/76)*
19. **Nico F. Declercq**, Joris Degrieck, Oswald Leroy, "The inhomogeneous wave decomposition of 3D Gaussian-like bounded beams", **Ultrasonics** 42, 273-276, 2004. *(Imp. Fact. 0.844; SCI-index, Acoustics, rank:11 /28)*
20. **Nico F. Declercq**, Joris Degrieck, Oswald Leroy, " On the influence of fatigue on ultrasonic polar scans of fiber reinforced composites", **Ultrasonics** 42, 173-177, 2004. *(Imp. Fact. 0.844; SCI-index, Acoustics, rank:11 /28)*
21. **Nico F. Declercq**, Joris Degrieck, Oswald Leroy, "The Principle of a Chopped Series Equilibrium to Determine the Expansion Coefficients in the Inhomogeneous Waves Decomposition of a Bounded Beam", **Acta Acustica United with Acustica** 89, 1038-1040, 2003. *(Imp. Fact. 0.346; SCI-index, Acoustics, rank:21 /28)*
22. **Nico F. Declercq**, Joris Degrieck, Rudy Briers, Oswald Leroy, "Theoretical verification of the backward displacement of waves reflected from an interface having superimposed periodicity", **Appl. Phys. let.** 82(15), 2533-2535, 2003. *(Imp. Fact. 4.207; SCI-index, Physics-Applied, rank:3/76)*
23. Joris Degrieck, **Nico F. Declercq**, Oswald Leroy, "Ultrasonic Polar Scans as a possible means of nondestructive testing and characterization of composite plates", **Insight - The Journal of The British Institute of Non-Destructive Testing**, 45(3), 196-201, 2003. *(Imp. Fact. 0.311; SCI-index, Materials Science – Characterization & Testing, rank:11/23)*
24. **Nico F. Declercq**, Rudy Briers, Joris Degrieck, Oswald Leroy, "Diffraction of horizontally polarized ultrasonic plane waves on a periodically corrugated solid-liquid

interface for normal incidence and Brewster angle incidence", **IEEE Transactions on Ultrasonics, Ferroelectrics, and Frequency Control**, 49(11), 1516-1521, 2002. *(Imp. Fact. 1.595 ;SCI-index, Engineering – electrical & electronic, rank:46/205)*

25. **Nico F. Declercq**, Rudy Briers, Oswald Leroy, " The use of polarized bounded beams to determine the groove direction of a surface corrugation at normal incidence, the generation of surface waves and the insonification at Bragg-angles", **Ultrasonics** 40/1-8 pp. 345-348, 2002.*(Imp. Fact. 0.844; SCI-index, Acoustics, rank:11 /28)*
26. **Nico F. Declercq**, Joris Degrieck, Rudy Briers and Oswald Leroy, "Diffraction of homogeneous and inhomogeneous plane waves on a doubly corrugated liquid/solid interface" accepted for publication in **Ultrasonics**. *(Imp. Fact. 0.844; SCI-index, Acoustics, rank:11 /28)*
27. **Nico F. Declercq**, Joris Degrieck, Oswald Leroy, "On the theoretical possibility to apply an acoustic diffraction grating as a complex frequency filter device for electronic signals", accepted for publication in **Ultrasonics**. *(Imp. Fact. 0.844; SCI-index, Acoustics, rank:11 /28)*

Invited publications in congress proceedings

1. **Nico F. Declercq**, Rudy Briers, Joris Degrieck, Oswald Leroy, "Inhomogeneous waves in isotropic and anisotropic media", invited paper in Proceedings of VII International Conference for Young Researchers on Wave Electronics and its Applications in Information and Telecommunication Systems, St Petersburg, Russia , p 7-8, 12-15/09 2004.
2. **Nico F. Declercq**, Rudy Briers, Joris Degrieck, Oswald Leroy, "The diffraction of ultrasound on corrugated surfaces and its possible application for surface waves stimulation" , invited paper in Proceedings of 51st open seminar on Acoustics, Joint with 9th School of Acousto-Optics and Applications , Gdansk, Poland , 6-10/09 2004 | Proc. SPIE Int. Soc. Opt. Eng. 5828, 170 (2005).
3. Leroy Oswald, **Declercq Nico F.**, Degrieck Joris, "The Acousto-Optic interaction from a fundamental point of view to its applications in non-destructive testing", ULT-Gen-002, Proceedings of Forum Acusticum (3rd EAA European Congress on Acoustics, XXXIII Spanish Congress, Tecniacustica 2002, 3rd Iberian Congress on Acoustics, European and Japanese Symposium - EAA - SEA - ASJ, Expoacustica 2002), Sevilla Spain, 16-20 September 2002.

Contributed publications in congress proceedings

4. **Nico F. Declercq**, “Theoretical and experimental ultrasonics : bulk acoustic microscopy”, Proceedings of the 5th UGent PhD symposium, 1 December 2004, Aula UGent, Ghent, Belgium.
5. **Nico F. Declercq**, Joris Degrieck, Oswald Leroy, "Some properties of waves having complex frequency", paper in Proceedings of VII International Conference for Young Researchers on Wave Electronics and its Applications in Information and Telecommunication Systems, St Petersburg, Russia , p73-74, 12-15/09 2004.
6. **Nico F. Declercq**, Joris Degrieck, Oswald Leroy, "The possible connection between the non-trivial law of Snell and backscattering on smooth surfaces " , paper in Proceedings of VII International Conference for Young Researchers on Wave Electronics and its Applications in Information and Telecommunication Systems, St Petersburg, Russia , p63-65, 12-15/09 2004.
7. **Nico F. Declercq**, Joris Degrieck, Oswald Leroy, “The existence of a band-gap for Rayleigh waves on coated solids” , paper in Proceedings of VII International Conference for Young Researchers on Wave Electronics and its Applications in Information and Telecommunication Systems, St Petersburg, Russia , p66-68, 12-15/09 2004
8. **Nico F. Declercq**, Rudy Briers, Gennady Shkerdin, Oswald Leroy, Joris Degrieck, "The ultrasonic radiation mode theory " paper in Proceedings of 51st open seminar on Acoustics, Joint with 9th School of Acousto Optics and Applications , Gdansk, Poland , 6-10/09 2004 | Proc. SPIE Int. Soc. Opt. Eng. 5828, 181 (2005).
9. **Nico F. Declercq**, A. Teklu, M. A. Breazeale, Joris Degrieck, Oswald Leroy, "Schlieren photography as a great tool to study wave diffraction at the end of a thin plate " paper in Proceedings of 51st open seminar on Acoustics, Joint with 9th School of Acousto-Optics

and Applications , Gdansk, Poland , 6-10/09 2004 | Proc. SPIE Int. Soc. Opt. Eng. 5828, 117 (2005).

10. **Nico F. Declercq** , A. Teklu, M. A. Breazeale, Roger D. Hasse, Joris Degrieck, Oswald Leroy, "Fiber direction determination in composites by means of Schlieren photography " paper in Proceedings of 51st open seminar on Acoustics, Joint with 9th School of Acousto Optics and Applications , Gdansk, Poland , 6-10/09 2004 | Proc. SPIE Int. Soc. Opt. Eng. 5828, 123 (2005).
11. **Nico F. Declercq**, A. Teklu, M. A. Breazeale, Rudy Briers, Oswald Leroy, Joris Degrieck, "The diffraction of leaky Rayleigh waves at the extremity of a fluid loaded plate", J. Acoust. Soc. Am. 115(5), 2472, 2004.
12. **Nico F. Declercq**, Filip Van den Abeele, Joris Degrieck, Oswald Leroy, "The dependence of Lamb wave stimulation parameters on the impedance difference between upper and lower liquid", J. Acoust. Soc. Am. 115(5), 2472 , 2004.
13. Alem A. Teklu, **Nico F. Declercq**, Mack A. Breazeale, "Measurement of the frequency of the ultrasonic parametric threshold amplitude", J. Acoust. Soc. Am. 115(5), 2533 , 2004
14. **Nico F. Declercq**, A. Teklu, M. A. Breazeale, Joris Degrieck, Oswald Leroy, "The Schoch effect as a means to detect the principal axes of a piezoelectric crystal", J. Acoust. Soc. Am. 115(5), 2569 , 2004.
15. **Nico F. Declercq**, Rudy Briers, Joris Degrieck, Oswald Leroy, "Ultrasonic Inhomogeneous Waves: Three Decades of Fascination", J. Acoust. Soc. Am. 115(5), 2624, 2004
16. **Nico F. Declercq**, Joris Degrieck, Oswald Leroy, "Surface and plate mode stimulation in piezoelectric materials in the framework of inhomogeneous wave theory", J. Acoust. Soc. Am. 115(5), 2626 , 2004.
17. **Nico F. Declercq**, Joris Degrieck, Oswald Leroy, "Diffraction of plane waves having complex frequency and the excitation of transient leaky Rayleigh waves", J. Acoust. Soc. Am. 115(5), 2626 , 2004.
18. **Nico F. Declercq**, Joris Degrieck, Rudy Briers, Oswald Leroy, "On the existence of a Brewster angle for solid side incidence on periodically rough surfaces", pp V3623-V3626 in Proceedings of the ICA2004 18th International Congress on Acoustics, Kyoto International Conference Hall, 4-9 April 2004, Kyoto, Japan.
19. **Nico F. Declercq**, Joris Degrieck, Oswald Leroy, "The reflection of ultrasound from stressed piezoelectric crystals", pp V3429-3422 in Proceedings of the ICA2004 18th International Congress on Acoustics, Kyoto International Conference Hall, 4-9 April 2004, Kyoto, Japan.
20. **Nico F. Declercq**, Joris Degrieck, Oswald Leroy, "On the use of the localized inhomogeneity approach to describe bounded beams", pp II1661-II1662 in Proceedings of the ICA2004 18th International Congress on Acoustics, Kyoto International Conference Hall, 4-9 April 2004, Kyoto, Japan.
21. **Nico F. Declercq**, Filip Van den Abeele, Joris Degrieck, Oswald Leroy, "On the use of bounded beam effects to characterize fluids in containers", pp II1347-II1350 in Proceedings of the ICA2004 18th International Congress on Acoustics, Kyoto International Conference Hall, 4-9 April 2004, Kyoto, Japan.
22. **Nico F. Declercq**, Joris Degrieck, Rudy Briers, Oswald Leroy, "The extended model to simulate the Quetzal echo at the Mayan pyramid of Kukulkan at Chichen Itza in Mexico", proceedings of the Joint congress CFA/DAGA'04 22-25 March 2004 in Strasbourg, France.

23. **Nico F. Declercq**, Joris Degrieck, Oswald Leroy, "Two Improved Methods to Determine the Coefficients in the Inhomogeneous Wave Decomposition of Bounded Beams", Peer reviewed Section of the Proceedings of the 8th Western Pacific Acoustics Conference (Wespac8), paper WE41, 7-9 April, Melbourne, Australia, 2003.
24. **Nico F. Declercq**, Joris Degrieck, Oswald Leroy, "Ultrasonics, a Fascinating Field of Physics and its Applications", Paper 079, Proceedings of the 4th UGent FTW PhD symposium, December 3rd, Ghent, Belgium, 2003.
25. **Nico F. Declercq**, Joris Degrieck, Oswald Leroy, "Profiled plane waves as the framework for the interaction of 3D bounded beams with anisotropic materials", 995-998, Proceedings of the World Congress on ultrasonics 2003, September 7-10, 2003, Paris, France.
26. **Nico F. Declercq**, Joris Degrieck, Oswald Leroy, "The characterization of applied and residual stress in isotropic plates by means of multidirectional inspection", Paper N841, pp 4287-4292, Proceedings of InterNoise2003, August 25-28, 2003, International Convention Center Jeju, Seogwipo, Korea.
27. **Nico F. Declercq**, Joris Degrieck, Rudy Briers, Oswald Leroy, "On the possible application of doubly corrugated plates in advanced SAW devices", Paper N840, pp 3730-3737, Proceedings of InterNoise2003, August 25-28, 2003, International Convention Center Jeju, Seogwipo, Korea.
28. **Nico F. Declercq**, Joris Degrieck, Oswald Leroy, "On the theoretical discovery of a new kind of leaky surface waves", Paper P409 of the Proceedings of the Tenth International Congress on Sound and Vibration, 7-10 July 2003, Stockholm, Sweden.
29. **Nico F. Declercq**, Joris Degrieck, Oswald Leroy, "Numerical simulations of ultrasonic polar scans", pp75-80 in Emerging Technologies in Non Destructive Testing, Van Hemelrijck, Anastasopoulos and Melanitis (eds), Swets & Zeitlinger, Lisse, 2004.
30. **Nico F. Declercq**, Joris Degrieck, Rudy Briers, Oswald Leroy, "Some interesting features of the interaction of a bounded ultrasonic beam with a doubly corrugated interface between a solid and a liquid", pp 191-199, 'Modelling and Experimental Measurements in Acoustics III', Edts D. Almorza, C. A. Brebbia, R. Hernandez, WITPRESS, Southampton, Boston, 2003.
31. **Nico F. Declercq**, Joris Degrieck, Oswald Leroy, "On the ability of bounded inhomogeneous waves to experimentally verify the behavior of infinite inhomogeneous plane waves", J. Acoust. Soc. Am. 113(4), 2283, 2003.
32. **Nico F. Declercq**, Joris Degrieck, Rudy Briers, Oswald Leroy, " A full simulation of the Quetzal echo at the Mayan pyramid of Kukulkan at Chichen Itza in Mexico", J. Acoust. Soc. Am. 113(4), 2189, 2003.
33. **Nico F. Declercq**, Joris Degrieck, Oswald Leroy, "Numerical Simulations of Ultrasonic Polar Scans on Single Layered Fiber Reinforced Composites", proceedings of DAGA'03, 18-20 March 2003, Aachen**,** Germany.
34. **Nico Declercq**, Joris Degrieck, Oswald Leroy, "Nondestructive Materials Characterization by means of Ultrasound", Proceedings of the 3rd FTW PHD SYMPOSIUM, Ghent University, Gent Belgium 2002.
35. **Nico F. Declercq**, Joris Degrieck, Rudy Briers, Oswald Leroy, "A theoretical elucidation for the experimentally observed backward displacement of waves reflected from an interface having superimposed periodicity", Proceedings of the First Pan-American/Iberian Meeting on Acoustics (144th Meeting of the Acoustical Society of

America, 3rd Iberoamerican Congress of Acoustics, 9th Mexican Congress on Acoustics), 2-6 Dec. 2002, Cancun Q. R. Mexico.

36. **Declercq Nico F.**, Degrieck Joris, Leroy Oswald, "Hypercomplex Waves", PHA-Gen-006, Proceedings of Forum Acusticum (3rd EAA European Congress on Acoustics, XXXIII Spanish Congress, Tecniacustica 2002, 3rd Iberian Congress on Acoustics, European and Japanese Symposium - EAA - SEA - ASJ, Expoacustica 2002), Sevilla Spain, 16-20 Sepember 2002.
37. **Nico F. Declercq**, Joris Degrieck, Rudy Briers, Oswald Leroy, "The Diffraction of Inhomogeneous waves by a doubly corrugated liquid/solid interface", Proceedings of the 6th French Congress on Acoustics, Lille France, 2002.
38. **Nico F. Declercq**, Joris Degrieck, Oswald Leroy, "Characterization of layered Orthotropic Materials Using Ultrasonic Polar Scans", Proceedings of the 2nd FTW PHD SYMPOSIUM, Ghent University, Gent Belgium, 2001.
39. **Nico F. Declercq**, Rudy Briers, Oswald Leroy, "The Direct Superposition Method to predict Wood Anomalies in Acoustic Spectra obtained from Diffraction on Periodically Corrugated Surfaces", Proceedings of the 17th International Congress on Acoustics, Rome Italy, September 2-7, 2001.

Invited active communications at congresses

1. **Nico F. Declercq**, Rudy Briers, Joris Degrieck, Oswald Leroy, "Inhomogeneous waves in isotropic and anisotropic media" , plenary session, invited oral presentation at VII International Conference for Young Researchers on Wave Electronics and its Applications in Information and Telecommunication Systems, **St Petersburg**, Russia , 12-15/09 2004.
2. **Nico F. Declercq**, Rudy Briers, Joris Degrieck, Oswald Leroy, "The diffraction of ultrasound on corrugated surfaces and its possible application for surface waves stimulation" , oral (invited) presentation at 51st open seminar on Acoustics, Joint with 9th School of Acousto-Optics and Applications, **Gdansk**, Poland , 6-10/09 2004.

Contributed active communications at congresses

3. **Nico F. Declercq**, “Theoretical and experimental ultrasonics : bulk acoustic microscopy”, poster presentation at the 5th UGent PhD symposium, 1 December 2004, Aula UGent, **Ghent**, Belgium
4. **Nico F. Declercq**, Joris Degrieck, Oswald Leroy, "Some properties of waves having complex frequency", poster presentation at VII International Conference for Young Researchers on Wave Electronics and its Applications in Information and Telecommunication Systems, **St Petersburg**, Russia , 12-15/09, 2004.
5. **Nico F. Declercq**, Joris Degrieck, Oswald Leroy, "The possible connection between the non-trivial law of Snell and backscattering on smooth surfaces " , oral presentation at VII International Conference for Young Researchers on Wave Electronics and its

Applications in Information and Telecommunication Systems, **St Petersburg**, Russia , 12-15/09 2004.

6. **Nico F. Declercq**, Joris Degrieck, Oswald Leroy, "The existence of a band-gap for Rayleigh waves on coated solids", oral presentation at VII International Conference for Young Researchers on Wave Electronics and its Applications in Information and Telecommunication Systems, **St Petersburg**, Russia , 12-15/09 2004.
7. **Nico F. Declercq**, Rudy Briers, Gennady Shkerdin, Oswald Leroy, Joris Degrieck, "The ultrasonic radiation mode theory " oral presentation at 51st open seminar on Acoustics, Joint with 9th School of Acousto-Optics and Applications , **Gdansk**, Poland , 6-10/09 2004.
8. **Nico F. Declercq**, Joris Degrieck, Oswald Leroy, "Schlieren photography as a great tool to study wave diffraction at the end of a thin plate " oral presentation at 51st open seminar on Acoustics, Joint with 9th School of Acousto-Optics and Applications , **Gdansk**, Poland , 6-10/09 2004.
9. **Nico F. Declercq** , A. Teklu, M. A. Breazeale, Roger D. Hasse, Joris Degrieck, Oswald Leroy, "Fiber direction determination in composites by means of Schlieren photography " oral presentation at 51st open seminar on Acoustics, Joint with 9th School of Acousto-Optics and Applications , **Gdansk**, Poland , 6-10/09 2004.
10. **Nico F. Declercq**, A. Teklu, M. A. Breazeale, Rudy Briers, Oswald Leroy, Joris Degrieck, "The diffraction of leaky Rayleigh waves at the extremity of a fluid loaded plate", oral presentation at 75th Anniversary Celebration of the Acoustical Society of America (147th meeting of the Acoustical Society of America), Sheraton New York Hotel and Towers, **New York**, New York, 24-28 May 2004, USA.
11. **Nico F. Declercq**, Filip Van den Abeele, Joris Degrieck, Oswald Leroy, "The dependence of Lamb wave stimulation parameters on the impedance difference between upper and lower liquid", oral presentation at 75th Anniversary Celebration of the Acoustical Society of America (147th meeting of the Acoustical Society of America), Sheraton New York Hotel and Towers, **New York**, New York, 24-28 May 2004, USA.
12. **Nico F. Declercq**, A. Teklu, M. A. Breazeale, Joris Degrieck, Oswald Leroy, "The Schoch effect as a means to detect the principal axes of a piezoelectric crystal", oral presentation at 75th Anniversary Celebration of the Acoustical Society of America (147th meeting of the Acoustical Society of America), Sheraton New York Hotel and Towers, **New York**, New York, 24-28 May 2004, USA.
13. **Nico F. Declercq**, Rudy Briers, Joris Degrieck, Oswald Leroy, "Ultrasonic Inhomogeneous Waves: Three Decades of Fascination", oral presentation at 75th Anniversary Celebration of the Acoustical Society of America (147th meeting of the Acoustical Society of America), Sheraton New York Hotel and Towers, **New York**, New York, 24-28 May 2004, USA.
14. **Nico F. Declercq**, Joris Degrieck, Oswald Leroy, "Surface and plate mode stimulation in piezoelectric materials in the framework of inhomogeneous wave theory", oral presentation at 75th Anniversary Celebration of the Acoustical Society of America (147th meeting of the Acoustical Society of America), Sheraton New York Hotel and Towers, **New York**, New York, 24-28 May 2004, USA.
15. **Nico F. Declercq**, Joris Degrieck, Oswald Leroy, "Diffraction of plane waves having complex frequency and the excitation of transient leaky Rayleigh waves", oral presentation at 75th Anniversary Celebration of the Acoustical Society of America (147th meeting of the Acoustical Society of America), Sheraton New York Hotel and Towers, **New York**, New York, 24-28 May 2004, USA.

16. **Nico F. Declercq**, Joris Degrieck, Rudy Briers, Oswald Leroy, "On the existence of a Brewster angle for solid side incidence on periodically rough surfaces", oral presentation Fr3.C2.1 at the ICA2004 18th International Congress on Acoustics, Kyoto International Conference Hall, 4-9 April 2004, **Kyoto**, Japan.
17. **Nico F. Declercq**, Joris Degrieck, Oswald Leroy, "The reflection of ultrasound from stressed piezoelectric crystals", oral presentation Fr2.C2.2 at the ICA2004 18th International Congress on Acoustics, Kyoto International Conference Hall, 4-9 April 2004, **Kyoto**, Japan.
18. **Nico F. Declercq**, Joris Degrieck, Oswald Leroy, "On the use of the localized inhomogeneity approach to describe bounded beams", poster presentation Tu.P1.22 at the ICA2004 18th International Congress on Acoustics, Kyoto International Conference Hall, 4-9 April 2004, **Kyoto**, Japan.
19. **Nico F. Declercq**, Filip Van den Abeele, Joris Degrieck, Oswald Leroy, "On the use of bounded beam effects to characterize fluids in containers", oral presentation Tu4.1.3 at the ICA2004 18th International Congress on Acoustics, Kyoto International Conference Hall, 4-9 April 2004, **Kyoto**, Japan.
20. **Nico F. Declercq**, Joris Degrieck, Rudy Briers, Oswald Leroy, "The extended model to simulate the Quetzal echo at the Mayan pyramid of Kukulkan at Chichen Itza in Mexico", oral presentation at CFA/DAGA'04, 7ème Congrès Français d'Acoustique, Salon Européen de l'Acoustique - 30. Deutsche Jahrestagung für Akustik, Europäische Akustik-Ausstellung, Palais des Congrès et de la Musique, **Strasbourg**, France 22-25 March 2004.
21. **Nico F. Declercq**, Joris Degrieck, Oswald Leroy, "Ultrasonics, a Fascinating Field of Physics and its Applications", Poster presentation 079 at the 4th UGent FTW PhD symposium, December 3rd, **Ghent**, Belgium, 2003.
22. **Nico F. Declercq**, Joris Degrieck, Oswald Leroy, "Profiled plane waves as the framework for the interaction of 3D bounded beams with anisotropic materials", Orals Presentation TO-PM08.05 at the 5th World Congress on Ultrasonics WCU 2003, September 7-10, 2003, **Paris** , France.
23. **Nico F. Declercq**, Joris Degrieck, Oswald Leroy, "The characterization of applied and residual stress in isotropic plates by means of multidirectional inspection", Oral Presentation N841 at InterNoise2003, August 25-28, 2003, International Convention Center Jeju, **Seogwipo**, Korea.
24. **Nico F. Declercq**, Joris Degrieck, Rudy Briers, Oswald Leroy, "On the possible application of doubly corrugated plates in advanced SAW devices", Oral Presentation N840 at InterNoise2003, August 25-28, 2003, International Convention Center Jeju, **Seogwipo**, Korea.
25. **Nico F. Declercq**, Joris Degrieck, Oswald Leroy, "On the theoretical discovery of a new kind of leaky surface waves", Oral Presentation P409 at the Tenth International Congress on Sound and Vibration, 7-10 July 2003, **Stockholm**, Sweden.
26. **Nico F. Declercq**, Joris Degrieck, Oswald Leroy, "On the influence of fatigue on Ultrasonic Polar Scans of fiber reinforced composites", Oral Presentation 1.22B at Ultrasonics International 2003, 30 June- 3 July 2003, **Granada**, Spain.
27. **Nico F. Declercq,** Joris Degrieck, Oswald Leroy, "The representation of 3D gaussian beams by means of inhomogeneous waves", poster presentation P22 at Ultrasonics International 2003, 30 June- 3 July 2003, **Granada**, Spain.
28. **Nico F. Declercq**, Joris Degrieck, Rudy Briers, Oswald Leroy, "Some interesting features of the interaction of a bounded ultrasonic beam with a doubly corrugated interface

between a solid and a liquid", Oral Presentation at 'Acoustics 2003', University of Cadiz, **Cadiz**, Spain, 16-18 June 2003.

29. **Nico F. Declercq,** Joris Degrieck, Oswald Leroy, "Numerical Simulations of Ultrasonic Polar Scans", Oral presentation at the 3rd International Conference on Emerging Technologies in Non-Destructive Testing & Technology Transfer and Business Partnership Event, May 26-28, **Thessaloniki**, Greece, 2003.
30. **Nico F. Declercq,** Joris Degrieck, Oswald Leroy, "On the ability of bounded inhomogeneous waves to experimentally verify the behavior of infinite inhomogeneous plane waves", Oral Presentation at the 145th Meeting of the Acoustical Society of America, Nashville Convention Center, **Nashville**, Tennessee, USA, 28 April - 2 May 2003.
31. **Nico F. Declercq**, Joris Degrieck, Rudy Briers, Oswald Leroy, "A full simulation of the Quetzal echo at the Mayan pyramid of Kukulkan at Chichen Itza in Mexico", Oral Presentation at 145th Meeting of the Acoustical Society of America, Nashville Convention Center, **Nashville**, Tennessee, USA, 28 April - 2 May 2003.
32. **Nico F. Declercq**, Joris Degrieck, Oswald Leroy, "Two Improved Methods to Determine the Coefficients in the Inhomogeneous Wave Decomposition of Bounded Beams", oral presentation at the 8th Western Pacific Acoustics Conference (Wespac8), paper WE41, 7-9 April, **Melbourne**, Australia, 2003.
33. **Nico F. Declercq**, Joris Degrieck, Oswald Leroy, "Numerical Simulations of Ultrasonic Polar Scans on Single Layered Fiber Reinforced Composites", oral presentation at DAGA'03, 18-20 March 2003, **Aachen**, Germany.
34. **Nico Declercq**, Joris Degrieck, Oswald Leroy, "Nondestructive Materials Characterization by means of Ultrasound", Poster presentation at the 3rd FTW PHD SYMPOSIUM, Ghent University, **Ghent**, Belgium, 2002.
35. **Nico F. Declercq**, Joris Degrieck, Rudy Briers, Oswald Leroy, "A theoretical elucidation for the experimentally observed backward displacement of waves reflected from an interface having superimposed periodicity", Oral presentation (5aPA6) at the First Pan-American/Iberian Meeting on Acoustics (144th Meeting of the Acoustical Society of America, 3rd Iberoamerican Congress of Acoustics, 9th Mexican Congress on Acoustics), 2-6 Dec. 2002, **Cancun**, Q. R. Mexico**.**
36. **Declercq Nico F.**, Degrieck Joris, Leroy Oswald, "Hypercomplex Waves", oral presentation PHA-Gen-006 at Forum Acusticum (3rd EAA European Congres on Acoustics, XXXIII Spanish Congres, Tecniacustica 2002, 3rd Iberian Congres on Acoustics, European and Japanese Symposium - EAA - SEA - ASJ, Expoacustica 2002), **Sevilla** Spain, 16-20 September 2002 .
37. **Nico F. Declercq**, Joris Degrieck, Rudy Briers, Oswald Leroy, "The diffraction of inhomogeneous acoustic waves by a doubly corrugated solid/liquid interface", oral presentation 2c4-3 at 6th French Conference on Acoustics CFA Lille 2002, **Lille** 8-11 April 2002, France.
38. **Nico F. Declercq**, Joris Degrieck, Oswald Leroy," Characterization of layered Orthotropic Materials Using Ultrasonic Polar Scans", poster presentation at The 2nd FTW PHD SYMPOSIUM, December 12, 2001, Ghent University, **Ghent**, Belgium.
39. **Nico F. Declercq**, Rudy Briers, Oswald Leroy, "The Direct Superposition Method to predict Wood Anomalies in Acoustic Spectra obtained from Diffraction on Periodically Corrugated Surfaces", oral presentation at 17th International Congress on Acoustics, September 2-7 2001, **Rome**, Italy.

40. **Nico F. Declercq**, Rudy Briers, Oswald Leroy, "The use of polarized bounded beams to determine the groove direction of a surface corrugation", poster presentation P2/1.21 at Ultrasonics International 2001, 2-5 July 2001, Technical University of Delft, **Delft**, The Netherlands.

Awards

- **5th place in the contest for the "2004 J. L. Lions Award to Young Scientists in Computational Mathematics"** presented by "The European Community on Computational Methods in Applied Sciences" (ECCOMAS)
- "**Physical Acoustics Best Student Paper Award**" provided by the Physical Acoustics Technical Committee of the Acoustical Society of America at the First Pan-American/Iberian Meeting on Acoustics (144th Meeting of the Acoustical Society of America, 3rd Iberoamerican Congress of Acoustics, 9th Mexican Congress on Acoustics), 2-6 Dec. 2002, Cancun, Q. R. Mexico. (Ref: Echoes 13(2), 5, 2003)
- "**Best Presentation Award**" at the 2nd FTW PHD SYMPOSIUM, December 12, 2001, Ghent University

Grants in addition to IWT PhD-grant

- **Travel grant** to support contribution to the '‘51ST OPEN SEMINAR ON ACOUSTICS’ joint with ‘Polish-German Structured Conference on Acoustics’ and ‘9th Acoustooptics and Applications’, 6th - 10th September 2004 - Gdańsk, Poland' and the 'VII International Conference For Young Researchers Wave Electronics and Its Applications in Information and Telecommunication Systems, St. Petersburg, Russia, 12-15 September 2004', and also to make scientific visits to 'the Institute of Radio Engineering and Electronics (the Russian Academy of Sciences, Moscow, Russia)' and ' the Laboratory of Acoustic Microscopy, Institute of Biochemical Physcis, Russian Academy of Sciences, Moscow, Russia' in September 2004. This grant is offered by the 'Fund for Scientific Research Flanders-Belgium (**F. W. O.**)'
- '**Student grant transportation subsidy**' offered by the Acoustical Society of America (**ASA**) to travel to the 147th meeting of the Acoustical Society of America, New York, 24-28 May 2004.
- ‘**Young Scientist Conference Attendance Grant**’ offered by the International Commission for Acoustics (**ICA**) and the Committee on International Research and Education of the Acoustical Society of America (**ASA**), for attending the 18th ICA International Congress on Acoustics to be held in Kyoto, Japan from 4th-9th April 2004.
- **Project Coordinator of a NATO Science Program Collaboration Linkage Grant** between Soete Laboratory (University of Ghent, Belgium), the Institute of Radio Engineering and Electronics (the Russian Academy of Sciences, Moscow, Russia) and the National Center for Physical Acoustics (The University of Mississippi – Olemiss, Oxford, Mississippi, USA).
- **Travel grant** to support contribution to the '3rd International Conference on Emerging Technologies in Non-Destructive Testing & Technology Transfer and Business Partnership Event', May 26-28, Thessaloniki, Greece, 2003, offered by the 'Fund for Scientific Research Flanders-Belgium **(F. W. O.)**'.

Curriculum Vitae

Name:	**Nico F. Declercq**
Date of Birth :	**December 27th ,1975**
Place of Birth:	**Kortrijk (Belgium)**
Marital status:	**Married since 06/06/1997 to Shirani de Silva (Sri Lanka)**
	Father of Benjamin Jonathan Howard, born in Kortrijk on October 21st, 1999. Father of Anna-Laura Florence Marion, born on January 26th, 2005.
Preliminar Education:	**Latin-Maths-Sciences (Basisschool 'Yes' Deerlijk, Middenschool 'Groenhove' Waregem, Koninklijk Atheneum Waregem)**
Higher Education:	**BSc in Physics and MSc in Astrophysics, KUL Leuven University, July 2000**
Former Occupation	**Voluntary Researcher (without salary) at the Physical Acoustics and Acousto-Optics Research group of Prof O. Leroy, Interdisciplinary Research Center, Katholieke Universiteit Leuven Campus Kortrijk, September 2000 - September 2001.**
Current Occupation:	**PhD student at the Faculty of Engineering (Ghent University), since October 2001**
Financial Support:	**The Flemish Institute for the Encouragement of the Scientific and Technological Research in Industry (I.W.T.), see also GRANTS**
Promoters:	• **Prof Dr ir Joris Degrieck** • **Em. Prof. Dr Dr.H.C. Oswald Leroy**
Doctoral Program supervisors:	• **Prof Dr ir Joris Degrieck (Prof. at Ghent University)** • **Prof Em. Dr Dr.H.C. Oswald Leroy (Prof. Em. at KULeuven University Campus Kortrijk)** • **Prof Dr Rudy Briers (Professor at the faculty of medicine of KULeuven University Campus Kortrijk, Lecturer at KATHO - RENO dept.)**
Stays and visits abroad as a 'Visiting Scientist'	• **Acousto-Optics Lab, Oscillation Physics Division, Department of Physics, M. V. Lomonosov Moscow State University, Russia, September 2004** • **Lab of Acousto-Optic devices, Moscow State University of Metals and Alloys, Russia, September 2004** • **Acousto Optic-Lab of Prof S. V. Kulakov, St Petersburg State University of Aerospace Instrumentation, Russia, September2004**

	• **Institute of Radio Engineering and Electronics, Russian Academy of Sciences, Moscow, Russia, September 2004** • **Dept of Ultrasonic Microscopy, Institute of Biochemical Physics, Russian Academy of Sciences, Moscow, Russia, September 2004** • **The Laboratory for Acousto-Optics and Solid State Acoustics of Prof. Dr. Mack Breazeale, The National Center for Physical Acoustics (NCPA), The University of Mississippi (Ole Miss), Oxford - MS, USA: June 2004** • **Precision and Intelligence Laboratory, Tokyo Institute of Technology, April 2004, Yokohama, Japan** • **The Laboratory for Acousto-Optics and Solid State Acoustics of Prof. Dr. Mack Breazeale, The National Center for Physical Acoustics (NCPA), The University of Mississippi (Ole Miss), Oxford - MS, USA: December 2003 - January 2004** • **The Department of Materials Engineering, The University of Moratuwa, Moratuwa, Sri Lanka: July 2003** • **The Laboratory for Acousto-Optics and Solid State Acoustics of Prof. Dr. Mack Breazeale, The National Center for Physical Acoustics (NCPA), The University of Mississippi (Ole Miss), Oxford - MS, USA: May 2003**
Society Memberships:	• **The Canadian Acoustical Association CAA-ACA** • **American Physical Society APS** • **European Physical Society EPS** • **Acoustical Society of America ASA** • **Russian Acoustical Society RAS** • **Belgian Acoustical Society ABAV** • **French Acoustical Society SFA** • **Institute of Electrical and Electronics Engineers IEEE** • **British Institute of Non-Destructive Testing BINDT** • **International Institute of Acoustics and Vibration IIAV** • **Optical Society of America OSA**
Scientific Services	**Regular referee for** • **The Journal of the IEEE trans. on UFFC** *(Imp. Fact. 1.595 ;SCI-index, Engineering – electrical & electronic, rank:46/205)* • **The Journal of the Acoustical Society of America** *(Imp. Fact. 1.310; SCI-index, Acoustics, rank:7 /28)* • **Applied Physics Letters** *(Imp. Fact. 4.207; SCI-index, Physics-Applied, rank:3/76)* • **The Journal of Applied Physics** *(Imp. Fact. 2.281; SCI-index, Physics-Applied, rank:13/76)*

	• **Optics Communications** *(Imp. Fact.1.482; SCI-index, Optics, rank:16/53)* **Assisting in the organization of two presentation sessions for the World Congress on Ultrasonics (WCU – Paris, 2003)** **Organization of two presentation sessions for the World Congress on Ultrasonics – joint with Ultrasonics International (WCU-UI'05 - Bejing, 2005)**

Table of Contents

Chapter I
(Hoofdstuk 1)

Nederlandstalige Samenvatting
(Dutch Summary)

De hoofdstukken I tot en met III zijn gereserveerd voor de Nederlandstalige samenvatting, de inleiding en de Engelstalige samenvatting. De scriptie bestaat uit verschillende hoofdstukken die elk een aantal secties bevatten. Elke sectie is op een zodanige manier geschreven, dat het mogelijk is om de inhoud te vatten zonder alle voorgaande secties en hoofdstukken gelezen te hebben. De voornaamste reden voor deze aanpak is de verscheidenheid aan onderwerpen in deze thesis en de verwachting dat niet elke lezer die interesse vertoont voor één bepaald onderwerp zich ook geroepen voelt om gans de thesis door te nemen. Voorts is elk hoofdstuk voorzien van een voorwoord dat de context weergeeft van de geponeerde these. Hoofdstuk I geeft een beknopt overzicht van de voornaamste verwezenlijkingen van dit werk, zonder daarom in te gaan op de details. Er wordt getracht een schets te geven van het probleem, de oplossing van het probleem en de mogelijke gevolgen. Voor een gedetailleerde behandeling van de verschillende onderwerpen wordt de lezer graag doorverwezen naar de verschillende hoofdstukken in het Engels.
Bij elke figuur in deze Nederlandstalige samenvatting staat ter informatie aangegeven aan welke figuur uit de tekst deze identiek is. Desalniettemin is deze informatie niet noodzakelijk om de figuur te begrijpen.

Hoofdstuk IV Inhomogene golven en begrensde bundels

Sectie IV.A : De geschiedenis en de eigenschappen van ultrasone inhomogene golven.

- Aanvaard voor publicatie in **IEEE Transactions on Ultrasonics, Ferroelectrics, and Frequency Control** *(Imp. Fact. 1.595 ;SCI-index, Engineering – electrical & electronic, rank:46/205)*
- Mondelinge presentatie op uitnodiging tijdens: plenaire sessie, 'VII International Conference for Young Researchers on Wave Electronics and its Applications in Information and Telecommunication Systems', **St Petersburg**, Rusland , 12-15 september 2004
- Mondelinge presentatie tijdens '75th Anniversary Celebration of the Acoustical Society of America (147th meeting of the Acoustical Society of America), Sheraton New York Hotel and Towers, New York, **New York**, USA, 24-28 mei 2004

Inhomogene golven zijn een veralgemening van de klassieke vlakke golven. Ze worden beschreven met behulp van complexe golfparameters en vertonen typisch een exponentieel variërende amplitude langsheen het golffront. Dit type golven kwam voor het eerst voor in Amerikaanse publicaties, maar werd later grotendeels ontwikkeld door Franse en Belgische onderzoekers, nadat was aangetoond dat inhomogene golven de natuurlijke stimuli zijn voor oppervlaktegolven. Desalniettemin werd het fenomeen van de inhomogene golven nog al te vaak beschouwd als een wiskundig artefact, alhoewel experimenteel reeds was bewezen dat zulke golven ook daadwerkelijk kunnen worden opgewekt en dat hun eigenschappen overeenstemmen met de theorie. Met dit uniek overzicht van de

geschiedenis, eigenschappen en de experimentele opwekking van ultrasone inhomogene golven, menen wij te mogen stellen dat een definitieve doorbraak is bereikt bij een breed publiek van onderzoekers in de akoestiek. Het is tevens de eerste maal in de geschiedenis dat het exacte verband wordt uitgerekend tussen de elementen van de complexe Lamé parameters en de intrinsieke akoestische grootheden zoals demping en golfsnelheid.

Sectie IV.B : Het principe van het 'eindige reeks' evenwicht om de expansiecoëfficiënten te bepalen bij de ontbinding van een begrensde bundel in inhomogene golven

- Nico F. Declercq, Joris Degrieck, Oswald Leroy, "The Principle of a Chopped Series Equilibrium to Determine the Expansion Coefficients in the Inhomogeneous Waves Decomposition of a Bounded Beam", **Acta Acustica United with Acustica** 89, 1038-1040, 2003. *(Imp. Fact. 0.346; SCI-index, Acoustics, rank:21 /28)*
- Mondelinge presentatie tijdens 'the 8th Western Pacific Acoustics Conference (Wespac8)', **Melbourne**, Australië, 7-9 april, 2003.

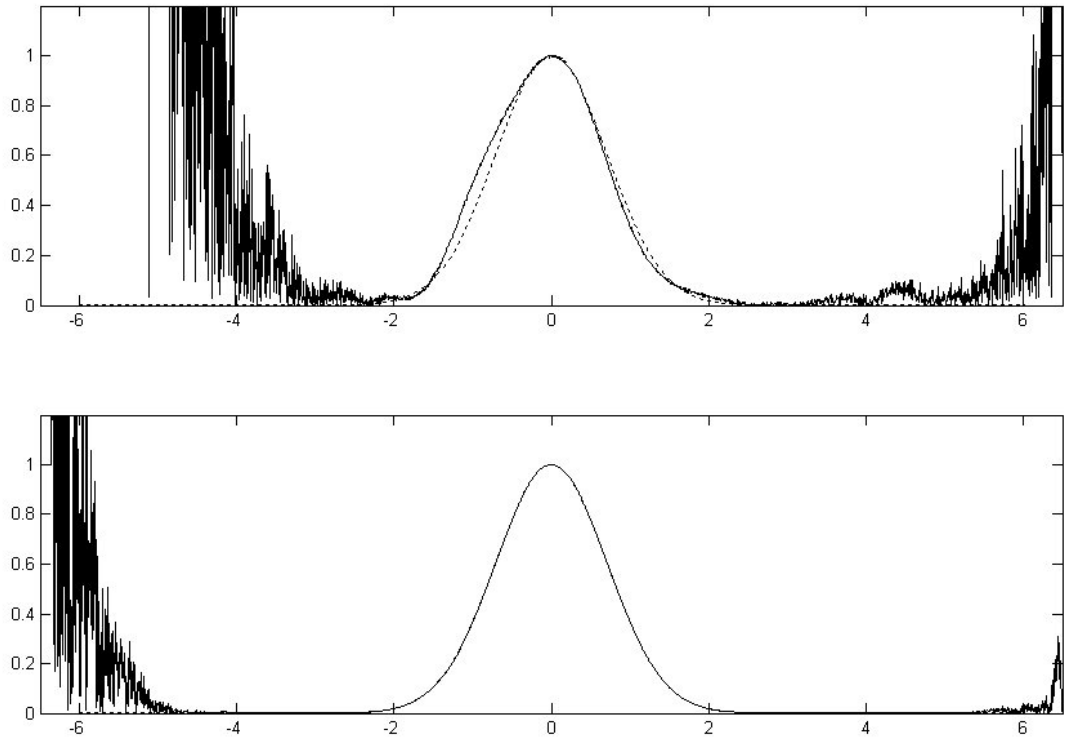

Fig I.1 (identiek aan Fig IV.B_2): ***De horizontale as is de genormaliseerde afstand tot het centrum van de bundel (dus de exacte afstand gedeeld door de gaussische breedte), terwijl de verticale as de amplitude voorstelt. Deze figuur toont een extreem geval van slechte conditionering. Het bovenste gedeelte toont met behulp van een stippellijn een Gaussisch profiel en met behulp van een volle lijn de benadering in de inhomogene golftheorie gebruik makend van klassieke methodes. Men merkt niet enkel sterke afwijkingen binnen de breedte van de bundel, maar ook de ontwikkeling van zogenaamde 'staarten' buiten de breedte van de bundel, waar normaliter de amplitude perfect nul zou moeten zijn. Het onderste gedeelte van de figuur toont de benadering onder dezelfde omstandigheden, doch nu gebruik makend van de optimalisatieprocedure met inbegrip van de eindige reeksenmethode zoals in deze sectie beschreven. Men merkt dat de optimalisatie nu nagenoeg perfect is binnen de breedte van de bundel en dat tevens de 'staarten' verder naar buiten verschoven zijn.***

In tegenstelling tot de klassieke Fourier methode, waarbij een begrensde bundel beschreven wordt als een sommatie van vlakke golven die elk een welbepaalde amplitude, fase en richting hebben, wordt in de inhomogene golftheorie een begrensde bundel gevormd door een sommatie van inhomogene golven die eveneens elk een welbepaalde amplitude en fase hebben, maar die daarenboven elk dezelfde richting hebben. Er werd vroeger reeds aangetoond dat deze laatste werkwijze correct is binnen een korte afstand langsheen de voortplantingsrichting van de bundel en binnen een korte afstand langsheen de breedte van de bundel. De opwekking van oppervlaktegolven, met behulp van een instralende begrensde bundel, langsheen een vloeistof-vaste stof scheiding gebeurt per definitie lokaal, wat betekent dat de beperkte geldigheid van de inhomogene golfmethode langsheen de voortplantingsrichting van de bundel, niet van primordiaal belang is. Wat echter wel belangrijk is, is de beperking langsheen de breedte van de bundel. Het is namelijk zo dat de opwekking van oppervlaktegolven, vaak gepaard gaat met drastische vormveranderingen en verbredingen van de gereflecteerde bundel. Indien de vormverandering ook optreedt in een gebied waarin de inhomogene golfmethode slecht geconditioneerd is, dan ontstaan cruciale fouten. De reden voor de beperkte doeltreffendheid van de inhomogene golfmethode in de breedte van de bundel, is het feit dat we uiteindelijk te maken hebben met een numerieke procedure die een sommatie van exponentiele functies optimaliseert. De karakteristieke aard van deze functies houdt ondermeer in dat de minste numerieke onvolkomenheid tot onoverzichtelijke fouten leidt vanaf een bepaalde afstand tot het centrum van de begrensde bundel.

In deze sectie is een techniek voorgesteld die de exponentiele functies representeert met behulp van hun Taylor reeksontwikkeling en er wordt aangetoond dat een optimale reekslengte bestaat waarop de numerieke fout minimaal wordt indien de optimalisatie in de inhomogene golfmethode gebeurt met behulp van die eindige reeksen en indien de bekomen coëfficiënten worden toegekend aan de respectievelijke exacte exponentiële functies. Het resultaat is een verruiming, langsheen de breedterichting van een te ontbinden begrensde bundel, en dus van de bruikbaarheid van de inhomogene golftheorie. Het valt te verwachten dat deze bevordering van de optimalisatieprocedure door gebruik te maken van eindige reeksontwikkelingen, ook in andere takken van de numerieke analyse zijn nut zal bewijzen.

Sectie IV.C : Een handige analytische beschrijving van de coëfficiënten in de ontbinding van symmetrische begrensde bundels in inhomogene golven

- Nico F. Declercq, Joris Degrieck, Oswald Leroy, "A useful analytical description of the coefficients in an Inhomogeneous Wave Decomposition of a symmetrical bounded beam", **Ultrasonics** 43(4), 279-282, 2005 *(Imp. Fact. 0.844; SCI-index, Acoustics, rank:11 /28)*
- Mondelinge presentatie tijdens ‘the 8th Western Pacific Acoustics Conference (Wespac8), **Melbourne**, Australië, 7-9 april, 2003.

In sectie IV.B kwam voornamelijk de numerieke natuur van de inhomogene golftheorie aan bod. Dit komt hoofdzakelijk doordat er voorheen nooit een analytische uitdrukking gevonden was voor de expansiecoëfficiënten in de inhomogene golfmethode. Sectie IV.C daarentegen toont aan op welke manier een analytische uitdrukking kan gevonden worden

en geeft ook het resultaat.

Indien de ruimtelijke beschrijving van een begrensde bundel verondersteld wordt beschreven te zijn als:

$$\varphi(x,z) = \sum_{n=-N}^{N} \frac{1}{2}\left(1+\delta_{n,0}\right) A_n \exp\left(\beta_n x\right) \exp\left(i\sqrt{\left(\frac{\omega^2}{v^2}+\beta_n^2\right)} z \right)$$

Dan is de analytische uitdrukking voor de expansiecoëfficiënten gegeven door:

$$A_n = \sum_{m=n}^{N} (-1)^n \frac{m!}{(m-n)!n!n!} \sum_{r=0}^{m} (-1)^r \frac{m!}{(m-r)!r!r!} I_r$$

met

$$I_r = \frac{1}{p} \int_{-\infty}^{+\infty} \exp\left[-\exp\left(\frac{x}{p}\right) + (r+1)\frac{x}{p} \right] f(x)\, dx$$

<u>Sectie IV.D</u> **: De Laplace transformatie om begrensde inhomogene golven te beschrijven**

- Nico F. Declercq, Joris Degrieck, Oswald Leroy, "The Laplace transform to describe bounded inhomogeneous waves", **J. Acoust. Soc. Am.** 116(1), 51-60, 2004. *(Imp. Fact. 1.310; SCI-index, Acoustics, rank:7 /28)*
- Mondelinge presentatie tijdens 'the 145th Meeting of the Acoustical Society of America', Nashville Convention Center, **Nashville**, Tennessee, USA, 28 april - 2 mei 2003.

Het mooie aan de inhomogene golftheorie is de beschrijving van golfkarakteristieken, die niet noodzakelijk hand in hand gaan met de menselijke intuïtie, maar die weliswaar in overeenstemming zijn met recente experimenten. Toch is het zo dat bij deze experimenten nooit echt 'wiskundige' inhomogene golven kunnen worden opgewekt die oneindig breed zijn, maar dat begrensde versies moeten worden gegenereerd. Die begrensdheid is uiteraard het gevolg van de eindige afmetingen van de experimentele geluidsbron. Desalniettemin is het eigenaardig dat eindige inhomogene golven beantwoorden aan de eigenschappen van 'oneindige' inhomogene golven. De reden wordt in deze sectie onthuld. Er wordt aangetoond dat begrensde inhomogene golven, via de Laplace transformatie, op een natuurlijke manier te ontbinden zijn in oneindige inhomogene golven. Bovendien wordt aangetoond dat het merendeel van de begrensde inhomogene golf bepaald wordt door het gedrag van één enkele oneindige inhomogene golf en dat alle andere inhomogene golven die aanwezig zijn in de ontbinding, enkel een bijdrage leveren aan de vorming van de randen van de begrensde golf en dus geen invloed hebben op het globaal gedrag.

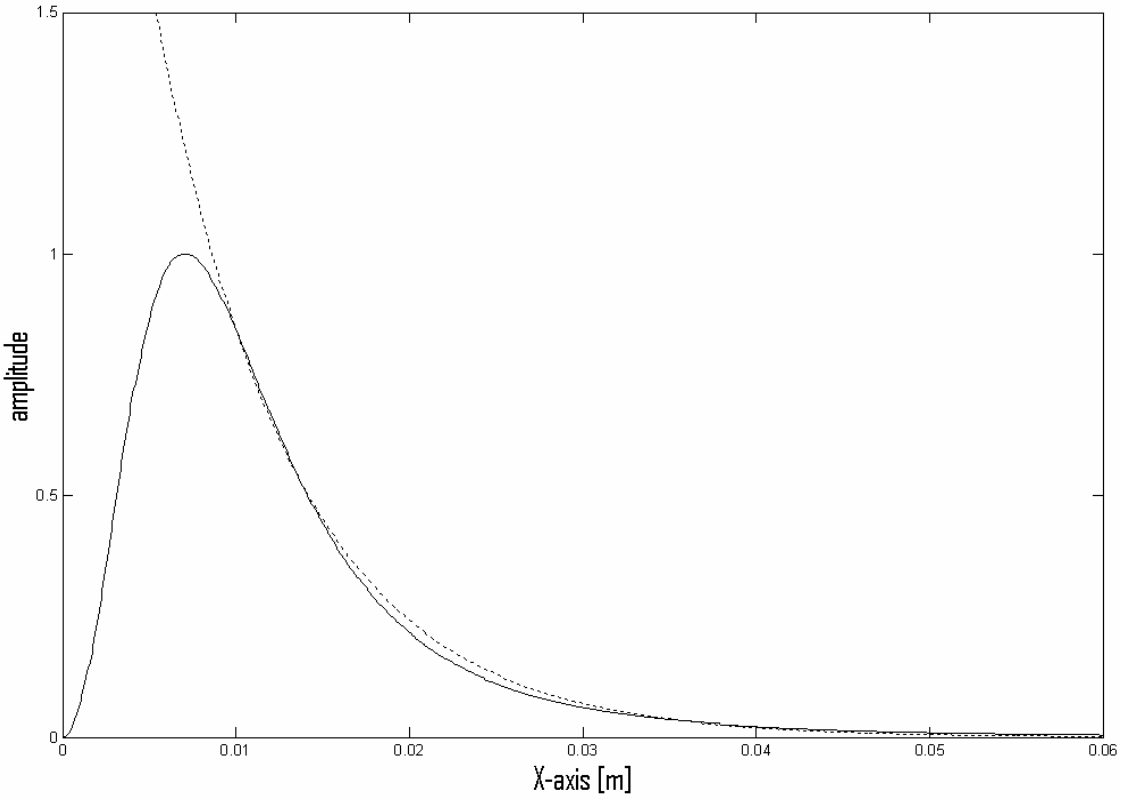

Fig. I.2 (identiek aan Fig. IV.D_5): ***De horizontale as duidt de afstand [m] aan langsheen het golffront. De verticale as duidt de amplitude aan. De stippellijn beschrijft het profiel van een oneindige inhomogene golf. De volle lijn beschrijft het profiel van een begrensde inhomogene golf.***

Sectie IV.E : De voorstelling van 3D Gaussische bundels met behulp van inhomogene golven

- Nico F. Declercq, Joris Degrieck, Oswald Leroy, "The inhomogeneous wave decomposition of 3D Gaussian-like bounded beams", **Ultrasonics** 42, 273-276, 2004. *(Imp. Fact. 0.844; SCI-index, Acoustics, rank:11 /28)*
- poster presentatie tijdens 'Ultrasonics International 2003', **Granada**, Spain, 30 June- 3 July 2003

De ontwikkeling van de inhomogene golftheorie ging gepaard met de ontdekking dat een begrensde bundel kan beschreven worden als een som van inhomogene golven. De methode om de coëfficiënten te bepalen was gebaseerd op de techniek van Prony, waarbij een vergelijking met exponentiele functies omgezet wordt in een veeltermvergelijking. Via identificatie met Laguerre veeltermen, wordt dan een waarde gevonden voor de onbekende coëfficiënten. Doch, de methode was tot hiertoe enkel toepasbaar in eendimensionale gevallen, waardoor het onmogelijk is om het exacte profiel van een bundel die in twee richtingen begrensd is, te beschrijven. De huidige sectie presenteert een alternatieve methode om de onbekende coëfficiënten te bepalen, die toelaat om ook bundels te beschrijven die in twee richtingen begrensd zijn.

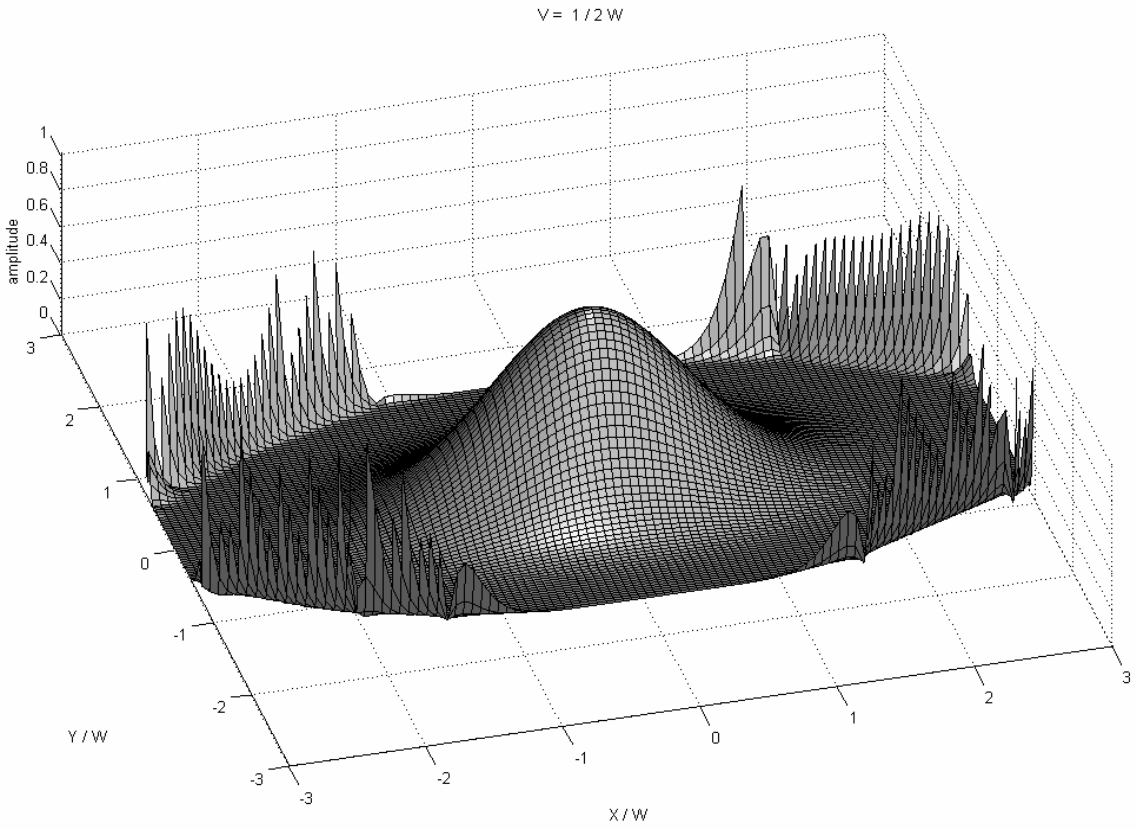

Fig. I.3 (identiek aan Fig. IV.E_4): Het profiel van een 3D quasi-Gaussische bundel, beschreven in de inhomogene golftheorie. De afstanden langs de x-as en langs de y-as, zijn genormaliseerd door te delen door de overeenkomsitege 'gausische' breedte. De 'staarten' die te zien zijn, zijn vergelijkbaar met de staarten die ook in Fig. I.1 te zien zijn.

<u>Sectie IV.F</u> : Controle van de focusafstand van complex harmonische en complex gepulste ultrasone begrensde bundels

- Nico F. Declercq, Joris Degrieck, Oswald Leroy, "Focal length control of complex harmonic and complex pulsed ultrasonic bounded beams", **J. Appl. Phys**. 97(5), 054904 1-8, 2005 *(Imp. Fact. 2.281; SCI-index, Physics-Applied, rank:13/76)*
- Poster presentatie tijdens 'VII International Conference for Young Researchers on Wave Electronics and its Applications in Information and Telecommunication Systems', **St Petersburg**, Rusland , 12-15 september 2004

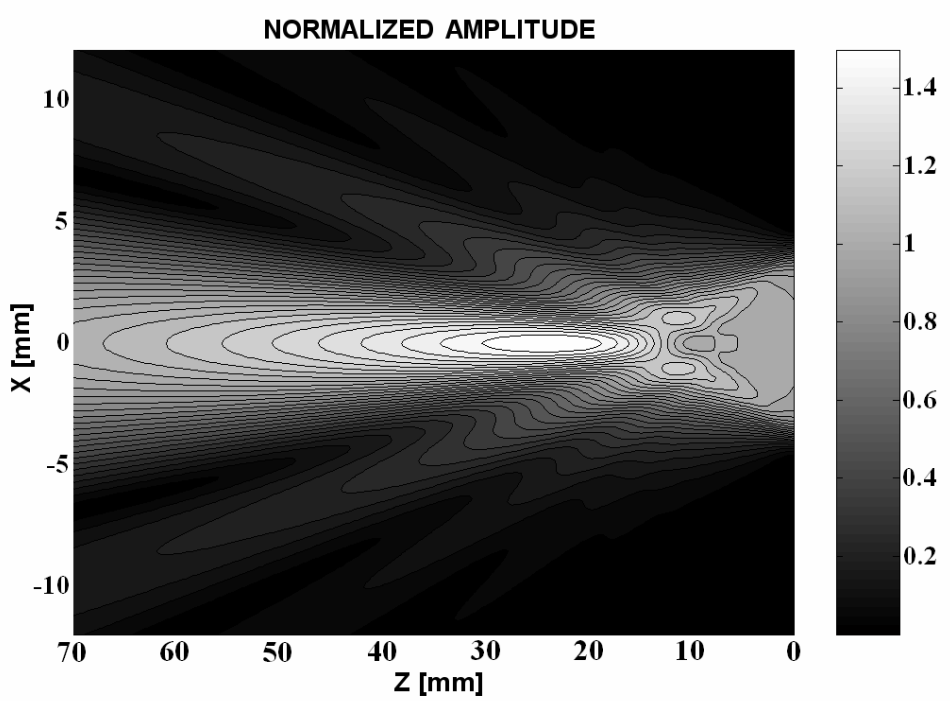

Fig. I.4 (identiek aan Fig. IV.F_5): ***Een voorbeeld van een gefocusseerde bundel die van rechts naar links gericht is. Het witgekleurde ovaal gebied is de focus.***

Het vermogen van ultrageluid, enerzijds om bloed te doen stollen of nierstenen te verbrijzelen en anderzijds om warmteontwikkeling te veroorzaken, maakt dit een uitstekend middel in de geneeskunde om interne wonden te stollen en om kanker te bestralen. Bovendien kan het effect zeer lokaal geïnduceerd worden, indien gebruik gemaakt wordt van gefocusseerde bundels. Deze bundels worden typisch gemaakt met 'phased array' technologie, waardoor een hoge mate van flexibiliteit verwezenlijkt wordt, vooral voor het instellen van de focusafstand. Deze technologie is echter uitermate duur, waardoor vooral ontwikkelingslanden achterna blijven huppelen. Een klassieke transducer zou in principe ook een flexibel instelbare focusafstand moeten bezitten, maar deze instelbaarheid is dan gebaseerd op het wijzigen van de frequentie, wat in principe zeer moeilijk is vermits transducers typisch enkel op discrete frequenties geluid kunnen genereren, rond hun grondtoon en rond oneven veelvouden ervan.

In deze sectie wordt echter aangetoond dat, indien men de amplitude van het signaal dat de gefocusseerde transducer aanstuurt, op een precieze manier laat variëren in de tijd, dit een belangrijke focusverschuiving veroorzaakt die afhangt van de mate van amplitudeverandering. Deze bevinding is gebaseerd op de complex harmonische golftheorie. Bovendien wordt aangetoond dat deze bevinding ook geldig is voor signalen die kort zijn in de tijd en die dus overeenstemmen met realistische signalen, in tegenstelling tot oneindige 'wiskundige' signalen. De techniek maakt het gebruik van 'phased array' technologie overbodig en bezit dus het potentieel om de kostprijs voor verscheidene medische behandelingen, drastisch te verlagen.

<u>Sectie IV.G</u> **: Over het bestaan en de opwekking van een nieuwe soort uitstralende oppervlaktegolven**

- Mondelinge presentatie tijdens 'Tenth International Congress on Sound and Vibration, **Stockholm**, Zweden, 7-10 juli 2003

Indien men de continuïteitsvoorwaarden voor geluidsgolven aan een scheiding tussen een vaste stof en een vloeistof, in formules giet, dan is het mogelijk om de karakteristieke vergelijking te bekomen voor een oppervlaktegolf. Deze vergelijking legt een verband tussen de voortplantingssnelheid en de materiaalparameters. Een complexe golfsnelheid komt dan neer op oppervlaktegolven die energie uitstralen. Praktisch komt die toestand, in overeenstemming met de karakteristieke vergelijking, neer op een (complexe) pool van de reflectiecoëfficiënt. De positie van die pool (in het complexe vlak), is echter functie van de tekens die men kiest voor de verschillende golfvectoren. Hier wordt aangetoond dat, indien men rekening houdt met recente bevindingen van Marc Deschamps betreffende de tekenkeuze (die overigens op experimenten gestoeld zijn), dat dan niet enkel het welgekende bestaan kan worden aangetoond van '(enkel) in de vloeistof energie-uitstralende' Rayleigh golven, maar ook van een nieuw type oppervlaktegolf dat zijn energie zowel uitstraalt in de vloeistof als in de vaste stof.

Hoofdstuk V De interactie van geluid met continu gelaagde media

Sectie V.A : De interactie van inhomogene golven en van Gaussische bundels met modder die zich bevindt tussen een harde vaste stof en een ideale vloeistof

- Nico F. Declercq, Oswald Leroy, Joris Degrieck, Jeroen Vandeputte "The interaction of inhomogeneous waves and Gaussian beams with mud in between a hard solid and an ideal liquid", **Acta Acustica United with Acustica** 90, 819-829, 2004 *(Imp. Fact. 0.346; SCI-index, Acoustics, rank:21 /28)*

In de scheepvaart en in de havennijverheid, is het van het grootste belang om met zekerheid te kunnen stellen of een schip al dan niet een havengeul of een sluis kan binnenvaren, zonder vast te komen zitten in de bodem. Indien men beslist om het schip te laten binnenvaren, met onvoldoende vrije ruimte onder de kiel, dan strandt het schip. Indien men verkeerdelijk beslist om het schip niet te laten binnenvaren, dan is de dagelijkse kost door onnodig voor anker te liggen, een ware economische ramp. De beslissing wordt bemoeilijkt door de aard van de bodem in havens en sluizen. Die is dikwijls bedekt met modder die meerdere meters dik kan zijn. De modder is niet homogeen en bestaat uit een doorvaarbare waterige bovenlaag op een ondoorvaarbare kleiachtige onderlaag. Tussenin bevindt zich een transitielaag die men de nautische bodem noemt. Detectie van die nautische bodem is dus de cruciale taak om te weten of een schip al dan niet kan binnenvaren. Klassieke echoloden maken enkel gebruik van longitudinale geluidsgolven, waardoor niet de nautische bodem, maar wel de bovenlaag van de modder ofwel de onderlaag detecteerbaar zijn.

Hier wordt aangetoond dat schuin invallende geluidsbundels, die naast longitudinaal

geluid ook transversaal geluid opwekken in de modder, wel gevoelig zijn voor de positie van de nautische bodem en dus indirect de diepte kunnen bepalen. Voor dit doeleinde wordt een nieuw ontwikkeld model beschreven dat de voortplanting van geluid in continue lagen (in tegenstelling tot een systeem van discrete lagen) kan nabootsen. Tevens wordt aangetoond hoe begrensde bundels zich voortplanten in het gelaagd systeem. Omwille van de wetenschappelijke waarde, wordt hier voor de eerste maal de interactie beschreven van inhomogene golven met zo'n gelaagd systeem en wordt aangetoond dat de eigenschappen van de reflectiecoëfficiënt voor zulke inhomogene golven, perfect toelaten te voorspellen wat de karakteristieken zijn van de reflectie van begrensde bundels op het moddersysteem.

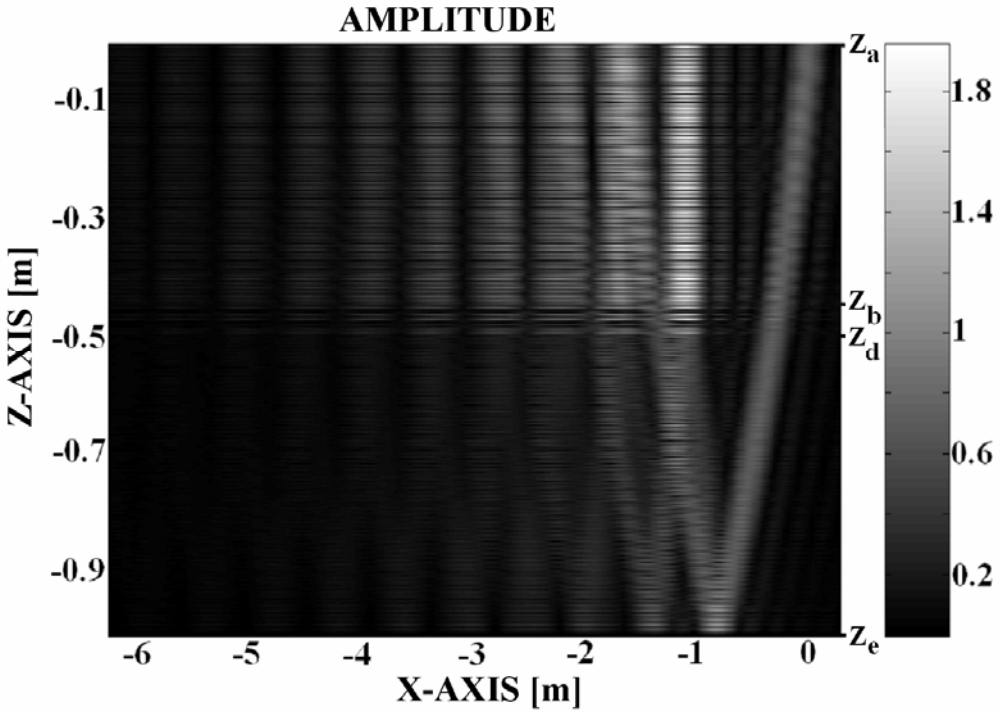

Fig. I.5 (identiek aan Fig. V.A_7): ***Een voorbeeld van de voortplanting van een begrensde geluidsbundel in modderlagen. De geluidsbundel vertrekt rechtsboven in de figuur en beweegt naar links beneden. Interne reflectie en reflectie op de harde bodem, bepalen de structuur van het totale gereflecteerde veld. De verticale as duidt de diepte [m] aan in de modder, terwijl de horizontale as de laterale afstand [m] tot de bron weergeeft.***

Hoofdstuk VI De interactie van geluid met gecoate materialen

Sectie VI.A : Frequentieband sprong voor Rayleigh golven op gecoate substraten

- Nico F. Declercq, Joris Degrieck, Oswald Leroy, "Frequency bandgap for Rayleigh waves on coated surfaces", **Appl. Phys Let**. 85(1), 148-150, 2004. *(Imp. Fact. 4.207; SCI-index, Physics-Applied, rank:3/76)*
- Mondelinge presentatie tijdens 'VII International Conference for Young Researchers on Wave Electronics and its Applications in Information and Telecommunication Systems', **St Petersburg**,

Rusland , 12-15 september 2004

De voortplantingssnelheid van Rayleighgolven hangt af van de fysische eigenschappen van het materiaal waarop deze oppervlaktegolven voortbewegen. Normaliter verwacht men dat Rayleighgolven op een gecoate plaat 'bestaan', en dat ze een snelheid hebben die zich bevindt ergens tussen de snelheid van Rayleighgolven op puur substraat en op pure coating. Deze sectie toont echter aan dat dit niet het geval is, indien de fysische eigenschappen van de coating erg verschillen van die van het substraat. In het laatste geval is het namelijk zo dat voor een gegeven dikte van de coating, er een frequentieband is waarin Rayleighgolven niet kunnen bestaan. Dat betekent dat het mogelijk is om een zodanige coating aan te brengen op een relatief dikke plaat, dat een elektrisch signaal ontdaan wordt van een bepaalde frequentieband, na omzetting in Rayleighgolven en opnieuw omzetten in een elektrisch signaal. Dit fenomeen kan zeer belangrijke toepassingen hebben in de elektronica en is complementair aan de welbekende bandpass filter, die net wel een bepaalde band doorlaat en alles wat zich daarbuiten bevindt, tegenhoudt.

Sectie VI.B : De dispersie van Lambgolven in buitengewone tweelagige platen.

In navolging van vorige sectie werd ook een studie gemaakt over het gedrag van Lambgolven in tweelagige platen, waarvan de twee lagen zeer sterk verschillen in fysische eigenschappen. Er wordt aangetoond dat het asymptotisch gedrag van de S_0 en de A_0 mode verdwijnt in de dispersiecurven. Tevens wordt aangetoond dat diezelfde S_0 en A_0 mode een vorm vertonen die afwijkt van de klassieke vorm.

Hoofdstuk VII Schlierenfotografie als een niet-destructieve testmethode

Sectie VII.A : Schlierenfotografie om de geluidsinteractie met sterk absorberende materialen te bestuderen.

- Aanvaard voor publicatie in **Ultrasonics**. *(Imp. Fact. 0.844; SCI-index, Acoustics, rank:11 /28)*

Bij de karakterisering van materialen, wordt vaak de reflectie van begrensde bundels bestudeerd en kan men daaruit afleiden welke de snelheid is van bulkgolven en van oppervlaktegolven in het te onderzoeken materiaal. Indien men echter te maken heeft met materialen die het geluid zeer sterk absorberen, dan is er eenvoudigweg geen gereflecteerd geluidsveld en kan men er dus ook geen eigenschappen uit bepalen. De huidige sectie toont aan dat in dit geval de warmte, die ontstaat door transformatie van het geluid, kan gedetecteerd worden samen met het invallende geluid, met behulp van Schlierenfotografie. Vermits Schlierenfotografie gebaseerd is op de interactie van zwak laserlicht met het medium waarin het materiaal zich bevindt en interactie met het materiaal zelf, en niet is

gestoeld op het aanbrengen van sensoren, is deze studiemethode 100% niet-destructief. De techniek kan gebruikt worden als 'meetmethode' om na te gaan hoever het geluid zich langsheen het oppervlak voortplant, of in welke mate warmte ontwikkeld wordt.

Sectie VII.B : Het begroten van de vezelrichting in composieten met gebruik van hoogfrequente brede bundels en Schlieren fotografie.

- Aanvaard voor publicatie in **Research in Nondestructive Evaluation** *(Imp. Fact 0.935; SCI-index, Materials Science – Characterization & Testing, rank:2/23)*
- Mondelinge presentatie tijdens '51st open seminar on Acoustics, joint with 9th School of Acousto-Optics and Applications', **Gdansk**, Polen , 6-10 september 2004.

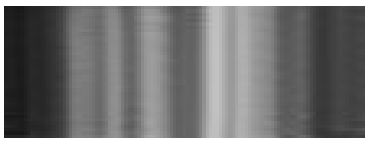

Fig. I.6 (identiek aan Fig. VII.B_4): ***Er worden Schlierenfoto's gemaakt van de gereflecteerde bundel. Deze figuur geeft een uitvergroot beeld weer van de bundel. De voortplantingsrichting van het geluid op deze foto is parallel met de verticale as, terwijl de horizontale as overeenstemt met de breedterichting van de bundel. Door de ruimtelijke inhomogeniteit van de reflectiecoëfficiënt, kan Schlierenfotografie, onder de juiste omstandigheden, een franjepatroon tonen in de gereflecteerde bundel. Deze informatie is eenvoudig bruikbaar om de vezelrichting te bepalen.***

Er bestaan zeer gesofisticeerde methodes om de vezelrichting in composieten te bepalen. Een van die methodes is de polaire scan en wordt verderop in deze thesis beschreven. Deze methodes hebben vaak gemeen dat ze heel wat meer te bieden hebben dan enkel het vastleggen van de vezelrichting, wat meteen ook de oorzaak is van het feit dat ze slechts door gespecialiseerd personeel interpreteerbaar en bruikbaar zijn. In deze sectie wordt een methode uiteengezet, gebaseerd op Schlierenfotografie en het gebruik van relatief hoogfrequente en brede ultrasone bundels. De methode buit de ruimtelijke inhomogeniteit van de reflectiecoëfficiënt uit in vezelversterkte composieten en is vrij makkelijk interpreteerbaar, waardoor ook minder gespecialiseerd personeel de vezelrichting kan begroten.

Hoofdstuk VIII Vloeistofkarakterisering in gesloten containers

Sectie VIII.A : Het Schoch effect om het onderscheid te maken tussen verschillende vloeistoffen in gesloten containers

- Nico F. Declercq, Filip Van den Abeele, Joris Degrieck, Oswald Leroy, "The Schoch effect to distinguish between different liquids in closed containers", **IEEE Transactions on Ultrasonics, Ferroelectrics, and Frequency Control** 51(10), 1354-1357, 2004. *(Imp. Fact. 1.595 ;SCI-index,*

Engineering – electrical & electronic, rank:46/205)

- Mondelinge presentatie tijdens 'ICA2004 18th International Congress on Acoustics', Kyoto International Conference Hall, **Kyoto**, Japan, 4-9 April 2004

De eenvoudigste methode om te onderzoeken welke vloeistof zich in een kleine gesloten container bevindt, is de snelheid van het geluid te meten in de vloeistof via een zogeheten puls-echo methode. Deze methode wordt dan ook vaak gebruikt in de voedingsindustrie om continu te controleren of de gefabriceerde vloeistof, of het nu om visolie dan wel om fruitsap of iets anders gaat, voldoet aan de vooropgestelde eisen, maar is enkel bruikbaar voor kleine containers die twee parallelle wanden bezitten en waarvan men de precieze afmetingen kent. In de praktijk doen zich echter heel wat situaties voor waarbij de containers zeer groot zijn of waarvan de geometrie geen eenduidige puls-echo experimenten toelaat. Deze moeilijkheden treft men vooral aan bij grenscontroles en in luchthavens en zeehavens. In deze thesis wordt een methode vooropgesteld die bruikbaar is op gelijk welke container waarvan ten minste 1 wand vlak is. De techniek is gebaseerd op het zogenaamde Schoch effect en laat vrij eenvoudig toe om na te gaan of een onbekende vloeistof in een container overeenkomst vertoont met de veronderstelde vloeistof. De techniek is dus bijzonder geschikt voor die situaties waarbij klassieke puls-echo technieken onbruikbaar zijn en waarbij men moet nagaan of de vloeistof in een gesloten container overeenstemt met de informatie op de bijgeleverde documenten.

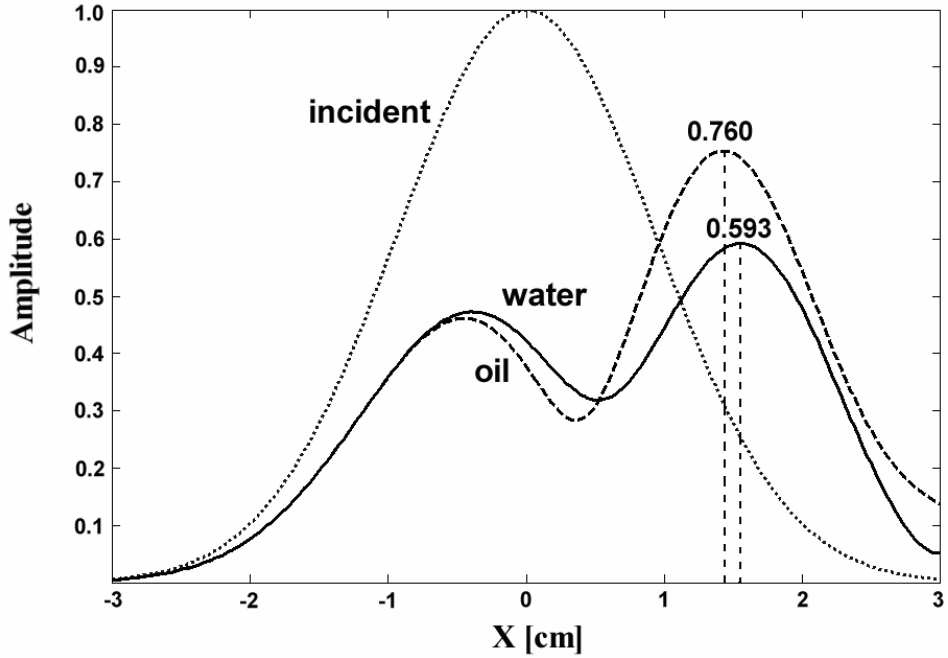

Fig. I.7 (identiek aan Fig. VIII.A_3): ***Het profiel van een gereflecteerde begrensde bundel op de wand van de gesloten vloeistofcontainer, in het geval een Lambgolf wordt opgewekt in de containerwand, hangt af van de onbekende vloeistof achter die wand. De horizontale as geeft de afstand weer langsheen de breedte van de bundels, terwijl de verticale as de amplitude weergeeft. De stippellijn toont het invallend profiel, de volle lijn toont het gereflecteerde profiel indien zich water in de container bevindt, terwijl de gestreepte lijn het gereflecteerde profiel toont indien zich zonnebloemolie in de container bevindt.***

Sectie VIII.B : Het vermogen van uitstralende Lambgolven om reële vloeistoffen te onderscheiden van fictieve vloeistoffen

- Mondelinge presentatie tijdens **'**75th Anniversary Celebration of the Acoustical Society of America (147th meeting of the Acoustical Society of America)', Sheraton New York Hotel and Towers, **New York**, New York, VSA, 24-28 mei 2004

In de bestaande literatuur worden dikwijls Lambgolven besproken in een plaat, ondergedompeld in een vloeistof. Deze sectie bestudeert Lambgolven in een plaat die twee verschillende vloeistoffen van elkaar scheidt. Er wordt aangetoond dat de complexe pool die overeenstemt met een Lambgolf die energie uitstraalt, een reëel deel heeft dat nauwelijks afhangt van de aard van de beide vloeistoffen en een imaginair deel dat functie is van het verschil in eigenschappen van beide vloeistoffen. Meerbepaald wordt aangetoond dat, voor een gegeven vloeistof aan de ene kant van de plaat, de waarde van het imaginaire gedeelte van de pool, een lineaire functie is van het akoestisch impedantieverschil tussen de vloeistoffen aan de twee kanten van de plaat, indien men te maken heeft met een bestaande of realistische vloeistof, en dat dit lineair verband niet meer opgaat indien men te maken heeft met een fictieve vloeistof. Dit fenomeen kan bijzonder behulpzaam zijn voor theoretici in verschillende takken van de natuurkunde, die in theoretische modellen de parameters van een vloeistof willen inbrengen en die willen nagaan of die parameters al dan niet realistisch zijn.

Hoofdstuk IX Geluid in systemen met discontinuïteiten in meer dan 1 dimensie

Sectie IX.A : De stralingsmode theorie in de studie der ultrageluiden

- Aanvaard voor publicatie in **IEEE Transactions on Ultrasonics, Ferroelectrics, and Frequency Control** *(Imp. Fact. 1.595 ;SCI-index, Engineering – electrical & electronic, rank:46/205)*
- Mondelinge presentatie tijdens '51st open seminar on Acoustics, Joint with 9th School of Acousto-Optics and Applications', **Gdansk**, Polen , 6-10 september 2004

Als voorbereiding op de overige secties binnen dit hoofdstuk, en met het oog gericht op onderzoek dat na dit doctoraat dient te gebeuren, wordt in deze sectie een overzicht gegeven van de totstandkoming en de stand van zaken in de zogeheten 'radiation mode theory', oftewel de stralingsmode theorie. Deze theorie is mathematisch zwaar geladen, maar is in staat om de interactie van geluid te beschrijven in systemen die discontinuïteiten vertonen in meerdere dimensies. Een typisch voorbeeld is een kubus. Desalniettemin wordt die moeilijke theorie in deze sectie in eenvoudige bewoordingen beschreven met een minimum aan wiskundige uitdrukkingen. Er wordt uitvoerig beschreven wat de historische gronden zijn, voor welke systemen de theorie reeds is ingezet en wat de toekomstverwachtingen zijn.

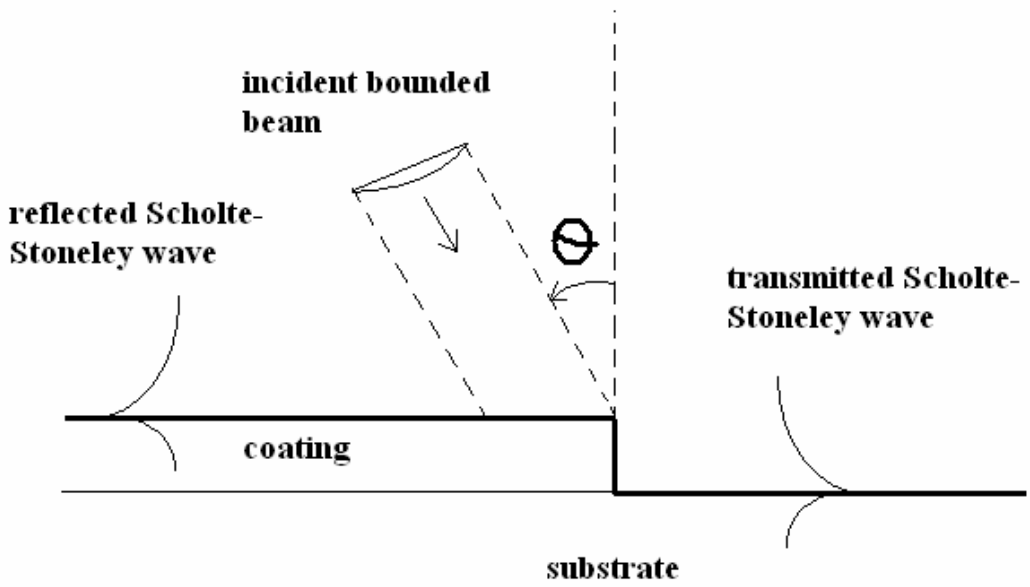

Fig. I.8 (identiek aan Fig. IX.A_7): ***Een voorbeeld van een geometrische configuratie voor dewelke de stralingsmode theorie nuttig is gebleken: een plaat ('substrate') die langsheen de linkerhelft voorzien is van een deklaag ('coating') en voor dewelke die deklaag ontbreekt aan de rechterkant. Een Gaussische ultrasone bundel ('incident bounded beam') valt in op het overgangsgebied en wekt ondermeer een doorgelaten ('transmitted') Scholte – Stoneley oppervlaktegolf op die naar rechts beweegt alsook eenzelfde golf ('reflected') die gereflecteerd wordt en naar links beweegt.***

Sectie IX.B : Een studie van de diffractie van uitstralende Rayleigh golven aan het uiteinde van een dikke plaat, ondergedompeld in een vloeistof.

- Nico F. Declercq, A. Teklu, M. A. Breazeale, Rudy Briers, Oswald Leroy, Joris Degrieck, Gennady N. Shkerdin, "Study of the scattering of leaky Rayleigh waves at the extremity of a fluid loaded thick plate", **J. Appl. Phys** 96(10),5836-5840, 2004 *(Imp. Fact. 2.281; SCI-index, Physics-Applied, rank:13/76)*
- Mondelinge presentatie tijdens '75th Anniversary Celebration of the Acoustical Society of America (147th meeting of the Acoustical Society of America)', Sheraton New York Hotel and Towers, **New York**, New York, VSA, 24-28 mei 2004

In de voorgaande sectie worden ondermeer resultaten weergegeven die bekomen zijn na een theoretische en een experimentele studie betreffende de interactie van een Scholte – Stoneley oppervlaktegolf die beweegt langsheen een vlakke plaat en die interageert met het uiteinde van die plaat. Het resultaat is dat de Scholte – Stoneley golf het merendeel van zijn energie uitstraalt in het verlengde van de plaat. Een eerste wetenschappelijke vraag die daar op natuurlijke wijze uit volgt is of het gedrag van een Rayleigh oppervlaktegolf gelijkaardig is. Een tweede daaropvolgende vraag is eerder gegroeid vanuit het standpunt van de technologie van het niet-destructief testen van materialen: Is het mogelijk om het oppervlak van een plaat te testen, indien men enkel toegang heeft tot de zijkant van die plaat?

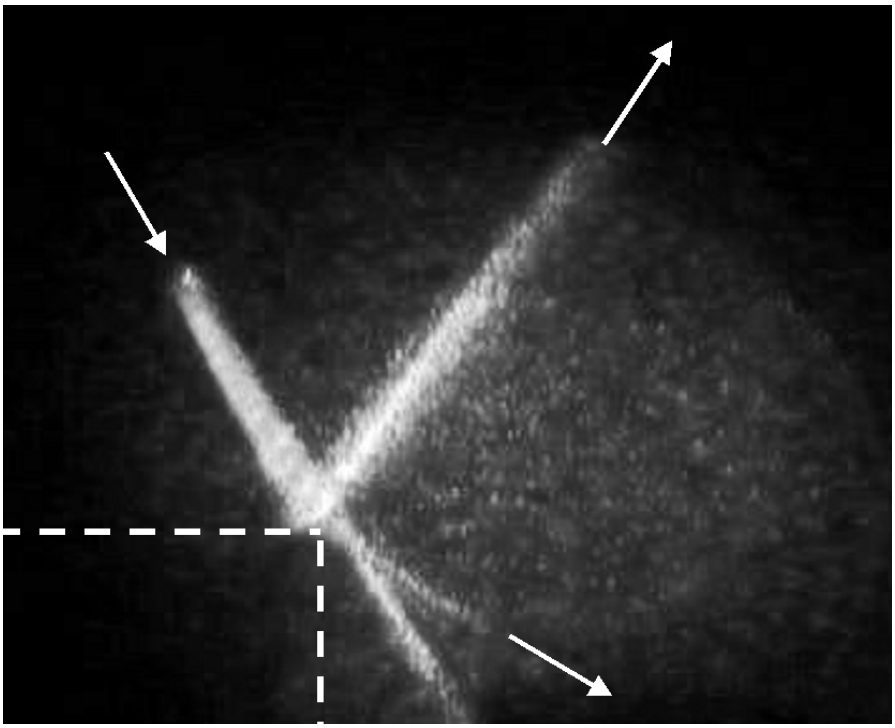

Fig. I.9 (identiek aan Fig. IX.B_6): ***Dit is een van de Schlierenfoto's die aantonen dat een Rayleigh golf, die opgewekt wordt langsheen de bovenkant van een dikke plaat met behulp van ultrasone instraling door middel van een begrensde bundel, 'om het hoekje' gaat en zich langs de verticale wand voortplant en zijn energie geleidelijk uitstraalt langsheen de Rayleigh hoek. De witte streepjeslijn komt precies overeen met de randen van de dikke plaat.***

De huidige studie toont aan dat Rayleigh oppervlaktegolven 'om het hoekje' gaan, wanneer ze het uiteinde van een plaat bereiken. De studie is gebaseerd op Schlierenfotografie en werd uitgevoerd voor verschillende materialen. Daarmee is aangetoond dat Rayleighgolven fundamenteel anders interageren met het uiteinde van een plaat. Daarmee is tevens aangetoond dat, indien enkel de zijkant van een dikke plaat toegankelijk is, een Rayleighgolf kan opgewekt worden op die zijkant, en dat die golf zich automatisch voortplant 'om het hoekje' naar het vlak van de plaat. Dit is bijzonder belangrijk voor het niet-destructieve onderzoek op moeilijk toegankelijke materiaalonderdelen.

Het is ondermeer de bedoeling om met de stralingsmode theorie in de toekomst deze experimentele studie theoretisch te begrijpen en numeriek te simuleren.

Intuïtief is echter duidelijk dat een Scholte – Stoneley golf die dieper doordringt in de omringende vloeistof dan in de vaste stof, eerder het pad van de vloeistof tracht te volgen, terwijl Rayleigh golven, die dieper doordringen in de vaste stof dan in de vloeistof, het pad van de vaste stof prefereren.

Bovendien licht de studie een tipje van de sluier en onthult ernstige aanwijzingen dat Rayleighgolven voornamelijk worden gestimuleerd door de randen van een begrensde bundel en niet zozeer door het centraal gedeelte van de bundel.

Sectie IX.C : De interactie van een begrensde bundel met het uiteinde van een plaat, onder de Lambhoek.

- Nico F. Declercq, Joris Degrieck, Oswald Leroy, "Bounded beam interaction with plate-edge at Lamb angle", Acta Acustica United with Acustica 91, 326-332, 2005 *(Imp. Fact. 0.346; SCI-index, Acoustics, rank:21 /28)*
- Mondelinge presentatie tijdens '51st open seminar on Acoustics, joint with 9th School of Acousto-Optics and Applications', **Gdansk**, Polen , 6-10 september 2004.

De twee voorgaande secties toonden aan hoe enerzijds Scholte – Stoneley golven en anderzijds Rayleigh golven interageren met het uiteinde van een dikke plaat. Indien men echter te maken heeft met een dunne plaat, dan is het interessanter om na te gaan wat er gebeurt indien een Lambgolf (een soort plaatgolf) interageert met het uiteinde van een plaat. Een combinatie van theoretische modellering en analyse van kwalitatief haarscherpe Schlierenfoto's toont aan welke Lambgolven worden omgezet in welke andere Lambgolven en toont tevens aan dat Lambgolven, wanneer ze het uiteinde van de plaat bereiken, een akoestische multipool teweegbrengen die, naargelang de omstandigheden, prachtige voorwaarts stralende ultrasone bundels kan opwekken.

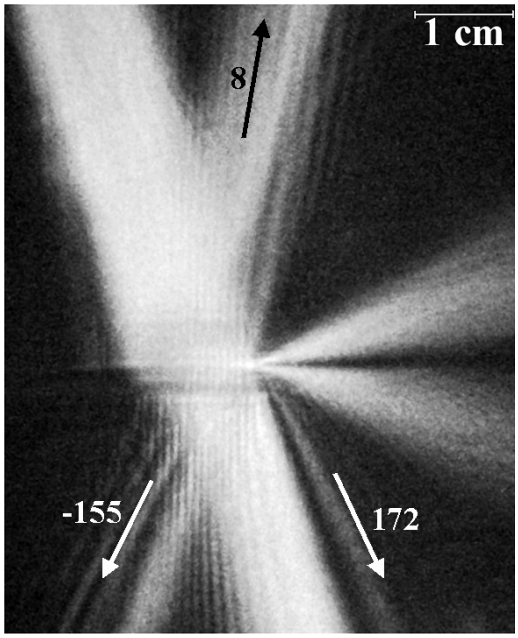

Fig. I.10 (identiek aan Fig. IX.C_5): Deze spectaculaire Schlierenfoto onthult de wondermooie interactie van een begrensde bundel met het uiteinde van een dunne aluminiumplaat, indien de invalshoek overeenstemt met de Lambhoek voor A_1 Lambgolven. Uit de foto wordt afgeleid welke Lambmodes na modeconversie ontstaan. Tevens wordt aangetoond, dat het voorwaarts patroon (de twee nagenoeg horizontale bundels) ontstaat door multipool-opwekking. De numerieke waarden op deze figuur komen overeen met de hoeken ten opzichte van de loodrechte op de plaat.

Hoofdstuk X Diffractieverschijnselen

- mondelinge presentatie op uitnodiging tijdens '51st open seminar on Acoustics, joint with 9th School

of Acousto-Optics and Applications', **Gdansk**, Polen , 6-10 september 2004.

<u>Secties X.A.1</u> **:** **Ultrasone Diffractieverschijnselen op eendimensionale ruwe oppervlakken**

<u>Sectie X.A.1.a</u> **:** **Een theoretische studie van de achterwaartse verplaatsing van een bundel op periodiek ruwe oppervlakken en het verband met uitstralende Scholte – Stoneley golven.**

- Nico F. Declercq, Joris Degrieck, Rudy Briers, Oswald Leroy, "Theory of the backward beam displacement on periodically corrugated surfaces and its relation to leaky Scholte-Stoneley waves", **J. Appl. Phys**. 96(11), 6869-6877, 2004 *(Imp. Fact. 2.281; SCI-index, Physics-Applied, rank:13/76)*
- Mondelinge presentatie tijdens First Pan-American/Iberian Meeting on Acoustics (144th Meeting of the Acoustical Society of America, 3rd Iberoamerican Congress of Acoustics, 9th Mexican Congress on Acoustics), **Cancun**, Mexico, 2-6 Dec. 2002.
- '**Best student paper award**' geschonken door de 'Acoustical Society of America'

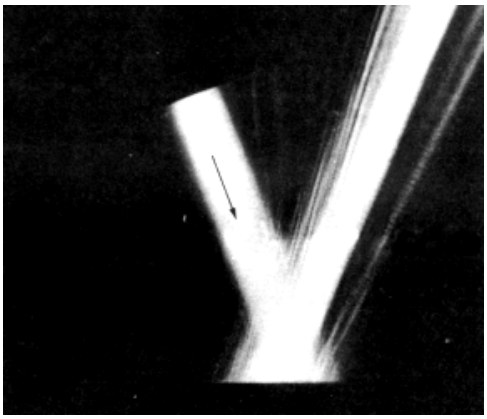

Fig. I.11 : ***De achterwaartse verschuiving van een begrensde bundel bij interactie met een periodiek ruw oppervlak. Het pijltje duidt de invalsrichting aan. Dit fenomeen bleef onverklaard sinds 1976, maar is nu volledig ontrafeld.***

In 1976 voerden Breazeale en Torbett Schlieren-experimenten uit op periodiek ruwe oppervlakken. Naar analogie met een fenomeen van de achterwaartse verschuiving van lichtbundels in het elektromagnetisme, verwachtten Breazeale en Torbett een gelijkaardig fenomeen in de akoestiek, mede door de voorspelling door Bertoni en Tamir dat het fenomeen bij een welbepaalde invalshoek zou moeten optreden, naargelang de gebruikte frequentie en naargelang de aard van de vaste stof en de periodiciteit van de groefjes die werden aangebracht op het oppervlak van die vaste stof. Maar, de experimenten toonden dat het fenomeen optreedt onder een zeer onverwachte invalshoek en bovendien bleek niemand in staat om deze achterwaartse verplaatsing te simuleren, niet bij de experimenteel waargenomen hoek, noch bij de theoretisch voorspelde hoek.

De huidige sectie toont aan op welke manier het fenomeen kan begrepen en gesimuleerd worden, namelijk door gebruik van de inhomogene golftheorie. Er wordt tevens aangetoond dat het fenomeen niet verklaarbaar is met de klassieke Fourier theorie. Bovendien wordt theoretisch aangetoond dat het fenomeen het gevolg is van een nieuw

type oppervlaktegolf, namelijk een uitstralende Scholte – Stoneley golf. Dit type golf was voorheen onbekend en bestaat enkel op ruwe oppervlakken en is min of meer vergelijkbaar met de klassieke Scholte – Stoneley golf op vlakke oppervlakken, die nooit uitstraalt. Bovendien voorspelt het theoretisch model dat, indien Breazeale en Torbett een smallere ultrasone bundel hadden geimplementeerd, dat ze dan hoogstwaarschijnlijk wel iets (een bundelverschuiving of profielvervorming) hadden gezien bij inval onder de hoek die door Bertoni en Tamir was voorspeld.

Voorts verklaart deze sectie de ware aard van zogenaamde Wood-anomalieën in het nulde-orde diffractiespectrum voor loodrecht invallend geluid op een periodiek ruw oppervlak. Alhoewel dit vroeger verondersteld werd te wijten te zijn aan Scholte - Stoneley golven, wordt hier aangetoond dat dit slechts een deel van de waarheid is en dat het daarenboven te wijten is aan een soort eigentrilling van het ruwe oppervlak bij de betreffende frequentie.

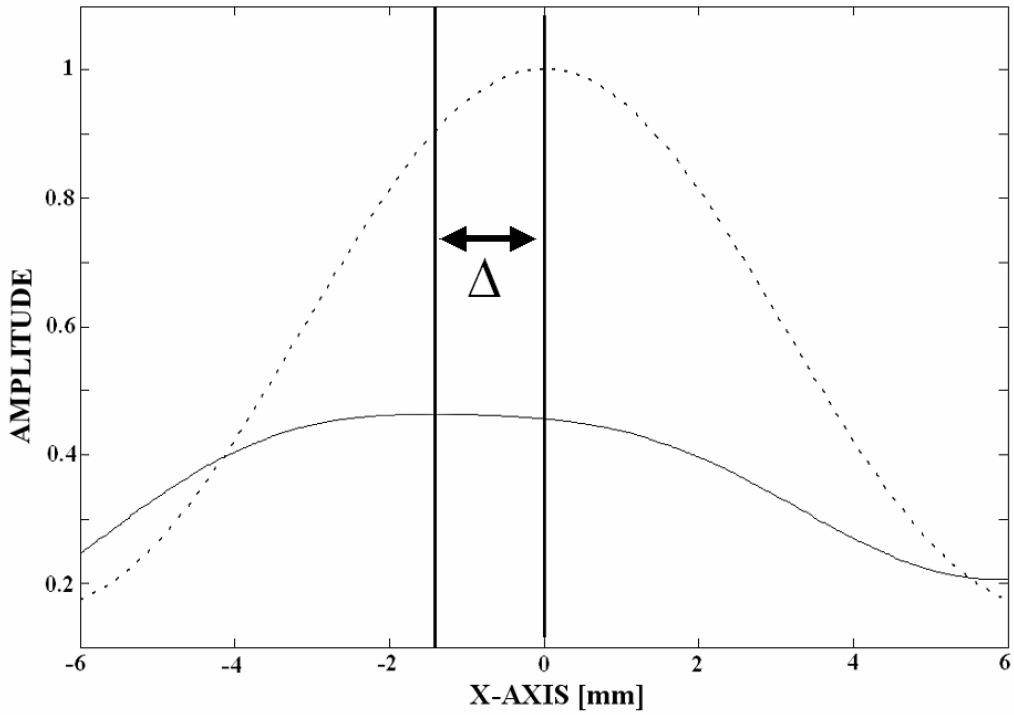

Fig. I.12 (identiek aan Fig. X.A.1.a_15): ***De stippellijn komt overeen met het profiel van de invallende bundel, terwijl de volle lijn overeenkomt met de achterwaarts verschoven gereflecteerde bundel, in overeenstemming met het experiment van Breazeale en Torbett in Fig. I.11. De horizontale as is de afstand tot het centrum van de invallende bundel, terwijl de verticale as de amplitude voorstelt.***

Sectie X.A.1.b : **Experimentele studie van de achterwaartse verplaatsing van een bundel op periodiek ruwe oppervlakken en het verband met uitstralende Scholte – Stoneley golven.**

- Aanvaard voor publicatie in **J. Appl. Phys.** *(Imp. Fact. 2.281; SCI-index, Physics-Applied, rank:13/76)*

Deze sectie volgt nauw op de vorige sectie en beschrijft resultaten die gehaald zijn uit experimenten die samen met Breazeale en anderen zijn uitgevoerd in Mississippi. Er wordt experimenteel aangetoond dat het fenomeen van de achterwaartse verplaatsing inderdaad het gevolg is van een uitstralend type Scholte – Stoneley golf. Bovendien wordt aangetoond dat smallere bundels inderdaad profielwijzigingen teweegbrengen, bij de hoek die door Bertoni en Tamir werd voorspeld. Deze experimenten zijn uitgevoerd nadat de theorie was bekendgemaakt en vormen daarom een perfecte bevestiging van de theoretische voorspellingen.

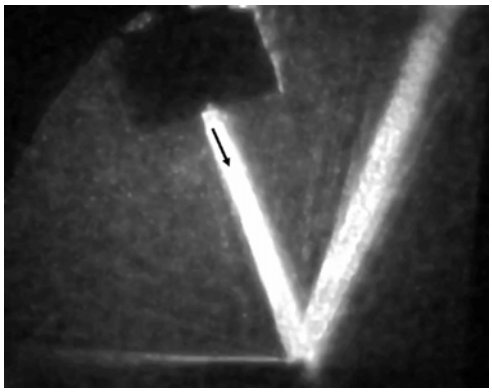

Fig. I.13 (identiek aan Fig. X.A.1.b_5): ***Deze foto vormt het experimentele bewijs van het feit dat de achterwaartse bundelverschuiving ontstaat door een naar achteren gerichte soort Scholte – Stoneley golf. De bewijsvoering is gebaseerd op het feit dat de Scholte – Stoneley golf uitstraalt in het verlengde van de plaat, wanneer ze de rand bereikt. De instraalhoek op deze foto is gelijk aan de instraalhoek van Fig. I.11, zij het voor een smallere bundel in de huidige figuur ten opzichte van Fig. I.11, vandaar ook een verwaarloosbare achterwaartse verplaatsing van de gereflecteerde bundel.***

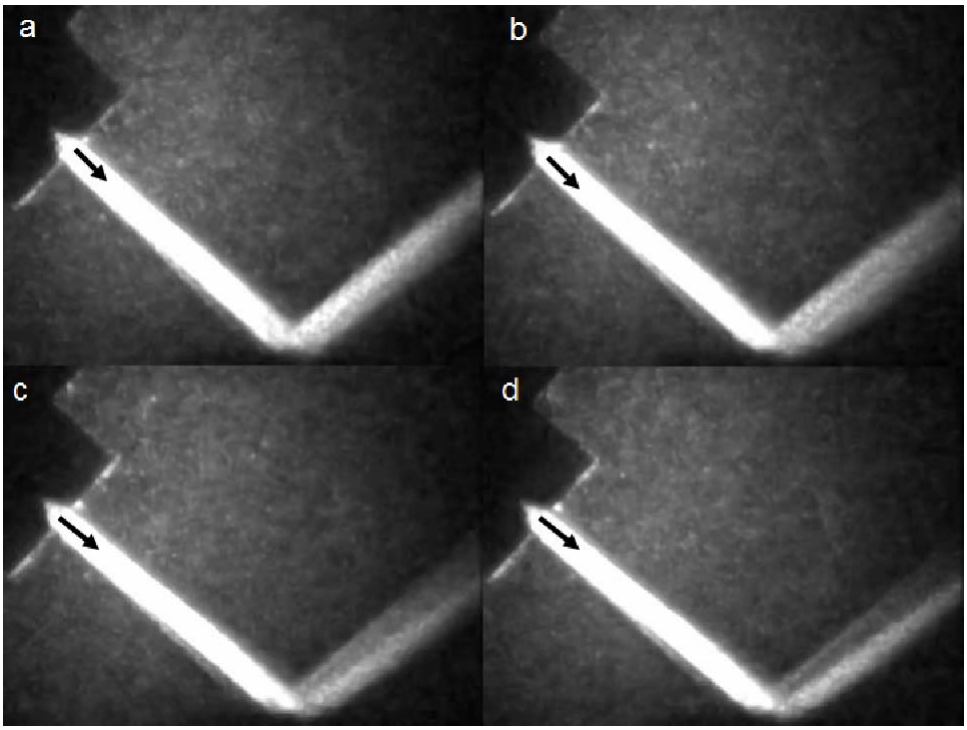

Fig. I.14 (identiek aan Fig. X.A.1.b_7): ***Deze foto's tonen aan dat er profielwijzigingen ontstaat bij de hoek die door Bertoni en Tamir was voorspeld, op voorwaarde dat de ingestraalde bundel smal genoeg is, wat theoretisch was voorspeld in de voorgaande sectie.***

<u>Sectie X.A.1.c</u> **: Opmerking over het gediffracteerd geluidsveld, gegenereerd door inhomogene golven na interactie met een ruwe periodiek ruwe scheiding tussen een vloeistof en een vaste stof**

Enkele jaren geleden werd door Briers *et al* vooropgesteld dat bij de diffractie van inhomogene golven aan een periodiek ruw oppervlak, de tekenkeuze voor de componenten van de golfvectoren volgens de normaal aan het oppervlak, volgens principes diende te gebeuren die wel resultaten opleverden in overeenstemming met de experimenten, maar die tegenstrijdig waren met principes die werden gehanteerd aan vlakke oppervlakken. Hier wordt aangetoond dat het perfect mogelijk is om dezelfde principes te hanteren als aan een vlakke scheiding, maar in een veralgemeende vorm, voor een periodiek ruwe scheiding. De berekende resultaten komen even goed overeen met de experimenten en houden geen contradictie meer in.

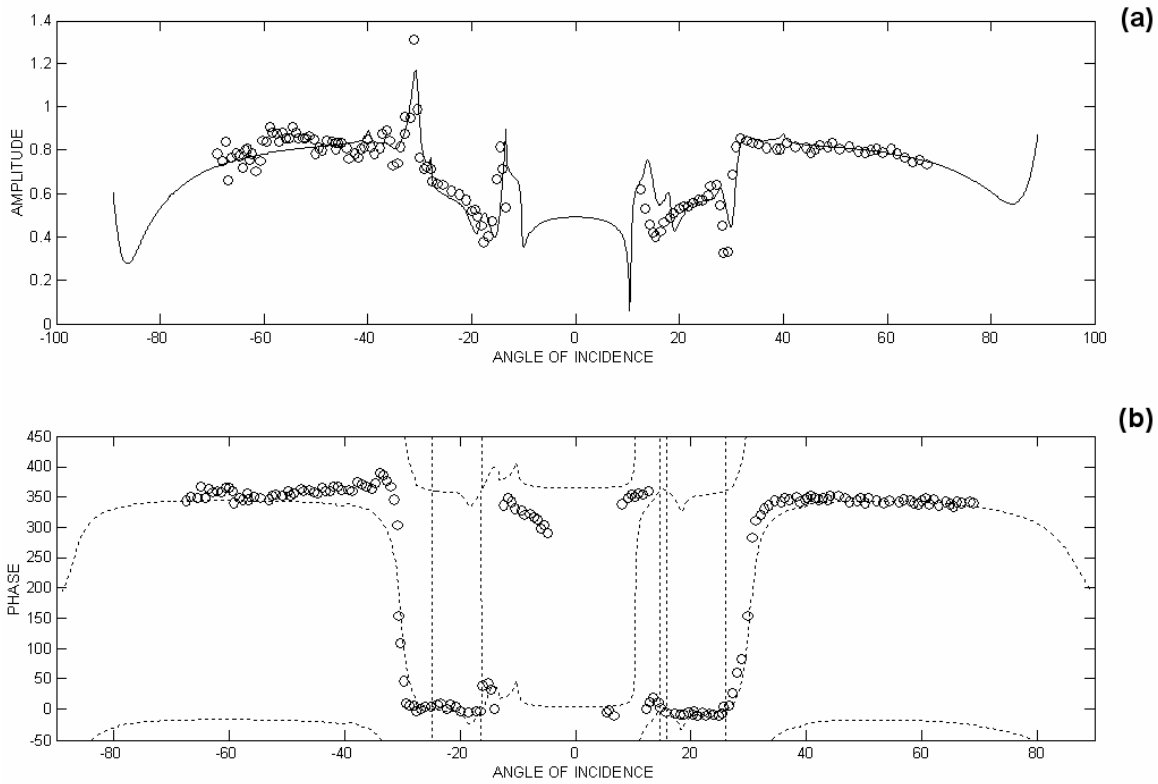

Fig. I.15 (identiek aan Fig. X.A.1.c_2): ***Vergelijking tussen experimentele waarden (cirkels) en theoretische waarden (lijnen) voor de nulde-orde reflectiecoëfficiënt voor verschillende invalshoeken tussen -90^0 en $+90^0$. Het bovenste gedeelte toont de amplitude, terwijl het onderste gedeelte de fase weergeeft. De horizontale as stelt telkens de invalshoek voor, terwijl de verticale as de amplitude (bovenste deel) weergeeft of de fase (onderste deel). De theoretische waarden werden berekend voor de nieuwe tekenkeuze die overeenstemt met die aan een vlakke scheiding. Er blijkt een duidelijke gelijkenis te bestaan tussen de theorie en het experiment.***

<u>Sectie X.A.1.d</u> : De diffractie van complex harmonische vlakke golven en de opwekking van voorbijgaande uitstralende Rayleigh golven

- Mondelinge presentatie tijdens '75th Anniversary Celebration of the Acoustical Society of America (147th meeting of the Acoustical Society of America)', Sheraton New York Hotel and Towers, **New York**, New York, VSA, 24-28 mei 2004

De meest veralgemeende vorm van vlakke golven bevat niet enkel een complexe golfvector, maar tevens een complexe frequentie. Indien aanwezig, dan veroorzaakt het imaginaire gedeelte van de frequentie een exponentieel dalende of stijgende amplitude als functie van de tijd. In deze sectie wordt bestudeerd hoe zulke golven interageren met een periodiek ruw oppervlak. Het is geweten dat periodiek ruwe oppervlakken in staat zijn om vlakke en inhomogene golven om te vormen tot oppervlaktegolven, maar is dit ook het geval voor complex harmonische golven? De studie toont aan dat loodrecht invallende complex harmonische golven in staat zijn (veel beter dan harmonische inhomogene

golven) om Rayleigh golven op te wekken die ‘voorbijgaand’ (Engels: ‘transient’) van aard zijn en die eveneens energie uitstralen in de vloeistof.

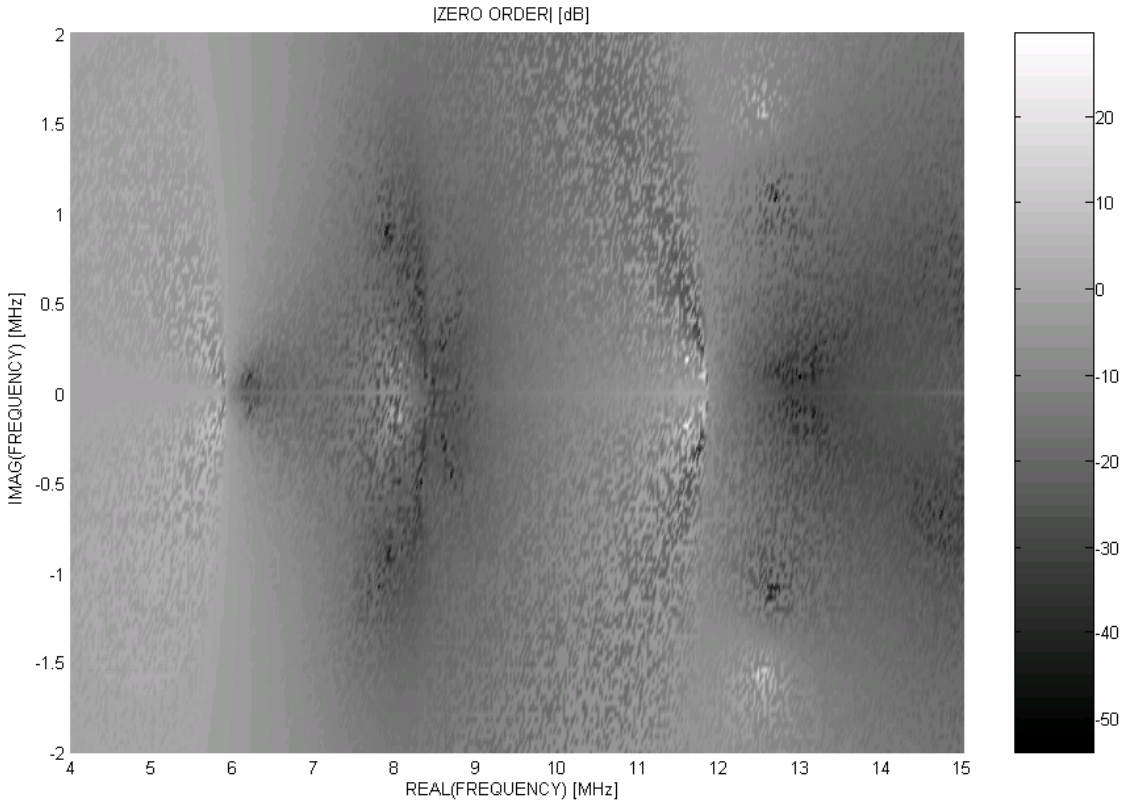

Fig. I.16 (identiek aan Fig. X.A.1.d_6): ***Een voorbeeld van het nulde orde diffractiespectrum (amplitude in dB), als functie van de reële frequentie (horizontale as) en de imaginaire frequentie (verticale as) Men merkt gebiedjes op met een zeer kleine amplitude en ook gebiedjes met een zeer grote amplitude. Deze gebiedjes zijn typisch een indicatie voor de opwekking van oppervlaktegolven.***

Deze bevinding is zeer belangrijk omdat het veel eenvoudiger is, en tevens flexibeler, om complex harmonische golven op te wekken dan inhomogene golven. Dit opent de weg naar de relatief eenvoudige opwekking van hoogenergetische Rayleighgolven met behulp van een diffractierooster en een invallende bundel met middelmatige amplitude.

Sectie X.A.1.e : Het akoestische diffractierooster: een filter voor complexe frequenties in elektronische signalen

In de elektronica is het begrip van het frequentiespectrum uiteraard heel goed ingeburgerd. Het spectrum kan fysisch bepaald worden via de nodige filters, of kan mathematisch berekend worden via de Fourier transformatie. Er bestaat echter ook de mogelijkheid om een elektronisch signaal lokaal voor te stellen als een sommatie van in de tijd exponentiële functies. Deze exponentiële functies komen in principe overeen met het effect van het imaginair gedeelte van de frequentie in complex harmonische akoestische golven. Alhoewel deze mathematische ontbinding mogelijk is via de nodige optimalisatieprocedures, blijft de vraag of het mogelijk is om een fysische filter te bouwen die het mogelijk maakt om dit ‘complexe spectrum’ te begroten in plaats van louter het

'reële spectrum'. De studie toont aan dat voor dit doel een periodiek ruw oppervlak kan dienst doen, in combinatie met acousto-optische cellen.

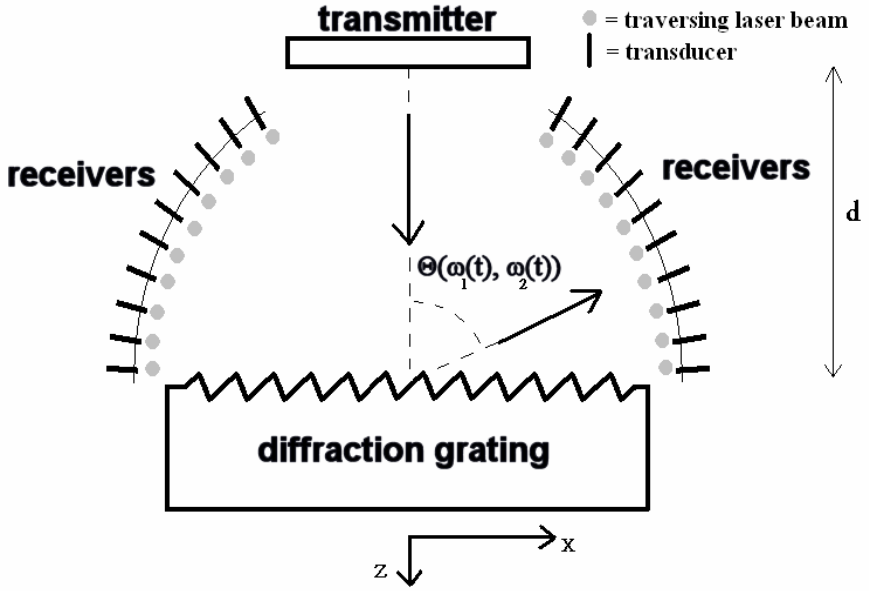

Fig. I.17 (identiek aan Fig. X.A.1.e_1): ***Een schematische voorstelling van hoe de filter er zou kunnen uitzien. Een vrij brede transducer ('transmitter') stuurt geluid naar een periodiek ruw oppervlak ('diffraction grating') waarna het gediffracteerd geluid kan gedetecteerd worden via omnidirectionele transducers ('receivers'). Deze transducers verschaffen zo informatie over de energierichting. Om de faserichting te kennen, wordt gebruik gemaakt van laserlicht ('traversing laserlight') dat het geluid doorstraalt en waarvan het diffractiepatroon loodrecht gevormd wordt ten opzichte van de fasevlakken van het geluid.***

<u>Sectie X.A.1.f</u> **: Het gebruik van gepolariseerde begrensde bundels om de groefrichting van een ruw oppervlak te bepalen bij loodrechte inval, de opwekking van oppervlaktegolven en de instraling bij Bragghoeken.**

- Nico F. Declercq, Rudy Briers, Oswald Leroy, " The use of polarized bounded beams to determine the groove direction of a surface corrugation at normal incidence, the generation of surface waves and the insonification at Bragg-angles", **Ultrasonics** 40/1-8 pp. 345-348, 2002.*(Imp. Fact. 0.844; SCI-index, Acoustics, rank:11 /28)*
- poster presentatie tijdens 'Ultrasonics International 2001', Technische Universiteit Delft, **Delft**, Nederland, 2-5 juli 2001.

Tijdens niet-destructieve testen gebeurt het soms dat men te maken krijgt met platen waarvan de onderkant gegroefd is. Een van de vragen die men dan dient te beantwoorden is: 'Volgens welke richting zijn de groeven gemaakt?'. Dit werk bestudeert en overhandigt een methode om de richting vrij eenvoudig te bepalen, gebruik makend van één enkele breedbandige contact-transducer die loodrecht geplaatst wordt op de plaat.

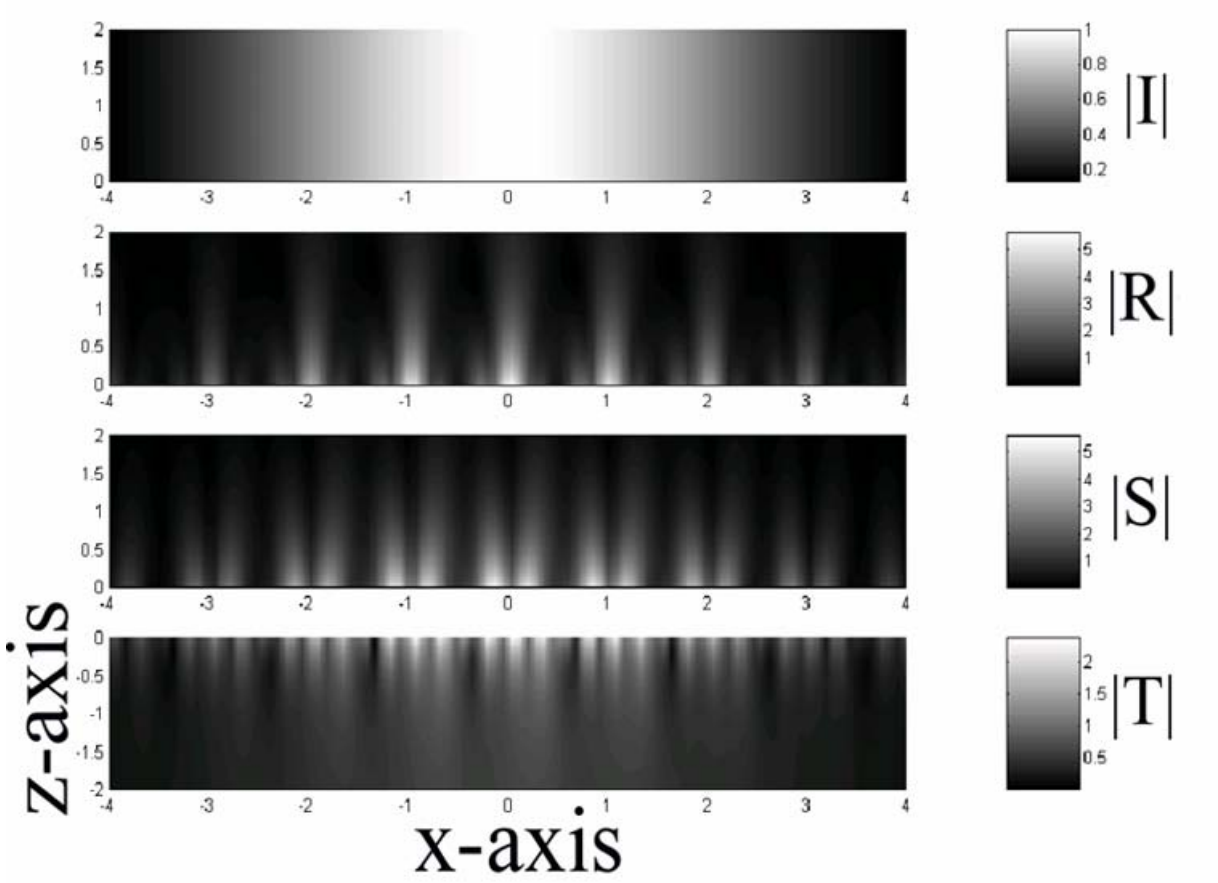

Fig. I.18 (identiek aan Fig. X.A.1.f_5): *|I| is de amplitude van de loodrecht invallende longitudinaal gepolariseerde Gaussische bundel, |R| is de amplitude van het gereflecteerde longitudinaal gepolariseerde geluid, |S| is de amplitude van het gereflecteerde transversaal gepolariseerde geluid en |T| is de amplitude van het doorgelaten longitudinaal gepolariseerde geluid. De frequentie is deze dewelke, voor de gegeven groeven, Scholte-Stoneley oppervlaktegolven opwekt. De horizontale as komt overeen met de richting langs de plaat, de verticale as komt overeen met de normaal op de plaat, gedeeld door de periode van het groefpatroon. Het is duidelijk dat er een franjepatroon optreedt, dit is het gevolg van de interferentie van Scholte-Stoneley oppervlaktegolven die van links naar rechts lopen en zij die van rechts naar links lopen. Alhoewel de amplitude het grootst is in de omgeving van de invallende bundel, is het zo dat het franjepatroon zich uitstrekt buiten de grenzen van de invallende bundel.*

Analyse van de gereflecteerde puls, bijvoorbeeld voor invallende circulair gepolariseerde golven, leert dat de polarisatierichting bij een frequentie die overeenstemt met deze dewelke Scholte-Stoneley oppervlaktegolven opwekt, parallel staat ten opzichte van de groeven en deze dewelke Love-oppervlaktegolven opwekt, loodrecht staat ten opzichte van de groeven. Bovendien wordt aangetoond dat, alhoewel strikt genomen enkel vlakke golven in staat zijn om Scholte-Stoneley golven op te wekken bij loodrechte inval, via diffractie op die groefjes onderaan de plaat, ook begrensde bundels daartoe in staat zijn.

<u>Sectie X.A.1.g</u> **: De diffractie van horizontaal gepolariseerde ultrasone vlakke golven aan een periodiek ruwe vaste stof – vloeistof scheiding bij loodrechte inval en bij inval onder de Brewster hoek.**

- Nico F. Declercq, Rudy Briers, Joris Degrieck, Oswald Leroy, "Diffraction of horizontally polarized

ultrasonic plane waves on a periodically corrugated solid-liquid interface for normal incidence and Brewster angle incidence", **IEEE Transactions on Ultrasonics, Ferroelectrics, and Frequency Control**, 49(11), 1516-1521, 2002. *(Imp. Fact. 1.595 ;SCI-index, Engineering – electrical & electronic, rank:46/205)*

- Mondelinge presentatie tijdens 'ICA2004 18th International Congress on Acoustics', Kyoto International Conference Hall, **Kyoto**, Japan, 4-9 April 2004

Net als in de vorige sectie, wordt hier het gedrag bestudeerd van geluid dat opgewekt wordt aan de vlakke kant van een plaat en dat interageert met de ruwe tegenovergestelde kant van dezelfde plaat. Men spreekt van horizontaal gepolariseerde golven indien de polarisatierichting evenwijdig is met de groeven en men spreekt van verticaal gepolariseerde golven indien de polarisatie loodrecht staat op de groefrichting. Ofschoon het gros van de onderzoekers altijd al aannam dat invallend verticaal gepolariseerd geluid geen horizontaal geluid kan opwekken en omgekeerd, wordt in deze sectie het theoretische bewijs van die stelling geleverd. Bovendien wordt de vergelijking opgesteld die een beschrijving toelaat van de interactie van horizontaal gepolariseerde golven met de groefjes. Het ontstaan van Love-oppervlaktegolven wordt numeriek aangetoond. Daarenboven wordt ook het bestaan van een Brewsterhoek aangetoond en wordt aldus bewezen dat deze bekende hoek uit de optica ook een tegenhanger heeft in de akoestiek.

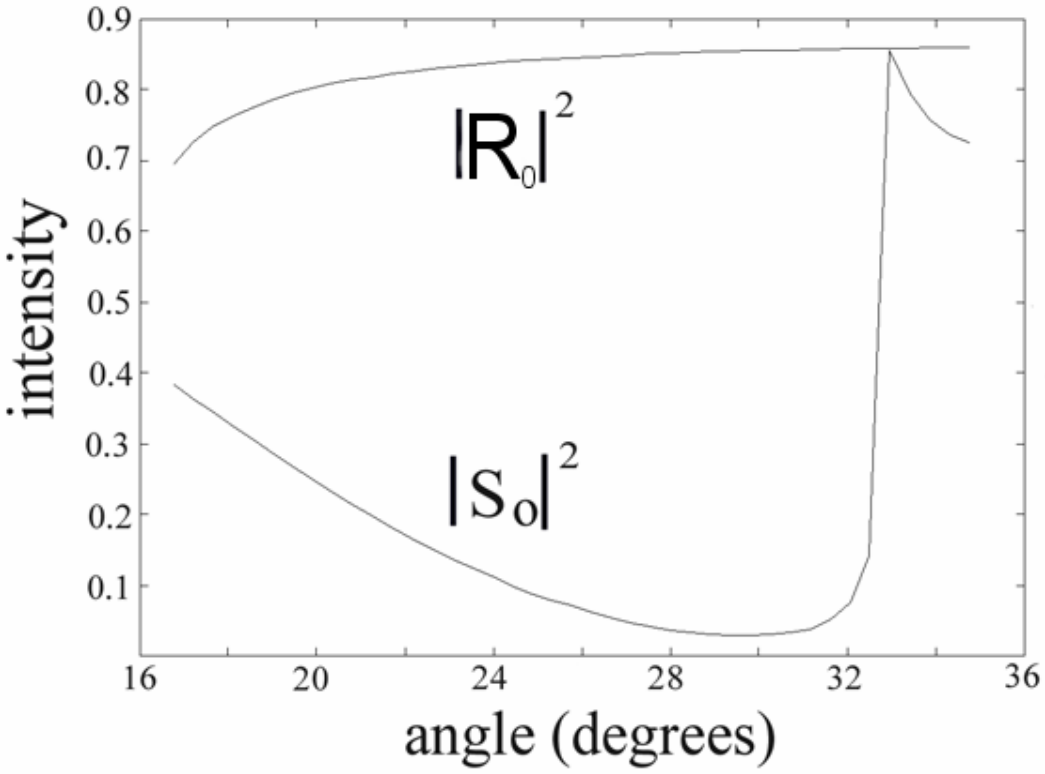

Fig. I.19 (identiek aan Fig. X.A.1.g_4): ***Deze figuur geeft de gereflecteerde intensiteit (verticale as) weer voor de verticaal gepolariseerde nulde orde gediffracteerde golf*** S_0 ***en de horizontaal gepolariseerde nulde orde gediffracteerde golf*** R_0 ***als functie van de invalshoek (horizontale as). De Brewsterhoek is deze hoek waarbij*** S_0 ***een minimum vertoont en waarbij het gereflecteerde geluid dus hoofdzakelijk horizontaal gepolariseerd is, net zoals bij de Brewsterhoek in de optica.***

Sectie X.A.1.h : Enkele bemerkingen bij het fenomeen van Scholte – Stoneley golven op periodiek ruwe oppervlakken

- Mondelinge presentatie tijdens '17th International Congress on Acoustics', **Rome**, Italië, 2-7 september 2001

Aan de hand van experimenten die uit de literatuur gehaald zijn, wordt aangetoond dat er aanwijzingen zijn dat Scholte-Stoneley oppervlaktegolven sneller voortbewegen langsheen een ruwe plaat dan langsheen een vlakke plaat. In 2001 werd een model voorgesteld dat het fenomeen bijna perfect kon simuleren, maar dat volgens de referees van het toen ingestuurde artikel te weinig de te verwachten dispersieve aard van oppervlaktegolven op ruwe oppervlakken weerspiegelde. Omwille daarvan werd een verbeterde versie van het model uitgesteld en is het oorspronkelijke model niet in deze thesis opgenomen.

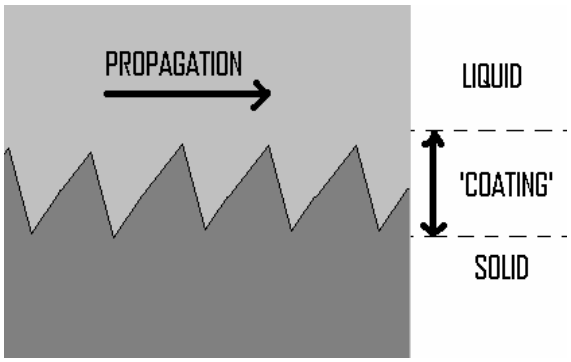

Fig. I.20 (identiek aan Fig. X.A.1.h_1): ***Er zijn sterkte aanwijzingen dat een ruw oppervlak door een Scholte – Stoneley oppervlaktegolf wordt 'gevoeld' als een deklaag op een plaat. Dit maakt het vanuit theoretisch standpunt niet onmogelijk dat zulke golven sneller voortbewegen langsheen een ruwe plaat dan langsheen een vlakke plaat, een fenomeen dat experimenteel wordt waargenomen. 'Propagation' duidt de voortplantingsrichting aan, terwijl 'liquid' de vloeistof, 'solid' de vaste stof en 'coating' de deklaag voorstellen.***

Sectie X.A.2 : Ultrasone Diffractieverschijnselen op tweedimensionale ruwe oppervlakken

Sectie X.A.2.a : De diffractie van homogene en inhomogene vlakke golven op een dubbel gegroefde vloeistof – vaste stof scheiding.

- Mondelinge presentatie tijdens 'InterNoise2003', International Convention Center Jeju, **Seogwipo**, Korea, 25-28 augustus, 2003
- Mondelinge presentatie tijdens 'Acoustics 2003', Universiteit van Cadiz, **Cadiz**, Spain, 16-18 juni 2003.

In de voorgaande secties werd steeds uitgegaan van een oppervlak dat parallelle groefjes vertoont. Het kan echter ook voorkomen dat groefjes worden aangebracht op een plaat, loodrecht op reeds aanwezige groefjes. Dan ontstaat er iets wat lijkt op een 'eierkrat'. De beschrijving van de diffractie op zo'n oppervlak en de stimulering van

oppervlaktegolven, was nog nooit gebeurd. In deze sectie wordt vooreerst aangetoond wat de fysische en theoretische verklaring is voor een veralgemening van de klassieke roostervergelijking in het geval van invallende inhomogene golven. De roostervergelijking in een richting (bvb de x-richting), is gegeven door

$$k_x^m = k_x^{inc} + m\frac{2\pi}{\Lambda_x}$$

waarbij k_x^m de golfvectorcomponent is voor de m-de orde gediffracteerde golf langsheen het oppervlak, waarbij k_x^{inc} diezelfde component is, maar voor de invallende vlakke golf, waarbij m de diffractieorde is en Λ_x de ruimtelijke periode van het ruwe oppervlak in de x-richting. Een veralgemening houdt in dat de vergelijking nog steeds opgaat, ook indien k_x^{inc} een complexe waarde heeft, dus in het geval van invallende inhomogene golven.

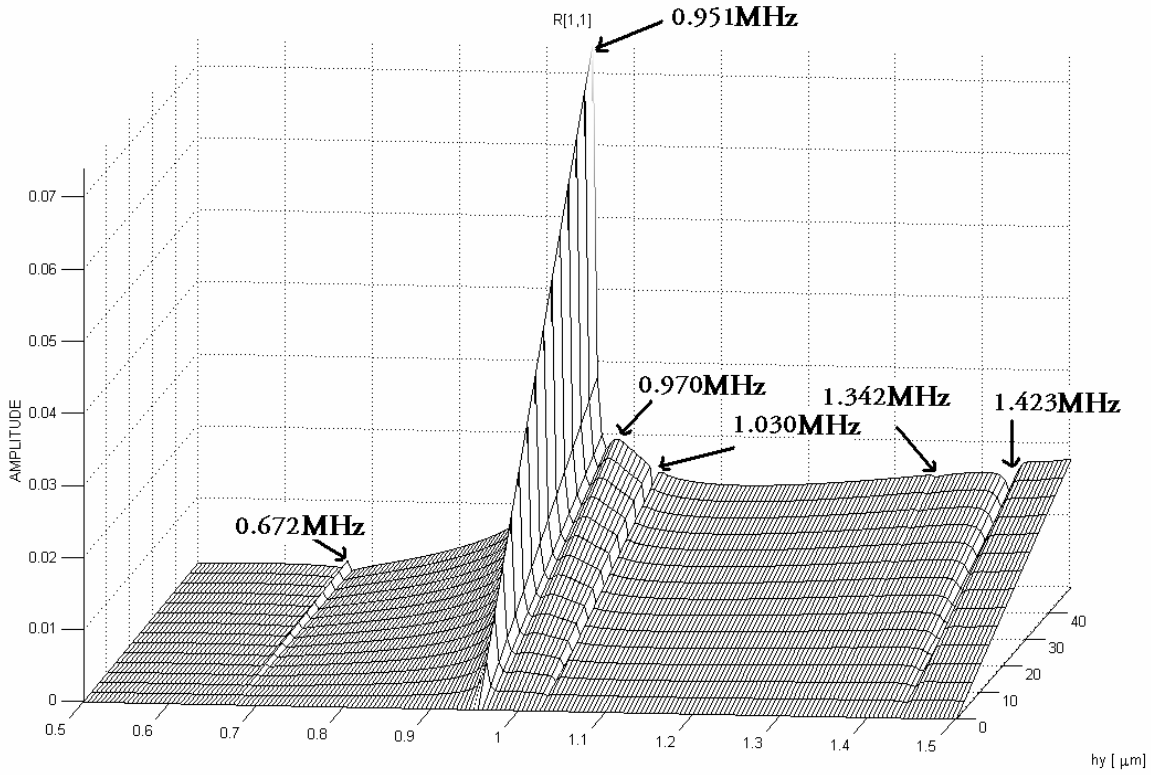

Fig. I.21 (identiek aan Fig. X.A.2.a_5): ***deze grafiek geeft de amplitude weer van het geluid dat diffracteert aan een tweedimensionaal gegroefd oppervlak, met*** $\Lambda_x = \Lambda_y = 2.2mm$***, en wiens voortplanting gericht is precies in het midden tussen de x-as en de y-as. De amplitude is weergegeven als functie van de frequentie (horizontale as [MHz]) en als functie van de hoogte van de groefjes(loodrecht op de y-richting), voor een vaste hoogte*** $h_x = 50\mu m$ ***van die groefjes (welke evenwijdig zijn aan de y-richting). De frequentie 0.951 MHz correspondeert met de opwekking van Scholte Stoneley golven langs die richting. Het is duidelijk dat de amplitude toeneemt naarmate de veranderlijke hoogte even groot wordt als*** $h_x = 50\mu m$***. Dit komt omdat in die omstandigheid de Scholte-Stoneley golf optimaal gestimuleerd wordt in die welbepaalde richting.***

Deze verklaring is specifieerbaar tot het eendimensionale geval waar de veralgemening vroeger reeds werd geponeerd en experimenteel geverifieerd, maar nooit theoretisch bewezen. Vervolgens worden in deze sectie de vergelijkingen opgesteld die het diffractieverschijnsel op tweedimensionaal gegroefde oppervlakken beschrijven en worden numerieke simulaties uitgevoerd, zowel voor invallende klassieke homogene vlakke golven als voor meer gesofisticeerde inhomogene golven. Er wordt numeriek aangetoond en theoretisch verklaard, hoe het mogelijk is om een bepaalde richting in het vlak te geven aan opgewekte Scholte-Stoneley oppervlaktegolven. Een gelijkaardige procedure wordt gevolgd om duidelijk te maken waarom inhomogene golven slechts in welbepaalde richtingen Rayleighgolven kunnen opwekken. Tevens wordt een studie gemaakt van de invloed van de relatieve dieptes van de orthogonale groeven op een tweedimensionaal gegroefde plaat.

Secties X.B : **Akoestische diffractieverschijnselen**

Sectie X.B.1 : **Een theoretische studie van speciale akoestische effecten die veroorzaakt worden aan de trappen van de El Castillo piramide in de Maya ruines van Chichen Itza in Mexico**

- **Nature News** 14 December 2004; | doi:10.1038/news041213-5
- Nico F. Declercq, Joris Degrieck, Rudy Briers, Oswald Leroy, "A theoretical study of special acoustic effects caused by the staircase of the El Castillo pyramid at the Maya ruins of Chichen-Itza in Mexico", **J. Acoust. Soc. Am.** 116(6), 3328-3335, 2004 *(Imp. Fact. 1.310; SCI-index, Acoustics, rank:7 /28)*
- Mondelinge presentatie tijdens '145th Meeting of the Acoustical Society of America', Nashville Convention Center, **Nashville**, Tennessee, USA, 28 april - 2 mei 2003.
- Mondelinge presentatie tijdens 'CFA/DAGA'04, 7ème Congrès Français d'Acoustique, Salon Européen de l'Acoustique - 30. Deutsche Jahrestagung für **Akustik, Europäische Akustik-Ausstellung', Palais des Congrès et de la Musique,** Strasbourg, France, 22-25 maart 2004
- Verschenen in tientallen **kranten** over de ganse wereld en in België, verschenen in 'De Nieuwe Wereld' (radio 1) en in het nieuws (VTM)

In tegenstelling tot alle voorgaande secties, die eigenschappen van ultrageluid beschreven, handelt deze sectie over akoestische signalen. Dit zijn dus laagfrequente signalen die voor het menselijk oor hoorbaar zijn. Meer specifiek komt in deze sectie een fenomeen aan bod waarbij een trap fungeert als diffractierooster voor hoorbaar geluid. Aangezien dit fenomeen nogal wat aandacht heeft gekregen in de pers, verdient het een iets uitgebreider stuk binnen deze korte samenvatting.

In Mexico, in de buurt van het toeristische Cancun, is er een archeologische Maya site, Chichen-Itza genaamd. Op die site zijn er verschillende bijzondere akoestische fenomenen waarneembaar, zoals bijvoorbeeld een balspel-terrein, omgeven door een muur, waarbij de trainer van het ene team kan spreken tegen de trainer van het andere team, op zo'n 100 meter afstand van elkaar, zonder zijn stem te moeten verheffen. Dit, terwijl de spelers op het veld, die zich tussenin de twee trainers bevinden, niets van de conversatie kunnen horen. Dit is een bizar fenomeen, maar is perfect verklaarbaar dankzij de structuur van de

muur, die het geluid geleidt van de ene trainer naar de andere.

Doch, op die site staat ook een piramide (El Castillo) die nog in vrij goede staat is. Men meent dat de piramide onder meer dienst deed als zonnekalender. Aan de vier zijden van de piramide bevindt zich een steile trap met treden die ietsje hoger zijn dan de treden die men tegenwoordig vindt in moderne trappenhallen. Het aantal treden komt overeen met het aantal dagen in een jaar en op de dag van de equinox, schijnt de opkomende zon precies op een gesculpteerde slang, die zich langs een van de trappen naar de top van de piramide bevindt. Nu is het zo dat men ergens anders, in het oude Maya rijk, hiërogliefen heeft aangetroffen, waarop diezelfde slang staat afgebeeld samen met een in Mexico zeer bekende vogel, namelijk de Quetzal. De nauwe band tussen de Quetzal en de Maya's is wellicht ontstaan toen de Maya's nog in de wouden leefden en dus nog geen piramides bouwden. Het is reeds vele decennia een raadsel waarom de piramide een echo teweegbrengt die verdacht goed lijkt op het geluid van een Quetzal, in respons op een handklap. Er zijn verschillende theorieën geponeerd in het verleden, gaande van de tussenkomst van UFO's tot een meer waarschijnlijke uitleg dat het hier gaat over een effect dat door de trappen van de piramide wordt teweeggebracht. Het fenomeen heeft reeds menig toerist en wetenschapper geboeid.

De jongste jaren zijn er dan ook extensieve akoestische metingen verricht, voornamelijk door David Lubman (California), die de structuur van de echo in kaart gebracht heeft. Echter, de gemeten signalen brachten enkel nieuwe speculaties teweeg, zonder een sluitende verklaring te geven. Zo werd, tot in 2002, verondersteld dat het hier ging om het fenomeen van Bragg scattering. Het was namelijk zo dat men via een zogenaamde 'ray-benadering' patronen kon voorspellen die min of meer ook te zien waren in de gemeten signalen.

Om het fenomeen te demonstreren organiseerde 'The Acoustical Society of America' daarom een post meeting tour naar de site, ter gelegenheid van het eerste Pan-American Congress on Acoustics (Cancun, 2002).

Op de archeologische site in Chichen-Itza, werden wij gevraagd om met de ganse groep voor de piramide te staan en in onze handen te klappen. De echo, die telkens volgde op het geklap, was zo mooi en fenomenaal, dat werkelijk iedereen ervan onder de indruk was. Toen ons verteld werd dat het wellicht om een puur Bragg fenomeen ging, was ik het daar niet mee eens. Voor een Bragg fenomeen heb je namelijk een diffractierooster nodig van dezelfde grootteorde als de geluidsbron of heb je op z'n minst een parallelle invallende geluidsbundel nodig. Op de site hadden we te maken met een, bijna, puntbron (de groep klappende handen) en een veel grotere, weliswaar eindige, piramide (bekleed met trappen). Bovendien, terwijl ik eventjes ging zitten onderaan de piramide, op de eerste trede, hoorde ik regendruppels vallen in een emmer water. Toen ik omhoog keek kon ik duidelijk het verband horen en zien tussen de voetstappen van mensen die hogerop de piramide aan het beklimmen waren, en de geluiden die ik kon waarnemen. De 'voetstap-pulsen' waren blijkbaar omgevormd tot regendruppelgeluiden. Nu is het zo dat de Maya cultuur op Yucatan grotendeels verweven is met de regen, het voorspellen van regen en de regengod. Vanuit die optiek is het dan ook niet verwonderlijk dat je zulke fenomenen zou kunnen waarnemen.

Bij terugkomst, heb ik mij dus aan het werk gezet en heb ik een diffractiemodel van Claeys en Leroy voor de diffractie van oneindige en harmonische vlakke golven op een oneindig en geribbeld oppervlak, verder uitgebreid. De uitbreiding omvatte het feit dat we in Chichen-Itza te maken hebben met een sferische golf, dus geen vlakke golf, die

bovendien niet harmonisch is, maar wel gepulst en die, vooraleer ze interageert met de piramide, eerst deels met de grond interageert. Bovendien wordt die puls veroorzaakt door de aard van de bron. Tevens werden de geometrische eigenschappen van het probleem (dimensies van de piramide, positie van de waarnemer,…) alsook de fysische eigenschappen van de tropische lucht in Yucatan en van het gesteente van waaruit de treden zijn vervaardigd, in rekening gebracht.

Eerst en vooral is aangetoond, met het klassieke straal-model, dat het fenomeen geen puur Bragg fenomeen is, vermits de zogenaamde Bragglijnen niet samenvallen met de harmonieken in de sonogrammen die David Lubman (California) heeft geregistreerd. Vervolgens werd met het nieuwe model, zoals hierboven beschreven, aangetoond dat een mathematsiche puls (een delta functie) wel een gefluit teweegbrengt, maar niet dat gefluit dat ter plekke is waargenomen. Vervolgens werd aangetoond dat, indien een werkelijke handklap in het model wordt aangebracht, de echo wel nabootsbaar is en dat een voornaam deel van de echo-structuur eigenlijk te wijten is aan de reeds aanwezige harmonieken in de handklap zelf. Dus met andere woorden, het fenomeen in Chichen-Itza wordt niet enkel veroorzaakt door de treden zelf, die door hun diffractie-vermogen als het ware een ruimtelijke geluidsfilter vormen, maar ook door de aard van de geluidsbron, namelijk een handklap. Indien men bijvoorbeeld een trommel zou gebruiken als geluidsbron, dan zou de echo helemaal anders klinken, ook al gaat het telkens om een korte ‘puls’.

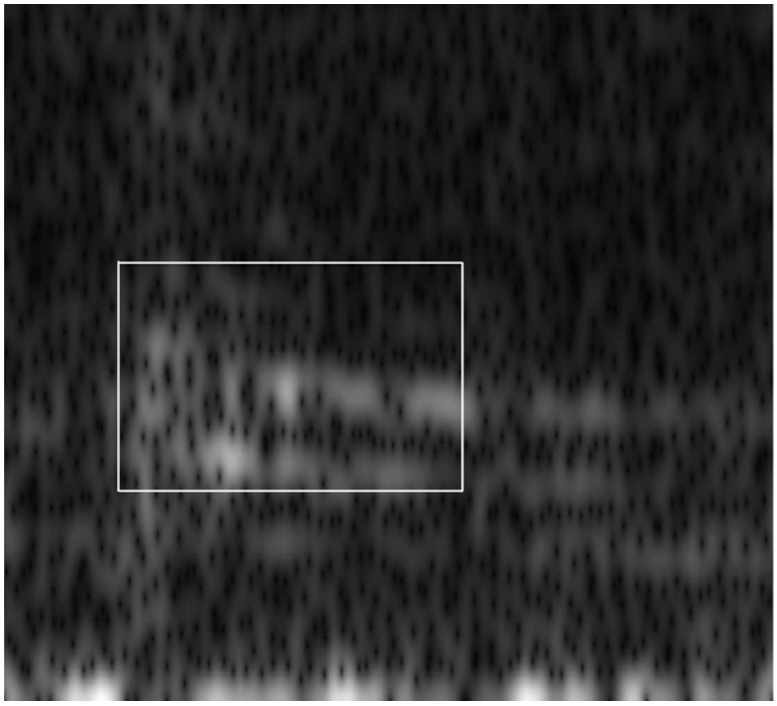

Fig. I.22 (identiek aan Fig. X.B.1_8): ***Sonogram van de geregistreerde echo aan de voet van de piramide in Chichen Itza. In deze figuur en ook in de hiernavolgende twee figuren, overspant het witte kadertje steeds hetzelfde gebied, terwijl de ganse figuur het gebied [0 Hz – 5000 Hz] bevat langs de verticale as en langs de horizontale as een tijd van 0.2 s overspant.***

Bovendien is aangetoond dat het zogenaamde regendruppel effect, dat hoger beschreven is, het gevolg is van diffractie van het geluid dat afkomstig is van voetstappen, die zich een weg banen, langsheen de trappen, naar de waarnemer onderaan de piramide.

Dus samengevat blijkt nu dat zowel de Quetzal echo als het regendruppel effect, verklaard zijn, weliswaar dankzij een nieuw en vrij omslachtig model dat qua rekentijd verschillende weken bestrijkt, vanuit fysische gronden, en dat die verklaring het raadsel van de echo enkel maar kracht bij zet. Men kan namelijk nog steeds niet met zekerheid weten of de piramide doelbewust gebouwd is om de verschillende geluiden te veroorzaken, dan wel of het hier om puur toeval gaat. Dus 'hoe' het effect ontstaat is nu onomstotelijk bewezen, maar het 'waarom' blijft een mysterie…

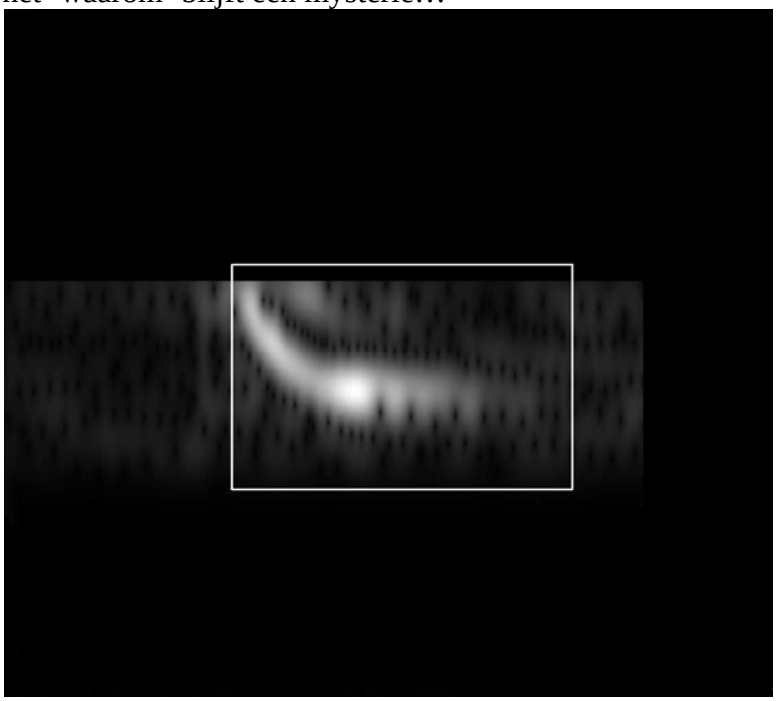

Fig. I.23 (identiek aan Fig. X.B.1_6): ***Sonogram van de gesimuleerde echo aan de voet van de piramide in Chichen Itza, volgend op een wiskundige 'delta' puls. Vergelijking met vorige figuur toont dat de lage frequenties niet in sterke mate aanwezig zijn. Vandaar de te hoge toonhoogte van de berekende echo.***

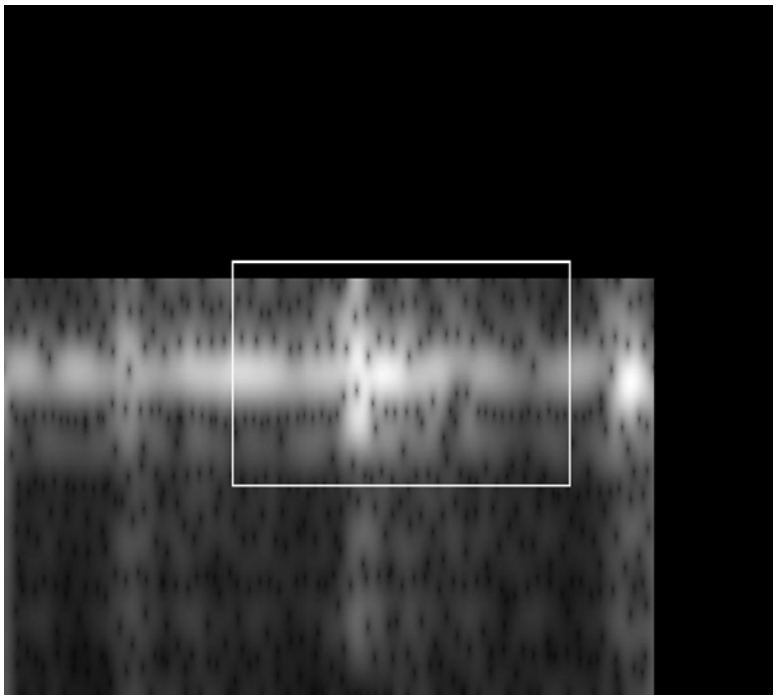

Fig. I.24 (identiek aan Fig X.B.1_11): ***Sonogram van de gesimuleerde echo aan de voet van de piramide in Chichen Itza, volgend op een echte handklap. Behalve het feit dat de simulatie door numerieke moeilijkheden niet de precieze duur van de echo kan aantonen, komen wel de lagere frequenties duidelijk naar voren. De reden is het feit dat de lagere frequenties reeds in hoge mate aanwezig zijn in de handklap zelf.***

Hoofdstuk XI Ultrasone Polaire Scans

Sectie XI.A : Ultrasone polaire scans als niet destructieve methode om vezelversterkte platen te testen en te karakteriseren.

- Joris Degrieck, Nico F. Declercq, Oswald Leroy, "Ultrasonic Polar Scans as a possible means of nondestructive testing and characterization of composite plates", **Insight - The Journal of The British Institute of Non-Destructive Testing**, 45(3), 196-201, 2003. *(Imp. Fact. 0.311; SCI-index, Materials Science – Characterization & Testing, rank:11/23)*

Ultrasone scans zijn in wezen niets anders dan de registratie van de gereflecteerde of doorgelaten amplitude van een vrij brede ultrasone bundel aan een te onderzoeken plaat, voor elke mogelijk ruimtelijke invalshoek. Een polaire scan vertoont een typisch patroon dat enerzijds bepaald wordt door de eigenschappen van de ingestraalde ultrasone bundel, en anderzijds bepaald wordt door de eigenschappen van de plaat. Daardoor is een polaire scan eigenlijk een vingerafdruk van de fysische eigenschappen van een plaat en brengt op een behoorlijke wijze de aard van de anisotropie aan het licht. Derhalve is de techniek van de polaire scans uitermate geschikt voor het karakteriseren van vezelversterkte composietplaten. De stand van zaken van ultrasone polaire scans, wordt in deze sectie uit de doeken gedaan.

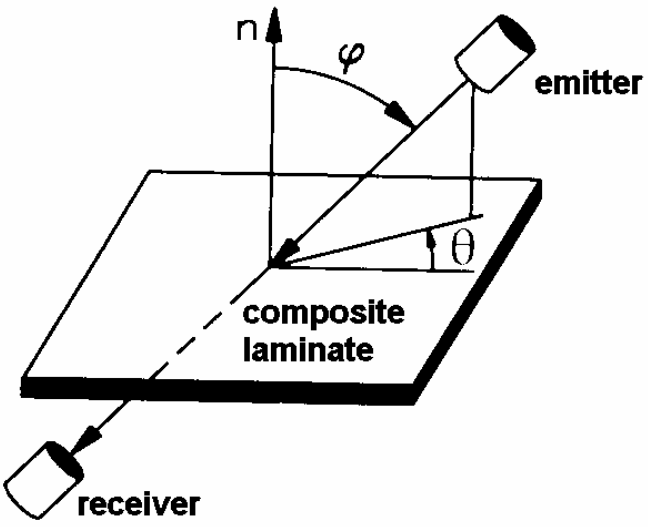

Fig. I.25 (identiek aan Fig. XI.A_1): ***In een ultrasone polaire scan wordt een bepaald gebiedje van een composietplaat ('composite laminate') bestraald met ultrageluid (afkomstig van de 'emitter' en ontvangen door de 'receiver') vanuit alle mogelijke hoeken*** (θ, φ)**.**

Sectie XI.B : Het simuleren van harmonische en gepulste polaire scans op orthotrope materialen en op meer algemene anisotrope kristallen

- Aanvaard voor publicatie in **NDT & E International** *(Imp. Fact. 0.752; SCI-index, Materials Science – Characterization & Testing, rank:3/23)*
- Mondelinge presentatie tijdens '3rd International Conference on Emerging Technologies in Non-Destructive Testing & Technology Transfer and Business Partnership Event', **Thessaloniki**, Griekenland, mei 26-28, 2003.

Voor 2001 was een 'polaire scan'-opstelling binnen onze vakgroep voorhanden en was het mogelijk om polaire scans te simuleren voor éénlagige orthotrope materialen. Aangezien vrijwel alle composieten meerlagig zijn en aangezien het af en toe voorkomt dat composieten een andere anisotropie bezitten dan orthotropie, was de oorspronkelijke doelstelling van dit werk de nodige modellering te ontwikkelen zodat ook polaire scans op zulke composieten te simuleren waren. De resultaten van deze studie en de wijze van modelleren, staan beschreven in de huidige sectie. Naast orthotrope materialen, is het nu ook mogelijk om elk mogelijk anisotroop materiaal aan een polaire scan te onderwerpen en de polaire scan te simuleren. Als voorbeelden komen bariumtitanaat aan bod en ook galliumarsenide. Gelijk welke oriëntatie van de kristallen kan in rekening worden gebracht. Bovendien kunnen verschillende kristallen gestapeld worden onder gelijk welke oriëntatie.

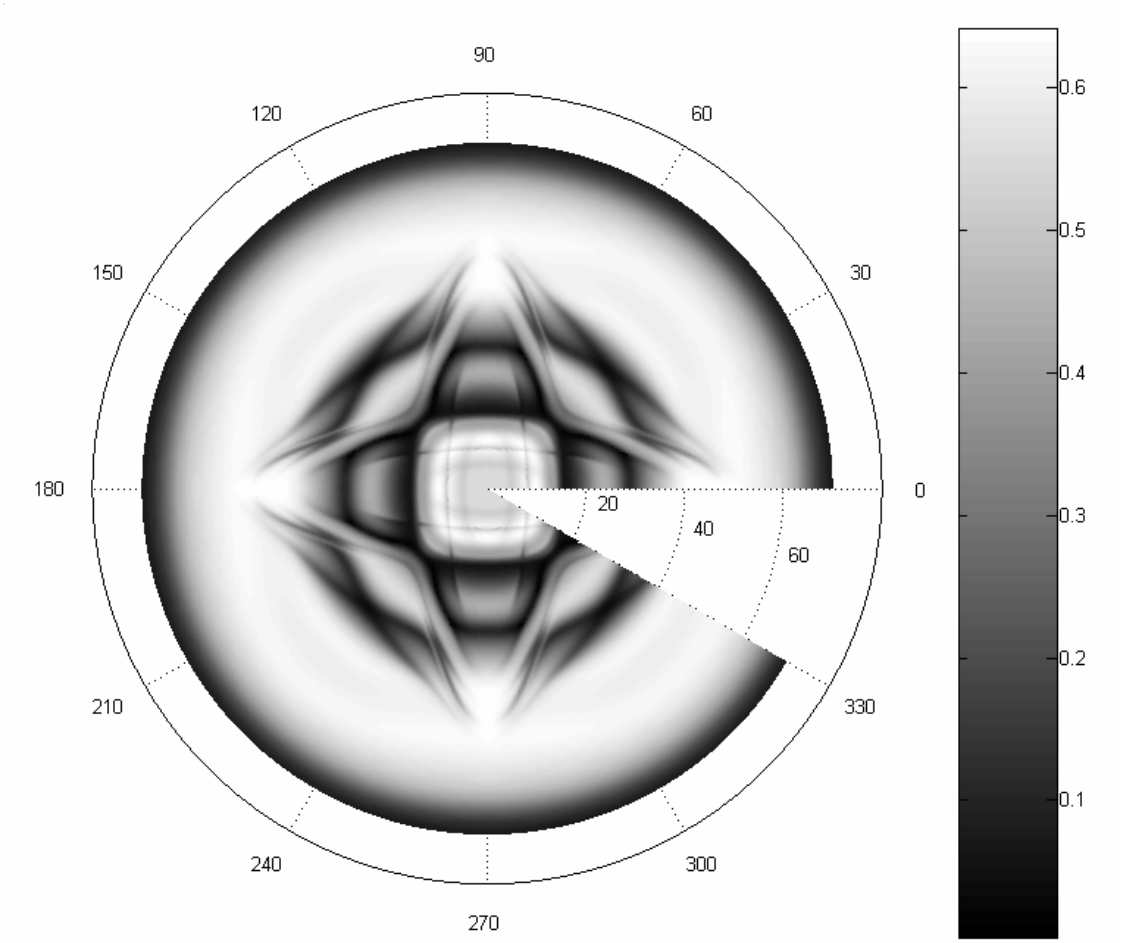

Fig. I.26 (identiek aan Fig. XI.B_10): ***gesimuleerde ultrasone polaire scan in transmissie op een 1mm dik, 10-lagig (0^0/90^0) 'cross ply' vezelversterkt composiet bij 5MHz.***

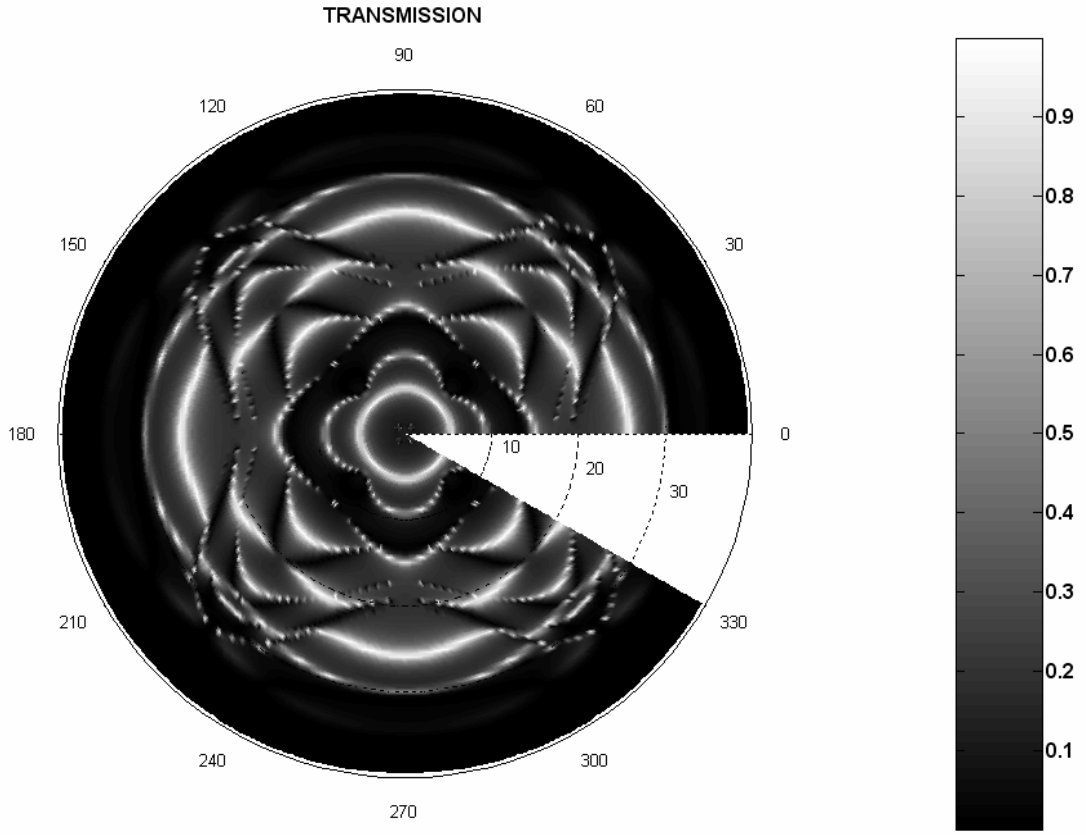

Fig. I.27 (identiek aan Fig. XI.B_15): ***gesimuleerde ultrasone polaire scan in transmissie op een 3mm dik, barium titanaat (z-cut) kristal, bij 2 MHz.***

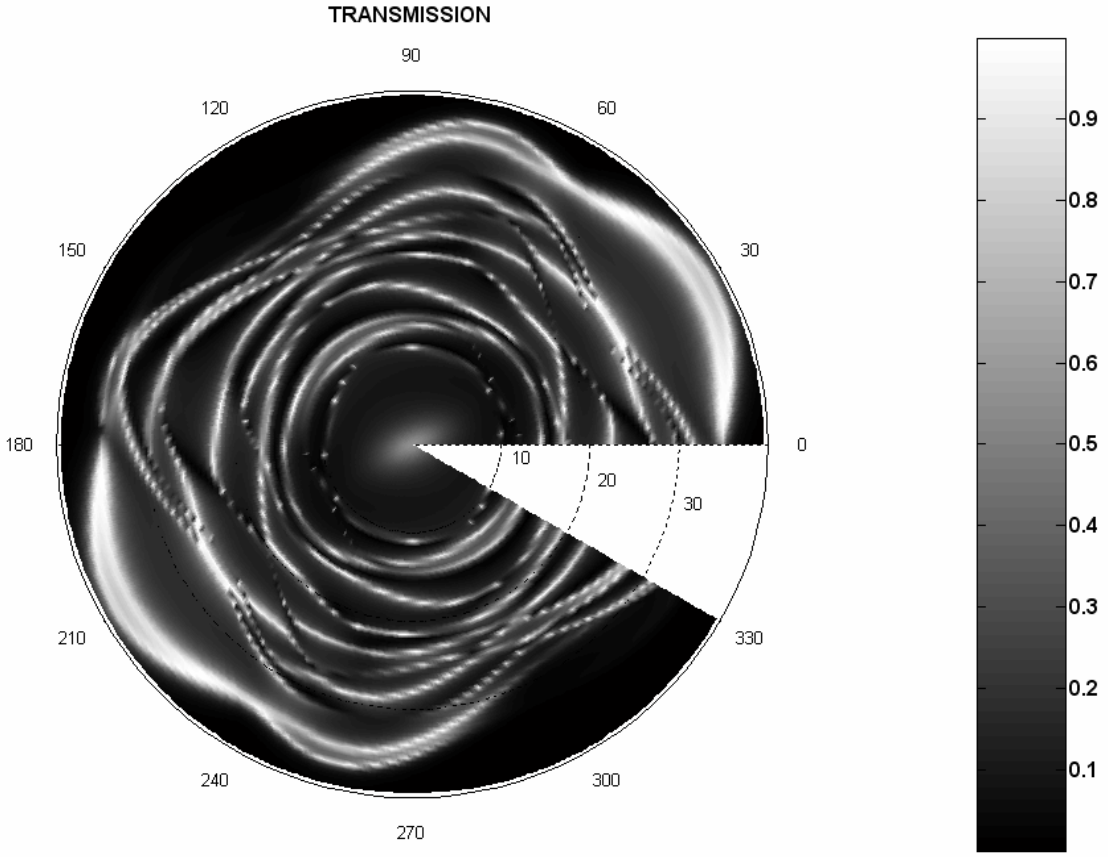

Fig. I.28 (identiek aan Fig. XI.B_26): ***gesimuleerde ultrasone polaire scan in transmissie op een 3mm dik, gelaagd kristal, bestaande uit een laag bariumtitanaat en een laag galliumarsenide met een willekeurig gekozen oriëntatie, bij 2 MHz.***

Sectie XI.C : Over de invloed van vermoeiing op ultrasone polaire scans op vezelversterkte composieten

- Nico F. Declercq, Joris Degrieck, Oswald Leroy, " On the influence of fatigue on ultrasonic polar scans of fiber reinforced composites", Ultrasonics 42, 173-177, 2004. *(Imp. Fact. 0.844; SCI-index, Acoustics, rank:11 /28)*
- Mondelinge presentatie tijdens 'Ultrasonics International 2003', **Granada**, Spanje, 30 juni- 3 juli 2003

Binnen onze vakgroep gebeurt ook onderzoek naar vermoeiing van composieten. Eén van de gevolgen van vermoeiing is het optreden van een verminderde stijfheid. Aangezien ultrasone polaire scans in belangrijke mate bepaald worden, precies door de stijfheid van het onderzochte materiaal, is het evident dat ze kunnen ingezet worden om vermoeiing op te volgen. Deze studie toont dan ook expliciet aan dat het zowel experimenteel als theoretisch mogelijk is (met vrij goede overeenstemming) om vermoeiing op te volgen in een vezelversterkt composiet. Dit is zeer belangrijk in vele takken van de industrie waar

composieten aan vermoeiing onderhevig zijn, zoals in de luchtvaartindustrie, de scheepsbouw, de controle van windmolens, enzovoort…

Sectie XI.D : Een numerieke studie van de haalbaarheid om spanning te visualiseren in isotrope platen met gebruik van de gereflecteerde amplitude van harmonische golven

- Mondelinge presentatie tijdens 'InterNoise2003', International Convention Center Jeju, **Seogwipo**, Korea, augustus 25-28, 2003

Heel veel materialen zijn onderhevig aan residuele spanningen, die meestal het gevolg zijn van het fabricageproces. Daarenboven zijn zo goed als alle materialen, eens ze een onderdeel vormen van een bepaalde constructie, onderhevig aan aangelegde spanningen. Bovendien kunnen elk van de genoemde spanningen plaatsafhankelijk zijn, waardoor het aangewezen is om lokaal na te gaan wat de spanningen zijn. Aangezien de polaire scan bepaald wordt door de lokale stijfheden op de plaats van uitvoering op een bepaald materiaal, lijkt de polaire scan een mogelijk middel om die spanningen in kaart te brengen. Voor die reden werd nagegaan, via numerieke simulatie, in welke mate de polaire scan gevoelig is aan spanningen. De modellering werd volledig uitgevoerd voor anisotrope materialen, in tegenstelling tot heel wat modellen in de literatuur die enkel isotrope materialen in beschouwing nemen. De reden is het feit dat zelfs isotrope materialen, anisotroop kunnen worden door de aanwezigheid van spanningen. De berekeningen voor een isotrope plaat tonen aan dat, net zoals de intuïtie dit verwacht, isotrope platen de isotropie in het vlak van de plaat behouden bij loodrechte spanningen (ten opzichte van de plaat) en dat spanningen in het vlak van de plaat het isotrope materiaal anisotroop maken. Bovendien wordt aangetoond dat de gevolgen van spanningen voor een polaire scan niet spectaculair zijn, behalve voor vrij hoge spanningen.

Hoofdstuk XII Geluid in piezo-elektrische materialen

Sectie XII.A : Het effect van verstijving van kristallen als gevolg van piezo-elektriciteit.

Ofschoon dit in den beginne absoluut niet gepland was, kon ik niet weerstaan aan de verleidelijke lokroep van de natuurlijke schoonheid van kristallen die een mysterieus piezo-elektrisch karakter bezitten dat een opmerkelijke invloed heeft op de stijfheid. Dit laatste induceert in belangrijke mate een richtingsafhankelijke snelheidswijziging van het geluid in deze materialen. Vandaar dat in deze sectie het piezo-elektrisch effect wordt beschreven en dat op grafische wijze wordt duidelijk gemaakt wat de invloed is van piezo-electriciteit op de stijfheid van kristallen, en dus op de traagheidskrommes voor vlakke golven die zich voortplanten in het beschouwde materiaal. De voorstellingswijze toont het verschil in traagheid voor elke richting en is uniek. Bovendien worden aan de berekende traagheidsverschil-oppervlakken pijltjes toegevoegd die, hetzij de wijziging van de

energieflux weergeven, hetzij de wijziging van de polarisatie.

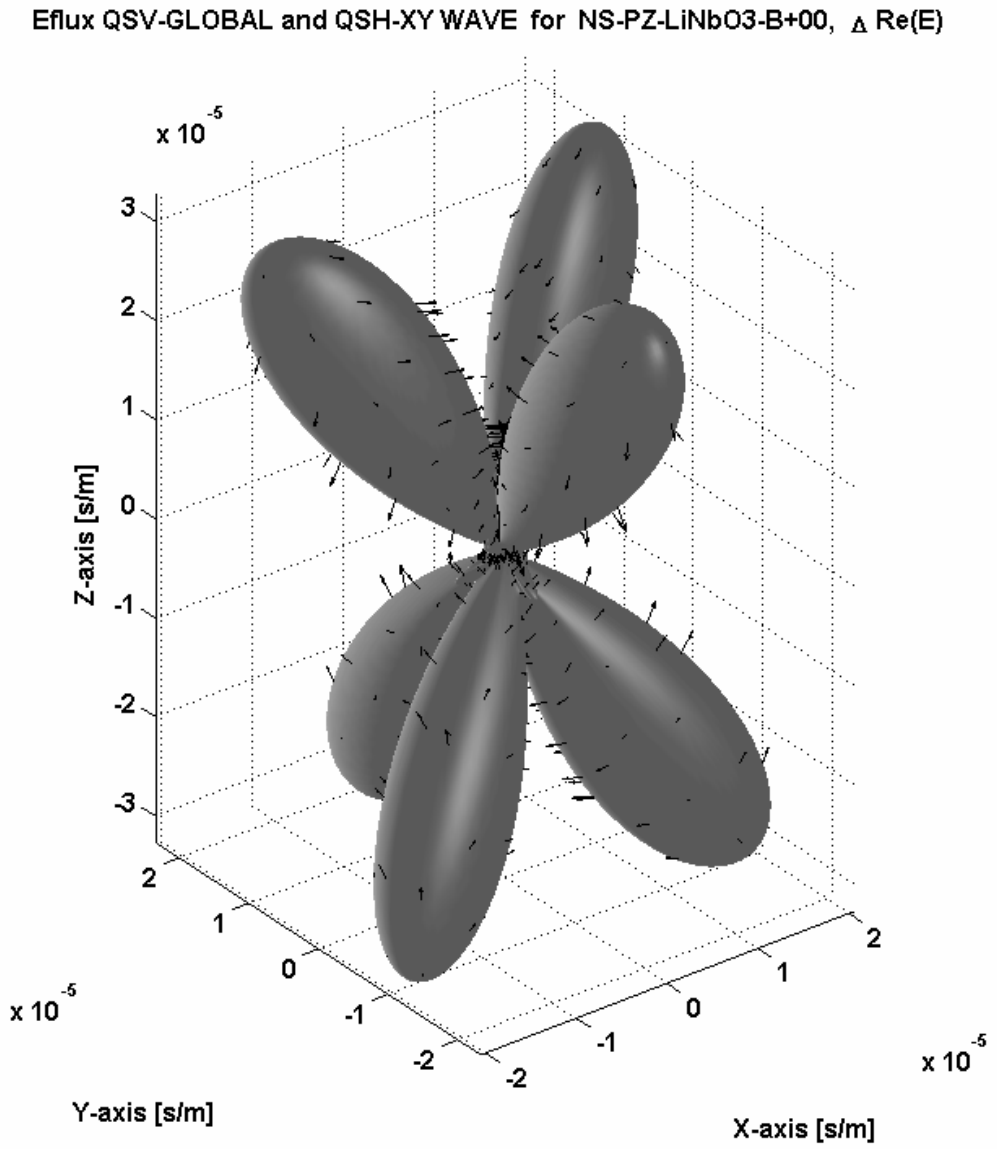

Fig. I.29 (identiek aan Fig. XII.A_5): ***het verschil tussen het traagheidsoppervlak voor de zogenaamde QSV-mode in lithiumniobaat met inbegrip van het piezo-elektrisch effect en met verwaarlozing van het piezo-elektrisch effect. De zwarte pijlen duiden het verschil in energieflux aan.***

Sectie XII.B.1 : Inhomogene golven in piezo-elektrische materialen

In de vele voorgaande secties wordt hier en daar onderzoek beschreven op inhomogene golven. Niet in deze secties, noch in de verschenen literatuur, wordt het gedrag van inhomogene golven bestudeerd in piezo-elektrische kristallen. Vandaar dat in de huidige sectie een studie wordt uiteengezet die het gedrag van inhomogene golven beschrijft en die

de gevoeligheid voor het piezo-elektrisch effect nagaat. Er wordt onder meer aangetoond dat inhomogene golven gevoeliger zijn voor het piezo-elektrisch effect dan klassieke homogene vlakke golven.

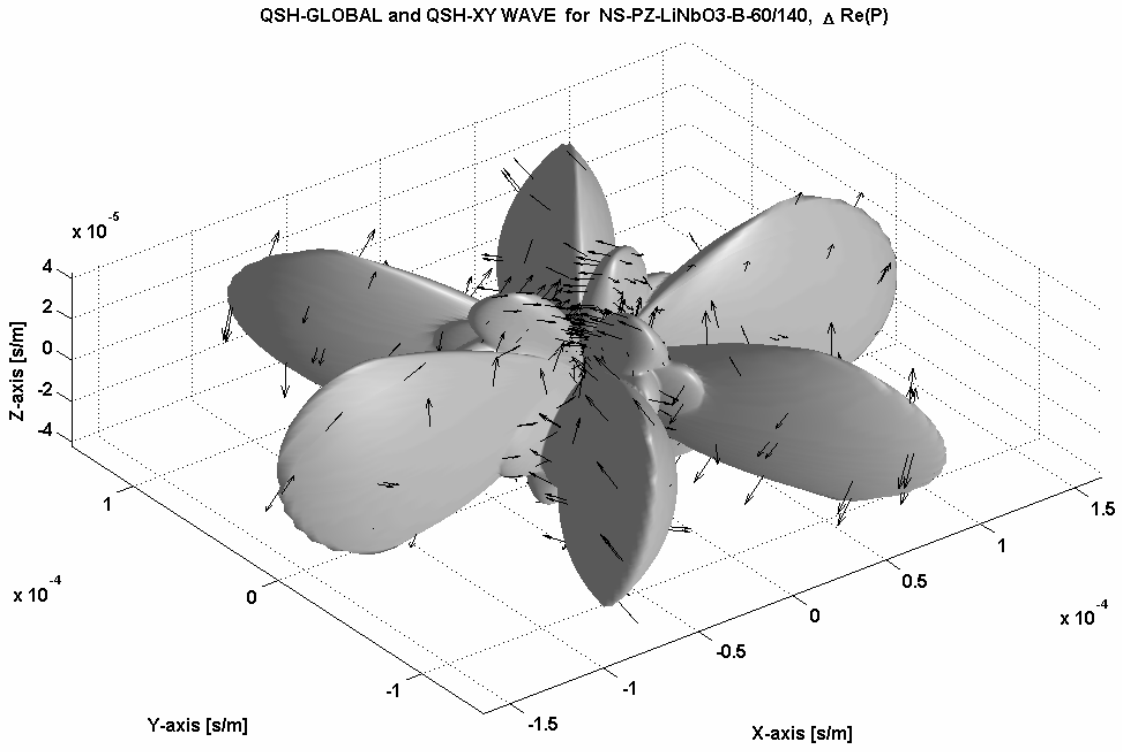

Fig. I.30 (identiek aan Fig. XII.B.1_12): ***het verschil tussen het traagheidsoppervlak voor de zogenaamde QSH-mode in lithiumniobaat met inbegrip van het piezo-elektrisch effect en met verwaarlozing van het piezo-elektrisch effect, voor inhomogene golven. De pijlen duiden het verschil in polarisatie aan.***

Sectie XII.B.2 : Versterkte anisotropie in paratellurium voor inhomogene golven en het mogelijke belang voor de toekomstige ontwikkeling van acousto-optische cellen

In acousto-optics wordt de interactie van licht met geluid bestudeerd. Deze tak van de wetenschap heeft veel toepassingen, vooral in het gebied van de optische informatieverwerking, in elektronische filters enzovoort. Een van de tegenwoordig vaak gebruikte kristallen om acousto-optische cellen mee te bouwen, is paratellurium. Een van de redenen is de hoge efficiëntie, die mede wordt veroorzaakt door de zeer sterke anisotropie van deze kristallen. Deze anisotropie wordt weerspiegeld in een zeer sterke richtingsafhankelijkheid van de geluidssnelheid. In deze sectie wordt aangetoond dat, indien inhomogene golven worden beschouwd in plaats van klassieke homogene vlakke golven, dat dan die sterke richtingsafhankelijkheid nog aangewakkerd wordt, waardoor

aanwijzingen ontstaan dat de kwaliteit van paratellurium in acousto-optische cellen nog verder kan uitgebuit worden door gebruik te maken van inhomogene golven.

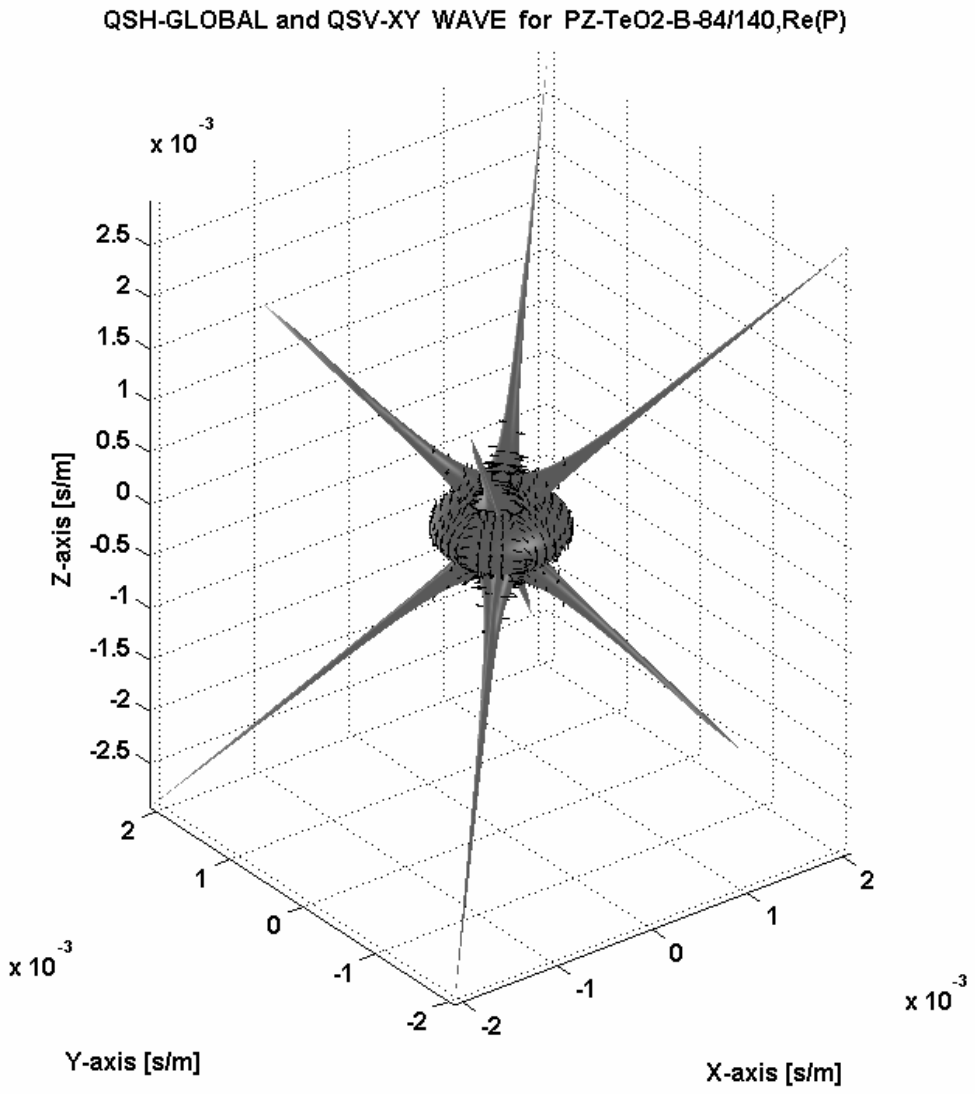

Fig. I.31 (identiek aan Fig. XII.B.2_11): traagheidsoppervlak voor de zogeheten QSH-mode in paratellurium, indien inhomogene golven worden beschouwd. Het bolvormig patroon, voorzien van uitgesproken 'naalden', legt een extreem sterke richtingsafhankelijk van de golfsnelheid bloot. Dit is een heel belangrijke eigenschap die mogelijk in de toekomst de kwaliteit van acousto-optische cellen verder kan opdrijven.

<u>Sectie XII.C</u> : Geluid in voorgespannen piezo-elektrische materialen van gelijk welke anisotropie.

- Mondelinge presentatie tijdens 'ICA2004 18th International Congress on Acoustics', Kyoto International Conference Hall, **Kyoto**, Japan, 4-9 april 2004

Onderzoek werkt zeer verslavend. Enerzijds wil men steeds meer begrijpen, anderzijds

wil men de moeilijkheidsgraad van datgene wat men begrijpt, steeds verhogen. Deze verslaving ligt aan de basis om ook voorgespannen piezo-elektrische materialen te bestuderen. Het probleem met voorgespannen piezo-elektrische materialen is dat zowel de elastische als de elektrische eigenschappen geconditioneerd worden door het aangelegde spanningsveld of door het aangelegde elektrische veld. Bovendien treedt dit fenomeen op in kristallen, wiens anisotropie meestal niet van het eenvoudigste type is. Dit alles maakt het probleem des te aantrekkelijker om te doorgronden. Aangezien conditioneringvelden over het algemeen beduidend zijn en dus veel groter dan de typische velden die een akoestische golf met zich meebrengt, dient bovendien rekening te worden gehouden met niet-lineaire effecten tijdens de conditionering. Dit maakt dat ook hogere-orde materiaalconstanten hun intrede doen, wat het leven alleen maar leuker maakt.

De huidige sectie presenteert een veralgemeende vergelijking van Christoffel, die geldig is in het geval van voorgespannen piezo-elektrische kristallen die gelijk welke anisotropie kunnen bezitten. Deze vergelijking wordt verkregen door het geluidsveld te beschouwen in een systeem dat via niet-lineaire eigenschappen is geconditioneerd door zowel een aangelegde spanning als een aangelegd elektrisch veld. Voorts wordt een uitdrukking gegeven voor de energieflux in dit gecompliceerde geval. Er worden numeriek resultaten gerapporteerd voor Lithiumniobaat. De symmetrierelaties voor de lineaire en de hogere orde materiaalconstanten worden berekend op grond van het invariant gedrag van de materiaaleigenschappen onder de specifieke symmetrierelaties voor dit kristal. De invloed van een aangelegde spanning wordt berekend zowel met inbegrip als met verwaarlozing van piezo-elektriciteit, zowel voor homogene als voor inhomogene golven. Bovendien wordt de invloed nagegaan van zowel de grootte als de richting van de aangelegde spanning. De bekomen wiskundige uitdrukkingen zijn zo omvangrijk, dat ze, om deze samenvatting binnen de perken te houden, hier niet worden opgenomen.

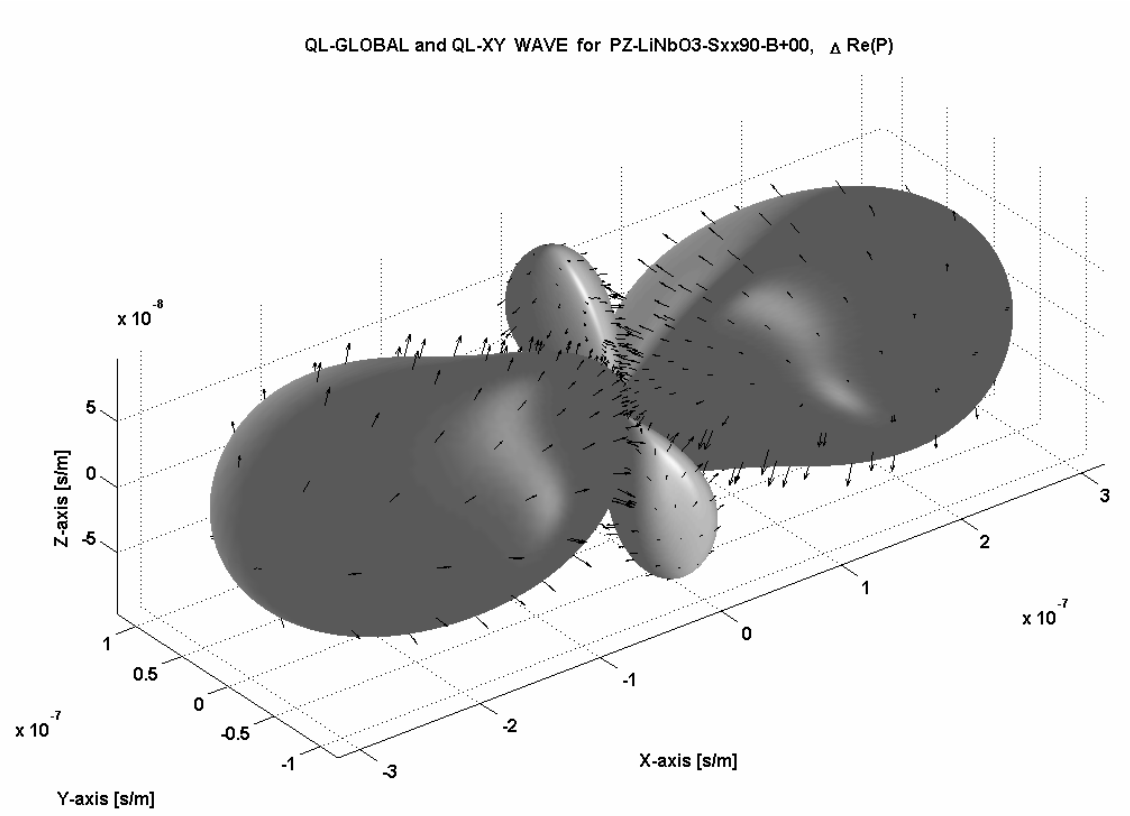

Fig. I.32 (identiek aan Fig. XII.C_2): ***De verandering van het traagheidsoppervlak voor de zogeheten QL-mode, in aanwezigheid van een aangelegde spanning van 90 MPa langs de x-richting, in het geval van piezo-elektrisch lithiumniobaat. De zwarte pijltjes duiden de verandering van de polarisatie aan.***

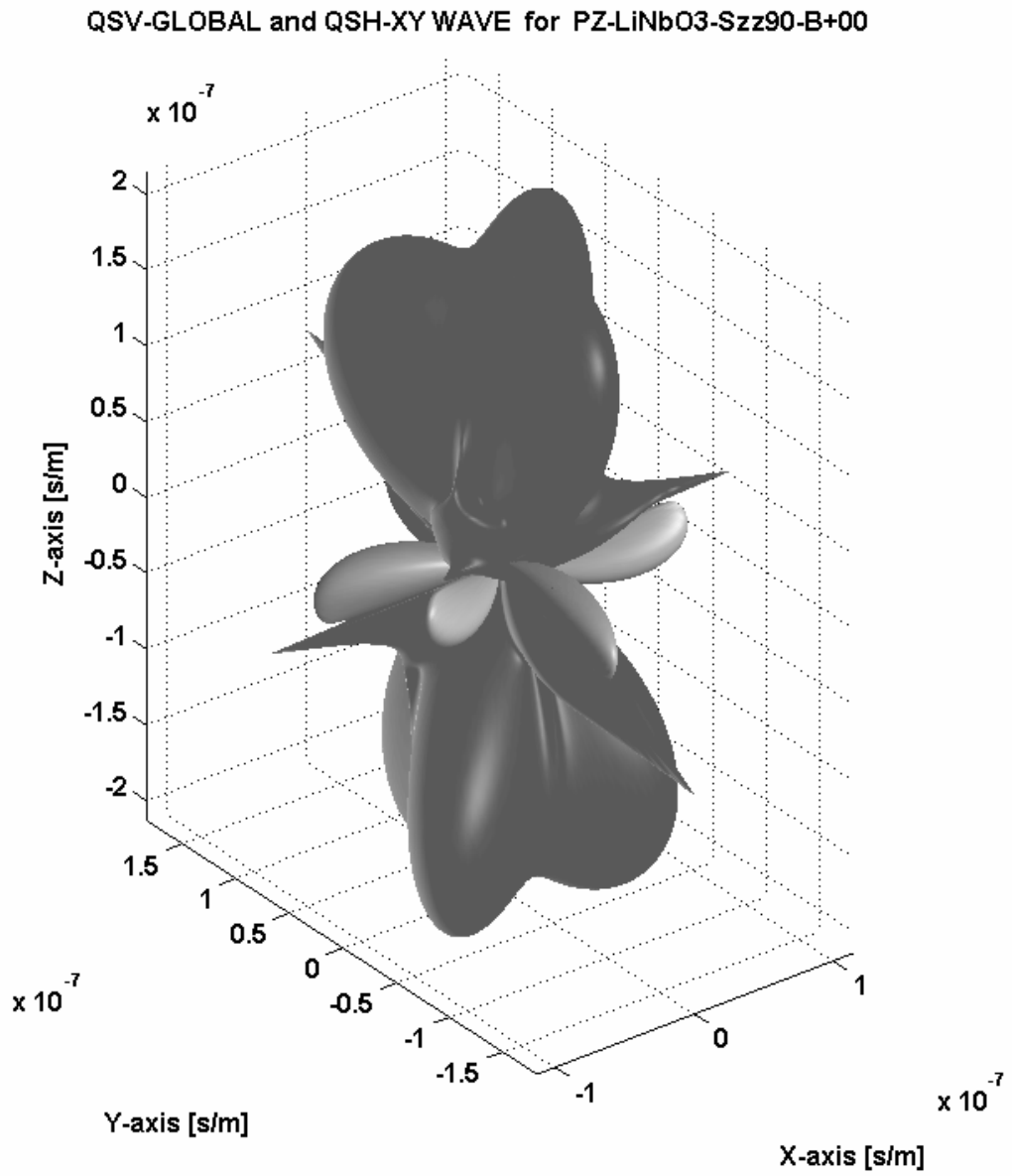

Fig. I.33 (identiek aan Fig. XII.C_18): ***De verandering van het traagheidsoppervlak voor inhomogene golven voor de zogeheten QSV-mode, in aanwezigheid van een aangelegde spanning van 90 MPa langs de z-richting, in het geval van piezo-elektrisch lithiumniobaat.***

Hoofdstuk XIII Akoestische microscopie

<u>Sectie XIII.A</u> **: Microscopische beeldvorming van het inwendige van vezelversterkte composieten**

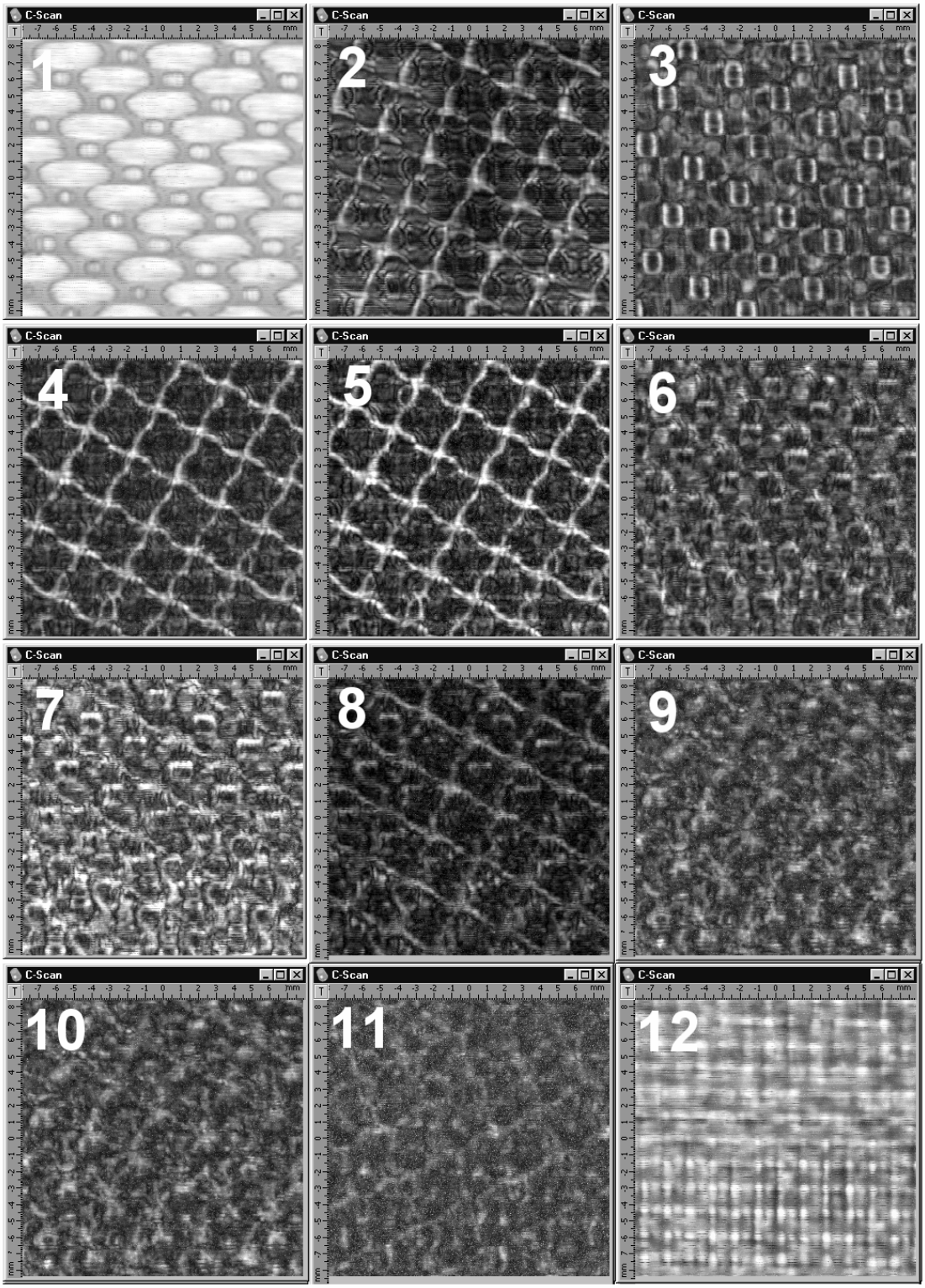

Fig. I.34 (identiek aan Fig. XIII.A_13): ***C-scan beelden op verschillende dieptes, beginnende met het bovenvlak (#1) en eindigend met het beeld van de bodemzijde (#12), voor een unidirectioneel, met een koolstofweefsel versterkt, composiet, gemaakt uit polyfenylsulfide (PPS). Het is duidelijk dat niet enkel de oppervlaktestructuur bestudeerd kan worden, maar ook het interne en zelfs de onderkant van de plaat.***

Klassieke C-scans zijn in staat om ‘over de diepte uitgemiddelde’ eigenschappen van dunne composietlaminaten te onderzoeken. Alhoewel C-scans zeker en vast zeer nuttig zijn, is het in vele gevallen echter noodzakelijk om ook dieptegevoelige informatie over composietlaminaten te begroten. Het is bijvoorbeeld niet enkel noodzakelijk om te weten dat ergens in een composiet een delaminatie optreedt, maar het is tevens belangrijk om te weten hoe diep precies in de plaat die delaminatie optreedt. Bovendien is het nuttig om in de verschillende laagjes van een composiet na te gaan hoe de vezelstructuur eruitziet, of er leegtes of harsophopingen aanwezig zijn, of er barstjes aanwezig zijn enzovoort. Al deze eisen nodigen het gebruik van microscopietechnieken uit. Echter, klassieke akoestische microscopie maakt gebruik van sterk gefocusseerde en zeer hoogfrequente ultrasone bundels, die uitermate geschikt zijn om het oppervlak te onderzoeken en niet zozeer het binnenste van een plaat. Daarom werd de laatste jaren een microscoop gebouwd in een laboratorium in Moskou, die het principe van een C-scan combineert met technologie uit de akoestische microscopie. Het verschil met klassieke microscopie is dat men slechts weinig gefocusseerde ultrasone bundels opwekt en dat de gebruikte frequenties net hoog genoeg zijn om voldoende resolutie te bekomen in de diepte van de plaat, zonder daarom de zeer hoge frequenties te bereiken die men in de klassieke microscopie gebruikt. Bovendien wordt gebruik gemaakt van geoptimaliseerde technologie om de geproduceerde akoestische puls extreem kort te maken, wat de resolutie uiteraard op een cruciale wijze verbetert. In dit labo werden door de auteur experimenten verricht op verschillende soorten vezelversterkte composieten met de bedoeling om na te gaan in welke mate de techniek geschikt is om de structuur van composieten in beeld te brengen. Het is de bedoeling dat later met die techniek de schadevorming in composieten door vermoeiing en door impact, kan worden onderzocht.

Hoofdstuk XIV Exotische onderwerpen

Sectie XIV.A : Dubbelzijdige ultrasone bundelverschuiving

- Nico F. Declercq, Joris Degrieck, Oswald Leroy, "The Double Sided Ultrasonic Beam Displacement", **Appl. Phys. let.** 85(18), 4234-4236, 2004 *(Imp. Fact. 4.207; SCI-index, Physics-Applied, rank:3/76)*

In het ultrasoon onderzoek is het zogenaamde Schoch fenomeen een welbekend fenomeen dat het gevolg is van de opwekking van Rayleigh golven of de opwekking van Lambgolven. Bij dit fenomeen wordt het profiel van een gereflecteerde bundel zodanig vervormd, dat er een voorwaarts verschoven deel ontstaat, samen met een niet-verplaatst gedeelte. De beide delen zijn van elkaar gescheiden door een geluidsarme zone. In hoofdstuk X van dit werk wordt ook het fenomeen van de achterwaartse verschuiving verklaard bij de diffractie op een ruw oppervlak. Echter, een situatie waarbij zowel een voorwaarts verschoven deel als een achterwaarts verschoven deel ontstaat, was totnogtoe niet gekend. In deze sectie wordt aangetoond, zowel experimenteel als numeriek, dat het ontstaan van een dubbelzijdige ultrasone bundelverschuiving, waarbij dus zowel een voorwaarts als een achterwaarts verschoven gereflecteerde bundel ontstaan, mogelijk is, onder specifieke, bijna toevallige omstandigheden. Het fenomeen kan namelijk ontstaan in een dunne glasplaat, wanneer onder precieze omstandigheden Lambgolven worden opgewekt.

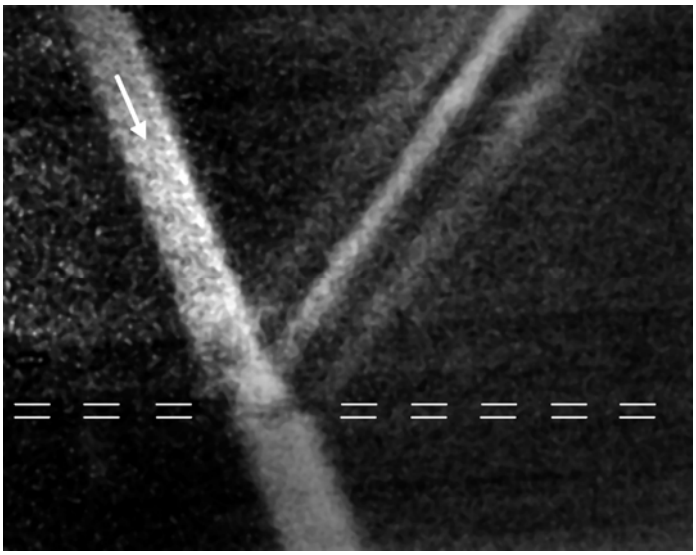

Fig. I.35 (identiek aan Fig. XIV.A_2): De dubbelzijdige bundelverschuiving. In het gereflecteerde profiel zijn zowel een achterwaarts verplaatste als een voorwaartse verplaatste bundel zichtbaar, naast een centrale bundel. De witte stippellijnen komen precies overeen met de bovenkant en de onderkant van de glasplaat.

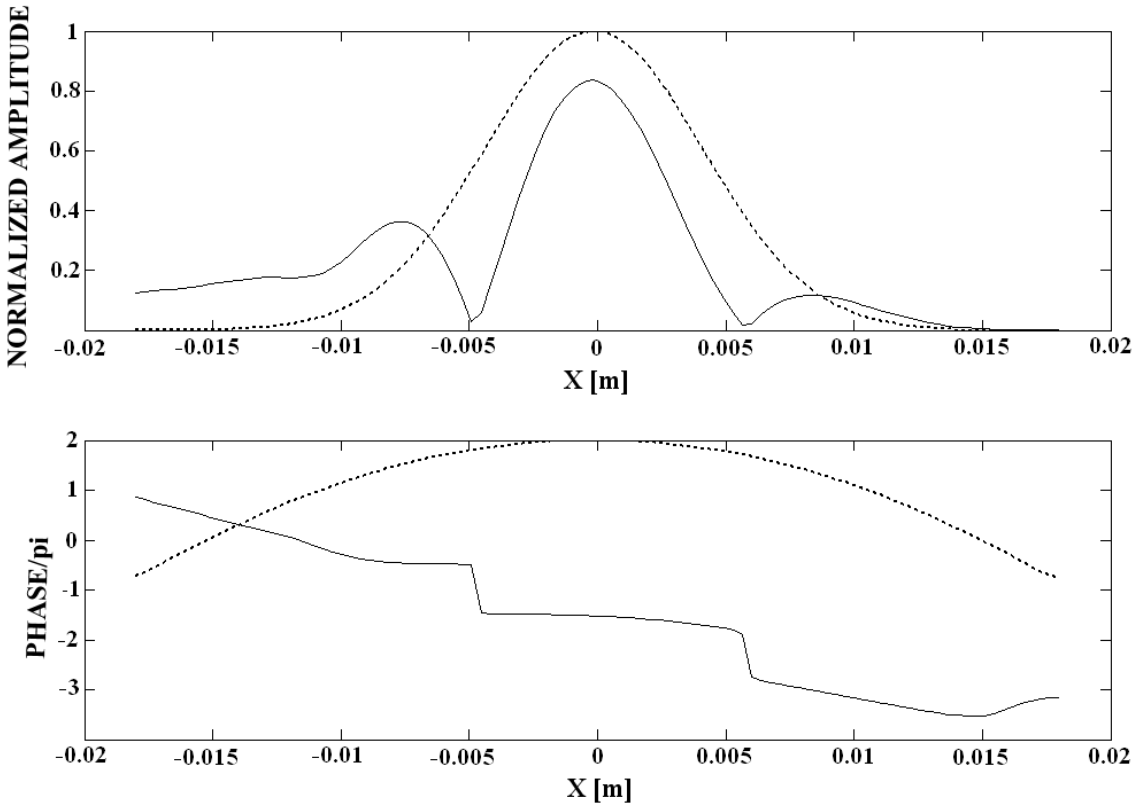

Fig. I.36 (identiek aan Fig. XIV.A_5): Simulering van de dubbelzijdige bundelverschuiving uit Fig. I.35. De stippellijn komt overeen met het invallend profiel, terwijl de volle lijn het gereflecteerde profiel voorstelt. De verticale as in bovenste deel van deze figuur geeft de amplitude weer, terwijl de verticale as in het onderste gedeelte de fase weergeeft. De horizontale as is de afstand tot het centrum van de bundel.

Hoofdstuk XV Conclusies en vooruitzichten

Gedurende de voorbije drie jaren zijn verscheidene waardevolle resultaten bereikt die gebundeld zijn in deze thesis. Het doel van een onderzoeker bestaat er echter in om de natuur te proberen te begrijpen en om de verworven kennis met de mensheid te delen. Het doel van een wetenschapper mag niet bestaan uit het nastreven van een palmares. Vandaar dat deze wettelijk verplichte Nederlandstalige samenvatting het gevaar in zich houdt om een palmares op te sommen, eerder dan de zuivere geest van wetenschappelijk onderzoek te reflecteren. Daarom zou het mij een plezier doen mocht de lezer de inhoud van de thesis, eerder dan deze beknopte samenvatting, koesteren.

Wat de vooruitzichten betreft, heb ik slechts twee aspecten in de hand en die hebben spijtig genoeg een onvoldoende vermogen om een heldere blik op de toekomst te werpen. Die twee aspecten zijn enerzijds mijn liefde voor de natuur en de bijhorende nieuwsgierigheid en anderzijds de vele potentiële toekomstplannen om zowel breed als diepgaand onderzoek te (blijven) verrichten.

Chapter II Introduction

My admiration for waves originates from the observation of sea waves in Sri Lanka in June 1997. Nevertheless, the destructive power of waves on that same spot on December 26, 2004, when a tsunami hit, destroying the lives of too many people, has uncovered the dark side of the sea. The message of the tsunami was loud and clear : "Nature gives and Nature takes! Scientists can only observe and attempt to understand."

This dissertation is the result of my research that started in October 2001. Prior to October 2001, I have written a Master's thesis under the supervision of Rudy Briers and Oswald Leroy, entitled "A theoretical treatment of the diffraction of linear and circular polarized ultrasonic plane waves at a periodically rough solid-liquid interface" (Institute of Astronomy, Department of Physics, KU Leuven, 2000). After my graduation in the summer of 2000, I have developed my background in acoustics as a volunteer researcher in the *Research Group on Physical Acoustics and Acousto-Optics* (KU Leuven Campus Kortrijk) of Oswald Leroy, under Leroy's promotership and the co-promotership of Rudy Briers and Joris Degrieck. After Leroy's retirement, I have joined the research team of Joris Degrieck (*Department of Mechanical Construction and Production*, Ghent University), under Degrieck's promotership and the co-promotership of Oswald Leroy. My salary has been paid since October 2001 by the IWT, for which I'm very grateful! So far, my work has resulted in 25 published/accepted papers in international journals of Thomson's science citation index. Furthermore, I've had the pleasure to make over 40 presentations at congresses all over the world. Professionally, this output is mainly the result of a motivation, coming from the collegial atmosphere at international conferences (following strict deadlines), as well as from the mutual respect for my promoters and colleagues.

Each chapter of this dissertation contains a number of sections. I have intended to make every section self-contained. This means that there are no cross references between different sections and it also means that, from time to time, short explanations or one or two figures are repeated. The reason for this is the ease to read the dissertation in relative short portions, which is a necessary requirement in nowadays academic world, overloaded by meetings and administration.

The sequence of chapters does not necessarily reflect the temporal development. Nevertheless, it is attempted to follow a constructive series, in which each chapter makes the consecutive pieces better understandable and each chapter makes the preceding portions better understood.

Chapter III English Summary

The style of this dissertation is such that each section, of every chapter, forms a unit that can possibly be understood independent from the other parts. The reason is that people who are interested in one certain section, do not necessarily like to read the whole work.
The current chapter presents a short summary of the remaining chapters. The summary mainly focuses on listing the results, rather than presenting the entire study itself.

Chapter IV Inhomogeneous waves and bounded beams

Section IV.A : The history and properties of ultrasonic inhomogeneous waves

- Accepted for publication in **IEEE Transactions on Ultrasonics, Ferroelectrics, and Frequency Control** *(Imp. Fact. 1.595 ;SCI-index, Engineering – electrical & electronic, rank:46/205)*
- Invited Oral presentation at: plenary session, 'VII International Conference for Young Researchers on Wave Electronics and its Applications in Information and Telecommunication Systems', **St Petersburg**, Russia , 12-15 September 2004
- Oral presentation at '75th Anniversary Celebration of the Acoustical Society of America (147th meeting of the Acoustical Society of America), Sheraton New York Hotel and Towers, New York, **New York**, USA, 24-28 May 2004

Inhomogeneous waves are generalized plane waves. They are described as classical plane waves, except that the wave parameters, such as the wave vector, are complex valued. The Americans have been the first to publish features of this kind of waves, but the theory was ultimately developed in Europe. This development was boosted after it was shown that inhomogeneous waves form a natural stimulus for surface waves. Nevertheless, the idea of inhomogeneous waves remained a mathematical 'artifact', even though experiments showed how these waves can be generated and showed that their behavior corresponds to theory. In this chapter, a historical overview is presented, together with an overview of the properties of inhomogeneous waves. This overview is likely to form the final breakthrough of inhomogeneous waves into the world of acoustics. Furthermore, for the first time in history, it is shown how the complex Lame parameters can be fully expressed in terms of intrinsic acoustic parameters such as damping and sound velocity.

Section IV.B : The principle of a chopped series equilibrium to determine the expansion coefficients in the inhomogeneous waves decomposition of a bounded beam

- Nico F. Declercq, Joris Degrieck, Oswald Leroy, "The Principle of a Chopped Series Equilibrium to Determine the Expansion Coefficients in the Inhomogeneous Waves Decomposition of a Bounded Beam", **Acta Acustica United with Acustica** 89, 1038-1040, 2003. *(Imp. Fact. 0.346; SCI-index, Acoustics, rank:21 /28)*
- Oral presentation at 'the 8th Western Pacific Acoustics Conference (Wespac8)', **Melbourne**, Australia, 7-9 April, 2003.

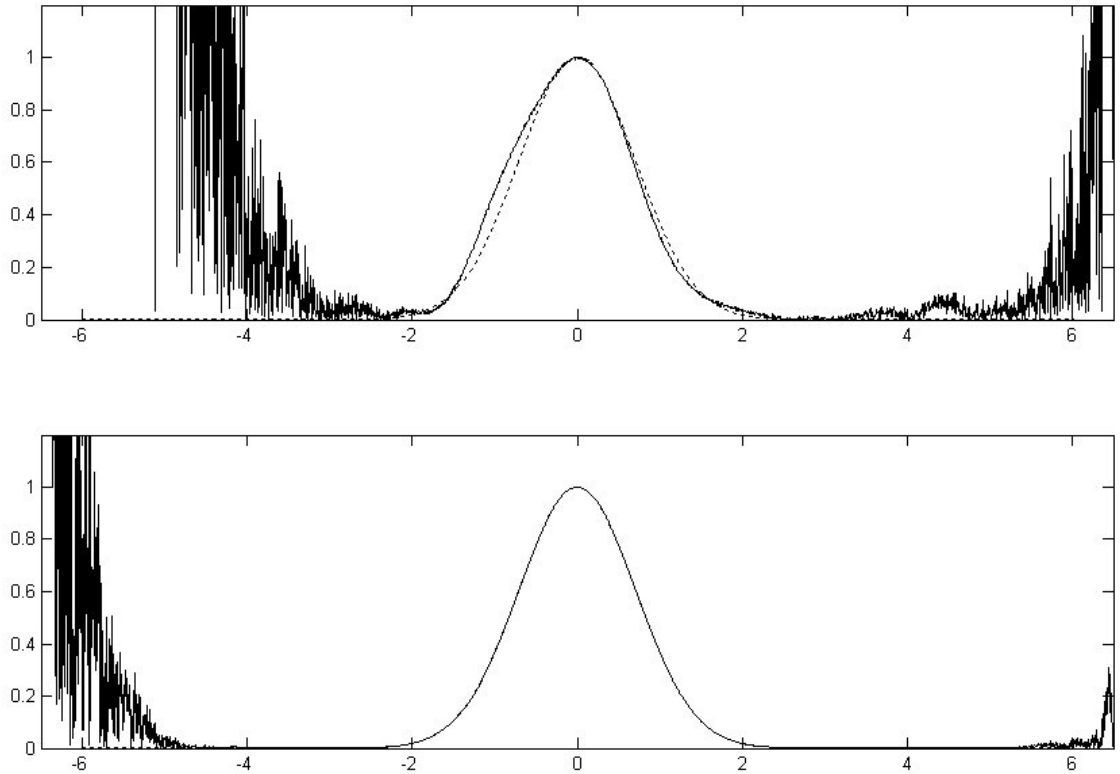

Fig. III.1 (identical to Fig IV.B_2): The horizontal axis is the distance to the center of the beam, divided by the Gausian beam width, whereas the vertical axis is the amplitude. This figure shows an extreme situation of a badly conditioned optimization. The upper part presents the exact gaussian profile as a dashed line and the numerically approached profile, applying classical methods, as a solid line. The approximation is quite different within the body of the profile and results in exponentially growing 'tails' outside the profile where a zero value is expected. The lower part of this figure shows the same result, though applying the chopped series equilibrium principle. Note that the result is much improved!

Contrary to the classical Fourier method, decomposing a bounded beam into pure plane waves, having different amplitudes, phases and directions, in the inhomogeneous wave method, a bounded beam is decomposed into inhomogeneous waves, having different amplitudes, phases, but having equal propagation directions. During the historical development of the inhomogeneous wave theory, it has been revealed that the method is correct within a limited distance along the propagation direction and within a limited range along the width of the bounded beam. The limited range of validity along the propagation direction is not crucial, because inhomogeneous wave are primarily considered in the case when a bounded beam interacts with a plane interface at relatively small angles. Nevertheless, the limitation along the width of the bounded beam is very important, because whenever strong beam shifts or beam profile deformations are induced in the case of surface wave generation, the effect can possibly occur in areas where the bounded beam, approximated by means of a superposition of inhomogeneous waves, is badly conditioned. The primary reason for the inhomogeneous wave method being badly conditioned along the width of the bounded beam, is the fact that the optimization is performed by means of exponential functions. This is a delicate question, because a very small numerical error

results in a very large difference between the numerical approximation and the exact profile, at significant distances from the origin.

This section presents a technique, based on a chopped Taylor series representation of the exponential functions, applying the optimization procedure for these chopped series and attributing the obtained coefficients to the original exponential functions. It is shown that there exists an optimum series length for that purpose. The result is an improvement of the optimization of the approximation of bounded beams by means of inhomogeneous waves. The principle of this technique can possibly be very important in other fields of numerical analysis as well.

Section IV.C : A useful analytical description of the coefficients in an inhomogeneous wave decomposition of symmetrical bounded beam

- Nico F. Declercq, Joris Degrieck, Oswald Leroy, "A useful analytical description of the coefficients in an Inhomogeneous Wave Decomposition of a symmetrical bounded beam", **Ultrasonics** 43(4), 279-282, 2005 *(Imp. Fact. 0.844; SCI-index, Acoustics, rank:11 /28)*
- Oral presentation at 'the 8th Western Pacific Acoustics Conference (Wespac8)', **Melbourne**, Australia, 7-9 April, 2003.

Section IV.B is primarily devoted to numerical problems in the inhomogeneous wave theory. This is due to the obvious fact that analytical expressions for the expansion coefficients in the decomposition of bounded beams into inhomogeneous waves, have never been found. Section IV.C explains how an analytical expression can be obtained and presents the result.
If the spatial description of a bounded beam is given by:

$$\varphi(x,z) = \sum_{n=-N}^{N} \frac{1}{2}\left(1+\delta_{n,0}\right) A_n \exp\left(\beta_n x\right) \exp\left(i\sqrt{\left(\frac{\omega^2}{v^2}+\beta_n^2\right)}\, z \right)$$

Then, the analytical expression for the expansion coefficients is given by:

$$A_n = \sum_{m=n}^{N} (-1)^n \frac{m!}{(m-n)!n!n!} \sum_{r=0}^{m} (-1)^r \frac{m!}{(m-r)!r!r!} I_r$$

with

$$I_r = \frac{1}{p} \int_{-\infty}^{+\infty} \exp\left[-\exp\left(\frac{x}{p}\right) + (r+1)\frac{x}{p} \right] f(x)\, dx$$

Section IV.D : The Laplace transform to describe bounded inhomogeneous waves

- Nico F. Declercq, Joris Degrieck, Oswald Leroy, "The Laplace transform to describe bounded inhomogeneous waves", **J. Acoust. Soc. Am.** 116(1), 51-60, 2004. *(Imp. Fact. 1.310; SCI-index, Acoustics, rank:7 /28)*
- Oral presentation at 'the 145th Meeting of the Acoustical Society of America', Nashville Convention Center, **Nashville**, Tennessee, USA, 28 April - 2 May 2003.

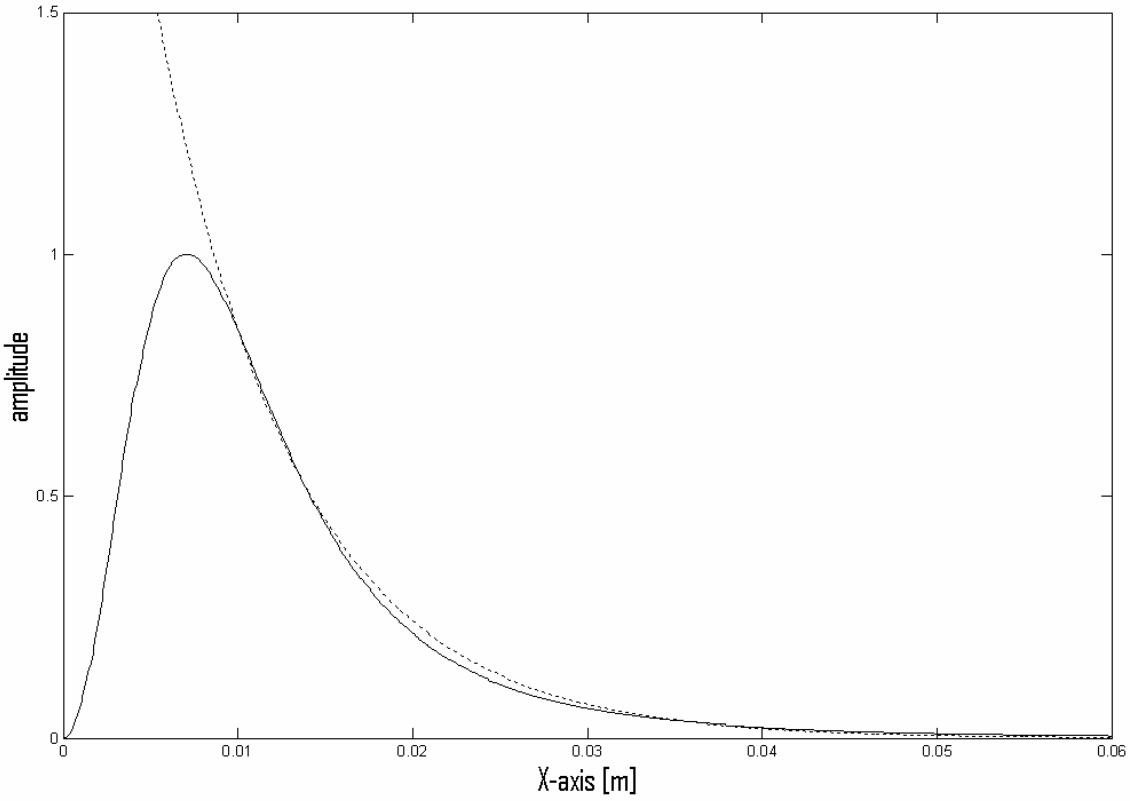

Fig. III.2 (identical to Fig. IIIV.D_5): ***The horizontal axis denotes the distance along the wave front, whereas the vertical axis denotes the amplitude. The dashed line corresponds to the profile of an infinite inhomogeneous wave, whereas the solid line corresponds to the profile of a bounded inhomogeneous wave.***

A beautiful aspect of the theory of inhomogeneous waves, is the fact that several features emerge that do not necessarily coincide with human intuition, but that are experimentally verifiable. Nevertheless, those specific experiments are performed by means of bounded inhomogeneous waves instead of infinite inhomogeneous waves. The reason is, of course, the finite dimension of transducers. Therefore, the correspondence between theory and experiment is not obvious. The cause of this correspondence is revealed in this section where, by means of the Laplace transform, the physical connection between infinite inhomogeneous waves and their bounded counterparts, is unveiled. It is shown that only one of the inhomogeneous waves within the superposition, is responsible for the global behavior of bounded inhomogeneous waves, whereas the other waves are merely responsible for the edge formation.

Section IV.E : The representation of 3D Gaussian beams by means of inhomogeneous waves

- Nico F. Declercq, Joris Degrieck, Oswald Leroy, "The inhomogeneous wave decomposition of 3D Gaussian-like bounded beams", **Ultrasonics** 42, 273-276, 2004. *(Imp. Fact. 0.844; SCI-index, Acoustics, rank:11 /28)*
- poster presentation at 'Ultrasonics International 2003', **Granada**, Spain, 30 June- 3 July 2003

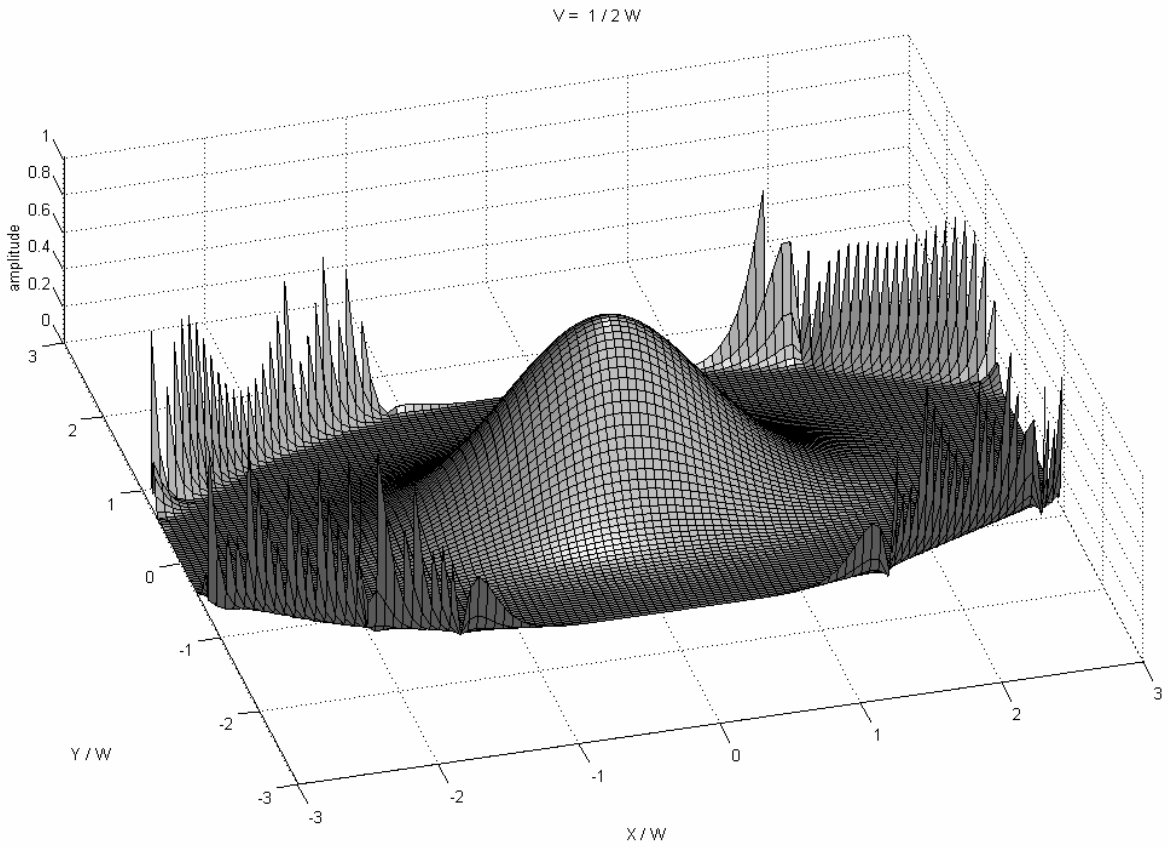

Fig. III.3 (identical to Fig. IV.E_4): ***The profile of a 3D quasi-Gaussian beam, approached by means of a superposition of inhomogeneous waves. The tails that appear are comparable to those in Fig. III.1.***

The development of the inhomogeneous wave theory has been accompanied by the discovery that bounded beam can be represented as a superposition of inhomogeneous waves. The method of determining the expansion coefficients in the decomposition, was based on Prony's technique, transforming an equation containing exponential functions, into a polynomial equation. After identification with Laguerre polynomials, the expansion coefficients can be determined. Nevertheless, the method has thus far been limited to beams that are bounded in only one direction. This is a serious shortcoming, because it limits application of the inhomogeneous wave theory to more realistic situations where sound beams are bounded in two directions. The current section introduces a novel method to determine the expansion coefficients, that is also applicable in the latter situation of realistic beams bounded in two directions.

Section IV.F : Focal length control of complex harmonic and comlex pulsed ultrasonic bounded beams

- Accepted for publication in **J. Appl. Phys**. *(Imp. Fact. 2.281; SCI-index, Physics-Applied, rank:13/76)*
- Poster presentation at 'VII International Conference for Young Researchers on Wave Electronics and its Applications in Information and Telecommunication Systems', **St Petersburg**, Russia , 12-15 September 2004

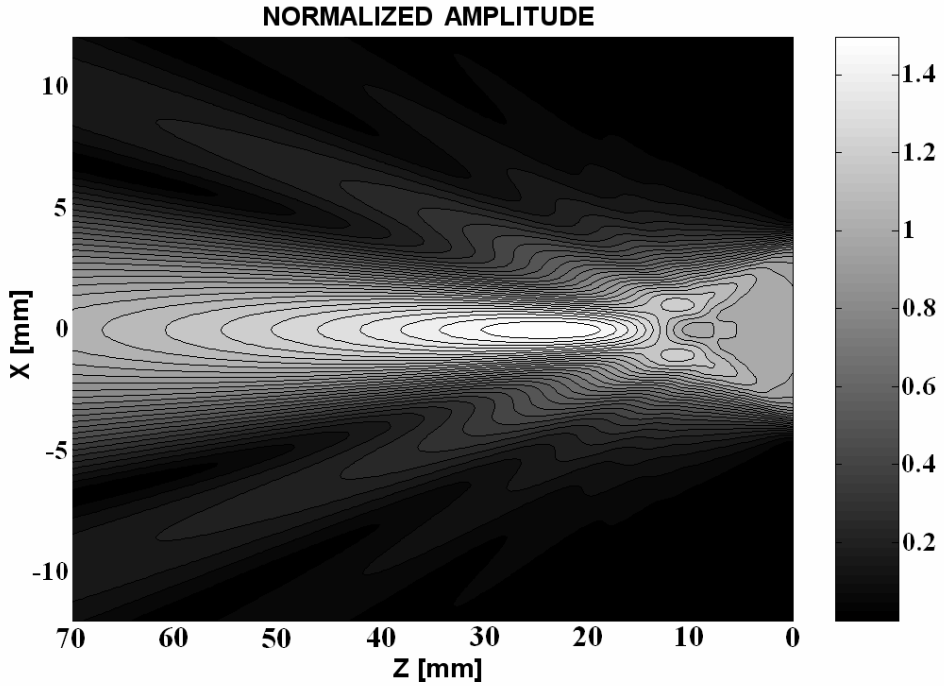

Fig. III.4 (identical to Fig. IV.F_5): ***Example of a square profile focused bounded beam, propagating from the right hand side to the left hand side. The white oval spot is the focus.***

The ability of ultrasound, on the one hand to coagulate thrombocytes and on the other hand to transform into heat, makes it an established tool for medical applications. In the case of focused ultrasound, the generated effects can be induced locally. At the moment, focused beams are commonly formed by means of phased array technology because of flexibility, especially when tuning the focal distance. This technology however is extremely expensive, which is an important and 'pity' disadvantage in developing countries. Principally, the focal distance of a single element focusing transducer, must also be tunable, though by changing the frequency, which most often results in a severe diminishing of the generated sonic amplitude, an effect resulting from the inability of most transducers to generate vibrations different from their first harmonic or odd multiples.

In this section, it is shown that it is possible to tune the focal distance of a single element focusing transducer, by changing the input amplitude in a distinct manner. The theory behind the effect is the complex harmonic wave theory. It is shown that the effect is generated, not only in the theoretical case of infinite signals, but also in the realistic situation of short signals. The result of this research may be important in the fabrication of

affordable medical equipment.

Section IV.G : On the existence and the excitation of a new kind of leaky surface waves

- Oral presentation at 'Tenth International Congress on Sound and Vibration', **Stockholm**, Sweden, 7-10 July 2003

By formulating the continuity conditions at a solid-liquid interface, it is possible to obtain the characteristic equation of surface waves. This equation relates the material parameters to the velocity of surface waves. Practically, the solution corresponds to a complex pole of the reflection coefficient of incident sound on the interface. A complex velocity then corresponds to leaky surface waves. Nevertheless, the result is also a function of the appropriate sign choice for the normal components of the wave vectors. By applying novel knowledge concerning the sign choice, obtained from experiments by Marc Deschamps, it is possible to established the well-known existence of leaky Rayleigh waves, a kind which radiates energy into the liquid, but also predict a novel type of surface waves, that leaks energy both into the liquid and into the solid.

Chapter V The interaction of sound with continuously varying layers

Section V.A : The interaction of inhomogeneous waves and Gaussian beams with mud in between a hard solid and an ideal liquid

- Nico F. Declercq, Oswald Leroy, Joris Degrieck, Jeroen Vandeputte, "The interaction of inhomogeneous waves and Gaussian beams with mud in between a hard solid and an ideal liquid", **Acta Acustica United with Acustica** 90, 819-829, 2004 *(Imp. Fact. 0.346; SCI-index, Acoustics, rank:21 /28)*

In the shipping and dredging industry, it is of primordial importance to estimate the nautical depth in rivers and harbors. The bottom is often covered by a layer of mud that is not homogeneous and consists of a fluid-like upper layer, a solid-like lower layer and a transition zone in between. The transition zone is the real nautical bottom. When taking the critical decision to enter a ship into a harbor or to remain anchored, knowledge of the exact nautical depth is crucial. Classical echo-sounding is not capable of detecting the nautical bottom, because it is based on normal incident sound and does not generated shear waves in the mud. The nautical bottom is characterized by an abrupt change of the shear parameters but not the compressional parameters. Therefore only the transition between water and fluid-like mud is detectable by means of classical echo-sounding, as well as the transition between the solid-like mud layer and the hard or sandy underground.

The present section describes a newly developed model that describes the interaction of sound in a continuous system of layers in mud. The propagation of bounded beams is simulated and it is shown that oblique incident bounded beams produce a reflected sound pattern that is susceptible to the position of the nautical depth. Therefore a method is discovered that is indirectly capable of detecting the position of the nautical depth.

Furthermore, primarily because of scientific reasons, the interaction of inhomogeneous waves with this mud system is described and it is shown that the reflection coefficient enables a prediction of the reflected beam characteristics.

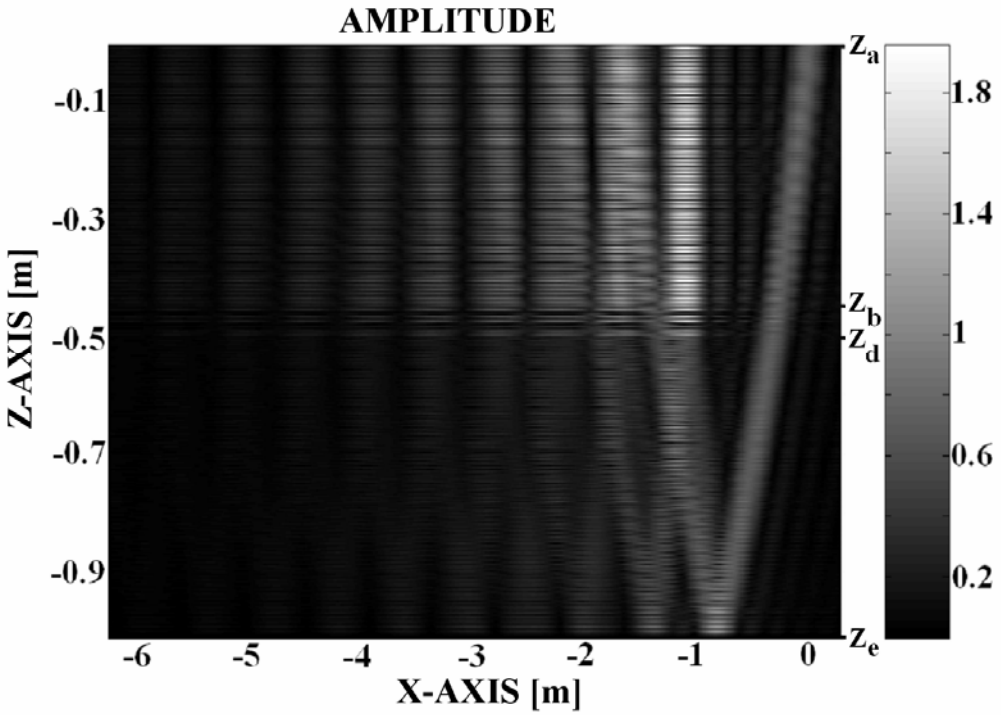

Fig. III.5 (identical to Fig. V.A_7): ***An example of the propagation of a bounded sound beam in mud. The bounded beam is generated at the origin and propagates from the upper right corner down. After interaction with the different layers, including the nautical bottom between z_b and z_d and the hard underground, a complicated reflection pattern is formed. This pattern is susceptible to the position of the nautical bottom.***

Chapter VI The interaction of sound with coated materials

Section VI.A : Frequency band gap for Rayleigh waves on coated substrates

- Nico F. Declercq, Joris Degrieck, Oswald Leroy, "Frequency bandgap for Rayleigh waves on coated surfaces", **Appl. Phys Let**. 85(1), 148-150, 2004. *(Imp. Fact. 4.207; SCI-index, Physics-Applied, rank:3/76)*
- Oral presentation at 'VII International Conference for Young Researchers on Wave Electronics and its Applications in Information and Telecommunication Systems', **St Petersburg**, Russia , 12-15 September 2004

The Rayleigh wave velocity depends on the material properties of the solid on which they propagate. Commonly, a Rayleigh wave on a coated substrate, has a velocity in between the Rayleigh wave velocity on pure substrate and on pure coating. In this section however, it is shown that whenever the physical properties of the coating differ extremely from the physical properties of the substrate, that there exists a frequency band in which

Rayleigh waves cannot exist. The presence of such a frequency band gap is complementary to a well known band pass filter in electronics. The existence of a band gap is very promising for developing new electronic filters based on surface acoustic waves..

Section VI.B : Lamb wave dispersion in extraordinary bilayered plates

Following the discovery of previous section, a study is performed on the properties of Lamb waves in bilayered plates, consisting of physically highly different layers. It is shown that the well-known asymptotical behavior of the S_0 and A_0 mode disappears and it is also shown that the shape of the dispersion curves of the S_0 and A_0 mode is quite different from their classical shape.

Chapter VII Schlieren photography as a tool for nondestructive testing

Section VII.A : Schlieren photography to study sound interaction with highly absorbing materials

- Accepted for publication in **Ultrasonics**. *(Imp. Fact. 0.844; SCI-index, Acoustics, rank:11 /28)*

Very often, characteristics of a reflected beam are studied in order to obtain information about the material on which the reflection occurs. Nevertheless, in the exceptional case where the material is so highly sound absorbing, there is no reflected beam and therefore it is impossible to examine reflected beam properties. In such situations, Schlieren photography is a promising tool because it enables simultaneous visualization of the incident sound beam and the generation of heat on the surface. The technique can be used to study the extent of sound along the surface and to study the heat transformation rate. In addition, the technique does not require the installation of sensors, whence it is completely nondestructive.

Section VII.B : Detection of fiber direction in composites by means of high frequency wide bounded beam and Schlieren photography

- Accepted for publication in **Research in Nondestructive Evaluation** *(Imp. Fact 0.935; SCI-index, Materials Science – Characterization & Testing, rank:2/23)*
- Oral presentation at '51st open seminar on Acoustics, joint with 9th School of Acousto-Optics and Applications', **Gdansk**, Poland , 6-10 September 2004.

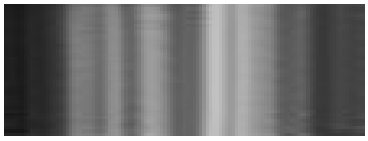

Fig. III.6 (identical to Fig. VII.B_4): ***This enlarged Schlieren image of a bounded ultrasonic beam, shows a fringing pattern that enables the determination of the fiber direction in composites.***

There are very sophisticated techniques available to determine the fiber direction in composites. However, those techniques enable extraction of much more information than just the fiber direction. This makes them generally complicated to perform and require highly specialized staff. The current section presents a very simple technique, applying Schlieren photography and a relatively high frequency wide bounded beam, to detect a spatially varying reflection coefficient on fiber reinforced composites. This spatial variation results in a fringing pattern that is straightforwardly related to the fiber direction.

Chapter VIII Characterization of liquids in closed containers

Section VIII.A : The Schoch effect to distinguish between different liquids in closed containers

- Nico F. Declercq, Filip Van den Abeele, Joris Degrieck, Oswald Leroy, "The Schoch effect to distinguish between different liquids in closed containers", **IEEE Transactions on Ultrasonics, Ferroelectrics, and Frequency Control** 51(10), 1354-1357, 2004. *(Imp. Fact. 1.595 ;SCI-index, Engineering – electrical & electronic, rank:46/205)*
- Oral presentation at 'ICA2004 18th International Congress on Acoustics', Kyoto International Conference Hall, **Kyoto**, Japan, 4-9 April 2004

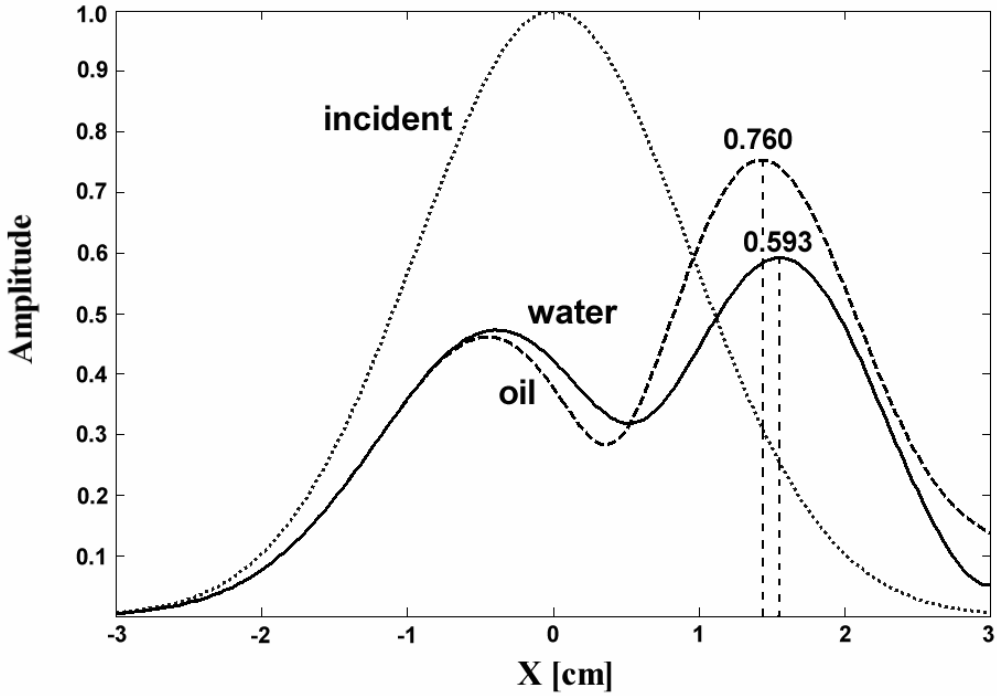

Fig. III.7 (identical to Fig. VIII.A_3): ***The profile of a reflected bounded beam on the container skin, in the event of Lamb wave generation, depends on the contained liquid. Different reflected beam profiles are shown for different contained liquids***

The simplest technique to examine a fluid in a closed container, is the use of a pulse-echo technique and the determination of the sonic velocity of the liquid. However, in many situations, the pulse-echo technique is not applicable because of the dimensions of the container or because there are no two parallel container skins. Therefore, the technique is, to a large extent, only used in the food and beverage industry. At border crossings or in harbors and airports, controllers regularly encounter large containers or containers of a shape that prohibits fluid characterization by means of the pulse echo technique. For such situations, a technique is presented here that only requires one flat area on the container skin. The technique is based on the Schoch effect. It is shown that the reflected beam parameters, in the event of the Schoch effect (due to the generation of Lamb waves within the container skin) are determined by the characteristics of the contained liquid.

Section VIII.B : On the capability of Leaky Lamb waves to discriminate between real and fictitious liquids

- Oral presentation at '75th Anniversary Celebration of the Acoustical Society of America (147th meeting of the Acoustical Society of America)', Sheraton New York Hotel and Towers, **New York**, New York, USA, 24-28 May 2004

The existing literature on Lamb waves only covers such waves in plates immersed in a liquid. Here, a study is performed on Lamb waves in a plate separating two different liquids. It is shown that the imaginary part of the complex pole, corresponding to a Lamb wave, is linearly dependent on the impedance difference between the two liquids if realistic liquids are considered and is randomly dependent on the impedance difference if unrealistic liquids are considered. This fact is important for theorists, who want to enter liquid parameters into their models and who need to know whether the considered liquid parameters are realistic or not.

Chapter IX Sound in media having discontinuities in more than one dimension

Section IX.A : The radiation mode theory in ultrasonics

- Accepted for publication in **IEEE Transactions on Ultrasonics, Ferroelectrics, and Frequency Control** *(Imp. Fact. 1.595 ;SCI-index, Engineering – electrical & electronic, rank:46/205)*
- Oral presentation at '51st open seminar on Acoustics, Joint with 9th School of Acousto-Optics and Applications', **Gdansk**, Poland , 6-10 September 2004

As an introduction to the consequent sections, the history and principles of the radiation mode theory are outlined in this part. Even though this theory is relatively difficult, it is attempted to make the description as simple as possible, with a minimum number of mathematical expressions. The radiation mode theory is suitable to study systems having discontinuities in more than one direction. A typical example is a cube. It is the author's

intention to develop this theory further the coming years.

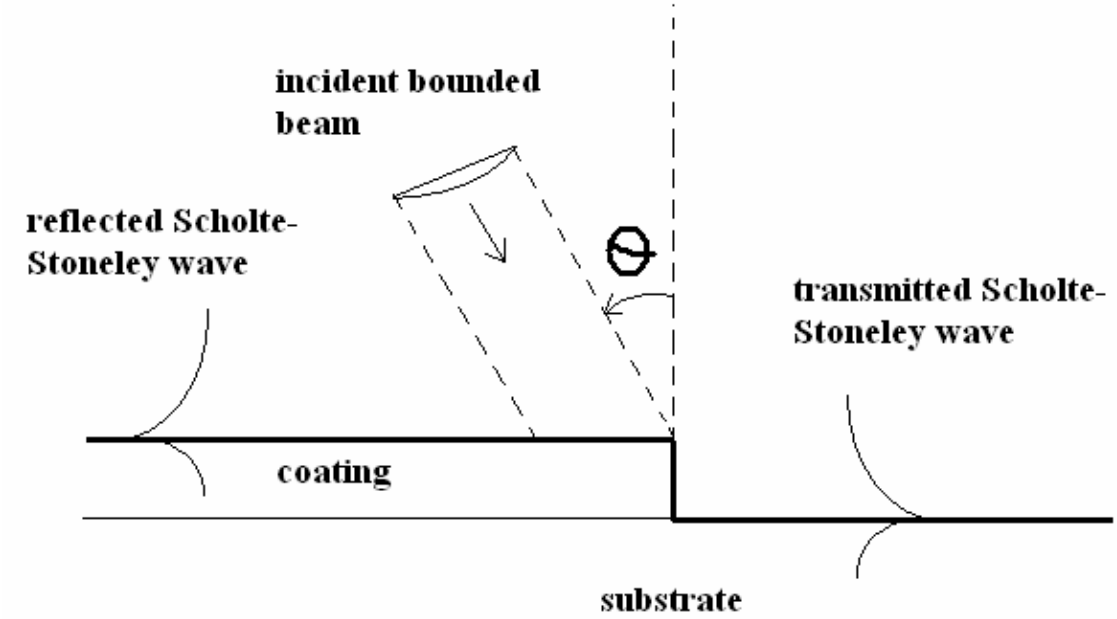

Fig. III.8 (identical to Fig. IIIX.A_7): ***Example of a geometrical configuration for which the radiation mode theory is extremely suitable. An incident beam generates transmitted and reflected Scholte-Stoneley waves at the downstep of a coated plate.***

Section IX.B : Study of the scattering of leaky Rayleigh waves at the extremity of a fluid loaded thick plate

- Nico F. Declercq, A. Teklu, M. A. Breazeale, Rudy Briers, Oswald Leroy, Joris Degrieck, Gennady N. Shkerdin, "Study of the scattering of leaky Rayleigh waves at the extremity of a fluid loaded thick plate", **J. Appl. Phys** 96(10),5836-5840, 2004 *(Imp. Fact. 2.281; SCI-index, Physics-Applied, rank:13/76)*
- Oral presentation at '75th Anniversary Celebration of the Acoustical Society of America (147th meeting of the Acoustical Society of America)', Sheraton New York Hotel and Towers, **New York**, New York, USA, 24-28 May 2004

In the previous section, it is outlined how a Scholte – Stoneley wave interacts with the edge of a thick plate. It is outlined that numerical simulations prove, in agreement with experiments, that Scholte – Stoneley waves, when reaching the end of a plate, primarily scatter into the forward direction. In the current section, a study is performed on the interaction of Rayleigh waves with the end of a thick plate. It is shown that when they reach the edge, they propagate 'around the corner'. This is important from a scientific point of view, but also from the point of view of nondestructive testing. If the surface of a plate needs to be examined without having access to it, whereas the edge of the plate is accessible, then the property of Rayleigh waves to propagate around the corner can be exploited. The reason why Rayleigh waves tend to travel around the corner and Scholte – Stoneley waves tend to scatter in the forward direction is probably due to the fact that Rayleigh waves penetrate deeper into the solid than into the liquid, whereas Scholte – Stoneley waves penetrate deeper into the liquid than in the solid. This makes that Rayleigh waves 'stick' better to the surface than Scholte – Stoneley waves and tend to follow its contours.

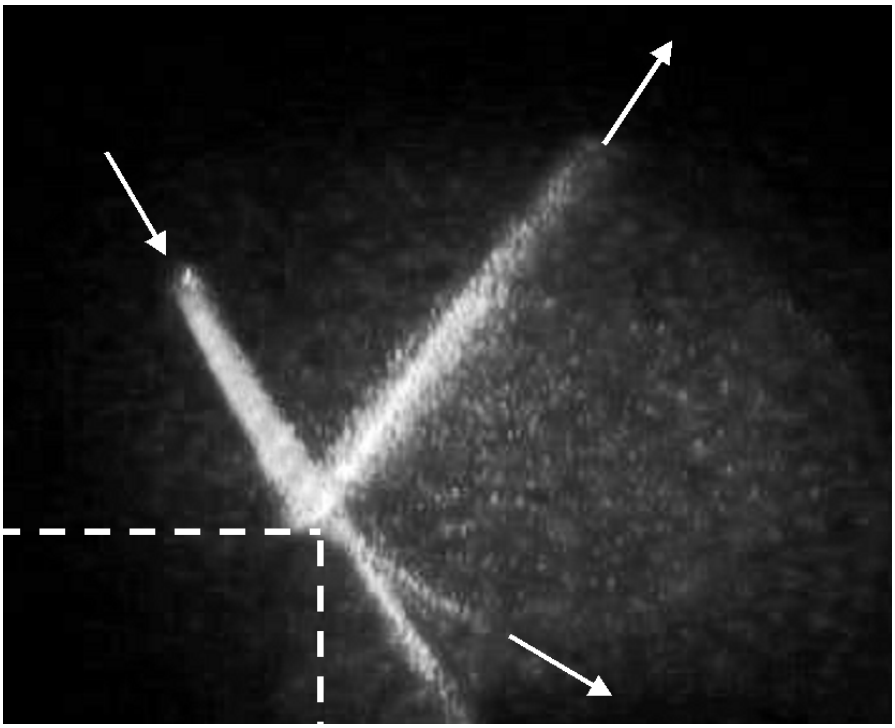

Fig. III.9 (identical to Fig. IIIX.B_6): ***This Schlieren picture proves that leaky Rayleigh waves, generated by means of an incident beam, propagate around the corner of a thick plate when reaching the end. The white dashed lines correspond to the edges of the thick plate.***

Section IX.C : Bounded beam interaction with plate-edge at Lamb angle

- Accepted for publication in **Acta Acustica United with Acustica** *(Imp. Fact. 0.346; SCI-index, Acoustics, rank:21 /28)*
- Oral presentation at '51st open seminar on Acoustics, joint with 9th School of Acousto-Optics and Applications', **Gdansk**, Poland , 6-10 September 2004.

The two previous sections study the interaction of surface waves with the edge of a thick plate. In thin plates however, it is more likely to generate Lamb waves and therefore it is interesting to study their interaction with the edge as well. By means of high quality Schlieren photography, this interaction is studied and it is revealed what types of mode conversion take place. Furthermore, it is shown that the edge of a plate can become an acoustic multipole, stimulated by the incident Lamb waves.

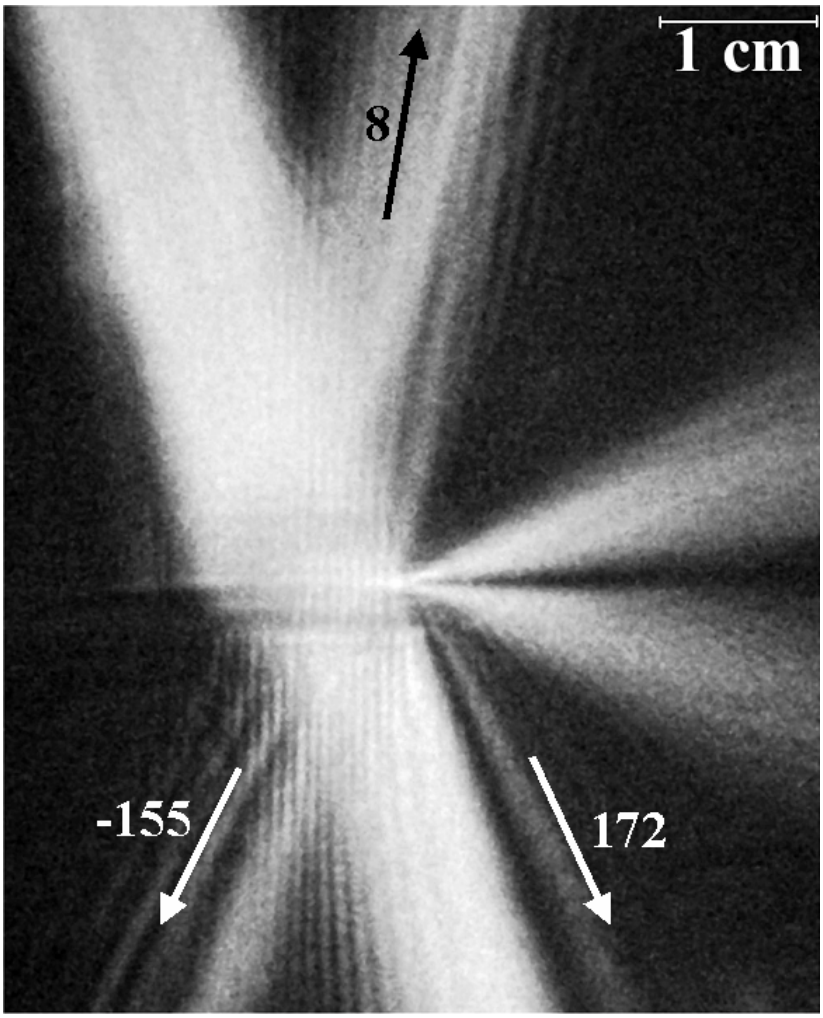

Fig. III.10 (identical to Fig. IIIX.C_5): This spectacular Schlieren picture reveals the wonderful interaction of a bounded beams with the edge of a thin aluminum plate, in the case of A_1 Lambmode stimulation. From pictures like this, it is possible to determine what types of mode conversion take place. The forward beams are due to multipole generation on the edge of the plate, whereas the other patterns can be explained as the interaction of different leaky fields.

Chapter X Diffraction phenomena

- Invited oral presentation at '51st open seminar on Acoustics, joint with 9th School of Acousto-Optics and Applications', **Gdansk**, Poland , 6-10 September 2004.

Sections X.A.1 : **Ultrasonic Diffraction phenomena on 1D rough surfaces**

Section X.A.1.a : **A theoretical treatment of the backward beam displacement**

on periodically corrugated surfaces and its relation to leaky Scholte – Stoneley waves.

- Nico F. Declercq, Joris Degrieck, Rudy Briers, Oswald Leroy, "Theory of the backward beam displacement on periodically corrugated surfaces and its relation to leaky Scholte-Stoneley waves", **J. Appl. Phys**. 96(11), 6869-6877, 2004 *(Imp. Fact. 2.281; SCI-index, Physics-Applied, rank:13/76)*
- Oral presentation at First Pan-American/Iberian Meeting on Acoustics (144th Meeting of the Acoustical Society of America, 3rd Iberoamerican Congress of Acoustics, 9th Mexican Congress on Acoustics), **Cancun**, Q. R. Mexico, 2-6 December 2002
- '**Best student paper award**' presented by the 'Acoustical Society of America'

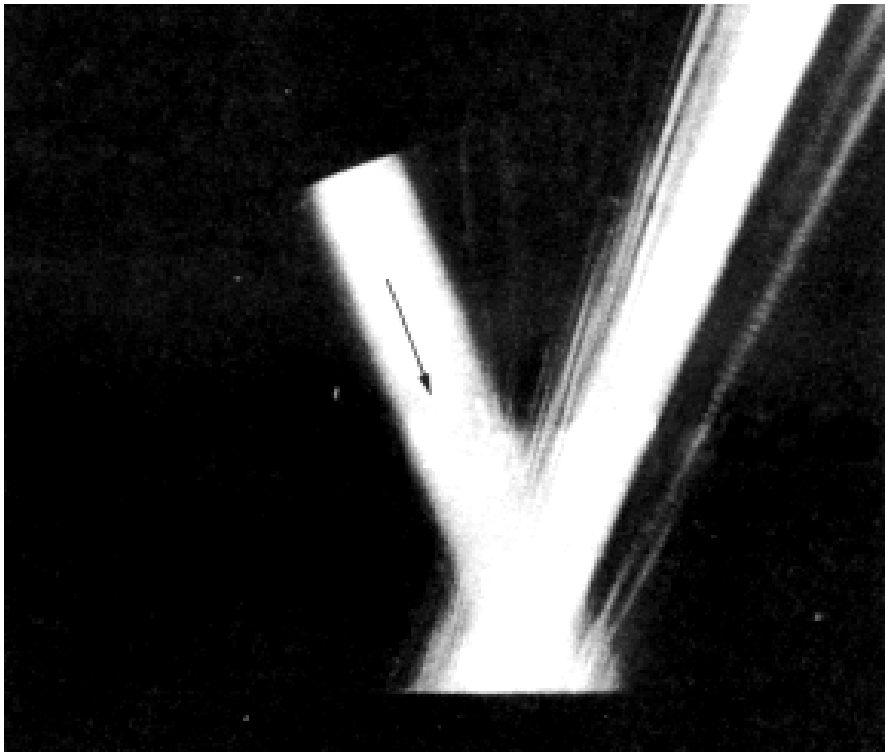

Fig. III.11 : ***Schlieren picture of the backward beam displacement, first observed by Breazeale and Torbett in 1976. This phenomenon has remained obscure ever since, but is now entirely explained.***

In 1976, Breazeale and Torbett performde an experiment that was aimed at verifying the prediction by Bertoni and Tamir, that, on a periodically corrugated surface, a backward beam displacement of the reflected beam was expected at a certain angle of incidence, depending on the applied frequency and the periodicity of the corrugated surface, and corresponding to generated backward propagating Rayleigh waves. However, the backward displacement was not observed at this angle, but at an unexpected angle. The reason remained obscure and the effect has never been simulated ever since. In this section, it is shown that the Fourier method cannot simulate the backward displacement. The inhomogeneous wave theory however is capable of simulating the effect and explaining it. It is obtained that the effect is due to a leaky version of Scholte – Stoneley waves. Furthermore, the theory predicts that if Breazeale and Torbett would have applied a narrower beam, that they would probably have observed beam profile deformations and

possibly also a backward beam displacement.

In addition, this section also uncovers the real nature of Wood anomalies in diffraction spectra. Whereas it has always been believed that Wood anomalies are due to the generation of Scholte – Stoneley waves, it is explained here that this is only a fraction of the truth. The Wood anomaly actually results from an eigenvibration of the corrugated surface and is only stimulated by means of normal incident sound.

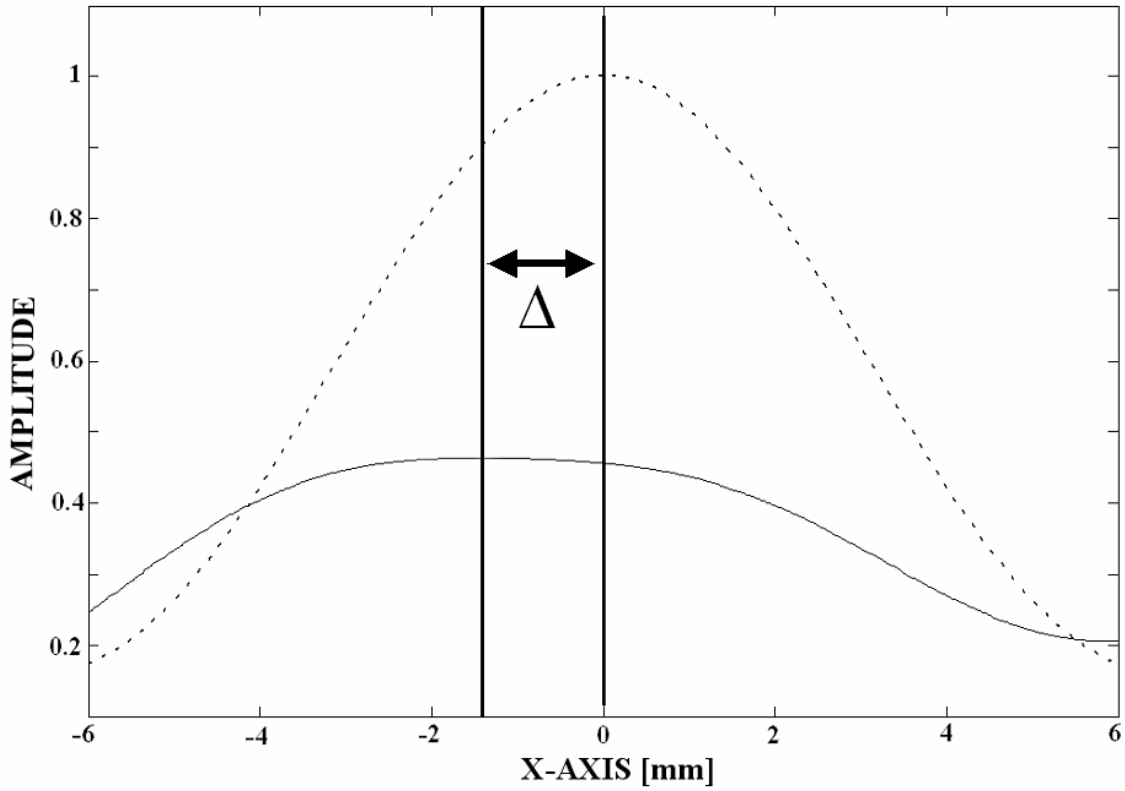

Fig. III.12 (identical to Fig. X.A.1.a_15): ***The dotted curve corresponds to the incident bounded beam, whereas the solid line is the simulated backward displacement of the reflected beam. This simulation corresponds to the experimental result of Breazeale and Torbett as depicted in Fig. III.11.***

<u>Section X.A.1.b</u> **: Experimental study of the backward beam displacement on periodically corrugated surfaces and its relation to leaky Scholte-Stoneley waves**

- Accepted for publication in **J. Appl. Phys.** *(Imp. Fact. 2.281; SCI-index, Physics-Applied, rank:13/76)*

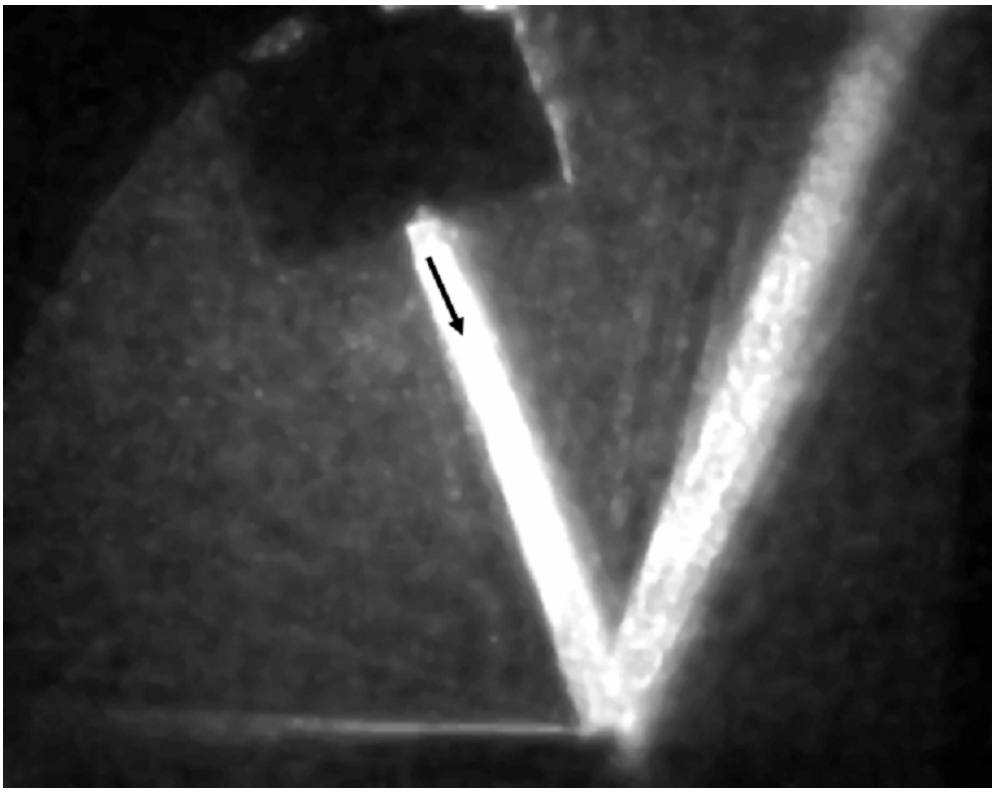

Fig. III.13 (identical to Fig. X.A.1.b_5): ***This Schlieren picture is the experimental evidence of the fact that the backward beam displacement is due to a type of Scholte – Stoneley waves. The angle of incidence in this figure corresponds to the angle at which the backward displacement occurs. The backward propagating surface wave is scattered 'in the forward direction' when reaching the end of the brass sample on the left hand side of the image. This is a strong indication that it is a Scholte – Stoneley wave.***

This section presents new experimental evidence for the phenomenon of the backward beam displacement, obtained at Olemiss in collaboration with Mack Breazeale *et al*. We have been able to repeat the experiments of 1976 and were able to find evidence for the fact that the backward beam displacement is the result of the generation of backward propagating (leaky) Scholte – Stoneley waves. Furthermore, the theoretical prediction of the former section has been verified, that beam profile deformations are possible at the angle predicted by Bertoni and Tamir, on the condition that narrow beams are used.

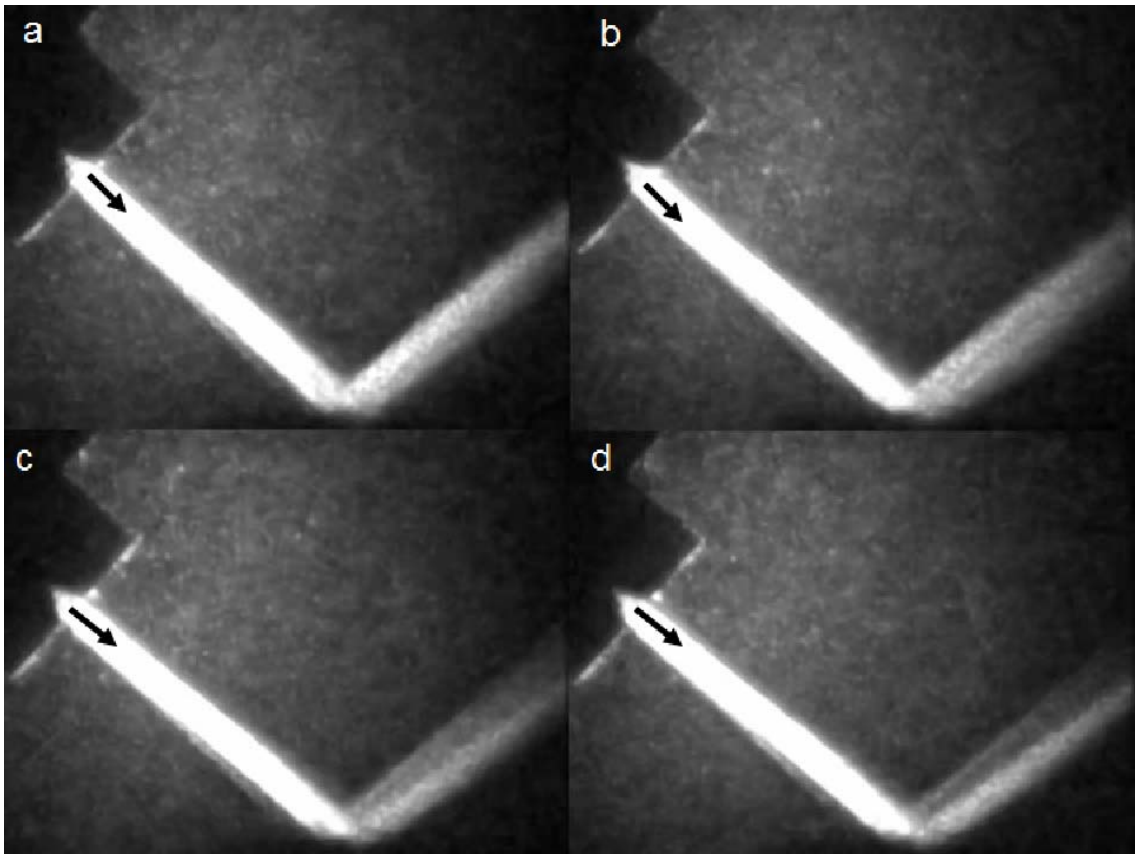

Fig. III.14 (identical to Fig. X.A.1.b_7): ***These pictures show experimental evidence of beam profile deformations near the angle predicted by Bertoni and Tamir, for a narrow incident beam.***

<u>Section X.A.1.c</u> : Note on the diffraction field generated by inhomogeneous waves obliquely incident on a periodically rough liquid-solid boundary

A number of years ago, it has been posed by Briers *et al* that, in order to simulate the diffraction of inhomogeneous waves on a periodically corrugated surface, a certain choice for the sign of the wave vector component perpendicular to the interface, was necessary in order to obtain numerical results in accordance with experiments. However, this sign choice, when applied in the case of zero-height corrugations, is in contradiction with the sign choice posed by Marc Deschamps for smooth surfaces. In the current section, it is shown that if the sign choice of Marc Deschamps is appropriately generalized to corrugated surfaces, that simulations can be obtained that equally well correspond to the experiments and that do not contain any contradictions anymore between the choice in the case of a smooth surface and in the case of a corrugated surface.

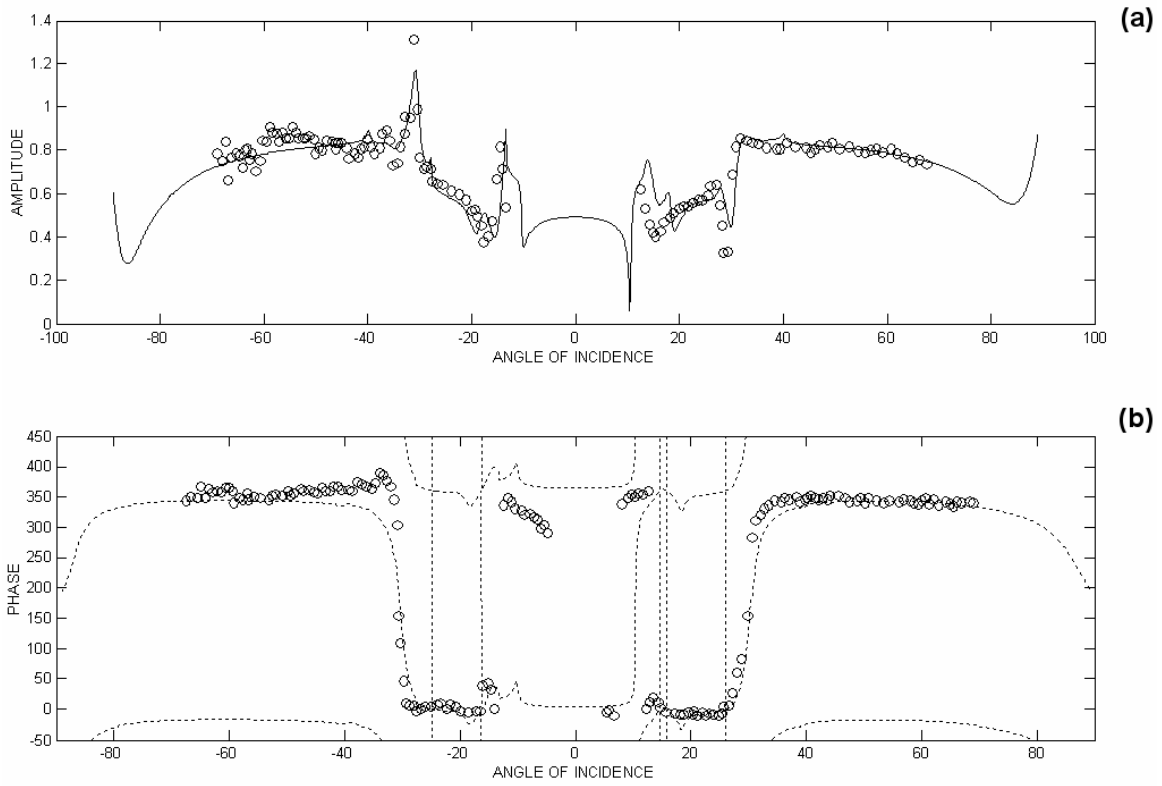

Fig. III.15 (identical to Fig. X.A.1.c_2): ***comparison between the calculated zero-order reflected phase (bottom) and amplitude (top) with experiments, when the new sign choice, as generalized from Deschamps' rule, is applied. The numerical results (lines) correspond fairly well to the experimental values (circles).***

Section X.A.1.d : Diffraction of complex harmonic plane waves and the stimulation of transient leaky Rayleigh waves

- Oral presentation at '75th Anniversary Celebration of the Acoustical Society of America (147th meeting of the Acoustical Society of America)', Sheraton New York Hotel and Towers, **New York**, New York, USA, 24-28 May 2004

The most extensive generalization of classical plane waves, is a wave whose frequency is complex valued. Then, the imaginary part of the frequency is the cause of an exponential change of the amplitude as a function of time. This section studies the interaction of such complex harmonic plane waves with a periodically corrugated surface. It is shown that normal incident complex harmonic waves possess a significant potentiality to stimulate high energy leaky Rayleigh waves. These Rayleigh waves are transient.

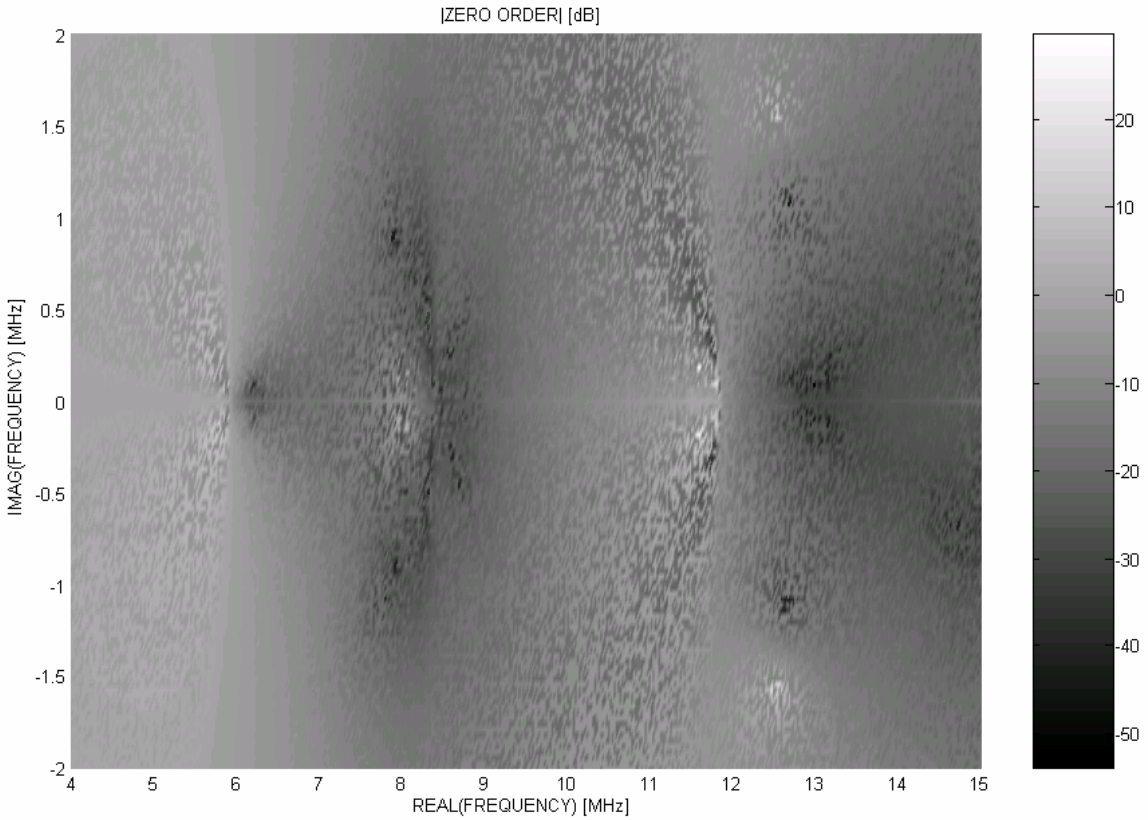

Fig. III.16 (identical to Fig. X.A.1.d_6): ***Example of the zero-order diffraction spectra as a function of the real and imaginary frequency. Areas of high amplitude are indications of the generation of surface waves.***

Section X.A.1.e : The acoustic diffraction grating: a complex frequency filter device for electronic signals

In electronics, the notion of a frequency spectrum is well established. The spectrum can be physically obtained by means of filters, or it can be obtained by means of the Fourier transformation. Nevertheless, an electronic signal can also be decomposed into exponentially varying signals. These signals correspond to complex harmonic waves in acoustics. Even though, mathematically, this decomposition is possible through optimization procedures, the question that arises is if a physical filter can be generated to perform this decomposition. The current section explains how an acoustic diffraction grating can be applied for that purpose, in combination with acousto-optics.

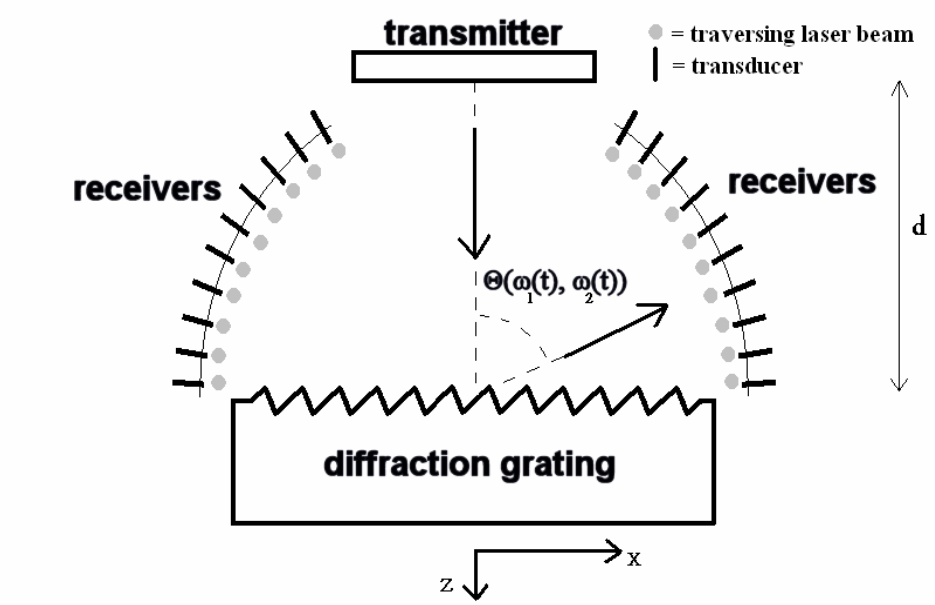

Fig. III.17 (identical to Fig. X.A.1.e_1): ***A schematic of the suggested filter system. A wide transducer generates sound that is diffracted on the grating. Then, the diffracted sound can be detected by means of omnidirectional transducers that detect the energy propagation direction, and acousto-optic cells, that detect the phase propagation direction. The combination of these two parameters make it, in principal, possible to determine the complex frequency spectrum.***

Section X.A.1.f : The use of polarized bounded beams to determine the groove direction of a surface corrugation at normal incidence, the generation of surface waves and the insonification at Bragg-angles

- Nico F. Declercq, Rudy Briers, Oswald Leroy, " The use of polarized bounded beams to determine the groove direction of a surface corrugation at normal incidence, the generation of surface waves and the insonification at Bragg-angles", **Ultrasonics** 40/1-8 pp. 345-348, 2002.*(Imp. Fact. 0.844; SCI-index, Acoustics, rank:11 /28)*
- poster presentation at 'Ultrasonics International 2001', Technical University of Delft, **Delft**, The Netherlands, 2-5 July 2001.

In the field of nondestructive testing, it happens that a plate must be examined, having grooves on the back. Then, it might be interesting to detect the direction of the grooves, because they are hidden behind the plate. This section describes how it is possible to apply circularly polarized normal incident sound for that purpose, using a contact transducer. Depending on the frequency, the reflected sound waves can be polarized along the direction of the grooves or perpendicular to them. Furthermore, this section simulates the interaction of a normal incident bounded beam at the Scholte – Stonley wave generating frequency. It is shown that bounded beams are able to stimulate Scholte – Stoneley waves and that the pattern that appears along the interface, is a set of fringes, resulting from interference between Scholte – Stoneley waves propagating from left to right and waves propagating from right to left.

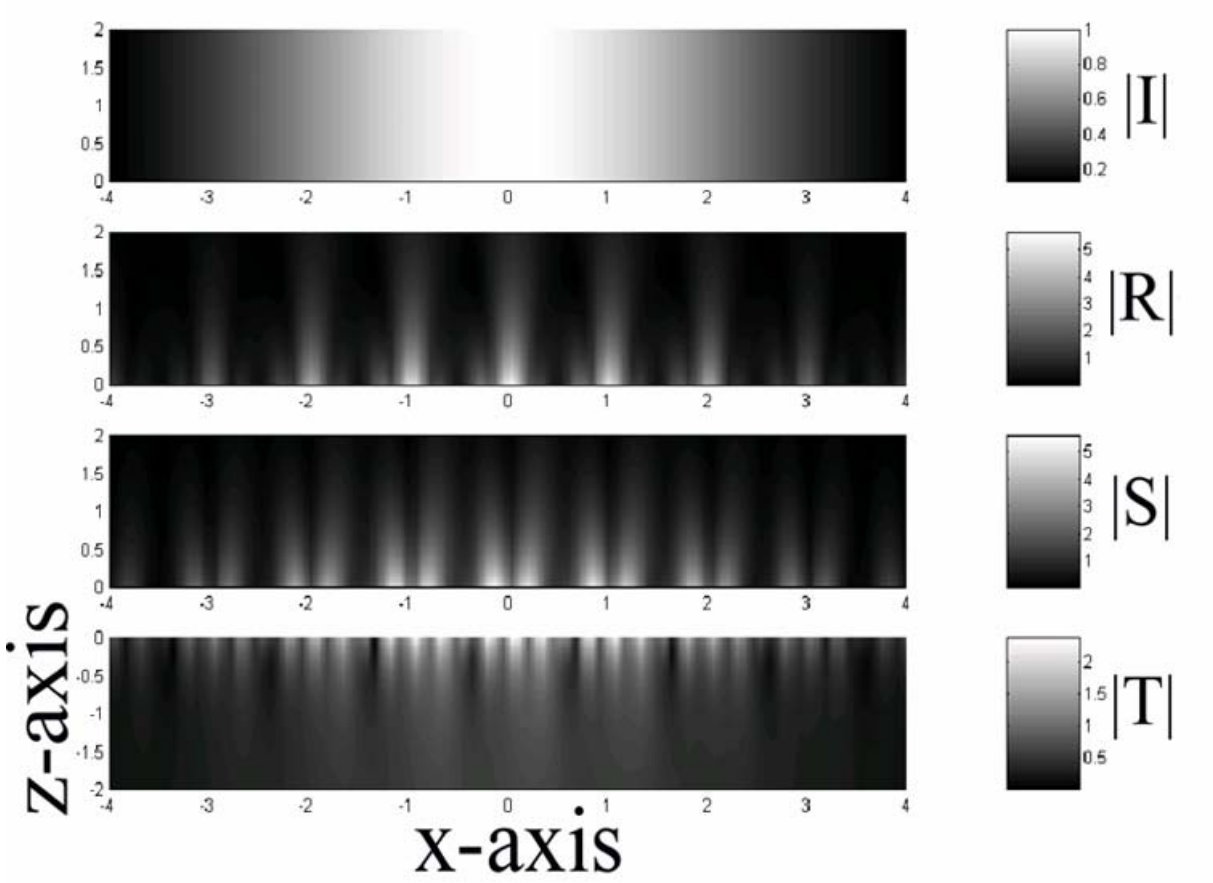

Fig. III.18 (identical to Fig. X.A.1.f_5): *|I| is the amplitude of the normal incident longitudinal polarized gaussian profiled sound, |R| of the reflected longitudinal, |S| of the reflected shear and |T| of the longitudinal transmitted sound. The frequency is 8.3 MHZ and the generation of second order Scholte-Stoneley waves occurs. This phenomenon does not occur at arbitrary frequencies.*
Notice the interference of the forward and backwards traveling surface wave. (x-coordinate: in numbers of the corrugation period)

Section X.A.1.g : Diffraction of horizontally polarized ultrasonic plane waves on a periodically corrugated solid-liquid interface for normal incidence and Brewster angle incidence

- Nico F. Declercq, Rudy Briers, Joris Degrieck, Oswald Leroy, "Diffraction of horizontally polarized ultrasonic plane waves on a periodically corrugated solid-liquid interface for normal incidence and Brewster angle incidence", **IEEE Transactions on Ultrasonics, Ferroelectrics, and Frequency Control**, 49(11), 1516-1521, 2002. *(Imp. Fact. 1.595 ;SCI-index, Engineering – electrical & electronic, rank:46/205)*
- Oral presentation at 'ICA2004 18th International Congress on Acoustics', Kyoto International Conference Hall, **Kyoto**, Japan, 4-9 April 2004

Similar to the latter section, the current section describes the interaction of sound, generated at the smooth side of a plate, possessing a periodical roughness on the opposite side. Horizontally polarized sound is polarized along the grooves, whereas vertically polarized sound is polarized perpendicular to the grooves. Even though it had been intuitively accepted by most researchers that horizontally polarized sound cannot be

transformed into vertically polarized sound through the diffraction phenomenon and vice versa, the current section presents a theoretical proof of this intuition. The current section also establishes the equation that enables simulation of the diffraction of horizontally polarized sound on the considered corrugated side of a plate. The generation of Love waves is shown numerically. Furthermore, the existence of a Brewster angle, similar to the Brewster angle in optics, is numerically shown. Incidence at this angle results in mainly horizontally polarized reflected sound.

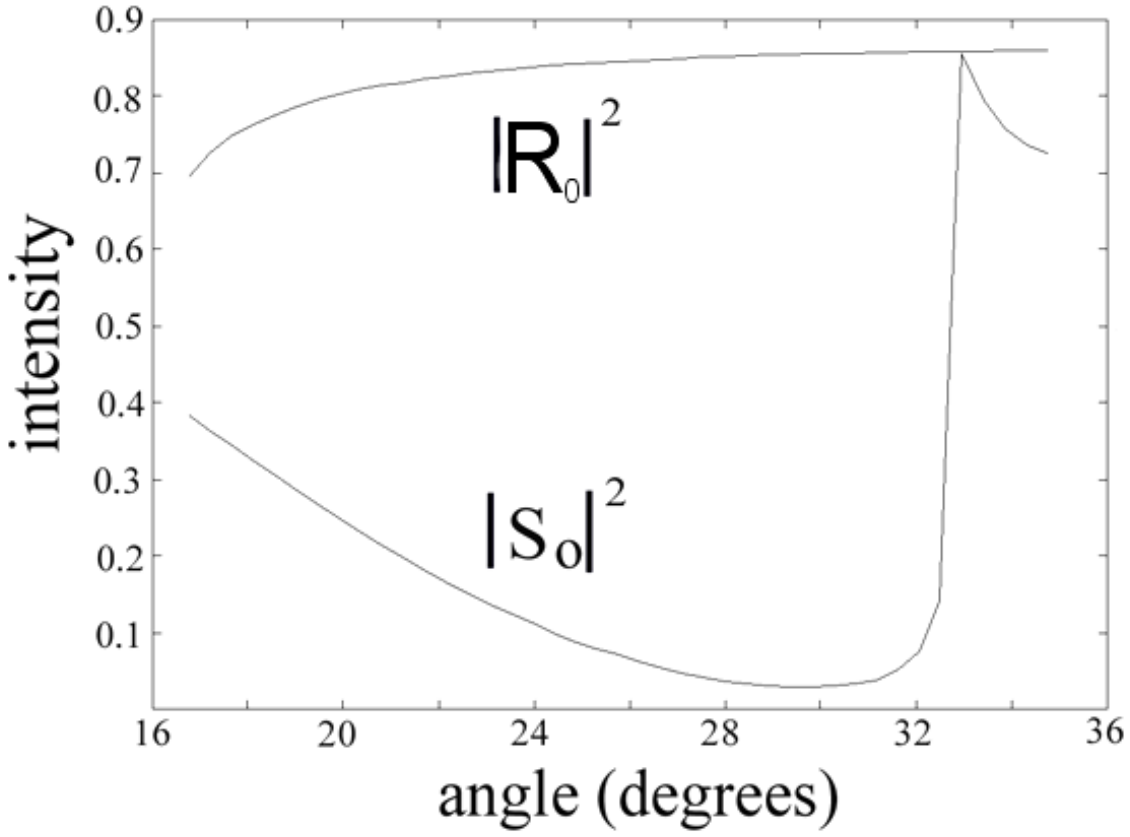

Fig. III.19 (identical to Fig. X.A.1.g_4): ***This figure depicts the intensity of the zero order reflected sound intensity of vertically polarized diffracted waves,*** S_0 ***, and the intensity of horizontally polarized diffracted waves,*** R_0 ***, as a function of the angle of incidence. The Brewster angle is defined as the angle at which*** S_0 ***shows a minimum, resulting in mainly horizontally polarized reflected sound. This angle is similar to the Brewster angle in optics.***

<u>Section X.A.1.h</u> **: Note on Scholte – Stoneley waves on a periodically corrugated surface**

- Oral presentation at '17th International Congress on Acoustics', **Rome**, Italy, 2-7 september 2001

This section describes experimental results obtained from the literature and shows that the experiments actually mean that the velocity of Scholte – Stoneley waves on rough

surfaces, is larger than on smooth surfaces. Intuitively, this effect is not really surprising, because the corrugated surface can be compared to a coating. It is known that a coating can increase the velocity of surface waves, or decrease it.

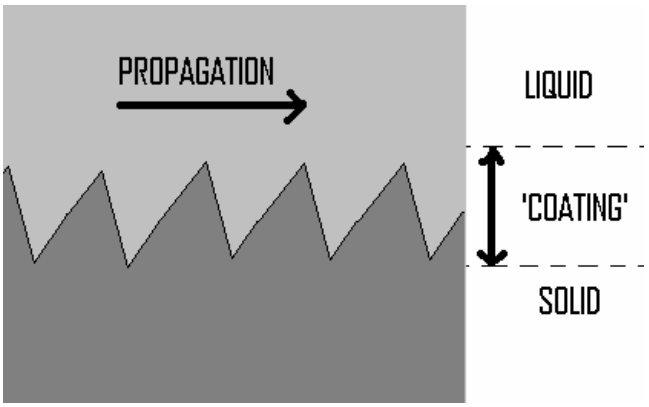

Fig. III.20 (identical to Fig. X.A.1.h_1): ***A corrugated interface between a liquid and a solid can be interpreted as a coated solid substrate in a liquid, when a Scholte – Stoneley wave travels along the interface with constant direction (propagation direction) of the real part of its wave vector.***

Section X.A.2 : Ultrasonic Diffraction phenomena on 2D rough surfaces

Section X.A.2.a : Diffraction of homogeneous and inhomogeneous plane waves on a doubly corrugated liquid/solid interface

- Oral presentation at 'InterNoise2003', International Convention Center Jeju, **Seogwipo**, Korea, August 25-28, 2003,
- Oral presentation at 'Acoustics 2003', University of Cadiz, **Cadiz**, Spain, 16-18 June 2003.

In the previous sections, only corrugations in one direction were considered. However, it is also possible to describe the interaction of sound with doubly corrugated surfaces. Such surfaces are similar to 'egg-crates' and can diffract sound into many spatial directions. This section begins with a proof that the classical grating equation, for homogeneous plane waves, can be generalized to the case of incident inhomogeneous waves. This proof is also valid in the situation of a one-dimensional corrugated surface, where the generalization of the grating equation had been proved experimentally, but not theoretically. Consequently, in this section, the equations are formed that enable simulation of the interaction of ultrasound on doubly corrugated surfaces. Numerical simulations are performed for incident homogeneous plane waves as well as for incident inhomogeneous plane waves.
It is numerically shown how the corrugation period has a steering influence on generated Scholte-Stoneley waves. It is also explained why a given inhomogeneous wave can only stimulate Rayleigh waves in one direction and not in other directions. A study is also revealed on the influence of the relative height of the two perpendicular sets of grooves that form together the doubly corrugated surface.

Sections X.B : Acoustic diffraction phenomena

Section X.B.1 : A theoretical study of special acoustic effects caused by the staircase of the El Castillo pyramid at the Maya ruins of Chichen-Itza in Mexico

- **Nature News** 14 December 2004; | doi:10.1038/news041213-5
- Nico F. Declercq, Joris Degrieck, Rudy Briers, Oswald Leroy, "A theoretical study of special acoustics effects caused by the staircase of the El Castillo pyramid at the Maya ruins of Chichen-Itza in Mexico", **J. Acoust. Soc. Am.** 116(6), 3328-3335, 2004 *(Imp. Fact. 1.310; SCI-index, Acoustics, rank:7 /28)*
- Oral presentation at '145th Meeting of the Acoustical Society of America', Nashville Convention Center, **Nashville**, Tennessee, USA, 28 April - 2 May 2003.
- Oral presentation at 'CFA/DAGA'04, 7ème Congrès Français d'Acoustique, Salon Européen de l'Acoustique - 30. Deutsche Jahrestagung für **Akustik, Europäische Akustik-Ausstellung', Palais des Congrès et de la Musique,** Strasbourg, France, 22-25 March 2004
- Reported in dozens of newspapers around the world, including Belgium. Also reported on the Belgian Television ('VTM Nieuws') and the Belgian National Radio ('De Nieuwe Wereld', on Radio 1)

Extract from Nature News, 14 December 2004:Mystery of 'chirping' pyramid decoded:

"Acoustic analysis shows how temple transforms echoes into sounds of nature", by Philip Ball

A theory that the ancient Mayans built their pyramids to act as giant resonators to produce strange and evocative echoes has been supported by a team of Belgian scientists. Nico Declercq of Ghent University and his colleagues have shown how sound waves ricocheting around the tiered steps of the El Castillo pyramid, at the Mayan ruin of Chichén Itzá near Cancún in Mexico, create sounds that mimic the chirp of a bird and the patter of raindrops. The bird-call effect, which resembles the warble of the Mexican quetzal bird, a sacred animal in Mayan culture, was first recognized by California-based acoustic engineer David Lubman in 1998. The 'chirp' can be triggered by a handclap made at the base of the staircase. Declercq was impressed when he heard the echo for himself at an acoustics conference in Cancún in 2002. After the conference, he, Lubman and other attendees took a trip to Chichén Itzá to experience the chirp of El Castillo at first hand. "It really sounds like a bird", says Declercq. *Sound structure* But did the pyramid's architects know exactly what they were doing? Declercq's calculations show that, although there is evidence that they engineered the pyramid to produce surprising sounds, they probably couldn't have predicted exactly what they would resemble. Lubman was at first convinced that the pyramid-builders did create the bird-chirp effect intentionally. But that's not necessarily so, Declercq and his colleagues argue. Their analysis of the pyramid's acoustics show that the precise sound caused by the echoes depends on the sound that excites them. Drums, for example, might produce a different type of resonance. The researchers hope that others will make more on-site measurements of El Castillo's acoustics to see what effects other sounds sources induce. Indeed, Declercq heard one such variation during the 2002 trip. As other visitors tramped up the steps of the 24-metre high pyramid, he noticed a flurry of pulse-like echoes that seemed to sound just like rain falling into a bucket of water.

Declercq wonders whether this, rather than the quetzal call, could have been the aim of El Castillo's acoustic design. "It may not be a coincidence," he says - the rain god played an important part in Mayan culture.

But perhaps such meaningful interpretations are fanciful. Declercq's team has shown that the height and spacing of the pyramid's steps creates like an acoustic filter that emphasizes some sound frequencies while suppressing others. But more detailed calculations of the acoustics shows that the echo is also influenced by other, more complex factors, such as the mix of frequencies of the sound source. Ultimately, then, it will be virtually impossible to prove that any specific echo effect is intentional. "Either you believe it or you don't," says Declercq. He himself is now sceptical of the quetzal theory - not least because he has now heard similar effects produced by staircases at other religious sites. At Kataragama in Sri Lanka, for example, a handclap by a staircase leading down to the Menik Ganga river produces an echo in response that resembles the quacking of ducks. [*end of Extract*]

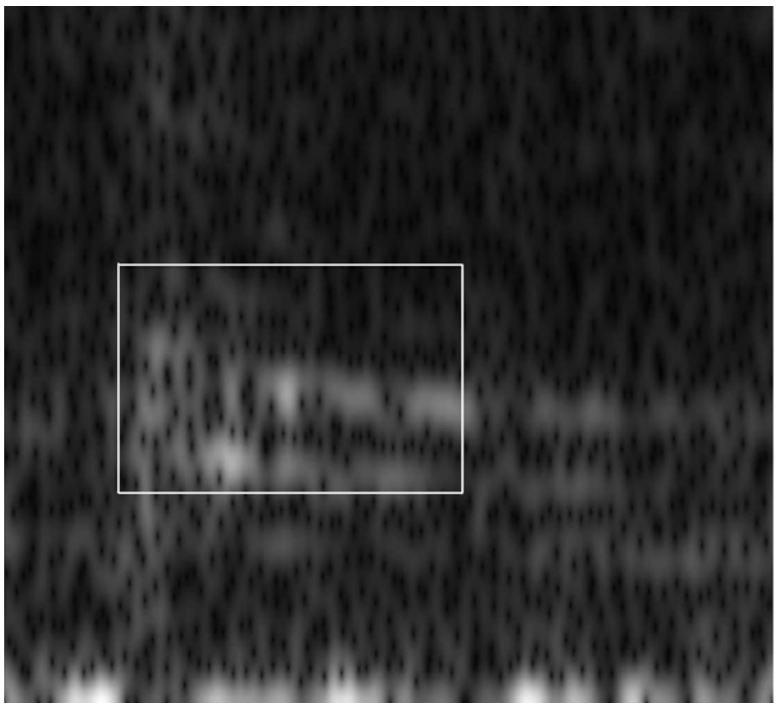

Fig. III.21(identical to Fig. X.B.1_8): ***Sonogram of the registered echo at the pyramid in Chichen Itza. In this figure, and in the consequent two figures, the white rectangle spans de same area, whereas the entire figure corresponds to a frequency interval [0 Hz – 5000 Hz] along the vertical direction and a time interval of 0.2s along the horizontal direction.***

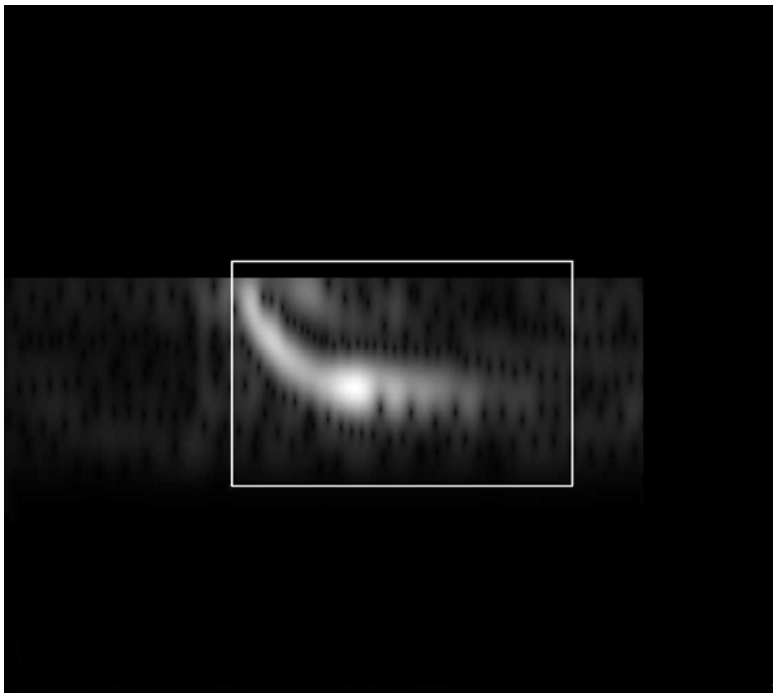

Fig. III.22 (identical to Fig. X.B.1_6): ***Sonogram of the simulated echo at the pyramid in Chichen Itza, in response to a mathematical delta-like pulse. Comparison with the previous figure shows that the calculated echo does not contain the required low frequency bands.***

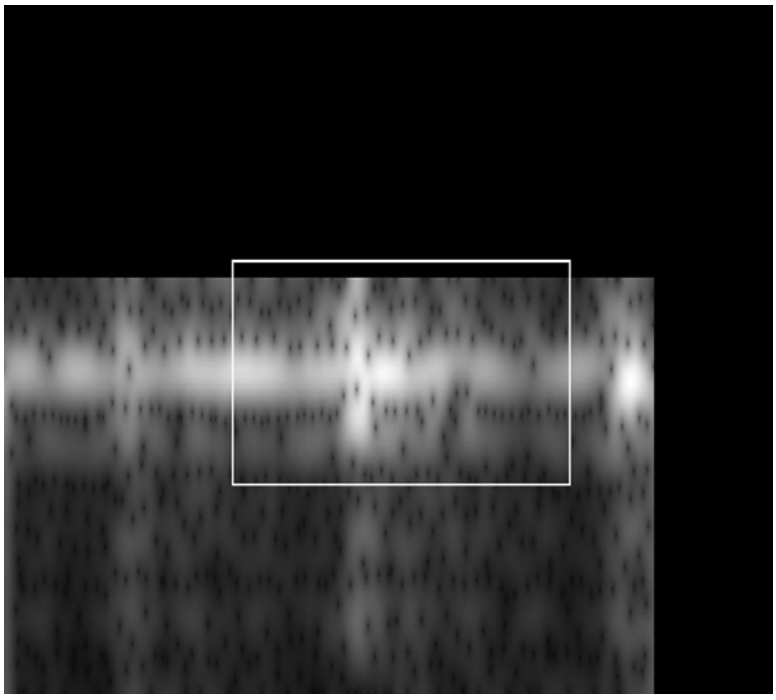

Fig. III.23 (identical to Fig X.B.1_11): ***Sonogram of the simulated echo at the pyramid in Chichen Itza, in response to a realistic handclap. Besides the fact that, due to numerical shortcomings, the exact length of the chirp cannot be determined, the low frequency bands are present. The reason is that these bands are present in the incident handclap, in advance to the formation of the echo.***

Chapter XI Ultrasonic Polar Scans

Section XI.A : Ultrasonic polar scans as a possible means of nondestructive testing and characterization of composite plates

- Joris Degrieck, Nico F. Declercq, Oswald Leroy, "Ultrasonic Polar Scans as a possible means of nondestructive testing and characterization of composite plates", **Insight - The Journal of The British Institute of Non-Destructive Testing**, 45(3), 196-201, 2003. *(Imp. Fact. 0.311; SCI-index, Materials Science – Characterization & Testing, rank:11/23)*

Ultrasonic polar scans form the registration of the transmitted (or reflected) amplitude for sound incident at all possible angles, on a given spot. A polar scans shows typical amplitude patterns that are like fingerprints of the material and that contain information about the stiffness and the anisotropy. The current section gives an overview of the state of the art in ultrasonic polar scans.

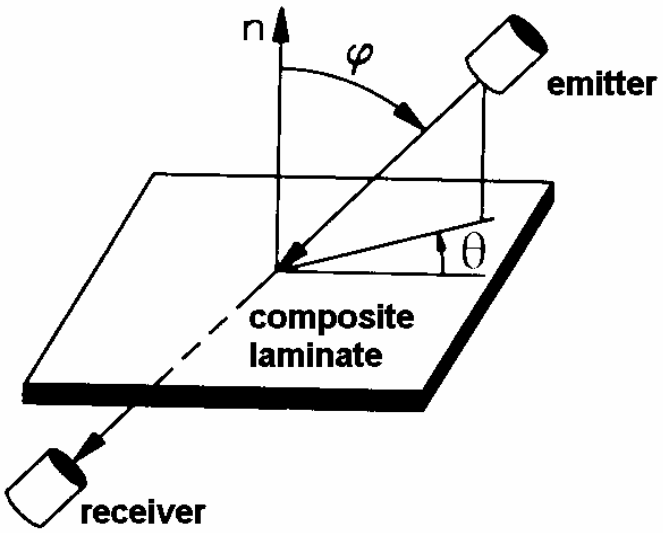

Fig. III.24 (identical to Fig. XI.A_1): ***In a polar scan, the target spot is impinged at a constant distance form all possible angles*** (θ, φ)**.**

Section XI.B : Simulation of harmonic and pulsed ultrasonic polar scans on orthotropic materials and more general anisotropic crystals

- Accepted for publication in **NDT & E International** *(Imp. Fact. 0.752; SCI-index, Materials Science – Characterization & Testing, rank:3/23)*
- Oral presentation at '3rd International Conference on Emerging Technologies in Non-Destructive Testing & Technology Transfer and Business Partnership Event', **Thessaloniki**, Greece, May 26-28, 2003.

Before I began my research in 2001, there was an ultrasonic polar scan experimental setup in our department and there was also a computer program available that enables the

simulation of ultrasonic polar scans for single layered orthotropic materials. Nevertheless, because most composites are multilayered and because some composites have a more general anisotropy, further extensions of the numerical possibilities have been established lately. The results and the simulation procedure are described in this section. Besides fiber reinforced composites, it is now possible to simulate ultrasonic polar scans on any kind of crystals of any kind of anisotropy and orientation. As examples, barium titanate and gallium arsenide are considered. Besides the possibility to consider any orientation, it is also possible to stack crystals mathematically and simulate the ultrasonic polar scan for any possible internal orientation.

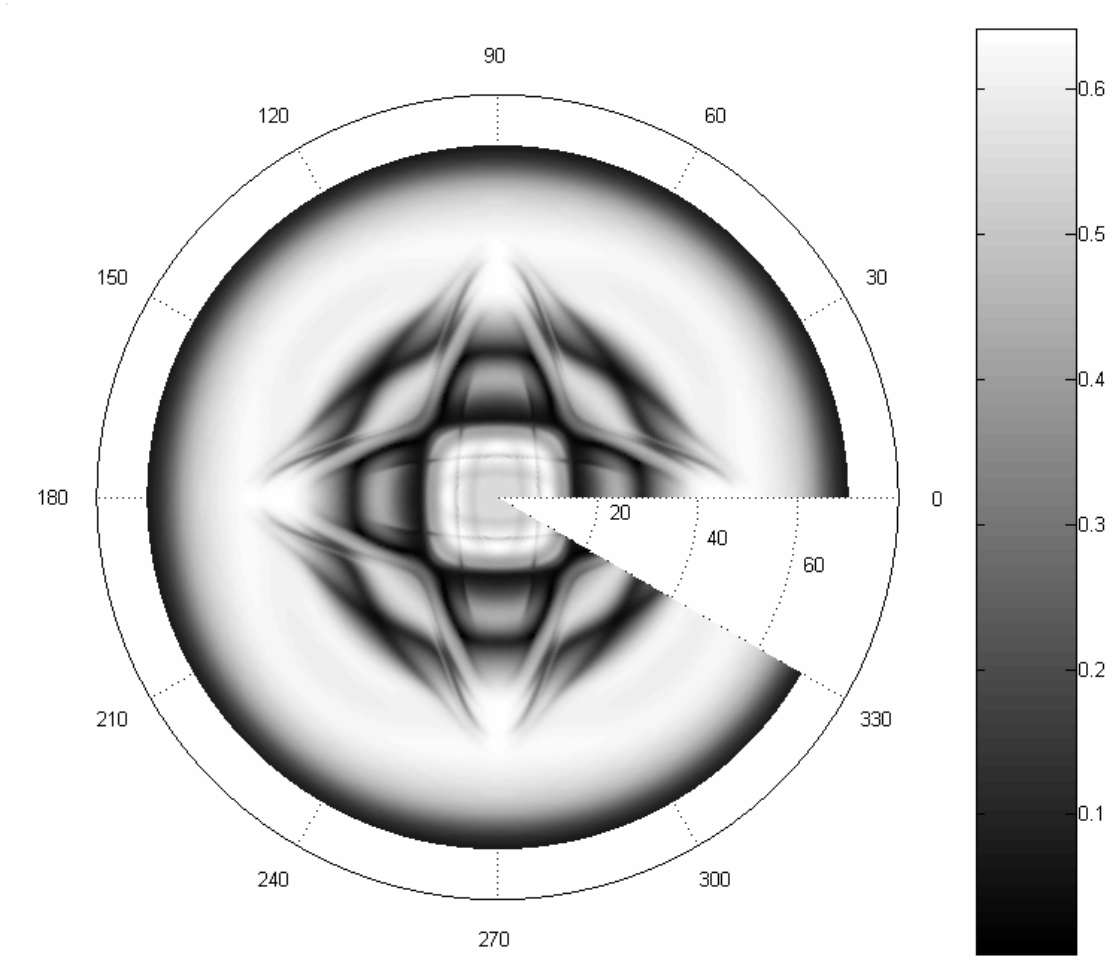

Fig. III.25 (identical to Fig. XI.B_10): ***Ultrasonic Polar Scan (harmonic 5MHz, in transmission) of a 1mm thick cross-ply reinforced composite consisting of 10 ($0^0/90^0$) stacked layers of unidirectional fiber reinforced material.***

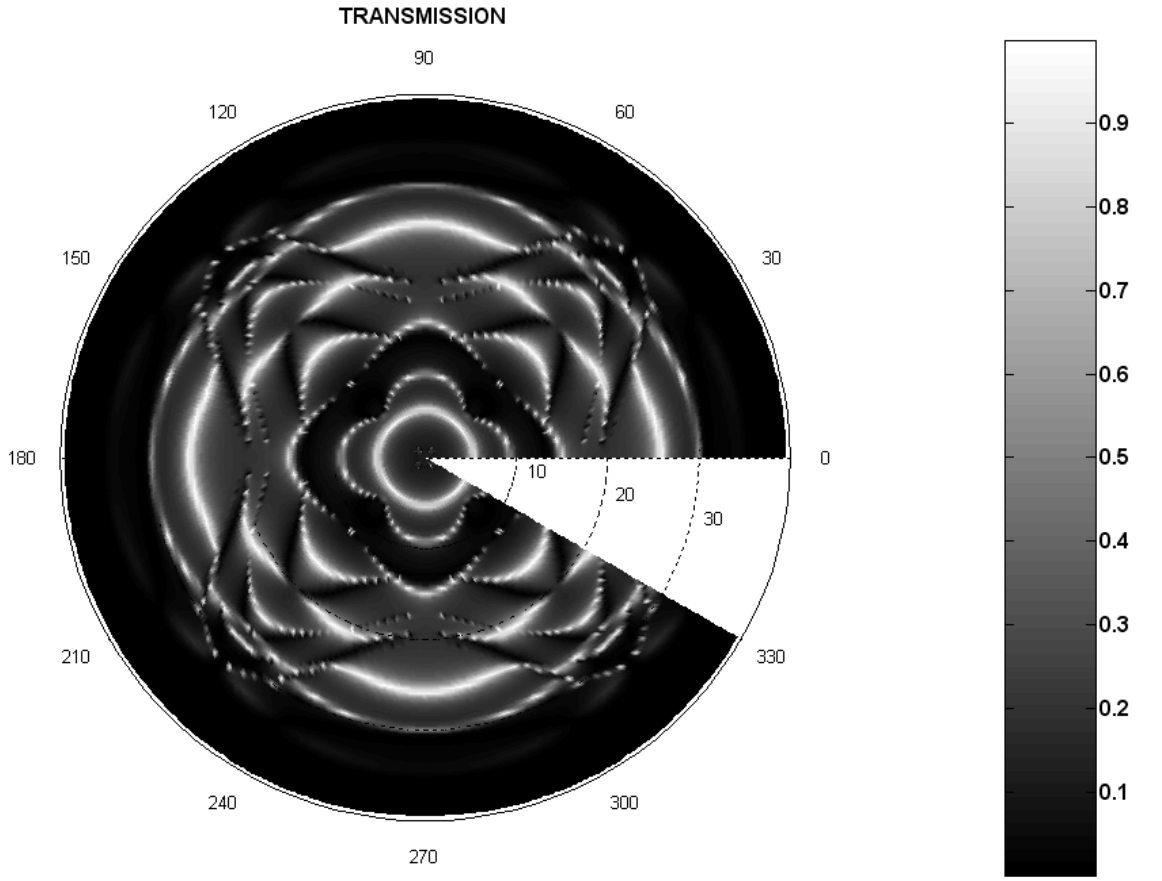

Fig. III.26 (identical to Fig. XI.B_15): ***simulated polar scan in transmission for a 3mm thick Z-cut Barium Titanate plate at 2 MHz.***

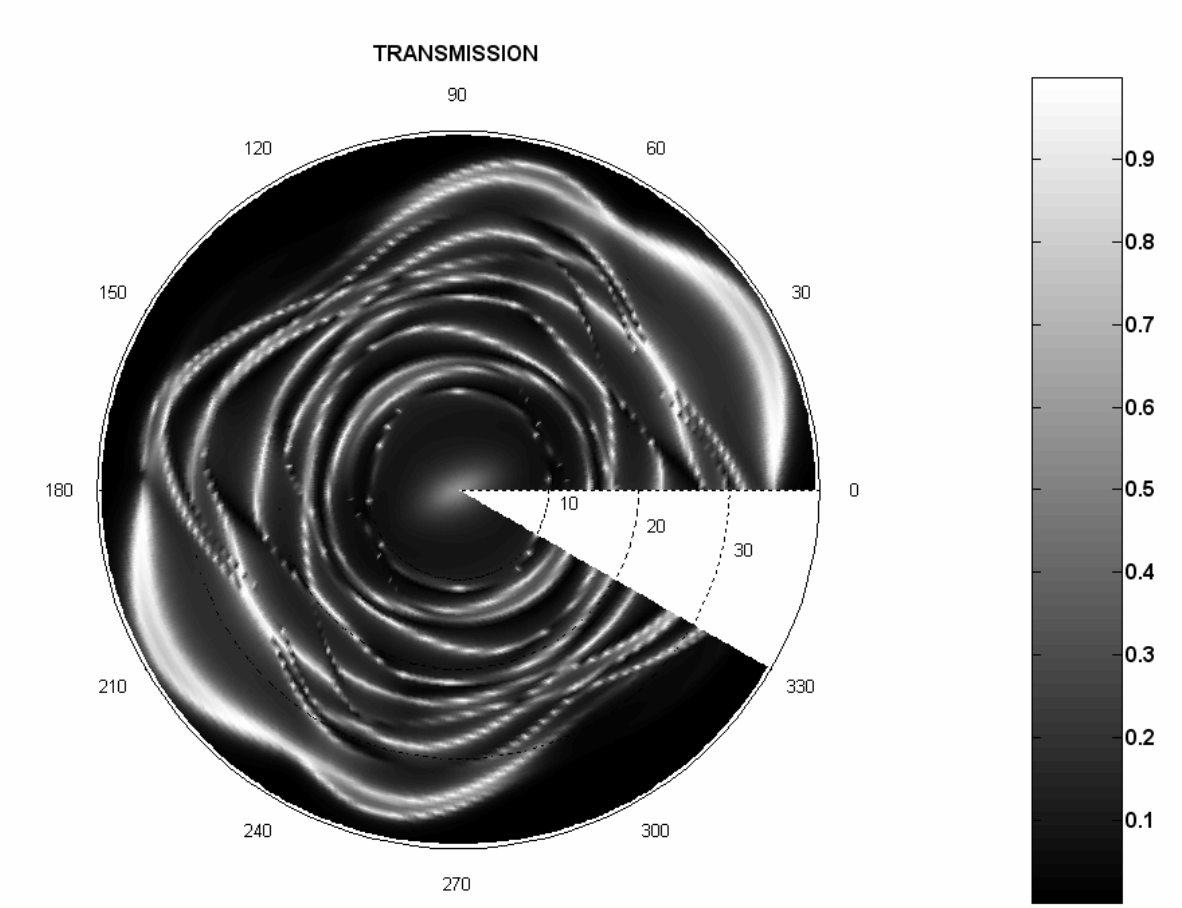

Fig. III.27 (identical to Fig. XI.B_26): ***simulated polar scan in transmission for a 3mm thick 'arbitrary'-cut layered plate at 2 MHz.***

Section XI.C : On the influence of fatigue on ultrasonic polar scans of fiber reinforced composites

- Nico F. Declercq, Joris Degrieck, Oswald Leroy, " On the influence of fatigue on ultrasonic polar scans of fiber reinforced composites", **Ultrasonics** 42, 173-177, 2004. *(Imp. Fact. 0.844; SCI-index, Acoustics, rank:11 /28)*
- Oral presentation at 'Ultrasonics International 2003', **Granada**, Spain, 30 June- 3 July 2003

In our department, extensive research is performed on fatigue of composites. One of the consequences of fatigue is a diminishing stiffness. Because characteristic patterns in ultrasonic polar scans are formed, to a large extent, by the stiffness of an examined laminate, it is natural to apply such scans for fatigue monitoring. In this section, it is shown by means of experiments and simulations (in good agreement), that ultrasonic polar scans are indeed capable of fatigue monitoring. This is important in many branches of the economy, such as the airline industry, etc.

Section XI.D : A numerical study on the feasibility of visualization of stress in isotropic plates by means of the reflected amplitude of harmonic ultrasonic waves

- Oral presentation at 'InterNoise2003', International Convention Center Jeju, **Seogwipo**, Korea, August 25-28, 2003

A lot of materials are subject to residual stress, as a consequence of the fabrication process. Furthermore, materials inside constructions, are also subject to applied stress. The magnitude and the direction of these stresses can be spatially dependent, whence a local characterization is required. For that purpose, ultrasonic polar scans seem inviting, because they collect local information of the investigated material. A model was applied for simulating the effect of stress in anisotropic laminates. Simulations are performed for the case of isotropic plates (that become anisotropic because of applied stress) and it is shown that ultrasonic polar scans are not very susceptible to stress, except in the exceptional case of very large stress.

Chapter XII Sound in piezoelectric materials

Section XII.A : The effect of stiffening of crystals due to piezoelectricity

The effect of stiffening of crystals due to piezoelectricity, is well known. Nevertheless, this section shows the effect graphically, by plotting the difference of the slowness surfaces with and without piezoelectricity. Furthermore, arrows can be added to the graphics, that denote the change of polarization or the change of energy flux.

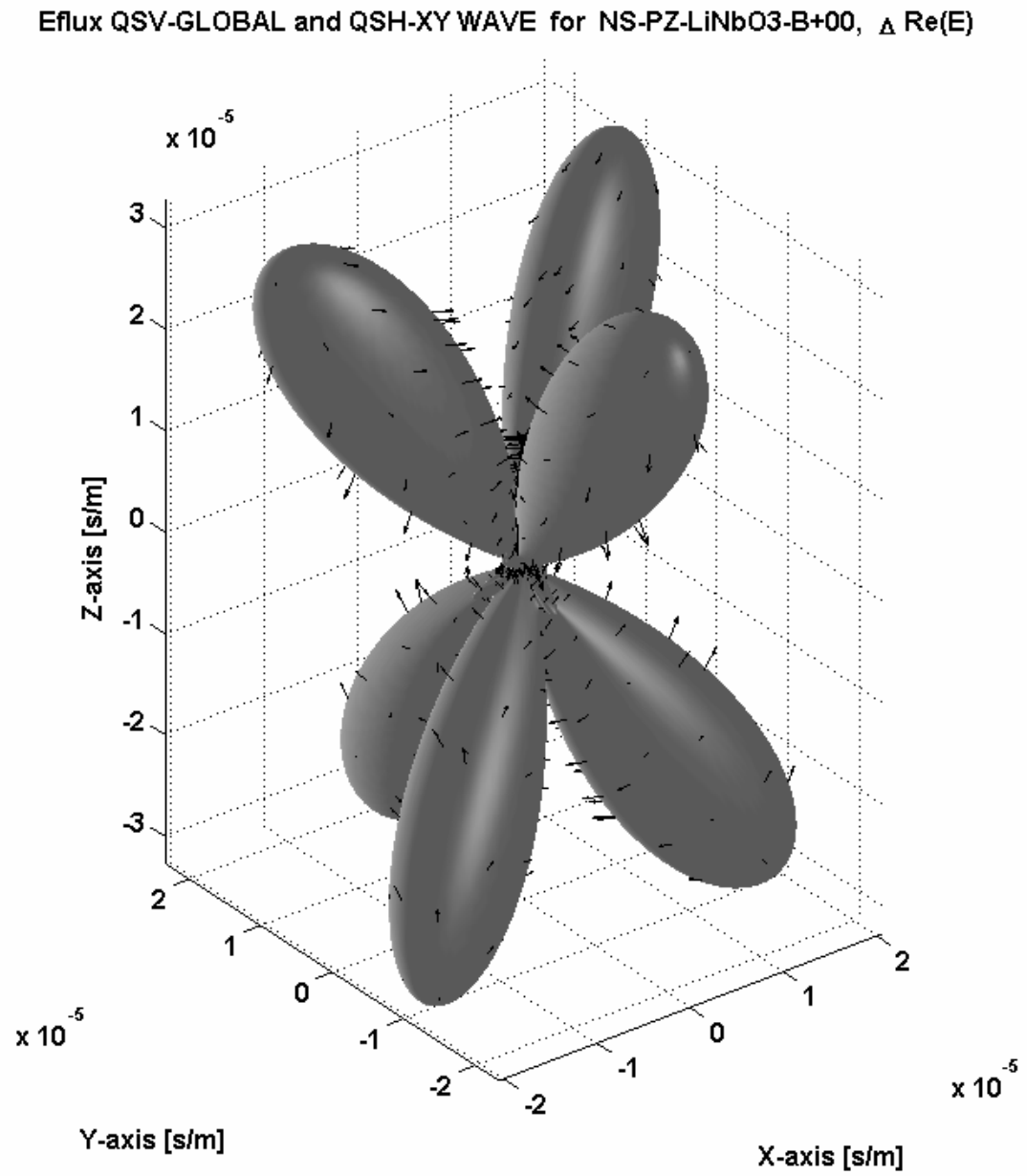

Fig. III.28 (identical to Fig. XII.A_5): ***The difference between the slowness surface for the QSV mode in Lithium Niobate, including piezoelectricity, and neglecting piezoelectricity. The black arrows denote the difference of energy flow for each spot.***

Section XII.B.1 : Inhomogeneous waves in piezoelectric crystals

In the existing literature, inhomogeneous waves in piezoelectric materials are not considered. Here, they are introduced and it is shown that they are better susceptible to the presence of piezoelectricity in crystals than homogeneous plane waves.

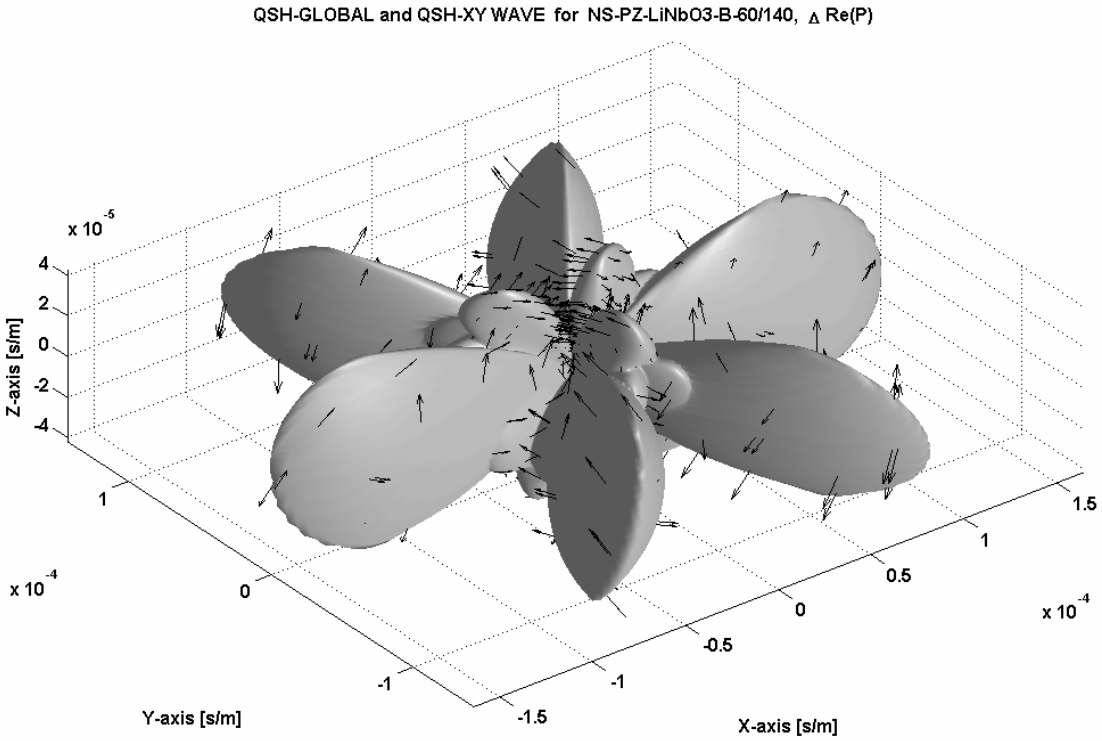

Fig. III.29 (identical to Fig. XII.B.1_12): ***The difference between the slowness surface for the QSH mode in Lithium Niobate, in the case of inhomogeneous waves, including piezoelectricity, and neglecting piezoelectricity. The black arrows denote the difference of polarization for each spot.***

Section XII.B.2 : Enhanced anisotropy in Paratellurite for inhomogeneous waves and its possible importance in the future development of acousto-optic devices

The strong anisotropy in paratellurite is very important for the fabrication of acousto-optic cells. Here, it is shown that the effect of anisotropy on inhomogeneous waves in this crystal, is much more outspoken than the effect on homogeneous plane waves. This makes it reasonable to consider fabricating acousto-optic cells, based on inhomogeneous waves instead of homogeneous waves.

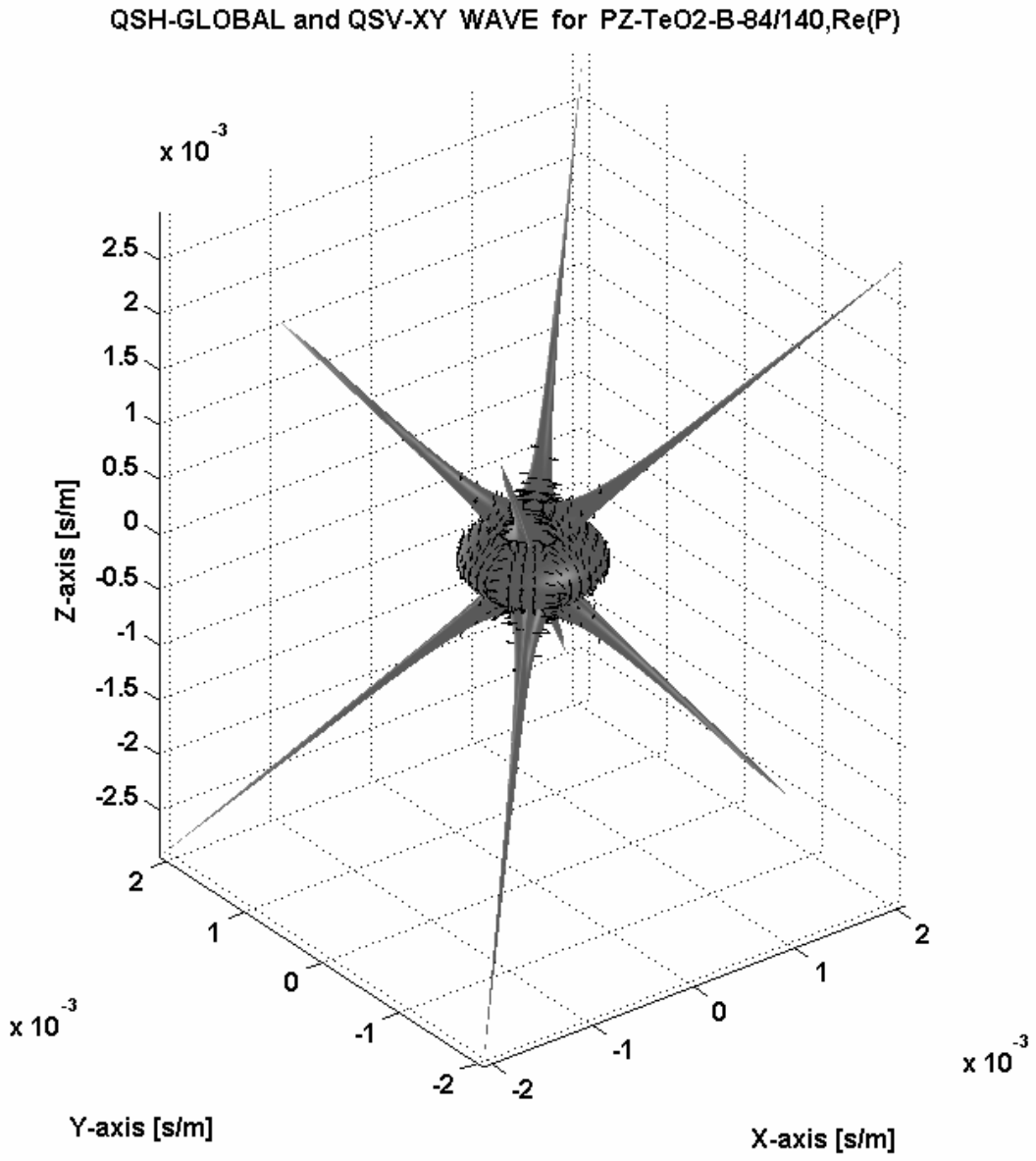

Fig. III.30 (identical to Fig. XII.B.2_11): ***Slowness surface of the QSH mode in paratellurite for inhomogeneous waves. The black arrows denote the polarization vector at each point on the slowness surface. The formation of a 'ball', covered by pins, denotes a very strong directional dependent velocity.***

Section XII.C : Sound in biased piezoelectric materials of general anisotropy

- Oral presentation at 'ICA2004 18th International Congress on Acoustics', Kyoto International Conference Hall, **Kyoto**, Japan, 4-9 April 2004

A generalized form of the Christoffel equation was formulated for biased piezoelectric crystals of general anisotropy. This is done by considering a linear acoustic regime in a crystal that is biased by nonlinear effects. An expression is given of the energy flux for the

considered situation of biased piezoelectric crystals. Numerical results are reported for Lithium Niobate. The influence is calculated of an initial pressure, in the piezoelectric case and in the non-piezoelectric case, for homogeneous plane waves and also for inhomogeneous plane waves. Furthermore, the influence of the magnitude and the direction of the considered pressure, on the change in the acoustic wave velocity, is studied as well.

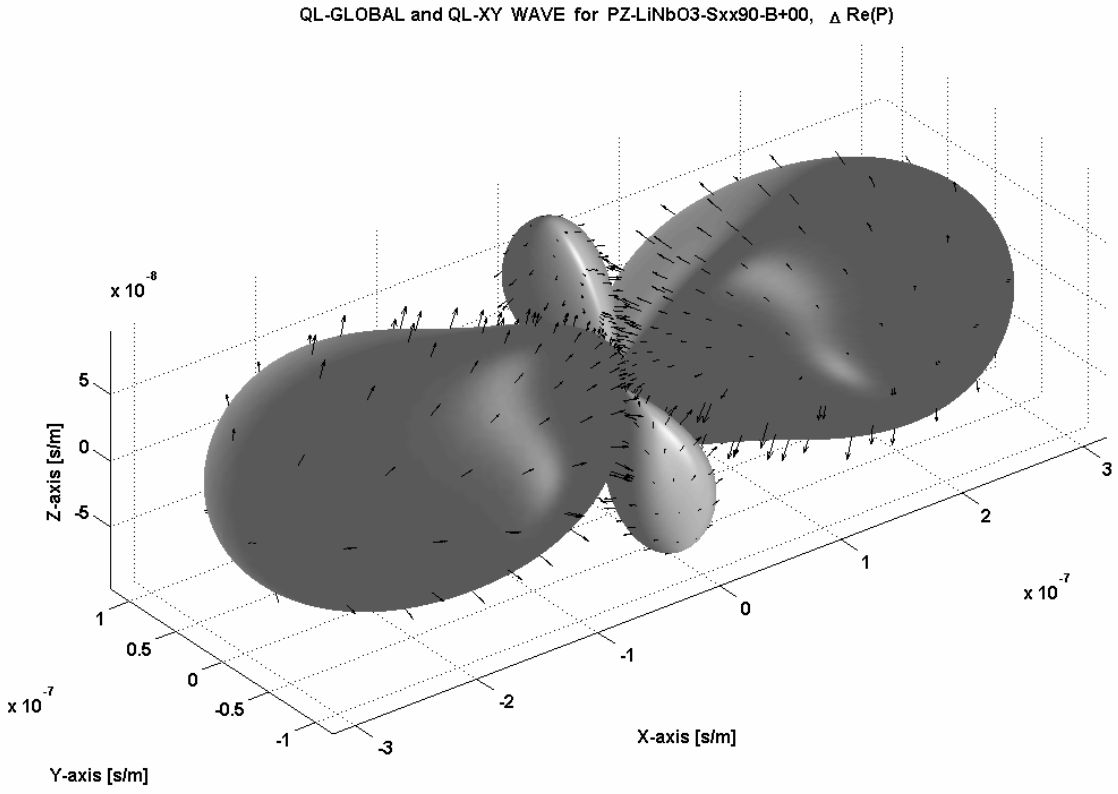

Fig. III.31 (identical to Fig. XII.C_2): ***The change of the slowness surface for the QL-mode, for a pressure of 90 MPa along the X-axis, in the case of homogeneous plane waves for piezoelectric Lithium Niobate. The arrows denote the change of polarization.***

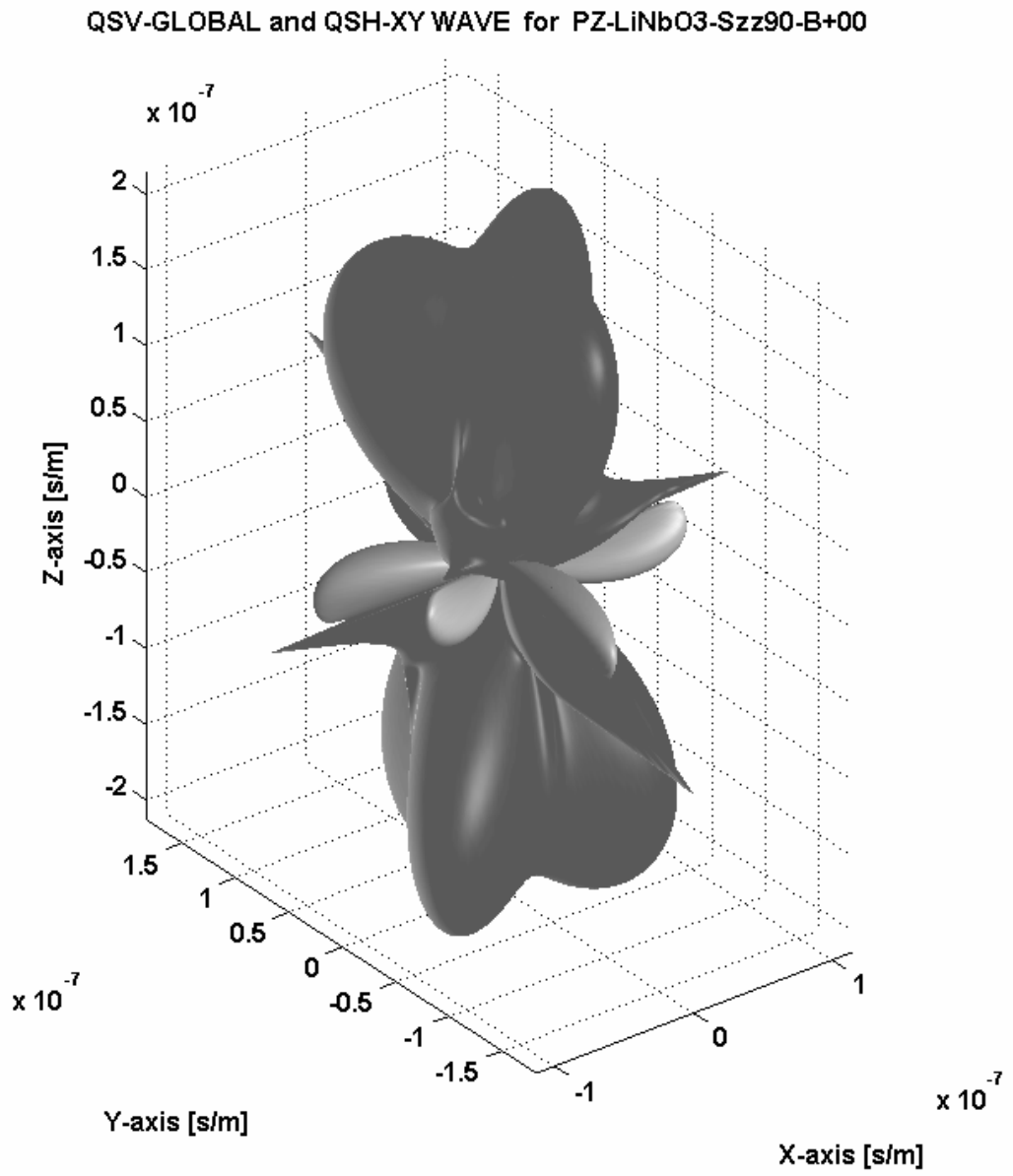

Fig. III.32 (identical to Fig. XII.C_18): ***The change of the slowness surface for the QSV-mode, for a pressure of 90 MPa along the Z-axis, in the case of homogeneous plane waves for piezoelectric Lithium Niobate.***

Chapter XIII Acoustic Microscopy

Section XIII.A : Microscopic Bulk Imaging of Fabric Fiber Reinforced Composites

Microscopic bulk imaging combines a newly developed C-scan apparatus and sophisticated data acquisition technology, with high quality ultrasonic microscopy

technology. The system generates ultra short ultrasonic pulses (less than two wavelengths long) having a nominal frequency of 50 MHz. The technique is also applicable at higher frequencies. The ultrasonic beam is focused, having a relatively small aperture. Layer-by-layer imaging of the internal microstructure of carbon fiber reinforced composites (CFRC) and glass fiber reinforced composites (GFRC) is achievable. The method provides a spatial lateral resolution in the order of 50 microns and an in-depth resolution in the order of 80 microns. Echo signals reflected from structural units, such as plies, fiber bundles and micro-flaws form acoustic images of the microstructure at different depths inside the samples. The images make it possible to see ply arrays, the stacking of bundles within plies and the binding material distribution within the bulk of the composite. They reveal failures of interply adhesion, buckling of single plies and fiber bundles, internal defoliations, disbonds and voids. The series of successive images offer outstanding possibilities to reconstruct the bulk structure, to estimate local variations of the properties, and the topological and geometrical characteristics of the structural components. The imaging technique has been applied to study different types of fiber packing – unidirectional, cross-ply and fabric laminates. In addition, high-resolution (one micron) acoustic images are also presented at higher frequencies, for larger aperture, that allow the investigation of the fiber distribution within a single bundle. The images also allow the visualization of the structure of fiber bundle crossovers and disbondings at interfaces and the evaluation of the interaction of a single fiber with the resin or even elastic characteristics of individual fibers.

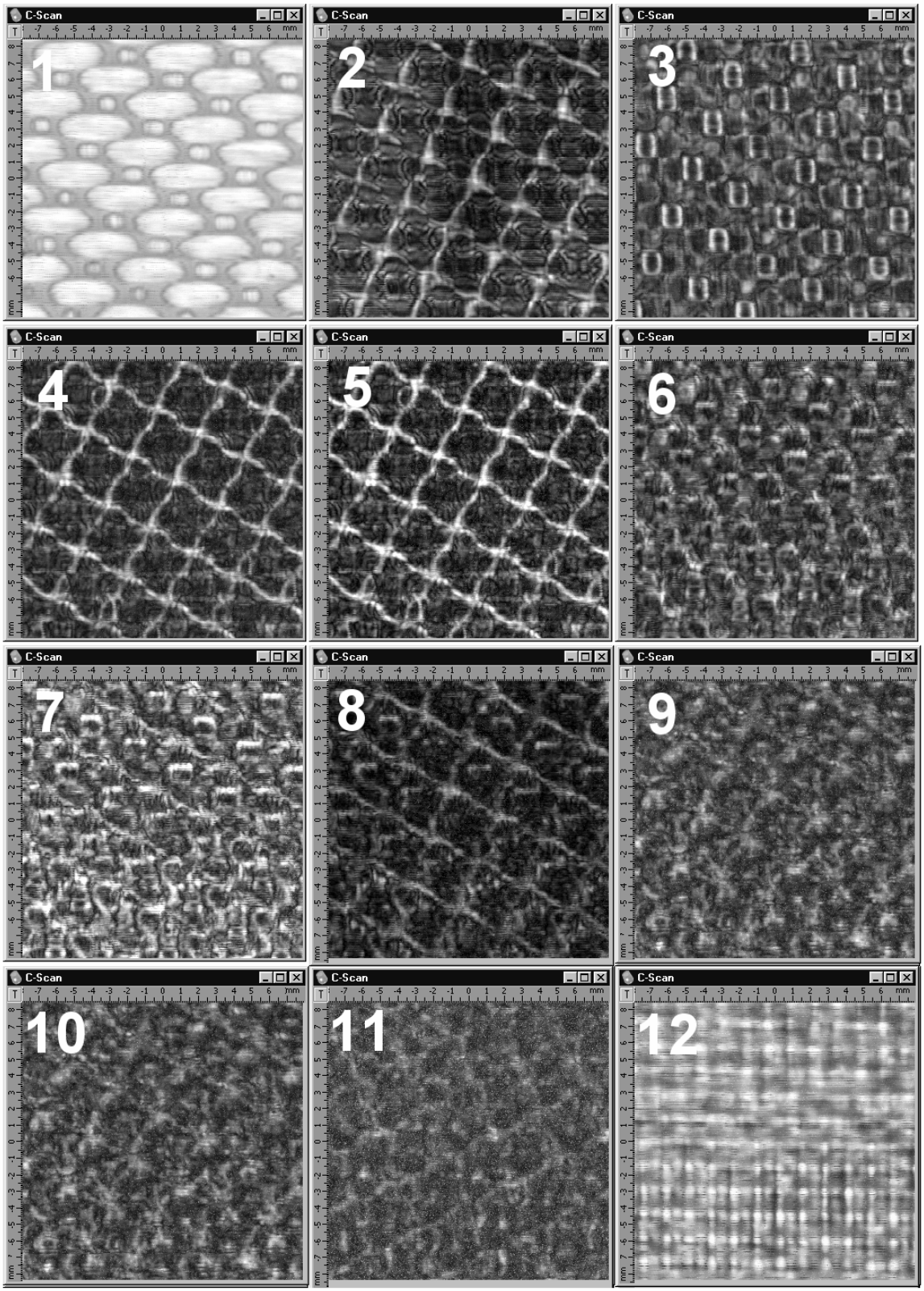

Fig. III.33 (identical to Fig. XIII.A_13): ***C-scan images at different depths, beginning with the upper surface (#1) and ending with an image of the bottom (#12), for unidirectional fabric carbon fibers in Poly Phenylene Sulfide (PPS).***

Chapter XIV Exotic Topics

Section XIV.A : The double sided ultrasonic beam displacement

- Nico F. Declercq, Joris Degrieck, Oswald Leroy, "The Double Sided Ultrasonic Beam Displacement", **Appl. Phys. let.** 85(18), 4234-4236, 2004 *(Imp. Fact. 4.207; SCI-index, Physics-Applied, rank:3/76)*

It is a well established idea in optics as well as in ultrasonics that a bounded Gaussian beam, when reflected from an interface, can be displaced in the forward or in the backward direction, depending on the propagation direction of leaky waves that are generated by the incident beam. Such a displacement is often accompanied by the so called Schoch effect characterized by a null strip in between a specular and a nonspecular reflected beam, and a trailing field that is much further displaced. The current paper shows experimentally and numerically that a simultaneous forward and backward displacement is possible accompanied by two null strips and being only the result of forward propagating Lamb waves.

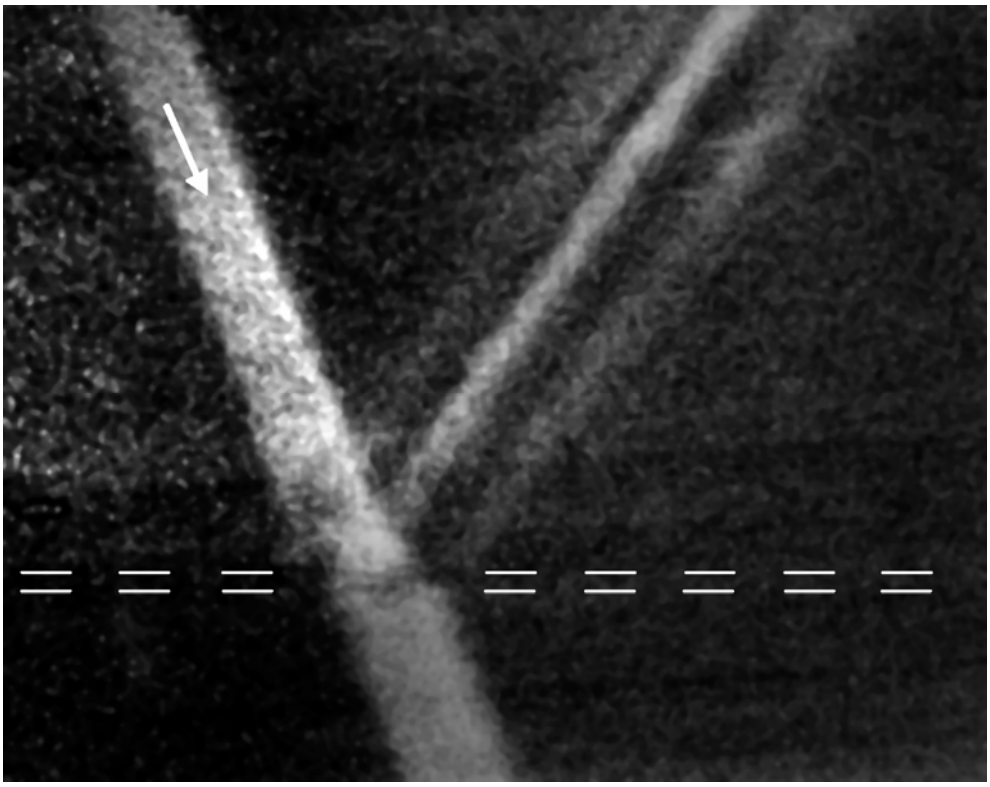

Fig. III.34 (identical to Fig. XIV.A_2): ***The double sided beam deformation. A backward and a forward displaced beam are visible together with the central specular reflected beam.***

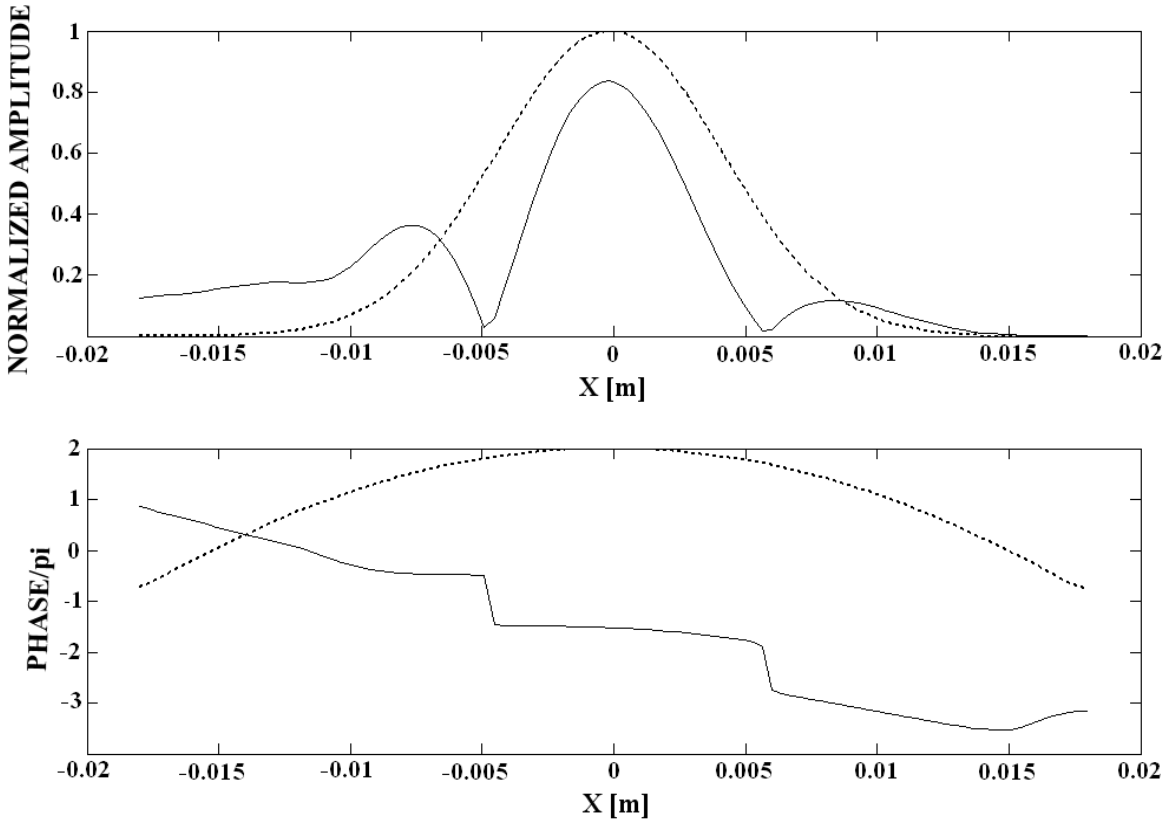

Fig. III.35 (identical to Fig. XIV.A_5): ***Simulation of Fig.* III.34*, i.e. incidence at 28.35^0. Dotted curve: incident beam profile, solid curve: reflected beam profile. Note that the forward and the backward displaced beams are out of phase with the specular central lobe.***

Chapter IV Inhomogeneous Waves and Bounded Beams

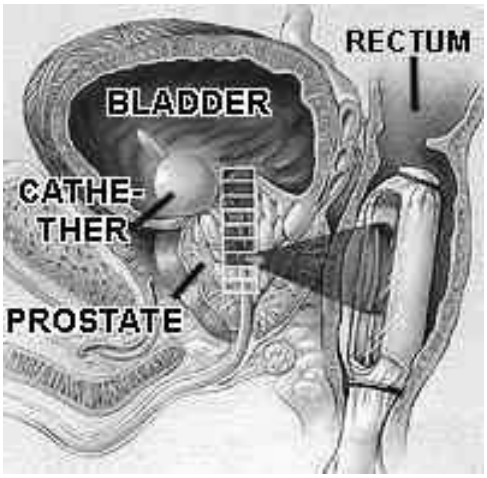

Focused ultrasound is sometimes used to cure prostate cancer. One of the sections of this chapter studies the flexible adjustment of focused ultrasound. The study may be important for the fabrication of achievable equipment for cancer therapy.

The problem of the square root of a negative number, already existed at the beginning of the Christian calendar, see for example 'Stereometrica', by Heron of Alexandria. Around 800 years later, the idea of the existence of a solution was crushed by the Indian mathematician Mahavira, who stated 'As in the nature of things, a negative is not a square, it has no square root'. Girolamo Cardano was the mathematician who first discovered a solution, in 1545, though he thought his discovery was fictitious and useless. The further development and spreading of the idea of complex numbers, was the result of brilliant scientists such as Caspar Wessel, Rene Descartes, Gottfried Wilhelm von Leibniz, Leonard Euler and Carl Friedrich Gauss.

In the theory of waves, and in particular the theory of acoustics and ultrasonics, a complex number has been introduced after the discovery by Leonhard Euler (in *Introductio in analysin infinitorum*, 1748) that an exponential function, containing an imaginary argument, is analytically equal to the combination of a cosine in the real space and a sine in the imaginary space, hence

$$e^{iS} = \cos S + i \sin S$$

This notion enables the addition of an imaginary twin to each real wave phenomenon and analyze the problem in the complex space. After this analysis, it is possible to extract the real solution from the complex result. The merit of this procedure is the fact that all mathematical expressions in the theory of waves, are contracted and simplified after the transformation into the complex space.

An acoustic wave is oscillatory in time and in space. From mechanical considerations, it is possible to obtain the wave equation, relating the temporal properties to the spatial properties of sound. The simplest solitary solution of this equation, is the so called homogeneous plane wave. It is characterized by a harmonic function like the one obtained by Euler,

possessing a real argument ‘S’. This involves a real wave vector and a real frequency. Even though pure plane waves are the simplest solitary solutions of the wave equation, they are able to generate more complicated sound fields by means of a superposition in the framework of the Fourier theory. Nevertheless, there are more solitary solutions possible. Most of them will probably never be discovered.

One, very useful, solitary solution is the inhomogeneous plane wave. It is a wave that contains temporal and spatial harmonic as well as spatial inharmonic amplitude variations. Being a solution of the wave equation, it fulfills strict relationships between the harmonic and the inharmonic amplitude variations, through the so called dispersion relation. If Euler’s notation is followed, inhomogeneous plane waves can easily be described as pure homogeneous plane waves, having a complex wave vector.

If also the temporal variation contains inharmonic contributions, a complex frequency is involved and the wave is called ‘complex harmonic’ and more specific ‘complex harmonic homogeneous’ or ‘complex harmonic inhomogeneous’, depending on the lack, respectively presence of an imaginary part of the wave vector.

Inhomogeneous waves are interesting phenomena, because their propagation properties differ from pure homogeneous plane waves. Also their polarization is different. Nevertheless, such kind of waves have always been considered mathematical artifacts that are only generated experimentally (along interfaces) under certain conditions during scattering.

It was not until Claeys and Leroy discovered that inhomogeneous waves are natural building blocks of bounded beams, resulting in a physical connection between the Schoch effect and the generation of Rayleigh waves on smooth surfaces, that the world of acoustics realized the physical importance of inhomogeneous waves. Inhomogeneous waves are present inside bounded beams and they are the origin of the stimulation of surface waves. Later, inhomogeneous waves have been generated experimentally and their excellent ability to stimulate surface waves, has been validated.

Because Oswald Leroy is my promoter, a study of inhomogeneous waves has been almost naturally a mandatory requirement before studying additional topics. While studying this wonderful subject, I have written a historical overview of the concept of inhomogeneous waves. This survey is given in section IV.A of this chapter.

The decomposition of bounded beams into inhomogeneous waves is mathematically well established, apart from numerical instabilities, for which there have not yet been found ultimate solutions. Two enhancements of the stability of the decomposition, are presented in sections IV.B and IV.C.

As mentioned above, inhomogeneous waves have been generated experimentally and it has been shown that their behavior corresponds to what is mathematically predicted. Nevertheless, the experimentally generated inhomogeneous waves only correspond to mathematical inhomogeneous waves within a limited spatial interval. This is, of course, due to the finite dimensions of transducers that generate such waves. An unavoidable question that immediately arises is, of course, “how is it possible that such bounded inhomogeneous waves behave like infinite inhomogeneous waves?” It is possible to simulate the behavior of bounded inhomogeneous wave by approaching them as a summation of infinite plane waves, in the framework

of the Fourier theory. But, this is merely a simulation, not a scientific answer to the posed question. Furthermore, it is a connection between 'homogeneous' plane waves and bounded 'inhomogeneous' waves. Besides, simulating a phenomenon is quite different from understanding it. The real answer is found in section IV.D, where the mathematical link between infinite inhomogeneous plane waves and bounded inhomogeneous waves is found through the Laplace transformation.

In the past, the study of bounded beams in terms of inhomogeneous waves, has always been limited to the 2D case, because it was impossible to expand a 3D bounded beam into inhomogeneous waves. This problem has been solved and the concept is outlined in section IV.E.

As mentioned earlier, also the frequency of plane waves can be considered complex valued. This results in a harmonic oscillation that is damped in time. In section IV.F, it will be outlined how the presence of a complex frequency , can change the focal length of a focused bounded beam. It is also shown that this phenomenon is not only true in the mathematical case of complex harmonic waves, but also in the realistic case of sound being limited in time and having temporal characteristics that correspond, within a limited time window, to the complex harmonic wave. This is very important, because it shows that adapting the temporal variation of the amplitude (a variation that is much more slowly than the oscillatory – harmonic - variation) makes it possible to change the focal length. Therefore, expensive phased array technology becomes unnecessary and makes the treatment of cancer by means of focused ultrasound better achievable, also for developing countries.

Section IV.G describes the discovery of a new type of surface waves. It radiates both into the solid and into the liquid and is based on novel calculations within the framework of the theory of inhomogeneous waves.

Further on in this dissertation, a study of inhomogeneous waves will be presented in mud layers (chapter V), in diffraction phenomena (chapter X) and in piezoelectric media (chapter XII). Most of these additional studies have not been included in the historical survey of section IV.A.

IV.A The History and Properties of Ultrasonic Inhomogeneous Waves

This section gives a historical survey of the development of the inhomogeneous wave theory, and its applications, in the field of ultrasonics. The references are listed chronologically and are as good as complete. Along the historical description, several scientific features of inhomogeneous waves are described. All topics of inhomogeneous wave research are taken into account, such as waves in viscoelastic solids and liquids, thermo-viscous liquids and solids, anisotropic viscoelastic materials. Also inhomogeneous waves having a complex frequency are described. Furthermore the formation of bounded beams by means of inhomogeneous waves is given and also the diffraction of inhomogeneous waves on periodically corrugated surfaces. The experimental generation of inhomogeneous waves is considered as well. The contents of this section are accepted for publication in IEEE Trans. on UFFC (Imp. Fact. 1.595 ;SCI-index, Engineering – electrical & electronic, rank:46/205)

INTRODUCTION

There is no better sentence to start this section than one which is similar to the one that was used to end a paper of Bernard Poirée [44], i.e. 'Ultrasonic inhomogeneous waves are a treasure'. It will be seen in what follows that inhomogeneous waves have been a goldmine for many researchers because it formed the core of their scientific activities for many years, but it will also be seen that inhomogeneous waves are actually a treasure of physics because of many theoretically predictable beautiful features, properties and behaviors. Furthermore it will be noticed that inhomogeneous waves often let nature poke fun at humans' intuition.

First of all we would like to show that inhomogeneous waves are of primordial importance in the correct description of reflection/transmission phenomena. Let's for example take a look at the interface between a viscoelastic liquid and an ideal liquid. A homogeneous plane wave incident from the viscoelastic fluid is damped along its propagation direction. The transmitted wave is not damped along its propagation direction but its amplitude is influenced by the one of the incident wave as shown in Fig. IV.A_1. It can be noticed in Fig. IV.A_1 that the transmitted wave will have an amplitude that grows exponentially along its wave front. Such waves are called inhomogeneous waves. Therefore inhomogeneous waves are entities that are necessary to describe even such a simple phenomenon as scattering on plane interfaces.

For some people, inhomogeneous waves are completely unknown, for others they are unavoidable when the interaction of sound with viscoelastic materials is to be described. Yet other people (the inhomogeneous wave freaks) study such waves in the bulk of a material, for example generated by means of some sort of a transducer, and let them interact with materials, such waves are often explicitely called inhomogeneous bulk waves. Because inhomogeneous waves are the most general plane wave solutions of the wave equation, there is actually no reason why one should neglect inhomogeneous waves and only study the very trivial case of homogeneous plane waves. This section describes, from a historical point of view, how the concept of inhomogeneous waves in ultrasonics has grown from an artifact to a fortune of physics. The references in this section are listed according to their submission date and the authors have tried to make this list complete. The historical approach is the 'red line' in this section and the scientific knowledge is distributed along the current section as to appear

whenever necessary to understand the historical development. Nowadays, inhomogeneous waves have become tools for nondestructive testing. Therefore it is expected that many applications will appear in papers the coming decade. The authors would like to express their wish that the current section may become an inspiring source for future scientists in this fantastic field of research.

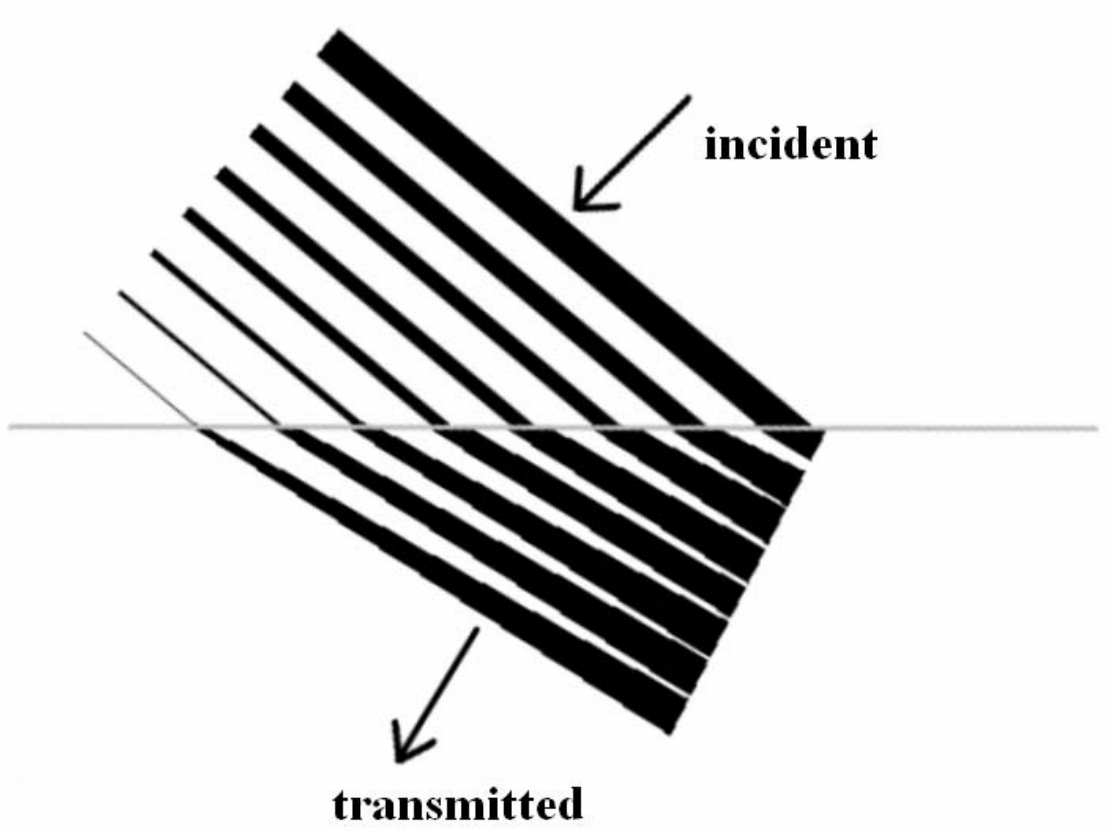

Fig. IV.A_1: ***An inhomogeneous wave is naturally 'born' in transmission at the interface between a viscoelastic liquid (top) and an ideal liquid (bottom). In general, whenever damping plays a role, inhomogeneous waves are part of the game. The black lines correspond to wave fronts, their thickness corresponds to the amplitude.***

In the past, several papers have appeared that give an overview of inhomogeneous waves, but never in a historical context and never spanning the whole area of inhomogeneous waves. In 1988, an overview appeared by Poirée [31], dealing with elastic solids and ideal fluids and also one by Deschamps [32], dealing with viscoelastic materials, conservation of energy and special attention also went to the generalized law of Snell-Descartes. A year later came another review by Leroy, Mampaert and Quentin [33]. Later reviews can be found in Deschamps [39] (mainly dealing with thermo-viscous materials and viscoelastic isotropic and anisotropic materials) and Poirée [44]. Leroy also wrote a review in 1996 [67] with special attention for non specular bounded beam effects at the Rayleigh angle of incidence.

The current section deals with all important aspects of inhomogeneous waves and does not go into detail in some areas that have been less important for the growth of the field of inhomogeneous waves in ultrasonics. These areas are dealing with waves in sediment layers [43], in inhomogeneous media such as rock layers [59], viscous fluids [63], porous materials [71, 24] and the interaction of inhomogeneous waves with defects [83]. However it is believed that the latter area will become more and more important in the coming decade since inhomogeneous waves are starting to be used in NDT.

BASIC PROPERTIES OF ULTRASONIC INHOMOGENOUS WAVES

An example of an inhomogeneous wave is shown in Fig. IV.A_2. The different parameters denoted in this figure will be outlined below. This paragraph summarizes some basic properties of inhomogeneous waves. How these properties were discovered and also supplementary developments will be described in subsequent paragraphs.

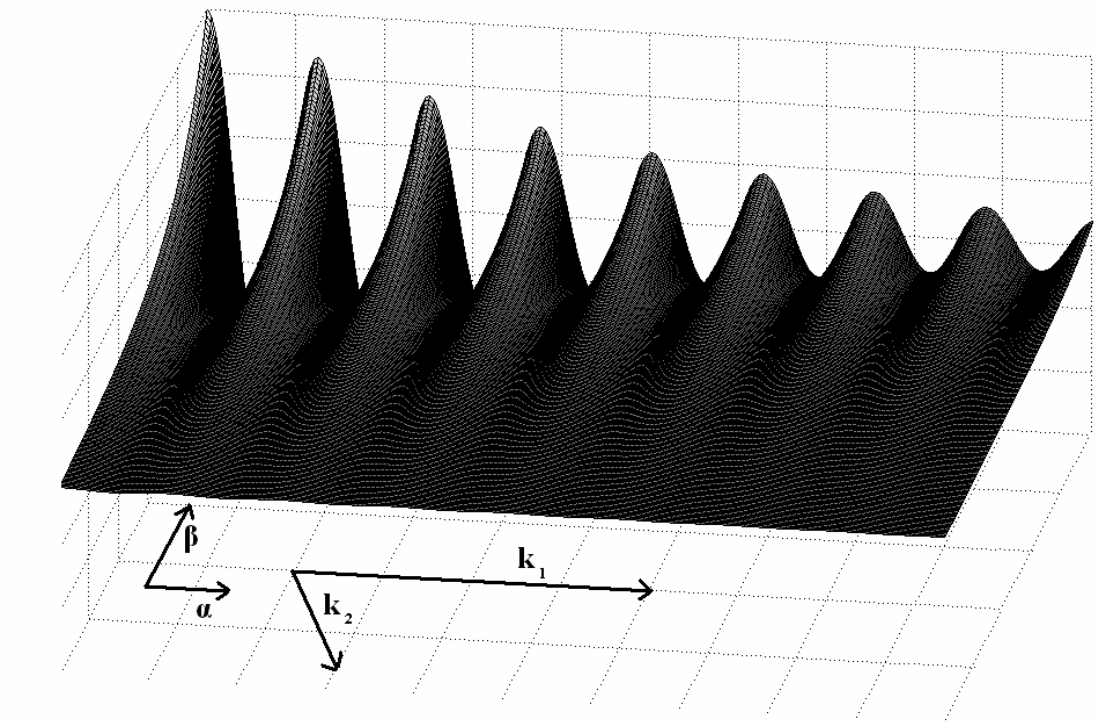

Fig. IV.A_2: ***An inhomogeneous wave. Damping occurs along the propagation direction and there is also an exponential amplitude decay along the wave front due to the inhomogeneity.***

Basically an inhomogeneous ultrasonic wave, represented by a particle displacement **u**, is written just as a homogeneous plane wave, i.e.

$$\mathbf{u} = A\mathbf{P}\exp\left(i\mathbf{k}\bullet\mathbf{r} - i\omega t\right) \qquad \text{(IV.A\_1)}$$

A being the amplitude, **P** being the polarization, **k** is the wave vector, ω is the angular frequency, **r** is the position, t is time, and $i = \sqrt{-1}$.
The wave (IV.A_1) is a solution of the viscoelastic wave equation

$$\tilde{\mu}\,\Delta\mathbf{u} + \left(\tilde{\lambda} + \tilde{\mu}\right)\nabla\nabla\cdot\mathbf{u} = \rho\,\ddot{\mathbf{u}} \qquad \text{(IV.A\_2)}$$

with

$$\tilde{\lambda} = \lambda + \lambda' \frac{\partial}{\partial t} \qquad \text{(IV.A\_3)}$$

$$\tilde{\mu} = \mu + \mu' \frac{\partial}{\partial t}$$

if

$$\mathbf{k} \bullet \mathbf{k} = \rho\omega^2 / \left(\tilde{\lambda} + 2\tilde{\mu} \right) \qquad \text{(IV.A\_4)}$$

and

$$\mathbf{k} \times \mathbf{P} = 0 \qquad \text{(IV.A\_5)}$$

or if

$$\mathbf{k} \bullet \mathbf{k} = \rho\omega^2 / \tilde{\mu} \qquad \text{(IV.A\_6)}$$

and

$$\mathbf{k} \bullet \mathbf{P} = 0 \qquad \text{(IV.A\_7)}$$

Waves that correspond to (IV.A_4-5) are called longitudinal, whereas waves corresponding to (IV.A_6-7) are called shear waves.

It is also convenient to take into account that $\partial / \partial t \approx -i\omega$ and use the following substitutions in (IV.A_4) and (IV.A_6):

$$\mu = \rho\omega^2 \frac{v_s^2 \left(\omega^2 - \alpha_{0,s}^2 v_s^2 \right)}{\omega^4 + 2\omega^2 \alpha_{0,s}^2 v_s^2 + \alpha_{0,s}^4 v_s^4} \qquad \text{(IV.A\_8)}$$

$$\mu' = -2\rho\omega^2 v_s^3 \frac{\alpha_{0,s}}{\omega^4 + 2\omega^2 \alpha_{0,s}^2 v_s^2 + \alpha_{0,s}^4 v_s^4} \qquad \text{(IV.A\_9)}$$

$$\lambda = \frac{-\rho\omega^2 M}{S} \qquad \text{(IV.A\_10)}$$

$$\lambda' = \frac{2\rho\omega^2 N}{S} \qquad \text{(IV.A\_11)}$$

with

$$M = \omega^6\left(2v_s^2 - v_d^2\right) + \omega^4\left(\alpha_{0,d}^2 v_d^4 - 2v_d^2\alpha_{0,s}^2 v_s^2 + 4v_s^2\alpha_{0,d}^2 v_d^2 - 2v_s^4\alpha_{0,s}^2\right) + \omega^2\left(-v_d^2\alpha_{0,s}^4 v_s^4 - 4v_s^4\alpha_{0,d}^2 v_d^2\alpha_{0,s}^2 + 2\alpha_{0,d}^2 v_d^4\alpha_{0,s}^2 v_s^2 + 2v_s^2\alpha_{0,d}^4 v_d^4\right) + \alpha_{0,d}^2 v_d^4\alpha_{0,s}^4 v_s^4 - 2v_s^4\alpha_{0,d}^4 v_d^4\alpha_{0,s}^2 \quad \text{(IV.A\_12)}$$

$$N = 2\alpha_{0,d}^4 v_d^4 v_s^3\alpha_{0,s} + 4\omega^2 v_s^3\alpha_{0,d}^2 v_d^2\alpha_{0,s} - 2\omega^2 v_d^3\alpha_{0,s}^2 v_s^2\alpha_{0,d} - v_d^3\alpha_{0,s}^4 v_s^4\alpha_{0,d} + 2\omega^4 v_s^3\alpha_{0,s} - \omega^4 v_d^3\alpha_{0,d} \quad \text{(IV.A\_13)}$$

$$S = \left(\omega^4 + 2\omega^2\alpha_{0,s}^2 v_s^2 + \alpha_{0,s}^4 v_s^4\right)\left(\omega^4 + 2\alpha_{0,d}^2 v_d^2\omega^2 + \alpha_{0,d}^4 v_d^4\right) \quad \text{(IV.A\_14)}$$

whence (IV.A_4) becomes

$$\mathbf{k}\bullet\mathbf{k} = \left(\frac{\omega}{v_d} - i\alpha_{0,d}\right)^2 \quad \text{(IV.A\_15)}$$

and (IV.A_6) becomes

$$\mathbf{k}\bullet\mathbf{k} = \left(\frac{\omega}{v_s} - i\alpha_{0,s}\right)^2 \quad \text{(IV.A\_16)}$$

In (IV.A_15-16) v_d and v_s are the longitudinal respectively shear wave velocity for pure homogeneous plane waves in the considered medium whilst $\alpha_{0,d}$ and $\alpha_{0,s}$ are the intrinsic damping coefficients in the medium for longitudinal respectively shear waves.

Whenever μ' and λ' are nil, it is perfectly possible that all quantities in (IV.A_1) are real valued. The amplitude A can be real, or complex, depending on the phase at the origin. Whenever μ' and/or λ' differ from zero, it follows from (IV.A_4) and (IV.A_6) that $\mathbf{k}$ is complex valued. Besides, regardless of the values of μ' and λ', $\mathbf{k}$ can be complex valued because of specific boundary conditions. Hence inhomogeneous waves are defined as waves described by (IV.A_1) and having a complex wave vector $\mathbf{k}$, i.e.

$$\mathbf{k} = \mathbf{k}_1 + i\mathbf{k}_2 \quad \text{(IV.A\_17)}$$

A summation of a real vector with an imaginary vector, as in (IV.A_17), is called the bi-vector formalism. Substitution of (IV.A_17) in (IV.A_1) reveals that $\mathbf{k}_1$ influences the phase of the considered sound wave, while $i\mathbf{k}_2$ influences the amplitude. Therefore it is common to write

$$\mathbf{k}_2 = \boldsymbol{\alpha} - \boldsymbol{\beta} \tag{IV.A_18}$$

with

$$\boldsymbol{\alpha} \parallel \mathbf{k}_1 \tag{IV.A_19}$$

and

$$\boldsymbol{\beta} \perp \mathbf{k}_1 \tag{IV.A_20}$$

$\boldsymbol{\alpha}$ is called the damping vector, while $\boldsymbol{\beta}$ is called the inhomogeneity vector.
Now if $\mathbf{k}$ is indeed complex, then from (IV.A_5) and (IV.A_7), it follows that the polarization vector $\mathbf{P}$ can also be complex, i.e.

$$\mathbf{P} = \mathbf{P}_1 + i\mathbf{P}_2 \tag{IV.A_21}$$

The vector P is normalized whence

$$\mathbf{P}\bullet\mathbf{P} = 1 \rightarrow \begin{cases} \mathbf{P}_1\bullet\mathbf{P}_1 = 1 + \mathbf{P}_2\bullet\mathbf{P}_2 \\ \mathbf{P}_1\bullet\mathbf{P}_2 = 0 \end{cases} \tag{IV.A_22}$$

An important feature of the polarization is consequently that the real component is always larger than the imaginary component.
Because of (IV.A_21) the values of $\mathbf{P}_1$ and $\mathbf{P}_2$ are determined by (IV.A_5) or (IV.A_7) as follows:
For longitudinal waves:

$$\mathbf{k}\times\mathbf{P} = 0 \rightarrow \mathbf{P} = \mathbf{k}/|\mathbf{k}| \rightarrow \mathbf{P} = \mathbf{k}\left(\omega/v_d - i\alpha_{0,d}\right)^{-1/2} \tag{IV.A_23}$$

or in other words

$$\mathbf{P}_1 = \frac{\frac{\omega}{v_d}\mathbf{k}_1 - \alpha_{0,d}\mathbf{k}_2}{\frac{\omega^2}{v_d^2} + \alpha_{0,d}^2} \tag{IV.A_24}$$

$$\mathbf{P}_2 = \frac{\alpha_{0,d}\mathbf{k}_1 + \frac{\omega}{v_d}\mathbf{k}_2}{\frac{\omega^2}{v_d^2} + \alpha_{0,d}^2}$$

while for shear waves:

$$\mathbf{k}\bullet\mathbf{P}=0\rightarrow\mathbf{P}=\mathbf{F}\times\mathbf{k}/|\mathbf{k}|\rightarrow\mathbf{P}=\left(\mathbf{F}\times\mathbf{k}\right)\left(\omega/v_s-i\alpha_{0,s}\right)^{-1/2} \tag{IV.A_25}$$

or in other words

$$\mathbf{P}_1=\frac{\frac{\omega}{v_s}\mathbf{F}\times\mathbf{k}_1-\alpha_{0,s}\mathbf{F}\times\mathbf{k}_2}{\frac{\omega^2}{v_s^2}+\alpha_{0,s}^2} \tag{IV.A_26}$$

$$\mathbf{P}_2=\frac{\alpha_{0,s}\mathbf{F}\times\mathbf{k}_1+\frac{\omega}{v_s}\mathbf{F}\times\mathbf{k}_2}{\frac{\omega^2}{v_s^2}+\alpha_{0,s}^2}$$

with $\mathbf{F}\perp\mathbf{k}$.

From (IV.A_24) we learn that longitudinal inhomogeneous waves are elliptically polarized with the ellipse of particle motion inside the plane formed by the real and imaginary part of the wave vector. From (IV.A_26) we learn that shear waves are also elliptically polarized, however the ellipse of particle motion is not anymore inside the plane formed by the real and imaginary part of the wave vector. These polarization properties involve that it would be more appropriate to talk about quasi-longitudinal and quasi-shear waves just as in anisotropic media, but this is seldom done in inhomogeneous wave theory.

In isotropic materials, it is very convenient to let relations (IV.A_4-7) automatically be taken into account by working with the Helmholtz decomposition

$$\mathbf{u}=\nabla\varphi+\nabla\times\psi\mathbf{e} \tag{IV.A_27}$$

where φ and ψ are scalar plane waves (having a complex wave vector) and **e** is an appropriately chosen unit vector so that

$$\nabla\bullet\psi\mathbf{e}=0 \tag{IV.A_28}$$

In anisotropic materials it is better to work directly with (IV.A_1).

In many papers the dispersion relations (IV.A_15) or (IV.A_16) are written in terms of the components of **k**, leading, for *m*=*s* or *m*=*d*, to

$$k_1^2-\beta^2-\alpha^2=\frac{\omega^2}{v_m^2}-\alpha_{0,m}^2 \tag{IV.A_29}$$

and

$$k_1\alpha = \frac{-\omega}{v_m}\alpha_{0,m} \tag{IV.A_30}$$

For the moment we have supposed that (IV.A_1) is a harmonic function of time. Implicitly this means that we supposed that the vibration is somehow generated by means of a harmonic source. However there are also other sources, such as damped or even critically damped sources, possible. Sound coming from such sources will have different characteristics in time and space. In fact the source affects the complex amplitude but also the frequency, whence depending on the characteristics of the source, this frequency can be real (harmonic), complex (harmonically damped) or even imaginary (critically damped). Hence in general

$$\omega = \omega_1 + i\omega_2 \tag{IV.A_31}$$

The concept of complex frequencies will be dealt with in detail further below.

THE CONCEPT OF COMPLEX ANGLES

In the early days of the inhomogeneous wave theory and in mathematical papers about this theory, the concept of complex angles is often used.
From the fact that (see (IV.A_15-16)), for *m*=*s* or *m*=*d*,

$$\mathbf{k}\bullet\mathbf{k} = \left(\frac{\omega}{v_m} - i\alpha_{0,m}\right)^2 \tag{IV.A_32}$$

and

$$\sin^2\theta + \cos^2\theta = 1 \tag{IV.A_33}$$

in the XZ-plane **k** can be formally written as

$$\mathbf{k} = \left(\frac{\omega}{v_m} - i\alpha_{0,m}\right)\left(\mathbf{e}_x \sin\theta + \mathbf{e}_z \cos\theta\right) \tag{IV.A_34}$$

Identification with

$$\mathbf{k} = \left(k_{1,x} + ik_{2,x}\right)\mathbf{e}_x + \left(k_{1,z} + ik_{2,z}\right)\mathbf{e}_z \tag{IV.A_35}$$

then results in

$$k_{1,x} = \frac{\omega}{v_m}\sin\theta_1\cosh\theta_2 + \alpha_{0,m}\cos\theta_1\sinh\theta_2 \qquad \text{(IV.A\_36)}$$

$$k_{2,x} = \frac{\omega}{v_m}\cos\theta_1\sinh\theta_2 - \alpha_{0,m}\sin\theta_1\cosh\theta_2$$

$$k_{1,z} = \frac{\omega}{v_m}\cos\theta_1\cosh\theta_2 - \alpha_{0,m}\sin\theta_1\sinh\theta_2$$

$$k_{2,z} = -\frac{\omega}{v_m}\sin\theta_1\sinh\theta_2 - \alpha_{0,m}\cos\theta_1\cosh\theta_2$$

with

$$\theta = \theta_1 + i\theta_2 \qquad \text{(IV.A\_37)}$$

The angle defined in (IV.A_34) is hence a complex angle.

THE GENERALIZED LAW OF SNELL-DESCARTES

When an inhomogeneous wave is incident on an interface between two media, reflected as well as transmitted inhomogeneous waves will be generated, at least if the mechanical continuity conditions allow them to be generated. The conditions are very often given by continuity of normal displacement and normal stress-vector for liquid-solid interfaces and total stress for solid-solid interfaces. However there is also the continuity of propagation-phase, which simply states that along the interface (for example parallel with the X-axis) incident sound coincidentally generates scattered sound. This principle is called the classical law of Snell-Descartes and is physically best formulated as continuity of

$$\mathbf{k}_1 \bullet \mathbf{r} \quad \text{for } \mathbf{r} \in \textit{interface} \qquad \text{(IV.A\_38)}$$

and

$$\text{continuity of } \omega_1 \qquad \text{(IV.A\_39)}$$

In linear acoustics however there is also the principle that the amplitude of the scattered sound is linearly dependent on the incident amplitude. If the incident amplitude differs from spot to spot (and/or from time to time) along the interface because this incident wave is inhomogeneous (and/or has complex frequency), then the scattered waves must be equally profiled in space (and/or in time) along the interface. This results in continuity of

$$\mathbf{k}_2 \bullet \mathbf{r} \quad \text{for } \mathbf{r} \in \textit{interface} \qquad \text{(IV.A\_40)}$$

and

$$\text{continuity of } \omega_2 \qquad \text{(IV.A\_41)}$$

Relations (IV.A_38-41) can be compressed as continuity of

$$\mathbf{k}\bullet\mathbf{r} \text{ for } \mathbf{r} \in interface \qquad \text{(IV.A\_42)}$$

and

$$\text{continuity of } \omega \qquad \text{(IV.A\_43)}$$

The principles formulated in (IV.A_42-43) are called 'the generalized law of Snell-Descartes'. The principle is schematically shown in Fig IV.A_3, for an interface between two liquids. The projections of each wave vector on the interface are the same for each of the present waves (incident 'ínc', reflected 'r' and transmitted 't').

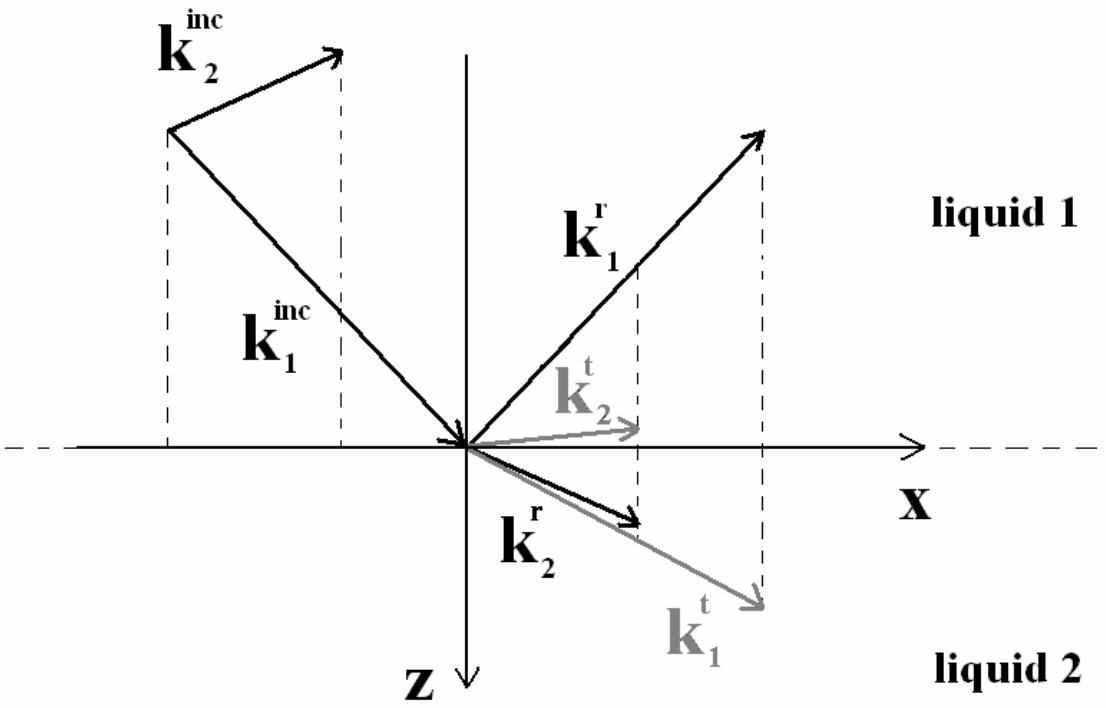

Fig. IV.A_3: ***Schematic of what is called the Generalized law of Snell-Descartes. All real wave vectors involved have the same projection on the interface, the same holds for the imaginary wave vectors.***

THE FOUNDER OF THE ULTRASONIC INHOMOGENOUS WAVE THEORY

In numerous papers concerning inhomogeneous waves, it can be found that Brekhovskikh [1] already mentions the fact that the wave number can be complex. The pioneering work of Henry F. Cooper JR [2, 3] is almost never mentioned. Most likely this work was 'forgotten' by the re-founders of ultrasonic inhomogeneous waves more than a decade later. However the work of Cooper can be considered as the foundation of the ultrasonic inhomogeneous wave theory. In this work, the existence of inhomogeneous waves (Cooper named them 'general plane waves') in viscoelastic media is proved and also the scattering of such waves on an isotropic solid-vacuum interface and an interface between two isotropic solids is considered. Note that there are some printing errors in Cooper's paper that have been discovered only in 1987 by Jones, Kwan and Yeatman [27]. Even less known is the

fact that Cooper already implements what has later been called 'the generalized law of Snell-Descartes', see (IV.A_42-43), and also the dispersion relation (IV.A_32) for inhomogeneous waves. Cooper does not apply any bi-vector formalism and does not consider the dispersion relation in its modern form resulting from that bi-vector formalism. Cooper also did not discover the fact that a reflection coefficient may exceed unity. Nevertheless there can be no doubt at all that Cooper should be considered the real founder of ultrasonic inhomogeneous wave theory.

THE RE-FOUNDERS AND BOOSTERS OF THE ULTRASONIC INHOMOGENEOUS WAVE THEORY

Single Ultrasonic Inhomogeneous Waves

In his paper, Frisk [6] deals with the fact that the description of the radiation field of tiny sources cannot occur without involving inhomogeneous waves. Therefore he studies the reflection of such waves from interfaces in the ocean bottom and states that Snell's law for real wave vector components can be generalized to the case of complex wave vector components without any problem. He also describes the fact that the reflection coefficient can exceed unity without violation of the principle of energy conservation. However Frisk studies inhomogeneous waves not as real physical entities, but as parts of the decomposition of the sound field produced by tiny sources. Therefore his inhomogeneous waves are of such a kind that they damp away from the source and would nowadays be called damped homogeneous plane waves. As a result inhomogeneous waves in Frisk's paper are only important very close to the sound source.

Because the work of Cooper [2, 3] seemed to be forgotten, in the period of Frisk, only those researchers were interested in inhomogeneous waves who were also interested in near field phenomena.

New life was given to the theory by an error in a paper of Atalar [7]. Atalar dealt with a lossy liquid – lossless isotropic solid interface and he explicitly prevented exponential amplitude growth away from the interface. The reason originated from the then well established idea (the Sommerfeld radiation condition) that the amplitude must always be zero at infinity. However Sommerfeld's rule is not really crucial if one is considering inhomogeneous incident waves. Apparently Atalar was not aware of this. The paper of Atalar shows a reflection coefficient that is so extraordinary that it inspired Claeys and Leroy [11] to study it deeper. They came to the conclusion that contrary to what Atalar had proposed, the transmitted waves in the case studied by Atalar must always be directed in such a way that there is exponential growth inside the solid. In a much later study, Deschamps and Roux [37, 45] have studied this problem in more detail and also came to the conclusion that the classical Sommerfeld radiation condition should not be used for inhomogeneous waves, stating that for surface waves it is not always necessary to impose that their amplitude should tend to zero at large distances away from the interface. Atalar [12] resolved this discussion by stating that Claeys and Leroy [11] were right below the critical angle and that he was right beyond the critical angle. Hence the discussion of Atalar, Claeys and Leroy resulted in what would later be discovered experimentally by Marc Deschamps [61]. These discussions also showed that ultrasonic inhomogeneous waves were concepts that were naturally generated during scattering whenever damping becomes a factor of importance.

One month later than Claeys' and Leroy's submission [11], Weston [10] published a paper that was also dealing with inhomogeneous waves. Weston was interested in very small inhomogeneities of sound in waveguides [8]. For such small inhomogeneities there are

regions in the angular interval $\left[0,\frac{\pi}{2}\right]$ where the reflection coefficient has practically constant amplitude. This lead Weston to consider a formulation, like Brekhovskikh [1] and Bertoni and Tamir (see ref 3 in [13]) did in the framework of homogeneous plane waves, of a beam shift due to constant amplitude and high phase shifts in a beam that is composed (in Fourier sense) of very weakly inhomogeneous waves. Even though his considerations practically only hold for guided waves in between lossy media, an important conclusion of his paper is that there can be an energy gain when inhomogeneous waves are reflected. Even more interesting is a crucial sentence in Weston's paper that would become one of the major ideas of inhomogeneous wave theorists, i.e. "In fact, there are the two viewpoints on the reflection of inhomogeneous waves, and it is worth stressing that these are equivalent: a displacement like other waves with no extra gain, or no displacement but with gain". This intuition was shared by Claeys and Leroy and they later proved [26] explicitly that there is energy conservation when inhomogeneous waves are reflected from an interface between two media. This intuition also formed the basic idea in unraveling the Schoch displacement [13].

The formation of bounded beams by means of inhomogeneous waves and their connection with leaky surface waves

The real breakthrough of inhomogeneous waves originated from a paper of Claeys and Leroy [13, 18] in which they described a bounded beam as a superposition of inhomogeneous waves by means of the Prony technique. Hence their superposition is performed not in Fourier-sense but in a sense that had only been done before in electronics and only in the time domain, e.g. Spitznogle and Quazi [4].

Essentially the method works as follows: In Fig. IV.A_4, a schematic is given of the different coordinates that are used below. On the left side there is the incident (gaussian) bounded beam with given profile, while on the right side there is the reflected profile.

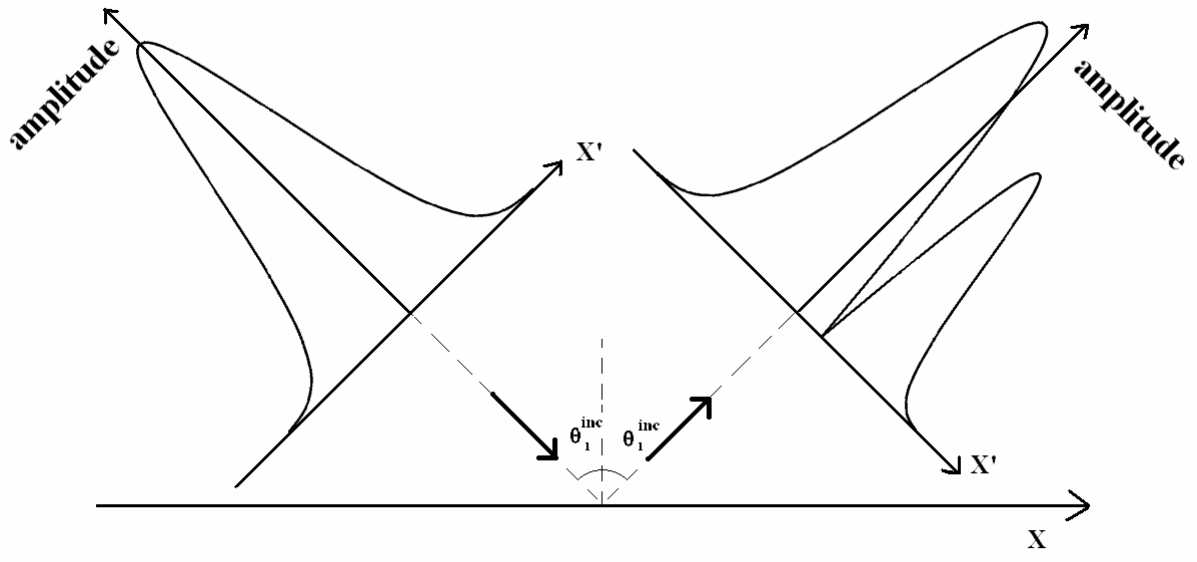

Fig. IV.A_4: ***A bounded beam with profile f(x') is incident on the left and is reflected on the right.***

The bounded beam $f(x,y)$ with profile $f(x')$ is written as

$$f(x') = \sum_{n=-N}^{N} I_n A_n \exp\left(\beta_n x'\right) \tag{IV.A_44}$$

with $I_n = 0$ if $n < 0$ and $I_n = 1$ if $n \geq 0$ in the original work of Claeys and Leroy and $I_n \equiv 1$ in a later extension of the original method (see further below).
For symmetrical profiles this leads to

$$f(x') = A_0 + \sum_{n=1}^{N} \left(I_n + I_{-n}\right) A_n \exp\left(\beta_n x'\right) \tag{IV.A_45}$$

The transformation $\beta_n = n / p$ and $x' = p \ln \gamma$ consequently results in

$$A_0 + \sum_{n=1}^{N} \left(I_n + I_{-n}\right) A_n \gamma^n = f\left(p \ln \gamma\right) \tag{IV.A_46}$$

The right side of equation (IV.A_46) can also be decomposed in Laguerre polynomials L_n of order *n* as

$$f\left(p \ln \gamma\right) = B_0 + \sum_{n=1}^{N} B_n L_n\left(\gamma\right) \tag{IV.A_47}$$

with

$$B_n = \int_0^{\infty} \exp(-\gamma) f\left(p \ln \gamma\right) L_n\left(\gamma\right) d\gamma \tag{IV.A_48}$$

The unknown coefficients A_n are then found elegantly by means of linear combinations of B_n or directly just by means of a numerical optimization of equation (IV.A_45). This superposition lead to simulations of the interaction of bounded Gaussian beams at all angles of incidence. Especially the simulation of the Schoch effect at the Rayleigh angle and at the Lamb angle, which had up until then only been done by means of the Fourier method for all angles of incidence and a more specialized form of the Fourier method at the Rayleigh angle (ref 3 in [13]), awakened many acousticians. From that moment on there existed an undisputable bond between inhomogeneous waves and leaky surface waves. Now, since leaky surface waves were known to be of extraordinary importance in non destructive testing, the breakthrough of the ultrasonic inhomogeneous wave theory was a fact.

In a later paper, Leroy, Poirée, Sebbag and Quentin [21, 28] and Leroy, Quentin and Claeys [26] highlighted the difference in the reflection coefficient at the Rayleigh angle of homogeneous plane waves and inhomogeneous plane waves. Inhomogeneous plane waves, as used in the bounded beam decomposition of Claeys and Leroy [13, 68], showed a minimum at the Rayleigh angle which was in intuitive agreement with energy transformation from incident sound to Rayleigh waves, while nothing like this was visible for homogeneous plane waves. This, together with their experience in the field of Acousto-Optics, lead to a new definition of the reflection coefficient for bounded beams. This coefficient was the complex amplitude of

the reflected sound integrated over the whole profile, divided by the one of the incident beam. This coefficient showed a minimum at the Rayleigh angle, in agreement with intuition. Furthermore, their definition was in accordance with a measurable entity in acousto-optics, where the second order diffracted light amplitude corresponded to their definition of the reflection coefficient and was directly measurable.

A vast study that revealed the fact that inhomogeneous waves are excellent tools to excite leaky Rayleigh waves was perfomed by Poirée and Sebbag [36] and also Quentin, Derem and Poirée [38]. They showed not only that leaky Rayleigh waves could be written as a combination of inhomogeneous waves, but also showed that it was from a physical point of view natural to generate such waves by means of incident inhomogeneous waves. Later, Duclos et al [52] also perfomed a study on the connection of Lamb waves with inhomogeneous waves.

Ten years after the findings of Claeys and Leroy, Van den Abeele and Leroy [49, 53, 54, 56, 62] extended the method as described above in (IV.A_44) but now with $I_n \equiv 1$ to form bounded beams, hence involving not only inhomogeneous waves having an inhomogeneity vector in one sense but also in the opposite sense. They studied in great detail the effects of frequency and beam width on the reflected beam profile. Later, a study has been performed by Vanaverbeke, Windels and Leroy [86], following experimental research of Devolder, Wevers, Demeester and Leroy (see ref(1) in [86]), on the possibility to measure the characteristics of a coating by means of phase-measuring (acousto-optic) techniques. One of their findings was that the results coming from the Fourier model correspond to the ones coming from the inhomogeneous wave model when studying the reflection of bounded beams on coated materials.

Nevertheless, the formation of bounded beams by means of inhomogeneous waves bares a drawback in that only an approximation can be found numerically in a relatively small area around the center of the beam. At large distances there are always exponentially growing amplitude tails. The presence of these tails can severely interfere with the areas of interest after reflection. Therefore some numerical techniques have been developed [91, 90] lately in order to shift those tails a little bit more outward. Furthermore since the Prony technique only works for one variable, it is impossible to build 3D bounded beams by means of inhomogeneous waves. Lately this shortcoming has been voided [95] by introducing a technique that is capable indeed of building 3D bounded beams. A result of a 3D gaussian beam profile formed by means of a summation of inhomogeneous waves is shown in Fig. IV.A_5. Just as in the 2D case there appear exponentially growing tails at some distance away from the center of the profile.

Very recently, mainly because of the fact that bounded inhomogeneous waves have been experimentally generated (see further below), there have appeared some papers dealing with the description of the behavior of bounded inhomogeneous waves (i.e. an exponential profile but chopped in space) in reflection/transmission at plane interfaces between a liquid and a solid. The first description consists of the formation of bounded inhomogeneous waves by means of a Fourier decomposition into homogeneous plane waves and has been published by Vanaverbeke, Windels and Leroy [82]. Still, because it is interesting not just to simulate what happens to bounded inhomogeneous waves when they interact with materials, but also to understand what the physical and theoretical connection is between bounded inhomogeneous waves and infinite inhomogeneous waves, it has been shown recently that a bounded beam is built up by means of infinite inhomogeneous waves and that the connection is made through the Laplace transform [92, 93]. Furthermore it is shown that this description shows why bounded inhomogeneous waves behave like infinite inhomogeneous waves. The reason is that the infinite inhomogeneous wave having the same inhomogeneity as the bounded

inhomogeneous wave determines what happens to the bulk of the bounded beam, whereas other inhomogeneities are only important to form the edges of the bounded beam.

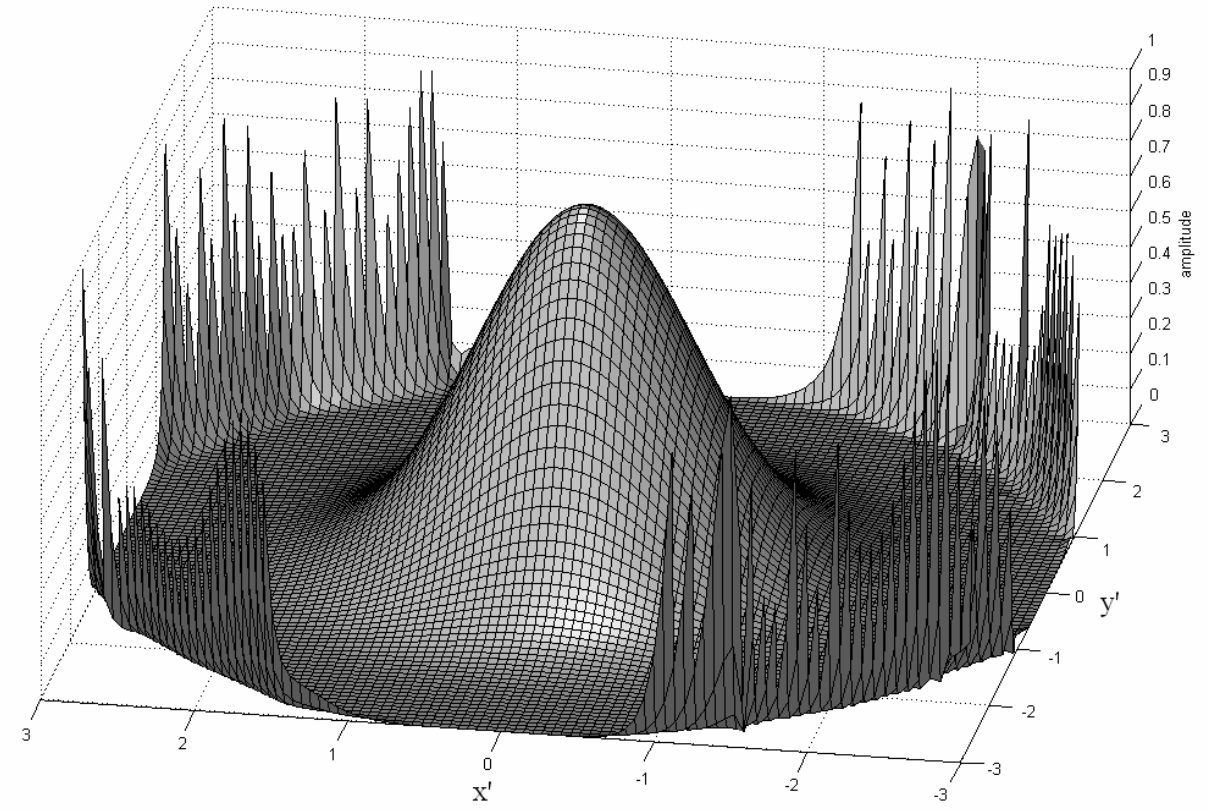

Fig. IV.A_5: ***The profile of a gaussian beam in 3D, built by means of a superposition of inhomogeneous waves.***

The heritage from electromagnetic wave theory

Inhomogeneous waves have been much earlier developed in electromagnetic wave theory than in ultrasonics theory. However, as is often the case in different branches of science, the connection between the two fields did not grow automatically. The first who connected inhomogeneous waves theory in ultrasonics with the one in electromagnetism was Michael Hayes. In a paper which appeared in the same year as the one of Atalar [7] and Claeys and Leroy [11], Hayes [9] published one dealing with inhomogeneous (surface) waves that was valid for both electromagnetic and ultrasonic waves. A few years later Hayes [16] published another paper where he introduced the bi-vector formalism (see also Boulanger [57]). The bi-vector formalism originates from Gibbs (see ref 1 in [16]) and Synge (see ref 2 in [16]) and Hayes revealed its importance in the description of ultrasonic and electromagnetic inhomogeneous waves. The bi-vector formalism of Hayes has formed the theoretical structure of inhomogeneous waves that is still used today.

THE FURTHER DEVELOPMENT OF THE THEORY FOR VISCOELASTIC ISOTROPIC MEDIA

Around 1984 the founders and the re-founders of the theory of ultrasonic inhomogeneous waves had considered the existence of such waves, they had shown peculiarities of the reflection coefficient, they had considered the principle which would later

be called the generalized law of Snell-Descartes (IV.A_42-43) and they had shown through the Schoch displacement that there was a strong connection between inhomogeneous waves and leaky surface waves. Nevertheless a lot of work still needed to be done before the theory could reach its nowadays proportions.
Michael Hayes [16] had already used the formalism of bi-vectors in the description of bulk inhomogeneous waves. Poirée [15] showed that this formalism could also be used to describe surface waves. Later, Poirée's findings were extended in a paper of Poirée and Luppé [48]. Meanwhile Hosten and Deschamps [14] had applied the concept of complex angles (IV.A_37) in the scattering of inhomogeneous waves. The latter two authors combined their efforts with the bi-vector formalism as used by Hayes [16] and Poirée [15] and extended the notion of damped homogeneous plane waves (see ref 3 in [19]) and surface waves to inhomogeneous bulk waves. For the first time ever Hosten and Deschamps [14] published the dispersion relation in the bi-vector formalism (as is currently always used, see (IV.A_29-30)) for viscoelastic isotropic media and for the first time they wrote about the generalized law of Snell-Descartes. The former was already calculated by Cooper [2, 3], the latter had already been obtained by Cooper [2, 3] and Frisk [6] but here it was for the first time explicitly written within the bi-vector formalism. Hosten and Deschamps [14] showed within the bi-vector formalism the fact that inhomogeneous waves are generated naturally on an ideal liquid/absorbing solid and therefore complemented what had been tackled before by Atalar, Claeys and Leroy [7, 11, 12].

The conservation of energy, which had been tackled before [26] for scattering of inhomogeneous waves on interfaces between ideal elastic media, was established by Deschamps [35] for viscoelastic materials. Hence after 1990 there were no doubts possible anymore considering energy conservation when inhomogeneous waves are reflected/transmitted. A further study can also be found in Chevée and Deschamps [47, 60]. Since the phase velocity of inhomogeneous waves is frequency dependent, it is also important to study the velocity of energy transport in such waves. This has been done by Poirée [46]. Because inhomogeneous waves were so astonishingly promising, Deschamps and Chevée [40] extended an approach (the expansion into a Debeye series), for describing the interaction of homogeneous plane waves with a solid layer immersed in a viscous liquid, to inhomogeneous waves. They found energy conservation laws. Nevertheless they also found some peculiarities of inhomogeneous waves which were not so attractive for intuitive interpretation, such as propagation directions within the layer exceeding 90^0 and they also found some convergence problems in their approach. Their paper in fact indicates that inhomogeneous waves can be considered as an excellent tool, but not the ultimate tool for describing the interaction of sound with materials.

A treatise on the reflection/transmission of inhomogeneous waves (including shear horizontal waves) between two isotropic viscoelastic solids can be found in a paper of Caviglia and Morro [72]. The latter paper differs slightly from the other papers in the framework of inhomogeneous waves because the Stroh formalism is used here.

Lately [89] it has also been shown that inhomogeneous waves must be able to stimulate a surface wave on a liquid/solid interface that radiates both into the liquid and into the solid and therefore differs from a leaky Rayleigh wave.

THE INTERACTION OF ULTRASONIC INHOMOGENEOUS WAVES WITH ANISOTROPIC MATERIALS

Contrary to for example the book of Fedorov (ref 8 in [55]) it could already be found in the book of Musgrave [5] that complex wave vectors are mathematically possible in crystals. However it was only much later that one has started to study this phenomenon

deeply. The most general approach for describing the interaction of sound with an interface between generally anisotropic materials before 1986 is found in a paper of Rokhlin, Bolland and Adler [20]. It is so general not only because of the possibility to calculate results for general anisotropy but also because the numerical approach is valid for all angles of incidence whereas most earlier papers only presented results below the bulk critical angles. Furthermore it has been shown by Lanceleur, Ribeiro and De Belleval [55] that Rokhlin et al. [20] must have implicitely implemented inhomogeneous waves because of correspondence with the later results of Lanceleur et al. [55]. One of the key factors is of course that Rokhlin et al [20] determine the wave vector direction (up/down) by considerations of the energy flow whence they obtain the correct choice of the sign even in the case of generated inhomogeneous waves. Nevertheless in the paper of Rokhlin et al. [20] there are no explicit studies described that reveal phenomena that are due to incident or scattered inhomogeneous waves. Therefore the work of Atalar, Claeys and Leroy [7, 12, 11] and Hosten and Deschamps [14], where it was shown that damped waves produce inhomogeneous waves in a reflection/transmission process, motivated Hosten, Deschamps and Tittmann [22] to describe transmitted waves in a viscous anisotropic material (e.g. a fiber reinforced composite) in the framework of the inhomogeneous wave theory. The description of bulk inhomogeneous waves in anisotropic media had already happened by Hayes [16], but not in the context of reflection/transmission and certainly not their influence on the reflection/transmission coefficient. Hosten et al [22] showed that the inhomogeneous wave theory produces results in agreement with experiments for propagation (through stiffness coefficients) and damping (through damping coefficients). This work was later further extended by Deschamps and Hosten [42] to a system where the reflection /transmission coefficients are expanded in a Debeye series. Now since the vast majority of composites are layered, it was appealing to Hosten [41] to try numerical techniques that already existed for describing the interaction of homogeneous plane waves with layered (composite) materials, e.g. the Thomson-Haskell method, in the field of inhomogeneous plane waves. However, since the classical Thomson-Haskell method produces numerical instabilities for high values of frequency times thickness, Hosten [41] modified the method to get more stability and tested it in the case of damped materials, where the then well established theory of inhomogeneous waves demanded the presence of bulk inhomogeneous waves inside the layered medium. Again he found excellent agreement with experiments. The rapid developments in the inhomogeneous wave theory together with some important attempts to include such waves in reflection/transmission phenomena in anisotropic media (along crystal axes [22]) inspired Lanceleur, Ribeiro and De Belleval [55] to study the presence and the consequences of inhomogeneous waves due to reflection/transmission phenomena in general anisotropic media (therefore also valid along the acoustical axes). Hence the paper of Lanceleur et al [55] complements the paper of Rokhlin et al [20]. For researchers in the field it is therefore necessary to study those papers together.

Besides, a thorough study on the differences of the Stroh formalism and the Christoffel equation formalism for inhomogeneous waves in anisotropic elastic materials can be found in Shuvalov [78].

Furthermore it is well know that for homogeneous plane waves the energy ray is directed along the direction of the wave vector, when this wave vector is directed perpendicular to the slowness surface in that direction. It is not always possible to have this situation, especially in anisotropic materials. Deschamps and Poncelet [85] showed that this is possible indeed if one deals with inhomogeneous waves because the inhomogeneity component becomes a steering factor. Hence it is always possible to find such conditions for inhomogeneous waves. They also show that there are always four solutions in each direction.

Further findings of the interaction of inhomogeneous waves with anisotropic materials can be found in Deschamps and Assouline [76], in Boulanger and Hayes [81] and in Rogé [80].

INHOMOGENEOUS WAVES IN THERMOVISCOUS LIQUIDS

In viscoelastic materials there are only vibrational modes, i.e. (quasi) longitudinal and (quasi) shear modes. In thermoviscous liquids however there is also an entropy (or thermal) mode. This mode, which formerly was only described as a pure homogeneous plane wave, was described in the framework of the inhomogeneous wave theory by Poiree [17, 23] for the case of a perfect thermoviscous gas by means of a first order perturbation of Navier-Stokes equations. Deschamps and Cheng [30] extended this model to the general case of thermoviscous liquids. The latter authors also showed that surface modes are possible that couple entropy modes with vibrational modes. The case of termoviscous solids can be found in Deschamps and Changlin [34]

THE EXPERIMENTAL GENERATION OF ULTRASONIC INHOMOGENEOUS WAVES

Up until 1988, inhomogeneous waves had mostly been important from a theoretical point of view and there were only indirect connections with experiments such as the Schoch effect or damping within materials. Most researchers in the field believed that bulk inhomogeneous waves could become an important tool for NDE, however such waves had never been generated and studied before. Deschamps and Hosten [29] were the very first to build a tool for exciting bulk inhomogeneous waves and they verified that experimentally excited bulk inhomogeneous waves had propagation properties in complete agreement with theory. From that moment on, bulk inhomogeneous waves became established physical entities. The excitation equipment consisted of a relatively wide transducer and the inhomogeneous wave was generated by transmitting the generated sound through a damping prism-like material.

The principle is shown in Fig. IV.A_6. A homogeneous plane sound wave impinges the prism. Its characteristics are given by $\mathbf{k}_0 = k_{1,0}\mathbf{e}_{x_0}$. Along the interface $y = x\tan\theta_1$ Snell's law must be fulfilled, whence within the damping prism a damped homogeneous plane wave is generated. This wave is in its turn transmitted along the interface $y = x\tan\theta_2$ whence also along this second interface it must fulfill Snell's law.

Now by demanding that the transmitted wave (in the lossless lower media) must be conform with $\mathbf{k}_2 = \sqrt{\beta^2 + (\omega/v)^2}\,\mathbf{e}_{x_2} - i\beta\mathbf{e}_{y_2}$, i.e. an inhomogeneous wave with given inhomogeneity vector $\boldsymbol{\beta}$, then it can be shown that implementation of Snell's law together with the dispersion relation inside the damping prism results in

$$\theta_1 = \arctan\left(-p\beta\frac{v}{\sqrt{\beta^2 v^2 + \omega^2 v_0}}\right) \qquad \text{(IV.A\_49)}$$

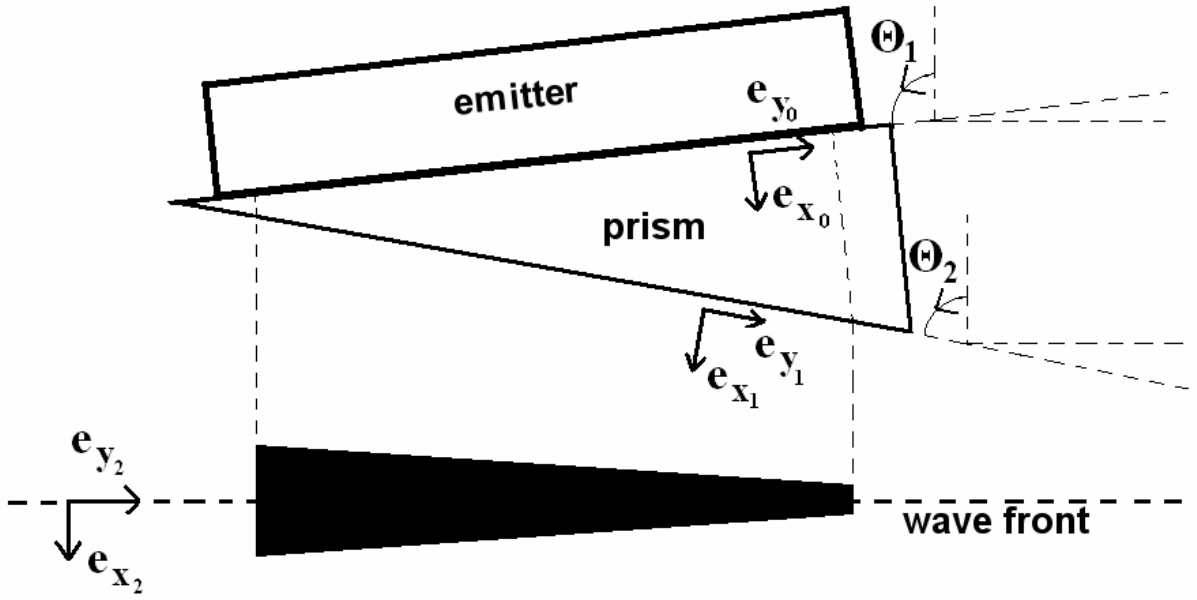

Fig. IV.A_6: ***The generation of an inhomogeneous wave by means of a damping prism. The black triangle represents the wave front, with the thickness being relative to the amplitude.***

and

$$\theta_2 = -\arctan\left(-\omega\beta\frac{v}{\sqrt{\beta^2 v^2+\omega^2}\,\alpha_0 v_0}\right) \tag{IV.A_50}$$

with

$$p=\frac{-\omega\alpha_0 v \pm \sqrt{\beta^2\left(-v_0^2\beta^2v^2+\omega^2\left(v^2-v_0^2\right)\right)+\alpha_0^2v_0^2\left(\beta^2v^2+\omega^2\right)}}{v\left(\alpha_0^2-\beta^2\right)} \tag{IV.A_51}$$

for α_0 being the intrinsic damping and v_0 the sound velocity inside the prism.

The reason why both angles θ_1 and θ_2 must be tuned is the fact that not only the amplitude variation must be correct but also the wave front and its direction of propagation. It is for example seen from (IV.A_49-51) that if one demands $\beta = 0$ that both angles are equal to $\pm\pi$.

It also follows from (IV.A_49-51) that if one demands $\beta = \alpha_0$ that $\theta_1 = \frac{\pi}{2}$ and that $\theta_2 = \arctan\left(-\frac{v}{v_0}\right)$ which would be $-\frac{\pi}{4}$ in the case of $v = v_0$.

This method using a damping prism was also used in [75] by Briers, Leroy, Poncelet and Deschamps in order to experimentally verify the theory of the diffraction of inhomogeneous waves on periodically rough surfaces (see further below).

A second method to experimentally generate bulk inhomogeneous waves has been presented by Huang, Briers, Rokhlin and Leroy [58] and basically works as follows. Consider a thick metal plate which is half immersed in a liquid (see Fig. IV.A_7). The other half is dry. When

a Rayleigh transducer generates a pulsed Rayleigh wave on the dry side in the direction of the wet side, the generated Rayleigh wave will propagate towards the liquid. When it reaches the liquid, it becomes leaky.

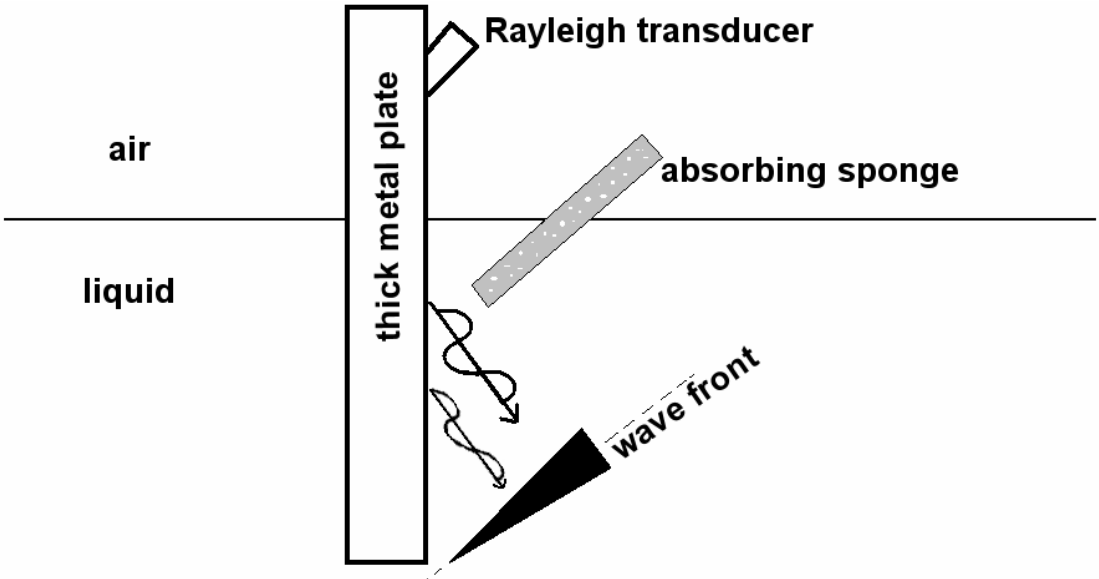

Fig. IV.A_7: ***A schematic of the generation of inhomogeneous waves by means of leaky Rayleigh waves. The black triangle denotes the wave front with thickness relative to the amplitude.***

This leakiness causes sound to be transmitted at the Rayleigh angle into the liquid and also causes damping of the remaining Rayleigh wave in the solid plate. Hence the amount that is leaked into the liquid diminishes along the propagation direction of the Rayleigh wave. This causes the radiated sound to be inhomogeneous, i.e. amplitude decay perpendicular to the propagation direction of the radiated sound. Furthermore the leakage of sound into the liquid is frequency dependent, whence the inhomogeneity in the generated bulk waves is also frequency dependent. An inhomogeneity can then be 'chosen' for further research by filtering out all frequencies that do not produce this particular inhomogeneity. The drawback of the latter method is clearly the fact that the frequency and the inhomogeneity cannot be chosen independent from each other. The drawback of the former method is the fact that a different prism (i.e. different angles θ_1 and θ_2) is needed whenever a different inhomogeneity is required.

THE DIFFRACTION OF ULTRASONIC INHOMOGENEOUS WAVES

Since the 1980's, it was known that periodically corrugated surfaces possessed the ability to transform incident bulk waves into Scholte-Stoneley waves. That is because under the right circumstances one of the diffracted modes propagates along the interface under advantageous conditions. Therefore such surfaces became appealing for nondestructive testing applications since for most materials it is otherwise not possible to stimulate Scholte-Stoneley waves on water-solid interfaces by means of sound incident from one of the two media. However in nondestructive testing it is also inviting to use Rayleigh waves. The problem arising from studies of the diffraction of pure plane waves (or wide bounded beams) on corrugated surfaces was that the leaky Rayleigh wave did not seem to get excited appropriately by this method. Hence the combination of the inhomogeneous wave theory and the diffraction of plane waves was unavoidable. The most important difference between the diffraction of pure plane waves and the diffraction of inhomogeneous waves is that the grating

equation must be generalized in a similar way as the law of Snell-Descartes had been generalized before.

The classical grating equation is given by

$$\sin\theta^n = \sin\theta^{inc} + n\frac{\lambda}{\Lambda} \qquad \text{(IV.A\_52)}$$

Unless one is attracted to working with complex angles it is easier to transform this equation into

$$k_x^n = k_x^{inc} + n\frac{2\pi}{\Lambda} \qquad \text{(IV.A\_53)}$$

The generalization, done by Briers and Leroy [50, 51, 64] consists of applying equation (IV.A_53) not just for real wave vectors but also for complex wave vectors. Hence it is seen from (IV.A_53) that the diffraction phenomenon adds or subtracts a real value and not an imaginary value. In other words the diffraction phenomenon does not alter $k_{2,x}$ but only $k_{1,x}$. The corresponding z-component of each of the diffracted waves is then found from the dispersion relation (IV.A_15-16). Now since leaky Rayleigh waves and leaky Lamb waves have a complex wave vector component along the interface, it is seen from (IV.A_53) that they cannot be stimulated by means of incident homogeneous plane waves and can only be stimulated by means of incident inhomogeneous waves. The results can also be found in a later paper of Van Den Abeele, Briers and Leroy [62, 65]. The theory was also experimentally verified by Huang, Briers, Rokhlin and Leroy [58] and Briers, Leroy, Poncelet and Deschamps [75]. An extension of the model from homogeneous solids to porous media can also be found in Briers and Leroy [77]. Recently the theory of the diffraction of inhomogeneous waves clarified the backward beam displacement phenomenon on periodically rough surfaces as experimentally found by Breazeale and Torbett (see ref [87]) and connected this phenomenon to a leaky Scholte-Stoneley wave [88, 94]. Lately the theory of the diffraction of inhomogeneous waves on periodically corrugated surfaces in 1D has been extended [84] to surfaces having a corrugation in 2D. This theory shows that Scholte-Stoneley waves can be steered in the in-plane directions depending on the frequency and the corrugation periodicities, while leaky Rayleigh waves cannot.

INHOMOGENEOUS WAVES HAVING COMPLEX FREQUENCY

Inhomogeneous waves having complex frequency are generally called complex inhomogeneous harmonic plane waves. They are also called inhomogeneous transient waves. The imaginary part of the frequency corresponds to a source that has exponentially decaying (or growing) amplitude as a function of time. The main reason for studying such waves is the simple fact that perfect harmonic waves do not exist in nature. Every wave has started some time and will also end to exist at some time. Especially in the field of geophysics, where relatively short earthquakes generate transient surface waves or transient Lamb waves, complex (inhomogeneous) harmonic plane waves are becoming very important.

Consequences of complex frequency in the early stages of the theoretical development can be found in Borejko [25], Poirée [44], Deschamps [61] and Scott [63]. The real development of this theory started with Deschamps, Poirée and Poncelet [66].

For real frequencies, it is known that $k_1 = \frac{\omega}{v}$, this is generalized for complex frequencies by working with the slowness vector **S**, resulting in

$$\mathbf{k} = \omega \mathbf{S} \tag{IV.A_54}$$

whence

$$\begin{aligned} \mathbf{k}_1 &= \omega_1 \mathbf{S}_1 - \omega_2 \mathbf{S}_2 \\ \mathbf{k}_2 &= \omega_2 \mathbf{S}_1 + \omega_1 \mathbf{S}_2 \end{aligned} \tag{IV.A_55}$$

It is important to note here that the direction of the real wave vector and that of the real slowness vector are in general different from each other. It is also important to note that the components of **k** along a given Cartesian axis only depend on the components of **S** along that same axis. This means that relation (IV.A_42) of the generalized Snell-Descartes law can also be expressed in terms of **S** without any inconsistency.
Hence for the case of complex frequencies, the dispersion relation (IV.A_15) or (IV.A_16) becomes for *m=d* or *m=s*

$$\left(\omega_1^2 - \omega_2^2\right)\left(S_1^2 - S_2^2\right) - 4\omega_1\omega_2 \mathbf{S}_1 \bullet \mathbf{S}_2 = \frac{1}{v_m^2}\left(\omega_1^2 - \omega_2^2\right) + 2\frac{\omega_2}{v_m}\alpha_{0,m} - \alpha_{0,m}^2 \tag{IV.A_56}$$

and

$$\omega_1\omega_2\left(S_1^2 - S_2^2\right) + \left(\omega_1^2 - \omega_2^2\right)\mathbf{S}_1 \bullet \mathbf{S}_2 = \frac{\omega_1\omega_2}{v_m^2} - \frac{\omega_1}{v_m}\alpha_{0,m} \tag{IV.A_57}$$

Relations (IV.A_56) and (IV.A_57) show that the complex frequency affects the spatial features of the sound wave.
Since it can be derived from (IV.A_1) that the imaginary part will result in an exponentially decaying amplitude as a function of time if $\omega_2 < 0$ and exponentially growing if $\omega_2 > 0$, the particle displacement will not be an ellipse anymore as in the case of inhomogeneous waves having a real frequency, but will be a collapsing elliptic spiral if $\omega_2 < 0$ and an expanding elliptic spiral if $\omega_2 > 0$.
An important question that might be posed in the case of transient inhomogeneous waves is 'how fast do they travel?'. For inhomogeneous waves having real frequency, it is clear that they travel at the phase velocity. For transient waves however, as a function of time you also get amplitude growth that is spreading in space. Therefore it is necessary to distinguish between phase velocity :

$$v_{ph} = \frac{\omega_1}{\mathbf{k}_1 \bullet \mathbf{k}_1}\mathbf{k}_1 \tag{IV.A_58}$$

and amplitude velocity

$$v_{amp} = \frac{\omega_2}{\mathbf{k}_2 \bullet \mathbf{k}_2} \mathbf{k}_2 \qquad \text{(IV.A\_59)}$$

Furthermore it can be found in Poncelet [70] that the velocity of energy propagation is given by

$$\mathbf{v}_E = \frac{\mathbf{S}_1}{\mathbf{S}_1 \bullet \mathbf{S}_{ph}} \qquad \text{(IV.A\_60)}$$

with phase slowness vector $\mathbf{S}_{ph}$ given by

$$\mathbf{S}_{ph} = \frac{\mathbf{k}_1}{\omega_1} \qquad \text{(IV.A\_61)}$$

This shows that the energy propagates in the direction of $\mathbf{S}_1$.

Expression (IV.A_60) is the main reason why one who is dealing with transient waves prefers to work with the complex slowness vector **S** instead of the complex wave vector **k**. Nevertheless it is always possible to switch between slowness space and wave vector space by applying relation (IV.A_55).

A thorough investigation of the energy flux for damped inhomogeneous complex plane waves in viscoelastic fluids can be found in Boulanger [73].

In the mid 1990's one got interested in applying complex inhomogeneous harmonic waves for non destructive testing. Therefore in 1996 Poncelet and Deschamps [69] started to study de generation by means of such waves of leaky Lamb waves in isotropic homogeneous plates. It is well known that the solutions (i. e. the possible wave vectors in the plane of the plate) of the Lamb wave characteristic equation (i.e. the dispersion equation for Lamb waves) for a fluid loaded plate, are complex. This actually means that such waves can be generated by means of inhomogeneous waves and more generally by means of complex harmonic inhomogeneous waves. In their paper, Poncelet and Deschamps [69] show that the dispersion equation for Lamb waves can be expressed in the two independent unknown variables ω and S_x (x-axis along the plane of the plate). This means that for each Lamb mode A_n and S_n there is an infinite number of dispersion curves possible. For that reason, a detailed study for the case of leaky inhomogeneous Lamb modes (i.e. complex slowness, real frequency) on the one hand and transient real Lamb modes (real slowness, complex frequency) on the other hand is performed. It is shown that the dispersion curves are different for both situations. Furthermore it is shown that there is a huge difference for the A_0 and S_0 mode for complex frequencies if compared with real frequencies. The difference is that both modes do not converge to the Rayleigh wave velocity for thick plates, but stop to exist at a certain threshold real frequency times plate thickness. Also below this threshold there are sometimes two possible imaginary parts of the frequency for the same mode at the same real frequency times thickness. Furthermore it is shown that, contrary to all other modes, the A_0 mode can only be stimulated with increasing amplitude as a function of time. A very important conclusion of complex harmonic inhomogeneous plane waves is perhaps the fact that they show that in time there is something similar (though not equivalent) as in space, which is that signals bounded

in time are also capable of stimulating Lamb waves, like signals bounded in space (bounded beams) are capable of stimulating Lamb waves. An exotic study for the case of both complex wave vector and complex frequency reveals fantastic effects such as coupling of the branches of the A_0 with other modes. The findings of Poncelet and Deschamps have later been experimentally verified in Deschamps and Poncelet [74].

Furthermore, in their paper, Poncelet and Deschamps [69] mention the important fact that the dispersion curves for complex frequencies correspond very well to the minima of the reflection coefficient calculated for an incident harmonic homogeneous plane wave, in contrast to the dispersion curves calculated for the solutions with complex slowness. This fact has later been studied in full detail by Bernard, Deschamps and Lowe [79] for a plate immersed in a solid.

Lately, research has been done [96, 97] on the diffraction of transient waves on a periodically corrugated surface. It is found that transient plane waves are excellent tools to stimulate leaky Rayleigh waves on such surfaces and it is also shown that such a surface can be used to filter any signal instantaneously into its complex frequency components.

CONCLUSIONS

This section has given an impression of what exists in the field of ultrasonic inhomogeneous waves, how each topic has started and how it evolved. Perhaps the most important finding is that the theory has grown due to the strong interaction between the different researchers in this field. It is therefore not surprising that all given references form a network that cannot be divided into subgroups. This complicated network of collaborations in the past is also the reason why the references cannot be sorted by author. Hence for historical reasons we have opted for chronological order and we have described the evolution of this wonderful field in ultrasonics according to this time sequence. Whenever needed for clarity we have selected sub fields of inhomogeneous wave research and described its evolution as a separate paragraph, however without hiding connections with other sub fields in different paragraphs.

The theoretical development of ultrasonic inhomogeneous waves has more or less reached its final destination. It is therefore expected that the coming decade will be the one of practical applications in non destructive testing and characterization of materials. Hence there is still a huge world of opportunities for further research in the field of ultrasonic inhomogeneous waves and their applications.

REFERENCES

[1] L. M. Brekhovskikh, Waves in Layered Media (Academic, New York, 1960)
[2] Henry F. Cooper, Jr, Edward L. Reiss, “Reflection of Plane Viscoelastic Waves from Plane Boundaries”, J. Acoust. Soc. Am. 39(6),1133-1138, 1966
[3] Henry F. Cooper, Jr, “Reflection and Transmission of Oblique Plane Waves at a Plane Interface between Viscoelastic Media”, J. Acoust. Soc. Am. 42(5), 1064-1069, 1967
[4] Frank R. Spitzenogle, Azizul H. Quazi, “Representation and Analysis of Time-Limited Signals Using a Complex Exponential Algorithm”, J. Acoust. Soc. Am., 47(5), 1150-1155, 1970
[5] M. J. P. Musgrave, Crystal Acoustics (Holden-Day, San Francisco, 1970)
[6] George V. Frisk, “Inhomogeneous waves and the plane wave reflection coefficient”, J. Acoust. Soc. Am. 66, 219-234, 1979
[7] Abdullah Atalar, “Reflection coefficient for a lossy liquid-lossless isotropic solid interface”, J. Acoust. Soc. Am. 65(5), 1101-1103, 1979
[8] D. E. Weston, C. T. Tindle, “Reflection loss and mode attenuation in a Pekeris model”, J. Acoust. Soc. Am. 66(3),872-879, 1979
[9] M. Hayes, “Energy flux for trains of inhomogeneous plane waves”, Proc. R. Soc. Lond. A 370, 417-429, 1980

[10] D. E. Weston, "Oblique reflection of inhomogeneous acoustic waves", J. Acoust. Soc. Am. 69(1), 54-59, 1981
[11] J. M. Claeys, O. Leroy, "How to choose a square root in calculating the reflection coefficient for a lossy liquid-lossless isotropic solid interface", J. Acoust. Soc. Am. 68(6), 1894-1896, 1980
[12] Abdullah Atalar, "On the reflection coefficient which exceeds unity", J. Acoust. Soc. Am. 70(4), 1182-1183, 1981
[13] J. M. Claeys and O. Leroy, "Reflection and transmission of bounded sound beams on half-spaces and through plates", J. Acoust. Soc. Am. 72(2), 585-590, 1982
[14] Hosten. B, Deschamps M., "Coefficients complexes de transmission ultrasonore à travers une lame a faces parallèles immergée", C. R. Acad. Sc. Paris, Serie II, 299, 519-522, 1984.
[15] Poirée B. "Vitesse de propagation de l'énergie de l'onde plane évanescente acoustique, Rev. CETHEDEC 79, 103-112, 1984
[16] Michael Hayes, "Inhomogeneous plane waves", Arch. Ration. Mech. Anal. 85, 41-79, 1984
[17] Poirée B. "L'onde plane hétérogène dans un fluide thermovisqueux". Trait. Signal 2, 223-226, 1985
[18] Jean-Marie Claeys, "Theoretical Models to describe reflection and diffraction of ultrasound from layered media", PhD Thesis KUL department of Sciences (in dutch), 1985
[19] B. Hosten, M. Deschamps, "Génération d'ondes hétérogènes a l'interface liquide-solide viscoélastique. Approximation par des ondes inhomogènes", ACUSTICA 59, 193-198, 1986
[20] S. I. Rokhlin, T. K. Bolland, L. Adler, "Reflection and refraction of elastic waves on a plane interface between two generally anisotropic media", J. Acoust. Soc. Am. 79(4), 906-918, 1986
[21] O. Leroy, B. Poirée, L. Sebbag, G. Quentin, "On the Reflection Coefficient of Acoustic Beams", ACUSTICA 66, 84-89, 1988
[22] B. Hosten, M. Deschamps, B. R. Tittmann, "Inhomogeneous wave generation and propagation in lossy anisotropic solids. Application to the characterization of viscoelastic composite materials", J. Acoust. Soc. Am. 82(5), 1763-1770, 1987
[23] Poirée B. "Plane Heterogeneous waves in a thermoviscous fluid", ACUSTICA 64(2), 73-79, 1987
[24] Allard J. F., Lauriks W., "Poles and zeros of the plane wave reflection coefficient for porous surfaces", ACUSTICA 83(6), 1045-1052, 1997
[25] P. Borejko, "Inhomogeneous plane waves in a constrained elastic body", Q. J. Mech. Appl. 40(1), 71-87, 1987
[26] O. Leroy, G. Quentin, J. M. Claeys, "Energy conservation for inhomogeneous plane waves", J. Acoust. Soc. Am. 84(1), 374-378, 1988
[27] H. W. Jones, H. W. Kwan, E. M. Yeatman, "A note on reflection and transmission of waves at a boundary between two viscoelastic media", J. Acoust. Soc. Am. 84(3), 1104-1106, 1988
[28] Landry Sebbag, "Les lois de la réflexion-réfraction des ondes planes évanescentes et les ondes d'interface", Thesis, University of Paris 7, 1987.
[29] M. Deschamps, B. Hosten, "Génération de l'onde hétérogène de volume dans un liquide non absorbant", Acustica 68, 92-95, 1989.
[30] M. Deschamps, C. L. Cheng, "Ondes hétérogènes et réflexion-réfraction à l'interface liquide-non-absorbant/liquide-thermovisqueux", Acustica 68, 96-103, 1989
[31] Bernard Poirée, "Les ondes planes évanescentes dans les fluides parfaits et les solides élastiques", J. Acoustique 2, 205-216, 1989 (in French)
[32] Marc Deschamps, Cheng Changlin, "Réflexion-réfraction de l'onde plane hétérogène : lois de Snell-Descartes et continuité de l'énergie", J. Acoustique 2, 229-240, 1989
[33] O. Leroy, K. Mampaert, G. Quentin ,"Inhomogeneous acoustic plane waves : generation, reflection and related phenomena", Proc. Acousto-optics and Applications: 4th Spring School 23-27 May 1989, Gdansk, pp. 153-174, 1989
[34] Deschamps M., Changlin C., "Liquid-thermoviscoelastic solids interface", ultrasonics 27, 308-313, 1989
[35] Marc Deschamps, "Réflexion-réfraction de l'onde plane hétérogène : répartition de l'énergie", J. Acoustique 3, 251-261, 1990
[36] Bernard Poirée, Landry Sebbag, "Les lois de la réflexion-réfraction des ondes planes harmoniques évanescentes. I. Mise en équations", J. Acoustique 4, 21-46, 1991
[37] M. Deschamps, J. Roux, "Some considerations concerning evanescent surface waves", Ultrasonics 1991 (29), 283-287, 1991
[38] Gérard Quentin, André Derem, Bernard Poirée, "The formalism of evanescent plane waves and its importance in the study of the generalized Rayleigh wave", J. Acoustique 3, 321-336, 1990
[39] Marc Deschamps, "L'onde plane hétérogène et ses applications en acoustique linéaire", J. Acoustique 4, 269-305, 1991

[40] M. Deschamps, P. Chevée, “Reflection and refraction of a heterogeneous plane wave by a solid layer”, Wave Motion 15, 61-75, 1992.
[41] B. Hosten, “Bulk heterogeneous plane waves propagation through viscoelastic plates and stratified media with large values of frequency domain”, Ultrasonics 29, 445-450, 1991
[42] Marc Deschamps, Bernard Hosten, “The effects of viscoelasticity on the reflection and transmission of ultrasonic waves by an orthotropic plate”, J. Acoust. Soc. Am. 91(4), 2007-2015, 1992
[43] Jens M. Hovem, Åge Kristensen, “Reflection loss at a bottom with a fluid sediment layer over a hard solid half-space”, J. Acoust. Soc. Am. 92(1), 335-339, 1992
[44] B. Poirée, “Complex harmonic waves”, 99-117, *Physical Acoustics*, Edited by O. Leroy and M. A. Breazeale, Plenum Press, New York, 1991
[45] Jose Roux, “Reflection and refraction of heterogeneous waves at plane interfaces”, “Physical Acoustics : Fundamentals and Applications”, Edited by O. Leroy and M. Breazeale, 155-164, Plenum, New York and London, 1991
[46] Poirée B., “Velocity of energy-transport in an acoustic complex plane wave”, ACUSTICA 74(1), 63-68, 1991
[47] Chevée P., Deschamps M., Interaction of plane heterogeneous waves within a damping layer – comparison between theory and experiment”, ACUSTICA 76(5), 224-230, 1992
[48] Bernard Poirée, Francine Luppé, “Evanescent plane waves and the Scholte-Stoneley interface wave”, J. Acoustique 4, 575-588, 1991
[49] K. Van Den Abeele, O. Leroy, “Complex harmonic wave scattering as the framework for investigation of bounded beam reflection and transmission at plane interfaces and its importance in the study of vibrational modes”, J. Acoust. Soc. Am. 93(1), 308-323, 1993
[50] Briers R. and Leroy O. " Reflection of inhomogeneous plane ultrasonic waves on periodically rough solid-vacuum interfaces". SPIE vol 1844 Acousto-Optics and Applications, Gdansk-Jurata, Poland. Proceed. pp. 196-205 (1992).
[51] R. Briers, O. Leroy, “Study of the behaviour of inhomogeneous harmonic waves in their diffraction from simple rough surfaces”, J. de Physique IV, C1(2), 679-682, 1992
[52] O. Lenoir, J. M. Conoir, J. L. Izbicki, “Description des ondes de Lamb en termes d’ondes evanescentes et de resonances”, Journal de Physique IV-C1, 691-694, 1992
[53] K. Van den Abeele, O. Leroy, “Bounded beam reflection and transmission effects in terms of complex harmonic waves”, J. de Physique IV, C1(2), 675-678, 1992
[54] Koen Van den Abeele, “Alternative fundamental theoretical descriptions for acousto-optic and acoustic investigation of pulsed and profiled ultrasound in view of nondestructive testing of layered structures”, Thesis, Katholieke Universiteit Leuven Campus Kortrijk, Belgium, 1992
[55] Patrick Lanceleur, Helder Ribeiro, Jean-François De Belleval, “The use of inhomogeneous waves in the reflection-transmission problem at a plane interface between two anisotropic media”, J. Acoust. Soc. Am., 93(4), 1882-1892, 1993
[56] K. Van Den Abeele, O. Leroy, “On the influence and width of an ultrasonic bounded beam in the investigation of materials: Study in terms of heterogeneous plane waves”, J. Acoust. Soc. Am. 93(5), 2688-2699, 1993
[57] Ph. Boulanger, M. Hayes, Bivectors and Waves in Mechanics and Optics (Chapman and Hall, London, 1993)
[58] W. Huang, R. Briers, S. I. Rokhlin, O. Leroy, “Experimental study of inhomogeneous wave reflection from a solid-air periodically rough boundary using leaky Rayleigh waves”, J. Acoust. Soc. Am. 96(1), 363-369, 1994
[59] Caviglia G., Morro A., “Wave-propagation in a dissipative stratified layer”, Wave Motion 19(1), 51-66, 1994
[60] Patrice Chevée, “Réflexion et transmission d’une faisceau borne ultrasonore sur une lame viscoélastique anisotrope immergée”, Thesis, University of Bordeaux I, France, 1993
[61] Marc Deschamps, “Reflection and refraction of the evanescent plane wave on plane interfaces”, J. Acoust. Soc. Am. 96(5), 2841-2848, 1994
[62] K. Van Den Abeele, R. Briers, O. Leroy, “Stimulated Material Vibration by Inhomogeneous Plane Waves and its Applications for Bounded Ultrasonic Beams”, IEEE, ULTRASONICS SYMPOSIUM 1994, 915-919, 1994
[63] N. H. Scott, “Inhomogeneous plane waves in compressible viscous fluids”, Wave Motion 22, 335-347, 1995
[64] Rudy Briers, “Contributions to the study of acoustic scattering and conversion phenomena in discontinuous structures by introducing a mode theory and by applying the inhomogeneous wave theory”, PhD Thesis KULeuven University, department of sciences, 1995

[65] Koen E.-A Van Den Abeele, Rudy Briers, Oswald Leroy, “Inhomogeneous plane-wave scattering and mode stimulation on periodic rough surfaces”, J. Acoust. Soc. Am. 99(5), 2883-2897 (1996)
[66] M. Deschamps, B. Poiree, O. Poncelet, “Energy velocity of complex harmonic plane waves in viscous fluids”, Wave Motion 25, 51-60, 1997.
[67] Oswald Leroy, “Nonspecular reflection-transmission phenomena of bounded beams described by inhomogeneous plane waves”, Acoustic Interaction with Submerged Elastic Structures, Part I, pp. 129-163, edited by A. Guran, J. Ripoche and F. Ziegler, Series on Stability, Vibration and Control of Systems Series B: Vol. 5., World Scientific (1996).
[68] Oswald Leroy, “Nonspecular reflection-transmission phenomena of bounded acoustic beams described by inhomogeneous plane waves”, Proc. Nordic Acoustical Meeting, 12-14 June 1996, 491-494, 1996
[69] O. Poncelet, M. Deschamps, “Lamb waves generated by complex harmonic inhomogeneous plane waves”, J. Acoust. Soc. Am., 102(1), 292-300, 1997
[70] Olivier Poncelet, “Ondes planes hétérogènes a fréquence complexe : modes propres de plaques immergées.”, PhD thesis University of Bordeaux 1, 1996.
[71] Allard JF, Lauriks W, “Poles and zeros of the plane wave reflection coefficient for porous surfaces”, Acustica 83(6), 1045-1052, 1997
[72] G. Caviglia, A. Morro, “A new approach to reflection-transmision between viscoelastic half-spaces”, J. Acoust. Soc. Am. 106(4), 1666-1672, 1999.
[73] Ph. Boulanger, “Energy flux for damped inhomogeneous plane waves in viscoelastic fluids”, Wave Motion 28, 215-225, 1998
[74] M. Deschamps, O. Poncelet, “Transient Lamb waves : Comparison between theory and experiment”, J. Acoust. Soc. Am. 107(6), 3120-3129, 2000
[75] R. Briers, O. Leroy, O. Poncelet, M. Deschamps, “Experimental verification of the calculated diffraction field generated by inhomogeneous waves obliquely incident on a periodically rough liquid-solid boundary”, J. Acoust. Soc. Am. 106(2), 682-687, 1999
[76] M. Deschamps, F. Assouline, “Attenuation Along the Poynting Vector Direction of Inhomogeneous Plane Waves in Absorbing and Anisotropic Solids”, Acustica – Acta Acustica, 86, 295-302, 2000
[77] R. Briers, O. Leroy, “Surface mode generation at porous interfaces by permanent and transient heterogeneous plane waves”, Poromechanics, Thimus et al. (eds), Balkema, Rotterdam, 179-183, 1998
[78] A. L. Shuvalov, “On the theory of plane inhomogeneous waves in anisotropic elastic media”, Wave Motion 34, 401-429, 2001
[79] Bernard, M. Deschamps, M. J. S. Lowe, “Comparison between the dispersion curves calculated in complex frequency and the minima of the reflection coefficients for an embedded layer”, J. Acoust. Soc. Am. 107(2), 793-800, 2000
[80] Bruno Rogé, “Réflexion/transmission d’une onde plane inhomogene incidente sur une interface plane séparant deux milieux anisotropes", Thesis, Université de Technologie de Compiègne, France, 1999
[81] Boulanger P, Hayes M, “Special inhomogeneous waves in cubic elastic materials”, Zeitschrift fur angewandte mathematik und physik 51(6), 1031-1038, 2000.
[82] S. Vanaverbeke, F. Windels, O. Leroy, “The reflection of bounded inhomogeneous waves on a liquid/solid interface”, J. Acoust. Soc. Am. 113(1), 73-83,2003
[83] Wei P. J., Zhang Z. M., “Scattering of inhomogeneous wave by viscoelastic interface crack”, acta mechanica 158(3-4), 215-225, 2002
[84] Nico F. Declercq, Joris Degrieck, Rudy Briers, Oswald Leroy, “Diffraction of homogeneous and inhomogeneous plane waves on a doubly corrugated liquid/solid interface” submitted elsewhere.
[85] M. Deschamps, O. Poncelet, “Inhomogeneous plane wave and the most energetic complex ray”, Ultrasonics 40, 293-296, 2002
[86] Vanaverbeke S., Windels F. Leroy O., “The influence of coating thickness on the phase shift of bounded ultrasonic beams: Comparison between Fourier analysis and inhomogeneous plane wave theory”, Acta Acustica united with ACUSTICA 89(4), 640-646, 2003
[87] Nico F. Declercq, Joris Degrieck, Rudy Briers, Oswald Leroy, “Theoretical verification of the backward displacement of waves reflected from an interface having superimposed periodicity”, Appl. Phys. Let. 82(15), 2533-2534, 2003
[88] | Nico F. Declercq, Joris Degrieck, Rudy Briers, Oswald Leroy, "Theory of the backward beam displacement on periodically corrugated surfaces and its relation to leaky Scholte-Stoneley waves", J. Appl. Phys. 96(11), 6869-6877, 2004
[89] Nico F. Declercq, Joris Degrieck, Oswald Leroy, "On the theoretical discovery of a new kind of leaky surface waves", Paper P409 of the Proceedings of the Tenth International Congress on Sound and Vibration, 7-10 July 2003, Stockholm, Sweden.

[90] Nico F. Declercq, Joris Degrieck, Oswald Leroy, "The Principle of a Chopped Series Equilibrium to Determine the Expansion Coefficients in the Inhomogeneous Waves Decomposition of a Bounded Beam", Acta Acustica United with Acustica 89, 1038-1040, 2003
[91] Nico F. Declercq, Joris Degrieck, Oswald Leroy, "Two Improved Methods to Determine the Coefficients in the Inhomogeneous Wave Decomposition of Bounded Beams", Peer reviewed Section of the Proceedings of the 8th Western Pacific Acoustics Conference (Wespac8), paper WE41, 7-9 April, Melbourne, Australia, 2003.
[92] Nico F. Declercq, Joris Degrieck, Oswald Leroy, "On the ability of bounded inhomogeneous waves to experimentally verify the behavior of infinite inhomogeneous plane waves", J. Acoust. Soc. Am. 113(4), 2283, 2003
[93] Nico F. Declercq, Joris Degrieck, Oswald Leroy, "The Laplace transform to describe bounded inhomogeneous waves", J. Acoust. Soc. Am. 116(1), 51-60, 2004.
[94] Nico F. Declercq, Joris Degrieck, Rudy Briers, Oswald Leroy, “A Theoretical elucidation for the experimentally observed backward displacement of waves reflected from an interface having superimposed periodicity”, J. Acoust. Soc. Am. 112(5), 2414, 2002
[95] Nico F. Declercq, Joris Degrieck, Oswald Leroy, "The inhomogeneous wave decomposition of 3D Gaussian-like bounded beams", Ultrasonics 42, 273-276, 2004.
[96] Nico F. Declercq, Joris Degrieck, Oswald Leroy, “Diffraction of Transient Harmonic Plane waves and the Stimulation of Transient Leaky Rayleigh Waves”, submitted
[97] Nico F. Declercq, Joris Degrieck, Oswald Leroy,” The Acoustic Diffraction Grating: a Complex Frequency Filter Device for Electronic Signals” submitted

IV.B The principle of a chopped series equilibrium to determine the expansion coefficients in the inhomogeneous waves decomposition of a bounded beam

Up until now, the technique of expanding a bounded beam into inhomogeneous plane waves sometimes suffered from insurmountable numerical problems. Avoidance of these troubles was possible solely by throwing the expansion overboard and producing a new one with different parameters such as the spatial interval upon which optimization had to be performed, or the inhomogeneity interval that had to be taken under consideration. The latter often resulted in imperfect descriptions of critical phenomena such as beam displacement, for which inhomogeneous waves have proved again and again to be very well suited. Here, we introduce an ameliorated technique that determines the expansion coefficients by means of a chopped series representation of the inhomogeneous waves. We show that, if the series has an optimized length, the so found coefficients, which we attribute to the exact inhomogeneous waves in the expansion, are more accurate. The contents of this section, have been published as:
Nico F. Declercq, Joris Degrieck, Oswald Leroy, "The Principle of a Chopped Series Equilibrium to Determine the Expansion Coefficients in the Inhomogeneous Waves Decomposition of a Bounded Beam", Acta Acustica United with Acustica 89, 1038-1040, 2003. (Imp. Fact. 0.346; SCI-index, Acoustics, rank:21 /28)

INTRODUCTION

It has been shown by many scientists that inhomogeneous waves are a great tool to describe the stimulation of critical waves like Rayleigh waves and Lamb waves [1-8]. This fact formed the impetus to describe bounded beams in terms of inhomogeneous waves in order to deal with experimentally observed phenomena such as beam displacement[9-12]. The latter description was first obtained by Claeys and Leroy [13] and was improved later by others [14-15]. The inhomogeneous waves description of a bounded beam by inhomogeneous waves differs from the classical Fourier description [16] in that all inhomogeneous waves travel in the same direction but differ in inhomogeneity. However the most important reason why not everybody is excited to apply the inhomogeneous waves description of bounded beams, is the appearance of exponential tails beyond a certain distance away from the center of the bounded beam (at the most 4 beam widths, but often much less due to numerical problems during optimization), since certain phenomena that might be important often appear at distances beyond the appearance of the tails. These tails emerge as a consequence of numerical instabilities when optimization methods are applied. That is because exponential functions are extremely sensitive in the sense that very small optimization errors become

visible as exponentially large errors. It may therefore be highly important to find a method that suppresses these optimization errors. This is the aim of this section.

THEORETICAL DEVELOPMENT

A narrow gaussian beam $\varphi(x,z)$ with profile $f(x)$ at $z=0$ is to be described as a superposition of inhomogeneous waves

$$\varphi(x,0)=f(x)=\sum_{n=-N}^{N} A_n \exp\left(\beta_n x\right) \text{ for } x\in[-L,L] \tag{IV.B_1}$$

in which β_n is called the inhomogeneity parameter, A_n is the corresponding amplitude and L determines the interval upon which the optimization occurs. If we apply a classical optimization method, then we find numbers A_n^* for the unknown coefficients A_n. Ideally, we would have $A_n^*=A_n$, but it is well known that on the contrary, $A_n^*\neq A_n$ whence

$$\sum_{n=-N}^{N} A_n^* \exp\left(\beta_n x\right)-f(x)=\xi(x)\neq 0 \tag{IV.B_2}$$

Numerous calculations have convinced us that $\xi(x)$ depends on the range of β_n taken under consideration, on the number of inhomogeneous waves considered as well as on the interval on which the optimization is performed. Moreover, the behavior of the numerical error $\xi(x)$ as a function of these parameters is really unpredictable. The reason is not a matter of physics but purely a matter of the optimization being well or bad conditioned for the selected parameters. It is our aim to find a method that improves the conditioning of the optimization, whence numbers A_n^{**} for the unknown coefficients A_n are found, so that

$$\sum_{n=-N}^{N} A_n^{**} \exp\left(\beta_n x\right)-f(x)=\varepsilon(x) \tag{IV.B_3}$$

with

$$|\varepsilon(x)|\leq|\xi(x)| \tag{IV.B_4}$$

First, we write $\exp(\beta_n x)$ as a series expansion so that

$$\exp\left(\beta_n x\right)=\sum_{r=0}^{\alpha}\frac{\left(\beta_n x\right)^r}{r!}+\Delta_n^{\alpha}(x) \tag{IV.B_5}$$

with

$$\Delta_n^{\alpha}(x) = \sum_{r=\alpha+1}^{+\infty} \frac{(\beta_n x)^r}{r!} \tag{IV.B_6}$$

We now seek for the coefficients A_n^{**} for which

$$\sum_{n=-N}^{N} A_n^{**} \left(\sum_{r=0}^{\alpha} \frac{(\beta_n x)^r}{r!} \right) = f(x) \text{ for } x \in [-L, L] \tag{IV.B_7}$$

There will still be a numerical error on this calculation, so that

$$\sum_{n=-N}^{N} A_n^{**} \left(\sum_{r=0}^{\alpha} \frac{(\beta_n x)^r}{r!} \right) - f(x) = \mu(x) \tag{IV.B_8}$$

It is known from our experience and from the simple fact that no polynomial is more difficult to deal with numerically in an optimization than an exponential function, that always

$$|\mu(x)| < |\xi(x)| \tag{IV.B_9}$$

And also that

$$\frac{\partial |\mu(x)|}{\partial |x|} < \frac{\partial |\xi(x)|}{\partial |x|} \tag{IV.B_10}$$

Now, if we utilize the found coefficients A_n^{**} in (IV.B_1), we will obtain

$$\sum_{n=-N}^{N} A_n^{**} \exp(\beta_n x) - f(x) = \varepsilon(x) \neq 0 \tag{IV.B_11}$$

The error $\varepsilon(x)$ contains an intrinsic contribution $\rho(x)$ due to the chop process and the numerical contribution $\mu(x)$ of (IV.B_8), whence

$$\varepsilon(x) = \rho(x) + \mu(x) \tag{IV.B_12}$$

Now, for α small in (IV.B_8), $\mu(x) < \rho(x)$. As α ups, $\mu(x)$ increases while $\rho(x)$ decreases. Consequently, $\varepsilon(x)$ shows a minimum for a certain α such that $\mu(x) = \rho(x)$ and hence $\varepsilon(x) = 2\mu(x)$. We call this situation the chopped series equilibrium. This equilibrium error $\varepsilon(x)$ can be larger, equal to or smaller than $\xi(x)$.

Besides this, there is also the dependence of the numerical error on the interval on which the optimization process is performed and on the number of inhomogeneous waves concerned. It is clear from the fact that functions that tend to exponentials are hard to utilize in an optimization if the function argument becomes large, that the larger the interval upon which the optimization process is performed, the larger the numerical errors will be. In other words, as L increases, the optimization upon the interval $[-L, L]$ shows larger numerical errors. As a consequence, $\mu(x)$ increases with *L,* but less significantly than $\xi(x)$. Hence, it is possible to obtain a situation in which $2\mu(x) < \xi(x)$ and hence $\varepsilon(x) = 2\mu(x)$ will be less than $\xi(x)$. If that situation does or does not occur depends on all parameters involved.

Hence we have shown that situations occur for which there exists an α for which $\varepsilon(x)$ shows a minimum that is smaller than $\xi(x)$. We have therefore found a method that in certain circumstances enhances the optimization process to find the expansion coefficients in an inhomogeneous waves decomposition of a bounded beam; hence the exponential tails that appear will be shifted outwards.

NUMERICAL RESULTS

We have performed a numerical optimization in order to find the expansion coefficients in (IV.B_1) for a gaussian profile

$$f(x) = \exp\left(-x^2 / W^2\right) \tag{IV.B_13}$$

As in [13-15], we have taken

$$\beta_n = n / p \tag{IV.B_14}$$

with p a real number. We have plotted the exact profile (IV.B_13) as a function of *x/W* in a dotted line and the obtained curve for the description of that profile by means of inhomogeneous waves in a solid line. In Figs IV.B_1 and IV.B_2, the upper plot is the case where we have worked directly with the exponential functions, while the lower plot is the case by means of the 'chopped series equilibrium' introduced here. In both cases, *N=29, L=6.5W, α=100.* In Fig IV.B_1, p=3W. We notice that in this case the optimization using the exponentials to obtain A_n in (IV.B_1) is quite stable and so is the optimization using the chopped series expansion. In Fig IV.B_2, we have taken p=6.7W, for which the optimization using exponentials becomes very unstable, while we see that the optimization using the chopped series expansion is far more stable. In the case of Fig IV.B_2, we conclude that the technique that is introduced here gives much better results.

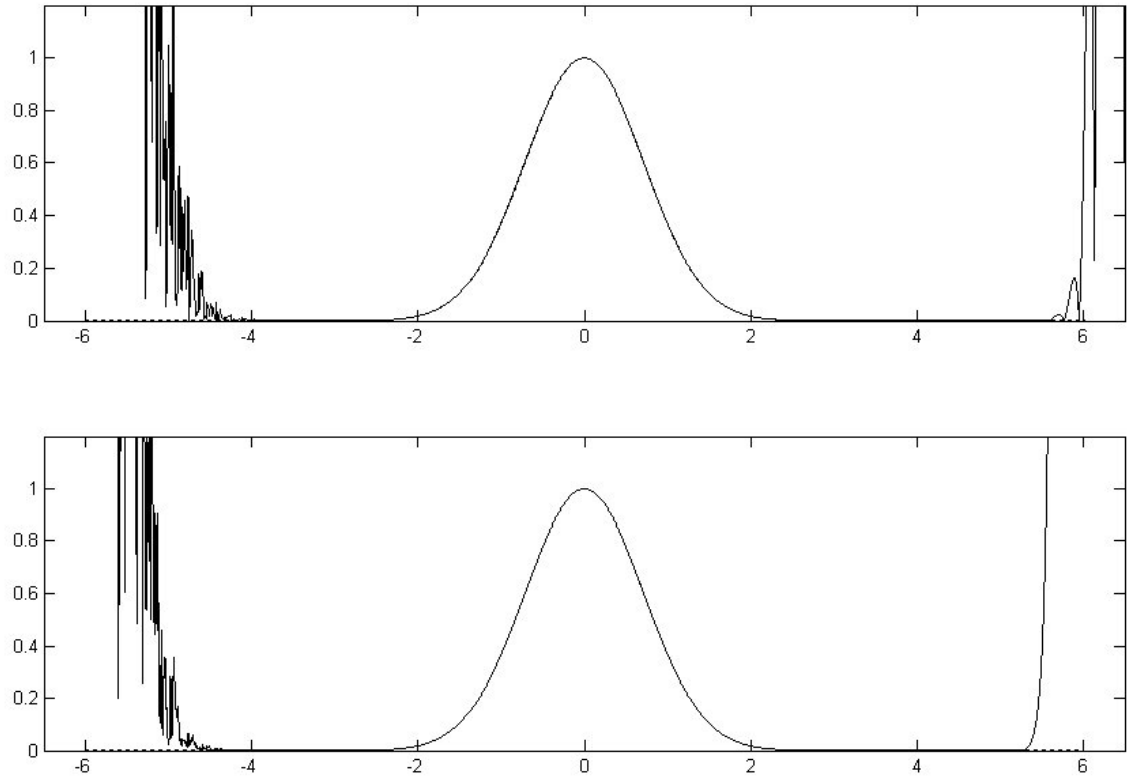

Fig IV.B_1: ***Results for p=3W. Dotted line: exact gaussian beam profile as a function of x/W. Solid line: inhomogeneous waves decomposition. Top: old method using*** A_n^****, see (IV.B_2). Bottom: new method using*** A_n^{**}***, see (IV.B_3).***

CONCLUSION

A technique is found that diminishes numerical instabilities in the determination of the expansion coefficients of an inhomogeneous waves decomposition of bounded beams. This result is important because up until now the inhomogeneous waves decomposition of bounded beams often suffered from numerical instabilities that could only be overcome by altering the parameters in the decomposition, whence these became insufficiently optimized to describe critical phenomena such as beam displacement.

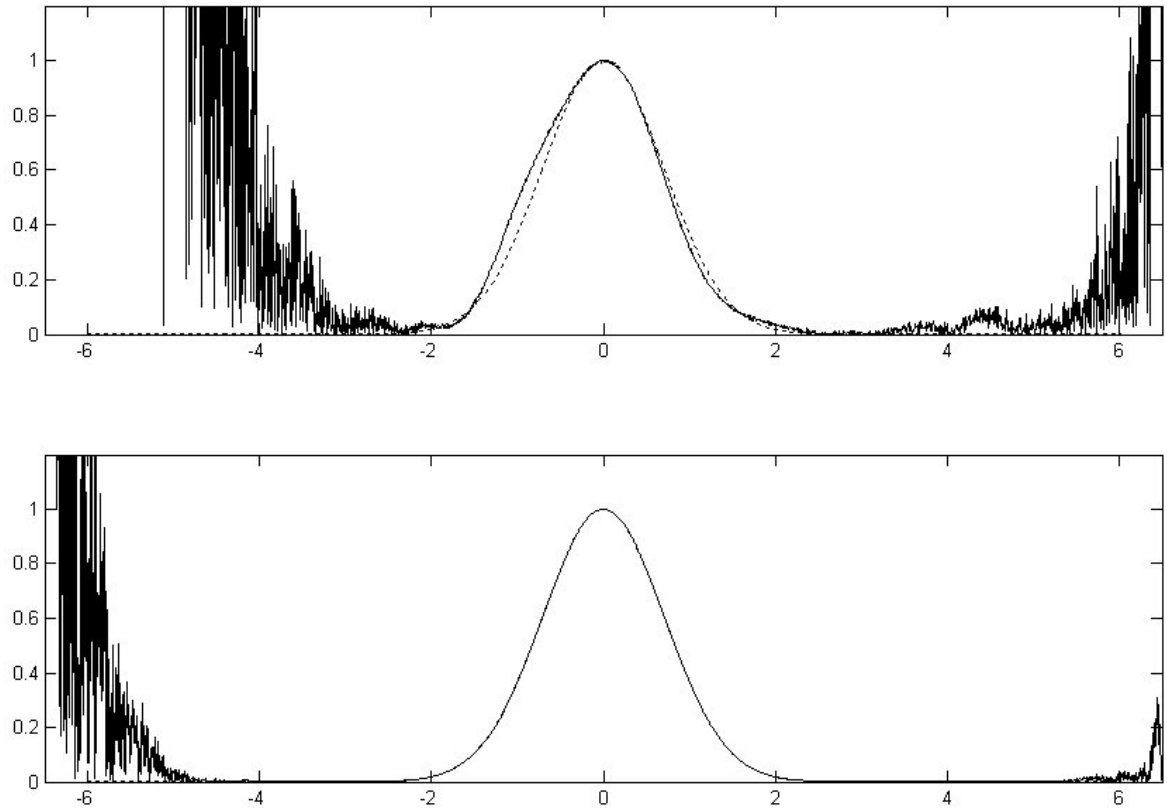

Fig IV.B_2: ***Results for p=6.7W. Dotted line: exact gaussian beam profile as a function of x/W. Solid line: inhomogeneous waves decomposition. Top: old method, method using*** A_n^****, see (IV.B_2). Bottom: new method using*** A_n^{**}***, see (IV.B_3).***

REFERENCES

[1] Marc Deschamps,"L'onde plane hétérogène et ses applications en acoustique linéaire" (in French), J. Acoustique 4, 269-305, 1991

[2] B. Poirée, "Complex Harmonic Waves", Physical Acoustics, Edited by O. Leroy and M. A. Breazeale, Plenum Press, New York, 1991

[3] Patrick Lanceleur, Helder Ribeiro, Jean-François De Belleval, "The use of inhomogeneous waves in the reflection-transmission problem at a plane interface between two anisotropic media", J. Acoust. Soc. Am., 93(4), 1882-1892, 1993

[4] W. Huang, R. Briers, S. I. Rokhlin, O. Leroy, "Experimental study of inhomogeneous wave reflection from a solid-air periodically rough boundary using leaky Rayleigh waves", J. Acoust. Soc. Am., 96(1), 363-369, 1994

[5] Marc Deschamps, "Reflection and refraction of the evanescent plane wave on plane interfaces", J. Acoust. Soc. Am., 96(5), 2841-2848, 1994

[6] O. Poncelet, M. Deschamps, "Lamb waves generated by complex harmonic inhomogeneous plane waves", J. Acoust. Soc. Am., 102(1), 292-300, 1997

[7] M. Deschamps, F. Assouline, "Attenuation Along the Poynting Vector Direction of Inhomogeneous Plane Waves in Absorbing and Anisotropic Solids", Acustica – Acta Acustica, 86, 295-302, 2000

[8] A. L. Shuvalov, "On the theory of plane inhomogeneous waves in anisotropic elastic media", Wave Motion 34, 401-429, 2001

[9] Werner G. Neubauer, "Ultrasonic reflection of a bounded beam at Rayleigh and critical angles for a plane liquid-solid interface", J. Appl. Phys., 44(1), 48-55, 1973

[10] M. A. Breazeale and Laszlo Adler, "Reflection of a Gaussian ultrasonic beam from a liquid-solid interface", J. Acoust. Soc. Am. 56(3), 866-872, 1974

[11] M. A. Breazeale, Laszlo Adler, Gerald W. Scott, "Interaction of ultrasonic waves incident at the Rayleigh angle onto a liquid-solid interface", J. Appl. Phys., 48(2), 530-537, 1977

[12] K. W. Ng, T. D. K. Ngoc, J. A. McClure, W. G. Mayer, “Nonspecular Transmission Effects for Ultrasonic Beams Incident on a Solid Plate in a Liquid”, Acustica 48, 168-173, 1981
[13] J. M. Claeys and O. Leroy, “Reflection and transmission of bounded sound beams on half-spaces and through plates”, J. Acoust. Soc. Am., 72(2), 585-590, 1982
[14] K. Van Den Abeele, O. Leroy, “Complex harmonic wave scattering as the framework for investigation of bounded beam reflection and transmission at plane interfaces and its importance in the study of vibrational modes”, J. Acoust. Soc. Am., 93(1), 308-323, 1993
[15] K. Van Den Abeele, O. Leroy, “On the influence of frequency and width of an ultrasonic bounded beam in the investigation of materials: Study in terms of heterogeneous plane waves”, J. Acoust. Soc. Am., 93(5), 2688-2699, 1993
[16] Nico F. Declercq, Rudy Briers, Oswald Leroy, " The use of polarized bounded beams to determine the groove direction of a surface corrugation at normal incidence, the generation of surface waves and the insonification at Bragg-angles", Ultrasonics 40/1-8, 345-348, 2002.

IV.C A useful analytical description of the coefficients in an Inhomogeneous Wave Decomposition of a symmetrical bounded beam

If a bounded beam is described using a superposition of infinite inhomogeneous waves, the values of the coefficients attributed to each inhomogeneous wave are found using a classical optimization procedure, whence it is impossible to describe the obtained values analytically. In this section, we develop a new and easy to apply straightforward analytical method to find the appropriate values of the sought coefficients. Supplementary to its analytical and straightforward nature, the method proves to reduce the inherent instabilities found in the inhomogeneous wave decomposition.
The contents of this section have been published as: Nico F. Declercq, Joris Degrieck, Oswald Leroy, "A useful analytical description of the coefficients in an Inhomogeneous Wave Decomposition of a symmetrical bounded beam", Ultrasonics 43(4), 279-282, 2005 (Imp. Fact. 0.844; SCI-index, Acoustics, rank:11 /28)

INTRODUCTION

In order to describe a bounded beam, one can apply the classical Fourier decomposition [1]. This method describes the beam as a superposition of plane waves all traveling in a different direction and works extremely well in the bulk of a material. If, however, the interaction with an interface is to be described, the theory reveals some shortcomings. First, physical contradictions appear when narrow obliquely incident beams are described, because plane waves have to be considered with 'incidence angles' exceeding 90°. Second, it has been shown in numerous publications that critical phenomena such as Rayleigh wave generation cannot be described sufficiently accurate using pure plane incident waves. As a consequence, one is often compelled to apply the inhomogeneous wave decomposition of a bounded beam [2,3]. The latter describes a bounded beam as a superposition of inhomogeneous waves (i.e. having a complex wave vector), all traveling in the same direction, but having different inhomogeneities. Claeys and Leroy [2] were the first to apply this technique. They considered only positive inhomogeneities. Later, Van Den Abeele and Leroy [3] extended the theory and included also negative inhomogeneities. Their theory followed the same steps as taken by Claeys and Leroy [2] but was better in really tackling the generation of interface waves. Up until now, there has not been developed a straightforward tool to find the coefficients attributed to each inhomogeneous wave, nor has there been found any analytical expression to describe them. The method applied so far invokes a classical optimization procedure to find the 'best' value for each coefficient. It is well known that this method works extremely well inside the beam, but exponentially growing amplitudes appear beyond one or at the most four beam widths. In this section, we introduce an analytical expression for the

coefficients, therefore one is not obliged anymore to apply the more or less 'stochastic' tool of before. Furthermore, it will be shown by a numerical example that the obtained 'analytical curve' may not fit the gauss curve perfectly, but that the annoying exponential growth appears further away from the center of the beam than would be the case using the classical 'best fit' method [2-6]. This property can be very useful because interesting phenomena (such as the Schoch effect [7]) often appear beyond the point where the classical curve tends to be exponential. The analytical method introduced here may cast away this problem.

THEORETICAL DEVELOPMENT

A bounded beam $\varphi(x,z)$ with profile

$$\varphi(x,0) = f(x) \tag{IV.C_1}$$

can be decomposed in a series of inhomogeneous waves [2-6]

$$\varphi(x,z) = \sum_{n=-N}^{N} \frac{1}{2}\left(1+\delta_{n,0}\right) A_n \exp\left(\beta_n x\right) \exp\left(i\sqrt{\left(\frac{\omega^2}{v^2}+\beta_n^2\right)} z \right) \tag{IV.C_2}$$

where $\delta_{n,0} = 1$ if $n = 0$ and $\delta_{n,0} = 0$ if $n \neq 0$, ω is the angular frequency, v is the velocity of plane sound waves, A_n is the amplitude that needs to be determined and β_n is the inhomogeneity attributed to the index n and is arbitrarily valued. Further below, in (IV.C_5), we choose β_n to be proportional to n.
We solely reckon with symmetrical profiles, whence

$$\beta_n = -\beta_{-n} \text{ and } A_n = A_{-n} \tag{IV.C_3}$$

In signal processing and in ultrasonics, the Prony technique [8] has been used a few times before. It is based on the transformation of an equation, containing exponentials, into a polynomial, whos unknown coefficients can be found using linear inversion procedures. The technique has been used before to describe any bounded beam profile as a superposition of Gaussian beams [9], but also, as in the current section, to describe bounded beams as a superposition of infinite inhomogeneous waves [2-3]. In (IV.C_2), the unknown coefficients A_n can be found using a specialized form of the Prony technique [2-6, 8-10] by solving the equation

$$\sum_{n=0}^{N} A_n y^n = f\left(p \ln y\right) \tag{IV.C_4}$$

With p being a constant value so that

$$y = \exp\left(x/p\right), \; p = n/\beta_n \tag{IV.C_5}$$

Equation (IV.C_4) can then be solved by applying a decomposition in Laguerre polynomials [2], whence

$$\sum_{n=0}^{N} B_n L_n(y) = f(p \ln y) \tag{IV.C_6}$$

with

$$B_n = \frac{1}{p} \int_0^{+\infty} \exp(-y) f(p \ln y) L_n(y) dy \tag{IV.C_7}$$

and L_n the n-th order Laguerre polynomial.
Consequently, one demands [2,3]

$$A_n = \sum_{j=0}^{N} c_j B_j \tag{IV.C_8}$$

It is not practical to find the unknowns c_j. The procedure is based on a least squares error estimation (or 'best fit' procedure) and the results are often tabulated for recycling purposes. Nevertheless, it might be useful to find an exact analytical expression for A_n. The latter has never been achieved thus far.
We combine (IV.C_4) and (IV.C_5) and we utilize [11]

$$L_n(y) = \sum_{m=0}^{n} (-1)^m \frac{n!}{(n-m)!m!m!} y^m \tag{IV.C_9}$$

whence

$$\sum_{n=0}^{N} A_n y^n = g \tag{IV.C_10}$$

with

$$g = \sum_{n=0}^{N} \sum_{m=0}^{n} C_{m,n} y^m \tag{IV.C_11}$$

$$C_{m,n} = B_n (-1)^m \frac{n!}{(n-m)!m!m!} \tag{IV.C_12}$$

Now, we rewrite (IV.C_11)

$$g = \sum_{q=0}^{N} D_q y^q \tag{IV.C_13}$$

with

$$D_q = \sum_{n=q}^{N} C_{q,n} \tag{IV.C_14}$$

Therefore coupling (IV.C_10), (IV.C_12), (IV.C_13) and (IV.C_14), and requiring coefficients belonging to equal powers of y to be the same

$$A_n = \sum_{m=n}^{N} (-1)^n \frac{m!}{(m-n)!n!n!} \sum_{r=0}^{m} (-1)^r \frac{m!}{(m-r)!r!r!} I_r \tag{IV.C_15}$$

with

$$I_r = \frac{1}{p} \int_{-\infty}^{+\infty} \exp\left[-\exp\left(\frac{x}{p}\right) + (r+1)\frac{x}{p} \right] f(x)\,dx \tag{IV.C_16}$$

Expression (IV.C_15) is an analytical expression for finding the unknown coefficients A_n in (IV.C_2).

It must be underlined that the values found by (IV.C_15) may be different from those found using other techniques. That is because (IV.C_15) is an analytical consequence of setting expression (IV.C_4) equal to expression (IV.C_5). The latter can only be analytically true for N infinitely large. Classical optimization procedures however demand (IV.C_4) to be equal to (IV.C_5) for a limited value of N, valid on a limited spatial interval. The concept is therefore different. The problem of the latter (least squares error estimation) approach is that the reconstructed profile differs a lot (exponentially!) beyond the limited spatial interval and when the interval is increased, the numerical optimization becomes numerically unstable and generates errors that again produce the 'exponential tails' at just a few (less than 4) beam widths from the center of the beam. The drawback of the analytical method presented here is that it is hard to have the numerical errors well in hand when solving expression (IV.C_16), especially for large 'r'. Moreover, these errors cumulate dramatically in (IV.C_15) and (IV.C_2) if N is set large. These problems would vanish of course if the integral (IV.C_16) could be solved analytically, which is as far as we know impossible.

NUMERICAL RESULTS

We have performed calculations for a Gaussian beam profile

$$f(x) = \exp(-x^2 / W^2) \tag{IV.C_17}$$

where W is the beam width and we have limited the number of inhomogeneous waves in (IV.C_2) setting $N=7$ and $p=3.6W$. In Table IV.C_I, we have listed the obtained coefficients for the applied methods. The reconstructed profiles, invoking the coefficients of Table IV.C_I are shown in Fig IV.C_1, together with the perfect Gauss curve.

Table IV.C_I: ***The values found for the coefficients $A_0,..,A_7$ using a classical 'best fit method' and using the analytical method formulated in this section.***

coefficients	A classical best fit method	Analytical method
A_0	2009.790×10^{5}	-23727.757×10^{-4}
A_1	-1791.024×10^{5}	130729.573×10^{-4}
A_2	1264.645×10^{5}	-150052.951×10^{-4}
A_3	-702.482×10^{5}	66625.670×10^{-4}
A_4	302.940×10^{5}	-13804.836×10^{-4}
A_5	-99.244×10^{5}	1411.210×10^{-4}
A_6	23.847×10^{5}	-68.201×10^{-4}
A_7	-3.960×10^{5}	1.231×10^{-4}

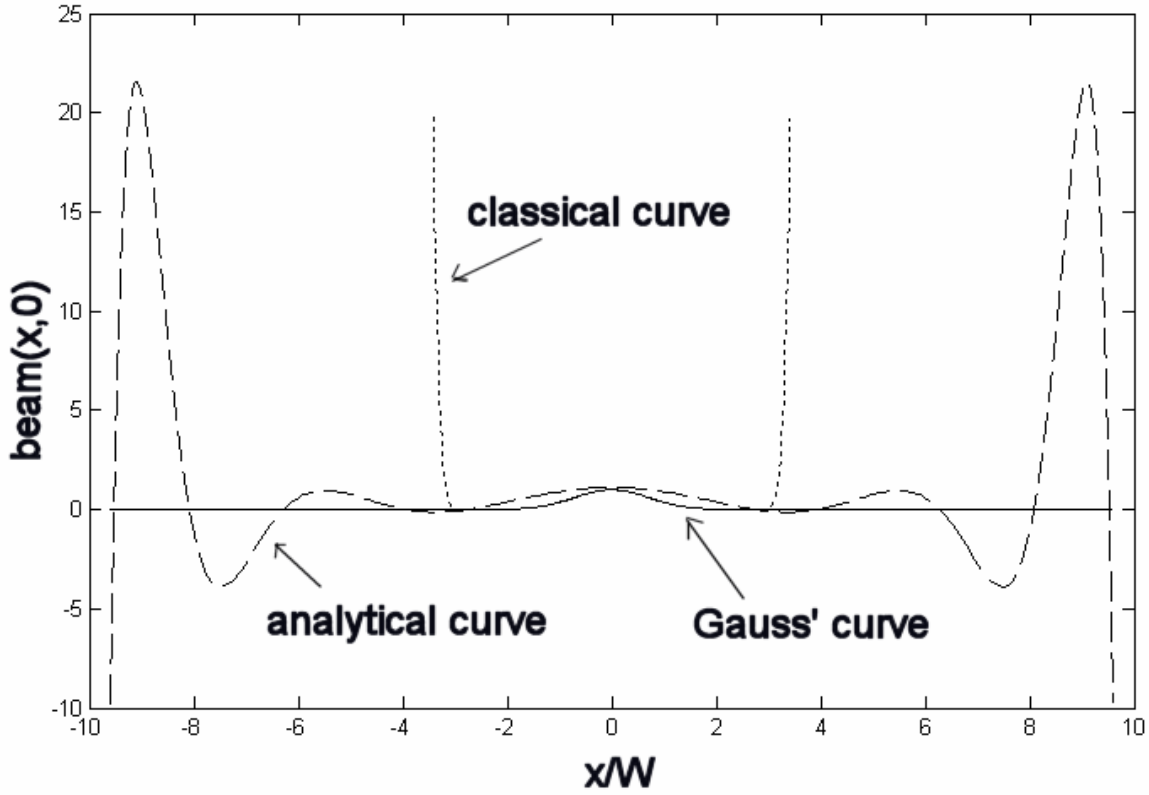

Fig IV.C_1: ***Calculated curves for gaussian beam profiles. Solid line: the exact gaussian beam. Dotted line: approximation of the gaussian beam applying a classical optimization method. Dashed line: approximation of the gaussian beam applying analytical expression (IV.C_15).***

CONCLUSION

We have presented an analytical expression for the unknown coefficients A_n in an inhomogeneous wave decomposition of a bounded beam. Such an expression has never been reported elsewhere. The numerical problems that occur when implementing the analytical expression to determine the unknown coefficients A_n are less dramatic than the ones occurring in 'least squares

error' methods used in the past.

REFERENCES

[1] Nico F. Declercq, Rudy Briers, Oswald Leroy, " The use of polarized bounded beams to determine the groove direction of a surface corrugation at normal incidence, the generation of surface waves and the insonification at Bragg-angles", Ultrasonics 40/1-8 pp. 345-348, 2002.

[2] J.M. Claeys, O. Leroy, "Reflection and transmission of bounded sound beams on halfspaces and through plates", J. Acoust. Soc. Am., 72, 585-590, 1982.

[3] K. Van Den Abeele and O. Leroy, "Complex harmonic wave scattering as the framework for investigation of bounded beam reflection and transmission at plane interfaces and its importance in the study of vibrational modes", J. Acoust. Soc. Am. 93, 908-323, 1993.

[4] Nico F. Declercq, Joris Degrieck, Oswald Leroy, "The inhomogeneous wave decomposition of 3D Gaussian-like bounded beams", Ultrasonics 42, 273-276, 2004.

[5] Nico F. Declercq, Rudy Briers, Joris Degrieck, Oswald Leroy, "The History and Properties of Ultrasonic Inhomogeneous Waves", accepted for publication in IEEE Transactions on Ultrasonics, Ferroelectrics, and Frequency Control

[6] Nico F. Declercq, Joris Degrieck, Oswald Leroy, "The Principle of a Chopped Series Equilibrium to Determine the Expansion Coefficients in the Inhomogeneous Waves Decomposition of a Bounded Beam", Acta Acustica United with Acustica 89, 1038-1040, 2003.

[7] M. A. Breazeale, Laszlo Adler, "Reflection of a Gaussian ultrasonic beam from a liquid-solid interface", J. Acoust. Soc. Am., 56(3), 8666-872, 1974.

[8] Frank R. Spitznogle, Azizul H. Quazi, "Representation and Analysis of Time-Limited Signals Using a Complex Exponential Algorithm", J. Acoust. Soc. Am. 47(5), 115-1155, 1970.

[9] Prange, M. and R. Shenoy, "A fast Gaussian beam description of ultrasonic fields based on Prony's method", Ultrasonics, 34, 117-119, 1996.

[10] R. Prony, "Essai expérimental et analytique sur les lois de la dilatabilité des fluides élastiques et sur celles de la force expansive de la vapeur de l'eau et de la vapeur de l'alcool, à différentes températures", J. l'Ecole Polytech. Paris 1, 2, 24-76 ,1795.

[11] George B. Arfken, Hans J. Weber, " Mathematical methods for physicists – International Fourth Edition", Academic Press, 778, 1995.

IV.D The Laplace transform to describe bounded inhomogeneous waves.

The inhomogeneous wave theory deals with plane waves having complex valued wave vectors and with their superposition to form bounded beams. Since infinite inhomogeneous plane waves cannot be formed experimentally, verifications of the theory have to be performed using bounded inhomogeneous waves.
This section clarifies how a bounded inhomogeneous wave is described as a superposition of inhomogeneous waves. This is done by applying the Laplace transform. The current section also shows, from a theoretical point of view, why bounded inhomogeneous waves behave like infinite inhomogeneous waves in numerous experiments.
The contents of this section have been published as: Nico F. Declercq, Joris Degrieck, Oswald Leroy, "The Laplace transform to describe bounded inhomogeneous waves", J. Acoust. Soc. Am. 116(1), 51-60, 2004. (Imp. Fact. 1.310; SCI-index, Acoustics, rank:7 /28)

INTRODUCTION

From the moment infinite inhomogeneous waves have made their entry in the 1980's, they have been used in the study of the propagation and the scattering of sound. They gained sympathy because of their ability to describe - often better than pure infinite homogeneous plane waves - critical phenomena like the generation of Leaky Rayleigh waves. An extensive survey on the properties of infinite inhomogeneous plane waves can be found in the literature [1-4]. While infinite inhomogeneous plane waves are often studied in the context of their superposition to form bounded beams [5-7], perhaps even more interesting is the theoretical and experimental study of individual inhomogeneous waves. A lot of experiments are reported that confirm theoretical predictions of the behavior of inhomogeneous waves while interacting with interfaces [2,8-11]. The interesting part of these confirmations is the fact that infinite inhomogeneous waves can only be approached experimentally within a limited spatial interval, depending on the apparatus that is used experimentally [8]. The overall experimentally generated wave is in fact a bounded inhomogeneous wave, being a chopped and smoothened version of the theoretical infinite inhomogeneous wave. The importance of bounded inhomogeneous waves, as compared with bounded gaussian beams, is the fact that they contain the inhomogeneity features of inhomogeneous waves (i.e. exponential decay of the amplitude along the wave front) and are hence capable of stimulating more efficiently critical phenomena such as leaky Rayleigh waves or leaky Lamb waves than gaussian beams. Furthermore, this resemblance with infinite inhomogeneous waves is the reason why at incidence angles that correspond to the stimulation of critical phenomena, a strong beam shift occurs [2,8-11] to the reflected beam as the principle effect, which is different from the Schoch effect (the creation of two reflected lobes with a null zone in between) that occurs if gaussian beams are used. In what follows, we investigate bounded inhomogeneous waves in terms of infinite inhomogeneous plane waves, using a numerical technique that has never been applied before in such a context, namely the Laplace transform. In fact, as far as we know, no reports exist at all where bounded inhomogeneous waves are described in terms of infinite inhomogeneous plane waves.

Whenever the expression 'profile' is used in this text, it refers to the normalized particle displacement amplitude profile. Further below, we will consider oblique incidence of a bounded inhomogeneous wave at an interface (X', Z'=0), see Fig IV.D_1. The profile of this bounded beam can be compared with the profile of the reflected beam if one considers the amplitude distribution along an axis X (see Fig. IV.D_1) that coincides with the wave front and for theoretical simplicity has the same origin as the fixed (X',Z') coordinate system. The latter enables us to compare for example possible shifts of the reflected profile along the X-axis with respect to the incident profile.

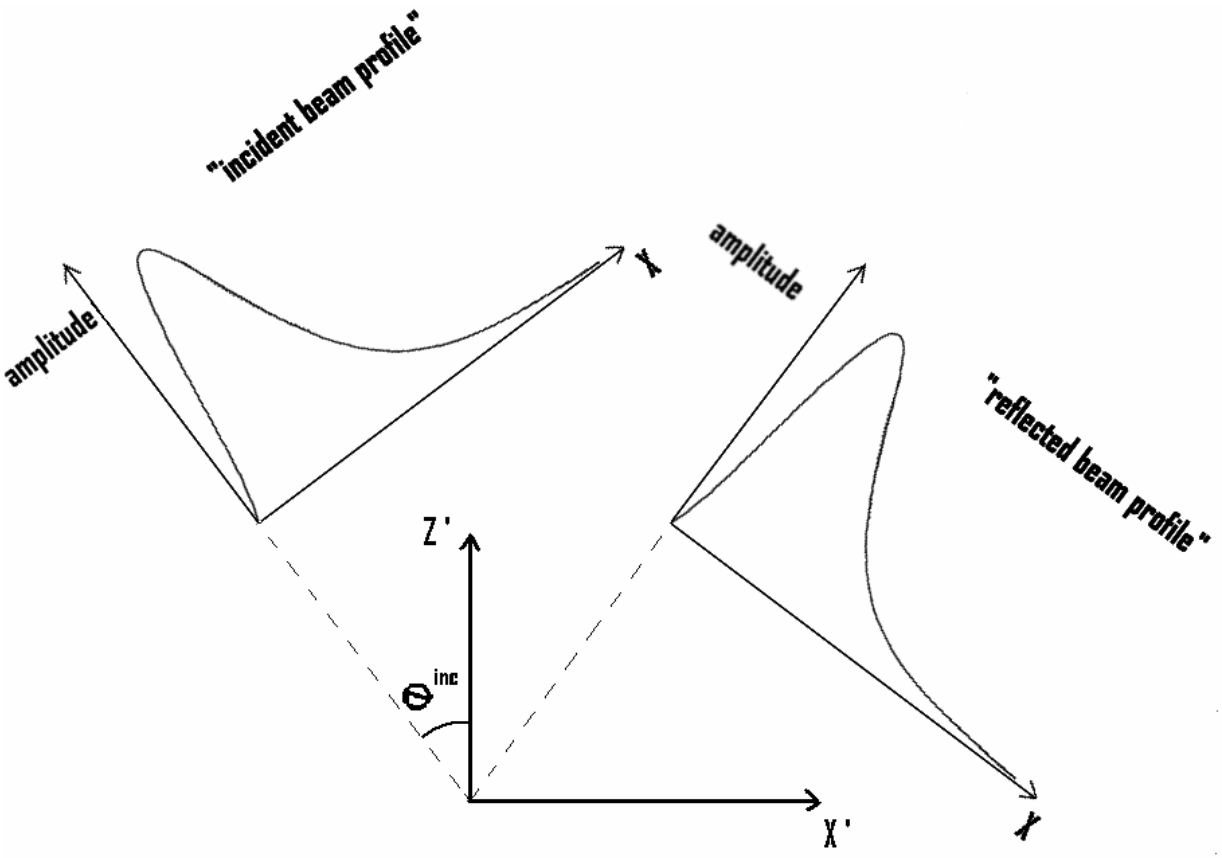

Fig. IV.D_1: ***Schematic of the different coordinate systems. The reflection interface coincides with the X'-axis. The incident beam profile is described along a rotated X'-axis, denoted by X, perpendicular to the propagation direction. The reflected beam profile is also described along a rotated X'-axis, denoted by the same symbol X. Hence it is possible to compare the profile of the incident beam with that of the reflected beam in a diagram where the amplitude is depicted as a function of the 'common' X-axis. For convenience, we suppose that the X-axis for both incident and reflected beams has the same origin as the (X',Z') coordinate system.***

INFINITE INHOMOGENEOUS PLANE WAVES IN A NUTSHELL

For the reader who is not familiar with the theory of infinite inhomogeneous waves, a first glimpse is offered in this section. Anyone who needs to get to know more about this theory is invited to read references [1,3-4,6-7]

If a 'plane wave solution' having an amplitude A, polarization $\mathbf{P}$, wave vector $\mathbf{k}$ and angular frequency ω

$$A\mathbf{P}\exp\left(i\mathbf{k}\bullet\mathbf{r}-i\omega t\right) \qquad \text{(IV.D\_1)}$$

is entered into the wave equation for visco-elastic media, then it can be shown that the dispersion relation must hold:

$$\mathbf{k} \bullet \mathbf{k} = \left(\frac{\omega}{v} + i\alpha_0 \right)^2 = \frac{\omega^2}{\left(\tilde{v} \right)^2} \tag{IV.D_2}$$

in which v is the phase velocity of traditional infinite homogeneous harmonic plane waves, $\tilde{v}$ is often called 'the complex wave velocity,, and α_0 is the intrinsic damping coefficient. Therefore in general the wave vector **k** can be complex valued, whence

$$\mathbf{k} = \mathbf{k}_1 + i\mathbf{k}_2 \; ; \; \mathbf{k}_1, \mathbf{k}_2 \in \Re^3 \tag{IV.D_3}$$

and

$$\mathbf{k}_2 = \boldsymbol{\alpha} + \boldsymbol{\beta} \text{ with } \boldsymbol{\beta} \perp \mathbf{k}_1 \text{ and } \boldsymbol{\alpha} \parallel \mathbf{k}_1 \tag{IV.D_4}$$

The vector $\mathbf{k}_1$ is called the propagation wave vector. The vector $\boldsymbol{\beta}$ is called the inhomogeneity vector whilst $\boldsymbol{\alpha}$ is called the damping vector. In many publications the opposite sign for $\boldsymbol{\beta}$ in (IV.D_4) can be found, but it is more convenient in this outline to use a positive sign. In order to prevent confusion with other papers, we will describe physical problems in terms of the imaginary part of the wave vector, i.e. k_2 , whence the sign convention of $\boldsymbol{\beta}$ will have no influence on these discussions. If (IV.D_3) and (IV.D_4) are entered in (IV.D_2), one finds

$$\mathbf{k}_1 \bullet \mathbf{k}_2 = k_1 \alpha = \frac{\omega}{v} \alpha_0 \tag{IV.D_5}$$

and

$$\left(k_1 \right)^2 - (\alpha)^2 - (\beta)^2 = \left(\frac{\omega}{v} \right)^2 - \left(\alpha_0 \right)^2 \tag{IV.D_6}$$

Relations (IV.D_5) and (IV.D_6) are called the dispersion equations. Due to (IV.D_5), the damping vector can only exist if there is intrinsic visco-elastic damping in the media. Furthermore, its value depends not only on the intrinsic damping α_0, but also on the inhomogeneity vector $\boldsymbol{\beta}$. Typical waves (IV.D_1) are depicted in Figs IV.D_2-4. In the context of what follows, it must be stressed that waves like (IV.D_1) have a wave front that extends to infinity, i.e. such waves are not bounded in space.
The term infinite inhomogeneous plane waves in the current section stands for 'plane waves' (IV.D_1) having a complex valued wave vector and a real valued frequency. The polarization will be complex too, but this fact has no influence on the amplitude distribution in space, whence it is not highlighted here.

Whenever an infinite inhomogeneous plane wave interacts with a plane interface between two media, continuity of the component of **k** along the interface is required. This is called the generalized Snell-Descartes law.

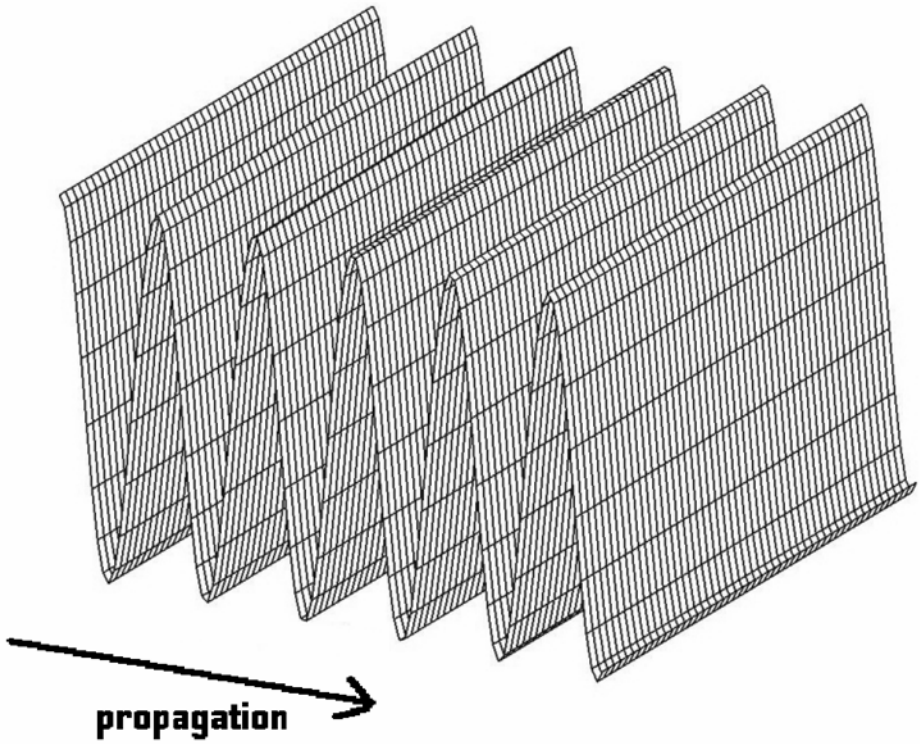

Fig. IV.D_2: ***An infinite pure plane wave (undamped). The amplitude along the wave front remains constant, as well as the amplitude along the propagation direction.***

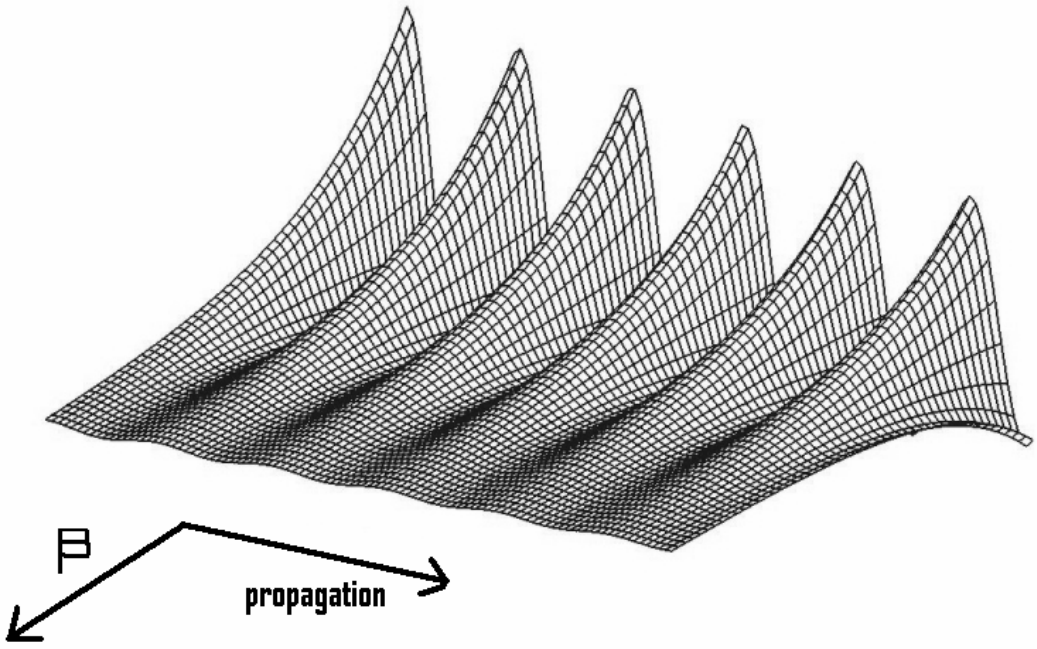

Fig. IV.D_3: ***An infinite inhomogeneous wave (undamped). The amplitude along the wave front decays exponentially down the inhomogeneity vector β (according to its definition in (IV.D_4)). The amplitude remains constant along the propagation direction.***

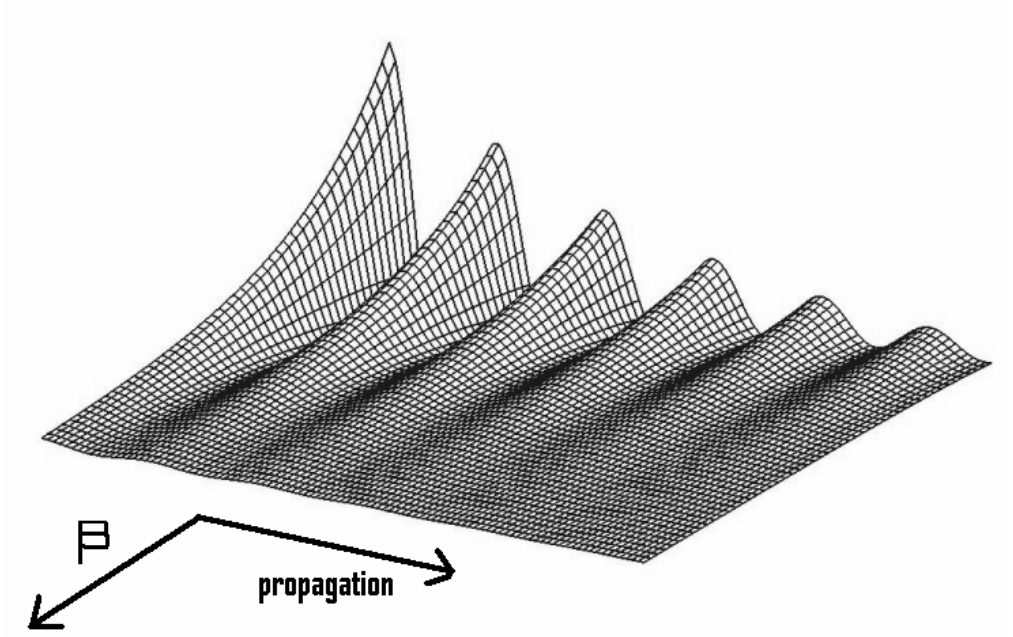

Fig. IV.D_4: ***Same as in Fig. IV.D_3, except that there is now damping, whence the amplitude also decays exponentially along the propagation direction.***

CLASSICAL BOUNDED BEAM FORMATION IN TERMS OF THE FOURIER THEORY

As this method is so widely known, we limit the discourse to a short description in words. In the Fourier theory, a bounded beam profile in X-space (consider Fig. IV.D_1) is transformed into $k_{1,x}$-space by means of the discrete Fourier transform. The amplitudes that correspond to each $k_{1,x}$ value are then attributed to a plane wave having a wave vector component $k_{1,x}$ and another component $k_{1,z}$ that is found as a function of $k_{1,x}$ and the dispersion relation for pure plane waves, i.e. (IV.D_6) for $\alpha = \beta = 0$. Physically this means that the bounded beam which profile is considered in the discrete Fourier transform, is built up by means of infinite plane waves all traveling in different directions and having amplitudes determined by that discrete Fourier transform. The beauty of this approach is of course that practically all kinds of beam profiles can be approximated by means of this method. However, from a theoretical point of view, the method is strictly only valid for beams that propagate in infinite space or at the most perpendicular to any boundary. That is because integration is performed from $X=-\infty$ to $X=+\infty$ which is strictly only possible if space is uninterrupted in this interval. Therefore, if oblique incidence is considered, the method is strictly wrong. Nevertheless, many authors apply the method even for oblique incidence. Furthermore, if large oblique incidence is considered of a narrow beam, there is yet another difficulty which is again a consequence of the fact that the method is strictly only valid for normal incidence, and that is that 'incident' infinite plane waves must be considered that are actually 'coming from the continuing media'. This is of course a contradictive situation which is not present in the inhomogeneous waves decomposition of bounded beams (see below). Yet another important problem that arises if the Fourier method is applied is the fact that no inhomogeneous waves are present in the bounded beam under consideration. This may lead to wrong numerical simulations especially whenever complicated surfaces (for example corrugated surfaces) are considered [12-15]. The reason is that inhomogeneous waves interact at interfaces differently from pure plane waves. This fact is very important because if one simulates a bounded inhomogeneous wave by means of the Fourier method, the resulting bounded beam may

simulate reality incorrectly, especially in cases where rough surfaces are considered [12-15]. That is the reason why this section focuses on the description of bounded inhomogeneous waves in terms of infinite inhomogeneous plane waves.

CLASSICAL GAUSSIAN BOUNDED BEAM FORMATION IN TERMS OF INFINITE INHOMOGENEOUS WAVES

The previous section suggests that it is not recommended to decompose a bounded inhomogeneous wave into plane waves (Fourier method) because 'contradictions' might occur and more important because the nature of plane waves is so different from that of (infinite) inhomogeneous (plane) waves that it is possible to perform wrong simulations especially if interaction is concerned with complicated interfaces such as periodically corrugated surfaces [12-15]. Therefore it is necessary to focus on the decomposition of bounded beams by means of a superposition of infinite inhomogeneous plane waves. Several years ago Leroy et al [5-7] proposed such a method. The method consists of the formation of a bounded beam as a superposition of infinite inhomogeneous plane waves all propagating in the same direction, but having different amplitudes and inhomogeneities. Let's consider a beam with profile *f(x)* which has to be decomposed as a superposition of inhomogeneous waves, then, if the sign convention (IV.D_4) is adopted, one has [5]

$$f(x) = \sum_{n=0}^{N} A_n \exp\left(-\beta_n x\right) \tag{IV.D_7}$$

Furthermore, one performs a coordinate transformation $x = p \ln y$ with $p \in \Re_0^+$ and $y \in (0,+\infty)$, whence, if $\beta_n = -n/p$,

$$\sum_{n=0}^{N} A_n y^n = f(p \ln y) \tag{IV.D_8}$$

on the other hand, one applies a decomposition into Laguerre polynomials [5] $L_n(y)$, such that

$$\sum_{n=0}^{N} B_n L_n(y) = f(p \ln y) \tag{IV.D_9}$$

with

$$B_n = \int_0^{+\infty} \exp(-y) f(p \ln y) L_n(y) dy \tag{IV.D_10}$$

then the coefficients A_n in (IV.D_7-8) are searched as a linear combination of B_i for $1 \le i \le N$. The drawback of this method is that (IV.D_10) can only be found numerically, while the mentioned linear combination is not found straightforwardly but as an optimization procedure. The procedure is found to be best suited if gaussian profiles are considered and is hence only applied for gaussian beams or beam profiles that can be approximated by means of

a small number of superposed gaussian beams [5-7]. Therefore, in what follows, we bring to light an analytical method that is valid for the kind of bounded beams f(x) that is important in this report and is called 'bounded inhomogeneous waves'.

THE DESCRIPTION OF BOUNDED INHOMOGENEOUS WAVES BY MEANS OF THE LAPLACE TRANSFORM

A bounded inhomogeneous wave looks like an infinite inhomogeneous wave except for the important fact that it is chopped as a small interval in x-space. Hence it does not extend to infinity and is bounded in space. The main feature of such a bounded inhomogeneous wave is that it is exponentially shaped inside the beam and that its amplitude drops at the borders. Hence, depending on the method that is used to generate such waves, the shape at the borders may differ a bit, but the exponential feature remains unchanged. There are therefore many mathematical functions possible that describe the profile of a bounded beam. We have chosen a function for which an analytical solution exists for the amplitudes A_n in (IV.D_7).

The profile of a bounded inhomogeneous wave, representing an exponentially decaying infinite inhomogeneous wave and traveling perpendicular to the x-axis, can sufficiently be described in the x-interval $[0,+\infty]$ by the analytical expression

$$f(x) = \frac{27W^4x^2}{4\left(x^2+W^2\right)^3} \tag{IV.D_11}$$

in which W is a parameter that is proportional to the 'width' of the beam profile. $f(x)$ reaches its maximum at

$$x_m = \frac{\sqrt{2}}{2}W \tag{IV.D_12}$$

Now, it would be possible to apply the numerical optimization technique of the previous section. However, it is here more convenient to apply an analytical approach. The first reason is that a numerical optimization procedure is far from natural and is in fact a fitting procedure. The expression 'give me enough parameters and I will fit you an elephant' is perhaps most suitable to understand the artificial character of any fitting procedure. The second reason is that it is known from experiments that bounded inhomogeneous waves behave like infinite inhomogeneous waves, whence there must be a physical and an inherent analytical relation between the two kinds of waves.

Therefore we decompose $f(x)$ into decaying infinite inhomogeneous waves and we let the interval of the inhomogeneities β_n mathematically tend to infinity, while decreasing the distance between the successive inhomogeneities; hence

$$f(x) = \sum_{n=0}^{N} B\left(-\beta_n\right)\exp\left(-\beta_n x\right) \cong \int_0^{+\infty} e^{-\beta x} A(\beta)\, d\beta \tag{IV.D_13}$$

$$\text{with } B\left(-\beta_n\right) = A\left(\beta_n\right)\Delta\beta_n$$

The integral in (IV.D_13) can be interpreted as the Laplace transform L of $A(\beta)$, whence the unknown coefficients $A(\beta)$ can be obtained applying the inverse Laplace transform L^{-1} of the profile (IV.D_11), thus releasing the problem of impractical numerical optimization procedures as they occur in the previous section. From textbooks containing tables of Laplace transforms, an analytical expression can be extracted

$$A(\beta) = L^{-1}\left(f(x)\right) = \frac{37W}{32}\left[\left(1+W^2\beta^2\right)\sin(W\beta) - W\beta\cos(W\beta)\right] \tag{IV.D_14}$$

This is an oscillating function with increasing amplitude as a function of β, involving very high amplitudes attributed to very rapidly decreasing inhomogeneous waves. Therefore, high β values will only contribute to the amplitude near the origin, since their amplitude becomes negligible at larger distances. Still, in practice, we shall have to chop the integral retaining a finite integration interval from $\beta = 0$ to a chosen $\beta = \beta_{\max}$, whence the recovered bounded inhomogeneous wave profile will deviate considerably near x=0. The two reasons for this chop process are 'numerical ease' and the requirement that $\mathbf{k}_1$ and $\mathbf{k}_2$ must be real, then considering (IV.D_5) and (IV.D_6) necessitates

$$\alpha \le \alpha_0 \tag{IV.D_15}$$

and

$$\beta^2 \le \omega^2 / v^2 - \left(\alpha_0\right)^2 \tag{IV.D_16}$$

The second step is the re-discretisation of the chopped integral in order to keep a finite number of infinite inhomogeneous waves forming the profile.

We therefore now examine the properties of the discrete and chopped summation of infinite inhomogeneous waves (see (IV.D_13)) representing the bounded inhomogeneous wave as described in (IV.D_11).

$$f(x) = \sum_{\beta=0}^{\beta_{\max}} A(\beta)\exp(-\beta)\Delta\beta \tag{IV.D_17}$$

It is always necessary to choose one value for W or respectively for β and then optimize the value of β respectively W in order to have best agreement between the bounded inhomogeneous wave and the infinite inhomogeneous wave under consideration. As an example we consider the case W=0.01m. It is seen from Fig. IV.D_5 that the upper part of profile (IV.D_11) can almost perfectly be approximated using one single inhomogeneous wave, having in this case an inhomogeneity $\beta = 125/m$.

This is as expected, since the profile (IV.D_11) was made to locally represent an infinite inhomogeneous wave. If we need to approximate the complete profile (IV.D_11), additional infinite inhomogeneous plane waves will be involved. In order to explain the behavior of a bounded inhomogeneous wave in the experiments cited above, we need to investigate the influence of the additional infinite inhomogeneous waves in the upper part of the bounded profile (IV.D_11).

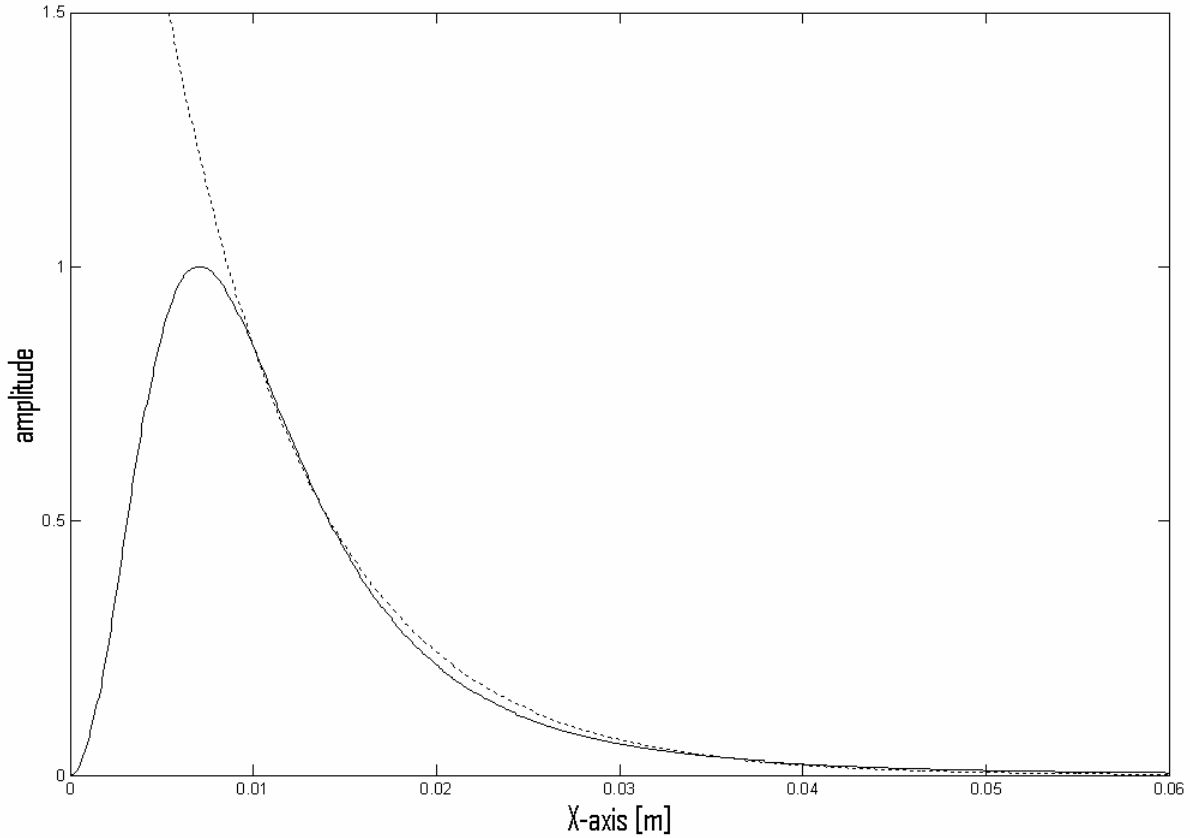

Fig. IV.D_5: ***Solid line: the exact profile (IV.D_11). Dotted line: the profile of an infinite inhomogeneous wave having an inhomogeneity 125/m.***

In Fig. IV.D_6, we have added each of the N terms in the summation (IV.D_17) for N=31 and for $\beta_{\max} = 3750/m$. The upper exponential is again the one for $\beta = 125/m$. It is clear that this infinite inhomogeneous plane wave still dominates the upper part, i.e. for higher x values, of the bounded inhomogeneous wave (IV.D_11). All other inhomogeneous waves dominate in the lower parts, i.e. for x values near zero, of the profile. That can explain why a bounded inhomogeneous wave in experiments behaves almost exactly (if the part of the beam near X=0 is not considered) as if it was an infinite inhomogeneous wave.

Next, in Fig. IV.D_7, all 31 inhomogeneous waves are summed to form the dashed line which is an approximation of the exact bounded inhomogeneous wave (solid line). A considerable deviation occurs near the origin, as explained above.

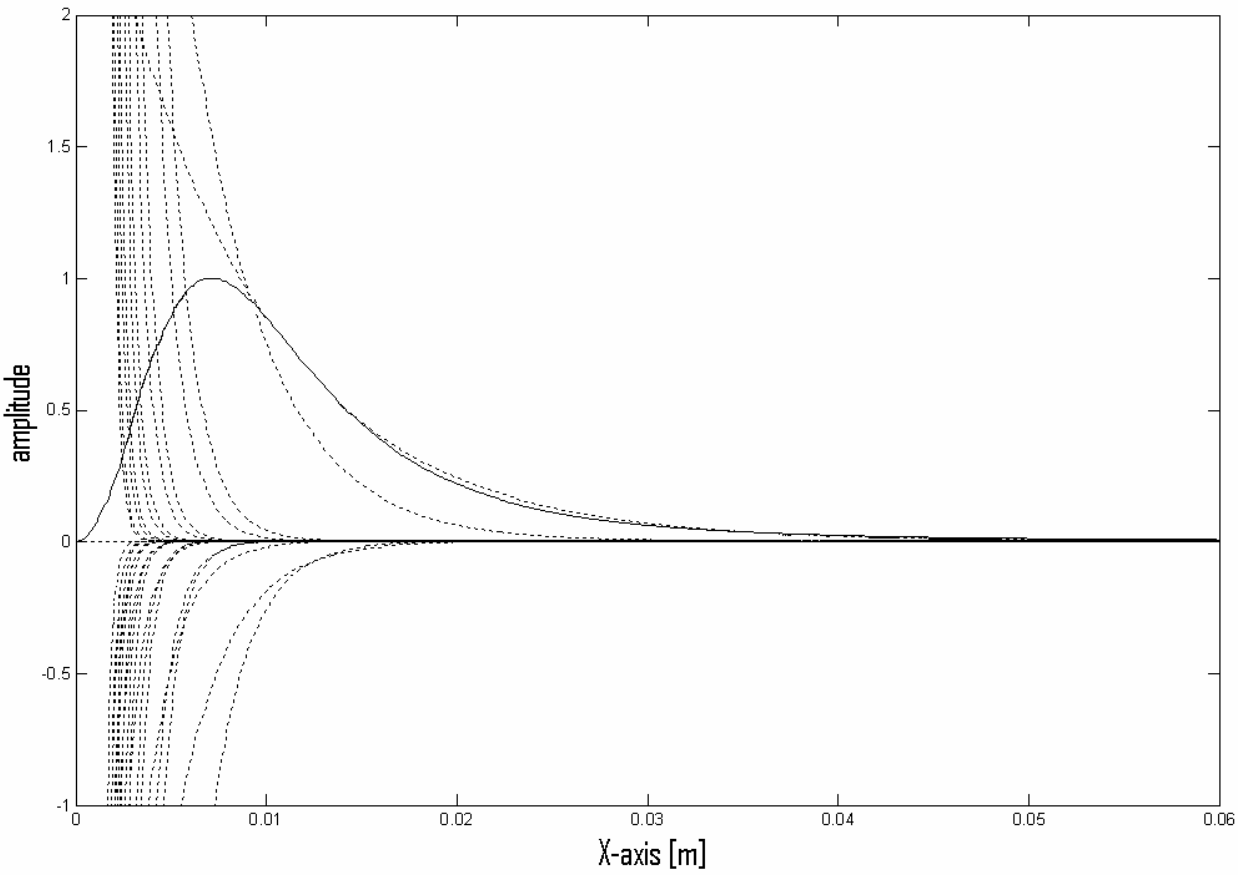

Fig. IV.D_6: Solid line: the exact profile (*IV.D*_11). Dotted lines: the profiles of the infinite inhomogeneous waves that form the exact profile as in (*IV.D*_13)

THE SCATTERING OF BOUNDED INHOMOGENEOUS WAVES

Theoretical development

We will now examine, by means of a numerical example, how a bounded inhomogeneous wave behaves during scattering at an interface between a liquid and an isotropic solid. We therefore highlight each individual incident infinite inhomogeneous wave and describe how it interacts with the interface.

Taking into account the generalized Snell-Descartes law (i.e. $k_x = k_x^{inc}$), we denote the potential for the incoming wave by

$$\varphi^{inc} = \exp i\left(k_x^{inc} x + k_z^{inc} z\right) \tag{IV.D_18}$$

for the reflected wave by

$$\varphi^{r} = R\ \exp i\left(k_x^{inc} x + k_z^{r} z\right) \tag{IV.D_19}$$

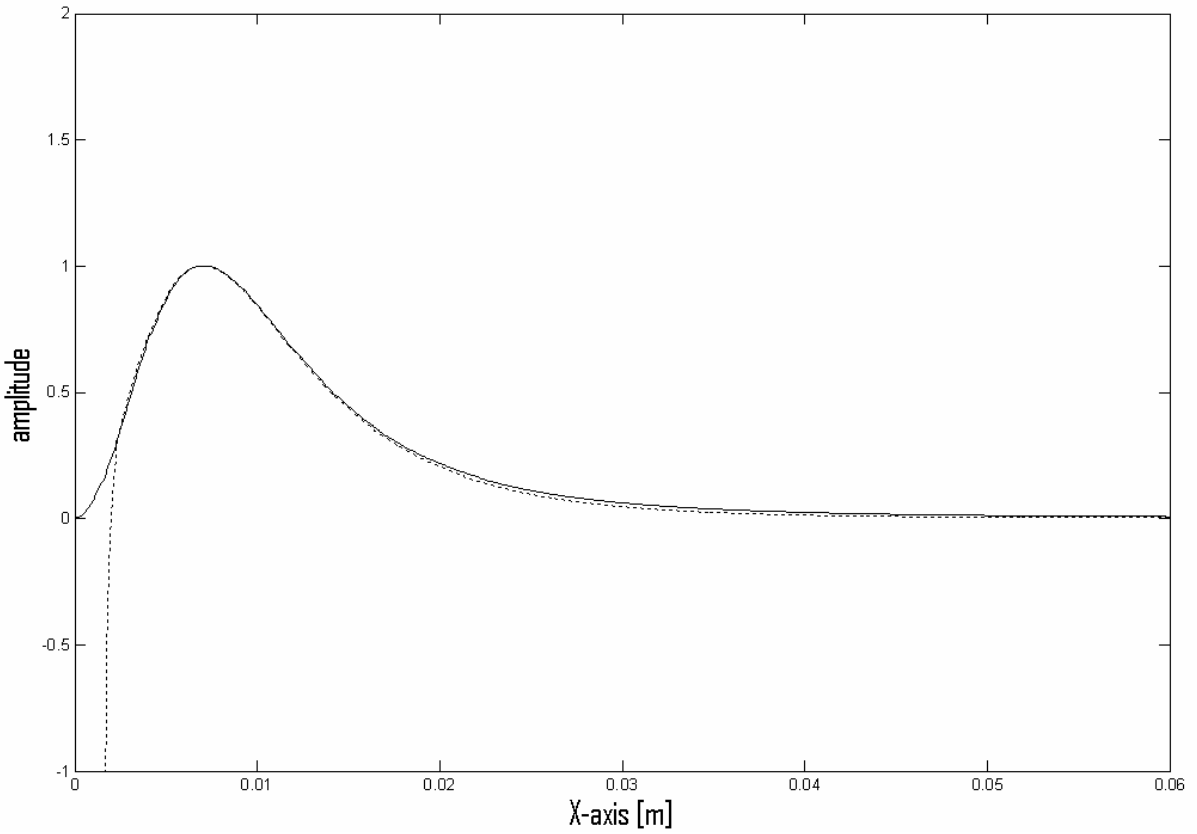

Fig. IV.D_7: ***Solid line: the exact profile (IV.D_11). Dotted line: the summation of the inhomogeneous waves as in (IV.D_13)***

for the transmitted longitudinal wave by

$$\varphi^t = T_d \exp i\left(k_x^{inc} x + k_z^{td} z\right) \tag{IV.D_20}$$

and for the transmitted shear wave by

$$\boldsymbol{\psi}^t = T_s \exp i\left(k_x^{inc} x + k_z^{ts} z\right)\mathbf{e}_y \tag{IV.D_21}$$

where R is the reflection coefficient, T_d is the transmission coefficient for longitudinal waves and T_s is the transmission coefficient for shear waves. All wave vectors involved in (IV.D_18-21) are supposed to be complex valued, cfr. (IV.D_3). Again we note that the sign of β is opposite to the one in ref. 5, however this is no problem because all the physics in the current section is expressed in terms of $\mathbf{k}_1$ and $\mathbf{k}_2$ immediately. Taking into account (IV.D_13), and taking into account the dispersion relation for inhomogeneous waves (IV.D_2), we have

$$\begin{bmatrix} k_x^{inc} \\ k_z^{inc} \end{bmatrix} = \begin{bmatrix} \cos\theta^{inc} & \sin\theta^{inc} \\ -\sin\theta^{inc} & \cos\theta^{inc} \end{bmatrix} \begin{bmatrix} i\beta^{inc} \\ \sqrt{\left(\omega/v + i\alpha_0\right)^2 - \left(\beta^{inc}\right)^2} \end{bmatrix} \tag{IV.D_22}$$

and

$$k_z^r = \sqrt{\left(\omega/v + i\alpha_0\right)^2 - \left(k_x^{inc}\right)^2} \tag{IV.D_23}$$

$$k_z^{td} = \sqrt{\left(\omega/v_d + i\alpha_{0d}\right)^2 - \left(k_x^{inc}\right)^2} \tag{IV.D_24}$$

$$k_z^{ts} = \sqrt{\left(\omega/v_s + i\alpha_{0s}\right)^2 - \left(k_x^{inc}\right)^2} \tag{IV.D_25}$$

In (IV.D_22-25), v is the wave velocity in the liquid, v_d and v_s are the longitudinal respectively shear wave velocities in the solid.
The intrinsic damping coefficients in the liquid for longitudinal waves, respectively in the solid for longitudinal and shear homogeneous plane waves are denoted by α_0, α_{0d} and α_{0s}. For simplicity, we will suppose that there is no damping involved in our calculations.
We then develop the continuity conditions along the interface for normal displacements

$$u_z^{liquid} = u_z^{solid} \tag{IV.D_26}$$

and for normal stress,

$$T_{p3}^{liquid} = T_{p3}^{solid} \tag{IV.D_27}$$

with

$$\mathbf{u}^{liquid} = \nabla\left(\varphi^{inc} + \varphi^r\right) \tag{IV.D_28}$$

$$\mathbf{u}^{solid} = \nabla\left(\varphi^t\right) + \nabla \times \boldsymbol{\psi}^t \tag{IV.D_29}$$

and

$$T_{pj}^q = \delta_{pj}\tilde{\lambda}^q \varepsilon_{rr}^q + 2\tilde{\mu}^q \varepsilon_{pj}^q \tag{IV.D_30}$$

in which we have used the Einstein double suffix notation convention, q=1 for the liquid and q=2 for the solid, and

$$\tilde{\lambda}^q = \lambda^q - i\omega\lambda'^q = \rho\left(\tilde{v}_d\right)^2 \tag{IV.D_31}$$

$$\tilde{\mu}^q = \mu^q - i\omega\mu'^q = \rho\frac{\left(\tilde{v}_s\right)^2 - \left(\tilde{v}_d\right)^2}{2} \tag{IV.D_32}$$

$$\varepsilon_{kl}^q = \frac{1}{2}\left[\partial_l u_k^q + \partial_k u_l^q\right] \tag{IV.D_33}$$

The Lamé constants are denoted by λ and μ, while the viscoelastic damping coefficients are given by λ' and μ'. The definition of the 'complex velocity $\tilde{v}$' is found in (IV.D_2), for the appropriate choice of shear or longitudinal wave material properties.
By applying the continuity conditions (IV.D_26) and (IV.D_27) we obtain

$$\begin{bmatrix} RD \\ TD \\ TS \end{bmatrix} \tag{IV.D_34}$$

$$= \begin{bmatrix} k_z^r & -k_z^{td} & -k_x^{inc} \\ 0 & -2k_z^{td}k_x^{inc} & \left(\frac{\omega}{v_s} + i\alpha_{0s}\right)^2 - 2\left(k_x^{inc}\right)^2 \\ -\tilde{\lambda}^1\left(\frac{\omega}{v} + i\alpha_0\right)^2 & \tilde{\lambda}^2\left(\frac{\omega}{v_d} + i\alpha_{0d}\right)^2 + 2\tilde{\mu}^2\left(k_z^{td}\right)^2 & 2\tilde{\mu}^2 k_z^{ts}k_x^{inc} \end{bmatrix}^{-1}$$

$$\times \begin{bmatrix} -k_z^{inc} \\ 0 \\ \tilde{\lambda}^1\left(\frac{\omega}{v} + i\alpha_0\right)^2 \end{bmatrix}$$

Remember that in order to obtain (IV.D_34), we have incorporated the dispersion relation for inhomogeneous waves. Solving (IV.D_34) requires proper choices of the signs of the z-components of the wave vector. The latter can be found in the literature [6] and is outlined in terms of $\mathbf{k}_1$ and $\mathbf{k}_2$, i.e. independent of the choice of the sign of β in (IV.D_4), as follows. The bulk critical angle for transmitted waves of type *c* (*c*=*s* for shear, *c*=*d* for longitudinal) is given by

$$\theta^c = \arcsin\frac{v}{v_c} \tag{IV.D_35}$$

Whenever $\theta^{inc} < \theta^{c}$, $\mathbf{k}_1$, for that particular transmitted mode must point into the solid, which corresponds to the classical Sommerfeld conditions. Whenever $\theta^{inc} \geq \theta^{c}$, $\mathbf{k}_2$, for that particular transmitted mode must point into the solid. For the reflected wave, it is always so that $\mathbf{k}_1$, must point into the liquid.

Numerical results

We consider a water/brass interface with $v = 1480 m/s$, $v_d = 4840 m/s$, $v_s = 2270 m/s$, $\rho_l = 1000 kg/m^3$, $\rho_s = 8100 kg/m^3$.

ρ_l respectively ρ_s are the densities of the liquid and the solid and are needed for the determination of the Lamé constants when applying the dispersion relation for inhomogeneous waves (IV.D_2).

We know from calculations of the reflection coefficient by means of (IV.D_34), involving inhomogeneous waves, that for 5MHz, a Rayleigh wave is stimulated when $\theta^{inc} = 44.045^0$ and $\beta^{inc} = 311.56/m$, corresponding to the so called Rayleigh pole.

We thus consider a bounded inhomogeneous wave, having a Rayleigh wave stimulating inhomogeneity, i.e. $\beta = 311.56/m \Leftrightarrow W = 0.004m$. We calculate the reflected profiles for different angles of incidence. All calculations are performed for $\beta_{\max} = 6231.2$ and for 21 inhomogeneous waves with equidistant inhomogeneity coefficients $\beta \in [0, \beta_{\max}]$. In Fig. IV.D_8, the angle of incidence θ^{inc} is 30^0. This angle is far less than the Rayleigh angle. We notice that each infinite inhomogeneous wave by which the bounded inhomogeneous wave is built up, is shifted very little and so is the bounded inhomogeneous wave.

In Fig. IV.D_9, the angle of incidence $\theta^{inc} = 42^0$, which is in the vicinity of the Rayleigh angle. We notice that the bounded inhomogeneous wave is shifted along the x-axis, by the same amount as its infinite inhomogeneous counterpart. At last, in Fig. IV.D_10 we have taken the exact Rayleigh angle of incidence $\theta^{inc} = 44.045^0$.

We observe that both the bounded inhomogeneous wave and its infinite counterpart are shifted by almost the same distance along the interface. We must stress however that Figs. IV.D_5-10 cannot be used to check energy conservation, but solely to check displacement. The reason for that is the fact that the bounded inhomogeneous wave is written as a finite sum over a finite inhomogeneity interval. This causes deviations near x=0, whence energy conservation cannot be checked. It is impossible to use the exact integral expression (IV.D_13) without encountering numerical problems, otherwise such calculations would undoubtedly better involve conservation of energy and hence limit the calculated intensities of the dotted line near x=0 in Fig IV.D_10.

In contrast to bounded gaussian beams, a bounded inhomogeneous wave does not cause a null zone or other peculiarities due to the Schoch effect. Hence nondestructive testing of materials using bounded inhomogeneous waves is quite different from the use of other types of bounded beams.

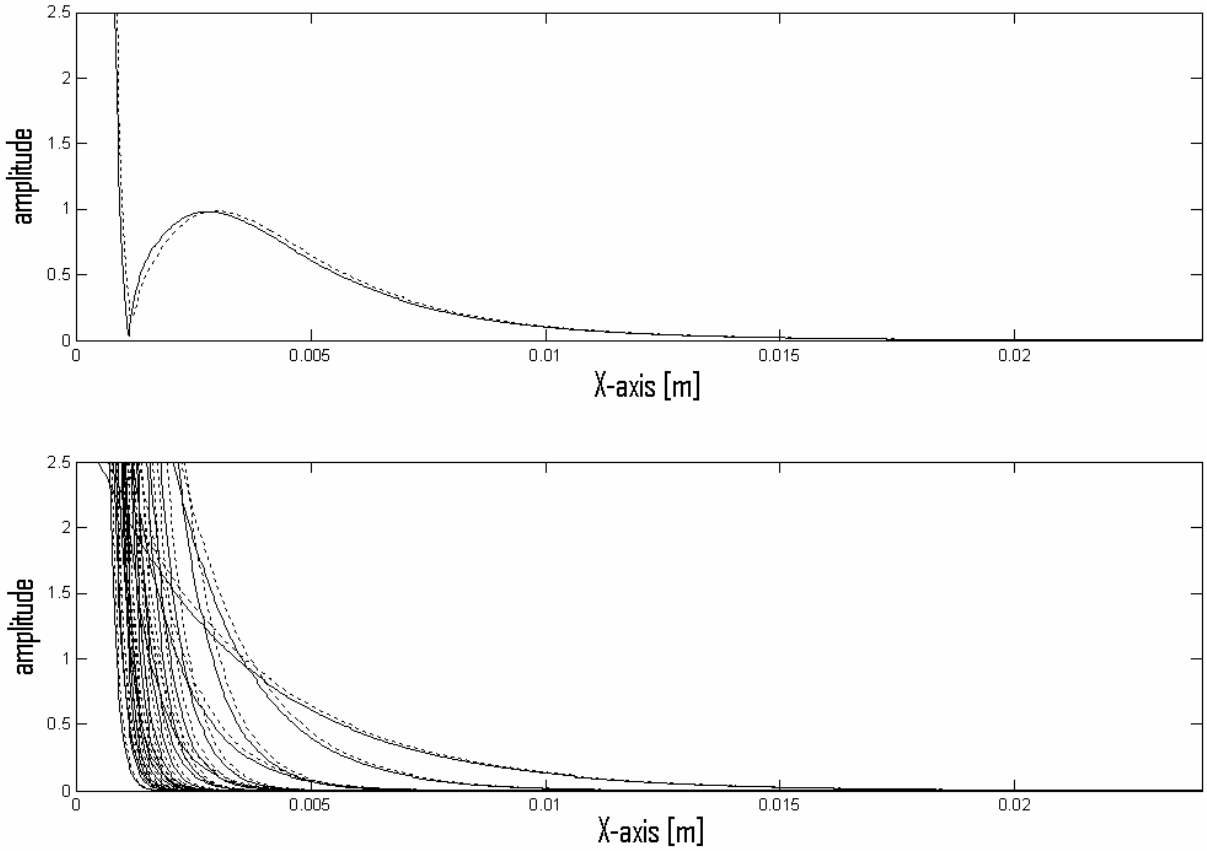

Fig. IV.D_8: ***Solid line: absolute value of the amplitude of the incident bounded inhomogeneous beam profile (top) and its infinite inhomogeneous waves building blocks (bottom). Dotted line: absolute value of the amplitude of the reflected bounded inhomogeneous beam profile (top) and its reflected infinite inhomogeneous waves building blocks (bottom). Inhomogeneity: 311.56/m. Angle of incidence : 30^0 (not in the vicinity of the Rayleigh angle).***

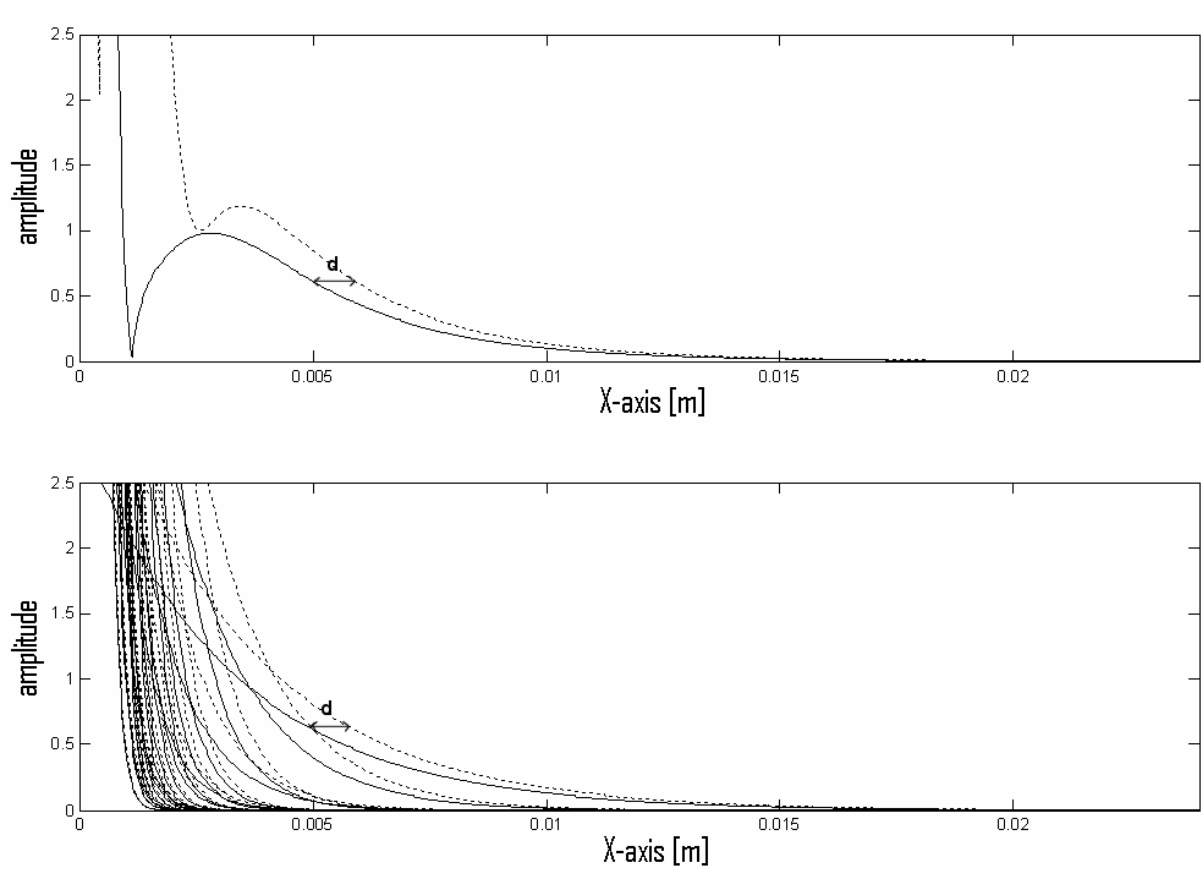

Fig. IV.D_9: ***Solid line: absolute value of the amplitude of the incident bounded inhomogeneous beam profile (top) and its infinite inhomogeneous waves building blocks (bottom). Dotted line: absolute value of the amplitude of the reflected bounded inhomogeneous beam profile (top) and its reflected infinite inhomogeneous waves building blocks (bottom). Inhomogeneity: 311.56/m. Angle of incidence : 42^0 (in the neighborhood of the Rayleigh angle). It is seen that both the infinite and the bounded inhomogeneous wave are displaced by a distance d.***

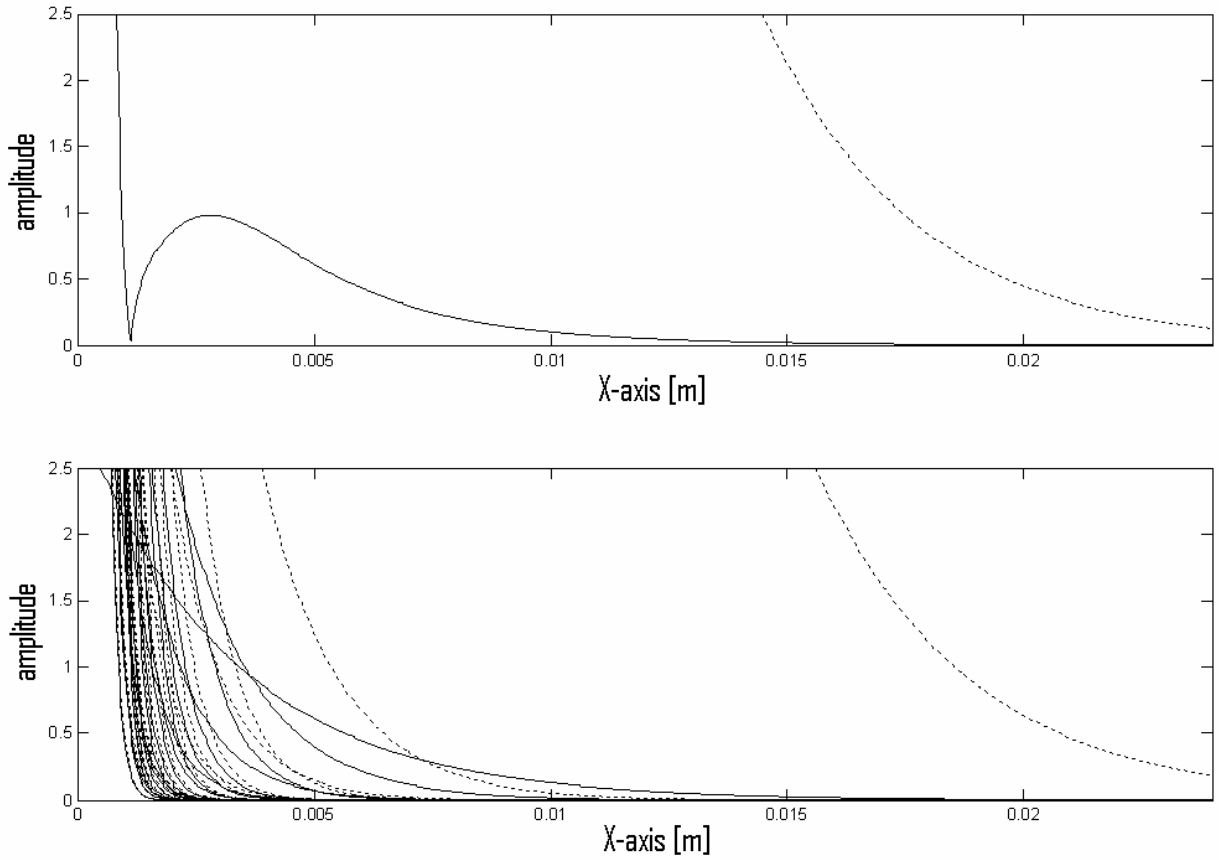

Fig. IV.D_10: ***Solid line: absolute value of the amplitude of the incident bounded inhomogeneous beam profile (top) and its infinite inhomogeneous waves building blocks (bottom). Dotted line: absolute value of the amplitude of the reflected bounded inhomogeneous beam profile (top) and its reflected infinite inhomogeneous waves building blocks (bottom). Inhomogeneity: 311.56/m. Angle of incidence : 44.045^0 (exactly the Rayleigh angle).***

CONCLUSIONS

We have presented the Laplace transform as a tool for analytically determining the unknown coefficients in the infinite inhomogeneous plane waves decomposition of a bounded inhomogeneous wave. We have also shown that it is understood from a theoretical point of view why in experiments bounded inhomogeneous waves behave almost as if they were infinitely extended. As an example, we have exposed how a bounded inhomogeneous wave is deformed after interaction with a water/brass interface and have verified that it is shifted in space by the same amount as its infinite inhomogeneous counterpart. This shift which is not really accompanied by a deformation, is typical for bounded as well as for infinite inhomogeneous waves and differs much from strong deformations such as the well known Schoch effect for gaussian beams.

REFERENCES

[1] Bernard Poirée, "Les ondes planes évanescentes dans les fluides parfaits et les solides élastiques", J. Acoustique 2, 205-216, 1989.

[2] Marc Deschamps, "L'onde plane hétérogène et ses applications en acoustique linéaire", J. Acoustique 4, 269-305, 1991

[3] B. Poirée, "Complex harmonic waves", 99-117, *Physical Acoustics*, Edited by O. Leroy and M. A. Breazeale, Plenum Press, New York, 1991

[4] Gérard Quentin, André Derem, Bernard Poirée, "The formalism of evanescent plane waves and its importance in the study of the generalized Rayleigh wave", J. Acoustique 3, 321-336, 1990
[5] J. M. Claeys, O. Leroy, "Reflection and transmission of bounded sound beams on half spaces and through plates", J. Acoust. Soc. Am. 72(2), 585-590, 1982
[6] K. Van Den Abeele, O. Leroy, "Complex harmonic wave scattering as the framework for investigation of bounded beam reflection and transmission at plane interfaces and its importance in the study of vibrational modes", J. Acoust. Soc. Am. 93(1), 308-323, 1993
[7] K. Van Den Abeele, O. Leroy, "On the influence of frequency and width of an ultrasonic bounded beam in the investigation of materials: Study in terms of heterogeneous plane waves", J. Acoust. Soc. Am. 93(5), 2688-2699, 1993
[8] M. Deschamps, B. Hosten, "Génération de l'onde hétérogène de volume dans un liquide non absorbant", Acustica 68, 92-95, 1989.
[9] W. Huang, R. Briers, S. I. Rokhlin, O. Leroy, "Experimental study of inhomogeneous wave reflection from a solid-air periodically rough boundary using leaky Rayleigh waves", J. Acoust. Soc. Am. 96(1), 363-369, 1994
[10] Marc Deschamps, "Reflection and refraction of the evanescent plane wave on plane interfaces", J. Acoust. Soc. Am. 96(5), 2841-2848, 1994
[11] R. Briers, O. Leroy, O. Poncelet, M. Deschamps, "Experimental verification of the calculated diffraction field generated by inhomogeneous waves obliquely incident on a periodically rough liquid-solid boundary", J. Acoust. Soc. Am. 106(2), 682-687, 1999
[12] Nico F. Declercq, Joris Degrieck, Rudy Briers, Oswald Leroy, "Theoretical verification of the backward displacement of waves reflected from an interface having superimposed periodicity", Appl. Phys. Let. 82(15), 2533-2534, 2003
[13] Nico F. Declercq, Joris Degrieck, Rudy Briers, Oswald Leroy, "A theoretical treatment of the backward beam displacement on periodically corrugated surfaces and its relation to leaky Scholte-Stoneley waves", submitted to JASA (reviewed + revised + resubmitted)
[14] Nico F. Declercq, Joris Degrieck, Rudy Briers, Oswald Leroy, "A Theoretical elucidation for the experimentally observed backward displacement of waves reflected from an interface having superimposed periodicity", J. Acoust. Soc. Am. 112(5), 2414, 2002
[15] A. A. Teklu, M. A. Breazeale, "Backward displacement of ultrasonic waves reflected from a corrugated interface", J. Acoust. Soc. Am. 113(4), 2283-2284, 2003.

IV.E The representation of 3D gaussian beams by means of inhomogeneous waves

There are different methods to mathematically represent a bounded beam. Perhaps the most famous method is the classical Fourier method that consists of the superposition of pure homogeneous plane waves all traveling in different directions and having an amplitude that can be found by the Fourier transform of the required profile. This method works perfectly for 2D as well as for 3D bounded beams. However, some researchers prefer the Inhomogeneous Wave theory to represent a bounded beam because some phenomena, e.g. the Schoch effect, are explained by this method by means of concepts that agree better with intuition. There are several papers dealing with this method for 2D gaussian beams. Until now, it has never been considered possible to represent 3D gaussian beams as well. The present section shows a method to overcome this shortcoming and presents different sorts of 3D gaussian beams that are built up by means of inhomogeneous plane waves.
The contents of this section have been published as: Nico F. Declercq, Joris Degrieck, Oswald Leroy, "The inhomogeneous wave decomposition of 3D Gaussian-like bounded beams", Ultrasonics 42, 273-276, 2004. (Imp. Fact. 0.844; SCI-index, Acoustics, rank:11 /28)

INTRODUCTION

There are several ways of mathematically representing bounded beams. The most common technique is the Fourier method [1] in which a bounded beam is built up by pure plane waves all incident at different angles. One of the other methods is the decomposition of a bounded beam into inhomogeneous waves [2,3]. Inhomogeneous waves differ from pure plane waves in that their wave vector is complex, involving an exponentially decaying/growing amplitude along their wave fronts. If a bounded beam is imagined to be built up by inhomogeneous waves, one approaches the bounded beam by means of a summation of inhomogeneous waves in a limited interval. Beyond the limits of that interval, exponentially growing tails appear [2,3]. The approach has always been understood as a least squares approximation and applies the so called Prony technique [2] and the orthogonality of Laguerre polynomials. This method, which was first applied on bounded beams by Claeys and Leroy [2], has always been applied to 2D gaussian beams, involving polynomials containing one single variable. The extension to 3D gaussian beams has never been performed since a similar reasoning would involve polynomials containing 2 variables. As until now, one has never found a promising technique to deal with these polynomials in this context, 3D gaussian beams remained non-existing in inhomogeneous wave theory. The present communication reports a simple technique to represent 3D gaussian-like beams by means of inhomogeneous waves. The technique is based on a fitting procedure in a limited number of spots and not on a least squares approximation on a certain interval.

REPRESENTING 3D GAUSSIAN-LIKE BEAMS

The profile of a 3D gaussian-like beam is given by

$$f(x,y) = \exp\left(-\frac{x^2}{W^2} - \frac{y^2}{V^2}\right) \tag{IV.E_1}$$

and is decomposed into inhomogeneous waves as

$$f(x,y) = \sum_{m=-M}^{M} \sum_{n=-N}^{N} A_{m,n} \exp\left(\boldsymbol{\beta}_{m,n} \bullet \mathbf{r}\right) \tag{IV.E_2}$$

The amplitude attributed to the inhomogeneous wave of number (m,n) is $A_{m,n}$, the inhomogeneity is $\boldsymbol{\beta}_{m,n}$ with

$$\boldsymbol{\beta}_{m,n} = \beta_m^x \mathbf{e}_x + \beta_n^y \mathbf{e}_y \tag{IV.E_3}$$

In accordance with the method of Claeys and Leroy [2,3], we apply

$$\beta_m^x = \frac{m}{p_x} \text{ and } \beta_n^y = \frac{n}{p_y} \tag{IV.E_4}$$

with p_x and p_y real numbers.

Furthermore, we choose $(2M+1)\times(2N+1)$ spots in the xy-plane in which we demand (IV.E_2) to hold. Due to the smoothness of exponential functions, equation (IV.E_2) will hold rather well for intermediate points if the $(2M+1)\times(2N+1)$ spots are chosen well thought-out. It is found that almost perfect results are found if the spots are chosen to lay equidistantly on concentric ellipses defined by

$$\frac{x^2}{r^2W^2} + \frac{y^2}{r^2V^2} = 1 \tag{IV.E_5}$$

for r determined by

$$\frac{r}{W} \in \{0.001, 0.2\} \cup \{1.2, ..., \mu\} \tag{IV.E_6}$$

Fig. IV.E_1 shows the considered spots for a 3D gaussian beam profile defined by $V = W$. μ is chosen to be *3/W*.

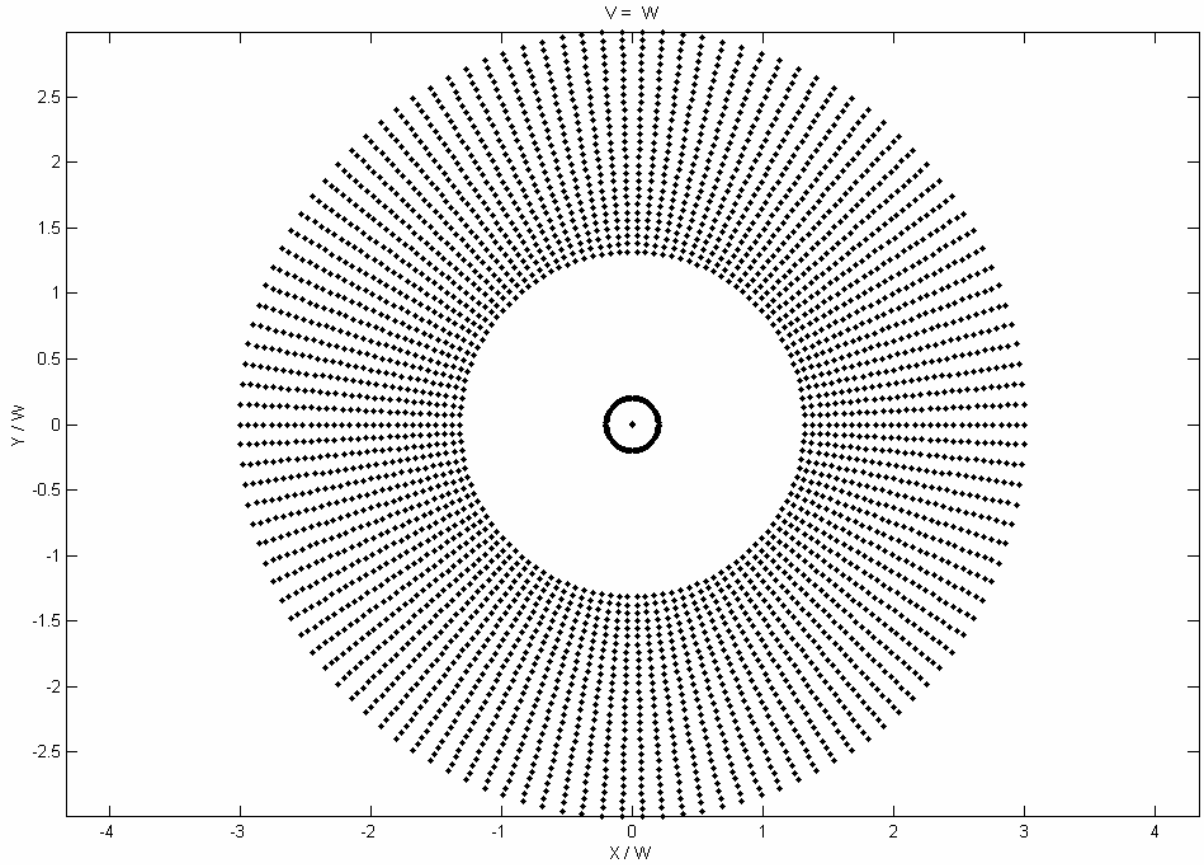

Fig IV.E_1: ***The distribution of spots where the fit procedure (IV.E_2) is performed for a perfectly gaussian beam profile (V=W).***

In Fig. IV.E_2, the obtained gaussian profile is shown by means of a superposition of inhomogeneous waves for $p_x = p_y = 6.7$ and for $M = N = 30$. It is seen that the approximation is promising within a certain radius. Beyond that radius, exponential tails appear in a similar way as in approximations of 2D gaussian beams [2,3]. As is already supposed in (IV.E_1), the method can also be used if the bounded beam is not perfectly gaussian, but is characterized by $W \neq V$.

The chosen spots for the situation $V = \frac{W}{2}$ are depicted in Fig. IV.E_3. In Fig. IV.E_4, the approximation is shown by a superposition of the same inhomogeneous waves as in Fig. IV.E_2, except of course that the coefficients $A_{m,n}$ are different.

Special attention must be paid to the number of inhomogeneous waves that is used, because the larger the number of waves, the larger the number of spots in which the fitting procedure is performed. The latter results in an enhanced overall beam profile approximation. In Fig. IV.E_5, the approximation of Fig. IV.E_2 is shown for $M = N = 10$. It is clear that wrinkles appear which are not visible in Fig. IV.E_2.

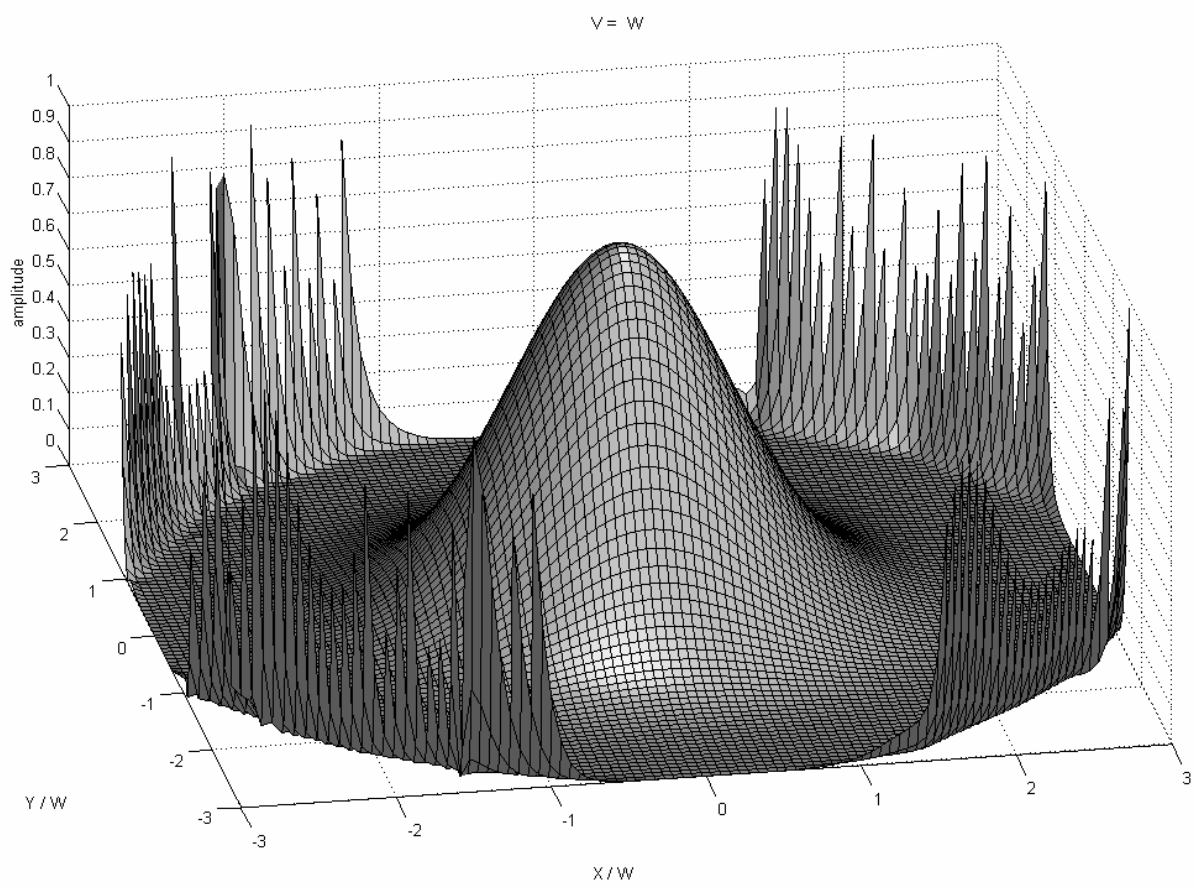

Fig IV.E_2: ***The profile of a 3D gaussian beam approached by a superposition of inhomogeneous waves (V=W).***

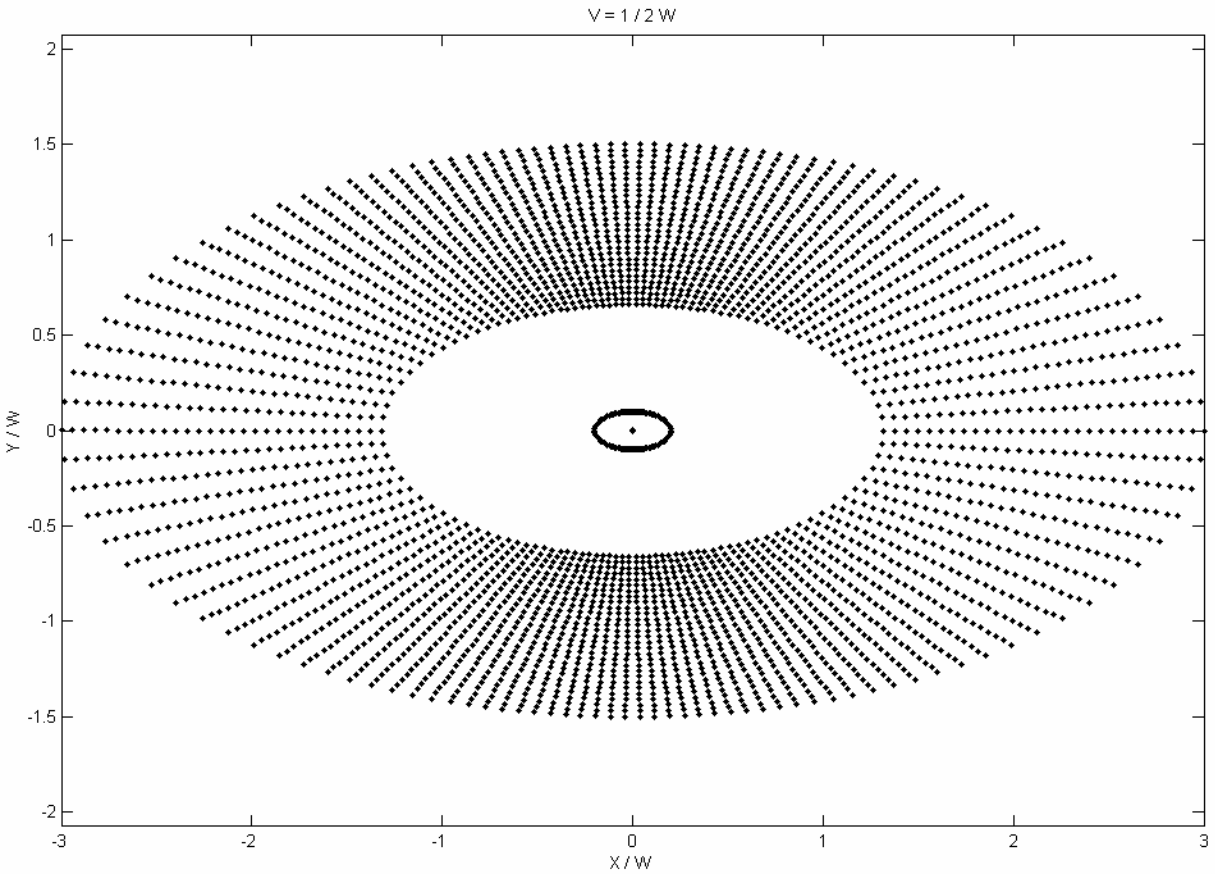

Fig IV.E_3: ***The distribution of spots where the fit procedure (IV.E_2) is performed for a gaussian like beam profile (V=W/2).***

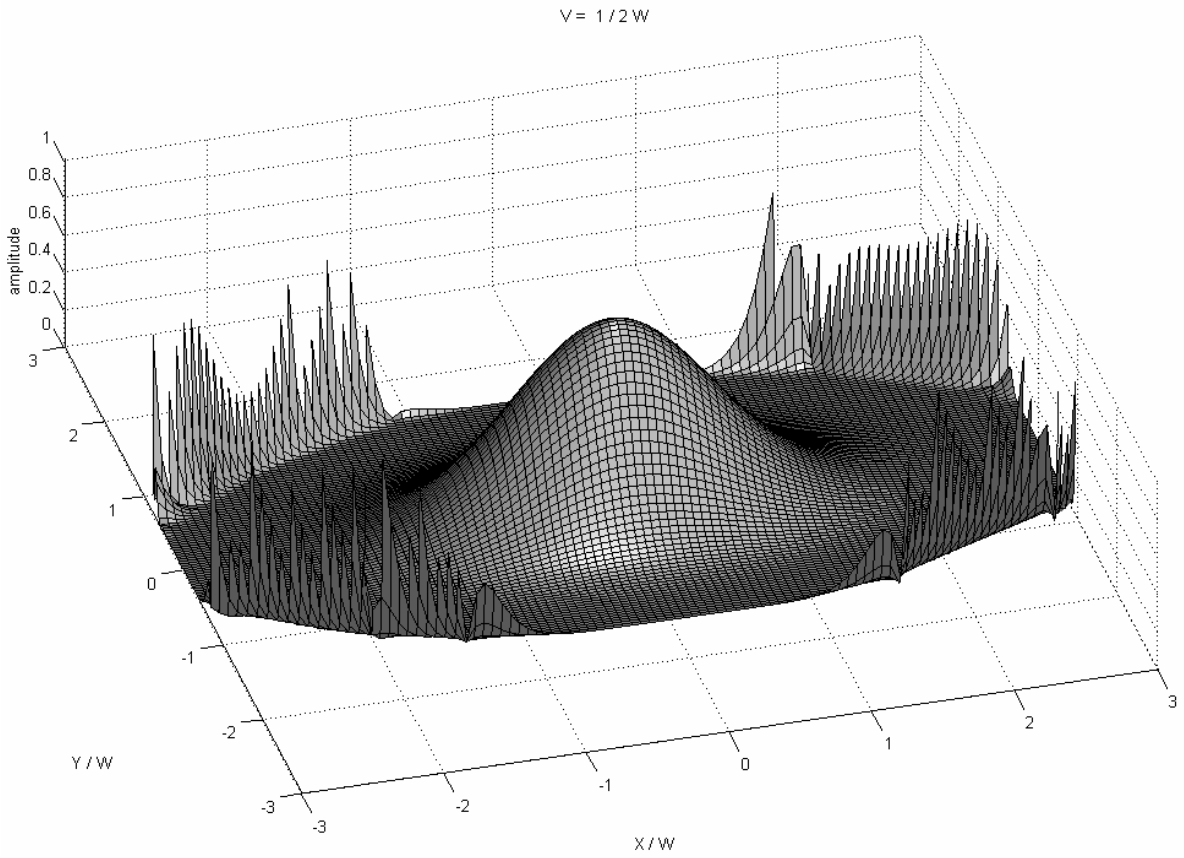

Fig IV.E_4: ***The profile of a 3D gaussian-like beam approached by a superposition of inhomogeneous waves (V=W/2).***

CONCLUSION AND PROSPECTS

A method is presented to approximate 3D gaussian beams by a superposition of inhomogeneous waves. The method seems to work very well, especially if the number of inhomogeneous waves is large. In future, research has to be performed as to investigate how steady this method is for utilization in scattering phenomena, because it is known from the application of 2D gaussian beams that numerical stability is critical [2,3].

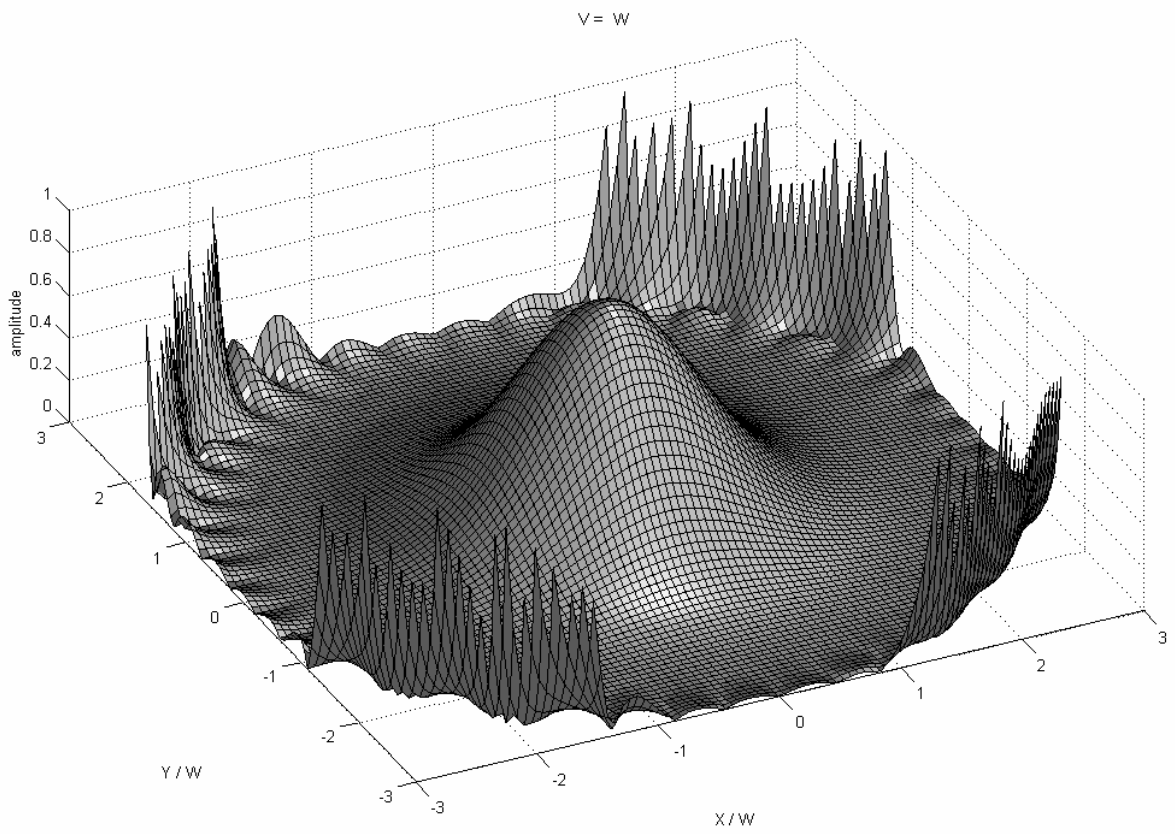

Fig IV.E_5: ***Same result as in Fig.*** **IV.E***_2, except that a much smaller number of inhomogeneous waves is used (M=N=10)*

REFERENCES

[1] Nico F. Declercq, Rudy Briers, Oswald Leroy, " The use of polarized bounded beams to determine the groove direction of a surface corrugation at normal incidence, the generation of surface waves and the insonification at Bragg-angles", Ultrasonics 40/1-8 pp. 345-348, 2002.

[2] J.M. Claeys, O. Leroy, "Reflection and transmission of bounded sound beams on halfspaces and through plates", J. Acoust. Soc. Am., 72, 585-590, 1982.

[3] K. Van Den Abeele and O. Leroy, “Complex harmonic wave scattering as the framework for investigation of bounded beam reflection and transmission at plane interfaces and its importance in the study of vibrational modes”, J. Acoust. Soc. Am. 93, 308-323, 1993.

IV.F Focal length control of complex harmonic and complex pulsed ultrasonic bounded beams

This section describes a way to change the focal length of a single transducer without phased array technology and without changing the (real) frequency. The physical effect is induced by changing the signal's amplitude in a precise manner in order to approach the complex harmonic wave regime. In this regime, changing the imaginary frequency results in a change of the focal length. A study is performed for different beam shapes and for complex harmonic signals as well as for complex pulsed signals.
The contents of this section have been publishded as: Nico F. Declercq, Joris Degrieck, Oswald Leroy, "Focal length control of complex harmonic and complex pulsed ultrasonic bounded beams", J. Appl. Phys., 97(5), 054904 1-8, 2005 *(Imp. Fact. 2.281; SCI-index, Physics-Applied, rank:13/76)*

INTRODUCTION

Focused transducers are widely used in acoustic microscopy [1] and in general NDT [2-4]. In the medical field, pulsed focused ultrasound has long been used to destroy kidney stones and the High Intensity Focused Ultrasound (HIFU) technique is applied in the treatment of cancer [5] and internal wounds. The latter is realized by 'stimulating' thrombocytes to locally coagulate [6-9], i.e. acoustic hemostasis. The technique is also used to seal air leaks in lungs [10]. It is also possible to treat cancer by means of the local hyperthermia technique where low(er) intensity focused ultrasound is used during a much longer period of time. For the moment, one is limited to the use of single focused transducers, which have almost no flexibility to change the focal length, or phased arrays, which are more flexible but posses their own inherent shortcomings, such as a very high cost.

For a given single transducer, the only known technique to change the focal length for a given medium, is changing the input frequency. However, unless the new frequency is an odd number of the transducer's first harmonic, the generated power is negligible. The current section describes a technique to change the focal length without changing the frequency but with altering the amplitude in a very distinctive manner. In what follows, we redefine the word frequency. What is classically called 'frequency' is now explicitly called 'real frequency'. The 'real frequency' is a specific part of a more general 'complex frequency' and is responsible for the phase of the considered signal. The 'imaginary frequency' is then, as will be explained further below, responsible for the temporal amplitude change.

Furthermore, even though focusing of ultrasound is often accompanied by non-linear effects, especially when very high amplitudes are involved, such as in HIFU, for simplicity we limit this discourse to a linear regime in visco-elastic media.

THEORY

In the linear elasticity regime, sound fields can be divided into the long-lasting or the harmonic type and the short time, pulsed type. Practically, all sound fields are bounded in space, whereas mathematically, infinite waves are also possible.

building blocks of the bounded beam description

Harmonic infinite plane waves are orthogonal solutions of the wave equation and form therefore the building blocks for the description of complicated sound fields. However, more sophisticated, though more general, solutions of the wave equation are so called complex harmonic inhomogeneous plane waves. Such waves are described as classical homogeneous plane waves,

$$\varphi(r,t) = A\mathbf{P}\exp(\gamma\mathbf{k}\cdot\mathbf{r} - 2\pi\gamma ft) \text{ with } \gamma = \pm 1 \tag{IV.F_1}$$

except that each of the quantities in (IV.F_1), apart from time t and position **r**, are complex valued instead of simply real valued. An extensive historical overview of such waves, has recently been reported by Declercq et al [11].
Besides the amplitude A, the polarization is, in general, complex valued

$$\mathbf{P} = \mathbf{P}_1 + i\mathbf{P}_2 \tag{IV.F_2}$$

and so is the frequency f

$$f = \left(f_{\mathrm{Re}} + if_{\mathrm{Im}}\right) \tag{IV.F_3}$$

The complex wave vector is decomposed as [11]

$$\mathbf{k} = \mathbf{k}_{\mathrm{Re}} + i\mathbf{k}_{\mathrm{Im}} = \mathbf{k}_{\mathrm{Re}} + i\left(\boldsymbol{\alpha} - \boldsymbol{\beta}\right) \tag{IV.F_4}$$

with $\boldsymbol{\alpha} \parallel \mathbf{k}_{\mathrm{Re}}$ and $\boldsymbol{\beta} \perp \mathbf{k}_{\mathrm{Re}}$, then, it can be verified that

$$\mathbf{u} = A\mathbf{P}\exp\left(2\pi\gamma f_{\mathrm{Im}}t\right)\exp\left(-\gamma\boldsymbol{\alpha}\bullet\mathbf{r}\right)\exp\left(\gamma\boldsymbol{\beta}\bullet\mathbf{r}\right)\exp i\left(\gamma\mathbf{k}_{\mathrm{Re}}\bullet\mathbf{r} - 2\pi\gamma f_{\mathrm{Re}}t\right) \tag{IV.F_5}$$

The parameter $\mathbf{k}_{\mathrm{Re}}$ is called the propagation wave vector, f_{Re} is the real frequency, $\boldsymbol{\alpha}$ is called the damping vector, whereas $\boldsymbol{\beta}$ is called the inhomogeneity vector. The parameter γ is included in (IV.F_1) and (IV.F_5) and determines the sign convention that is used. Most often it is set equal to '+1', though some researchers prefer to set it equal to '-1'. The need to distinguish between different values of γ will be clear later on, when we describe focusing of bounded beams. The parameter f_{Im} determines the transient feature of the wave under consideration and is called the source parameter. If γf_{Im} is positive, the wave is amplified in time, if it is negative, the wave diminishes in time.
If we take a closer look at (IV.F_5), then we see that only the last factor determines the phase of the complex harmonic inhomogeneous wave. All the other factors determine the amplitude. Nevertheless, (IV.F_5) must be a solution of the wave equation, because otherwise it cannot physically exist.

For visco-elastic media, the wave equation for waves described by (IV.F_1) results in the dispersion relation [11] , i.e.

$$\mathbf{k} \bullet \mathbf{k} = \left(\frac{2\pi f}{v_b} - i\alpha_{0,b} \right)^2 \qquad \text{(IV.F\_6)}$$

where $b=d$ for longitudinal waves or $b=s$ for shear waves. v_b is the phase velocity for harmonic homogeneous plane waves (i.e. having a real wave vector and real frequency) and $\alpha_{0,b}$ is the intrinsic damping coefficient. Contrary to a harmonic wave, whose amplitude is constant in time and contains only one single (real) frequency f_{Re}, a complex harmonic wave shows exponential amplitude decay in time and contains one single complex frequency $f = f_{\mathrm{Re}} + if_{\mathrm{Im}}$. The generation of complex harmonic waves has already been achieved experimentally [12] by application of a proper electrical input signal to a single transducer.
Lately, it has been shown [11,13] that, for complex harmonic waves, it is necessary to distinguish between phase velocity :

$$v_{ph} = \frac{2\pi f_{\mathrm{Re}}}{\mathbf{k}_{\mathrm{Re}} \bullet \mathbf{k}_{\mathrm{Re}}} \mathbf{k}_{\mathrm{Re}} \qquad \text{(IV.F\_7)}$$

and amplitude velocity

$$v_{amp} = \frac{2\pi f_{\mathrm{Im}}}{\mathbf{k}_{\mathrm{Im}} \bullet \mathbf{k}_{\mathrm{Im}}} \mathbf{k}_{\mathrm{Im}} \qquad \text{(IV.F\_8)}$$

Then, the velocity of energy propagation is given by

$$\mathbf{v}_E = \frac{\mathbf{S}_{\mathrm{Re}}}{\mathbf{S}_{\mathrm{Re}} \bullet \mathbf{S}_{ph}} \qquad \text{(IV.F\_9)}$$

with phase slowness vector $\mathbf{S}_{ph}$ given by [11]

$$\mathbf{S}_{ph} = \frac{\mathbf{k}_{\mathrm{Re}}}{2\pi f_{\mathrm{Re}}} \qquad \text{(IV.F\_10)}$$

and with $\mathbf{S}_{\mathrm{Re}}$ the real part of the slowness vector, defined as [11]

$$\mathbf{S}_{\mathrm{Re}} = \left(\mathbf{k}_{\mathrm{Im}} f_{\mathrm{Im}} + \mathbf{k}_{\mathrm{Re}} f_{\mathrm{Re}} \right) / 2\pi \left(f_{\mathrm{Re}}^2 + f_{\mathrm{Im}}^2 \right) \qquad \text{(IV.F\_11)}$$

the bounded beam description

A bounded sound beam is determined by a profile along the direction perpendicular to the sound propagation direction, and a propagation pattern determined by physical laws. In isotropic homogeneous media, the properties of a real 3D bounded beam is sufficiently represented by a 2D bounded beam. This approach has been followed in many papers before

[14-33]. Therefore we assume a bounded beam having a given profile along the x-direction and propagating in the z-direction. Furthermore, this assumption involves constant properties along the y-direction and results in relative numerical and representational ease.

The profile (along the x-direction) of a focused bounded harmonic beam $g\left(x,z,t,f_{\mathrm{Re}},f_{\mathrm{Im}}\right)$, i.e. Gaussian [34] if ξ=2, or square if ξ=8, can be described as

$$g\left(x,0,0,f_{\mathrm{Re}},f_{\mathrm{Im}}\right)=\exp\left(-x^{\xi}/W^{\xi}\right)\exp\left(-\gamma i x^{2}/\left(W^{2}W_{foc}^{2}\right)\right) \qquad \text{(IV.F\_12)}$$

W being the (Gaussian) beam width and W_{foc} being a focusing parameter. For unfocussed beams, $W_{foc}=\infty$, whereas for focused beams W_{foc} is typically smaller than or equal to unity. The profile (IV.F_12) shows amplitude as well as phase variation. The result can be seen in Fig. IV.F_1, for a Gaussian beam profile (ξ=2, $W=4mm$, $W_{foc}=0.9$) and a square profile (ξ=8, $W=4mm$, $W_{foc}=1$).

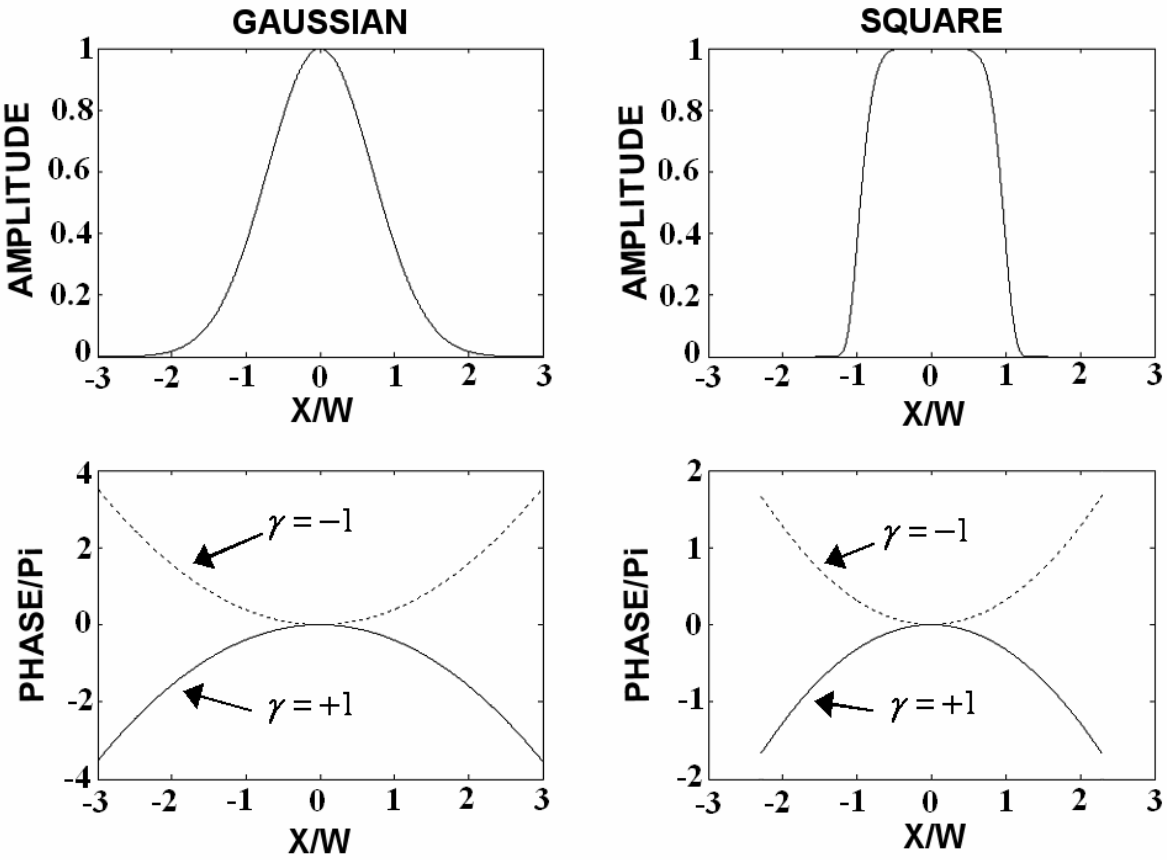

Fig IV.F_1: ***Graphical representation of a Gaussian and a square profile, in amplitude as wel as in phase.***

Here, it is necessary to distinguish between the positive sign choice ($\gamma=+1$) and the negative sign choice ($\gamma=-1$) in the building blocks (IV.F_1) and (IV.F_5) and the profile (IV.F_12). The reason is that focusing occurs when the center of the beam is behind in time, compared to the edges of the beam. This principle is incorporated by a positive or a negative phase shift of the center compared to the edges, depending on whether the material particle vibrations are

represented by a clockwise respectively counterclockwise rotating phase vector in the complex phase space.

For the moment, we deal with (complex) harmonic beams, which means that there is only one (complex) frequency involved. Later on, when pulsed beams are considered, more frequencies will be involved through a temporal Fourier transform.
Because a Gaussian function is not a solution of the wave equation, it is necessary to decompose the profile function (IV.F_12) into plane waves, i.e.

$$g\left(x,z,t,f_{\mathrm{Re}},f_{\mathrm{Im}}\right)=\left[\sum_{m=-M}^{M} A_m \exp i\gamma\left(k_x^m x+k_z^m z\right)\right]\exp\left(-2\pi\gamma\left(f_{\mathrm{Re}}+if_{\mathrm{Im}}\right)t\right) \qquad \text{(IV.F\_13)}$$

$$\text{with } k_x^m = mk_x^1 \in \mathbb{R}$$

using the spatial discrete Fourier transform for obtaining the Fourier coefficients A_m and the wave vector components k_x^m and applying the dispersion relation (IV.F_6) in order to obtain the remaining wave vector components k_z^m. The value of k_x^1 depends on the considered spatial interval and will be explained later.

Given the values k_x^m, obtained from the discrete Fourier transform, each wave vector component k_z^m determines the propagation direction of the plane wave denoted by the integer 'm' and is a function of the complex frequency *f* through the dispersion relation (IV.F_6). The effect of the phase profile of the bounded beam (see bottom of Fig. IV.F_1) on the propagation structure, also depends on the frequency. This effect is well known for the concept of real frequencies. If a focused transducer is driven at different real frequencies, the focal length changes because the propagation direction of the present Fourier components change as well. However, driving a given transducer is often only possible at frequencies near a given first harmonic or at odd multiples. Nevertheless, the effect of a change of the complex frequency, and in particular of the source parameter f_{Im}, on the focal length, is unknown. Because changing f_{Im} actually does not mean applying a different driving frequency but essentially means relaxation of the input signal. The influence on the focal length of the input signal relaxation is of practical interest. The next section describes the effect of the source parameter f_{Im} on the focal length of a complex harmonic Gaussian beam and also of a square beam.

COMPLEX HARMONIC FOCUSED BOUNDED BEAMS

From a mathematical point of view, harmonic bounded beams are easily described, because they can be decomposed into Fourier components having the same (complex) frequency, see equation (IV.F_13). The situation of pulsed bounded beams will be dealt with in the next paragraph. We take the example of focused bounded beams in water. The longitudinal wave velocity *v* is 1480m/s. For simplicity, except when explicitly stated, we only reckon with a lossless liquid, i.e. $\alpha_{0,d}=0$. The real frequency is 2 MHz. We define the focal length as the distance between the origin and the spot of highest amplitude within the focused beam. Because the profile of a bounded beam is by definition described by a function that differs from zero within a limited spatial interval, the Fast Fourier Transform (FFT) method is applicable. The spatial interval of the transform must be chosen large enough because the resulting representation is automatically periodic in space, with a period equal to

that spatial interval, and we want to avoid interference, along the propagation path, between neighboring beams in the mathematical representation. For that reason we have chosen a large spatial interval [*-20W, 20W*]. This spatial interval determines the lower bound of the considered nonzero values of $|k_x^m|$, i.e. $k_x^1 = 2\pi/40W$. The upper bound is determined by Nyquist-Shannon's theorem [35-37]. Very briefly, Nyquist-Shannon's theorem states that, when sampling at a given rate, the highest frequency that can appear in the sampled signal is half the sampling frequency. In the considered interval [*-20W, 20W*], we found for our purposes, that the beam profile could sufficiently well be represented by 2^{12} points, involving, when translating Nyquist-Shannon's theorem to spatial samples, an upper bound for k_x^m of $2\pi/40W \times 2^{11}$. We choose powers of 2, because the FFT is much faster for a number of samples being equal to a power of 2.

Focused Gaussian beams

First of all, a filled contour plot displays isolines calculated from the amplitude distribution and fills the areas between the isolines using constant colors. In Fig. IV.F_2, a filled contour plot of the amplitude pattern of the Gaussian bounded beam in water, originating at $(x,z)=(0,0)$, is shown, characterized by $W = 4mm$, $W_f = 0.9$, $f_{\mathrm{Re}} = 2MHz$ and $f_{\mathrm{Im}} = -1500Hz$.

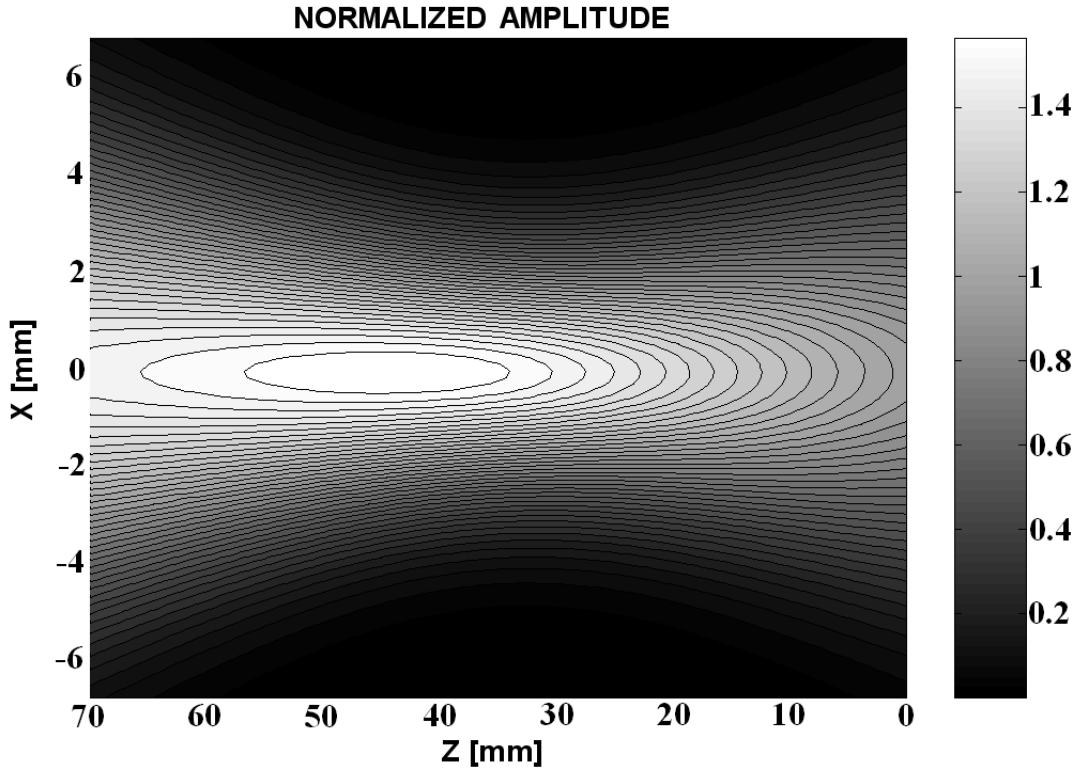

Fig IV.F_2: ***filled contour plot of the amplitude pattern of a complex harmonic bounded Gaussian beam in water, originating at*** $(x,z)=(0,0)$***, and characterized by*** $W = 4mm$, $W_f = 0.9$, $f_{\mathrm{Re}} = 2MHz$ ***and*** $f_{\mathrm{Im}} = -1500Hz$. ***The focal spot is situated at*** $z \approx 48mm$. ***In this figure, sound is propagating from right to left.***

It is seen that the focal spot is situated at $z \approx 48mm$. The pattern for the case of $f_{\mathrm{Im}} = 1500Hz$ is shown in Fig. IV.F_3, where it is seen that the focal spot is situated at $z \approx 20mm$. The difference in focal spot position is significant. In fact, in Fig. IV.F_4, the focal spot position is calculated as a function of f_{Im} and it is seen that the focal length changes when altering f_{Im}. The change is remarkable and spans over 4cm.

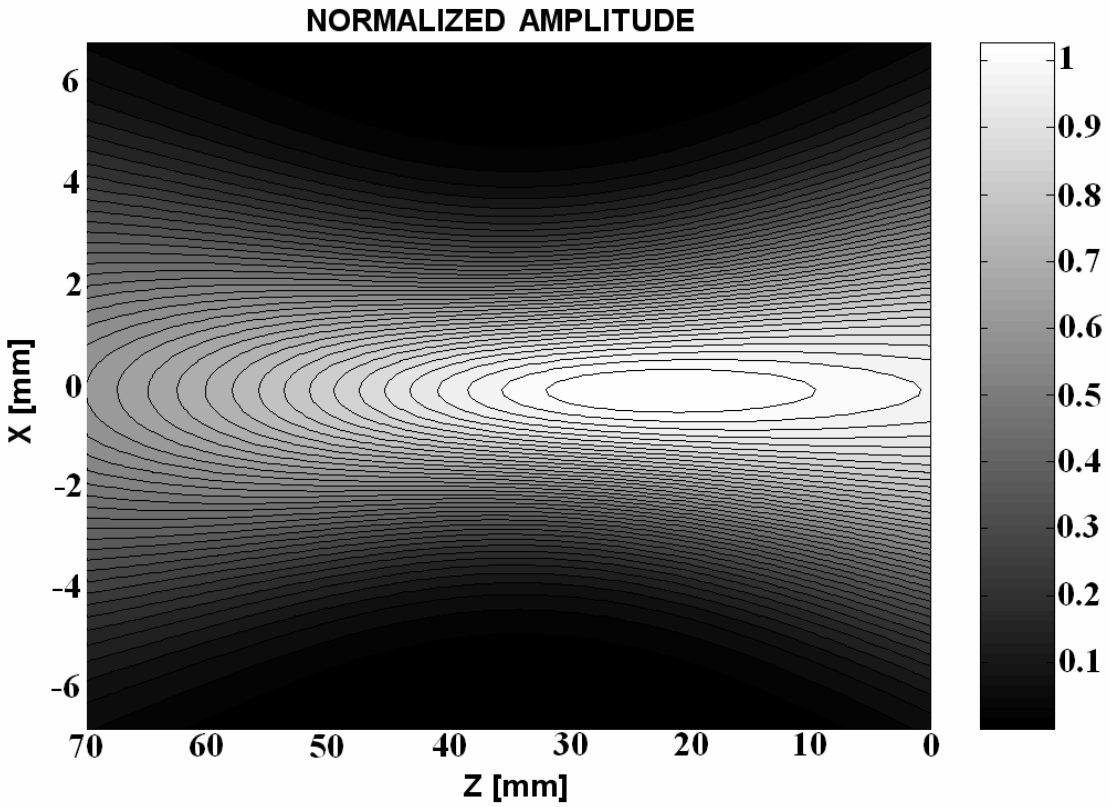

Fig IV.F_3: ***Similar to Fig. IV.F_2, except that*** $f_{\mathrm{Im}} = 1500Hz$ ***. Here, the focal spot is situated at*** $z \approx 20mm$ ***. In this figure, sound is propagating from right to left.***

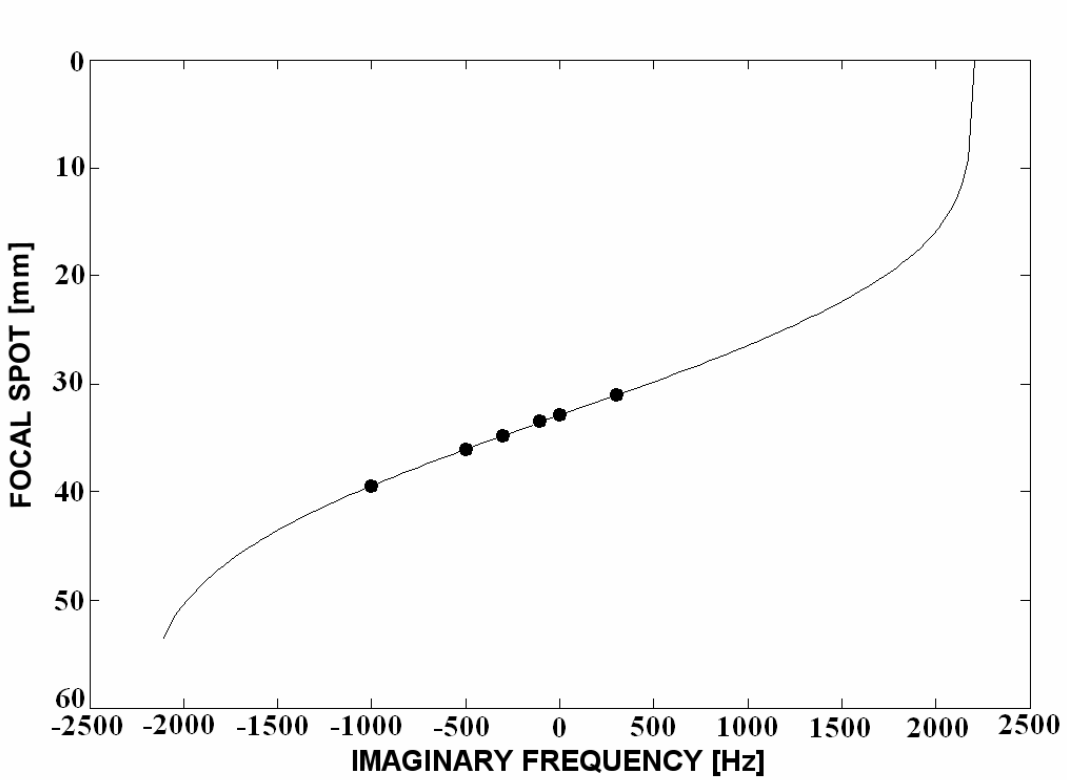

Fig IV.F_4: ***Focal length of a complex harmonic Gaussian beam in water as a function of*** f_{Im} ***and for*** $W = 4mm$, $W_f = 0.9$ ***and*** $f_{\mathrm{Re}} = 2MHz$

This is as good as what is to be expected from a phased array transducer of comparable size that is used in HIFU [38]. We have repeated the calculations for a nonzero damping $\alpha_{0,d} = p\alpha_w$, with $\alpha_w = 0.6\times10^{-15}$, the damping in physical water, and with $p \in \{0,5,..,50\}$. Even though damping influences the amplitude at the focal spot, no change was noticeable in the focal length. For this Gaussian beam, we have also calculated the focal length as a function of f_{Re} for $f_{\mathrm{Im}} = 0$ and we have found that beyond a threshold frequency of 0.5MHz, the distance D (in mm) of the focal spot is given by a linear function of f_{Re} (in MHz) described by

$$D = 16.77 f_{\mathrm{Re}} - 0.8534 \qquad \text{(IV.F\_14)}$$

The existence of a threshold frequency is due to a considerable near field for low frequencies. As stated earlier, changing f_{Re} is practically not always realistic, even though mathematically, a considerable focal shift is possible, as seen in equation (IV.F_14).

Focused Square beams

In order to show that the effect of the focal length change is not just a mathematical trick that is only valid for Gaussian beams, we have performed similar calculations as in the previous section, for a square profiled bounded beam, as depicted on the right side of Fig. IV.F_1.

In Fig. IV.F_5, the amplitude pattern of the square shaped bounded beam in water originating at (0,0) is shown, characterized by $W = 4mm$, $W_f = 1$, $f_{\mathrm{Re}} = 2MHz$ and $f_{\mathrm{Im}} = -100Hz$. The focal spot is situated at 23.4mm. In Fig. IV.F_6, the change of focal length as a function of f_{Im} is given. Even though the change in focal spot distance as a function of f_{Im} and the interval in which focalization occurs, is different from the case of a Gaussian beam (cfr Fig. IV.F_4), the effect of f_{Im} is again significant. It is therefore shown that f_{Im} does not solely influence the focal length of Gaussian beams, but also of other types.

COMPLEX PULSED FOCUSSED BOUNDED BEAMS

signal representation

The previous paragraph described focusing of complex harmonic beams. Such beams are mathematically very elegant, though they never exist in reality. Real signals are always limited in time and they can only be approximated by a (complex) harmonic beam within a restricted time interval that is smaller than the duration of the signal. A very short signal is generally called a pulse and is classically generated by means of a capacitor unloading its charge rapidly to a transducer. By complex pulsed signals, we actually mean a somewhat longer signal that approaches the complex harmonic signal structure within a limited temporal interval.

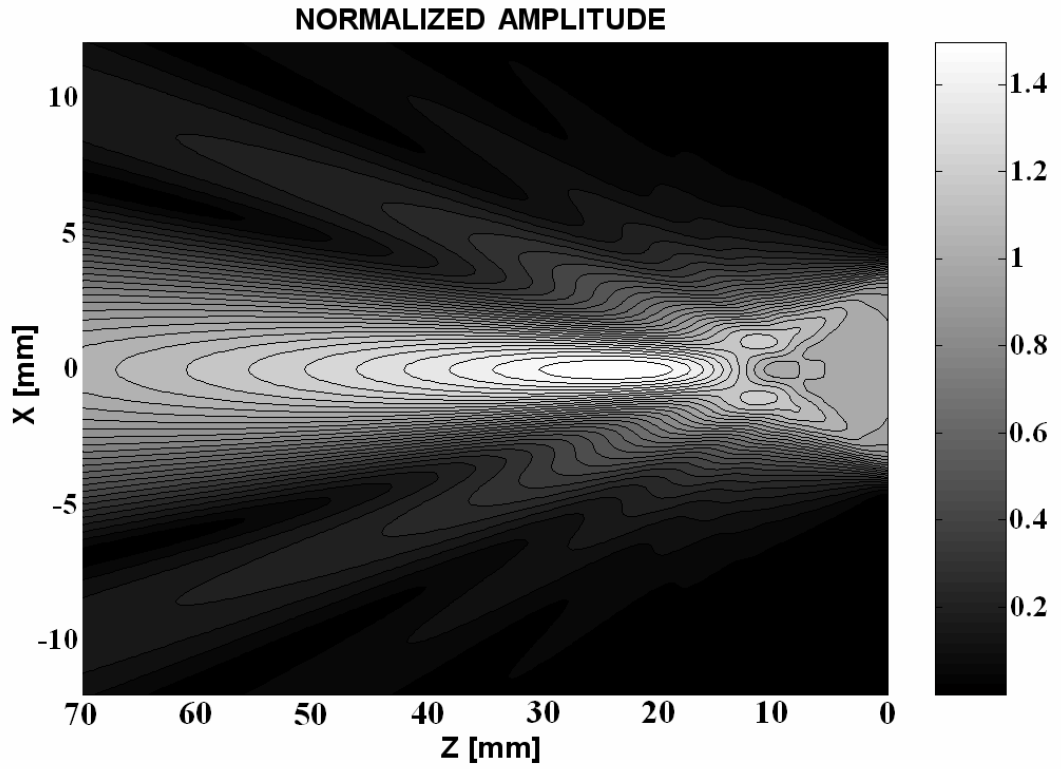

Fig IV.F_5: ***Amplitude propagation pattern of a complex harmonic bounded square shaped beam in water originating at (0,0), characterized by*** $W = 4mm$, $W_f = 1$, $f_{\mathrm{Re}} = 2MHz$ ***and*** $f_{\mathrm{Im}} = -100Hz$. ***The focal spot is situated at 23.4mm. In this figure, sound is propagating from right to left.***

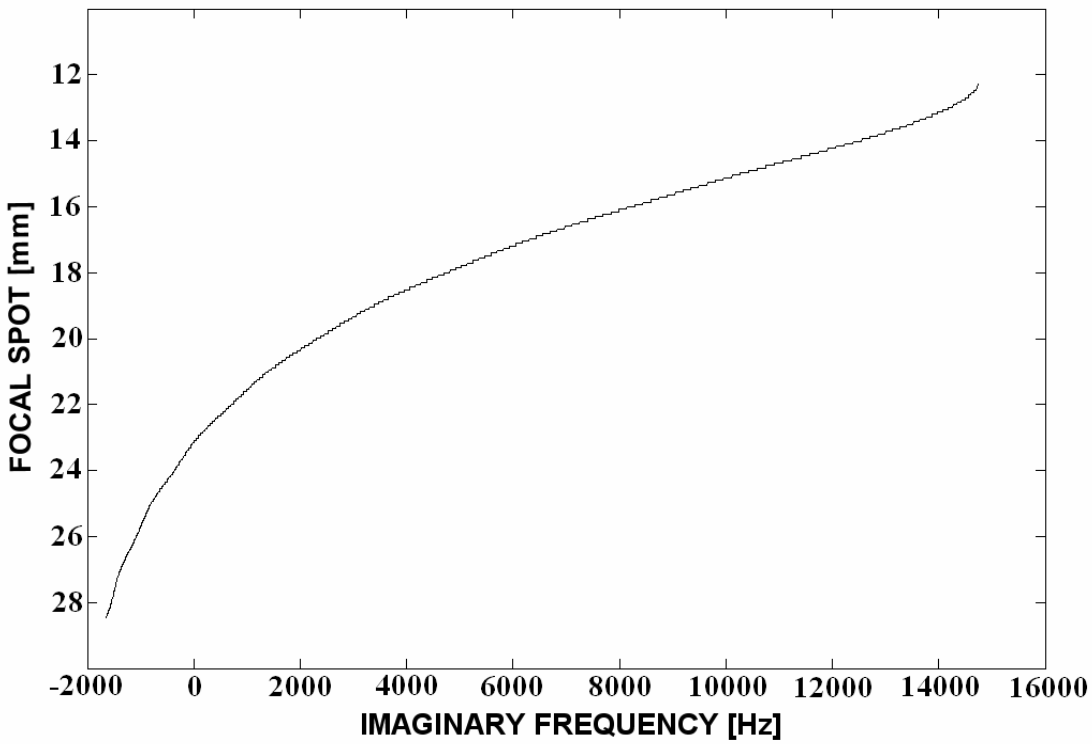

Fig IV.F_6: ***Focal length of a complex harmonic square shaped beam in water as a function of*** f_{Im} ***and for*** $W = 4mm$, $W_f = 1$ ***and*** $f_{\mathrm{Re}} = 2MHz$

Therefore, there is a complex harmonic regime, preceded by a start regime and followed by a stop regime. The start regime is characterized by a relatively rapid increase of the amplitude from zero to a start maximum, whereas the stop regime has the opposite effect. A realistic function that describes complex pulsed signals is given by

$$h(t) = \exp\left(-\left(\frac{t-1.08m}{m}\right)^{18}\right) \times \exp\left(-i\gamma 2\pi f\left(t-\frac{1}{4f_{\mathrm{Re}}}\right)\right) \qquad \text{(IV.F\_15)}$$

with $m = 0.455/R$ and with R the pulse rate and $1/R$ the duration of the complex harmonic pulse. The symbol γ is defined earlier and represents the sign choice of the wave description. Because the signal (IV.F_15) is not a solution of the wave equation, a decomposition into Fourier components is again mandatory. In this perspective, it is necessary to paraphrase Nyquist-Shannon's theorem [35-37] as "the sampling rate must be equal to, or greater than, twice the highest frequency component in the signal". We considered a pulse rate of $(2\ \mathrm{ms})^{-1}$, which means that the considered pulses cannot last longer than 2 ms. We have again used $f_{\mathrm{Re}} = 2MHz$ and several numerical simulations revealed that the frequency components of the considered time limited signals are always situated in the short vicinity of the central frequency of 2MHz. We therefore limit the upper frequency to $(2+\delta)MHz$. Nyquist-Shannon's theorem shows that the sampling rate must then be larger than $(4+2\delta)MHz$, or,

given the pulse rate of $(2\text{ms})^{-1}$, the number of samples must be $8000+4000\delta$. Several trial calculations showed that the frequency components, for the signals tackled in this section, are always negligible above a value determined by $\delta = 0.048$. This value results in a number of samples given by $2N=2^{13}$. Therefore, N is the number of Fourier components and the time limited signal $h(t)$ is represented by

$$h(t) = \sum_{n=0}^{N} B_n \exp\left(-i2\pi f_n t\right) \text{ with } f_n = nR \in \mathbb{R} \tag{IV.F_16}$$

A first example of a complex pulsed signal is given in Fig. IV.F_7, for $f = 2MHz - i1000Hz$ and a duration of 2 ms. The corresponding Fourier spectrum is also given in Fig. IV.F_7. It can be seen that the relevant frequency components are distributed in a very small range around the central frequency of 2MHz. We would like to point out that a signal that is described by a complex frequency, can always be represented by a summation of signals having a real frequency, if it is a time limited signal. Furthermore, the distribution of the frequency components around the real part of the considered complex frequency, depends on the imaginary part. The effect of changes in the focal length is then understood as follows: The presence of different frequency components in the Fourier spectrum causes a different propagation pattern, as described earlier. In Fig. IV.F_7, the amplitude of the considered complex pulse, shows a maximum at a certain position in time. The side left of the maximum is called the 'start regime', whereas the side right of the maximum is the 'complex harmonic regime'. The stop regime is situated near 2ms, and is invisible here, because the amplitude of the signal has dropped so much in the complex harmonic regime.

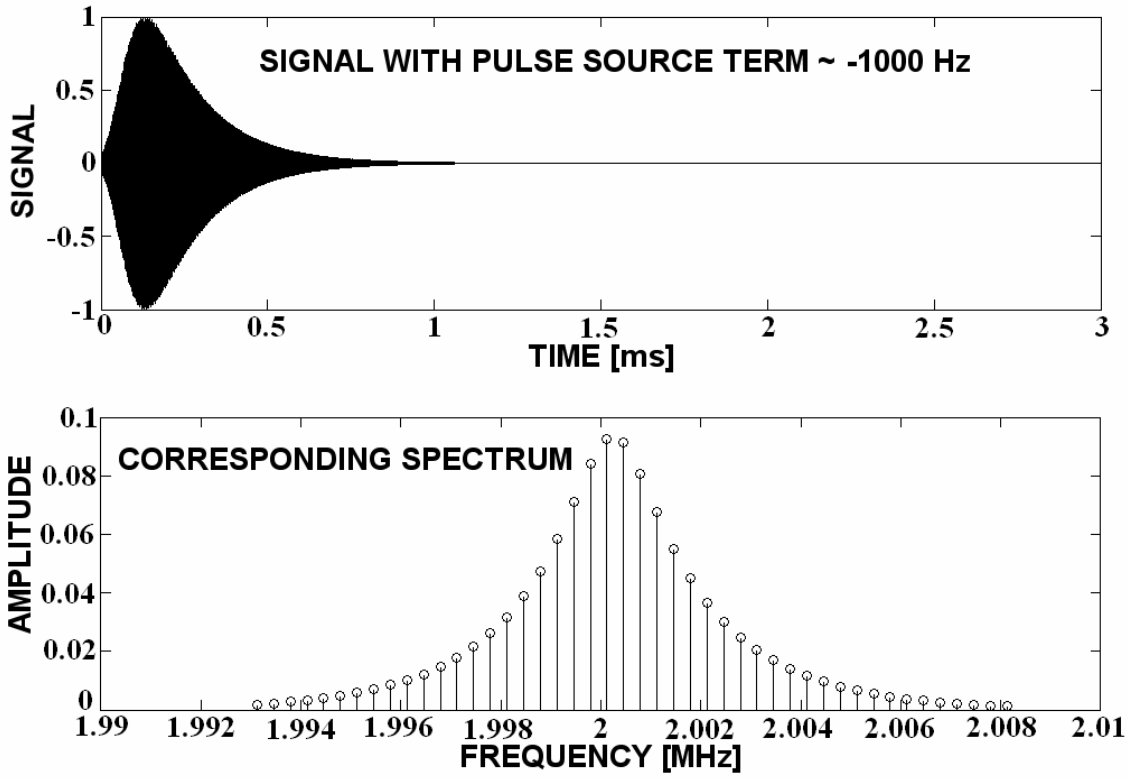

Fig. IV.F_7: ***Top: complex pulsed signal given by (IV.F_15), for $f = 2MHz - i1000Hz$ and a duration of 2 ms. Bottom: The corresponding Fourier spectrum.***

bounded beam representation

The description of a bounded beam that is generated by an input complex pulsed signal at the origin, is performed by a superposition of harmonic plane waves as follows:

$$g\left(x,z,t,f_{\mathrm{Re}},f_{\mathrm{Im}}\right)=\sum_{m=-M}^{M}\sum_{n=0}^{N}C_{m,n}\exp i\left(k_x^m x+k_z^{m,n}z-2\pi f_n t\right), \qquad k_x^m,f_n\in\mathbb{R} \tag{IV.F_17}$$

If $C_{m,n}$ is rewritten as

$$C_{m,n}=a_m b_n \tag{IV.F_18}$$

then, identification with the expression within the brackets of equation (IV.F_13) and with equation (IV.F_16), results in $a_m=A_m$, $b_m=B_m$ and $k_z^{m,n}$ is determined by k_x^m and f_n through the dispersion equation (IV.F_6). Actually, this means that the number of plane waves in the decomposition equation (IV.F_17) is the product of the number in equation (IV.F_13) for the spatial description and in equation (IV.F_16) for the temporal description, which means that we are dealing with 2^{24} samples, or in other words, more than 8 million building blocks that, when superposed, form the considered bounded, pulsed beams. This results in a relatively large computation time. It is clear that a similar description of 3D beams would require far too much calculation time, which is an additional reason why only 2D bounded beams are considered here.

Numerical implementation of equation (IV.F_17) enables us to visualize the beam pattern at any instant in time. Because this section primarily highlights focusing of bounded beams, we show, by means of a filled contour plot in Fig. IV.F_8, the amplitude profile along the Z-axis (x=0) for 125 instants of time from the beginning to the end of the signal of Fig. IV.F_7. It can be seen that, as soon as the complex harmonic regime is reached, a stable focusing effect occurs at a distance equal to the one for complex harmonic bounded beams characterized by the same beam width, focusing parameter and complex frequency. In fact, the focal length in the complex harmonic regime was calculated for different values of the imaginary frequency. The results are added to Fig. IV.F_4 as bold dots. The signal, corresponding to an imaginary frequency of 300Hz, is given in Fig. IV.F_9. Its spatial structure along the z-axis for each instant of time is given in Fig. IV.F_10. Again, in the complex harmonic regime, a focal spot is visible at the position corresponding to the case of a complex harmonic beam. The focus disappears in the stop regime. The stop regime is significant here, because, contrary to the signal in Figs IV.F_7-8, this signal increases its amplitude before reaching the stop regime.

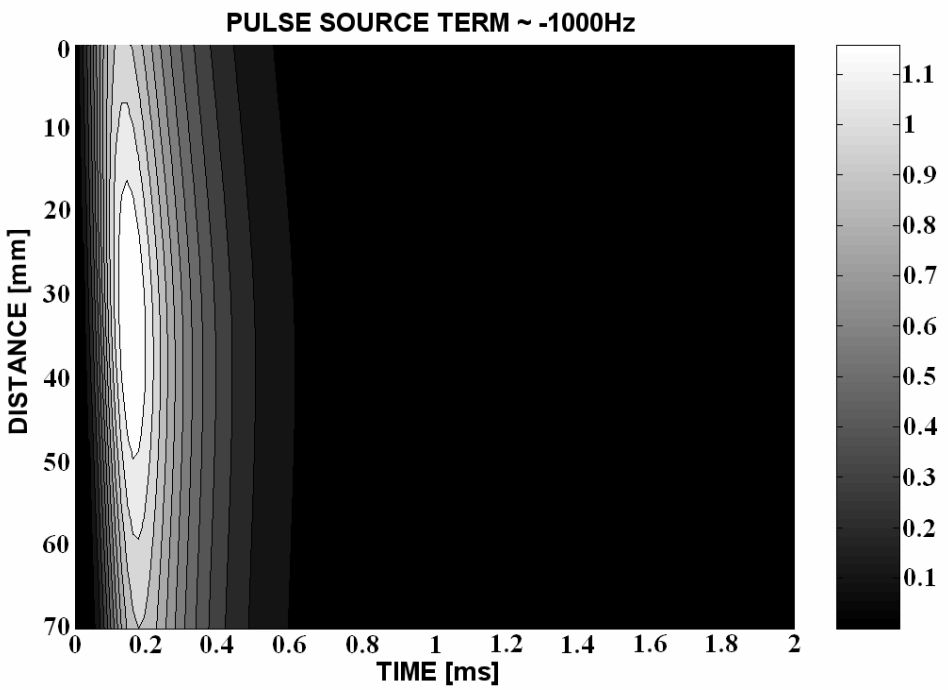

Fig. IV.F_8: ***Amplitude profile along the Z-axis (x=0) for 125 instants of time from the beginning to the end of the signal of Fig. IV.F_7. In the complex harmonic regime, the presence of a focal spot is clear and the focal length corresponds to that of the corresponding complex harmonic bounded beam.***

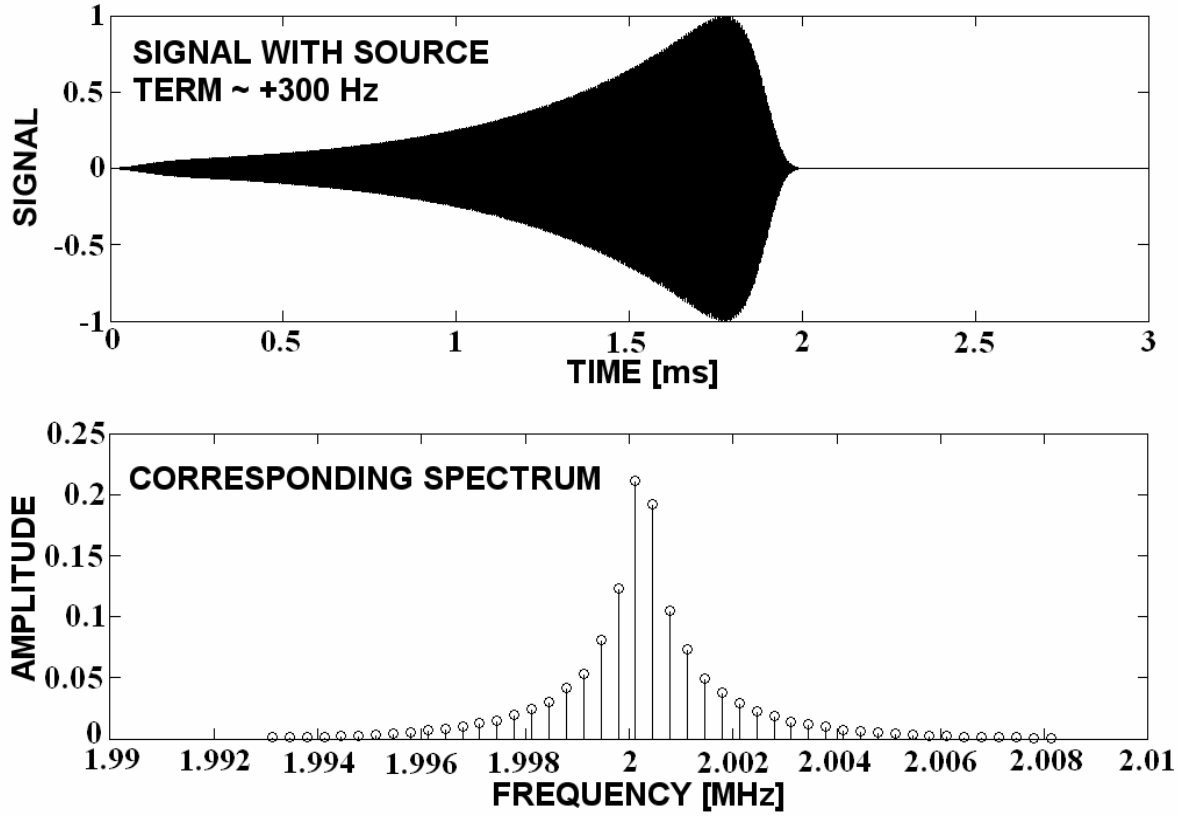

Fig. IV.F_9: ***Same as* Fig. IV.F_*7, except that the the frequency is now*** $f = 2MHz + i300Hz$ ***. This corresponds to a complex pulse having increasing amplitude.***

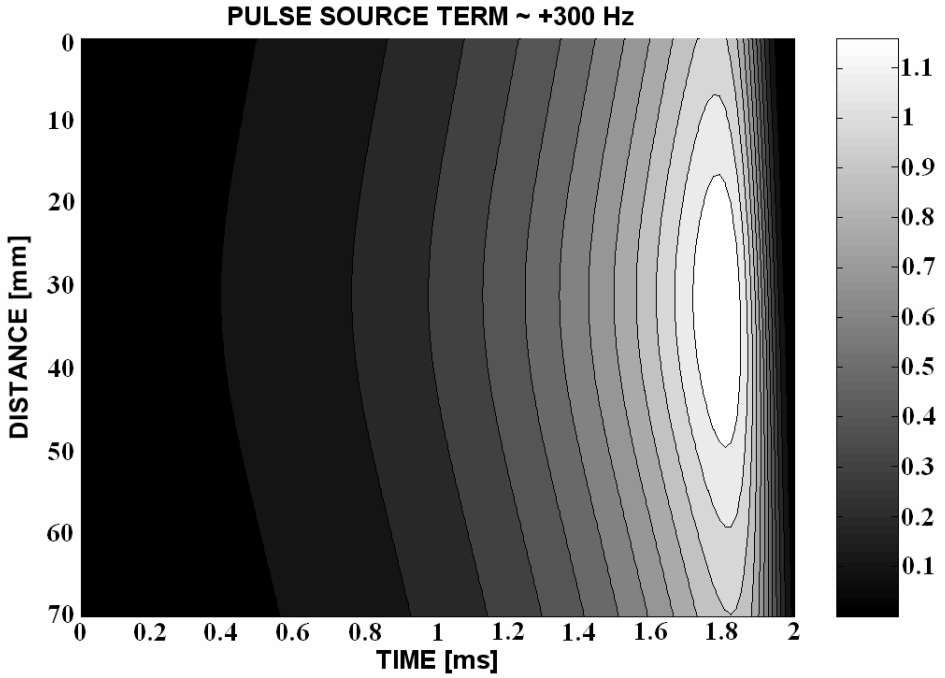

Fig. IV.F_10: ***Same as Fig. IV.F_8, except that the the frequency is now*** $f = 2MHz + i300Hz$ ***. This corresponds to a complex pulse having increasing amplitude.***

It is also clear that the amplitude at the focal spot, changes in time due to the shape of the complex pulse. In Fig. IV.F_11, the amplitude at the focal spot is given for each instant of time and for 6 cases that correspond to the bold dots of Fig. IV.F_4. Furthermore, the position of the focal spot is also a function of time, especially in the start and stop regimes. This is seen in Fig. IV.F_12, where the line code is the same as in Fig. IV.F_11. It is seen that the focal spot position is constant in the complex harmonic regime, and changes in the other regimes and also that the amplitude at the focal spot follows the amplitude of the input signal.

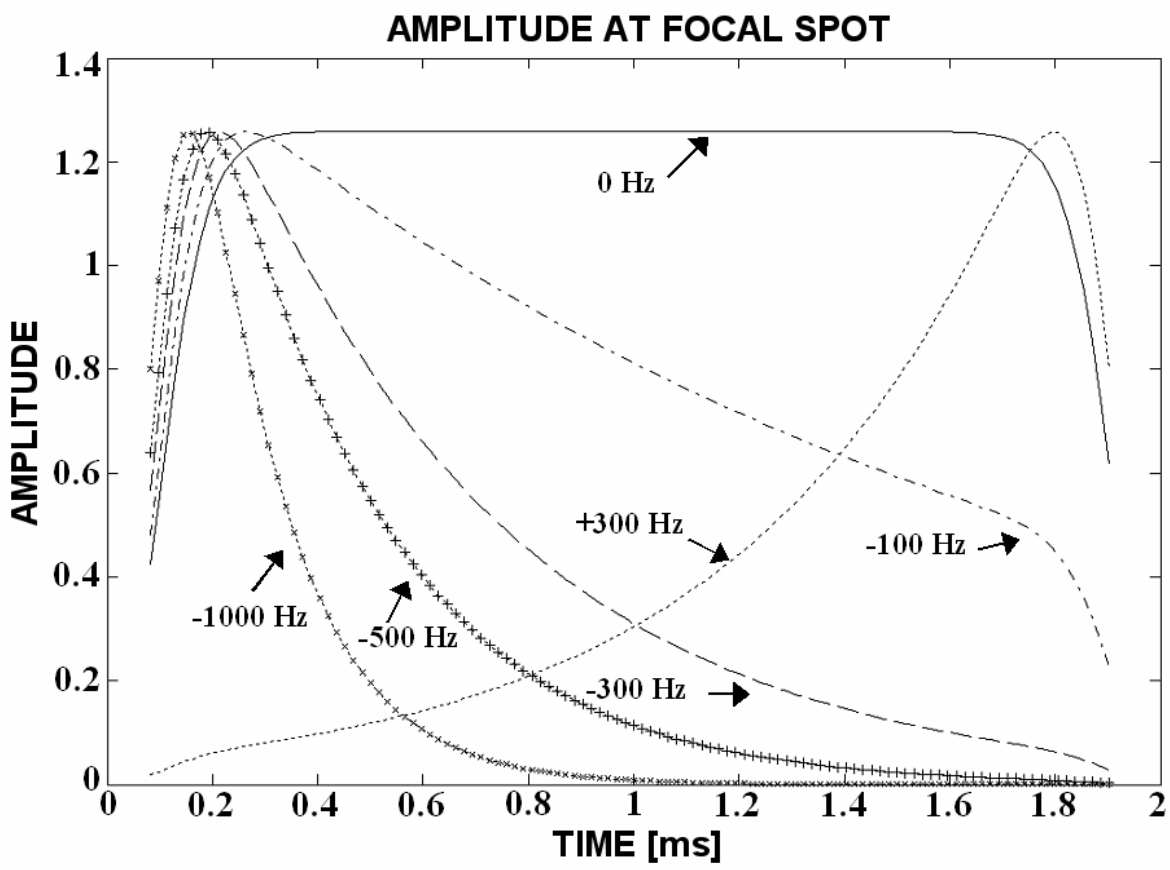

Fig. IV.F_11: ***The amplitude at the focal spot for each instant of time and for 6 cases that correspond to the bold dots of Fig. IV.F_4.***

An important question to be asked is where such a temporal and spatially limited beam produces the largest power. Of course, it must be on the focal spot, but because the position of the focal spot and the accompanied amplitude both change in time, it is not evident to give an immediate answer. For that reason, we have calculated the following function:

$$Q\left(z, f_{\mathrm{Re}}, f_{\mathrm{Im}}\right) = \int_{0}^{1/R} \frac{A\left(z,t, f_{\mathrm{Re}}, f_{\mathrm{Im}}\right)}{P\left(f_{\mathrm{Re}}, f_{\mathrm{Im}}\right)} \times \frac{P\left(f_{\mathrm{Re}}, 0\right)}{\mathrm{H}\left(f_{\mathrm{Re}}\right)} dt \qquad \text{(IV.F\_19)}$$

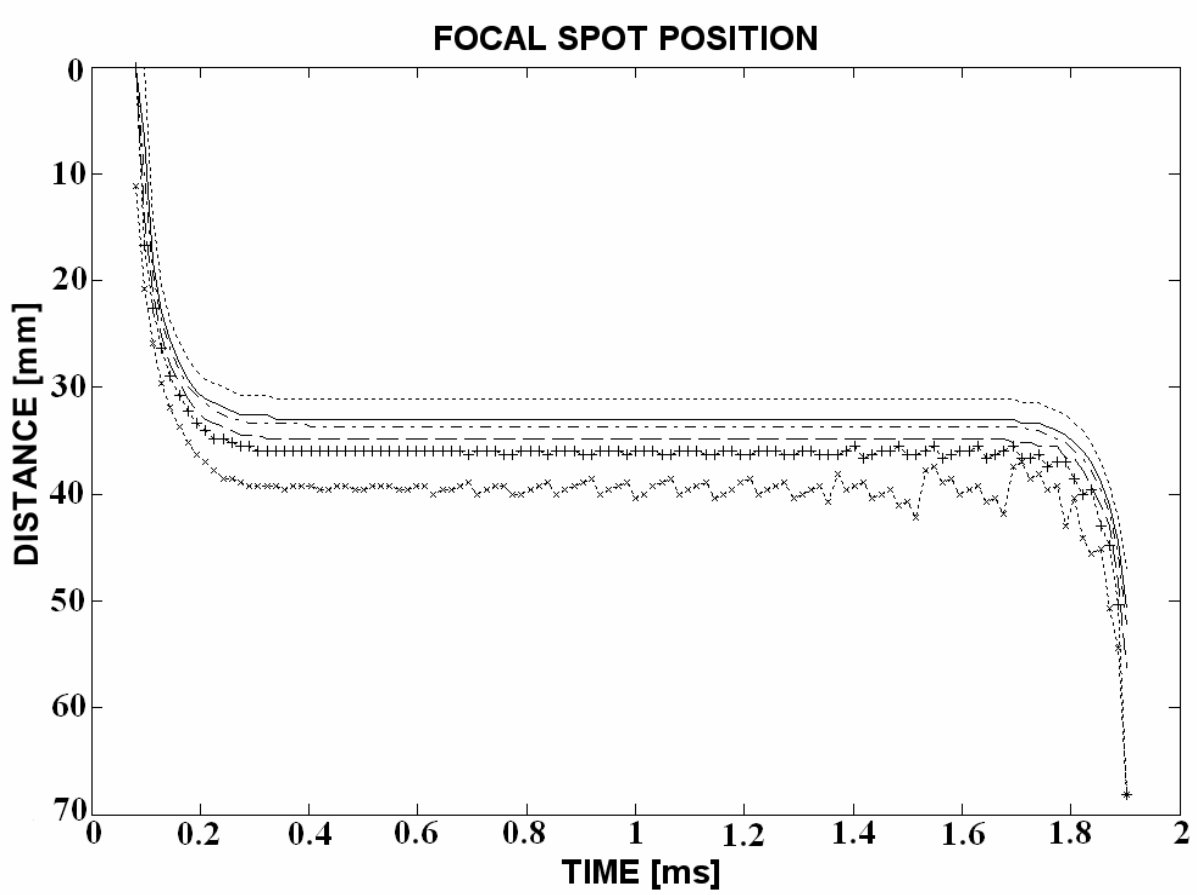

Fig. IV.F_12: ***The position of the focal spot as a function of time, the line code is the same as in Fig. IV.F_11.***

with

$$P\left(f_{\mathrm{Re}}, f_{\mathrm{Im}}\right) = \int_{0}^{1/R} \left| g\left(0,0,t, f_{\mathrm{Re}}, f_{\mathrm{Im}}\right)\right| dt \tag{IV.F_20}$$

being the amplitude of the input signal, integrated over the duration of the complex pulse and characterized by a frequency $f = f_{\mathrm{Re}} + if_{\mathrm{Im}}$. Furthermore,

$$H\left(f_{\mathrm{Re}}\right) = Max\left(\int_{0}^{1/R} A\left(z,t, f_{\mathrm{Re}}, 0\right) dt\right) \tag{IV.F_21}$$

and

$$A\left(z,t, f_{\mathrm{Re}}, f_{\mathrm{Im}}\right) = \left| g\left(0,z,t, f_{\mathrm{Re}}, f_{\mathrm{Im}}\right)\right|_{FocalSpot} \tag{IV.F_22}$$

The function of equation (IV.F_19) is a measure of the total energy received during the duration of the pulse on a certain spot along the z-axis, and normalized so that the total power of the input signals under consideration is the same for each of those signals. Fig. IV.F_13 shows the result for 190 discrete positions along the z-axis and for incorporation of 125 instants of time. Only the results in between 30 mm and 40 mm are given, because the values

were negligible elsewhere. It is seen that, even though the focal spot changes its position in time, and even though the amplitude at the focal spot changes in time, overall, the largest amount of energy is delivered on the constant focal spot in the complex harmonic regime. This is really important, especially when not the peak value of the amplitude at the focal spot is important, but the overall energy delivery, such as in the use of the local hyperthermia technique as mentioned in the introduction.

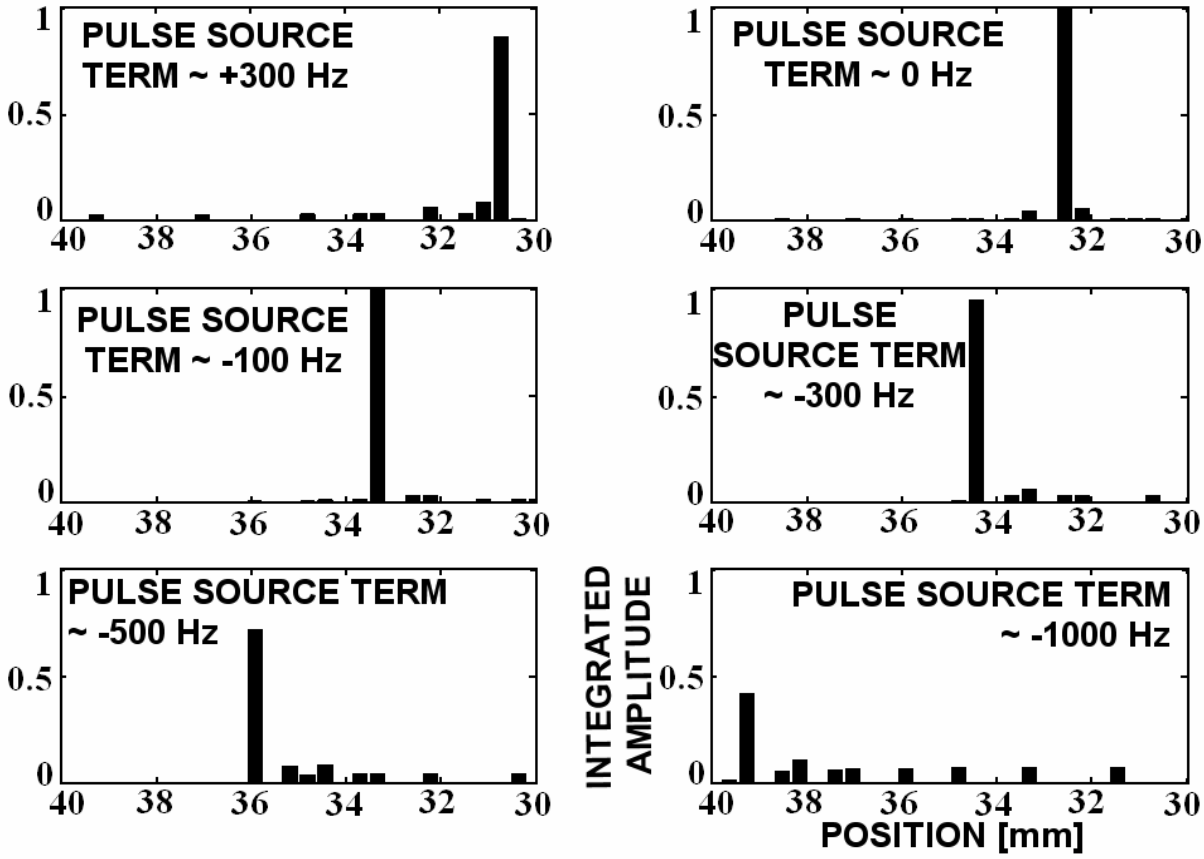

Fig. IV.F_13: ***A measure of the total deliverd power at the focal spot within one complex pulse, as a function of the distance along the Z-axis, calculated by means of (IV.F_19). It is clear that the maximum power release happens at the focal length corresponding to the complex harmonic regime.***

CONCLUSIONS

We have described the influence of the frequency on the focal length of a bounded beam. The effect of the real frequency is well known and has only been given short consideration. More attention was drawn to the effect of the imaginary part of the frequency. This imaginary part is responsible for an exponential change of the amplitude in time and different imaginary frequencies result in different focal lengths. We have shown that this effect happens for Gaussian beams as well as for square beams. We have also shown that the value of the focal length does not depend on the intrinsic damping parameter.

Because real signals are always limited in time, we have also studied complex pulses and have shown that the effect of the imaginary part on the focal length of complex pulsed bounded beams is essentially the same as for complex harmonic bounded beams, except in the start and stop regimes. Even though we only considered a linear

regime in an isotropic and homogeneous medium like water, it is likely that similar effects will occur in more complicated media like human tissue [39], and that for many applications, especially in the medical field, the cost of equipment may be reduced if for some treatments, expensive phased arrays can be replaced by much cheaper single transducers.

REFERENCES

[1] Zhang Q. L., Levin V. M., Zhang J., Zhang H. Z., He J. S., Zhang S. G., Liu S. P., "Preliminary study on morphology of in-situ hybrid composites by using acoustic microscopy", Progress Nat. Sc. 11, S160-S164, 2001

[2] Fei D., Chimenti D.E., Teles S. V. , "Material property estimation in thin plates using focused, synthetic-aperture acoustic beams", J. Acoust. Soc. Am 113 (5), 2599-2610, 2003

[3] Chimenti D. E., Fei D., "Scattering coefficient reconstruction in plates using focused acoustic beams", Int. J. Sol. Struct. 39 (21-22), 5495-5513, 2002

[4] Kazushi Yamanaka, "Surface acoustic wave measurements using an impulsive converging beam", J. Appl. Phys. 54(8), 4323-4329, 1983

[5] Chan AH, Huynh G, Paun M, Fujimoto VY, Moore DE, and Vaezy S, "Focused Ultrasound Therapy Of The Uterus: A Device For Potential Treatment Of Leiomyoma," in Therapeutic Ultrasound, Proceedings of the 2nd International Symposium, MA Andrew, LA Crum, S Vaezy, eds (American Institute of Physics Press), pp. 391-399, 2003.

[6] George W. Keilman, Peter J. Kaczkowski, "High-intensity focused ultrasound transducer design for surgical and hemostatic applications", J. Acoust. Soc. Am. 103(5), 2831, 1998

[7] Sandra L. Poliachik, Pierre D. Mourad, and Lawrence A. Crum , Wayne L. Chandler "Effect of high-intensity focused ultrasound on platelet activation, aggregation, and adhesion", J. Acoust. Soc. Am. 107(5), 2787, 2000

[8] Lawrence A. Crum, Michael Bailey, Kirk Beach, Stephen Carter, Wayne Chandler, Peter Kaczkowski, Roy Martin, Pierre Mourad, Sandra Poliachik, and Shahram Vaezy , George Keilman, Thomas L Anderson, Lee Weng, and David M. Perozek, "Acoustic hemostasis", J. Acoust. Soc. Am. 106(4), 2228, 1999

[9] Hwang JH, Vaezy S, Martin R, Cho, M-Y, Noble ML, Crum LA, and Kimmey M, "High-intensity focused US: a Potential new treatment for GI bleeding," Gastrointestinal Endoscopy, 58 (1), 111-115, 2003.

[10] Vaezy S, Cornejo C, Martin R, and Crum L, "Hemostasis and sealing air leaks in lung using HIFU," in Therapeutic Ultrasound, Proceedings of the 2nd International Symposium, MA Andrew, LA Crum and S Vaezy, eds (American Institute of Physics Press), pp. 163-167, 2003.

[11] Nico F. Declercq, Rudy Briers, Joris Degrieck, Oswald Leroy, "The History and Properties of Ultrasonic Inhomogeneous Waves" accepted for publication by IEEE-UFFC, intended for publication in the special 50th anniversary issue in the summer of 2004.

[12] M. Deschamps, O. Poncelet, "Transient Lamb waves: Comparison between theory and experiment", J. Acoust. Soc. Am. 107(6), 3120-3129, 2000

[13] O. Poncelet, M. Deschamps, "Lamb waves generated by complex harmonic inhomogeneous plane waves", J. Acoust. Soc. Am., 102(1), 292-300, 1997 - Olivier Poncelet, "Ondes planes hétérogènes a fréquence complexe : modes propres de plaques immergées.", PhD thesis University of Bordeaux 1, 1996.

[14] J. M. Claeys, O. Leroy, "Reflection and transmission of bounded sound beams on half-spaces and through plates", J. Acoust. Soc. Am. 72(2), 585-590, 1982

[15] Tribikram Kundu, "On the nonspecular reflection of bounded acoustic beams", J. Acoust. Soc. Am. 83(1), 18-24, 1988

[16] Nico F. Declercq, Joris Degrieck, Oswald Leroy, "Frequency bandgap for Rayleigh waves on coated surfaces", Appl. Phys. Let. 85(1), 148-150, 2004.

[17] Nico F. Declercq, Joris Degrieck, Oswald Leroy, "The Laplace transform to describe bounded inhomogeneous waves", J. Acoust. Soc. Am. 116(1), 51-60, 2004.

[18] Nico F. Declercq, Joris Degrieck, Oswald Leroy, "The Principle of a Chopped Series Equilibrium to Determine the Expansion Coefficients in the Inhomogeneous Waves Decomposition of a Bounded Beam", Acta Acustica United with Acustica 89, 1038-1040, 2003.

[19] Nico F. Declercq, Joris Degrieck, Rudy Briers, Oswald Leroy, "Theoretical verification of the backward displacement of waves reflected from an interface having superimposed periodicity", Appl. Phys. Let. 82(15), 2533-2535, 2003.

[20] Nico F. Declercq, Rudy Briers, Oswald Leroy, " The use of polarized bounded beams to determine the groove direction of a surface corrugation at normal incidence, the generation of surface waves and the insonification at Bragg-angles", Ultrasonics 40/1-8 pp. 345-348, 2002
[21] Nico F. Declercq, Joris Degrieck, Oswald Leroy, "A useful analytical description of the coefficients in an Inhomogeneous Wave Decomposition of a symmetrical bounded beam", accepted for publication in Ultrasonics
[22] Nico F. Declercq, Filip Van den Abeele, Joris Degrieck, Oswald Leroy, "The Schoch effect to distinguish between different liquids in closed containers", accepted for publication in IEEE Transactions on Ultrasonics, Ferroelectrics, and Frequency Control
[23] Nico F. Declercq, Oswald Leroy, Joris Degrieck, Jeroen Vandeputte, "The interaction of inhomogeneous waves and Gaussian beams with mud in between a hard solid and an ideal liquid", accepted for publication in Acta Acustica United with Acustica
[24] John Pott, John G. Harris, "Scattering of an acoustic Gaussian beam from a fluid-solid interface", J. Acoust. Soc. Am. 76(6), 1829-1838, 1984
[25] Abdellatif Bey Temsamani, Steve Vandenplas, Leo Van Biesen, "Experimental investigation of bounded beam reflection from plane interfaces in the vicinity of leaky waves angles", Ultrasonics 38, 749-753, 2000
[26] Tran D. K. Ngoc, Walter G. Mayer, "Numerical integration method for reflected beam profiles near Rayleigh angle", J. Acoust. Soc. Am. 67(4), 1149-1152, 1980
[27] M. A. Breazeale, Laszlo Adler, Larry Flax, "Reflection of a Gaussian ultrasonic beam from a liquid-solid interface", J. Acoust. Soc. Am. 56(3), 866-872, 1974
[28] Peter B. Nagy, Kangra Cho, Laszlo Adler, D. E. Chimenti, "Focal shift of convergent ultrasonic beams reflected from a liquid-solid interface", J. Acoust. Soc. Am. 81(4), 835-839, 1987
[29] Theodore E. Matikas, Martine Rousseau, Philippe Gatignol, "Theoretical analysis for the reflection of a focused ultrasonic beam from a fluid-solid interface", J. Acoust. Soc. Am. 93(3), 1407-1416, 1993
[30] Leslie E. Pitts, Thomas J. Plona, Walter G. Mayer, "Theory of Nonspecular Reflection Effects for an Ultrasonic Beam Incident on a Solid Plate in a Liquid", IEEE Trans. on Sonics and Ultrasonics, SU-24(2), 101-109, 1977
[31] K. W. Ng, T. D. K. Ngoc, J. A. McClure, W. G. Mayer, "Nonspecular Transmission Effects for Ultrasonic Beams Incident on a Solid Plate in a Liquid", Acustica 48, 168-173, 1981
[32] Andrew N. Norris, "Back reflection of ultrasonic waves from a liquid-solid interface", J. Acoust. Soc. Am. 73(2), 427-434, 1983
[33] Ralph A. Stephen, "Optimum and standard beam widths for numerical modeling of interface scattering problems", J. Acoust. Soc. Am. 107(3), 1095-1102, 2000
[34] J. Vandeputte, O. Leroy, R. Briers, G. Shkerdin, "Extension of the mode method for viscoelastic media and focused ultrasonic beams", J. Acoust. Soc. Am. 108(4), 1614-1621, 2000
[35] Leon W. Couch II, *Digital and analog communication systems – fifth edition*, Prentice Hall, New Jersey, 1997
[36] H. Nyquist, "Certain topics in telegraph transmission theory," Trans. AIEE, vol. 47, pp. 617-644, Apr. 1928.
[37] A. E. Shannon, "Communication in the presence of noise," Proc. Institute of Radio Engineers, vol. 37, no.1, pp. 10-21, Jan. 1949.
[38] S. Vaezy, B. Huguenin, G. Fleury, J. R. Flexman, R.Held, "A transvaginal image-guided high intensity ultrasound array", paper 2B-3, proceedings of 2003 IEEE International Symposium, Honolulu, Hawaii, October 5-8, 2003
[39] M. Tabei, T.D. Mast, R.C. Waag, "Simulation of ultrasonic focus aberration and correction through human tissue", J. Acoust. Soc. Am. 113 (2), 1166-1176, 2003

IV.G On the existence and the excitation of a new kind of leaky surface waves

The inhomogeneous wave theory has proved to be well suited to predict and to describe properties and the excitation of surface waves such as the leaky Rayleigh wave. The theory is applied here for a water/brass interface and shows that a new kind of leaky surface waves can exist and can be excited by impinging sound. Properties such as polarization, propagation and amplitude distribution are described and systematically compared with features of leaky Rayleigh waves.

INTRODUCTION

A surface wave can be defined as a wave whos spatial amplitude distribution contains a lobe that travels along the interface. For Scholte – Stoneley waves, the 'lobe' is simply an exponentially decreasing function -in the solid and in the liquid- of the distance from the interface and the 'lobe' does not leak, i.e. its amplitude remains along its travel path. For leaky Rayleigh waves [1-4], the 'lobe' is a small region in the solid, close to the surface, which emits its energy into the liquid (it 'leaks'), therefore having a decreasing amplitude as a function of the traveled distance. The new kind of surface waves that is discussed here, contains a 'lobe' in the solid close to the interface, turning into a bulk wave at larger distances due to energy emission into the solid and it also leaks energy into the liquid.

As far as we know, there is only one paper that discusses a similar phenomenon at a solid/vacuum interface, i.e. a paper by Nesvijski [5]. Nesvijski [5] has discovered that the Rayleigh equation shows some poles in addition to the well known Rayleigh poles that correspond to situations under which waves may exist that show a lobe near the surface and turn into a bulk wave at larger distances. Nesvijski [5] also discusses some important applications of this phenomena. However, since it is usual in non destructive testing to couple a transducer to a solid by means of a liquid, the impact of such a solid/vacuum special surface wave in most of the applications might not be that considerable. Just as the classical Rayleigh wave has become really important in non destructive testing when its leaky counterpart [1-3,6] was discovered and applied [7-13], the new kind of surface wave of Nesvijski [5] might only become significant due to the existence of its leaky counterpart which is discussed here. The generation of such new kind of leaky surface waves must be taken into account when new models are created or experiments are performed to study the generation of surface waves by impinging sound [14-17] or even by laser light [18-19].

We have met the new kind of surface waves not when considering poles of the Rayleigh equation or the Scholte-Stoneley equation [20-21], but when calculating the reflection coefficient as a function of the angle of incidence and the inhomogeneity of impinging inhomogeneous waves. The reflection coefficient for a brass/water interface shows a peak in addition to the well known leaky Rayleigh wave peak. We have compared its location with those of the poles and branch cuts that are discussed by Pott and Harris [15-16]. They distinguish between the four surface wave poles (two for leaky Rayleigh waves and two for Scholte – Stoneley waves) and four 'branch cuts', that give rise to lateral waves (two for shear lateral waves and two for longitudinal lateral waves). The latter can be found experimentally in the article of Couchman and Bell [22]. The new kind of surface waves that we have discovered, is different from phenomena resulting form these eight critical points.

In what follows, we fully apply the properties of inhomogeneous waves, which can be found in numerous articles [23-29].

In our calculations, we apply the Deschamps' principles [30-31] for the appropriate choice of the sign of scattered wave vectors and we translate them into easy to apply rules. Furthermore, we show numerical results and illustrate some calculated properties of the new kind of leaky surface waves and compare them to the ones of leaky Rayleigh waves.

THE SCATTERING OF INHOMOGENEOUS WAVES

The wave potentials, the application of the generalized Snell's law and rules translating Deschamps' principles

The generalized Snell's law involves continuity of the complex valued k_x. Hence, the potential for the incident wave is described by

$$\varphi^{inc} = \exp i\left(k_x x + k_z^{inc} z\right) \tag{IV.G_1}$$

and the reflected, the transmitted longitudinal and the transmitted shear respectively by

$$\varphi^{r} = RD \exp i\left(k_x x + k_z^{r} z\right) \tag{IV.G_2}$$

$$\varphi^{t} = TD \exp i\left(k_x x + k_z^{td} z\right) \tag{IV.G_3}$$

$$\boldsymbol{\psi}^{t} = TS \exp i\left(k_x x + k_z^{ts} z\right)\mathbf{e}_y \tag{IV.G_4}$$

with

$$\mathbf{k}^{\xi} = k_x \mathbf{e}_x + k_z^{\xi}\mathbf{e}_z = \mathbf{l}^{\xi} + i\boldsymbol{\alpha}^{\xi} - i\boldsymbol{\beta}^{\alpha} \tag{IV.G_5}$$

with $\xi = inc, r, td, ts$, and with $\mathbf{l}^{\xi}$ being the real part and $\boldsymbol{\alpha}^{\xi} - \boldsymbol{\beta}^{\xi}$ the imaginary part of the complex wave vector $\mathbf{k}^{\xi}$. $\boldsymbol{\beta}^{\xi}$ is called the inhomogeneity vector, while $\boldsymbol{\alpha}^{\xi}$ is called the damping vector and $\mathbf{l}^{\xi} \perp \boldsymbol{\beta}^{\xi}$ while $\mathbf{l}^{\xi} \parallel \boldsymbol{\alpha}^{\xi}$.

In Fig. IV.G_1, we have depicted $\mathbf{l}^{inc}$ and $\boldsymbol{\beta}^{inc}$. Furthermore, we get

$$\begin{bmatrix} k_x \\ k_z^{inc} \end{bmatrix} = \begin{bmatrix} \cos\theta^{inc} & \sin\theta^{inc} \\ -\sin\theta^{inc} & \cos\theta^{inc} \end{bmatrix} \begin{bmatrix} -i\beta^{inc} \\ \sqrt{\left(\omega/v + i\alpha_0\right)^2 - \left(\beta^{inc}\right)^2} \end{bmatrix} \tag{IV.G_6}$$

β^{inc} is the inhomogeneity of the incident inhomogeneous wave, θ^{inc} is the angle of incidence, α_0, α_{0d} and α_{0s} are the intrinsic damping coefficients for the liquid respectively for the longitudinal waves in the solid and the shear waves in the solid.

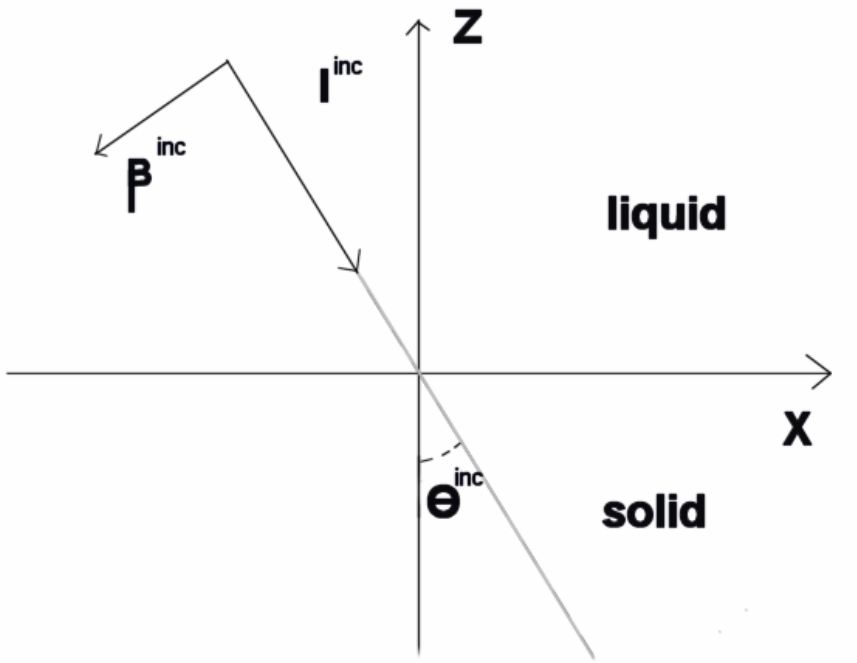

Fig IV.G_1: ***The real part*** $\mathbf{l}^{inc}$ ***of a complex incident wave vector*** $\mathbf{k}^{inc}$ ***together with the inhomogeneity*** $\boldsymbol{\beta}^{inc}$

From the dispersion relation for inhomogeneous waves [23-29], we know that

$$k_z^r = \pm\sqrt{\left(\omega/v + i\alpha_0\right)^2 - \left(k_x\right)^2} \tag{IV.G_7}$$

$$k_z^{td} = \pm\sqrt{\left(\omega/v_d + i\alpha_{0d}\right)^2 - \left(k_x\right)^2} \tag{IV.G_8}$$

$$k_z^{ts} = \pm\sqrt{\left(\omega/v_s + i\alpha_{0s}\right)^2 - \left(k_x\right)^2} \tag{IV.G_9}$$

The wave velocity in the liquid is v, the longitudinal respectively shear wave velocities in the solid are v_d and v_s.

The signs in (IV.G_7-9) are to be chosen according to Deschamps' principles, in order to correspond to experimentally verified properties[30-31].

Deschamps principles state that if $\mathrm{Re}(k_z)=0$, one has to deal with Scholte-Stoneley-like surface modes and the sign of k_z must be so that there is exponential decay of the amplitude away from the interface, i.e. the Sommerfeld conditions must hold. If $\mathrm{Re}(k_z)\neq 0$, then the sign of k_z depends on the angle of propagation of the liquid-side companion, of the considered longitudinal or shear mode in the solid

$$|\theta| = \arctan\left[\frac{|k_x|}{|k_z^r|}\right] \tag{IV.G_10}$$

If

$$\left|\theta^p\right| = \arctan\left[\frac{|k_x|}{|k_z^p|}\right] \tag{IV.G_11}$$

is 'close enough' to $\pi/2$, then that particular mode 'p' (p=d for longitudinal waves, p=s for shear waves) must show leaky Rayleigh wave features, whence the real parts of the wave vector must point into the liquid. Deschamps [31] states that 'close enough' to $\pi/2$ means the liquid side companion must fulfill

$$|\theta| > \left|\arcsin\left(\frac{v}{v_p}\right)\right| \tag{IV.G_12}$$

Whenever

$$|\theta| \le \left|\arcsin\left(\frac{v}{v_p}\right)\right| \tag{IV.G_13}$$

the Sommerfeld conditions hold, demanding that the mode 'p' travels away from the interface. For reasons of practicality, it is convenient to translate these principles into easy to apply rules leading to the following procedure:
First, apply Sommerfeld rules, i.e. the real parts of the wave vectors should all point away from the interface, except the incoming wave vector. Then, if the inhomogeneity vector of the incoming wave (this is minus the imaginary part of the incoming wave vector) points to the interface, one must check if relation (IV.G_12) holds for each mode in the solid. If so, the sign of that particular wave vector must be reversed.

The continuity conditions and the expression for the reflection coefficient

The straintensor is given by

$$\varepsilon_{i,j} = \frac{1}{2}\left(\frac{\partial u_i}{\partial x_j} + \frac{\partial u_j}{\partial x_i}\right) \tag{IV.G_14}$$

with displacement vector

$$\mathbf{u} = \nabla\varphi \tag{IV.G_15}$$

in the liquid, and

$$\mathbf{u} = \nabla\varphi + \nabla\times\boldsymbol{\psi} \tag{IV.G_16}$$

in the solid in which the respective potentials are given in (IV.G_1-4).
If we denote the stress tensor by $T_{i,j}$, then

$$T_{i,j} = \delta_{i,j}\tilde{\lambda}\varepsilon_{n,n} + 2\tilde{\mu}\varepsilon_{i,j} \tag{IV.G_17}$$

In which $\delta_{i,j}$ is the Kronecker delta, and λ and μ are the complex Lamé constants.
The continuity of normal stress and displacement (upper index 1: liquid, 2: solid) along the interface are respectively given by

$$T^1_{m,3} = T^2_{m,3};\ m=1,2,3 \tag{IV.G_18}$$

and

$$u^1_z = u^2_z \tag{IV.G_19}$$

Relations (IV.G_18-19) result in the following continuity condition:

$$\begin{bmatrix} RD \\ TD \\ TS \end{bmatrix} = \begin{bmatrix} k_z^r & -k_z^{td} & -k_x^{inc} \\ 0 & -2k_z^{td}k_x & \left(\frac{\omega}{v_s}+i\alpha_{0s}\right)^2 - 2\left(k_x\right)^2 \\ -\tilde{\lambda}^1\left(\frac{\omega}{v}+i\alpha_0\right)^2 & \tilde{\lambda}^2\left(\frac{\omega}{v_d}+i\alpha_{0d}\right)^2 + 2\tilde{\mu}^2\left(k_z^{td}\right)^2 & 2\tilde{\mu}^2k_z^{ts}k_x \end{bmatrix}^{-1} \times \begin{bmatrix} -k_z^{inc} \\ 0 \\ \tilde{\lambda}^1\left(\frac{\omega}{v}+i\alpha_0\right)^2 \end{bmatrix} \tag{IV.G_20}$$

in which the complex Lamé constants are given by

$$\tilde{\lambda}^1 = \rho\omega^2 \Big/ \left(k_x\right)^2 + \left(k_z^{inc}\right)^2 \qquad \text{(IV.G\_21)}$$

$$\tilde{\mu}^2 = \rho_s\omega^2 \Big/ \left(k_x\right)^2 + \left(k_z^{td}\right)^2 \qquad \text{(IV.G\_22)}$$

$$\tilde{\lambda}^2 = \rho_s\omega^2 \Big/ \left(k_x\right)^2 + \left(k_z^{inc}\right)^2 - 2\tilde{\mu}^2 \qquad \text{(IV.G\_23)}$$

ρ being the density of the liquid and ρ_s the density of the solid.
The reflection coefficient is then RD and is found from (IV.G_20).

NUMERICAL RESULTS

We neglect damping and consider a water/brass interface characterized by $\rho = 1000kg/m^3$, $v = 1480m/s$, $\rho_s = 8100kg/m^3$, $v_s = 2270m/s$ and $v_d = 4840m/s$.
In Fig. IV.G_2, we have plotted the absolute value of the reflection coefficient as a function of the inhomogeneity β^{inc} and the angle of incidence θ^{inc} for a frequency of 5MHz. As expected, a peak can be found at the leaky Rayleigh wave angle. The exact values for that peak are: $\beta_R = -317.268/m$ and $\theta_R = 44.04762^0$. However, for this water/brass interface, there appears another peak (as seen in Fig. IV.G_2), for the values $\beta_D = -1269.38847/m$ and $\theta_D = 19.00752^0$. If Snell's law is applied to recover the corresponding velocity of both the leaky Rayleigh and the new phenomena, we get respectively $v_R = 2128.7124m/s$ and $v_D = 4544.1675m/s$. The latter differs form the former and also differs from the bulk velocities in the solid, whence it is not a leaky Rayleigh wave and not a lateral wave corresponding to a 'branch cut' [15-16,21]. If we examine the reflection coefficient for 1MHz, we get $\beta_R = -63.42105/m$ and $\beta_D = -253.87719/m$ for exactly the same angles.

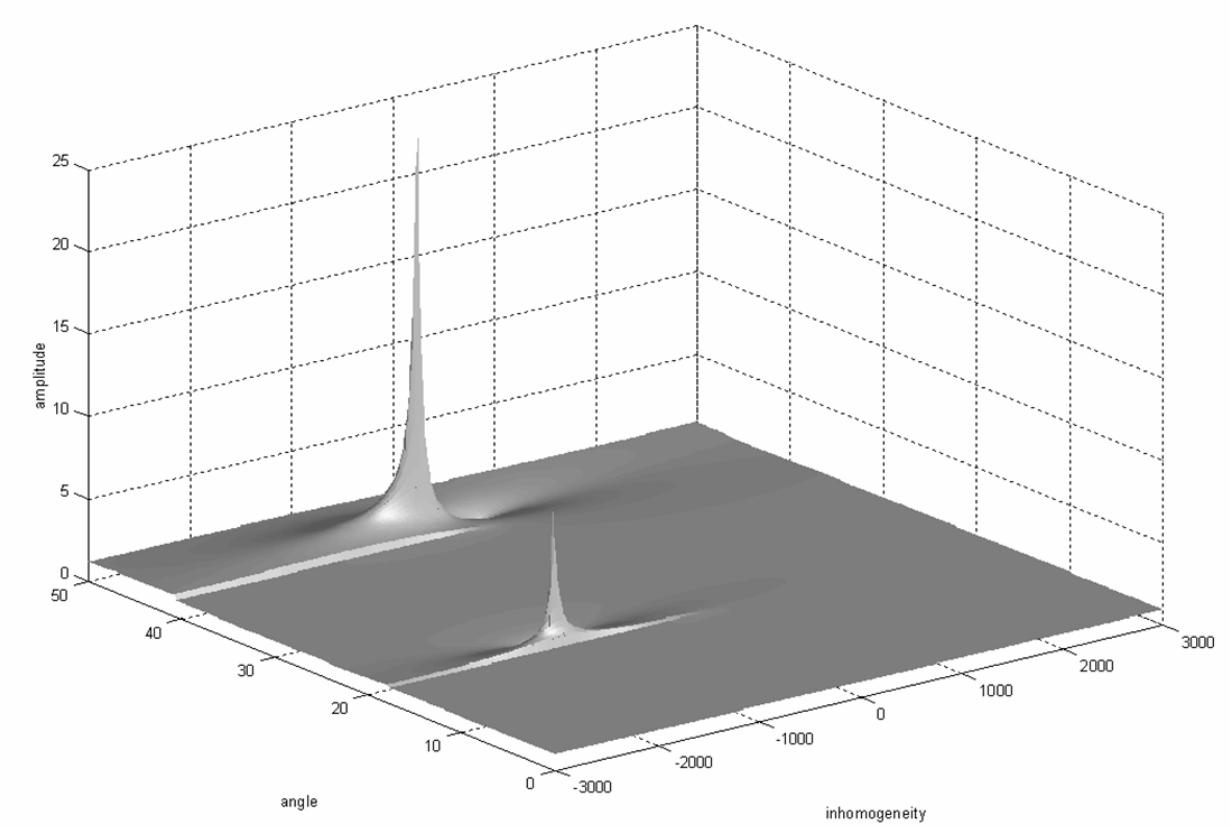

Fig IV.G_2: ***The amplitude of the reflected waves for different inhomogeneities and for different incidence angles on a brass/water interface. On should notice the appearance of two peaks. The one at an angle of 44.0476 degrees is the Rayleigh peak, while the one at an angle of 19.0075 degrees is the one corresponding to the new kind of surface waves.***

PROPERTIES OF THE NEW KIND OF SURFACE WAVES

In what follows, we have taken a frequency of 5MHz.

We recall that the displacement is given by (IV.G_15-16)

In Fig. IV.G_3, the profile of a leaky Rayleigh wave at 5MHz is plotted, for an angle of incidence of 44.0472 degrees and inhomogeneity –317.268/m. The propagation of this profile is depicted in Fig. IV.G_4 and Fig. IV.G_5., where we can see that the leaky Rayleigh wave is damped due to emission of sound into the liquid. In Fig. IV.G_6, the particle displacement (in the solid side) at the spot $[x,z]=[0,0]$ is given for each instant of time $t\in\left[0,\frac{2\pi}{\omega}\right]$. Figs. IV.G_5-6 learn us that leaky Rayleigh waves are elliptically polarized.

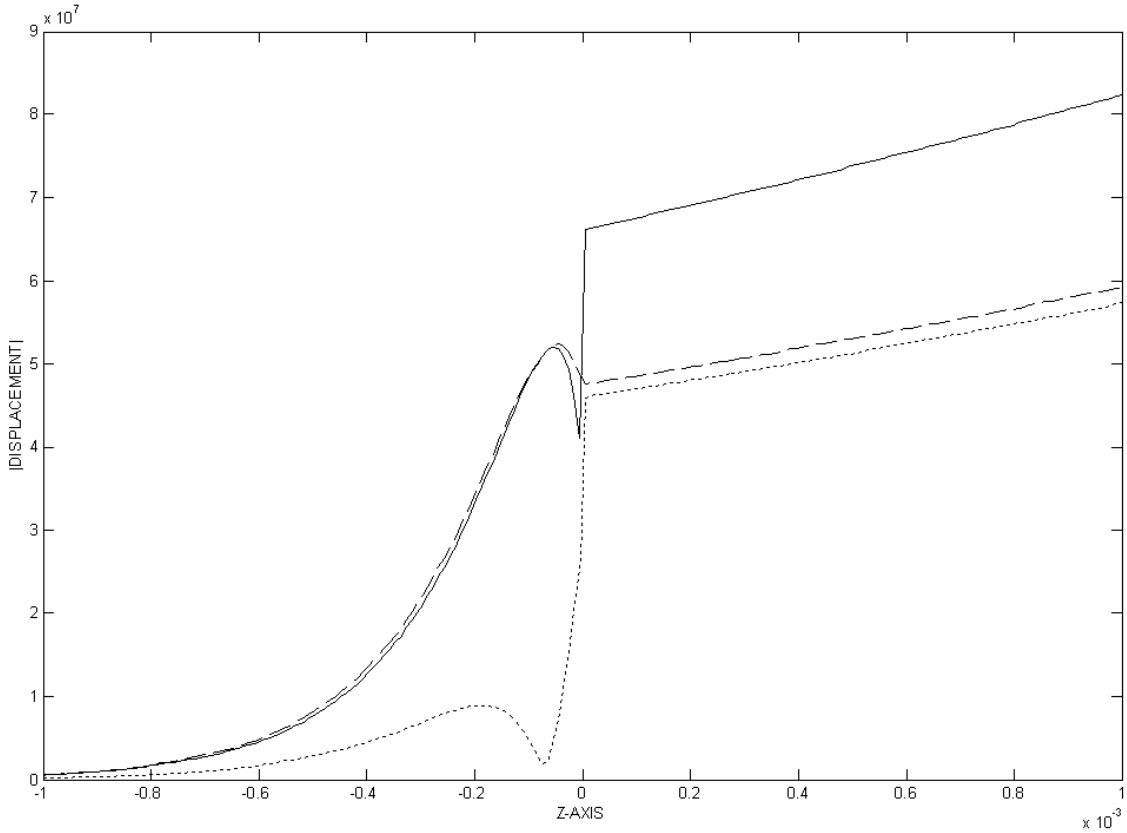

Fig IV.G_3: ***The profile of a Rayleigh wave at 5MHz. The angle of incidence is 44.0472 degrees, with inhomogeneity –317.268/m. The dotted line corresponds to*** $|\mathbf{u}_x|$***, the dashed line to*** $|\mathbf{u}_z|$***, while the solid line corresponds to*** $|\mathbf{u}|$**.**

In Fig. IV.G_7, the profile of the new kind of surface wave at 5MHz, for an angle of incidence of 19.0075187 degrees and inhomogeneity -1269.38884711/m is shown. The new kind of surface wave shows a lobe of increased amplitude near the interface that remains so while propagating (see Fig. IV.G_8 and Fig. IV.G_9), except for a decrease due to radiation into the liquid, just as in the case of leaky Rayleigh waves. However, the decrease is slightly higher than in the case of leaky Rayleigh waves. We will discuss this phenomenon further below. It is also noticed form Fig IV.G_10, that the polarization of the new kind of surface waves is also elliptically, though it differs from the polarization of a leaky Rayleigh wave (cfr. Fig. IV.G_6).

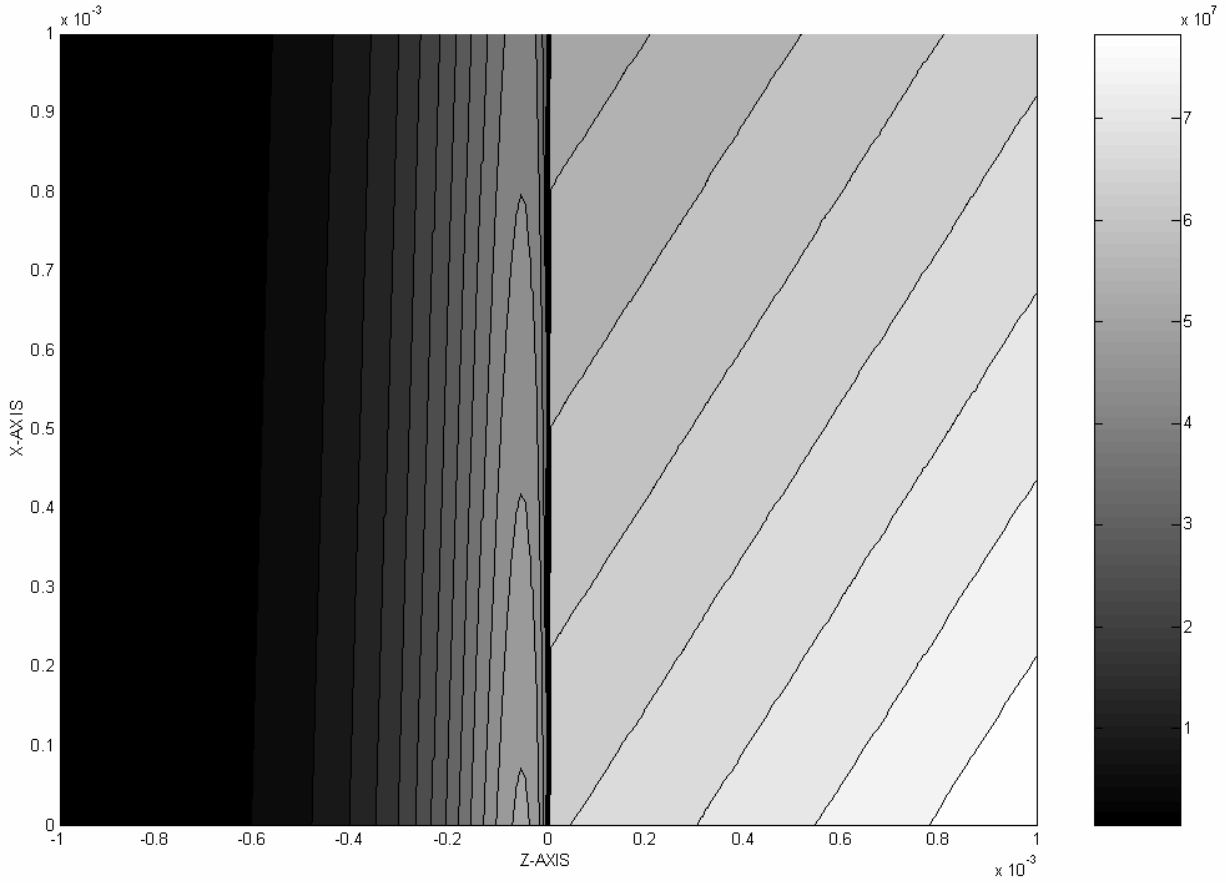

Fig IV.G_4: ***A filled contour plot of the total displacement $|\mathbf{u}|$ of a Rayleigh wave (the one of Fig IV.G_3) as a function of z and the propagation distance x.***

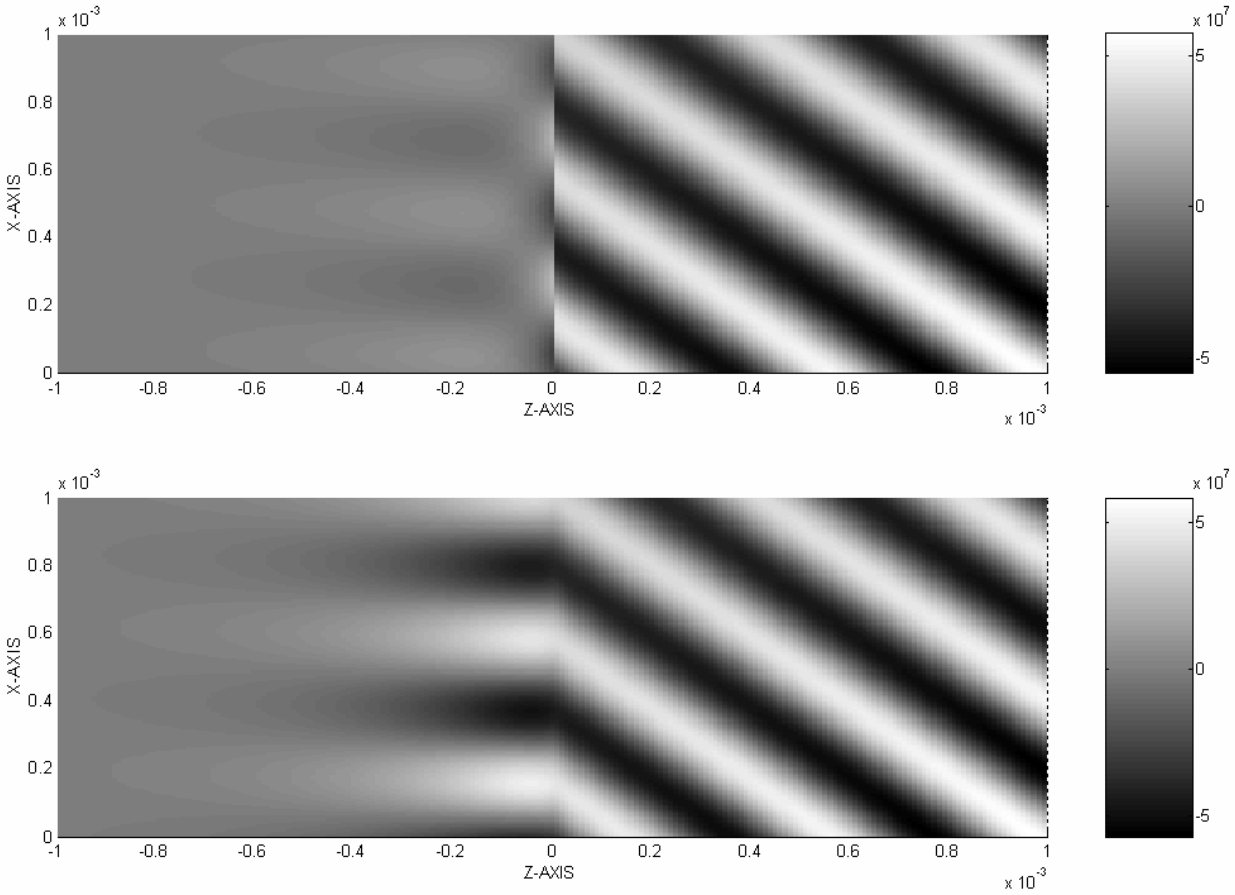

Fig IV.G_5: ***The real part of the displacement (u_x : top; u_z :bottom) for time t=0, as a function of z and the propagation distance x for the leaky Rayleigh wave of Fig IV.G_4. It is possible to observe that the leaky Rayleigh wave is circularly polarized, which is a well known feature of such surface waves.***

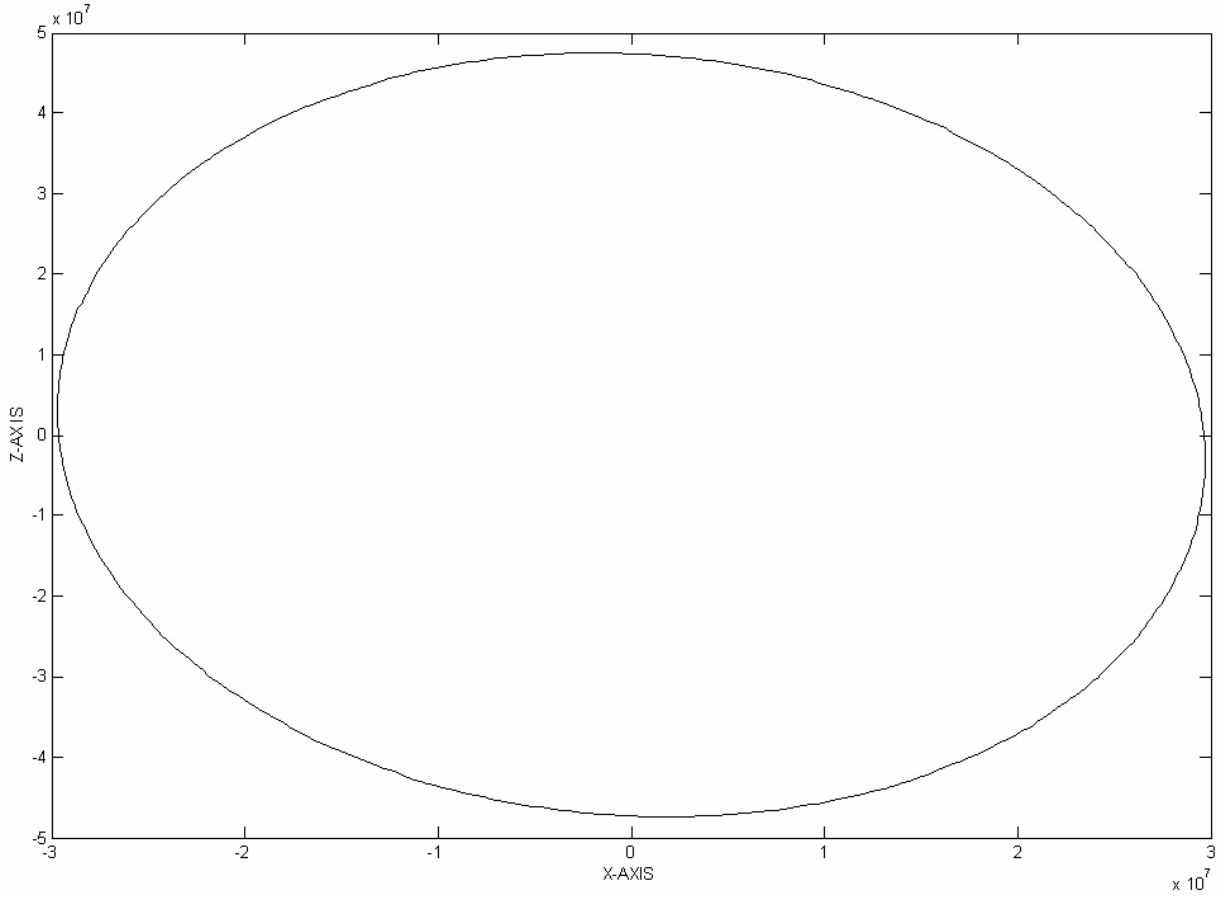

Fig. IV.G_6: ***The particle displacement in the solid for the leaky Rayleigh wave of Fig. IV.G_5 at*** $[x, z] = [0,0]$**,** ***depicted over 1 period of time. It is clear that this corresponds to elliptical polarization.***

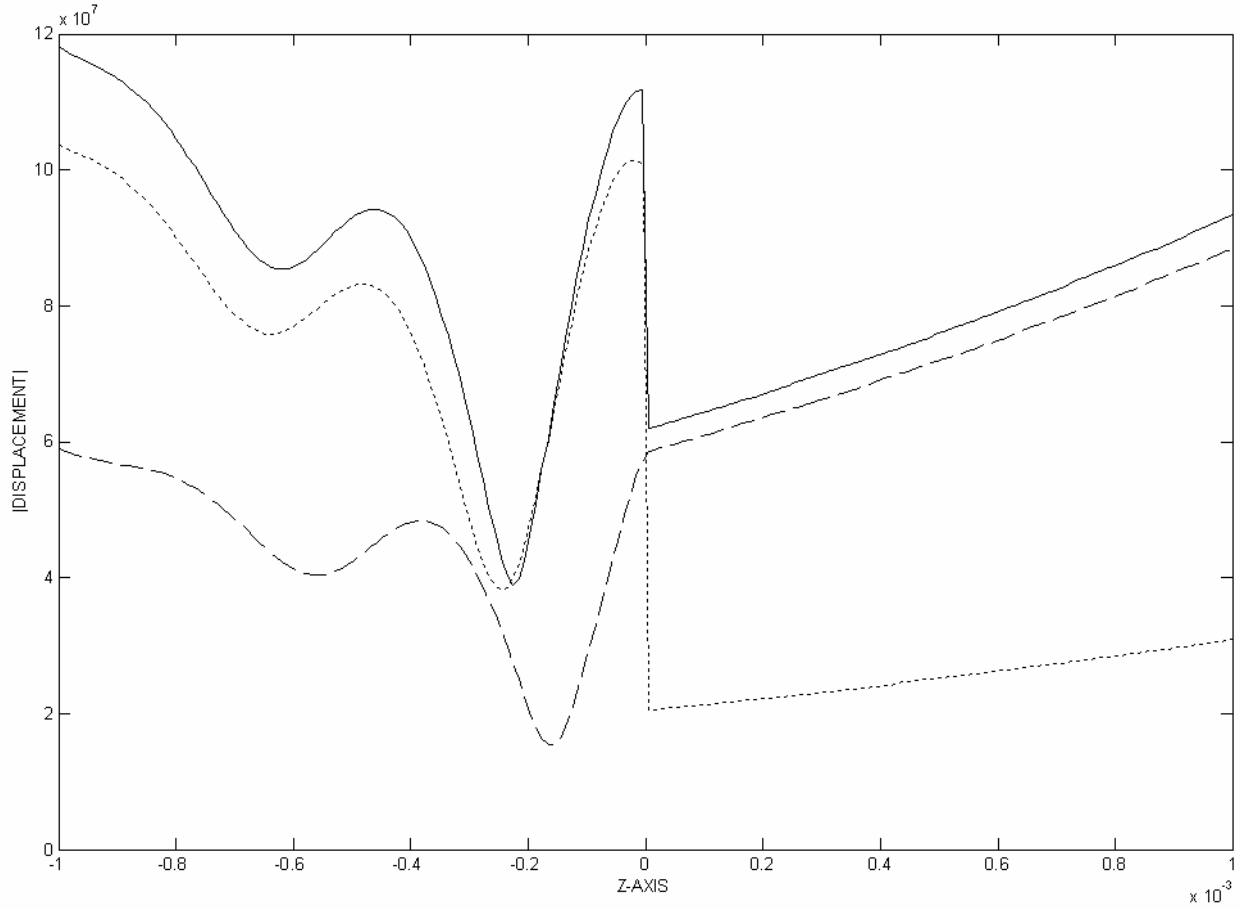

Fig IV.G_7: ***The profile of the new kind of surface wave at 5MHz The angle of incidence is 19.0075187 degrees, with inhomogeneity -1269.38884711/m. The dotted line corresponds to*** $|\mathbf{u}_x|$ ***, the dashed line to*** $|\mathbf{u}_z|$ ***, while the solid line corresponds to*** $|\mathbf{u}|$ ***.***

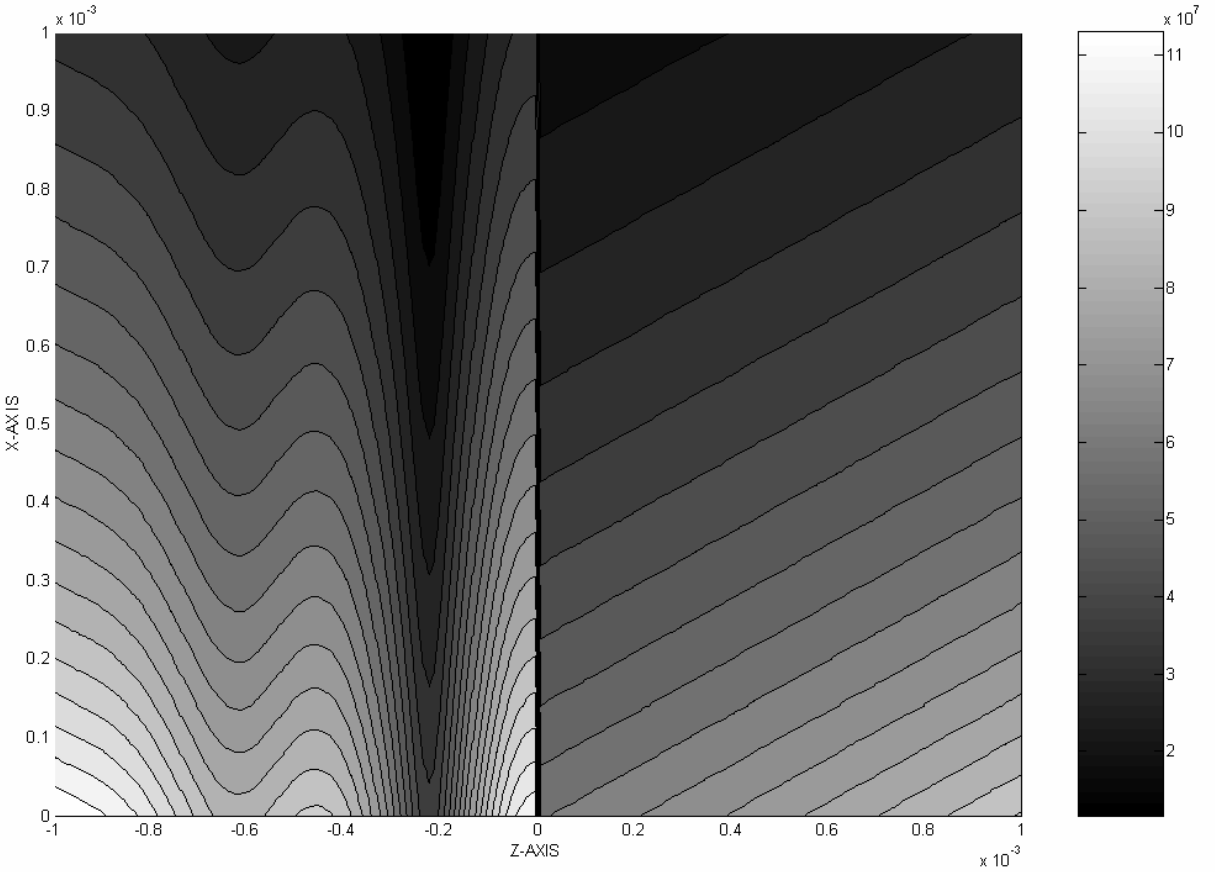

Fig. IV.G_8: ***A filled contour plot of the total displacement*** $|\mathbf{u}|$ ***of the new kind of surface wave (the one of Fig IV.G_7) as a function of z and the propagation distance x.***

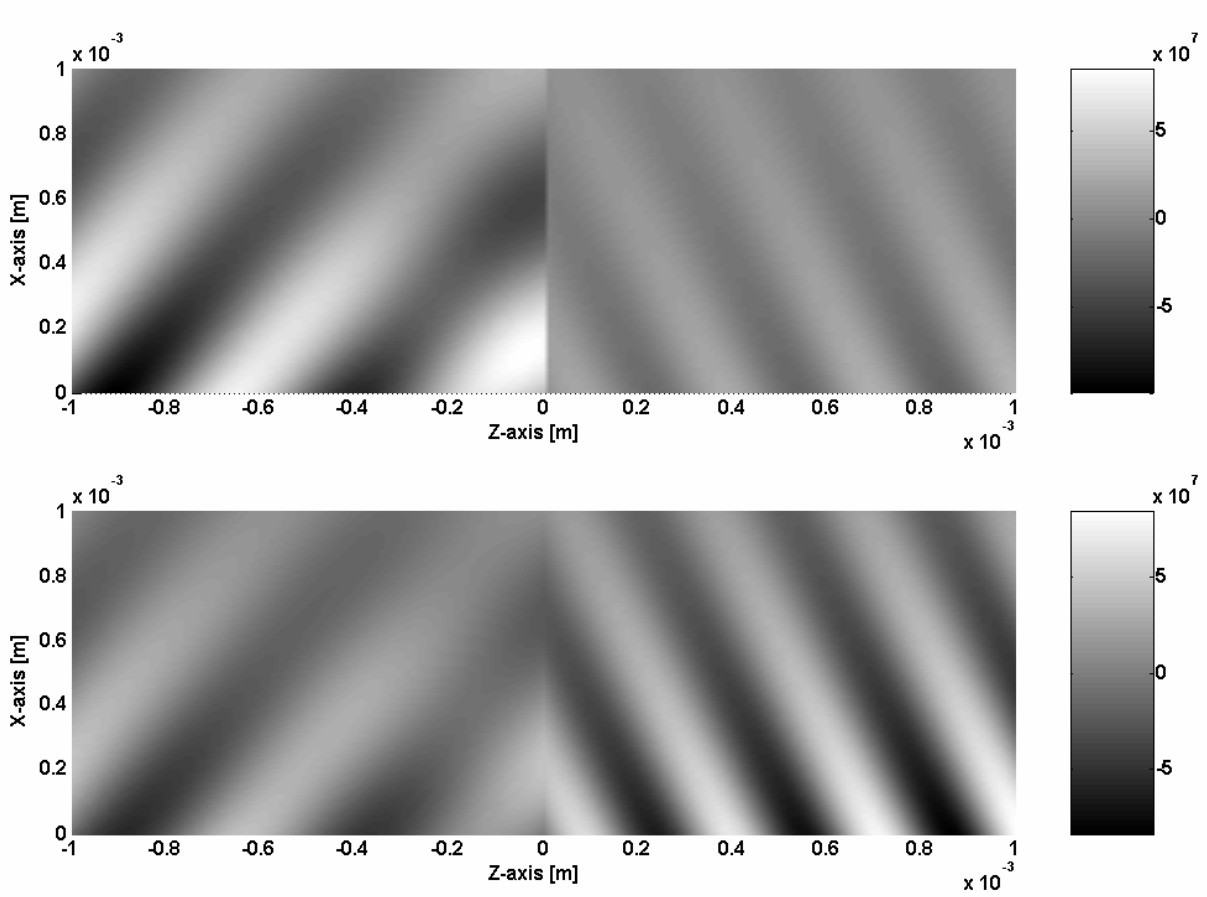

Fig IV.G_9: ***The real part of the displacement (u_x : top; u_z :bottom) as a function of z and the propagation distance x for the new kind of surface wave of Fig IV.G_8. It is possible to observe that the new kind of surface wave is elliptically polarized (almost linearly).***

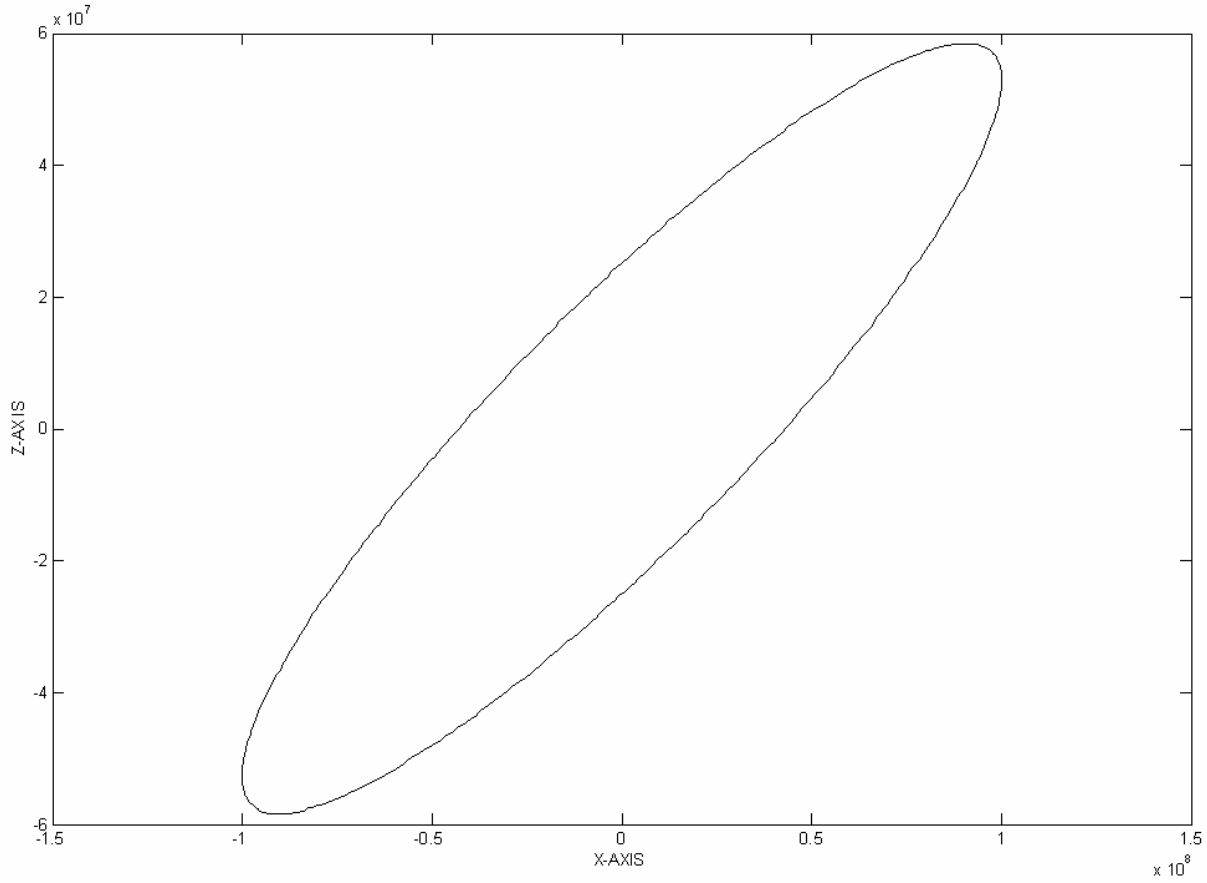

Fig. IV.G_10: ***The particle displacement in the solid for the new kind of surface wave of Fig. IV.G_9 at*** $[x,z]=[0,0]$***, depicted over 1 period of time. It is clear that this corresponds to elliptical polarization, though it differs from the polarization of a leaky Rayleigh wave (seen Fig. IV.G_6).***

It is widely known that a leaky Rayleigh wave consists of two inhomogeneous waves in the solid whose real parts point into the liquid and one inhomogeneous wave in the liquid whose real part also points into the liquid. Hence, radiation solely occurs in the direction of the liquid, i.e. the leaky Rayleigh wave leaks into the liquid. The exact wave vector components for the case of a leaky Rayleigh waves are shown in Fig. IV.G_11 and listed in Table IV.G_I.

Table IV.G_I: ***the calculated values of the components of the wave vectors corresponding to the case of leaky Rayleigh waves and the new kind of surface waves, corresponding to the peaks that appear in Fig. IV.G_2. The wave vectors are depicted in Fig. IV.G_9 and Fig. IV.G_10.***

	Leaky Rayleigh wave	New kind of surface wave
$k_x\left[m^{-1}\right]$	14759+228i	6926+1200i
$k_z^{inc}\left[m^{-1}\right]$	-15259+221i	-20105+413i
$k_z^{r}\left[m^{-1}\right]$	15259-221i	20105-413i
$k_z^{td}\left[m^{-1}\right]$	254-13256i	2530-3286i
$k_z^{ts}\left[m^{-1}\right]$	652-5166i	-12062+689i

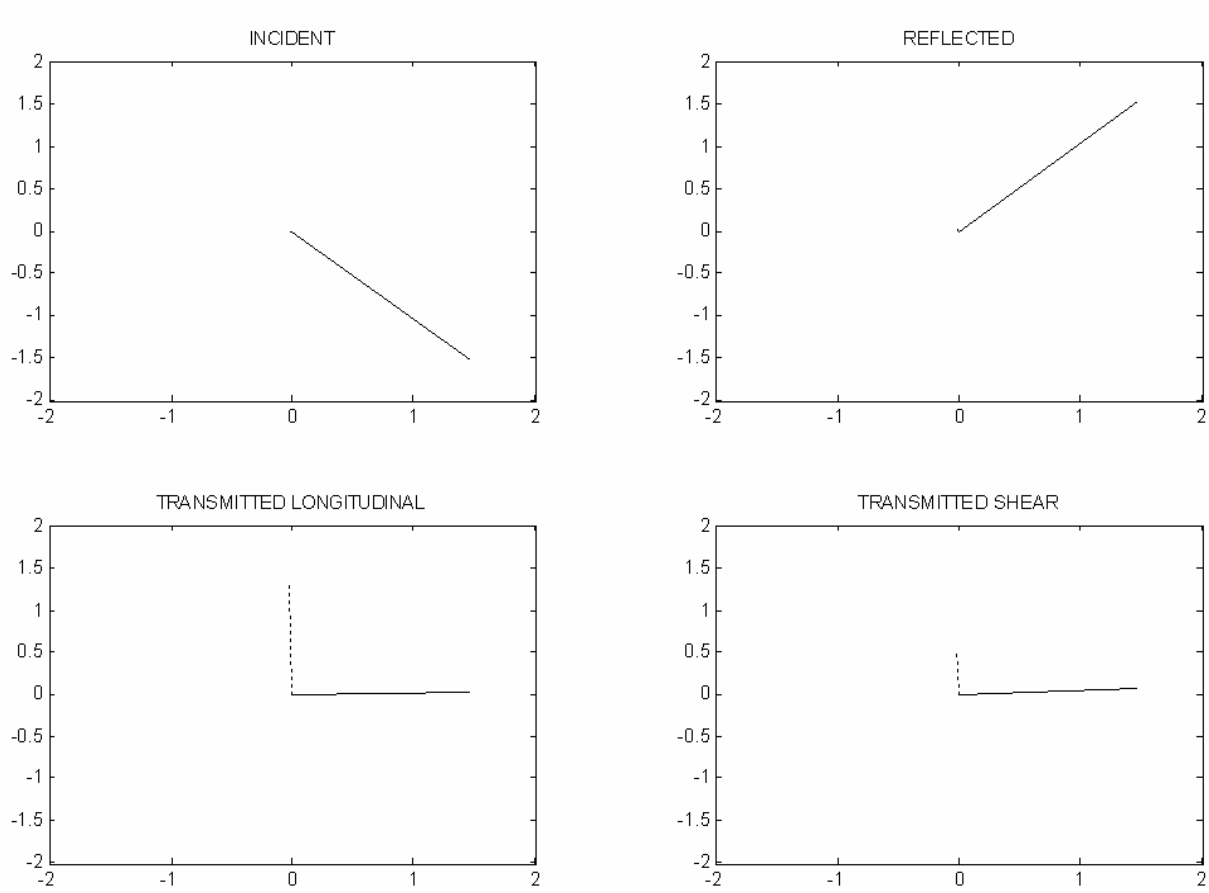

Fig. IV.G_11: ***The exact wave vectors as given in Table IV.G_I ($\times 10^{-4}$) for the leaky Rayleigh wave. Solid vectors: real vectors, dotted vectors: minus imaginary vectors (i.e. the inhomogeneity vectors β). It is seen that the leaky Rayleigh wave radiates into the liquid.***

In the case of the new kind of surface waves (see Fig IV.G_12 and Table IV.G_I), radiation occurs both into the liquid as well as into the solid (through shear waves). This is the reason why the new kind of surface waves diminish more rapidly than leaky Rayleigh waves.

POSSIBILITIES FOR THE GENERATION OF THE NEW KIND OF SURFACE WAVES

Since bounded beams must be narrow enough for beam deformations (such as a Schoch-displacement) to occur when leaky Rayleigh waves are generated and since the incidence inhomogeneity for the generation of the new kind of surface waves is much larger than for the generation of a leaky Rayleigh wave, it is expected that the generation by and the effect on an incident bounded beam will be solely visible when it is much narrower than upon the excitation of leaky Rayleigh waves. This is the reason why it is not visible in reported experiments [10]

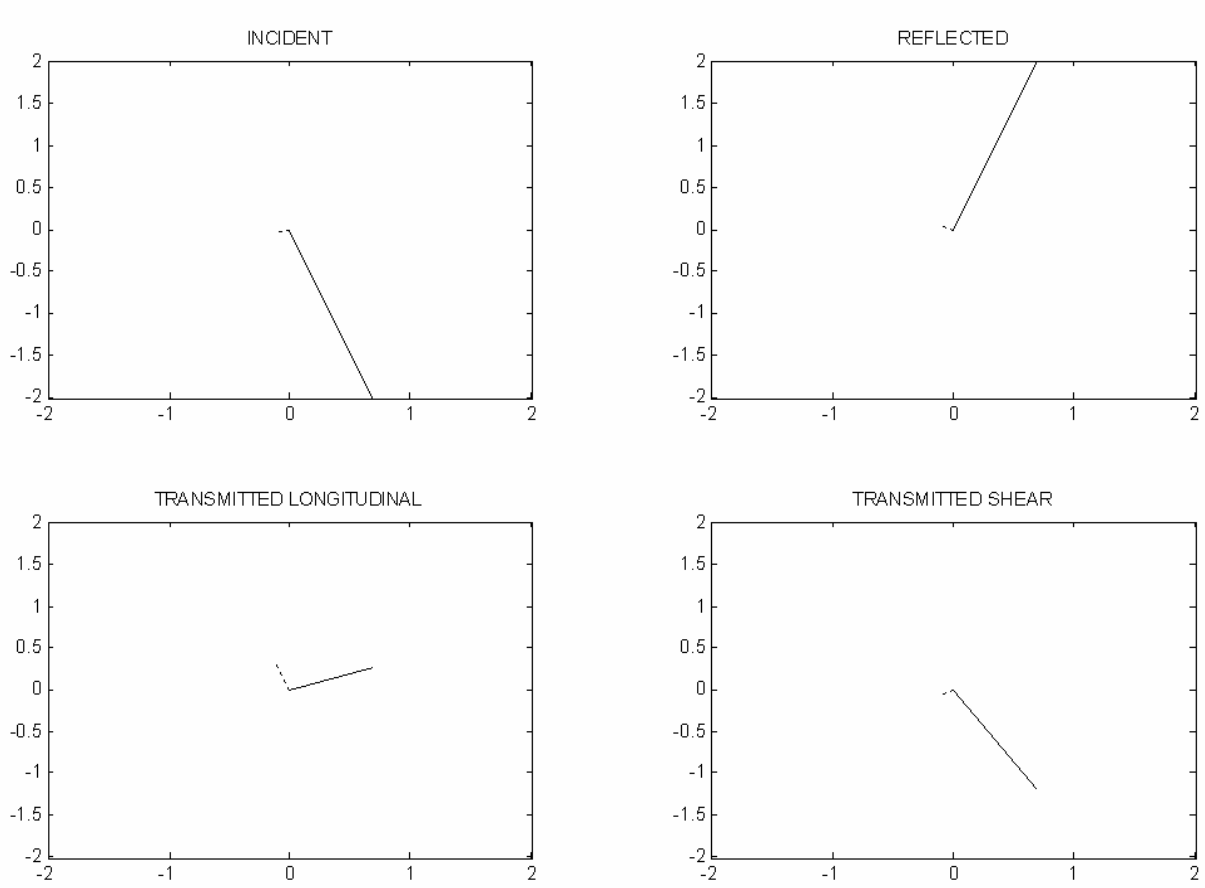

Fig IV.G_12: ***The exact wave vectors as given in Table IV.G_I ($\times 10^{-4}$) for the new kind of surface wave. Solid vectors: real vectors, dotted vectors: minus imaginary vectors (i.e. the inhomogeneity vectors β). It is seen that the new kind of surface wave radiates into the liquid and into the solid.***

CONCLUSION

It is shown that the inhomogeneous waves theory predicts the existence and the excitation of a new kind of surface waves on a water/brass interface that radiates both into the solid and into the liquid. Its polarization is elliptical (almost linear). The importance of this new phenomena lies in the areas where leaky surface waves have found to be very important, such as geology, electronics and especially non destructive testing of materials. It is expected that the new kind of surface waves will be generated by bounded beams that must be much narrower than in the case of the generation of leaky Rayleigh waves.

REFERENCES

[1] A. Viktorov, "Leaky surface waves in an isotropic solid", Sov. Phys. Dokl., 21(5), 1976
[2] T. J. Plona, M. Behravesh, W. G. Mayer, "Rayleigh and Lamb waves at liquid-solid boundaries", Ultrasonics, July 1975, 171-174, 1975
[3] J. H. M. T. van der Hijden, "Quantitative analysis of the pseudo-Rayleigh phenomenon", J. Acoust. Soc. Am., 75(4), 1041-1047, 1984
[4] REFCCAWei Li, Jan D. Achenbach, "V(z) measurement of multiple leaky wave velocities for elastic constant determination", J. Acoust. Soc. Am., 100(3), 1529-1537, 1996
[5] E. G. Nesvijski, "On a possibility of Rayleigh Transformed Sub-Surface Waves Propagation", The e-journal of NDT (www.NDT.net), 5(09), 2000
[6] Bernard Poirée, Francine Luppé, "Evanescent plane waves and the Scholte-Stoneley interface wave », J. Acoustique 4, 575-588, 1991

[7] M.A. Breazeale, Lazlo Adler, Gerald W. Scott, "Interaction of ultrasonic waves incident at the Rayleigh angle onto a liquid-solid interface", J. Appl. Phys, 48(2),530-537, 1977
[8] J. M. Claeys, O. Leroy, "Reflection and transmission of bounded sound beams on half-spaces and through plates", J. Acoust. Soc. Am., 72(2), 585-590, 1982
[9] René Lucas, "Etude de l'évolution du faisceau ultrasonore réfléchi par une interface eau-métal au voisinage du second angle critique, C. R. Acad. Sc. Paris, t. 273, Serie B, 61-64, 1974
[10] M. A. Breazeale, Laszlo Adler, Larry Flax, "Reflection of a gaussian ultrasonic beam from a liquid-solid interface", J. Acoust. Soc. Am., 56(3), 866-872, 1974
[11] Werner G. Neubauer, "Ultrasonic refelction of a bounded beam at Tayleigh and critical angles for a plane liquid-solid interface », J. Apll. Phys. 44(1),48-55, 1973
[12] Peter B. Nagy, Kangra Cho, Laszlo Adler, D. E. Chimenti, " Focal shift of convergent ultrasonic beams reflected from a liquid-solid interface", J. Acoust. Soc. Am., 81(4), 835-839, 1987
[13] Theodore E. Matikas, Martine Rousseau, Philippe Gatignol, "Theoretical analysis for the reflection of a focused ultrasonic beam from a fluid-solid interface", J. Acoust. Soc. Am., 93(3), 1407-1416, 1993
[14] Robert J. Hallermeier, Orest I. Diachok, "Simple technique for Exciting and probing Elastic Surface Waves", J. Appl. Phys., 41(12), 4763-4764, 1970
[15] John Pott, John G. Harris, "Scattering of an acoustic Gaussian beam from a fluid-solid interface", J. Acoust. Soc. Am. 76(6), 1829-1838, 1984
[16] John Pott, John G. Harris, "Further studies of the scattering of a gaussian beam from a fluid-solid interface", J. Acoust. Soc. Am. 78(3), 1072-1080, 1985
[17] Robert j. Hallemeier, Orest I. Diachok, "Simple Technique for Exciting and Probing elastic Surface Waves", J. Appl. Phys 41(12), 4763-4764, 1970
[18] M. Liu, H. P. Ho, M. G. Somekh, J. M. R. Weaver, "Noncontacting optical generation of focused surface acoustic waves using a customized zoneplate", Electr. Let., 31(4), 264-265, 1995
[19] V. Husev, C. Desmet, W. Lauriks, C. Glorieux, J. Thoen, "Theory of Scholte, leaky Rayleigh, and lateral wave excitation via the laser-induced thermoelastic effect", J. Acoust. Soc. Am. 100(3), 1514-1528, 1996
[20] N. Favretto-Anrès, "Theoretical Study of the Stoneley-Scholte Wave at the Interface between an Ideal Fluid and a Viscoelastic Solid", ACUSTICA-acta acustica, 82, 829-838, 1996
[21] Frédéric Padilla, Michel de Billy, Gérard Quentin, "Theoretical and experimental studies of surface waves on solid-fluid interfaces when the value of the fluid sound velocity is located between the shear and the longitudinal ones in the solid", J. Acoust. Soc. Am. 106(2), 666-673, 1999
[22] J. C. Couchman, J. R. Bell, "Prediction, detection and characterization of a fast surface wave produced near the first critical angle", Ultrasonics, November 1978, 272-274, 1978
[23] Oswald Leroy, "Nonspecular reflection-transmission phenomena of bounded beams described by inhomogeneous plane waves", Series on Stability, Vibration and Control of Systems Series B: Vol5, World Scientific, 1996
[24] Bernard Poirée, "Complex harmonic plane waves", Proc. Symposium on "Physical Acoustics : Fundamentals and Applications", Kortrijk, Belgium, Eds. O. Leroy and M. Breazeale, 99-117, Plenum, New York and London, 1990
[25] Bernard Poirée, "Les ondes planes évanescentes dans les fluides parfaits et les solides élastiques", J. Acoustique 2, 205-216, 1989 (in French)
[26] Jose Roux, "Reflection and refraction of heterogenous waves at plane interfaces", Proc. Symposium on "Physical Acoustics : Fundamentals and Applications", Kortrijk, Belgium, Eds. O. Leroy and M. Breazeale, 155-164, Plenum, New York and London, 1990
[27] M. Deschamps, P. Chevée, "Reflection and refraction of a heterogeneous plane wave by a solid layer", Wave motion 15, 61-75, 1992
[28] Gérard Quentin, André Derem, Bernard Poirée, "The formalism of evanescent plane waves and its importance in the study of the generalized Rayeligh wave", J. Acoustique 3, 321-336, 1990
[29] Marc Deschamps, "L'onde plane hétérogène et ses applications en acoustique linéaire", J. Acoustique 4, 269-305, 1991 (in French)
[30] M. Deschamps, J. Roux, "Some considerations concerning evanescent surface waves", Ultrasonics 1991 (29), 283-287, 1991
[31] Marc Deschamps, "Reflection and refraction of the evanescent plane wave on plane interfaces", J. Acoust. Soc. Am. 96(5), 2841-2848,1994.

Chapter V The Interaction of Sound with Continuously Varying Layers

Near the coastline and especially in rivers and harbors, it is of vital importance for a captain of a ship, to know the nautical depth. Overestimations of the nautical depth make ships strand, underestimations often result in unnecessary delays when entering harbors.

At the beginning of my research as a PhD student, my Co-promoter Oswald Leroy planned to join a collaboration with Haecon Harbour & Engineering Consultants (Drongen, Belgium), Verhaert Space Instruments & Applied Technologies (Kruibeke, Belgium), the Department of Chemical Engineering Techniques (Katholieke Universiteit Leuven, Heverlee, Belgium) and later also our department in Gent, dealing with fundamental and applied research in the field of echo-sounding of the bottom of rivers and harbors. The goal was to find a method to discover the real nautical bottom.

The bottom of rivers and harbors mainly consists of mud on a hard underground. This mud contains a navigable upper layer, a non-navigable lower layer and a transition layer in-between. Current echo-sounding techniques are only able to detect the water-mud interface and the mud-hard bottom interface. The nautical depth, which is determined by the transition zone, is not detectable.

Before the collaboration started, I performed some test calculations in order to study the feasibility. Later, when the project started, I joined as a volunteer and offered my evenings and weekends in order to build a fresh model that could investigate the interaction of sound with such a layered system. The main difficulty was the continuity of the layers (instead of abrupt changes), which made the use of special mathematical functions necessary, instead of the often used plane wave solutions. I puzzled, read a lot of literature and worked very hard until finally, after encountering a lot of mathematical functions that I had never met before (Whitaker functions, Kummer functions, Airy functions,…), I found a consistent system for which solutions existed.

The model is described in this chapter. Because I had only joined the project as a volunteer and because time consuming continuous feedback was necessary between the experiments and the theory, colleague Jeroen Vandeputte joined the project as an employee. For reasons of computational simplicity and flexibility, he decided not to use the model of this chapter, but to apply a model of discrete layers, for which, if the number of layers was large enough, the continuous model was approachable. Nevertheless, his model applied the Thomson-Haskell method, which makes the use of inhomogeneous waves very difficult and which makes it impossible to obtain a view of the interior of the layered structure. The model of this chapter on the other hand, has no difficulty to consider inhomogeneous waves and makes visualization of the propagation of bounded beams inside the layered structure, achievable.

This chapter describes how inhomogeneous waves and bounded beams interact with the mud system. The first had never been done before for continuous layers, the latter was never considered before, because echo-sounding is classically performed by means of pulsed sound instead of harmonic bounded beams, making ray-approaches more inviting. Consistency between the two types of interacting sound waves is proved in this chapter. Furthermore, it is highlighted how the nautical depth influences the reflected sound pattern. This influence is the key factor in the determination of the real nautical depth.

V.A The Interaction of Inhomogeneous Waves and Gaussian Beams with Mud in Between a Hard Solid and an Ideal Liquid

Mud is classified as a Bingham liquid, which, situated in between a hard solid and an ideal liquid, forms a rheological system in which the physical parameters vary continuously. Moreover, inside this liquid, there is often a transition zone (at the nautical bottom) in which the shear wave velocity varies almost exponentially. First we translate this rheological system into a theoretical rheological model that is numerically susceptible to predict its physical influence on impinging sound. Then, we show theoretically how the interaction of sound with this rheological model is solved. Finally, we present some numerical results for impinging inhomogeneous waves and we show how a bounded beam interacts with this continuously layered system. This section shows that it is theoretically possible to apply the inhomogeneous wave theory for such a system and also that the Fourier description of bounded beams works excellent for describing the propagation of bounded beams through mud. Even though it is widely known that echo sounding cannot reveal the position of the nautical bottom, we show that its position influences the reflected beam pattern for oblique incidence, which is promising for nautical depth determination in harbors and rivers.
The contents of this section have been published as: Nico F. Declercq, Oswald Leroy, Joris Degrieck, Jeroen Vandeputte "The interaction of inhomogeneous waves and Gaussian beams with mud in between a hard solid and an ideal liquid", Acta Acustica United with Acustica 90, 819-829, 2004 (Imp. Fact. 0.346; SCI-index, Acoustics, rank:21 /28)

INTRODUCTION

It is known from various textbooks that a Bingham liquid is a liquid that behaves like solid under static conditions, but starts to flow if a yield force is applied that exceeds a critical value. This phenomenon is often called plastic flow. The description of this flow is beyond our intentions and is left as a matter of investigation for rheologists. Bingham liquids also have other properties that are more interesting at this point. We are primarily interested in the consequences of a Bingham liquid at rest, i.e. under macroscopic static conditions, on traversing sound. An important feature of liquids, showing Bingham behavior, at rest, is the appearance of a spatial phase transition zone below which the liquid can be fully described as a Bingham liquid and above which the liquid behaves almost as if it were an ideal liquid. Such liquids appear in many branches of science and everyday life materials such as fresh concrete [1-2] , lava [3-4], mud [5-8], molten plastic and even ketchup. The range of applications where Bingham-like behaving liquids appear, is even wider. They appear in the study of periodical river floods [9], gravity

driven floods [10], sediment mobility [11], climate evolution [12], archeology [13-15], meteorology [16], geology [17], emulsion [18], and even in engineering problems when bridges have to be built [19] or in the oil industry and ecology [20].

Especially in the shipping and dredging industry, it is of primordial importance to know the nautical depth in rivers and harbors. The nautical depth is determined by mud characteristics at the bottom of waterways, see Fig. V.A_1. It forms the transition between navigable mud and non-navigable mud. Navigable mud is almost like water, whereas non-navigable mud is almost like clay.

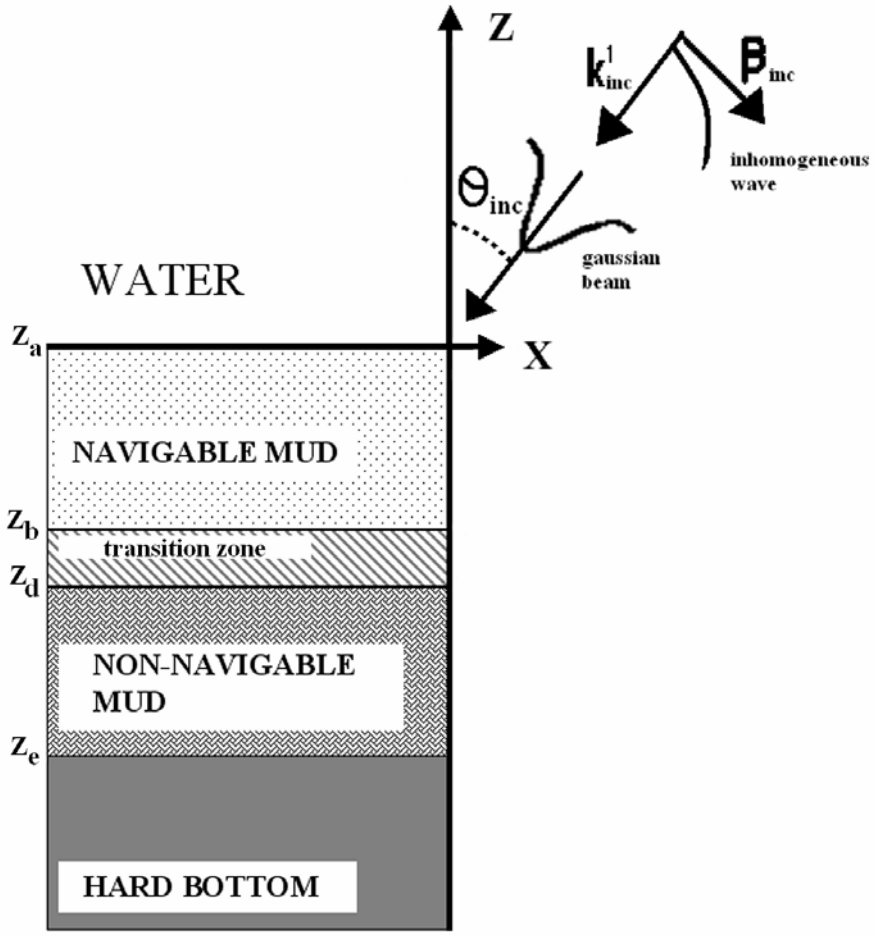

Fig. V.A_1: ***A schematic of the different layers in a system of mud in between a hard solid and an ideal liquid.***

In many of the mentioned fields and especially for monitoring waterways, the use of ultrasound is already generally adopted in its simplest form such as echo-sounding [21-23], where it is highly competitive with other techniques such as laser bathymetry [24]. Nevertheless, the problem with echo-sounding is the fact that the nautical bottom cannot be detected when normal incidence is applied. The reason is that this transition zone consists of an almost abrupt change in shear sound parameters, but not in longitudinal sound parameters. Since normal incident sound doesn't stimulate shear waves, it is not susceptible to the transition zone. Echo sounding is hence only practicable for determination of the depth where the hard bottom starts (sand, rocks, concrete, …) and where the transition between water and navigable mud occurs, not for determining the

nautical depth, which is always located somewhere in between. It is therefore interesting to develop a theoretical model that describes a more advanced interaction of sound with liquids showing Bingham behavior. More particularly, understanding of the interaction with inhomogeneous waves and obliquely incident bounded beams might be a stimulus to create more sophisticated technologies to detect the transition zone.

In what follows, we study a rheological system which is quite similar to mud in a harbor. The parameters used in the numerical examples for describing mud do not perfectly correspond to the exact parameters, but they are realistic. For simplicity we have neglected damping in the numerical examples, except for the hard bottom. Nevertheless, because damping plays an important role in real physical mud, we have incorporated damping in the theoretical description.

THEORETICAL DESCRIPTION OF THE RHEOLOGICAL MODEL

Bulk properties

The different layers that are mentioned below, are depicted in Fig. V.A_1. For reasons of simplicity, we limit our model to where the rheological system of interest is for our purpose fully characterized by its dimensions and its density and sound velocity. The latter two are supposed to vary continuously with depth. The influence of the specific microscopic structure on what we are interested in, is hence considered to be fully contained in the density and velocity values. Therefore, we do not consider explicitly the occurrence of air bubbles [25-26] or the presence of grains [27]. The latter assumption is justified by the known fact that liquids showing Bingham behavior, like for example mud, cannot be reduced to special cases of grainy solids like sand [28].

The rheological system consists of a layer of liquid showing Bingham behavior (for brevity called ‘Bingham layer’), covered by water and resting on an infinitely thick layer of material with constant bulk properties (‘the underground or the hard bottom’). The Bingham layer itself is built-up by three interlayers. The upper interlayer is that where the liquid finds itself under such physical conditions that it is almost an ideal fluid (e.g. navigable mud). The lower interlayer is that where the liquid has been transformed into a Bingham liquid (e.g. non-navigable mud). The middle layer is the so called ‘transition zone’.

Moreover, the upper interlayer, respectively the lower interlayer, has low respectively high constant shear velocity, while the transition zone has a nonlinearly continuously varying shear velocity, connecting that of the upper interlayer to that of the lower interlayer. It is in this layer that the so called ‘phase transition’ appears. We always consider the density varying linearly throughout the system. The dilatational velocity is considered to be quasi linearly varying with depth, i.e. linearly if we only take a look at the particular points mathematically separating each layer. Demanding pure linearity would be too rigorous, leading to inconsistency of the physical parameters.

If the density and the sound velocities vary sufficiently slow with the depth within each layer, then, locally, plane waves as well as inhomogeneous waves will be solutions of the wave equation. Under these circumstances, it has been shown by Brekhovskikh and Godin [29] that if φ is the longitudinal wave potential and ψ the shear wave potential, then, omitting the time dependence $\exp(-i\omega t)$

$$\varphi(x,z) = \Phi(z)\exp\left(ik_{d,x}x\right) \tag{V.A_1}$$

$$\boldsymbol{\psi}(x,z) = \psi(x,z)\mathbf{e}_y = \Psi(z)\exp\left(ik_{s,x}x\right)\mathbf{e}_y \tag{V.A_2}$$

with

$$\frac{\partial^2\Phi(z)}{\partial z^2} + g_d(z)\Phi(z) = 0 \tag{V.A_3}$$

$$\frac{\partial^2\Psi(z)}{\partial z^2} + g_s(z)\Psi(z) = 0 \tag{V.A_4}$$

Because inhomogeneous waves are local solutions of the wave equation, the dispersion relation for inhomogeneous waves [30] holds locally and we get

$$g_d(z) + k_{d,x}^2 = \frac{\omega^2}{\left(v_d^p(z)\right)^2} - \left(\alpha_{d,0}^p(z)\right)^2 = \frac{\omega^2\rho(z)}{\lambda(z)+2\mu(z)} \tag{V.A_5}$$

$$g_s(z) + k_{s,x}^2 = \frac{\omega^2}{\left(v_s^p(z)\right)^2} - \left(\alpha_{s,0}^p(z)\right)^2 = \frac{\omega^2\rho(z)}{\mu(z)} \tag{V.A_6}$$

The system is considered to behave viscoelastic, whence [31-35] for each spot in layer ‘p’

$$\lambda^p(z) = \lambda_1^p(z) - i\omega\lambda_2^p(z) \tag{V.A_7}$$

$$\mu^p(z) = \mu_1^p(z) - i\omega\mu_2^p(z) \tag{V.A_8}$$

with the Lamé constants λ_1^p and μ_1^p and viscoelastic constants λ_2^p and μ_2^p of (V.A_7-8) related to the intrinsic damping coefficient for shear waves $\alpha_{s,0}^p$, the shear wave velocity v_s^p, the intrinsic damping coefficient for longitudinal waves $\alpha_{d,0}^p$ and the longitudinal wave velocity v_d^p, through the dispersion relations [30] (V.A_5-6), giving

$$\mu_1^p = \omega^2 \left(v_s^p \right)^2 \rho^p \left(\omega - \alpha_{s,0}^p v_s^p \right) \frac{\alpha_{s,0}^p v_s^p + \omega}{\left(\omega^2 + \left(\alpha_{s,0}^p v_s^p \right)^2 \right)^2} \tag{V.A_9}$$

$$\mu_2^p = 2\alpha_{s,0}^p \omega^2 \left(v_s^p \right)^3 \frac{\rho^p}{\left(\omega^2 + \left(\alpha_{s,0}^p v_s^p \right)^2 \right)^2} \tag{V.A_10}$$

$$\lambda_2^p = 2\alpha_{d,0}^p \omega^2 \left(v_d^p \right)^3 \frac{\rho^p}{\left(\omega^2 + \left(\alpha_{d,0}^p v_d^p \right)^2 \right)^2} - 2\mu_2^p \tag{V.A_11}$$

$$\lambda_1^p = \omega^2 \left(v_d^p \right)^2 \rho^p \left(\omega - \alpha_{d,0}^p v_d^p \right) \frac{\alpha_{d,0}^p v_d^p + \omega}{\left(\omega^2 + \left(\alpha_{d,0}^p v_d^p \right)^2 \right)^2} - 2\mu_1^p \tag{V.A_12}$$

Whenever necessary, the longitudinal wave velocity v_d^p and the shear wave velocity v_s^p can be extracted from (V.A_9-12) and written as a function of the Lamé coefficients and the frequency. For brevity, in the sequel, we write

$$\lambda_3^p = -i\omega\lambda_2^p \tag{V.A_13}$$

$$\mu_3^p = -i\omega\mu_2^p \tag{V.A_14}$$

Relations (V.A_9-12) and the straightforward extraction of v_d^p and v_s^p are reported here for the first time. Before, solely approximations were published for extremely low damping coefficients [36-38].

The differential equations (V.A_3-4) can only be solved if $g_q; q = d, s$ are sufficiently 'uncomplicated [29]'. We limit the level of difficulty to g_q being constant or a linear function of *z*. Before describing the interaction of sound with the rheological system (see next paragraph), it is necessary to determine g_q for each layer. Taking into account the above stated properties of the sound velocities as a function of depth, we find for the intervals defined in Fig. V.A_1,

interval	$g_s(z)$	$g_d(z)$
$z_a \to z_b$	$g_{s,ab}(z) = \tilde{k}_{s,ab}$	$g_{d,ab}(z) = \tilde{k}_{d,ab} + \tilde{p}_{d,ab}\, z$
$z_b \to z_d$	$g_{s,bd}(z) = \tilde{k}_{s,bd} + \tilde{p}_{s,bd}\, z$	$g_{d,bd}(z) = \tilde{k}_{d,bd} + \tilde{p}_{d,bd}\, z$
$z_d \to z_e$	$g_{s,de}(z) = \tilde{k}_{s,de}$	$g_{d,de}(z) = \tilde{k}_{d,de} + \tilde{p}_{d,de}\, z$

(V.A_15)

where each $\tilde{k}$ and $\tilde{p}$ have to be determined, so that the rheological system is consistent with (V.A_9-12) and the above stated properties of the density and sound velocities as a function of depth. The 'tilde' is there in order not to mix up with classical wave numbers. In what follows in this paragraph, all parameters describe the upper interlayer, the transition layer and the lower interlayer and not the covering ideal liquid or the solid underground. Therefore, for example a parameter ζ_e is the value of ζ at the spot $\lim_{\substack{z \to z_e \\ z<z_e}}(z)$.

The Lamé constants in the layers $\left[z_a, z_b\right]$, $\left[z_b, z_d\right]$ and $\left[z_d, z_e\right]$ are assumed to be continuous through their respective interfaces, whereas for μ_a, λ_a, ρ_a, μ_e λ_e and ρ_e given edge parameters, we demand the following boundary conditions:

Boundary Conditions for Shear Parameters

We demand that for each $z \in \left[z_a, z_b\right]$

$$\frac{\mu_{ab}(z)}{\rho_{ab}(z)} = \frac{\mu_a}{\rho_a} \tag{V.A_16}$$

and that for each $z \in \left[z_d, z_e\right]$

$$\frac{\mu_{de}(z)}{\rho_{de}(z)} = \frac{\mu_e}{\rho_e} \tag{V.A_17}$$

which involves a constant shear velocity in the intervals $\left[z_a, z_b\right]$ and $\left[z_d, z_e\right]$

Boundary Conditions for Longitudinal Parameters

$$\lambda_{ab}\left(z_a\right)=\lambda_a \tag{V.A_18}$$

$$\lambda_{de}\left(z_e\right)=\lambda_e \tag{V.A_19}$$

Quasi Linearity of the Complex Longitudinal Velocity

Quasi linearity means linear if only the mathematical spots z_a, z_b, z_d and z_e are considered. The complex longitudinal velocity in a layer 'p', of which the real part is the genuine longitudinal wave velocity is defined as:

$$v_d^p=\sqrt{\frac{\lambda^p+2\mu^p}{\rho^p}} \tag{V.A_20}$$

Note that this is consistent with (V.A_5), because it is the expression of the generalized complex wave velocity and not the real wave velocity.

Set of Equations of Boundary and Continuity Conditions

In what follows, we denote $\mu_{gn}=\mu_g\left(z_n\right)$.

Conditions (V.A_16-20) ultimately give:

$$\tilde{k}_{s,ab}=\frac{\rho_a\omega^2-\left(\mu_{1a}+\mu_{3a}\right)\left(k_{s,x}\right)^2}{\left(\mu_{1a}+\mu_{3a}\right)} \tag{V.A_21}$$

$$\tilde{k}_{s,de}=\frac{\rho_e\omega^2-\left(\mu_{1e}+\mu_{3e}\right)\left(k_{s,x}\right)^2}{\left(\mu_{1e}+\mu_{3e}\right)} \tag{V.A_22}$$

$$\begin{pmatrix}-1 & -z_b\\ 1 & z_d\end{pmatrix}\begin{pmatrix}\tilde{k}_{s,bd}\\ \tilde{p}_{s,bd}\end{pmatrix}=\begin{pmatrix}-\tilde{k}_{s,ab}\\ \tilde{k}_{s,de}\end{pmatrix} \tag{V.A_23}$$

and

$$\begin{pmatrix} 0 & 0 & 1 & z_d & 0 & 0 \\ 1 & z_b & 0 & 0 & 0 & 0 \\ 0 & 0 & 0 & 0 & 1 & z_e \\ 0 & 0 & 1 & z_d & -1 & -z_d \\ 1 & z_b & -1 & -z_b & 0 & 0 \\ 1 & z_a & 0 & 0 & 0 & 0 \end{pmatrix} \begin{pmatrix} \tilde{k}_{d,ab} \\ \tilde{p}_{d,ab} \\ \tilde{k}_{d,bd} \\ \tilde{p}_{d,bd} \\ \tilde{k}_{d,de} \\ \tilde{p}_{d,de} \end{pmatrix} \tag{V.A_24}$$

$$= \begin{pmatrix} \omega^2 \left[\sqrt{\frac{\lambda_{ab}(z_a)+2\mu_{ab}(z_a)}{\rho_{ab}(z_a)}} \left(\frac{z_e - z_d}{z_e - z_a} \right) + \sqrt{\frac{\lambda_{de}(z_e)+2\mu_{de}(z_e)}{\rho_{de}(z_e)}} \frac{z_d - z_a}{z_e - z_a} \right]^{-2} - \left(k_{d,x}\right)^2 \\ \omega^2 \left[\sqrt{\frac{\lambda_{ab}(z_a)+2\mu_{ab}(z_a)}{\rho_{ab}(z_a)}} \left(\frac{z_e - z_b}{z_e - z_a} \right) + \sqrt{\frac{\lambda_{de}(z_e)+2\mu_{de}(z_e)}{\rho_{de}(z_e)}} \frac{z_b - z_a}{z_e - z_a} \right]^{-2} - \left(k_{d,x}\right)^2 \\ \frac{\omega^2 \rho_e}{\lambda_e + 2\mu_{de}} - \left(k_{d,x}\right)^2 \\ 0 \\ 0 \\ \frac{\omega^2 \rho_a}{\lambda_a + 2\mu_{ab}} - \left(k_{d,x}\right)^2 \end{pmatrix}$$

Equations 21-24 enable us to determine the self consistent values $\tilde{k}_{s,ab}$, $\tilde{k}_{s,de}$, $\tilde{k}_{s,bd}$, $\tilde{p}_{s,bd}$, $\tilde{k}_{d,ab}$, $\tilde{p}_{d,ab}$, $\tilde{k}_{d,bd}$, $\tilde{p}_{d,bd}$, $\tilde{k}_{d,de}$, $\tilde{p}_{d,de}$ that determine the rheological system that is considered here. In Fig. V.A_2, an example is given as how the wave velocities and density may evolve as a function of depth. More details concerning Fig. V.A_2 will follow in the next paragraph.

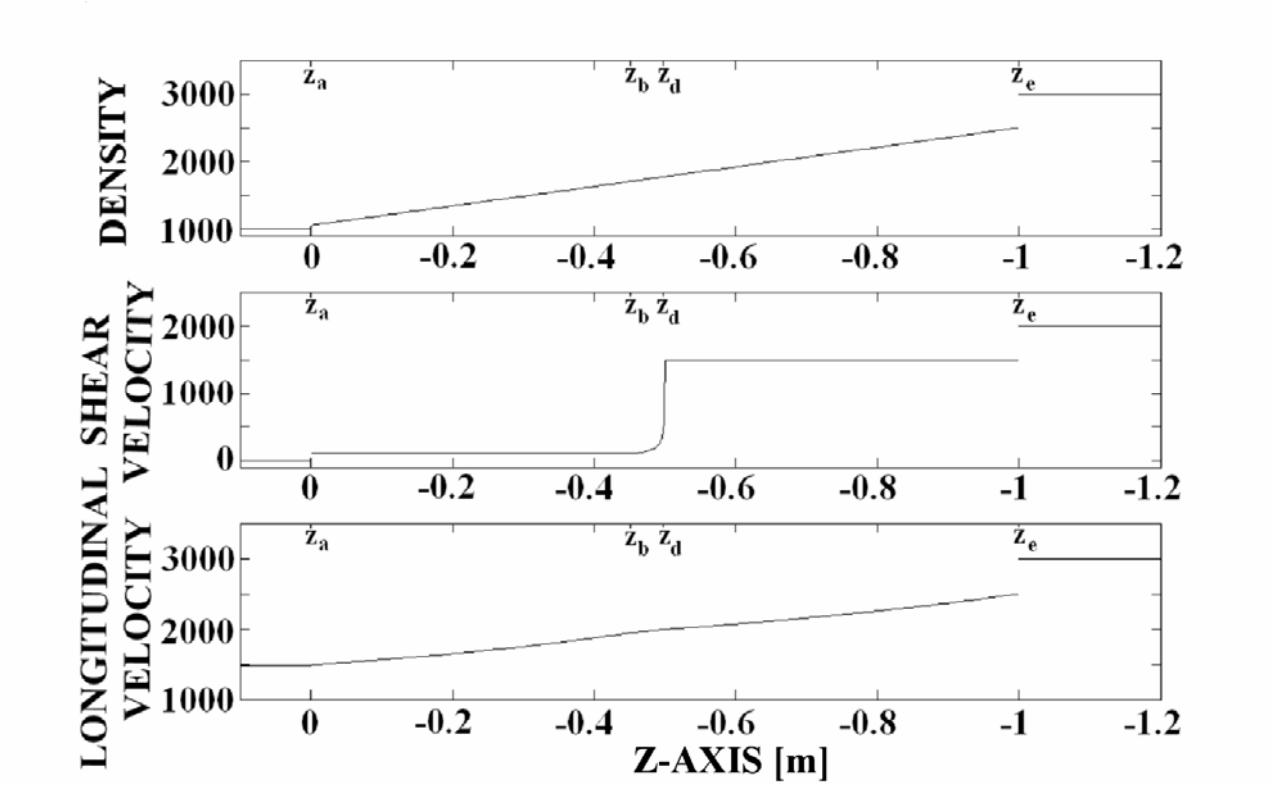

Fig. V.A_2: ***Density and sound velocities as a function of depth for the system shown in Fig. V.A_1 and applied in calculations that produce Figs V.A_3-10.***

THE INTERACTION OF INHOMOGENEOUS WAVES WITH THE RHEOLOGICAL MODEL

Before building a continuity matrix, it is first necessary to find solutions of (V.A_1-4). If we rewrite equations (V.A_3-4) for $f = \Phi$ or $f = \Psi$ as

$$\frac{\partial^2 f}{\partial z^2} - \left(-\tilde{p}\, z - \tilde{k} \right) f = 0 \qquad \text{(V.A\_25)}$$

and take

$$\gamma = \left(-\tilde{p} \right)^{-2/3} \left(-\tilde{p}\, z - \tilde{k} \right) \qquad \text{(V.A\_26)}$$

then (V.A_25) becomes

$$\frac{\partial^2 f}{\partial \gamma^2} - \gamma f = 0 \tag{V.A_27}$$

which is the Airy equation, whence [39]

$$f = C_m Airy_0(\gamma) + C_w Airy_2(\gamma) \tag{V.A_28}$$

with

$$\frac{\partial f}{\partial z} = -\frac{\tilde{p}}{\left(-\tilde{p}\right)^{2/3}}\left[C_m Airy_1(\gamma) + C_w Airy_3(\gamma)\right] \tag{V.A_29}$$

The Airy function of the first kind is denoted by $Airy_0$ with derivative $Airy_1$, while the Airy function of the second kind is denoted by $Airy_2$ with derivative $Airy_3$.

In the case $\tilde{p} = 0$,

$$f = C_m \exp\left(i\sqrt{\tilde{k}}z\right) + C_w \exp\left(-i\sqrt{\tilde{k}}z\right) \tag{V.A_30}$$

Taking into account relations (V.A_15), we use the following acoustical potentials ('inc'=incident, 'r'=reflected, 'u'=underground):

$$\Phi^{inc} = A\exp\left(ik_{inc,z}z\right) \tag{V.A_31}$$

$$\Phi^{r} = Q\exp\left(-ik_{inc,z}\left(z - z_a\right)\right) \tag{V.A_32}$$

$$\Psi_{ab}(z) = C_{ms,ab}\exp\left(i\sqrt{\tilde{k}_{s,ab}}\left(z - z_a\right)\right) + C_{ws,ab}\exp\left(-i\sqrt{\tilde{k}_{s,ab}}\left(z - z_b\right)\right) \tag{V.A_33}$$

$$\Phi_{ab}(z) = C_{md,ab}Airy_0\left(\gamma_{d,ab}\right) + C_{wd,ab}Airy_2\left(\gamma_{d,ab}\right) \tag{V.A_34}$$

$$\Psi_{bd}(z) = C_{ms,bd}\, Airy_0\left(\gamma_{s,bd}\right) + C_{ws,bd}\, Airy_2\left(\gamma_{s,bd}\right) \tag{V.A_35}$$

$$\Phi_{bd}(z) = C_{md,bd}\, Airy_0\left(\gamma_{d,bd}\right) + C_{wd,bd}\, Airy_2\left(\gamma_{d,bd}\right) \tag{V.A_36}$$

$$\Psi_{de}(z) = C_{ms,de} \exp\left(i\sqrt{\tilde{k}_{s,de}}\left(z - z_d\right)\right) + C_{ws,de} \exp\left(-i\sqrt{\tilde{k}_{s,de}}\left(z - z_e\right)\right) \tag{V.A_37}$$

$$\Phi_{de}(z) = C_{md,de}\, Airy_0\left(\gamma_{d,de}\right) + C_{wd,de}\, Airy_2\left(\gamma_{d,de}\right) \tag{V.A_38}$$

$$\Psi_u(z) = S \exp\left(ik^s_{u,z}\left(z - z_e\right)\right) \tag{V.A_39}$$

$$\Phi_u(z) = D \exp\left(ik^d_{u,z}\left(z - z_e\right)\right) \tag{V.A_40}$$

The unknown parameters Q, S, D and all $C's$ can now be obtained by creating a continuity matrix that connects the sound fields in each layer. The spots z_a and z_e involve abrupt changes of the sound velocity and density. Hence, we demand continuity of normal stress and displacement there. All other spots involve continuous changes of density and sound velocity, whence we demand continuity of the acoustical potentials (V.A_31-40) and their first derivatives.

The stress tensor is given by

$$\sigma_{ij} = \delta_{ij} \tilde{\lambda}\, \varepsilon_{kk} + 2\, \tilde{\mu}\, \varepsilon_{ij} \tag{V.A_41}$$

where we have used the double suffix Einstein notation convention. The strain tensor ε is denoted by its elements

$$\varepsilon_{ij} = \frac{1}{2}\left[\frac{\partial u_i}{\partial r_j} + \frac{\partial u_j}{\partial r_i} \right] \tag{V.A_42}$$

with displacement vector

$$\mathbf{u} = \nabla\varphi + \nabla \times \boldsymbol{\psi} \tag{V.A_43}$$

The continuity matrix can be found straightforwardly from the continuity conditions given above and taking into account Snell's law stating that the lateral component of the wave vector remains unaltered in the layered system. The result is:

$$[CONT]_{15\times 15}[U]_{15\times 1} = [K]_{15\times 1} \tag{V.A_44}$$

with

$$U = \Big[Q, C_{md,ab}, C_{wd,ab}, C_{ms,ab}, C_{ws,ab}, C_{md,bd}, C_{wd,bd}, C_{ms,bd}, .. \\ ..C_{ws,bd}, C_{md,de}, C_{wd,de}, C_{ms,de}, C_{ws,de}, D, S \Big]^T \tag{V.A_45}$$

$$K = \left[-2\mu_w k_{inc,x} k_{inc,z} \Phi^{inc}, ik_{inc,z} \Phi^{inc}, \left(-\omega^2 \rho_w + 2\mu_w k_{inc,x}^2 \right) \Phi^{inc}, 0, .., 0 \right]^T \tag{V.A_46}$$

and

$$CONT = \begin{bmatrix} c1 & 0 & 0 & 0 \\ c2 & c3 & 0 & 0 \\ 0 & c4 & c5 & 0 \\ 0 & 0 & c6 & c7 \end{bmatrix} \tag{V.A_47}$$

with in [*CONT*] blocks of zeros denoted by '0' and the other elements given in Appendix (V.A_A1- V.A_A7).

NUMERICAL RESULTS FOR INCIDENT INHOMOGENEOUS WAVES

To keep things short, incident inhomogeneous waves are described as pure plane waves, except that their wave vector is complex valued. Hence

$$\mathbf{k}_{inc} = \mathbf{k}_{inc}^1 + i\mathbf{k}_{inc}^2 \tag{V.A_48}$$

with

$$\mathbf{k}_{inc}^2 = \boldsymbol{\alpha}_{inc} - \boldsymbol{\beta}_{inc} \tag{V.A_49}$$

$\boldsymbol{\alpha}_{inc}$ is the damping vector, while $\boldsymbol{\beta}_{inc}$ is the inhomogeneity vector. More properties can be found in numerous articles [30,40]. An example of the amplitude profile and wave vectors of an undamped inhomogeneous wave is shown in the right upper corner of Fig. V.A_1. It is known

that if pure homogeneous plane waves, i.e. $\mathbf{k}_{inc}^2 = 0$, scatter from plane interfaces, that in general inhomogeneous waves will be transmitted into the opposing medium if damping is present. However, it has also been shown before that incident inhomogeneous waves can deliver some insight into what will happen to the profile of bounded beams if they are reflected from the interface [41]. The main problem however with the formation of bounded beams by a superposition of inhomogeneous waves is that, besides its great opportunities to describe and understand beam displacements like the Schoch effect, the propagation of such mathematical beams is often not very convenient. Since it is our aim to depict exactly how a transmitted bounded beam propagates into the layers, we choose not to decompose bounded beams into inhomogeneous waves, but into pure plane waves using the Fourier decomposition.
Nevertheless, a limited study of the reflection coefficient of inhomogeneous waves gives us the opportunity to predict already some phenomena that will occur in the next paragraph, where the reflection and transmission of bounded beams are studied. As an example, we have taken the parameters of Table V.A_I and Table V.A_II, which are graphically given in Fig. V.A_2.

Table V.A_I: ***Boundary values at some particular spots in the layered system***

Spot	Position [m]	Density [kg/m^3]	Longitudinal velocity [m/s]
z_0	0. 1	-	-
z_a	0	1050	1490
z_b	-0.45	-	-
z_d	-0.50	-	-
z_e	-1	2500	2500

Table V.A_II: **Boundary values in some particular intervals in the layered system**

Interval	Density [kg/m^3]	Longitudinal velocity [m/s]	Shear velocity [m/s]
$z_0 \rightarrow z_a$	1050	1480	0
$z_a \rightarrow z_b$	-	-	100
$z_d \rightarrow z_e$	-	-	1500
Underground (hard bottom)	3000	3000	2000

Furthermore, we have solely considered (strong) damping in the underground, not in the other layers. In Fig. V.A_3, a frequency of 150 kHz is applied. It is seen that the reflection coefficient (shown as its intensity in dB) as a function of the angle of incidence (defined in Fig. V.A_1) and as a function of the incident inhomogeneity (a positive inhomogeneity β_{inc} is also shown in Fig. V.A_1), shows an elevated intensity (peaks) in some regions and much smaller intensity in other regions.

This phenomenon also appears if the interaction of inhomogeneous waves with metal plates is considered. It is well known that a reflection coefficient less than unity shifts an inhomogeneous wave to the direction in which it shows exponential growth, while a reflection coefficient exceeding unity shifts an inhomogeneous wave to direction in which it shows exponential decay. Furthermore, the smaller the value of $|\beta_{inc}|$, the larger the shift to left or right. Because the reflection coefficients for positive inhomogeneities is nowhere negative (in dB), it can already be concluded that inhomogeneous waves will never be shifted in the positive x-direction. Hence, a backward beam shift will never occur.

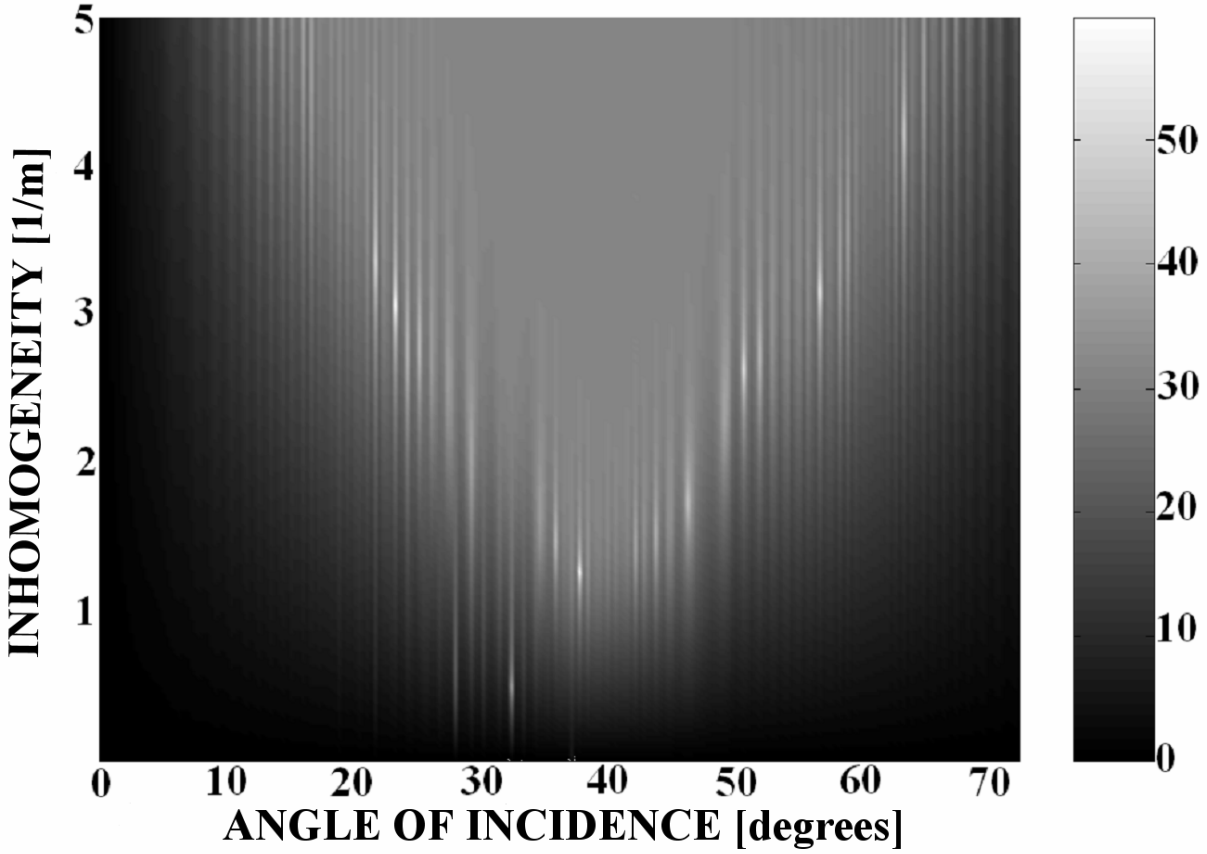

Fig. V.A_3: ***Intensity in dB of reflected inhomogeneous waves as a function of the angle of incidence and inhomogeneity***

It is seen in Fig. V.A_3 that, at 38.07^0, an amplitude peak occurs for very low inhomogeneity. Hence, a very strong beam shift can be expected there. Furthermore, all other peaks for relatively low inhomogeneities are roughly situated in between 20^0 and 50^0. It can therefore be expected that strong beam shifts will occur within that interval of incidence angles and that the strongest shift will appear at 38.07^0.

NUMERICAL RESULTS FOR INCIDENT BOUNDED BEAMS

It is worthwhile to present the total displacement field inside the rheological system in order to visualize how an incident bounded beam propagates and scatters through the different layers. We know that each incident inhomogeneous wave generates the acoustical potentials (V.A_31-40). If we take into account (V.A_31-40) and (V.A_43), then the displacement fields can be obtained. They are listed in the appendix (V.A_A25- V.A_A29). A continuous Gaussian beam of frequency 150kHz and width 0.3m, decomposed into plane waves using the Fourier decomposition, is impinging at the spot $(z = z_a, x = 0)$. This is schematically visualized in Fig. V.A_1. The thereby generated normalized amplitude of the particle displacements along $z = z_a$ are depicted in Fig. V.A_4 as a function of the angle of incidence.
Hence, the incident beam can be noticed at x=0 and also the reflected sound is visible. Furthermore, it is noticed that the reflected 'beam' undergoes a sweep to larger distances and then back to smaller distances as the angle of incidence grows. This sweep exceedingly occurs in the interval between 20^0 and 50^0 and is strongest at 38.07^0 as was predicted in the previous paragraph.

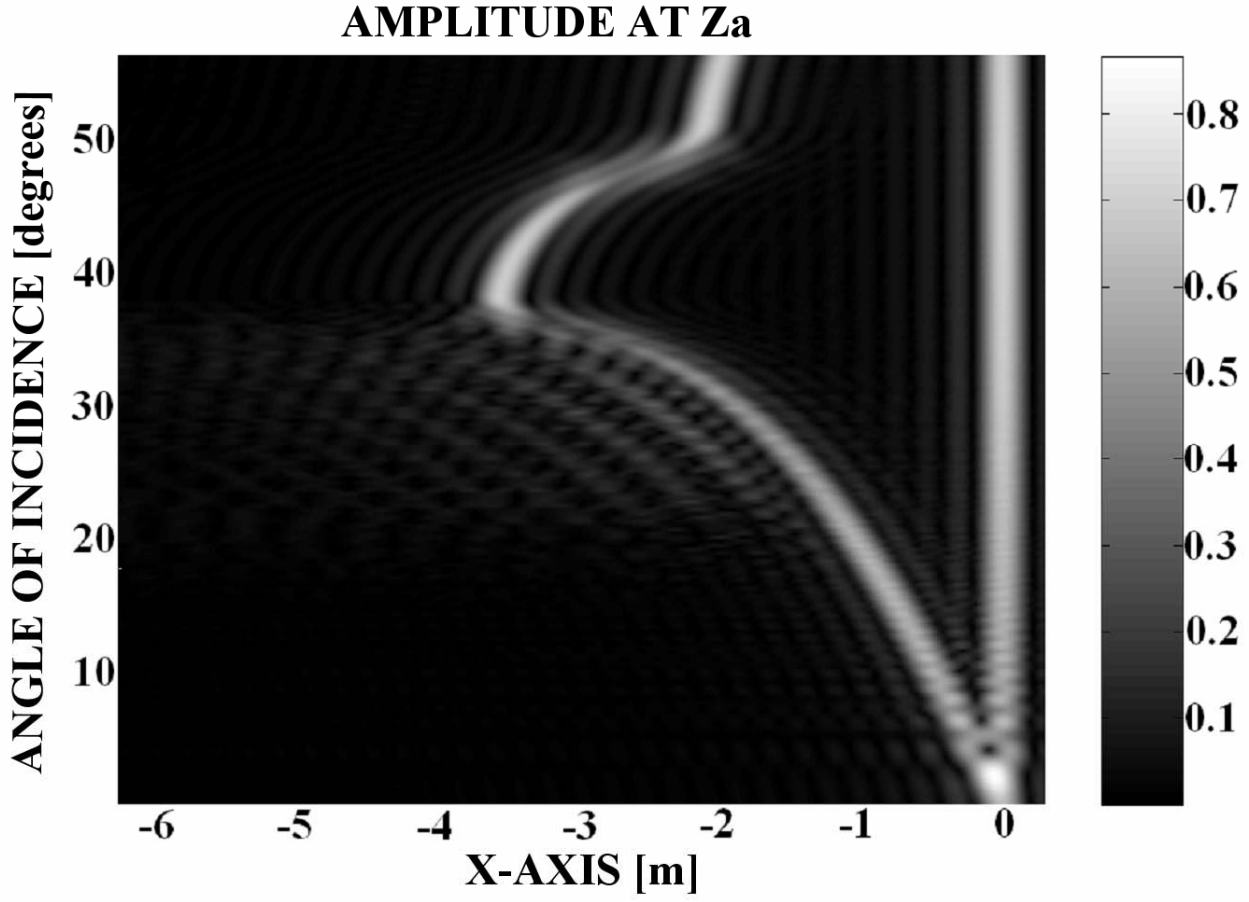

Fig. V.A_4: ***Total amplitude at $z = z_a$ as a function of the lateral distance (x-axis) and as a function of the angle of incidence. The incident beam impinges the layers at $(z = z_a, x = 0)$.***

The phenomenon that causes this sweep is explained below, where the physical appearance of the bounded beam inside the layers is depicted. In Figs V.A_5-10, the normalized amplitude of the particle displacements is depicted inside the layers and for angles of incidence corresponding to some remarkable spots in Fig. V.A_4. It is seen from Fig. V.A_5 that for normal incidence, there is complete transmission through the transition layer.
This is the reason why in echo sounding the transition layer is not detectable. From Fig. V.A_6 and Fig. V.A_7, it is seen that at more or less randomly chosen angles 7.36^0 respectively 27.93^0 , part of the sound is transmitted through the transition layer, while part is reflected.
This shows that, even though there is no abrupt change but a strong continuous change in physical parameters, contrary to normally incident sound, obliquely incident sound is susceptible to the presence of the transition zone. There is however an angle of 38.07^0 at which the transition layer let incident sound pass completely. It is at this angle that a large beam sweep (or shift) is visible in Fig. V.A_4 and Fig. V.A_8.
The sweep happens because the bounded beam propagates over a large distance up to the underground, without being affected by the transition layer that crosses its path. For larger angles, incident sound is reflected (see Fig. V.A_9) again in the transition layer. Furthermore, there is an angle of 55.53^0 (see Fig. V.A_10) at which the incident sound is perfectly reflected from the transition layer.

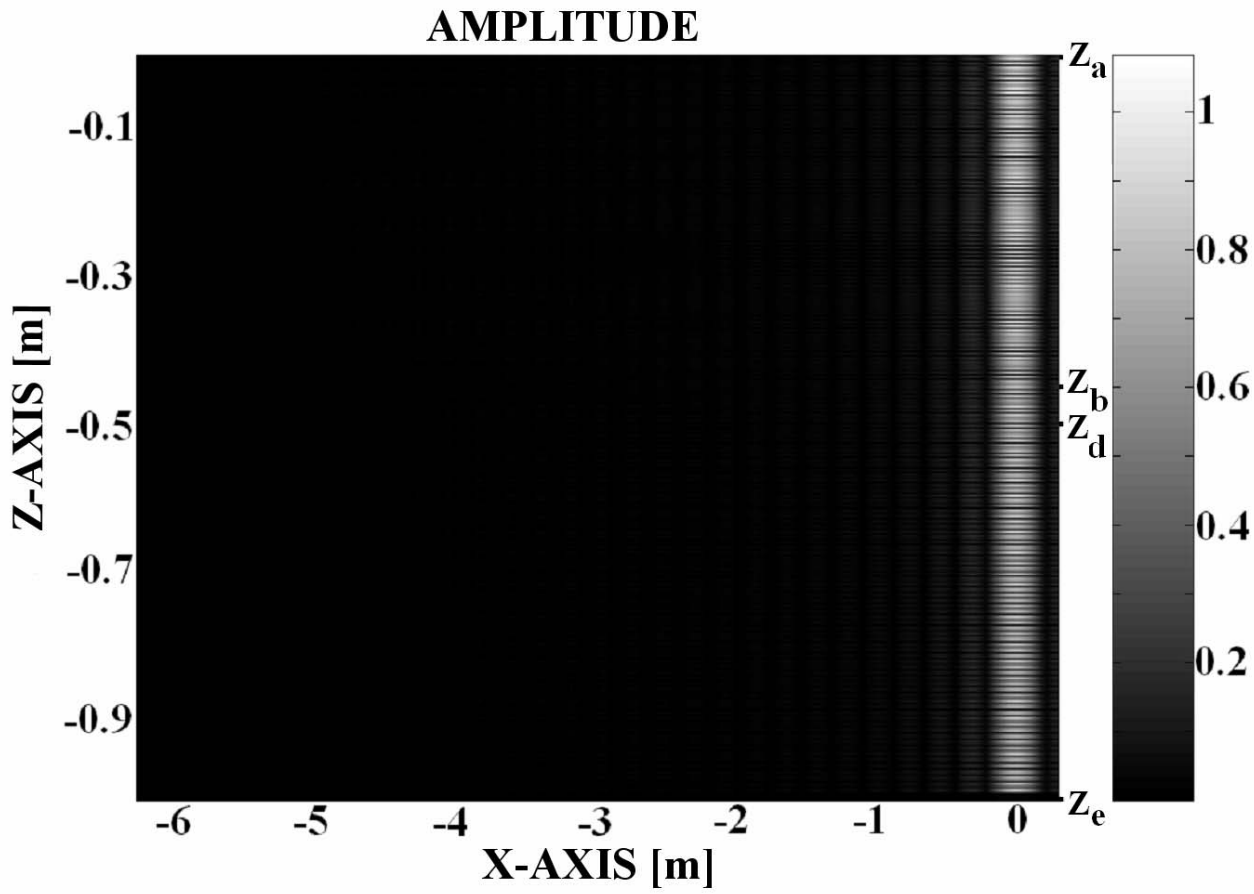

Fig. V.A_5: ***Total sound field inside the layers for angle of incidence 0^0. This situation corresponds with classical echo sounding. The transition zone has no influence on the reflected beam.***

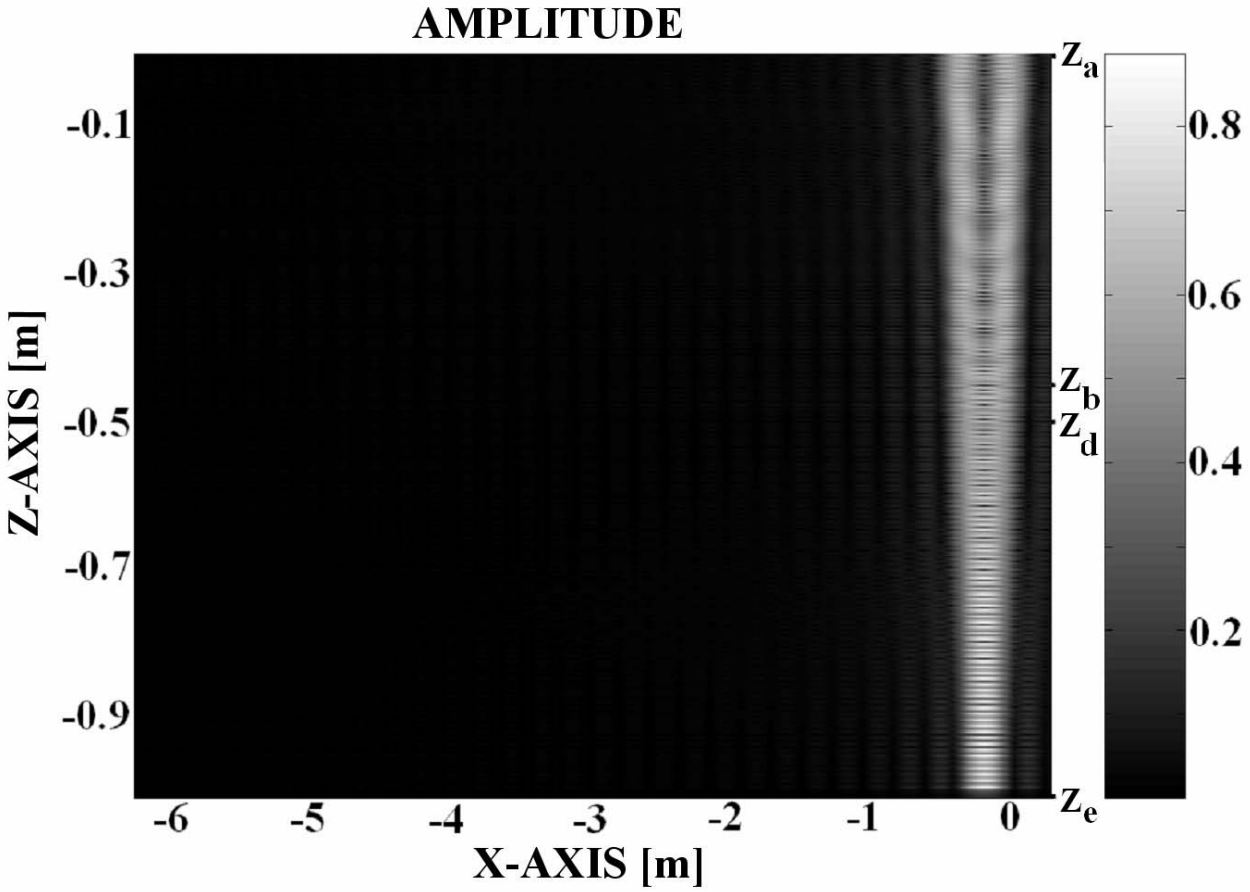

Fig. V.A_6: ***Total sound field inside the layers for angle of incidence*** 7.36^{0} .

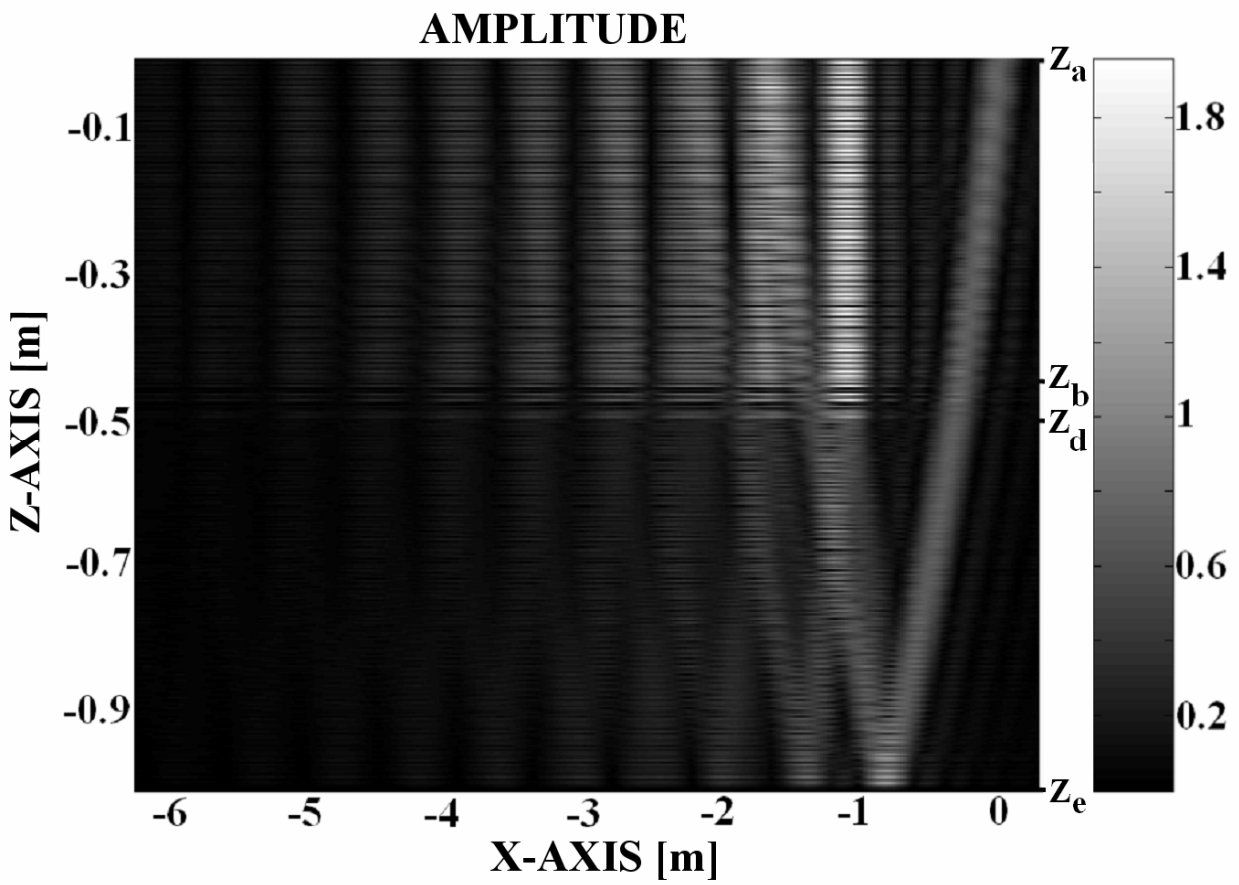

Fig. V.A_7: ***Total sound field inside the layers for angle of incidence 27.93^0. It is clear that, contrary to Fig. V.A_5, the transition zone influences the reflected beam.***

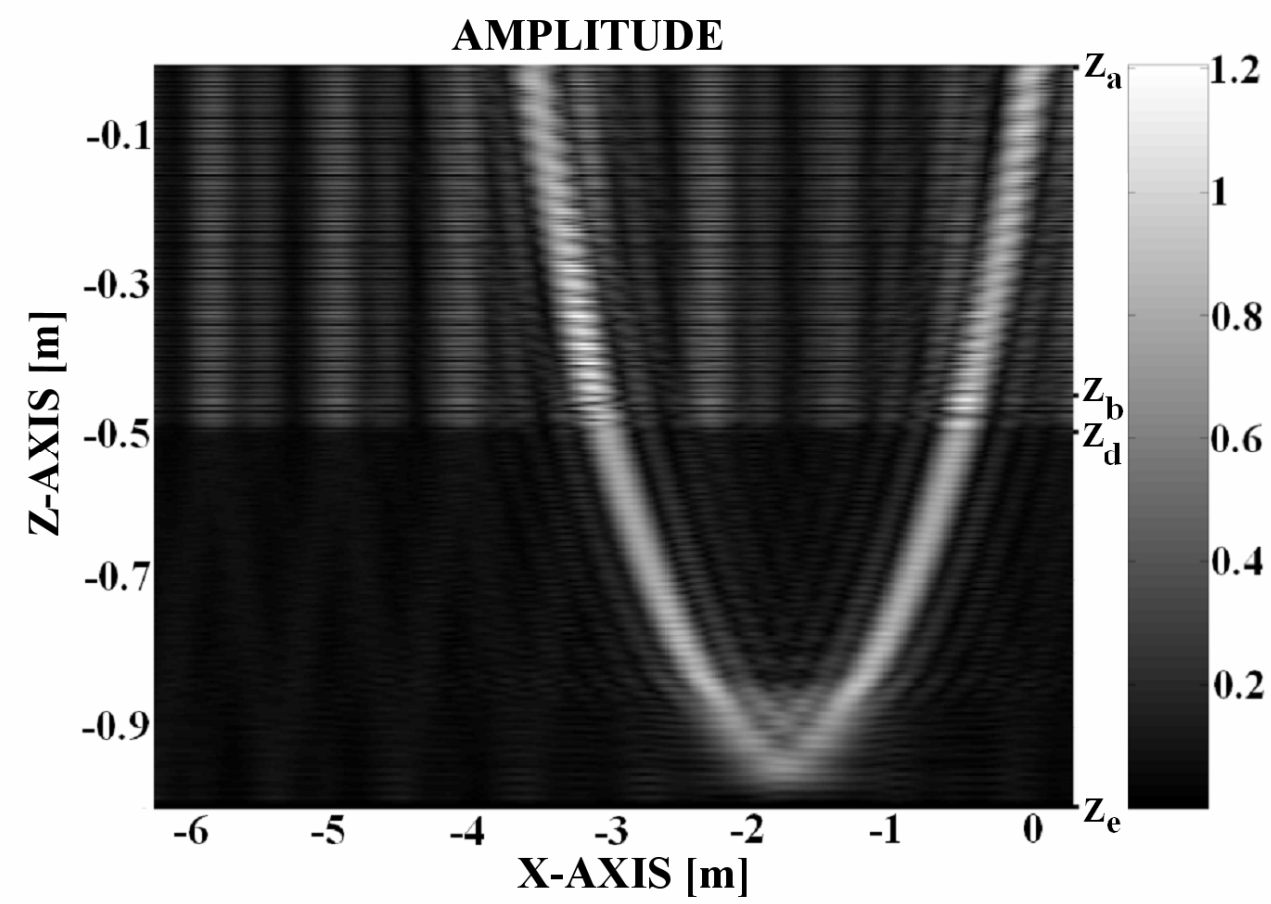

Fig. V.A_8: ***Total sound field inside the layers for angle of incidence 38.07^0. This corresponds with the maximum sweep in Fig. V.A_4.***

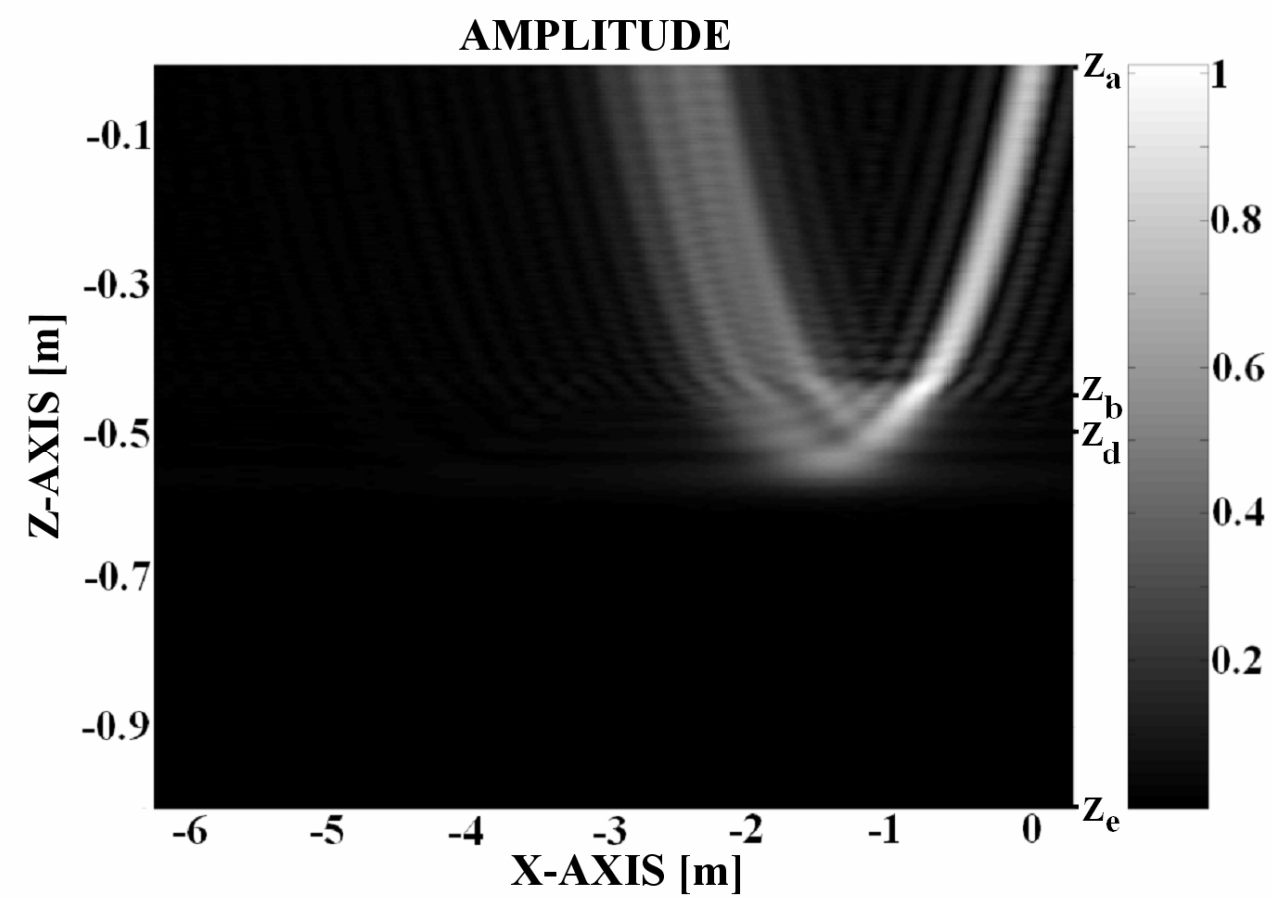

Fig. V.A_9: ***Total sound field inside the layers for angle of incidence 48.04^0. There is no penetration into the non-navigable mud.***

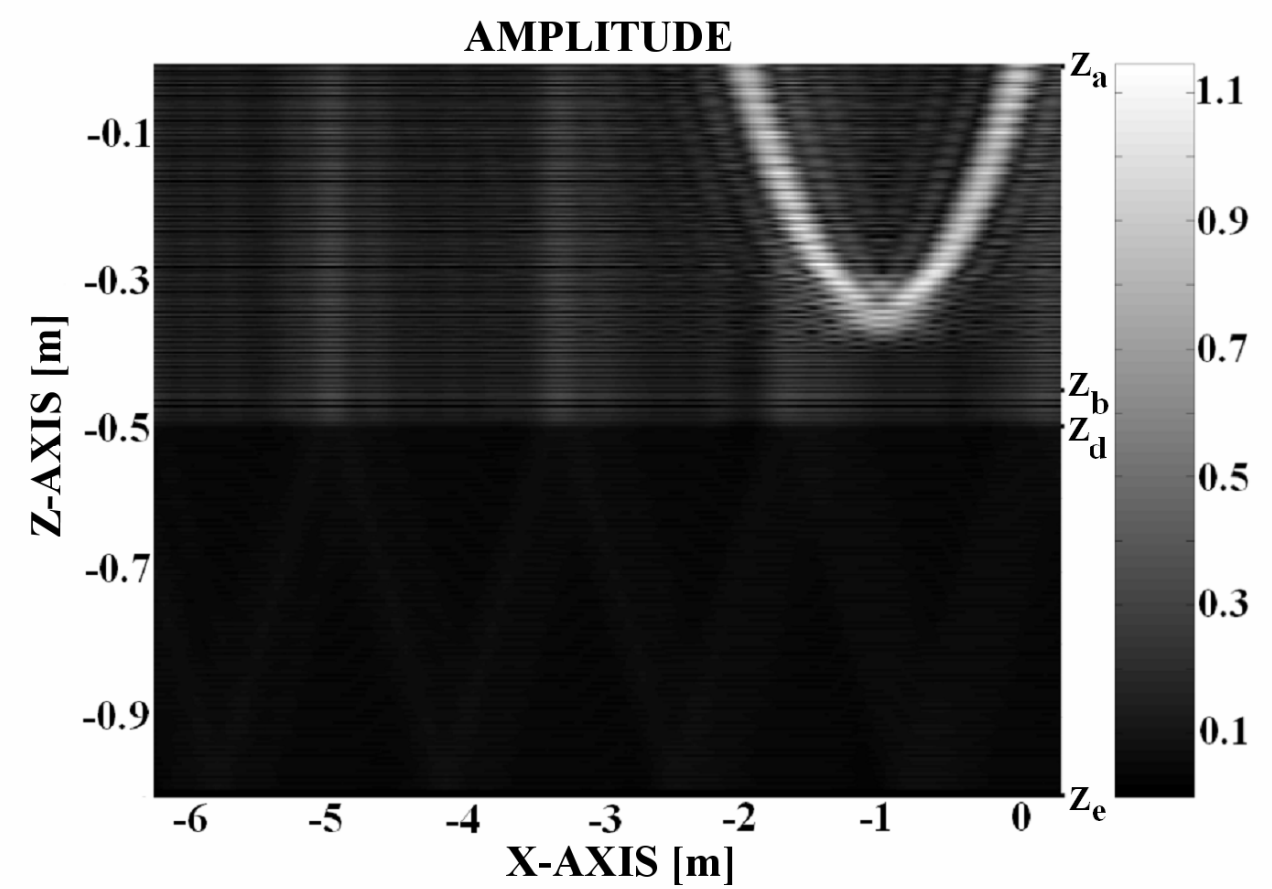

Fig. V.A_10: ***Total sound field inside the layers for angle of incidence*** 55.53^0 .

In the shipping and the dredging industry, it is important to find out where exactly the transition zone is situated in order to determine the depth of the nautical bottom. Even though the physical parameters that are incorporated here do not perfectly correspond to the parameters of physical mud, it is interesting to show that the position of the transition zone influences the reflected beam profile for oblique incidence.

Therefore we have repeated the calculation of Fig. V.A_4 in Fig. V.A_11, except for the only difference that the transition zone is now 10cm deeper, i.e. $z_b = -0.55m$ and $z_d = -0.60m$. Comparison of Fig. V.A_11 with Fig. V.A_4 shows that the reflected beam profile is indeed influenced by the depth of the transition zone, especially in the practicable range of small angles of incidence. The study of the reflected beam profile is hence a promising technique for determination of the nautical bottom. Further details are beyond the scope of this section.

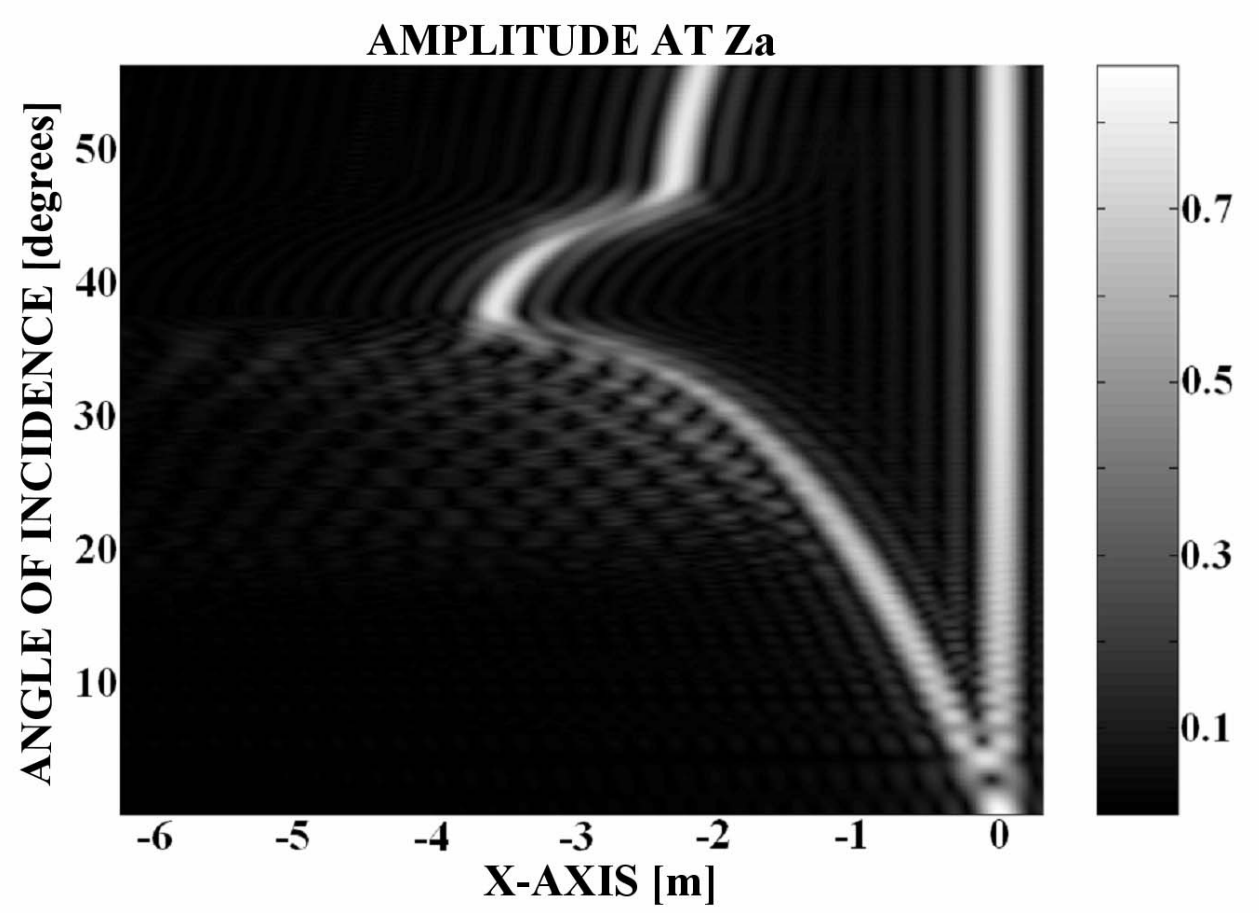

Fig. V.A_11: ***This figure is equal to Fig. V.A_4, except that here*** $z_b = -0.55m$ ***and*** $z_d = -0.60m$***, which means that the transition layer is 10 cm lower. The difference is noticeable in the reflected beam pattern and can be used to measure the nautical depth in harbors.***

CONCLUDING REMARKS

Contrary to existing models [42-43] for 'discrete layers of homogeneous sediment material', a model is developed that is susceptible to simulate the interaction of sound with a liquid showing Bingham features (like mud), where layers of very fine sediment are involved possessing 'continuously varying material parameters', situated in between an ideal liquid and a hard solid. It is shown that the reflection coefficient for incident inhomogeneous waves shows peaks exceeding unity which are also present in earlier studies on discontinuously layered materials such as coated metal plates swamped in water. A qualitative study of these peaks has revealed strong beam displacements at certain angles. This was numerically confirmed by studying the interaction of bounded beams with the rheological system using the Fourier decomposition. This work shows that strong varying physical properties inside a continuously layered system may have serious consequences on impinging sound, such as total reflection or total transmission. Furthermore it is shown that the reflected beam profile for oblique incidence is influenced by the nautical depth. This may have important applications in the shipping

and dredging industry.

APPENDIX

The different elements of the continuity matrix given in (V.A_47) are obtained and given in (V.A_A1- V.A_A7). For brevity, the symbol ‘a’ is used instead of ‘Airy’, in the expressions in this appendix.

$$c1=\begin{bmatrix} -2\mu_w k_{inc,x} k_{inc,z} & P_{md,ab,0} \\ ik_{inc,z} & P_{md,ab,1} \\ \rho_w\omega^2 - 2\mu_w k_{inc,x}^2 & P_{md,ab,2} \end{bmatrix}$$

$$\begin{bmatrix} P_{wd,ab,0} & \mu_{ab}\left(z_a\right)\left[-k_{inc,x}^2 + g_{s,ab}\left(z_a\right)\right] & P_{ws,ab,0} \\ P_{wd,ab,1} & ik_{inc,x} & P_{ws,ab,1} \\ P_{wd,ab,2} & -2\mu_{ab}\left(z_a\right)k_{inc,x}\sqrt{\tilde{k}_{s,ab}} & P_{ws,ab,2} \end{bmatrix} \qquad \text{(V.A\_A1)}$$

$$c2=\begin{bmatrix} 0 & 0 & 0 \\ 0 & a_0\left(\gamma_{d,ab}\left(z_b\right)\right) & a_2\left(\gamma_{d,ab}\left(z_b\right)\right) \\ 0 & 0 & 0 \\ 0 & -\dfrac{\tilde{p}_{d,ab}\, a_1\left(\gamma_{d,ab}\left(z_b\right)\right)}{\left(-\tilde{p}_{d,ab}\right)^{2/3}} & -\dfrac{\tilde{p}_{d,ab}\, a_3\left(\gamma_{d,ab}\left(z_b\right)\right)}{\left(-\tilde{p}_{d,ab}\right)^{2/3}} \end{bmatrix}$$

$$\begin{bmatrix} \exp\left(i\sqrt{\tilde{k}_{s,ab}}\left(z_b - z_a\right)\right) & 1 \\ 0 & 0 \\ i\sqrt{\tilde{k}_{s,ab}}\exp\left(i\sqrt{\tilde{k}_{s,ab}}\left(z_b - z_a\right)\right) & -i\sqrt{\tilde{k}_{s,ab}} \\ 0 & 0 \end{bmatrix} \qquad \text{(V.A\_A2)}$$

(V.A_A3)

$$c3 = \begin{bmatrix} 0 & 0 \\ -a_0\left(\gamma_{d,bd}\left(z_b\right)\right) & -a_2\left(\gamma_{d,bd}\left(z_b\right)\right) \\ 0 & 0 \\ \dfrac{\tilde{p}_{d,bd}\, a_1\left(\gamma_{d,bd}\left(z_b\right)\right)}{\left(-\tilde{p}_{d,bd}\right)^{2/3}} & \dfrac{\tilde{p}_{d,bd}\, a_3\left(\gamma_{d,bd}\left(z_b\right)\right)}{\left(-\tilde{p}_{d,bd}\right)^{2/3}} \\ -a_0\left(\gamma_{s,bd}\left(z_b\right)\right) & -a_2\left(\gamma_{s,bd}\left(z_b\right)\right) \\ 0 & 0 \\ \dfrac{\tilde{p}_{s,bd}\, a_1\left(\gamma_{s,bd}\left(z_b\right)\right)}{\left(-\tilde{p}_{s,bd}\right)^{2/3}} & \dfrac{\tilde{p}_{s,bd}\, a_3\left(\gamma_{s,bd}\left(z_b\right)\right)}{\left(-\tilde{p}_{s,bd}\right)^{2/3}} \\ 0 & 0 \end{bmatrix}$$

(V.A_A4)

$$c4 = \begin{bmatrix} 0 & 0 \\ a_0\left(\gamma_{d,bd}\left(z_d\right)\right) & a_2\left(\gamma_{d,bd}\left(z_d\right)\right) \\ 0 & 0 \\ -\dfrac{\tilde{p}_{d,bd}\, a_1\left(\gamma_{d,bd}\left(z_d\right)\right)}{\left(-\tilde{p}_{d,bd}\right)^{2/3}} & -\dfrac{\tilde{p}_{d,bd}\, a_3\left(\gamma_{d,bd}\left(z_d\right)\right)}{\left(-\tilde{p}_{d,bd}\right)^{2/3}} \\ a_0\left(\gamma_{s,bd}\left(z_d\right)\right) & a_2\left(\gamma_{s,bd}\left(z_d\right)\right) \\ 0 & 0 \\ -\dfrac{\tilde{p}_{s,bd}\, a_1\left(\gamma_{s,bd}\left(z_d\right)\right)}{\left(-\tilde{p}_{s,bd}\right)^{2/3}} & -\dfrac{\tilde{p}_{s,bd}\, a_3\left(\gamma_{s,bd}\left(z_d\right)\right)}{\left(-\tilde{p}_{s,bd}\right)^{2/3}} \\ 0 & 0 \end{bmatrix}$$

(V.A_A5)

$$c5 = \begin{bmatrix} 0 & 0 \\ -a_0\left(\gamma_{d,de}\left(z_d\right)\right) & -a_2\left(\gamma_{d,de}\left(z_d\right)\right) \\ 0 & 0 \\ \dfrac{\tilde{p}_{d,de}\, a_1\left(\gamma_{d,de}\left(z_d\right)\right)}{\left(-\tilde{p}_{d,de}\right)^{2/3}} & \dfrac{\tilde{p}_{d,de}\, a_3\left(\gamma_{d,de}\left(z_d\right)\right)}{\left(-\tilde{p}_{d,de}\right)^{2/3}} \end{bmatrix} \begin{bmatrix} -1 & -\exp\left(-i\sqrt{\tilde{k}_{s,de}}\left(z_d - z_e\right)\right) \\ 0 & 0 \\ -i\sqrt{\tilde{k}_{s,de}} & i\sqrt{\tilde{k}_{s,de}}\exp\left(-i\sqrt{\tilde{k}_{s,de}}\left(z_d - z_e\right)\right) \\ 0 & 0 \end{bmatrix}$$

(V.A_A6)

$$c6 = \begin{bmatrix} ik_{inc,x}\, a_0\left(\gamma_{d,de}\left(z_e\right)\right) & ik_{inc,x}\, a_2\left(\gamma_{d,de}\left(z_e\right)\right) \\ -\dfrac{\tilde{p}_{d,de}\, a_1\left(\gamma_{d,de}\left(z_e\right)\right)}{\left(-\tilde{p}_{d,de}\right)^{2/3}} & -\dfrac{\tilde{p}_{d,de}\, a_3\left(\gamma_{d,de}\left(z_e\right)\right)}{\left(-\tilde{p}_{d,de}\right)^{2/3}} \\ P_{md,de,13} & P_{wd,de,13} \\ P_{md,de,14} & P_{wd,de,14} \end{bmatrix} \begin{bmatrix} -i\sqrt{\tilde{k}_{s,de}}\exp\left(i\sqrt{k_{s,de}}\left(z_e - z_d\right)\right) & i\sqrt{\tilde{k}_{s,de}} \\ ik_{inc,x}\exp\left(i\sqrt{\tilde{k}_{s,de}}\left(z_e - z_d\right)\right) & ik_{inc,x} \\ P_{ms,de,13} & P_{ws,de,13} \\ P_{ms,de,14} & P_{ws,de,14} \end{bmatrix}$$

$$c7 = \begin{bmatrix} -ik_{inc,x} & ik^{s}_{u,z} \\ -ik^{d}_{u,z} & -ik_{inc,x} \\ 2\mu_u k_{inc,x} k^{d}_{u,z} & \mu_u\left(k^{2}_{inc,x} - \mu_u g_{s,u}\right) \\ \lambda_u k^{2}_{inc,x} + \left(\lambda_u + 2\mu_u\right) g_{d,u} & 2\mu_u k_{inc,x} k^{s}_{u,z} \end{bmatrix} \tag{V.A_A7}$$

with in (V.A_A1- V.A_A7):

$$P_{md,ab,0} = -2i\mu_{ab}\left(z_a\right) k_{inc,x} \frac{\tilde{p}_{d,ab}\, a_1\left(\gamma_{d,ab}\left(z_a\right)\right)}{\left(-\tilde{p}_{d,ab}\right)^{2/3}} \tag{V.A_A8}$$

$$P_{wd,ab,0} = -2i\mu_{ab}\left(z_a\right) k_{inc,x} \frac{\tilde{p}_{d,ab}\, a_3\left(\gamma_{d,ab}\left(z_a\right)\right)}{\left(-\tilde{p}_{d,ab}\right)^{2/3}} \tag{V.A_A9}$$

$$P_{ws,ab,0} = \mu_{ab}\left(z_a\right)\left[-k^{2}_{inc,x} + g_{s,ab}\left(z_a\right)\right] \exp\left(-i\sqrt{\tilde{k}_{s,ab}}\left(z_a - z_b\right)\right) \tag{V.A_A10}$$

$$P_{md,ab,1} = -\frac{\tilde{p}_{d,ab}}{\left(-\tilde{p}_{d,ab}\right)^{2/3}} a_1\left(\gamma_{d,ab}\left(z_a\right)\right) \tag{V.A_A11}$$

$$P_{wd,ab,1} = -\frac{\tilde{p}_{d,ab}}{\left(-\tilde{p}_{d,ab}\right)^{2/3}} a_3\left(\gamma_{d,ab}\left(z_a\right)\right) \tag{V.A_A12}$$

$$P_{ws,ab,1} = ik_{inc,x} \exp\left(-i\sqrt{\tilde{k}_{s,ab}}\left(z_a - z_b\right)\right) \tag{V.A_A13}$$

$$P_{md,ab,2} = \left[-\lambda_{ab}\left(z_a\right)k_{inc,x}^2 - \left(\lambda_{ab}\left(z_a\right) + 2\mu_{ab}\left(z_a\right)\right)g_{d,ab}\left(z_a\right)\right] a_0\left(\gamma_{d,ab}\left(z_a\right)\right) \tag{V.A_A14}$$

$$P_{wd,ab,2} = \left[-\lambda_{ab}\left(z_a\right)k_{inc,x}^2 - \left(\lambda_{ab}\left(z_a\right) + 2\mu_{ab}\left(z_a\right)\right)g_{d,ab}\left(z_a\right)\right] a_2\left(\gamma_{d,ab}\left(z_a\right)\right) \tag{V.A_A15}$$

$$P_{ws,ab,2} = 2\mu_{ab}\left(z_a\right)k_{inc,x}\sqrt{\tilde{k}_{s,ab}} \exp\left(-i\sqrt{\tilde{k}_{s,ab}}\left(z_a - z_b\right)\right) \tag{V.A_A16}$$

$$P_{md,de,13} = -2i\mu_{de}\left(z_e\right)k_{inc,x}\frac{\tilde{p}_{d,de}}{\left(-\tilde{p}_{d,de}\right)^{2/3}} a_1\left(\gamma_{d,de}\left(z_e\right)\right) \tag{V.A_A17}$$

$$P_{wd,de,13} = -2i\mu_{de}\left(z_e\right)k_{inc,x}\frac{\tilde{p}_{d,de}}{\left(-\tilde{p}_{d,de}\right)^{2/3}} a_3\left(\gamma_{d,de}\left(z_e\right)\right) \tag{V.A_A18}$$

$$P_{ms.de,13} = \mu_{de}\left(z_e\right)\left[-k_{inc,x}^2 + g_{s,de}\left(z_e\right)\right] \exp\left(i\sqrt{\tilde{k}_{s,de}}\left(z_e - z_d\right)\right) \tag{V.A_A19}$$

$$P_{ws,de,13} = \mu_{de}\left(z_e\right)\left[-k_{inc,x}^2 + g_{s,de}\left(z_e\right)\right] \tag{V.A_A20}$$

$$P_{md,de,14} = -\left[\left(\lambda_{de}\left(z_e\right) + 2\mu_{de}\left(z_e\right)\right)g_{d,de}\left(z_e\right) + \lambda_{de}\left(z_e\right)k_{inc,x}^2\right] a_0\left(\gamma_{d,de}\left(z_e\right)\right) \tag{V.A_A21}$$

$$P_{wd,de,14} = -\left[\left(\lambda_{de}\left(z_e\right)+2\mu_{de}\left(z_e\right)\right)g_{d,de}\left(z_e\right)+\lambda_{de}\left(z_e\right)k_{inc,x}^2\right]a_2\left(\gamma_{d,de}\left(z_e\right)\right) \tag{V.A_A22}$$

$$P_{ms,de,14} = -2\mu_{de}\left(z_e\right)k_{inc,x}\sqrt{\tilde{k}_{s,de}}\exp\left(i\sqrt{\tilde{k}_{s,de}}\left(z_e-z_d\right)\right) \tag{V.A_A23}$$

$$P_{ws,de,14} = 2\mu_{de}\left(z_e\right)k_{inc,x}\sqrt{\tilde{k}_{s,de}} \tag{V.A_A24}$$

The particle displacement fields within the different layers of the rheological system are given as:

$$\mathbf{u}_w = ik_{inc,x}\left[Q\exp\left(-ik_{inc,z}\left(z-z_a\right)\right)+A\exp\left(ik_{inc,z}\left(z-z_0\right)\right)\right]\exp\left(ik_{inc,x}x\right)\mathbf{e}_x \tag{V.A_A25}$$
$$+ik_{inc,z}\left[-Q\exp\left(-ik_{inc,z}\left(z-z_a\right)\right)+A\exp\left(ik_{inc,z}\left(z-z_0\right)\right)\right]\exp(ik_{inc,x}x)\mathbf{e}_z$$

$$\mathbf{u}_{ab} = ik_{inc,x}\left(C_{md,ab}a_0\left(\gamma_{d,ab}\right)+C_{wd,ab}a_2\left(\gamma_{d,ab}\right)\right)\exp\left(ik_{inc,x}x\right)\mathbf{e}_x \tag{V.A_A26}$$
$$-i\sqrt{\tilde{k}_{s,ab}}$$
$$\times\left(C_{ms,ab}\exp\left(i\sqrt{\tilde{k}_{s,ab}}\left(z-z_a\right)\right)-C_{ws,ab}\exp\left(-i\sqrt{\tilde{k}_{s,ab}}\left(z-z_b\right)\right)\right)$$
$$\times\exp\left(ik_{inc,x}x\right)\mathbf{e}_x$$
$$-\frac{\tilde{p}_{d,ab}}{\left(-\tilde{p}_{d,ab}\right)^{2/3}}\exp\left(ik_{inc,x}x\right)\left(C_{md,ab}a_1\left(\gamma_{d,ab}\right)+C_{wd,ab}a_3\left(\gamma_{d,ab}\right)\right)\mathbf{e}_z$$
$$+ik_{inc,x}\exp\left(ik_{inc,x}x\right)\left(C_{ms,ab}\exp\left(i\sqrt{\tilde{k}_{s,ab}}\left(z-z_a\right)\right)\right)\mathbf{e}_z$$
$$+ik_{inc,x}\exp\left(ik_{inc,x}x\right)\left(C_{ws,ab}\exp\left(-i\sqrt{\tilde{k}_{s,ab}}\left(z-z_b\right)\right)\right)\mathbf{e}_z$$

$$\mathbf{u}_{bd} = ik_{inc,x}\left(C_{md,bd}a_0\left(\gamma_{d,bd}\right)+C_{wd,bd}a_2\left(\gamma_{d,bd}\right)\right)\exp\left(ik_{inc,x}x\right)\mathbf{e}_x \qquad \text{(V.A\_A27)}$$

$$+\frac{\tilde{p}_{s,bd}}{\left(-\tilde{p}_{s,bd}\right)^{2/3}}\exp\left(ik_{inc,x}x\right)\left(C_{ms,bd}a_1\left(\gamma_{s,bd}\right)+C_{ws,bd}a_3\left(\gamma_{s,bd}\right)\right)\mathbf{e}_x$$

$$-\frac{\tilde{p}_{d,bd}}{\left(-\tilde{p}_{d,bd}\right)^{2/3}}\exp\left(ik_{inc,x}x\right)\left(C_{md,bd}a_1\left(\gamma_{d,bd}\right)+C_{wd,bd}a_3\left(\gamma_{d,bd}\right)\right)\mathbf{e}_z$$

$$+ik_{inc,x}\exp\left(ik_{inc,x}x\right)\left(C_{ms,bd}a_0\left(\gamma_{s,bd}\right)+C_{ws,bd}a_2\left(\gamma_{s,bd}\right)\right)\mathbf{e}_z$$

$$\mathbf{u}_{de} = ik_{inc,x}\left(C_{md,de}a_0\left(\gamma_{d,de}\right)+C_{wd,de}a_2\left(\gamma_{d,de}\right)\right)\exp\left(ik_{inc,x}x\right)\mathbf{e}_x \qquad \text{(V.A\_A28)}$$

$$-i\sqrt{\tilde{k}_{s,de}}$$

$$\times\left(C_{ms,de}\exp\left(i\sqrt{\tilde{k}_{s,de}}\left(z-z_d\right)\right)-C_{ws,de}\exp\left(-i\sqrt{\tilde{k}_{s,de}}\left(z-z_e\right)\right)\right)$$

$$\times\exp\left(ik_{inc,x}x\right)\mathbf{e}_x$$

$$-\frac{\tilde{p}_{d,de}}{\left(-\tilde{p}_{d,de}\right)^{2/3}}\exp\left(ik_{inc,x}x\right)\left(C_{md,de}a_1\left(\gamma_{d,de}\right)+C_{wd,de}a_3\left(\gamma_{d,de}\right)\right)\mathbf{e}_z$$

$$+ik_{inc,x}\exp\left(ik_{inc,x}x\right)\left(C_{ms,de}\exp\left(i\sqrt{\tilde{k}_{s,de}}\left(z-z_d\right)\right)\right)\mathbf{e}_z$$

$$+ik_{inc,x}\exp\left(ik_{inc,x}x\right)\left(C_{ws,de}\exp\left(-i\sqrt{\tilde{k}_{s,de}}\left(z-z_e\right)\right)\right)\mathbf{e}_z$$

$$\mathbf{u}_u = \left[ik_{inc,x} D \exp\left(ik^d_{u,z} \left(z - z_e \right) \right) - ik^s_{u,z} S \exp\left(ik^s_{u,z} \left(z - z_e \right) \right) \right] \exp\left(ik_{inc,x} x \right) \mathbf{e}_x + \left[ik^d_{u,z} D \exp\left(ik^d_{u,z} \left(z - z_e \right) \right) + ik_{inc,x} S \exp\left(ik^s_{u,z} \left(z - z_e \right) \right) \right] \exp\left(ik_{inc,x} x \right) \mathbf{e}_z \quad \text{(V.A_A29)}$$

REFERENCES

1. H. Okamura, K. Maekawa, K. Ozawa, "High performance Concrete", Gihou-Dou Pub., 1993 (in Japanese)
2. F. DeLarrard, C. Hu, T. Sedran, J. C. Sitzkar, M. Joly, F. Claux, F. Derkx, "A New Rheometer for Soft-to-Fluid Fresh Concrete", ACI Materials Journal, Vol. 94 (3), May-June, 234-243, 1997
3. M. Dragoni, M. Bonafede, E. Boschi, "Downslope flow models of Bingham liquid : implications for lava flows", J. Vulcanol. Geotherm. Res. 30, 305-325, 1986
4. Tracy K. P. Gregg, Susan E. H. Sakimoto, "Inside the black box: velocity distributions and flow rates in lava channels from laboratory, analytic and computational fluid dynamics methods", Lunar and Planetary science XXIX p1499, Proceedings of 'Lunar and Planetary Science Conference', Houston, Texas 1998
5. Earl Brown, "What is bottom?", Soundings, Lighthouse journal of the Canadian Hydrographic Association (CHA) edition 60, 2002
6. Wolfgang Dasch and Rewert Wurpts , "Isoviscs as Useful Parameters for Describing Sedimentation",Terra et Aqua International Journal on Public Works, Ports and Waterways Developments 82, 2001
7. R. Wurpts ,"The Question of Definition of the Nautical Depth in Fluid Mud by the Aid of Rheological Properties", Proceedings of the 15th World Dredging Congress 'Dredging into the 21st century', 457, 1998
8. XU Jian-yi, YUAN Jian-zhong. "Study on the Fluid Mud in the Yangtze Estuary", Journal of Sediment Research 3, 2001
9. Stanislas Wartel, "Mud layers and cyclic sedimentation patterns in the estuary of the Schelde (Belgium)", Proceedings of 'IGCP, Réunion Internationale PICG274, Evolution côtiere au Quaternaire, Dakar, Mai 1993', 46-47, 1993
10. Samuel Bentley, Harry H. Roberts, "Fluid Mud: Worldwide Importance in Rapid Coastal Dispersal of Fine-Grained Sediments", paper 43322, at 'AAPG Annual Meeting 2002: Our Heritage-Key to Global Discovery', March 10-13, 2002, Houston, 2002
11. Peter T. Harris, Richard Coleman, "Estimating global shelf sediment mobility due to swell waves", Marine Geology 150,171-177, 1998
12. "Mud Study to trace evolution, Sediment from sea-depths reveal secrets of Earth's changes", The Malay Mail, July 23, 1993
13. H. Singh, J. Adams, D. Mindell, and B.P. Foley, "Imaging Underwater for Archaeology," Journal of Field Archaeology 27(3), 319-328, Fall 2000
14. D.A. Mindell and B. Bingham, "A High-frequency, Narrow-beam Sub-bottom Profiler for Archaeological Applications" ,Proceedings of IEEE Oceans 2001 Conference, 2001.
15. Jean-Daniel Stanley, Franck Goddio, Gerard Schnepp, "Nile flooding sank two ancient cities", Nature 412, 293 – 294,19 Jul 2001
16. Dirk Verschuren, Kathleen R. Laird, Brian F. Cumming, "Rainfall and drought in equatorial east Africa during the past 1,100 years", Nature 403, 410 – 414, 27 Jan 2000
17. R. G. Rothwell, J. Thomson, G. Kähler, "Low-sea-level emplacement of a very large Late Pleistocene 'megaturbidite' in the western Mediterranean Sea",Nature 392, 377 – 380, 26 Mar 1998
18. Jie Li, Yuriko Renardy, " Shear-induced rupturing of a viscous drop in a Bingham liquid", J. Non-Newtonian Fluid Mechanics, vol. 95/2-3, pp. 235-251, 2000.
19. Tom Byerly, "Building a Better Bridge", Government Technology, November 98, 1998
20. Atema, Jelle, Dale F. Leavitt, Diana E. Barshaw and M. Carmela Cuomo, "Effects of Drilling Muds on Behavior of the American Lobster, Homarus americanus, in Water Column and Substrate Exposures" Can. J. Fish. Aquat. Sci. 39(5), (ERL,GB X298), 675-689, 1982
21. H. De Vlieger, "Navitracker – A towed density probe for continous measurement of sediment density", Terra et Aqua, International Journal on Public Works, Ports and Waterways development, 1987
22. James V. Gardner, Peter Dartnell, Helen Gibbons, and Duncan MacMillan, "Exposing the Sea Floor: High-Resolution Multibeam Mapping Along the U.S. Pacific Coast", U.S. Geological Survey Fact Sheet 013-00, 2000

23. Ralph A. Stephen, ”Bottom penetration at subcritical grazing angles by scattering”, J. Acoust. Soc. Am. 99(4), 2475-2500, 1996
24. J. R. Banic, A. G. Cunningham, “Airborne Laser Bathymetry: A Tool for the Next Millennium,” EEZ Technology 3, Aug/Sep, 75-80, 1998
25. Frank A. Boyle and Nicholas P. Chotiros , “A model for acoustic backscatter from muddy sediments”, J. Acoust. Soc. Am. 98(1), 525-530, 1995
26. Kevin B. Briggs, Michael D. Richardson, Darrell R. Jackson , “High-frequency bottom backscattering: Volume scattering from gassy mud”, J. Acoust. Soc. Am. 96(5), 3218, 1994
27. P.D.M.Spelt, M.A.Norato, A.S.Sangani, L.L.Tavlarides and M.S.Greenwood, "Attenuation of sound in concentrated suspensions: theory and experiments," Journal of Fluid Mechanics 430,51-86, 2001
28. William R. Bryant, Michael D. Richardson, “Permeability and porosity of clayey sediments in seismo-acoustics”, J. Acoust. Soc. Am. 92(4), 2308, 1992
29. L.M. Brekhovskikh, O. A. Godin, “Acoustics of Layered Media I”, Springer Series on Wave Phenomena 1998.
30. B. Poirée, “Complex Harmonic Plane Waves”, in “Physical Acoustics”, Edited by O. Leroy and M. A. Breazeale, Plenum Press, New York, 1991.
31. J. P. Charlier, F. Crowet, “Wave equations in linear viscoelastic materials”, J. Acoust. Soc. Am. 79(4), 895-900, 1986
32. M. Deschamps, C.L. Cheng, “Liquid-Thermoviscoelastic Solids Interface”, Ultrasonics 27, 308-313, 1989
33. Michael J. Buckingham ,“Theory of compressional and shear waves in fluidlike marine sediments”, J. Acoust. Soc. Am. 103(1), 288-299, 1998
34. Edwin L. Hamilton , “Attenuation of shear waves in marine sediments”, J. Acoust. Soc. Am. 60(2), 334-338, 1976
35. Edwin L. Hamilton , “Sound attenuation as a function of depth in the sea floor”, J. Acoust. Soc. Am. 59(3), 528-535, 1976
36. Koen Van Den Abeele, “Alternative fundamental theoretical descriptions for acousto-optic and acoustic investigation of pulsed and profiled ultrasound in view of nondestructive testing of layered structures”, PhD Thesis Department of Sciences, KUL Campus Kortrijk, 1992.
37. K.F. Herzfeld, T. A. Litovitz, “Absorption and dispersion of ultrasound waves”, Academic, New York, 1959
38. W. M. Madigosky, R. W. Warfield, “The magnitude of ultrasonic volume viscosity”, Acustica 55, 123-127, 1984.
39. Milton Abramowitz, Irene A. Stegun, edts, “Handbook of mathematical functions”, Dover publications, 1972
40. M. Deschamps, P. Chevée, “Reflection and refraction of a heterogeneous plane wave by a solid layer”, Wave Motion 15, 61-75, 1992.
41. J. M. Claeys, O. Leroy, “Reflection and transmission of bounded sound beams on half-spaces and through plates”, J. Acoust. Soc. Am. 72(2), 585-590, 1982
42. Henrik Schmidt, Finn B. Jensen, “A full wave solution for propagation in multilayered viscoelestic media with application to Gaussian beam reflection at fluid-solid interfaces”, J. Acoust. Soc. Am. 77(3), 813-825, 1985
43. Finn B. Jensen, Henrik Schmidt, “Subcritical penetration of narrow Gaussian beams into sediments”, J. Acoust. Soc. Am. 82(2), 574-579, 1987

Chapter VI The Interaction of Sound with Coated Materials

Many filters that are used in nowadays high-tech electronic devices and communication systems, such as satellites , are based on surface acoustic waves (SAW).

Acoustic waves have been used in electronics for many years, often in quartz resonators. Also, delay lines, exploiting the typical low values of acoustic velocities, give a long delay in a small space. The first surface acoustic wave (SAW) devices were made in 1965, introducing exceptional versatility because the propagation path was accessible to components for generating, receiving or modifying the waves. During the following 30 years there has been an explosion in the development of these devices. A huge range of device types have emerged, and they are now present everywhere in applications ranging from professional radar and communications systems to everyday devices such as television and mobile phones. Despite this, the devices are not generally well known, because they are hidden inside.

SAW technology, is eminently suitable for linear analogue devices. Within this area, the versatility is so great that the devices cover almost all the functions imaginable – bandpass filters, pulse compression filters, resonators and so on. This has all been achieved since the SAW-device emerged in 1965, and the devices have demonstrated steadily-improving reproducible performance with, when needed, cost effectiveness.

The interest in surface waves for electronics applications arises originally from radar requirements. Radar became established in the second world war. It was shown that the range capability of a radar can in principle be substantially improved if the radiated pulse is lengthened without changing its power level, and preferably without changing its bandwidth since this determines the resolution. This could be done by transmitting a chirp pulse. In the receiver, there would be a 'matched filter' to optimize the signal-to-noise ratio, basically a dispersive delay line such that the various frequencies of the received signal are delayed by different amounts, arriving at the output at the same time.

The long pulse lengths, in the order of 10-100 msec, implied that the filter would need a technology giving substantial signal delays, and 'conventional' methods such as dispersive L-C circuits or cables would be very bulky.

It was natural to consider acoustic waves, with velocities more than 100 times smaller than those of electromagnetic waves.

This chapter deals with Rayleigh waves and Lamb waves in coated substrates. Section VI.A describes the possibility to use a relatively thick coated plate as a frequency filter. As a matter of fact, the filter operates as the compliment of a Bandpass filter, i.e. a bandgap filter. This effect is new and is promising for the development of advanced frequency filters. The filter, as proposed in section VI.A, is adaptable simply by changing the coating thickness. The special features of the coated substrate are the result of the enormous difference in physical properties between the substrate and the coating.

Actually, the concept itself of frequency filtering is not new in SAW-devices. A surface acoustic wave filter is manufactured on a substrate of quartz or Lithium Niobate. Surface acoustic wave filters create Rayleigh waves. Each Rayleigh wave is generated by a series of interdigital strips of gold that collectively form an interdigital transducer (IDT). The wave is launched across the substrate to another IDT that converts the mechanical energy back to electrical. It is the spacing and length of each metal strip on the IDT that determines the bandpass and central frequency of the resulting filter.

In addition, in section VI.B, the same coating as proposed for the filter in section VI.A, is considered on a thin plate. It will be shown that Lamb waves show strange dispersive properties in this coated plate.

VI.A Frequency bandgap for Rayleigh waves on coated substrates

The Rayleigh wave velocity for a coated substrate must have a value in between the ones for the substrate material and the coating material. Nevertheless, Adler and McCathern [J. Appl. Phys. 49(4), 2576-2576, 1978] have performed measurements, based on the Schoch effect, on a stainless steel substrate covered with an aluminum oxide coating that seems contradict this phenomenon. The current section describes the frequency bandgap effect for Rayleigh waves on coated substrates and explains how this phenomenon is related to the cited measurements. The existence of such a gap can be very important for the development of frequency filters.
The contents of this section have been published as: Nico F. Declercq, Joris Degrieck, Oswald Leroy, "Frequency bandgap for Rayleigh waves on coated surfaces", Appl. Phys Let. 85(1), 148-150, 2004. (Imp. Fact. 4.207; SCI-index, Physics-Applied, rank:3/76)

INTRODUCTION

Coatings are very common in materials technology [1]. Rayleigh waves are often used in nondestructive testing and in electronic devices. They are also important in seismology. In the past they have frequently been used as a means to characterize coatings on substrates [2-4]. When bounded beams are incident from water onto a coated surface at the 'substrate Rayleigh angle', the Schoch phenomenon appears and its characteristics are determined by the properties of the coating [2-4]. Because a Rayleigh wave on a coated substrate is influenced by both the coating and the substrate, it is clear that the characteristics of this Rayleigh wave must be situated in between the ones of such waves on homogeneous solids consisting of pure substrate material or consisting of pure coating material. Therefore one expects a Rayleigh wave velocity bounded by the Rayleigh wave velocities on the pure solids. It is believed that the Rayleigh wave velocity can be found by measuring the angle at which the Schoch effect occurs when a bounded sound beam is reflected from a solid in water [2-6]. Laszlo Adler and D. A. McCathern [5] found a combination of coating (Al_2O_3) and substrate (stainless steel) for which the Schoch effect corresponds with a Rayleigh wave velocity that is lower than the one on any of the composed materials. This is so surprising that an explanation has only been found later, when it was found that the aluminum oxide was actually porous. In this section, we will focus on the consequences of a non-porous aluminum oxide coating on stainless steel In what follows it will be seen that if the properties of the coating and the substrate differ too much (e.g. Al_2O_3 on stainless steel), that there exists a frequency gap in which Rayleigh waves, leaking into the liquid, cannot exist in the composite system.

THEORY

The interaction of sound with the system of isotropic layers has been simulated by a linear combination of all possible plane wave solutions in the coating, i.e. for each type of waves (shear and longitudinal) we have one upward propagating shear wave and one downward propagating

shear wave. For the incidence media (water) there is only one incident wave and one reflected wave, for the substrate there is one shear and one longitudinal transmitted wave. The wave vectors of each of the waves are determined by the law of Snell-Descartes [8-12] and by the dispersion relation for plane waves [8-12]. The amplitude attributed to each wave is found by considering continuity of the normal stress vector and normal displacement on the water-solid interface and continuity of the normal stress vector and total displacement on the solid-solid interface [13]. In our calculations and on the figures that are given below, the Cartesian axes x and z are used with z pointing from the incidence media into to solid media, whereas x is parallel to the interface. The z=0 position corresponds with the coating-substrate interface.

NUMERICAL RESULTS AND DISCUSSION

The physical properties of the considered materials are given in Table VI.A_I.

Table VI.A_I : ***physical properties of used materials***

	Density [kg/m^3]	Longitudinal wave velocity [m/s]	Shear wave Velocity [m/s]
water	1000	1480	-
stainless steel	8090	5610	3180
Al_2O_3	4000	10460	6010
brass	8100	4840	2270

Just as in [5] we have considered a coating thickness of 0.24 mm. In Fig. VI.A_1 the reflected 'homogeneous plane wave' amplitude and phase are plotted as a function of the angle of incidence for 1 MHz. It is noticed that, for a given configuration, a phase shift of π occurs at the Rayleigh angle.

This angle is 30.33^0 for a stainless steel half space, 15.52^0 for a Al_2O_3 half space, 28.15^0 for a Al_2O_3 coating on stainless steel substrate and 17.18^0 for a stainless steel coating on a Al_2O_3 substrate. Hence nothing extraordinary happens because the Rayleigh angles (and hence their velocities) for the coated substrates are situated in between the ones for the uncoated substrates. However, in Fig. VI.A_2 the reflected amplitude and phase are plotted for a Al_2O_3 coated stainless steel substrate not only as a function of the angle of incidence, but also as a function of the frequency. It is noticed that in between 1.57 MHz and 23.23 MHz no phase shift of π occurs. Therefore Rayleigh waves are not stimulated in that region. This 'forbidden' region is therefore a frequency 'gap'. The gap exists because the physical properties of stainless steel and Al_2O_3 differ too much. For certain frequencies the coating does not just disturb the Rayleigh wave on the substrate, but simply destroys it. In Fig. VI.A_3 it can be seen, by means of the example of a brass coating on stainless steel, that no gap appears if the coating and substrate are more alike.

Fig. VI.A_4 shows the particle displacement pattern, for the Al_2O_3 coating on stainless steel, at the Rayleigh angle outside the gap (the Rayleigh wave pattern is visible), whereas Fig. VI.A_5 shows the pattern inside the gap, exactly at the angle where in [5] the Schoch effect was observed. It is seen that there is no Rayleigh wave pattern present in Fig. VI.A_5. It is also

interesting to note in Figs. VI.A_2-3 that the presence of a coating makes Rayleigh waves dispersive, i.e. their velocity depends on the frequency [14].

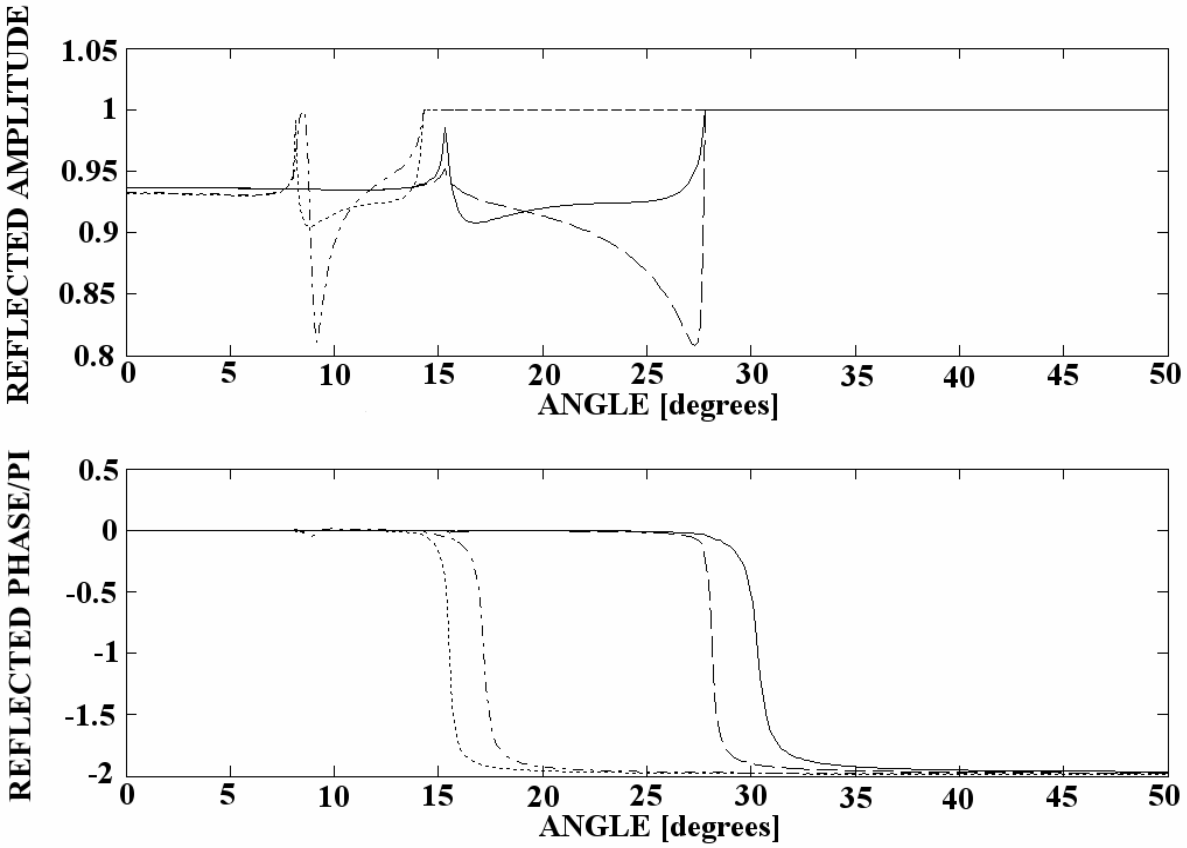

Fig. VI.A_1: ***Reflected amplitude (top) and reflected phase (bottom), at 1 MHz, as a function of the angle of incidence, for a stainless steel (solid line),*** Al_2O_3 ***(dotted line), 0.24 mm*** Al_2O_3 ***coating on stainless steel (dashed line), 0.24 mm stainless steel coating on*** Al_2O_3 ***(dash-dot line).***

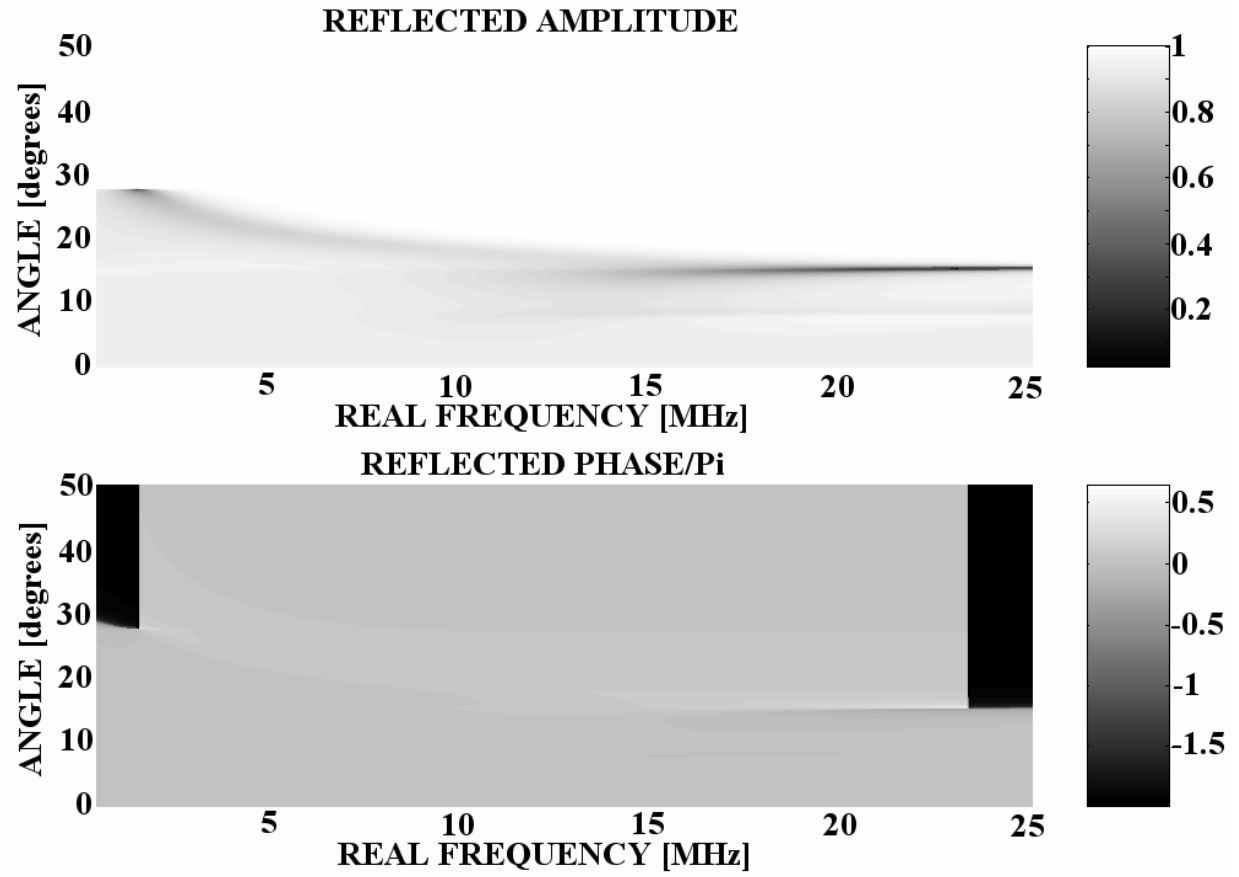

Fig. VI.A_2: ***Reflected amplitude (top) and reflected phase (bottom) for 0.24 mm*** Al_2O_3 ***coating on Stainless steel as a function of the angle of incidence and on the frequency. It is seen that there is a gap between 1.57 MHz and 23.23 MHz where Rayleigh waves cannot exist.***

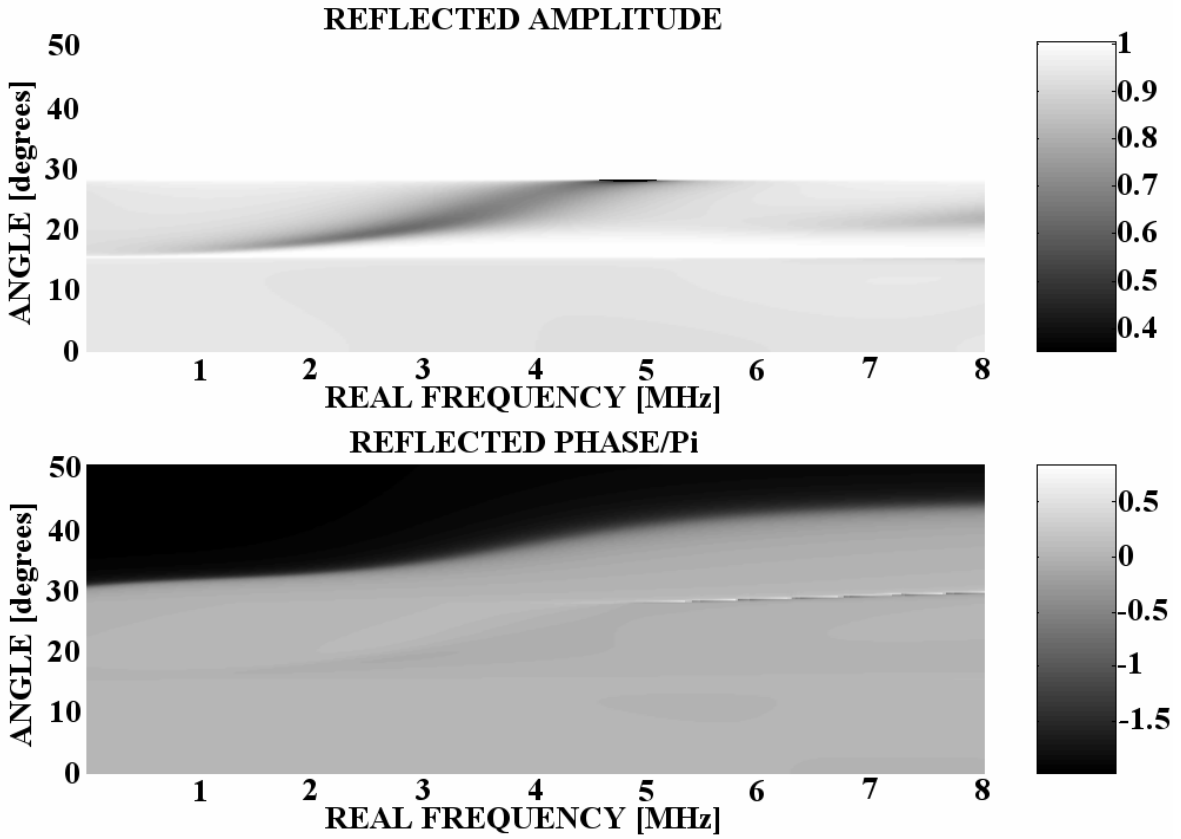

Fig. VI.A_3: ***Reflected amplitude (top) and reflected phase (bottom) for 0.24 mm brass coating on Stainless steel as a function of the angle of incidence and on the frequency. There is no frequency gap visible.***

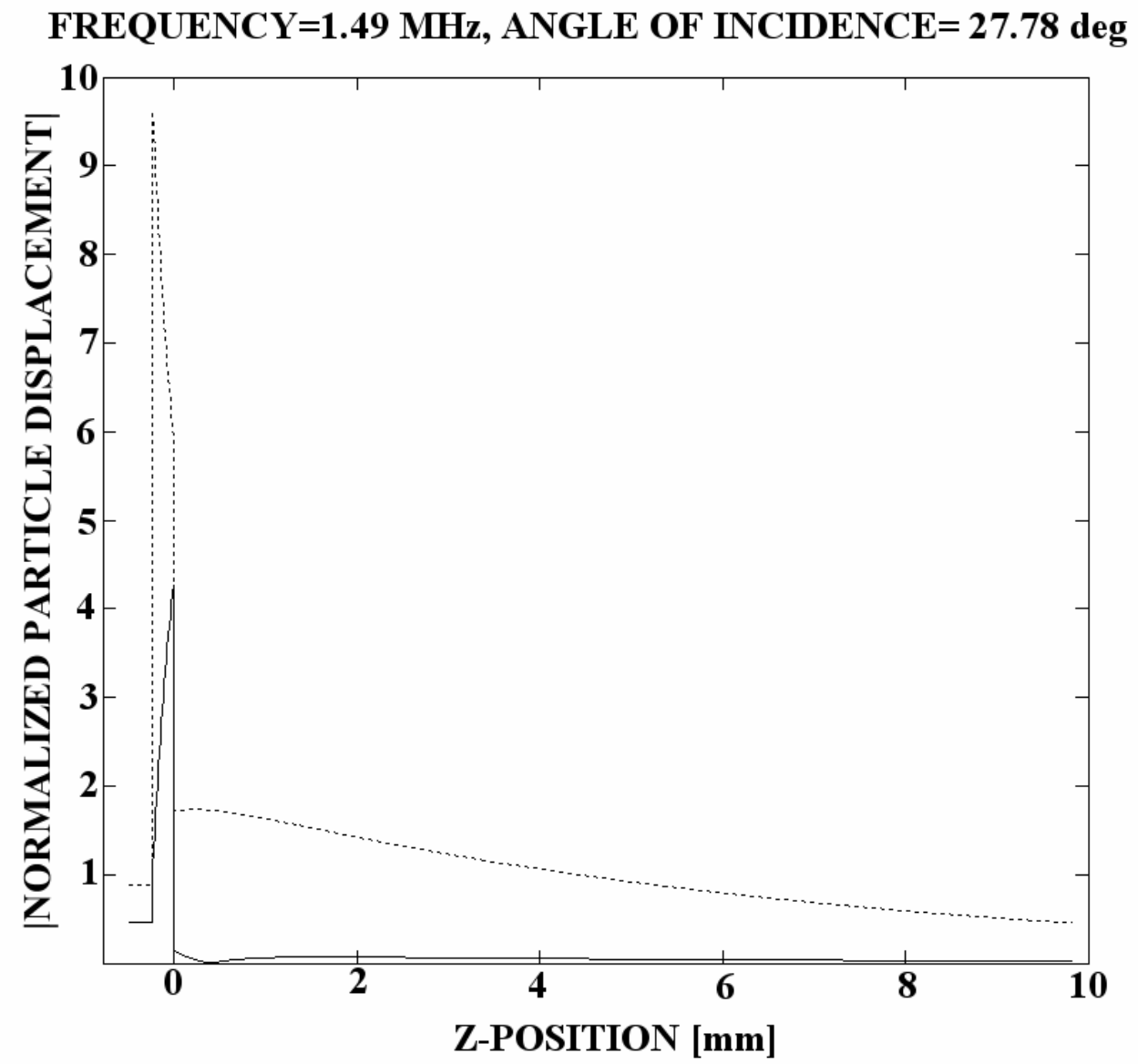

Fig. VI.A_4: ***Particle displacement (u) profile at 1.49MHz and incidence angle 27.78^0. Solid line: $|u_x|$, dotted line $|u_z|$. Although disturbed by the coating (0<x<-0.24mm), a typical Rayleigh wave pattern is visible in the substrate (x>0). The amplitude is also fairly high.***

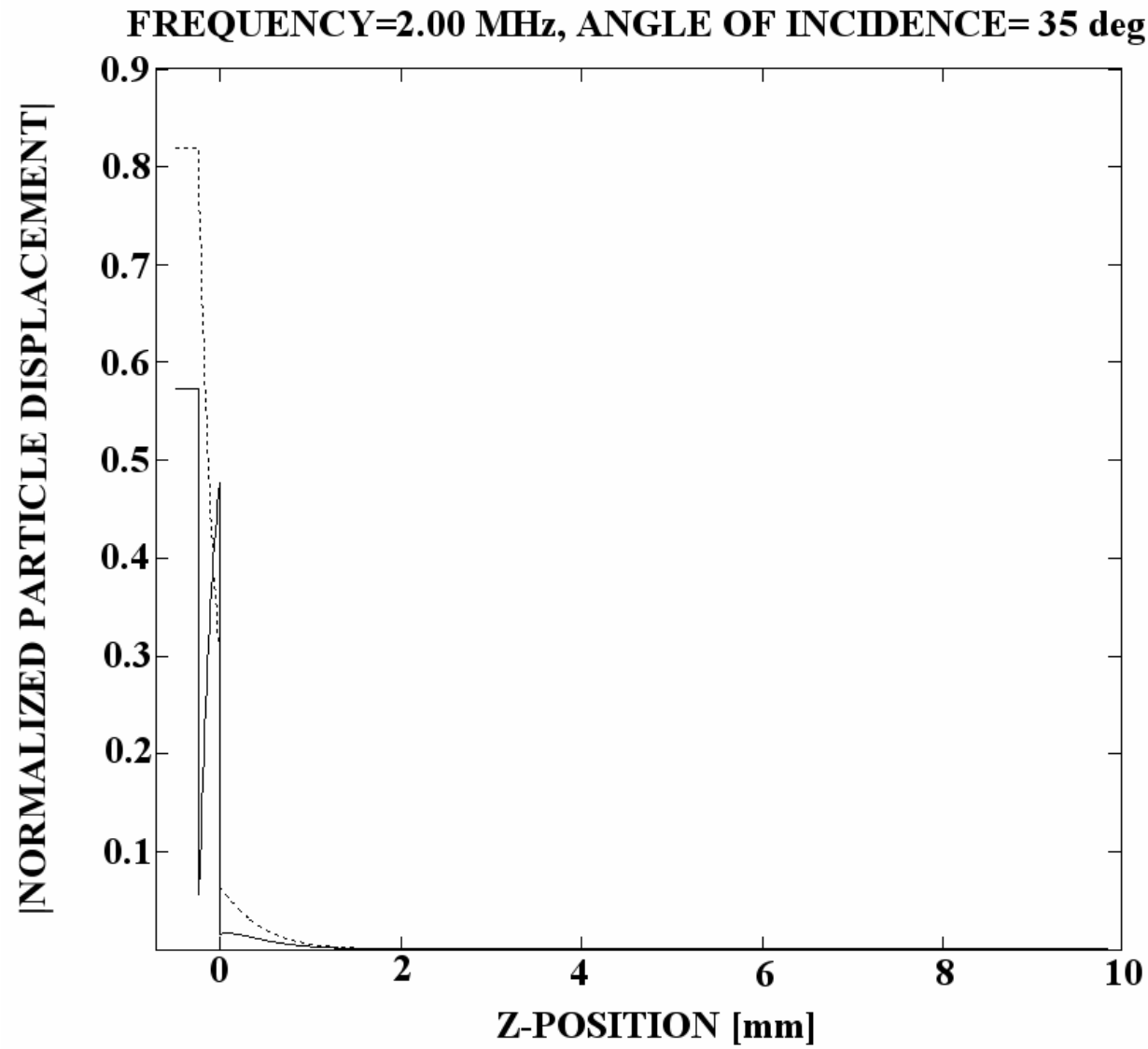

Fig. VI.A_5: ***Particle displacement (u) profile at 2MHz and incidence angle 35^0. Solid line: $|u_x|$, dotted line $|u_z|$. This corresponds to the situation of ref [5]. Because the frequency is part of the gap, no Rayleigh wave pattern is visible. Also the amplitude in the substrate is very small if compared with Fig. VI.A_4.***

CONCLUSIONS

It has been shown that if the physical properties of the coating and the substrate differ too much, that there exists a frequency gap in which there is no phase jump of the reflection coefficient. Therefore, no classical Rayleigh waves can exist. The gap extent is a function of the coating thickness and the coating material. Gennady Shkerdin [private communication], has warned me that in fact there is a type of Rayleigh wave generated within the gap, but it is so disturbed that it leaks into the solid. For the latter reason, its amplitude will drop significantly and the gap, which is therefore not a perfect gap, will be characterized by a strongly diminished amplitude of the transmitted surface wave. The experiments in ref [5] have been performed in that gap region. However, it has been

shown later by Adler et al [18] that the aluminum oxide in the original experiment was porous, this caused the effect that has been observed.

REFERENCES

1. Dekempeneer E., Van Acker K, Meneve J, Neerinck D, Eufinger S, Pappaert W, "Abrasion resistant low friction diamond-like multilayers", Surface & Coating Technology 142, 669-673, 2001
2. S. Devolder, O. Leroy, M. Wevers, P. De Meester, "Relation between the phase of the reflected ultrasound and the thickness of a thin layer placed on a solid halfspace", Acustica – acta acustica 82, 372 – 375, 1996
3. Filip W. Windels, S. Vanaverbeke, O. Leroy, "Thin coating charaterization by Rayleigh waves: An analytical model based on normal-mode theory", J. Acoust. Soc. Am. 110(3), 1349-1359, 2001
4. S. Vanaverbeke, F. Windels, O. Leroy, "The influence of coating thickness on the phase shift of bounded ultrasonic beams: comparison between fourier analysis and inhomogeneous plane wave theory", Acta Acustica United with Acustica 89, 640-646, 2003
5. Laszlo Adler, D. A. McCathern, "Reflection of a Gaussian ultrasonic beam from Al_2O_3 layer-stainless steel in water at the Rayleigh angle", J. Appl. Phys., 49(4), 2576-2577, 1978
6. A. Schoch, "Der Schalldurchgang durch plate", Acustica 2, 1-17, 1952
7. A. Schoch, "Seitliche Versetzung eines total-reflektierten Strahls bei Ultraschallwellen", Acustica 2, 18-19, 1952
8. R. Briers, O. Leroy, O. Poncelet, M. Deschamps, "Experimental verification of the calculated diffraction field generated by inhomogeneous waves obliquely incident on a periodically rough liquid-solid boundary", J. Acoust. Soc. Am. 106(2), 682-687, 1999
9. M. Deschamps, B. Poiree, O. Poncelet, "Energy velocity of complex harmonic plane waves in viscous fluids", Wave Motion 25, 51-60, 1997.
10. W. Huang, R. Briers, S. I. Rokhlin, O. Leroy, "Experimental study of inhomogeneous wave reflection from a solid-air periodically rough boundary using leaky Rayleigh waves", J. Acoust. Soc. Am. 96(1), 363-369, 1994
11. Jose Roux, "Reflection and refraction of heterogeneous waves at plane interfaces", "Physical Acoustics : Fundamentals and Applications", Edited by O. Leroy and M. Breazeale, 155-164, Plenum, New York and London, 1991
12. Nico F. Declercq, Joris Degrieck, Oswald Leroy, Appl. Phys. Let. 4245-4247, 84(21), 2004.
13. Adnan H. Naefeh, *Wave propagaton in layered anisotropic media with applications to composites*, North-Holland, 1995
14. Don E. Bray, Davis M. Egle, Leon Reiter, "Rayleigh wave dispersion in the cold-worked layer of used railroad rail", J. Acoust. Soc. Am. 64(3), 845-851, 1978
15. Nico F. Declercq, Rudy Briers, Oswald Leroy, " The use of polarized bounded beams to determine the groove direction of a surface corrugation at normal incidence, the generation of surface waves and the insonification at Bragg-angles", Ultrasonics-Elsevier 40/1-8 pp. 345-348, 2002.
16. Nico F. Declercq, Joris Degrieck, Rudy Briers, Oswald Leroy, "A Theoretical elucidation for the experimentally observed backward displacement of waves reflected from an interface having superimposed periodicity", J. Acoust. Soc. Am. 112(5), 2414, 2002
17. Nico F. Declercq, Joris Degrieck, Rudy Briers, Oswald Leroy, "Theoretical verification of the backward displacement of waves reflected from an interface having superimposed periodicity", Appl. Phys. Let. 82(15), 2533-2534, 2003
18. Adler and Butler, IEEE Ultrasonic proceedings #79CH1482-9SU | Nayfeh, Chimenti, Adler and Crane J.Appl.Phys. 52(8) 4985-4994 (1981)

VI.B Lamb wave dispersion in extraordinary bilayered plates

The dispersion curves for Lamb waves in a bilayered plate are situated in between those for a plate containing pure substrate and a plate containing only coating material. Mostly, the shape of the curves is not spectacularly altered by the presence of a second layer. Especially the A0 and S0 dispersion curves always seem to have the same shape, for all homogeneous plates and for all bilayered plates. The current section reports dispersion curves for a stainless steel layer covered by an aluminum oxide layer, whose physical parameters differ very much from those of the stainless steel layer. It is shown that the shape of the A0 and S0 curves become extraordinary.

INTRODUCTION

The use of coatings is very popular [1-3] and is frequently used to control friction and wear in all kinds of sliding contacts, to protect a substrate from corrosion, to provide an electrically conducting layer to an insulator or simply to color a surface. A number of implementations is also given in [4-13]. For many applications, it is essential to extract information about the coating thickness or about the physical parameters, such as density and stiffness. Nondestructive testing of coatings can be performed by means of ultrasound. There are a number of papers dealing with the interaction of ultrasound with coatings on half infinite substrates [4-10] and, because coatings are also used on thin plates, studies have also appeared on the interaction of ultrasound with coated plates [10-13]. No matter what bilayered system is considered, it is always found that the characteristics of the interaction of sound with the material are in between those of the interaction of sound with each of the constituents. In particular, if one considers dispersion curves of Lamb waves in bilayered plates, the dispersion curves shift from their original position for one of the constituents, towards the position for the other constituent, when the relative thickness is increased continuously. The shape of the dispersion curves changes only slightly. Sometimes curves start to cross one another, sometimes they move apart from each other, but there are no spectacular changes in shape. There are however changes in the absolute position and dimensions of the curves. Especially, according to traditional knowledge, the dispersion curves corresponding to A_0 and S_0 Lamb modes for lossless isotropic plates can always immediately be recognized because their shape is qualitatively always the same.

However, in what follows, it will be shown that some spectacular changes appear in the shape of the dispersion curves of the A_0 and S_0 Lamb modes when an extraordinary bilayered plate is used. This means constituents having physical properties (density and stiffness) that are much different from the properties of the substrate. This study is motivated by the fact that it is known [16] that an extraordinary coating on a semi-infinite substrate, sometimes results in the non-existence of Rayleigh waves.

ALUMINUM OXIDE LAYER ON STAINLESS STEEL LAYER

An aluminum oxide (Al_2O_3) layer on a stainless steel layer is a configuration that exists. It has been used in experiments reported in [4, 16]. Stainless steel is characterized by a density of

8090 kg/m^3, a longitudinal wave velocity of 5610 m/s and a shear wave velocity of 3180 m/s. Aluminum oxide is characterized by a density of 4000 kg/m^3, a longitudinal wave velocity of 10460 m/s and a shear wave velocity of 6010 m/s. It is clear that the physical difference between both materials is extraordinary. We have considered a coated plate that is submerged in water (density 1000 kg/m and longitudinal wave velocity 1480 m/s). The problem of incident sound interacting with the plate is resolved by expressing the sound field into acoustic potentials [14] and demanding continuity of normal stress and normal particle displacement on the solid-liquid interfaces, whereas continuity of normal stress and total displacement on the solid-solid interface [15]. The dispersion curves are obtained by extracting the velocities, through Snell's law, from the angles of incidence for which the reflection coefficient for pure plane waves tends to zero, a procedure which is repeated for each value of frequency times plate thickness. The dispersion curves are obtained for plates consisting of layers with different relative thickness. By plate thickness, we always mean complete thickness, i.e. lower layer plus upper layer. The thickness of the upper layer is then given as a certain percentage of the total plate thickness. Fig. VI.B_1 shows a schematic of a plate immersed in water.

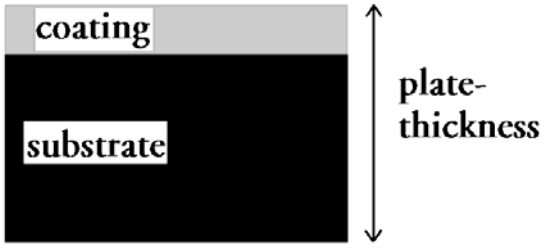

Fig. VI.B_1: ***Schematic of a bilayered plate immersed in water. The plate thickness is always substrate plus coating.***

In Figs. VI.B_2-4, the Rayleigh wave velocity [16] is indicated on the right side of each partition for a stainless steel half space (0%) and for an Al_2O_3 plate (100%). Furthermore, the dispersion curves are shown for different percentages of upper layer thickness. It can be seen that there is a tendency of dispersion curves to transform from the original configuration (100% stainless steel, i.e. 0% coating) to the ultimate configuration (100% aluminum oxide, i.e. 100% coating). However, something extraordinary happens with the A_0 and S_0 curves. Even though they also evolve from the original configuration to the ultimate configuration, some spectacular shape transformations occur. The most striking feature is the A_0 mode having a maximum velocity at some point along the frequency times thickness axis for an upper layer thickness exceeding 30%. That is extraordinary because normally, an A_0 mode tends asymptotically to its maximum velocity which is the Rayleigh velocity. Here it first reaches a maximum before showing asymptotical behavior.

The S_0 mode behaves more as expected, except for some kinks when the Al_2O_3 percentage is 80%-90%. Furthermore, it is known that the S_0 and A_0 mode tend simultaneously to the Rayleigh velocity for homogeneous plates. Here, they appear to get separated from each other for the bilayered plate. This separation increases until the upper layer thickness is 75% of the plate thickness. For thicker upper layers the distance between the A_0 and S_0 modes tends to decrease again until they show normal behavior for a plate consisting 100% of the upper layer.
All these extraordinary phenomena do not occur when ordinary bilayered plates are used such as brass on stainless steel.

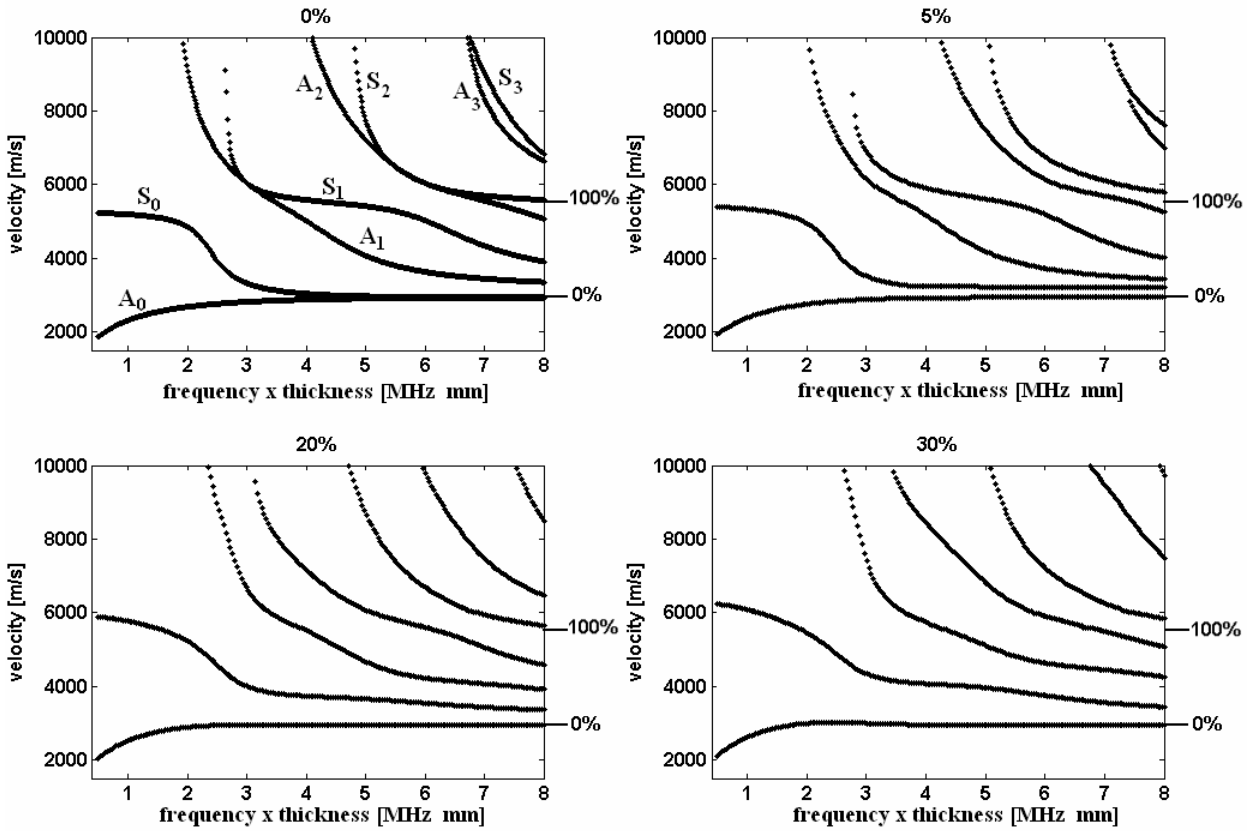

Fig. VI.B_2: ***Dispersion curves for a plate consisting of 0%, 5%, 20% and 30% of 'upper layer'.***

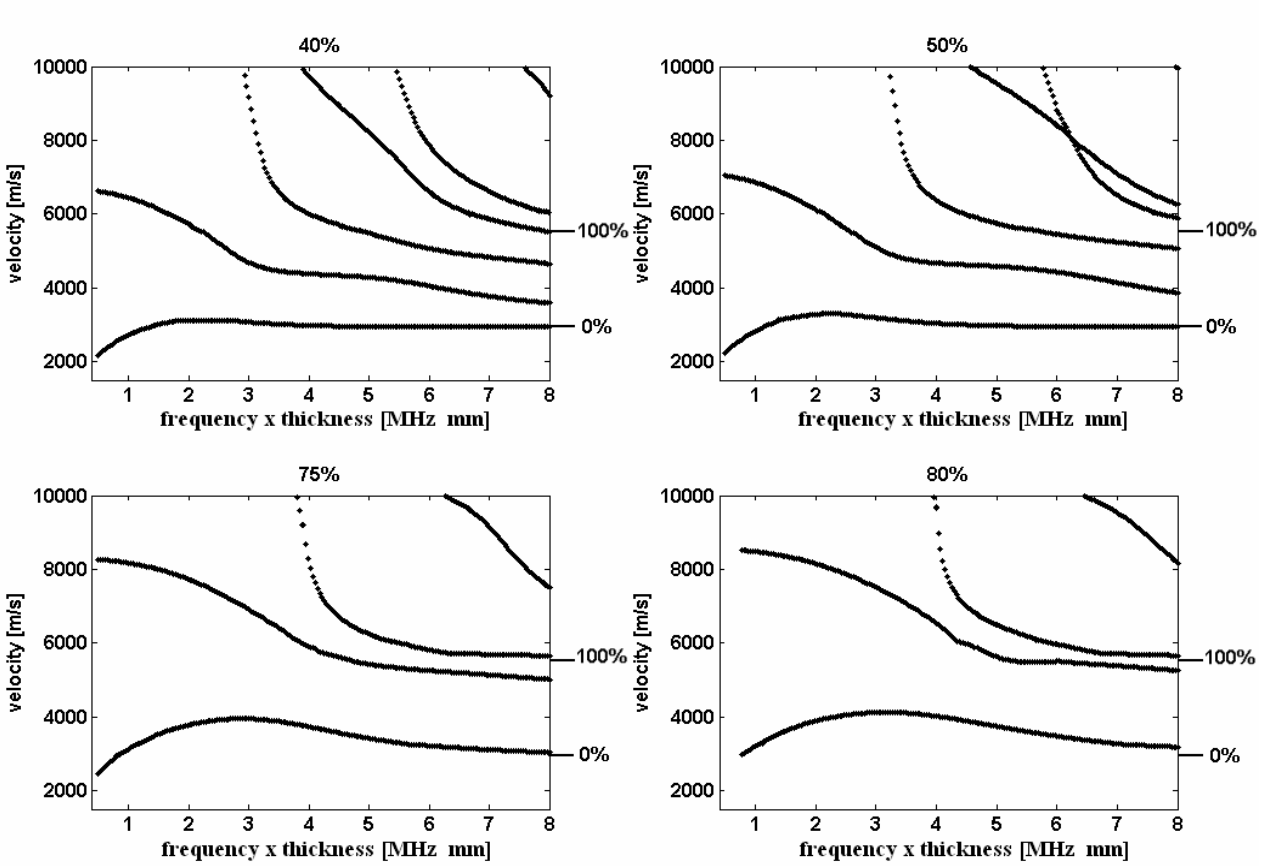

Fig. VI.B_3: ***Dispersion curves for a plate consisting of 40%, 50%, 75% and 80% of 'upper layer'.***

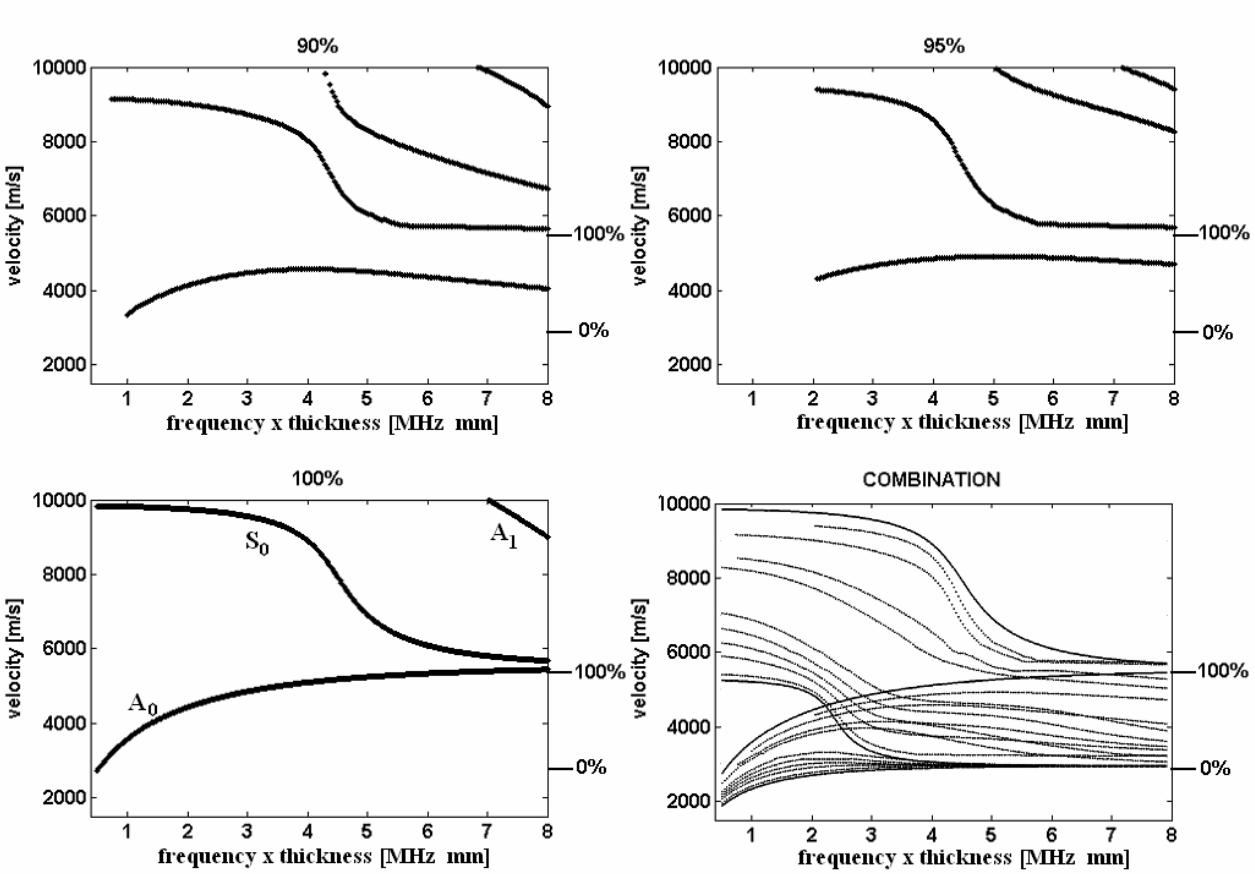

Fig. VI.B_4: ***Dispersion curves for a plate consisting of 90%, 95% and 100% of 'upper layer'. The lower right figure combines all A_0 and S_0 dispersion curves of Figs VI.B_2-4.***

CONCLUSION

It is shown that the dispersion curves for Lamb modes in extraordinary bilayered plates show some peculiarities that have not been reported before for ordinary bilayered plates or for pure homogeneous plates. First, there is the extraordinary shape of the S_0 mode and especially the A_0 mode, secondly there is the separation of the S_0 and A_0 mode at frequencies where they would have been almost indistinguishable for pure plates or for ordinary bilayered plates.

REFERENCES

[1] D. Neerinck, P. Persoone, M. Sercu, A. Goel, C. Venkatraman, D. Kester, C. Halter, P. Swab, D. Bray, "Diamond-like nanocomposite coating for low-wear and low-friction applications in humid environments", Thin Solid Films 317, 402-404, 1998

[2] Dekempeneer E., Van Acker K., Vercammen K., Meneve J., Neerinck D., Eufinger S., Pappaert W., Sercu M. Smeets J., "Abrasion resistant low friction diamond-like multilayers", Surface & Coatings Technology 142,669-673, 2001

[3] De Scheerder I., Szilard M., Huang Y. M., Ping X. B., Verbeken E., Neerinck D., Demeyere E., Coppens W., Van de Werf F., "Evaluation of the biocompatibility of two new diamond-like stent coatings (Dylyn (TM)) in a porcine coronary stent model", J. Invasive Cardiology 12(8), 389-394, 2000

[4] Laszlo Adler, D. A. McCathern, "Reflection of a Gaussian ultrasonic beam from Al2O3 layer-stainless stainless steel in water at the Rayleigh angle", J. Appl. Phys. 49(4), 2576-2577, 1978

[5] Filip W. Windels, S. Vanaverbeke, o. Leroy, “Thin coating characterization by Rayleigh waves: An analytical model based on normal-mode theory”, J. Acoust. Soc. Am. 110(3), 1349-1359, 2001
[6] S. Devolder, O. Leroy, M. Wevers, P. De Meester, “Relation between the Phase of the Reflected Ultrasound and the thickness of a thin layer placed on a solid halfspace”, Acustica – acta acustica 82, 372-375, 1996
[7] S. Vanaverbeke, F. Windels, O. Leroy, “The influence of coating thickness on the phase shift of bounded ultrasonic beams: comparison between Fourier analysis and inhomogeneous plane wave theory”, Acta Acustica united with Acustica 89, 640-646, 2003
[8] Z. Wang, X. Li, J. David N. Cheeke, “A modified modal frequency spacing method for coating characterization”, J. Acoust. Soc. Am. 104(5), 3119-3122, 1998
[9] Vikram K. Kinra, Changyi Zhu, “Ultrasonic nondestructive evaluation of thin (sub-wavelength) coatings”, J. Acoust. Soc. Am. 93(5), 2454-2467, 1993
[10] G. Every, “Measurement of the near-surface elastic properties of solids and thin supported films”, Meas. Sci. Technol. 13, R21-R39, 2002
[11] Yung-Chun Lee, Sheng-Wen Cheng, “Measuring Lamb wave dispersion curves of a bi-layered plate and its application on material characterization”, IEEE transaction son ultrasonics, ferroelectrics and frequency control 48(3), 830-837, 2001
[12] Yusuke Tsukahara, noritaka Nakaso, jun-Ichi Kushibiki, Noriyoshi Chubachi, “Excitation of plate waves in thickness measurements of layers dposited on thin plates”, IEEE transaction son ultrasonics, ferroelectrics and frequency control 36(6), 638-642, 1989
[13] P.-C. Xu, K.-E. Lindenschmidt, S. A. Meguid, “A new high-frequency analysis of coatings using leaky Lamb waves”, J. Acoust. Soc. Am. 94(5), 2954-2962, 1993
[14] J. D. Achenbach, *wave propagation in elastic solids*, North Holland, 1975
[15] Adnan H. Nayfeh, *wave propagation in layered anisotropic media with applications to composites*, North-Holland, 1995
[16] Nico F. Declercq, Joris Degrieck, Oswald Leroy, "Frequency bandgap for Rayleigh waves on coated surfaces", Appl. Phys. Let. 85(1), 148-150, 2004.

Chapter VII Schlieren Photography as a Tool for Nondestructive Testing

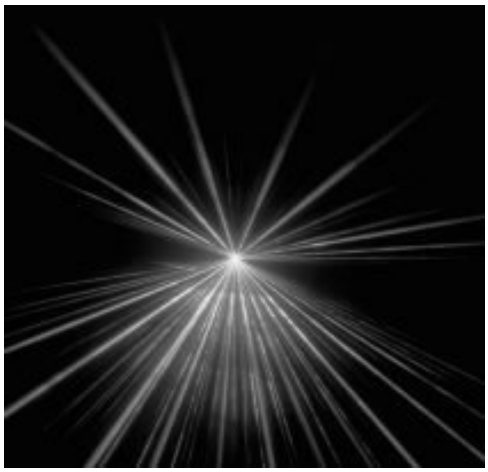

A spectacular view on the diffraction of laser light.

Schlieren photography is an old technique, based on optic diffraction, to visualize changes of the refractive index of a transparent media. The technique can be used to study flows, heat, ultrasound,…

The technique has been introduced to me by Joris Degrieck. Thanks to his enthusiastic transfer of knowledge, I have been able to build the Schlieren experimental setup relatively fast. Afterwards, it was only a matter of adjustment and improvement and last but no least, a lot of patience, in order to obtain many of the pictures that are presented in this dissertation. The Schlieren setup that I have built here in our Lab in Gent, is based on a combination of a lens and a parabolic mirror.

Later, when I visited the Laboratory of Mack Breazeale, I have been able to improve my knowledge about Schlieren photography better. The experimental setup at NCPA in Oxford (University of Mississippi), is based on two sophisticated lenses. The Schlieren pictures in this dissertation, in sections that describe results obtained in collaboration with Mack Breazeale, have been made by this experimental setup.

Eventhough Schlieren pictures are distributed throughout this dissertation, the current section focuses on two problems. The first is the problem of the study of the interaction of sound with highly absorbing media (section VII.A), whereas the second is the problem of the fast detection of the fiber direction in composites (section VII.B).

VII.A Schlieren Photography to Study Sound Interaction with Highly Absorbing Materials

Strong absorption of sound is often caused by the conversion of sound energy into heat. When this happens, it is not possible to study the interaction of sound with the absorbing material by means of reflected sound characteristics, because there is no reflected sound. Detecting, for example, the distance that sound travels in a strongly absorbing material, can be done by heat detection systems. However, the presence of temperature detectors in such materials interferes with the sound field and is therefore not really suitable. Infrared measurements are a possible option. Another option is the use of Schlieren photography for simultaneous visualization of sound and heat. This technique is briefly outlined with a 3MHz sound beam incident on a highly absorbing sponge. The contents of this section have been accepted for publication in Ultrasonics (Imp. Fact. 0.844; SCI-index, Acoustics, rank:11 /28)

INTRODUCTION

Schlieren photography is based on the acousto-optic effect [1-5] and is important when ultrasound is to be visualized [6-10]. In a Schlieren experiment, a wide beam of coherent laser light propagates through a transparent medium in which ultrasound propagates. The presence of sound generates a light-diffraction grating which is caused by the spatially periodically varying refractive index which in its turn is caused by the traversing soundwaves. Hence, light is diffracted into several spatial orders [1-5]. Since only orders different form zero deviate from light that is not diffracted, the zero order field must be eliminated in order to visualize the presence of sound by means of the diffracted light. The obtained light is then projected on a screen and can be used to visualize ultrasound.

However, if an inhomogeneity in the refractive index is present due to other effects, it may also be visible on a Schlieren picture. The visualization of heat often occurs in other scientific areas by means of Schlieren photography as well [11-16]. Nevertheless, as far as we know, the simultaneous visualization of sound and sound induced heat, has not been reported yet.

EXPERIMENTAL SETUP

The experimental setup is sketched in Fig. VII.A_1. A strongly absorbing sponge is glued on an iron plate and is immersed in water at approximately 20^0 C. A 1.6W sound beam of 1 cm physical beam width and having a frequency of 3MHz impinges the sponge. No reflected sound is visible due to the strong sound absorption. The sponge forms an angle with the incident beam. The angle is chosen randomly since the described effect occurs at each angle. Nevertheless the distance that sound propagates in the sponge can be angle dependent. The sound emitter is turned on for approximately 1 minute after which it is turned off. The coherent light that is used to form the Schlieren pictures is emitted by a '633nm/20mW' laser apparatus.

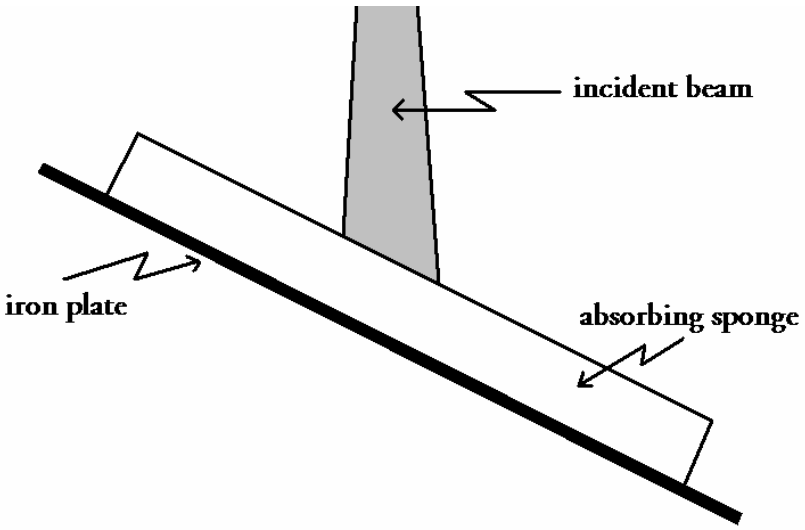

Fig VII.A_1: ***Experimental setup. An incident ultrasonic beam impinges a highly absorbing sponge.***

SCHLIEREN PICTURES

Figs. VII.A_2a-i show Schlieren pictures coming from the experimental setup described above. The sponge is impinged by sound for approximately 1 minute. Then the sound emitter is turned off while the Schlieren image is continuously observed. In Fig. VII.A_2a , the situation is shown an instant after the sound emitter is turned on. It is seen that no reflection occurs. This is due to the strong absorption of sound by the sponge. Figs VII.A_2a-c show the situation as time passes. It is seen that heat is formed on the spot of incidence and that this heat zone 'grows' slowly. Fig. VII.A_2d shows the situation right after the incident sound beam is turned off. It is seen that the surface remains hot for a while. This hot zone diminishes slowly as is seen in Figs. VII.A_2d-i. Meanwhile, the formation of a heat convection cell is visible in Fig. VII.A_2e. This cell rises slowly in Fig. VII.A_2f, tends to tear itself away in Fig. VII.A_2g and dissolves completely in Fig. VII.A_2h. The situation after approximately 30 sec is seen in Fig. VII.A_2i. Some instants later, no hot zone is visible anymore.

CONCLUSION AND PROSPECTS

It is shown that the formation and the evolution of heat due to sound absorption is visible on Schlieren pictures simultaneously with an incident sound beam. Further research is necessary to build a theory that describes the effect correctly. The method could possibly be used to find critical angles in the absence of a reflected beam.

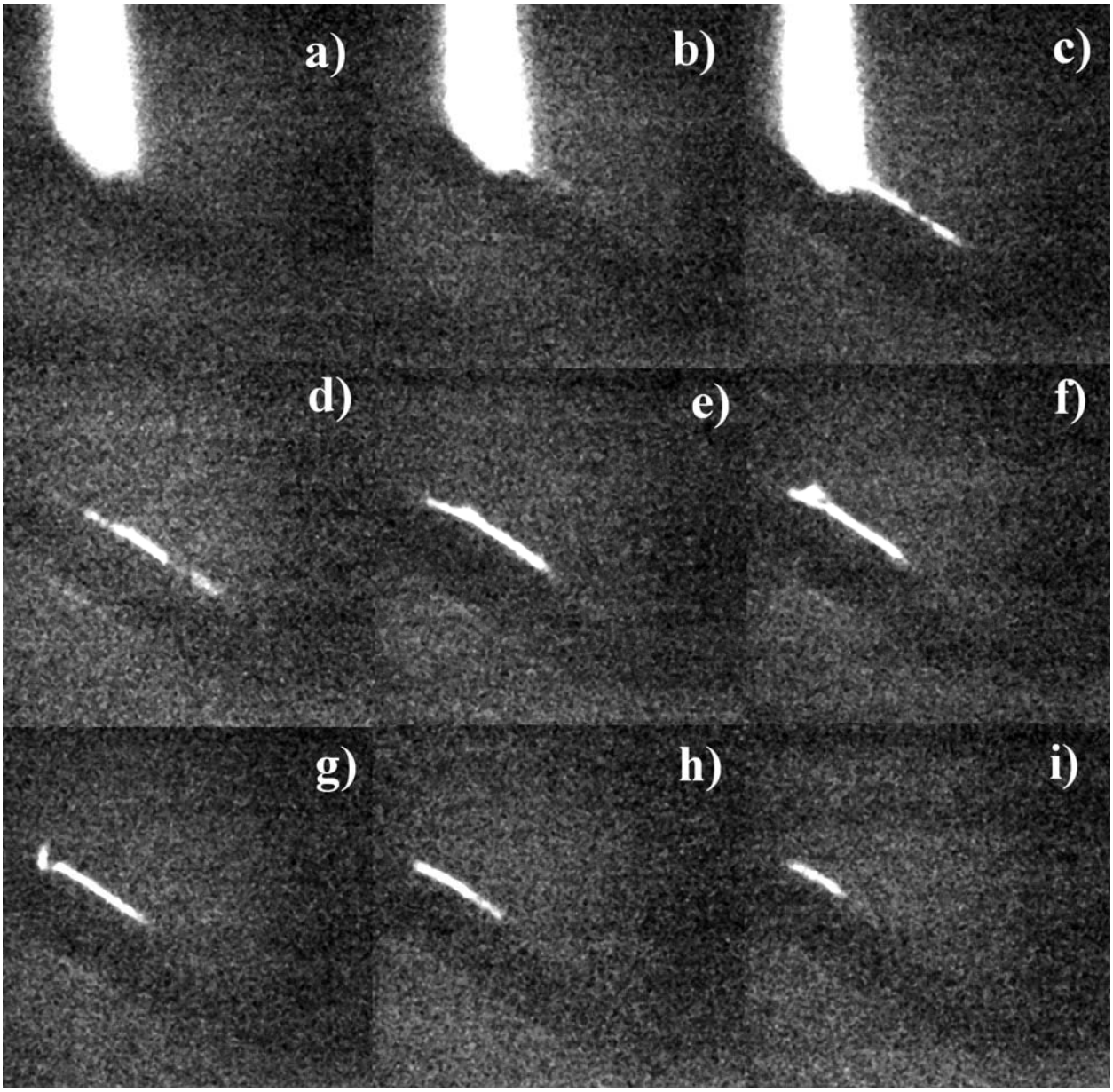

Fig VII.A_2: ***Sequence of Schlieren pictures of a sound beam impinging a sponge and the generated heat. Figs 2a-2c show the situation while the sound source is turned on and corresponds approximately to a period of 60s, whereas Figs. 2d-2i show the evolution after the sound source has been turned off and span a period of approximately 30s.***

REFERENCES

[1] W. Hereman, R. Mertens, F. Verheest, O. Leroy, J. M. Claeys, E. Blomme, "Interaction of light and ultrasound : Acousto-Optics",Physicalia Mag. 6(4), 213-245, 1984

[2] Blomme E. and Leroy O, " Diffraction of light by ultrasound : Finite analytical expressions for the spectra up to order 3", Acustica 57, 168-174, 1985.

[3] V. F. Humphrey, S. M. Knapp, C. Beckett, "Visualisation of the Resonances of a Fluid-Filled Cylindrical Shell Using a Low Frequency Schlieren System", Physical Acoustics, Edited by o. Leroy and M. A. Breazeale, plenum press, New York, 1991.

[4] Adrian Korpel (editor), "Selected Papers on Acousto-Optics", SPIE Milestone Series, Vol. MS 16, 1990

[5] Adrian Korpel, "Acousto-Optics, second edition", Marcel Dekker Inc., 1997

[6] Paul A. Chinnery and Victor F. Humphrey ,"On the overlapping acoustic resonances of a fluid-filled cavity: Schlieren visualization of an insonified circular-cylindrical shell",J. Acoust. Soc. Am. 102(3), 1383-1387, 1997
[7] Toru Tuziuti, Teruyuki Kozuka, and Hideto Mitome ,"Evaluation of source sound pressure of an ultrasonic transducer using schlieren visualization", J. Acoust. Soc. Am. 98(5), 2876, 1995
[8] Thomas H. Neighbors, Walter G. Mayer, and Herbert J. Ruf, "Acousto-optic imaging of focused ultrasound pressure fields", J. Acoust. Soc. Am. 98(3), 1751-1756, 1995
[9] M. de Billy, J. F. Piet, S. Mahaut, and G. Quentin, "Ray theory applied to the internal caustic identification of liquid cavities acoustically insonified", J. Acoust. Soc. Am. 95(2), 1143-1146, 1994
[10] W. E. Moore and J. A. Bucaro, "Measurement of acoustic fields using schlieren and holographic techniques", J. Acoust. Soc. Am. 63(1), 60-67, 1978
[11] Agrawal A.K., Butuk N.K., Gollahalli S.R., Griffin D., "Three-dimensional rainbow schlieren tomography of a temperature field in gas flows", Appl. Optics 37 (3), 479-485, 1998
[12] Qin X., Xiao X.D., Puri I.K., Aggarwal S.K. , "Effect of varying composition on temperature reconstructions obtained from refractive index measurements in flames", Combustion and flame 128 (1-2), 121-132, 2002
[13] Tanda G., Devia F., "Application of a schlieren technique to heat transfer measurements in free-convection", Exp. in fluids 24 (4), 285-290, 1998
[14] Marchesse Y., Gervais Y., Foulon H. ,"Optical measurements of the temperature in a supersonic jet", AIAA J. 41 (3), 470-475, 2003
[15] Albers B.W., Agrawal A.K., "Schlieren analysis of an oscillating gas-jet diffusion flame", Combustion and Flame 119 (1-2), 84-94, 1999
[16] Tanda G., Misale M., Devia F., "Experimental heat transfer from a vertical plate within a naturally ventilated cabinet", Heat and mass transf. 36 (6), 511-516, 2000

VII.B Detection of Fiber Direction in Composites by means of a High Frequency Wide Bounded Ultrasonic Beam and Schlieren Photography

This section describes an experimental method, based on the combination of schlieren photography and a wide bounded ultrasonic beam of frequency 10 MHz, used to detect the fiber direction in composites. Experiments are described on unidirectional and fabric fiber reinforced composites. This method is not based on Lamb wave phenomena, which can be complicated for interpretation by NDT engineers, but rather is based on relatively simple principles, i.e. inhomogeneity and symmetry of composites.

The work in this section has been performed at the National Center for Physical Acoustics, The University of Mississippi, Oxford, Mississippi, USA, in collaboration with A. Teklu, M. A. Breazeale, and Roger D. Hasse. The contents of this section have been accepted for publication in Research in Nondestructive Evaluation (Imp. Fact 0.935; SCI-index, Materials Science – Characterization & Testing, rank:2/23).

INTRODUCTION

Since fiber reinforced composites are mostly tuned to decrease their weight and to get the necessary stiffness in certain vital directions as well, it is important to know the fiber direction at any time during the construction or maintenance processes. The impact response, fatigue damage, and stiffness all depend upon the direction [1-5] . There are methods available to assess the fiber direction, such as ultrasonic polar scans [6-9] or ultrasonic reflected bounded beam deformation properties [10] . These methods are based on Lamb wave phenomena and the direction dependent mechanical properties of the composite. Furthermore the applied frequencies are small enough (1 MHz - 5 MHz) that one is dealing with a 'homogeneous' composite. Other possible techniques are optical micrography [11] or Moiré interferometry [12] and are mainly surface layer fiber direction characterizing methods, which are actually best applied when some of the fibers are exposed after polishing the sample of interest.

The technique described here is based on the interaction of relatively high frequency sound (10 MHz) with the composite under investigation and is based on imperfections [13-15] in the fiber density of the fiber reinforced layers that are relatively close to the surface. These imperfections are practically always present and actually consist of small areas in the composite where the fiber density is higher, accompanied by a small neighboring region where the fiber density is lower. For low frequency sound the imperfections are 'invisible' whence the composite can be considered homogeneous. For higher frequency sound, however, the composite is inhomogeneous, resulting in a spatially dependent reflection coefficient. If, in addition, a relatively wide beam is used, the reflected beam profile will be fringed due to the spatially dependent reflection coefficient. This fringing will be there for any type of imperfection. However, for imperfections along the fiber direction, such as spatial fiber density variations, which normally span several mm or cm parallel to the fibers, the fringes will 'cleave' the

reflected sound beam along the fiber direction. Hence, when schlieren photography [16] is used to visualize the reflected beam, the fringing will be visible on the schlieren picture as a pattern of high intensity light alternated with low intensity light. Contrary to reflected beam spatial intensity patterns when the frequency is low enough (1-5MHz), which are due to a form of the Schoch effect caused by multilayer Lamb waves or Rayleigh waves [10], the pattern described here is independent of the angle of incidence and is solely due to inhomogeneities near the surface.

EXPERIMENTAL CONFIGURATION AND PROCEDURE

Schlieren photography is based on the diffraction of light by ultrasound and is well described in ref 16. A monochromatic schlieren experimental setup is used as shown in Fig. VII.B_1. Two large (f/6.3, 1.2192 m focal length) lenses are used (L2 and L3). A monochromatic laser light beam generated by a 10mW He-Ne laser source is focused by the first lens L1 onto a pinhole that is placed exactly at 1.2192 m of L2. After passage through L2, the light is collimated in order to get a perfect parallel wide laser beam passing through the water tank. This light beam is then focused by L3 onto a spatial filter that blocks all undiffracted light. Therefore only diffracted light reaches the projection screen, whence visualization of ultrasound is achieved. The image is then captured by a digital camera and stored on a computer.

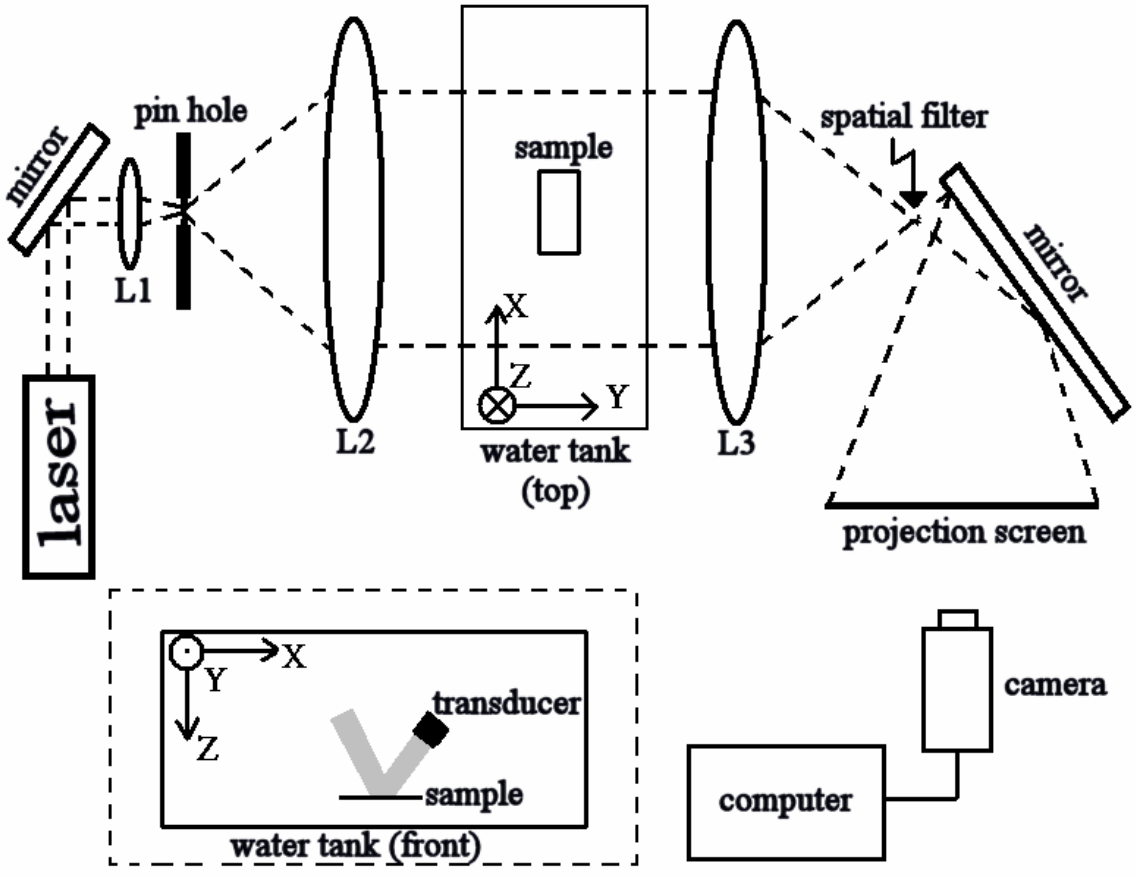

Fig. VII.B_1. ***Schematic of the experimental configuration. 'L' stands for lens.***

A 2.5 cm wide ultrasonic beam of 10 MHz impinges the surface of the sample under investigation at an angle of 33^0 . This angle is not crucial, as a matter of fact it is randomly chosen and the results shown below are valid for each angle of incidence. The configuration is shown in Fig. VII.B_2, where the sample under investigation (the reflector) is a relatively thick aluminum sample. It is noticed that even though the amplitude of the reflected beam is smaller than that of the incident beam, the pattern is the same, i.e. gaussian. This pattern, studied in the white rectangle of Fig. VII.B_2, is shown in Fig. VII.B_3. In fact, Fig. VII.B_3 serves as a reference figure for all results discussed below. As soon as the reflected pattern for a certain sample under given conditions differs from the one in Fig. VII.B_3, it will be discussed in what follows. Remark that Fig. VII.B_2 is a monochromatic schlieren photograph of the incident and reflected ultrasonic beam. The laser light that is used in order to obtain this picture, propagates normal to the picture i.e. normal to the plane of ultrasound incidence on the samples in the experiments described below. In what follows, this direction is referred to as the laser light direction. In all experiments the samples under consideration are placed on a highly ultrasound absorbing material in order to prevent side effects coming from reflections on the base where the samples are positioned.

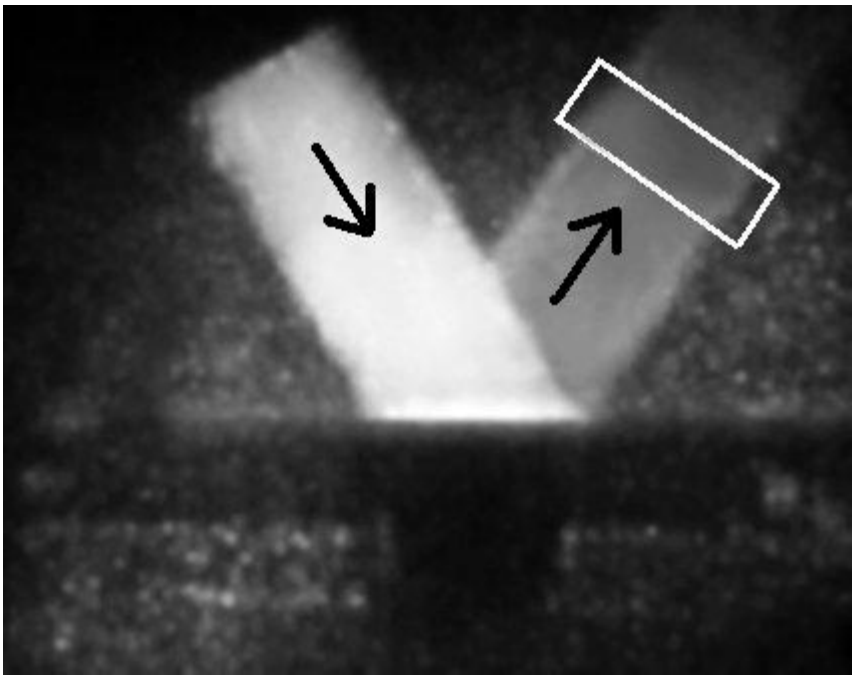

Fig. VII.B_2: ***Experimental setup for a 2.5 cm wide 10MHz ultrasonic beam (here incident on an aluminum sample). From the visualized reflected beam we always extract the area on the picture denoted by the white rectangle for studying the reflected beam pattern.***

Fig. VII.B_3: ***The reflected beam pattern for an aluminum sample. No fringes are visible.***

RESULTS AND DISCUSSION

unidirectional carbon fiber reinforced epoxy and glass fiber reinforced epoxy

If a unidirectional carbon fiber reinforced epoxy laminate is placed in the experimental setup of Fig. VII.B_2, there is always a pattern visible as in Figs. VII.B_2-3, except for the case when the laser light direction is parallel to the fiber direction, which generates a pattern as in Fig. VII.B_4. Equal findings hold for a unidirectional glass fiber reinforced epoxy. The result is seen in Fig. VII.B_5. Note that the fibers in both samples are supposed to be perfectly parallel to each other. However, due to spatial variations in fiber density, caused by imperfect prepreg and caused by the fabrication process, a pattern as in Figs VII.B_4-5 is possible. The reason is described in the previous paragraph.

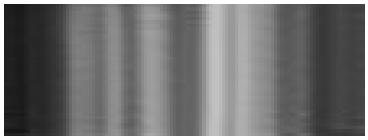

Fig. VII.B_4: ***The reflected beam pattern for a carbon epoxy unidirectional composite***

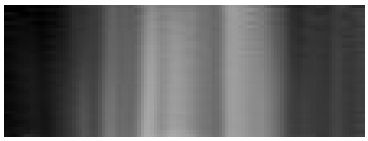

Fig. VII.B_5: ***The reflected beam pattern for a glass epoxy unidirectional composite***

unidirectional ($[0°]_8$) stacked 4 harness glass fabric reinforced epoxy and cross ply ($[0°/90°]_{2s}$) stacked glass fabric reinforced epoxy

The patterns of Figs VII.B_4-5 (especially the one of Fig. VII.B_5) do not show spectacular differences when compared with Fig. VII.B_3. That is of course because the pattern is based on small density variations. However, in practical applications, pure unidirectional materials are seldom used, whereas many kinds of fabrics are much more common. In Fig. VII.B_6 a photograph is shown of the type of fabric that is often used for the same purposes as a purely unidirectional material. Most of the fibers (in tiny bunches) in Fig. VII.B_6 are directed along the 0^0 direction. However, in order to hold them together, a small number of fibers are woven in the 90^0 direction. This does not result in different stiffness properties when compared to a purely unidirectional material, but rather it is more commonly found in a typical lay-up fabrication process. Nevertheless, the presence of weft fibers (90^0) results in the formation of bunches of fibers, instead of pure homogeneously distributed fibers in the 0^0 direction. This phenomenon is appealing for using the described schlieren technique in order to ascertain the fiber direction. Experiments are performed on unidirectional ($[0°]_8$) stacked glass fabric reinforced epoxy and have shown that the reflected beam profile is always equal to Fig. VII.B_3, except when the laser light direction θ (see Fig. VII.B_6) is equal to 0^0, 45^0 or 90^0 as can be seen in Fig. VII.B_7. The reason for 0^0 is the presence of bunches of fibers, that for 90^0 is the presence of the spatial separation of the weft fiber bunches, whereas the cause for the 45^0 is that this is also a symmetry direction for the used fabric.

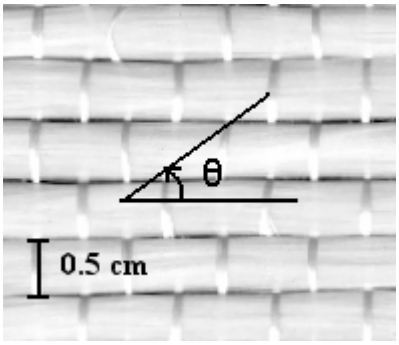

Fig. VII.B_6: ***Photograph of the fibers that are used in manufacturing the unidirectional glass fabric reinforced epoxy samples. The width of the warp bunches (horizontal) is 5mm.The angle θ is shown and corresponds to the angles denoted in Figs VII.B_7-8.***

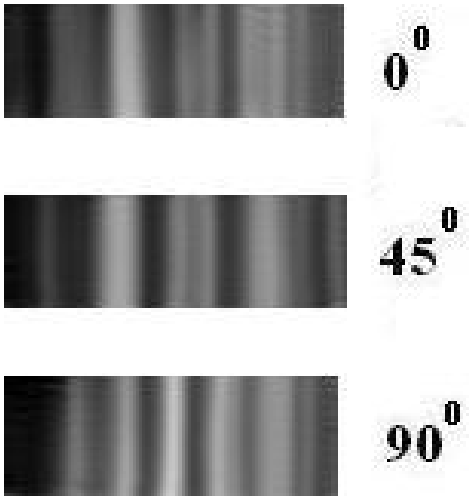

Fig. VII.B_7: ***The reflected beam pattern for a $[0°]_8$ stacked glass epoxy laminate with layers reinforced with unidirectional composite as in Fig. VII.B_5.***

If the same experiment is repeated for cross ply ($[0°/90°]_{2s}$) stacked glass fabric reinforced epoxy, then again no fringes are visible except if laser light is directed at 0^0, 45^0 or 90^0 measured from the fiber direction for the upper layer. The results are shown in Fig. VII.B_8. The fact that the patterns in the 0^0 and 90^0 direction are approximately the same as far as the spacing between the fringes is concerned (which is not the case in Fig. VII.B_7) shows that the pattern is not solely influenced by the properties of the upper layer, but also by lower layers in the composite sample. Ultrasound penetrates deep enough to be influenced by more than one layer. One of the consequences of this feature of the technique is that when the composite is covered with a coating (homogeneous and isotropic), the fringes will still be visible.

unidirectional 5-harness satin weave fabric ($[0°]_8$) stacked and cross ply 5-harness satin weave fabric ($[0°/90°]_{2s}$) stacked carbon fabric reinforced PPS

The previous paragraph describes experiments on samples that consist of quasi unidirectional fibers. That is because the weft bunches are much smaller than the warp bunches. In the aviation industry one often uses real fabric layers, i.e. layers where the weft and warp bunches have comparable size. For that reason we have also performed experiments on unidirectional 5-harness satin weave fabric ($[0°]_8$) stacked carbon fabric reinforced Poly Phenyl Sulfide (PPS). A photograph is shown in Fig. VII.B_9. The directions 1 (-25^0), 2 (0^0), 3 (19^0) and 4 (65^0) correspond to symmetry directions of the composite that result in fringed patterns if the laser light is passing in those directions. The results are shown in Fig. VII.B_10 for each of those directions.

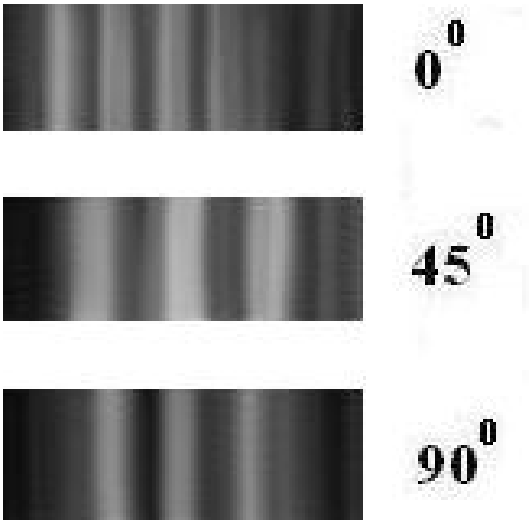

Fig. VII.B_8: ***The reflected beam pattern for a*** $[0°/90°]_{2s}$ ***stacked glass epoxy laminate with layers reinforced with unidirectional composite as in Fig. VII.B_5.***

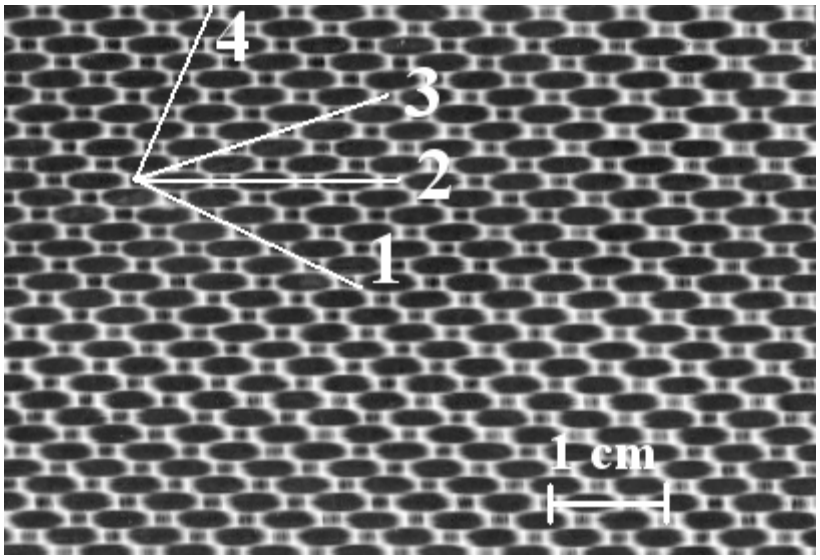

Fig. VII.B_9: ***Definition of the direction 1 (-25^0), 2 (0^0), 3 (19^0) and 4 (65^0) on the upper surface of a PPS 5-harness satin weave fabric carbon fiber reinforced composite.***

Because the symmetry for the pattern shown in Fig. VII.B_9 is quite different when compared to the symmetry observed in Fig. VII.B_6, it is expected that a composite consisting of a stacking of such layers in 0^0 and 90^0 directions will result in serious 'effect-canceling' of the outcome of each layer on reflected ultrasound. It is expected, therefore, that no fringes can be visible in directions labeled 4 and 1, because those direction form an angle of approximately 90^0 with one another. Indeed, in Fig. VII.B_11 the result is shown for direction 4 (a similar result was found for direction 1), for a cross ply 5-harness satin weave fabric ($[0°/90°]_{2s}$) stacked carbon fabric reinforced PPS. In that direction a fringe pattern was visible, although not as distinct as in Fig. VII.B_10, whereas no fringes were visible in other directions.

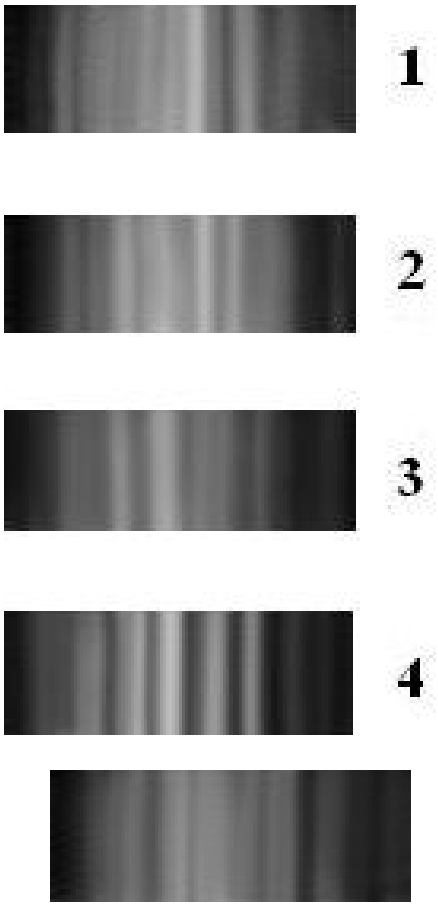

Fig. VII.B_10: ***The reflected beam pattern along the directions as defined in Fig. VII.B_8 for a [0°]$_8$ stacked laminate with layers as described in Fig. VII.B_9 and the upper layer having the direction equal to the layer shown photographically in Fig. VII.B_9.***

Fig. VII.B_11: ***The reflected beam pattern along the directions as defined in Fig. VII.B_8 for a [0°/90°]$_{2s}$ stacked laminate with layers as described in Fig. VII.B_8 and the upper layer having the direction equal to the layer shown photographically in Fig. VII.B_8.***

CONCLUSIONS

This section shows that the use of a wide beam having a relatively high frequency, combined with a schlieren photography experimental setup enables the determination of the symmetry directions of a composite. This technique can be used to detect the fiber direction(s) in composites. Results are shown for different types of composites.

REFERENCES

[1] H. Fukunaga, G. N. Vanderplaats, "Strength optimization of laminated composites with respect to layer thickness and or layer orientation angle", Computers and structures 40 (6), 1429-1439, 1991

[2] R. W. Rydin, A. Locurcio, V. M.Karbhari, "Influence of reinforcing layer orientation on impact response of plain weave RTM composites", J. Reinforsed Plastics and Composites 14 (11), 1199-1225 NOV 1995

[3] O.S. Es-Said, J. Foyos, R. Noorani, M. Mendelson, R. Marloth, B.A. Pregger "Effect of layer orientation on mechanical properties of rapid prototyped samples" Materials and Manufacturing Processes 15 (1): 107-122 2000

[4] W.S. Lee, W.C. Sue, S.T. Chiou "Effect of reinforcement orientation on the impact fracture of carbon fiber reinforced 7075-T6 aluminum matrix composite", Materials Trans. JIM, 41 (8), 1055-1063 AUG 2000

[5] Tetsusei Kurashiki, Masaru Zako, Ignaas Verpoest, "Damage development of woven fabric composites considering an effect of mismatch of lay up", Proc. Tenth European Conf. On Composite Materials ECCM-10, June 3-7, Bruges, Belgium, 2002

[6] W. H. M. Vandreumel, J. L. Speijer, "Polar-Scan, a non-destructive test method for the inspection of layer orientation and stacking order in advanced fiber composites", Materials Evaluation 41 (9), 1060-1062, 1983

[7] Degrieck J.,. Some possibilities of nondestructive characterization of composite plates by means of ultrasonic polar scans. Non Destructive Testing. Van Hemelrijck & Anastassopoulos (eds), Balkema, Rotterdam, 225-236, 1996.
[8] Degrieck J.& Declercq N. F.& Leroy O.. Ultrasonic Polar Scans as a possible means of nondestructive testing and characterization of composite plates. Insight – The Journal of the British Institute of Non-Destructive Testing 45(3), 196-201, 2003.
[9] Nico F. Declercq, Joris Degrieck, Oswald Leroy, "Numerical simulations of ultrasonic polar scans", pp75-80 in Emerging Technologies in Non Destructive Testing, Van Hemelrijck, Anastasopoulos and Melanitis (eds), Swets & Zeitlinger, Lisse, 2004
[10] A.U. Rehman, C. Potel, J.F. de Belleval , "Numerical modeling of the effects on reflected acoustic field for the changes in internal layer orientation of a composite" Ultrasonics 36 (1-5), 343-348, 1998
[11] C.J. Creighton, M.P.F. Sutcliffe, T.W. Clyne "A multiple field image analysis procedure for characterisation of fibre alignment in composites", Composites part A – Applied Science and Manufacturing 32 (2), 221-229, 2001
[12] R.D. Hale, D.O. Adams, "Influence of in-plane fiber misalignment on Moiré interferometry results" , J. Composite Materials 31 (24), 2444-2459 1997
[13] J. Chen, T.M. McBride, S.B. Sanchez ," Sensitivity of mechanical properties to braid misalignment in triaxial braid composite panels", J. Composite Technology & Research 20 (1), 13-17, 1998
[14] A. Vincenti, P. Vannucci, G. Verchery, "Influence of orientation errors on quasi-homogeneity of composite laminates", Composites Science and Technology 63, 739-749, 2003
[15] S.C. Barwick, T.D. Papathanasiou "Identification of fiber misalignment in continuous fiber composites", Polymer Composites 24 (3), 475-486, 2003
[16] M. A. Breazeale, "From monochromatic light diffraction to colour schlieren photography", J. Opt. A: Pure Appl. Opt. 3, S1-S7, 2001

Chapter VIII Characterization of Liquids in Closed Containers

In the dock industry and for port officials in a modern society, it is mandatory to possess the necessary practical tools or fast inspections of ships and their cargo.

When studying the Schoch effect on thick and thin plates immersed in water, I noticed that not a single study was reported in the literature on the effects of the liquids surrounding the plate, on the Schoch phenomenon (see chapter IV). The reason is obvious. It is known that dispersion curves of Lamb waves in classical plates (steel, brass,…), are relatively unaffected by the immersion liquid. Nevertheless, when studying the interaction of sound with composites, I read in Adnan H. Nayfeh's book (*Wave propagation in layered anisotropic media*) that the dispersion curves are significantly affected by the immersion liquids, if the physical properties (density,…) are of the same order of magnitude. This made me believe that there must be small differences as well for classical plates immersed in liquids such as water. This difference, if small, is perhaps best noticed by an incident bounded beam, if this beam interacts very intimately with the plate. This happens, of course, when Lamb waves are generated, resulting in the Schoch effect. Therefore, I believed that the Schoch effect must be sensitive to the properties of the surrounding liquids. For containers, the surrounding liquids consist of a liquid that functions as carrier for incident sound (typically water), and the contained liquid underneath the container skin.

It was my desire to guide a student and introduce him/her in the field of ultrasonics. Therefore I proposed the subject of characterizing liquids in containers, as a subject for a Master's thesis. Filip Van den Abeele (who is now a brilliant and hard working researcher in the field of continuum damage mechanics) was interested and that's how we started to collaborate. He has really done a good job by first achieving the necessary basics of the homogeneous and inhomogeneous wave theory and then dealing with whatever I requested in the particular case of liquids in containers.

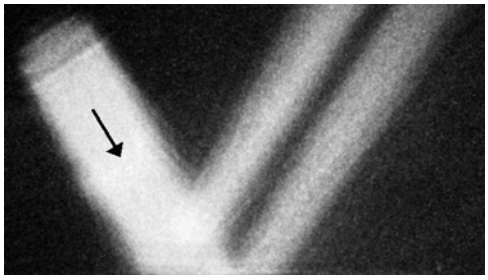

The Schoch effect consists of an incident bounded beam, being reflected as two parallel beams with a null zone in between. The effect occurs on smooth surfaces, due to the generation of leaky surface waves or leaky Lamb waves.

I promised him from the beginning that I would guide him as well as possible in order to make his work publishable in an international journal. We worked hard together and obtained interesting results that are described in this chapter. Section VIII.A shows that the Schoch effect is a promising tool to characterize liquids in containers. Section VIII.B describes a very interesting phenomenon that makes it possible to distinguish between realistic liquids and unrealistic liquids, simply by verifying the Lamb wave pole for a given plate separating water and a liquid under examination.

VIII.A The Schoch effect to distinguish between different liquids in closed containers

In different industrial branches it is necessary to characterize liquids in closed containers. For small cans, accessibility to both sides is almost trivial. However in industries where larger containers are used and especially in the dock industry, only one side is accessible practically and damping often prevents through-transmission ultrasonic measurements or pulse echo techniques. It is known that built-in sensors can be used to determine the density and the wave velocity of liquids, but normally, containers are not equipped with such sensors. It is also known that differences in the reflection coefficient at a solid-liquid interface can determine the density and sound velocity of liquids but only if the difference in acoustical impedance between the solid and the liquid is small. For most containers this condition is not provided, and therefore a more sensitive method is needed. This section reports simulations that show how identical containers, having different liquids inside, can be distinguished from one another by means of differences in the Schoch effect at a Lamb wave angle of incidence for harmonic bounded ultrasonic beams.

The work in this section was performed in collaboration with my graduate student Filip Van den Abeele and is published as: Nico F. Declercq, Filip Van den Abeele, Joris Degrieck, Oswald Leroy, "The Schoch effect to distinguish between different liquids in closed containers", IEEE Transactions on Ultrasonics, Ferroelectrics, and Frequency Control 51(10), 1354-1357, 2004.
(Imp. Fact. 1.595 ;SCI-index, Engineering – electrical & electronic, rank:46/205)

INTRODUCTION

The purpose of this section is to formulate an answer to the many requests and suggestions of several sources in the beverage industry and especially in the dock industry over the last couple of years for studying the possibility of fluid characterization in closed containers in a non-destructive way. In the dock industry and for port officials [1,2] it is desirable to possess practical tools to characterize the fluid content of containers. This can be done by removing liquid and performing chemical tests. Even though this is the only test that produces 100% certainty, it is also helpful to use other means that are equivalent to non-destructive testing. This might be due to the risk of poisoning, the lack of speed when sampling, the risk of contamination, ...
It has been shown before that, besides other techniques [3], it is possible to apply ultrasound for that purpose. One method is based on time of flight measurements [4-6]. This method requires access to both sides of a container or at least requires containers that are small enough so that damping does not prevent sound from traversing the container. Hence, even though this method

seems to work for small containers within a production line, application to large containers is not realistic.
Another method is based on laser excitation of sound in fluids [7]. This method is interesting, but the fact that it can only be used in the case of open containers, makes it less applicable.
Yet another - very sensitive - method, developed by Greenwood et al [8-11], applies a sensor that can be submerged in the liquid or built in the container skin; and is actually based on the 'sensitivity' of the reflection coefficient at the solid-liquid interface between the sensor and the liquid. Nevertheless, submerging the sensor in the liquid requires opening the container or embedding the sensor in the cargo container's skin, which is not practicable.
Ultimately, application of the sensor's principle to an existing container skin without built-in sensor is not realistic because the difference in acoustical impedance between the skin and the contained liquid is too large to make the technique sensitive enough [8-11]. Hence the method developed by Greenwood et al is probably only really practicable for pipelines [10].
The method studied here is based on beam deformations in reflection on the existing skin of a closed container, which solely requires access from one side, does not require an echo that has traversed the liquid, and is therefore an inviting technique for relatively large containers. Because the method makes use of the existing container skin, it doesn't require built-in sensors. This is only possible because it is more sensitive than the reflection coefficient as used by Greenwood et al [8-11]. The beam deformations are induced by the generation of Lamb waves in the container skin and their characteristics are influenced by the properties of the liquid. It is known that harmonic bounded beams show nonspecular reflection phenomena when incident at the Rayleigh angle for liquid-solid structures [12-20] or at a Lamb wave generating angle on a liquid-solid-liquid structure [21-26] : this is called the Schoch effect.
However, all papers dealing with this effect, study the situation where a plate separates two identical liquids, instead of two different ones.
In this section, we consider an isotropic plate between two different liquids. A schematic is presented in Fig. VIII.A_1. The upper liquid is always water, while the lower liquid can be of any kind. If a bounded beam is incident from the upper liquid on a plate in between that upper liquid and a lower liquid, the generation of leaky Lamb waves will induce deformation of the reflected beam, widely known as the Schoch effect, generating two reflected lobes instead of only one. The first lobe is called the specular lobe and its position corresponds almost perfectly with the position of a reflected beam if no deformation occurs. The second lobe is called the nonspecular lobe and is displaced along the interface. The displacement itself is also called Schoch displacement. The influence of the lower liquid on the deformed beam can be noticed in the phase and amplitude of the nonspecular lobe and also in the position and depth of the 'null zone' in between the specular and nonspecular lobe. The purpose of this section is to show that it is possible to distinguish between two liquids in a similar container by studying differences in the Schoch effect.
Finally it is shown by means of a numerical simulation that measuring the characteristics of the reflected deformed beam enables one to distinguish between oil and water. This work might be an impetus for further study using phased array techniques and may also inspire other labs to try ultrasonic focussed beams [27-28]. It is likely that focal spot shifts might also be influenced by the characteristics of the unknown liquid.

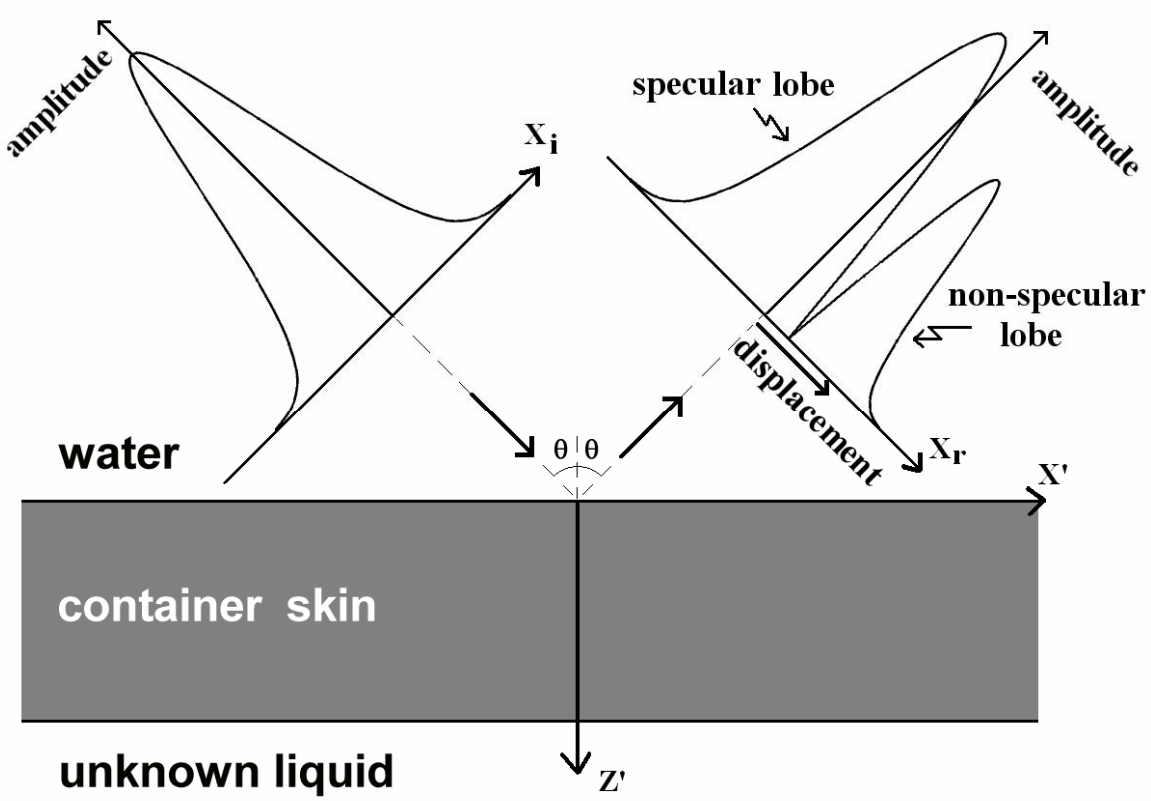

Fig. VIII.A_1: ***Schematic of a container skin separating an 'unknown' liquid and water. The incident and (deformed) reflected bounded beam profiles are also shown. The short solid arrows denote propagation direction for incident and reflected beam.***

NUMERICAL APPROACH

We consider the system depicted in Fig. VIII.A_1. A gaussian incident bounded beam is considered with profile

$$f(x) = \exp\left(-x^2 / W^2\right) \qquad \text{(VIII.A\_1)}$$

with W the gaussian half width. The beam itself is decomposed into infinite homogeneous plane waves by means of the Fourier transform. The sound field generated by each incident infinite homogeneous plane wave is calculated by application of the Helmholtz decomposition [29] of the particle displacement field, by incorporating the dispersion relation for bulk waves and the classical Snell's law [30] and by considering continuity of normal stress and normal displacement along each of the interfaces [31].

NUMERICAL RESULTS

It can be found in Greenwood et al [8-11] that if the reflection coefficient is used to determine liquid characteristics, the difference in acoustical impedance between the solid and the liquid must not be too large. Nevertheless, for containers, the impedance of the skin mostly differs very

much from that of the contained liquid. It is hence not reasonable to use the reflection coefficient for liquid characterization in such containers.
In order to show this, we have calculated the reflected beam amplitude and phase at the center of the beam, for normal incidence and for a number of liquids in a container. We have taken the example of a glass plate container skin of 1.86 mm thickness and a 3MHz normal incident Gaussian beam of 1.25 cm gaussian half width. For glass, the density is 2500 kg/m³, whereas the longitudinal wave velocity is 5660 m/s and the shear wave velocity 3520 m/s. The liquid characteristics and the numerical results are listed in Table VIII.A_I, where the following parameters are used:

$$\Delta A_L^r(x) = \frac{A_L^r(x) - A_W^r(x)}{Z_L - Z_W} \qquad \text{(VIII.A\_2)}$$

$A_L^r(x)$ being the x-dependent reflected amplitude for a given liquid underneath the plate and Z_L the liquid's impedance, equal to ρv [kg/m²s].

$$\Delta PH_L^r(x) = \frac{PH_L^r(x) - PH_W^r(x)}{Z_L - Z_W} \qquad \text{(VIII.A\_3)}$$

$PH_L^r(x)$ being the x-dependent reflected phase for a given liquid underneath the plate. The values, for L replaced by W, correspond to water. It is seen that the difference in reflected amplitude and phase, for any given liquid, when compared with the ones for water underneath the plate, is poor.

One way to increase the sensitivity of the reflection coefficient for the properties of the unknown liquid is to apply multiple reflections, because then the resulting reflection coefficients are separated further from one another. Hence the larger the number of contacts between the pulse and the unknown liquid, the more the pulse is influenced by the liquid. For a harmonic incident beam, the largest contact with the liquid occurs when Lamb waves are stimulated in the container skin. The fluid will influence the characteristics of the leakage field emitted by the Lamb wave. When the Schoch effect occurs, the second (nonspecular) lobe contains most information about the liquid, for this lobe originates from the presence of a leakage field. Again, we have taken the example of a glass plate of 1.86 mm thickness and a 3MHz incident Gaussian beam of 1.25 cm gaussian half width. From the corresponding dispersion curves of Fig VIII.A_2, it can be found that an A_1 Lamb mode will be generated at an angle of incidence of 19.36°. In Fig. VIII.A_3 the incident beam profile together with the calculated reflected beam amplitude profile in the case of oil and in the case of water underneath the plate are shown for an angle of incidence of 19.36° corresponding with stimulated A_1 Lamb waves. It is seen that the reflected profiles differ considerably.

Table VIII.A_I : ***The central reflected amplitude*** $A_L^r(0)$***, the central reflected phase*** $PH_L(0)$***, and the differences of those parameters for a given liquid underneath the plate, compared to their values in the case of water underneath the plate,*** $\Delta A_L^r(0)$ ***respectively*** $\Delta PH_L^r(0)$ ***. The density*** ρ ***, plane wave velocity v and the impedance Z of the listed liquids is also given.***

liquid	ρ [kg/m³]	v [m/s]	$A_L^r(0)$	$\frac{PH_L(0)}{\pi}$	$\Delta A_L^r(0)$ $\times 10^9$	$\Delta PH_L^r(0)$ $\times \frac{10^5}{\pi}$
methanol	791	1103	0.9975	-0.138	-2.4690	3793
acetone	791	1174	0.9981	-0.1091	-3.8087	6609
ethanol	790	1207	0.9968	-0.1008	-1.5195	2574
gasoline	803	1250	0.9981	-0.136	-4.4094	8913
kerosene	810	1320	0.9984	-0.1168	-5.8422	13821
benzene	870	1295	0.9916	-0.0831	12.4522	-35705
Sunflower oil	920	1450	0.9879	-0.1635	55.4794	-381122
Cyclo-hexanole	962	1450	0.9874	-0.1644	101.0575	-1189447
water	1000	1480	0.996	-0.133	-	-
Nitro-methane	1130	1330	0.9958	-0.1029	-8.7336	-374201
sea water	1025	1531	0.9961	-0.1298	1.1201	14388
glycerin	1260	1904	0.9221	0.009	-80.4099	-87314
bromoform	2890	920	0.9567	-0.1827	-33.3389	-28142
mercury	13500	1450	0.9851	0.0033	-0.6023	-24

When the reflected beam phase profiles are compared, one notices a considerable difference too (Fig. VIII.A_4). If we define x^* as the position where the nonspecular reflected lobe has maximum amplitude, then for sunflower oil $\Delta A_L^r(x^*) = -1144 \times 10^{-9}$ whereas $\Delta PH_L^r(x^*) = 6379 \times 10^{-10}\pi$. These values are much larger than the values for normal incidence of Table VIII.A_I. In other words, the use of the Schoch effect is much more sensitive than the use of the reflection coefficient. However, contrary to the method of Greenwood et al, when the Schoch effect is used to obtain information about the unknown liquid, it is not possible to come to a direct inversion method to find the liquid characteristics from the reflected profile. When inversion is necessary, optimization procedures must be applied in order to estimate the liquid parameters. Nevertheless it is not certain that the liquid parameters corresponding to a given reflected profile, are unique. The method presented here can therefore be used to discriminate between given liquids (e.g. water and oil), rather than to find out the exact physical parameters of an unknown liquid.

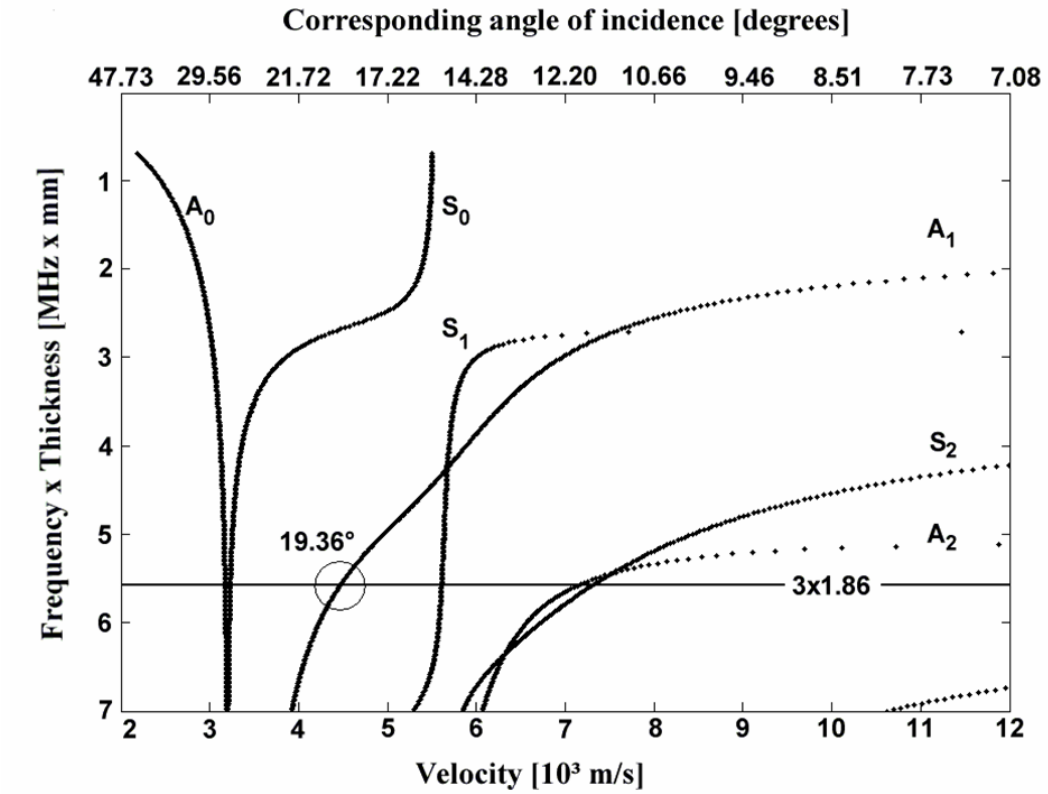

Fig. VIII.A_2: ***Dispersion curves for the glass plate under consideration. It is seen that an angle of incidence of 19.36° corresponds with the stimulation of the A_1 mode when a 3MHz ultrasonic beam is incident on a plate of 1.86 mm thickness.***

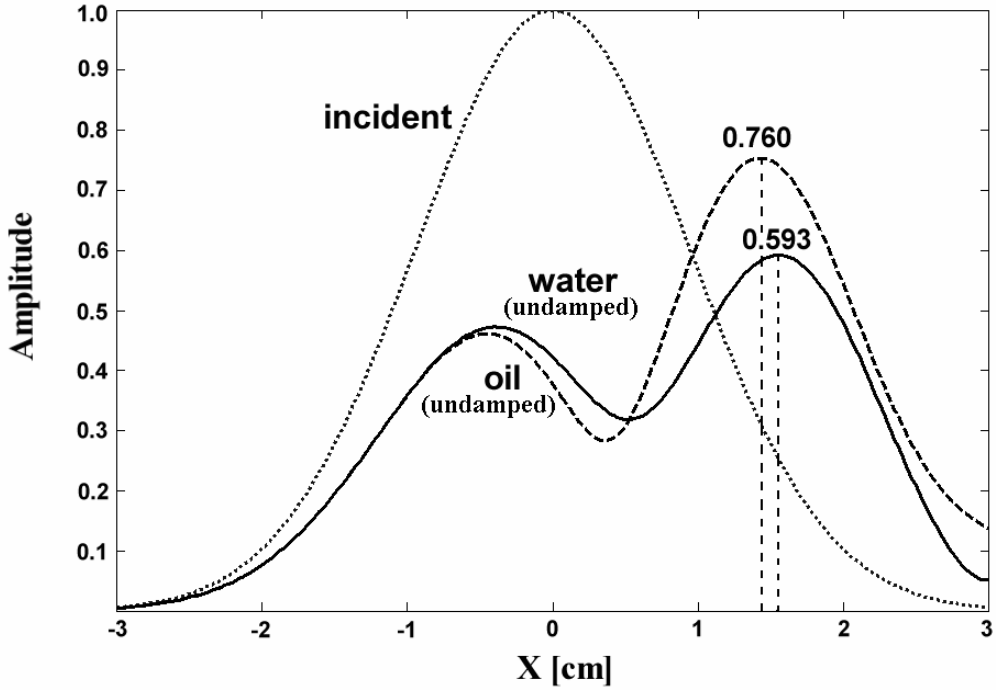

Fig. VIII.A_3: ***Reflected amplitude profiles, for a 3MHz bounded beam incident at 19.36° on a 1.86 mm thick glass plate, when the unknown liquid underneath the container skin is water (solid line) or sunflower oil (dashed line). The incident beam profile is given in a dotted line. The maximum amplitude of the nonspecular reflected beam is explicitly given.***

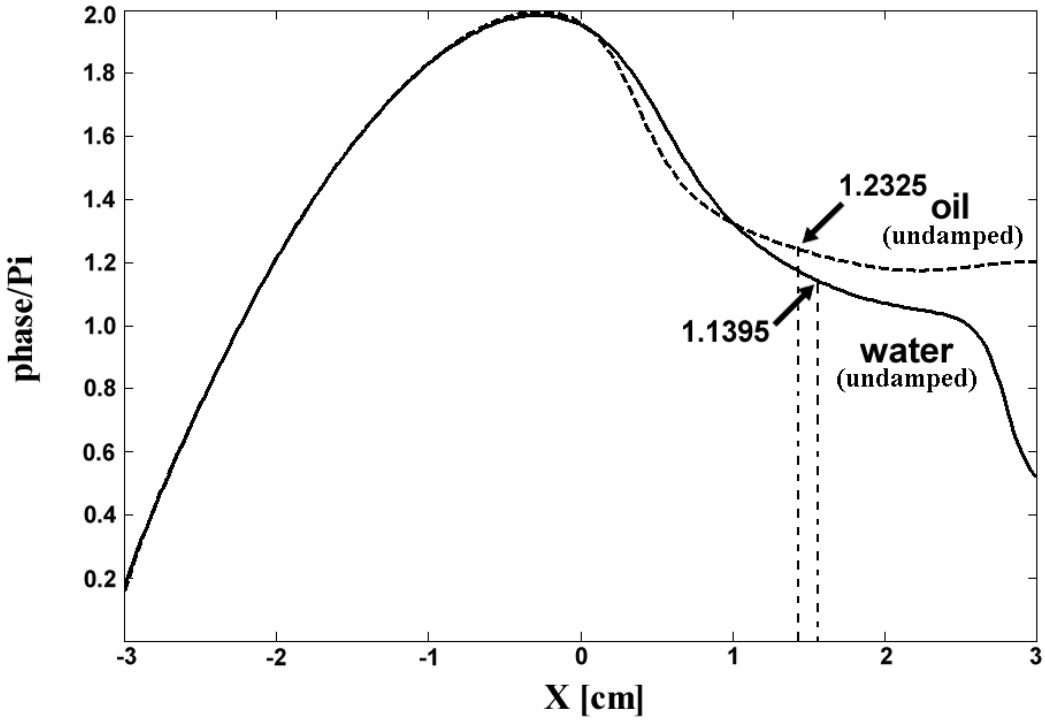

Fig. VIII.A_4: ***Corresponding phase profiles for the geometry of Fig. VIII.A_3.. The phase, at the position corresponding with the maximum amplitude of Fig. VIII.A_3, is explicitly given.***

CONCLUSIONS

First, an overview has been given of different techniques to characterize liquids in containers and the necessity of introducing a new technique based on the Schoch effect caused by Lamb wave stimulation in the skin of a container. It is shown that the Schoch effect can be used to distinguish between different liquids in containers. The method does not apply built-in or submerged sensors and does not require opening of the container. Numerical comparison was made between the sensitivity of the outlined method and another technique that is based on the reflection coefficient. An example was given for a glass container, where it is seen that the Schoch effect is much more sensitive than the reflection coefficient. We believe that the presented technique can be very effective, due to its flexibility and its non-requirement of built in sensors, if it is combined with phased array techniques to emit and receive the involved sound fields.

REFERENCES

[1] Newsletter of the contact group of customs managers of northern ports EU, RALFH(3), 1-6, July 2002.
[2] Containerscan op de Rotterdamse Maasvlakte, Brochure of The Netherlands port customs, External and Internal Communication, May 1999 (in Dutch).
[3] Michael P. Snell, "Gamma-Ray Technology: The Practical Container Inspection Alternative", Port Technology International 9(3), 83-91.
[4] J. Abrehouch, R. Latif, A. Moudden, B. Faiz, "Non Destructive Ultrasonic Characterization of Canned Fish Oil", Acta Acustica United with Acustica, 88, 587-591, 2002 (In French).

[5] John M. Doyle, "Detector can scan containers for contraband without unsealing", Aviation Weeks Homeland Security & Defense, Feb 20, 2003.
[6] PASS (Product Acoustic signature system), brochure found on http://www.mehlgriffinbartek.com/html/press_frames.htm.
[7] S. Petillion, N. Van Riet, C. Glorieux, "Laser ultrasonic characterization of complex acoustic properties of viscous liquids", poster P112 at Ultrasonics International 2003, Granada, Spain.
[8] M.S. Greenwood, J. R. Skorpik, J. A. Bamberger, R. V. Harris, "On-line ultrasonic density sensor for process control of liquids and slurries", Ultrasonics 37, 159-171, 1999.
[9] Margaret Stautberg Greenwood, Judith Ann Bamberger, "Measurement of viscosity and shear wave velocity of a liquid or slurry for on-line process control", Ultrasonics 39, 623-630, 2002.
[10] Margaret S. Greenwood, Judith A. Bamberger, "Ultrasonic sensor to measure the density of a liquid or slurry during pipeline transport", Ultrasonics 40, 413-417, 2002.
[11] Margaret S. Greenwood, Jason C. Lail, "Ultrasonic fluid densitometry and densitometer", J. Acoust. Soc. Am. 104(2), 614, 1998.
[12] M. A. Breazeale, Laszlo Adler, Gerald W. Scott, "Interaction of ultrasonic waves incident at the Rayleigh angle onto a liquid-solid interface", J. Appl. Phys, 48(2), 530-537, 1977.
[13] M. A. Breazeale, Laszlo Adler, Larry Flax, "Reflection of a Gaussian ultrasonic beam from a liquid-solid interface", J. Acoust. Soc. Am. 56(3), 866-872, 1974.
[14] Tran D. K. Ngoc, Walter Mayer, "Numerical integration method for reflected beam profiles near Rayleigh angle", J. Acoust. Soc. Am. 67(4),1149-1152, 1980.
[15] Abdellatif Bey Temsamani, Steve Vandenplas, Leo Van Biesen, "Experimental investigation of bounded beam reflection from plane interfaces in the vicinity of leaky waves angles", Ultrasonics 38, 749-753, 2000.
[16] M. de Billy, I. Molinero, "On the nonobservance of nonspecular bounded beam reflection effects of Lamb modes", J. Acoust. Soc. Am. 83(4), 1249-1254, 1988.
[17] John Pott, John G. Harris, "Scattering of an acoustic Gaussian beam from a fluid-solid interface", J. Acoust. Soc. Am. 76(6), 1829-1838, 1984.
[18] J. M. Claeys, O. Leroy, "Reflection and transmission of bounded sound beams on half-spaces and through plates", J. Acoust. Soc. Am. 72(2), 585-590, 1982.
[19] Tribikram Kundu, "On the nonspecular reflection of bounded acoustics beams", J. Acoust. Soc. Am. 83(1), 18-24, 1988.
[20] Werner G. Neubauer, "Ultrasonic reflection of a bounded beam at Rayleigh and critical angles for a plane liquid-solid interface", J. Appl. Phys 44(1), 48-55, 1973.
[21] Tran D. K. Ngoc, Walter G. Mayer, "Influence of Plate Mode Structure and Gaussian Beam Profile Characteristics on Ultrasonic Reflection and Transmission", IEEE Trans. on Sonics and Ultrasonics, SU-29(2), 112-114, 1982.
[22] Thomas J. Plona, Leslie E. Pitts, Walter G. Mayer, "Ultrasonic bounded beam reflection and transmission effects at a liquid/solid-plate/liquid interface", J. Acoust. Soc. Am. 59(6), 1324-1328, (1976).
[23] K. W. Ng, T. D. K. Ngoc, J. A. McClure, W. G. Mayer, "Nonspecular Transmission Effects for Ultrasonic Beams Incident on a Solid Plate in a Liquid", Acustica 48, 169-173, 1981.
[24] Tran D. K. Ngoc, Walter G. Mayer, "A General Description of Ultrasonic Nonspecular Reflection and Transmission Effects for Layered Media", IEEE Trans. on Sonics and Ultrasonics , SU-27(5), 229-236, 1980.
[25] Leslie E. Pitts, Thomas J. Plona, Walter G. Mayer, "Theory of Nonspecular Reflection Effects for an Ultrasonic Beam Incident on a Solid Plate in a Liquid", IEEE Trans. on Sonics and Ultrasonics, SU-24(2), 101-109, 1977.
[26] Smaine Zeroug, Leopold B. Felsen, "Nonspecular reflection of two- and three-dimensional acoustic beams from fluid-immersed plane-layered elastic structures", J. Acoust. Soc. Am. 95(6), 3075-3089, 1994.
[27] Theodore E. Matikas, Martine Rousseau, Philippe Gatignol, "Theoretical analysis for the reflection of a focussed ultrasonic beam from a fluid-solid interface", J. Acoust. Soc. Am. 93(3), 1407-1416, 1993.
[28] Peter B. Nagy, Kangra Cho, Laszlo Adler, D. E. Chimenti, "Focal shift of convergent ultrasonic beams reflected from a liquid-solid interface",J. Acoust. Soc. Am. 81(4), 835-839, 1987.
[29] J.D. Achenbach, wave propagation in elastic solids, north-holland 1975.
[30] Nico F. Declercq, Joris Degrieck, Oswald Leroy, "On the generalized Snell's law and its possible relation to coherent backscattering of ultrasonic waves", Appl. Phys. let. , 4245-4247, 84(21), 2004.
[31] Adnan H. Nayfeh, wave propagation in layered anisotropic media with applications to composites, north-holland, 1995.

VIII.B On the capability of Leaky Lamb waves to discriminate between real and fictitious liquids

Leaky Lamb waves are complex poles of the reflection coefficient for (inhomogeneous) waves incident on a plate surrounded by liquid. When the plate is separating two different liquids, the real part of the pole is almost independent of the liquids, whereas the imaginary part highly depends on the physical difference between the two liquids. It is found that this dependence shows linear characteristics if both liquids are real. If one of the liquids is fictitious, then the dependence does not obey this linearity anymore. The method is inviting for theorists when, in certain numerical models in whatever physical problem, they need to figure out whether their assumed liquid parameters are realistic or not.

The work in this section was performed in collaboration with my graduate student Filip Van den Abeele.

INTRODUCTION

A study, intended to reveal changes of the Schoch effect due to Lamb wave stimulation, in order to characterize liquids in closed containers [1], showed that this effect is quite susceptible to the physical properties of contained liquids. Furthermore, in many studies in ultrasonics, the interaction of ultrasound with 'objects' immersed in a liquid is investigated. For theorists, when modeling such situations, it is then desirable to consider an existing liquid, having a measured density and sound velocity, in order to avoid possible prediction of artificial phenomena due to 'impossible' characteristics of the chosen liquid. Nevertheless, it is obvious that minor deviations from the exact values, due to experimental errors when measuring the density or measuring the sound velocity, will not make the existence of that particular chosen liquid, in the theoretical model, impossible, or make its influence on the obtained numerical results unreliable.
However, the immediate question arising here is : When do we consider a liquid to be realistic and when do we agree that it cannot exist and is therefore fictitious? In what follows, it will be shown that the imaginary part of the complex pole corresponding to Lamb wave generation, depends on the impedance difference between the two liquids on both sides of the plate. Furthermore, it will be shown that this dependency is linear for all existing liquids and realistic liquids, but that it is not linear and even random, in the case when one of the liquids is fictitious.

LEAKY LAMB WAVES IN A PLATE SEPARATING TWO DIFFERENT LIQUIDS

In this report, we consider 3 solids: stainless steel (density = 7900 kgm^{-3}, shear wave velocity = 3200 m/s, longitudinal wave velocity = 5790 m/s), brass (density = 8600 kgm^{-3}, shear wave velocity = 2150 m/s, longitudinal wave velocity = 4410 m/s) and glass (density = 2500 kgm^{-3}, shear wave velocity = 3520 m/s, longitudinal wave velocity = 5660 m/s).

For a plate in vacuum, Lamb waves are solutions of the equations, expressing the disappearance of normal stress at the vacuum/solid interfaces. The solutions are real. For a plate immersed in a liquid, Lamb waves are solutions of the continuity equations, expressing continuity of normal stress and normal displacements at the liquid/solid interfaces. Here, the solutions are complex, because Lamb waves radiate energy into the liquid, resulting in a complex wave vector of its plane wave components. These complex solutions correspond to poles, or singularities, of the reflection coefficient for inhomogeneous plane waves incident from the liquid onto the plate. Therefore, it is inviting to apply the theoretical development of [1] and extract information about the position of those poles. Special attention will be drawn on the cases where the liquids on both sides of the plate differ from each other.

NUMERICAL RESULTS

According to the generalized law of Snell-Descartes [3-7], the wave vector component parallel to the plate is, for a given liquid (liquid 1) from which sound is incident, completely determined by the real angle of incidence θ and the inhomogeneity vector β. Then, a pole corresponding to leaky Lamb waves, is determined by this real angle θ and inhomogeneity vector β. We noticed that, for a given 'liquid 1', the real angle is independent of the liquid on the other side of the plate (liquid 2). Therefore, the real angle θ is applied to determine the kind of leaky Lamb wave that is generated, whereas the inhomogeneity β contains information about liquid 2.

In Fig. VIII.B_1, the dispersion curves for Lamb waves in a stainless steel plate are given. We consider a [frequency x thickness] equal to 3 MHz x mm. Three types Lamb waves are indicated, i.e. A_0, S_0 and A_1 Lamb waves. Moreover, the reflection coefficient for this case is shown as a function of the real angle of incidence θ and the inhomogeneity β in the situation where the plate is immersed in water. Note that for each type of Lamb wave, there is a position [θ, β] where the reflection coefficient corresponds to a pole or singularity. For reasons of readability, the plot in Fig. VIII.B_1 is made for a limited grid. Therefore the 'peaks' appear to be finite. In reality however, they tend to infinity. In what follows, the position of the different peaks are determined for a sufficiently fine grid. As a matter of fact, the positions are determined by restricting the 2D interval around the peaks and create zoom-in calculations, in order to avoid unnecessary calculations in uninteresting areas. Table VIII.B_I lists the different liquids considered. Because the number of possible fictitious liquids is infinite, we have only listed 5 of them (A-E). As a reference, each time, we take the considered plate immersed in water (liquid 1 = liquid 2) and determine the inhomogeneity β_0 at which the pole exists (for the given impedance Z_0 of water).

Then, if liquid 2 changes, we determine the new values β and Z, and plot $\Delta\beta = \beta - \beta_0$ as a function of $\Delta Z = Z - Z_0$. The results for the stainless steel plate, in the case of A_1 Lamb wave stimulation, are shown in Fig. VIII.B_2. The codes corresponding to the different liquids are also added. Subsequently, in the other figures, these codes are ignored and can always be reconstructed because the numbers follow the impedance sequence, see Table VIII.B_I. Note that the values corresponding to existing liquids all follow a linear tendency, whereas the values corresponding to fictitious liquids are distributed within the coordinate plane. In fact, a larger number of calculations showed that whenever fictitious liquids are considered, the results are randomly distributed and only accidentally coincide with the straight line.

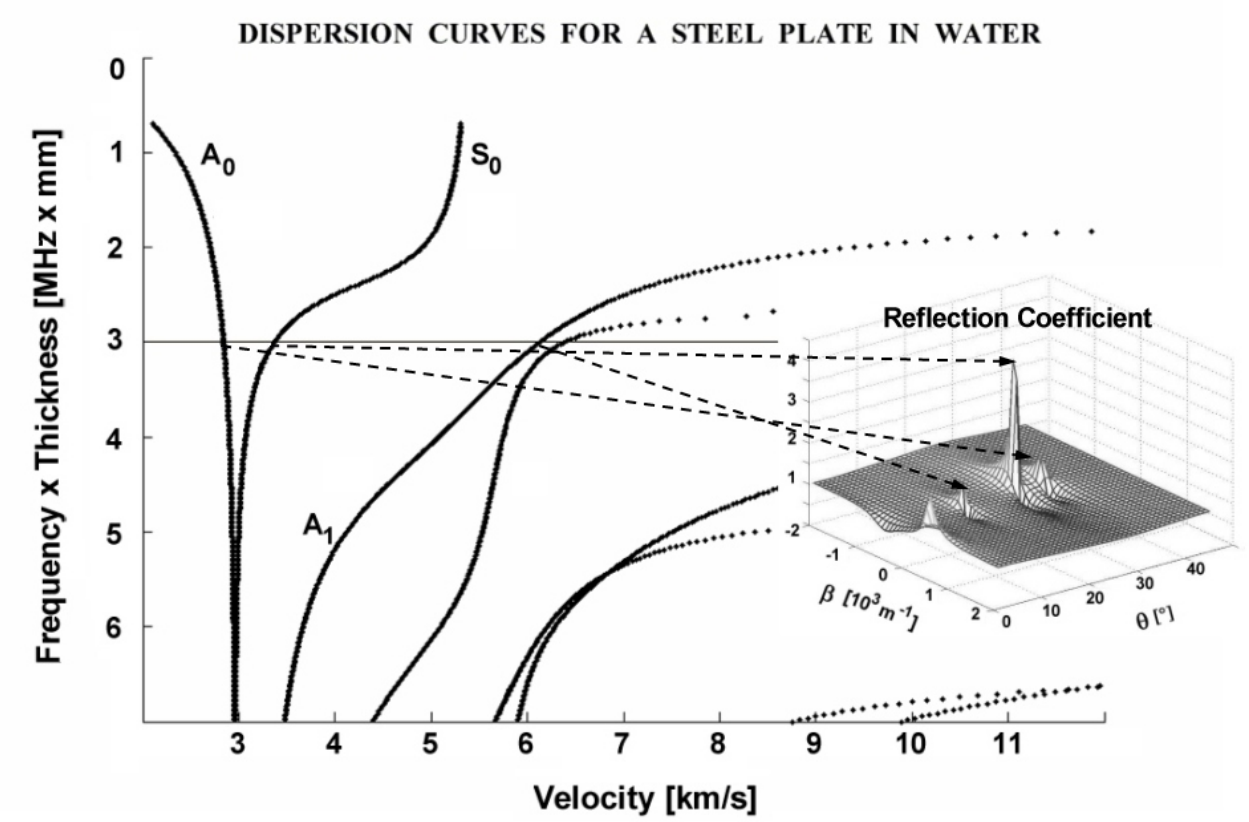

Fig. VIII.B_1: ***The dispersion curves for Lamb waves in a stainless steel plate are given. The horizontal indicated line corresponds to a [frequency x thickness] equal to 3 MHz x mm. Three types Lamb waves are indicated, i.e. A_0, S_0 and A_1 Lamb waves. On the right, a small image is added of the reflection coefficient for this case as a function of the real angle of incidence θ and the inhomogeneity β in the situation where the plate is immersed in water. For each type of Lamb wave, there is a position [θ, β] where the reflection coefficient corresponds to a pole or singularity.***

The straight line that is drawn in Fig. VIII.B_2 and also in the other figures further on, is obtained through a least squares approximation. In Fig. VIII.B_3, the same procedure was followed for different materials of container skin and only for existing liquids. Note that the results follow straight lines once again and the direction of each straight line is a function of the solid under consideration. In Fig. VIII.B_4, the case of a brass container skin is considered under the same circumstances as in Fig. VIII.B_2 and Fig. VIII.B_3, though for different Lamb waves. Note that the direction appears to be is dependent of the type of Lamb wave. Finally in Fig. VIII.B_5, the result is shown for other combinations of [frequency(f) x thickness(d)]. Again, the existing liquids follow a linear tendency with a direction depending on f x d.

Table VIII.B_I : List of liquids, ordered according to for increasing acoustical impedance

Code	name	ρ [kg/m³]	**C** [m/s]
1	Ch4h9Cl	840	980
2	Alcohol, methanol	791	1103
3	Alcohol, isopropyl	786	1170
4	Acetone	791	1174
5	Ethanol at 25°C	790	1204
6	Alcohol, ethanol	790	1207
7	Alcohol, propyl	804	1220
A	Fictitious liquid A	147	6750
8	Gasoline	803	1250
9	Alcohol, butyl	810	1240
B	Fictitious liquid B	309	3440
10	Petroleum	825	1290
11	Kerosene	810	1320
12	Acetate, butyl	871	1270
13	Benzene	870	1295
14	Benzol	878	1330
15	Univis 800	870	1350
16	Fish Oil	880	1440
17	Transformer Oil	920	1390
18	Safflower Oil	900	1450
19	Peanut Oil	914	1436
20	Soybean Oil	930	1430
C	Fictitious liquid C	465	2860
21	Sunflower Oil	920	1450
22	Corn Oil	922	1460
23	Olive Oil	948	1430
24	Cyclohexanole	962	1450
25	**Water**	1000	1480
D	Fictitious liquid D	400	3700
26	Silicon dow oil	1110	1352
27	Nitromethane	1130	1330
28	Glycol-butylene	1019	1480
29	Sea water	1025	1531
30	Alcohol, furfuryl	1135	1450
E	Fictitious liquid E	568	2900
31	Glycol-PE 400	1060	1620
32	Ethanol amide	1018	1720
33	Dimethyl phthalate	1200	1460
34	Glycol-PE 200	1087	1620
35	Glycol-ethylene II	1108	1590
36	Glycol-diethylene	1116	1580
37	Glycol-tetraethylene	1120	1580
38	Glycol-triethylene	1123	1610
39	Formamide	1134	1620
40	Glycol-ethylene	1113	1658

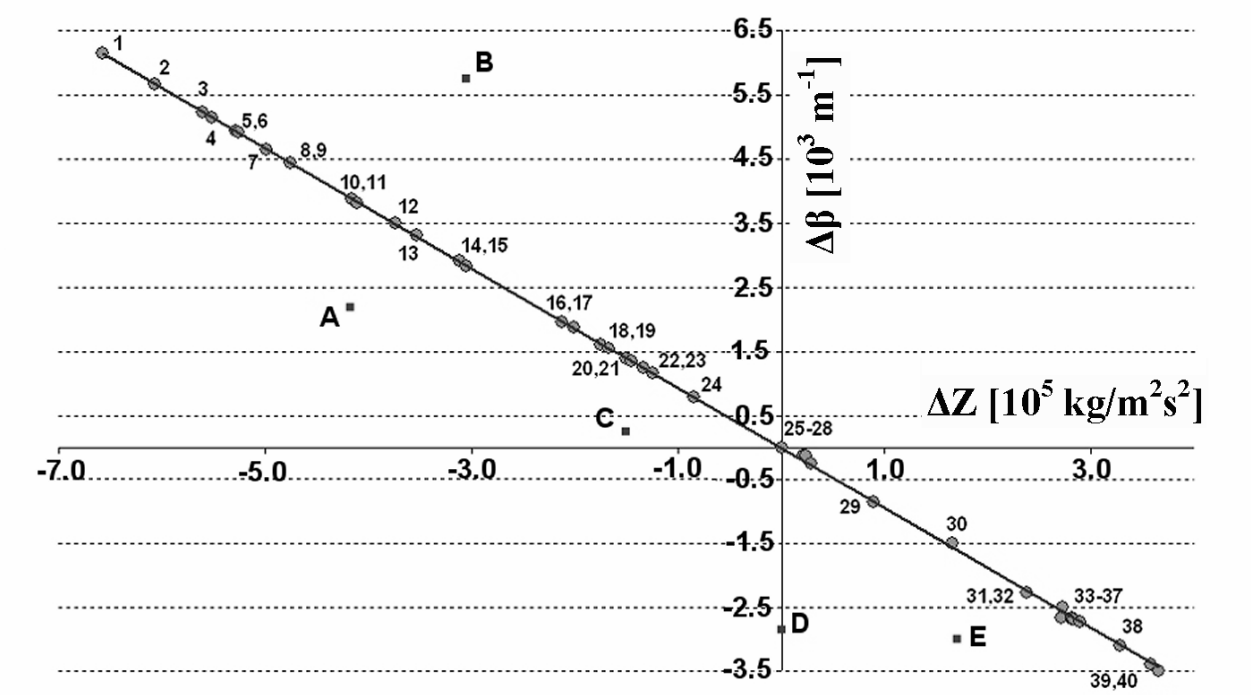

Fig. VIII.B_2: $\Delta\beta = \beta - \beta_0$ ***as a function of*** $\Delta Z = Z - Z_0$***. The results for the stainless steel plate, in the case of*** A_1 ***Lamb wave stimulation, for 'liquid 1' = water and 'liquid 2' listed in Table VIII.B_1. The codes corresponding to the different liquids are also added.***

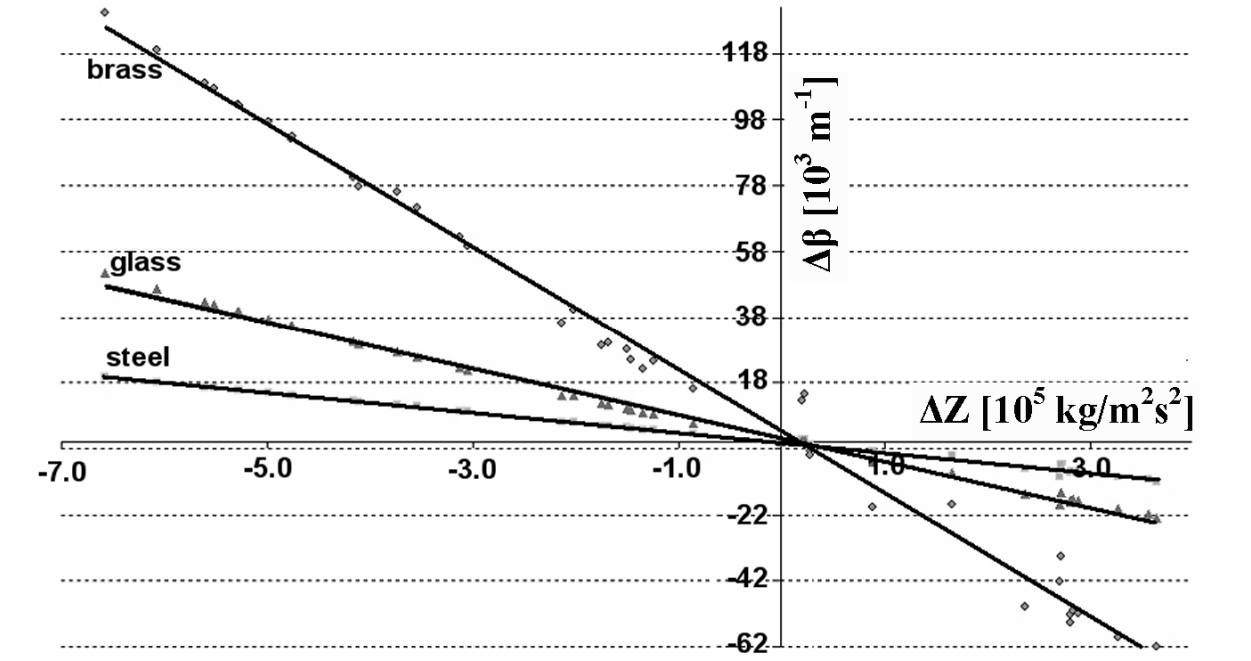

Fig. VIII.B_3: ***The same procedure was followed as in Fig. VIII.B_2, but for different materials of container skin and only for existing liquids. Note that the results follow straight lines and the direction of each straight line is a function of the solid under consideration.***

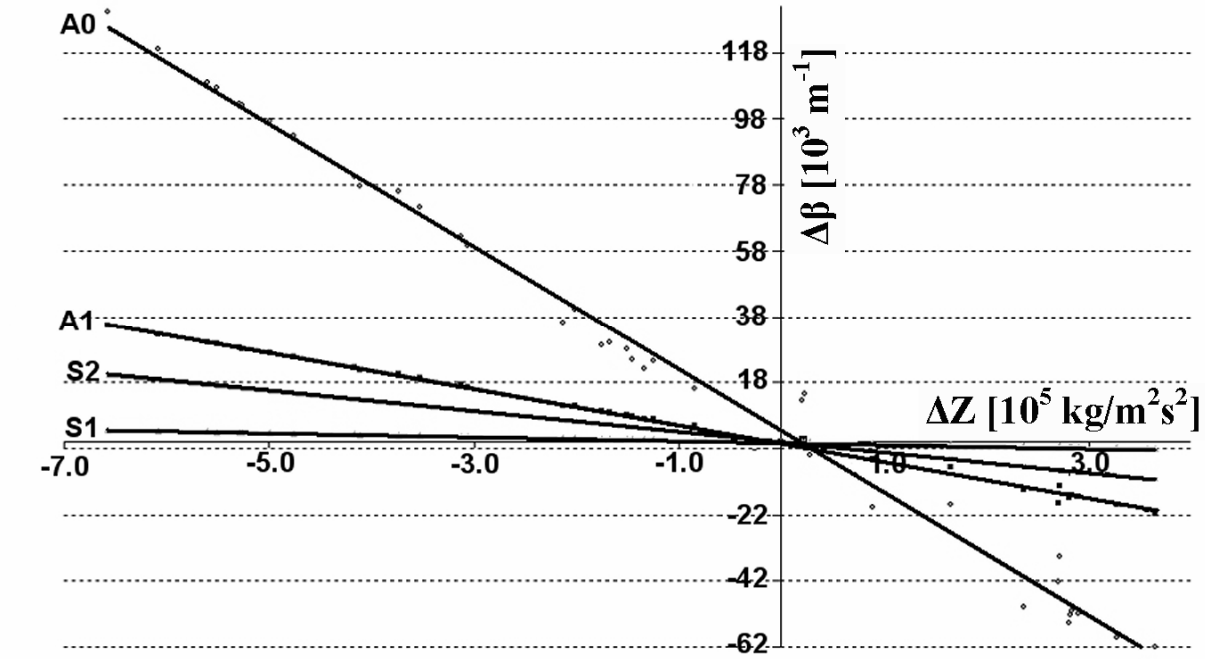

Fig. VIII.B_4: ***A brass container skin is considered under the same circumstances as in Fig. VIII.B_2 and Fig. VIII.B_3, though for different Lamb waves. The direction depends on the type of Lamb wave.***

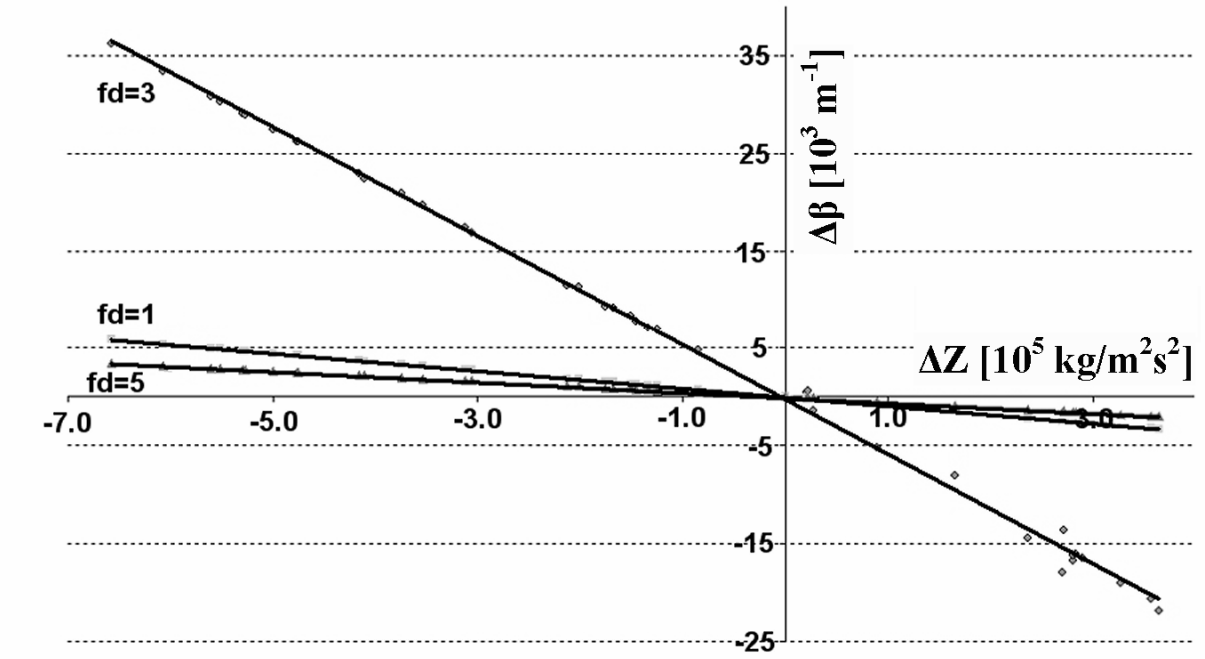

Fig. VIII.B_5: ***The result is shown for other combinations of [frequency(f) x thickness(d)]. Again, the existing liquids follow a linear tendency with a direction depending on f x d.***

CONCLUSIONS

It is shown that the imaginary part of the complex pole of the reflection coefficient is linearly dependent of the impedance difference between 'liquid 1' and 'liquid 2'. This linear tendency depends on the kind of Lamb wave, on the considered frequency and on the material of which the solid plate is made of. Furthermore, the linear trend only holds for existing liquids. Fictitious liquids do not follow this linear trend and produce randomly scattered results.

REFERENCES

[1] Nico F. Declercq, Filip Van den Abeele, Joris Degrieck, Oswald Leroy, "The Schoch Effect to Distinguish Between Different Liquids in Closed Containers", IEEE Trans. on UFFC 51(10), 1354-1357, 2004
[2] Igor Aleksandrovich Viktorov, "Rayleigh and Lamb Waves, Physical Theory and Applications", Plenum press New York, 1967
[3] Nico F. Declercq, Rudy Briers, Joris Degrieck, Oswald Leroy, "The History and Properties of Ultrasonic Inhomogeneous Waves", accepted for publication in IEEE Trans. on UFFC.
[4] Marc Deschamps, Bernard Hosten, "The effects of viscoelasticity on the reflection and transmission of ultrasonic waves by an orthotropic plate", J. Acoust. Soc. Am. 91(4), 2007-2015, 1992
[5] B. Poirée, "Complex harmonic waves", 99-117, Physical Acoustics, Edited by O. Leroy and M. A. Breazeale, Plenum Press, New York, 1991
[6] Allard JF, Lauriks W, "Poles and zeros of the plane wave reflection coefficient for porous surfaces", Acustica 83(6), 1045-1052, 1997
[7] M. Deschamps, O. Poncelet, "Inhomogeneous plane wave and the most energetic complex ray", Ultrasonics 40, 293-296, 2002

Chapter IX Sound in Media Having Discontinuities in More Than One Direction

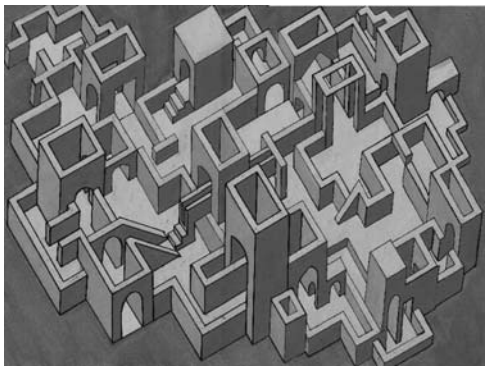

The exact description of sound inside a labyrinth will probably never be accomplished. It is simply far too complicated.

One of the main principles in acoustics, is the conservation of symmetry. The symmetry of a sound field is always equal to the symmetry of its source. After interaction with an object, this symmetry is distorted and becomes partly determined by the symmetry of that object. Therefore, the interaction of sound with an infinite plate can be relatively easy described by means of a decomposition into infinite plane waves. On the other hand, the interaction of sound with a finite plate or with a plate containing an inclusion or anything else, cannot be described anymore by means of a decomposition into infinite plane waves.

One of the most sophisticated theoretical models that resembles the physical reality best, is the so called 'Radiation Mode Theory'. Even though this theory is mathematically 'heavy loaded', it is described very 'friendly' in section IX.A. The reason for this description is that it is my intention to make the Radiation Mode Theory one of the major research subjects in my life after this PhD-dissertation. Furthermore, in section IX.B, while describing the interaction of Rayleigh waves with the edge of a plate, there will be referred to the Radiation Mode Theory of section IX.A. Also, in the next chapter (section X.A.1.b), facts about Scholte – Stoneley waves, obtained from section IX.A, will be hard experimental evidence for the statement that the backward beam displacement is due to a leaky form of Scholte – Stoneley waves.

Section IX.C describes the (beautiful) interaction of a bounded beam with the edge of a plate, incident at the Lamb angle.

IX.A The Radiation Mode Theory in Ultrasonics

This section describes the history and the state of the art in radiation mode theory (RMT) in ultrasonics. The RMT originates from electromagnetism where it has proved to be very efficient in the field of wave guides and discontinuities. In ultrasonics the RMT made its entrance only a decade ago and has already proved to be very efficient in describing the interaction of sound with discontinuities such as a step on a plate, a liquid wedge, the extremity of a plate and much more. It is likely that the development of the RMT for 2D isotropic media has come almost to an end. This section lists the results obtained so far. Further extensions to more complicated media are to be expected the coming decade.
The contents of this section have been accepted for publication in IEEE Transactions on Ultrasonics, Ferroelectrics, and Frequency Control (Imp. Fact. 1.595 ;SCI-index, Engineering – electrical & electronic, rank:46/205)

INTRODUCTION

The general rule in acoustics is to describe sound in the same symmetrical system as the scatterer or as the sound source. For example sound emitted by a cylinder is described in cylindrical coordinates, while sound emitted by a sphere is described in spherical coordinates.

When the interaction of sound needs to be described in a system with only discontinuities in one dimension, e.g. an infinite plate swamped in water, the theory of plane waves is very suitable. That is because plane waves extend to infinity and so does the considered system. If however the interaction of sound is to be described with a system containing discontinuities in more than one dimension, e.g. a cube swamped in water, then the plane wave theory becomes unsuitable because it does not reflect the symmetry of the system under consideration. In such systems a description by means of 'modes' becomes very suitable. Furthermore, whenever an incident bounded beam is considered, most scientists decompose this bounded beam into plane waves. However from a mathematical point of view that is only correct if normal incidence is taken under consideration. The reason is that if a decomposition into plane waves is considered, the Fourier method is applied. This method consists of an integration of the beam profile along the z'-axis (see Fig. IX.A_1) and thus implicitly imposes that there are no discontinuities along that direction. If the profile is considered far away from the interface, the mentioned problem is avoided by the fact that the profile becomes almost zero at large distances away from the beam center, but if the profile is considered closer to the interface it is clear that the Fourier method should actually not be applied. Moreover whenever the Fourier method is applied it is always assumed that the reflected sound depends on the incident sound and not vice versa. In other words the incident sound is not disturbed by the reflected sound. This again follows from the incorrectly assumed fact that the incident sound pattern would solely depend on its amplitude distribution along an infinite line (z' in Fig. IX.A_1) and cannot depend on the fact that there is an interface present along the integration path in the Fourier analysis. The RMT, first created and applied in electromagnetism [1-2] and later developed in acoustics [3-13], provides a physical and mathematical solution to such problems. In the RMT no integration path is needed in the Cartesian axes system (X,Y,Z) but only in the phase space (k_y). Furthermore discontinuity

conditions in two dimension are dealt with by dividing the system into substructures that only contain discontinuities in one direction.
In what follows we will describe the basics of RMT, followed by some of the main results that have been obtained in the first decade of its existence.

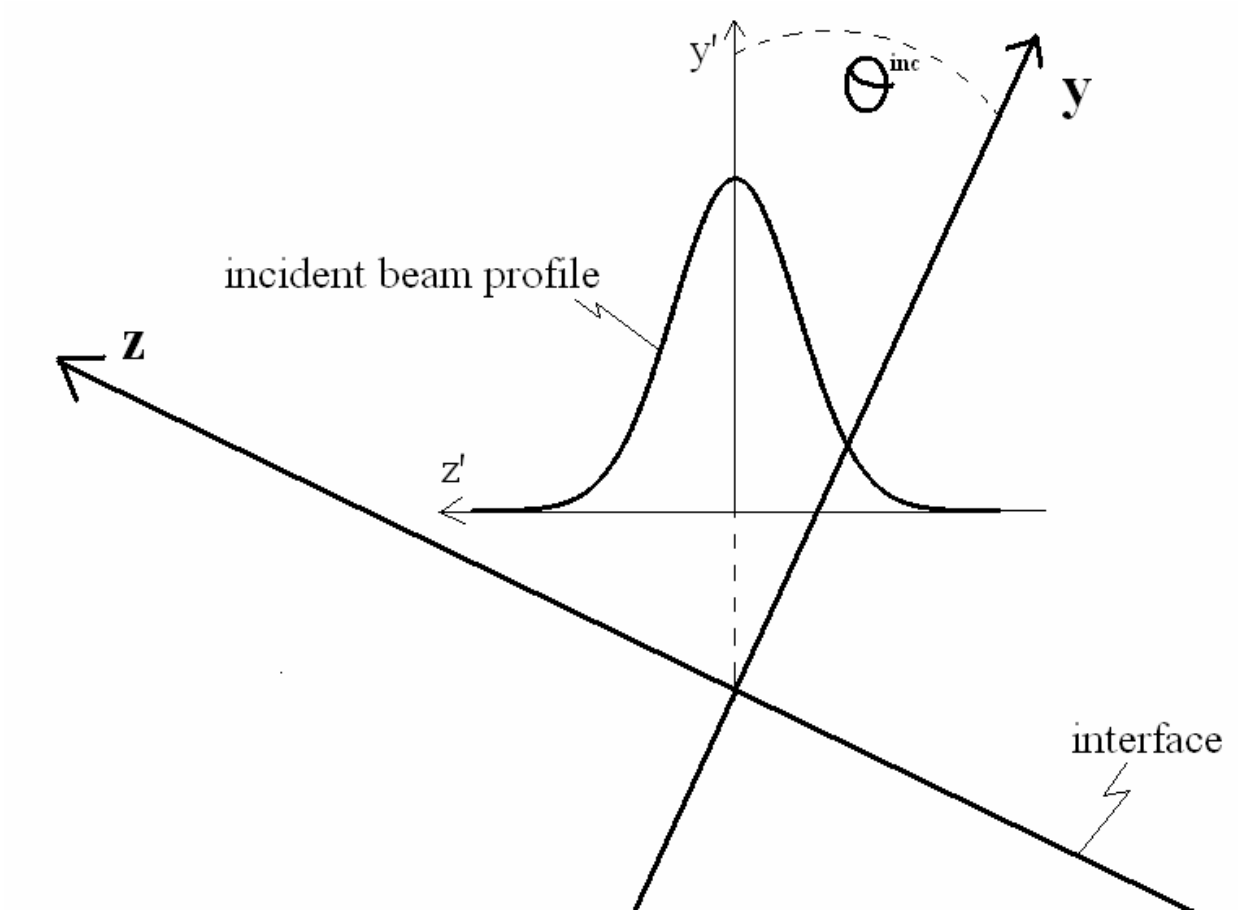

Fig. IX.A_1: ***A bounded beam incident on the interface at an angle*** θ^{inc}

THE BASICS OF RADIATION MODE THEORY IN WORDS

There are three ways to describe the basics of radiation mode theory. The first is a description in words and may give the wrong impression that it is in fact a simple theory. The other two methods consist of giving the mathematics behind the theory with or without poetic explanations. The latter two methods can be found in the few papers [3-13] that already exist on RMT and are automatically lengthy and cumbersome. For that reason we will deal with the first method and explain the basics in words, therefore running the risk of giving the misplaced impression that it is a simple theory.

A mode is the combination of all possible reflected and transmitted waves for a given incident plane wave on a system containing only discontinuities in one dimension, e.g. a plate swamped in water. Hence for each possible incident plane wave, coming from each possible direction above or below the system, there is a mode. For example in a system consisting of a liquid half space and a solid half space, the radiation mode having a component of sound incident from the liquid, consists of that incident plane sound wave, together with one reflected plane

wave and two transmitted plane waves. Such modes that are in fact consisting of radiated energy, are called 'radiation modes'. In the RMT there are however also non-radiating modes available, called eigenmodes. These modes contain all possible transmitted and reflected waves given the fact that there is no radiation of sound. For example on a solid/fluid interface, such eigenmodes are the Scholte-Stoneley modes. Lambmodes are no eigenmodes in that sense because in a system where there are also radiation modes present (i.e. there is a coupling medium), Lamb modes become leaky and hence radiate sound. Furthermore a Lamb wave can be written as a linear combination of radiation modes. The relative amplitude attributed to each component of a given mode is relatively simply calculated from continuity conditions along the one dimensional discontinuity system. For example if a radiation mode is considered in a solid/liquid system with incident sound coming from the liquid side, then the relative amplitudes of each component of the mode are calculated by considering the condition of normal stress and normal displacement and by building a continuity matrix from which each amplitude attributed to each component is calculated.

Since actually one should deal with the system in which discontinuities are present in two dimensions instead of one, as in Fig. IX.A_2, one generates all possible modes for each subsystem which has only discontinuities in one dimension. For example if a step is present on a solid plate swamped in water, then this system containing discontinuities in two directions is divided into two systems which have only discontinuities in one direction, i.e. two infinite plates are considered.

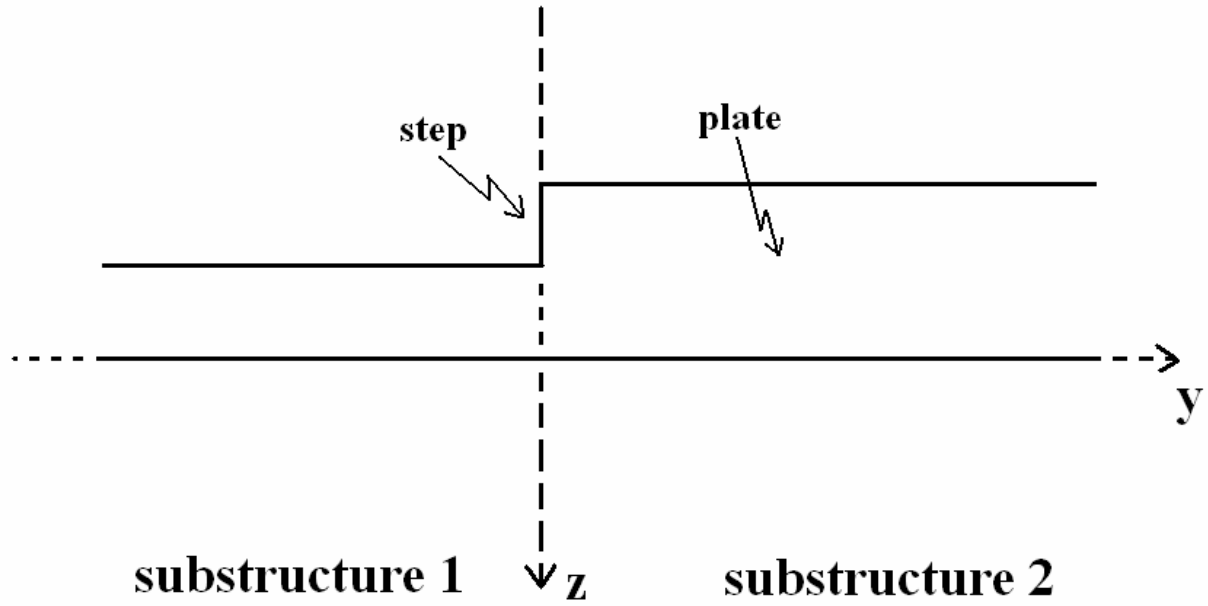

Fig. IX.A_2: ***Schematic of a step on a plate. This system having discontinuities in two dimensions is divided into two substructures, each having only discontinuities in one dimension.***

The complete sound field in each substructure is fully described by means of a linear combination of al possible radiation modes and all possible eigenmodes.
This is done as follows: The particle displacement $\mathbf{u}(\mathbf{r})$ is written as

$$u(r) = \sum_j C_j \mathbf{u}^j(\mathbf{r}) + \int_0^{+\infty} \sum_m C_m\left(k_y\right)\mathbf{u}^m\left(k_y, \mathbf{r}\right) dk_y \tag{IX.A_1}$$

whereas the stress tensor components are written as

$$T_{kl}(\mathbf{r}) = \sum_j C_j T_{kl}^j(\mathbf{r}) + \int_0^{+\infty} \sum_m C_m\left(k_y\right) T_{kl}^m\left(k_y, \mathbf{r}\right) dk_y \tag{IX.A_2}$$

The index *j* is attributed to eigenmodes, whereas the index *m* is attributed to radiation modes. The position vector is denoted by **r**. The linear combination in (IX.A_1) and (IX.A_2) is called mode expansion. The set $\left\{C_j, C_m\right\}$ is the set of expansion coefficients. They are the actual unknown parameters for describing the complete acoustic system. If necessary, the expansion coefficients can also be made position dependent, whence rough surfaces can be considered as well. Furthermore the expansion coefficients in each structure are related to each other by expressing continuity conditions on the interface that separates the two substructures, e.g. the z-axis in Fig. IX.A_2. This latter continuity condition hence relates the sound fields in the substructures to one another and therefore reduces the number of independent expansion coefficients. Finally the remaining independent expansion coefficients are related to boundary conditions. Such boundary conditions are for example: a Gaussian bounded beam incident on a given spot under a given angle. For a more detailed explanation of the basics of RMT, we kindly refer to refs [1-13]

APPLICATIONS

half spaces

Even though the RMT was well established in electromagnetism [1-2], it took until 1990 before the same concept was first used in acoustics. The pioneering work can be found in a paper by Leroy and Shkerdin [3] for a so called solid wedge, which is simply two solids attached to one another, both being bounded by vacuum on one side. This pioneering work describes the interaction of a bulk wave and also of a Rayleigh wave with the transition between both solids. The aim of that paper was actually to show that a translation of the RMT from electromagnetism to acoustics was possible and worked pretty well. Later on the search for a challenge for the RMT began. The first challenge came from a dispute between two scientific groups. Like so often in science, insight and progress follows disputes between people who are courageous enough to defend their opinion. Around 1993, there were two quite different views on the subject of generating a Scholte – Stoneley wave by means of a liquid wedge technique. A Scholte – Stoneley waves is known to travel along a liquid – solid interface without radiating energy into one of the two media. This is due to the fact that such surface waves have a velocity which is less than any of the bulk sound velocities in the surrounding media. However this low velocity is also the reason why such waves cannot be generated on a liquid-solid interface by means of an incident sound beam. One way of surmounting this handicap is the application of a liquid wedge. The principle is depicted in Fig. IX.A_3 and is based on complicated scattering effects in the region where the three involved media are in contact with each other.

The first opinion on the mechanism of Scholte – Stoneley wave generation by means of a liquid wedge is described in refs 1 and 2 in [4] and states that according to a formula which is

similar to the classical Snell's law, Sholte – Stoneley waves would mainly be generated at one particular angle that resulted from that formula. Experiments on an alcohol-water wedge (incidence from alcohol side) confirmed indeed that Scholte - Stoneley waves were generated at that angle. It was not believed that Scholte – Stoneley waves could also be generated by means of a water-alcohol wedge because this would contradict the posed formula. However there was also the opinion of J. Chamuel (private communication with Briers and Leroy) that, based on extended experiments, Scholte – Stoneley waves would actually be generated at every angle of incidence (from the alcohol side) and not just the one corresponding to the experiments in cited refs.

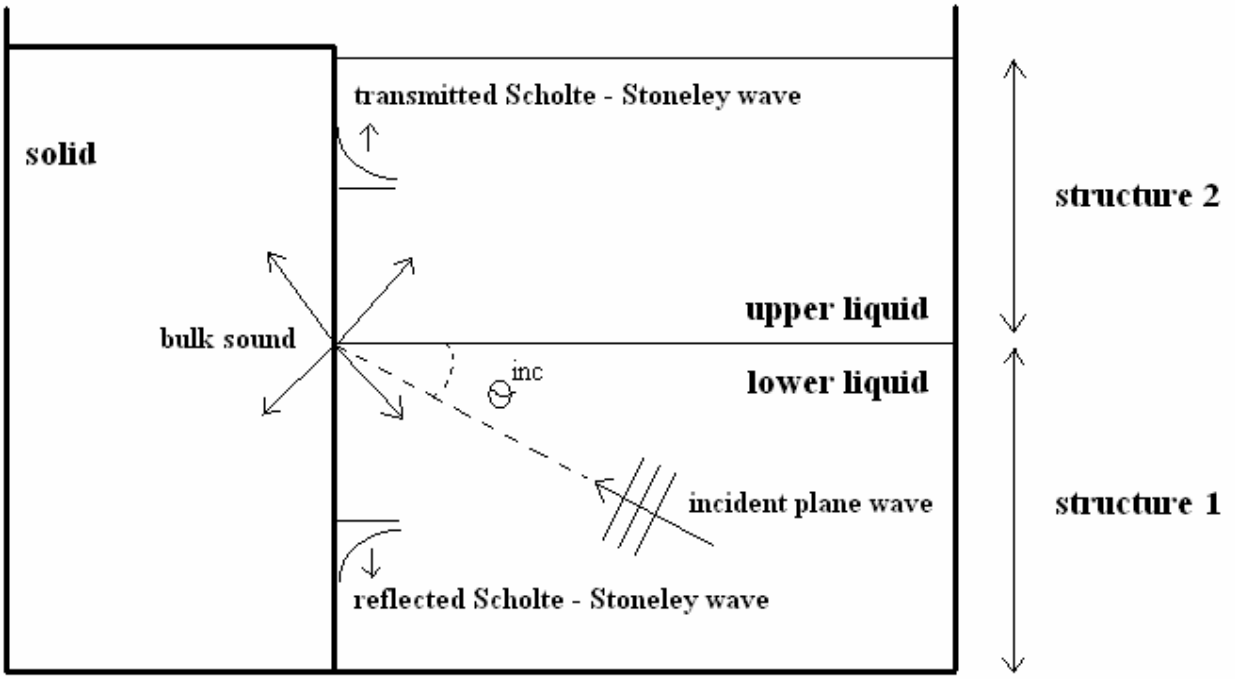

Fig. IX.A_3: ***Geometrical configuration of a liquid wedge***

This dispute challenged the further development of the RMT in order to clarify the problem. Briers et al [4] found numerical results that were quite astonishing.
They found that indeed all angles of incidence produce Scholte – Stoneley waves but the largest amplitude corresponded to an angle of approximately 87^0. Furthermore they found that Scholte – Stoneley waves could also be excited by incidence from the water side (instead of the alcohol side), which was surprising and proved that the formula which looked like Snell's law is not in all situations applicable. This study of the liquid wedge was later followed by a more thorough study [5] indicating that also incidence at the Rayleigh angle produced larger stimulation of Scholte – Stoneley waves if compared to other angles, though not as large as the one in the vicinity of 87^0 as described in the earlier paper [4]. Furthermore in practical situations one is often faced with incident Gaussian beams instead of incident plane waves or plane waves diffracted by a narrow slit (as was the case in [4]). Therefore in [5] the RMT decomposition of a Gaussian beam is presented. As far as we know there is no such analogy described yet in electromagnetism.

plates

Until 1996, only half spaces had been described in RMT. An extension to a plate was the next challenge and was performed in [6]. This model shows how a Scholte – Stoneley wave is scattered at the extremity of a fluid loaded plate, see Fig. IX.A_4.

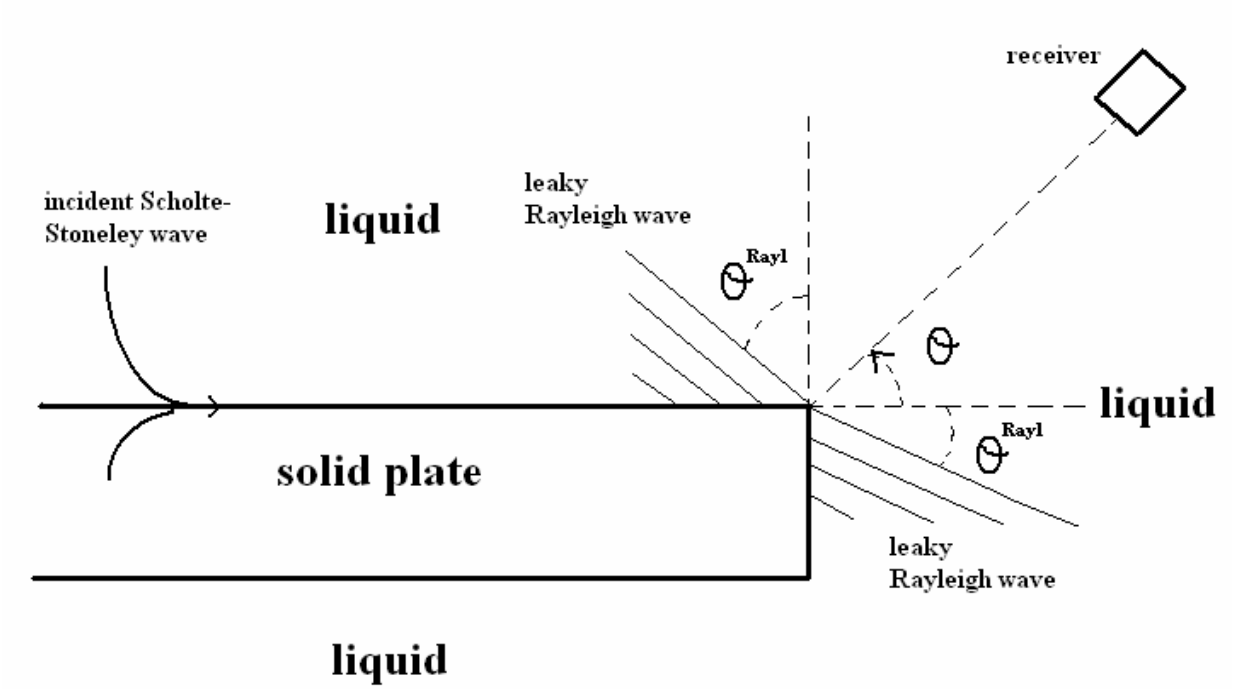

Fig. IX.A_4: ***Experimental configuration for the scattering and mode conversion of a Scholte – Stoneley wave at the edge of a fluid loaded thick plate.***

Because of the complexity, a zero order approximation was performed, followed by a first order approximation. The difference between the two approximations is the leaky Rayleigh wave traveling from top to bottom along the extremity edge of the plate, i.e. included in the first order approximation and excluded in the zero order approximation. The results for the transmitted bulk wave in a zero order approximation for a 5MHz Scholte- Stoneley wave at the end of a water loaded aluminum plate of 1cm thickness is shown in Fig. IX.A_5.
This shows that the largest amplitude is transmitted in line with the plate. There was good agreement with experiments of Tinel (ref 13 in [6]), except in the vicinity of the Rayleigh angle, where Tinel measured an amplitude dip. The latter shortcoming was swept away by using a first order approximation. The latter generated results in perfect agreement with experiments of Tinel, see Fig. IX.A_6.

This proves that the dip in the graphs of Tinel were due to a leaky Rayleigh wave traveling from top to bottom along the extremity edge of the plate. In [6], it is also shown that the incident Scholte – Stoneley wave generates a leaky Rayleigh wave on the upper interface of the plate and also on the lower interface of the plate. This is visible in ref [6] as maxima in the radiated fields at the angles corresponding to the leakage of energy of those leaky Rayleigh waves. An important consequence is of course that due to the reversibility of mode conversion phenomena, a Scholte – Stoneley wave can also be generated by means of sound incident at the Rayleigh angle on the edge of the plate. Hence Scholte – Stoneley waves can be generated by means of sound incident on the edge of a plate.

Because the liquid wedge technique had proved to be excellent for generating Scholte – Stoneley waves, as described above, the question remained as to how the generation of Lamb waves could be described. It was widely known that Lamb waves could also be stimulated by means of a liquid wedge technique.

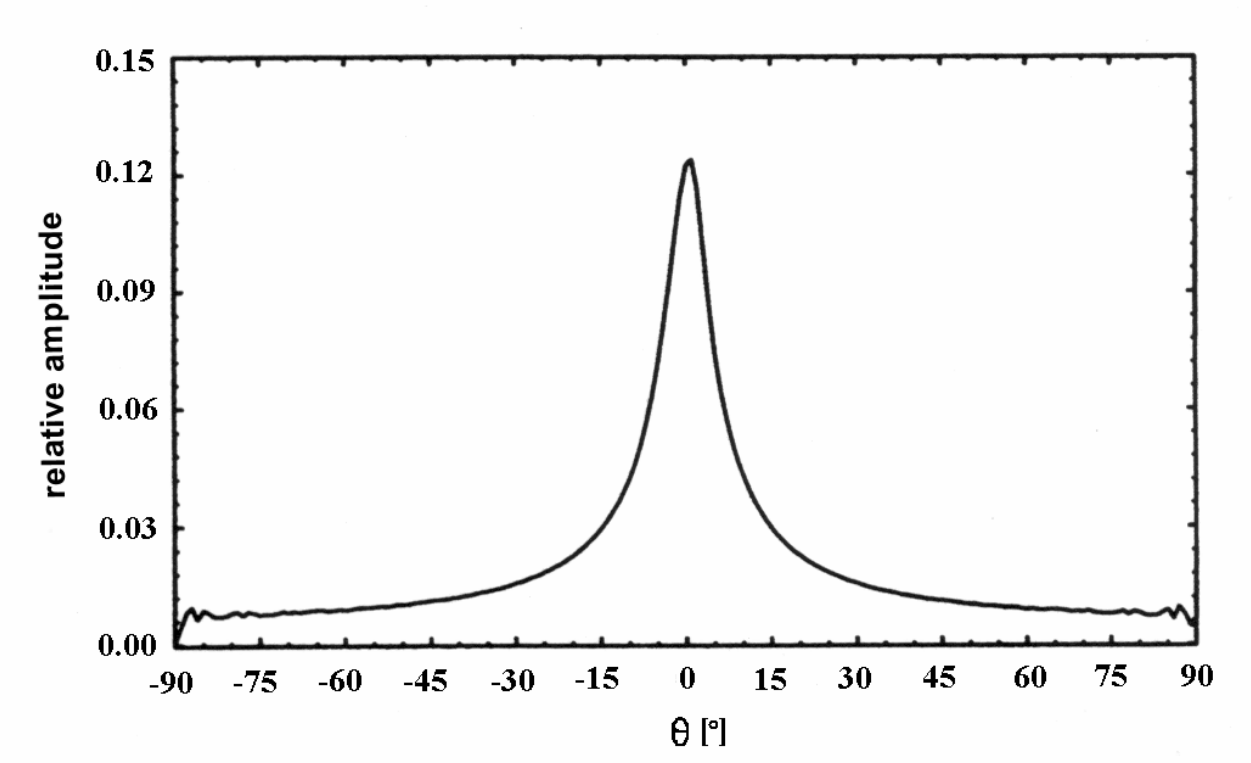

Fig. IX.A_5: ***Transmitted amplitude as a function of the transmission direction θ for a 5MHz Scholte – Stoneley wave on a water loaded 1 cm thick aluminum plate (zero order)***

The technique existed in generating leaky Lamb waves on a plate in a liquid whence those leaky Lamb waves could propagate in the plate to the liquid free half space (vacuum or air) and be turned into pure (non leaky) Lamb waves. No one had ever described this well established phenomenon numerically. Besides generating Lamb waves, the technique can also be used to stimulate Rayleigh waves. Both phenomena have been extensively described and simulated by Briers et al [8].

layered systems

Now that the problem of a plate had been tackled extensively, a study of a bilayered system was the next road ahead. The impetus for this study came from the gained knowledge that Scholte – Stoneley waves could be generated by means of scattering effects in a liquid wedge. The question to be answered was if one would be able to generate Scholte – Stoneley waves at the down step of a thin layer on a substrate, see Fig. IX.A_7.

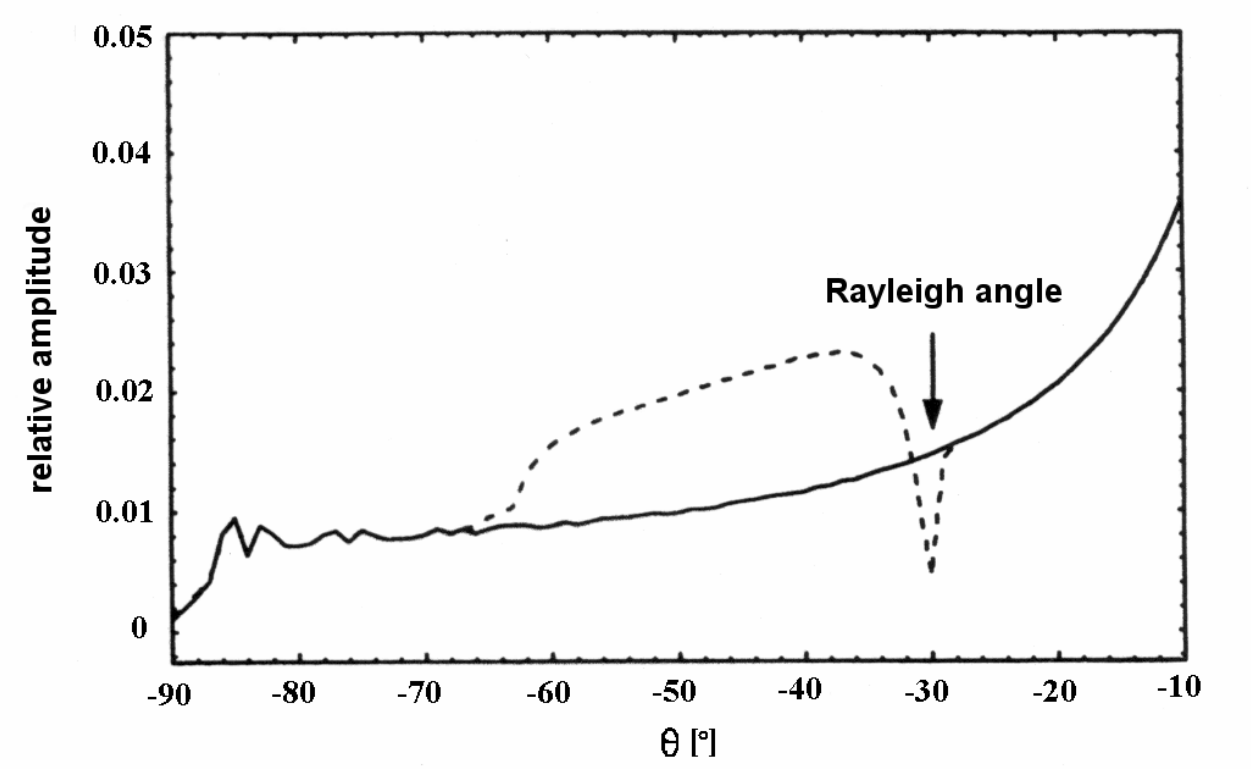

Fig. IX.A_6: ***Same as Fig. IX.A_5, though shortened angle interval. Dashed line is the first order approximation and solid line is zero order approximation.***

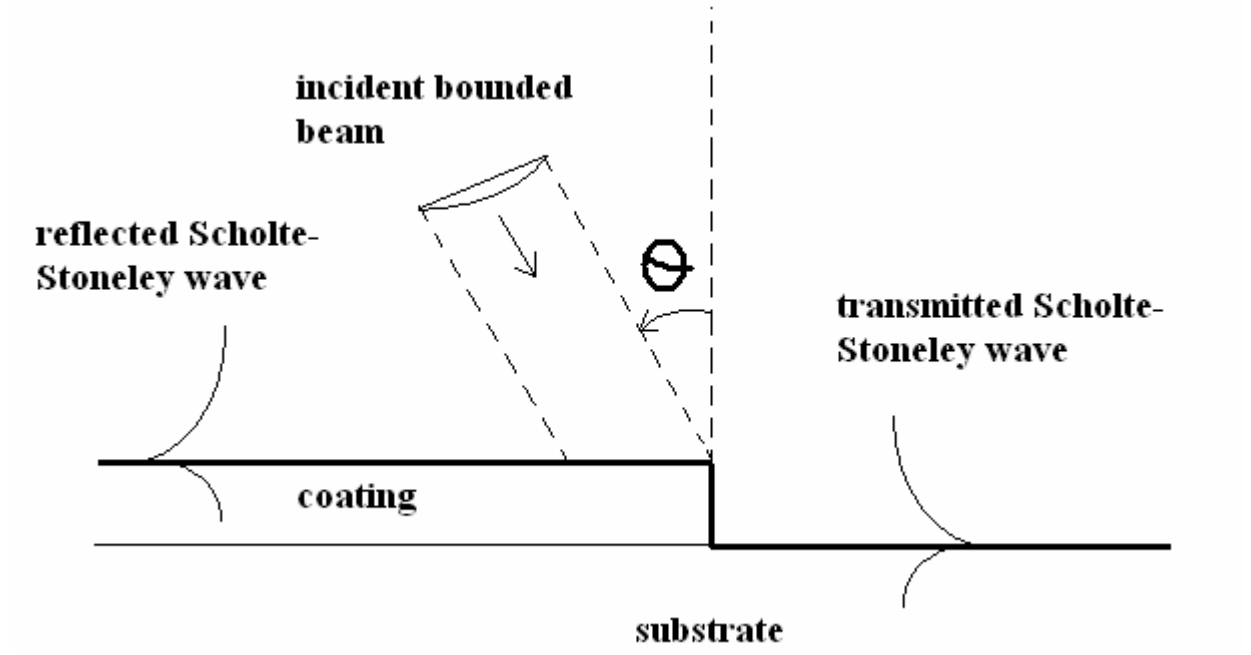

Fig. IX.A_7: ***Geometrical configuration of Scholte – Stoneley wave generation at downstep.***

If the answer was positive [7,9], a new technique would be born which would be much more practical than the use of a liquid wedge. It was found indeed that Scholte – Stoneley waves could be generated at an angle of incidence of approximately 87^0 and also at the Rayleigh angle. The numerical results are shown in Fig. IX.A_8. IT was also shown that the amplitude at the Rayleigh angle is actually independent of the coating material and is only dependent of the substrate characteristics. Recently the RMT has also been further extended to multilayered systems [12].

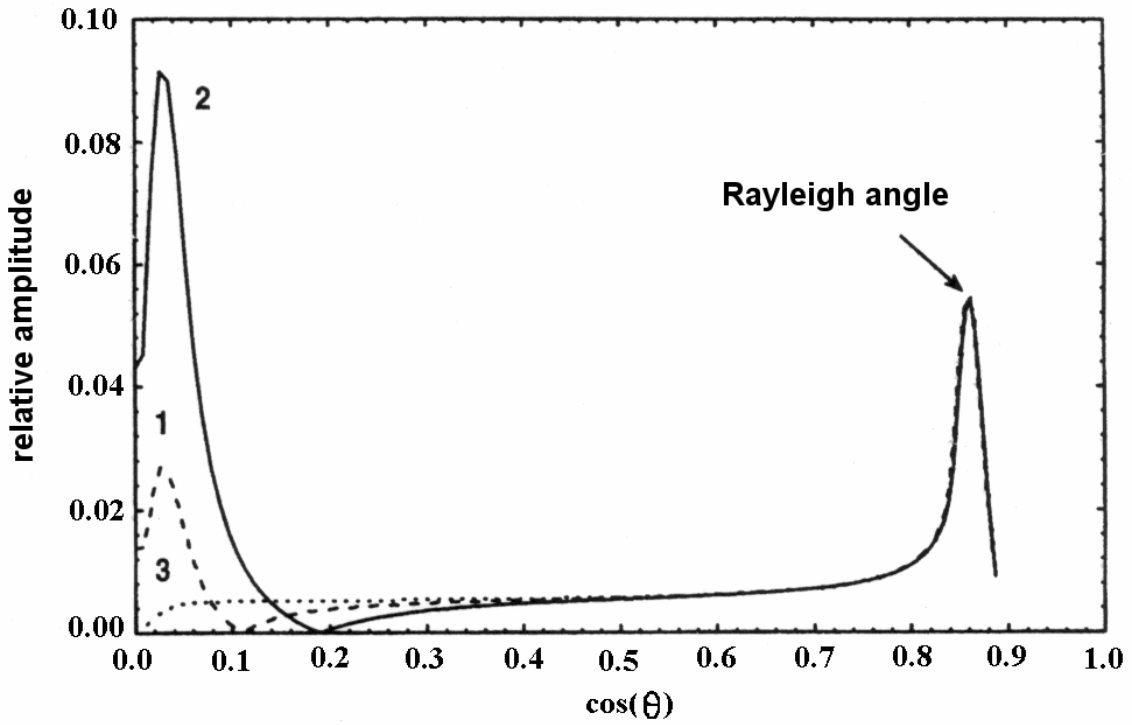

Fig. IX.A_8: ***Relative amplitude of the transmitted Scholte – Stoneley wave generated by a 4 MHz Gaussian beam (beam width 5mm) at 15 cm radial distance from the downstep, incident from water as a function of the angle of incidence. The substrate is steel and the thin layer consists of (1) copper, (2) Pyrex glass, (3) steel.***

inclusions

Mainly caused by the importance of NDT and more precisely the technique of finding defects in materials and a lack of models that were able to describe the interaction of sound with inclusions, a study started that dealt with the interaction of sound with inclusions at the surface [9-10]. It is intuitively reasonable that the Schoch effect, which is caused by leaky Rayleigh waves, must be sensitive to inclusions on or near the surface, because the accompanied Rayleigh waves must 'feel' the presence of such inclusions since their amplitude is located mostly near the surface. Definitely the RMT showed that a measurement of phase differences between the specular and the nonspecular reflected lobe when the Schoch effect happens, is an indication of the dimensions and position of inclusions. In Fig. IX.A_9, the characteristics of a reflected gaussian beam are shown for incidence at the Rayleigh angle on a stainless steel half space, on a half space covered with a thin coating and on a half space with a thin inclusion at the surface. The

configuration is as such that the center of the incident beam coincides with the beginning of the inclusion. The thickness of the inclusion and the coating is the same. It is seen that the reflected beam profile shows some important aspects that are related to the characteristics of such a thin coating/inclusion. It is also seen that the results for the coating fall in between the results for the inclusion.
Later a study was performed on inclusions near the surface [13], similar results were also found for that case.

viscoelastic media

In all previous studies, damping was neglected in all considered materials. Therefore Vandeputte et al extended the RMT to the case of viscoelastic media [11]. It was shown that absorption weakens the nonspecular lobe and amplifies the specular lobe in the case of the Schoch effect at Lamb angles of incidence. They also showed that beam focusing has effects on the presence or absence of a null zone when the Schoch effect occurs. This is because the Lamb wave profiles are disturbed by the focusing effect.

PROSPECTS AND CONCLUSIONS

The development of the RMT has been completed for 2D isotropic systems. The theory has up until now showed its value in the understanding and simulation of the generation of Scholte – Stoneley waves, Rayleigh waves and Lamb waves by means of a liquid wedge. It also showed how a Scholte – Stoneley wave interacts with the extremity of a plate. The RMT also paved the way for the use of a downstep an a substrate to generate Scholte – Stoneley waves. Lately extensions have occurred for multilayered media and for visco-elastic media. Further development is expected to happen for 3D systems and for anisotropic media as well. The RMT is far from easy to apply, but it works and it is very powerful to deal with problems which cannot be dealt with in the framework of other theories.

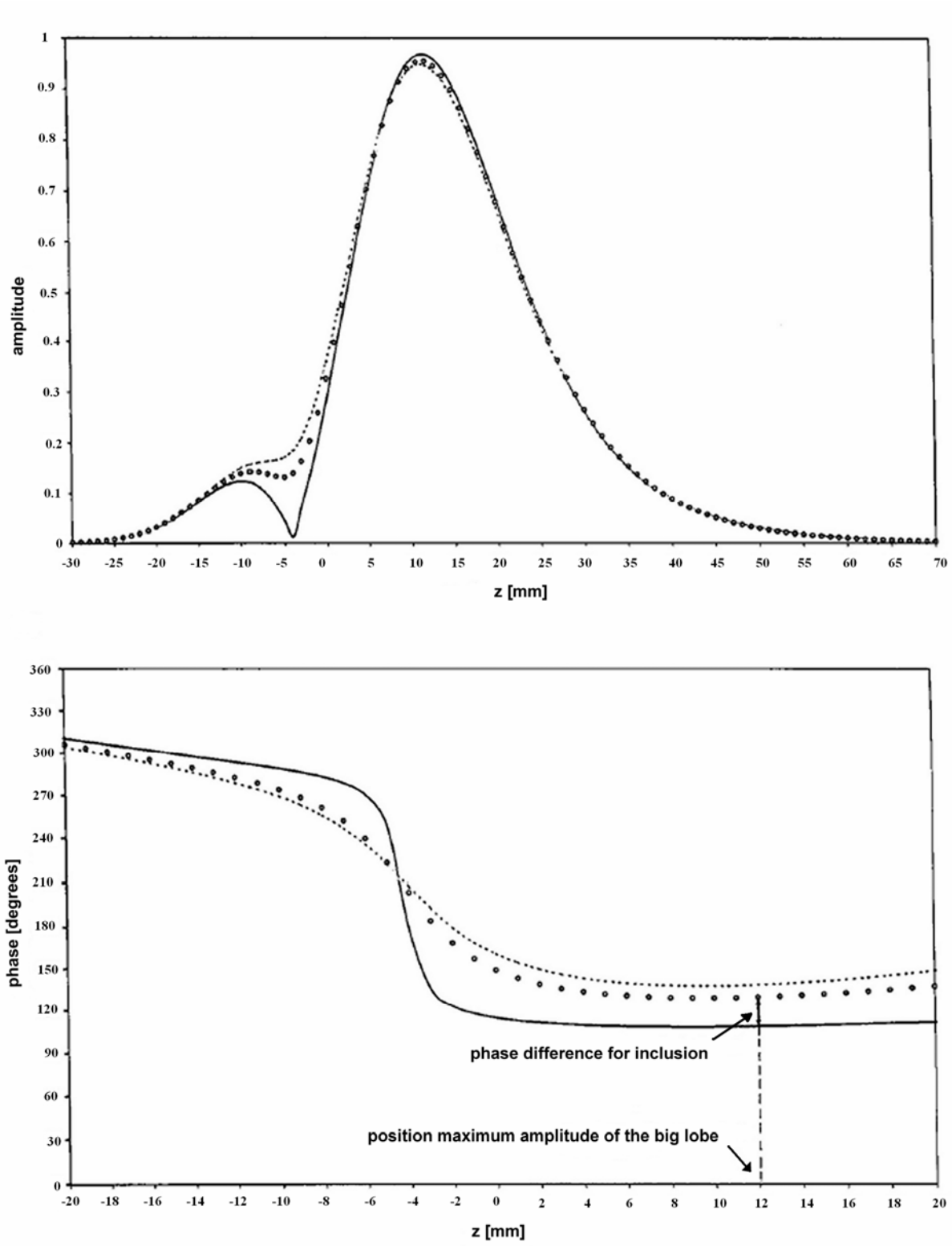

Fig. IX.A_9: ***Amplitude distribution (top), bottom: phase distribution (bottom) of a reflected 4MHz Gaussian beam, of 12mm half width, onto a stainless steel half space (solid line), onto a 5µm layer on a stainless steel substrate (dashed line), onto an inclusion of 5µm thickness (length 15mm) in stainless steel (circles line). The Gaussian beam is incident at the Rayleigh angle. The arrow defines the phase difference.***

REFERENCES

[1] V. V. Shevchenko, *Continuous Transitions in Open Waveguides*, The Golem Press, 1971

[2] Dietrich Marcuse, *Light Transmission Optics*, Bell Laboratories Series, 1972

[3] O. Leroy, G.N. Shkerdin, "The mode method in the theory of acoustic wave diffraction on division boundaries between different structures", in *Physical Acoustics*, edited by O. Leroy and M. A. Breazeale, plenum press, New York, 1991.

[4] R. Briers, O. Leroy, G. N. Shkerdin, Yu. V. Gulyaev, "Mode theory as a framework for the investigation of the generation of a Stoneley wave at a liquid-solid interface", J. Acoust. Soc. Am. 95(4), 1953-1966, 1994

[5] R. Briers, O. Leroy, G. N. Shkerdin, "A fundamental study of the excitation of a Stoneley wave at a liquid-solid interface: Rayleigh angle and Gaussian beam incidence", J. Acoust. Soc. Am. 95(4), 1967-1976, 1994

[6] R. Briers, O. Leroy, G. N. Shkerdin, "Conversion of a Stoneley wave at the extremity of a fluid loaded plate", J. Acoust. Soc. Am. 101(3), 1347-1357, 1997

[7] R. Briers, O. Leroy, G. Shkerdin, "Stoneley wave excitation by a bounded beam at the down-step of a thin layer on a substrate", J. Acoust. Soc. Am. 102(4), 2108-2112, 1997

[8] R. Briers, O. Leroy, G. Shkerdin, "A liquid wedge as a generating technique for Lamb and Rayleigh waves", J. Acoust. Soc. Am. 102(4), 2117-2124, 1997

[9] R. Briers, O. Leroy, G. Shkerdin, "The interaction of bulk and surface waves with thin layers and inclusions modeled by a mode theory", 51-57, Proc. The 4th International Conf. Of Slovenian Soc. For Nondestr. Testing, Ljubljana, Slovenia, 24-25 April, 1997

[10] R. Briers, O. Leroy, G. Shkerdin, "Bounded beam interaction with thin inclusions. Characterization by phase differences at Rayleigh angle incidence", J. Acoust. Soc. Am. 108(4), 1622-1630, 2000

[11] J. Vandeputte, O. Leroy, R. Briers, G. Shkerdin, "Extension of the mode method for viscoelastic media and focused ultrasonic beams", J. Acoust. Soc. Am. 108(4), 1614-1621, 2000

[12] J. Vandeputte, G. N. Shkerdin, O. Leroy, "Radiation Mode Model for multilayered structures", in *Mechanical Waves for Composite Structures*, Kluwer Academic Publishers, Dordrecht, 141-149, 2000

[13] J. Vandeputte, O. Leroy, G, Shkerdin, "Influence of planar cracks in plates on reflected and transmitted fields of Gaussian acoustic beams", J. Acoust. Soc. Am. 114(2), 634-643, 2003

IX.B Study of the scattering of leaky Rayleigh waves at the extremity of a fluid loaded thick plate

A study by means of the Schlieren technique for visualization of ultrasonic beams, has revealed that when leaky Rayleigh waves, propagating along the horizontal edge of a thick, fluid loaded solid plate, are scattered at the extremity of the plate, they travel around the corner and start leaking into the liquid along the Rayleigh angle measured from the normal to the vertical edge of the plate. Furthermore the study reveals that leaky Rayleigh waves are stimulated by the border of an incident ultrasonic bounded beam, more than by the interior of the beam. Comparison with an earlier work shows that the characteristics of the scattering of leaky Rayleigh waves at the edge of the plate is very different from that of Scholte - Stoneley waves.

This work was performed at the National Center for Physical Acoustics, in collaboration with A. Teklu, M. A. Breazeale, and is published as: Nico F. Declercq, A. Teklu, M. A. Breazeale, Rudy Briers, Oswald Leroy, Joris Degrieck, Gennady N. Shkerdin, "Study of the scattering of leaky Rayleigh waves at the extremity of a fluid loaded thick plate", J. Appl. Phys 96(10),5836-5840, 2004 (Imp. Fact. 2.281; SCI-index, Physics-Applied, rank:13/76)

INTRODUCTION

Rayleigh waves are acoustic eigenmodes of a solid-vacuum interface. They are surface waves involving elliptic polarization of material particles near the interface. Rayleigh waves have a counterpart on solid-liquid interfaces, quite similar, except that they leak energy into the liquid and are therefore called leaky Rayleigh waves. Leaky Rayleigh waves leak energy at an angle (measured from the normal to the interface) that is called the Rayleigh angle θ^{Rayl}. Accordingly, they can be generated by means of sound incident at the Rayleigh angle through mode conversion of bulk waves into surface waves. In the literature, a number of papers can be found that deal with the interaction of Rayleigh waves with a corner, i.e. the extremity of a thick plate [1-10]. Other papers deal with the interaction of Rayleigh waves with inhomogeneities and discontinuities [11-14]. However, all cited papers study non-leaky Rayleigh waves, i.e. Rayleigh waves on a solid-air or solid-vacuum interface. The question arises how 'leaky' Rayleigh waves, interact with the extremity of a thick plate. Will they be transmitted and travel around the corner, or will they only be reflected and be accompanied by a radiation field in all directions? Earlier, some papers have been published [15-17] concerning surface waves on a solid-liquid interface and their interaction with the extremity of a thick plate. Nevertheless these papers only consider incident Scholte – Stoneley waves and no incident (leaky) Rayleigh waves. Scholte – Stoneley waves are eigenmodes on a solid-liquid interface and their velocity is smaller than any of the sound velocities in both surrounding media. Therefore, according to Snell's law, they cannot leak energy and are different from Leaky Rayleigh waves. However, it is interesting to discus the results of Refs 15-17 for comparison with the results for leaky Rayleigh waves as given further below. For this reason we first focus on Fig. IX.B_1, where the different angles are defined. The angles are measured from the horizontal to the surface in the half space beyond the edge of the

plate (see right side of Fig. IX.B_1), with the clockwise sense involving negative angles and the anti-clockwise sense involving positive angles. The angle of incidence is θ^{inc}, the angle of reflection is θ^{r}, whereas the angle of sound coming from the emitter and left undisturbed by the solid, is θ^{t}. Whenever an additional sound field is visible, it is given by an angle θ^{s}.

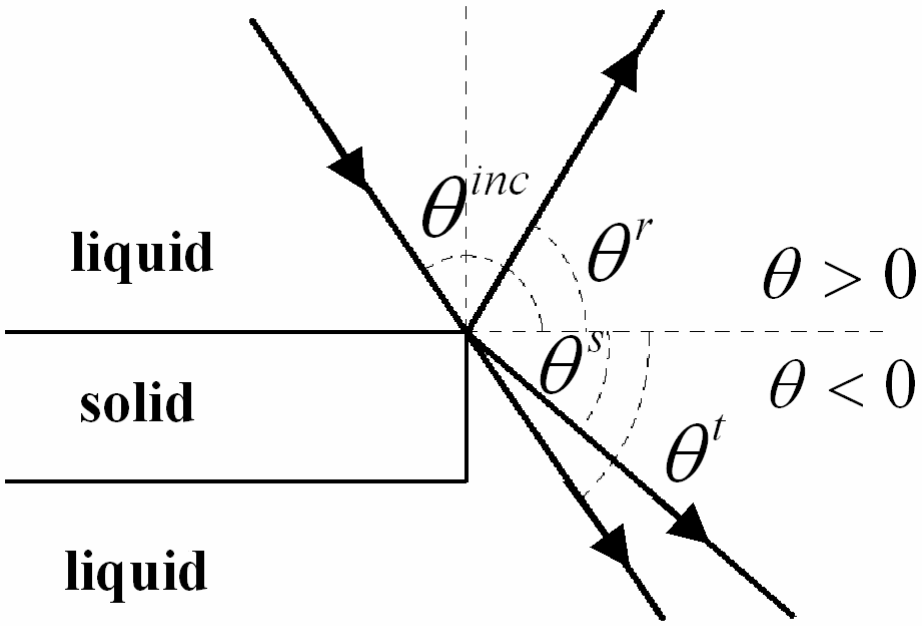

Fig. IX.B_1: ***Definition of the different angles θ^{inc}, θ^{r}, θ^{s}, θ^{t}. The angles are measured from the horizontal axis left from the plate. Positive angles are anti clockwise, negative angles are clockwise.***

The studies reported in refs [15-17] show that Scholte – Stoneley waves ($\theta^{inc}=180^{0}$) are primarily scattered in the forward direction ($\theta^{r}=\theta^{s}=\theta^{t}=0^{0}$). However sound is also scattered in all other directions, but this scattered sound is accompanied by a much smaller amplitude than that in the forward direction. A relatively strong mode conversion also occurs into reflected leaky Rayleigh waves. These surface waves radiate (leak) energy into the direction $\theta = 90 + \theta^{Rayl}$ with θ^{Rayl} the Rayleigh angle. In addition, the scattered sound shows a minimum in the $-\theta^{Rayl}$ direction, which means that leaky Rayleigh waves are hardly stimulated along the vertical edge of the plate ($\theta = -90^{0}$). Still, Scholte – Stoneley waves exist both in transmission (along the vertical edge, i.e. $\theta = -90^{0}$) and in reflection (along the horizontal edge, i.e. $\theta = 180^{0}$). This knowledge, together with the lack of literature concerning the event of scattering of leaky Rayleigh waves at the edge of a thick plate formed the reason for studying this phenomenon.

EXPERIMENTAL PROCEDURE

We have used thick solid plates (3cm high, 5cm width, 10cm long) in order to avoid Lamb wave stimulation. Lamb waves are plate waves that are easily stimulated in thin plates. At the frequencies we have used in the experiments, 3-6 MHz, a thickness of 3cm in this regard can be considered as 'infinity'. Furthermore, the thick plates were polished, because we wanted to avoid secondary effects, such as additional scattering or diffraction phenomena, caused by the surface roughness.

Incident and diffracted sound are experimentally visualized by means of the monochromatic Schlieren technique. This technique is described in ref [18]. Ultrasound is generated by apodized quartz transducers of the same type as in ref 18, that produce gaussian sound beams.

A leaky Rayleigh wave is generated on the solid-water interface by means of a bounded beam incident at the Rayleigh angle θ^{Rayl}. This angle is determined through observation of the Schoch effect [19-21] , i.e. the appearance of two reflected amplitude lobes with a null strip in between, for an incidence spot relatively far from the edge of the plate. Then, the plate is moved without altering the incident bounded beam, until the beam reaches the edge of the plate. This configuration is shown schematically in Fig. IX.B_2, where W is the physical horizontal width of the beam and where Δ is the distance from the left border of the beam to the extremity of the solid plate. Whenever $\Delta < W$, a fraction of the incident sound beam will propagate without severe disturbance coming from the solid edge, this is direct and undisturbed transmitted sound. Whenever $\Delta \geq W$ there is no direct and undisturbed transmitted sound.

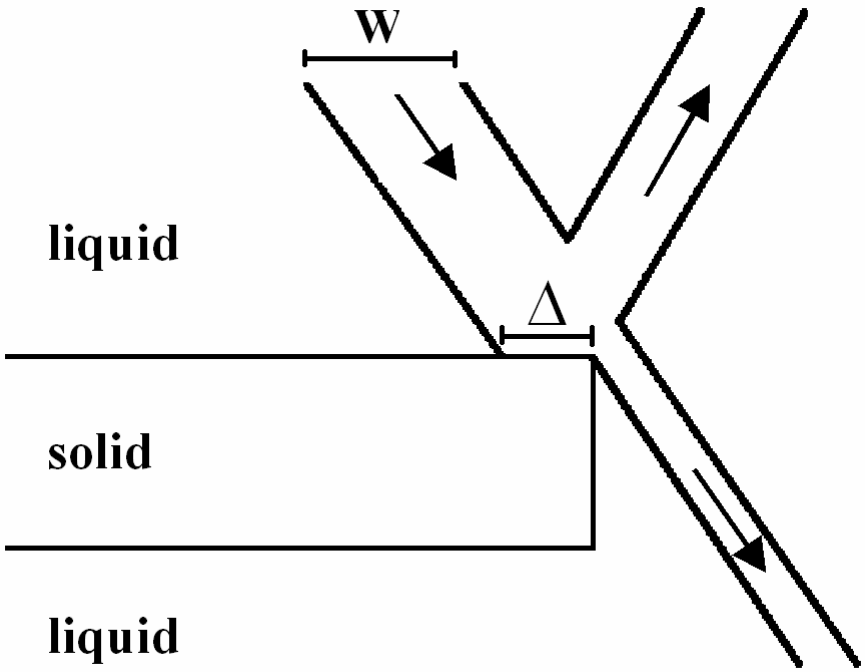

Fig. IX.B_2: ***Definition of Δ : the distance between first beam edge and plate edge, W: the horizontal physical width of the beam.***

RESULTS AND DISCUSSION

results for an aluminum sample

First, we consider an incident 2.5 cm wide bounded beam of 3MHz, incident on a brass plate. The dimensions of the plate are given above. According to ref [22], the Rayleigh wave velocity for aluminum is 2906 m/s. This corresponds to a Rayleigh angle θ^{Rayl} of 31^0 for the velocity of sound in water being 1480m/s. It was observed that if $\Delta \approx W$ for $\theta^{inc} = 90^0 + \theta^{Rayl}$, that in addition to a reflected beam in the direction $\theta^r = 90^0 - \theta^{Rayl}$, a 'scattered' sound beam was generated along the direction $\theta^s = -\theta^{Rayl}$. This scattered sound beam was not there for other angles of incidence. The phenomenon for an aluminum plate can be seen in Fig. IX.B_3, where $\theta^{Rayl} = 31^0$. As soon as $\Delta < W$, there is also a direct, undisturbed transmitted beam visible as can be seen in Fig. IX.B_4 ($\Delta \approx 0.78W$). Now, since $\theta^s = -\theta^{Rayl}$ for the 'scattered' sound beam, and since this beam disappears as soon as the incidence angle differs from $\theta^{inc} = 90^0 + \theta^{Rayl}$, it is likely that the beam is actually energy leakage coming from a leaky Rayleigh wave propagating along the vertical edge of the thick plate, i.e. along $\theta = -90^0$, and stimulated by interaction of the leaky Rayleigh wave on the horizontal side of the plate with the edge of the plate. We believe that this interpretation is more reasonable than the interpretation that the sound beam would be radiated by the incident leaky Rayleigh wave when reaching the extremity of the plate. Hence the incident leaky Rayleigh wave reaches the extremity of the plate and partly propagates around the corner onto the vertical edge of the plate. While doing so, it keeps leaking its energy and that is what is visible as a 'bounded beam' in the direction $\theta^s = -\theta^{Rayl}$.

As a matter of fact the effect of 'surface wave propagation around the corner' is reasonable because leaky Rayleigh waves are elliptically polarized. This elliptical particle motion at the corner stimulates elliptical motions on the vertical edge. That is also the reason why Scholte – Stoneley waves can travel around the corner [15-17]. However it is noticed that the characteristics of the scattering of leaky Rayleigh waves is much different from the scattering of Scholte – Stoneley waves at the corner.

Whereas Scholte – Stoneley waves scatter mostly in the forward direction ($\theta = 0$), leaky Rayleigh waves scatter mostly in the direction $\theta = -90^0$, resulting in a leakage field in the $\theta^s = -\theta^{Rayl}$ direction.

Remark that this phenomenon is invisible whenever $\Delta > W$. This is probably due to the leaky feature of the generated surface waves. When they have leaked too much energy into the liquid, their amplitude when propagating around the corner is too small to generate a leaky field in the direction $\theta^s = -\theta^{Rayl}$ that is visible by the Schlieren imaging technique.

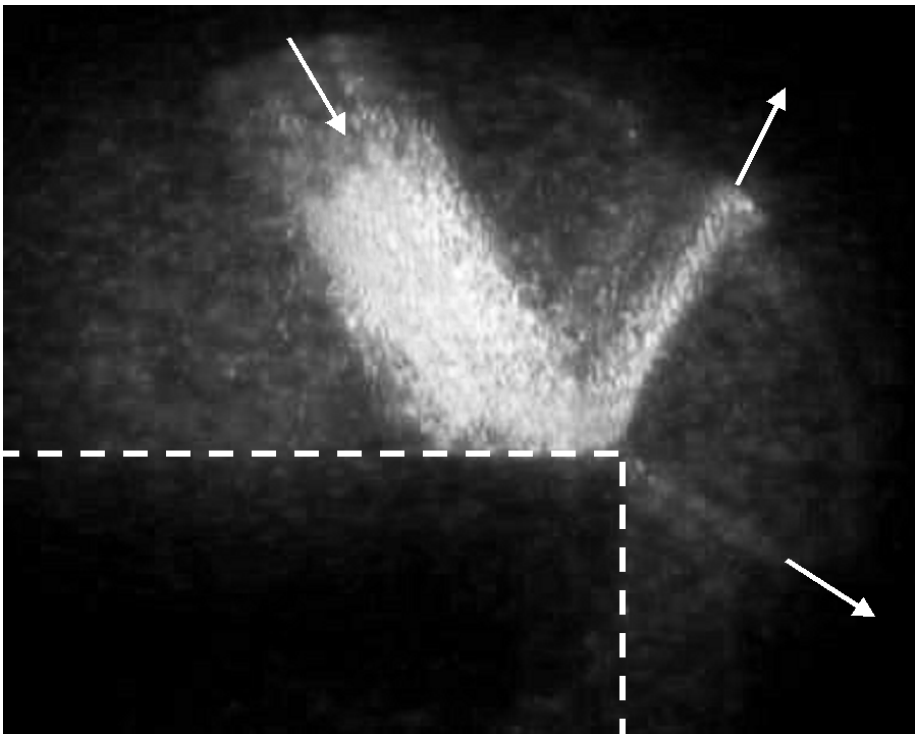

Fig. IX.B_3: ***Incidence of 3 MHz, 2.5 cm wide bounded beam on aluminum.*** $W \approx 2.9cm,\ \Delta \approx W$ ***(Schlieren picture). The dashed lines show where the plate is situated in the experiment. The arrows show the sound propagation direction.***

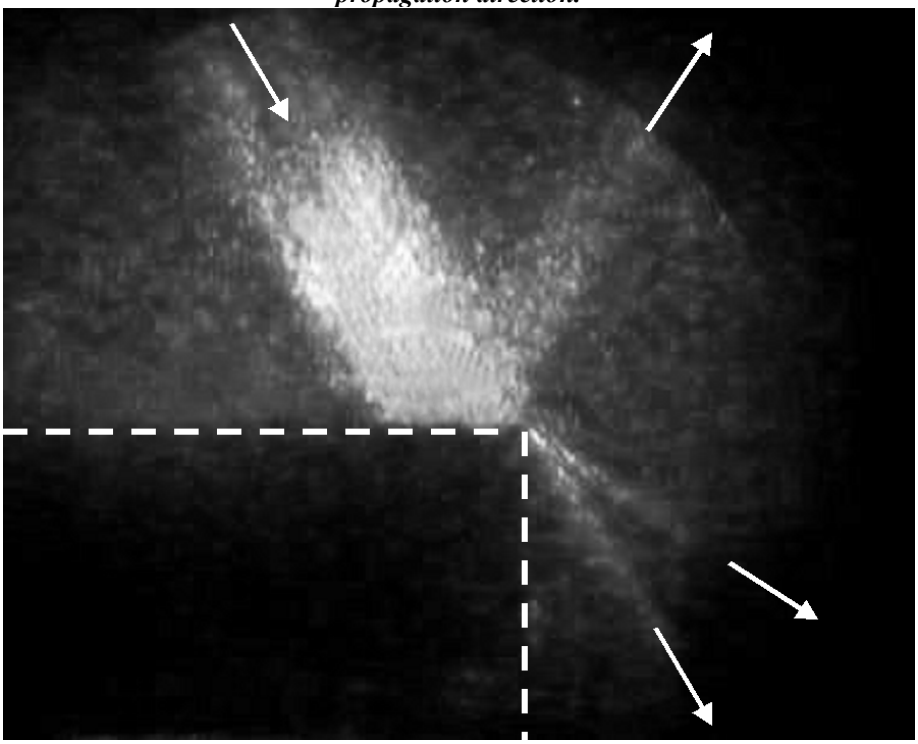

Fig. IX.B_4: ***Incidence of 3 MHz, 2.5 cm wide bounded beam on aluminum.*** $W \approx 2.9cm,$ $\Delta \approx 0.78W$ ***(Schlieren picture). The dashed lines show where the plate is situated in the experiment. The arrows show the sound propagation direction.***

The beam edges are responsible for leaky Rayleigh wave generation

Besides, because the generated bounded beam at the angle $\theta^s = -\theta^{Rayl}$ is directly proportional to the amplitude of the leaky Rayleigh wave propagating along the vertical edge and therefore also directly proportional to the amplitude of the leaky Rayleigh wave propagating along the horizontal edge in the region of incidence, it is possible to reveal what part of the incident beam is mostly responsible for the stimulation of leaky Rayleigh waves. If it is the center of the beam, then the amplitude of the sound beam at $\theta^s = -\theta^{Rayl}$ must increase whenever Δ increases from very small to $W/2$. In Fig. IX.B_5, Δ is very small ($\Delta \approx 0.2W$)and becomes larger in Fig. IX.B_6 ($\Delta \approx 0.6W$). Nevertheless no important amplitude change, except for a small amplitude drop, is visible in the bounded beam along the direction $\theta^s = -\theta^{Rayl}$.

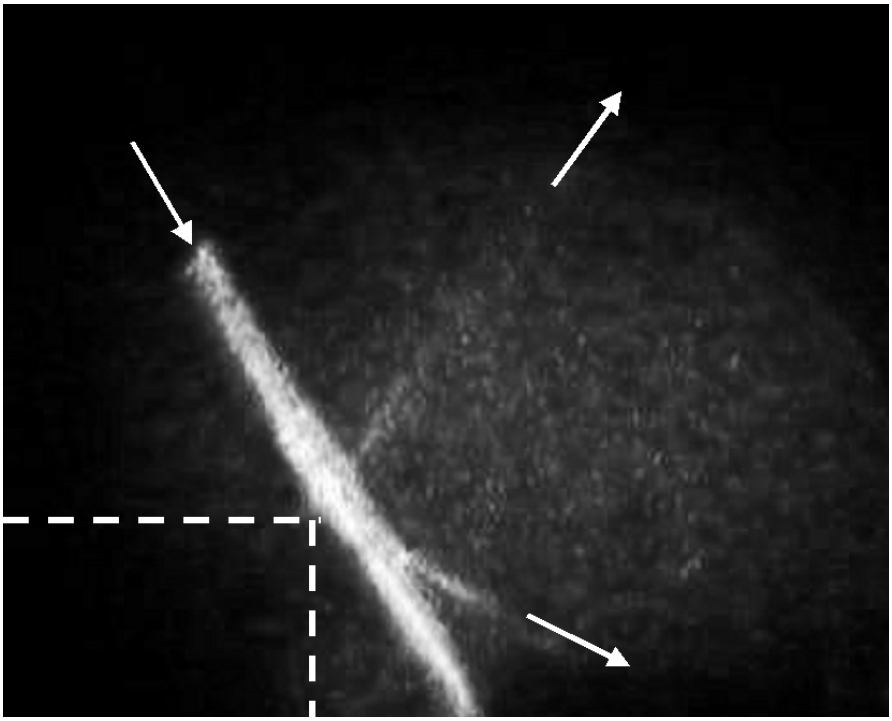

Fig. IX.B_5: ***Incidence of 6 MHz, 0.6 cm wide bounded beam on aluminum.*** $W \approx 0.7cm$, $\Delta \approx 0.2W$ ***(Schlieren picture). The dashed lines show where the plate is situated in the experiment. The arrows show the sound propagation direction.***

This means that the center of the beam does not add any noticeable energy to the Rayleigh wave. In other words the leaky Rayleigh wave is stimulated by the borders of the bounded beam. In fact this is not really surprising in the framework of inhomogeneous wave theory, where it is known [23-26] that leaky Rayleigh waves are stimulated not by homogeneous plane waves but by inhomogeneous plane waves. As a matter of fact, a bounded beam is a physical entity which behavior can be simulated in different frameworks of bounded beam models. The most famous model is the Fourier model, where a bounded beam is formed by means of a superposition of plane waves [25-26]. A less famous model is the superposition of inhomogeneous waves [25]. Nevertheless, those descriptions are global descriptions, where only a global resulting effect can be simulated, such as the Schoch effect.

Those models cannot describe what happens locally to sound when it is incident on an interface between two different media. Locally, it is clear that the border, contrary to the center, of a bounded beam is more similar to an inhomogeneous wave than to a homogeneous plane wave. As can be seen in Fig. IX.B_7, the border of a gaussian beam has a profile quite similar to that of an inhomogeneous wave, i.e. exponential amplitude growth/decay along the wave front, whereas the center of the beam has properties similar to homogeneous plane waves. Because inhomogeneous waves are better suited to stimulate Rayleigh waves, it is understandable that the edge of a bounded beam is more important than the center, for that cause.

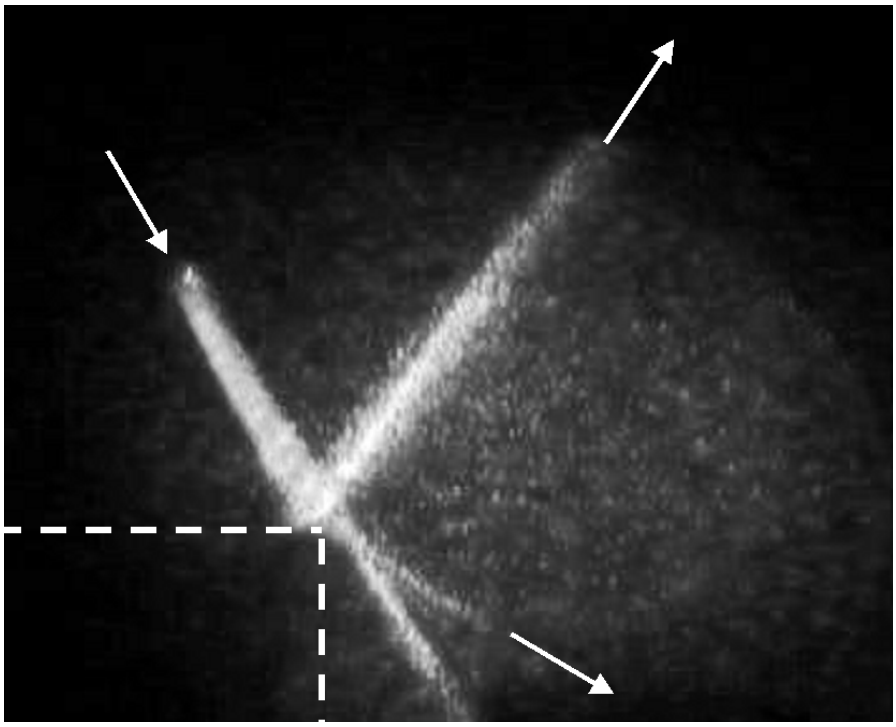

Fig. IX.B_6: ***Incidence of 6 MHz, 0.6 cm wide bounded beam on aluminum.*** $W \approx 0.7cm$, $\Delta \approx 0.6W$ ***(Schlieren picture). The dashed lines show where the plate is situated in the experiment. The arrows show the sound propagation direction.***

From the theory of inhomogeneous waves, it is also known that some inhomogeneities are better capable of stimulating Rayleigh waves than others. Everything depends on the kind of interface and on the frequency. It is therefore likely that the beam profile and also the beam width are important parameters. For example if a bounded beam would be used that is not gaussian, but that has an exponentially varying amplitude profile with bounded edges, then the center is not homogeneous-like but inhomogeneous and the whole beam will be responsible for the stimulation of Rayleigh waves. This is the effect of bounded inhomogeneous waves and has been described in refs [25,27].

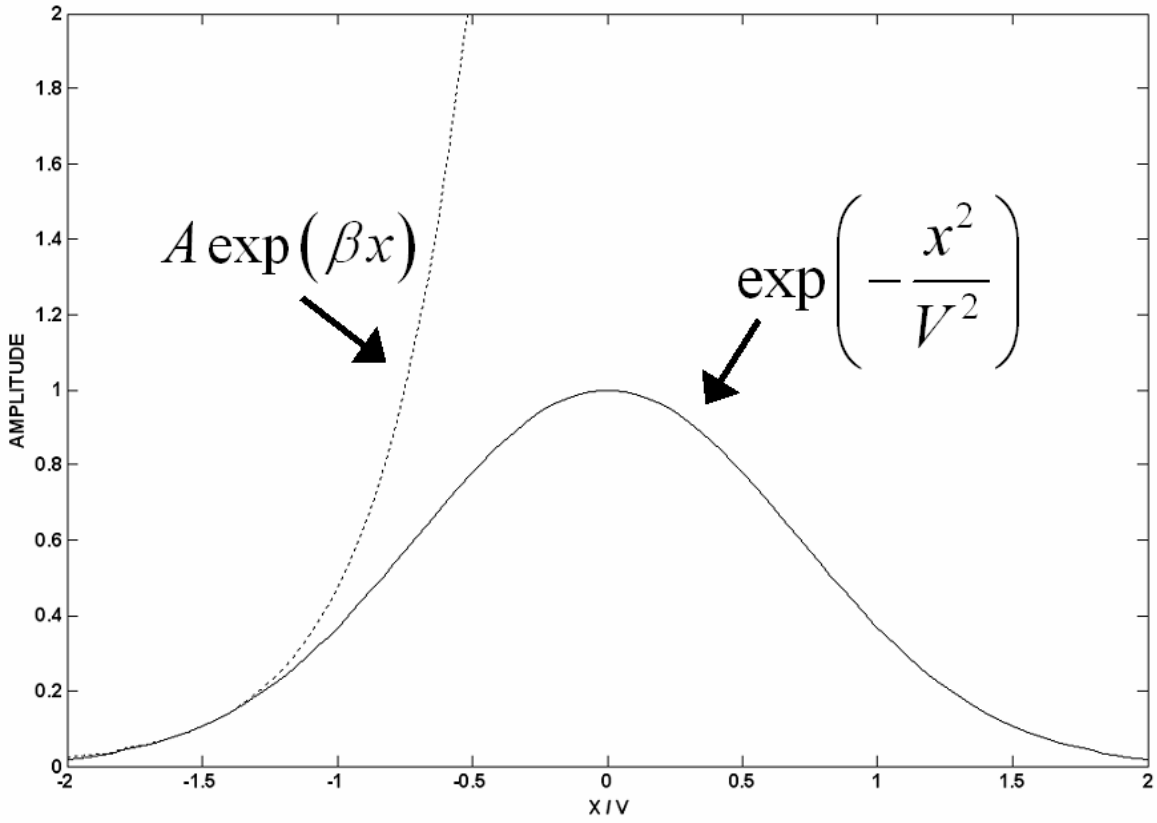

Fig. IX.B_7: ***The edges of a Gaussian beam have a profile that is relatively similar to that of an inhomogeneous wave. This is probably the reason why the edges of a Gaussian beam stimulate leaky Rayleigh waves. The x-axis is directed along the wave front. The value β is called the inhomogeneity of the accompanied inhomogeneous wave.***

results for a brass sample

Until now, we have only discussed results for an aluminum sample. In order to make sure that our conclusions do not just hold for aluminum, but also for a different solid, we have repeated the experiments for a brass plate. According to ref [22], the Rayleigh wave velocity for brass is 1964 m/s. This corresponds to a Rayleigh angle θ^{Rayl} of 49^0 for the velocity of sound in water being 1480m/s. One configuration is shown in Fig. IX.B_8, for a 0.6 cm wide bounded beam of 6 MHz, incident on a spot defined by $\Delta \approx 0.8W$,where it can be verified that the physical phenomenon remains unchanged except that here $\theta^{Rayl} = 49^0$. In fact, contrary to the phenomenon on aluminum, here $\left|\theta^s\right| > \left|\theta^t\right|$.

the disappearance of the Schoch phenomenon

It is also worthy to note that the Schoch displacement, as it appears whenever sound is incident at the Rayleigh angle on a spot relatively far from the edge of the plate, is disturbed when the incidence spot is near the corner and even seems to disappear whenever $\Delta \le W$. This is

of course because the Schoch phenomenon is due to the interaction between the reflected bounded beam and the sound field coming from generated leaky Rayleigh waves. Whenever the extremity of the plate is reached, the leaky Rayleigh waves are scattered by the edge and are partly propagating along the vertical edge. Now, the interesting part of this phenomenon is that the leaky Rayleigh waves leak energy around the corner that does not interfere anymore with the directly reflected sound beam. Hence the 'bounded' beam that is generated along the direction $\theta^s = -\theta^{Rayl}$ is a pure leakage field. Nevertheless it is not a pure inhomogeneous wave, because it results from a Gaussian incident beam and not from an exact distinct inhomogeneous wave.

The disappearance of the Schoch phenomenon when $\Delta > W$ is best seen when Fig. IX.B_8 is compared with Fig. IX.B_9. In both figures, the angle of incidence is the same, and so are the frequency and beam width, however the Schoch phenomenon is only visible in Fig. IX.B_9, where the incidence spot is relatively far from the corner, and not in Fig. IX.B_8.

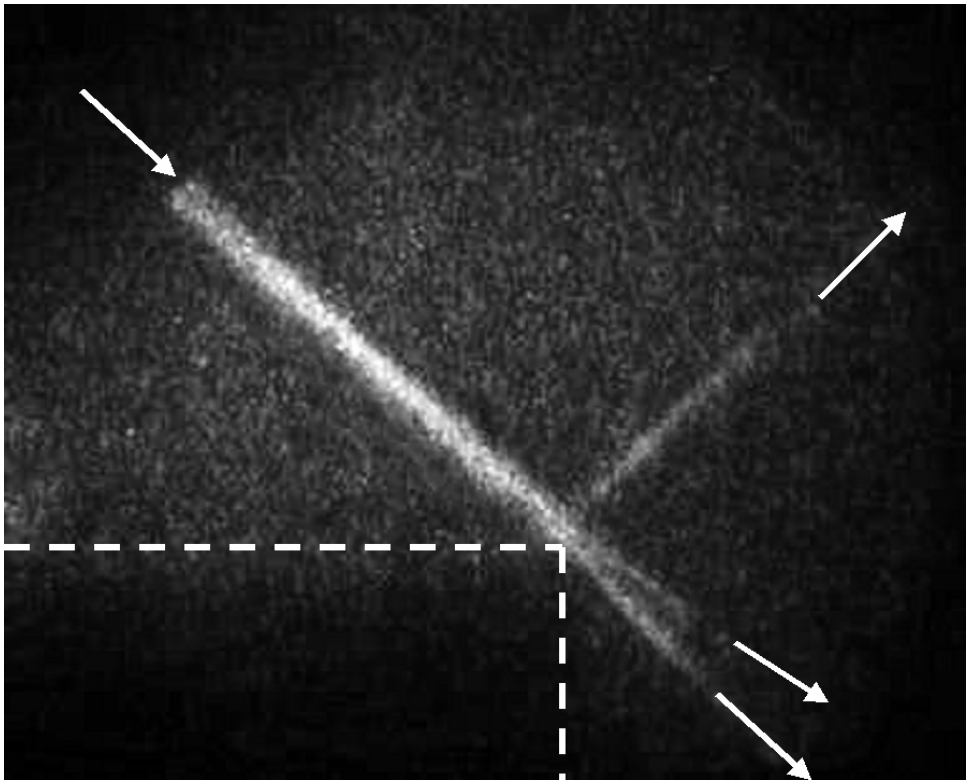

Fig. IX.B_8: ***Incidence of 6 MHz, 0.6 cm wide bounded beam on brass.*** $W \approx 0.9cm$, $\Delta \approx 0.8W$ ***(Schlieren picture). The dashed lines show where the plate is situated in the experiment. The arrows show the sound propagation direction. The dashed lines show where the plate is situated in the experiment. The arrows show the sound propagation direction.***

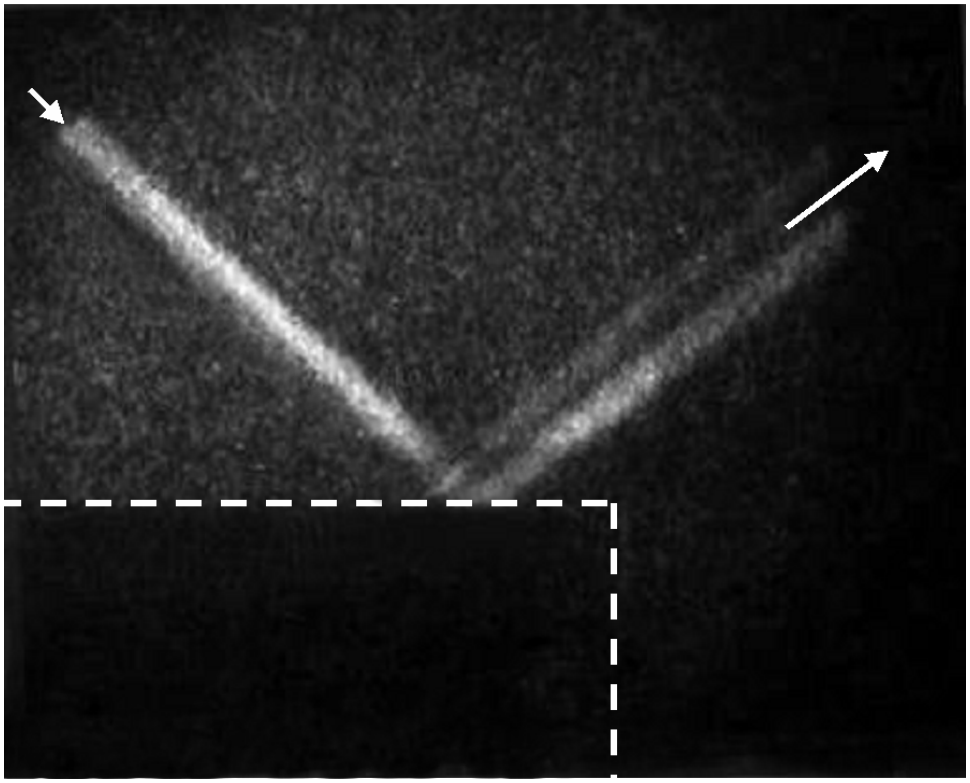

Fig. IX.B_9: ***Incidence of 6 MHz, 0.6 cm wide bounded beam on brass.*** $W \approx 0.9cm$***, far from the edge, the Schoch phenomenon is visible. (Schlieren picture). The dashed lines show where the plate is situated in the experiment. The arrows show the sound propagation direction. The dashed lines show where the plate is situated in the experiment. The arrows show the sound propagation direction.***

CONCLUSIONS

It is shown that leaky Rayleigh waves partly propagate around the corner of a thick solid plate. It is also shown that leaky Rayleigh waves are physically generated by the borders of the incident beam and not so much by the center. As far as we know, there are no other experiments described in the literature that have revealed this feature. This shows that only the beam borders are responsible for the physical generation of leaky Rayleigh waves, whereas mathematical models that describe bounded beams by means of a superposition of homogeneous or inhomogeneous infinite plane waves, ascribe responsibility for leaky surface wave generation to the complete area occupied by the bounded beam. Consistent experimental results are given for aluminum and brass. Comparison with cited earlier reports shows that whenever, along the vertical edge, at the extremity of a plate, leaky Rayleigh waves need to be generated, that it is better to use incident leaky Rayleigh waves than Scholte – Stoneley waves. This might be very important for nondestructive testing of materials.

REFERENCES

[1] Tsukasa Yoneyama, Shilgeo Nishida, “Further calculation on Rayleigh wave diffraction by elastic wedges”, J. Acoust. Soc. Am. 59(1), 206-208, 1976

[2] Z. L. Li, J. D. Achenbach, I. Komsky, Y. C. Lee, “Reflection and transmission of obliquely incident surface-waves by an edge of a quarter space – theory and experiment”, J. Appl Mech – Trans. of ASME 59(2), 349-355, 1992

[3] V. V. Krylov, “Calculation of the reflection coefficient for Rayleigh-waves at the edge of an obtuse-angle wedge”, Sov. Phys. Acoust.-USSR 331(1), 86-87, 1987

[4] V. V. Krylov, V. G. Mozhaev, “Reflection and transmission of Rayleigh-waves in a wedge”, Sov. Phys. Acoust.-USSR 31(6), 457-459, 1985

[5] V. G. Mozhaev, V. V. Krylov, ”Oscillation mechanism of Rayleigh-wave reflection and transmission in elastic wedge”, Vestnik Moskovskogo Universiteta Seriya 3 Fizika Astronomiya 26 (4), 76-79, 1985

[6] D. A. Bruttomesso, L. J. Jacobs, C. Fiedler, “Experimental and numerical investigation of the interaction of Rayleigh surface waves with corners”, J. Nondestr. Eval. 16(1), 21-30, 1997

[7] A. K. Gauetesen, “Scattering of a Rayleigh wave by an elastic quarter space – revisited”, Wave Motion 35(1), 91-98, 2002

[8] D.A. Bruttomesso, L.J. Jacobs,” Transfer functions to remove the effect of corners on Rayleigh waves”, J. Eng. Mech. – ASCE 125(1), 111-117, 1999

[9] Kane and Spence, “Rayleigh wave transmission on Elastic wege”, Geophys. 28, 715-723, 1963

[10] B. V. Budaev, D. B. Bogy, “Rayleigh wave scattering by a wedge”, Wave Motion 22(3), 239-257, 1995

[11] V. V. Popov, “Rayleigh wave diffraction by a weak inhomogeneity”, Acoust. Phys. 40(4), 577-579, 1994

[12] V. V. Popov, “Rayleigh-wave diffraction at a weak discontinuity in the boundary-conditions”, Acoust. Phys. 40(3), 377-380, 1994

[13] B. R. Tittmann, L. A. Ahlberg, A. K. Mal, “Rayleigh-wave diffraction from surface-breaking discontinuities”, Appl. Phys. Lett. 49(20), 1333-1335, 1986

[14] J. Pohl, Crack characterization using ultrasonic Rayleigh waves”, Materialprufung 43 (11-12), 446-451, 2001

[15] A. Tinel, “Diffraction de l’onde de Scholte par un dièdre et par un réseau de stries”, PhD thesis, Université le Havre, France, in French (1991)

[16] R. Briers, O. Leroy, G. N. Shkerdin, “Conversion of a Stoneley wave at the extremity of a fluid loaded plate”, J. Acoust. Soc. Am. 101(3), 1347-1357, 1997

[17] A. Tinel, J. Duclos, “Diffraction and conversion of the Scholte-Stoneley wave at the extremity of a solid”, J. Acoust. Soc. Am. 95(1), 13-20, 1994

[18] M. A. Breazeale, “From monochromatic light diffraction to colour schlieren photography”, J. Opt. A: Pure Appl. Opt. 3, S1-S7, 2001

[19] A. Schoch, “Der Schalldurchgang durch plate”, Acustica 2, 1-17, 1952

[1] Schoch, “Seitliche Versetzung eines total-reflektierten Strahls bei Ultraschallwellen”, Acustica 2, 18-19, 1952

[20] Werner Neubauer, “Observation of Acoustic Radiation from Plane and Curved Surfaces”, in *Physical Acoustics Vol 10*, W. P. Mason and R. N. Thurston, eds., 61, Academic Press, New York (1973)

[21] Tables of Physical and Chemical Constants,G.W.C. Kaye and T.H. Laby, 14th edition,Longman Group Limited 1973

[2] Hosten, M. Deschamps, “Génération d’ondes hétérogènes a l’interface liquide-solide viscoélastique. Approximation par des ondes inhomogènes”, ACUSTICA 59, 193-198, 1986

[22] Gérard Quentin, André Derem, Bernard Poirée, “The formalism of evanescent plane waves and its importance in the study of the generalized Rayleigh wave”, J. Acoustique 3, 321-336, 1990

[23] Nico F. Declercq, Rudy Briers, Joris Degrieck, Oswald Leroy, "The History and Properties of Ultrasonic Inhomogeneous Waves", accepted for publication in IEEE Transactions on Ultrasonics, Ferroelectrics, and Frequency Control - Nico F. Declercq, Rudy Briers, Joris Degrieck, Oswald Leroy, "Ultrasonic Inhomogeneous Waves: Three Decades of Fascination", J. Acoust. Soc. Am. 115(5), 2624, 2004

[24] Bertone H. L. and Tamir T., Unified theory of Rayleigh angle phenomena for acoustic beams at liquid-solid interfaces, Appl. Phys. 2, 157-172, 1973

[25] Nico F. Declercq, Joris Degrieck, Oswald Leroy, "The Laplace transform to describe bounded inhomogeneous waves", accepted for publication in J. Acoust. Soc. Am. - Nico F. Declercq, Joris Degrieck,

Oswald Leroy, "On the ability of bounded inhomogeneous waves to experimentally verify the behavior of infinite inhomogeneous plane waves", J. Acoust. Soc. Am. 113(4), 2283, 2003

IX.C Bounded beam interaction with plate-edge at Lamb angle

There are many papers dealing with the scattering of Lamb waves at the edges of free and immersed plates. Nevertheless, since such Lamb waves are often generated by means of bounded beams, here, a study is revealed, based on Schlieren photography, of the interaction of a bounded beam, incident near the edge of a plate at the Lamb angle. The study shows that retro reflection occurs of the generated Lamb waves and that more complicated mode conversion takes place whenever the border of the beam reaches the edge of the plate. The difference is shown between scattering of the A_1 and the S_1 Lamb mode. Furthermore, it is shown that Lamb waves excite a radiating acoustic multipole when encountering the edge of the plate.

The contents of this section have been accepted for publication in Acta Acustica United with Acustica (Imp. Fact. 0.346; SCI-index, Acoustics, rank:21 /28)

INTRODUCTION

Lamb waves are frequently applied in nondestructive testing of plates because they propagate over long distances. Whenever defects are encountered, mode conversion appears and this can be detected [1]. When Lamb waves reach the edge of a plate, complicated interactions occur, resulting in retro reflected Lamb modes and stimulations of additional Lamb modes [2-9]. Lamb waves also have a leaky counterpart when the plate is submerged in a liquid. Several studies have also been published on the interaction of a leaky Lamb wave with the edge of a plate [7-9]. Nevertheless, when a plate is submerged in a liquid, a commonly used technique for Lamb wave excitation is the application of a bounded beam incident at a Lamb wave generating angle, resulting in the Schoch effect, see Fig. IX.C_1.

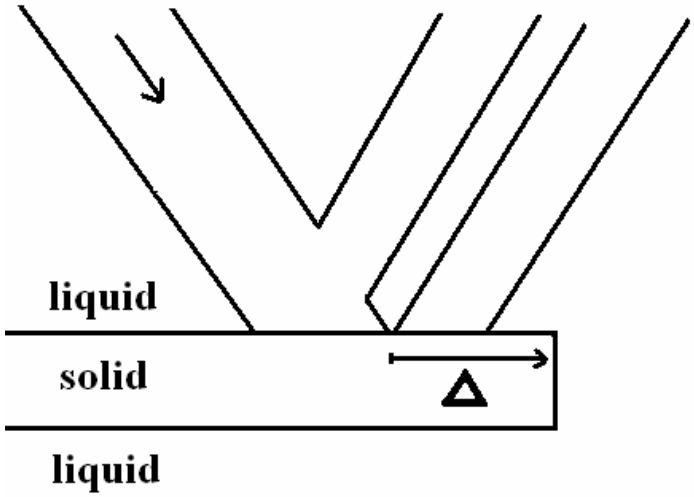

Fig. IX.C_1: ***Schematic of the experimental setup. The parameter Δ is the distance between the border of the incident beam and the edge of the plate.***

This angle depends on the frequency and on the plate thickness, as well as on the liquid and solid properties, and therefore must correspond to a dispersion curve. An example of dispersion curves for an aluminum plate is given in Fig. IX.C_2. This use of a bounded beam is also applied in a complex form (pulsed and focused) to discover a relatively large area of the dispersion curves for a given plate [10]. Nevertheless as far as we know, the interaction of the combination of an incident bounded beam and a generated leaky Lamb wave with the edge of a plate, has not been studied before. The most important reason is probably because modeling this complicated combination is difficult to do. However, a semi-quantitative experimental study is possible by means of the Schlieren technique [11]. This technique enables one to visualize sound fields and results in beautiful and scientifically interesting pictures that will be shown and discussed further on.

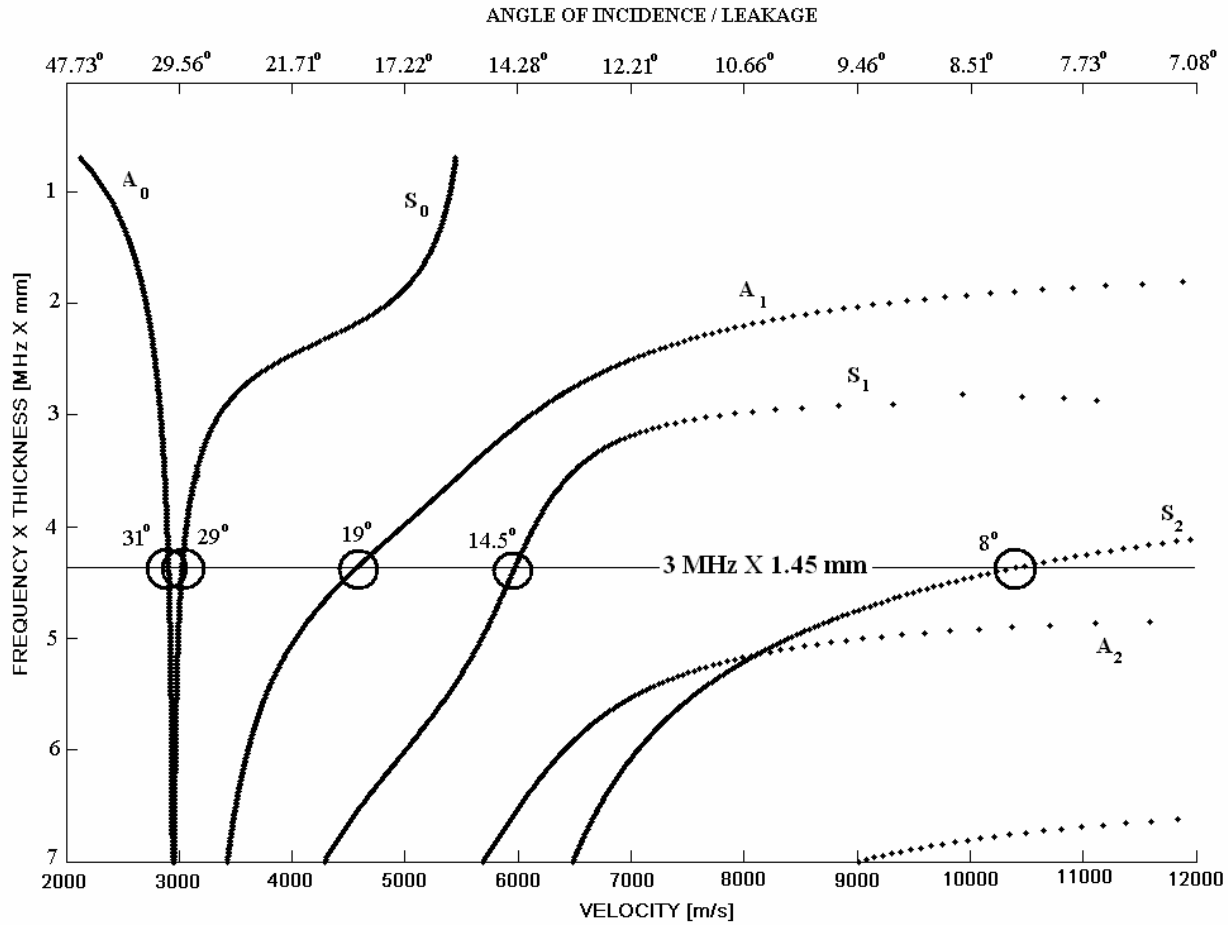

Fig. IX.C_2: ***Dispersion curves for Lamb waves in an aluminum plate. The horizontal line denotes the experimental situation for 3MHz sound incident on a 1.45 mm thick plate.***

In what follows, the interaction of a bounded beam with the edge of a plate is described for a Lamb wave angle of incidence. First of all, the experimental procedure will be outlined, then the situation of excitation of an A_1 mode in aluminum will be considered, followed by the excitation of an S_1 mode in glass.

It will be shown that one of the main differences between the two situations is the forward transmitted sound field. Subsequently, an explanation of the difference will be revealed in terms of acoustic multipole generation at the plate-edge.

EXPERIMENTAL SETUP AND PROCEDURE

A Schlieren experimental setup [11] is used. Schlieren images are obtained by means of a wide coherent and collimated light beam that passes through the water tank in which the ultrasonic experiments are performed. This light is bended and/or diffracted due to inhomogeneities in the liquid or by the presence of sound. The passed light is focused onto a black ink spot. Therefore, collimated light is trapped on the spot whereas light, that deviates from the collimated light beam, passes beyond the ink spot and ultimately reaches a projection screen. Hence, only disturbed light is visible on the projection screen and this is the reason why sound can be visualized.

The generation of a Lamb wave by means of a bounded beam can be visualized by this technique, because it involves the Schoch effect, resulting in a reflected specular lobe and a reflected nonspecular lobe (shifted to the right) with a null strip in between (see Fig. IX.C_1). This null strip is caused by the out of phase characteristic of the two lobes.

A considered plate is clamped on one side, leaving a free edge on the other side. The whole thing is immersed in water. Then, a 3MHz harmonic bounded Gaussian ultrasonic beam of 1 cm physical width is incident in a plane perpendicular to the coherent light and its interaction with the plate can be visualized and studied on the projection screen. The angle of incidence can be altered by means of a sophisticated mechanism that maintains the distance between the transducer (sound emitter) and the spot of incidence, while changing the angle of incidence. As usual, the angles defined in what follows are measured from the normal to the plate, clockwise, with the zero angle defined as the direction of the upwards pointing normal to the surface. A positive angle is attributed to sound that propagates from left to right (i.e. the incident beam and forward scattered sound), whereas a negative angle is attributed to sound propagating from right to left (i.e. backwards scattered sound, exists only in the occurrence of interaction with the edge of the plate).

In Fig. IX.C_1, a schematic is shown of the acoustical part of the experimental setup. The parameter Δ is the distance between the border of the incident beam and the edge of the plate.

INTERFERENCE PATTERN OF TWO PLANE WAVES

Suppose that a sound field in water is built up by two plane waves, then the sound potential is given by

$$\varphi = \sum_{\mu=1,2} A_\mu \exp i\left(k_{\mu,x}x + k_{\mu,z}z\right) \tag{IX.C_1}$$

The intensity is given by

$$|\varphi|^2 = |A_1|^2 + |A_2|^2 + 2|A_1||A_2|\cos\left(F_2 - F_1\right)\cos\left(\left(k_{2,x} - k_{1,x}\right)x + \left(k_{2,z} - k_{1,z}\right)z\right) \tag{IX.C_2}$$

with

$$F_{\mu} = phase\left(A_{\mu} \right) \tag{IX.C_3}$$

The Euclidean subspace that is characterized by an amplitude equal to the amplitude at the origin and that contains the origin itself, is then given by

$$0 = \left(k_{2,x} - k_{1,x} \right) x + \left(k_{2,z} - k_{1,z} \right) z \tag{IX.C_4}$$

In other words, this subspace (representing energy rays) is a straight line. Now, we consider the direction θ of this straight line, measured from the z-axis, whence we may replace z by $x\cot\left(\theta\right)$, and therefore

$$\theta = -\cot^{-1}\left(\frac{\sin\theta_2 - \sin\theta_1}{\cos\theta_2 - \cos\theta_1} \right) \tag{IX.C_5}$$

with θ_{μ} the phase propagation angle measured from the z-axis for the wave labeled by μ. In what follows, we consider plates normal to the z-axis, pointing upwards into the halfspace that contains the incident beam. The significance of formula (IX.C_5) will be outlined further on. Again, in formula (IX.C_5), we attribute a positive angle to propagation directions from left to right, and a negative angle to propagation directions from right to left. This is important, because it makes the interpretation of the angle θ straightforward and in agreement with this sign convention.

ANTISYMMETRICAL LAMB WAVES

Fig. IX.C_2 shows the different calculated dispersion curves for an aluminum plate immersed in water. The calculations are based on a longitudinal wave velocity of $6370 m/s$, a shear wave velocity of $3160 m/s$ and a density of $2770 kg/m^3$ for aluminum, whereas a longitudinal wave velocity of $1480 m/s$ and a density of $1000 kg/m^3$ for water. Each of the curves corresponds to a Lamb mode. The experiments are performed on a 1.45 mm thick aluminum plate using a 3 MHz bounded beam of 1 cm physical width. The horizontal line in Fig. IX.C_2 corresponds to the experimental configuration. It is seen that 5 Lamb modes can be stimulated depending on the angle of incidence, i.e. a A_0 mode at 31^0, and S_0 mode at 29^0, an A_1 mode at 19^0, an S_1 mode at 14.5^0 and a S_2 mode at 8^0. We have found the Schoch effect up to a certain extend for each of these modes. However the clearest effect was found at 19^0. Therefore, the reported experiments are performed using a fixed angle of 19^0. Another reason why we have used this angle is that it is seen in Fig. IX.C_2 that this angle generates A_1 Lamb waves. This is an antisymmetrical Lamb mode. Further below, the case of a symmetrical Lamb mode (for a glass plate) will be considered as well in order to observe any possible differences.

We have followed the experimental procedure outlined before. The distance Δ, as in Fig. IX.C_1, can be set by maintaining the incident beam and by shifting the position of the plate without changing its angle relative to the incident beam.

Lamb waves are partly retro-reflected when they reach the edge of the plate, which means that a standing wave pattern will be formed in the plate as a result of forward and backward propagating identical Lamb modes. Hence, whenever the Lamb mode reaches the edge, a standing wave pattern will be formed with an inter notch distance *d* given by

$$2d = \frac{v}{3MHz} \tag{IX.C_6}$$

with v the velocity of the Lamb waves. Fig. IX.C_2 shows that $v = 4546m/s$ and therefore $d = 0.76mm$. Indeed if we take a look at the Schlieren picture given in Fig. IX.C_3, when the considered bounded beam is incident at 19^0 with the furthest part of the right reflected lobe reaching the edge of the plate without surpassing it, a fringed pattern of vertical lines of thickness 0.76 mm appears superposed on the other sound patterns. This standing wave pattern can only radiate in vertical directions because it is steady and because Snell's law predicts that sound, that does not propagate along the interface, will radiate perpendicularly to that interface. Also, from a mathematical point of view, the pattern is actually caused by plane waves propagating along the same Lamb wave angle, though in opposite sense (when measured from the normal to the plate), which corresponds to energy rays along the angle 0^0, in accordance with formula (IX.C_5). Furthermore because it consists of anti-phase vibrations of consequent half wavelength regions, there are null strips generated in between the narrow vertical sound strips. This is the reason why this sound field is radiated in vertical 'lines' instead of a homogeneous sound field.

However, apart from identical retro-reflected Lamb waves, there can also exist retro-reflected Lamb waves of a different kind. The latter can be generated by the incident Lamb wave or by the direct interaction of the incident bounded beam with the edge of the plate. It can be calculated by means of (IX.C_5) that the combination of incident A_1 modes and reflected A_0 modes, result in rays along the directions 8^0 and 172^0. Furthermore, the combination of reflected A_1 modes and reflected A_0 modes, result in rays along the directions -25^0 and -155^0. In Figs IX.C_3 and IX.C_4, where the incident beam is situated very close to the edge of the plate ($\Delta \approx 0.20cm$) and respectively surpasses the edge of the plate slightly ($\Delta \approx 0.10cm$), it can be seen that there is, in addition to the vertical lines or the vertical rays as described above, an additional pattern consisting of rays along the angles 8^0 and 172^0.

This means that incident A_1 modes have been partly transformed into reflected A_0 modes. The energy leakage of both modes combines and forms the described rays. In Fig IX.C_5, where a larger part of the incident beam surpasses the edge of the plate ($\Delta \approx -0.30cm$), an additional pattern is formed consisting of rays along the -155^0 direction. This is an indication of the existence of mode conversion of A_1 modes into reflected A_1 modes and A_0 modes. The latter two form an interference pattern consisting of rays along -155^0. However, we could not find the expected -25^0 that also corresponds to the same mode conversion. Maybe it is too weak, or it is masked by the incident beam. Other combinations of mode conversion would have resulted in other angles, but these were not observed and are therefore not mentioned. The fact that the observed rays can be explained by means of mode conversion of Lamb modes, justifies that more complicated phenomena such as edge modes [12,13] are probably not involved here.

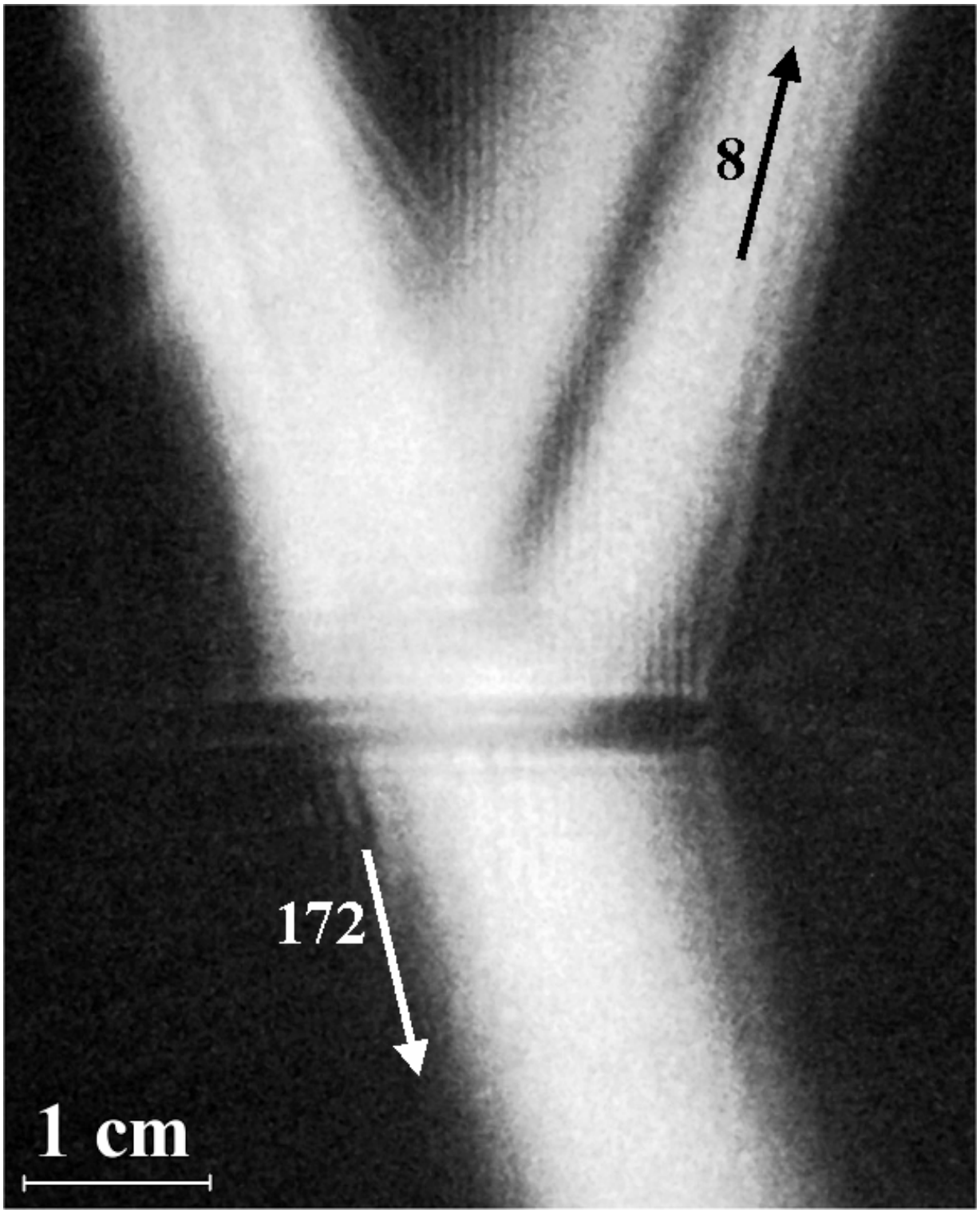

Fig. IX.C_3: ***Incidence at the Lamb wave angle of 19^o with the incident beam almost reaching the edge of the plate $\Delta \approx 0.20cm$. A typical Schoch effect is visible as on an infinite plate, however a pattern of vertical lines appears in addition. In addition, 'rays' appear in the directions 8^0 and 172^0.***

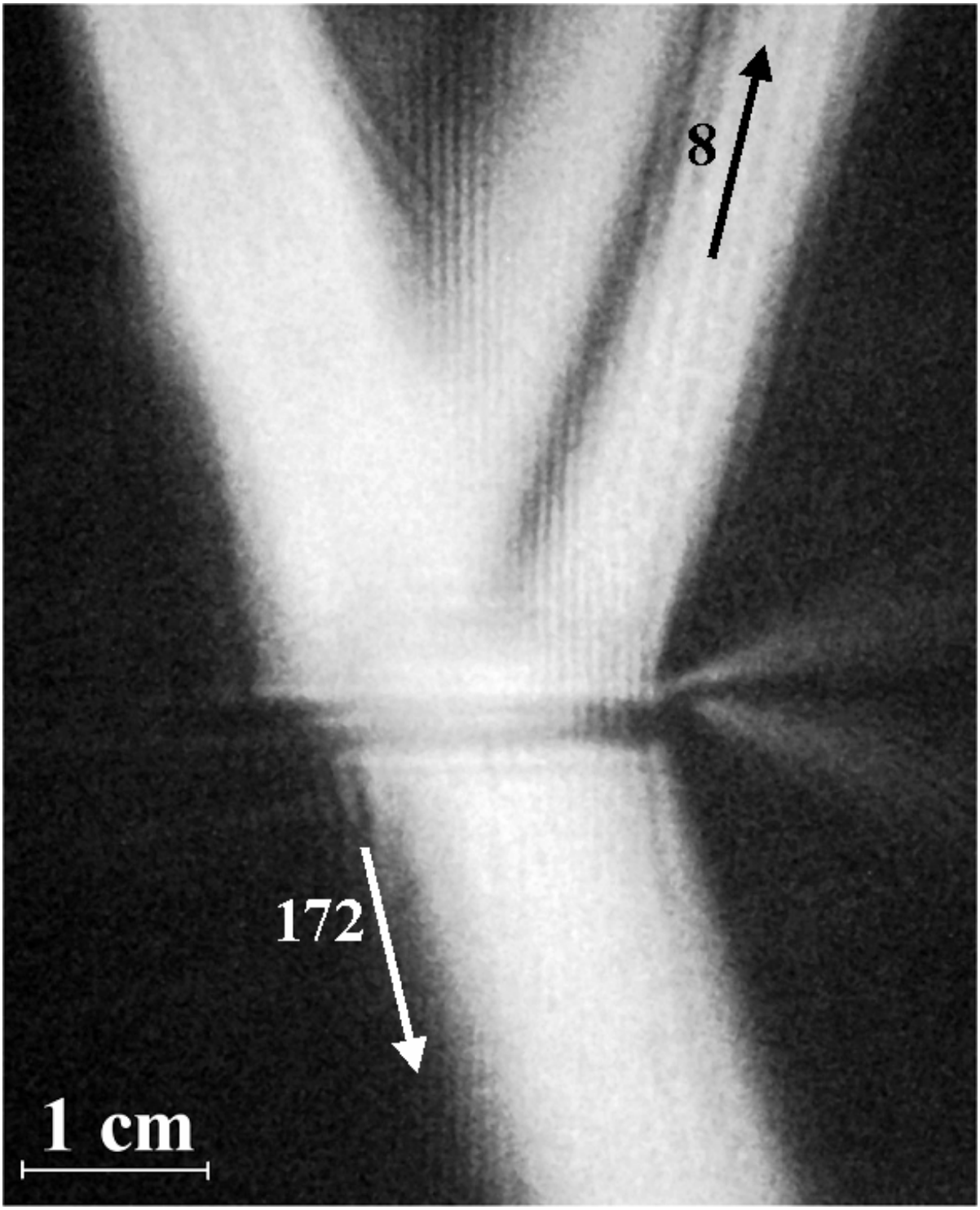

Fig. IX.C_4: ***Same as in Fig. IX.C_3, however here the incident beam surpasses the edge of the plate a distance of*** $\Delta \approx -0.10cm$. ***This is the reason why a scattered sound pattern is now visible emitted at the end of the plate. The pattern of vertical lines is still visible and is even a bit more outspoken than in Fig. IX.C_3. That is because the end of the plate is closer to the center of the beam. The additional rays are more outspoken than in Fig. IX.C_3.***

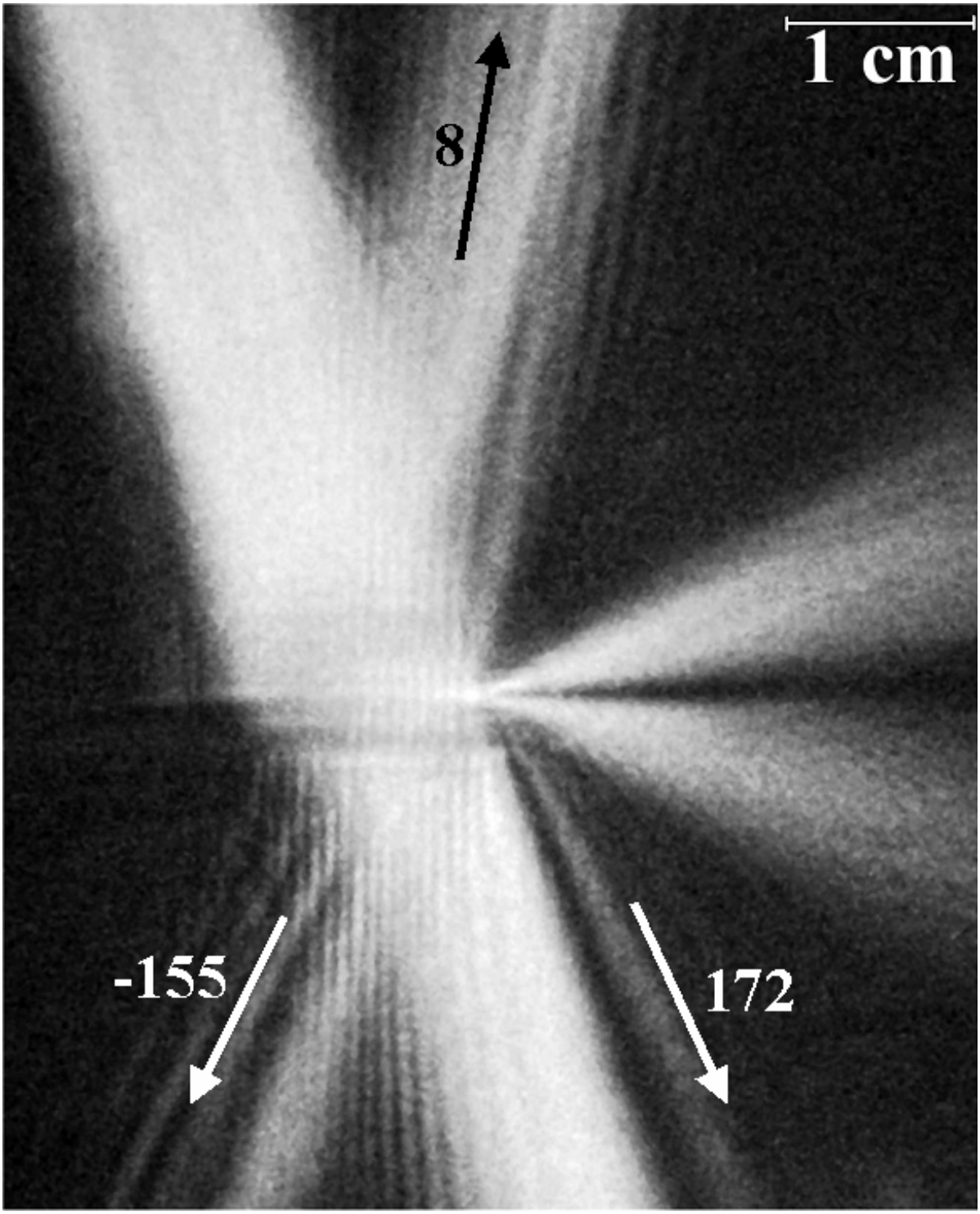

Fig. IX.C_5: ***Same as Fig. IX.C_4, except that the incident beam surpasses the edge of the plate even more,*** $\Delta \approx -0.30cm$. ***In addition other scattered beam patterns are visible and are probably due to mode converted Lamb waves. The vertical line pattern is still clearly visible. Apart from the rays in Figs IX.C_3 and IX.C_4, rays appear in the direction of*** -155^0.

In addition, a very weak radiation pattern appears beyond the edge of the plate, almost in-line with the plate itself. It is as if the edge becomes a sound source for beams directed to the right of the plate. These radiation patterns become stronger in Fig. IX.C_4, where it is shown what happens if $\Delta \approx -0.10cm$ and in Fig. IX.C_5, where $\Delta \approx -0.30cm$. A possible explanation why the right hand side pattern is more outspoken in Fig. IX.C_5 than in Fig. IX.C_3 is found in the fact that the amplitude of the excited Lamb waves is larger in the center of the beam than at the edges of the incident beam. This is reasonable, because we are dealing with an incident beam having a Gaussian amplitude profile. In section 6, it will be shown that Lamb waves, when reaching the end of the plate, generate an acoustic multipole that causes this typical radiation field.

SYMMETRICAL LAMB WAVES

Here, we consider a glass plate of thickness 1.23 mm. The angle of incidence is set at 15^0 which corresponds to the generation of the S_1 Lamb mode. The latter is known by considering the dispersion curves of the glass plate in Fig. IX.C_6 and by noting the Schoch effect during the experiments. Then the distance Δ, see Fig. IX.C_1, can be set by maintaining the incident beam and by shifting the position of the glass plate without changing its angle relative to the incident beam. The longitudinal sound velocity in glass is 5660 m/s, whereas the transversal sound velocity is 3520 m/s. The density is 2500 kg/m^3. Again, water is characterized by a longitudinal sound velocity of 1480 m/s and a density of 1000 kg/m^3. Calculation of the dispersion curves in Fig. IX.C_6 results in the existence of A_0 modes at an angle of 28.6^0, S_0 modes at 25.5^0, S_1 modes at 15^0, A_1 modes at 14^0 and (not seen in Fig. IX.C_6) S_2 modes at 3.45^0.

Fig. IX.C_7 corresponds to S_1 mode stimulation for the bounded beam incident at $\Delta \approx 0.84cm$. Note that vertical lines or rays are generated. The vertical rays are equidistant and the distance between them is a little less than 1mm. Indeed, Fig. IX.C_6 shows that for a S_1 Lamb wave angle of 15^0, $v = 5718m/s$ and therefore, according to relation (IX.C_6), $d = 0.95mm$. Therefore, as explained earlier, the vertical rays originate from the standing wave formation of forward propagating leaky S_1 Lamb waves and retro reflected S_1 Lamb waves.

If we consider formula (IX.C_5), then we see that incident S_1 modes and reflected S_2 modes result in rays at the angles 6^0 and 174^0, that incident S_1 modes and reflected S_0 modes result in rays at the angles -5^0 and -175^0, and that reflected S_1 modes and reflected S_2 modes result in rays at the angles -20^0 and -160^0. In Fig. IX.C_8, where the incident beam reaches the end of the plate, rays are visible at angles corresponding to the interaction of the leakage fields of reflected S_2 modes and incident S_1 modes, and also of reflected S_0 and S_1 modes. This shows that there is mode conversion of incident S_1 modes into reflected S_0, S_1 and S_2 modes. Furthermore, in Fig IX.C_9, in addition to those patterns, when the incident beam surpasses partly the edge of the plate, rays are also visible at the angles -5^0 and -175^0, which is due to the interference of the leakage fields of incident S_1 modes and reflected S_0 modes. Theoretically, also other combinations are possible, but the corresponding angles have not been observed experimentally. Nevertheless, we have not yet attempted to explain the possibility of sound patterns inline with the plate. This will be done in the next section.

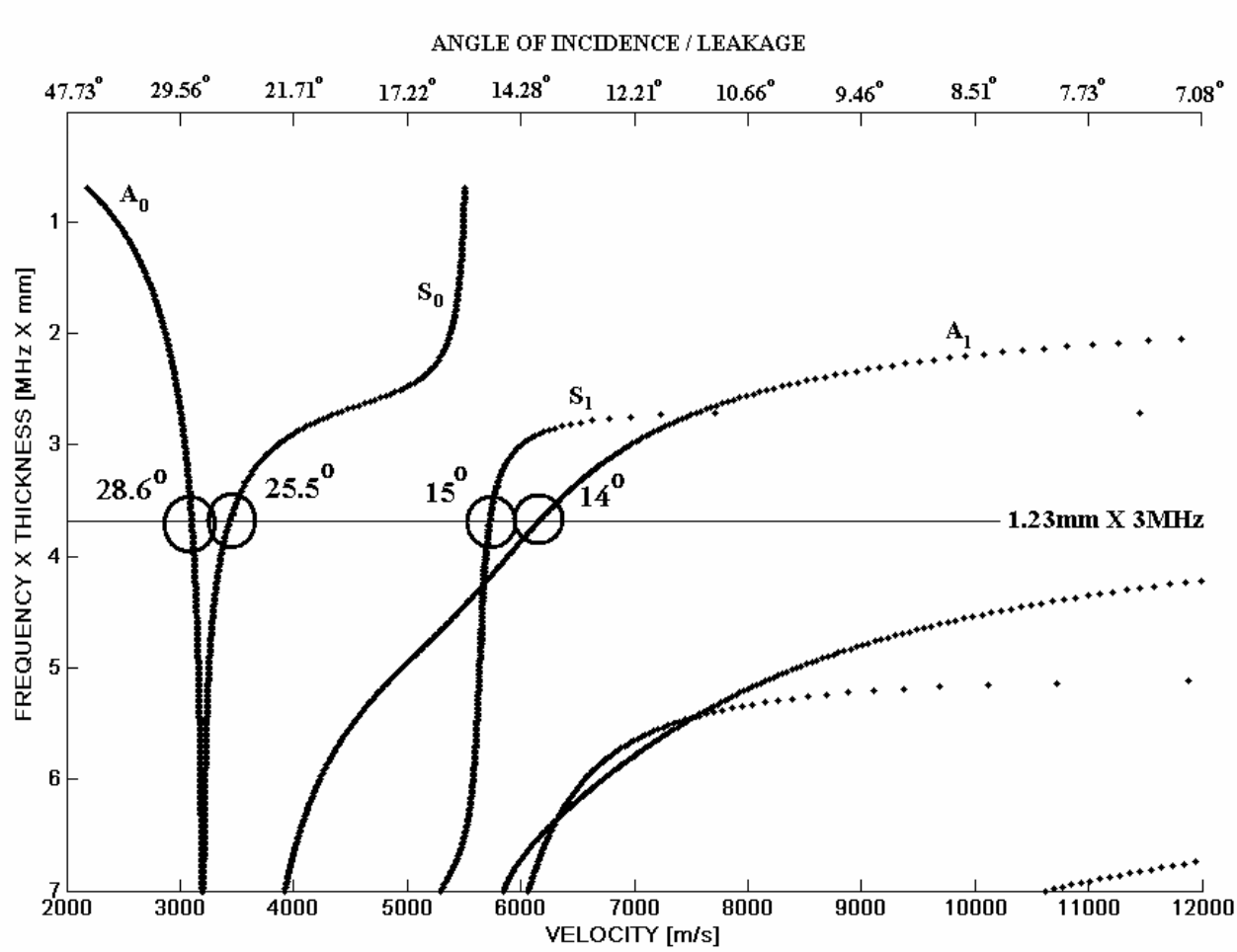

Fig. IX.C_6: ***Dispersion curves of Lamb waves in a glass plate. The added horizontal line corresponds with the combination of 3MHz on a plate of thickness 1.23 mm.***

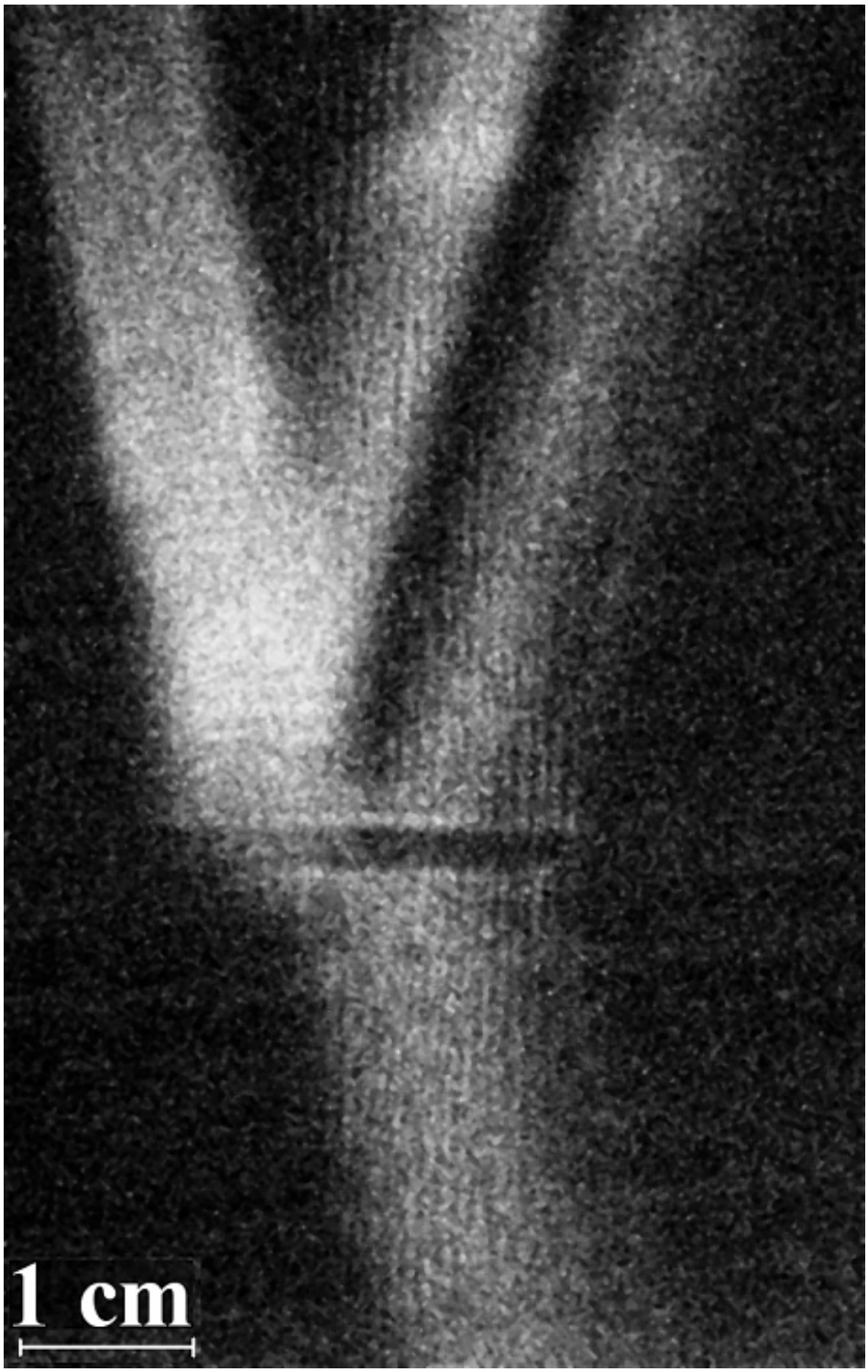

Fig. IX.C_7: ***Incidence of a 3 MHz Gaussian beam having a 1cm physical beam width at the S_1 Lamb wave angle (15^0), $\Delta \approx 0.84cm$. A vertical line pattern is visible, which is due to retro reflected S_1 modes.***

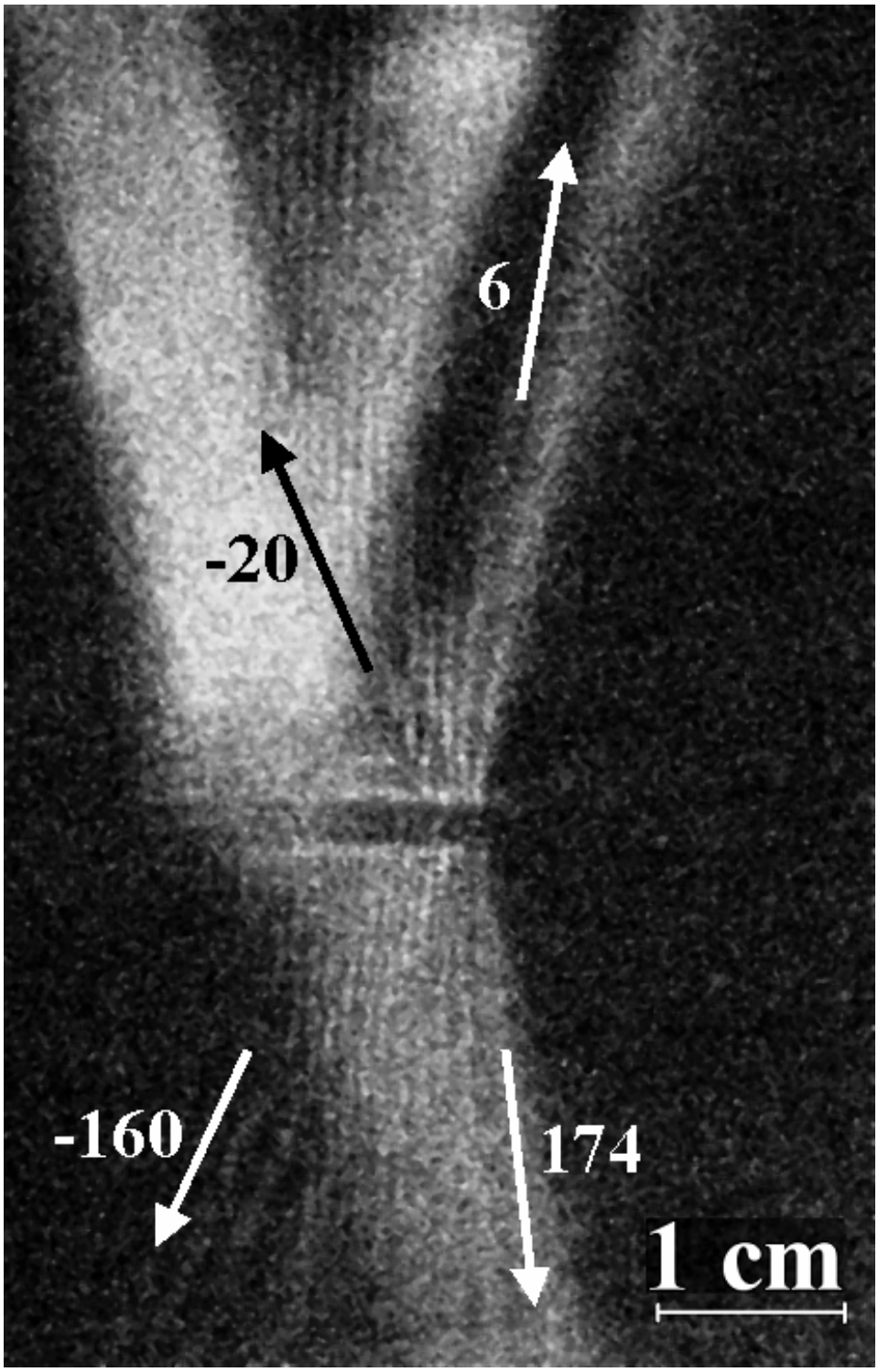

Fig. IX.C_8: ***Same as Fig. IX.C_7, except that*** $\Delta = 0cm$. ***A vertical line pattern is still visible, which is due to retro reflected*** S_1 ***modes. In addition, rays are visible along the directions*** 6^0, 174^0, -20^0 ***and*** -160^0.

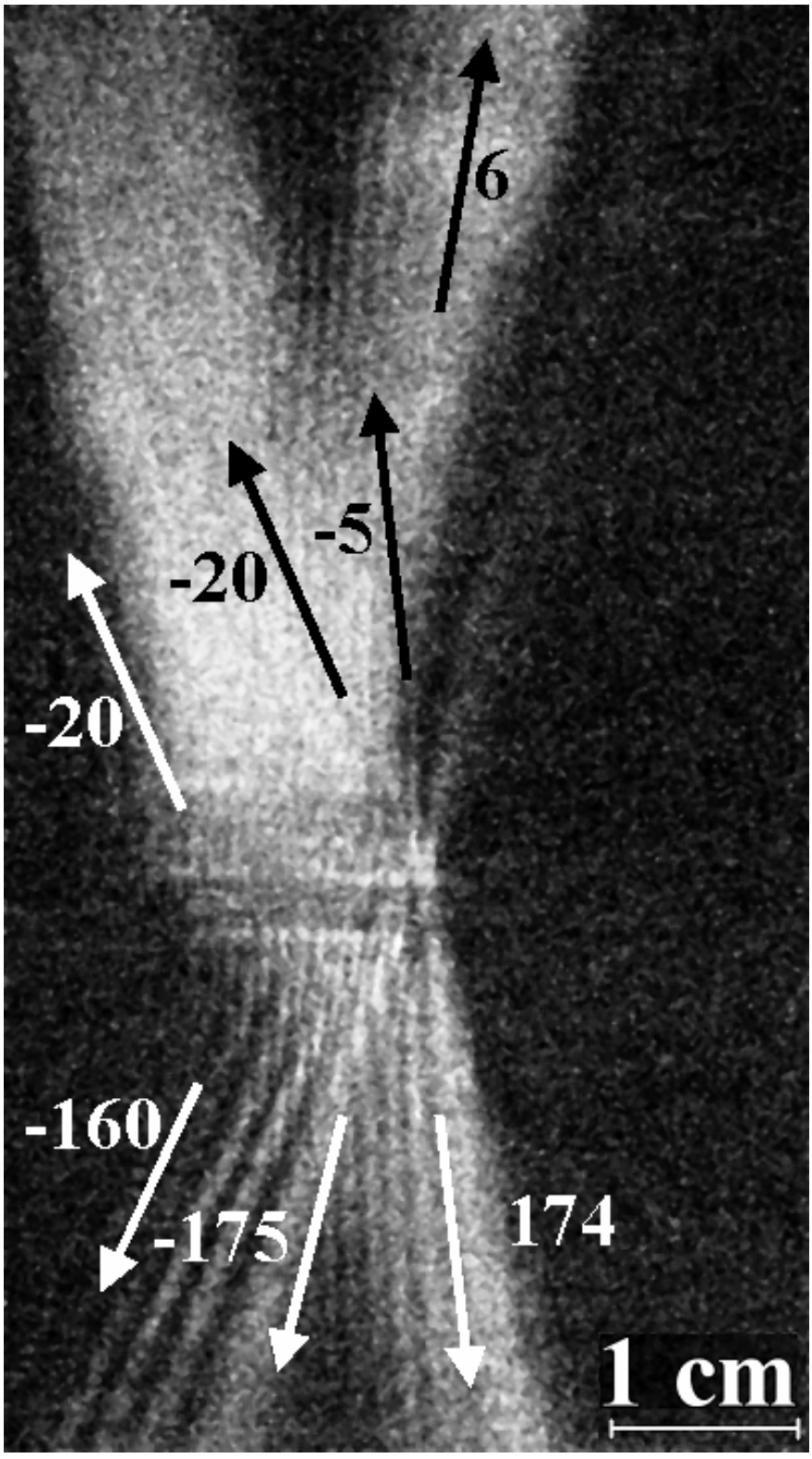

Fig. IX.C_9: ***Same as Fig. IX.C_7, except that*** $\Delta = -0.2cm$. ***Apart from the additional rays in Fig. IX.C_8, rays are also visible along*** -5^0 ***and*** -175^0.

PHYSICAL EXPLANATION FOR THE DIFFERENCE IN FORWARD SCATTERED FIELD WHEN A_1 AND S_1 LAMB WAVES REACH THE EDGE OF THE PLATE

From, for example, [14], we know that the particle displacement pattern along the thickness of the plate, depends on the kind of Lamb wave. For explaining the radiation field at the end of a plate, we have considered, as a trade off between realism and simplicity, along the edge of the plate, the particle displacement parallel to the plate (i.e. the x-direction, or the forward direction) and have replaced the positions along the thickness of the plate where that parallel displacement is maximum, by point sources having the same amplitude and phase.

In the upper part of Fig. IX.C_10, a schematic is shown, by means of horizontal arrows, of the maximum parallel displacements for different kinds of Lamb modes. The sense of the arrows corresponds to the phase. The lower part of Fig. IX.C_10 shows how these arrows are then replaced by point sources (denoted by a circle) where the sign ('+' or '-') denotes the phase ('+' is equivalent to phase '0', whereas '-' is equivalent to phase 'π'). In other words, this simplification results in a system where the edge of the plate is replaced by a 'multipole'. In reality, the situation will slightly deviate from this 'multipole' representation, because there will be intermediate radiation points in between the maxima as well. Nevertheless, this approximation results in an explanation of the radiated sound fields beyond the edge of a plate.

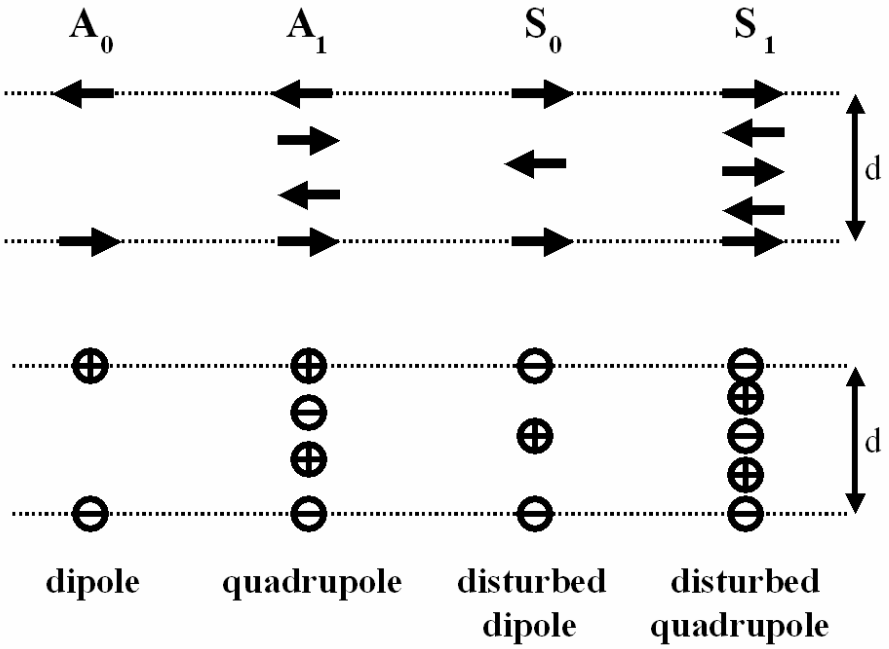

Fig. IX.C_10: ***A schematic of the horizontal particle displacement along the edge of the plate and its translation to multipoles. Top: the position of the arrows corresponds to the spots of maximum horizontal displacement for the given Lamb modes. The sense indicates the phase. Bottom: translation of the arrows to point sources whose combination forms a multipole. The sources are indicated with circles, provided with a sign that indicates the phase.***

This is seen in Figs IX.C_11-13, where the radiation field is shown at 3MHz in water, for different multipoles, characterized by d=1.5 mm. Because the plates in the two examples given in this section have a different thickness, it is difficult to study the independent influence of the multipole system on the radiation pattern. That is the reason for the fixed value of the thickness in the simulations. Therefore, the simulations are not exact simulations, though they can indicate that the multipole representation is a possible explanation of what is experimentally observed. The gray scale is equal for all Figs IX.C_11-13, therefore exact intensity comparison is possible. The resemblance of Fig IX.C_12 with Fig IX.C_5 and of Fig IX.C_13 with Fig IX.C_9, is striking. The strong forward scattering in Fig. IX.C_12 is due to a quadrupole and it is seen that this corresponds to an A_1 mode, which is the case in Fig IX.C_5. The very weak forward scattering in Fig. IX.C_13 corresponds to a so called 'disturbed quadupole' and according to Fig. IX.C_10, it corresponds to an S_1 mode, which is also the case in Fig. IX.C_9. Fig. IX.C_11 is added as information, it would correspond to an incident A_0 mode, which is not considered here.

In other words, it is shown in this section that the forward scattering pattern, or its absence, can be explained by means of an acoustic multipole on the edge of the plate, that is generated by means of an incident Lamb wave.

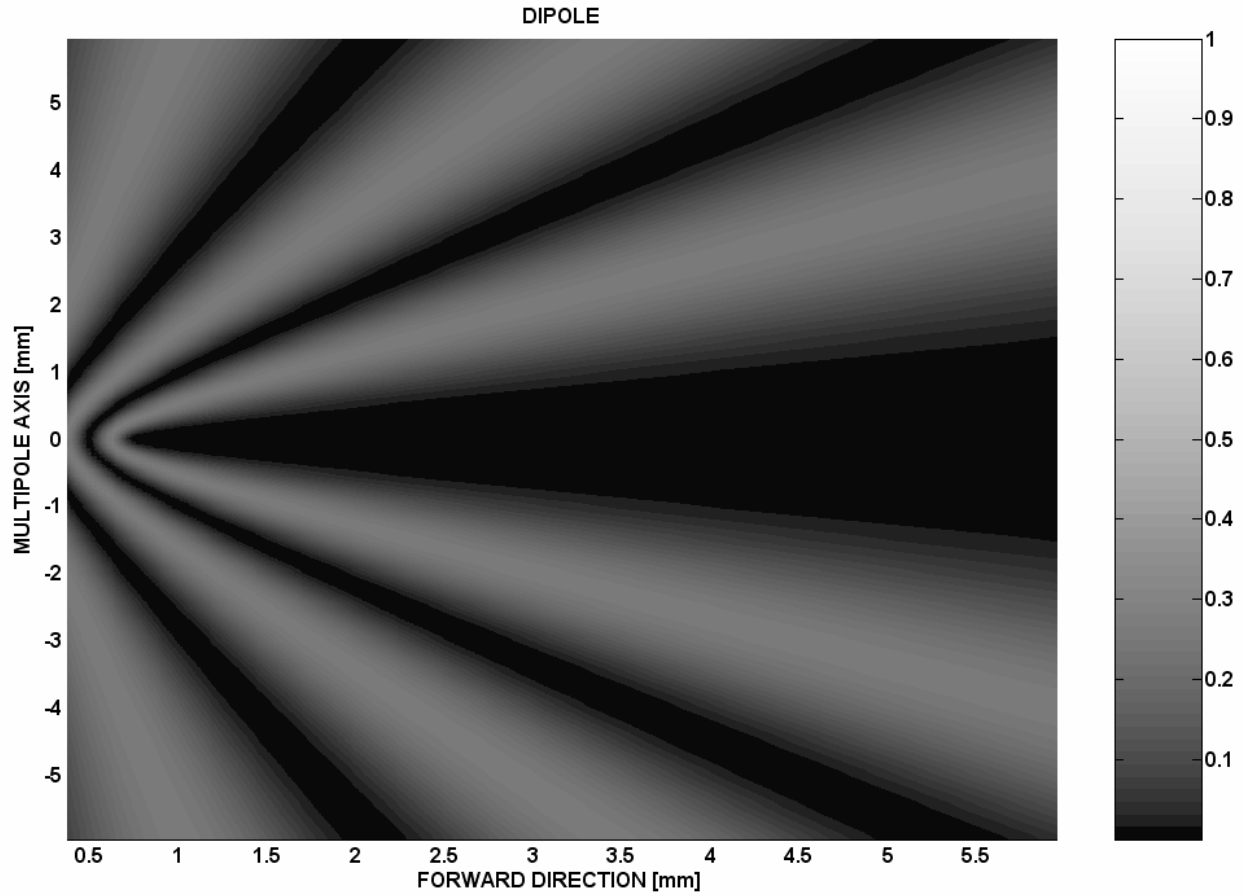

Fig. IX.C_11: ***Radiation of a dipole source ($\approx A_0$ mode) in water at 3MHz for d=1.5 mm***

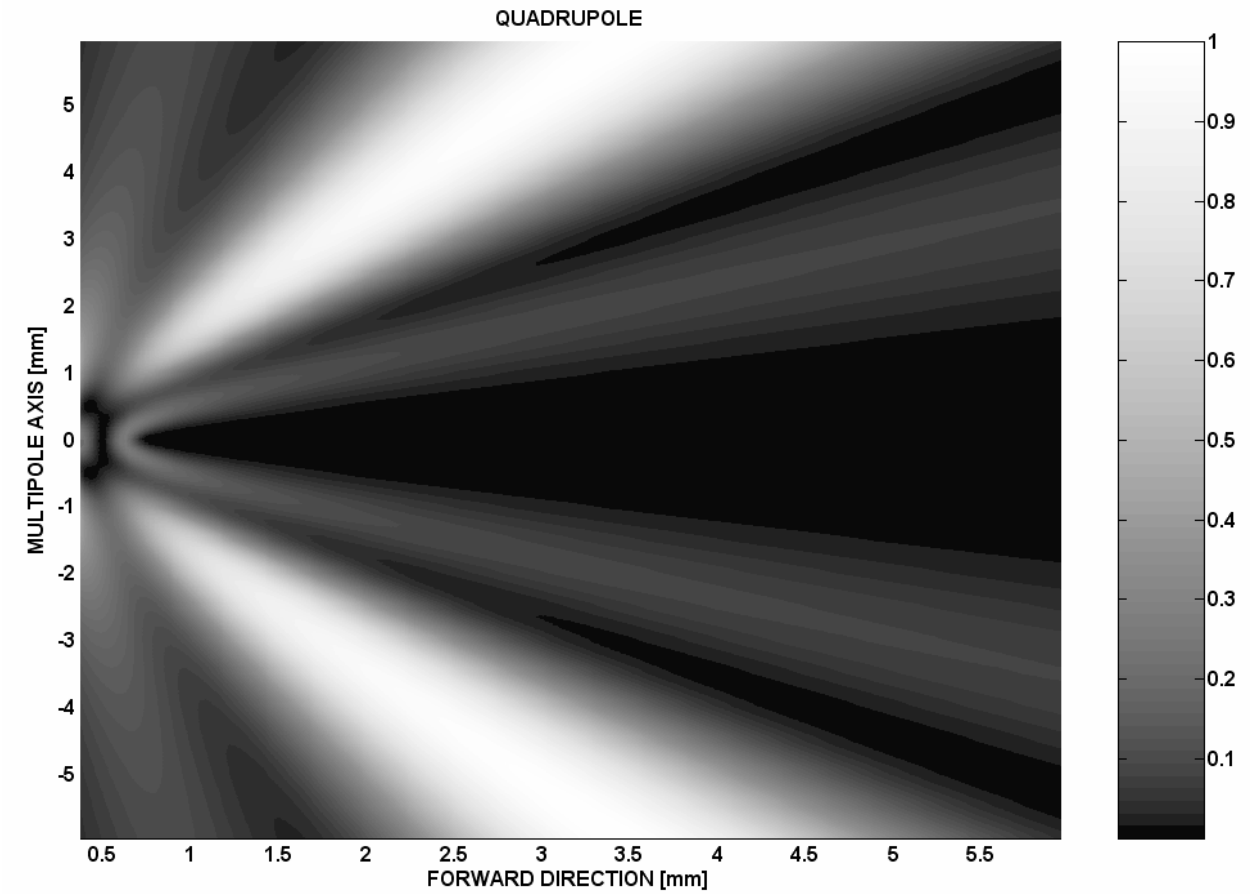

Fig. IX.C_12: ***Radiation of a quadrupole source ($\approx A_1$ mode) in water at 3MHz for d=1.5 mm. This pattern is also noticed in Fig. IX.C_5.***

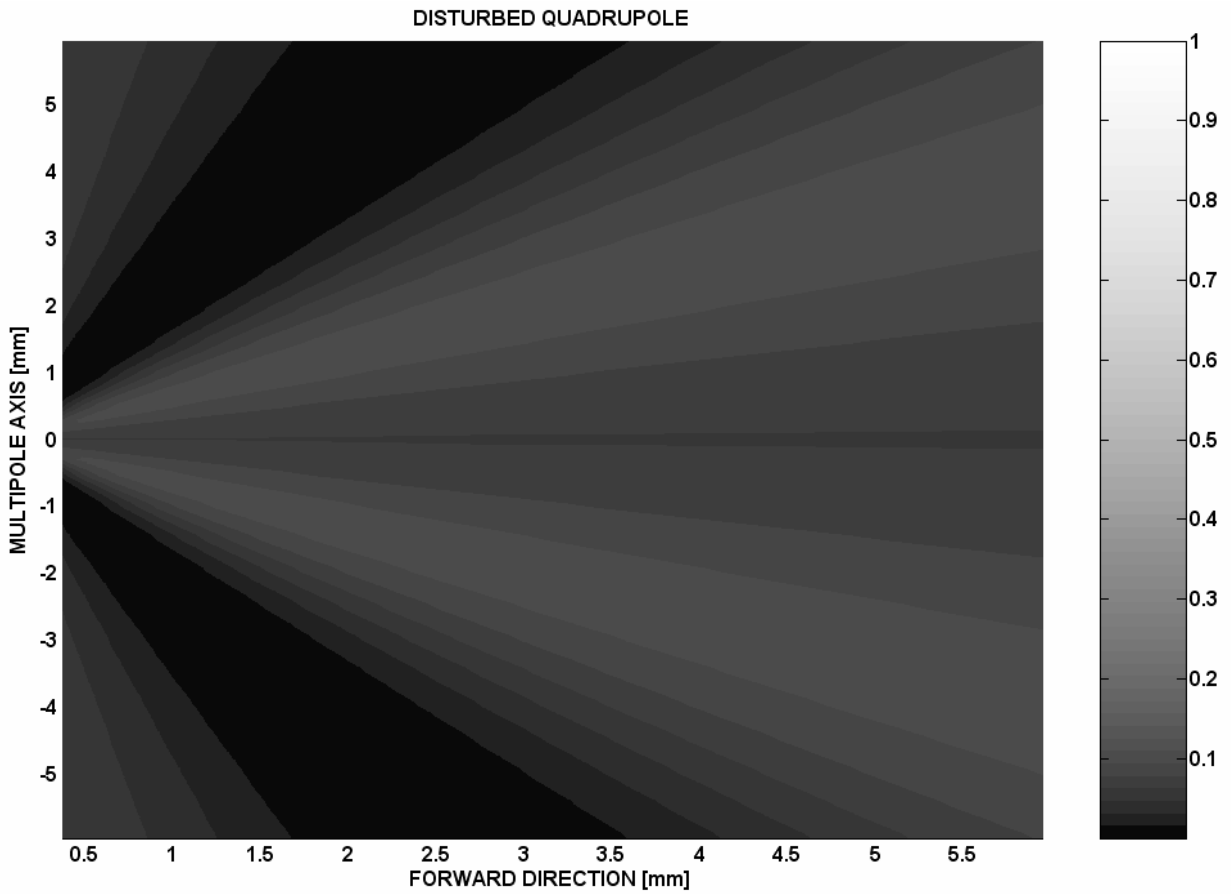

Fig. IX.C_13: ***Radiation of a disturbed quadrupole source ($\approx S_1$ mode) in water at 3MHz for d=1.5 mm. This pattern (or lack of pattern) is also noticed in Fig. IX.C_9.***

CONCLUSIONS

It is shown that incident leaky Lamb waves generate identical retro-reflected Lamb waves and other Lamb waves of the same symmetry (i.e. symmetrical or i.e. anti-symmetrical), when reaching the end of a plate. This results in typical leaky Lamb wave patterns consisting of rays. The physical origin of each of the observed rays is explained as the interference between leakage fields of different kinds of mode converted Lamb waves. Furthermore, sometimes Lamb waves also radiate in the forward direction when reaching the end of the plate. It is demonstrated that this is due to the formation of an acoustic multipole on the edge of the plate.

REFERENCES

[1] Kaczmarek H., "Lamb wave interaction with impact-induced damage in aircraft composite: Use of the A(0) mode excited by air-coupled transducer", J. Composite. Mat. 37(3), 217-232, 2003

[2] Bruno Morvan, Nicolas Wilkie-Chancellier, Hugues Duflo, Alain Tinel, Jean Duclos, "Lamb wave reflection at the free edge of a plate", J. Acoust. Soc. Am. 113(3), 1417-1425, 2003

[3] Predoi M. V., Rousseau M., "Recent results about Lamb waves reflection at the free edge of an elastic layer", Acta Acustica United with Acustica 89(4), 632-639, 2003

[4] Cho Y. H., Rose J. L., "A boundary element solution for a mode conversion study on the edge reflection of Lamb waves", J. Acoust. Soc. Am. 99(4), 2097-2109, 1996

[5] Diodati P., Tassi G., Alippi A., "Lamb wave reflection at the plate edges", Appl. Phys. Lett. 47(6), 573-575, 1985
[6] Galan J. M., Abascal R., "Numerical simulation of Lamb wave scattering in semi-infinite plates", Int. J. Num. Meth. Eng. 53(5), 1145-1173, 2002
[7] Elkettani M. E., Pareige P., Luppé F., "Conversion of Lamb waves at the edge of a submerged plate", J. de Physique IV 4(C5), 873-876, 1994
[8] Pareige P., Luppe F., Ripoche J., "Scattering of Lamb waves at the edge of a semi infinite plate embedded in water", J. Acoust. Soc. Am. 92(2), 1056-1060, 1992
[9] Zhu Q. G., Ruf H. J., Mayer W. G., "Lamb wave radiation from plate termination in a liquid", Ultrasonics 29(6), 459-463, 1991
[10] Fei D., Chimenti D. E., Teles S. V., "Materials property estimation in thin plates using focused, synthetic-aperture acoustic beams", J. Acoust. Soc. Am. 113(5), 2599-2610, 2003
[11] A. Breazeale, "From monochromatic light diffraction to colour schlieren photography", J. Opt. A: Pure Appl. Opt. 3, S1-S7, 2001
[12] Emmanuel le Clezio, Mihai Velentin Predoi, Michel Castaings, Bernard Hosten, Martine Rousseau, "Numerical predictions and experiments on the free-plate edge mode", Ultrasonics 41, 25-40, 2003
[13] Diligent O., Lowe M. J. S., Le Clezio E., Castaings M., Hosten B., "Prediction and measurement of nonpropagating Lamb modes at the free end of a plate when the fundamental antisymmetric A(0) is incident", J. Acoust. Soc. Am. 113(6), 3032-3042, 2003
[14] Igor Aleksandrovich Viktorov, *Rayleigh and Lamb Waves, Physical Theory and Applications*, Plenum Press, New York, 1967

Chapter X Diffraction Phenomena

The aerospace industry is an example where not a single error is tolerated. Therefore the equipment is subject to high tech nondestructive testing in order to discover faults and cracks in an early stage – enabling replacement, if necessary. One of the physical phenomena that are applied for the examination of surface and sub-surface cracks, is the phenomenon of surface waves, i.e. Scholte – Stoneley waves and Rayleigh waves. A diffraction grating can be used for their generation.

When a stone is thrown in a pond, a circular wave pattern is formed. When two stones are thrown simultaneously, two circular patterns are formed that interfere with each other. This results in directions on the water surface where only small waves are propagating and directions where larger waves are propagating. This phenomenon is called ‘diffraction’. Nevertheless, the term ‘diffraction’ is not limited to this phenomenon. Also the widening of a bounded beam while propagating, or the spreading of waves around obstacles, are sometimes called ‘diffraction’. In this chapter, by ‘diffraction’ we mean the interference pattern of sound caused by the interaction with a diffraction grating. An example of a diffraction grating in optics is a compact disk (CD). When a laser beam is pointed at the CD, the reflected light contains several beams, each of which corresponds to a so called diffraction order. In acoustics, a diffraction grating is comparable to a long row of stones that are thrown simultaneously or almost simultaneously in a pond, generating wave ‘beams’ in some directions and not in other directions.

The curious aspect of diffraction in ultrasonics is that under specific conditions, surface waves are generated. This is the reason why a diffraction grating is sometimes applied in nondestructive testing of materials. Especially the generation of Scholte – Stoneley waves by means of an incident bounded sound beam, which is not possible on smooth surfaces, occurs efficiently by means of a diffraction grating.

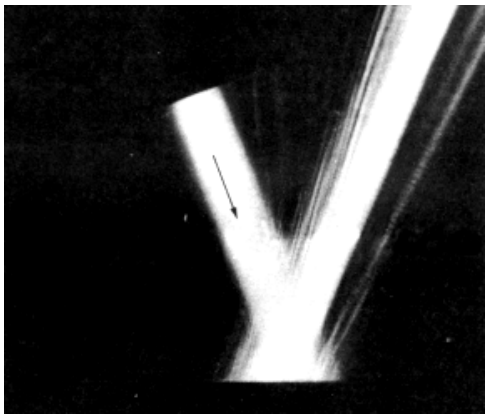

The extraordinary phenomenon of the backward displacement of bounded ultrasonic beams, incident on a periodically rough surface, is explained in this chapter, more than two decades after it has first been observed by Breazeale and Torbett in 1976.

I have been introduced to the subject of diffraction by Rudy Briers and later by Oswald Leroy, on the occasion of my Master's thesis. Later, Rudy Briers told me about a bizarre phenomenon that was observed and published by Breazeale and Torbett in 1976 and remained unexplained ever since. I was able to obtain a copy of this paper in 'Applied Physics Letters' and discovered that the paper actually reported two bizarre phenomena. First, there was the fact of a backward beam shift, which, on itself, is remarkable, but the angle at which the phenomenon appeared did not match predictions based on a theoretical model by Bertoni and Tamir.

This obscurity attracted me and occupied my days and nights for many weeks thereafter. First, I tried to simulate the effect applying the classical Fourier decomposition of bounded beams and found that the effect could not be simulated. Because I had already been working in the field of Inhomogeneous Waves (see Chapter IV) and because it had been experimentally proved by Briers *et al* that the Rayleigh decomposition of the sound field after diffraction, was also valid for inhomogeneous waves, I decided to try this theory and find out what was possible. I discovered that the effect that Breazeale and Torbett had observed, was due to something special, it was due to a new type of surface waves. I also found that if Breazeale and Torbett would have used another beam width, that they probably would have observed a backward beam shift, or at least reflected beam deformations, at the angle predicted by the model of Bertoni and Tamir. That's when I decided to contact Mack Breazeale and inform him about these new theoretical predictions. Dr Breazeale, who is one of the most brilliant scientists that I have ever met, was really enthusiastic about the predictions and promised me he would try to repeat the experiments.

In the meantime, I presented the theoretical results at the First Pan-American congress on Acoustics in Cancun (Mexico), in December 2002, for which I have been lucky enough to receive the Physical Acoustics Best Student Paper Award from the Acoustical Society of America.

Meanwhile, Alem Teklu, had asked Mack Breazeale to collaborate and to perform experiments in the field of ultrasonics. This coincidence made that the experiments by Breazeale and Torbett were soon thereafter repeated by Teklu and Breazeale. Furthermore, they found indications that some of the theoretical predictions were correct. In May 2003, during a congress of the Acoustical Society in Nashville (TN), I met Mack Breazeale and Alem Teklu for the first time and we all went to Oxford (MS) after the conference in order to plan future collaboration and to see the experiments in reality.

Later, during December 2003 and January 2004, I stayed at the National Center for Physical Acoustics (University of Mississippi) in Oxford (MS) and performed a lot of experiments together with Alem Teklu and Mack Breazeale. This work was continued in May 2004, after a congress of the Acoustical Society in New York. One of the tasks we fulfilled, was the validation of all the theoretical predictions. We found experimental evidence of the fact that the backward beam displacement is caused by a leaky type of Scholte –Stoneley waves, and we found that beam shifts were present at the angle predicted by Bertoni and Tamir, if only a narrower beam was used than in the original experiments in 1976. The theory is outlined in section X.A.1.a, whereas the experiments are outlined in section X.A.1.b.

The diffraction of ultrasound on corrugated surfaces really interested me. Therefore I extended the theory to the case where transient ultrasound is incident instead of harmonic ultrasound. This resulted in the knowledge that transient leaky Rayleigh waves can be stimulated surprisingly well on a corrugated surface (see section X.A.1.d). Furthermore, it was found that a diffraction grating can be used as a complex frequency filter device for electronic signals (see section X.A.1.e). It was also found that the groove direction (on the inaccessible side of a thick plate) can be determined be means of circularly polarized ultrasound (see section X.A.1.f). Furthermore, in section X.A.1.g, it is shown that a Brewster angle exists in ultrasonics, similar to the Brewster angle in optics.

I also believed that it could be interesting to study the diffraction on doubly corrugated surfaces (e.g. egg crates), which is, of course, much more complicated, though more interesting than in the case of single corrugated surfaces. This study is outlined in section X.A.2.a and explains the effect of the double corrugation on the generation of surface waves and also the steering effect on those surface waves.

An excellent example of an acoustic diffraction grating is the staircase of the El Castillo pyramid at Chichen Itza in Mexico. The explanation, of the Quetzal echo and the raindrop effect, which has been reported in Nature and in numerous newspapers around the world, is described in this chapter.

I already mentioned the congress in Cancun in 2002. After this congress, there was a post-meeting tour to the archaeological Maya site Chichen Itza. The reason was that special acoustic phenomena were reported there. After being convinced by colleagues and by kind Mexican students during the conference, I decided to join the post meeting tour and that's how I first heard the Quetzal echo in front of the El Castillo pyramid. This effect was well known to tourists, archaeologists and acousticians, but it had not been explained thoroughly. The quetzal chirp echo occurs in response to a handclap in front of the staircase of the pyramid. It was clear that the stairs were responsible for this phenomenon, but how this really happened and what else influenced the generation of this specific echo, remained obscure. Because I had been working on the diffraction of ultrasound on periodically corrugated surfaces, I decided to try to simulate the quetzal effect. Furthermore, when I was describing some of the ruins that I had seen, to a fellow student, being seated on the lower steps of the staircase, we both heard the sound of raindrops falling in a bucket filled by water. It sounded like music. We discovered that the effect was caused by other people climbing the stairs higher up – not by the 'tequila sunrise' we drunk the evening before. At that moment, I planned to try to simulate this effect as well.

So, when I returned to Belgium, I started to create the model, based on a theory of Claeys and Leroy for the diffraction of infinite plane waves on an infinite corrugated surface. I adapted the model to the finite staircase and the spherical pulsed incident sound. The information about the pyramid and the digitized recordings by David Lubman, were downloaded from the internet. I took into account the exact physical dimensions of the pyramid, as well as the physical parameters of the tropical air at Chichen Itza and the material of which the pyramid was built. I proved that the so called Lipmann conditions were fulfilled and therefore knew that the errors of the model were insignificant within the frequency interval of interest. I used a 'delta function'-like pulse as input and was able to calculate the result, which was a beautiful chirp. Nevertheless, the frequency of the chirp was too high compared to the recordings by David Lubman.

After comparison of the sonogram (a kind of signal representation that has been introduced to me by Joris Degrieck) of the handclap that was recorded by David Lubman and the sonogram of the reflected chirp, and considering my simulations, I stated that the lower frequencies in the registered echo, originated from the frequency pattern within the handclap itself. So, I collected the results and submitted them to the J. Acoust. Soc. Am. After a few months, I received comments by the reviewers that they were not 100% satisfied by the results because I had not taken into account the exact handclap as input and I had not considered possible influence of the ground in front of the pyramid. Therefore I returned to the model once again and extended it in order to satisfy the reviewers. The calculation time was now extremely long (almost 2 months), but the results matched the recordings by Lubman and showed that indeed a large part of the echo-pattern is caused by patterns that are already present in the incident handclap itself. The results also showed that the influence of the ground in front of the pyramid is not significant. The theory about the formation of the quetzal echo in front of the pyramid of Chichen Itza, can be found in section X.B.1. Surprisingly, the paper that has been published in the J. Acoust. Soc. Am. in December 2004, has resulted in a report in Nature News and has consequently been reported in numerous newspapers around the world. Before, I had never thought that this phenomenon was so important to so many people…

Sections X.A Ultrasonic Diffraction Phenomena

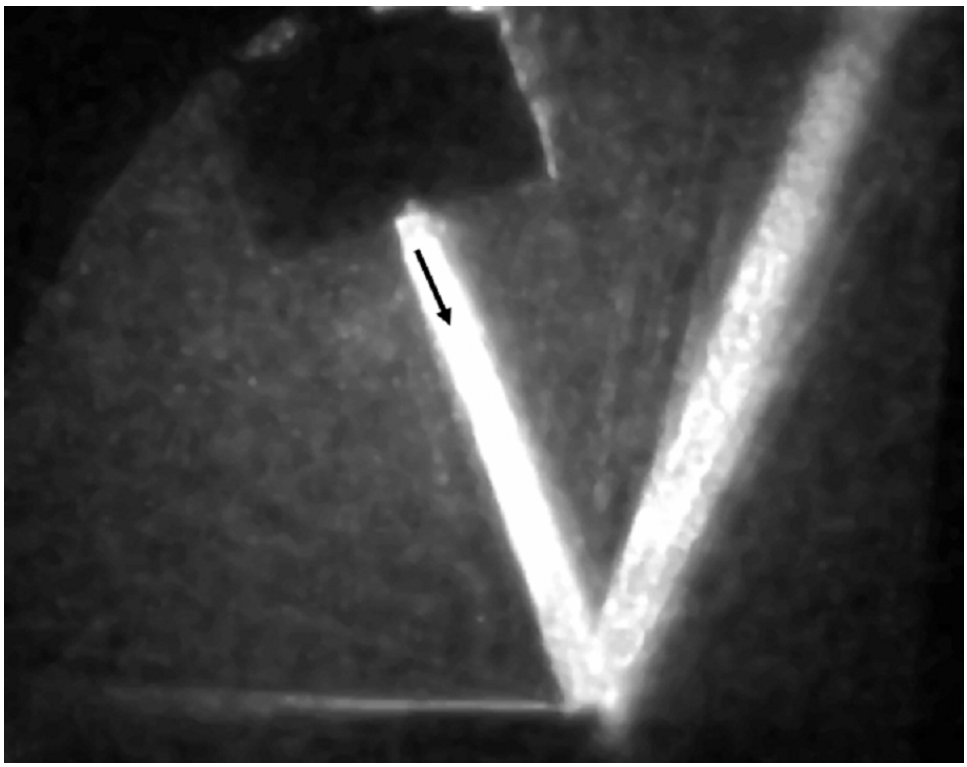

Fig. X.A: ***Schlieren image of a 6 mm wide ultrasonic beam incident upon a brass reflector at 22.5^{o}; a sound field is visible on the interface in the backward direction, being scattered in the forward direction at the extremity of the sample. This is evidence that it is a Scholte – Stoneley wave.***

X.A.1.a A Theoretical Treatment of the Backward Beam Displacement on Periodically Corrugated Surfaces and its relation to Leaky Scholte-Stoneley waves

Backward displacement of bounded ultrasonic beams reflected from a periodically corrugated surface between a liquid and a solid was first experimentally observed by Breazeale and Torbett [M. A. Breazeale, Michael A. Torbett, Appl. Phys. Let., 29(8), 456-458, 1976]. However, the phenomenon, which was expected to be a direct consequence of generated Rayleigh waves, did not appear at an angle of incidence that could have induced a leaky Rayleigh wave. The real explanation for this observed backward beam displacement has never been found. A demonstration of the capability of the inhomogeneous wave theory to simulate backward displacement of ultrasonic bounded beams (observed by Breazeale and Torbett, Appl. Phys. Let., 29(8), 456-458, 1976) has been demonstrated very recently [Nico F. Declercq, Joris Degrieck, Rudy Briers, Oswald Leroy, Appl. Phys. Let. 82(15), 2533-2534, 2003]. The current section applies the theory of the diffraction of inhomogeneous waves and shows how this theory is capable of simulating, explaining and understanding the experiments mentioned above. The theory reveals the existence of leaky Scholte – Stoneley waves, which is a novel phenomenon that was first reported from a theoretical point of view [Nico F. Declercq, Joris Degrieck, Rudy Briers, Oswald Leroy, J. Acoust. Soc. Am. 112(5), 2414, 2002] and was shortly after discovered experimentally [A. A. Teklu, M. A. Breazeale, J. Acoust. Soc. Am. 113(4), 2283-2284, 2003.]. Moreover, the present section shows that the classical Fourier decomposition of bounded beams is unable to simulate the backward beam displacement. This work also elucidates the nature of Wood anomalies in Diffraction spectra.

The contents of this section have been published as : Nico F. Declercq, Joris Degrieck, Rudy Briers, Oswald Leroy, "Theory of the backward beam displacement on periodically corrugated surfaces and its relation to leaky Scholte-Stoneley waves", J. Appl. Phys. 96(11), 6869-6877, 2004 (Imp. Fact. 2.281; SCI-index, Physics-Applied, rank:13/76), and also briefly as: Nico F. Declercq, Joris Degrieck, Rudy Briers, Oswald Leroy, "Theoretical verification of the backward displacement of waves reflected from an interface having superimposed periodicity", Appl. Phys. let. 82(15), 2533-2535, 2003. (Imp. Fact. 4.207; SCI-index, Physics-Applied, rank:3/76)

Furthermore, after presenting the paper at the First Pan-American Congress on Acoustics, Cancun, Mexico, December 2002, the author has been presented the physical acoustics best student paper award by the Acoustical Society of America [Echoes 13(2), 5, 2003].

INTRODUCTION

There are several ways to tackle the diffraction of sound by a periodically corrugated surface [1]. The method applied here is the one that is based on the 'Rayleigh decomposition' of the diffracted sound field into single bulk inhomogeneous waves, all traveling in directions that are determined by the classical grating equation. The validity of this approach has been proved by Briers et al [2,3]. In fact, it is an inhomogeneous waves extension of the more classical approach that can be found in Claeys et al [4,5] where the generation of diffracted plane waves is assumed. The validity of the latter method, where a decomposition into plane waves is used, is shown by Lippmann [6] , who states that it is correct whenever two conditions are fulfilled which say that the incident wavelength must be of the same order of magnitude as the corrugation period and that the height of the corrugation must be small compared to it. Claeys et al [4,5] studied the diffraction of plane waves on periodically corrugated liquid-solid interfaces, Jungman et al [7], Mampaert et al [8,9], and Declercq et al [10], studied this phenomenon on solid-liquid periodically corrugated interfaces. The latter showed that the diffraction of plane waves can be used to simulate the appearance of so called Wood anomalies [5] in diffraction spectra for normal incident sound. Wood anomalies are strong amplitude dips in the reflection spectra and are caused by energy transformation of incident sound into Scholte - Stoneley waves. Briers [2], Briers et al [3], Deschamps and Cheng [11] and Briers and Leroy [12,13] extended the theory of the diffraction of homogeneous plane waves to that of inhomogeneous plane waves and experimentally proved the validity of their approach. They also studied the diffraction on periodically corrugated solid plates immersed in water [2]. Besides the success of the mentioned papers, there remains the obscurity of the exact nature of Wood anomalies [5] and the explanation of what really happens in the experiments of Breazeale and Torbett [14] that show the appearance of a backward beam displacement on periodically corrugated surfaces. The present work focuses on the explanation of the experiments of Breazeale and Torbett [14] by applying the theory of the diffraction of inhomogeneous plane waves, properly involving some considerations of Deschamps [15] , and gives a comprehensive explanation of the nature of Wood anomalies in diffraction spectra.

THE EXPERIMENT OF MACK A. BREAZEALE AND MICHAEL TORBETT [14]

Breazeale and Torbett [14] have performed experiments that originally were intended to verify the prediction of Tamir and Bertoni [16], that, similar to their counterpart in optics, backward traveling acoustic surface waves, originating from diffraction, would cause a backward acoustical beam shift of the reflected sound. Breazeale and Torbett [14] let a bounded sound beam impinge from the liquid side, onto a periodically corrugated interface between water and brass. According to the classical diffraction equation, a backward traveling first order lateral wave (for example a lateral bulk wave, a Scholte-Stoneley wave or a leaky Rayleigh wave) exists if sound is incident from a real angle ξ^{inc} ('inc' stands for incident) with [14]

$$\sin \xi^{inc} = v_l \left(\frac{1}{f\Lambda} - \frac{1}{v_{BT}} \right) \qquad \text{(X.A.1.a\_1)}$$

in which v_l is the sound velocity in the covering liquid, f is the frequency, Λ is the corrugation period and v_{BT} is the velocity of the surface wave. If the velocity of leaky Rayleigh waves (2015m/s) on a smooth water-brass interface is entered in (X.A.1.a_1), at a frequency of 6MHz, one finds an angle of incidence of 41^0. This stimulated Breazeale and Torbett [14] to seek for a backward beam shift around 41^0. The result was negative. Furthermore, they looked at other angles of incidence and found the backward beam shift in the vicinity of 22.5^0 which led them to the primary conclusion that if the effect was caused by a backward traveling lateral wave, it would have a velocity $v_{BT} = 1470 m/s$ which differs quite a lot from the Rayleigh velocity. They concluded that more experimental and theoretical research was necessary to determine what really was the cause of this backward beam shift. Moreover, if they kept that particular angle of incidence and changed the frequency to 2MHz, the backward beam shift was not there anymore. In what follows, the inhomogeneous wave theory will show us that it is not a simple expression as (X.A.1.a_1) that determines the effect, but a complicated interaction between all diffracted orders. The next chapter treats the theoretical description of the interaction of one single inhomogeneous wave. Further, such single inhomogeneous waves will be superposed to form a bounded beam that interacts with the periodically corrugated surface under consideration.

THE DIFFRACTION OF INHOMOGENEOUS WAVES

Description of the Incident and the Diffracted Wave Field

Consider a periodically corrugated interface between a liquid and a solid as depicted in Fig. X.A.1.a_1.

The corrugation is periodic with period Λ and is given by

$$z = f(x) \tag{X.A.1.a_2}$$

with

$$f(x+\Lambda) = f(x) \tag{X.A.1.a_3}$$

It is convenient to write (X.A.1.a_2) as

$$g(x,z) = f(x) - z = 0 \tag{X.A.1.a_4}$$

Taking into account the Rayleigh decomposition of the diffracted wave field and taking into account characteristics of dilatational and shear waves, the displacement of the incident waves $\mathbf{N}^{inc}$, the (dilatational) reflected waves $\mathbf{N}^{r}$, the dilatational respectively shear waves in the solid $\mathbf{N}^{d}$ and $\mathbf{N}^{s}$, may be written as

$$\mathbf{N}^{inc} = A^{inc}\varphi^{inc}\left(ik_x^{inc}\mathbf{e}_x + ik_z^{inc}\mathbf{e}_z\right) \tag{X.A.1.a_5}$$

$$\mathbf{N}^{r} = \sum_m A_m^r\varphi^{m,r}\left(ik_x^{m,r}\mathbf{e}_x + ik_z^{m,r}\mathbf{e}_z\right) \tag{X.A.1.a_6}$$

$$\mathbf{N}^{d} = \sum_m A_m^d\varphi^{m,d}\left(ik_x^{m,d}\mathbf{e}_x + ik_z^{m,d}\mathbf{e}_z\right) \tag{X.A.1.a_7}$$

$$\mathbf{N}^{s} = \sum_m A_m^s\mathbf{P}^{m,s}\varphi^{m,s} \tag{X.A.1.a_8}$$

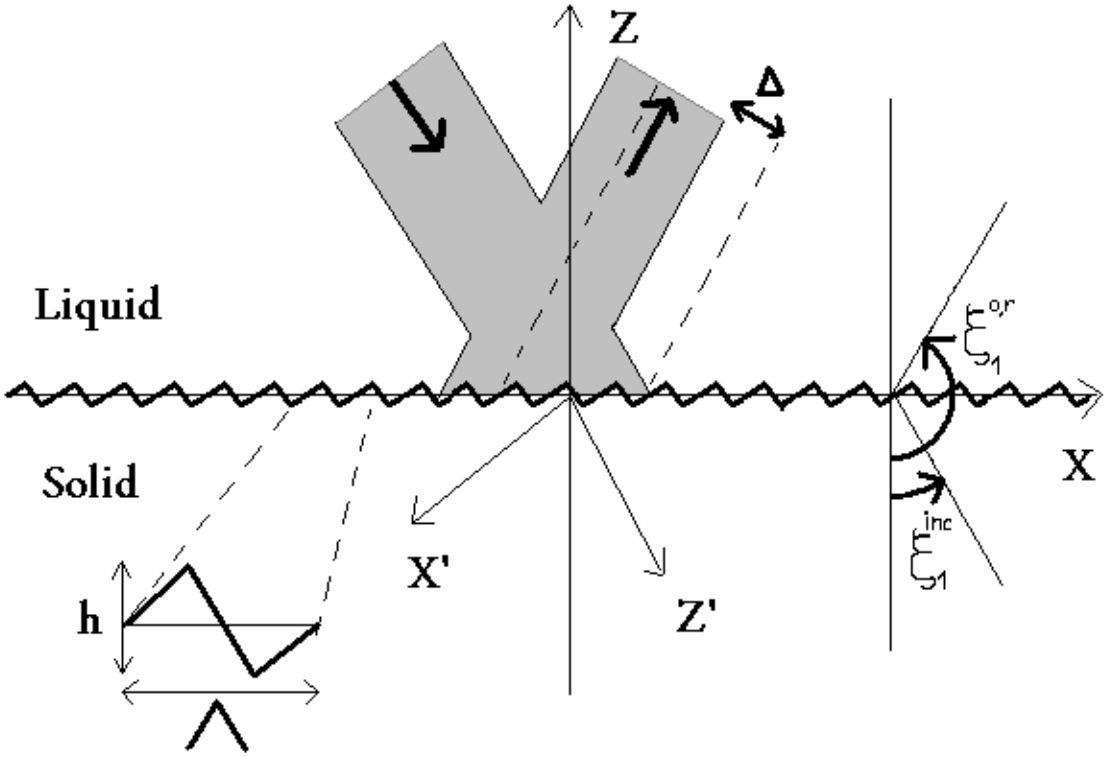

Fig. X.A.1.a_1: ***Diagram of the backward beam displacement*** Δ ***on a periodically corrugated surface with period*** Λ ***and height*** h***. The exact definition of the angles used in the text are here defined.***

with

$$\varphi^{\varsigma} = e^{i\left(\mathbf{k}^{\varsigma}\bullet\mathbf{r}\right)} \tag{X.A.1.a_9}$$

and

$$k_x^{m,s} P_x^{m,s} + k_y^{m,s} P_y^{m,s} + k_z^{m,s} P_z^{m,s} = 0 \qquad \text{(X.A.1.a\_10)}$$

In relations (X.A.1.a_5-10), A stands for the amplitude, while P stands for the polarization vector, whereas the index 'm' denotes the diffraction order and ς represents "inc", "m,r", "m,d" or "m,s".
The following properties that hold for inhomogeneous waves [17] also need to be taken into account:

$$\mathbf{k}^{\varsigma} = \mathbf{k}_1^{\varsigma} + i\mathbf{k}_2^{\varsigma} \qquad \text{(X.A.1.a\_11)}$$

$$\mathbf{k}_2^{\varsigma} = \boldsymbol{\alpha}^{\varsigma} - \boldsymbol{\beta}^{\varsigma} \qquad \text{(X.A.1.a\_12)}$$

$$\mathbf{k}_1^{\varsigma} \bullet \mathbf{k}_2^{\varsigma} = k_1^{\varsigma} \alpha^{\varsigma} \qquad \text{(X.A.1.a\_13)}$$

$$\boldsymbol{\beta}^{\varsigma} \perp \mathbf{k}_1^{\varsigma} \qquad \text{(X.A.1.a\_14)}$$

$$\alpha^{\varsigma} \left\| k_1^{\varsigma} \right. \qquad \text{(X.A.1.a\_15)}$$

$$\left(k_1^{\varsigma}\right)^2 - \left(\alpha^{\varsigma}\right)^2 - \left(\beta^{\varsigma}\right)^2 = \left(\frac{\omega}{v_{\varsigma}}\right)^2 - \left(\alpha_0^{\varsigma}\right)^2 \qquad \text{(X.A.1.a\_16)}$$

with v_{ς} the sound velocity and α_0^{ς} the intrinsic damping coefficient. The vector $\boldsymbol{\alpha}^{\varsigma}$ is called the damping vector, while the vector $\boldsymbol{\beta}^{\varsigma}$ is called the inhomogeneity vector.

The Continuity Conditions

The incident wave is described by the amplitude A^{inc}, the real part, k_1^{inc}, and imaginary part, k_2^{inc}, of the wave vector and incidence angle ξ_1^{inc}, so that, for non absorbing media

$$
\begin{aligned}
k_{1,x}^{inc} &= k_1^{inc} \sin \xi_1^{inc} \\
k_{1,z}^{inc} &= -k_1^{inc} \cos \xi_1^{inc} \\
k_{2,x}^{inc} &= k_2^{inc} \sin \xi_2^{inc} \\
k_{2,z}^{inc} &= -k_2^{inc} \cos \xi_2^{inc}
\end{aligned}
\qquad \text{(X.A.1.a\_17)}
$$

with $\xi_2^{inc} = \xi_1^{inc} - \pi/2$.

The signs in (X.A.1.a_17) are chosen to fulfill the definitions of the angles and axes in Fig. X.A.1.a_1.

In media τ ($\tau = 1$ in the liquid, $\tau = 2$ in the solid) the stress tensor T^{τ} is given [11,18] by its elements

$$
T_{ij}^{\varsigma} = \sum_{\eta} \left(\lambda_1^{\tau} + \lambda_2^{\tau} \frac{\partial}{\partial t} \right) \varepsilon_{\eta\eta}^{\tau} \delta_{i,j} + 2 \left(\mu_1^{\tau} + \mu_2^{\tau} \frac{\partial}{\partial t} \right) \varepsilon_{i,j}^{\tau} \qquad \text{(X.A.1.a\_18)}
$$

in which the strain tensor ε_{ij}^{τ} is

$$
\varepsilon_{ij}^{\tau} = \frac{1}{2} \left[\partial_i N_j^{\tau} + \partial_j N_i^{\tau} \right] \qquad \text{(X.A.1.a\_19)}
$$

The Lamé constants are denoted by λ_1^{τ} and μ_1^{τ}, while the viscosity coefficients are given by λ_2^{τ} and μ_2^{τ}. They obey the dispersion relations [17] (X.A.1.a_13) and (X.A.1.a_16) if

$$
\mathbf{k}^{\varsigma} \bullet \mathbf{k}^{\varsigma} = \frac{\rho\omega^2}{\left(\lambda_1^{\tau} - i\omega\lambda_2^{\tau} \right) + 2\left(\mu_1^{\tau} - i\omega\mu_2^{\tau} \right)} \qquad \text{(X.A.1.a\_20)}
$$

for dilatational waves (ς = “inc” or “m,r”,) in the liquid and ς = “m,d” or “m,s” in the solid) and if

$$
\mathbf{k}^{\varsigma} \bullet \mathbf{k}^{\varsigma} = \frac{\rho\omega^2}{\left(\mu_1^{\tau} - i\omega\mu_2^{\tau} \right)} \qquad \text{(X.A.1.a\_21)}
$$

for shear waves ($\varsigma = s,2$) in the solid). The Lamé constants are related to the shear velocity v_s^τ, the dilatational velocity v_d^τ, the intrinsic damping coefficient for shear waves $\alpha_{s,0}^\tau$ and the intrinsic damping coefficient for dilatational waves $\alpha_{d,0}^\tau$ through the dispersion relations (X.A.1.a_13) and (X.A.1.a_16).

In order to find the unknown coefficients $A_m^r, A_m^d, A_m^s P_x^{m,s}, A_m^s P_y^{m,s}, A_m^s P_z^{m,s}$, the equations that describe the continuity of normal stress and strain along the interface (X.A.1.a_4) must be solved, i.e.

$$\left(\mathbf{N}^{inc} + \mathbf{N}^r\right) \bullet \nabla g = \left(\mathbf{N}^d + \mathbf{N}^s\right) \bullet \nabla g \text{ along } g = 0 \qquad \text{(X.A.1.a\_22)}$$

$$\sum_j T_{ij}^1 \left(\nabla g\right)_j = \sum_j T_{ij}^2 \left(\nabla g\right)_j \text{ along } g = 0 \qquad \text{(X.A.1.a\_23)}$$

and also (see (X.A.1.a_10))

$$\left(A_m^s P_x^{m,s} k_x^{m,s} + A_m^s P_y^{m,s} k_y^{m,s} + A_m^s P_z^{m,s} k_z^{m,s} \right) \varphi^{m.s} = 0 \qquad \text{(X.A.1.a\_24)}$$

Conditions (X.A.1.a_22-24) lead to 5 equations that are periodic in x, whence a sufficient condition for a correct solution is that the Fourier coefficients (for a discrete Fourier transform over the interval $[0 \to \Lambda]$) are equal. The wave vectors that are introduced by this discrete Fourier transform are denoted by the order 'p'.

The 5 equations for each integer *p* are:

Equation 1:

$$\begin{aligned} & A^{inc} I^{inc,p}{}_i \left(-\left(k^1\right)^2 + k_x^{inc} k_x^p \right) \\ & + \sum_m A_m^r I^{m,r,p}{}_i \left(-\left(k^1\right)^2 + k_x^m k_x^p \right) \\ & + \sum_m A_m^d I^{m,d,p}{}_i \left(\left(k^{d,2}\right)^2 - k_x^m k_x^p \right) \\ & - \sum_m A_m^s P_x^{m,s} I^{m,s,p} \left(k_x^p - k_x^m \right) \\ & + \sum_m A_m^s P_z^{m,s} I^{m,s,p} \left(k_z^{m,s} \right) = 0 \end{aligned} \qquad \text{(X.A.1.a\_25)}$$

Equation 2:

$$
\begin{aligned}
&-A^{inc} I^{inc,p} \rho_1 \left(k_x^p - k_x^{inc} \right) \\
&-\sum_m A_m^r I^{m,r,p} \rho_1 \left(k_x^p - k_x^m \right) \\
&+\sum_m A_m^d I^{m,d,p} \rho_2 \left(-k_x^m + \left(1 + 2 \frac{\left(k_x^m \right)^2 - \left(k^{d,2} \right)^2}{\left(k^{s,2} \right)^2} \right) k_x^p \right) \\
&+\sum_m A_m^s P_x^{m,s} I^{m,s,p} i \rho_2 \left(1 - \frac{k_x^m k_x^p}{\left(k^{d,2} \right)^2} + \right. \\
&\left. ... + \left(\frac{1}{\left(k^{d,2} \right)^2} - \frac{1}{\left(k^{s,2} \right)^2} \right) \left(k_x^m \right)^2 \right) \\
&+\sum_m A_m^s P_z^{m,s} I^{m,s,p} \rho_2 i \left(k_z^{m,s} \right) \left(\left(\left(\frac{1}{\left(k^{d,2} \right)^2} - \frac{1}{\left(k^{s,2} \right)^2} \right) k_x^m ... \right. \right. \\
&\left. \left. ... - \left(\frac{1}{\left(k^{d,2} \right)^2} - \frac{2}{\left(k^{s,2} \right)^2} \right) k_x^p \right) = 0
\end{aligned}
\qquad \text{(X.A.1.a\_26)}
$$

Equation 3:

$$
+\sum_m A_m^s P_y^{m,s} I^{m,s,p} i \rho_2 \left(1 - \frac{k_x^m k_x^p}{\left(k^{s,2} \right)^2} \right) = 0
\qquad \text{(X.A.1.a\_27)}
$$

Equation 4:

$$
\begin{aligned}
&+A^{inc} I^{inc,p} \rho_1 k_z^{inc} \\
&+\sum_m A_m^r I^{m,r,p}\left(k_z^{m,r}\right)\rho_1 \\
&+\sum_m A_m^d I^{m,d,p}\left(k_z^{m,d}\right)\rho_2\left(-1+\frac{2}{\left(k^{s,2}\right)^2}\left(k_x^m k_x^p\right)\right) \\
&+\sum_m A_m^s P_x^{m,s} I^{m,s,p} i\left(k_z^{m,s}\right)\rho_2\left(\left(\frac{1}{\left(k^{d,2}\right)^2}-\frac{1}{\left(k^{s,2}\right)^2}\right)k_x^m-\frac{k_x^p}{\left(k^{s,2}\right)^2}\right) \\
&+\sum_m A_m^s P_z^{m,s} I^{m,s,p} i\rho_2\left(\left(\frac{1}{\left(k^{d,2}\right)^2}-\frac{1}{\left(k^{s,2}\right)^2}\right)\left(k_z^{m,s}\right)^2+1-\frac{k_x^m k_x^p}{\left(k^{s,2}\right)^2}\right)=0
\end{aligned}
\tag{X.A.1.a_28}
$$

Equation 5:

$$
\left(A_m^s P_x^{m,s} k_x^{m,s}+A_m^s P_y^{m,s} k_y^{m,s}+A_m^s P_z^{m,s} k_z^{m,s}\right)\delta_{m,p}=0 \tag{X.A.1.a_29}
$$

with $\left(k^1\right)^2$ and $\left(k^{d,2}\right)^2$ given by (X.A.1.a_20) and $\left(k^{s,2}\right)^2$ given by (X.A.1.a_21) and with the grating equation [3]

$$
k_x^m = k_x^{inc} + m\frac{2\pi}{\Lambda} \tag{X.A.1.a_30}
$$

(an equivalent expression holds of course for k_x^p) and

$$
I^{inc,\eta} = \frac{1}{k_z^{inc}}\int_\Lambda e^{i\left(k_x^{inc}-k_x^\eta\right)x} e^{i\left(k_z^{inc} f(x)\right)} dx \tag{X.A.1.a_31}
$$

$$
I^{m,\xi,\eta} = \frac{1}{k_z^{m,\xi}}\int_\Lambda e^{i\left[\left(k_x^m-k_x^\eta\right)x+k_z^{m,\xi} f(x)\right]} dx \tag{X.A.1.a_32}
$$

For $\delta_{m,p}$ Kronecker's delta. It is already seen from (X.A.1.a_27) that

$$A_m^s P_y^{m,s} = 0 \tag{X.A.1.a_33}$$

Consideration of Deschamps' Rule

A mode 'm,q' inside the solid (q=s or q=d), is accompanied by a reflected companion 'm,r'. The angle of propagation of the considered mode 'm,q' is

$$\left|\xi_1^{m,q}\right| = \arctan\left[\frac{\left|k_{1,x}^m\right|}{\left|k_{1,z}^{m,q}\right|}\right] \tag{X.A.1.a_34}$$

whereas the angle of propagation of the reflected companion is

$$\left|\xi_1^{m,r}\right| = \arctan\left[\frac{\left|k_{1,x}^m\right|}{\left|k_{1,z}^{m,r}\right|}\right] \tag{X.A.1.a_35}$$

From Deschamps [15] , we learn that each diffracted wave must travel away from the interface. However, if $\mathrm{Re}(k_z) = k_{1,z} \neq 0$, then the sign of k_z for the considered mode 'm,q', depends on the angle of propagation of the liquid-side companion, denoted by 'm,r'. If the considered mode 'm,q' inside the solid (q=s or q=d) is 'close enough' to $\pi/2$, then that particular mode 'm,q' must show leaky Rayleigh wave features, whence the inhomogeneity vector must point into the liquid. 'Close enough' to $\pi/2$ means the liquid side companion must fulfill

$$\left|\xi_1^{m,r}\right| > \left|\arcsin\left(\frac{v_l}{v_q}\right)\right| \tag{X.A.1.a_36}$$

v_l is the wave velocity in the liquid, v_q is the wave velocity of the considered mode 'q,m'. Whenever

$$\left|\xi_1^{m,r}\right| \leq \left|\arcsin\left(\frac{v_l}{v_q}\right)\right| \tag{X.A.1.a_37}$$

Deschamps' rule doesn't need to be considered, whence the Sommerfeld conditions hold, demanding that the mode 'q,m' travels away from the interface.

Truncation of Infinite Summations

The linear set of equations (X.A.1.a_25-29) is infinite since *m*,*p* may take every possible integer value for $-\infty \to +\infty$. However, it has been shown [4,9,10] that the interval of integers may be truncated to $\{-N,-N+1,..,N-1,N\}$, for N larger than 6.
From refs. [19-20], it is known that for a sawtooth profile

$$f(x)=\frac{2hx}{\Lambda}-\frac{h}{2} \text{ if } 0\le x<\frac{\Lambda}{2} \qquad \text{(X.A.1.a\_38)}$$

$$f(x)=\frac{3h}{2}-\frac{2hx}{\Lambda} \text{ if } \frac{\Lambda}{2}\le x<\Lambda \qquad \text{(X.A.1.a\_39)}$$

the integrals (X.A.1.a_31) and (X.A.1.a_32) become

$$I^{inc,\eta}=ih\Lambda e^{-ihk_z^{inc}/2}\frac{1-(-1)^{-\eta}e^{ihk_z^{inc}}}{\left(hk_z^{inc}\right)^2-(\pi\eta)^2} \qquad \text{(X.A.1.a\_40)}$$

$$I^{m,\eta,\xi}=ih\Lambda e^{-ihk_z^{inc}/2}\frac{1-(-1)^{(m-\eta)}e^{ihk_z^{m,\xi}}}{\left(hk_z^{m,\xi}\right)^2-\pi^2(m-\eta)^2} \qquad \text{(X.A.1.a\_41)}$$

In this work, only sawtooth profiles (X.A.1.a_38-39) have been taken under consideration.

THE DIFFRACTION OF A BOUNDED BEAM

This section describes very short two often used decompositions of bounded beams $\Omega(x',z')$, namely the Fourier decomposition and the inhomogeneous waves decomposition. The coordinates (x',z') are the eigencoordinates with *z*' parallel to the mean travel direction and $x'\perp z'$. It will follow from the numerical results below that whereas the inhomogeneous waves decomposition is able to describe the experiments of Breazeale and Torbett [14] properly, the Fourier decomposition is not.

The Fourier Decomposition

The current section deals with gaussian beam profiles with a beam width given wherever appropriate. Here, the beam profile $\Omega(x',c)$, for c a chosen constant, is subject to the discrete Fourier transform

$$\Omega(x',c) \leftrightarrow B\left(k_x^{n'},c\right) \mid k_x^{n'} \in \Re \tag{X.A.1.a_42}$$

whence

$$\Omega(x',z') = \sum_{n=-\infty}^{n=+\infty} B\left(k_x^{n'},c\right) e^{ik_x^{n'}x'} e^{ik_z^{n'}(z'-c)} = \sum_{n=-\infty}^{n=+\infty} B\left(k_x^{n'},c\right) e^{i\mathbf{k}^{n'}\bullet\left(\mathbf{r}'-\mathbf{r}_0'\right)} \tag{X.A.1.a_43}$$

with $k_z^{n'}$ related to $k_x^{n'}$ through the physical properties of the medium, with

$$\mathbf{k}^{n'} = k_x^{n'}\mathbf{e}_x' + k_z^{n'}\mathbf{e}_z' \tag{X.A.1.a_44}$$

and with $\mathbf{r}' \cong (x',z')$ and $\mathbf{r}_0' \cong (x',c)$. For physical reasons, the dispersion relations [17] (X.A.1.a_13) and (X.A.1.a_16) must hold, whence the range of *n* in (X.A.1.a_43) will be limited to $n \in \{-N,..,+N\}$.

The right part of expression (X.A.1.a_43) states that a bounded beam is described by a superposition of plane waves all having different travel directions and having different attributed amplitudes. It has been shown by Leroy et al [21-23] that the description of bounded beams by Fourier decomposition leads to contradictions such as waves considered incident at angles exceeding 90^0. Claeys et al [22,23] showed that this decomposition was not sufficiently appropriate to describe and to understand what happens if bounded beams are incident at critical angles such as the Rayleigh angle.

The Inhomogeneous Waves Decomposition

The concept of using inhomogeneous waves to decompose a bounded beam was introduced by Claeys and Leroy [20,22] and is based on the mathematical fact that a smooth beam profile can be locally approached by a summation of exponential functions [24]. This leads to the perception that a bounded beam can be decomposed in a series of inhomogeneous waves all traveling in the same direction, but having different amplitudes and inhomogeneities. Hence,

$$\Omega(x',z') = \sum_{n=-\infty}^{n=+\infty} B(n,c) e^{-\beta^n x'} e^{ik_z^{n'}(z'-c)} \tag{X.A.1.a_45}$$

Even here, due to the dispersion relations [17] (X.A.1.a_13) and (X.A.1.a_16), the range of n is limited to $n \in \{-N,..,+N\}$.

The Description of the Zero Order Reflected Beam

Each of the individual waves in the decompositions (X.A.1.a_43) or (X.A.1.a_45) is diffracted into an infinite number of diffraction orders, whence the reflected sound field is:

$$\Xi(x,z)=\sum_{n=-N}^{n=+N} D_n R_0 \gamma_0(x,z)+\sum_{n=-N}^{n=+N} D_n \sum_{m=-\infty}^{m=+\infty}\left(1-\delta_{n,0}\right) R_m \gamma_m(x,z) \qquad \text{(X.A.1.a\_46)}$$

In which, depending on whether decomposition (X.A.1.a_43) or (X.A.1.a_45) is applied, $D_n = B\left(k_x^{n'}, c\right)$ or $D_n = B(n,c)$, R_m is the reflection coefficient of diffraction order *m*, and γ_m is the wave function of diffraction order *m* (i.e. a plane wave or an inhomogeneous wave).
We call

$$\Xi_0(x,z)=\sum_{n=-N}^{n=+N} D_n R_0 \gamma_0(x,z) \qquad \text{(X.A.1.a\_47)}$$

the zero order reflected beam. It is this beam that is considered below, the so called 'reflected beam profile' is considered.

DISCUSSION OF NUMERICAL RESULTS

What really causes Wood Anomalies in Diffraction Spectra?

In the articles of Claeys et al [5], Mampaert et al [7-9] and Declercq et al [10] , one deals with the diffraction of pure plane waves on periodically corrugated surfaces. It is seen there that diffraction spectra for normal incidence show Wood anomalies at certain frequencies. These anomalies are believed to originate from the generation of Scholte-Stoneley waves. In what follows, we show that Wood anomalies originate from the resonant interaction between forward and backward traveling Scholte-Stoneley waves.
If one reconsiders the grating equation (X.A.1.a_30) and if one writes any of the diffraction displacements as

$$\mathbf{N}^{\varsigma}=\sum_{m=-M}^{m=M} \mathbf{A}_m^{\varsigma} \exp\left[i\left(k_x^{m,\varsigma} x + k_z^{m,\varsigma} z\right)\right] \qquad \text{(X.A.1.a\_48)}$$

with

$$\mathbf{A}_m^{\varsigma}=\left(A_{m,x}^{\varsigma}\mathbf{e}_x + A_{m,y}^{\varsigma}\mathbf{e}_y + A_{m,z}^{\varsigma}\mathbf{e}_z\right) \qquad \text{(X.A.1.a\_49)}$$

then, for normal incidence

$$\mathbf{N}^{\varsigma}=\sum_{m=1}^{m=M}\left[2\mathbf{A}_m^{\varsigma}\cos\left(\frac{2\pi m}{\Lambda}x\right)\right]\exp\left(ik_z^{m,\varsigma}z\right)+\mathbf{A}_0^{\varsigma}\exp\left[i\left(\frac{\omega}{v^{\varsigma}}z\right)\right] \qquad \text{(X.A.1.a\_50)}$$

If the frequency and the material parameters, are such that for a certain diffraction order 'm', a Scholte-Stoneley wave is stimulated, then the one of diffraction order *–m* also is stimulated and

both interact to create a standing wave phenomenon whose wavelength λ^S fits an integer number of times into one corrugation wavelength Λ (see (X.A.1.a_50)). In other words : The superposition of the backward and forward traveling Scholte-Stoneley waves causes a vibration eigenstate of the corrugated surface. This eigenstate is the actual reason why under these circumstances almost all of the incident energy is absorbed by the surface, resulting in the observation of a 'Wood anomaly' in the diffraction spectra.
For oblique incidence, relation (X.A.1.a_50) does not hold, whence the generation of a Scholte-Stoneley wave does not cause an eigenstate. The absence of an eigenstate diminishes the effect of the generated Scholte-Stoneley wave on the reflected sound intensity, as seen in Fig. 4 of ref. 25. A more precise explanation is the fact that the Scholte-Stoneley wave of a particular diffraction order, traveling in one direction, is disturbed by the bulk wave of the opposite diffraction order.
Obliquely incident waves do not cause strong stimulation of Scholte-Stoneley waves. The same reasoning holds for leaky Rayleigh waves if inhomogeneous incident waves are considered. Briers et al [2,3] showed that normally incident inhomogeneous waves under the correct circumstances may induce pure leaky Rayleigh waves having the same amplitude distribution as for leaky Rayleigh waves on smooth interfaces. It is expected that for oblique incidence, a generated Rayleigh wave is disturbed by diffraction orders.

Results and Discussion of the Reflection Coefficients for Single Inhomogeneous Waves incident where Breazeale and Torbett [14] observed a Backward Displacement

The calculations that have been performed here make use of the equations (X.A.1.a_25-29) taking into account (X.A.1.a_38-41) for orders ranging from –8 to +8. This results in a matrix equation where all the amplitudes of the diffracted wave orders are found at once. Zero order reflected waves travel along the specular direction. Other orders travel in directions that are governed by (X.A.1.a_30) and (X.A.1.a_34) together with the dispersion relations (X.A.1.a_20-21) since not only the x-component of the wave vectors determine the propagation direction, but also the z-component.
Numerical results are presented for oblique incidence of inhomogeneous waves of 6 MHz on a periodically sawtooth corrugated water-brass interface. The physical properties of water and brass listed in Table X.A.1.a_I are applied. In consistency with Breazeale and Torbett [14], a corrugation period $\Lambda = 178\mu m$ and a corrugation height $h = 25\mu m$ is used.
In Fig. X.A.1.a_2, the absolute value of the zero order reflection coefficient is depicted near the angle where in ref. [14] a backward beam shift is found. It is seen that an amplitude dip appears at an angle of incidence of 22.59^0 and inhomogeneity $-71.86 m^{-1}$. This means that the corresponding zero order reflected inhomogeneous wave is backwards displaced relatively to its incident companion.

Table X.A.1.a_I: ***the physical properties of water and brass, used in our calculations***

	water	brass
density [kg/m^3]	1000	8100
longitudinal wave velocity [m/s]	1480	4840
shear wave velocity [m/s]	0	2270

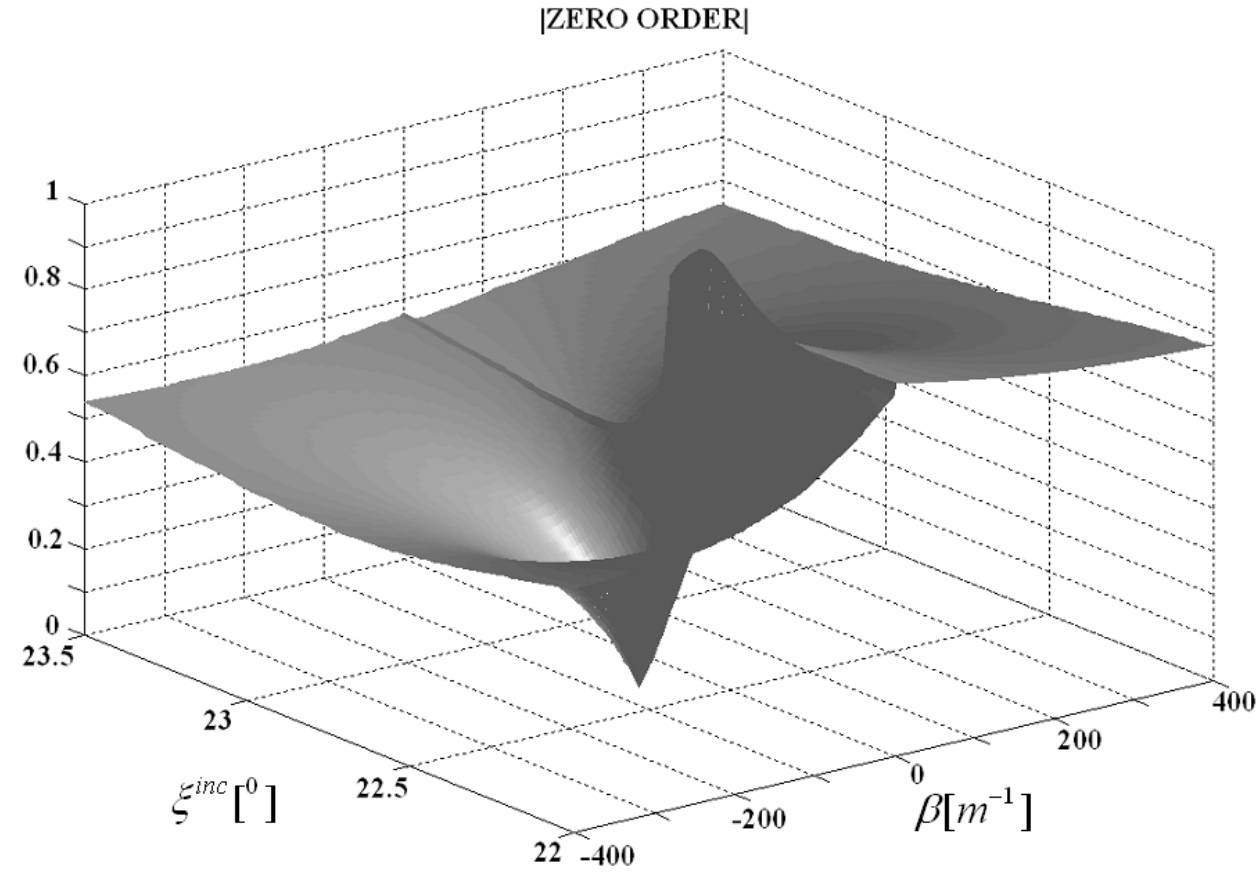

Fig. X.A.1.a_2: ***The absolute value of the zero order reflection coefficient, as a function of the angle of incidence and the incident inhomogeneity 'beta', shows a dip at 22.59^0 and inhomogeneity –71.86 m^{-1} .***

That this effect also appears for bounded beams, is described below, where results are shown for bounded beams. Fig. X.A.1.a_3, shows that the conditions at which the dip is there in Fig. X.A.1.a_2, do not correspond to a strong maximum of the –1 order reflection coefficient. In fact, the actual maximum is situated very close to but not at $\beta^{inc} = 0$, at an angle of incidence of 22.56^0. In addition, a strong maximum observed in the –1 order, corresponds to the generation of leaky Scholte-Stoneley waves.

First, under the assumption that it is a surface wave, the velocity corresponding to this angle of incidence reveals a velocity of 1477m/s, which is lower than the velocity of plane waves in water, and which is reasonable for Scholte-Stoneley waves. Second, the maximum is close to $\beta^{inc} = 0$ but is not equal to it. If we compare with the discussion of Wood anomalies in the previous section, we can come to the following interpretation: The Scholte-Stoneley wave is not much stimulated at $\beta^{inc} = 0$ due to the oblique incidence. Stronger stimulation occurs if the incident wave contains already some negative inhomogeneity (by which a higher amplitude is situated closer to the interface than if pure plane waves were incident).
This is the reason for $\beta^{inc} \approx 1$ a maximum is observed in the –1 reflection coefficient. Still, it remains a limited maximum, not a pole. Briers et al [2] have shown that due, to the grating equation (X.A.1.a_30), only pure plane waves are capable of stimulating Scholte-Stoneley waves.

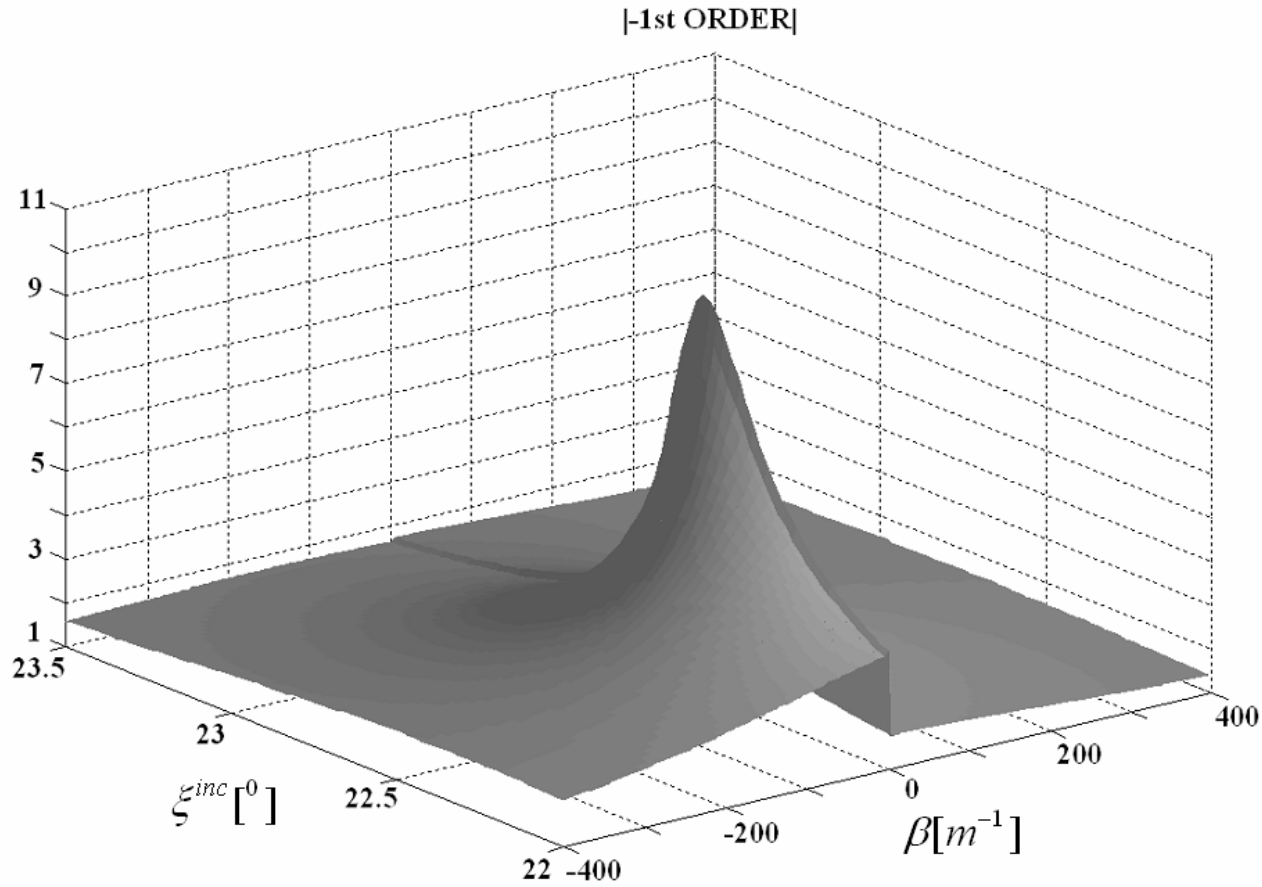

Fig. X.A.1.a_3: ***The absolute value of the –1 order reflection coefficient shows a maximum (not a pole) at 22.56^0 and inhomogeneity approximately –1m^{-1} .***

In order to discover the actual nature of what is really stimulated there, one must invoke relations (X.A.1.a_30) and (X.A.1.a_34) whence it is found that $\xi_1^{-1,r} = 269.996^0$, $\xi_1^{-1,d} = 269.998^0$ and $\xi_1^{-1,s} = 269.997^0$. It is important to remember that the angles are measured anti-clockwise starting from the negative z-axis. This means that it radiates into the liquid almost but not perfectly parallel to the interface. Hence it is a leaky Scholte-Stoneley wave.

If one needs to understand what causes the amplitude dip in the zero order reflection coefficient, one must not only take into account this leaky Scholte-Stoneley wave, but also sound stimulated by additional diffraction orders.
In Fig. X.A.1.a_4, it is seen that the amplitude of the +1 order reflected wave nowhere exceeds unity. However, it also seems to be stimulated more or less depending on the angle and inhomogeneity of incidence. It is the interaction of the –1 order with that of the +1 order that determines what happens with the zero order reflection coefficient. The same conclusion holds for higher order diffracted waves, even though their influence is more negligible. That is the reason why the position of the dip in Fig. X.A.1.a_2 differs from the position of the peak of Fig. X.A.1.a_3. However, the dip of Fig. X.A.1.a_2 is situated where the –1 order reflection coefficient is still considerably exceeding unity. In fact, if relations (X.A.1.a_30) and (X.A.1.a_34) are taken into account for the dip, one finds that $\xi_1^{-1,r} = 267.77^0$, $\xi_1^{-1,d} = 269.84^0$ and $\xi_1^{-1,s} = 269.80^0$. Hence, it must be concluded that the situation under which the backward traveling leaky Scholte-Stoneley wave is not in its highest stimulated state, will, due to its interaction with other diffracted orders, cause the amplitude dip of Fig. X.A.1.a_2.
For clarity, Figs X.A.1.a_2-4 are represented in Fig. X.A.1.a_5, but now viewed from the top and expressed in dB.

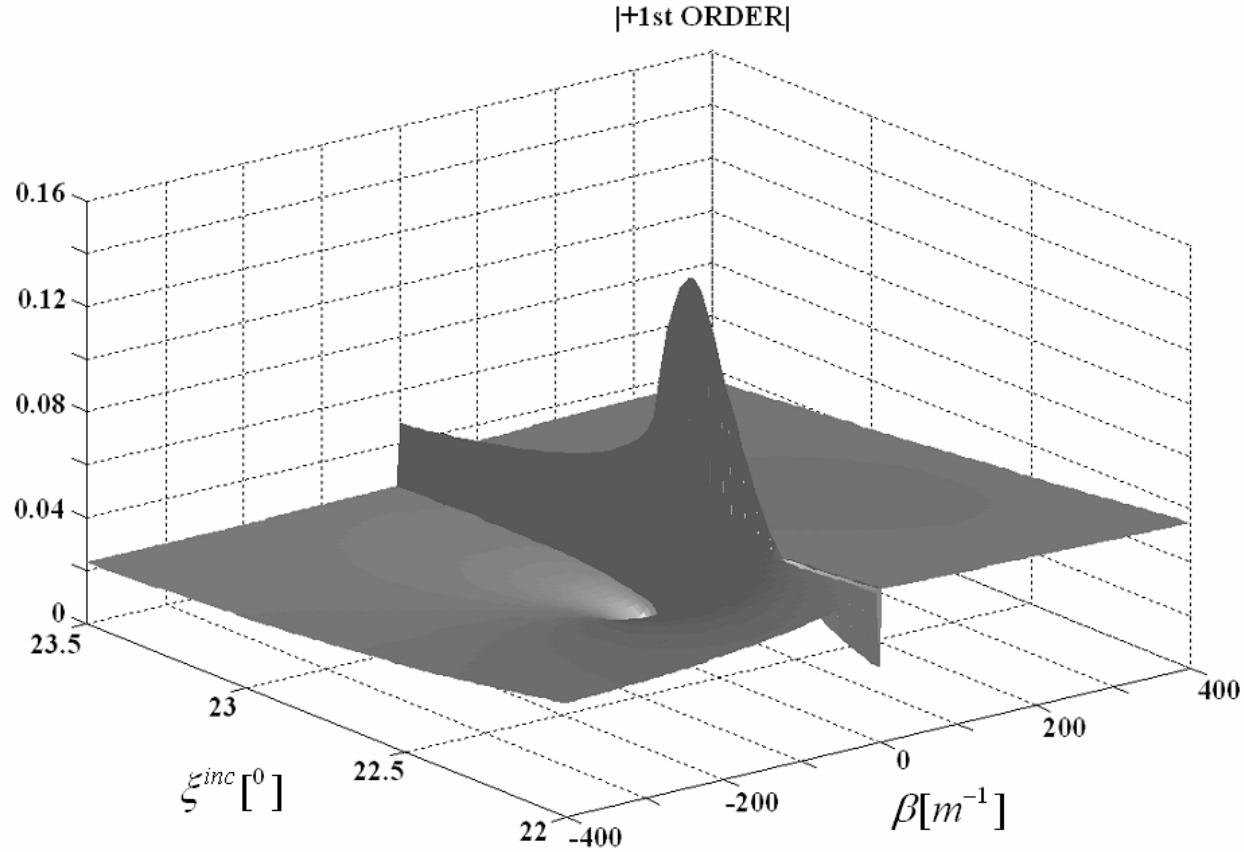

Fig. X.A.1.a_4: ***The absolute value of the +1 order reflection coefficient. Even though the amplitude is overall rather small, still there are fluctuations observable.***

Results and Discussion of the Reflection Coefficients for Single Inhomogeneous Waves incident near the Expected Rayleigh Angle.

In Fig. X.A.1.a_6, we present the results in dB, viewed from above. It is seen that the area between 42^0 and 47^0 contains a distribution of peaks and dips of the zero order reflection coefficient at inhomogeneities that are much larger than in the case of Fig. X.A.1.a_2. It is important to note that a peak (or a valley) in the zero order reflection coefficient for negative (or positive) inhomogeneities causes a shift to the right and a valley (or a peak) in the zero order reflection coefficient for positive, respectively negative, inhomogeneities causes a shift to the left. Therefore, two peaks or two valleys at symmetrical positions relative to the axis of the angle of incidence, thwart each others effect in a bounded beam. (This situation does not occur in Fig. X.A.1.a_6). A peak and a valley at symmetrical positions relative to the axis of the angle of incidence, causes a strong cooperation in shifting waves to the left or to the right. This situation appears more or less in Fig. X.A.1.a_2.

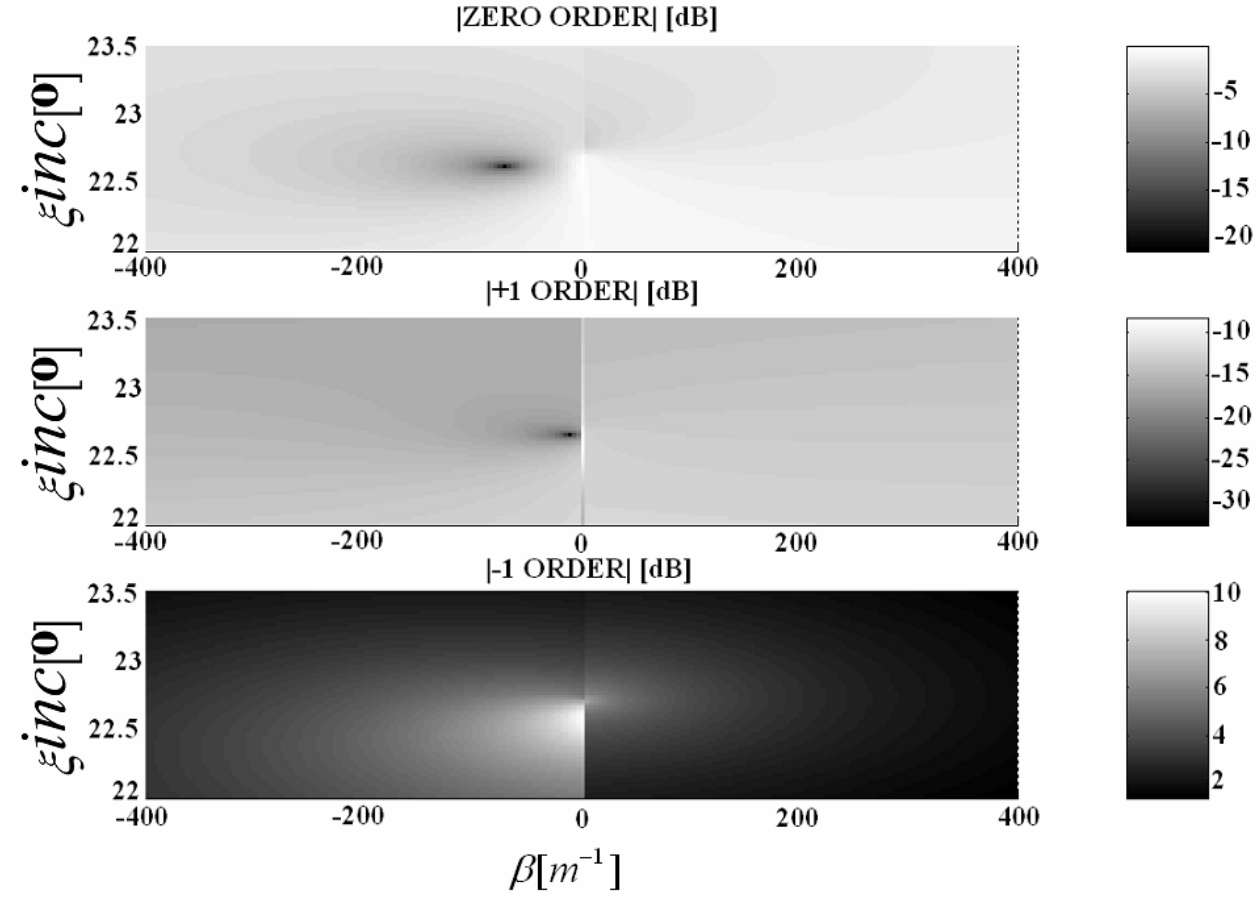

Fig. X.A.1.a_5: ***The information of Fig. X.A.1.a_2, Fig. X.A.1.a_3 and Fig. X.A.1.a_4 are collected and plotted in dB. Direct comparison with Fig. X.A.1.a_6 is therefore possible.***

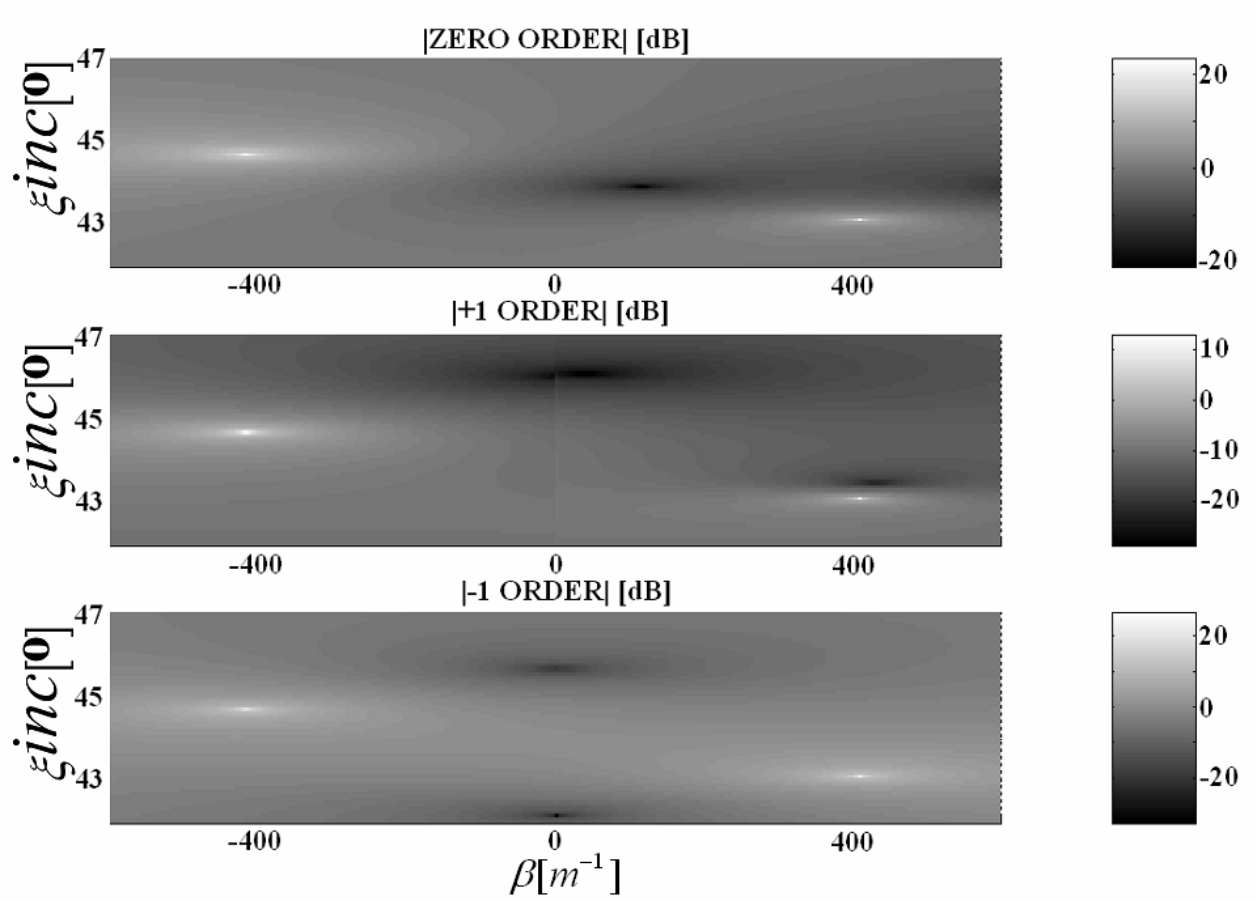

Fig. X.A.1.a_6: ***The amplitude in dB of the 0-order, 1-order and –1-order reflection coefficients as a function of the angle of incidence and the incident inhomogeneity. It is seen that the peaks and valleys in the 0-order reflection coefficient have flanks that appear to be uninfluenced if beta turns from positive to negative values.***

Actually, what we do see in Fig. X.A.1.a_6 is a dense distribution of peaks and dips in the zero order reflection coefficient that all extend beyond $\beta = 0$. It is as if the flanks of the peaks and valleys are uninfluenced by the transition of positive inhomogeneities into negative inhomogeneities and vice versa. Hence there is certainly not a strong, cooperation between a peak and a valley in a bounded beam. Furthermore, it is known that the highest inhomogeneity that is taken into account in the decomposition of a bounded beam into inhomogeneous waves is inversely proportional to the beamwidth [22]. Hence, for relatively large beamwidths, only the area $[-\beta_{\max}, \beta_{\max}]$ in which a small slope in the zero order reflection coefficient is observable, will be taken under consideration. This might be the reason why Breazeale and Torbett [14] couldn't observe any beamshift beyond 40^0, perhaps, if they had used a much narrower beam, they would have observed a beam shift indeed. An additional reason might be the intuitive fact that a real bounded beam (i.e. a beam that is not perfectly parallel, but is slightly spreading) is actually built up by several parallel beams (~'building blocks') coming from different directions close to a mean angle of incidence. Hence the consequential reflected beam will be the result of the superposition of many reflected beams that have undergone different deformations and in which the deformation of one 'building block' will be (partly) invisible due to the deformation of another 'building block'. The latter effect might cause all peaks and dips around 44^0 to 'interact' with each other and to thwart each others' effect, resulting in unobservable beam shifts.

Results and Discussion of Displacement Fields near the Expected Rayleigh Angle

There is however a critical question to be answered: Why do the peaks and dips in Fig. X.A.1.a_6 have different characteristics (i.e. a peak at β is not accompanied by a valley or dip near $-\beta$) than the peaks and dips that explain the excitation of leaky Rayleigh waves on smooth interfaces [23]. Our explanation is that the reason is to be found in the disturbance due to the other diffraction orders (see comments above in section **V.A** concerning Wood anomalies). Fig. X.A.1.a_7 shows the amplitude of the different displacements of the diffracted field in the case of $\theta^{inc} = 44.64^0$ and $\beta^{inc} = -419.0m^{-1}$, which corresponds to a peak in the +1 order reflection coefficient. Even though one would expect this peak to correspond to a generated forward traveling leaky Rayleigh wave, Fig. X.A.1.a_7 does not show any characteristic that corresponds to such a situation.
However, since it is the +1 order that is expected to be a 'leaky Rayleigh wave peak', it is interesting to plot the displacement field of only positive reflection orders. This is achieved in Fig. X.A.1.a_8, where it is seen that this pattern corresponds much better to that of a leaky Rayleigh wave on a smooth interface. However, the similarity is rather poor. The latter is probably due to the fact that even though their displacement is not plotted, the influence of negative orders is still present in the continuity conditions. Hence we may conclude that what causes the peaks in Fig. X.A.1.a_6 is the excitation of leaky Rayleigh wave-like phenomena.

Results and Discussion of Particle Displacement Fields near the Angle where Breazeale and Torbett [14] observed a Backward Beamshift

Fig. X.A.1.a_9 shows the displacement for the total diffraction field under the conditions that correspond to the dip in Fig. X.A.1.a_2. This field is much different than the field that would be expected if a pure Scholte-Stoneley wave was depicted. However, this is due to the fact that it is formed by the interaction of a leaky Scholte-Stoneley wave and the other diffraction orders (as discussed above). Its propagation is shown in Figs X.A.1.a_10-11.
What is really interesting in Fig. X.A.1.a_9 is the fact that it shows the same pattern as Fig. X.A.1.a_8.

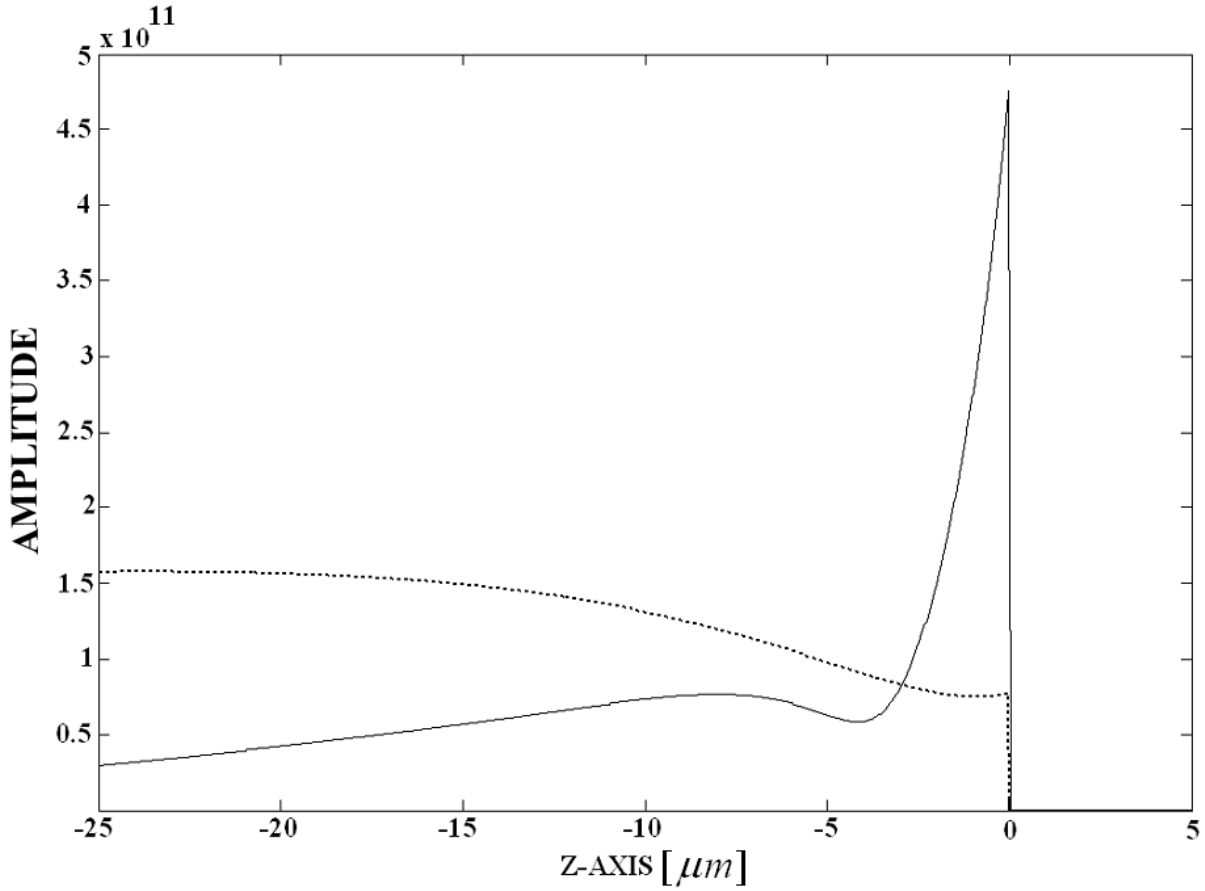

Fig. X.A.1.a_7: ***Amplitude of the complete particle displacement field as a function of depth (negative z-values in the solid, positive z-values in the liquid) for*** $\theta^{inc} = 44.64^0$, $\beta^{inc} = -419.0m^{-1}$ ***and a frequency of 6MHz. Solid line: x-displacement, dotted line: z-displacement. There is no Rayleigh characteristic observable.***

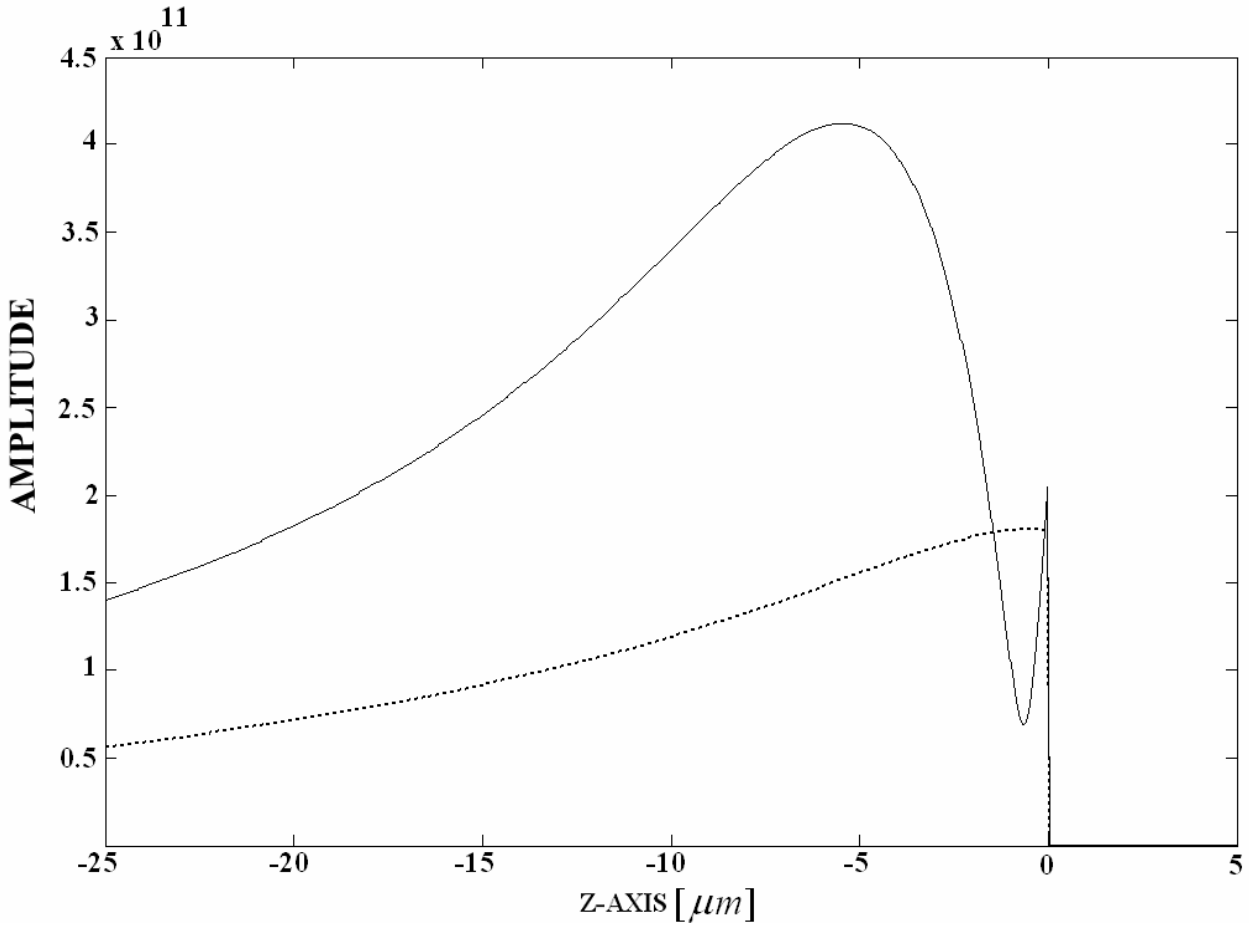

Fig. X.A.1.a_8: ***Same as Fig. X.A.1.a_7, except that solely the contribution to the displacement of the positive diffraction orders has been taken into account. This plot uncovers a characteristic that is more or less similar to the one of a leaky Rayleigh wave (cfr Fig 19 of Ref [26]).***

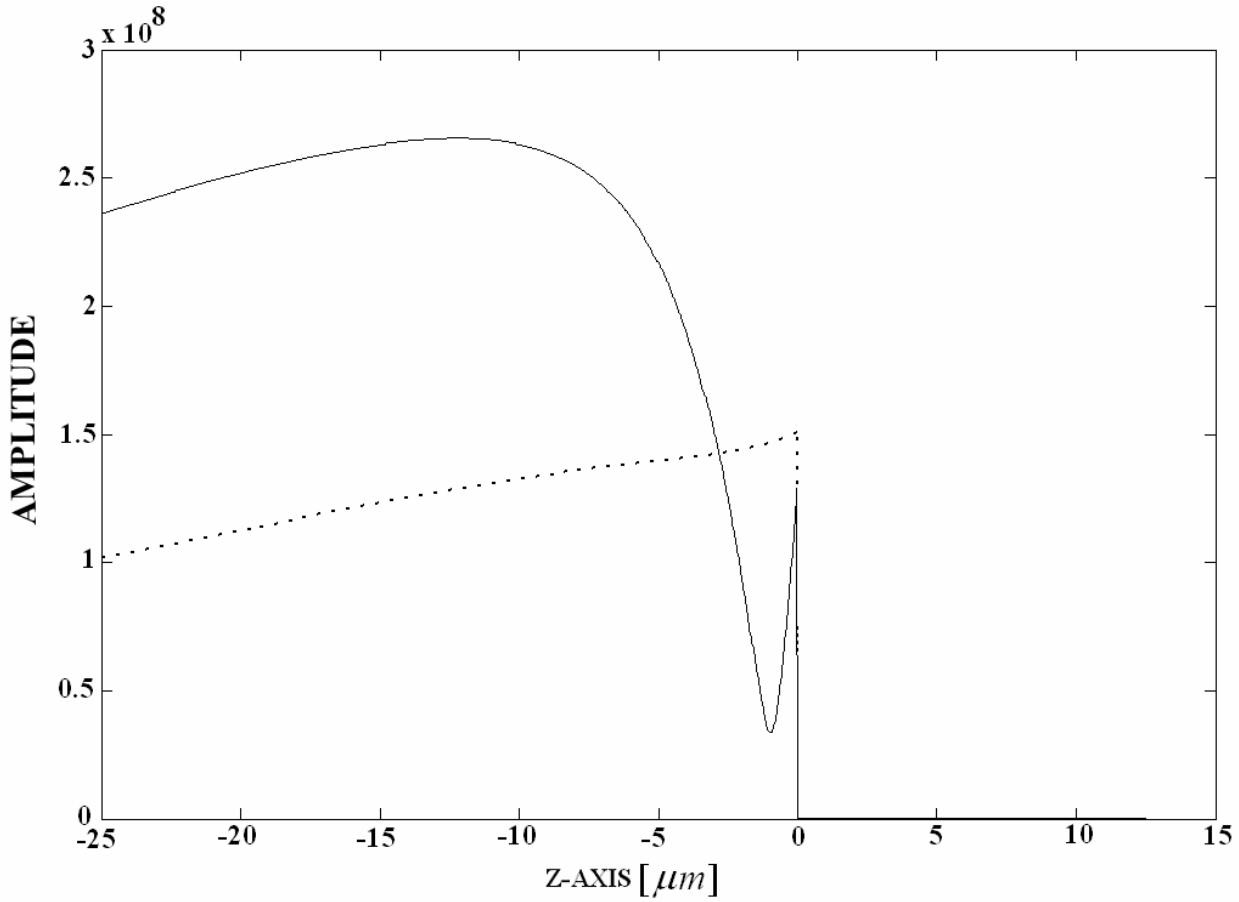

Fig.X.A.1.a_ 9: ***Amplitude of the complete particle displacement field as a function of depth (negative z-values in the solid, positive z-values in the liquid) for*** $\theta^{inc} = 22.59^0$, $\beta^{inc} = -71.86m^{-1}$ ***and a frequency of 6MHz. Solid line: x-displacement, dotted line: z-displacement. The pattern shows some resemblance with the typical pattern of Rayleigh waves. The reason of the similarity of Fig. X.A.1.a_9 and Fig. X.A.1.a_8 is rather surprising.***

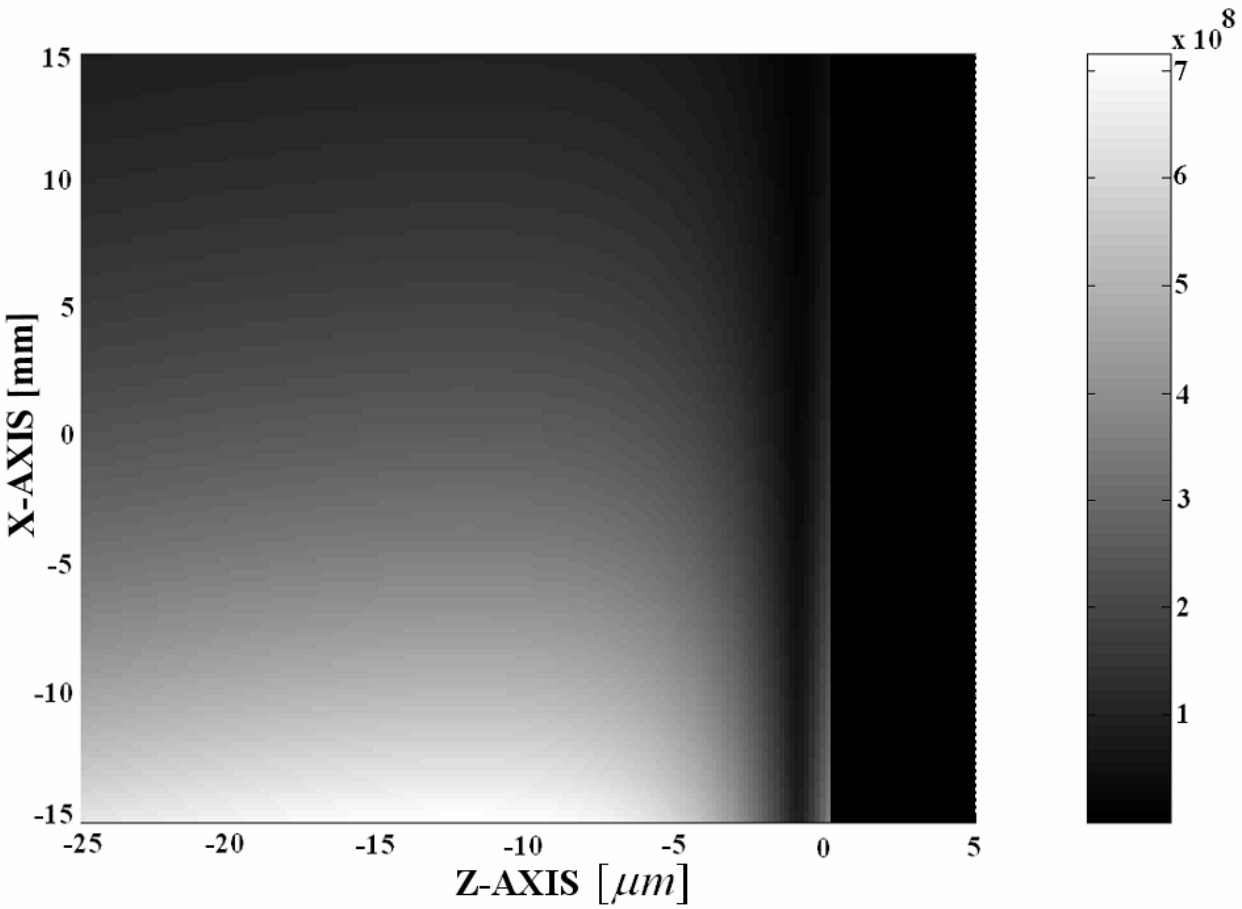

Fig. X.A.1.a_10: ***The amplitude of the x-displacement as a function of depth and propagation. Same physical circumstances as in Fig. X.A.1.a_9.***

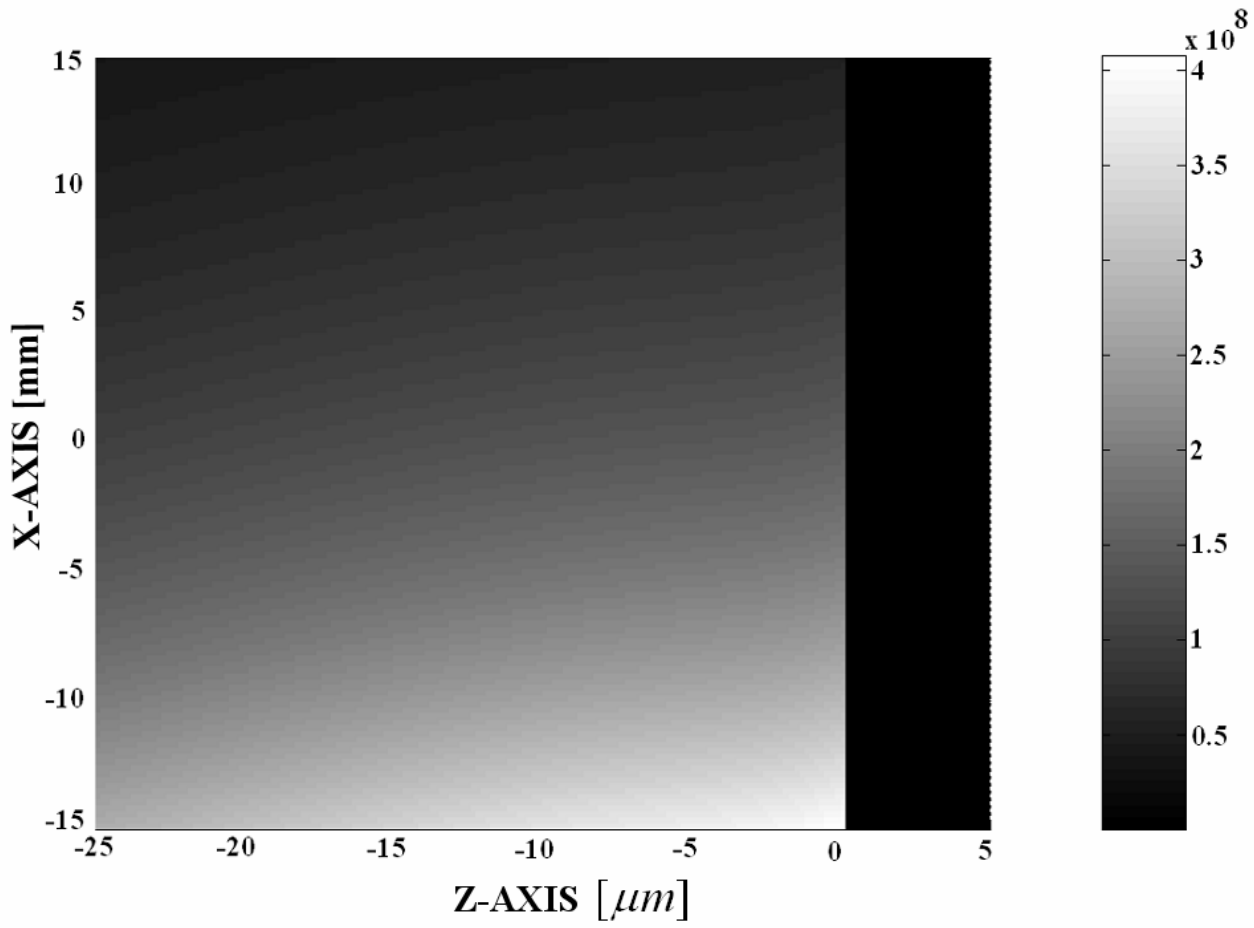

Fig. X.A.1.a_11: ***The amplitude of the z-displacement as a function of depth and propagation. Same physical circumstances as in Fig. X.A.1.a_9.***

Hence, the complete diffraction field that corresponds to the dip in Fig. X.A.1.a_2, shows the same amplitude pattern (not the exact values of course) as that corresponding to the leaky Rayleigh wave peak in Fig. X.A.1.a_6 at $\theta^{inc} = 44.64^0$ and $\beta^{inc} = -419.0m^{-1}$ if in the latter, only the particle displacements field due to waves traveling in the direction of the Rayleigh wave are plotted. We have no explanation for this.

Results for Bounded Beams using the Fourier Decomposition

If a bounded beam, described as a superposition of plane waves (see (X.A.1.a_43)), would fully explain what Breazeale and Torbett [14] observed experimentally, then the more elaborate study using inhomogeneous waves would be unnecessary. In Figs. X.A.1.a_12-13, the reflected beam pattern at 6MHz is shown as a function of the angle of incidence, using the Fourier method. Fig X.A.1.a_12 shows that for a very wide beam (approximately 10cm physical width), there is not really any significant beam shift observable, except for some small disturbance at bulk critical angles. If however a physical beamwidth of approximately 1 cm is used (Fig. X.A.1.a_13), which corresponds to the beamwidth in the experiments of Breazeale and Torbett [14], significant beam deformations and beam shifts appear between 35^0 and 45^0. The latter have not been observed experimentally. There is also nothing significant observable on Fig. X.A.1.a_13 near the angle

where Breazeale and Torbett [14] observed a significant backward beamshift. We must therefore conclude that the Fourier method is unable to describe the diffraction experiments of ref. [14].

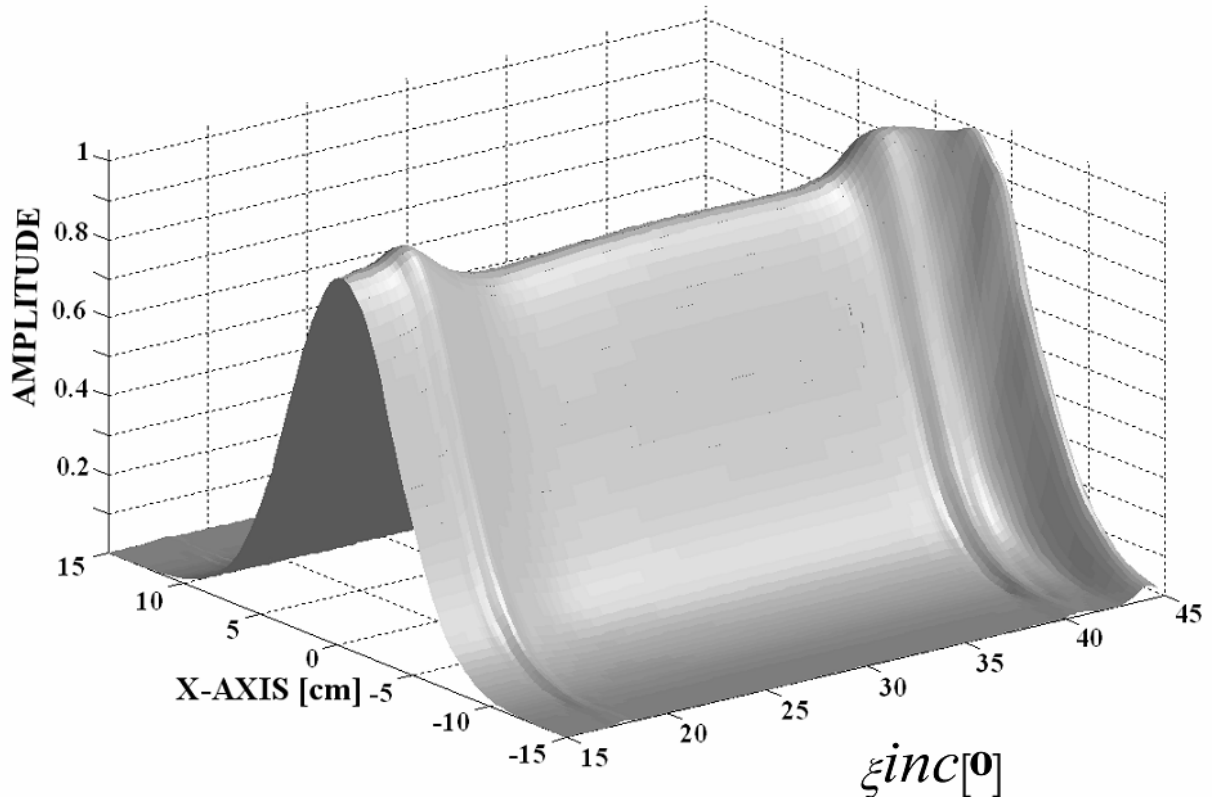

Fig. X.A.1.a_12: ***The reflected beam profile as a function of the angle of incidence at a frequency of 6 MHz. The Fourier method is used. The physical beamwidth is approximately 10 cm. No explicit beam displacement is observable. There is some effect at 17.80^0 , which is due to the critical angle for dilatational lateral bulk waves, and also at 40.69, which is due to the critical angle for shear lateral bulk waves.***

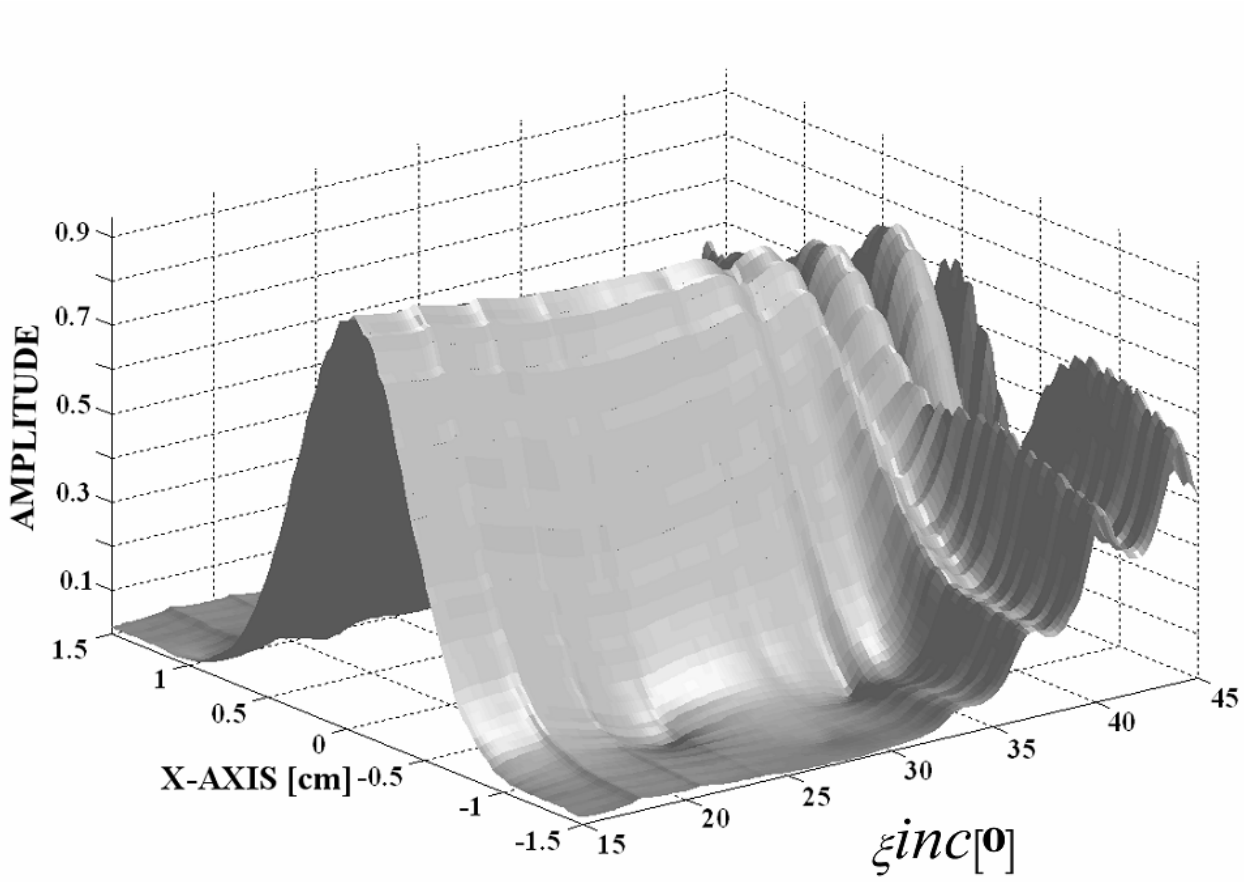

Fig. X.A.1.a_13: ***Same legend as Fig. X.A.1.a_12, except that a physical beamwidth of 1 cm is used. Hence one should expect to find what Breazeale and Torbett have experimentally observed, which is certainly not the case.***

Results for Bounded Beams using the Inhomogeneous Waves Decomposition

Fig. X.A.1.a_14 shows the theoretical result for 2MHz, $\theta^{inc} = 22.59^0$ and a physical beamwidth of approximately 1cm. No beamshift is seen. Fig. X.A.1.a_15 shows the same result, but now for a frequency of 6MHz. Clearly a beamshift Δ is observable. Figs X.A.1.a_14 and X.A.1.a_15 correspond so well to what Breazeale and Torbett [14] have observed, that they are almost exact copies of their pictures [14].

If the same incident beam is used as in Fig. X.A.1.a_15, but now at $\theta^{inc} = 43.07^0$, Fig. X.A.1.a_16 is obtained. At $\theta^{inc} = 44.63^0$ Fig. X.A.1.a_17 is obtained. It is seen that Figs. X.A.1.a_16-17 also show no beamshift (Fig. X.A.1.a_16) or an almost negligible forward beam shift (Fig. X.A.1.a_17). This is also in agreement with the observations in ref. [14], where no significant beam shift beyond 40^0 is found.

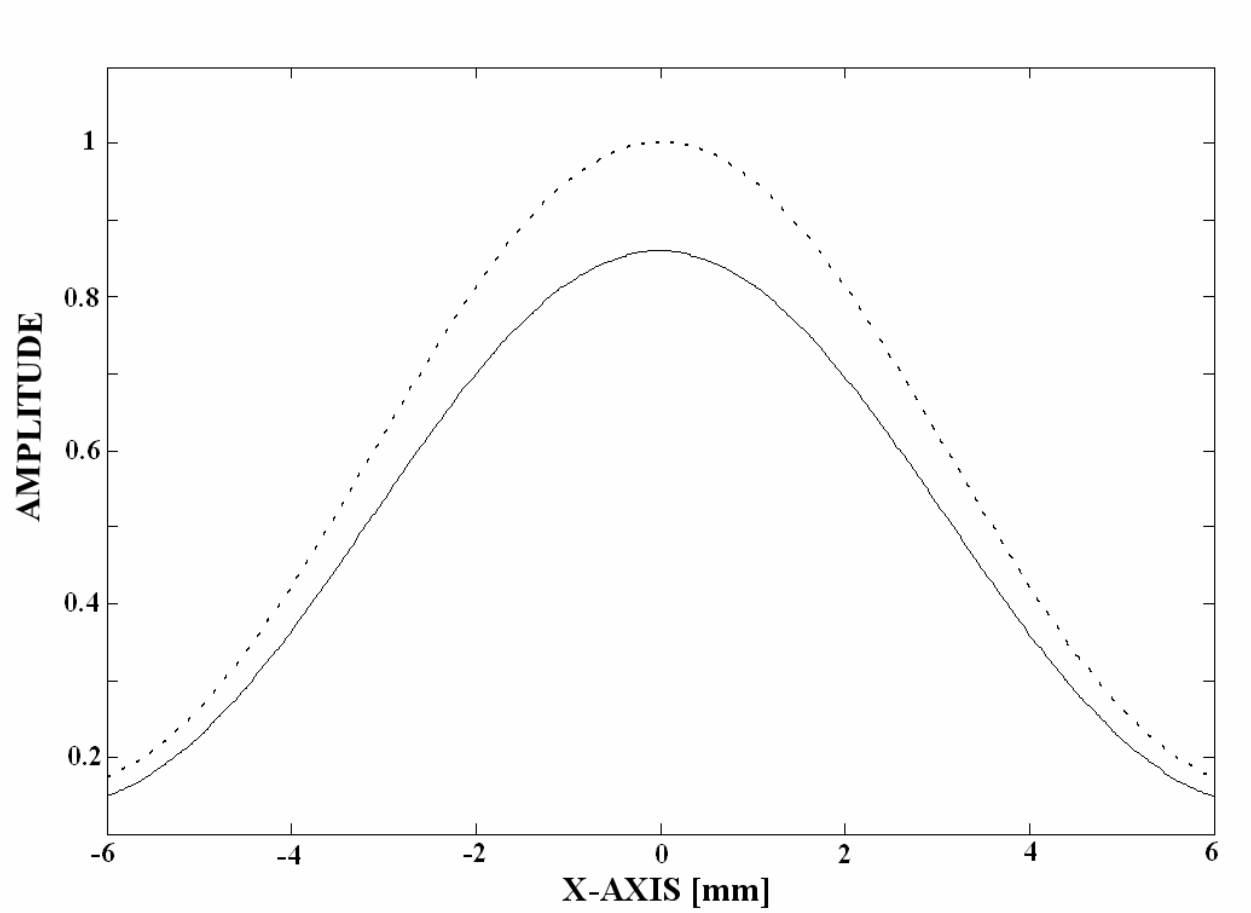

Fig. X.A.1.a_14: ***Here the inhomogeneous waves theory is used. The incident (dotted line) and the reflected (solid line) beam profile at a frequency of 2 Mhz and an angle of incidence 22.59^0 . No displacement is observed, in agreement with the experiments of Breazeale and Torbett.***

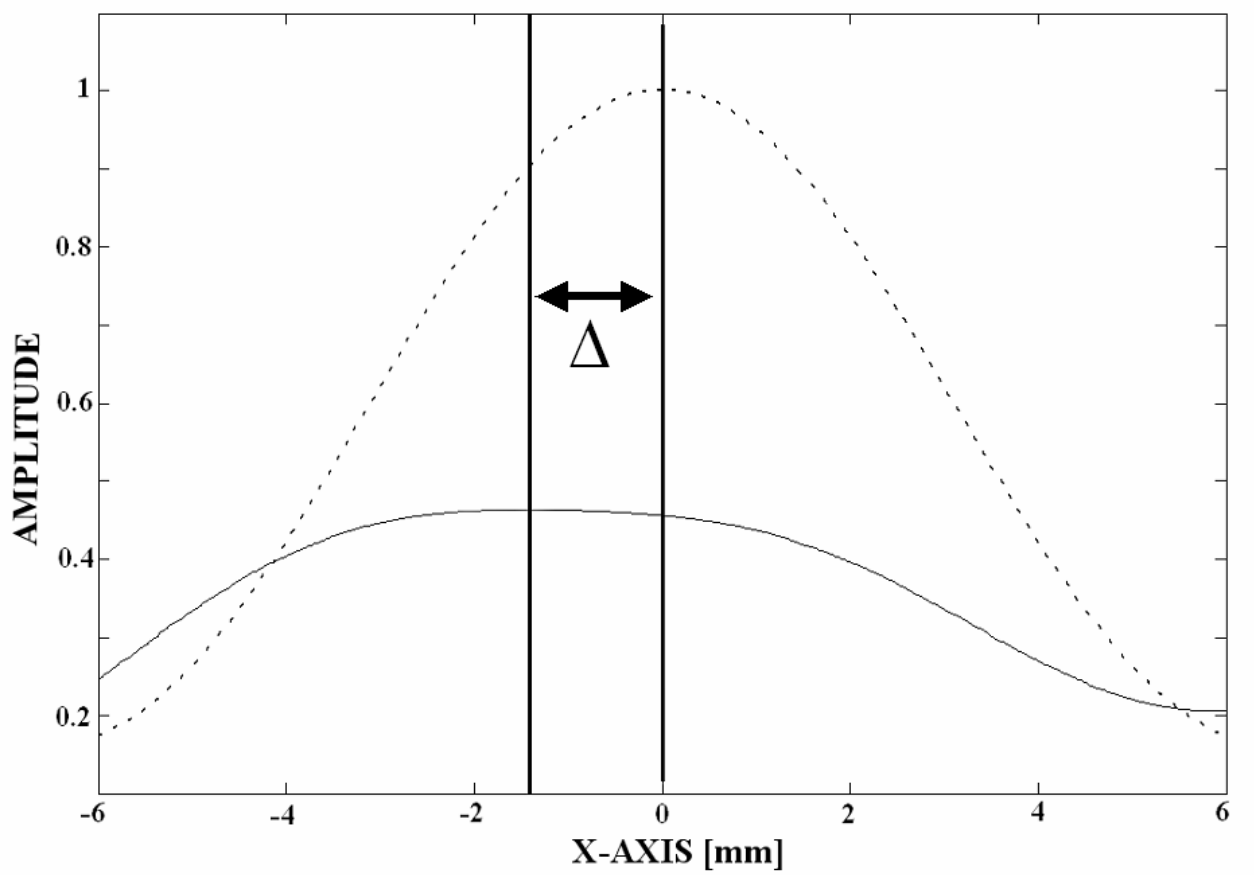

Fig. X.A.1.a_15: ***Same situation as in Fig. X.A.1.a_14, except that the frequency is now 6 MHz. A backward beam shift is observed in agreement with the experiments of Breazeale and Torbett.***

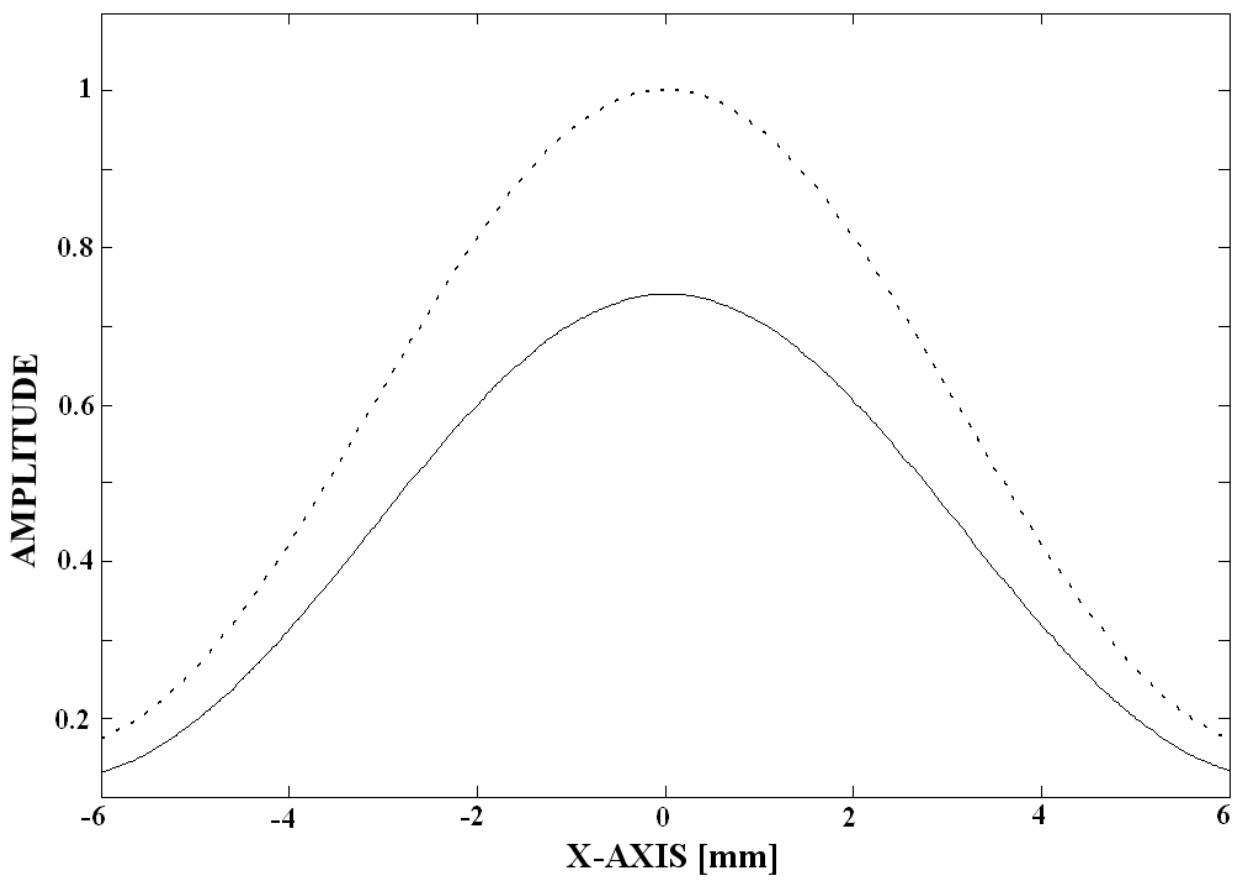

Fig. X.A.1.a_16: ***Same legend as in Fig. X.A.1.a_15, except that the angle of incidence is here 43.07^0, which is the angle at which the zero order reflection coefficient shows a maximum. (see Fig. X.A.1.a_6). No displacement is observed, in agreement with the experiments of Breazeale and Torbett.***

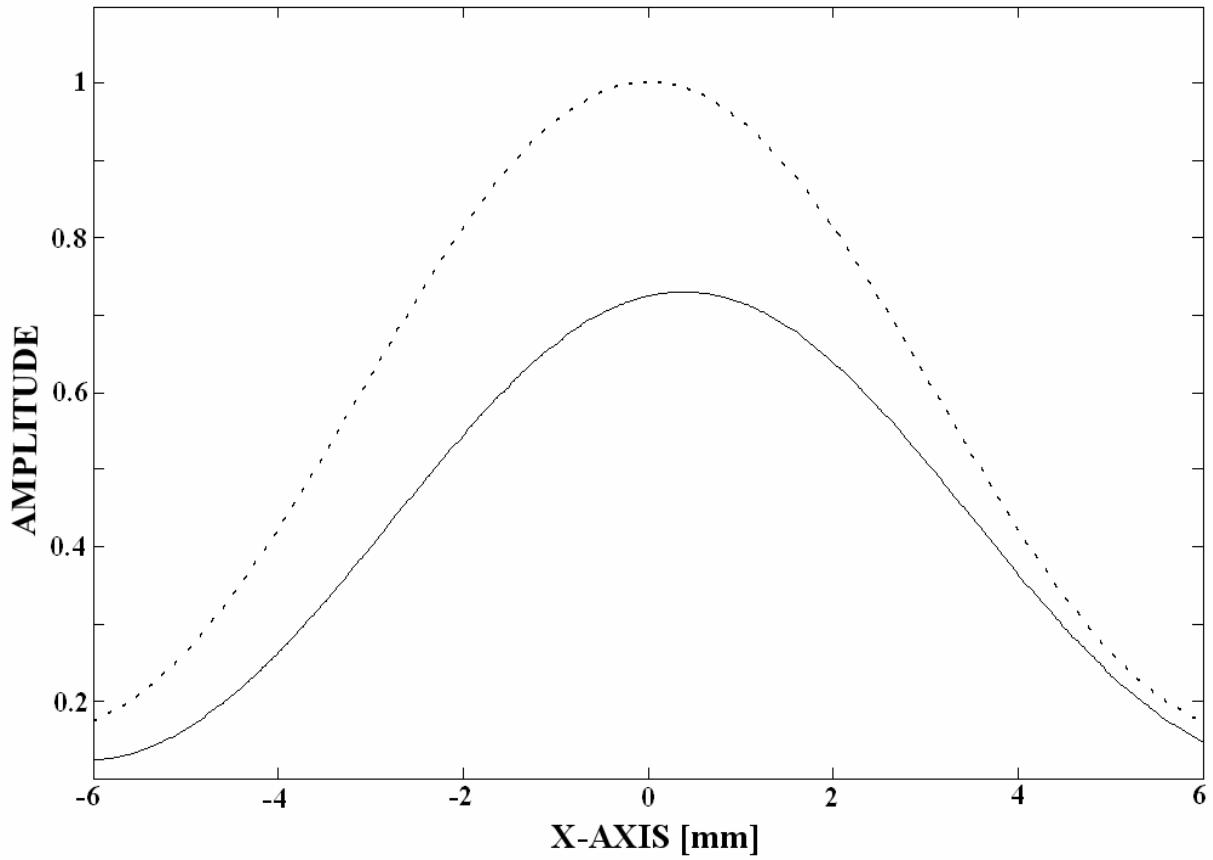

Fig. X.A.1.a_17: ***Same legend as in Fig. X.A.1.a_16, except that the angle of incidence is here 44.63^0, which is the angle at which the –1 order reflection coefficient shows a maximum (see Fig. X.A.1.a_6). Only a negligible displacement is observed which is in agreement with the experiments of Breazeale and Torbett.***

CONCLUDING REMARKS

This section has proved that the inhomogeneous waves theory is capable of elucidating the backward beam shift that has been observed by Breazeale and Torbett [14] and, besides a short demonstration [27] of the capability of the inhomogeneous waves theory to simulate the phenomenon, has been unexplained ever since. It is found that this effect is caused by the interaction of a leaky Scholte-Stoneley wave, with other diffracted waves. This is a new phenomenon and was first theoretically proved [28], shortly before its experimental discovery [29]. Furthermore, a better insight is given into the nature of Wood anomalies in diffraction spectra. Hence, even though the described diffraction theory has also been proved to be very valuable in architectural acoustics [30], perhaps one of the most beautiful phenomena it has ever explained, is the one described in the current section.

REFERENCES

[1] D. Maystre, “Selected Papers on Diffraction Gratings”, SPIE Milestone Series Vol. MS 83, SPIE, Washington, DC, 1993

[2] Rudy Briers, “Contributions to the study of acoustic scattering and conversion phenomena in discontinuous structures by introducing a mode theory and by applying the inhomogeneous wave theory”, PhD Thesis KULeuven University, department of sciences, 1995

[3] R. Briers, O. Leroy, O. Poncelet, M. Deschamps, “Experimental verification of the calculated diffraction field generated by inhomogeneous waves obliquely incident on periodically rough liquid-solid boundary”, J. Acoust. Soc. Am. 106(2), 682-687, 1999

[4] J.-M. Claeys, O. Leroy, “ Diffraction of plane waves by periodic surfaces”, Revue du Cethedec 72, 183-193, 1982

[5] J. M. Claeys, Oswald Leroy, Alain Jungman, Laszlo Adler, “ Diffraction of ultrasonic waves from periodically rough liquid-solid surface”, J. Appl. Phys 54(10, 5657-5662, 1983

[6] B.A. Lippmann, “Note on the Theory of Gratings”, J. Opt. Soc. Am.43, 408, 1953

[7] Jungman, O. Leroy, G. Quentin, K. Mampaert, “Theoretical and experimental study of ultrasonic surface modes at a solid-fluid interface”, J. Appl. Phys. 63(10), 4860-4870, 1988

[8] K. Mampaert, O. Leroy, “Reflection and transmission of normally incident ultrasonic waves on periodic solid-liquid interfaces”, J. Acoust. Soc. Am. 83(4), 1390-1398, 1988

[9] K. Mampaert, P.B. Nagy, O. Leroy, L. Adler, A. Jungman, G. Quentin, “On the origin of the anomalies in the reflected ultrasonic spectra from periodic surfaces”, J. Acoust. Soc. Am. 86(1), 429-431, 1989

[10] Nico F. Declercq, Rudy Briers, Oswald Leroy, " The use of polarized bounded beams to determine the groove direction of a surface corrugation at normal incidence, the generation of surface waves and the insonification at Bragg-angles", Ultrasonics 40/1-8 pp. 345-348, 2002.

[11] M. Deschamps, C.L. Cheng,“Liquid-Thermoviscoelastic Solids Interface“, Ultrasonics 27, 308-313, 1989

[12] Briers R. and Leroy O. "Study of the behaviour of inhomogeneous harmonic waves in their diffraction from simple rough surfaces". J. de Physique IV, C1(2), 679-682, 1992.

[13] Briers R. and Leroy O. " Reflection of inhomogeneous plane ultrasonic waves on periodically rough solid-vacuum interfaces". SPIE vol 1844 Acousto-Optics and Applications, Gdansk-Jurata, Poland. Proceed. pp. 196-205, 1992

[14] M. A. Breazeale, Michael Torbett, “Backward displacement of waves reflected from an interface having superimposed periodicity”, Appl. Phys. Let., 29(8), 456-458, 1976.

[15] Marc Deschamps, “Reflection and refraction of the evanescent plane wave on plane interfaces”, J. Acoust. Soc. Am. 96(5), 2841-2848, 1994

[16] T. Tamir, H. L. Bertoni, “Lateral Displacement of Optical Beams at Multilayered and Periodic Structures”, J. opt. Soc. Am., 61(10), 1397-1413, 1971

[17] Bernard Poirée, “Les ondes planes évanescentes dans les fluides parfaits et les solides élastiques”, J. Acoustique 2, 205-216, 1989.

[18] J.P. Charlier, F. Crowet, “Wave Equations in linear Viscoelastic Materials“, J. Acoust. Soc. Am. 79(4), 895-9000, 1986

[19] M. Abramowitz, I. A. Stegun, “Handbook of mathematical functions”, Dover Publications, 1972

[20] Jean-Marie Claeys, “Theoretical Models to describe reflection and diffraction of ultrasound from layered media”, PhD Thesis KUL department of Sciences (in dutch), 1985

[21] Oswald Leroy, “Nonspecular reflection-transmission phenomena of bounded beams described by inhomogeneous plane waves”, Acoustic Interaction with Submerged Elastic Structures, Part I, pp. 129-163, edited by A. Guran, J. Ripoche and F. Ziegler, Series on Stability, Vibration and Control of Systems Series B: Vol. 5., World Scientific (1996).

[22] J. M. Claeys and O. Leroy, “Reflection and transmission of bounded sound beams on half-spaces and through plates”, J. Acoust. Soc. Am. 72(2), 585-590, 1982

[23] K. Van Den Abeele, O. Leroy, “On the influence and width of an ultrasonic bounded beam in the investigation of materials: Study in terms of heterogeneous plane waves”, J. Acoust. Soc. Am. 93(5), 2688-2699, 1993

[24] Frank R. Spitzenogle, Azizul H. Quazi, “Representation and Analysis of Time-Limited Signals Using a Complex Exponential Algorithm”, J. Acoust. Soc. Am., 47(5), 1150-1155, 1970

[25] Nico F. Declercq, Rudy Briers, Joris Degrieck, Oswald Leroy, "Diffraction of horizontally polarized ultrasonic plane waves on a periodically corrugated solid-liquid interface for normal incidence and Brewster

angle incidence", IEEE Transactions on Ultrasonics, Ferroelectrics, and Frequency Control, 49(11), 1516-1521, 2002.

[26] Koen E.-A. Van Den Abeele, Rudy Briers, Oswald Leroy, “Inhomogeneous plane-wave scattering and mode stimulation on periodic rough surfaces”, J. Acoust. Soc. Am. 99(5), 2883-2897, 1996

[27] Nico F. Declercq, Joris Degrieck, Rudy Briers, Oswald Leroy, “Theoretical verification of the backward displacement of waves reflected from an interface having superimposed periodicity”, Appl. Phys. Let. 82(15), 2533-2534, 2003

[28] Nico F. Declercq, Joris Degrieck, Rudy Briers, Oswald Leroy, “A Theoretical elucidation for the experimentally observed backward displacement of waves reflected from an interface having superimposed periodicity”, J. Acoust. Soc. Am. 112(5), 2414, 2002

[29] A. Teklu, M. A. Breazeale, “Backward displacement of ultrasonic waves reflected from a corrugated interface”, J. Acoust. Soc. Am. 113(4), 2283-2284, 2003.

[30] Nico F. Declercq, Joris Degrieck, Rudy Briers,Oswald Leroy , “A theoretical study of special acoustic effects caused by the staircase of the El Castillo pyramid at the Maya ruins of Chichen-Itza in Mexico”, J. Acoust. Soc. Am. 116(6), 3328-3335, 2004

X.A.1.b Experimental Study of the Backward Displacement of Ultrasonic Waves Reflected from a Periodically Corrugated Interface

New experiments using the schlieren technique to image sound incident on a corrugated, water-brass interface show a backward displacement of the reflected beam at an angle of 22.5 degrees, confirming the observations of Breazeale and Torbett [Appl. Phys. Lett. 29, 456 (1976)]. However, a new theory hypothesizes that this beam displacement results from excitation of a new type of leaky surface wave. Further experiments with a sufficiently narrow incident beam reveal a backward displacement also at angles around 44 degrees, resulting from excitation of Rayleigh surface waves, as predicted by the theory of Tamir and Bertoni [J. Acoust. Soc. Am. 61, 1397-1413 (1971)]. Thus, a wide beam gives backward displacement at 22.5 degrees only. A narrow beam gives backward displacement also at angles around 44 degrees.

This work has been performed at the National Center for Physical Acoustics, The University of Mississippi, Oxford, Mississippi, USA, in collaboration with A. Teklu, M. A. Breazeale and Roger Hasse, and is accepted for publication in J. Appl. Phys. (Imp. Fact. 2.281; SCI-index, Physics-Applied, rank:13/76)

INTRODUCTION

The Goos-Hänchen theory predicts that light incident near the critical angle on a dielectric interface from an optically denser medium has a reflected beam that is laterally shifted from the position predicted by geometrical optics [1]. The incident light beam transfers a portion of its energy into the optically rarer medium and excites an electromagnetic field that travels longitudinally for a certain distance along the interface. This energy is leaked back into the denser medium and interferes with the specularly reflected beam. This interference results in a reflected beam which exhibits a lateral displacement that appears as a forward beam shift. More complex structures such as multilayered media and periodically corrugated configurations of the optical grating type guide electromagnetic fields of the leaky-wave variety as well. The lateral displacement of a light beam reflected from a leaky-wave structure when a Gaussian light beam is incident upon it was studied by Tamir and Bertoni [2]. The theory of Tamir and Bertoni [2] predicts that at a certain critical angle, a reflected beam shift may occur either in the forward or in the backward direction with respect to the incident beam.

The early experiments of Schoch [3,4] using the acoustic analog of the Goos-Hänchen effect for an ultrasonic beam reflected from a liquid-solid interface showed a forward lateral displacement of the reflected ultrasound beam. Later, Breazeale and Torbett [5], using a schlieren photographic technique, observed a backward beam shift of a 6 MHz ultrasonic beam of 10 mm width, reflected from a superimposed periodic grating, confirming the backward beam

displacement predicted by the theory of Tamir and Bertoni [2]. Angles of incidence are measured from the normal to the surface. According to the theory of Tamir and Bertoni [2], the angle of incidence θ_i at which the phenomenon occurs is 41^0 for an ultrasonic beam of frequency 6 MHz and is imaginary for 2 MHz; thus the effect would not be observed at 2MHz. If this theory is valid, at θ_i=41°, leaky Rayleigh surface waves with a velocity of 2015 m/s should be excited on a corrugated brass reflector leading to backward beam shift. The experiment confirmed the existence of a surface wave at 6 MHz, but not at 2 MHz, when frequency was the only parameter altered in the system. The predicted angle for a 6 MHz beam is significantly different from the value of 22.5° measured by Breazeale and Torbett [5]. Using the measured angle of incidence of 22.5°, they calculated the velocity of this leaky surface wave as 1470 m/s which is considerably smaller than that of the Rayleigh surface wave. This suggests that either the theory of Tamir and Bertoni [2] does not accurately describe the backward displacement phenomenon or that the surface wave that is responsible for the phenomenon differs from the leaky Rayleigh wave.

Recently, Declercq et. al. [6,7] used the inhomogeneous wave theory to account for the discrepancies between the predictions of Tamir and Bertoni [2] and the experimental observations of Breazeale and Torbett [5]. They represented a bounded ultrasonic beam as a sum of infinite inhomogeneous waves and applied the theory of the diffraction of inhomogeneous waves to account for the behavior of each individual wave upon incidence on the periodically rough surface. Furthermore, they applied sign reversal rules, based on experiments, as described by Deschamps [8]. Using this approach, Declercq et. al. [6,7] have calculated the angle of incidence for the generation of leaky surface waves in order to resolve disagreements between theory and experiment. Their calculated value of the angle of incidence agrees very well with our measured value. However, the most striking result of the inhomogeneous wave theory is the prediction of the excitation of a new kind of leaky surface wave [7] on a periodically corrugated brass-water interface that is different from the leaky Rayleigh wave. Declercq et. al. [7] also showed that in the vicinity of the angle of 44°, where Breazeale and Torbett [5] expected only a backward beam displacement due to leaky Rayleigh waves, there is excitation of propagating leaky Rayleigh waves which may result in changes of the beam profile but probably not in an outright backward beam displacement. It was also shown that any such changes in the beam profile can occur only near 44° when a bounded beam is used that is narrower than the one of 10 mm width that was used in the original experiments of Breazeale and Torbett.

Here, we report new experimental results obtained with modern imaging techniques using a bounded beam of only 6 mm beam width. This allowed us to study the cause of the backward displacement at 22.5° and to verify the prediction of Declercq et. al. [6,7] that changes in the beam profile can occur for such a narrow beam around 44°. These experiments indicate that the backward beam shift is caused by the generation of a Scholte-Stoneley like surface wave and that indeed there are changes in the beam profile around 44° when a narrow beam is used instead of the wider beam used in the original experiments.

EXPERIMENT

The schlieren photographic technique was used to image an incident ultrasonic bounded beam reflected by a periodically corrugated brass surface. Fig. X.A.1.b_1 is a schematic of the experimental set-up. To provide a large field of view, two large (f/6.3, 48 inch focal length) lenses were chosen.

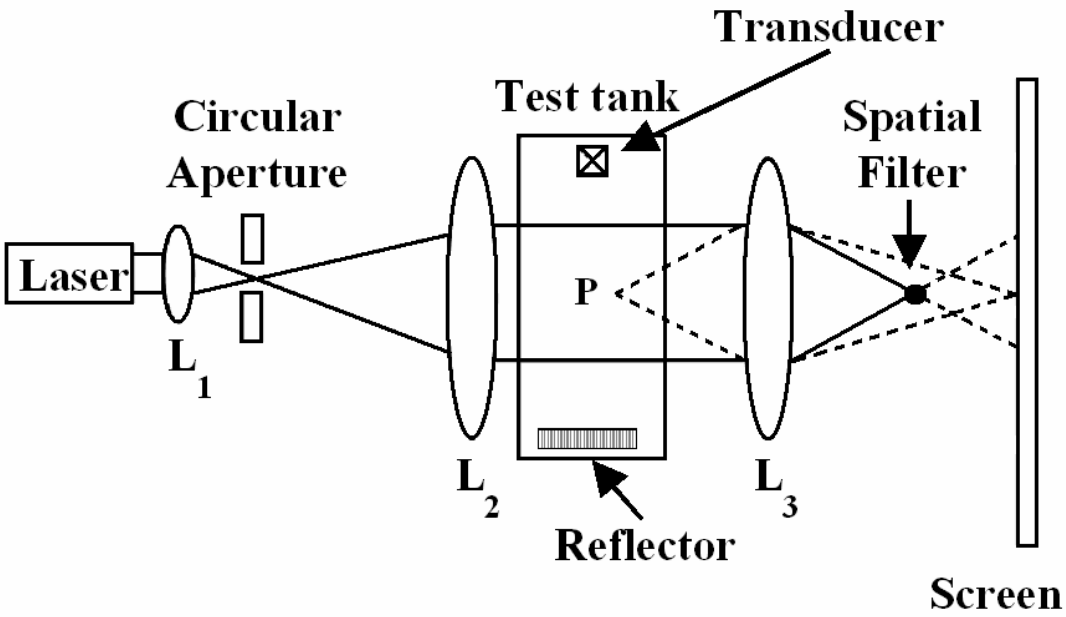

Fig X.A.1.b_1: ***Experimental set-up of the schlieren optical system.***

Monochromatic laser light is focused by the first lens L_1 onto a circular aperture (diameter 15 μm) that is placed at the focal point of lens L_1. After passing through the aperture, the light is collimated by lens L_2 and passes through the test tank. Two extreme light rays from the source passing parallel through the test tank are shown in Fig. X.A.1.b_1. The light rays are then focused by a third lens L_3. They pass through a focal point and providing an inverted image on the screen. An object placed inside the test tank, such as a reflecting surface or a transducer, thus can be imaged. A black ink spot is placed at the focal point of the third lens L_3 to act as a spatial filter [10]. The black spot obstructs all the light and produces a dark screen except for regions where the medium is disturbed by sound or by a density gradient of any kind. In our experiments, the test tank is filled with water that is disturbed by ultrasonic waves which produce the beams seen in our pictures.

A 6 MHz apodized quartz transducer is used to generate the bounded ultrasonic beam of 6.0 mm width. This beam is reflected from a brass interface ruled with square parallel grooves of period d = 0.178 mm and depth t = 0.025 mm (Fig. X.A.1.b_2). The angle of incidence of the beam is varied in order to observe the angles at which the backward beam displacement occurs. Fig. X.A.1.b_2 shows the arrangement of the transducer and the reflection diffraction grating. The inset in Fig. X.A.1.b_2 is a photograph of a side view of the ruled section of the grating as seen under a microscope. The schlieren image on the screen is recorded by a digital camera connected to a computer with image acquisition and analysis software.

RESULTS AND DISCUSSIONS

A schlieren image of an ultrasonic beam of frequency 6 MHz and a width of 6 mm, reflected from a brass-water interface is shown in Fig. X.A.1.b_3. For many angles of incidence, the angle of the reflected beam is equal to that of the incident beam, and the reflected beam experiences no lateral displacement. As the angle of incidence is varied, the first order diffracted beam appears in addition to the reflected beam as is shown in Fig. X.A.1.b_3.

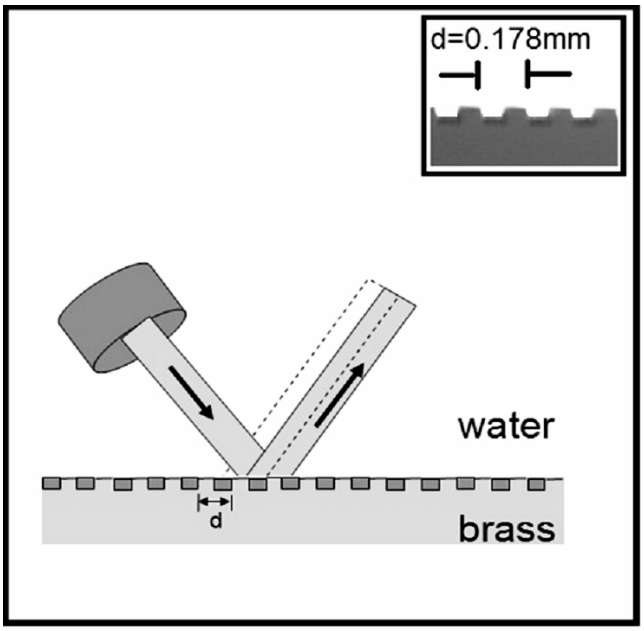

Fig. X.A.1.b_2: ***Schematic arrangement of the transducer and grating shown in Fig. X.A.1.b_1. The inset is a photograph of the ruled section of the grating.***

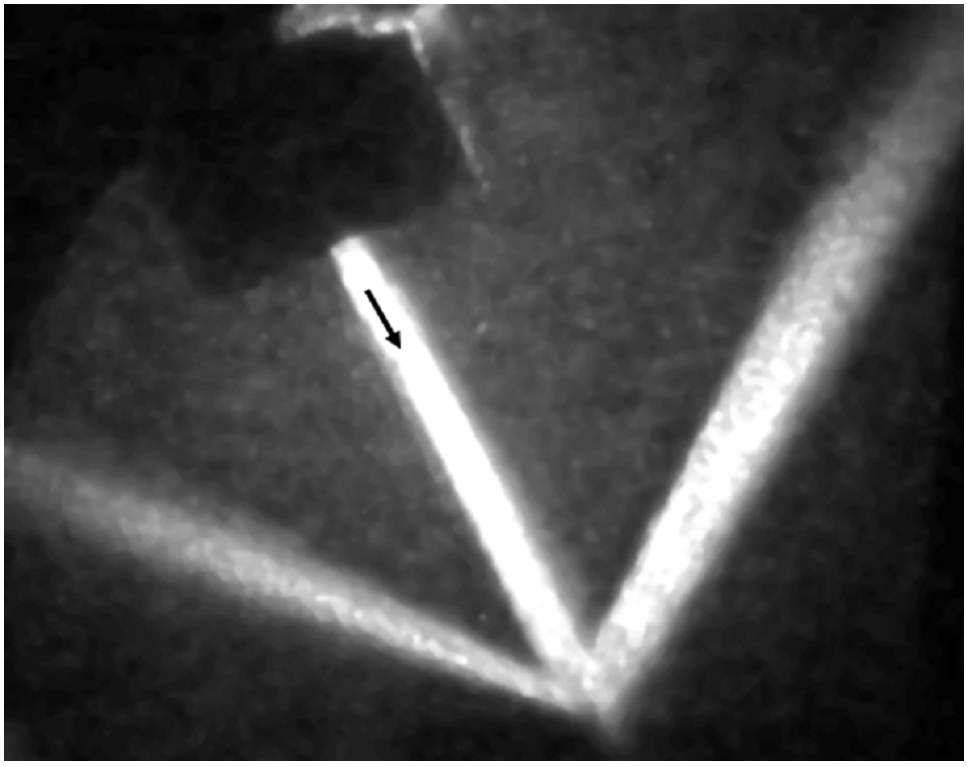

Fig. X.A.1.b_3: ***Schlieren image of a 6mm wide ultrasonic beam incident upon a brass reflector at a certain angle of incidence different from any critical angle.***

As the incident angle approaches 22.5°, in Fig. X.A.1.b_4, the first order diffracted beam approaches the tangent to the surface; also, illumination of the top surface of the brass reflector is

visible. As is seen on the left of the figure, the illumination extends beyond the left edge of the corrugated sample. In fact, the illumination is caused by a surface wave that is scattered in the forward direction when reaching the edge of the sample. This suggests that the generated surface wave is of the Scholte–Stoneley type. According to Briers et al [9], such a surface wave is scattered primarily forward when reaching the edge of a plate.

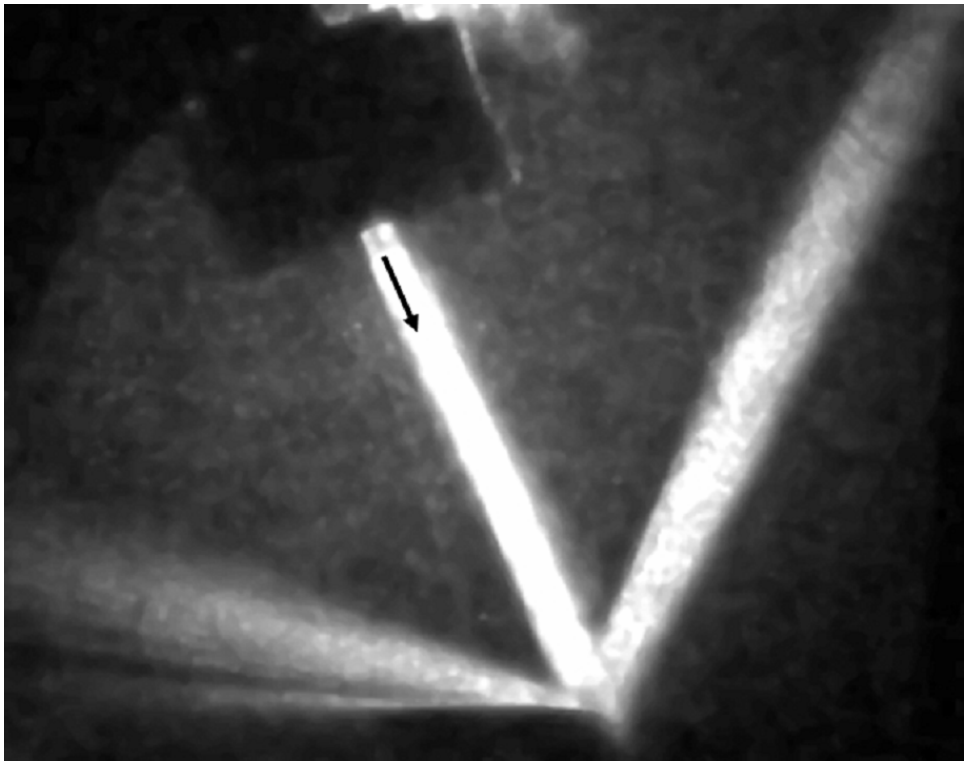

Fig. X.A.1.b_4: ***Schlieren image of a 6 mm wide ultrasonic beam incident upon a brass reflector at an angle of incidence slightly larger than 22.5^o; besides a diffracted beam near the interface, a sound beam is visible that propagates along the interface, being scattered in the forward direction at the extremity of the sample.***

Fig. X.A.1.b_5 shows the schlieren image in the case of a bounded beam incident at exactly 22.5°. Although illumination of the surface is still visible, a distinct backward displacement is not observed because the incident beam is much narrower than that in the original experiments of Breazeale and Torbett [5]. This phenomenon was predicted by Declercq et. al. [6] Furthermore, they predicted that the backward displacement occurs naturally for wide beams, as is seen in Fig. X.A.1.b_6, for a 12 mm wide beam. For narrow beams they also showed that at angles around 44° either forward or backward propagating leaky Rayleigh waves can be generated. Narrow beams are more likely to show variations of the beam profile at this angle. Indeed, in Fig. X.A.1.b_7 we see that alterations of the beam profile of the reflected bounded beam are visible for a narrow beam of 6 mm width. For the wider beam they were not observed [5].

As described, when the angle of incidence is equal to the angle of 22.5°, a reflected wide beam is laterally displaced backwards to a sizable extent as is shown in Fig. X.A.1.b_6. As can be seen from Figs. X.A.1.b_3-5, the ultrasonic phenomenon is a diffraction phenomenon, so the mathematical representation of the experiments by means of diffraction of inhomogeneous waves to account for backward beam displacement seems appropriate.

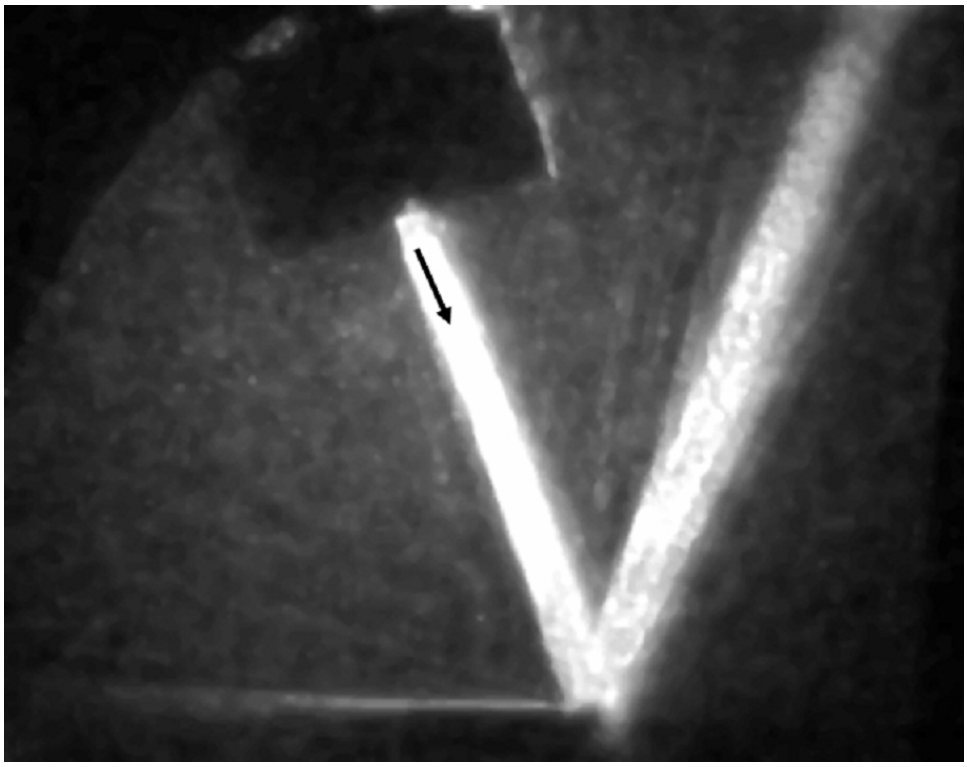

Fig. X.A.1.b_5: ***Schlieren image of a 6 mm wide ultrasonic beam incident upon a brass reflector at 22.5^{o}; a sound field is visible on the interface in the backward direction, being scattered in the forward direction at the extremity of the sample. This is evidence that it is a Scholte – Stoneley wave.***

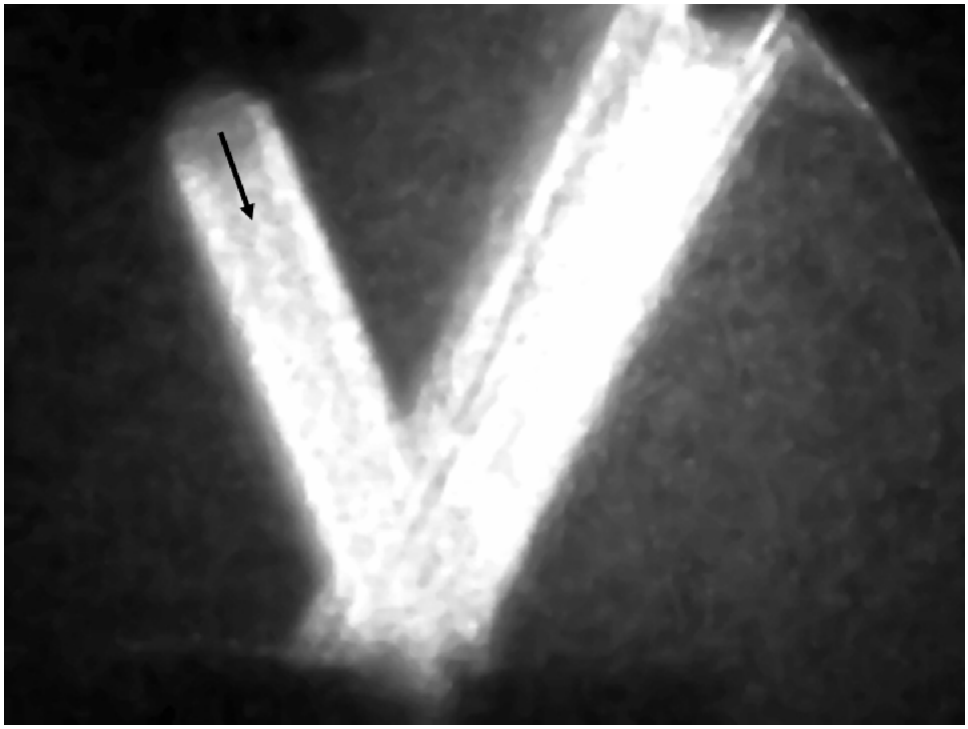

Fig. X.A.1.b_6: ***Same situation as in Fig. X.A.1.b_5, except that the width of the incident beam is now 12 mm.***

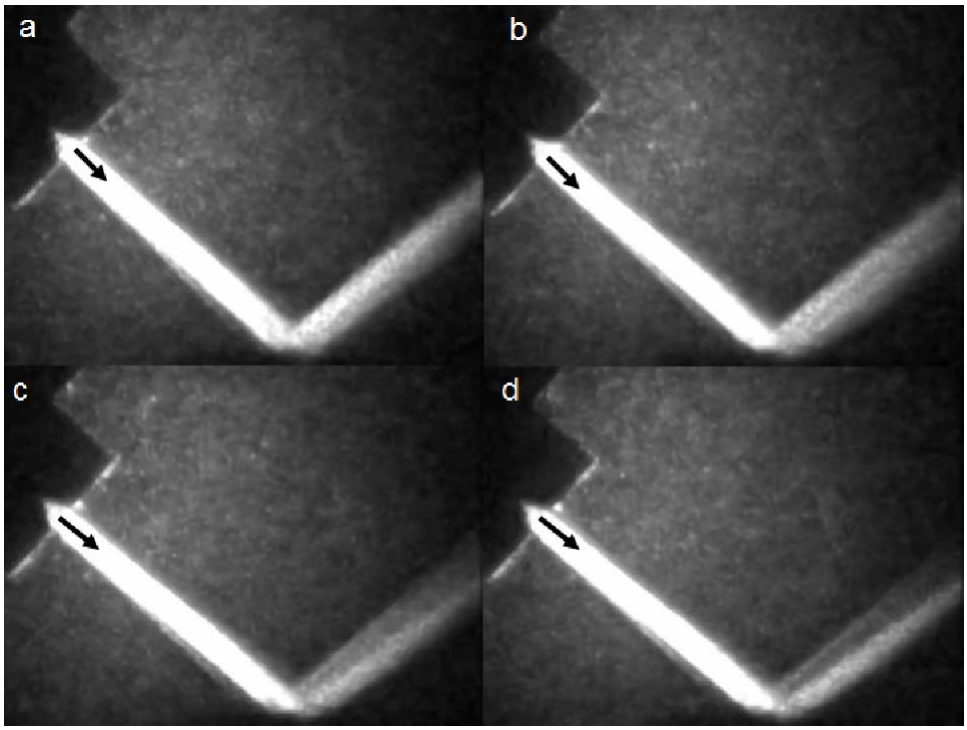

Fig. X.A.1.b_7: ***Schlieren pictures of a 6 mm wide bounded beam, incident at angles in the vicinity of 45. Changes of the reflected beam's profile are visible.***

It is known that for a bounded ultrasonic narrow beam incident on a water-brass interface, the condition for total internal reflection is given by [5]

$$\sin\theta_i = \frac{1}{K_{liq}}\left(\frac{2\pi}{d} - K_R\right) = V_{liq}\left(\frac{1}{fd} - \frac{1}{V_S}\right) \qquad \text{(X.A.1.b\_1)}$$

where d is the period, f is the frequency, V_{liq} is the propagation velocity in the liquid, and V_S is the propagation velocity of the leaky wave. At this angle, the incident beam interacts strongly with the leaky-wave field since it is phase matched to one of the space harmonics of the leaky wave. This interaction leads to an additional reflected beam which is laterally displaced in the negative x direction. (Note that the right-hand-side of Equation 1 can become greater than unity for certain values of the frequency f corresponding to an imaginary angle of incidence, at which angle the phenomenon of backward displacement is not observed.)

Using the measured values of θ_i = 22.5°, d = 0.178 mm and V_{liq} = 1490 m/s, one calculates, using Equation 1, the propagation velocity of the leaky surface wave V_S = 1470 m/s. This value is considerably smaller than the propagation velocity of leaky Rayleigh wave (2015 m/s) and is reasonable for a Scholte–Stoneley wave. Nevertheless, its influence on the reflected beam can only be explained by considering it to be of the leaky type, again in agreement with ref [7].

POSSIBLE APPLICATIONS

Scholte-Stoneley waves are excellent tools to examine the smooth surface and subsurface region of a solid immersed in water. Their basic advantages are a small penetration depth and propagation without energy loss over large distances. Nevertheless, they are hard to generate. One of the techniques of Scholte-Stoneley wave generation is the use of a small diffraction grating created on the smooth surface. Only normal incidence has been studied in detail; however, for some applications in the field of nondestructive testing or in underwater acoustics, normal incidence is not realizable—then oblique incidence is required. It is shown [10] that the generation of Scholte-Stoneley waves is possible for oblique incidence in the forward direction and it is explained [7] that for oblique incidence, stimulation of Scholte-Stonely waves is less outstanding, and actually only results in a leaky form of these waves. The current section proves for oblique incidence, that Scholte-Stoneley waves are indeed leaky, and that it is possible to generate them in the backward direction—resulting in the backward beam displacement. This phenomenon is of interest when backward-propagating Scholte-Stoneley waves are to be generated in a situation where only forward oblique incidence is possible.

CONCLUSIONS

The experiments of Breazeale and Torbett [5] have been verified. When sound is incident on a corrugated brass surface backward beam displacement can be observed. This backward displacement appears at 22.5°, rather than 41°, as predicted by the theory of Tamir and Bertoni [2]. Present experiments show that there is a generation of some other type of surface wave with a velocity far below that of a Rayleigh wave. This work confirms the excitation of a leaky surface wave at 22.5°, and provides visual evidence that it exhibits the behavior expected by a Scholte – Stoneley type of wave[7,9], in agreement with the theory developed by Declercq et. al. [6,7]

The narrow beam predictions of Declercq et. al. [7] also are verified. A beam of 6 mm in width (as opposed to the 10 mm beam used in the original experiments of Breazeale and Torbett [5]) cause the excitation of a leaky Rayleigh wave for angles of incidence near 44°, which is near the angle predicted by Tamir and Bertoni. [5]

The backward beam displacement is accompanied by backward propagating leaky Scholte – Stoneley waves, which is of interest in nondestructive testing when only oblique incidence is feasible in the forward direction.

REFERENCES

[1] Von F. Goos and H. Hänchen, Annalen der Physik., vol. **6**. No. 1, 333-64 (1947)
[2] T. Tamir and H. L. Bertoni, J. Acoust. Soc. Am. **61**, 1397-1413 (1971)
[3] A. Schoch, Nuovo Cimento (Suppl.) **7**, (9), 302 (1950)
[1] Schoch, Acustica **2**, 1 (1952)
[4] M. A. Breazeale and Michael A. Torbett, Appl. Phys. Lett. **29**, 456 (1976)
[5] N. F. Declercq, J. Degrieck, R. Briers, and O. Leroy, Appl. Phys. Lett., **82** (15), 2533-2535 (2003)
[6] Nico F. Declercq, Joris Degrieck, Rudy Briers, Oswald Leroy, "Theory of the backward beam displacement on periodically corrugated surfaces and its relation to leaky Scholte-Stoneley waves", J. Appl. Phys. 96(11),

6869-6877, 2004 - Nico F. Declercq, Rudy Briers, Joris Degrieck, Oswald Leroy, J. Acoust. Soc. Am. 112(5), 2414, 2002
[7] Marc Deschamps, J. Acoust. Soc. Am. **96**, 2841-48 (1994)
[8] R. Briers, O. Leroy, and G. N. Shkerdin, J. Acoust. Soc. Am. 101(3), 1347-1357, 1997
[9] James E. A. John, Gas Dynamics, Allyn & Bacon Inc., Boston, p. 341 (1969).
[10] Nico F. Declercq, Rudy Briers, Joris Degrieck, Oswald Leroy, IEEE trans. on UFFC 49(11), 1516-1521, 2002

X.A.1.c Note on the Diffraction Field Generated by Inhomogeneous Waves Obliquely Incident on a Periodically Rough Liquid-Solid Boundary

It is shown by Deschamps [J. Acoust. Soc. Am. 96(5), 2841-2848, 1994] that when inhomogeneous waves scatter from a plane interface, one should make an appropriate choice of the sign of the corresponding wave vectors. In an article of Briers et al [J. Acoust. Soc. Am. 106(2), 682-687, 1999], an extension of that sign rule is incorporated, in order to meet the requirements of correspondence of the theory of diffraction on periodically corrugated surfaces, with experimentally obtained data. The current section states that the extension is not necessary and that the rule of Deschamps can be applied as it is in order to meet agreement between theory and experiment.

INTRODUCTION

A corrugated interface between a liquid and a solid is depicted in Fig. X.A.1.c_1. The article of Briers et al [2] has proved to be very valuable as experimental evidence for the existence of physical phenomena that are predicted by the inhomogeneous wave theory, such as a reflection coefficient exceeding unity, and diffraction phenomena in the regime where the Rayleigh assumption for diffraction holds [2-4] This Rayleigh assumption is extensively explained in [2-4] and is in fact the decomposition of the diffracted sound field into pure and inhomogeneous plane waves, governed by the continuity of normal stress and displacement and by the generalized diffraction equation as well as the dispersion relation for inhomogeneous waves. Ref [2] also proved the validity of the generalized diffraction equation for complex valued wave vectors.
For smooth interfaces, the law of Snell-Descartes [5-23] holds and demands continuity of the incident and scattered complex wave vectors along the interface. The components perpendicular to the interface are often, especially in the pure homogeneous plane wave theory, chosen as to meet the causality principle stating that all diffracted waves must propagate away from the interface and the Sommerfeld condition stating that pure evanescent surface waves must show amplitude decay away from the interface. Deschamps [1] however shows that Sommerfeld's condition and the causality principle do not always have to be fulfilled if incident bulk inhomogeneous waves are considered.

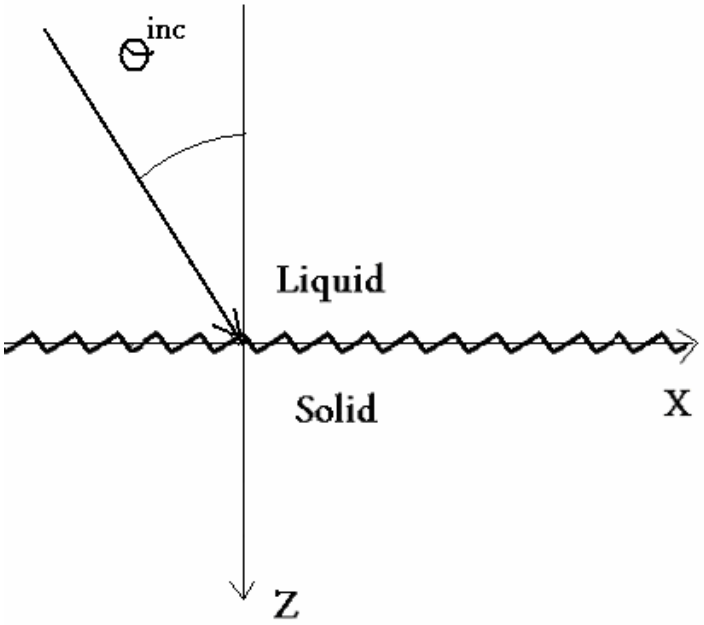

Fig. X.A.1.c_1: ***Schematic of the corrugated surface with incidence from the liquid side***

He states that the theory of the scattering of inhomogeneous waves can solely correspond fully with observations if the sign of the wave vector of a transmitted inhomogeneous wave is chosen to be 'leaky Rayleigh wave'-like whenever the direction of propagation is almost parallel to the interface. Furthermore, Deschamps states that 'almost parallel' is fulfilled whenever an incident plane wave that would generate a transmitted plane wave in the same direction as the transmitted inhomogeneous wave, would be incident at an angle beyond the critical angle for that particular transmitted mode. In the article of Briers et al [2], a sign choice is proposed in the theoretical treatment of diffraction on corrugated surfaces, that leads to almost perfect correspondence with experiments, but that differs from the sign choice in the article of Deschamps [1], because also the sign of the wave vectors of the reflected inhomogeneous waves are to be reversed beyond a critical angle. Mathematically, this extension of Deschamps' rule [2] is appropriate since it predicts the phase and the amplitude of the reflected waves rather well, however in what follows, we show that such an extension is not mandatory. Hence, the scientific requirement, that, physical principles for corrugated surfaces must become equal to those for plane surfaces in the limit of the corrugation height tending to zero, forces us to replace the extended rule [2].

THE SIGN CHOICE UNDER CONSIDERATION

In the referred article [2], the sign choice follows the causality principle and Sommerfeld's rule for each diffracted order m and for each mode p ($p=s$ for transmitted shear, $p=d$ for transmitted longitudinal, $p=r$ for reflected longitudinal waves) involving a (complex) angle $\theta^{p,m}$ that is defined by the diffraction equation for an incident homogeneous plane wave coming from the same angle of incidence as the incident inhomogenous wave [2]. If however for an order m and mode p

$$\left|\sin\theta^{p,m}\right| > 1 \qquad \text{(X.A.1.c\_1)}$$

Then the sign of the *z*-component of the corresponding wave vector should be reversed, also if the respective mode is a reflected wave. On plane interfaces, reversion of the reflected *z*-component of the wave vector never occurs for incident inhomogeneous waves [1]. Even if, on corrugated surfaces, Scholte-Stoneley waves are excited (by incident homogeneous plane waves), Sommerfeld's relations do not need to be reversed [3-4].

A MORE APPROPRIATE SIGN CHOICE

We state that Deschamps' rule [1] for a plane interface does not need to be extended for a rough surface. Hence reflected sound should always propagate into the half space of incidence. If for a plane interface, we denote the incoming wave vector as

$$\mathbf{k}^{inc} = \mathbf{k}_1^{inc} - i\mathbf{k}_2^{inc} \tag{X.A.1.c_2}$$

For $\mathbf{k}_1^{inc}$ and $\mathbf{k}_2^{inc}$ being real wave vectors and $i = \sqrt{-1}$, then the angle of incidence is θ^{inc} with

$$\left|\theta^{inc}\right| = \arctan\left[\left|k_{1,x}^{inc}\right| \Big/ \left|k_{1,z}^{inc}\right|\right] \tag{X.A.1.c_3}$$

However, in order to use this rule also for corrugated surfaces, one should focus not on the angle of incidence (as is literally the case in the article of Deschamps [1]), but on the angle of reflection θ^r, which is the same as the angle of incidence in the case of plane surfaces. Then, Deschamps' rule [1] becomes:
always use the causality principle for transmitted waves of mode *p*, except whenever.

$$\left|\theta^r\right| > \left|\arcsin\left(v_l / v_p\right)\right| \tag{X.A.1.c_4}$$

In which v_l is the sound velocity in the liquid and v_p is the sound velocity of the transmitted mode under consideration. In the case of (X.A.1.c_4), the choice of the sign of $k_{2,z}^p$ must be chosen as to fulfill the condition for leaky Rayleigh waves, i.e. $\mathbf{k}_2^p$ must point into the liquid. It is important to note that $\mathbf{k}_2^p$ is accompanied by $\mathbf{k}_2^r$ and that the sign choice of $k_{2,z}^p$ is completely determined by the nature of its counterpart $\mathbf{k}_2^r$.
If these principles are used for corrugated surfaces, then we obtain that for a transmitted wave of mode *p* and of order *m,* the sign choice of $k_{2,z}^{m,p}$ is completely determined by the nature of its counterpart $\mathbf{k}_{2,z}^{m,r}$, i.e the causality principle holds except when

$$\left|\theta^{r,m}\right| = \arctan\left[\left|k_{1,x}^{r,m}\right| \Big/ \left|k_{1,z}^{r,m}\right|\right] > \left|\arcsin\left(v_l / v_p\right)\right| \tag{X.A.1.c_5}$$

Then, whenever (X.A.1.c_5) holds, the sign of $\mathbf{k}_{2,z}^{m,p}$ must be chosen as to be Rayleigh wave like, i.e. $\mathbf{k}_{2}^{m,p}$ must point into the liquid.

COMPARISON WITH EXPERIMENTAL DATA

We have taken experimental data form Briers et al [2]. We have implemented Deschamps rule as described above, without creating extensions such as in Briers et al [2] and performed calculations under exactly the same circumstances [2] (i.e. the same material parameters are used).
In Fig. X.A.1.c_2, the zero order reflection coefficient is depicted and can be compared with Fig. X.A.1.c_5 in Briers et al [2]. Fig. X.A.1.c_2a shows the amplitude of the calculated reflection coefficient (full line) and the experimentally observed one (depicted by circles). It is seen, that the theoretical values correspond quite as well to the experimental values as in the cited article [2]. Around -15^0 we even get better results. In Fig X.A.1.c_2b, we have plotted the experimental values of the phase in circles and the calculated phase in doted lines. We need to stress the fact that for each phase φ, we have also plotted $\varphi \pm 360^0$ in order to avoid misinterpretations such as 0^0 that seems very different from 360^0. It is seen that the calculated phase corresponds quite well to the experimentally observed phase. The latter would not have been the case if the traditional causality principles held in any situation as is very well stated by Briers et al [2].

CONCLUSIONS

It is shown that the Deschamps' rule [1] for scattering at plane interfaces can be used without extension for diffraction on corrugated surfaces. This is shown by a numerical calculation showing that the original Deschamps' rule [1] leads to equally well correspondence with experiments as the extended rule in the commented article [2]. The same principle has also been implicitly incorporated in ref [24] and lead to correspondence with other diffraction experiments as well.

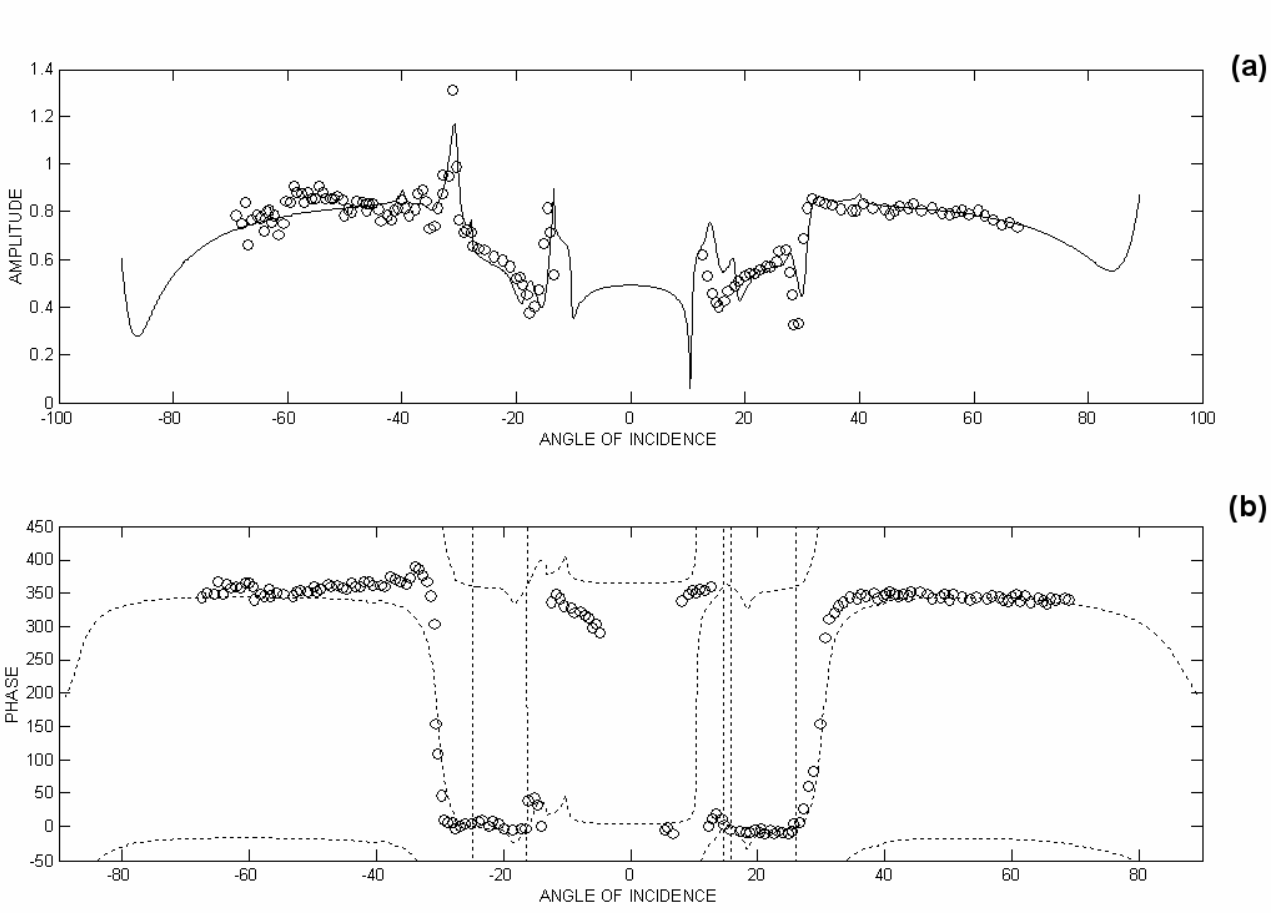

Fig. X.A.1.c_2: ***Comparison between experimentally obtained[2] zero order reflection coefficient and theoretical values, for angles of incidence ranging from -90^0 to $+90^0$. Fig. X.A.1.c_1a depicts the amplitude (circles=experimental values, full line=theoretical values), Fig. X.A.1.c_1b depicts the phase in degrees (circles=experimental values, dotted lines=theoretical values). For each angle of incidence, the theoretically obtained phase φ is accompanied by $\varphi \pm 360^0$.***

REFERENCES

[1] Marc Deschamps, "Reflection and refraction of the evanescent plane wave on plane interfaces", J. Acoust. Soc. Am. 96(5), 2841-2848, 1994

[2] R. Briers, O. Leroy, O. Poncelet, M. Deschamps, "Experimental verification of the calculated diffraction field generated by inhomogeneous waves obliquely incident on a periodically rough liquid-solid boundary", J. Acoust. Soc. Am. 106(2), 682-687, 1999

[3] J. M. Claeys, Oswald Leroy, Alain Jungman, Laszlo Adler, "Diffraction of ultrasonic waves from periodically rough liquid-solid surface", J. Appl. Phys. 54(10), 5657-5662, 1983

[4] K. Mampaert, O. Leroy, "Reflection and transmission of normally incident ultrasonic waves on periodic solid-liquid interfaces", J. Acoust. Soc. Am. 83 (4), 1390-1398, 1988

[5] Nico F. Declercq, and Joris Degrieck, Oswald Leroy, "On the generalized Snell's law and its possible relation to coherent backscattering of ultrasonic waves", in Press at Applied Physics letters

[6] M. Deschamps, O. Poncelet, "Inhomogeneous plane wave and the most energetic complex ray", Ultrasonics 40, 293-296, 2002

[7] Bruno Rogé, "Réflexion/transmission d'une onde plane inhomogene incidente sur une interface plane séparant deux milieux anisotropes", Thesis, Université de Technologie de Compiègne, France, 1999

[8] Bernard, M. Deschamps, M. J. S. Lowe, “Comparison between the dispersion curves calculated in complex frequency and the minima of the reflection coefficients for an embedded layer”, J. Acoust. Soc. Am. 107(2), 793-800, 2000
[9] M. Deschamps, F. Assouline, “Attenuation Along the Poynting Vector Direction of Inhomogeneous Plane Waves in Absorbing and Anisotropic Solids”, Acustica – Acta Acustica, 86, 295-302, 2000
[10] Ph. Boulanger, “Energy flux for damped inhomogeneous plane waves in viscoelastic fluids”, Wave Motion 28, 215-225, 1998
[11] Allard JF, Lauriks W, “Poles and zeros of the plane wave reflection coefficient for porous surfaces”, Acustica 83(6), 1045-1052, 1997
[12] O. Poncelet, M. Deschamps, “Lamb waves generated by complex harmonic inhomogeneous plane waves”, J. Acoust. Soc. Am., 102(1), 292-300, 1997
[13] Ph. Boulanger, M. Hayes, Bivectors and Waves in Mechanics and Optics (Chapman and Hall, London, 1993)
[14] Patrick Lanceleur, Helder Ribeiro, Jean-François De Belleval, “The use of inhomogeneous waves in the reflection-transmission problem at a plane interface between two anisotropic media”, J. Acoust. Soc. Am., 93(4), 1882-1892, 1993
[15] Chevée P., Deschamps M., Interaction of plane heterogeneous waves within a damping layer – comparison between theory and experiment”, ACUSTICA 76(5), 224-230, 1992
[16] Poirée B., “Velocity of energy-transport in an acoustic complex plane wave”, ACUSTICA 74(1), 63-68, 1991
[17] Jose Roux, “Reflection and refraction of heterogeneous waves at plane interfaces”, “Physical Acoustics : Fundamentals and Applications”, Edited by O. Leroy and M. Breazeale, 155-164, Plenum, New York and London, 1991
[18] Poirée, “Complex harmonic waves”, 99-117, *Physical Acoustics*, Edited by O. Leroy and M. A. Breazeale, Plenum Press, New York, 1991
[19] M. Deschamps, P. Chevée, “Reflection and refraction of a heterogeneous plane wave by a solid layer”, Wave Motion 15, 61-75, 1992.
[20] Gérard Quentin, André Derem, Bernard Poirée, “The formalism of evanescent plane waves and its importance in the study of the generalized Rayleigh wave”, J. Acoustique 3, 321-336, 1990
[21] M. Deschamps, J. Roux, “Some considerations concerning evanescent surface waves”, Ultrasonics 1991 (29), 283-287, 1991
[22] Bernard Poirée, Landry Sebbag, “Les lois de la réflexion-réfraction des ondes planes harmoniques évanescentes. I. Mise en équations”, J. Acoustique 4, 21-46, 1991
[23] Marc Deschamps, “Réflexion-réfraction de l’onde plane hétérogène : répartition de l’énergie”, J. Acoustique 3, 251-261, 1990
[24] Nico F. Declercq, Joris Degrieck, Rudy Briers, Oswald Leroy, "Theoretical verification of the backward displacement of waves reflected from an interface having superimposed periodicity", Appl. Phys. lett. 82(15), 2533-2535, 2003

X.A.1.d Diffraction of Complex Harmonic Plane waves and the Stimulation of Transient Leaky Rayleigh Waves

This section describes the interaction of complex harmonic plane waves with a periodically corrugated surface. It is shown that their ability to stimulate leaky Rayleigh waves on a corrugated surface is similar to the ability of harmonic inhomogeneous waves to stimulate such waves on a smooth interface. Because the experimental generation of harmonic inhomogeneous waves is more complicated and less flexible than the generation of complex harmonic waves, the combination with a diffraction grating therefore offers an excellent alternative. The theoretical model developed here is based on the well know and experimentally verified complex harmonic wave theory and the famous Rayleigh decomposition of the diffracted field. The numerical examples are given for combinations of frequency and corrugation dimensions that justify the use of the Rayleigh theory. A study of the influence of a complex frequency on the generation of Scholte – Stoneley waves is performed as well.

INTRODUCTION

In the 1980's a lot of attention was drawn on the use of Scholte – Stoneley waves for nondestructive testing purposes. Such waves possess the important feature of propagation along a solid-liquid interface with only minor damping, because their velocity is lower that the velocity of sound in the bulk of both surrounding media, whence no radiation happens. Hence, Scholte – Stoneley waves are excellent tools for long distance nondestructive testing. The main problem however is their experimental generation. The same reason why they do not radiate into the surrounding media is the reason why they cannot be generated by means of incident sound, at least not on smooth surfaces. One method to avoid this problem is the use of a periodically corrugated surface. Then, Scholte – Stoneley waves can be generated by means of diffraction. This phenomenon has been studied in great extent before [1-9]. In this section, we use the term harmonic (homogeneous) plane wave for a classical sinusoidal plane wave, i.e. a plane wave determined by a real wave vector and a real frequency. When the wave vector is complex valued, we use the term inhomogeneous wave or harmonic inhomogeneous wave. Furthermore, we use the term complex harmonic plane wave for the case when the frequency is complex valued and the wave vector is real. For complex harmonic plane waves having a complex valued wave vector as well, we explicitly use the term complex harmonic inhomogeneous wave. It is widely accepted that it is possible to stimulate leaky Rayleigh waves on smooth interfaces by means of harmonic inhomogeneous waves incident at the Rayleigh angle [10-14]. Harmonic inhomogeneous waves are plane waves which amplitude shows exponential decay along the wave front but not in the time domain. Furthermore, similar to the case of smooth interfaces, these waves are able to stimulate leaky Rayleigh waves on periodically corrugated surface for normal incidence [15-19]. The main problem however has always been that the experimental generation of inhomogeneous waves is not quite convenient. More precisely, all methods of generation are based on rigid and

complicated experimental setups and are expensive and time consuming [16, 19-20], because for each requested inhomogeneous wave different equipment is necessary.
The generation of complex harmonic plane wave is simpler and is much more flexible [21-25]. The theoretical model and the numerical simulations in this section are based on two well established theories, i.e. the theory of complex harmonic waves and the Rayleigh theory of sound diffraction on periodically rough surfaces. The theory of complex harmonic waves is based on complex solutions of the wave equation, they have also been generated experimentally [21-25]. The Rayleigh theory of sound diffraction on periodically rough surfaces, is also well established and is actually a simplified approach of more complicated models such as the differential [26-27] and integral equation approach [28-32] and the Waterman theory [33-37]. We apply the Rayleigh theory because of two important reasons, first the theory is convenient to include complex harmonic and inhomogeneous waves, second, it has been shown by Wirgin [38], that "contrary to prevailing opinion, the Rayleigh theory is fully capable of describing the scattering phenomena produced by a wide class of corrugated surfaces, including those whose roughness is rather large". Furthermore, Wirgin [38] proves that the Rayleigh theory is valid, for λ the largest wavelength involved in the diffraction phenomenon, for Λ the corrugation period and for h the corrugation height, whenever

$$h < 0.34\Lambda \qquad \text{(X.A.1.d\_1)}$$

and

$$\lambda > 1.53348h \qquad \text{(X.A.1.d\_2)}$$

In this section it will be shown that, similar to harmonic inhomogeneous waves, complex harmonic waves are excellent tools for stimulating (transient) leaky Rayleigh waves on periodically corrugated surfaces. Furthermore it will be shown that this stimulation effect is absent on smooth surfaces.

TRANSIENT HARMONIC PLANE WAVES

It is well known that plane waves are a solution of the wave equation in visco-elastic media [25]. Plane waves are described by a displacement vector **u** as follows:

$$\mathbf{u} = A\mathbf{P}\exp\left(i\mathbf{k}\bullet\mathbf{r} - i\omega t\right) \qquad \text{(X.A.1.d\_3)}$$

Besides time t and space **r**, all parameters in (X.A.1.d_3), i.e. the amplitude A, the polarization **P**, the wave vector **k** and the angular frequency ω can be complex valued [21-25]. The nomenclature for the different kinds of possible plane waves is found in Table X.A.1.d_I.
In the case that

$$\omega = \omega_1 + i\omega_2 \qquad \text{(X.A.1.d\_4)}$$

and

$$\mathbf{k} = \mathbf{k}_1 + i\mathbf{k}_2 = \mathbf{k}_1 + i(\boldsymbol{\alpha} - \boldsymbol{\beta}) \tag{X.A.1.d_5}$$

Table X.A.1.d_I: ***Different plane wave definitions depending on the values of k and ω***

k	ω	nomenclature
real	real	harmonic (homogeneous) plane wave
real	complex	complex harmonic (homogeneous) plane wave
complex	real	(harmonic) inhomogeneous wave
complex	complex	complex harmonic inhomogeneous wave

with $\boldsymbol{\alpha} \parallel \mathbf{k}_1$ and $\boldsymbol{\beta} \perp \mathbf{k}_1$, it can be verified that

$$\mathbf{u} = A\mathbf{P}\exp(\omega_2 t)\exp(-\boldsymbol{\alpha}\bullet\mathbf{r})\exp(\boldsymbol{\beta}\bullet\mathbf{r})\exp i(\mathbf{k}_1\bullet\mathbf{r} - \omega_1 t) \tag{X.A.1.d_6}$$

In (X.A.1.d_6) it is noticed that k_1 and ω_1 influence the vibration itself, while all other parameters influence the amplitude attributed to that vibration. The parameter k_1 is called the propagation wave vector, ω_1 is the real angular frequency, $\boldsymbol{\alpha}$ is called the damping vector, while $\boldsymbol{\beta}$ is called the inhomogeneity vector. The parameter ω_2 determines the transient feature of the wave under consideration and is called the source parameter. If it is positive, the wave is amplified in time, if it is negative, the wave diminishes in time. Important to remark is the fact that a first glimpse on (X.A.1.d_6) shows that the amplitude of **u** changes instantaneously throughout space. If for each instant of time the amplitude would be the same everywhere, then an instantaneous change throughout space would be a violation of the principle of energy conservation (energy cannot just vanish or appear) and also a violation of the fact that no signal can ever be transported faster than the speed of light under the assumption that time and space are real quantities. Therefore it is necessary to demand that expression (X.A.1.d_3) must be a solution of the wave equation [21-25]. For visco-elastic media, this means that the dispersion relation must hold [21-25], i.e.

$$\mathbf{k}\bullet\mathbf{k} = \left(\frac{\omega}{v_b} - i\alpha_{0,b}\right)^2 \tag{X.A.1.d_7}$$

where $b=d$ for longitudinal waves or $b=s$ for shear waves. v_b is the phase velocity for harmonic homogeneous plane waves (i.e. having a real wave vector and real frequency) and $\alpha_{0,b}$ is the intrinsic damping coefficient.

It is precisely this dispersion relation that relates the phase velocity and the amplitude distribution in space to the real angular frequency ω_1 and the source parameter ω_2. Even though the effect of (X.A.1.d_7) on sound waves is mathematically covered in [21-25], it is interesting to find out what the physical consequences are. The effect of (X.A.1.d_7) on a transient wave with respect to time is the description of the amplitude migration in space as a function of time. Let's consider a transient plane wave having an inhomogeneity vector **β** different from zero and propagating along the z-axis. Then if we plot the amplitude along the x-axis as a function of time, we get something like in Fig. X.A.1.d_1 where the amplitude changes exponentially along the x-axis due

to **β**, but also changes exponentially in time. This amplitude change in time can easily be interpreted as a position shift in time to the right or to the left, depending on the value of ω_2 and the inhomogeneity **β**. Hence the effect of ω_2 should be interpreted as the effect of lateral amplitude migration in time. In the case that also **α** differs from zero, this amplitude migration also occurs in the direction of phase propagation.

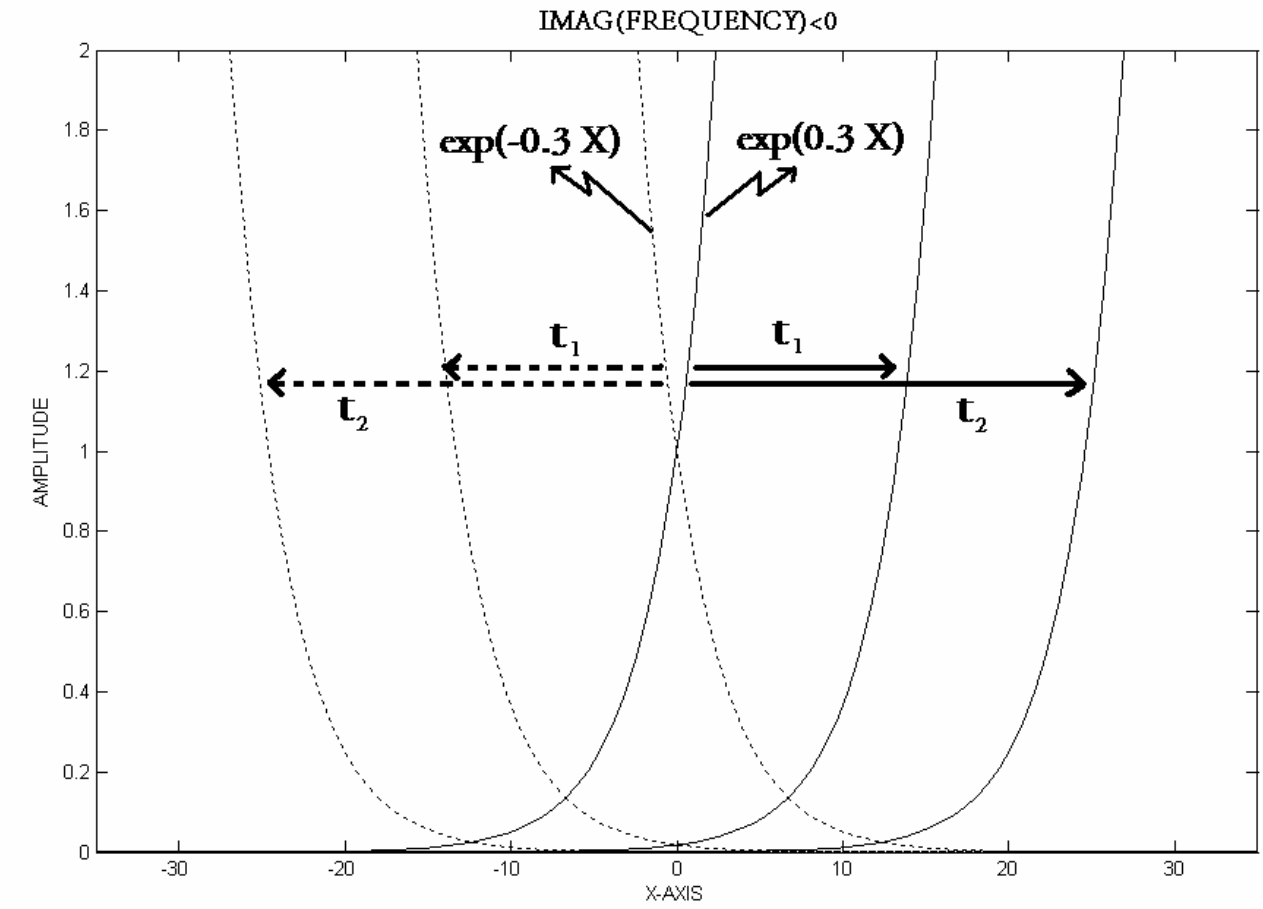

Fig. X.A.1.d_1: ***Schematic view of the amplitude migration that occurs, as time passes, of a complex harmonic inhomogeneous wave. The amplitude along the wave front is depicted at different instants and for positive and negative inhomogeneity.***

If **β**=0 then the dispersion relation makes sure that **α** differs from zero, whence there is amplitude migration along the phase propagation direction. This amplitude migration prevents physical impossibilities such as magical (dis)appearance of energy as described before.
Whenever sound is transmitted/reflected at a smooth interface between two different media, it is necessary to determine in what direction the vector **k** is pointing for each of the generated waves. For smooth surfaces, the lateral direction is always determined by the well known generalized Snell's law, which states that along the interface there is continuity of the complex wave vector and that the complex frequency remains unchanged [25], but the component perpendicular to the interface must be chosen carefully. We will show that this choice must be performed with consideration of the energy propagation no matter what this means for the wave vector itself. The reason is that the wave vector itself is not of primordial importance to determine what happens to

a sound wave, since amplitude migration due to the source parameter ω_2 must be considered as well. For that reason it is convenient to work with the slowness vector

$$\mathbf{k} = \omega \mathbf{S} \tag{X.A.1.d_8}$$

whence

$$\begin{aligned} \mathbf{k}_1 &= \omega_1 \mathbf{S}_1 - \omega_2 \mathbf{S}_2 \\ \mathbf{k}_2 &= \omega_2 \mathbf{S}_1 + \omega_1 \mathbf{S}_2 \end{aligned} \tag{X.A.1.d_9}$$

It has been shown by Deschamps, Poirée and Poncelet [22] that the vector corresponding to the energy velocity is given by

$$\mathbf{v}_E = \frac{\mathbf{S}_1}{\mathbf{S}_1 \bullet \mathbf{S}_{ph}} \tag{X.A.1.d_10}$$

with phase slowness vector $\mathbf{S}_{ph}$ given by

$$\mathbf{S}_{ph} = \frac{\mathbf{k}_1}{\omega_1} \tag{X.A.1.d_11}$$

This shows that the energy propagates in the direction of $\mathbf{S}_1$, i.e.

$$\mathbf{v}_E \simeq \frac{\mathbf{k}_2 \omega_2 + \omega_1 \mathbf{k}_1}{\omega_1^2 + \omega_2^2} \tag{X.A.1.d_12}$$

From a numerical point of view, if one considers the dispersion relation (X.A.1.d_7) and also Snell's law for smooth interfaces (or the grating equation in the case of corrugated surfaces, see further below), only the exact value of the wave vector of diffracted waves along the interface is determined. For the component perpendicular to the interface only the complex magnitude is determined and not the sign that is to be attributed to that magnitude. For inhomogeneous waves having a real frequency, this choice has been discussed and determined before [17, 39-42], i.e. reflected waves must always propagate away from the interface, while the same holds for transmitted waves, given the fact that the reflected companion (of the same order m) propagates at an angle below the critical angle for the transmitted wave under consideration. If this reflected companion propagates at an angle beyond the critical angle, then the transmitted wave under consideration must propagate towards the interface. Furthermore, whenever a diffracted wave is evanescent, i.e. having a real wave vector component along the interface and an imaginary wave vector component perpendicular to the interface, then exponential amplitude decay away from the interface must be imposed [1,6]. Now for the case of transient waves, we have translated all of these sign choice principles to energy propagation directions instead of just (phase) propagation

directions. We have then adapted the sign choice of the wave vector to the correct corresponding sign choice of the energy propagation vector. The reason is that the real part of the wave vector does not determine the energy propagation on its own (as in the case of harmonic inhomogeneous plane waves in isotropic media), but only in combined action with the source term ω_2 .

THE SYSTEM OF EQUATIONS

Description of the Incident and the Diffracted Wave Field

Let's consider a periodically corrugated interface between a liquid and a solid as depicted in Fig. X.A.1.d_2. The corrugation is periodic with period Λ and is given by

$$g(x,z) = f(x) - z = 0 = g(x+\Lambda, z) \qquad \text{(X.A.1.d\_13)}$$

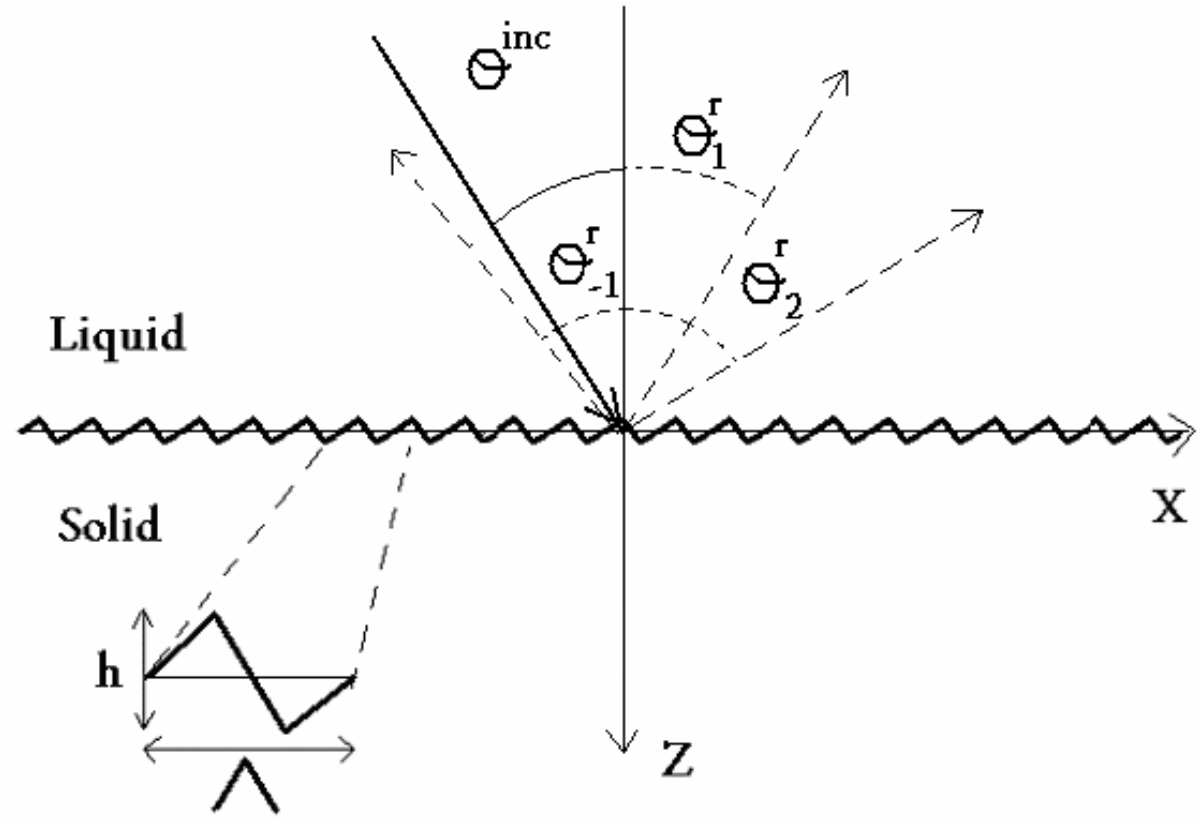

Fig. X.A.1.d_2: ***Schematic view of the considered corrugated interface. The different reflection angles are schematically shown for different diffraction orders and for obliquely incident sound.***

We take into account the Rayleigh decomposition [1-9, 15-19, 38, 46-47] of the diffracted wave field and also characteristics of longitudinal and shear waves, whence the displacement of the incident waves $\mathbf{N}^{inc}$, the (longitudinal) reflected waves $\mathbf{N}^{r}$, the longitudinal respectively shear waves in the solid $\mathbf{N}^{d}$ and $\mathbf{N}^{s}$, are written as

$$\mathbf{N}^{inc} = A^{inc}\varphi^{inc}\left(ik_x^{inc}\mathbf{e}_x + ik_z^{inc}\mathbf{e}_z\right) \tag{X.A.1.d_14}$$

$$\mathbf{N}^{r} = \sum_m A_m^r\varphi^{m,r}\left(ik_x^{m,r}\mathbf{e}_x + ik_z^{m,r}\mathbf{e}_z\right) \tag{X.A.1.d_15}$$

$$\mathbf{N}^{d} = \sum_m A_m^d\varphi^{m,d}\left(ik_x^{m,d}\mathbf{e}_x + ik_z^{m,d}\mathbf{e}_z\right) \tag{X.A.1.d_16}$$

$$\mathbf{N}^{s} = \sum_m A_m^s\mathbf{P}^{m,s}\varphi^{m,s} \tag{X.A.1.d_17}$$

with

$$\varphi^{\varsigma} = \exp i\left(\mathbf{k}^{\varsigma}\bullet\mathbf{r}\right) \tag{X.A.1.d_18}$$

and

$$k_x^{m,s}P_x^{m,s} + k_y^{m,s}P_y^{m,s} + k_z^{m,s}P_z^{m,s} = 0 \tag{X.A.1.d_19}$$

The index ‘m’ denotes the diffraction order and ς represents “inc”, “m,r”, “m,d” or “m,s”. The properties of transient waves as described in previous paragraph are taken into account, except for Snell’s law. When diffraction occurs, Snell’s law needs to be replaced by the generalized grating equation [15-19, 25]:

$$k_x^{m,b} = k_x^{inc} + m\frac{2\pi}{\Lambda} \tag{X.A.1.d_20}$$

With $b=r$ for the reflected field in the liquid and $b=d$ or $b=s$ for the transmitted longitudinal respectively shear waves in the solid. Equation (X.A.1.d_20) shows that only the real part of the lateral wave vector component is affected by the grating, not the imaginary part, whereas if we rewrite (X.A.1.d_20) in the slowness vector components (see (X.A.1.d_8)),

$$S_{1,x}^{m,b} = S_{1,x}^{inc} + m\frac{2\pi\omega_1}{\Lambda\left(\omega_1^2+\omega_2^2\right)} \tag{X.A.1.d_21}$$

$$S_{2,x}^{m,b} = S_{2,x}^{inc} - m\frac{2\pi\omega_2}{\Lambda\left(\omega_1^2+\omega_2^2\right)} \tag{X.A.1.d_22}$$

Equation (X.A.1.d_22) shows that the imaginary part of the lateral component of the slowness vector is affected by the grating.
To summarize, each wave in the Rayleigh decomposition of the diffracted field is characterized by a wave vector component along the interface determined by the grating equation (X.A.1.d_20) and a wave vector component perpendicular to the interface, having a value determined by the wave equation (through dispersion relation (X.A.1.d_7)) and a sign determined by the causality principle. However, each wave must also have an amplitude that is determined by continuity conditions. This is explained in the next section.

The Continuity Conditions

In media τ ($\tau = 1$ in the liquid, $\tau = 2$ in the solid) the stress tensor T^{τ} is given [43-44] by its elements

$$T_{ij}^{\varsigma} = \sum_{\eta}\left(\lambda_1^{\tau} + \lambda_2^{\tau}\frac{\partial}{\partial t}\right)\varepsilon_{\eta\eta}^{\tau}\delta_{i,j} + 2\left(\mu_1^{\tau} + \mu_2^{\tau}\frac{\partial}{\partial t}\right)\varepsilon_{i,j}^{\tau} \qquad \text{(X.A.1.d\_23)}$$

in which the strain tensor ε_{ij}^{τ} is

$$\varepsilon_{ij}^{\tau} = \frac{1}{2}\left[\partial_i N_j^{\tau} + \partial_j N_i^{\tau}\right] \qquad \text{(X.A.1.d\_24)}$$

The Lamé constants are denoted by λ_1^{τ} and μ_1^{τ}, while the viscosity coefficients are given by λ_2^{τ} and μ_2^{τ}. They accomplish the dispersion relation (X.A.1.d_7) if

$$\mathbf{k}^{\varsigma} \bullet \mathbf{k}^{\varsigma} = \frac{\rho\omega^2}{\left(\lambda_1^{\tau} - i\omega\lambda_2^{\tau}\right) + 2\left(\mu_1^{\tau} - i\omega\mu_2^{\tau}\right)} = \left(\frac{\omega}{v_d} - i\alpha_{0,d}\right)^2 \qquad \text{(X.A.1.d\_25)}$$

for longitudinal waves (ς = “inc” or “m,r”, in the liquid and ς = “m,d” or “m,s” in the solid) and if

$$\mathbf{k}^{\varsigma} \bullet \mathbf{k}^{\varsigma} = \frac{\rho\omega^2}{\left(\mu_1^{\tau} - i\omega\mu_2^{\tau}\right)} = \left(\frac{\omega}{v_s} - i\alpha_{0,s}\right)^2 \qquad \text{(X.A.1.d\_26)}$$

for shear waves ($\varsigma = s,2$ in the solid). In order to find the unknown coefficients A_m^r, A_m^d, $A_m^s P_x^{m,s}, A_m^s P_y^{m,s}, A_m^s P_z^{m,s}$, the equations that describe the continuity of normal stress and strain along the interface (X.A.1.d_13) need to be solved, i.e.

$$\left(\mathbf{N}^{inc}+\mathbf{N}^{r}\right)\bullet\nabla g=\left(\mathbf{N}^{d}+\mathbf{N}^{s}\right)\bullet\nabla g \text{ along } g=0 \qquad \text{(X.A.1.d\_27)}$$

$$\sum_j T_{ij}^{1}\left(\nabla g\right)_j=\sum_j T_{ij}^{2}\left(\nabla g\right)_j \text{ along } g=0 \qquad \text{(X.A.1.d\_28)}$$

and also, because for shear waves the complex displacement is perpendicular to the complex wave vector

$$\left(A_m^s P_x^{m,s} k_x^{m,s}+A_m^s P_y^{m,s} k_y^{m,s}+A_m^s P_z^{m,s} k_z^{m,s}\right)\varphi^{m.s}=0 \qquad \text{(X.A.1.d\_29)}$$

Conditions (X.A.1.d_27-29) lead to 5 equations that are periodic in x, whence a sufficient condition for a correct solution is that the Fourier coefficients (for a discrete Fourier transform over the interval $[0\to\Lambda]$) of the left and right sides of the equations are equal to each other. The wave vectors that are introduced by this discrete Fourier transform are denoted by the order 'p'. The 5 equations for each integer *p* are:

Equation 1:

$$\begin{aligned}
&A^{inc} I^{inc,p}{}_i\left(-\mathbf{k}^{inc}\bullet\mathbf{k}^{inc}+k_x^{inc}k_x^{p}\right)\\
&+\sum_m A_m^r I^{m,r,p}{}_i\left(-\mathbf{k}^{inc}\bullet\mathbf{k}^{inc}+k_x^{m}k_x^{p}\right)\\
&+\sum_m A_m^d I^{m,d,p}{}_i\left(\mathbf{k}^{d,2}\bullet\mathbf{k}^{d,2}-k_x^{m}k_x^{p}\right)\\
&-\sum_m A_m^s P_x^{m,s} I^{m,s,p}\left(k_x^{p}-k_x^{m}\right)\\
&+\sum_m A_m^s P_z^{m,s} I^{m,s,p}\left(k_z^{m,s}\right)=0
\end{aligned} \qquad \text{(X.A.1.d_30)}$$

Equation 2:

$$-A^{inc} I^{inc,p} \rho_1 \left(k_x^p - k_x^{inc} \right) \qquad \text{(X.A.1.d\_31)}$$

$$-\sum_m A_m^r I^{m,r,p} \rho_1 \left(k_x^p - k_x^m \right)$$

$$+\sum_m A_m^d I^{m,d,p} \rho_2 \left(-k_x^m + \left(1 + 2 \frac{\left(k_x^m \right)^2 - \mathbf{k}^{d,2} \bullet \mathbf{k}^{d,2}}{\mathbf{k}^{s,2} \bullet \mathbf{k}^{s,2}} \right) k_x^p \right)$$

$$+\sum_m A_m^s P_x^{m,s} I^{m,s,p} i \rho_2 \left(1 - \frac{k_x^m k_x^p}{\mathbf{k}^{d,2} \bullet \mathbf{k}^{d,2}} + \left(\frac{1}{\mathbf{k}^{d,2} \bullet \mathbf{k}^{d,2}} - \frac{1}{\mathbf{k}^{s,2} \bullet \mathbf{k}^{s,2}} \right) \left(k_x^m \right)^2 \right)$$

$$+\sum_m A_m^s P_z^{m,s} I^{m,s,p} \rho_2 i \left(k_z^{m,s} \right) \left(\left(\frac{1}{\mathbf{k}^{d,2} \bullet \mathbf{k}^{d,2}} - \frac{1}{\mathbf{k}^{s,2} \bullet \mathbf{k}^{s,2}} \right) k_x^m \ldots \right.$$

$$\left. \ldots - \left(\frac{1}{\mathbf{k}^{d,2} \bullet \mathbf{k}^{d,2}} - \frac{2}{\mathbf{k}^{s,2} \bullet \mathbf{k}^{s,2}} \right) k_x^p \right) = 0$$

Equation 3:

$$+\sum_m A_m^s P_y^{m,s} I^{m,s,p} i \rho_2 \left(1 - \frac{k_x^m k_x^p}{\mathbf{k}^{s,2} \bullet \mathbf{k}^{s,2}} \right) = 0 \qquad \text{(X.A.1.d\_32)}$$

Equation 4:

$$
\begin{aligned}
&+A^{inc} I^{inc,p} \rho_1 \left(k_z^{inc}\right)^2 \\
&+\sum_m A_m^r I^{m,r,p} \left(k_z^{m,r}\right) \rho_1 \\
&+\sum_m A_m^d I^{m,d,p} \left(k_z^{m,d}\right) \rho_2 \left(-1+\frac{2}{\mathbf{k}^{s,2}{}_{\bullet}\mathbf{k}^{s,2}}\left(k_x^m k_x^p\right)\right) \\
&+\sum_m A_m^s P_x^{m,s} I^{m,s,p} i\left(k_z^{m,s}\right) \rho_2 \left(\left(\frac{1}{\mathbf{k}^{d,2}{}_{\bullet}\mathbf{k}^{d,2}}-\frac{1}{\mathbf{k}^{s,2}{}_{\bullet}\mathbf{k}^{s,2}}\right)k_x^m-\frac{k_x^p}{\mathbf{k}^{s,2}{}_{\bullet}\mathbf{k}^{s,2}}\right) \\
&+\sum_m A_m^s P_z^{m,s} I^{m,s,p} i \rho_2 \left(\left(\frac{1}{\mathbf{k}^{d,2}{}_{\bullet}\mathbf{k}^{d,2}}-\frac{1}{\mathbf{k}^{s,2}{}_{\bullet}\mathbf{k}^{s,2}}\right)\left(k_z^{m,s}\right)^2+1-\frac{k_x^m k_x^p}{\mathbf{k}^{s,2}{}_{\bullet}\mathbf{k}^{s,2}}\right) \\
&=0
\end{aligned}
\qquad \text{(X.A.1.d\_33)}
$$

Equation 5:

$$\left(A_m^s P_x^{m,s} k_x^{m,s} + A_m^s P_y^{m,s} k_y^{m,s} + A_m^s P_z^{m,s} k_z^{m,s}\right)\delta_{m,p} = 0 \qquad \text{(X.A.1.d\_34)}$$

with

$$I^{inc,\eta} = \frac{1}{k_z^{inc}} \int_\Lambda \exp i\left[\left(k_x^{inc} - k_x^\eta\right)x + \left(k_z^{inc} f\left(x\right)\right)\right] dx \qquad \text{(X.A.1.d\_35)}$$

$$I^{m,\xi,\eta} = \frac{1}{k_z^{m,\xi}} \int_\Lambda \exp i\left[\left(k_x^m - k_x^\eta\right)x + k_z^{m,\xi} f\left(x\right)\right] dx \qquad \text{(X.A.1.d\_36)}$$

For $\delta_{m,p}$ Kronecker's delta. It is already seen from (X.A.1.d_32) that

$$A_m^s P_y^{m,s} = 0 \qquad \text{(X.A.1.d\_37)}$$

Hence $u_y = 0$ and therefore there are no horizontally polarized waves generated.

Remark that $f\left(x\right)$ only appears in the exponentials of integrals (X.A.1.d_35-36). This is due to the use of partial integration for integrals containing df/dx while equating the Fourier coefficients [1].

Truncation of Infinite Summations

The linear set of equations (X.A.1.d_30-34) is infinite since *m*,*p* may take every possible integer value from $-\infty \to +\infty$. However, it has been shown before [2, 8-9] that the interval of integers may be truncated to $\{-N,-N+1,..,N-1,N\}$, for N larger than 6.
From refs. [45-46], it is known that for a sawtooth profile

$$f(x)=\frac{2hx}{\Lambda}-\frac{h}{2} \text{ if } 0\le x<\frac{\Lambda}{2} \qquad \text{(X.A.1.d\_38)}$$

$$f(x)=\frac{3h}{2}-\frac{2hx}{\Lambda} \text{ if } \frac{\Lambda}{2}\le x<\Lambda \qquad \text{(X.A.1.d\_39)}$$

the integrals (X.A.1.d_35) and (X.A.1.d_36) become

$$I^{inc,\eta}=ih\Lambda e^{-ihk_z^{inc}/2}\frac{1-(-1)^{-\eta}e^{ihk_z^{inc}}}{\left(hk_z^{inc}\right)^2-(\pi\eta)^2} \qquad \text{(X.A.1.d\_40)}$$

$$I^{m,\eta,\xi}=ih\Lambda e^{-ihk_z^{inc}/2}\frac{1-(-1)^{(m-\eta)}e^{ihk_z^{m,\xi}}}{\left(hk_z^{m,\xi}\right)^2-\pi^2(m-\eta)^2} \qquad \text{(X.A.1.d\_41)}$$

In this work, only sawtooth profiles (X.A.1.d_38-39) have been taken under consideration, but the model equally works for other shapes as well.

THE NEED FOR DIFFRACTION

In many NDT-applications, it is desirable to generate surface waves. It is well known that for most liquid-solid interfaces Scholte – Stoneley waves cannot be generated by means of incident sound because their velocity is too slow compared with the sound velocities in the surrounding media. One of the techniques that can be used to stimulate Scholte – Stoneley waves is the use of a periodic corrugation on the surface. Then, these waves can be generated under the right conditions by means of diffraction. Even though this has been very successful for relatively wide beams, this success was not shared for the stimulation of leaky Rayleigh waves. It has been shown by Briers et al [15-19, 25] that inhomogeneous waves are needed in order to really stimulate leaky Rayleigh waves. Furthermore it is also known that this stimulation will never exceed the one by means of obliquely incident inhomogeneous waves on a plane interface at the Rayleigh angle. Hence the question that may arise: Why would anyone apply a diffraction grating to stimulate leaky Rayleigh waves if this can be better accomplished on a plane surface?
The answer is simple: A diffraction grating in combination with complex harmonic homogeneous waves, has a similar effect as the use of harmonic inhomogeneous waves incident on a smooth

interface. As an introduction to this matter, we have calculated the reflection coefficient as a function of the angle of incidence for a constant real frequency and variable imaginary frequency. This has been done for incident complex harmonic plane waves. Before, it has been shown that such waves show exponential amplitude variation along the wave propagation direction. Therefore the imaginary wave vector is directed parallel with the propagation wave vector, which is not the structure that a typical leaky Rayleigh wave consists of [10-14]. Furthermore this structure is maintained after reflection due to the dispersion relation and Snell's law. It is therefore unlikely that any actual leaky Rayleigh wave stimulation might occur, as would have been the case if harmonic inhomogeneous waves were considered [10-14]. The result is shown in Fig. X.A.1.d_3 for a water-brass interface and for a real frequency of 5 MHz and different imaginary frequencies. The material properties for water and brass are listed in Table X.A.1.d_II.

Table X.A.1.d_II: ***material properties used in this work***

material	$\rho[kg/m^3]$	$v_d[m/s]$	$v_s[m/s]$
water	1000	1480	0
brass	8100	4700	2100

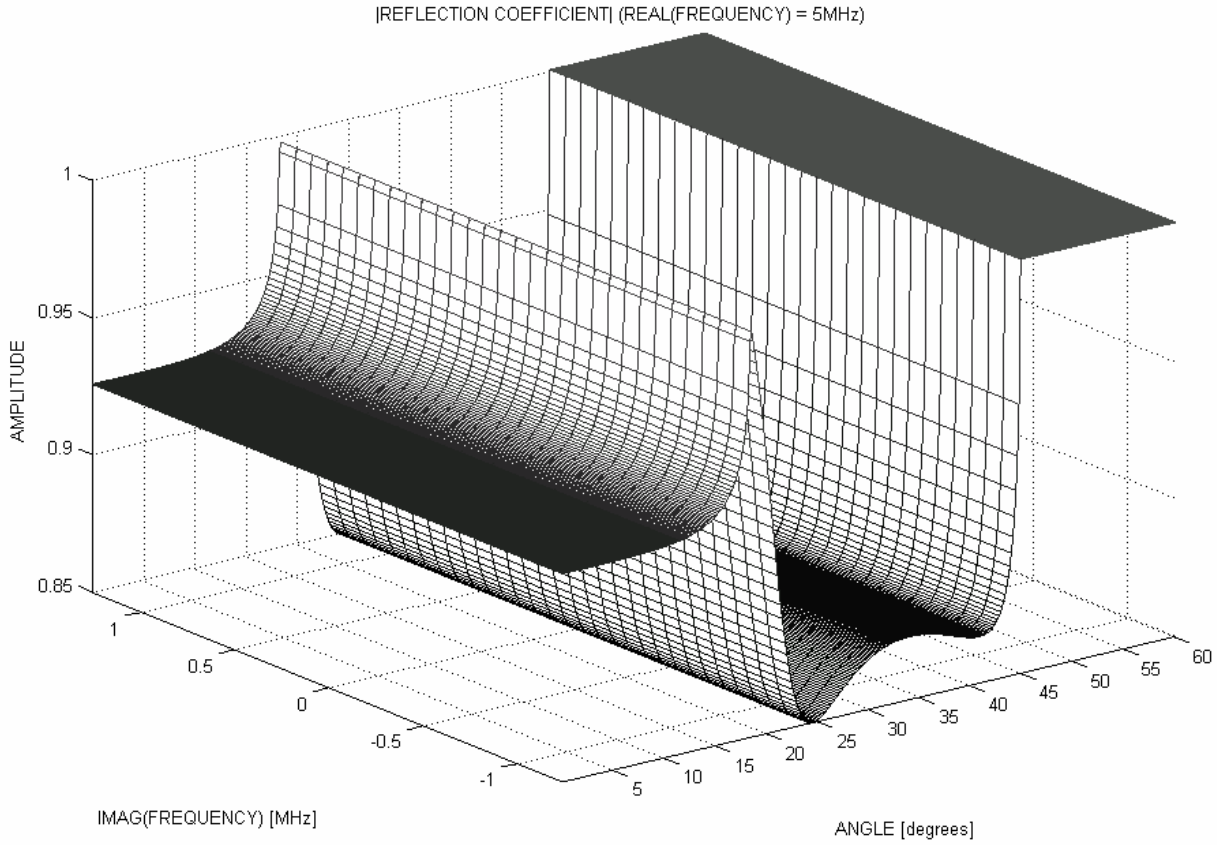

Fig. X.A.1.d_3: ***The absolute value of the reflection coefficient on a smooth water-brass interface constant real frequency and different imaginary frequencies. The Rayleigh angle is 48^0 .***

For simplicity we have neglected intrinsic damping in the numerical examples. It is verified that the amplitude of the reflection coefficient is independent of the imaginary frequency and it is certainly seen form Fig. X.A.1.d_3 that no typical peaks arise as would have been in the case for harmonic inhomogeneous waves [10-14].
In Fig. X.A.1.d_4 the two Cartesian components of the particle displacement are shown relative to the incident particle displacement amplitude, for a Rayleigh angle of incidence (48^0) at 5 MHz and without any transient feature. It is seen that the z-component reaches a value of approximately 1.5. This height is independent of the imaginary frequency that is used. We keep this pattern as a reference for further discussions. This amplitude is so low because there is no leaky feature in the liquid side.

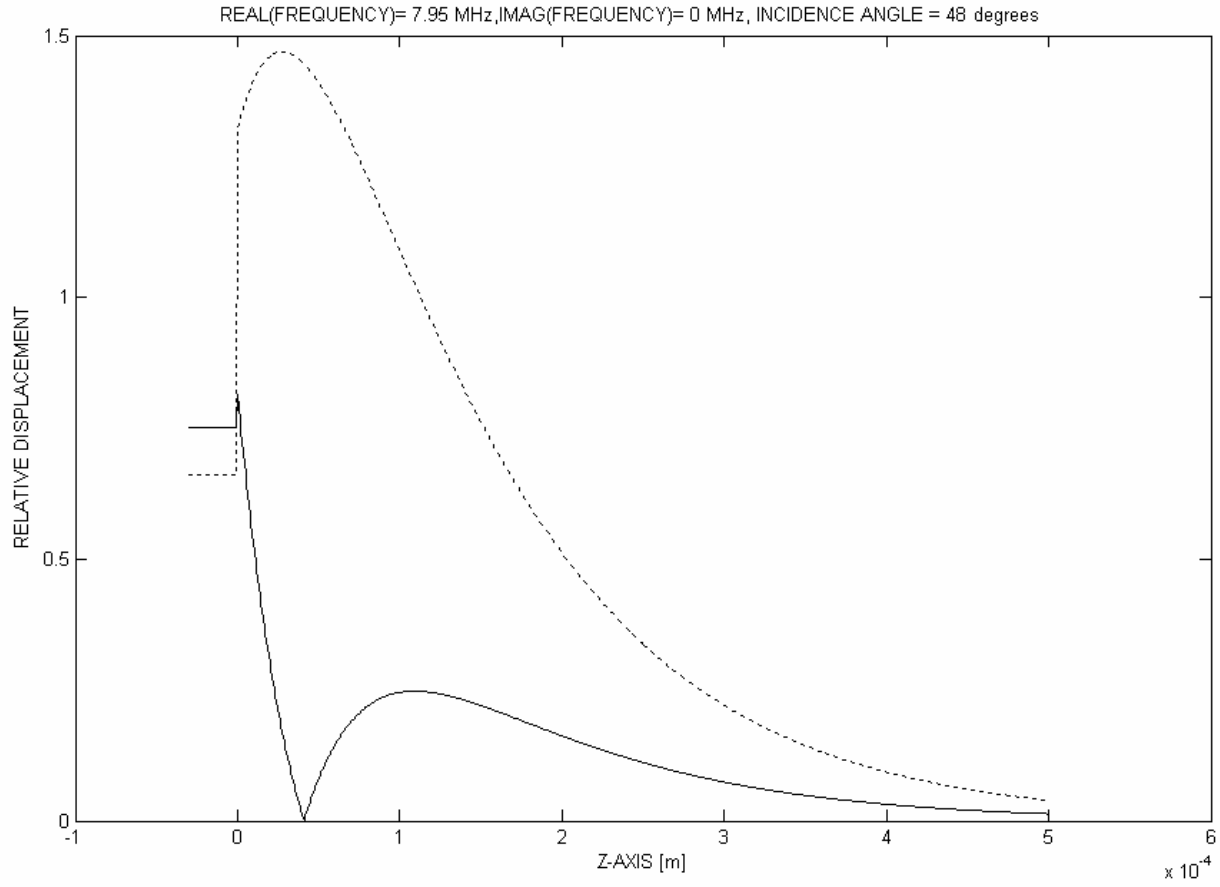

Fig. X.A.1.d_4: ***Relative displacement amplitude for transmitted and reflected sound resulting from harmonic homogeneous plane waves incident on a smooth water-brass interface at the Rayleigh angle. Solid line :*** $\left|\mathbf{u}_x\right|$, ***dotted line:*** $\left|\mathbf{u}_z\right|$. ***A typical Raleigh wave profile is noticeable in the solid.***

Now we study results obtained for diffraction on a periodically rough surface. All diffraction spectra tackled in this section are performed for normal incidence on a water/brass periodically corrugated interface having a periodicity $\Lambda = 250\mu m$ and height $h = 66\mu m$. According to (X.A.1.d_1-2) and the material properties given in Table X.A.1.d_II, this means that the applied Rayleigh theory for diffraction is valid within the frequency interval [4MHz, 15MHz].

Furthermore, the dispersion equation (X.A.1.d_25-26) has to be taken into account as well as the grating equation (X.A.1.d_20), in order to ensure the physicals validity of the approach. In Fig. X.A.1.d_5 the calculated reflection spectra are shown for normal incident harmonic plane waves.

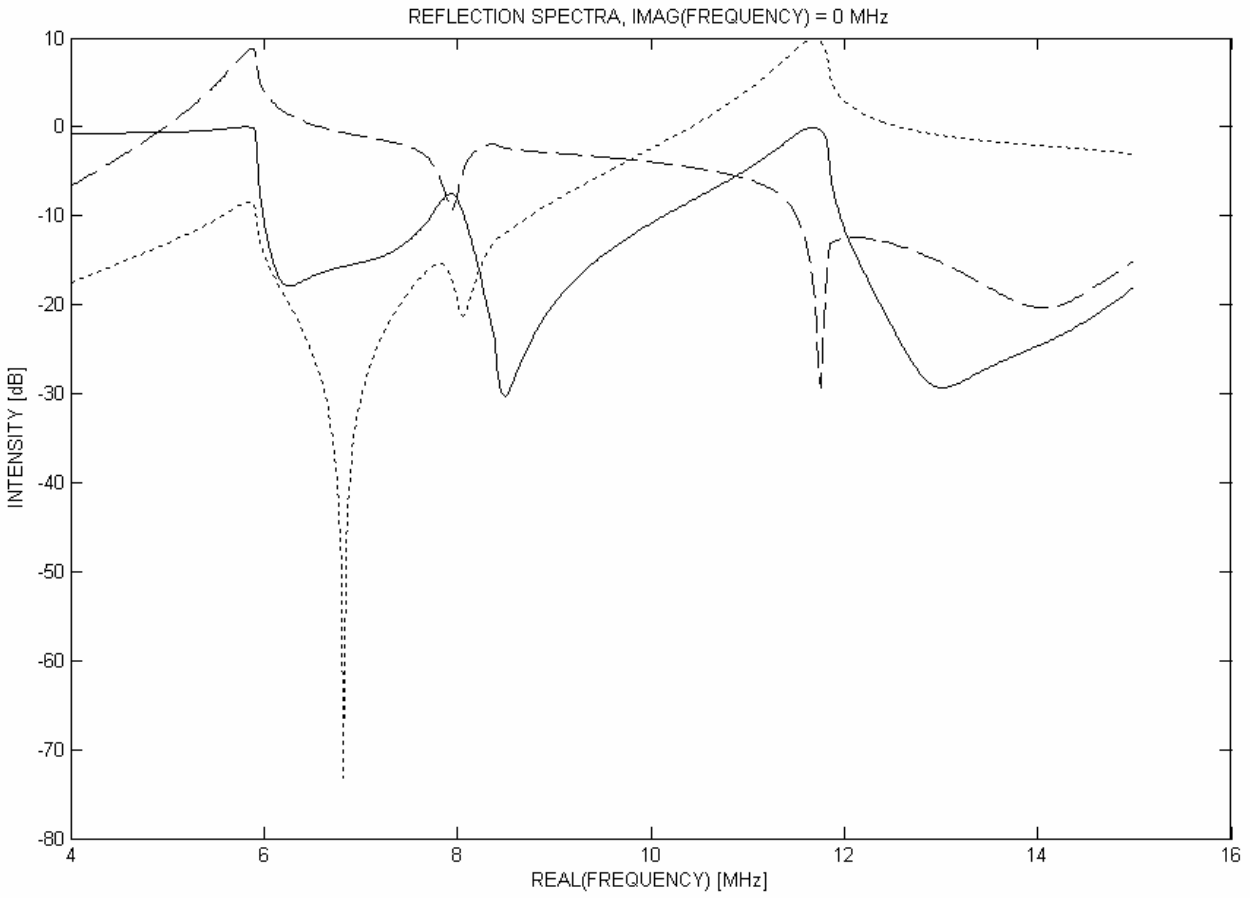

Fig. X.A.1.d_5: ***Diffraction spectra (in dB) of different orders for normal incident harmonic homogeneous plane waves. Solid line:*** $\left|A_0^r\right|^2$***, dashed line:*** $\left|A_{\pm 1}^r\right|^2$***, dotted line :*** $\left|A_{\pm 2}^r\right|^2$

It is seen for example that the zero order reflection coefficient is a function of the incident frequency. This figure corresponds to Fig. X.A.1.d_4 in the work of Claeys et al. [1]. In Figs X.A.1.d_6-8 these spectra are shown not only as a function of the real frequency, but also as a function of the imaginary frequency.

In Figs X.A.1.d_9-10 the propagation direction is shown for first order reflected waves. Fig. X.A.1.d_9 shows the phase propagation direction whereas Fig. X.A.1.d_10 shows the energy propagation direction. Noteworthy is the fact that the imaginary frequency has a steering effect on reflected waves. For example, below 6 MHz first order reflected waves are completely evanescent, which means that their wave vector component perpendicular to the surface is completely imaginary. This also means that these waves 'propagate' along the interface. Fig. X.A.1.d_9 shows that this evanescence is broken through if complex frequencies are used. For high imaginary frequencies, first order reflected waves below 6 MHz can perfectly be erected and propagate in the bulk instead of being evanescent. Nevertheless, this statement is only through if

phase propagation direction is considered. The energy still flows parallel with the interface, as can be seen in Fig. X.A.1.d_10.

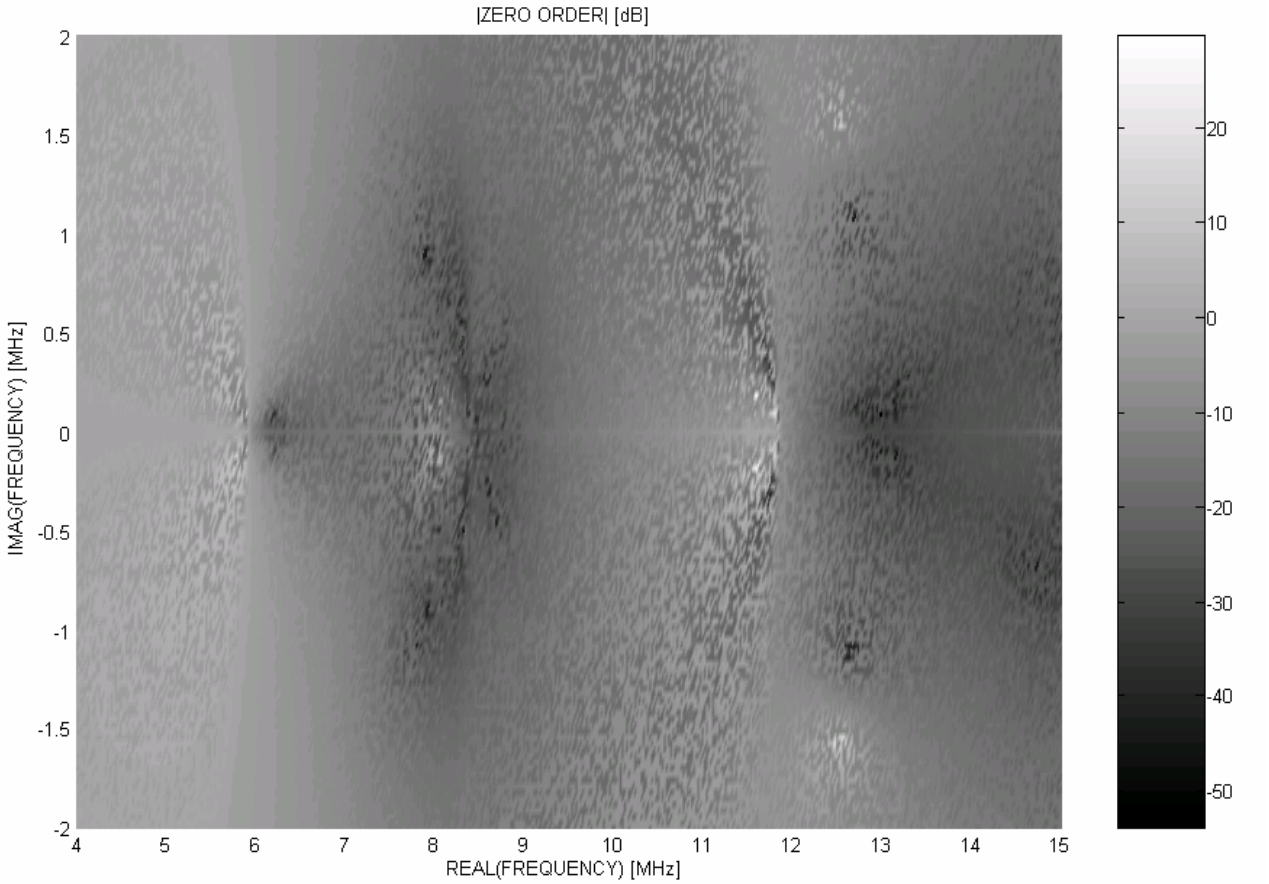

Fig. X.A.1.d_6: ***Diffraction spectra of the zero order reflected sound ($\left|A_0^r\right|^2$ in dB) as a function of the real and imaginary frequency.***

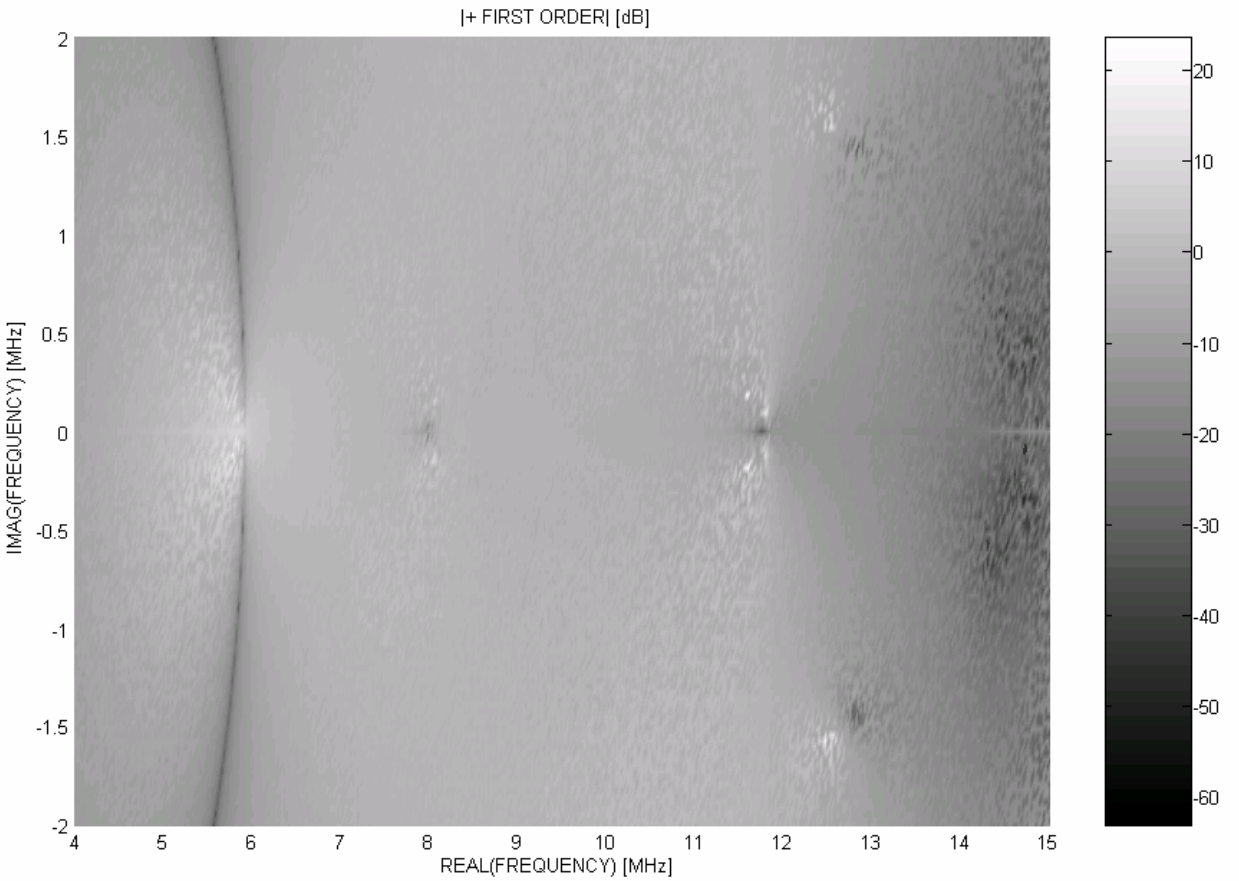

Fig. X.A.1.d_7: ***Diffraction spectra of the first order reflected sound ($\left|A_{\pm 1}^{r}\right|^2$ in dB) as a function of the real and imaginary frequency.***

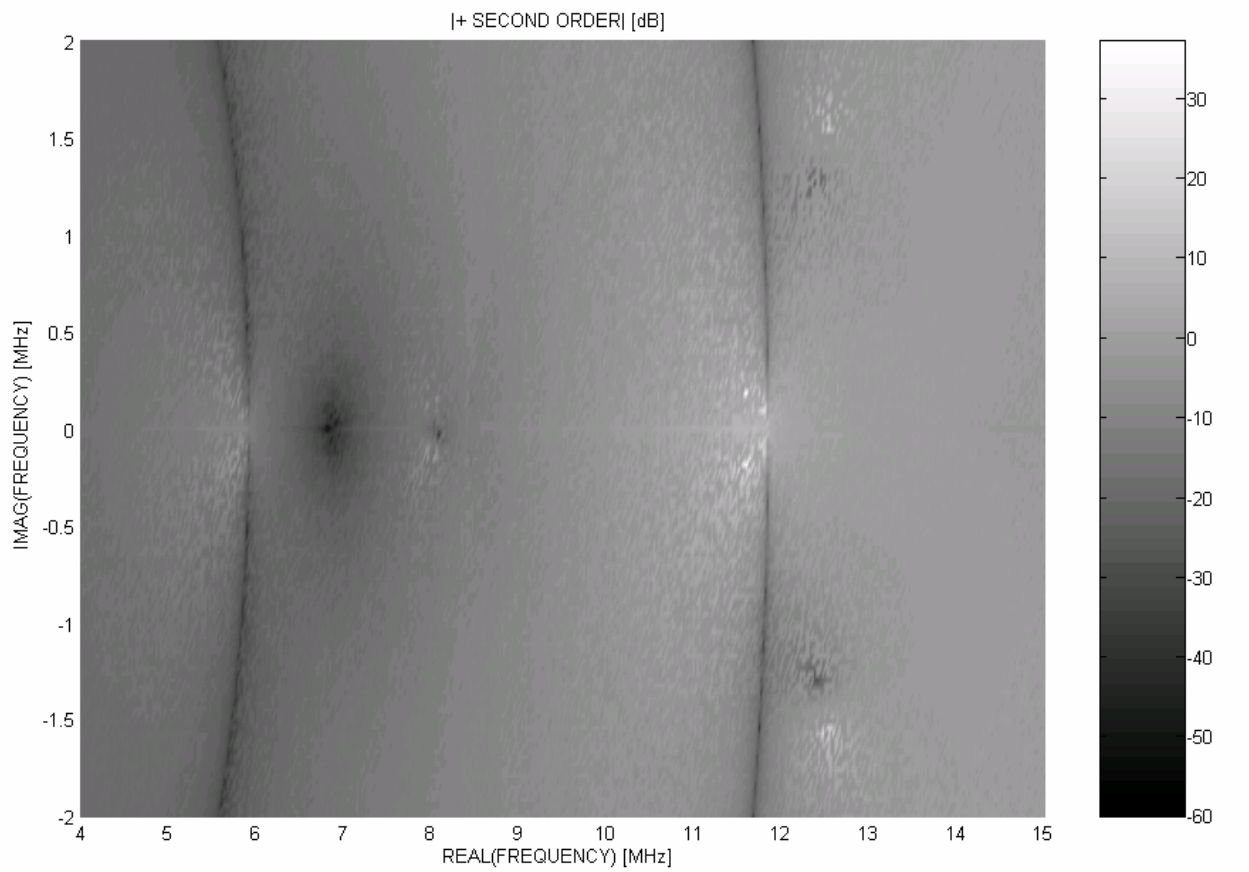

Fig. X.A.1.d_8: ***Diffraction spectra of the second order reflected sound ($\left|A^r_{\pm 2}\right|^2$ in dB) as a function of the real and imaginary frequency.***

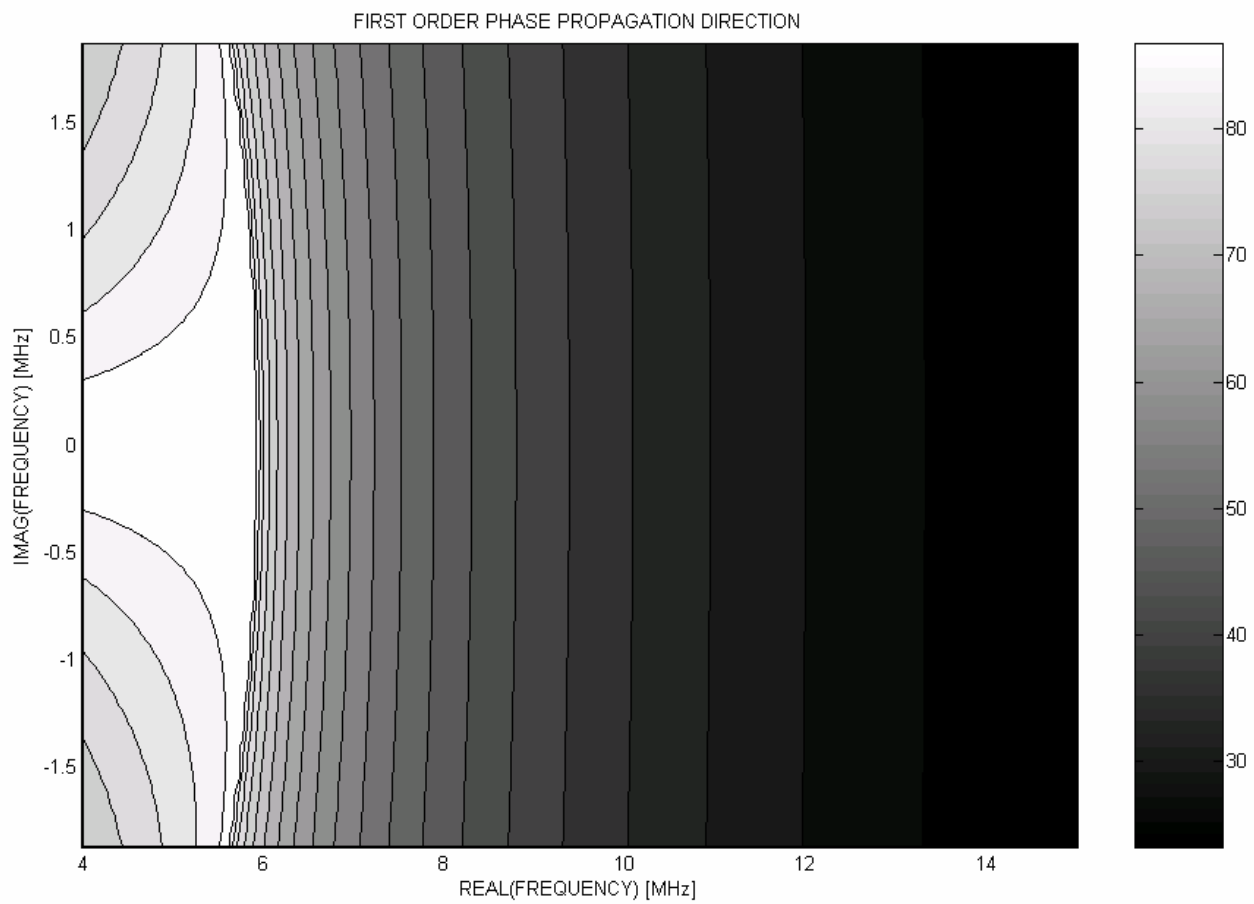

Fig. X.A.1.d_9: ***Phase propagation direction of the first order reflected waves.***

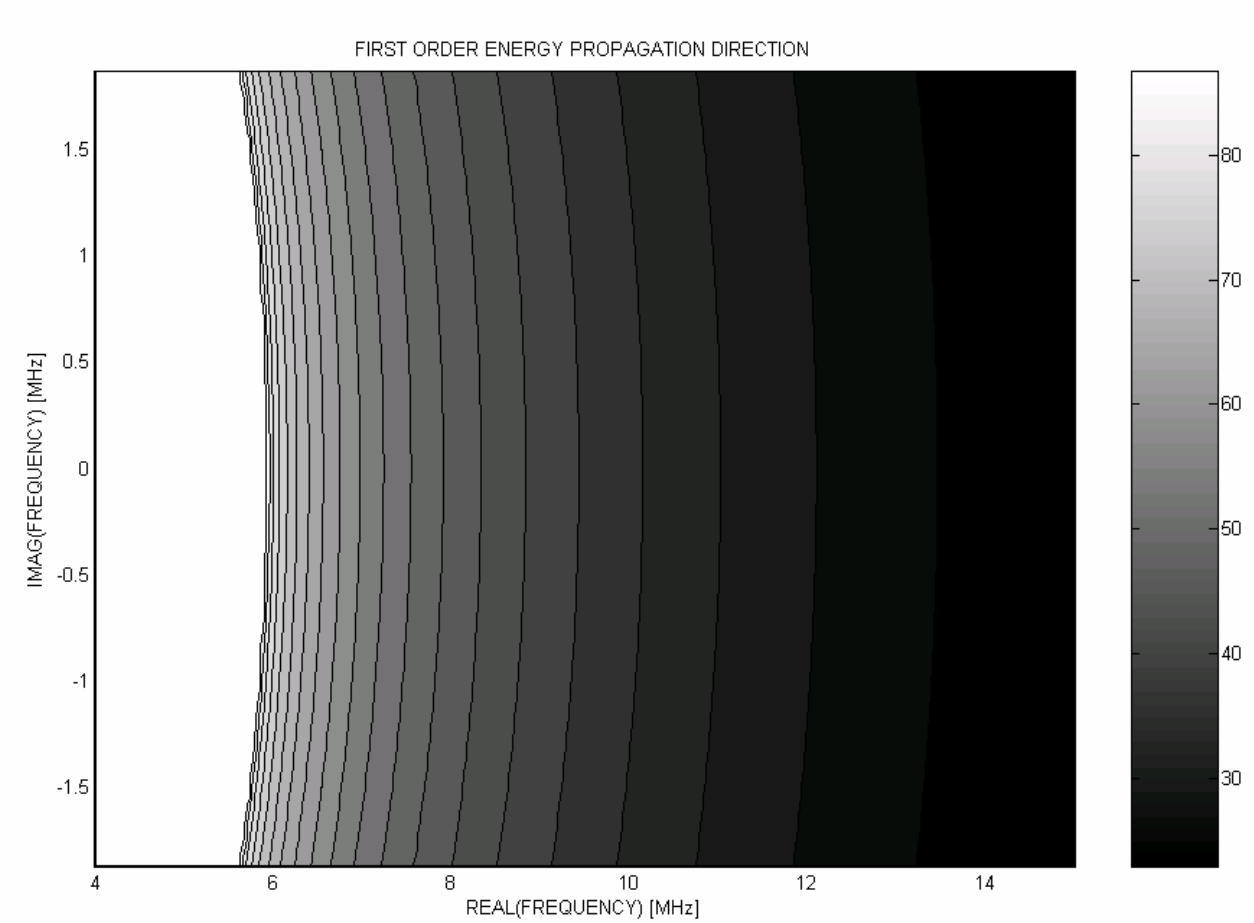

Fig. X.A.1.d_10: ***Energy propagation direction of the first order reflected waves.***

THE STIMULATION OF TRANSIENT SCHOLTE STONELEY WAVES

In Fig. X.A.1.d_5 it is seen that the zero order reflected sound shows some strong amplitude dips. When these dips are associated with the generation of Scholte – Stoneley waves, they are called Wood anomalies. It is know from earlier work [1,4] that the anomaly near 5.83 MHz corresponds to first order diffracted Scholte Stoneley waves, while the one at double that value corresponds to generated second order Scholte – Stoneley waves. Fig. X.A.1.d_11 shows the particle displacement components relative to the displacement amplitude of incident waves at 5.83 MHz and with no imaginary frequency component. This is a typical Scholte – Stoneley wave pattern. Most of the amplitude of a Scholte – Stoneley wave is situated in the liquid. In Fig. X.A.1.d_6, it can be seen that in the vicinity of 5.83 MHz there are regions with a lower amplitude than the first Wood anomaly. We have studied these stronger anomalies. Fig. X.A.1.d_12 shows again the displacement pattern for one of those anomalies, i.e. the one at real frequency of 6.18 MHz and an imaginary frequency of 0.03 MHz. It is seen that something comparable is visible as in Fig. X.A.1.d_11. However the amplitude is much smaller and the wave extends much further into the liquid than its harmonic counterpart. Probably this wave should be called a transient Scholte - Stoneley wave, which is different from a harmonic Scholte - Stoneley wave.

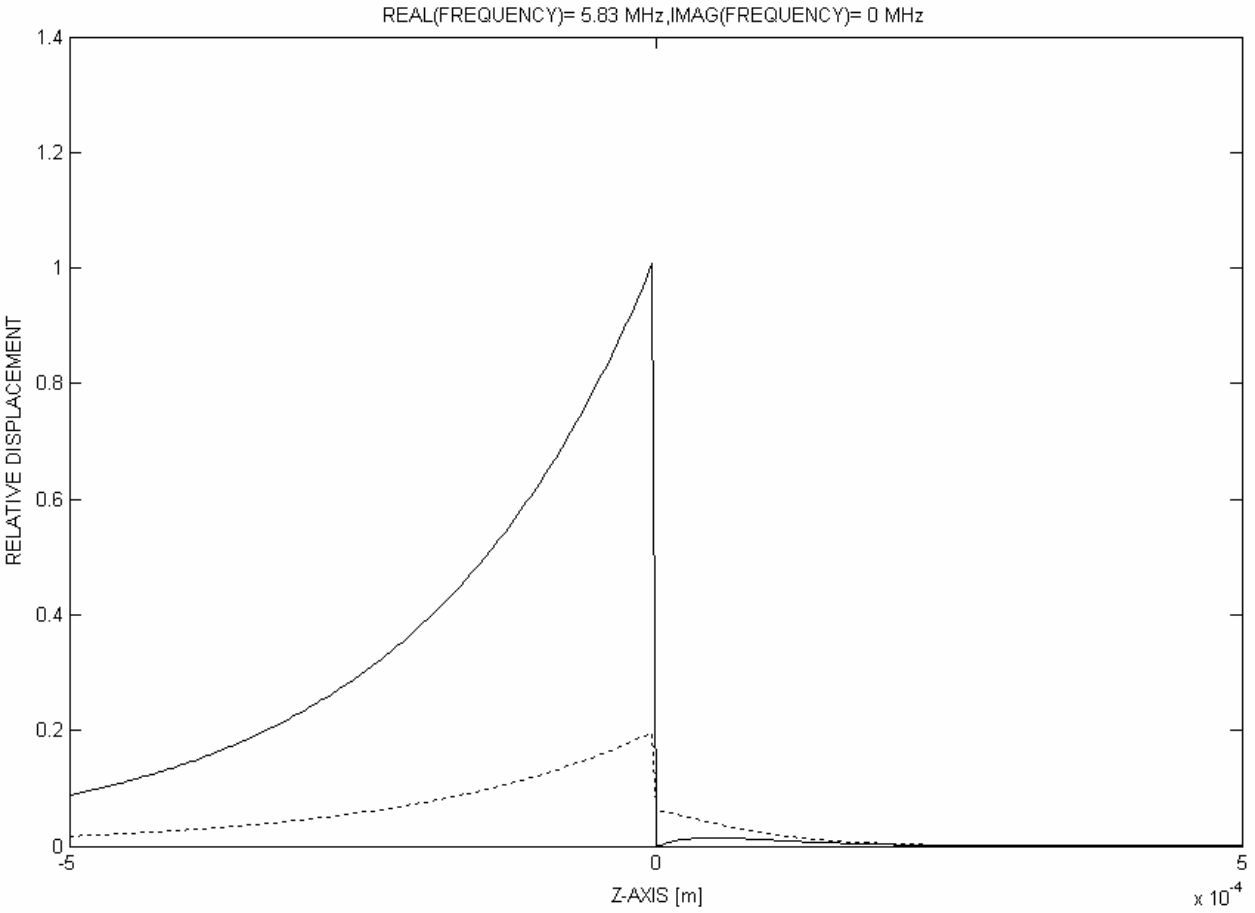

Fig. X.A.1.d_11: ***Relative displacement amplitude for first order transmitted and reflected sound resulting from harmonic homogeneous plane waves incident on the considered periodically rough water-brass interface at normal incidence having a real frequency of 5.83 MHz. Solid line :*** $|\mathbf{u}_x|$***, dotted line:*** $|\mathbf{u}_z|$***. A typical Scholte – Stoneley wave profile is visible.***

THE STIMULATION OF TRANSIENT LEAKY RAYLEIGH WAVES

In Fig. X.A.1.d_5, there is also an anomaly at 7.95 MHz. It is known from almost similar calculations for harmonic waves in [18] that this anomaly corresponds to the generation of a Rayleigh wave. However, just as in the case of Fig. X.A.1.d_4 there is no strong stimulation because the leaky feature is not present. This leaky feature can only be there if incident harmonic inhomogeneous waves were used instead of harmonic homogeneous plane waves [18]. Furthermore, the amplitudes in Fig. X.A.1.d_13, which describe the wave field patterns for the first order generated waves, are much less than the ones in Fig. X.A.1.d_4.

This shows why it is absolutely not beneficial to use a diffraction grating instead of a plane surface for stimulation of Rayleigh waves by means of harmonic homogeneous plane waves. The next option is of course the use of inhomogeneous waves, as in [15-19, 47]. However this has up until now only been practical in laboratory conditions and the generation of such waves is not really flexible [16, 19-20]. The generation of complex harmonic waves is much more flexible. Therefore the question immediately arises if it is possible to use incident complex harmonic plane

waves. For that purpose we have focused on the frequency area of 7.95 MHz. The results are seen in Figs X.A.1.d_14-15.

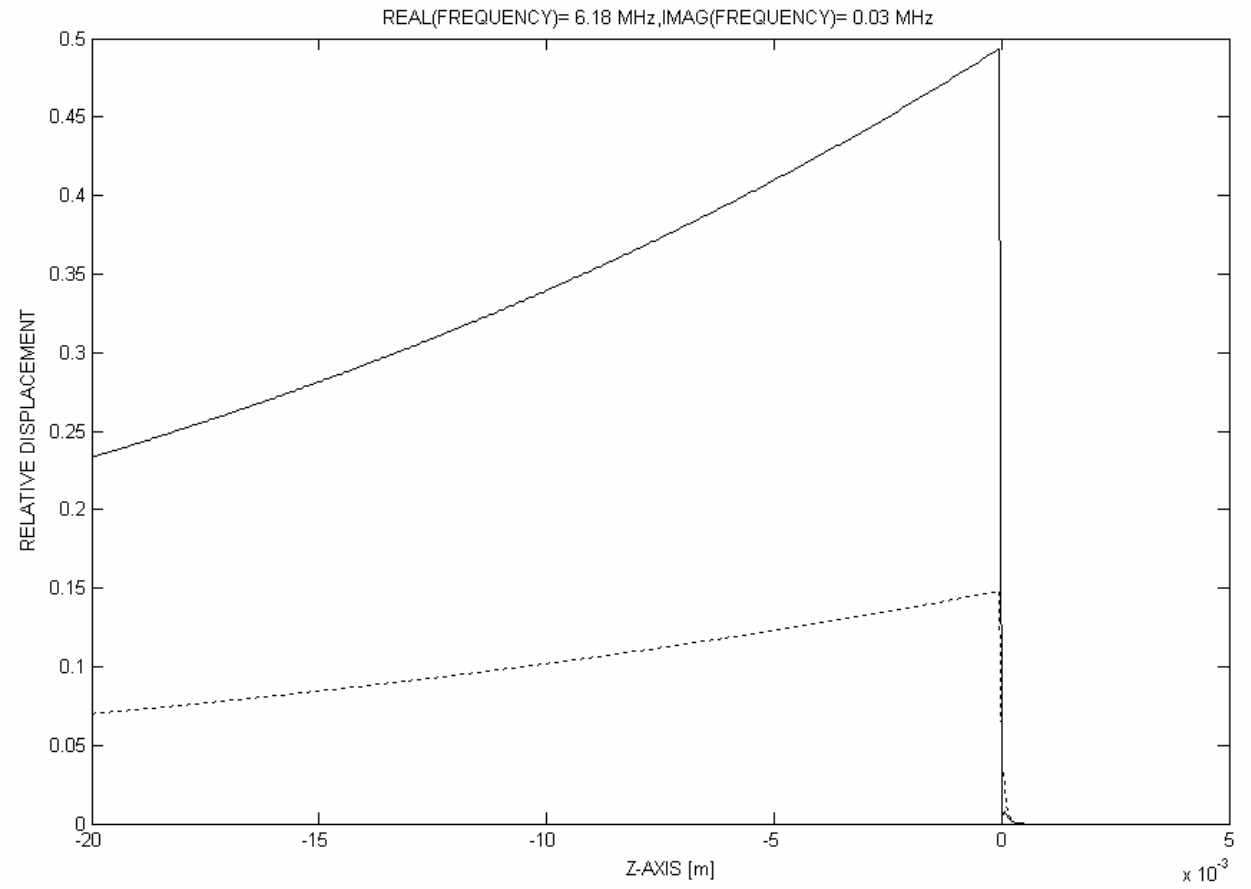

Fig. X.A.1.d_12: ***Relative displacement amplitude for first order transmitted and reflected sound resulting from complex harmonic homogeneous plane waves incident on the considered periodically rough water-brass interface at normal incidence having a real frequency of 6.18 MHz and an imaginary frequency of 0.03 MHz. Solid line :*** $\left|\mathbf{u}_x\right|$***, dotted line:*** $\left|\mathbf{u}_z\right|$***. A typical Scholte – Stoneley wave profile is visible though it reaches mush deeper into the liquid than in the harmonic case.***

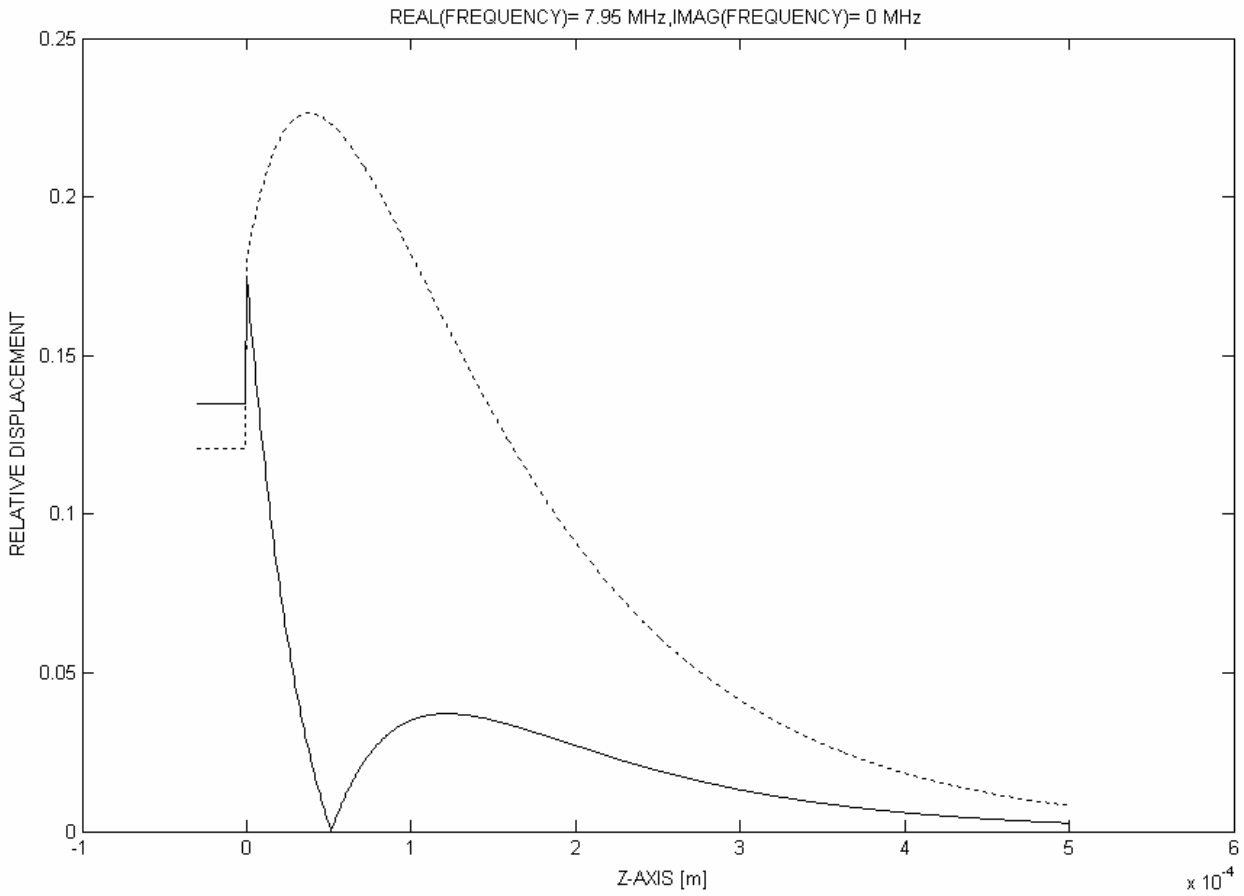

Fig. X.A.1.d_13: ***Relative displacement amplitude for first order transmitted and reflected sound resulting from harmonic homogeneous plane waves incident on the considered periodically rough water-brass interface at normal incidence having a real frequency of 7.95 MHz. Solid line :*** $\left|\mathbf{u}_x\right|$***, dotted line:*** $\left|\mathbf{u}_z\right|$***. A typical Raleigh wave profile is noticeable in the solid.***

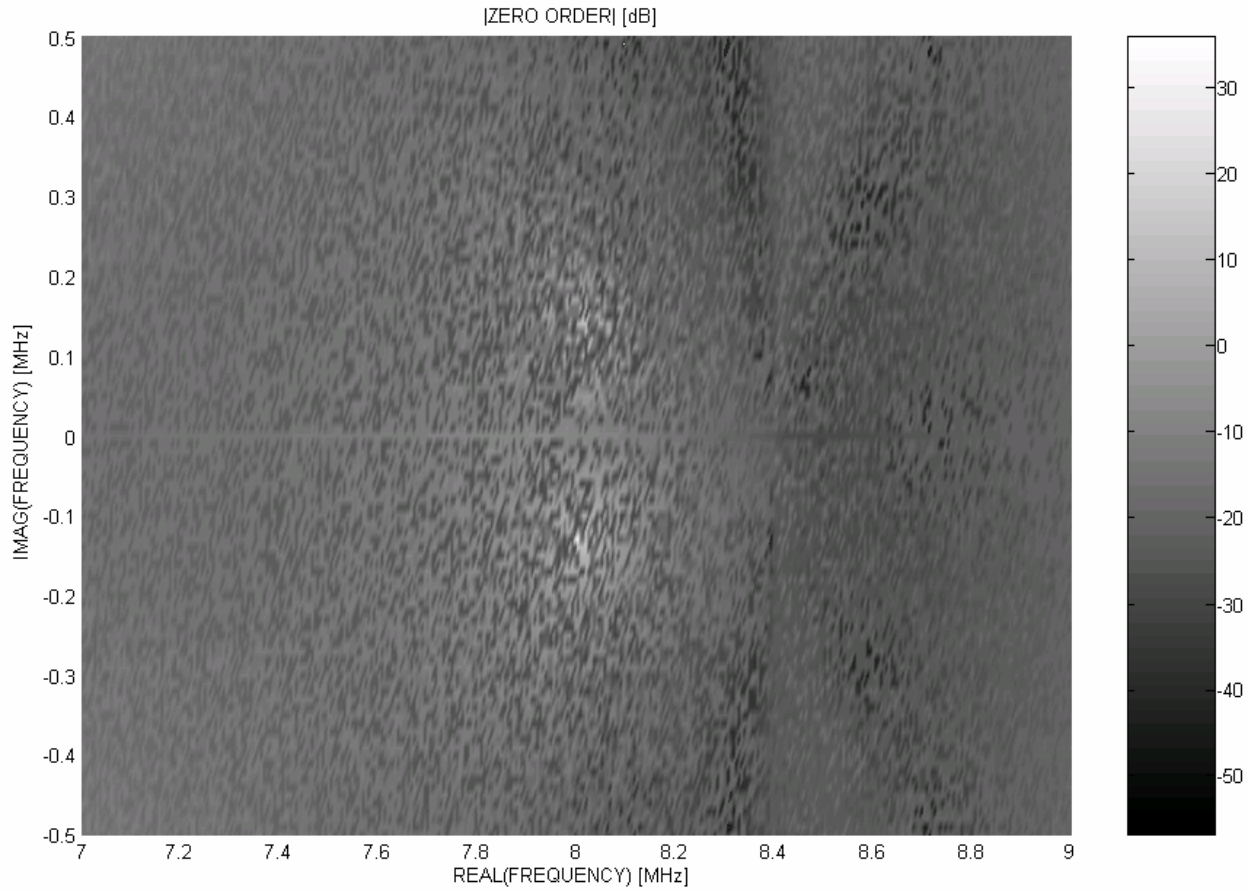

Fig. X.A.1.d_14: ***A high resolution close up of Fig. X.A.1.d_6 near the Rayleigh wave generating frequency.***

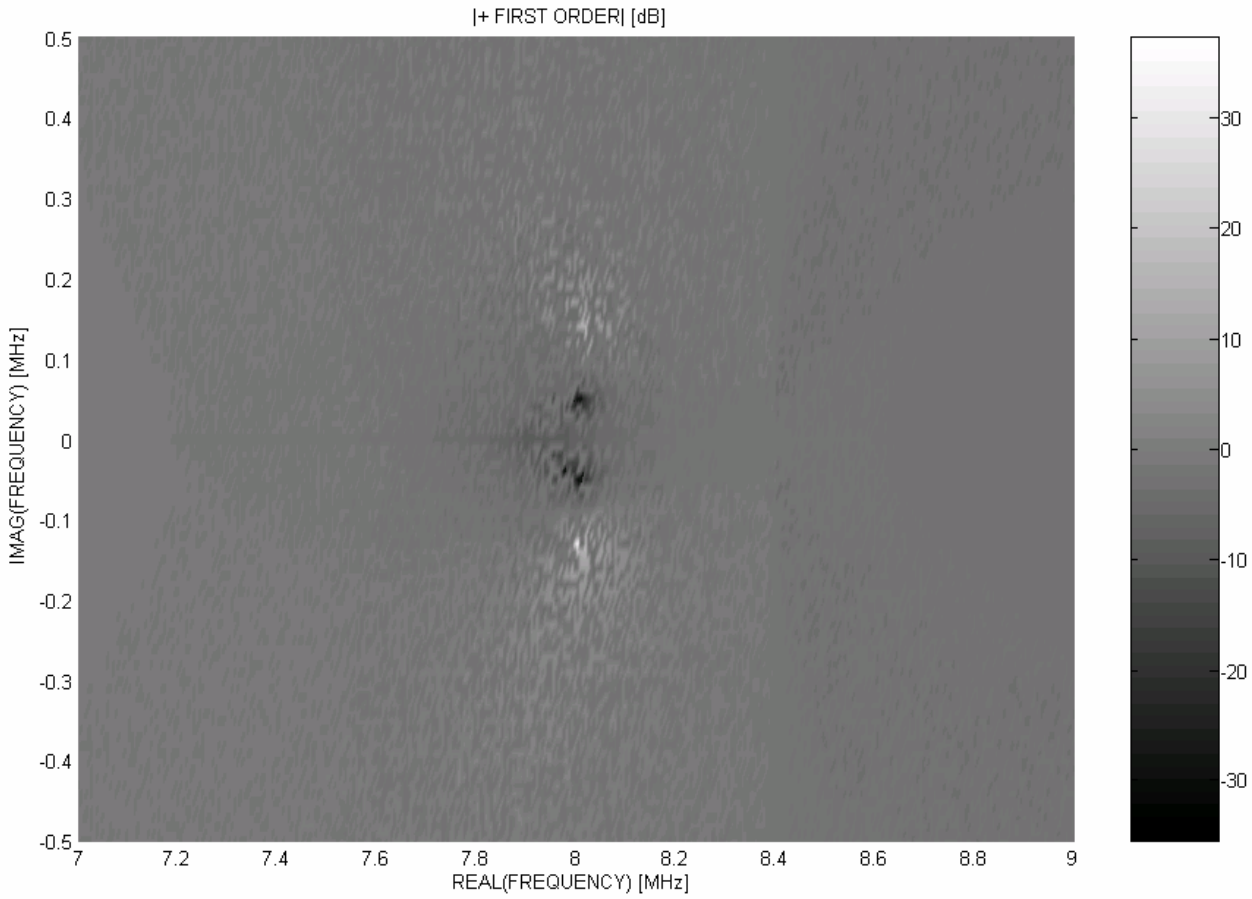

Fig. X.A.1.d_15: ***A high resolution close up of Fig. X.A.1.d_7 near the Rayleigh wave generating frequency.***

For the possible stimulation of Rayleigh waves, it is necessary to look at Fig. X.A.1.d_15, i.e. the first order reflection coefficient. It is seen that 4 regions of importance are present, i.e. two amplitude peaks and two amplitude dips. Fig. X.A.1.d_16 shows the corresponding relative displacement field for the peak at negative imaginary frequency, while Fig X.A.1.d_17 shows the result for the peak at positive imaginary frequency. Fig. X.A.1.d_18 shows the result for the dip corresponding to a negative imaginary frequency, whilst Fig. X.A.1.d_19 shows the result for the dip at positive imaginary frequency. It is seen that only the peak and dip for negative imaginary frequency show Rayleigh features. Furthermore it is seen that the amplitude corresponding to the Rayleigh wave which corresponds to the peak for negative imaginary frequency, has an amplitude that is more than 50 times the amplitude of the wave described in Fig. X.A.1.d_4 at a plane interface. This shows that complex harmonic homogeneous plane waves are able to really stimulate Rayleigh waves on periodically corrugated surfaces and that it is hence unnecessary to use more complicated harmonic inhomogeneous waves for that purpose. However there is one important question that we would still like to answer, i.e. why does this stimulation occur? We have calculated the propagation direction in reflection for the Rayleigh wave as depicted in Fig. X.A.1.d_16. The result is 48^0 for both the phase propagation direction and the energy propagation direction. But this is not the only clue. Even though the amplitude distribution pattern of Fig. X.A.1.d_16 is the one of a leaky Rayleigh wave at a fixed position along the interface, it is completely different if one would also look at its variation along the interface. A leaky Rayleigh

wave that is stimulated by means of a harmonic wave, must have a decaying amplitude along the interface (because of energy leakage), whereas here the amplitude does not change at all along the interface. The reason is that, due to the grating equation (X.A.1.d_20), no complex wave vector components can be generated along the interface if the incident wave has none along the interface, which is the exact case here. However, due to the transient feature, here one must not just take a look in space but also in time. Because the amplitude for negative imaginary frequencies drops with increasing time, the amplitude would, if a part of the wave would be followed while it travels along the interface, have decreasing amplitude indeed. Therefore there is, if not just space but also time is considered, amplitude decay along the interface and that is the reason why the energy leaks at a calculated angle, equal to the Rayleigh angle. Hence this is a transient leaky Rayleigh wave. For a positive imaginary frequency however there is no leakage but gain of energy while propagating, whence the nature of this phenomenon is very different, see Fig. X.A.1.d_17 and Fig. X.A.1.d_19, and cannot be called a transient leaky Rayleigh wave.

We have also performed calculations for oblique incidence, because for oblique incidence there is an imaginary part of the incident wave vector along the interface. We intended to figure out if this would be advantageous or not. The results, which are not depicted here, show that it is possible to generate leaky Rayleigh waves, but there is no strong stimulation and we have not found a relative displacement amplitude exceeding unity. Therefore we must conclude that for homogeneous plane waves, only normal incident complex harmonic waves are able to stimulate leaky Rayleigh waves.

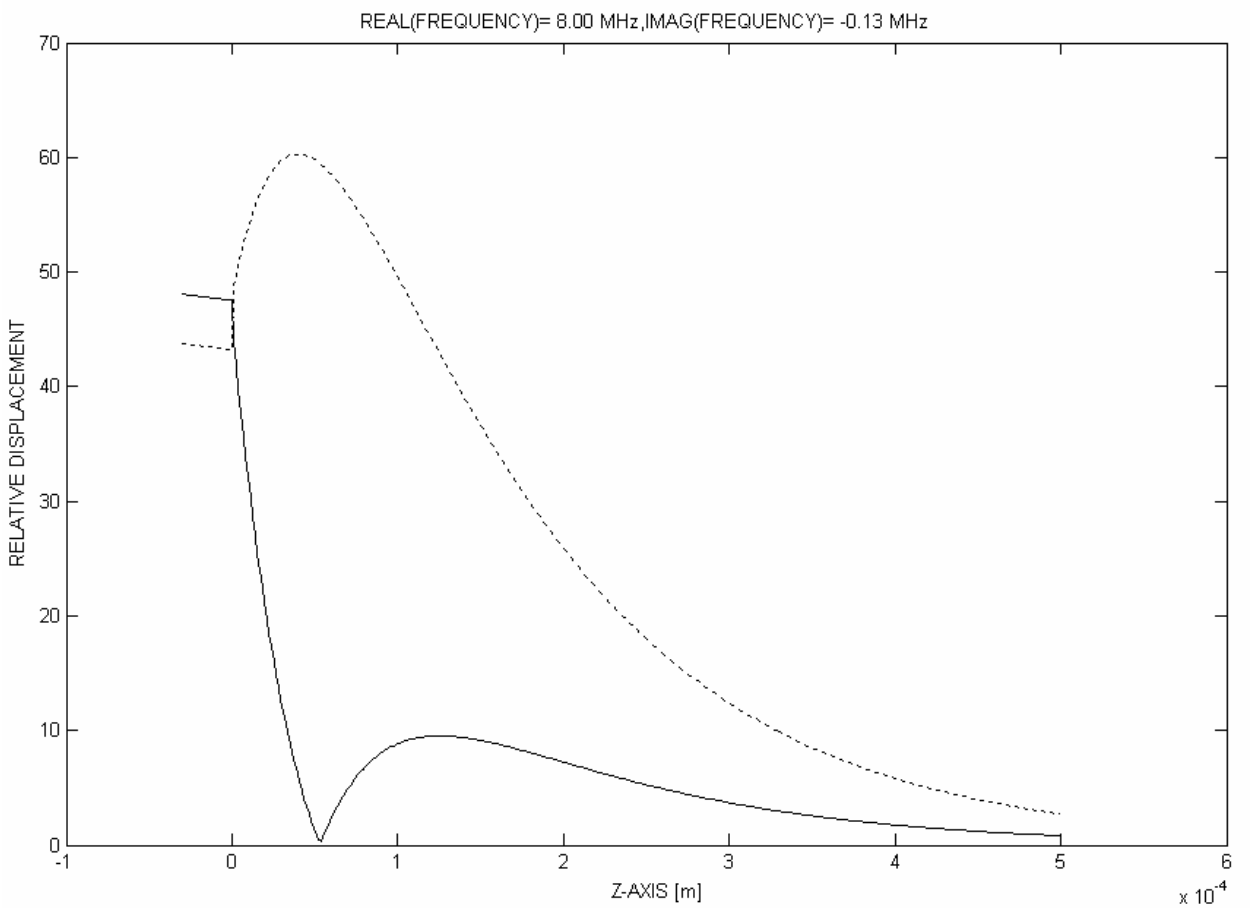

Fig. X.A.1.d_16: ***Relative displacement amplitude for first order transmitted and reflected sound resulting from complex harmonic homogeneous plane waves incident on the considered periodically rough water-brass interface at normal incidence having a real frequency of 8.00 MHz and an imaginary frequency of –0.13MHz. Solid line :*** $\left|\mathbf{u}_x\right|$, ***dotted line:*** $\left|\mathbf{u}_z\right|$. ***A typical Raleigh wave cross section profile is noticeable in the solid and also in the liquid.***

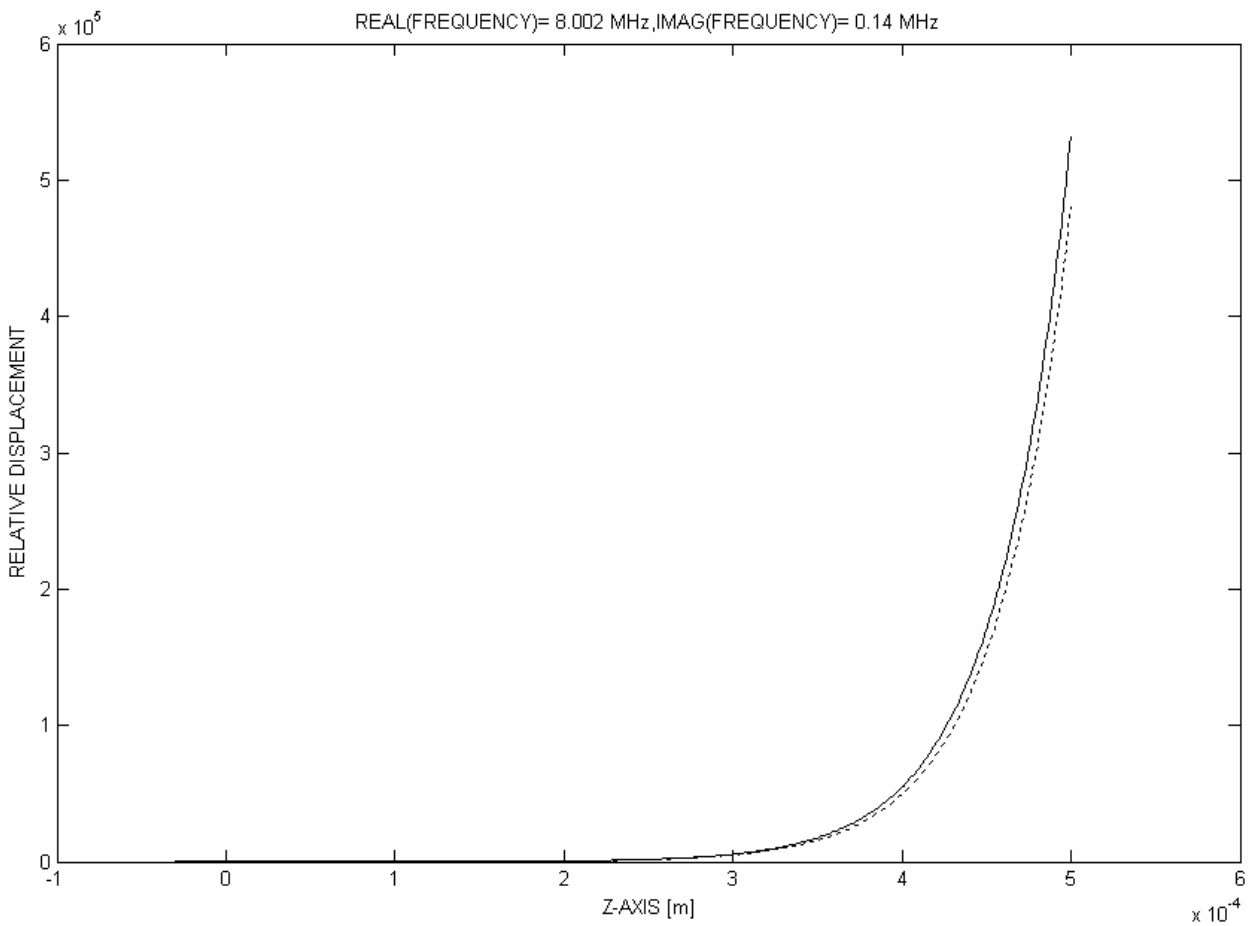

Fig. X.A.1.d_17: ***Same as Fig. X.A.1.d_16, but for having a real frequency of 8.00 MHz and an imaginary frequency of 0.14 MHz. Solid line :*** $|\mathbf{u}_x|$***, dotted line:*** $|\mathbf{u}_z|$**.**

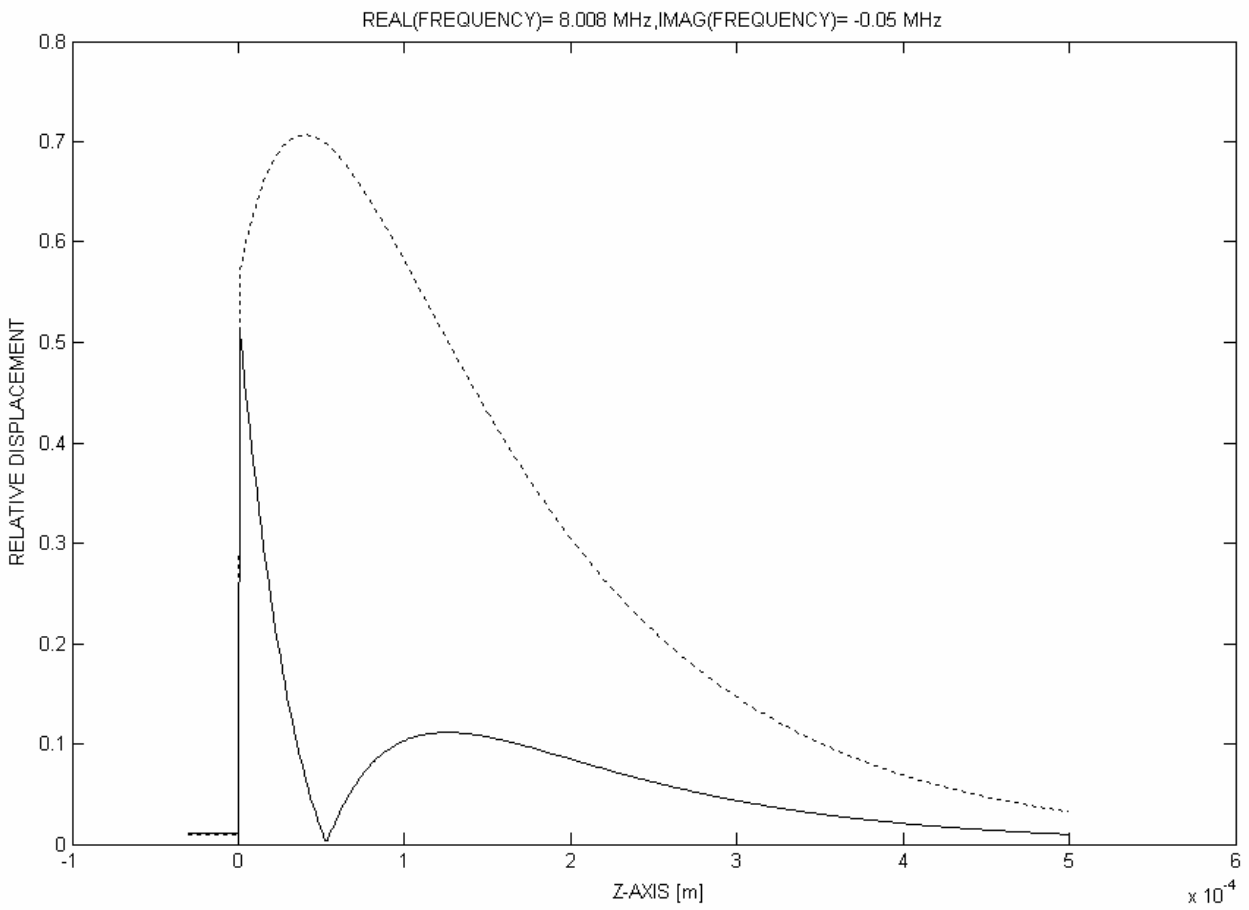

Fig. X.A.1.d_18: ***Same as Fig. X.A.1.d_16, but for having a real frequency of 8.008 MHz and an imaginary frequency of -0.05 MHz. Solid line :*** $|\mathbf{u}_x|$***, dotted line:*** $|\mathbf{u}_z|$**.**

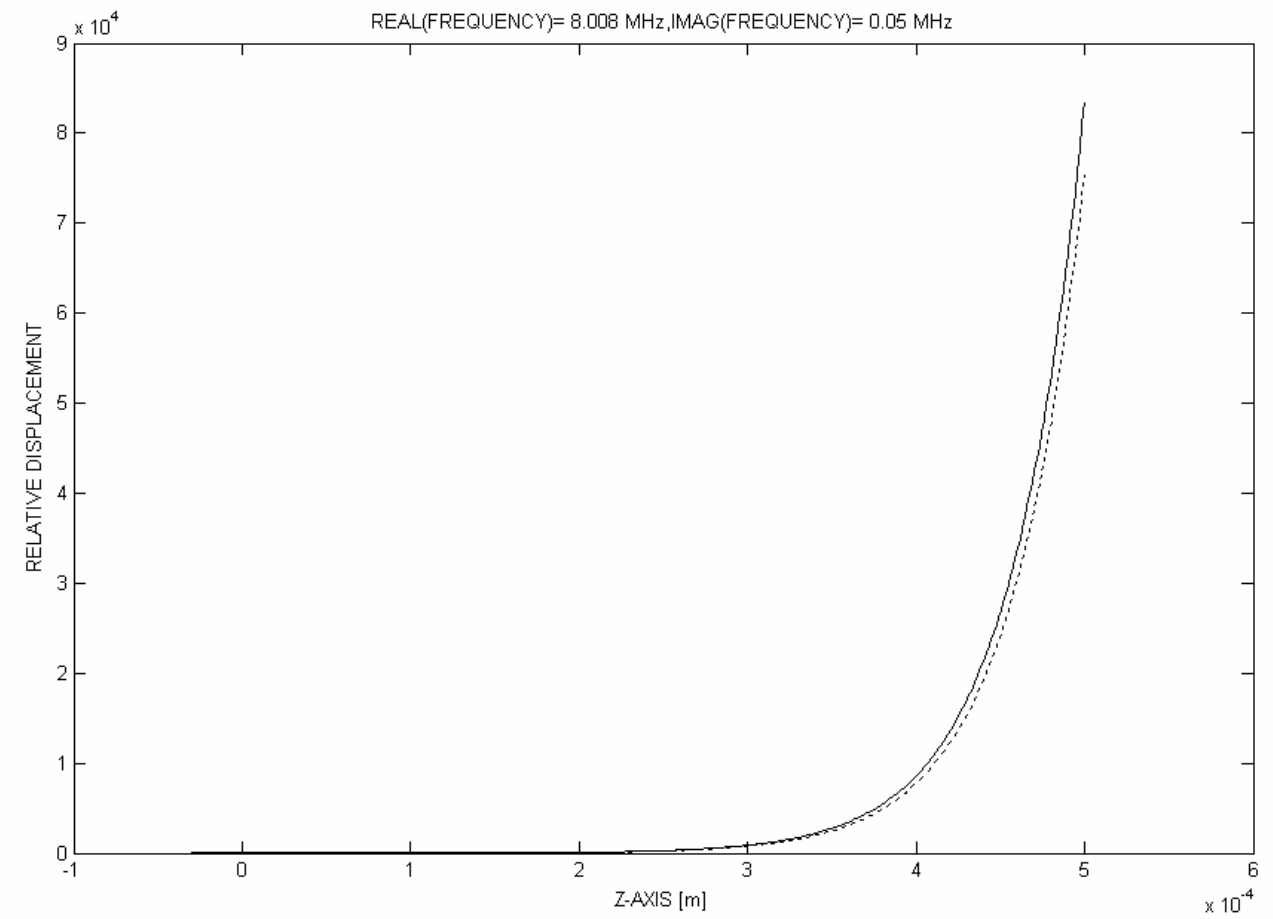

Fig. X.A.1.d_19: ***Same as Fig. X.A.1.d_16, but for having a real frequency of 8.008 MHz and an imaginary frequency of 0.05 MHz. Solid line :*** $|\mathbf{u}_x|$***, dotted line:*** $|\mathbf{u}_z|$**.**

CONCLUSIONS

The diffraction of complex harmonic plane waves is described on a periodically corrugated interface between a liquid and a visco-elastic isotropic solid. It is shown that, contrary to harmonic homogeneous plane waves, complex harmonic homogeneous plane waves are not advantageous for stimulating Scholte – Stoneley waves, whereas they can be extremely advantageous for stimulating transient leaky Rayleigh waves. Furthermore, because the generation of complex harmonic plane waves is much more simple than the generation of harmonic inhomogeneous plane waves, the described technique is an important step forward in the practical generation of high amplitude Rayleigh waves. This kind of wave is in its turn extremely important for NDT purposes of solids near the surface.

REFERENCES

[1] J. M. Claeys, Oswald Leroy, Alain Jungman, Laszlo Adler, "Diffraction of ultrasonic waves from periodically rough liquid-solid surface", J. Appl. Phys. 54(12), 5657-5662, 1983

[2] J. M. Claeys, O. Leroy, "Diffraction of plane waves by periodic surfaces", Rev. Cethedec 72, 183-193, 1982

[3] Alain Jungman, Laszlo Adler, Jan D. Achenbach, Ronald Roberts, "Reflection from a boundary with periodic roughness: Theory and experiment", J. Acoust. Soc. Am. 74(5), 1025-1032, 1983

[4] A. Jungman, o. Leroy, G. Quentin, K. Mampaert, “Theoretical and experimental study of ultrasonic surface modes at a solid-fluid periodic interface”, J. Appl. Phys. 63(12), 4860-4871, 1988
[5] Alain Jungman, Laszlo Adler, Gerard Quentin, “Ultrasonic anomalies in the spectrum of acoustic waves diffracted by periodic interfaces”, J. Appl. Phys. 53(9), 4673-4680, 1982
[6] K. Mampaert, O. Leroy, “Reflection and transmission of normally incident ultrasonic waves on periodic solid-liquid interfaces”, J. Acoust. Soc. Am. 83(6), 1390-1398, 1988
[7] Nico F. Declercq, Rudy Briers, Joris Degrieck, Oswald Leroy, "Diffraction of horizontally polarized ultrasonic plane waves on a periodically corrugated solid-liquid interface for normal incidence and Brewster angle incidence", IEEE Transactions on Ultrasonics, Ferroelectrics, and Frequency Control, 49(13), 1516-1521, 2002.
[8] Nico F. Declercq, Rudy Briers, Oswald Leroy, " The use of polarized bounded beams to determine the groove direction of a surface corrugation at normal incidence, the generation of surface waves and the insonification at Bragg-angles", Ultrasonics 40/1-8 pp. 345-348, 2002
[9] K. Mampaert, P. B. Nagy, O. Leroy, L. Adler, A. Jungman, G. Quentin, “On the origin of the anomalies in the reflected ultrasonic spectra from periodic surfaces”, J. Acoust. Soc. Am. 86(3), 429-431, 1989
[10] O. Leroy, B. Poirée, L. Sebbag, G. Quentin, “On the Reflection Coefficient of Acoustic Beams”, ACUSTICA 66, 84-89, 1988
[11] Landry Sebbag, “Les lois de la réflexion-réfraction des ondes planes évanescentes et les ondes d’interface”, Thesis, University of Paris 7, 1987.
[12] O. Leroy, G. Quentin, J. M. Claeys, “Energy conservation for inhomogeneous plane waves”, J. Acoust. Soc. Am. 84(3), 374-378, 1988
[13] Bernard Poirée, Landry Sebbag, “Les lois de la réflexion-réfraction des ondes planes harmoniques évanescentes. I. Mise en équations”, J. Acoustique 4, 21-46, 1991
[14] Gérard Quentin, André Derem, Bernard Poirée, “The formalism of evanescent plane waves and its importance in the study of the generalized Rayleigh wave”, J. Acoustique 3, 321-336, 1990
[15] R. Briers, O. Leroy, “Study of the behavior of inhomogeneous harmonic waves in their diffraction from simple rough surfaces”, J. de Physique IV, C1(4), 679-682, 1992
[16] W. Huang, R. Briers, S. I. Rokhlin, O. Leroy, “Experimental study of inhomogeneous wave reflection from a solid-air periodically rough boundary using leaky Rayleigh waves”, J. Acoust. Soc. Am. 96(3), 363-369, 1994
[17] Rudy Briers, “Contributions to the study of acoustic scattering and conversion phenomena in discontinuous structures by introducing a mode theory and by applying the inhomogeneous wave theory”, PhD Thesis KULeuven University, department of sciences, 1995
[18] Koen E.-A Van Den Abeele, Rudy Briers, Oswald Leroy, “Inhomogeneous plane-wave scattering and mode stimulation on periodic rough surfaces”, J. Acoust. Soc. Am. 99(7), 2883-2897 (1996)
[19] R. Briers, O. Leroy, O. Poncelet, M. Deschamps, “Experimental verification of the calculated diffraction field generated by inhomogeneous waves obliquely incident on a periodically rough liquid-solid boundary”, J. Acoust. Soc. Am. 106(4), 682-687, 1999
[20] M. Deschamps, B. Hosten, “Génération de l’onde hétérogène de volume dans un liquide non absorbant”, Acustica 68, 92-95, 1989.
[21] M. Deschamps, B. Poiree, O. Poncelet, “Energy velocity of complex harmonic plane waves in viscous fluids”, Wave Motion 25, 51-60, 1997.
[22] M. Deschamps, B. Poiree, O. Poncelet, “Energy velocity of complex harmonic plane waves in viscous fluids”, Wave Motion 25, 51-60, 1997.
[23] O. Poncelet, M. Deschamps, “Lamb waves generated by complex harmonic inhomogeneous plane waves”, J. Acoust. Soc. Am., 102(3), 292-300, 1997
[24] A. Bernard, M. Deschamps, M. J. S. Lowe, “Comparison between the dispersion curves calculated in complex frequency and the minima of the reflection coefficients for an embedded layer”, J. Acoust. Soc. Am. 107(4), 793-800, 2000
[25] Nico F. Declercq, Rudy Briers, Joris Degrieck, Oswald Leroy, “The History and Properties of Ultrasonic Inhomogeneous Waves”, submitted elsewhere
[26] G. Wolken, “Theoretical studies of atom-solid elastic scattering – He+LiF”, J. Chem. Phys., 58 (7), 3047-3064 1973
[27] M Neviere, M. Cadilhac, R. Petit, Applications of conformal mappings to diffraction of electromagnetic waves by a grating, IEEE T Antenn. Propag. AP21(1), 37-46, 1973
[28] J. L. Uretsky, The scattering of plane waves from periodic surfaces, Ann. Phys. 33(3), 400-427, 1965

[29] N. Garcia, N. Cabrera, New method for solving scattering of waves from a periodic hard surface – solutions and numerical comparisons with various formalisms, Phys. Rev. B 18(2), 576-589, 1978
[30] B. A. Lippmann, Note on the theory of gratings, J. Opt. Soc. Am. 43, 408, 1953
[31] W. C. Meecham, Variational method for the calculation of the distribution of energy reflected from a periodic surface. J. Appl. Phys. 27(4), 361-367, 1956
[32] R. Petit, Electromagnetic grating theories – limitations and successes, Nouv. Rev. D. Opt. 6(3), 129-135, 1975
[33] P. C. Waterman, "Scattering by periodic surfaces", J. Acoust. Soc. Am. 57(4), 791-802, 1975
[34] P. C. Waterman, "Comparison of the T-matrix and Helmholtz integral equation methods for wave scattering calculations – comments", J. Acoust. Soc. Am, 78(2), 804, 1985
[35] G. Whitman, Schwering F., Scattering by periodic metal-surfaces with sinusoidal height profiles – theoretical approach, IEEE Trans. Ant. Prop. 25(6), 869-876, 1977
[36] A. Wirgin, "New theoretical approach to scattering from a periodic interface", Opt. Comm. 27(2), 189-194, 1978
[37] A. K. Jordan, R. H. Lang, "Electromagnetic scattering patterns fron sinusoidal surfaces", Radio Science 14(6), 1077-1088, 1979
[38] A.Wirgin, "Reflection from a corrugated surface", J. Acoust. Soc. Am. 68(4), 692-699, 1980
[39] Abdullah Atalar, "Reflection coefficient for a lossy liquid-lossless isotropic solid interface", J. Acoust. Soc. Am. 65(7), 1101-1103, 1979
[40] J. M. Claeys, O. Leroy, "How to choose a square root in calculating the reflection coefficient for a lossy liquid-lossless isotropic solid interface", J. Acoust. Soc. Am. 68(8), 1894-1896, 1980
[41] Abdullah Atalar, "On the reflection coefficient which exceeds unity", J. Acoust. Soc. Am. 70(6), 1182-1183, 1981
[42] Marc Deschamps, "Reflection and refraction of the evanescent plane wave on plane interfaces", J. Acoust. Soc. Am. 96(7), 2841-2848, 1994
[43] M. Deschamps, C.L. Cheng, "Liquid-Thermoviscoelastic Solids Interface", Ultrasonics 27, 308-313, 1989
[44] J.P. Charlier, F. Crowet, "Wave Equations in linear Viscoelastic Materials", J. Acoust. Soc. Am. 79(6), 895-9000, 1986
[45] M. Abramowitz, I. A. Stegun, "Handbook of mathematical functions", Dover Publications, 1972
[46] Jean-Marie Claeys, "Theoretical Models to describe reflection and diffraction of ultrasound from layered media", PhD Thesis KUL department of Sciences (in dutch), 1985
[47] Nico F. Declercq, Joris Degrieck, Rudy Briers, Oswald Leroy, "Theoretical verification of the backward displacement of waves reflected from an interface having superimposed periodicity", Appl. Phys. lett. 82(17), 2533-2535, 2003

X.A.1.e On the Theoretical Possibility to Apply an Acoustic Diffraction Grating as a Complex Frequency Filter Device for Electronic Signals

In electronics, it is well known that filtering devices can be made that are able to decompose a signal instantaneously into a number of real frequency components. This procedure is equivalent to a numerical real time Fourier transform. However, it is also known that an electronic signal can be decomposed not just in real frequency components, but also in complex frequency components. The current section shows that it is theoretically possible to create a device, made of a periodically rough surface and a system that transforms the electronic signal into acoustic waves, that can be used to measure the amplitude attributed to considered complex frequency components of an electronic signal, in real time. This 'thought device' is mainly based on the directivity of diffracted sound and the complex frequency dependence of this directivity.
The contents of this section have been accepted for publication in Ultrasonics. (Imp. Fact. 0.844; SCI-index, Acoustics, rank:11 /28)

INTRODUCTION

From an old paper of Spitzenogle and Quazi [1] it can be learned that a 'time limited signal' can be decomposed into a summation of signals with exponentially varying amplitude as a function of time. This principle has later been translated [2] to space limited acoustic signals (bounded beams) and appeared to be excellent in explaining what happens to sound at the Rayleigh angle of incidence. The latter formed a strong impetus for the development of the inhomogeneous wave theory, which explains the behavior of plane waves having complex parameters. Lately, special attention was drawn on the case of inhomogeneous waves having complex frequency [3-6]. Such complex harmonic plane waves therefore return the inhomogeneous wave theory back to the paper of Spitzenogle and Quazi [1]. In acoustics, complex harmonic waves are building blocks of sound beams, bounded in space and in time. In electronics, signals are often not really bounded in time. However one is frequently interested in the instant properties of such signals. For that reason, a numerical spectrogram can be obtained that gives the amplitude as a function of the real frequency and as a function of time. An experimental spectrogram can also be formed (with some errors) in real time by an electronic filter system. Nevertheless, it may likewise be important to consider a 'spectrogram' of a signal not just in the real frequency space, but also in the more general complex frequency space. This is mathematically reachable within a time limited window [1], but it must also be possible to build a device that performs such a spectrogram in real time somehow by means of a filter system. In what follows, it is shown from a theoretical point of view, that an acoustic diffraction grating is a possible tool for that purpose.

COMPLEX HARMONIC PLANE WAVES

A thorough description of complex harmonic plane waves can be found in [3-6]. Therefore, we make this discourse very short. Complex harmonic plane waves are described by a particle displacement vector **u** as follows:

$$\mathbf{u} = A\mathbf{P}\exp\left(i\mathbf{k}\bullet\mathbf{r} - i\omega t\right) \tag{X.A.1.e_1}$$

Besides time *t* and space **r**, all parameters in (1), i.e. the amplitude *A*, the polarization **P**, the wave vector **k** and the angular frequency ω can be complex valued. Complex harmonic plane waves differ from harmonic plane waves by an angular frequency ω that is complex valued instead of real valued. Hence,

$$\omega = \omega_1 + i\omega_2\ ;\ \omega_1, \omega_2 \in \Re \tag{X.A.1.e_2}$$

and

$$\mathbf{u}\left(\mathbf{r}=0,t\right) = A\mathbf{P}\exp\left(\omega_2 t\right)\exp i\left(-\omega_1 t\right) \tag{X.A.1.e_3}$$

Henceforth, the term 'frequency' denotes $\omega/(2\pi)$ while the term angular frequency will be specifically used for ω itself. It is seen in (3) that the amplitude changes exponentially in time, through ω_2. For consistency with ref [1], we only consider $\omega_1 \geq 0$ and $\omega_2 \geq 0$. Complex harmonic waves are a solution of the visco-elastic wave equation if the dispersion relation holds [6]:

$$\mathbf{k}\bullet\mathbf{k} = \left(\frac{\omega}{v_0} - i\alpha_0\right)^2 \tag{X.A.1.e_4}$$

with v_0 the phase velocity of plane waves having a real wave vector and real frequency and with α_0 the intrinsic damping of the considered media.

Important for what follows is the definition of the energy velocity vector $\mathbf{v}_E$. It can be found in [3-4,6] that $\mathbf{v}_E$ is proportional to:

$$\frac{\mathbf{k}_2\omega_2 + \omega_1\mathbf{k}_1}{\omega_1^2 + \omega_2^2} \tag{X.A.1.e_5}$$

with $\mathbf{k}_1 = \mathrm{Re}(\mathbf{k})$ and $\mathbf{k}_2 = \mathrm{Im}(\mathbf{k})$.

THE DIFFRACTION OF COMPLEX HARMONIC PLANE WAVES

When harmonic plane waves, possessing a wave vector component k_x^{inc} along the interface, interact with a corrugated surface (see Fig. X.A.1.e_1), having a periodicity Λ, they diffract into harmonic plane waves of different orders 'm'.

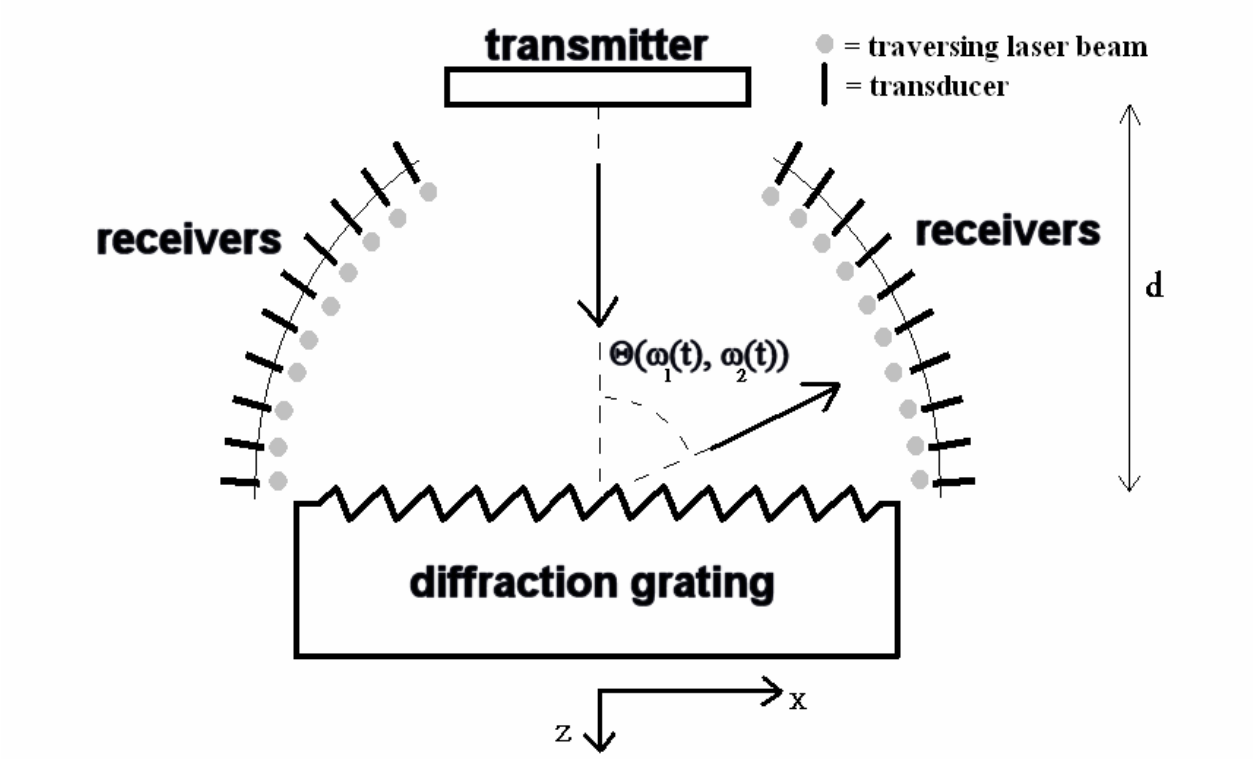

Fig. X.A.1.e_1: ***A schematic of the 'thought device', based on sound normally incident on a diffraction grating and diffracted into several directions. A discrete number of omni-directional transducers is placed at constant distance and different angles. In front of each transducer there is a laser beam traversing the sound beam in order to obtain the phase propagation direction as distinguished from the energy propagation direction.***

Each of these waves have a wave vector component

$$k_x^m = k_x^{inc} + m\frac{2\pi}{\Lambda} \qquad \text{(X.A.1.e\_6)}$$

along the interface and a component k_z^m perpendicular to the interface given by the dispersion relation (4). It has been shown before that this grating equation (6) is also valid for incident inhomogeneous waves. This is because it represents the spatial periodicity of the phase along the periodic interface and not the amplitude. Because the imaginary part of the frequency, of a given incident sound wave, influences the amplitude and not the phase, it is evident that the grating equation (6) also holds for incident complex harmonic plane waves.

For a given diffraction order 'm' and its wave vector component k_x^m along the interface, the sign of the wave vector component k_z^m normal to the interface is chosen according to well known sign

choice conventions [7-10] in terms of the phase propagation direction, based on causality principles, interpreted here in terms of the energy propagation direction.

HOW THE ACOUSTIC DIFFRACTION GRATING MAY WORK

The dispersion relation (4) represents 2 real equations, whereas the propagation of a complex harmonic plane wave is characterized by 2 unknown vectors, $\mathbf{k}_1$ and $\mathbf{k}_2$, and 2 unknown scalars, ω_1 and ω_2. For a chosen Euclidian space, the grating equation and incident wave propagation direction determine 1 vector component (in 2D space) or 2 vector components (in 3D space) of both $\mathbf{k}_1$ and $\mathbf{k}_2$. This means that in order to be identified, there must be two independent parameters quantified, for example ω_1 and ω_2, or for example two independent quantities that contain unambiguous information about $\mathbf{k}_1$ and $\mathbf{k}_2$.

In what follows, we show numerically that, under the right conditions, the direction of the energy velocity vector $\mathbf{v}_E$ as well as the direction of the phase velocity vector can be applied for that purpose, because for a given direction of the energy velocity vector $\mathbf{v}_E$ as well as the direction of the phase velocity vector, a unique couple (ω_1, ω_2) exists.

Consider an electronic signal s(t) that is decomposed into a series of complex frequency signals, i.e.

$$s(t) = \sum_n F_n(t) \exp\left(i\Omega_n(t)t\right) \tag{X.A.1.e_7}$$

Within a time limited interval around a certain t_0, a representation is possible with constant $S_n = F_n(t_0)$ and $\omega_n = \Omega_n(t_0)$, whence

$$s(t)_{t \simeq t_0} = \sum_n S_n \exp i\omega_n t \tag{X.A.1.e_8}$$

In the 'thought device' of Fig. X.A.1.e_1, this signal can be transmitted to a transducer (emitter) perpendicularly directed to a diffraction grating at a distance *d*. If for a moment the diffraction grating is not considered, then a receiver at distance 2d will receive the acoustic signal and will transform it again into an electronic signal. This output signal will differ from the input signal because the system signal>transducer>propagation medium>transducer>signal has a transfer characteristic different from unity. Hence, the output signal S_{out} is related to the input signal S_{in} as follows:

$$S_{out} = T\left(S_{in}\right) \tag{X.A.1.e_9}$$

in which *T* is an operator who changes the amplitude attributed to each complex frequency component in the signal. If there is a grating and if the receiving transducer (see short bold lines in Fig. X.A.1.e_1) is placed at a distance *d* from the surface at a certain direction, then there will

also a transfer operator *R* be involved, which corresponds to the reflection coefficient for the received reflected order.
Therefore, the received signal is ultimately described by

$$s(t)_{t \simeq t_0} = \sum_n RTS_n \exp i\omega_n t \qquad \text{(X.A.1.e\_10)}$$

As a consequence, if *R* and *T* are known for each possible ω_n, then measuring RTS_n reveals the values of S_n, i.e. the problem is reduced to measuring RTS_n as a function of each required ω_n. Therefore, the problem is reduced to defining what experimental 'condition' corresponds with each ω_n and measuring the accompanying amplitude for each of those 'conditions'. In what follows, it will be shown that measuring the phase propagation direction together with the energy propagation direction, defines a unique 'condition'. The energy propagation direction can practically be determined by a classical omni-directional transducer, whereas the phase propagation direction can be determined by the diffraction of laser light. The first is possible because an omni-directional transducer at a given spot measures by definition the encountered sound intensity, whereas the latter is possible because sound forms a diffraction grating for laser light en diffracts a laser light beam into different diffraction orders perpendicular to the sound wave fronts. The is the basic principle of acousto-optics. Both principles are depicted in Fig. X.A.1.e_2, where gray circular areas denote a cross section of a (diffracted) laser beam and where again the bold line represents the receiver. The set of short parallel lines in Fig. X.A.1.e_2 represent the wave fronts. The energy propagation direction and the phase propagation direction are denoted by a long arrow.

NUMERICAL SIMULATIONS

As explained, measuring the amplitude corresponding to a certain phase propagation direction and energy propagation direction, reveals the magnitude of a particular complex frequency component of a signal. There is however a limitation. When sound is received at a certain angle, it can only be attributed for certain to an order 'm' if there is no interference possible with other diffraction orders. Hence, a complex frequency spectrogram is solely possible within a certain interval in which there is no confusion possible between different diffraction orders. For that purpose the grating periodicity must be so that the maximum considered real frequency corresponds to the critical frequency for second order reflected waves. This critical frequency is defined as the largest frequency for which the second order reflected wave is evanescent (i.e. sticking to the interface). Practically this corresponds to the second order Scholte-Stoneley wave generating frequency, see for example ref [7-8]. The lowest frequency under consideration is then the critical frequency for first order waves, i.e. the first order Scholte-Stoneley wave generating frequency, because below this frequency, except for zero order reflected sound, there is no sound reflected from the interface.
We consider a periodically corrugated interface between water and a solid. The density of water is 1000 kg/m^3, the plane wave velocity in water is 1480 m/s and the periodicity of the corrugation is $\Lambda = 250\mu m$. For simplicity, we have only considered zero intrinsic damping. In Fig. X.A.1.e_3, the calculated phase propagation direction (here equal to the energy propagation direction) is depicted for normal incident harmonic homogeneous plane waves having real

frequencies between 4 MHz and 16 MHz. The dotted line corresponds to the first order reflected plane waves, whereas the solid line corresponds to second order reflected plane waves. The critical frequencies mentioned above, are directly visible as the frequencies at which the propagation direction starts to deviate from 90^0, measured from the normal to the interface.

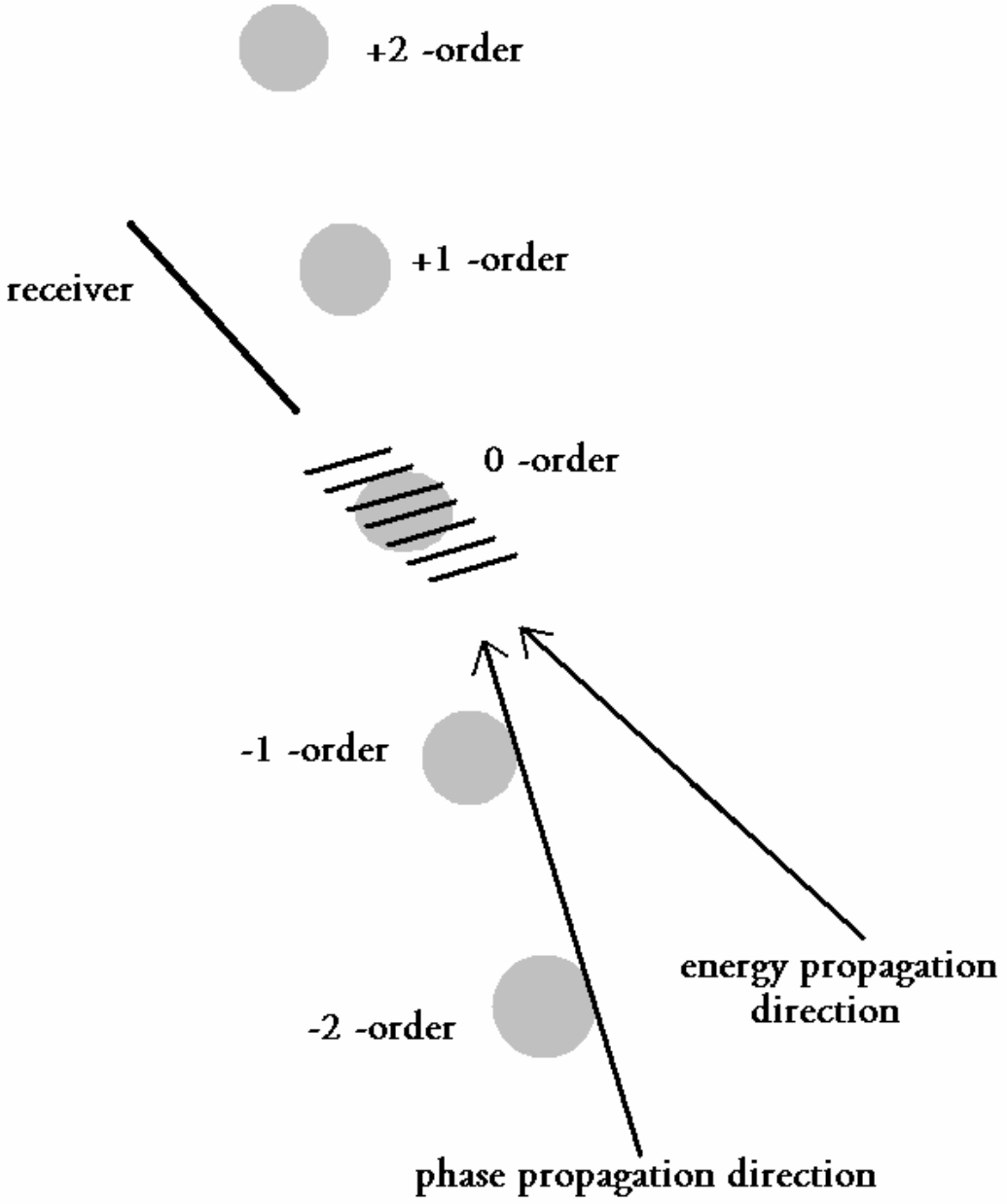

Fig. X.A.1.e_2: ***A close up of the omni-directional transducers of Fig. X.A.1.e_1, with attention to the diffraction direction of the traversing laser light. The difference between energy propagation direction and phase propagation must be measurable with this principle.***

Note that between approximately 6MHz and 12MHz there are only bulk reflected waves of the first order. This is the frequency region that we will focus on here in order to avoid interference between second and first order reflected sound waves. A 'thought device', as considered here,

will therefore only be able to filter between a limited frequency interval, i.e. between 6MHz and 12 MHz. Whenever necessary, this interval can be changed by using another grating periodicity.
In Fig. X.A.1.e_4 respectively Fig. X.A.1.e_5, the phase propagation direction and energy propagation direction are depicted as a function of the real and imaginary frequency. Comparison of these figures reveals, that for every couple (ω_1, ω_2) within the considered interval, there is one energy propagation direction and there is one phase propagation direction.
Furthermore, note that the projected iso-amplitude lines of one figure do not intersect more than once the projected lines in the other figure and therefore, for every combination of an energy propagation direction and a phase propagation direction, there corresponds only one couple (ω_1, ω_2). This shows numerically that there is a 'one to one' relation between the measurable quantities and (ω_1, ω_2). In other words, if the phase propagation direction and the energy propagation direction are measured instantaneously, together with the amplitude of the received sound, the complex frequency and its attributed amplitude are found.

CONCLUSIONS

It is recalled that a time varying electronic signal can be decomposed not just into real frequencies, but also into complex frequencies. The first method can be performed electronically by means of a filtering device. The second is more difficult. Here we have theoretically proposed a method based on a diffraction grating together with the use of omni-directional transducers and the diffraction of laser light. The basic principle is the fact that for each complex frequency there is a unique couple of energy propagation and phase propagation direction.

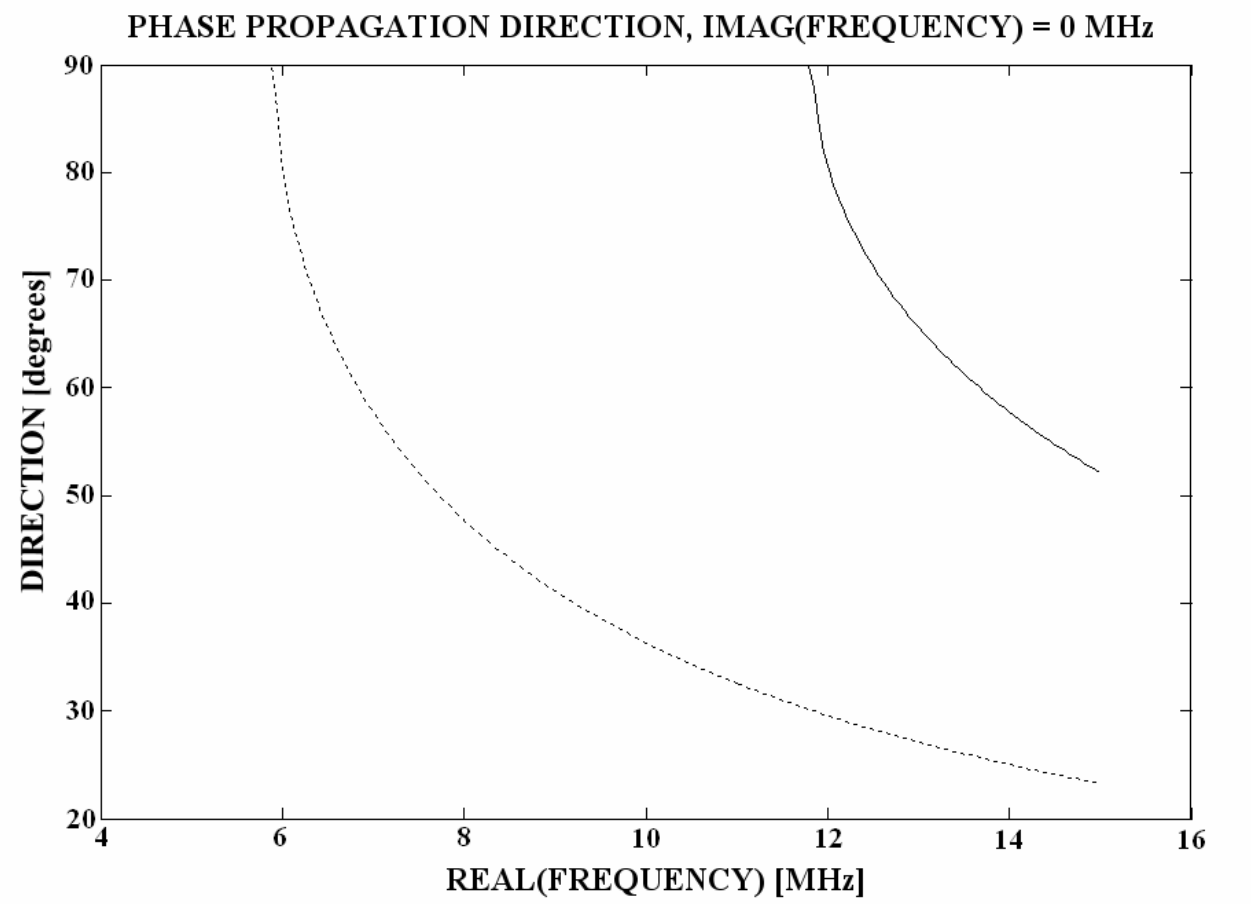

Fig. X.A.1.e_3: ***The phase propagation direction for first and second order reflected sound coming from normal incident harmonic sound at different real frequencies. Dotted line: first order, solid line: second order.***

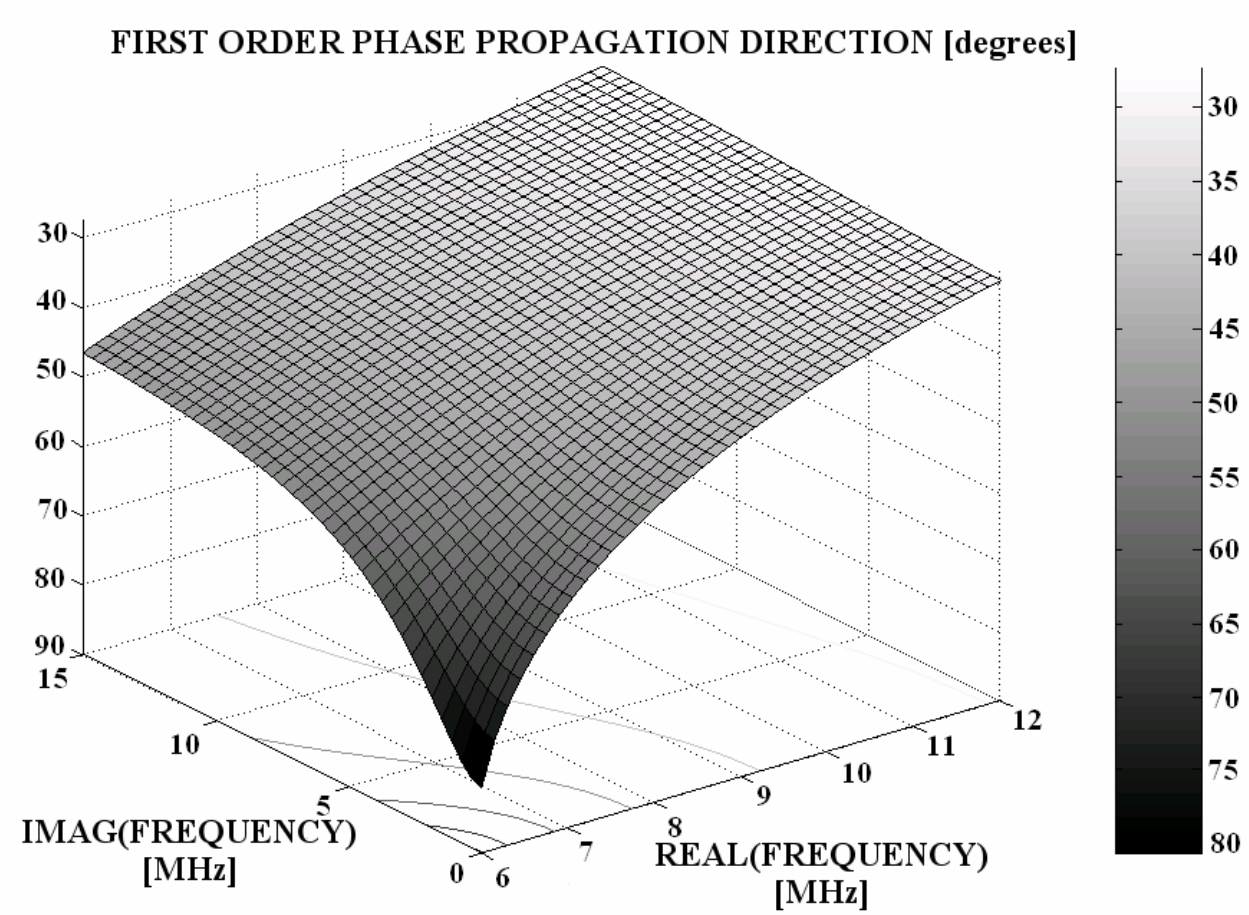

Fig. X.A.1.e_4: ***The first order phase propagation direction as a function of the complex frequency for normal incident sound. The lines on the horizontal surface are projected iso-amplitude lines.***

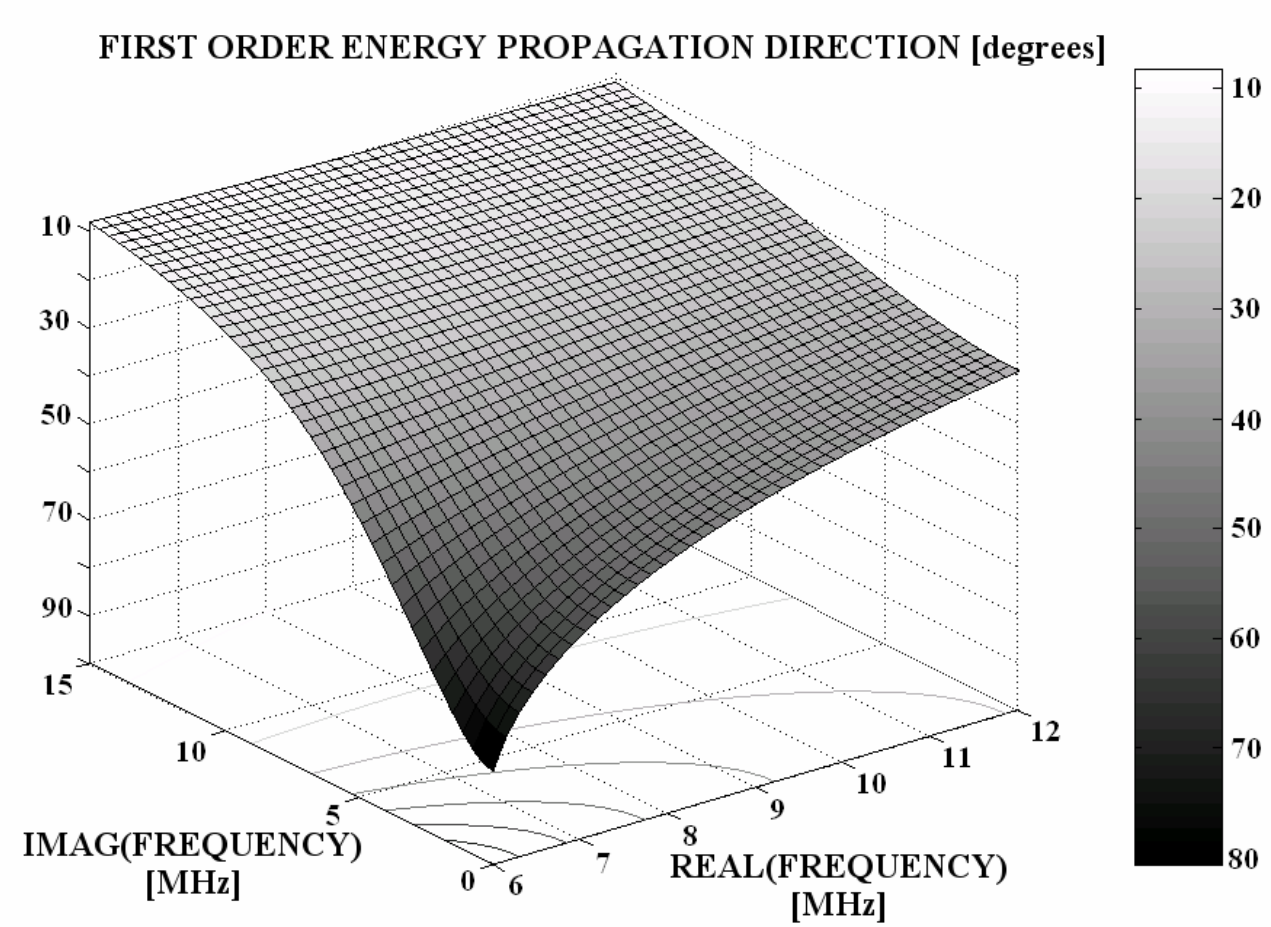

Fig. X.A.1.e_5: ***The first order energy propagation direction as a function of the complex frequency for normal incident sound. The lines on the horizontal surface are projected iso-amplitude lines. Comparison with Fig. X.A.1.e_5 reveals that for a given phase propagation direction and energy propagation direction, there corresponds only one couple*** (ω_1, ω_2)***. The reason is that each iso-amplitude line here does not cross a iso-amplitude line of Fig. X.A.1.e_4 twice.***

REFERENCES

[1] Frank R. Spitzenogle, Azizul H. Quazi, "Representation and Analysis of Time-Limited Signals Using a Complex Exponential Algorithm", J. Acoust. Soc. Am., 47(5), 1150-1155, 1970

[2] J. M. Claeys and O. Leroy, "Reflection and transmission of bounded sound beams on half-spaces and through plates", J. Acoust. Soc. Am. 72(2), 585-590, 1982

[3] M. Deschamps, B. Poiree, O. Poncelet, "Energy velocity of complex harmonic plane waves in viscous fluids", Wave Motion 25, 51-60, 1997.

[4] O. Poncelet, M. Deschamps, "Lamb waves generated by complex harmonic inhomogeneous plane waves", J. Acoust. Soc. Am., 102(1), 292-300, 1997

[5] A. Bernard, M. Deschamps, M. J. S. Lowe, "Comparison between the dispersion curves calculated in complex frequency and the minima of the reflection coefficients for an embedded layer", J. Acoust. Soc. Am. 107(2), 793-800, 2000

[6] Nico F. Declercq, Rudy Briers, Joris Degrieck, Oswald Leroy, "The History and Properties of Ultrasonic Inhomogeneous Waves", accepted for publication in IEEE-UFFC

[7] J. M. Claeys, Oswald Leroy, Alain Jungman, Laszlo Adler, "Diffraction of ultrasonic waves from periodically rough liquid-solid surface", J. Appl. Phys. 54(10), 5657-5662, 1983

[8] K. Mampaert, P. B. Nagy, O. Leroy, L. Adler, A. Jungman, G. Quentin, “On the origin of the anomalies in the reflected ultrasonic spectra from periodic surfaces”, J. Acoust. Soc. Am. 86(1), 429-431, 1989
[9] Koen E.-A Van Den Abeele, Rudy Briers, Oswald Leroy, “Inhomogeneous plane-wave scattering and mode stimulation on periodic rough surfaces”, J. Acoust. Soc. Am. 99(5), 2883-2897, 1996
[10] Rudy Briers, “Contributions to the study of acoustic scattering and conversion phenomena in discontinuous structures by introducing a mode theory and by applying the inhomogeneous wave theory”, PhD Thesis KULeuven University, department of sciences, 1995

X.A.1.f The Use of Polarized Bounded Beams to Determine the Groove Direction of a Surface Corrugation at Normal Incidence, the Generation of Surface Waves and the Insonification at Bragg-Angles.

Zero order reflected sound from a singly corrugated interface between a solid and a liquid, insonified from the solid side by circular polarized shear waves, can become almost perfect linearly polarized in a direction parallel or perpendicular to the corrugations, depending on the frequency, and can therefore reveal the direction of the corrugations.
When narrow bounded beams, formed by a summation of infinite plane waves, are diffracted at certain frequencies, depending on the angle of incidence, or vice versa, one can predict phenomena like backscattering at Bragg angle incidence and also the creation of Scholte-Stoneley waves.
The contents of this section have been published as: Nico F. Declercq, Rudy Briers, Oswald Leroy, " The use of polarized bounded beams to determine the groove direction of a surface corrugation at normal incidence, the generation of surface waves and the insonification at Bragg-angles", Ultrasonics 40/1-8 pp. 345-348, 2002.(Imp. Fact. 0.844; SCI-index, Acoustics, rank:11 /28)

INTRODUCTION

Consider an interface between a solid and a liquid, that is insonified from the solid side, with corrugations parallel to the y-axis, that is described by

$$p(x,z) = f(x) - z = p(x+\Lambda, z) = 0 \qquad \text{(X.A.1.f\_1)}$$

with Λ the period of the corrugation. The plane in which the diffracted orders are spread can reveal the direction of the grooves, using two transducers, while the polarization of the echo can also reveal the direction using only one transducer, i.e. when circularly polarized normal incident shear waves are used. The latter is discussed here. The results found for polarization will not differ if bounded beams were used instead of plane waves. If however, we wish to describe the complete amplitude distribution in space after diffraction, we must also reckon with bounded beams. The latter is worked out for normal incidence at the frequency that generates a second order Scholte – Stoneley surface wave and for oblique incidence at the Bragg angle.

NORMAL INCIDENT ELLIPTICALLY POLARIZED PLANE SHEAR WAVES

Theoretical considerations

Plane waves, having a polarization in a plane parallel to the surface generally have a horizontal y-component as well as a vertical x-component, whence a normally incident shear polarized wave field is characterized by its displacement field

$$\mathbf{u}_i = \left[B\mathbf{e}_x + C\mathbf{e}_y \right] e^{i\left(z\eta_i - \omega t\right)} \tag{X.A.1.f_2}$$

which corresponds to a potential

$$\boldsymbol{\psi}_i = \left[A\mathbf{e}_y - i\frac{C}{\eta_i}\mathbf{e}_x \right] e^{i\left[z\eta_i - \omega t\right]} \tag{X.A.1.f_3}$$

if we rewrite B as $B = -iA\eta_i$.

η_i is the wave number of the incident wave, while ω is its angular frequency.

The x component of Eq (X.A.1.f_2) or the y-component of Eq. (X.A.1.f_3) corresponds to a vertically polarized normally incident shear wave with continuity conditions developed by Mampaert et al [1,2], while the y component of Eq (X.A.1.f_2) corresponds to a horizontally polarized normally incident shear wave with continuity conditions developed by Declercq et al [3].

If B and C are in phase, Eq. (X.A.1.f_2) describes linearly polarized waves, while elliptically if they are out of phase. The particular case $C/B = e^{i\pi/2}$ involves circularly polarized anti clock wise rotating incident waves.

The horizontal component of the incident field generates horizontal reflected waves [3], while the vertical component generates vertical reflected waves [1,2], whence the zero order reflected transversal sound is described by the following potential

$$\boldsymbol{\psi}_r = \left[-i\frac{CP_0}{\eta_i}\mathbf{e}_x + \frac{iB}{\eta_i}S_0\mathbf{e}_y \right] e^{i\left(z\eta_{s0} - \omega t\right)} \tag{X.A.1.f_4}$$

or displacement

$$\mathbf{u}_r = \left[D\mathbf{e}_x + E\mathbf{e}_y \right] e^{i\left(z\eta_{s0} - \omega t\right)} = \left[BS_0\mathbf{e}_x + CP_0\mathbf{e}_y \right] e^{i\left(z\eta_{s0} - \omega t\right)} \tag{X.A.1.f_5}$$

with η_{s0} the wave number of the zero order reflected wave and S_0 and P_0 complex amplitudes that follow from the Mode Conversion Theory of diffraction [1-3].
The values of *D* and *E* determine the polarization of the reflected wave, just as *A* and *B* do for the incident wave.

Calculations

All calculations are performed using a sine shaped stainless steel – water interface, described in Table X.A.1.f_I.

Table X.A.1.f_I.: **Characteristics of the considered stainless steel – water interface**

	Stainless steel	water
$\rho(kg/m^3)$	7900	1000
$v_{shear}(m/s)$	3100	-
$v_{long}(m/s)$	5700	1480
$\Lambda = 350\mu m$ $Max(f) = 30\mu m$		

We consider a normally incident anti clock wise circularly polarized plane wave having unit amplitude

$$\mathbf{u}_i = \left[\mathbf{e}_x + e^{i\pi/2}\mathbf{e}_y\right] e^{i\left(z\eta_i - \omega t\right)} \qquad \text{(X.A.1.f\_6)}$$

that generates [1-3] a zero order reflected plane wave described in (X.A.1.f_5). In Fig. X.A.1.f_1, the intensity of *D* and *E* are plotted as a function of the frequency, while *phase(E)-phase(D)* is plotted in Fig. X.A.1.f_2.
It is seen in Fig. X.A.1.f_1, that both $|D|^2$ and $|E|^2$ show a distinct minimum, i.e. a frequency position at which Scholte Stoneley waves [1] are generated (minimum in $|D|^2$ at *8.4 MHz*), or Love waves [3] (minimum in $|E|^2$ at *8.88 MHz*). From Fig. X.A.1.f_2, we learn that the displacement rotation of the reflected wave is opposite to that of the incident wave for low frequencies and switches its rotation sense whenever a threshold frequency is surpassed at which surface waves are generated. For each frequency, one can draw an ellipse that is the displacement in real space at each instant of time during one vibration period. The special cases of *8.4 MHz* and *8.88 MHz* are shown in Fig. X.A.1.f_3, where it is seen that at the Scholte – Stoneley wave generating frequency, the reflected wave has a polarization that is almost linear and parallel to the wrinkles on the surface, while at the Love frequency the same effect happens but now the polarization is perpendicular to the wrinkles. Hence this reveals a method for determining the direction of the corrugation.

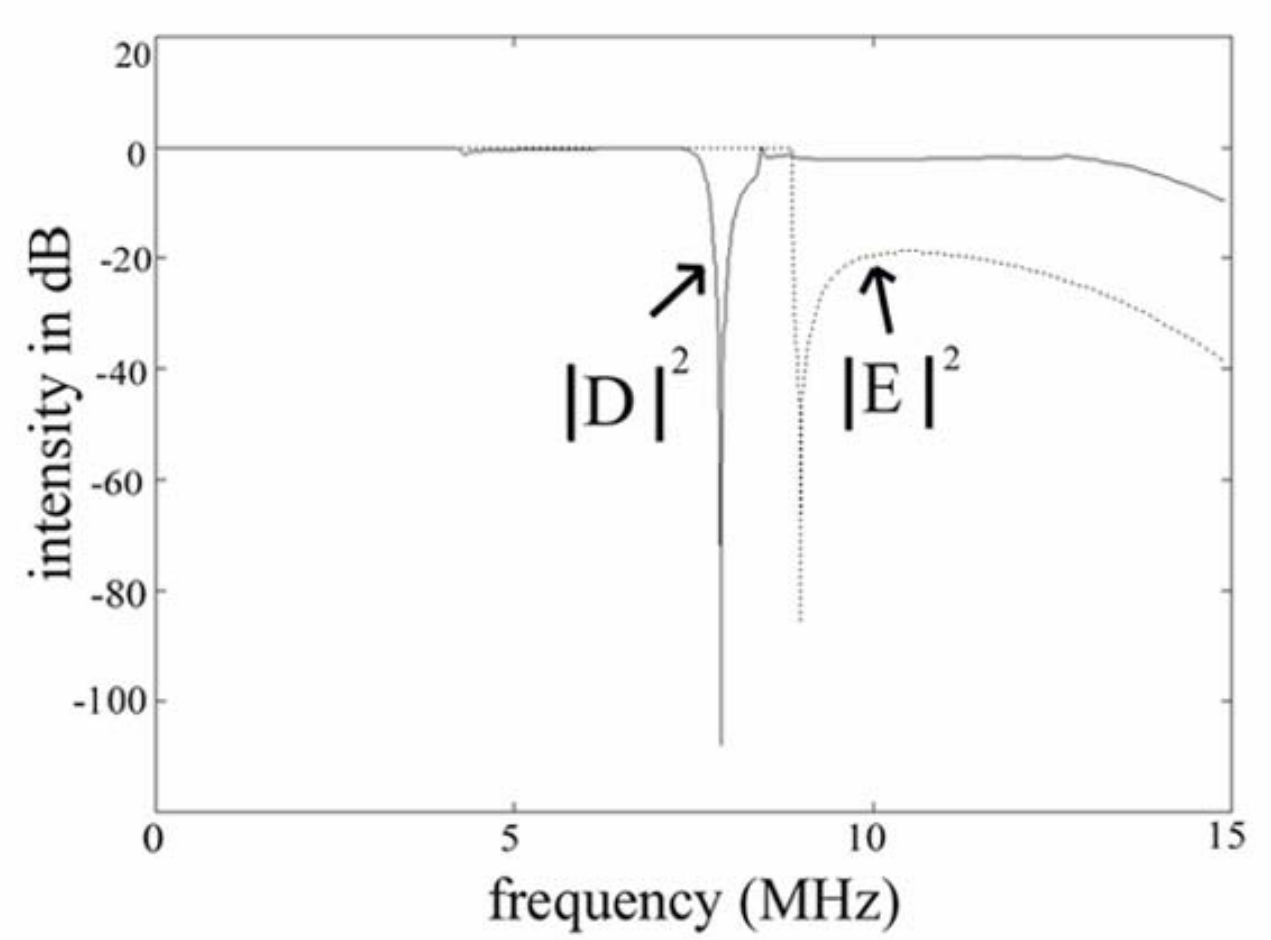

Fig X.A.1.f_1: ***The intensity spectrum of E and D.***

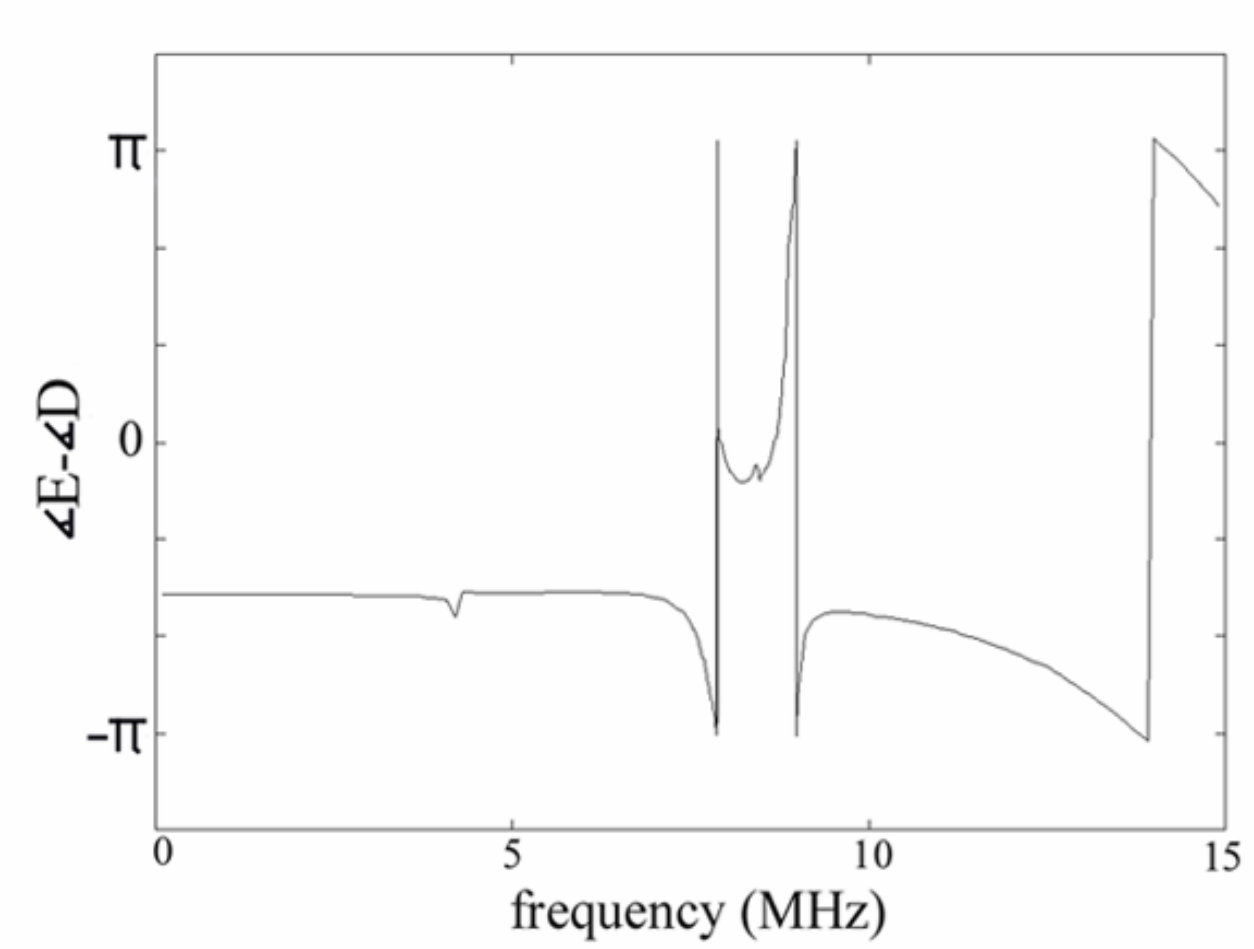

Fig X.A.1.f_2: ***The spectrum of the phase difference between E and D.***

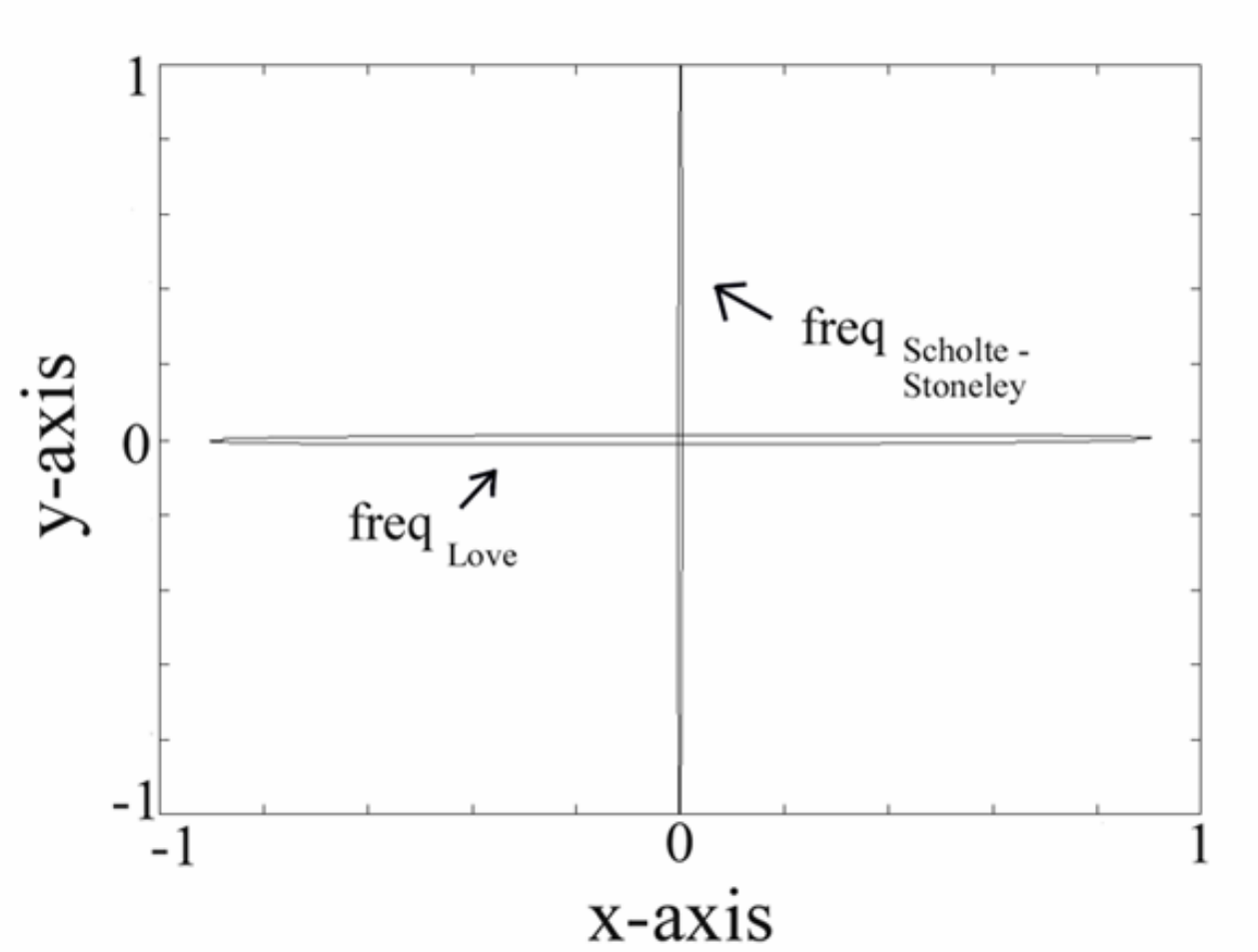

Fig X.A.1.f_3: ***The almost linear ellipses that are the displacements in one period of time, at the 'Scholte – Stoneley frequency' and the 'Love frequency'. Remember that the grooves in the surface are directed along the y-axis.***

INCIDENT GAUSSIAN BEAMS

Theoretical considerations

Now let us consider an incident beam that is gaussian bounded in one dimension, i.e. in the XZ-plane.
We denote the incoming gaussian beam as

$$\Psi_i(\mathbf{r}) = \int e^{-i\mathbf{k}\bullet\mathbf{r}}\phi_i(\mathbf{k})d\mathbf{k} = \frac{k}{2\pi N}\int e^{-ik\left(x\sin\theta + z\cos\theta\right)}e^{\frac{-k^2\left(1-\cos\left(\theta-\theta_0\right)\right)}{\sigma_k^2}}d\theta \qquad \text{(X.A.1.f\_7)}$$

with a spatial beam width

$$\sigma = \frac{1}{\sigma_k}\sqrt{\frac{\pi}{2}} \tag{X.A.1.f_8}$$

and angular beam width

$$\sigma_\theta = \arcsin\sqrt{-\frac{\pi \ln\left(1/2\right)}{\sigma^2 k^2}} \tag{X.A.1.f_9}$$

The angular beam width is defined as the angle $\theta - \theta_0$ for which

$$e^{\frac{-k^2\left(1-\cos\left(\theta-\theta_0\right)\right)}{\sigma_k^2}} = 1/2 \tag{X.A.1.f_10}$$

while the spatial beam width is defined as the x value for which $e^{\frac{-x^2}{2\sigma^2}} = 1/2$.

Calculations

Bragg - angle incidence

We consider longitudinally polarized sound (velocity v_l) incoming from the solid side and we solely reckon with the longitudinally polarized reflected sound. In agreement with diffraction of electromagnetic plane waves [4-6], we define the Bragg angle for a certain frequency as the angle of incidence for which most of the incoming energy is first order back scattered, or

$$\mathbf{k}_i = -\mathbf{k}_1 \Leftrightarrow \sin\theta_i = -\sin\theta_{l1} \tag{X.A.1.f_11}$$

whence the classical grating equation gives

$$\theta_{Bragg} = \arcsin\left(\frac{-v_l}{2\Lambda freq}\right) \tag{X.A.1.f_12}$$

The Bragg angle can only exist if

$$freq \geq \frac{v_l}{2\Lambda} \tag{X.A.1.f_13}$$

Relation (X.A.1.f_12) is a very practical tool for determining Λ from θ_{Bragg}, i.e. the angle at which the source receives the strongest echo.
In Fig. X.A.1.f_4, one can not only see that the reflected bounded beam is very divergent (due to the very narrow incident beam), but also that at the Bragg frequency, most of the reflected energy is sent back in the direction of the incident field.
There is no immediate relation between the here defined Bragg angle and the existence of surface waves on a corrugated interface.

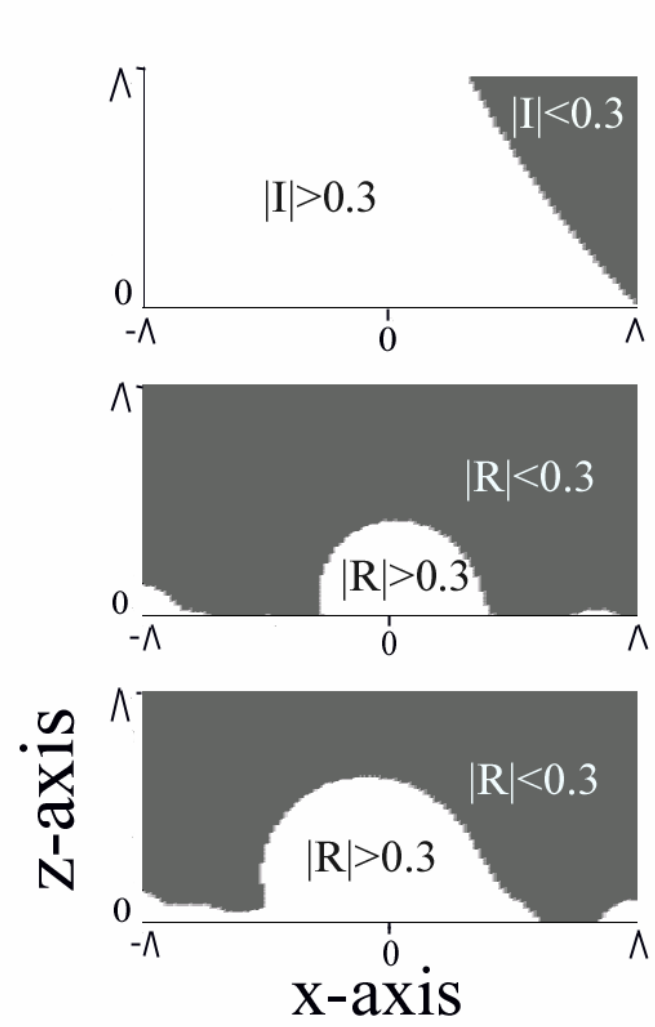

Fig X.A.1.f_4: ***Amplitude |I| of the incident longitudinally polarized gaussian profiled sound (top) and |R| of the longitudinally polarized reflected sound field, for an angle of incidence of –35.03°, for an arbitrary frequency of 10.34 MHz (middle) and for the Bragg frequency, calculated using (X.A.1.f_12), of 14.18MHz (bottom). In the white region, the amplitude exceeds an arbitrary chosen value of 0.3, while in the dark region the amplitude is less than 0.3. Despite of the divergence of the narrow reflected beam, it is clear that there is backscattering at the Bragg frequency (bottom).***

Normal incidence at the second order Scholte – Stoneley wave generating frequency

We know [1,2] that at certain frequencies, normal incident longitudinal plane waves can generate Scholte – Stoneley waves. In Fig. X.A.1.f_5, one can see that this also occurs when a bounded beam is used. Near the surface, amplitudes are calculated that exceed the incoming unit amplitude and this amplitude decreases exponentially for larger values of |z|. It is interesting to notice the maxima and minima along the x-axis, as a result of forward and backwards traveling surface waves.

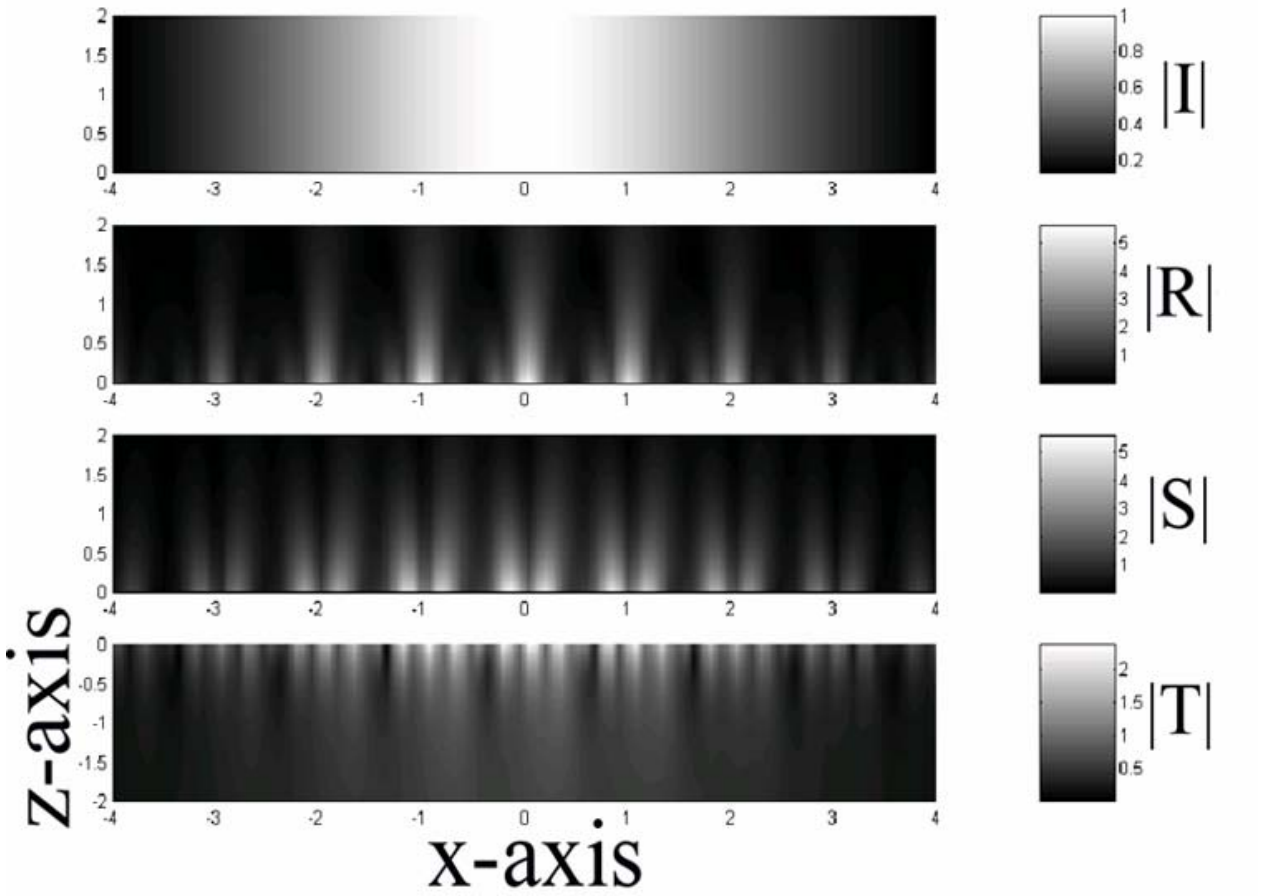

Fig. X.A.1.f_5: |I| is the amplitude of the normal incident longitudinal polarized gaussian profiled sound, |R| of the reflected longitudinal, |S| of the reflected shear and |T| of the longitudinal transmitted sound. The frequency is 8.3 MHZ and the generation of second order Scholte-Stoneley waves occurs. This phenomenon does not occur at arbitrary frequencies.
Notice the interference of the forward and backwards traveling surface wave. (x-coordinate: in numbers of Λ, z-coordinate: in numbers of $2\max\left[f\left(x\right)\right]$)

CONCLUSIONS

We have shown a method for discovering the wrinkle direction by using normal incident circularly polarized sound and we have shown the existence of Bragg angles and critical phenomena, i.e. surface wave generation, when gaussian bounded beams are used.

REFERENCES

[1] K. Mampaert and O. Leroy, Reflection and transmission of normally incident ultrasonic waves on periodic solid-liquid interfaces, J. Acoust. Soc. Am. 83(4) (1988) 1390-1398.
[2] J.M. Claeys and Oswald Leroy, Diffraction of ultrasonic waves from periodically rough liquid-solid surface, J. Appl. Phys. 54(10) (1983) 5657-5662
[3] Nico F. Declercq, Rudy Briers, Oswald Leroy, submitted to J. Acoust. Soc. Am.
[4] R. Adler, Interaction between light and sound, IEE Spectrum 4 (1967), 52-54
[5] M.G. Cohen, E.I. Gordon, Acoustic beam probing using optical techniques, Bell Syst. Tech. J. 44 (1965), 693-721

[6] Neil W. Ashcroft, N. David Mermin, Solid State Physics, International edition, Saunders College Publishing (1973), 96-97

X.A.1.g Diffraction of Horizontally Polarized Ultrasonic Plane Waves on a Periodically Corrugated Solid-Liquid Interface for Normal Incidence and Brewster Angle Incidence

The theory, and the use at normal incidence, of shear-vertically polarized waves (with polarization vector in the plane containing the incident wave vector and the normal on the interface) using the mode conversion method was tackled by Mampaert et al [J. Acoust. Soc. Am. 83(4), 1390-1398 (1988)]. Here we develop the theory for shear-horizontally polarized incident waves (with polarization vector perpendicular to both the normal on the interface and the incoming wave vector). We take into account normal incidence as well as oblique incidence. For normal incidence, we discover the generation of Love waves. If oblique incidence is considered, we discover the existence of a Brewster angle of incidence, comparable with the Brewster angle in optics, whence a diffraction grating can be used as a polarization filter.
The contents of this section have been published as: Nico F. Declercq, Rudy Briers, Joris Degrieck, Oswald Leroy, "Diffraction of horizontally polarized ultrasonic plane waves on a periodically corrugated solid-liquid interface for normal incidence and Brewster angle incidence", IEEE Trans. on UFFC, 49(11), 1516-1521, 2002. (Imp. Fact. 1.595 ;SCI-index, Engineering – electrical & electronic, rank:46/205)

INTRODUCTION

The diffraction of sound by a periodically corrugated surface that is traction free, or is the interface between a solid and a liquid, has been a hot topic for many years [1-4] and many methods have been developed in order to tackle the diffraction problem. Claeys et al [8] and Mampaert et al [6] use one method, the mode conversion theory of diffraction. The method describes the diffracted field as a summation of plane waves, traveling in directions determined by the classical grating equation and having amplitudes and phases determined by continuity of normal stresses and normal displacements at the interface. They report calculations tackling diffraction of incident plane waves with polarization perpendicular to the corrugations, i.e. the grooves, on the surface. Their results correspond very well with experiments. The present work reports calculations, using the same mode conversion principle, for incidence from the solid side and for a polarization that is parallel to the grooves, i.e. horizontally polarized waves. Contrary to Claeys and Mampaert who solely consider normal incidence in their calculations, we also take a look at other angles of incidence, more specifically at an angle that we define as the Brewster angle, involving similar effects as in optical scattering at plane interfaces. The geometry of the solid-liquid corrugated interface is depicted in Fig X.A.1.g_1.

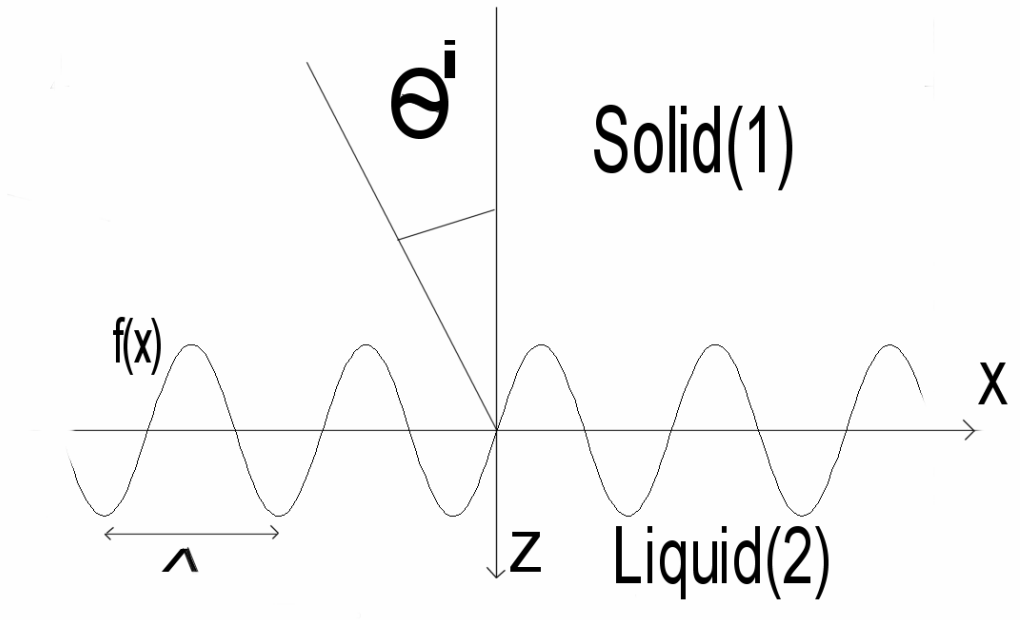

Fig. X.A.1.g_1: ***The geometry of the solid-liquid periodically corrugated interface***

THERE IS NO INTERSUBSET MODE CONVERSION

Consider a periodically corrugated surface that is the interface between a solid (henceforth upper index 1) and a liquid (henceforth upper index 2), described by

$$p(x,z) = f(x) - z = p(x+\Lambda, z) = 0 \qquad \text{(X.A.1.g\_1)}$$

Λ being the period. The wrinkles are directed parallel to the y-axis, whence one can easily distinguish between horizontally polarized waves having a polarization vector parallel to the grooves, and vertically polarized waves having a polarization vector perpendicular to the grooves. If $\mathbf{u}^1 = \mathbf{u}^i + \mathbf{u}^r$, with i = incident and r = reflected, is the particle displacement in the solid and $\mathbf{u}^2 = \mathbf{u}^t$, with t = transmitted, the particle displacement in the liquid, then we can establish continuity conditions for normal displacements and normal stresses as

$$\mathbf{u}^1 \bullet \mathbf{grad} p = \mathbf{u}^2 \bullet \mathbf{grad} p \qquad \text{(X.A.1.g\_2)}$$

$$\sum_{j=1}^{3} T_{kj}^1 grad(p)_j = \sum_{j=1}^{3} T_{kj}^2 grad(p)_j \qquad \text{(X.A.1.g\_3)}$$

with $\lfloor T_{kj} \rfloor$ the stress tensor. Relations (X.A.1.g_2-3) yield

$$A\mathbf{u}^i = B\mathbf{u}^r + M\mathbf{u}^t \qquad \text{(X.A.1.g\_4)}$$

A, *B* and *M* being operators depending, due to (X.A.1.g_1), solely on x,z and time. Since $\mathbf{u}^i$ also depends exclusively on x, z and time, relation (X.A.1.g_4) yields that both $\mathbf{u}^r$ and $\mathbf{u}^t$ also depend only on x, z and time. Taking this into account, we obtain for (X.A.1.g_2)

$$u_x^1 \frac{\partial f}{\partial x} - u_z^1 = u_x^2 \frac{\partial f}{\partial x} - u_z^2 \tag{X.A.1.g_5}$$

and for (X.A.1.g_3), we get

$$\left[\lambda^1 \frac{\partial u_z^1}{\partial z} + \left(2\mu^1 + \lambda^1\right) \frac{\partial u_x^1}{\partial x} \right] \frac{\partial f}{\partial x} - \mu^1 \left[\frac{\partial u_x^1}{\partial z} + \frac{\partial u_z^1}{\partial x} \right] \tag{X.A.1.g_6a}$$
$$= \left[\lambda^2 \frac{\partial u_z^2}{\partial z} + \left(2\mu^2 + \lambda^2\right) \frac{\partial u_x^2}{\partial x} \right] \frac{\partial f}{\partial x} - \mu^2 \left[\frac{\partial u_x^2}{\partial z} + \frac{\partial u_z^2}{\partial x} \right]$$

$$\mu^1 \left[\frac{\partial u_y^1}{\partial x} \frac{\partial f}{\partial x} - \frac{\partial u_y^1}{\partial z} \right] = \mu^1 \left[\frac{\partial u_y^2}{\partial x} \frac{\partial f}{\partial x} - \frac{\partial u_y^2}{\partial z} \right] \tag{X.A.1.g_6b}$$

$$\mu^1 \left[\frac{\partial u_z^1}{\partial x} + \frac{\partial u_x^1}{\partial z} \right] \frac{\partial f}{\partial x} - \left[\lambda^1 \frac{\partial u_x^1}{\partial x} + \left(2\mu^1 + \lambda^1\right) \frac{\partial u_z^1}{\partial z} \right] \tag{X.A.1.g_6c}$$
$$= \mu^2 \left[\frac{\partial u_z^2}{\partial x} + \frac{\partial u_x^2}{\partial z} \right] \frac{\partial f}{\partial x} - \left[\lambda^2 \frac{\partial u_x^2}{\partial x} + \left(2\mu^2 + \lambda^2\right) \frac{\partial u_z^2}{\partial z} \right]$$

The Lamé constants λ and μ are related to the bulk velocities of the respective media (superscript 1 for solid, 2 for liquid). Remark that further below, the symbol λ will also be used for the wavelength, but never using the superscripts 1 or 2.
The harmonic nature of the particle vibrations is accomplished by

$$\mathbf{u}^n = \left[u_x^n(x,z,t), u_y^n(x,z,t), u_z^n(x,z,t) \right] \; ; \; \dot{\mathbf{u}}^n = i\omega \mathbf{u}^n \tag{X.A.1.g_7}$$

for *n*=*i*,*r* or *t*
Conservation of linear momentum $\mathbf{P}$ when particle vibrations are conveyed yields

$$\mathbf{P}^i = \mathbf{P}^r + \mathbf{P}^t \tag{X.A.1.g_8}$$

The vibrating particles have a mass m^s and frequency ω in the solid and a mass m^l and the same frequency ω in the liquid, whence (X.A.1.g_8) imparts

$$u_j^r = u_j^i - \frac{m^l}{m^s} u_j^t \;;\; j=x,y,z \tag{X.A.1.g_9}$$

Equations (X.A.1.g_6) and (X.A.1.g_9) yield straightforwardly

$$\mathbf{u}^i = \left(0, u_y^i, 0\right) \Rightarrow \begin{cases} \mathbf{u}^t = (0,0,0) \\ \mathbf{u}^r = \left(0, u_y^i, 0\right) \end{cases} \tag{X.A.1.g_10a}$$

$$\mathbf{u}^i = \left(u_x^i, 0, u_z^i\right) \Rightarrow \begin{cases} \mathbf{u}^t = \left(u_x^t, 0, u_z^t\right) \\ \mathbf{u}^r = \left(u_x^r, 0, u_z^r\right) \end{cases} \tag{X.A.1.g_10b}$$

Therefore it is proved that an incident horizontally polarized wave doesn't produce any wave in the bulk of the fluid and will merely generate a horizontally polarized reverberated wave, while a vertically polarized wave, either dilatational or vertically shear polarized, will generate a vertical polarized reflected wave and a compressional transmitted wave. Hence, there is no mode conversion from horizontally incident waves to vertical refracted waves and there is also no mode conversion from vertically incident waves to horizontal refracted waves, i.e. there is no mode conversion from the horizontally polarized subset to the vertically polarized subset and vice versa.

HORIZONTALLY POLARIZED INCIDENT PLANE WAVES

In section II, it is shown that only shear horizontally polarized reflected waves are generated when horizontally polarized (shear) incident waves are considered. The velocity potential for the incoming plane wave is

$$\boldsymbol{\psi}^i = C \frac{-ik_z^i}{\left(k_x^i\right)^2 + \left(k_z^i\right)^2} e^{i\left(xk_x^i + zk_z^i\right)} \mathbf{e}_x + C \frac{ik_x^i}{\left(k_x^i\right)^2 + \left(k_z^i\right)^2} e^{i\left(xk_x^i + zk_z^i\right)} \mathbf{e}_z \tag{X.A.1.g_11}$$

while the velocity potential for the reflected sound is

$$\boldsymbol{\psi}^s = \xi(x,z)\mathbf{e}_x + \zeta(x,z)\mathbf{e}_z \tag{X.A.1.g_12}$$

where i = incident horizontally shear polarized, s = reflected horizontally shear and C is an amplitude. We decompose the reflected sound field into a Fourier series, therefore only considering sound that is traveling away from the surface and neglecting sound that is propagating towards the surface due to secondary scattering effects. According to Meecham [5], $\xi(x,z)$ as well as $\zeta(x,z)$ are allowed to be decomposed in a Fourier series [7] whenever the following conditions hold:

$$\max\left|f(x)\right| < \lambda^i \tag{X.A.1.g_13}$$

where

$$\lambda^i \approx \Lambda \tag{X.A.1.g_14}$$

Relations (X.A.1.g_13-14) are called the Lippman conditions [10] and state that the height of the roughness must be small compared to the wavelength of the ultrasonic wave and that the wavelength must be comparable with the roughness period.
Therefore

$$\begin{aligned}\boldsymbol{\psi}^s = C \sum_{m=-\infty}^{+\infty} R_m \Bigg[& \frac{-ik^s_{z,m}}{k^2_{x,m} + \left(k^s_{z,m}\right)^2} e^{i\left(xk_{x,m} + zk^s_{z,m}\right)} \mathbf{e}_x + \ldots \\ & \ldots + \frac{ik_{x,m}}{k^2_{x,m} + \left(k^s_{z,m}\right)^2} e^{i\left(xk_{x,m} + zk^s_{z,m}\right)} \mathbf{e}_z \Bigg]\end{aligned} \tag{X.A.1.g_15}$$

where m is the order of the plane wave functions, R_m is the reflection coefficient, $k^s_{z,m}$ is the wave number along the z-axis and $k_{x,m}$ is the wave number along the x-axis, of the m^{th} order plane wave. $k_{x,m}$ and $k^s_{z,m}$ are related to each other through the wave speed. The classical grating equation holds

$$\sin\theta^s_m = \sin\theta^i + m\frac{\lambda^s}{\Lambda} \Leftrightarrow k_{x,m} = k^i_x + m\frac{2\pi}{\Lambda} \tag{X.A.1.g_16}$$

where θ^i is the incidence angle with the z-axis, θ^s_m the reflection angle with the z-axis of the m^{th} order reflected plane wave and λ^s is the wavelength of the diffracted wave, governed by the frequency (not to be confused with the Lamé constant λ_1 or λ_2). Since, omitting the time dependence,

$$\mathbf{u}^1 = C\left[e^{i\left(xk_x^i + zk_z^i\right)} + \sum R_m e^{i\left(xk_{x,m} + zk_{z,m}^s\right)}\right]\mathbf{e}_y \qquad \text{(X.A.1.g\_17)}$$

The continuity conditions (X.A.1.g_2-3), at $z = f(x)$, demand

$$T_{yx}^1 grad(p)_x + T_{yz}^1 grad(p)_z = 0 \qquad \text{(X.A.1.g\_18)}$$

or likewise,

$$\left[\frac{\partial f}{\partial x}k_x^i - k_z^i\right]e^{i\left[xk_x^i + f(x)k_z^i\right]} = -\sum\left[\frac{\partial f}{\partial x}k_{x,m} - k_{z,m}^s\right]R_m e^{i\left[xk_{x,m} + f(x)k_{z,m}^s\right]} \qquad \text{(X.A.1.g\_19)}$$

Due to the periodicity of the tracks on the surface, both sides of (X.A.1.g_19) are periodic, whence we can write them as a Fourier series in $e^{ik_{x,n}x}$ with $k_{x,n}$ defined in (X.A.1.g_16) for 'm' replaced by 'n'. Then, equation (X.A.1.g_19) holds if and only if the Fourier coefficients of both sides in (X.A.1.g_19) are equal to each other. This results in

$$\left(k_x^i k_{x,n} - \frac{\omega^2}{v_s^2}\right)I_{i,n}^{k_z^i} = \sum R_m\left[-k_{x,m}k_{x,n} + \frac{\omega^2}{v_s^2}\right]I_{m,n}^s \qquad \text{(X.A.1.g\_20)}$$

where

$$I_{i,n}^{k_z^i} = \frac{1}{k_z^i}\int_0^\Lambda e^{i\left[\left(k_x^i - k_{x,n}\right)x + f(x)k_z^i\right]}dx \qquad \text{(X.A.1.g\_21)}$$

$$I_{m,n}^s = \frac{1}{k_{z,m}^s}\int_0^\Lambda e^{i\left[\left(k_{x,m} - k_{x,n}\right)x + f(x)k_{z,m}^s\right]}dx \qquad \text{(X.A.1.g\_22)}$$

involving

$$k_{x,m}^2 = \frac{\omega^2}{\left(v^s\right)^2} - \left(k_{z,m}^s\right)^2 \qquad \text{(X.A.1.g\_23)}$$

and

$$\left(k_x^i\right)^2 = \frac{\omega^2}{\left(v^s\right)^2} - \left(k_z^i\right)^2 \qquad \text{(X.A.1.g\_24)}$$

in which v^s is the shear wave velocity. As a consequence of the disability of fluids to carry shear waves, it is seen from (X.A.1.g_20) that the theory is also valid for pressure release surfaces. Equation (X.A.1.g_20) is valid for each *m* and *n* and therefore generates a transformation, having an infinite number of coefficients, of an infinite number of variables R_m. The discrete nature of this transformation enables us to calculate the value of the variables R_m using a computer procedure, whence it is also necessary to truncate the set of *m* and *n* values. The infinite transformation may be reduced to a finite transformation due to energy considerations. That is because it is physically necessary that only a finite number of R_m are significant since the incoming sound solely delivers finite energy per unit of time. We have performed calculations for m=1,2,3,.. and we have noticed that the alteration of the results when m or n exceed 3 does not exceed the smallest representable number of our computer. It can therefore be concluded that the results have converged as perfect as possible if we chop $\{R_m\}$ at |m|=3. For practical reasons however, we have chopped $\{R_m\}$ at |m|=8. Therefore we only consider $m,n \in \{-8,..,8\}$, i.e. a transformation of 17 by 17 is considered and also 17 unknown variables R_m. Even though the rapid convergence of our results makes numerical error estimation superfluous, it is interesting to remark that such an estimation can be made when necessary through power flow considerations [6] resulting in

$$\sum \left|\cos\theta_m^s\right| \left|R_m\right|^2 = \left|\cos\theta^i\right| \qquad \text{(X.A.1.g\_25)}$$

for the summation over all *m* for which $\sin\theta_m^s$ exists, determined by the classical grating equation (X.A.1.g_16).

CALCULATIONS

Normal incidence of horizontally polarized plane waves

The material properties are listed in Table X.A.1.g_I.

Table X.A.1.g_I: ***Material properties, and calculated frequencies and velocities (v_L) of Love waves for different solid-water interfaces with*** $\max|f(x)| = 35\mu m$ ***and*** $\Lambda = 350\mu m$

	$\rho(kg/m^3)$	$v_d(m/s)$	$v_s(m/s)$	Love-freq.(MHz)	v_L (m/s)
stainless steel	7850	5700	3100	8.83	3094.32
brass	8100	4700	2100	5.98	2092.49

perspex	1060	2350	1150	3.27	1144.13

Following Claeys et al [8] and Mampaert et al [6] who found anomalies in reflection spectra, for vertically polarized waves, that correspond to generated surface waves, we have calculated reflection spectra for horizontally polarized waves. It is seen from Fig. X.A.1.g_2, for a horizontally polarized plane wave with 0dB intensity, striking a sine shaped interface between stainless steel and water with $\max|f(x)| = 30\mu m$ and $\Lambda = 350\mu m$, that at 8.83 MHz, the zero order shows an anomaly accompanied by a maximum for the first order wave.

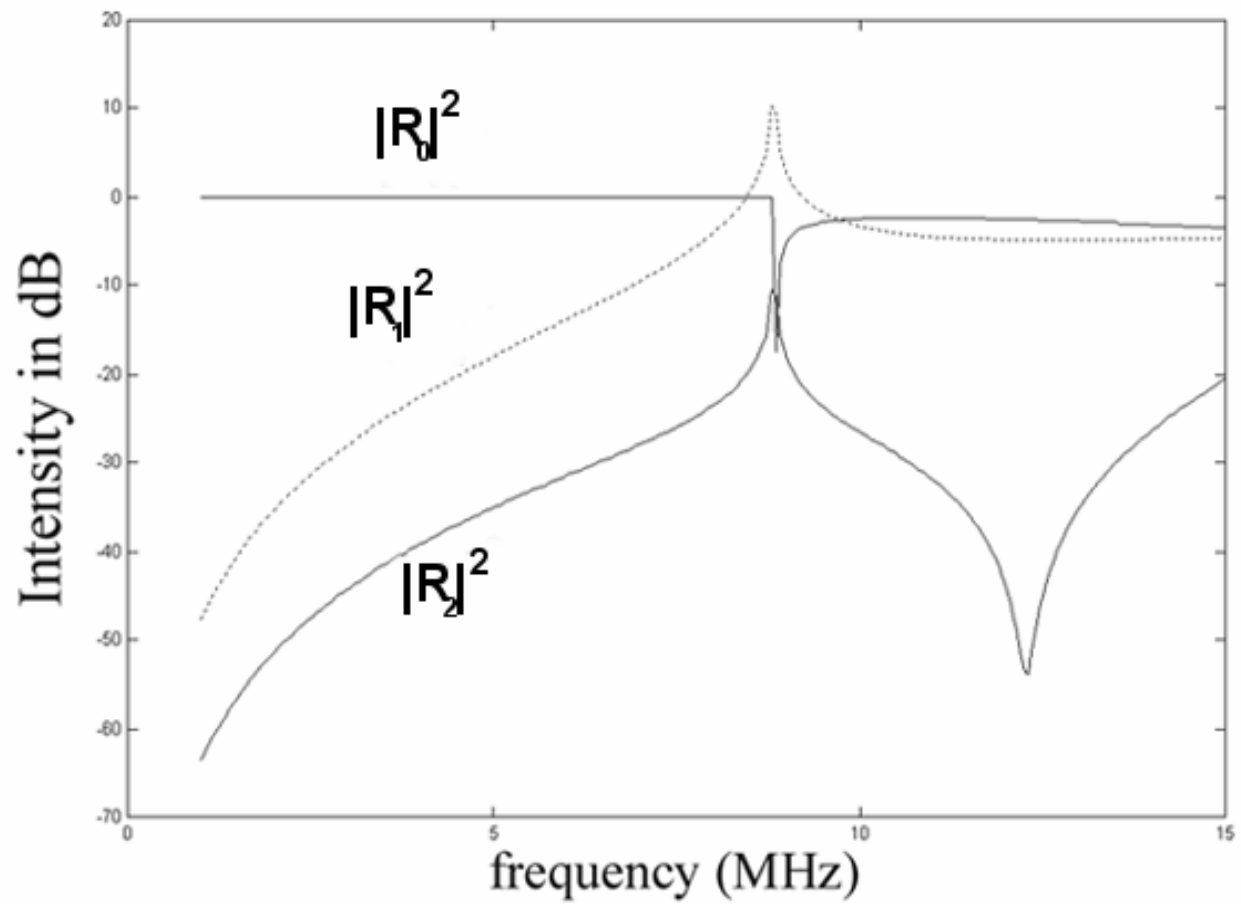

Fig. X.A.1.g_2: ***The intensities of the 3 first reflected orders in dB.***

The maximum exceeds 0dB whence it must be an inhomogeneous plane wave, which is in agreement with the fact that up to and beyond 8.83MHz, (X.A.1.g_23) shows that $k_{z,1}^{s}$ is pure imaginary. Since this surface wave is pure shear polarized, it is a Love like wave. It is also seen from Fig. X.A.1.g_3 that at 8.83 MHz the phase of the different orders undergo a strong phase shift. For low frequencies there is no diffraction because waves having a large wavelength are not susceptible for small corrugations, and hence all the energy, see Fig X.A.1.g_2, stays in the zero order wave during reflection. The reflected wave shows no phase difference with the zero phase of the incident wave. For higher frequencies, the incoming energy is distributed in the excited orders and the specular zero order reflected wave shows a phase difference with the incoming wave.

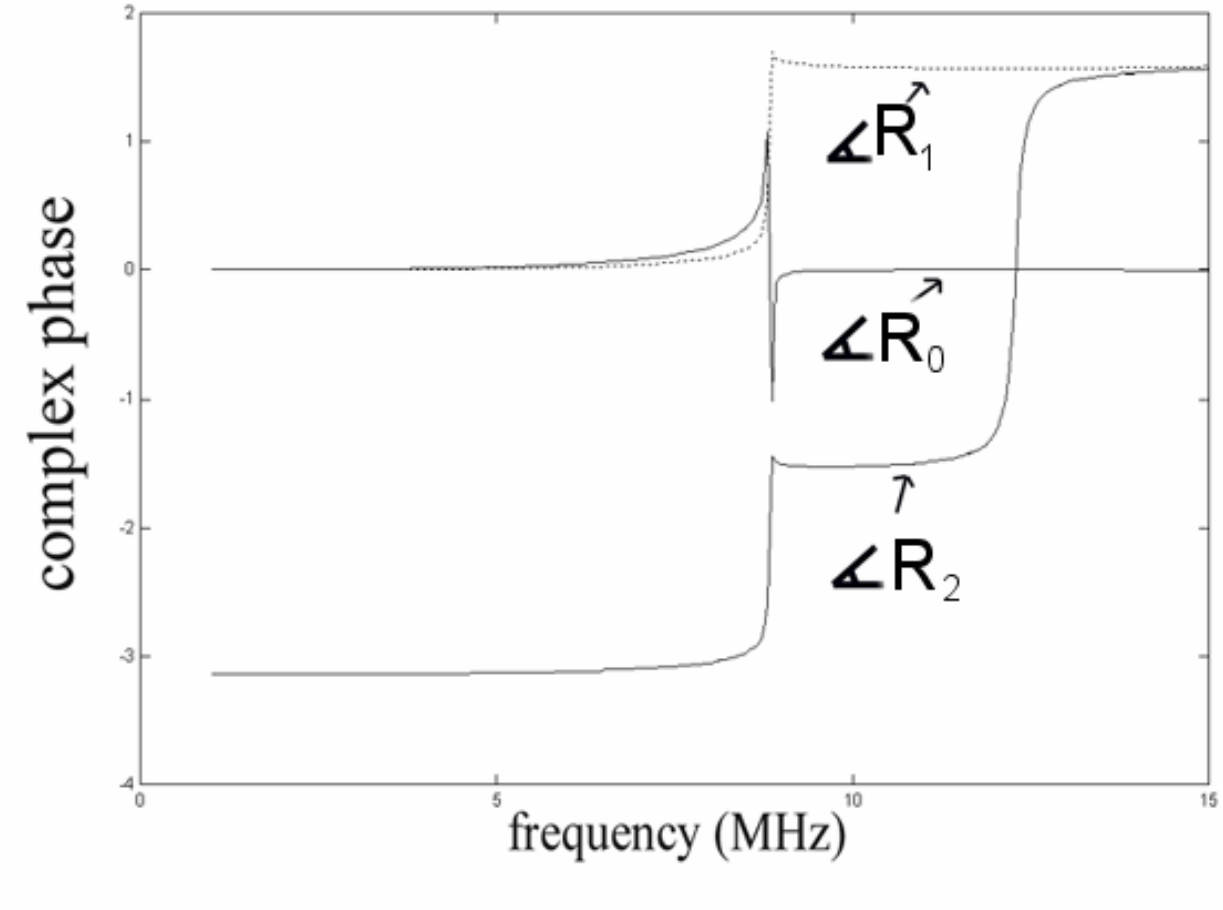

Fig. X.A.1.g_3: ***The phase of the 3 first reflected orders.***

Incidence at Brewster angle of shear polarized plane waves

In optics, it is well known [9] that for arbitrarily shear polarized light, incident at the Brewster angle, the specular reflected light has a polarization parallel to the interface and perpendicular to the incident light ray. In acoustics, we can, for a periodically corrugated surface, also define a Brewster angle θ^i in solids as the angle of the incident sound, at a chosen frequency and with arbitrary shear polarization, for which the zero order reflected sound, in the $-\theta^i$ direction, is horizontally polarized. In other words, the zero order reflected sound will contain a considerable amplitude R_0 of a horizontally polarized reflected wave and a negligible amplitude S_0 of a vertically polarized reflected shear wave. There will also be a longitudinal polarized wave, but it will propagate in a different direction and can be filtered out if bounded beams are used instead of plane waves. We know [6] that for normal incidence, vertically polarized incident waves will generate Scholte – Stoneley waves (SST) at certain frequencies $freq_{SST,m}$, m being the diffraction order, that absorb much, if not all, of the incident vertically polarized sound. We also know from

the classical grating equation (X.A.1.g_16) that in case SST are generated, the classical grating equation for an incident plane wave with k_x^i different from zero, may be written as

$$k_{x,m}^{SST} = k_x^i + m\frac{2\pi}{\Lambda} \tag{X.A.1.g_26}$$

As mentioned in section IV.1, SST contain an imaginary z-component and a real x-component of their wave vector. The wave vector is therefore complex. From the dispersion equation in the complex waves theory, which can be found in numerous papers concerning such waves, we know that we can write any wave vector as the angular frequency divided by a complex wave velocity. We may therefore express the real component of the wave vector, i.e. $k_{x,m}^{SST}$, as the angular frequency divided by its real (i.e. measurable) velocity *v*. We must however also take into account the direction of propagation (plus for positive m, minus for negative m). If we also assume that the velocity *v* of SST is independent of the frequency, i.e. *v* is equal to a frequency independent value v^{SST}, then

$$k_{x,m}^{SST} = sign(m)\frac{2\pi\, freq}{v^{SST}} \tag{X.A.1.g_27}$$

while for the (real) incident plane waves

$$k_x^i = \frac{2\pi\, freq}{v^s}\sin\theta^i \tag{X.A.1.g_28}$$

hence relations (X.A.1.g_26-28) result in

$$freq = \frac{m}{\Lambda}\frac{v^{SST}v^s}{sign(m)v^s - v^{SST}\sin\theta^i} \tag{X.A.1.g_29}$$

and

$$\theta^i = sign(m)\arcsin\left[\left(\frac{freq}{v^{SST}} - \frac{|m|}{\Lambda}\right)\frac{v^s}{freq}\right] \tag{X.A.1.g_30}$$

Relations (X.A.1.g_29-30) tell us at what angle θ^i the surface must be insonified with sound of frequency *freq* if SST are to be generated, and vice versa. It is this θ^i that we define as the Brewster angle of incidence, since zero order reflected sound will be created that, due to the extremely small amplitude of the reflected vertically polarized waves, does not, or almost not, contain any vertically polarized waves and thus solely horizontally polarized waves.
Now, we will see some consequences of the so far found formulas (X.A.1.g_29) and (X.A.1.g_30). It is important to note that for normal incidence [6] an SST generating frequency generates both an m'th order and a –m'th order SST. For oblique incidence however, as seen

from (X.A.1.g_29-30) for a certain angle of incidence, the m'th order and the –m'th order will be generated at different frequencies and for a chosen frequency, a θ^i will produce the m'th order, while $-\theta^i$ will generate the –m'th order. It is equally important to remark that only a θ^i can be found for a given frequency *freq*, using (X.A.1.g_30) if

$$0 < \left(\frac{v^S}{v^S + v^{SST}} \right) freq^{SST} \le freq \le freq^{SST} \left(\frac{v^S}{v^S - v^{SST}} \right) \qquad \text{(X.A.1.g\_31)}$$

$freq^{SST}$ being the frequency at which SST of the considered m'th order are generated using normal incidence and that for a given angle of incidence θ^i, a positive frequency can only be found, using (X.A.1.g_29), if

$$\sin\theta^i \, sign(m) < \frac{v^S}{v^{SST}} \qquad \text{(X.A.1.g\_32)}$$

It is also seen from (X.A.1.g_30) that

$$\begin{aligned} sign(\theta^i) = sign(m) &\Leftrightarrow freq \ge freq^{SST} \\ sign\left(\theta^i\right) = -sign(m) &\Leftrightarrow freq \le freq^{SST} \end{aligned} \qquad \text{(X.A.1.g\_33)}$$

One consequence of (X.A.1.g_31) is the necessity of $v^{SST} < v^s$, by which (X.A.1.g_32) is fulfilled too. Calculations have convinced us that the defined Brewster angle (X.A.1.g_30) never generates horizontally polarized surface waves since the Love wave frequency is always different from the SST frequency, whence θ^i is clearly a Brewster angle in every sense. An example is given in Fig X.A.1.g_3 for a shear polarized wave, of frequency 7Mhz, isonifying a sine shaped stainless steel – water interface with $\Lambda = 350\mu m$ and $\max\left|f\left(x\right)\right| = 30\mu m$, for which (X.A.1.g_31) gives

$$5.72MHz \le freq \le 16.16MHz \qquad \text{(X.A.1.g\_34)}$$

$v_2^{SST} = 1478.87 m/s$ was used, obtained from calculations using normal incidence at the second order SST generating frequency of *8.45 MHz*. Formula (X.A.1.g_30) for *7MHz* predict $\theta^i = 26°$, which is indeed part of the calculated broad valley of almost zero amplitude as shown in Fig. X.A.1.g_4, while the exact minima, i.e. the deepest spot in that broad valley of $\left|S_0\right|^2$ for 7MHz is at $\theta^i = 29.5°$, which would have been predicted by formula (X.A.1.g_30) if $v_2^{SST} = 1523.80 m/s$ was used. Since normal spectra predict $v_2^{SST} \approx v_1^{SST}$, we do not believe that the SST velocity alters because of a slightly different frequency, but due to a different angle of incidence. It is as if the continuously and obliquely insonifying sound field stimulates the SST to travel faster than in the event of normal incidence.

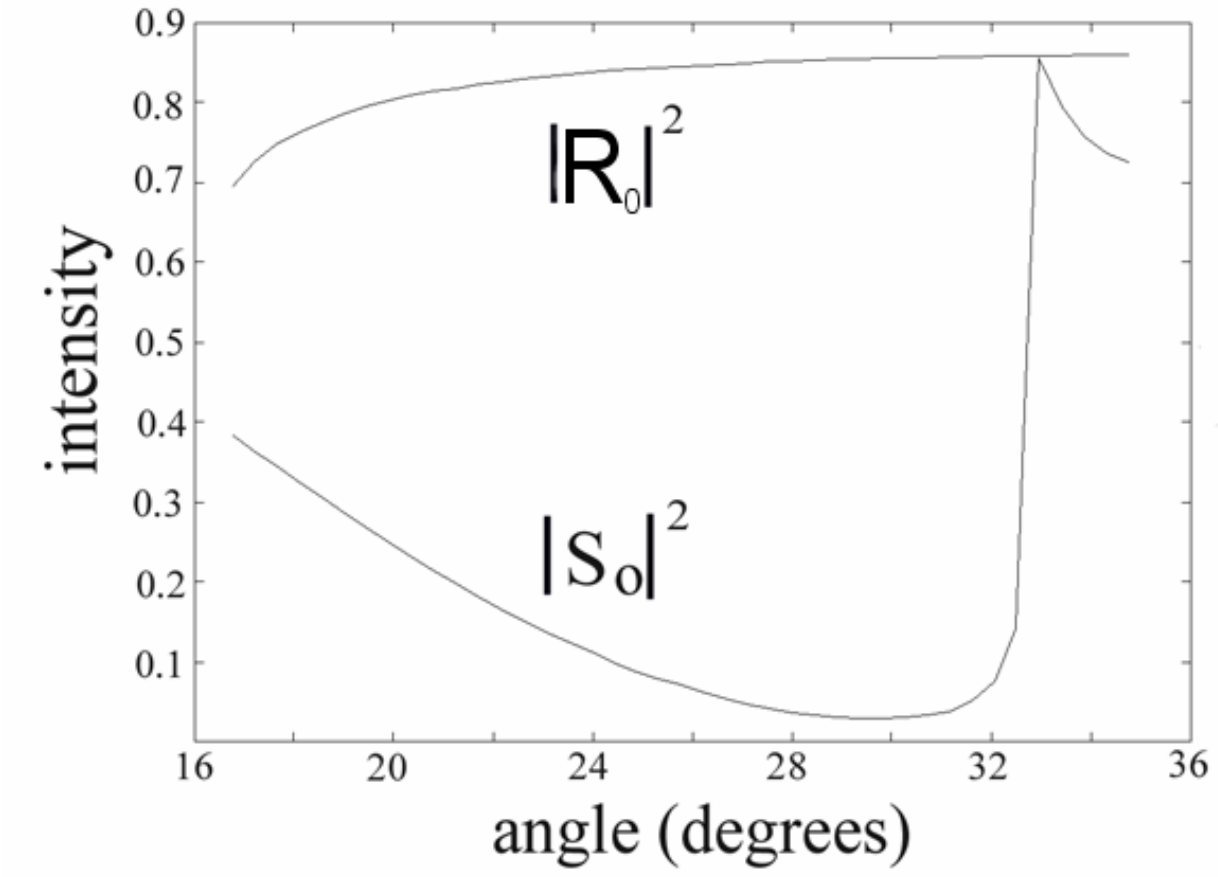

Fig. X.A.1.g_4: ***The intensity of*** S_0 ***and*** R_0 ***as a function of the angle of incidence.*** S_0 ***shows a minimum at 29.5° which we define as the Brewster angle.***

CONCLUDING REMARKS

A method has been developed to tackle the diffraction of horizontally polarized shear incident plane waves at a periodically corrugated interface between a solid and an ideal liquid. The creation of Love like waves has been predicted. The existence of a Brewster angle has been discovered and calculations using vertically polarized incident waves with continuity conditions obtained by Mampaert et al [6] show indications that Scholte – Stoneley waves, generated by diffraction have larger velocities for oblique incidence than for normal incidence.

REFERENCES

[1] R. Briers, O. Leroy, O. Poncelet, M. Deschamps, "Experimental verification of the calculated diffraction field generated by inhomogeneous waves obliquely incident on a periodically rough liquid-solid boundary", J. Acoust. Soc. Am. 106(2), 682-687 (1999)

[2] J. A. DeSanto, P. A. Martin, "On angular-spectrum representations for scattering by infinite rough surfaces", Wave Motion 24, 421-433 (1996)

[3] Richard C. McNamara, John A. DeSanto, "Numerical determination of scattered field amplitudes for rough surfaces", J. Acoust. Soc. Am. 100(6), 3519-3526 (1996)

[4] P. E. McSharry, D. T. Moroney, P. J. Cullen, "Wave scattering by a two-dimensional pressure-release surface based on a perturbation of the Green's function", J. Acoust. Soc. Am. 98(3), 1699-1716 (1995)
[5] W. C. Meecham, "Variational method for the calculation of the distribution of energy reflected from a periodic surface", J. Appl. Phys. , 27, 361-367 (1956)
[6] K. Mampaert, O. Leroy , "Reflection and transmission of normally incident ultrasonic waves on periodic solid-liquid interfaces", J. Acoust. Soc. Am. 83(4), 1390-1398 (1988)
[7] J. L. Uretsky, "The scattering of plane waves from periodic surfaces", Ann. Phys. 33, 400-427 (1965)
[8] J.M. Claeys, Oswald Leroy, Alain Jungman, Laszlo Adler, "Diffraction of ultrasonic waves from periodically rough liquid-solid surface", J. Appl. Phys. 54(10) 5657-5662 (1983)
[9] David Halliday, Robert Resnick, Jearl Walker, "Fundamentals of Physics, fourth edition", John Wiley & sons, 1017-1018 (1993)
[2] A. Lippmann, J. Opt. Soc. Am. 43, 408 (1953)

X.A.1.h Note on Scholte – Stoneley Waves on a Periodically Corrugated Surface

It is k*nown that the amplitude distribution and velocity of surface waves on a solid-liquid interface is influenced by the presence and the properties of a coating. It is shown that the effect on Scholte-Stoneley waves of roughness is intuitively comparable to the effect of a coating. Furthermore, this effect may be considered as an explanation for reported results concerning generated Scholte – Stoneley waves on rough surfaces.*

INTRODUCTION

On plane solid-liquid interfaces, Scholte – Stoneley waves are a solution of the Scholte – Stoneley equation [1], which is a generalization of the Rayleigh equation on solid-vacuum interfaces, and do not radiate. In several papers, the presence of Scholte-Stoneley waves on corrugated surfaces is also considered [2-4]. It is known from experiments that Scholte – Stoneley waves on corrugated interfaces do not radiate inherently (contrary to leaky Rayleigh waves) but solely through diffraction. If such a wave would travel along the corrugated interface with the real part of the wave vector directed parallel to the interface at each particular spot, then this would result in consecutive altering of that part of the wave vector direction during propagation. This effect would almost for certain result in inherent radiation of energy into one or both of the media. Since this effect does not appear for Scholte – Stoneley waves, it must be concluded that the real part of their wave vector is constantly directed along the direction of propagation, just as on a smooth interface.

The effect of the roughness is therefore comparable to the presence of a coating, with properties that differ from those of the solid and those of the liquid, comparable with the effect that fiber reinforced composites have properties that differ from the fibers as well as from the resin. For classical (smooth) coatings, we know that if for example a brass substrate is covered by an aluminum coating, surface waves will travel at a velocity corresponding to the water/brass case if the coating thickness is zero and corresponding to the water/aluminum case if the coating is sufficiently thick. From Franklin et al [5], we know that the effect of a coating on Scholte – Stoneley waves is a decrease or even an increase of their velocity, depending on the nature of the coating.

If the ‘coating’ is formed by a corrugation, its physical properties near the pure liquid will be almost exclusively determined by the properties of the liquid due to the relatively negligible presence of solid corrugations, while the opposite effect will occur near the pure solid side, as shown in Fig. X.A.1.h_1.

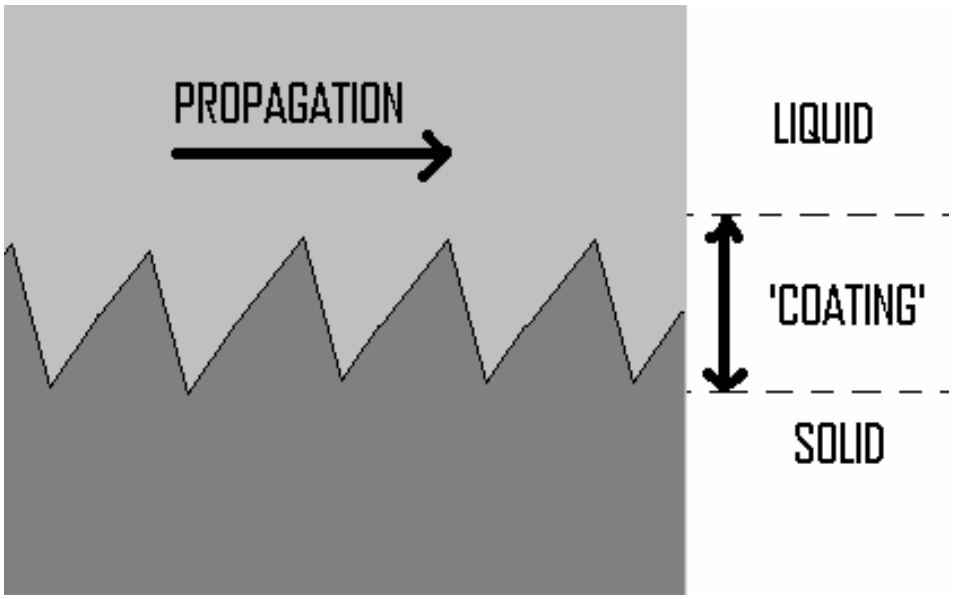

Fig. X.A.1.h_1: ***A corrugated interface between a liquid and a solid can be interpreted as a coated solid substrate in a liquid, when a Scholte – Stoneley wave travels along the interface with constant direction (propagation direction) of the real part of its wave vector.***

Hence the physical properties of the 'coating' will vary from 'almost liquid – like' to 'almost solid – like'. This continuity will have serious effects on the amplitude distribution of Scholte – Stoneley waves and also on their velocity. On smooth interfaces, the energy distribution of Scholte – Stoneley waves is more significant in the liquid part than in the solid part. It is expected that in the case of a corrugated surface, enhanced influence of the solid appears.
In what follows, some situations will be listed (found in the literature) in which a velocity increase is noticeable or is at least a plausible explanation of the observations.

NUMERICAL EXAMPLES EXTRACTED FROM REPORTED EXPERIMENTS

Diffraction experiments of Claeys et al [2]

Claeys et al [2] present diffraction curves for normal incident ultrasound on periodically corrugated surfaces, for several materials. The corrugation period is denoted by Λ. We do not aim at investigating their theory or at presenting a new theory, whence we solely focus on their experimental results. Their diffraction curves show so called Wood anomalies, which are believed to result from generated Scholte – Stoneley waves [2]. If we connect these Wood anomalies to the Scholte – Stoneley velocity v_{St} through the diffraction equation [2], we get for each diffraction order m

$$v_{St}(m) = f\Lambda/m \qquad \text{(X.A.1.h\_1)}$$

in which f is the frequency corresponding to the Wood anomaly.
The results for the velocities are listed in Table X.A.1.h_I. We call v_{smooth} the Scholte – Stoneley velocity for a smooth surface. It is seen from Table X.A.1.h_I that

$$v_{St}(m) > v_{smooth} \qquad \text{(X.A.1.h\_2)}$$

In other words, the velocity of Scholte – Stoneley waves appears to be higher for corrugated surfaces than for smooth surfaces and it even seems to exceed the velocity of sound in water (1480 m/s).

Table X.A.1.h_I: ***The velocities $v_{St}(m)$ [m/s]of Scholte – Stoneley waves corresponding to experimentally obtained Wood anomalies in diffraction spectra[2]. The diffraction order is m. The velocity on smooth surfaces is denoted by v_{smooth} and is numerically obtained form the Scholte – Stoneley equation[1]. The surfaces form the interface between a solid and water***

solid	v_{smooth}	$v_{St}(1)$	$v_{St}(2)$	$v_{St}(3)$
stainless steel	1479.568	1755 ± 2	1665 ± 2	1655 ± 2
brass	1476.759	1487 ± 2	1563 ± 2	1505 ± 2
perspex	885.817	1170 ± 2	1185 ± 2	1126 ± 2

Diffraction experiments of Tinel et al [4]

Tinel et al [4] report diffraction experiments for which the velocity of a Scholte – Stoneley wave on a corrugated interface (they call it a pseudo Scholte wave) between duraluminum and water is 1484.995 m/s, while only 1481.988 m/s on a smooth interface. Even here, a velocity increase seems to appear.

Field experiments of Chamuel and Brooke [3]

The Bragg frequency [3] f_{Bragg} of a corrugated surface is defined by

$$f_{Bragg} = v_{St} / (2\Lambda) \qquad \text{(X.A.1.h\_3)}$$

Chamuel and Brooke [3] report experiments in the shallow waters of the (corrugated) Barrow Strait of the Canadian Arctic that have been carried out by Brook, Thomson and MacKinnon [6] and that measure a Bragg frequency to which a Scholte - Stoneley wave velocity of 1460 m/s can be attributed, for averaged corrugations characterized by a height of 4m and Λ=75m, for dense limestone. If the Scholte-Stoneley equation is solved, one gets a Scholte – Stoneley velocity of only 1444m/s on a smooth surface characterized by the material properties of the Barrow Strait. Also here, a velocity increase seems to appear.

CONCLUDING REMARKS

It is shown from examples in the literature, that the increased velocity effect on Scholte-Stoneley waves seems to appear in many situations. We intuitively attribute this phenomena to the fact that the effect of a corrugation on a Scholte – Stoneley wave is comparable to the effect of a coating. The authors kindly invite readers to study this

phenomenon more properly or even to make an accurate theoretical model as to predict this effect.

REFERENCES

[1] Frédéric Padilla, Michel de Billy, Gérard Quentin, "Theoretical and experimental studies of surface waves on solid-liquid interfaces when the value of the fluid sound velocity is located between the shear and the longitudinal ones in the solid", J. Acoust. Soc. Am. 106(2), 666-673, 1999.

[2] J. M. Claeys, Oswald Leroy, Alain Jungman, Laszlo Adler, "Diffraction of ultrasonic waves from periodically rough liquid-solid surface", J. Appl. Phys. 54(10), 5657-5662, 1983

[3] Jacques R. Chamuel, Gary H. Brooke, "Transient Scholte wave transmission along rough liquid-solid interfaces", J. Acoust. Soc. Am. 83(4), 1336-1344, 1988

[4] Alain Tinel, Jean Duclos, Michel Leduc, "Scholte wave diffraction by a periodically rough surface", Physical Acoustics, Edited by O. Leroy and M. A. Breazeale, Plenum Press New York, 635-639,1991

[5] Franklin, M. Rousseau, P. Gatignol, "Scholte – Stoneley waves ina multilayered medium with elastic bond conditions at an interface", Physical Acoustics, Edited by O. Leroy and M. A. Breazeale, Plenum Press New York, 327-334,1991

[6] H. Brooke, D. J. Thomson, R. F. MacKinnon, "Propagation characteristics in shallow water with a high speed bottom", DREP Tech. Memo. 85, 18, 1985

X.A.2.a Diffraction of Homogeneous and Inhomogeneous Plane Waves on a Doubly Corrugated Liquid/Solid Interface

This section extends the theory of diffraction of sound on 1D corrugated surfaces to 2D corrugated surfaces. Such surfaces that are egg crate shaped, diffract incoming sound into all polar directions, which is fundamentally different from 1D corrugated surfaces. Even though the present section presents a theory which is valid for all angles of incidence, special attention is given to the particular case of the stimulation of surface waves by normal incident sound. The most interesting conclusion is that, depending on the frequency and the incident inhomogeneity, Scholte- Stoneley waves and leaky Rayleigh waves can be generated in different directions. This effect might be of particular interest in the development of Surface Acoustic Wave devices and the basic idea of this steering effect can be of importance for planar actuators.

INTRODUCTION

There are several papers available, applying many different methods, on the diffraction of sound by 1D corrugated surfaces. Many of them are listed in the book of Maystre [1]. The diffraction of sound on doubly corrugated surfaces ('egg crates') has only been sporadically taken under consideration in the literature. As far as we know, only three papers are available which tackle a similar physical problem.

The first is the paper of Boag et al [2], that describes a method using a so called source model. However, even though the title shows some resemblance with our title, actually, an investigation is performed on the diffraction caused by periodically distributed objects beneath a scattering surface.

The second paper is the one of Milder and Sharp [3] , which is based on a paper of Milder [4] , and describes a method which is in fact meant to be used in cases where scattering on complex rough surfaces, such as the ocean surface, appear. Their method is actually based on the Helmholtz integral expression of the scattered field and even though it is of practical interest in simulating scattering at very complex corrugations, whereas the current section is specialized to periodical surfaces, there is no consideration at all of generated surface waves and of the existence of anomalies in the reflection coefficient.

The third one is the paper of Bishop and Smith [5], in which research is reported on the diffraction on quite the same corrugated surfaces as is undertaken in the present section. However, Bishop and Smith [5] use a different method which consists of a 'T-matrix' formalism applying the Helmholtz-Kirchoff integral equations to represent the scattered pressure field in the liquid and the displacement field in the solid. Moreover, Bishop and Smith [5] limit their discourse to pure homogeneous incident plane waves, whereas the current section applies not only to homogeneous, but also to inhomogeneous plane waves. The reason for our focus on

inhomogeneous waves is the well known fact [6-8] that leaky Rayleigh waves can only be practically stimulated by inhomogeneous plane waves and not by homogeneous plane waves. Bishop and Smith [5] particularly focus on the interesting fact that the roughness shape is qualitatively unimportant for the phenomena that appear during diffraction and is completely unimportant in the positioning of anomalies that appear in the diffraction spectra as a function of the frequency or as a function of the angle of incidence. The present section does not investigate this phenomenon because it has been done by Bishop and Smith [5]. Another reason is because it can also be found in an earlier paper by Mampaert et al [9], in which a similar approach is formulated as in the present section, that for a singly corrugated surface, the shape of the corrugation is indeed relatively unimportant and has no effect at all on the position of anomalies in the reflection spectra. Furthermore, even though Bishop and Smith [5] observe some anomalies in their reflection spectra, they do not prove what exactly causes these anomalies, which could be done for example by means of depicting the displacement field of the diffracted sound. Finally, Bishop and Smith [5] apparently have not found any situation under which a reflection or transmission coefficient exceeds unity. However, it is known from earlier research [9-14] that Wood anomalies are caused by Scholte-Stoneley waves (SSTW) and that they must correspond to the specific property of diffracted waves having an amplitude exceeding unity accompanied by a pure imaginary wave vector component along the normal to the interface. Hence, although the paper of Bishop and Smith [5] is really interesting, the present section intends to better focus on the influence of the doubly corrugation on the generation of critical phenomena such as SSTW and leaky Rayleigh waves and tackles the diffraction of inhomogeneous waves which are known to be excellent tools to actually stimulate Rayleigh waves [6-8].

The current section follows the method of Claeys et al [10,15] and Mampaert et al [9,12-14] for incident homogeneous plane waves (i.e. the Rayleigh decomposition) and the extension of Briers et al [6-8,16,17] for inhomogeneous plane waves. This latter particular method applies a decomposition of the diffracted wave fields into inhomogeneous waves that travel each in a direction, and have an inhomogeneity, governed by the classical grating equation and the dispersion relation. This method has only been performed until now on singly corrugated surfaces, where it has been experimentally verified for incident homogeneous plane waves [9,15] as well as for incident inhomogeneous plane waves [8]. Actually, the limitations of the method are discussed in [6-10,12-17] and in this section we limit the discussion to examples where the method is valid, i.e. where the considered wavelengths meet the required Lippmann conditions. In the discussion below, we omit the time dependence $\exp(-i\omega t)$ of the sound field, since this factor can be added at any time in the results without altering any of the developed equations. The properties of inhomogeneous waves that appear in this section can also be found in [6-8,16,17] and in numerous papers dealing with such waves.

THEORETICAL DEVELOPMENT

Boundary Conditions

The doubly corrugated interface is described by

$$z = f(x,y) = f_x(x) + f_y(y) \qquad \text{(X.A.2.a\_1)}$$

with

$$f_x\left(x+\Lambda_x\right)=f_x\left(x\right) \text{ and } f_y\left(y+\Lambda_y\right)=f_y\left(y\right) \tag{X.A.2.a_2}$$

whence the boundary condition is given by

$$g\left(x,y\right)=f\left(x,y\right)-z=0 \tag{X.A.2.a_3}$$

An example of a doubly corrugated surface is given in Fig. X.A.2.a_1.

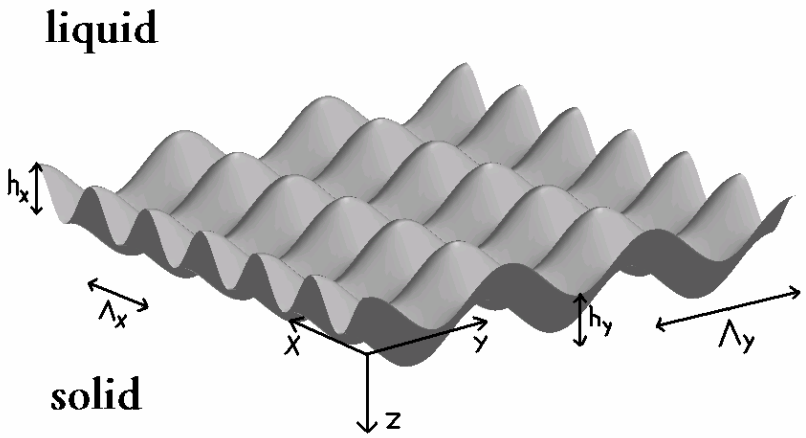

Fig. X.A.2.a_1: ***Example of a doubly corrugated interface between a liquid and a solid.***

The Rayleigh Decomposition in the Case of Doubly Corrugated Surfaces

If an inhomogeneous wave $\mathbf{N}^{inc}$ with complex wave vector $\mathbf{k}^{inc}$ is impinging the corrugated interface, it is scattered due to the corrugation into wave fields $\mathbf{N}^{p,scat}$, where p stands for any of the possible generated types of waves, e.g. reflected dilatational. One may write

$$\mathbf{k}^{inc}=\left(k_1^{inc}+i\alpha^{inc}\right)\mathbf{e}-i\beta^{inc}\mathbf{e}_{\perp} \tag{X.A.2.a_4}$$

where $\mathbf{e}$ is a unit vector along the direction of propagation and $\mathbf{e}_{\perp}\perp\mathbf{e}$.
k_1^{inc} is the propagation wave number, α^{inc} is the damping coefficient and β^{inc} is the inhomogeneity. Omitting the time dependence, one may write

$$N^{inc}=M\left(\alpha_{x,y}^{inc},\beta_{x,y}^{inc},x,y\right)M'\left(\alpha_z^{inc},\beta_z^{inc},z\right)F\left(k_{1,x,y}^{inc},x,y\right)F'\left(k_{1,z}^{inc},z\right) \tag{X.A.2.a_5}$$

where *M,* respectively *M'*, describe the amplitude and collect x- and y-, respectively z-, dependent quantities, while *F,* respectively *F'*, represent the phase and collect x- and y-, respectively z-, dependent quantities. The scattered fields are also written in that notation:

$$N^{p,scat} = M^{p,scat} M'^{p,scat} F^{p,scat} F'^{p,scat} \tag{X.A.2.a_6}$$

In the xy-plane, the amplitude of the scattered field is directly proportional to the amplitude of the incident field, whence

$$M\left(\alpha_{x,y}^{inc}, \beta_{x,y}^{inc}, x, y\right) = K^{p,scat} M^{p,scat} \tag{X.A.2.a_7}$$

in which $K^{p,scat}$ is a complex number that depends on the continuity conditions. Furthermore, it is supposed that the scattered field is described by an amplitude that is related to the overall structure of the surface (farfield approach), hence neglecting explicit dependence of individual spots inside the grooves. Therefore it is stated that $K^{p,scat}$ does not depend on x and y. Hence $M^{p,scat}$ and M have the same functional dependence on x and y and therefore

$$\alpha_{x,y}^{inc} = \alpha_{x,y}^{p,scat} \text{ and } \beta_{x,y}^{inc} = \beta_{x,y}^{p,scat} . \tag{X.A.2.a_8}$$

From the particular case of singly corrugated surfaces, it is known that this farfield assumption is valid whenever the Lippmann conditions [18] are fulfilled, stating that the corrugation period must be of the order of the incident wavelength and that the corrugation height is less than the incident wave length [19].
Whereas the amplitude in the farfield is thought of as being independent of particular spots inside the grooves, the same assumption cannot hold for the phase. That is because the phase is spatial dependent along the direction of propagation, whence it cannot be thought of as being equalized inside the grooves. Hence the phase $F^{p,scat} F'^{p,scat}$ is related to $F\left(k_{1,x,y}^{inc}, x, y\right) F'\left(k_{1,z}^{inc}, z\right)$ through a dependence on x and y. Furthermore, any coordinate translation

$$\Gamma(x,y) = \left(x + m\Lambda_x, y + n\Lambda_y\right), \; m,n \text{ integers} \tag{X.A.2.a_9}$$

leaves $F^{p,scat} F'^{p,scat}$ unaffected because (as the amplitude $M^{p,scat} M'^{p,scat}$ is neglected here) translating the grating using (X.A.2.a_9) does not alter the physical situation for these quantities. Therefore

$$F^{p,scat}(x,y) = F^{p,scat}\left(x + m\Lambda_x, y + n\Lambda_y\right) \tag{X.A.2.a_10}$$

whence a Fourier decomposition may be used

$$F^{p,scat}(x,y) = c \sum_{m=-\infty}^{+\infty} \sum_{n=-\infty}^{+\infty} C_{mn} e^{i\left(k^m x + k^n y\right)}, \tag{X.A.2.a_11}$$

$$k^m = m\frac{2\pi}{\Lambda_x},\ k^n = n\frac{2\pi}{\Lambda_y}$$

Relation (X.A.2.a_10) must be valid for all values (Λ_x, Λ_y), whence

$$c = e^{i\left(k_{1,x}^{inc}x + k_{1,y}^{inc}y\right)} \qquad \text{(X.A.2.a\_12)}$$

in order to fulfill Snell's law in the case of $(\Lambda_x = \infty, \Lambda_y = \infty)$
Relations (X.A.2.a_6-8) and (X.A.2.a_11-12) lead to the conclusion that

$$N^{p,scat} \qquad \text{(X.A.2.a\_13)}$$
$$= \sum_{m=-\infty}^{+\infty}\sum_{n=-\infty}^{+\infty} A^{mn} e^{i\left(\left(k_x^{inc} + \frac{2\pi m}{\Lambda_x}\right)x + \left(k_y^{inc} + \frac{2\pi n}{\Lambda_y}\right)y + k_z^{p,scat}z\right)}$$

A^{mn} having a complex value depending on the continuity conditions and k_x^{inc} respectively k_y^{inc} being the x and y components of the complex incident wave vector. It is clear that for example A^{mn}

$$k_x^m = k_x^{inc} + m\frac{2\pi}{\Lambda_x} \qquad \text{(X.A.2.a\_14)}$$

is the well known grating equation in the x direction. The one in the y direction for k_y^n is of course similar.
For the case of a singly corrugated surface, expression (X.A.2.a_13) has been used before [6-8, 16, 17] and was experimentally verified, but it had never been theoretically proved up to now that this extension of the famous grating equation for plane waves [9, 10, 12-15] is also valid for inhomogeneous waves.

Acoustic Potentials

Taking into account (X.A.2.a_13) and taking into account the characteristics of dilatational and shear waves, one may now write the incident waves $\mathbf{N}^{inc}$, the (dilatational) reflected waves $\mathbf{N}^r$, the dilatational respectively shear transmitted waves $\mathbf{N}^d$ and $\mathbf{N}^s$, as

$$\mathbf{N}^{inc} = A^{inc}\varphi^{inc}\left(ik_x^{inc}\mathbf{e}_x + ik_y^{inc}\mathbf{e}_y + ik_z^{inc}\mathbf{e}_z\right) \qquad \text{(X.A.2.a\_15)}$$

$$\mathbf{N}^r = \sum_{m,n} R^{m,n} \varphi^{m,n,r} \left(ik_x^{m,n,r} \mathbf{e}_x + ik_y^{m,n,r} \mathbf{e}_y + ik_z^{m,n,r} \mathbf{e}_z \right) \tag{X.A.2.a_16}$$

$$\mathbf{N}^d = \sum_{m,n} A^{m,n,d} \varphi^{m,n,d} \left(ik_x^{m,n,d} \mathbf{e}_x + ik_y^{m,n,d} \mathbf{e}_y + ik_z^{m,n,d} \mathbf{e}_z \right) \tag{X.A.2.a_17}$$

$$\mathbf{N}^s = \sum_{m,n} A^{m,n,s} \mathbf{P}^{m,n,s} \varphi^{m,n.s} \tag{X.A.2.a_18}$$

with

$$\varphi^{\varsigma} = e^{i\left(\mathbf{k}^{\varsigma} \bullet \mathbf{r} \right)} \tag{X.A.2.a_19}$$

and

$$k_x^{m,n,s} P_x^{m,n,s} + k_y^{m,n,s} P_y^{m,n,s} + k_z^{m,n,s} P_z^{m,n,s} = 0 \tag{X.A.2.a_20}$$

and with the following properties that hold for inhomogeneous waves:

$$\mathbf{k}^{\varsigma} = \mathbf{k}_1^{\varsigma} + i\mathbf{k}_2^{\varsigma} \tag{X.A.2.a_21}$$

$$\mathbf{k}_2^{\varsigma} = \boldsymbol{\alpha}^{\varsigma} - \boldsymbol{\beta}^{\varsigma} \tag{X.A.2.a_22}$$

$$\mathbf{k}_1^{\varsigma} \bullet \mathbf{k}_2^{\varsigma} = k_1^{\varsigma} \alpha^{\varsigma} \tag{X.A.2.a_23}$$

$$\boldsymbol{\beta}^{\varsigma} \perp \mathbf{k}_1^{\varsigma} \tag{X.A.2.a_24}$$

$$\alpha^{\varsigma} \left\| k_1^{\varsigma} \right. \tag{X.A.2.a_25}$$

$$\left(k_1^{\varsigma} \right)^2 - \left(\alpha^{\varsigma} \right)^2 - \left(\beta^{\varsigma} \right)^2 = \left(\frac{\omega}{v^{\varsigma}} \right)^2 - \left(\alpha_0^{\varsigma} \right)^2 \tag{X.A.2.a_26}$$

with v^{ς} the sound velocity and α_0^{ς} the intrinsic damping coefficient. Relation (X.A.2.a_20) can be found as the property of one of the possible propagation modes (pseudo shear) by demanding

inhomogeneous waves to be solutions of the wave equation. The properties of the pseudo dilatational waves are already present in the potential representation (X.A.2.a_15-18).

The Continuity Conditions

An incident inhomogeneous plane wave can be described by 7 initial values, i.e. the amplitude A^{inc}, and $k_1^{inc}, \xi_1^{inc}, \theta_1^{inc}, k_2^{inc}, \xi_2^{inc}, \theta_2^{inc}$ such that

$$\begin{aligned} k_{1,x}^{inc} &= k_1^{inc} \sin\xi_1^{inc} \cos\theta_1^{inc} \\ k_{1,y}^{inc} &= k_1^{inc} \sin\xi_1^{inc} \sin\theta_1^{inc} \\ k_{1,z}^{inc} &= k_1^{inc} \cos\xi_1^{inc} \\ k_{2,x}^{inc} &= k_2^{inc} \sin\xi_2^{inc} \cos\theta_2^{inc} \\ k_{2,y}^{inc} &= k_2^{inc} \sin\xi_2^{inc} \sin\theta_2^{inc} \\ k_{2,z}^{inc} &= k_2^{inc} \cos\xi_2^{inc} \end{aligned} \qquad \text{(X.A.2.a\_27)}$$

In media τ ($\tau = 1$ for liquid, $\tau = 2$ for solid) the stress tensor T^{τ} is given by its elements [20, 21]

$$T_{mn}^{\tau} = \sum_{\eta} \left(\lambda_1^{\tau} + \lambda_2^{\tau} \frac{\partial}{\partial t} \right) \varepsilon_{\eta\eta}^{\tau} \delta_{m,n} + 2 \left(\mu_1^{\tau} + \mu_2^{\tau} \frac{\partial}{\partial t} \right) \varepsilon_{mn}^{\tau} \qquad \text{(X.A.2.a\_28)}$$

in which the strain tensor ε_{mn}^{τ} is given by its elements

$$\varepsilon_{mn}^{\tau} = \frac{1}{2} \left[\partial_m N_n^{\tau} + \partial_n N_m^{\tau} \right] \qquad \text{(X.A.2.a\_29)}$$

The Lamé constants are given by λ_1^{τ} and μ_1^{τ}, while the viscosity coefficients are given by λ_2^{τ} and μ_2^{τ}. They fulfill the dispersion relation if

$$\mathbf{k}^{\tau} \bullet \mathbf{k}^{\tau} = \frac{\rho_{\tau} \omega^2}{\left(\lambda_1^{\tau} - i\omega\lambda_2^{\tau} \right) + 2 \left(\mu_1^{\tau} - i\omega\mu_2^{\tau} \right)} \qquad \text{(X.A.2.a\_30)}$$

for dilatational waves and if

$$\mathbf{k}^{\tau} \bullet \mathbf{k}^{\tau} = \frac{\rho_{\tau}\omega^2}{\left(\mu_1^{\tau} - i\omega\mu_2^{\tau}\right)} \tag{X.A.2.a_31}$$

for shear waves where ρ_{τ} is the density. The Lamé constants are related to the shear velocity v_s^{τ}, the dilatational velocity v_d^{τ}, the intrinsic damping coefficient for shear waves $\alpha_0^{s,\tau}$ and the intrinsic damping coefficient for dilatational waves $\alpha_0^{d,\tau}$ through the dispersion relation (X.A.2.a_26) and (X.A.2.a_30-31) as

$$\lambda_1^{\tau} = \omega^2\left(v_d^{\tau}\right)^2 \rho_{\tau}\left(\omega - \alpha_0^{d,\tau} v_d^{\tau}\right)\frac{\alpha_0^{d,\tau} v_d^{\tau} + \omega}{\left(\omega^2 + \left(\alpha_0^{d,\tau} v_d^{\tau}\right)^2\right)^2} - 2\mu_1^{\tau} \tag{X.A.2.a_32}$$

$$\mu_1^{\tau} = \omega^2\left(v_s^{\tau}\right)^2 \rho_{\tau}\left(\omega - \alpha_0^{s,\tau} v_s^{\tau}\right)\frac{\alpha_0^{s,\tau} v_s^{\tau} + \omega}{\left(\omega^2 + \left(\alpha_0^{s,\tau} v_s^{\tau}\right)^2\right)^2} \tag{X.A.2.a_33}$$

$$\lambda_2^{\tau} = 2\alpha_0^{d,\tau}\omega^2\left(v_d^{\tau}\right)^3 \frac{\rho_{\tau}}{\left(\omega^2 + \left(\alpha_0^{d,\tau} v_d^{\tau}\right)^2\right)^2} - 2\mu_2^{\tau} \tag{X.A.2.a_34}$$

$$\mu_2^{\tau} = 2\alpha_0^{s,\tau}\omega^2\left(v_s^{\tau}\right)^3 \frac{\rho_{\tau}}{\left(\omega^2 + \left(\alpha_0^{s,\tau} v_s^{\tau}\right)^2\right)^2} \tag{X.A.2.a_35}$$

In order to find the unknown coefficients $R^{m,n}$, $A^{m,n,d}$, $A^{m,n,s}P_x^{m,n,s}$, $A^{m,n,s}P_y^{m,n,s}$, $A^{m,n,s}P_z^{m,n,s}$, it is necessary to solve the equations that describe the continuity of normal stress and strain along the interface (X.A.2.a_3), i.e.

$$\left(\mathbf{N}^{inc} + \mathbf{N}^{r}\right) \bullet \nabla g = \left(\mathbf{N}^{d} + \mathbf{N}^{s}\right) \bullet \nabla g \ \text{ along } \ g = 0 \tag{X.A.2.a_36}$$

$$\sum_j T^1_{ij} (\nabla g)_j = \sum_j T^2_{ij} (\nabla g)_j \text{ along } g = 0 \qquad \text{(X.A.2.a\_37)}$$

and also (see (X.A.2.a_20))

$$\left(A^s_{mn} P^{m,n,s}_x k^{m,n,s}_x + A^s_{mn} P^{m,n,s}_y k^{m,n,s}_y + A^s_{mn} P^{m,n,s}_z k^{m,n,s}_z \right) \varphi^{m,n.s} = 0 \qquad \text{(X.A.2.a\_38)}$$

Conditions (X.A.2.a_36-38) lead to 5 equations that are periodic in x and y, whence a sufficient condition for a correct solution is that the Fourier coefficients (of the left and right side of the continuity equations) are equal for a Fourier transform $x \mapsto A\left(k^p, k^q\right)$ over the interval $\left[0 \to \Lambda_x, 0 \to \Lambda_y\right]$.

The 5 equations for each integer ‘p’ and ‘q’ are:

Equation 1:

$$\begin{aligned}
& A^{inc} I^{inc,p}_x I^{inc,q}_y i k^{inc}_z \left(-\left(k^1\right)^2 + k^{inc}_x k^p_x + k^{inc}_y k^q_y \right) \\
& + \sum_{m,n} R^{m,n} I^{m,n,r,p}_x I^{m,n,r,q}_y \left(i k^{m,n,r}_z \right) \left(-\left(k^1\right)^2 + k^m_x k^p_x + k^n_y k^q_y \right) \\
& + \sum_{m,n} A^{m,n,d} I^{m,n,d,p}_x I^{m,n,d,q}_y \left(i k^{m,n,d}_z \right) \left(\left(k^d\right)^2 - k^m_x k^p_x - k^n_y k^q_y \right) \\
& - \sum_{m,n} A^{m,n,s} P^{m,n,s}_x I^{m,n,s,p}_x I^{m,n,s,q}_y k^{m,n,s}_z \left(k^p_x - k^m_x \right) \\
& - \sum_{m,n} A^{m,n,s} P^{m,n,s}_y I^{m,n,s,p}_x I^{m,n,s,q}_y k^{m,n,s}_z \left(k^q_y - k^n_y \right) \\
& + \sum_{m,n} A^{m,n,s} P^{m,n,s}_z I^{m,n,s,p}_x I^{m,n,s,q}_y \left(k^{m,n,s}_z \right)^2 = 0
\end{aligned} \qquad \text{(X.A.2.a_39)}$$

Equation 2:

$$
\begin{aligned}
&-A^{inc} I_x^{inc,p} I_y^{inc,p} k_z^{inc} \rho_1\left(k_x^p - k_x^{inc}\right) \\
&- \sum_{m,n} R^{m,n} I_x^{m,n,r,p} I_y^{m,n,r,q} k_z^{m,n,r} \rho_1\left(k_x^p - k_x^m\right) \\
&+ \sum_{m,n,\pm} A^{m,n,d} I_x^{m,n,d,p} I_y^{m,n,d,q} k_z^{m,n,d} \\
&\times \rho_2\left(-k_x^m + \left(1 + 2\frac{\left(k_x^m\right)^2 - \left(k^d\right)^2}{\left(k^s\right)^2}\right) k_x^p + \frac{2k_y^n k_x^m k_y^q}{\left(k^s\right)^2}\right) \\
&+ \sum_{m,n} A^{m,n,s} P_x^{m,n,s} I_x^{m,n,s,p} I_y^{m,n,s,q} ik_z^{m,n,s} \\
&\times \rho_2\left(1 - \frac{k_x^m k_x^p}{\left(k^d\right)^2} + \left(\frac{1}{\left(k^d\right)^2} - \frac{1}{\left(k^s\right)^2}\right)\left(k_x^m\right)^2 - \frac{k_y^n k_y^q}{\left(k^s\right)^2}\right) \\
&+ \sum_{m,n} A^{m,n,s} P_y^{m,n,s} I_x^{m,n,s,p} I_y^{m,n,s,q} ik_z^{m,n,s} \\
&\times \rho_2\left(\left(\frac{2}{\left(k^s\right)^2} - \frac{1}{\left(k^d\right)^2}\right) k_y^n k_x^p - \frac{k_x^m k_y^q}{\left(k^s\right)^2} + \left(\frac{1}{\left(k^d\right)^2} - \frac{1}{\left(k^s\right)^2}\right) k_x^m k_y^n\right) \\
&+ \sum_{m,n} A^{m,n,s} P_z^{m,n,s} I_x^{m,n,s,p} I_y^{m,n,s,q} \rho_2 i\left(k_z^{m,n,s}\right)^2 \\
&\times \left(\left(\frac{1}{\left(k^d\right)^2} - \frac{1}{\left(k^s\right)^2}\right) k_x^m - \left(\frac{1}{\left(k^d\right)^2} - \frac{2}{\left(k^s\right)^2}\right) k_x^p\right) = 0
\end{aligned}
\qquad \text{(X.A.2.a\_40)}
$$

Equation 3:

$$
\begin{aligned}
&-A^{inc} I_x^{inc,p} I_y^{inc,p} k_z^{inc} \rho_1 \left(k_y^q - k_y^{inc} \right) \\
&- \sum_{m,n} R^{m,n} I_x^{m,n,r,p} I_y^{m,n,r,q} k_z^{m,n,r} \rho_1 \left(k_y^q - k_y^n \right) \\
&+ \sum_{m,n} A^{m,n,d} I_x^{m,n,d,p} I_y^{m,n,d,q} k_z^{m,n,d} \\
&\times \rho_2 \left[-2 \frac{\left(k^d \right)^2}{\left(k^s \right)^2} k_{y,n} + 2 \frac{\left(k_y^n \right)^2}{\left(k^s \right)^2} k_y^q + \ldots \right. \\
&\left. \ldots + 2 \frac{k_y^n k_x^m k_x^p}{\left(k^s \right)^2} + \left(1 - 2 \frac{\left(k^d \right)^2}{\left(k^s \right)^2} \right) \left(k_y^q - k_y^n \right) \right] \\
&+ \sum_{m,n} A^{m,n,s} P_x^{m,n,s} I_x^{m,n,s,p} I_y^{m,n,s,q} i k_z^{m,n,s} \\
&\times \rho_2 \left(-\frac{k_y^n}{\left(k^s \right)^2} \left(k_x^p - k_x^m \right) - \left(\frac{1}{\left(k^d \right)^2} - \frac{2}{\left(k^s \right)^2} \right) k_x^m \left(k_y^q - k_y^n \right) \right) \\
&+ \sum_{m,n} A^{m,n,s} P_y^{m,n,s} I_x^{m,n,s,p} I_y^{m,n,s,q} i k_z^{m,n,s} \\
&\times \rho_2 \left(1 - \frac{k_x^m k_x^p}{\left(k^s \right)^2} - \frac{k_y^n k_y^q}{\left(k^d \right)^2} + \left(\frac{1}{\left(k^d \right)^2} - \frac{1}{\left(k^s \right)^2} \right) \left(k_y^n \right)^2 \right) \\
&+ \sum_{m,n} A^{m,n,s} P_z^{m,n,s} I_x^{m,n,s,p} I_y^{m,n,s,q} i \left(k_z^{m,n,s} \right)^2 \\
&\times \rho_2 \left(\frac{k_y^n}{\left(k^s \right)^2} - \left(\frac{1}{\left(k^d \right)^2} - \frac{2}{\left(k^s \right)^2} \right) \left(k_y^q - k_y^n \right) \right) = 0
\end{aligned}
\qquad \text{(X.A.2.a\_41)}
$$

Equation 4:

$$
\begin{aligned}
&+A^{inc} I_x^{inc,p} I_y^{inc,p} k_z^{inc} \rho_1 \left(k_z^{inc}\right)^2 \\
&+\sum_{m,n} R^{m,n} I_x^{m,n,r,p} I_y^{m,n,r,q} \left(k_z^{m,n,r}\right)^2 \rho_1 \\
&+\sum_{m,n} A^{m,n,d} I_x^{m,n,d,p} I_y^{m,n,d,q} \left(k_z^{m,n,d}\right)^2 \rho_2 \left(-1+\frac{2}{\left(k^s\right)^2}\left(k_x^m k_x^p + k_y^n k_y^q\right)\right) \\
&+\sum_{m,n} A^{m,n,s} P_x^{m,n,s} I_x^{m,n,s,p} I_y^{m,n,s,q} i \left(k_z^{m,n,s}\right)^2 \\
&\times \rho_2 \left(\left(\frac{1}{\left(k^d\right)^2} - \frac{1}{\left(k^s\right)^2} \right) k_x^m - \frac{k_x^p}{\left(k^s\right)^2} \right) \\
&+\sum_{m,n} A^{m,n,s} P_y^{m,n,s} I_x^{m,n,s,p} I_y^{m,n,s,q} i k_z^{m,n,s} \\
&\times \rho_2 \left(\left(\frac{1}{\left(k^d\right)^2} - \frac{2}{\left(k^s\right)^2} \right) k_y^n - \frac{k_z^{m,n,s}}{\left(k^s\right)^2} \right) \left(k_y^q - k_y^n\right) \\
&+\sum_{m,n} A^{m,n,s} P_z^{m,n,s} I_x^{m,n,s,p} I_y^{m,n,s,q} i k_z^{m,n,s} \\
&\times \rho_2 \left(\left(\frac{1}{\left(k^d\right)^2} - \frac{1}{\left(k^s\right)^2} \right) \left(k_z^{m,n,s}\right)^2 + 1 - \frac{k_x^m k_x^p + k_y^n k_y^q}{\left(k^s\right)^2} \right) = 0
\end{aligned}
\qquad \text{(X.A.2.a\_42)}
$$

Equation 5:

$$
\begin{aligned}
&\left(A^{m,n,s} P_x^{m,n,s} k_x^{m,n,s} + A^{m,n,s} P_y^{m,n,s} k_y^{m,n,s} + \ldots \right. \\
&\left. \ldots + A^{m,n,s} P_z^{m,n,s} k_z^{m,n,s} \right) \delta_{m,p} \delta_{n,q} = 0
\end{aligned}
\qquad \text{(X.A.2.a\_43)}
$$

with $\left(k^1\right)^2$ and $\left(k^d\right)^2$ given by (X.A.2.a_30) and $\left(k^s\right)^2$ given by (X.A.2.a_31) and with

$$k_\gamma^\eta = k_\gamma^{inc} + \eta \frac{2\pi}{\Lambda_\gamma} \tag{X.A.2.a_44}$$

and

$$I_\gamma^{inc,\eta} = \frac{1}{k_z^{inc}} \int_{\Lambda_\gamma} e^{i\left(k_\gamma^{inc} - k_\gamma^\eta\right)x} \, e^{i\left(k_z^{inc} f_\gamma(\gamma)\right)} d\gamma \tag{X.A.2.a_45}$$

$$I_\gamma^{m,n,\eta,\xi} = \frac{1}{k_z^{m,n,\xi}} \int_{\Lambda_\gamma} e^{i\left[\delta_{\gamma,x}\left(k_x^m - k_x^\eta\right)x + \delta_{\gamma,y}\left(k_y^n - k_y^\eta\right)y + k_z^{m,n,\xi} f_\gamma(\gamma)\right]} d\gamma \tag{X.A.2.a_46}$$

where δ means Kronecker's delta.
Deschamps [11] shows that there are no a priori mathematical constraints on the choice of the sign of k_z. The choice needs to fulfill experiments. Hence if $\mathrm{Re}(k_z) = 0$, one has to deal with Scholte-Stoneley-like surface modes and the sign of k_z must be so that there is exponential decay of the amplitude away from the interface. If $\mathrm{Re}(k_z) = k_{1,z} \neq 0$, then the sign of k_z depends on the angle of propagation of the liquid-side companion, denoted by 'm,n,r', of the considered mode 'm,n,p' inside the solid (p=shear or p=dilatational)

$$\left|\theta_1^{m,n,r}\right| = \arctan\left[\frac{\left|k_{1,x}^{m,n} + k_{1,y}^{m,n}\right|}{\left|k_{1,z}^{m,n,r}\right|}\right] \tag{X.A.2.a_47}$$

If

$$\left|\theta_1^{m,n,p}\right| = \arctan\left[\frac{\left|k_{1,x}^{m,n} + k_{1,y}^{m,n}\right|}{\left|k_{1,z}^{m,n,p}\right|}\right] \tag{X.A.2.a_48}$$

is 'close enough' to $\pi/2$, then that particular mode 'm,n,p' must show leaky Rayleigh wave features, whence the inhomogeneity vector must point into the liquid. Deschamps [11] shows that 'close enough' to $\pi/2$ is fulfilled if

$$\left|\theta_1^{m,n,r}\right| > \left|\arcsin\left(\frac{v_l}{v_p}\right)\right| \qquad \text{(X.A.2.a\_49)}$$

v_l being the wave velocity in the liquid, v_p is the velocity of the considered mode 'm,n,p'. Whenever

$$\left|\theta_1^{m,n,r}\right| \leq \left|\arcsin\left(\frac{v_l}{v_p}\right)\right| \qquad \text{(X.A.2.a\_50)}$$

the causality principles hold, demanding that the mode 'm,n,p' travels away from the interface. Before explicitly tackling numerical results, it is worthwhile to look at some analytical relations between incident and diffracted waves. The same notation is used as in (X.A.2.a_27), for 'inc' replaced by the diffraction order 'm,n' in one of the media through which diffracted waves travel. The grating equation (X.A.2.a_44) results in the following properties:

$$\theta_1^{m,n} = \arctan\left(\frac{k_1^{inc}\sin\xi_1^{inc}\sin\theta_1^{inc} + n\frac{2\pi}{\Lambda_y}}{k_1^{inc}\sin\xi_1^{inc}\cos\theta_1^{inc} + m\frac{2\pi}{\Lambda_x}}\right) \qquad \text{(X.A.2.a\_51)}$$

$$\xi_1^{m,n} = \arcsin\left(\frac{1}{k_1^{m,n}} sqrt\left(\left(k_1^{inc}\sin\xi_1^{inc}\right)^2 + ..\right.\right. \qquad \text{(X.A.2.a\_52)}$$

$$\left..+ 4\pi k_1^{inc}\sin\xi_1^{inc}\left(\frac{m}{\Lambda_x}\cos\theta_1^{inc} + \frac{n}{\Lambda_y}\sin\theta_1^{inc}\right) + 4\pi^2\left(\left(\frac{m}{\Lambda_x}\right)^2 + \left(\frac{n}{\Lambda_y}\right)^2\right)\right)\right)$$

$$\theta_2^{m,n} = \theta_2^{inc} \qquad \text{(X.A.2.a\_53)}$$

$$\sin\xi_2^{m,n} = \frac{k_2^{inc}}{k_2^{m,n}}\sin\xi_2^{inc} \qquad \text{(X.A.2.a\_54)}$$

This means that the inhomogeneity vector remains its direction inside the xy-plane (X.A.2.a_53) and solely changes its direction in the plane of incidence (X.A.2.a_54). As a consequence of this property, an inhomogeneous wave with for example an inhomogeneity vector in the xz-plane, will not stimulate any waves (except SSTW) that have inhomogeneity vectors in the yz-plane.

This has a very important outcome on the generation of leaky Rayleigh waves, i.e. no matter what the angle under which incidence occurs, if leaky Rayleigh waves are stimulated, they will always have inhomogeneity vectors governed by the polar angle of incident inhomogeneity. Moreover, if SSTW emerge (i.e. $\xi_2^{m,n}=0$, $k_2^{m,n}\neq 0$), then $k_2^{inc}=0$ and/or $\xi_2^{inc}=j\pi$, for j an integer. This implies that SSTW can only be generated if homogeneous plane waves are incident or if $\mathbf{k}_2^{inc}\|\mathbf{e}_z$. For normal incident waves, this means that always $\beta^{inc}=0$. It can be verified that this reasoning can be turned the other way around, whence Rayleigh waves cannot be generated using incident homogeneous plane waves.
Relation (X.A.2.a_51) shows that zero order diffracted waves have a direction of propagation along the plane of incidence. This direction changes for orders different from zero. Relation (X.A.2.a_52) is Snell's law for zero order diffracted waves, for other orders it shows that $\xi_1^{m,n}$ depends on the plane of incidence and on the values of *m* and *n* of the diffracted order.

NUMERICAL CALCULATIONS

Preliminary Considerations

The linear system of equations (X.A.2.a_39-43) is infinite since *m*,*n*,*p* and *q* may take every possible integer value $\in\{-\Omega,..,+\Omega\}$ for Ω arbitrarily large. However, it has been shown before [10-14] (for singly corrugated surfaces) that the interval of integers may be truncated to $\{-N,-N+1,..,N-1,N\}$, for N larger than 6. The same truncation for doubly corrugations is now applied, allowing

$$m,p\in\left\{-N_x,..,+N_x\right\} \qquad \text{(X.A.2.a\_55)}$$

$$n,q\in\left\{-N_y,..,+N_y\right\} \qquad \text{(X.A.2.a\_56)}$$

$N_x=N_y=7$ is taken for both $f_x(x)$ and $f_y(y)$. In the case that a singly corrugated surface is to be tackled, then $N_x=0$ if $f_x(x)$ is constant and $N_y=0$ if $f_y(y)$ is constant. For both $f_x(x)$ and $f_y(y)$ constant (i.e. a plane interface), $N_x=N_y=0$. Hence the presented model holds for plane, singly corrugated and doubly corrugated interfaces! The number of entries in the continuity matrix formed by equations (X.A.2.a_39-43) is $25\left(2N_x+1\right)^2\left(2N_y+1\right)^2$, which results in 1265625 entries in the case $N_x=N_y=7$. It is hence clear that the calculations which are presented below are time consuming, even on a relatively fast computer.
From refs. 22-23, it can be derived that for a sinusoidal corrugation

$$f_\gamma(\gamma) = \frac{h_\gamma}{2}\cos\left(\frac{2\pi\gamma}{\Lambda_\gamma}\right) \tag{X.A.2.a_57}$$

the integrals become

$$I_\gamma^{inc,\eta} = \frac{\Lambda_\gamma (i)^{-\eta}}{k_z^{inc}} J_{-\eta}\left(\frac{h_\gamma k_z^{inc}}{2}\right) \tag{X.A.2.a_58}$$

$$I_\gamma^{m,n,\eta,\xi} = \frac{\Lambda_\gamma i^{\left(\delta_{\gamma,x}m+\delta_{\gamma,y}n-\eta\right)}}{k_z^{m,n,\xi}} J_{\left(\delta_{\gamma,x}m+\delta_{\gamma,y}n-\eta\right)}\left(\frac{h_\gamma k_z^{m,n,\xi}}{2}\right) \tag{X.A.2.a_59}$$

and for a sawtooth corrugation

$$f_\gamma(\gamma) = \frac{2h_\gamma\gamma}{\Lambda_\gamma} - \frac{h_\gamma}{2} \text{ if } 0 \le \gamma < \frac{\Lambda_\gamma}{2} \tag{X.A.2.a_60}$$

$$f_\gamma(\gamma) = \frac{3h_\gamma}{2} - \frac{2h_\gamma\gamma}{\Lambda_\gamma} \text{ if } \frac{\Lambda_\gamma}{2} \le \gamma < \Lambda_\gamma \tag{X.A.2.a_61}$$

the integrals become

$$I_\gamma^{inc,\eta} = ih_\gamma\Lambda\gamma e^{-ih_\gamma k_z^{inc}/2}\frac{1-(-1)^{-\eta}e^{ih_\gamma k_z^{inc}}}{\left(h_\gamma k_z^{inc}\right)^2-(\pi\eta)^2} \tag{X.A.2.a_62}$$

$$I_\gamma^{m,n,\eta,\xi} = ih_\gamma\Lambda\gamma e^{-ih_\gamma k_z^{inc}/2}\frac{1-(-1)^{\left(\delta_{\gamma,x}m+\delta_{\gamma,y}n-\eta\right)}e^{ih_\gamma k_z^{m,n,\xi}}}{\left(h_\gamma k_z^{m,n,\xi}\right)^2-\pi^2\left(\delta_{\gamma,x}m+\delta_{\gamma,y}n-\eta\right)^2} \tag{X.A.2.a_63}$$

whence both sinusoidal and triangular profiles involve relatively fast calculations since numerical integration is avoided. J_j is the j^{th} order Bessel function of the first kind.

Discussion of Numerical Results for Normal Incident Homogeneous Plane Waves

In this section, focusing occurs on the situation for which pure plane waves ($\beta^{inc} = 0$) are normally incident on a sawtooth-shaped doubly corrugated water/brass interface with $\Lambda_x = \Lambda_y$ and h_y varying from *0* to h_x. The material properties are shown in Table X.A.2.a_I.

Table X.A.2.a_I : Properties of the materials used in our calculations

Water:	$\rho^1 = 1000 kg/m^3$	$v_d^1 = 1480 m/s$	$v_s^1 = 0 m/s$
Brass:	$\rho^2 = 8100 kg/m^3$	$v_d^2 = 4840 m/s$	$v_s^2 = 2270 m/s$

First of all, it is important to note that due to the linearity of (X.A.2.a_1), for each direction θ in the xy-plane, there exists a corrugation period

$$\Lambda_\theta = \sqrt{\left(a\Lambda_x\right)^2 + \left(b\Lambda_y\right)^2} \qquad \text{(X.A.2.a\_64)}$$

with a and b integers containing no common dividers except unity. Furthermore, if the grating equation (X.A.2.a_14) or (X.A.2.a_44) is taken into account for that direction and also normal incidence, then a SSTW of order *c* with velocity v_{SST} can possibly be generated along the interface in the direction θ if the frequency is

$$freq_{SST}^c = c\frac{v_{SST}}{\sqrt{\left(a\Lambda_x\right)^2 + \left(b\Lambda_y\right)^2}} \qquad \text{(X.A.2.a\_65)}$$

Furthermore, this frequency must correspond to pure imaginary wave vector components perpendicular to the interface, because otherwise one would be dealing with a bulk lateral wave instead of a SSTW. The latter is true whenever

$$\frac{c}{\sqrt{\left(a\Lambda_x\right)^2 + \left(b\Lambda_y\right)^2}} v_B > freq_{SST}^c \qquad \text{(X.A.2.a\_66)}$$

in which v_B is the wave velocity that corresponds to the slowest bulk wave in both neighboring media.

It is therefore expected that for each frequency, it is virtually possible that a SSTW is generated. However, if or if not an SSTW is actually generated at a certain frequency not only depends on the considerations (X.A.2.a_65) and (X.A.2.a_66), but also on the continuity conditions. For the case $\Lambda_x = \Lambda_y$, it is intuitively reasonable that there are 3 main directions, measured from the x-axis in the xy-plane, in which SSTW are considerably stimulated, i.e. 0^0, 45^0 and 90^0, because

perpendicular to these directions the largest effective corrugations are associated. In the case of 45^0, (X.A.2.a_65) becomes

$$freq_{SST}^{c} = c\frac{v_{SST}}{\Lambda_x\sqrt{2}} \qquad \text{(X.A.2.a\_67)}$$

Hence, the frequency at which a c'th order SSTW is generated is expressed as

$$\left[freq_{SST}^{c}\right]_{45}0 = \frac{1}{\sqrt{2}}\left[freq_{SST}^{c}\right]_{0}0 \qquad \text{(X.A.2.a\_68)}$$

Figs X.A.2.a_2-16 show numerical results for the case $\Lambda_x = \Lambda_y = 2{,}2mm$, $h_x = 50\mu m$ and $h_y = 0 \to h_x$. The previous discussions already lead to the following results.
For each number a and b, it is always so that

$$\left[freq_{SST}^{c}\right] < c \times 0.6727MHz \qquad \text{(X.A.2.a\_69)}$$

with particular situations listed in Table X.A.2.a_II.

Table X.A.2.a_II : ***The maximum frequency f_M at which a SSTW of order c can be generated for some particular cases.***

a	b	f_M [MHz]
1	1	$c \times 0.476$
0	1	$c \times 0.673$
0	2	$c \times 0.336$
1	2	$c \times 0.300$
1	3	$c \times 0.212$

In Fig. X.A.2.a_2, the absolute value of $R^{0,0}$ is plotted as a function of the frequency and as a function of the height h_y. At $h_y = 0$, there is a strong dip visible at 0.672 MHz. Since this is lower than 0.673 MHz (see Table X.A.2.a_II), it can be concluded that this dip is a so called Wood anomaly and corresponds to the generation of a first order SSTW in the 0^0 direction.
Indeed, if one takes a look at Fig. X.A.2.a_3, the amplitude of the total displacement field due to all diffracted orders except the zero order, shows to be exponentially decaying away from the interface and it is seen that the energy is mostly situated in the liquid side.

The latter two properties are typical characteristics of SSTW. Since $\Lambda_x = \Lambda_y$, a second SSTW is generated in the 90^0 direction at the same frequency when h_y is increased. Ultimately, when $h_y = h_x$, equal SSTW are running in the 0^0 direction and in the 90^0 direction.

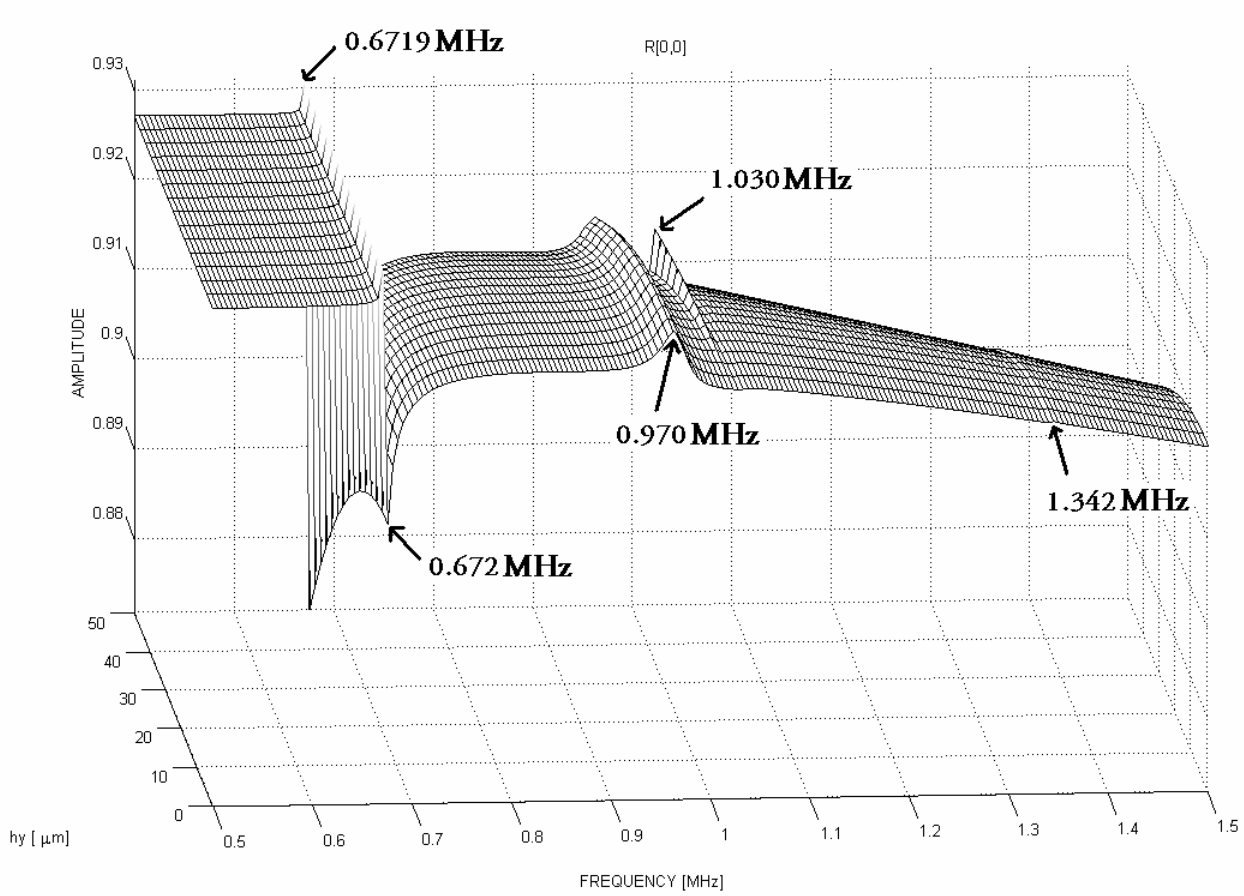

Fig. X.A.2.a_2: $\left|R^{0,0}\right|$ ***as a function of the frequency of normally incident homogeneous plane waves and the height*** h_y ***, for*** $h_x = 50\mu m$ ***and*** $\Lambda_x = \Lambda_y = 2.2mm$ **.**

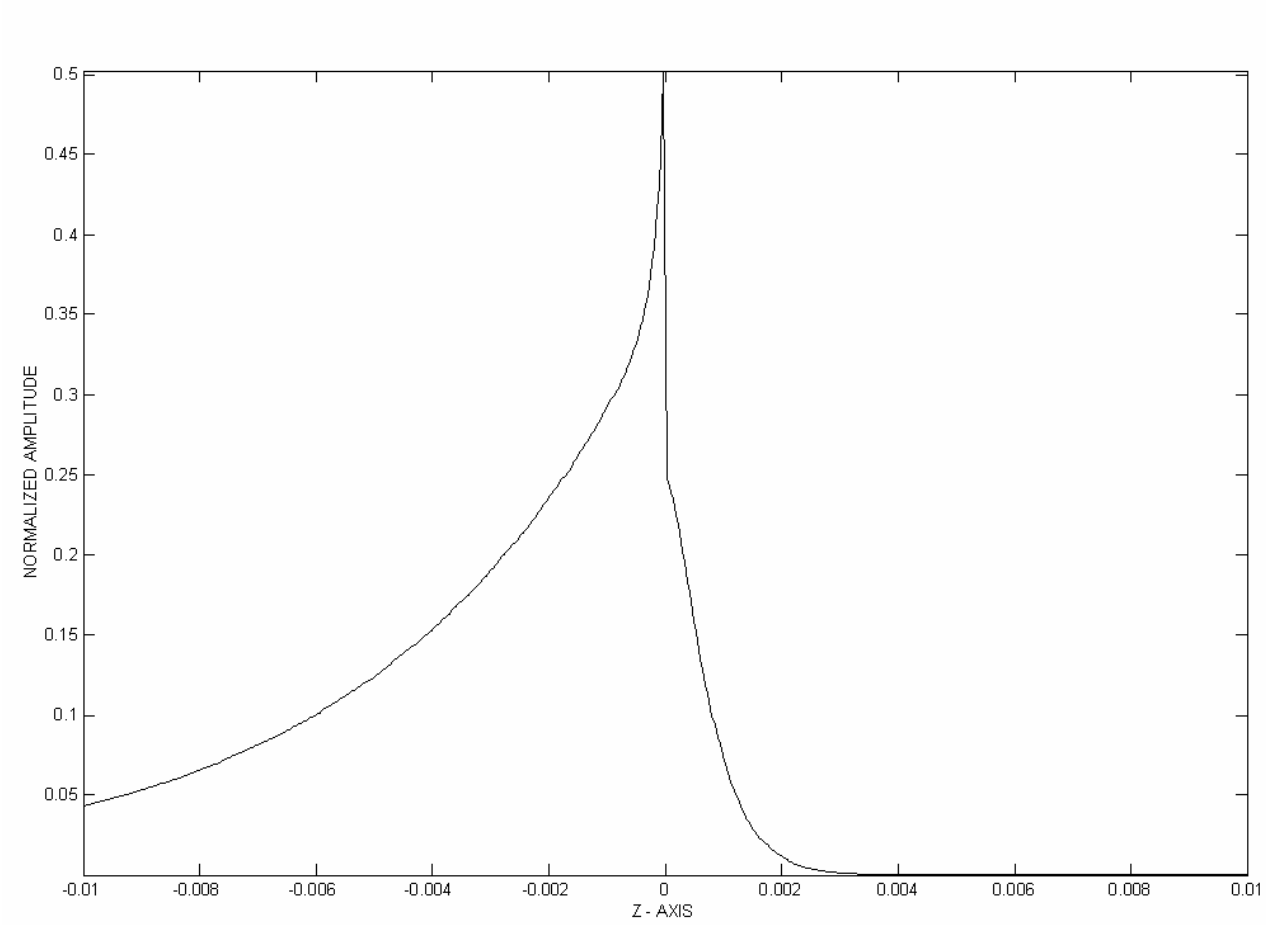

Fig. X.A.2.a_3: ***Amplitude of the total particle displacement field due to all diffraction orders except the zero order, at 0.672MHz for*** $h_x = 50\mu m$ **,** $h_y = 0$ ***and*** $\Lambda_x = \Lambda_y = 2.2mm$ **.**

This effect is visible in Fig. X.A.2.a_2, where the Wood anomaly (0.672 MHz) gets more definite, and also in Fig. X.A.2.a_4, where a first order SSTW in the 90^0 direction gets more and more stimulated as h_y approaches h_x.

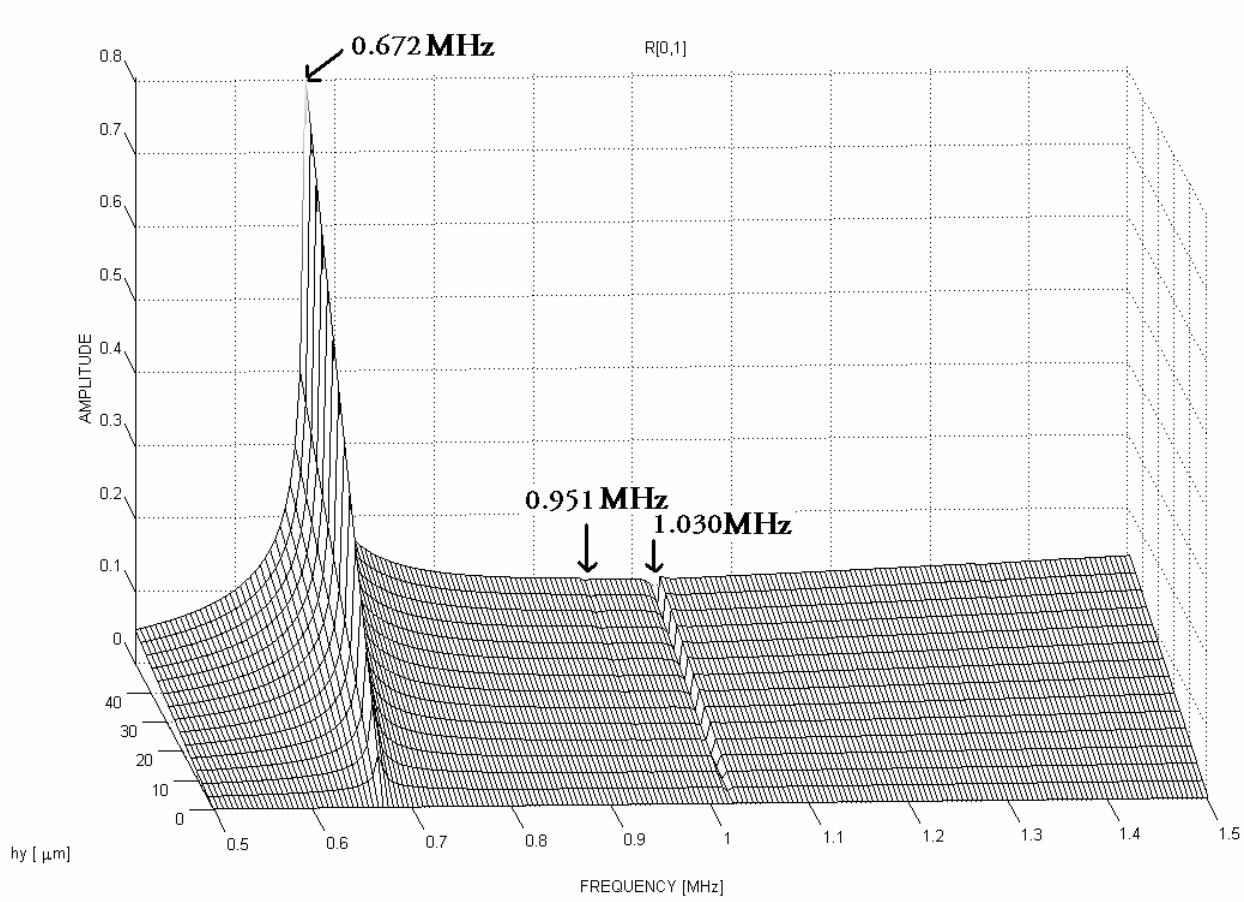

Fig. X.A.2.a_4: $\left|R^{0,1}\right|$ ***as a function of*** h_y ***and the frequency for*** $h_x = 50\mu m$ ***and*** $\Lambda_x = \Lambda_y = 2.2mm$**.**

Even more interesting is the fact that due to (X.A.2.a_67) and the Wood anomaly at 0.672 MHz, secondary SSTW may be generated in the 45^0 direction for c=1 at 0.475 MHz, which is out of reach in our calculations, and for c=2 at 0.951 MHz, which is still visible in Fig. X.A.2.a_5 as an amplitude peak in $\left|R^{1,1}\right|$. That this is a SSTW is proved by Table X.A.2.a_II, where it is seen that its frequency may not reach beyond 0.952 MHz, which is fulfilled.
In Fig. X.A.2.a_2, it is also seen that there is a peak at 1.030 MHz. This corresponds through the grating equation (X.A.2.a_44) to the generation of first order lateral bulk shear waves in the solid, which are obviously not excited very well since a peak in the reflection coefficient for pure homogeneous incident plane waves occurs. This phenomenon is equivalent to 'the first critical angle' on plane interfaces. For $h_y = 0$, a bulk shear lateral wave is generated in the 0^0 direction at 1.030 MHz. As h_y increases, the influence of another one in the 90^0 is more and more present, whence the effect on the zero order reflection coefficient is enhanced and noticed as an increased peak in Fig. X.A.2.a_2.

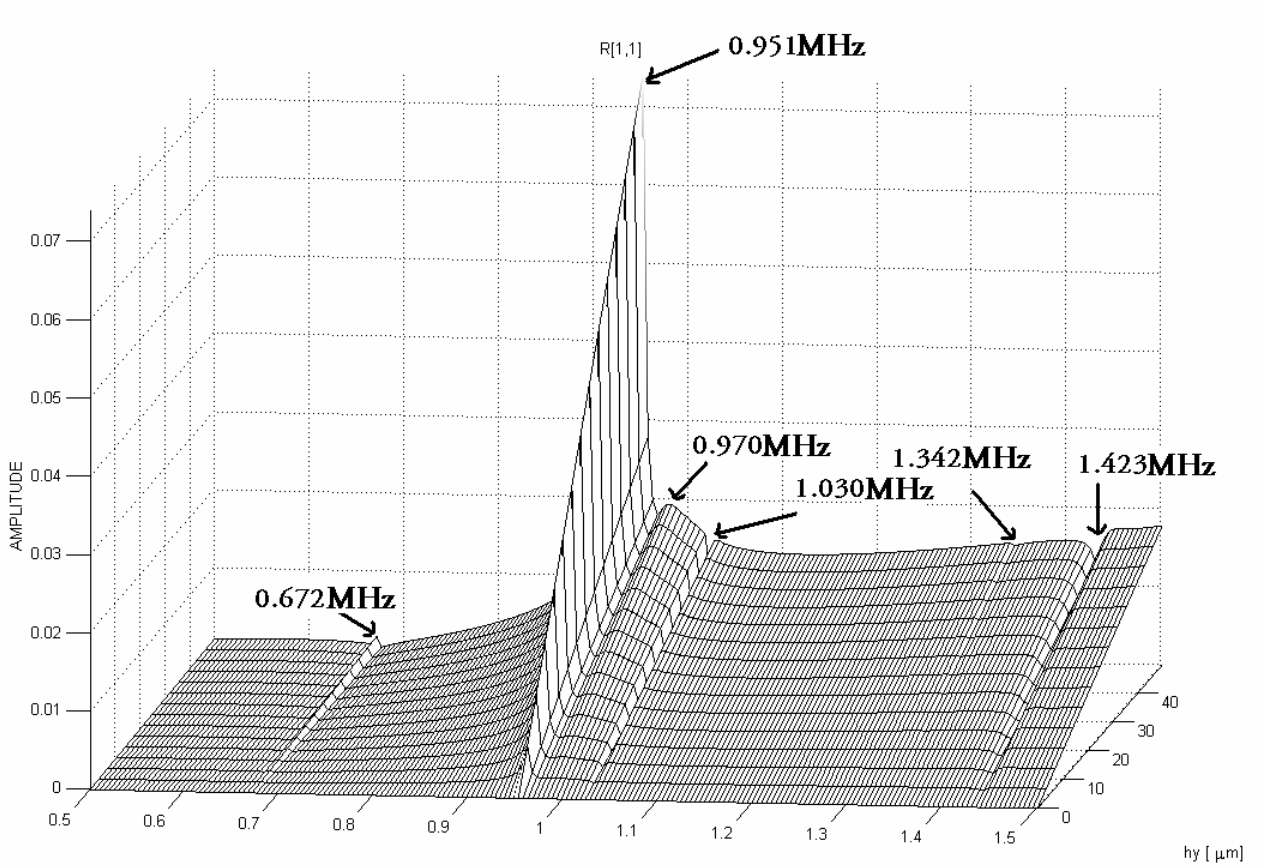

Fig. X.A.2.a_5: $\left|R^{1,1}\right|$ ***as a function of*** h_y ***and the frequency for*** $h_x = 50\mu m$ ***and*** $\Lambda_x = \Lambda_y = 2.2mm$**.**

The frequency at which a first order bulk wave in the liquid is formed, is situated at 0.673 MHz. However, due to the vicinity of the Wood anomaly at 0.672 MHz, the formation of an amplitude peak $R^{0,0}$ is highly disturbed, whence only a 'flank' of the 'would be peak' remains at 0.6719 MHz.

Furthermore, in Fig. X.A.2.a_2, a wrinkle is visible at 0.970 MHz. This is the Leaky Rayleigh wave frequency. However, since pure plane waves are unable to stimulate such a wave (see comments under (X.A.2.a_51-54)), the significance of this frequency will only become clear in the next section where incident inhomogeneous waves are considered.

In Fig. X.A.2.a_2, there is also a disturbance visible at 1.342 MHz, which is due to the generation of second order SSTW.

Yet another disturbance is visible in Fig. X.A.2.a_5 at 1.423 Mhz. This is exactly the frequency at which a third order SSTW is generated in the 45^0 direction, equivalent to the second order SSTW that is generated under the same angle at 0.951 MHz and is discussed above.

Discussion of Numerical Results for Normal Incident Inhomogeneous Plane Waves

In the previous section, the appearance of a wrinkle in Fig. X.A.2.a_2 at 0.970 MHz was acclaimed to be the leaky Rayleigh frequency. In order to prove this, one should take a look at Fig. X.A.2.a_6 in which the amplitude of the first order reflection coefficient is shown on a

singly corrugated surface, i.e. $h_y = 0$, with all other parameters equal as in the doubly corrugated surface of the previous section, as a function of the frequency and the incident inhomogeneity.

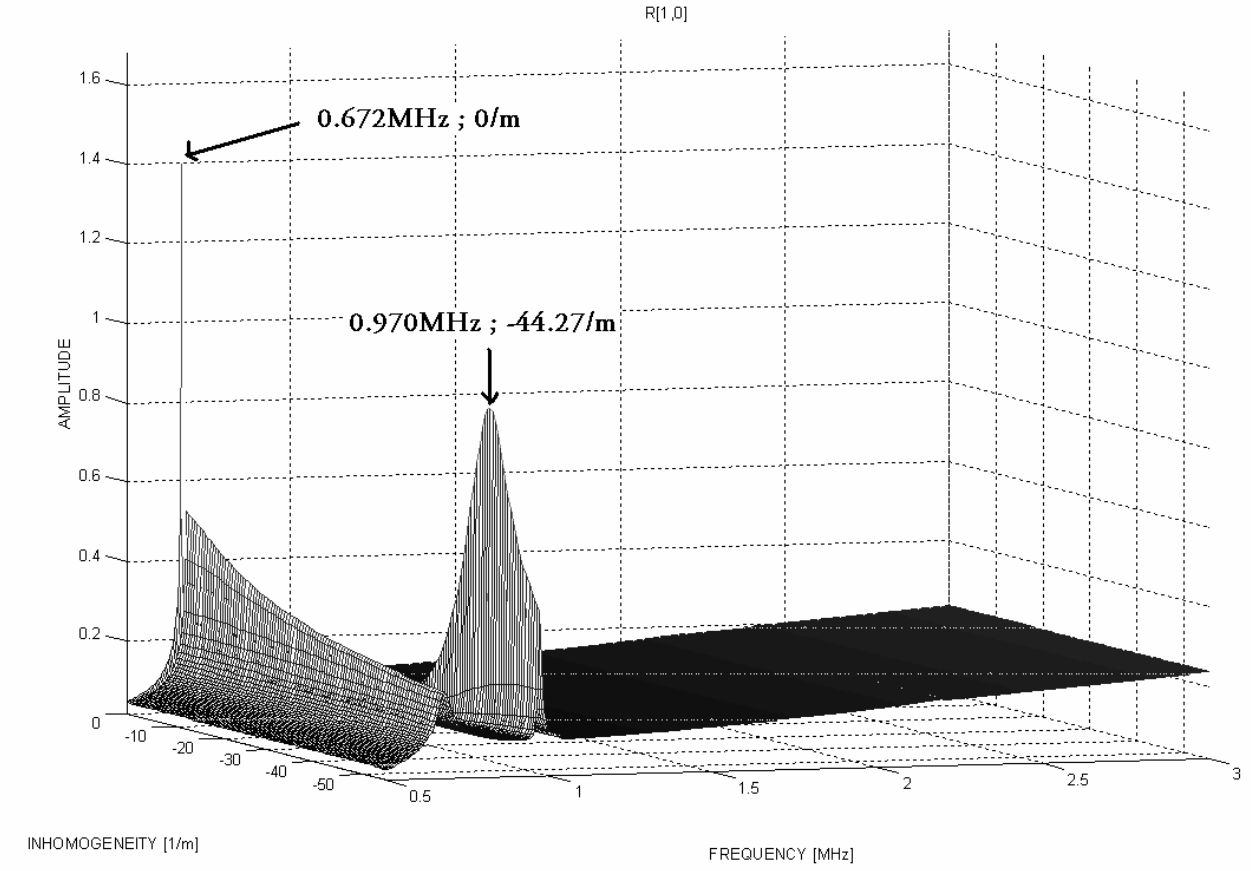

Fig. X.A.2.a_6: $\left|R^{1,0}\right|$ ***on a singly corrugated surface as a function of the frequency and the incident inhomogeneity, for*** $h_x = 50\mu m$ ***and*** $\Lambda_x = \Lambda_y = 2.2mm$**.**

The largest peak is the one at 0.672 MHz and zero inhomogeneity, i.e. for pure homogeneous plane waves, and is due to the excitation of SSTW, as is fully described in the previous section. The second peak is the one at 0.970 MHz and inhomogeneity –44.27m^{-1}. It is seen in Fig. X.A.2.a_7 that for incident inhomogeneous waves, the 1st order reflection coefficient is different from the –1st reflection coefficient, which is logically explained by the fact that whereas the incident field is symmetric if homogeneous plane waves are considered, it is not if inhomogeneous plane waves are considered.

The latter peak in Fig. X.A.2.a_6 at 0.970 MHz and inhomogeneity –44.27m^{-1}, represents the stimulation of a first order leaky Rayleigh wave. The latter is proved by Fig. X.A.2.a_8, in which the amplitude of the displacement field due to all diffracted orders except the zero order is plotted as a function of the x-coordinate. The typical leaky Rayleigh wave profile is visible.

Furthermore, simulation occurs on what happens to a normally incident inhomogeneous wave having inhomogeneity $\boldsymbol{\beta}^{inc} = -44.27m^{-1}\mathbf{e}_x$, impinging the same doubly corrugated interface as in the previous section. As stated above, the main difference between such inhomogeneous waves

and pure plane waves is the fact that they can generate SSTW in the y-direction, but not in the x-direction. Furthermore, they can generate leaky Rayleigh waves in the x-direction, but not in the y-direction.

First of all, let us take a look at Fig. X.A.2.a_9 where $\left|R^{0,0}\right|$ is plotted as a function of the frequency and the height of h_y.

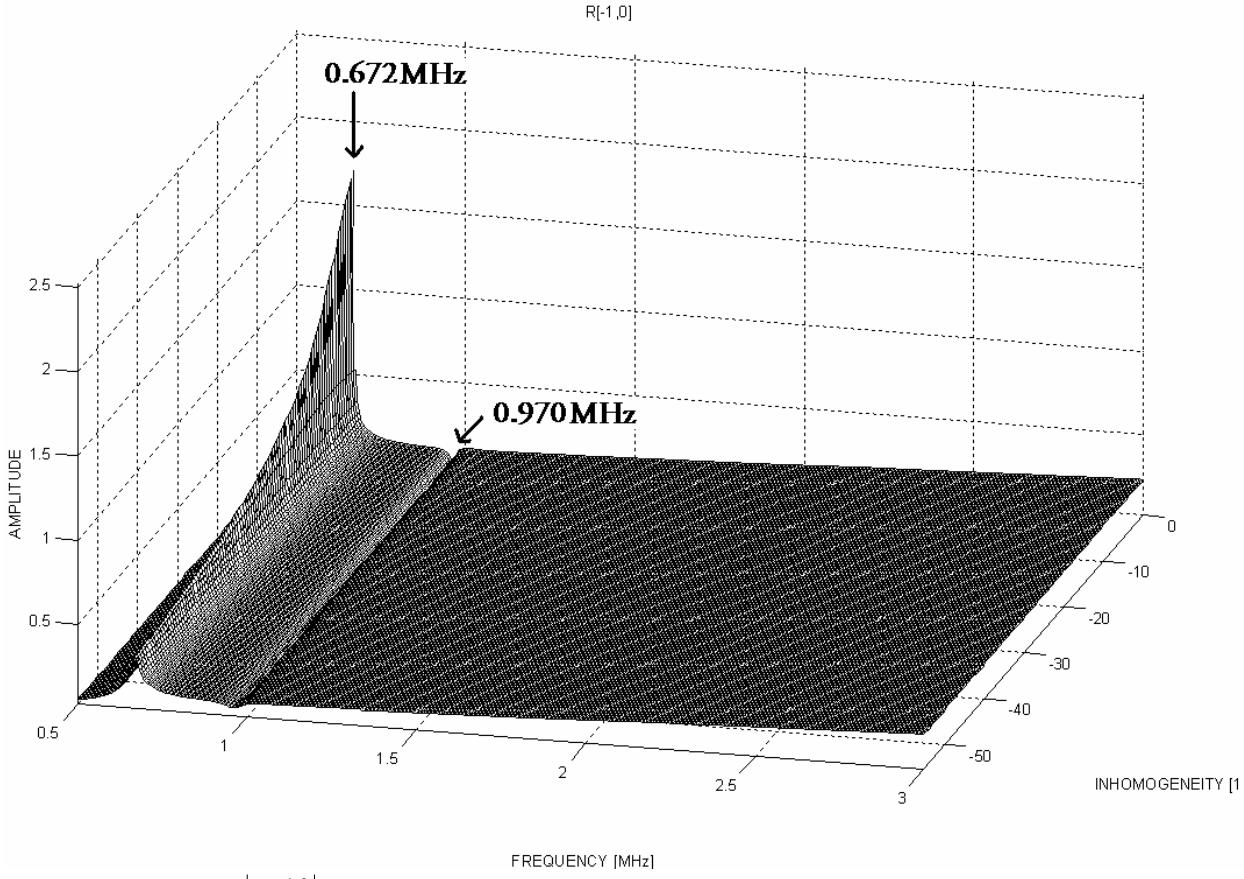

Fig. X.A.2.a_7: $\left|R^{-1,0}\right|$ ***on a singly corrugated surface as a function of the frequency and the incident inhomogeneity for*** $h_x = 50\mu m$ ***and*** $\Lambda_x = \Lambda_y = 2.2mm$**.**

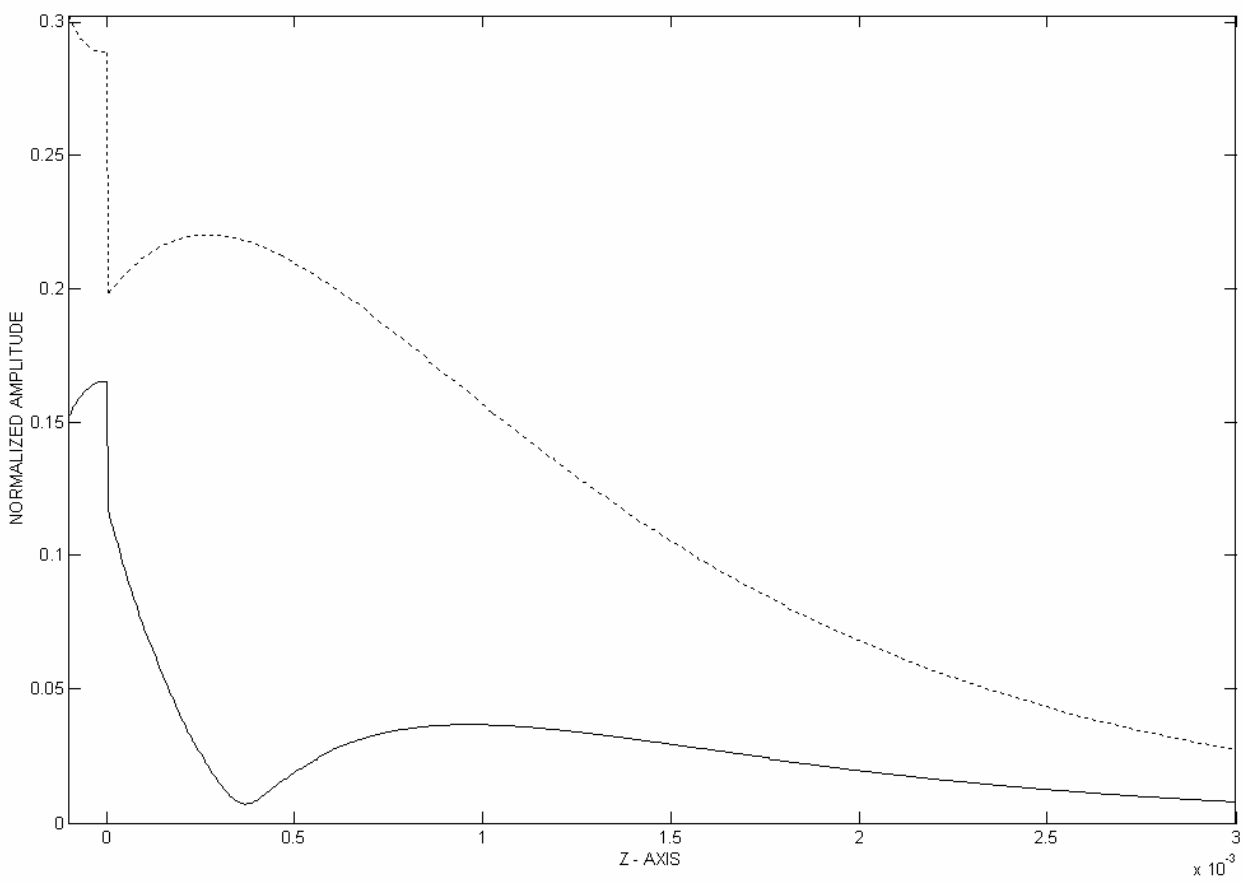

Fig. X.A.2.a_8: ***Amplitude of the particle displacement for*** $h_x = 50\mu m$ **,** $h_y = 0$ **, at 0.970 MHz and** $\boldsymbol{\beta}^{inc} = -44.27 m^{-1}\mathbf{e}_x$ **.** ***Solid line:*** $|N_x|$ ***.Dotted line:*** $|N_z|$ **.**

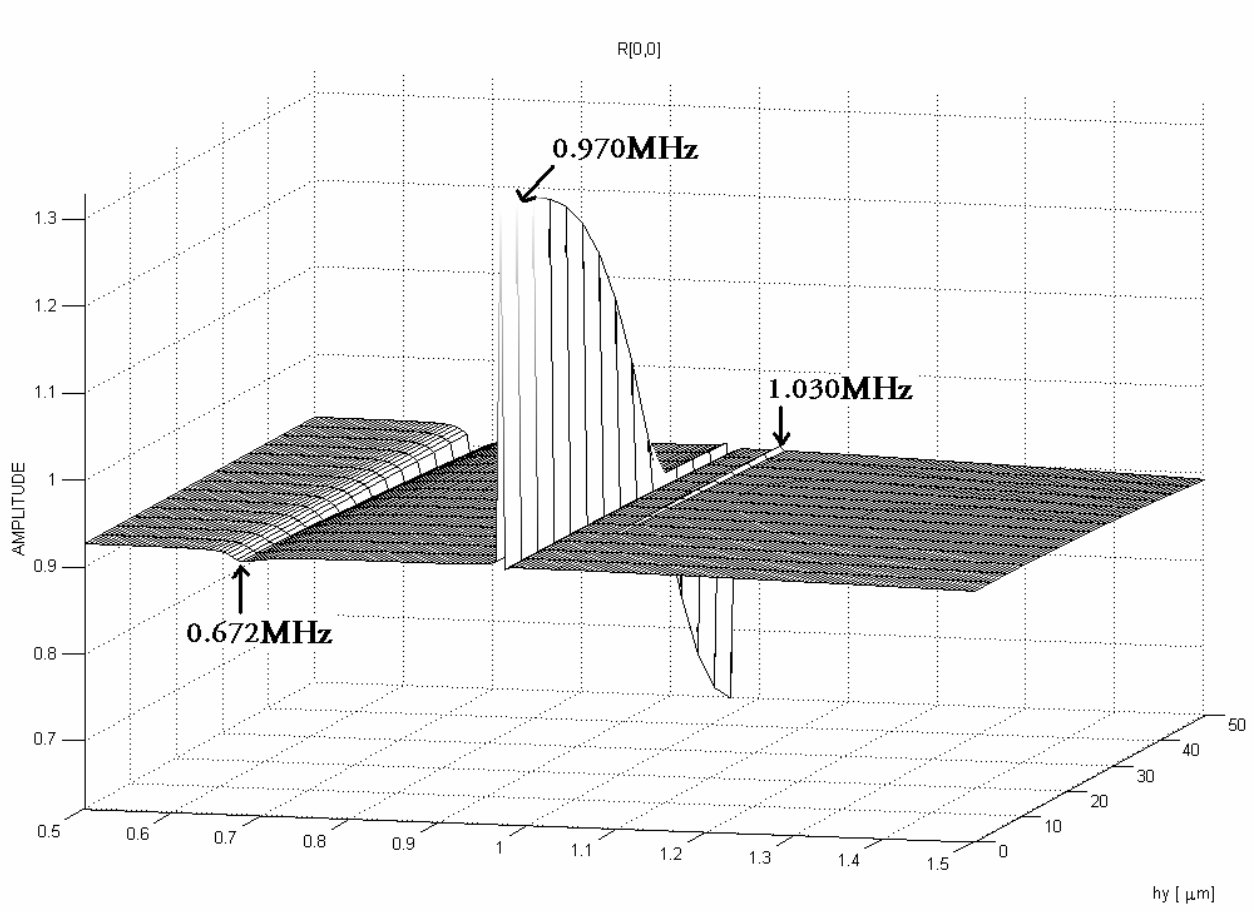

Fig. X.A.2.a_9: $\left|R^{0,0}\right|$ ***as a function of the frequency of normally incident inhomogeneous plane waves*** ***(*** $\boldsymbol{\beta}^{inc} = -44.27m^{-1}\mathbf{e}_x$ ***) and of the height*** h_y ***for*** $h_x = 50\mu m$ ***and*** $\Lambda_x = \Lambda_y = 2.2mm$ **.**

It is noticed that as h_y increases, there appears a Wood anomaly at 0.672MHz, which is exactly the same frequency as that where the Wood anomaly appears in Fig. X.A.2.a_2 and Fig. X.A.2.a_6 and which becomes more severe as h_y increases. Moreover, at 0.970 Mhz, an amplitude exceeding unity is noticed, which is due to the generation of a leaky Rayleigh wave (proved in Figs X.A.2.a_6-8) and induces a shift towards positive x values of the zero order reflected wave. When h_y increases, this maximum becomes a minimum, which results in a change in the displacement shift direction of the zero order reflected wave. In order to prove that 0.970 MHz remains a leaky Rayleigh wave frequency even if $h_y = h_x$, the displacement fields are plotted resulting from all diffraction orders in Fig. X.A.2.a_10, and for pure diffraction orders in the 0^0 direction in Fig. X.A.2.a_11.

The displacement fields for pure diffraction orders in the 90^0 direction are shown in Fig. X.A.2.a_12.

It is seen that even though the total diffraction field does not show any characteristic of a leaky Rayleigh wave, the displacement field due to pure diffraction orders in the 0^0 direction remains possessing leaky Rayleigh wave characteristics. Furthermore, Fig. X.A.2.a_13 and Fig. X.A.2.a_14 are revealing images.

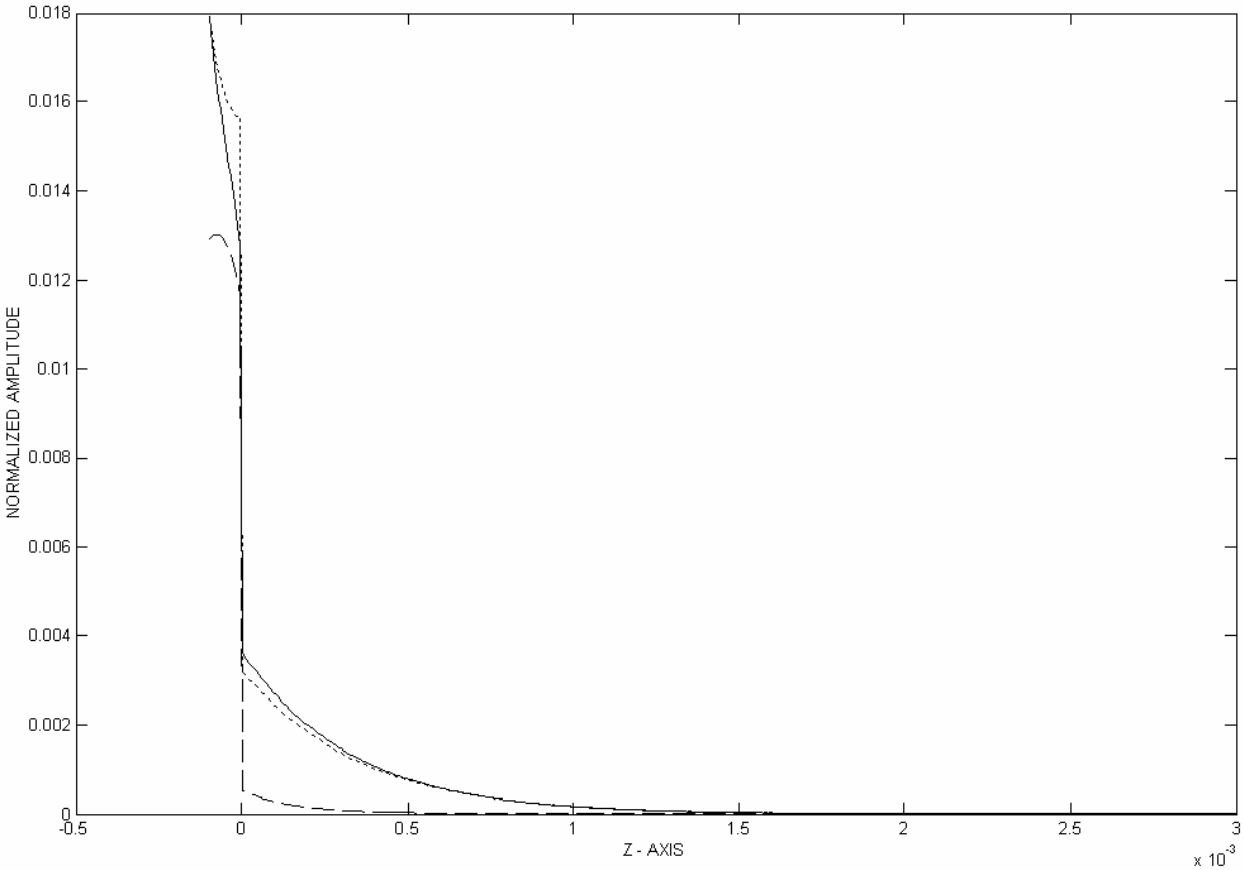

Fig. X.A.2.a_10: ***Amplitude of the particle displacement for*** $h_x = h_y = 50\mu m$ ***, at 0.970 MHz and*** $\boldsymbol{\beta}^{inc} = -44.27m^{-1}\mathbf{e}_x$ ***, for all diffraction order except for the zero order. Solid line:*** $|N_x|$ ***.Dotted line:*** $|N_z|$ ***. Dashed line:*** $|N_y|$ ***.***

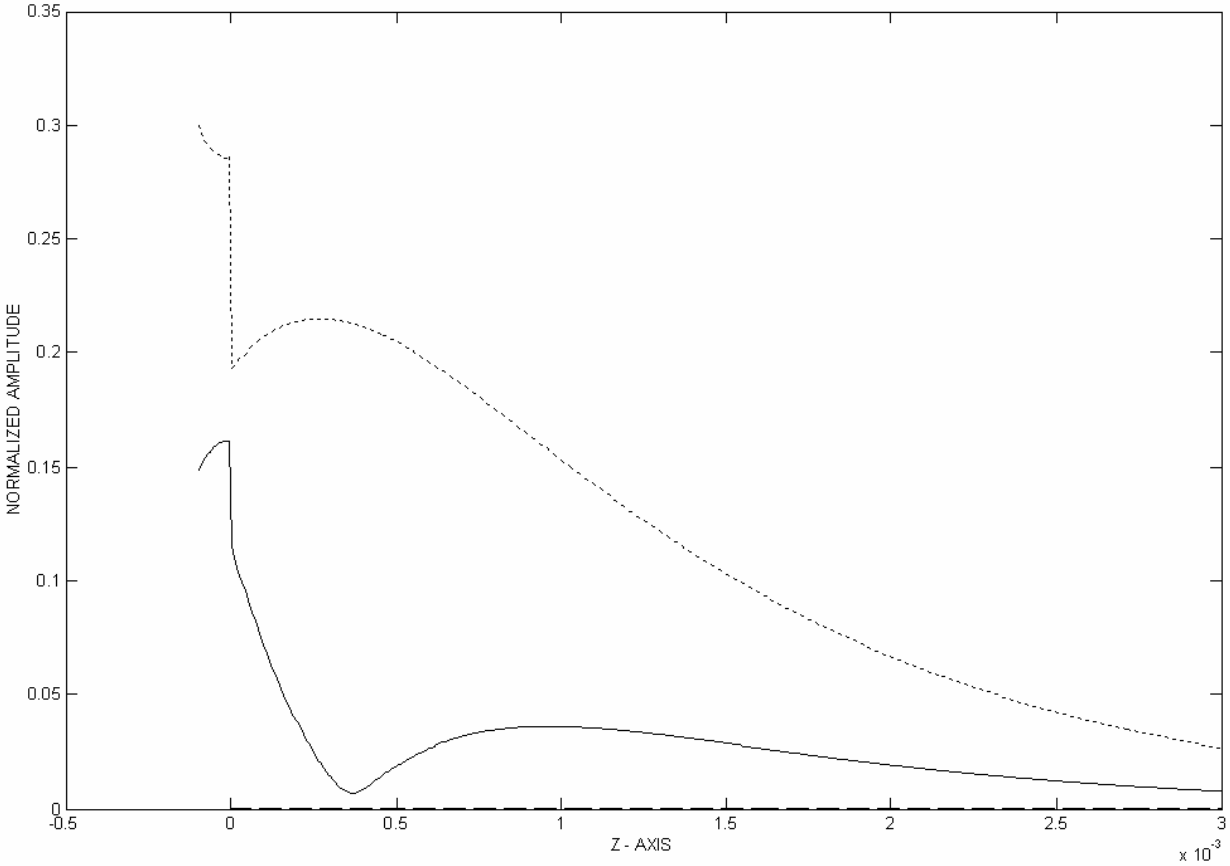

Fig. X.A.2.a_11: ***same as in Fig. X.A.2.a_10, except that only order for n=0 are taken into account.***

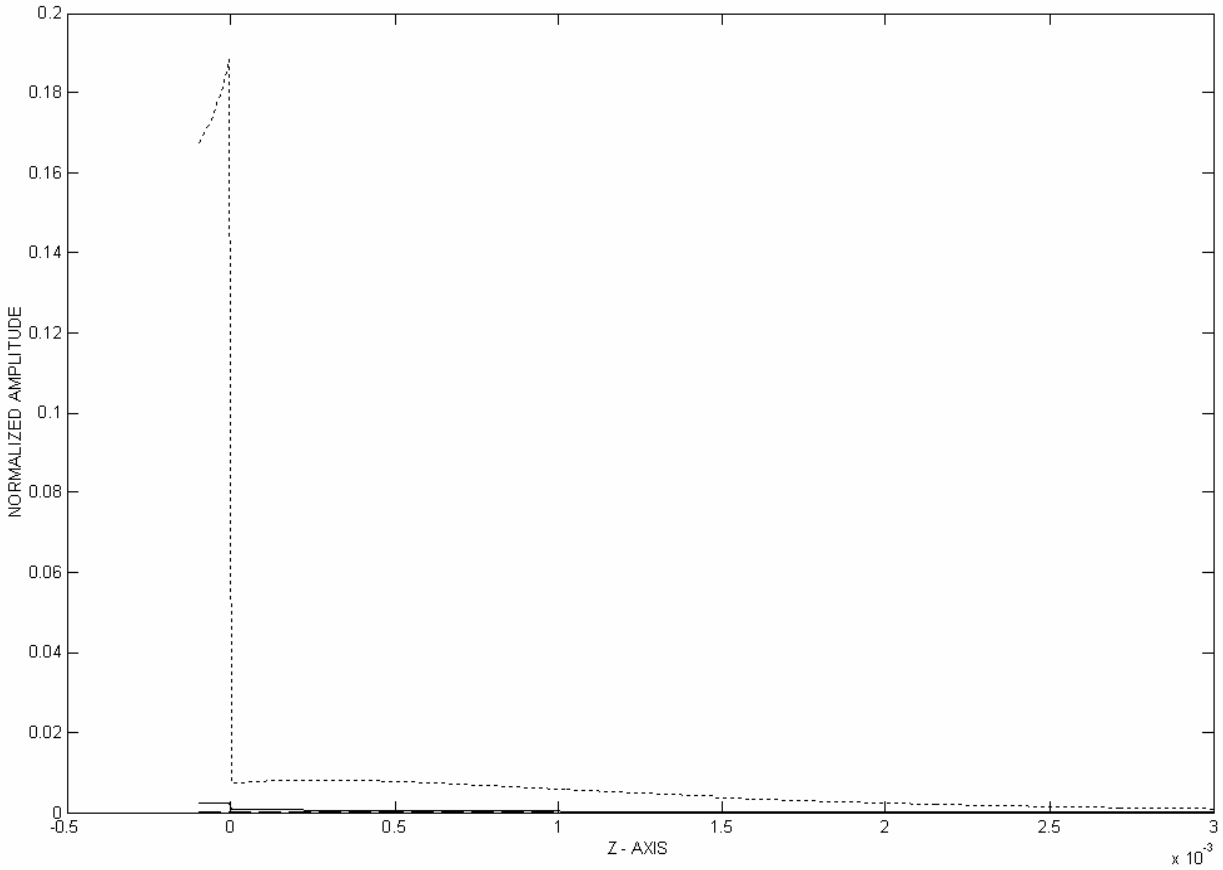

Fig. X.A.2.a_12: ***same as in Fig. X.A.2.a_10, except that only order for m=0 are taken into account.***

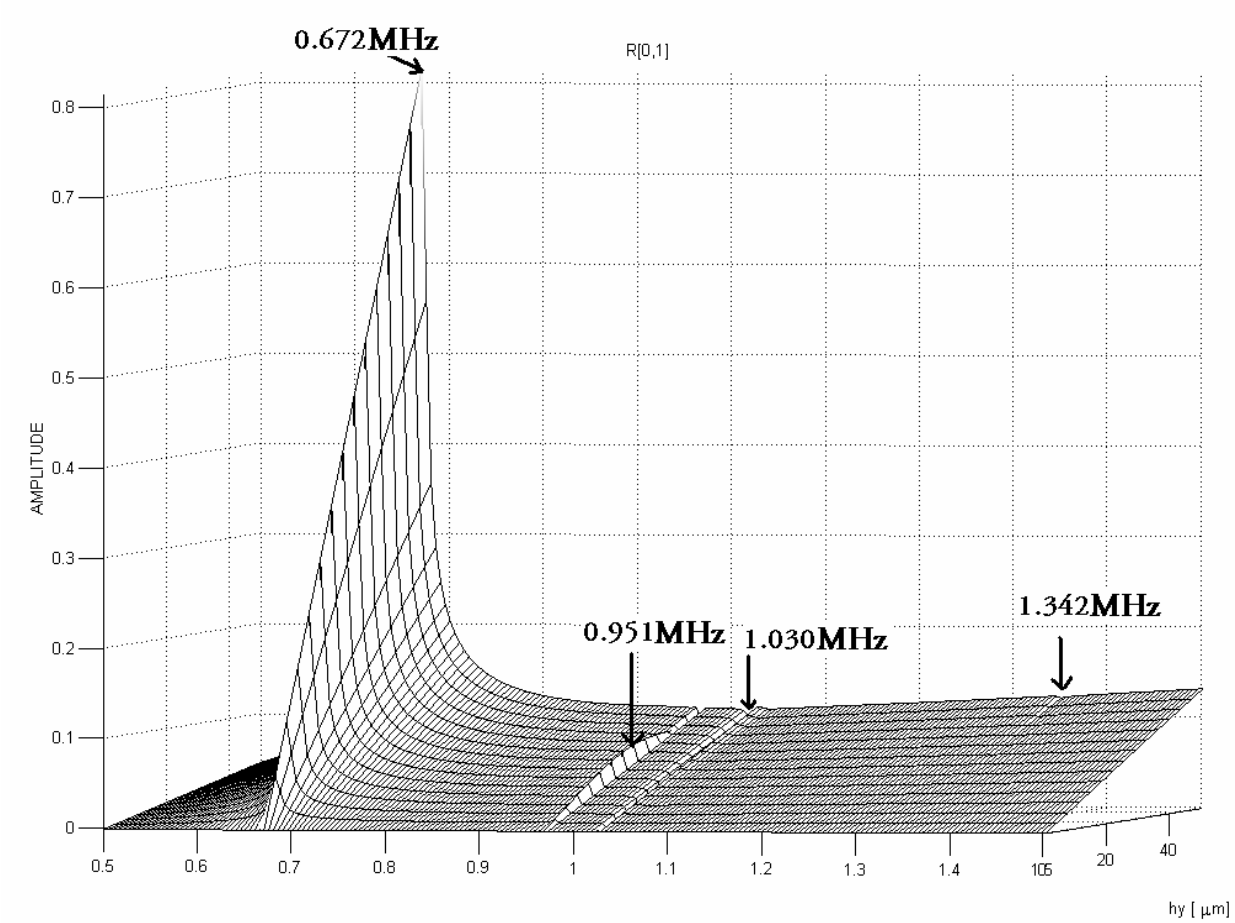

Fig. X.A.2.a_13: $\left|R^{0,1}\right|$ ***as a function of*** h_y ***and the frequency for*** $h_x = 50\mu m$ **,** $\Lambda_x = \Lambda_y = 2.2mm$ ***and*** $\boldsymbol{\beta}^{inc} = -44.27m^{-1}\mathbf{e}_x$**.**

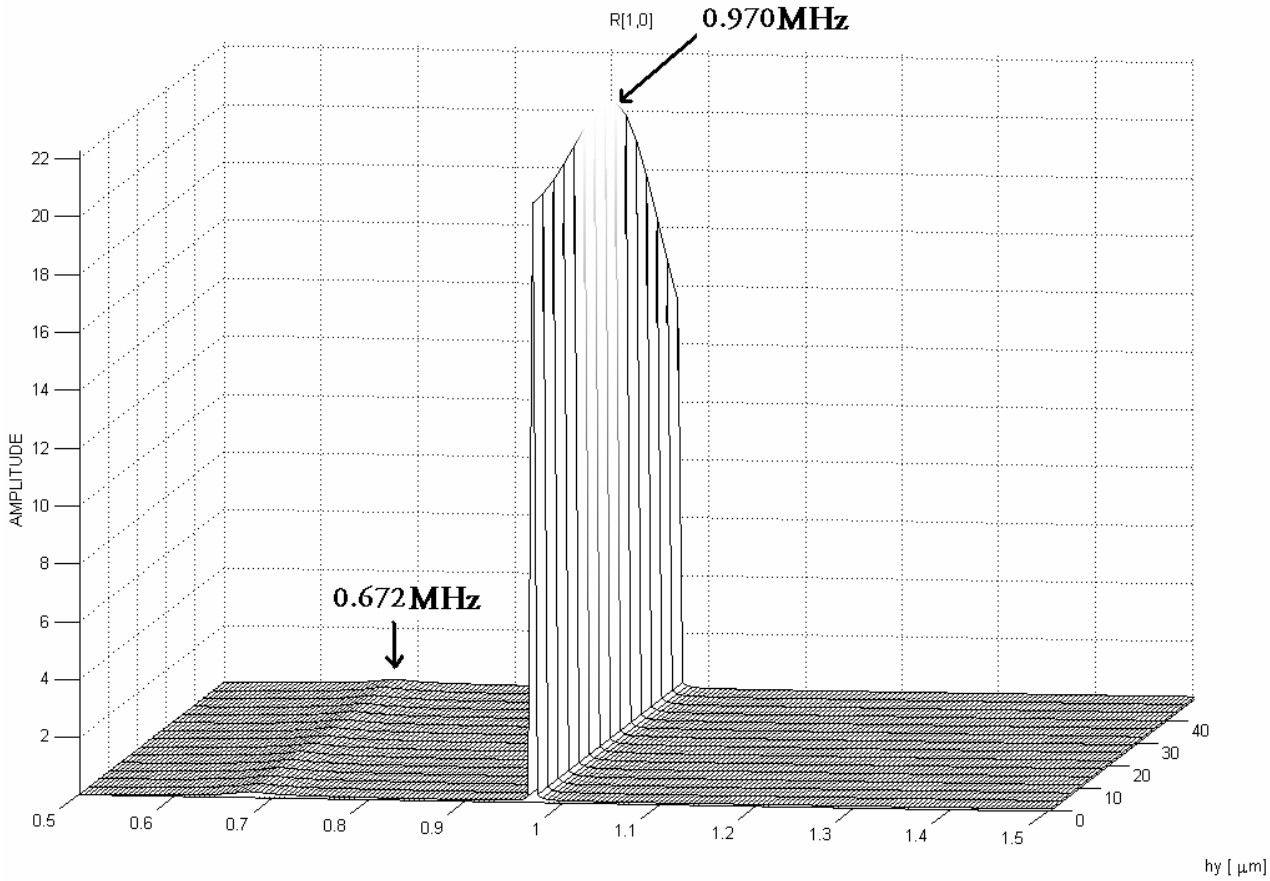

Fig. X.A.2.a_14: $\left|R^{1,0}\right|$ ***as a function of*** h_y ***and the frequency for*** $h_x = 50\mu m$ **,** $\Lambda_x = \Lambda_y = 2.2mm$ ***and*** $\boldsymbol{\beta}^{inc} = -44.27m^{-1}\mathbf{e}_x$**.**

It is seen in Fig. X.A.2.a_13 that in the 90^0 direction, an SSTW is generated at 0.672 MHz when h_y increases. There is also a small excitation visible at 0.951 MHz, due to the projection of the SSTW in the 45^0 direction on the 90^0 direction. In Fig. X.A.2.a_14 it is seen that in the 0^0 direction, a Rayleigh wave is generated at 0.970 MHz. The projection of the SSTW in the 45^0 direction on the 0^0 direction is invisible here since its influence on $R^{0,1}$ is negligible compared to that immense peak due to the Rayleigh wave.

Besides, if the reflection coefficient $R^{m,n}$ is considered with m different from zero, then the leaky Rayleigh wave phenomenon always overwhelms the effect of other phenomena. If $R^{m,n}$ is considered with m equal to zero, no influence is visible form the leaky Rayleigh wave phenomenon. This forms a numerical prove of the fact that leaky Rayleigh waves can only be stimulated in the x-direction if $\boldsymbol{\beta}^{inc} = \beta^{inc}\mathbf{e}_x$ and that in the opposite direction, solely SSTW can be generated. The latter two statements are visible in two telling examples, depicted in Fig. X.A.2.a_15 and Fig. X.A.2.a_16. It is seen that in Fig. X.A.2.a_15, a first order leaky Rayleigh wave is dominant at 0.970 MHz, while in Fig. X.A.2.a_16 a second order SSTW is dominant at 1.342 MHz. The second order leaky Rayleigh wave would of course be much more dominating, but its frequency reaches beyond the calculated frequency interval of Fig. X.A.2.a_15.

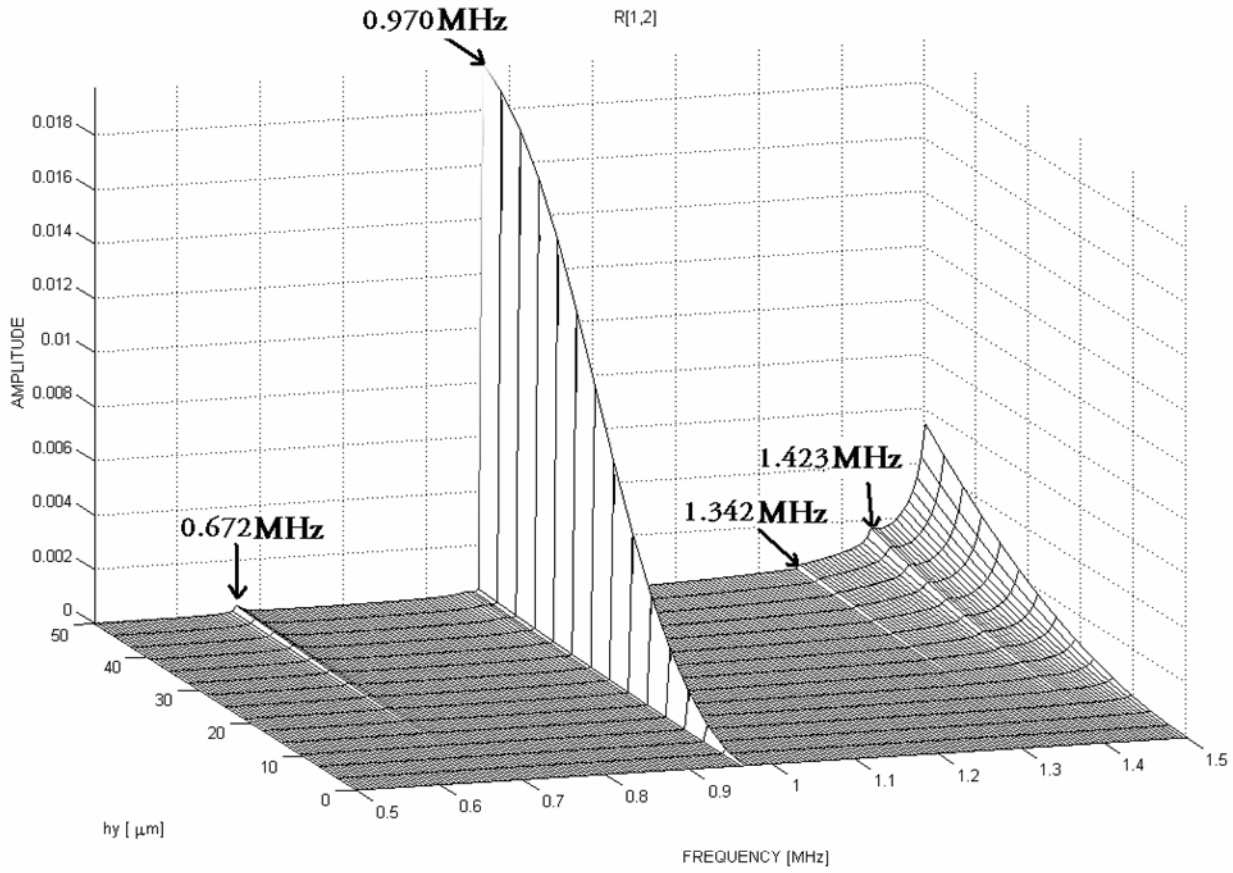

Fig X.A.2.a_15: $\left|R^{1,2}\right|$ ***as a function of*** h_y ***and the frequency for*** $h_x = 50\mu m$ **,** $\Lambda_x = \Lambda_y = 2.2mm$ ***and*** $\boldsymbol{\beta}^{inc} = -44.27m^{-1}\mathbf{e}_x$ **.**

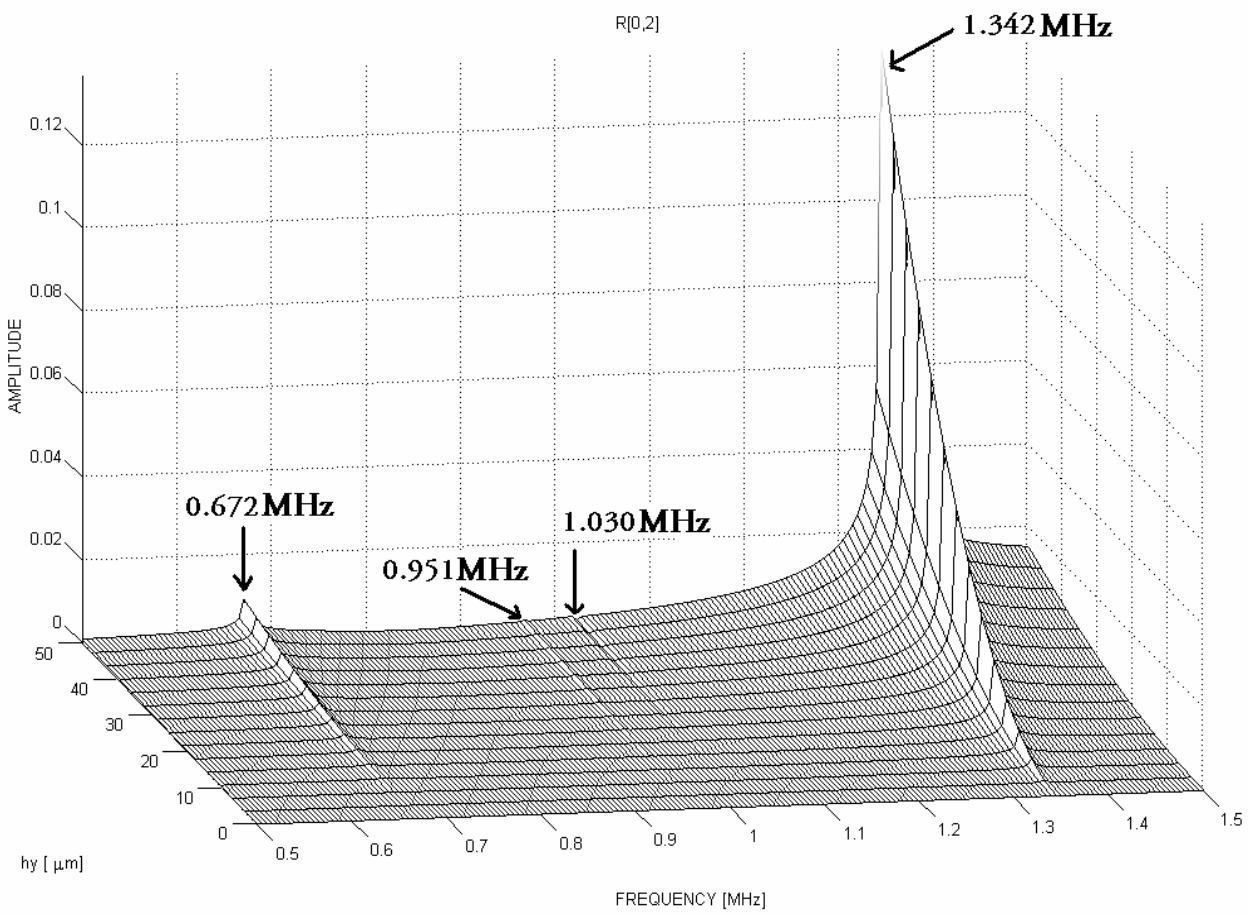

Fig. X.A.2.a_16: $\left|R^{0,2}\right|$ ***as a function of*** h_y ***and the frequency for*** $h_x = 50\mu m$ **,** $\Lambda_x = \Lambda_y = 2.2mm$ ***and*** $\boldsymbol{\beta}^{inc} = -44.27m^{-1}\mathbf{e}_x$**.**

CONCLUDING REMARKS

It is proved that the classical grating equation for singly corrugated surfaces can be extended to doubly corrugated surfaces and that it is also valid for incident inhomogeneous waves. From this equation, some properties are derived in (X.A.2.a_51-54) that relate the inhomogeneity and propagation direction to the inhomogeneity and angle of incidence.

Furthermore, it is shown through symmetry relations and through numerical calculations that normally incident homogeneous plane waves stimulate SSTW along the 0^0 , 45^0 and 90^0 directions in the xy-plane, measured from the x-axis, depending on the incident frequency. It is also numerically shown that normal incident inhomogeneous plane waves, having an inhomogeneity vector along the x-axis, can stimulate SSTW along the y-axis and not along the x-axis, whereas they can stimulate leaky Rayleigh waves along the x-axis and not along the y-axis.

The presented theory can be important in developing new Surface Acoustic Wave devices because of new possibilities of directivity as a function of the frequency and as a function of the inhomogeneity pattern of the impinging sound. Furthermore the basic

idea of this steering effect as a function of the surface symmetry and the frequency, can be important for developing planar actuators [24-28] by means of saw elements that have an equivalent effect as the doubly corrugated surface described in this section.

REFERENCES

[1] D. Maystre, "Selected Papers on Diffraction Gratings", SPIE: Milestone Series Vol. MS83 (SPIE, Washington, DC, 1993)

[2] Amir Boag, Yehuda Leviatan, Alona Boag, "Analysis of three-dimensional acoustic scattering from doubly periodic structures using a source model", J. Acoust. Soc. Am. 91(2), 572-580, 1992

[3] D. Michael Milder, H. Thomas Sharp, "An improved formalism for rough-suface scattering. II: Numerical trials in three dimensions", J. Acoust. Soc. Am. 91(5), 2620-2626, 1992

[4] D. Michael Milder, "An improved formalism for wave scattering from rough surfaces", J. Acoust. Soc. Am. 89(2), 529-541, 1991

[5] Garner C. Bishop, Judy Smith, "A T matrix for scattering from a doubly infinite fluid-solid interface with doubly periodic surface roughness", J. Acoust. Soc. Am. 94(3), 1560-1583, 1993

[6] Rudy Briers, "Contributions to the study of acoustic scattering and conversion phenomena in discontinuous structures by introducing a mode theory and by applying the inhomogeneous wave theory", PhD Thesis KULeuven University, department of sciences, 1995

[7] Koen E.-A Van Den Abeele, Rudy Briers, Oswald Leroy, "Inhomogeneous plane-wave scattering and mode stimulation on periodic rough surfaces", J. Acoust. Soc. Am. 99(5), 2883-2897 (1996)

[8] R. Briers, O. Leroy, O. Poncelet, M. Deschamps, "Experimental verification of the calculated diffraction field generated by inhomogeneous waves obliquely incident on a periodically rough liquid-solid boundary", J. Acoust. Soc. Am. 106(2), 682-687, 1999

[9] A. Jungman, O. Leroy, G. Quentin, K. Mampaert, "Theoretical and experimental study of ultrasonic surface modes at a solid-fluid interface", J. Appl. Phys. 63(10), 4860-4870 (1988)

[10] J.-M. Claeys, O. Leroy, " Diffraction of plane waves by periodic surfaces", Revue du Cethedec 72, 183-193 (1982)

[11] Marc Deschamps, "Reflection and refraction of the evanescent plane wave on plane interfaces", J. Acoust. Soc. Am. 96(5), 2841-2848 (1994)

[12] K. Mampaert, O. Leroy, "Reflection and transmission of normally incident ultrasonic waves on periodic solid-liquid interfaces", J. Acoust. Soc. Am. 83(4), 1390-1398 (1988)

[13] K. Mampaert, P.B. Nagy, O. Leroy, L. Adler, A. Jungman, G. Quentin, "On the origin of the anomalies in the reflected ultrasonic spectra from periodic surfaces", J. Acoust. Soc. Am. 86(1), 429-431 (1989)

[14] Nico F. Declercq, Rudy Briers, Oswald Leroy, " The use of polarized bounded beams to determine the groove direction of a surface corrugation at normal incidence, the generation of surface waves and the insonification at Bragg-angles", Ultrasonics 40/1-8 pp. 345-348, 2002.

[15] J. M. Claeys, Oswald Leroy, Alain Jungman, Laszlo Adler, " Diffraction of ultrasonic waves from periodically rough liquid-solid surface", J. Appl. Phys 54(10), 5657-5662 (1983)

[16] Briers R. and Leroy O. "Study of the behaviour of inhomogeneous harmonic waves in their diffraction from simple rough surfaces". J. Phys. IV, Colloque C1 suppl. au Journal de Physique III, vol 2, pp. C1-679-C1-682 (1992).

[17] Briers R. and Leroy O. " Reflection of inhomogeneous plane uitrasonic waves on periodically rough solid-vacuum interfaces". SPIE vol 1844 Acousto-Optics and Applications, Gdansk-Jurata, Poland. Proceed. pp. 196-205 (1992).

[18] B. A. Lippmann, "Note on the Theory of Gratings", J. opt. Soc. Am. 43, 408, 1953

[19] W. C. Meecham, "Variational Method for the Calculation of the Distribution of Energy reflected from a Periodic Surface", J. Appl. Phys. 27(4), 361-367, 1956

[20] M. Deschamps, C.L. Cheng, "Liquid-Thermoviscoelastic Solids Interface", Ultrasonics 27, 308-313 (1989)

[21] J.P. Charlier, F. Crowet, "Wave Equations in linear Viscoelastic Materials", J. Acoust. Soc. Am. 79(4), 895-9000 (1986)

[22] M. Abramowitz, I. A. Stegun, "Handbook of mathematical functions", Dover Publications, 1972

[23] Jean-Marie Claeys, "Theoretical Models to describe reflection and diffraction of ultrasound from layered media", PhD Thesis KUL department of Sciences (in dutch), 1985

[24] Friend J, Umeshima A, Ishii T, Nakamura K, Ueha S ,"A piezoelectric linear actuator formed from a multitude of bimorphs", SENSORS AND ACTUATORS A-PHYSICAL, 109 (3), 242-251, 2004

[25] Hu JH, Nakamura K, Ueha S , "Stability analysis of an acoustically levitated disk", IEEE TRANSACTIONS ON ULTRASONICS FERROELECTRICS AND FREQUENCY CONTROL, 50 (2), 117-127, 2003
[26] Friend JR, Satonobu J, Nakamura K, Ueha S, Stutts DS, "A single-element tuning fork piezoelectric linear actuator", IEEE TRANSACTIONS ON ULTRASONICS FERROELECTRICS AND FREQUENCY CONTROL, 50 (2), 179-186, 2003
[27] Yun CH, Ishii T, Nakamura K, Ueha S, Akashi K, "Holding mechanism using a resonance system for a high-power ultrasonic linear motor", JAPANESE JOURNAL OF APPLIED PHYSICS PART 1-REGULAR PAPERS SHORT NOTES & REVIEW PAPERS, 41 (5B), 3261-3266, 2002
[28] Satonobu J, Friend JR, Nakamura K, Ueha S, "Numerical analysis of the hybrid transducer ultrasonic motor: comparison of characteristics calculated by transmission-line and lumped-element models" ULTRASONICS 39 (8), 559-565, 2002

Sections X.B Acoustic Diffraction Phenomena

Fig. X.B: ***After the publication of the paper in J. Acoust. Soc. Am. and after Nature News published it, Wayne van Kirk sent me an important email, telling me that a mask of the Mayan rain god Chac is visible at the top of the pyramid. I did not know that when I discovered and modelled the raindrop effect… the presence of this mask makes the statement that the raindrop effect has been purposely induced by the pyramid builders, more plausible.***

X.B.1 A theoretical Study of Special Acoustic Effects Caused by the Staircase of the El Castillo Pyramid at the Maya Ruins of Chichen-Itza in Mexico

It is known that a handclap in front of the stairs of the great pyramid of Chichen Itza produces a chirp echo which sounds more or less like the sound of a Quetzal bird. The present work describes theoretical diffraction simulations and attempts to answer the critical question what physical effects cause the formation of the chirp echo. Comparison is made with experimental results obtained from David Lubman. Numerical simulations show that the echo shows a strong dependence on the kind of incident sound. Simulations are performed for a (delta function like) pulse and also for a real handclap. The effect of reflections on the ground in front of the pyramid is also discussed. The present work also explains why an observer seated on the lowest step of the pyramid hears the sound of raindrops falling in a water filled bucket instead of footstep sounds when people, situated higher up the pyramid, climb the stairs.

The contents of this section have been published as: Nico F. Declercq, Joris Degrieck, Rudy Briers, Oswald Leroy, "A theoretical study of special acoustic effects caused by the staircase of the El Castillo pyramid at the Maya ruins of Chichen-Itza in Mexico", J. Acoust. Soc. Am. 116(6), 3328-3335, 2004 (Imp. Fact. 1.310; SCI-index, Acoustics, rank:7 /28).

Furthermore, the results have been reported in numerous newspapers around the world, including Nature News [Nature News 14 December 2004; | doi:10.1038/news041213-5].

INTRODUCTION

During the post meeting tour of the first PanAmerican/Iberian meeting on Acoustics that was held in Cancun (Mexico) in 2002 (hereafter called 'the post meeting tour'), the participants were shown that there are plenty of interesting sound effects that occur at Chichen-Itza. Chichen Itza is a Maya ruin where, besides the famous 'ball court' [1], there is a pyramid (El Castillo) that produces a sound echo, in response to a handclap, which sounds like the chirp of a Quetzal bird. This effect has been one of the major subjects during plenty of talks given by David Lubman [2-5] and others [6-8]. Lubman has stressed the fact that the Quetzal bird chirp is actually caused by Bragg scattering. However, there has never been presented an actual simulation of the effect, except for some heuristic simulations based on the ray theory [2-5] or a heuristic approach for the case of incidence at 45^0 measured from the normal to the surface [8-12]. In what follows, a full diffraction simulation is presented of the echo, based on a (time-) delta function like handclap

and also a real handclap, based on the physical parameters of the staircase of the Pyramid at Chichen-Itza and based on the monofrequent single homogeneous plane wave diffraction theory of Claeys et al [9-10], which is a simplified case of the inhomogeneous plane wave diffraction theory [11]. The present work describes the first simulations of a spherical sound pulse, based on that monofrequent pure plane wave diffraction theory [9-10]. Furthermore, it is for the first time that the theory has been applied to audio frequencies.

Before presenting this development, it is of cultural importance to stress the fact that some people believe that the Quetzal bird chirp echo is caused by accident and others believe that it is caused as a consequence of the Pyramid builders' purpose. Nevertheless, it is known that the Quetzal bird has played a very important role in Mayan culture, which is probably due to the fact that Mayans originally lived for many centuries in the forest before getting involved in the construction of cities and religious sites. However, what is sure about this pyramid is that it certainly functioned as a great solar calendar. For example a large serpent is built on one side that causes special light effects around the time of spring and fall equinox. This serpent is culturally connected to the Quetzal bird (as can be seen on a Mayan glyph from the Dresden Codex), whence the generation of a Quetzal bird echo might not be a real coincidence. It is also known that an echo in Mayan culture represents a spirit. However, it must also be noted that a Quetzal bird echo also occurs at other Pre-Columbian sites and Ancient Mexican ruins [12]. Furthermore the first author encountered similar effects as in Chichen Itza at two religious sites in Sri Lanka. There, the short concrete staircase, that enables people to take a bath in the Menik Ganga river at the religious site of Katharagama, produces the low frequency sound of quacking ducks in response to a handclap. Furthermore high frequency echoes occur on the immense staircase leading to the religious site of Sri Pada (Adam's peak). Nevertheless, the effects in Sri Lanka are probably a coincidence and are not a result of purposely construction.

The last part of this section is devoted to the less known fact that an observer seated on the lowest stair step of the great pyramid at Chichen Itza, hears pulses that sound like raindrops falling in a water filled bucket, when other people are climbing the pyramid higher up. This phenomenon (hereafter called 'raindrop effect'), has been observed by the first author and by a student fellow Cécile Goffaux during the post meeting tour. Since the 'rain god' plays a very important role in the Yucatan Mayan culture, this finding might be an impetus for future cultural studies.

THEORETICAL DEVELOPMENT OF THE ECHO SIMULATION

The staircase is seen as a periodically corrugated (infinite) surface, being sawtooth shaped (see Fig. X.B.1_1).

This is only true within the interval of the physical staircase. This infinite mathematical model is matched to reality by modeling a handclap not by a truly spherical wave, but by a wave that only contains propagation directions from the emitter directly to the staircase within the angular interval $[\alpha_1, \alpha_2]$ that assures impingement on the staircase and within the interval $[\alpha_3, \alpha_4]$ if, in addition, reflections on the ground are considered as well. Hence, the handclap is only spherical if observed on the staircase. Whatever sound patterns are emitted to areas outside of the considered intervals is unimportant for the present study.

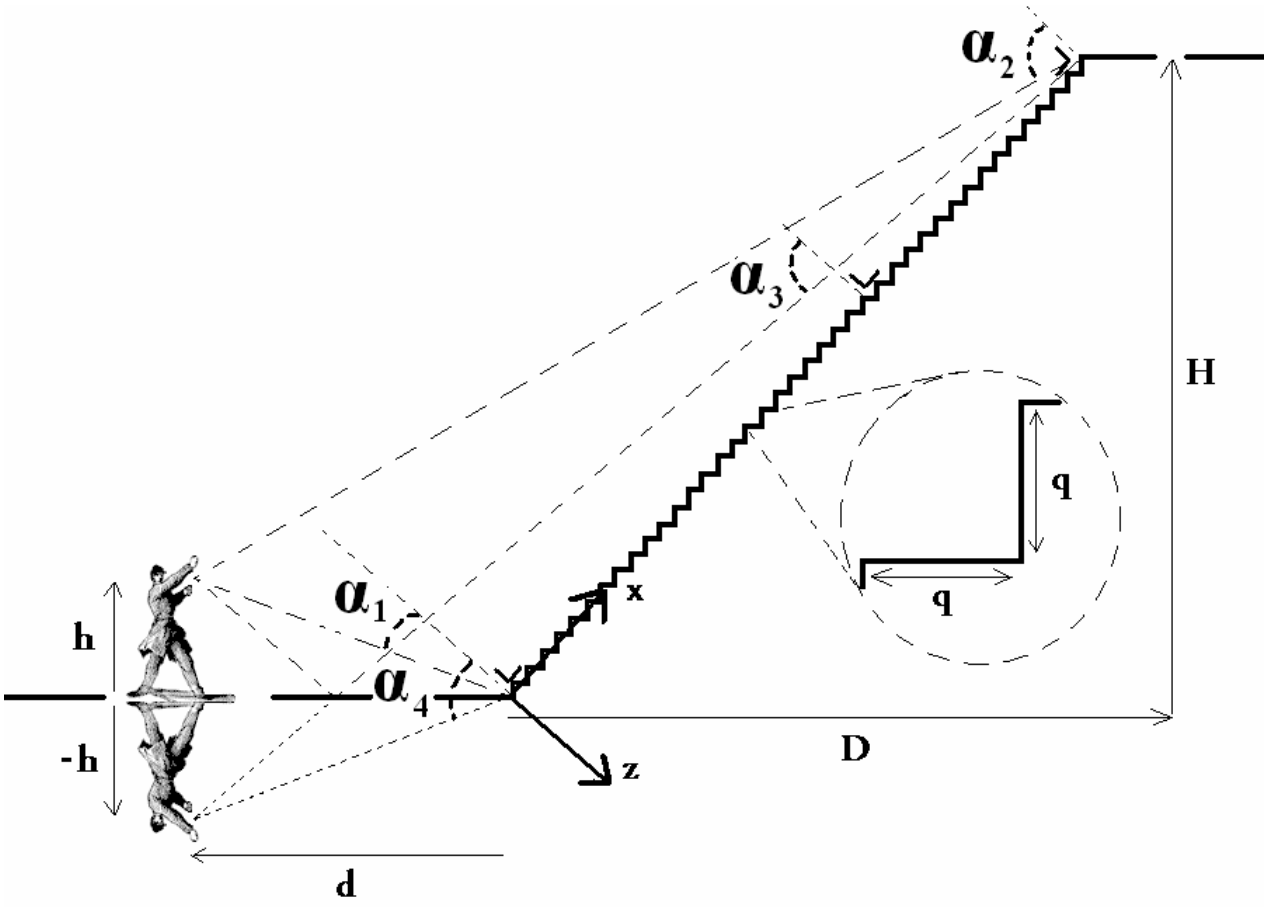

Fig. X.B.1_1: ***Depiction of the pyramid's staircase with and observer in front of it.***

The vectors **d, h, D** and **H** are defined in Fig. X.B.1_1. For $\mathbf{e}_x$ and $\mathbf{e}_z$ being unit vectors along the x, respectively z direction, straightforward geometrical considerations result in

$$\alpha_1 = \arccos \frac{(\mathbf{h}+\mathbf{d}) \bullet \mathbf{e}_z}{\sqrt{h^2 + d^2}} \qquad \text{(X.B.1\_1)}$$

$$\alpha_2 = \arccos \frac{(\mathbf{h}+\mathbf{d}) \bullet e_z}{\left|\mathbf{h}+\mathbf{d}-\sqrt{D^2+H^2}\,\mathbf{e}_x\right|} \qquad \text{(X.B.1\_2)}$$

$$\alpha_3 = \arccos \frac{(-\mathbf{h}+\mathbf{d}) \bullet e_z}{\left|-\mathbf{h}+\mathbf{d}-\sqrt{D^2+H^2}\,\mathbf{e}_x\right|} \qquad \text{(X.B.1\_3)}$$

$$\alpha_4 = \arccos \frac{(-\mathbf{h} + \mathbf{d}) \bullet \mathbf{e}_z}{\sqrt{h^2 + d^2}} \tag{X.B.1_4}$$

with

$$\begin{pmatrix} d_x \\ d_z \end{pmatrix} = \begin{pmatrix} \cos\xi & \sin\xi \\ -\sin\xi & \cos\xi \end{pmatrix} \begin{pmatrix} |d| \\ 0 \end{pmatrix} \tag{X.B.1_5}$$

$$\begin{pmatrix} h_x \\ h_z \end{pmatrix} = \begin{pmatrix} \cos\xi & \sin\xi \\ -\sin\xi & \cos\xi \end{pmatrix} \begin{pmatrix} 0 \\ |h| \end{pmatrix} \tag{X.B.1_6}$$

and

$$\xi = \arctan \frac{H}{D} + \frac{\pi}{2} \tag{X.B.1_7}$$

The diffraction theory of Claeys et al that is applied here can be found in the literature [9-11]. Nevertheless, some characteristics of that theory are outlined below. The theory is based on the decomposition of the diffracted acoustic field into pure plane waves, which is essentially only allowed whenever the Lipmann conditions [9-11] are fulfilled, stating that the incident wave length must be of the same order of magnitude as the corrugation period and that the corrugation height must not exceed the incident wave length. If these conditions do not hold, then errors will occur in the description of the sound field within the corrugation. Elsewhere the errors will be small, except when the Lipmann conditions are seriously violated of course. Basically, each of the reflected and transmitted wave fields are decomposed into a series of plane waves, each plane wave of order *m* having a wave vector

$$\mathbf{K}^m = k_x^m \mathbf{e}_x + k_z^m \mathbf{e}_z \tag{X.B.1_8}$$

with

$$k_x^m = k_x^{inc} + m \frac{2\pi}{\sqrt{2}q} \tag{X.B.1_9}$$

and k_z^m determined by k_x^m, the material properties of the considered medium and the dispersion relation $k^2 = \omega^2 / v^2$, ω being the angular frequency and *v* being the plane wave velocity. The sign of k_z^m is chosen such, as to fulfill the necessity of plane waves to propagate away from the interface and, whenever k_z^m is purely imaginary, the amplitude must decay away from the interface. The continuity conditions demand continuity of normal stress and normal particle displacements on each spot of the pyramid's staircase. It can be found in Claeys et al [9-11] that

this leads to a set of equations that is periodical in *x*, whence the discrete Fourier transform can be applied, resulting in an equal number of equations and unknown amplitudes of all diffracted orders. It can also be found in Claeys et al [9-11] that this discrete infinite set of equations and unknowns can be chopped to a square linear matrix equation that can be solved by a computer.

NUMERICAL RESULTS AND DISCUSSION

The following parameters are chosen such as to match the physical reality of the reported experiments [13] at 10 *m* in front of the pyramid (see Fig. X.B.1_1). The observer's height is chosen h=1.80 *m*, the observers distance d=10 *m*, the pyramid's dimensions D=23.84 *m*, H=24.02 *m*, q=0.263 *m*. It then follows from (X.B.1_1-4) that $\alpha_1 = 35.01^0$, $\alpha_2 = 78.15^0$, $\alpha_3 = 82.22^0$ and $\alpha_4 = 55.42^0$. The material properties in the humid Yucatan air have been taken as $\rho = 1.1466 \text{kg/m}^3$ for the density and $v = 343 m/s$ for the sound velocity. Those for the limestone [14] staircase have been taken as $\rho = 2000 kg/m^3$ for the density, $v_l = 4100 m/s$ for the longitudinal wave velocity and $v_s = 2300 m/s$ for the shear wave velocity. Damping has not been taken under consideration. For the parameters just given, the Lipmann conditions are given as follows: For frequencies lower than 1844 Hz, the numerical simulations will be perfect. For frequencies higher than 1844 Hz, there will be small errors in the description of the sound field within the corrugation, but not elsewhere. For very high frequencies, say more than 5000 Hz, errors may also occur in the prediction of the sound field outside of the corrugation, i.e. in the air and where the observer is situated. The errors gradually grow for higher frequencies and are due to 'shadow zones' and neglecting internal reflection within the stairs.

Direct echo coming from a delta pulse

Within the angular interval $[\alpha_1, \alpha_2]$, the incident sound is considered to be spherical and contains 500 frequencies equally distributed between 500Hz and 3000Hz. All incident plane waves have the same amplitude regardless of their direction and frequency. The former is necessary to produce the spherical wave, the latter is needed to produce a delta function like handclap. The spherical wave is modeled by 300 plane waves propagating along equally distributed angles within the interval $[\alpha_1, \alpha_2]$.

There is no serious violation of the Lipmann conditions. Only for frequencies above 1844 Hz can there be some errors in the sound field description within the corrugation, but that is not of significant importance here because we are only interested in effects at the observer's position.

In Fig. X.B.1_2, the calculated echo as a function of time is given, corresponding to an incident spherical pulse.

This signal looks very clean, i.e. there is not too much noise outside of the echo, and is somewhat similar to the normalized plot in Fig. X.B.1_3 of the actual sound of a real Quetzal bird in the forest.

The latter signal was downloaded in *.wav format from the website of David Lubman [13]. The few delta function like peaks in the middle of that latter plot are the result of cracks that can be heard in the recorded sound file and are probably due to wood creaks in the bird's biotope. Fig. X.B.1_4 shows a normalized plot of the pyramid's echo and is obtained from a *.wav file that was also downloaded from Lubman's website [13].

This signal is far from clean. This is primarily due to low frequency noise coming from the interaction of wind with the microphone. Since it is almost impossible to compare sound signals in time-space, it is necessary to study sonograms or spectrograms of the obtained signals [15]. A sonogram depicts the amplitude as a function of time '*t*' and as a function of frequency '*f*'.

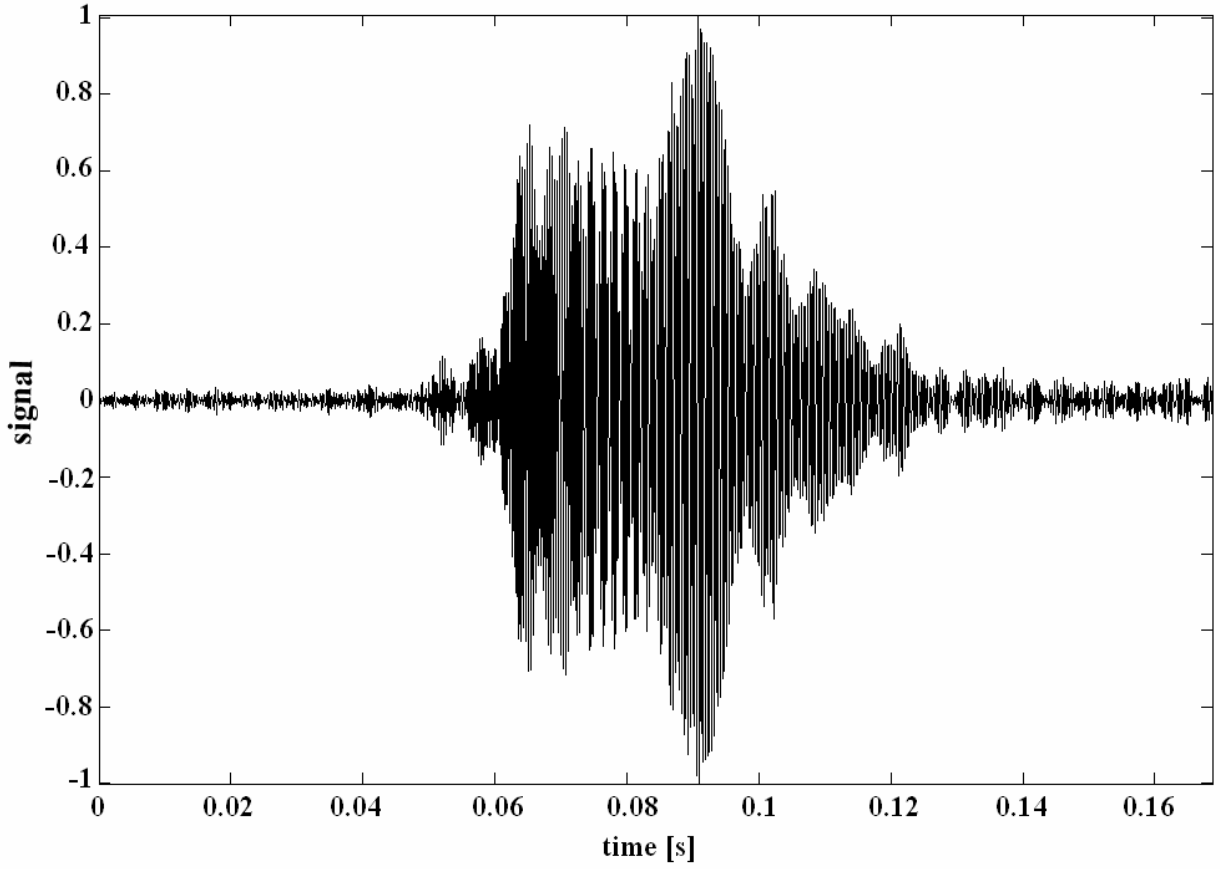

Fig. X.B.1_2: ***Normalized calculated direct echo coming from a delta pulse*.**

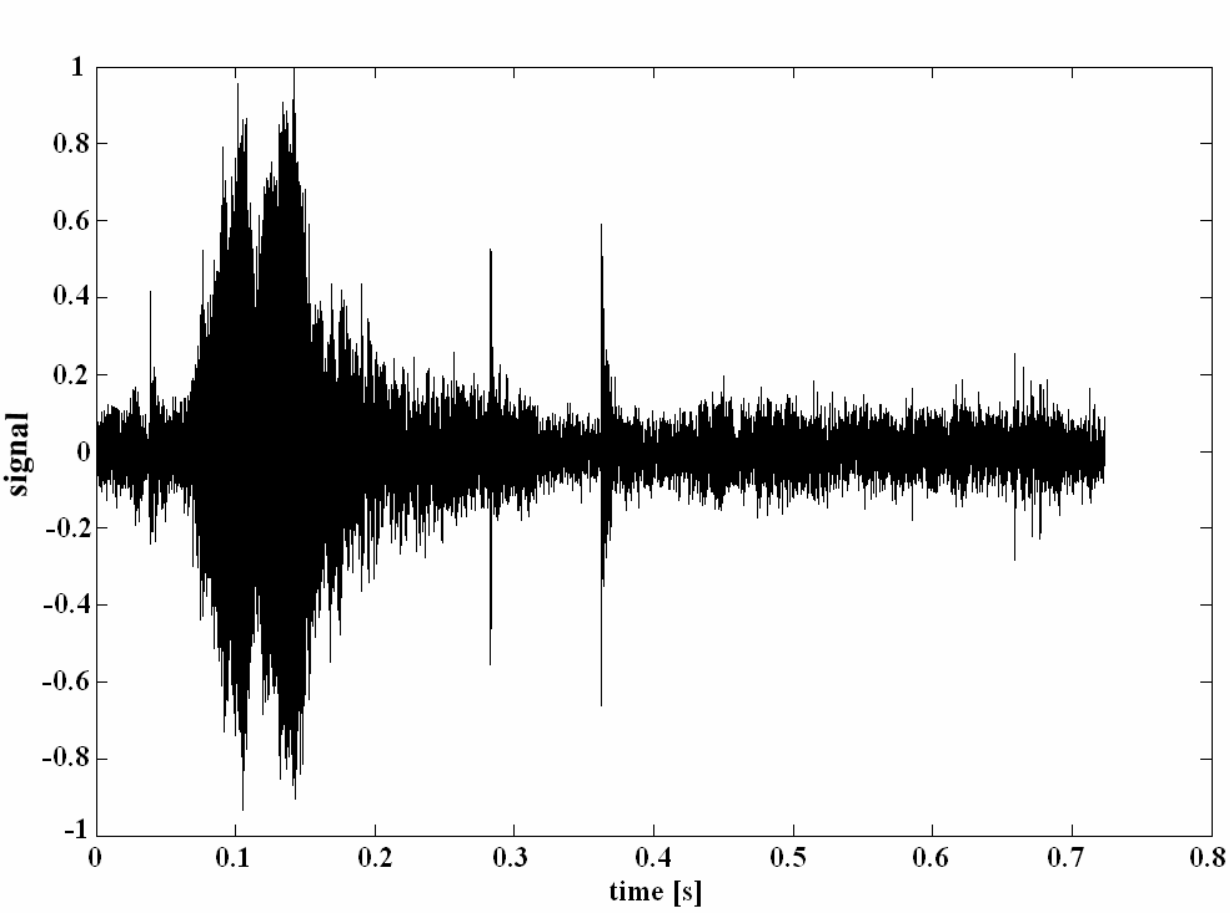

Fig. X.B.1_3: ***Normalized recorded signal produced by a Quetzal bird in the forest.***

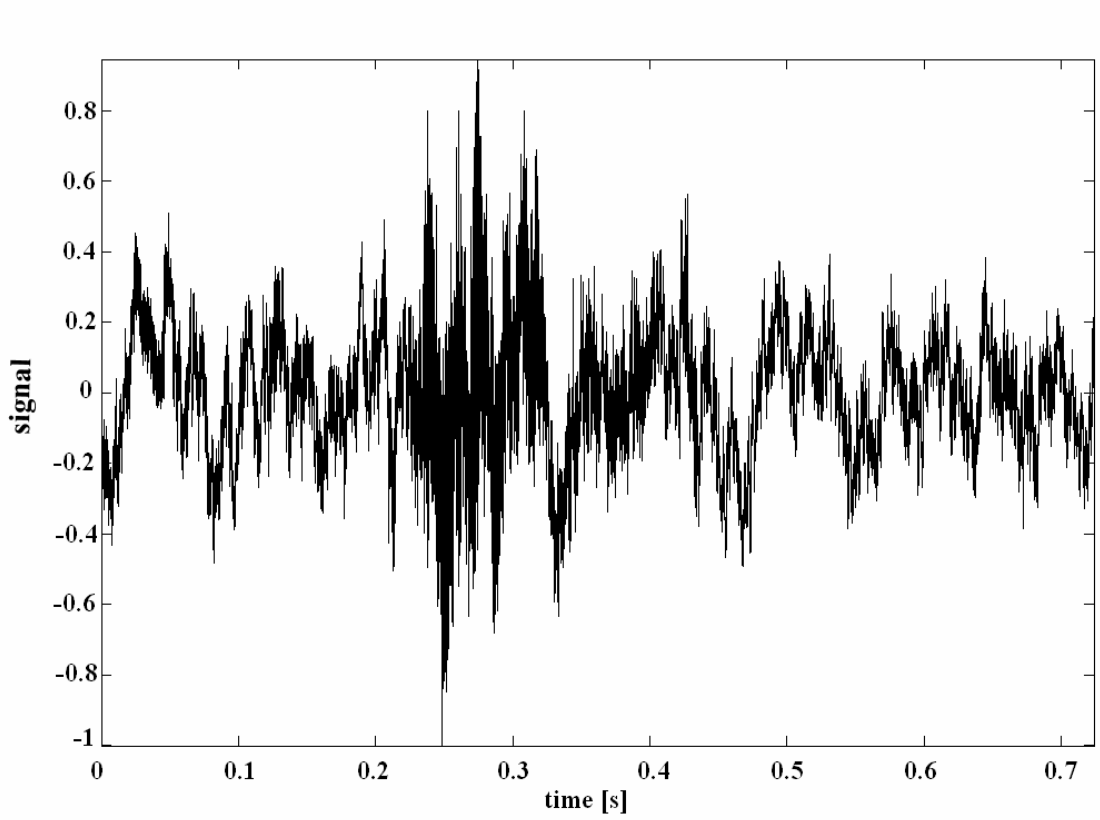

Fig. X.B.1_4: ***Normalized recorded signal of the echo coming from the pyramid.***

It is obtained by a time limited Fourier transform. Here, we used a gaussian window of 0.002s width. The sonograms are plotted by means of a gamma correction of 2. If the recorded sound is truly and solely an echo that comes from diffraction on the staircase, some patterns that will be mathematically described now, may appear in the sonogram. From (X.B.1_9) an -m'th order echo may appear if the following relation holds:

$$k_x^{inc} = m\frac{\pi}{\sqrt{2}q} \qquad \text{(X.B.1\_10)}$$

If this is combined with the dispersion relation, the angle, as a function of the frequency at which the echo may appear, can be calculated. If a ray-consideration is then applied, the time delay as a function of each angle, taking into account the wave speed in air, can also be obtained. This ultimately results in:

$$t(-m,f)=\frac{\left|d_z+h_z\right|}{v\cos\mathrm{Re}\left[\frac{\pi}{2}-\arctan\frac{\sqrt{\left(\frac{2\pi f}{v}\right)^2-\left(m\frac{\pi}{\sqrt{2}q}\right)^2}}{m\frac{\pi}{\sqrt{2}q}}\right]} \qquad \text{(X.B.1\_11)}$$

In Fig. X.B.1_5 the curves that are represented by (X.B.1_11) are depicted by means of a sonogram.

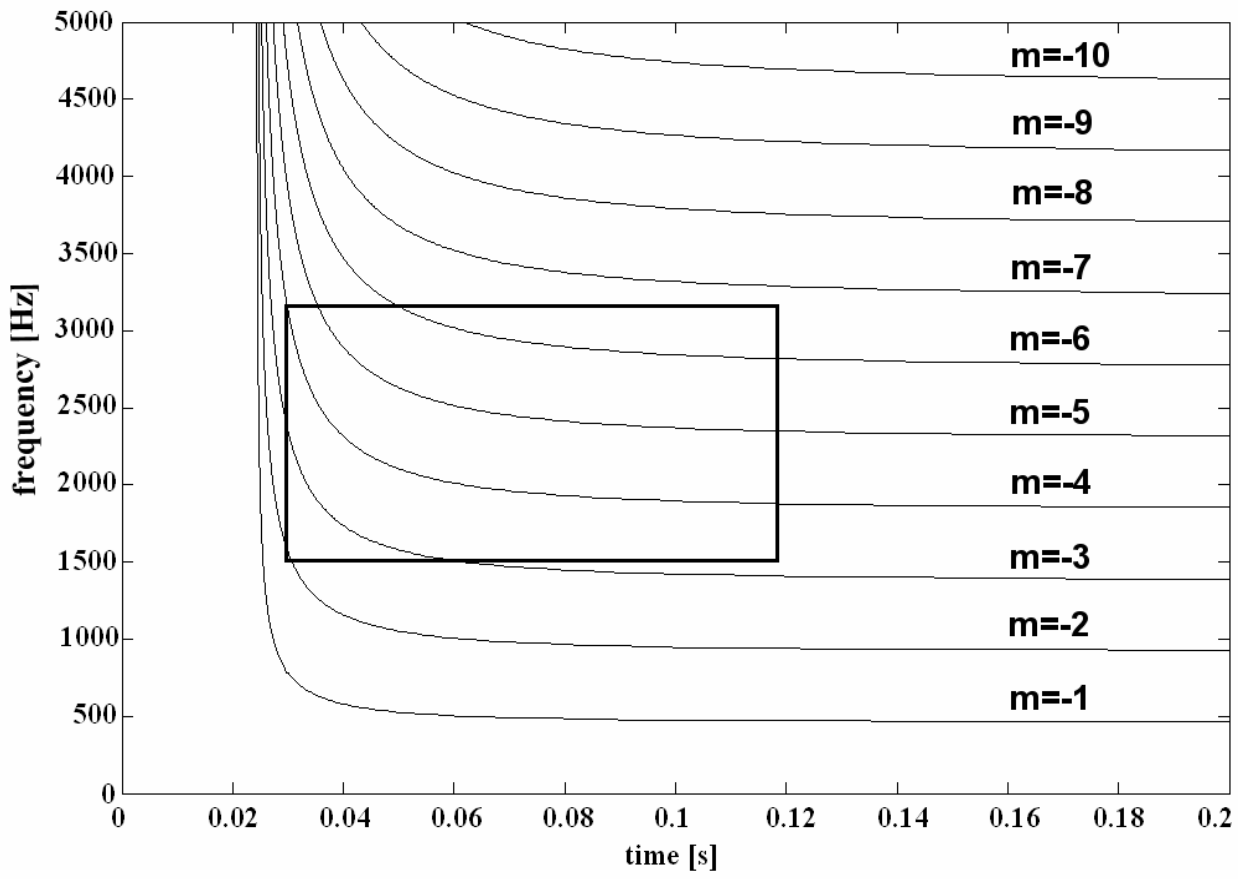

Fig. X.B.1_5: ***Bragg diffraction lines on a sonogram. The sonogram shows information as a function of time (horizontal axis) and frequency (vertical axis). The square window is a reference window that represents the same time/frequency values in each sonogram in this report.***

In all sonograms that are presented here, the vertical axis represents the frequency in the range from 0Hz (bottom) to 5000 Hz (top). The horizontal axis always spans a range of 0.2 s. However, the instant values on the horizontal axis do not always range from 0 s to 0.2 s. It is only the difference between the right side of the horizontal axis and the left side that is 0.2 s. This is of course due to the fact that sound recordings contain no information about the absolute values of

the start of recording and the end of recording. However, in order to compare the different sonograms that are presented here, we have taken into account physical considerations like the presence of the handclap in the recordings of Lubman [13] or the knowledge of the time-origin in our calculations, to draw a time/frequency window on each of the presented sonograms that is absolutely the same in each sonogram. This window will therefore function as the reference window for the discussions below. The absolute position of the window is chosen as to contain the relevant information that is present in Fig. X.B.1_6, which is the sonogram that corresponds to the calculated echo of Fig. X.B.1_2.

This sonogram shows almost the same structure as the one of Fig. X.B.1_7, which corresponds to the recorded Quetzal bird chirp in the woods (see also Fig. X.B.1_3). The only important difference is the frequency at which the patterns appear and their duration. The actual bird chirps at lower frequencies than the calculated pyramid's echo. The authors do not know how a young Quetzal bird sounds like, but perhaps the resemblance would then be better.

If Fig. X.B.1_5 is compared with Fig. X.B.1_6, it is noticed that even though the classical grating equation predicts the possibility of elevated amplitude lines in the sonogram, not all lines are associated with a relevant amplitude if the continuity conditions are also taken into account (see Fig. X.B.1_6).

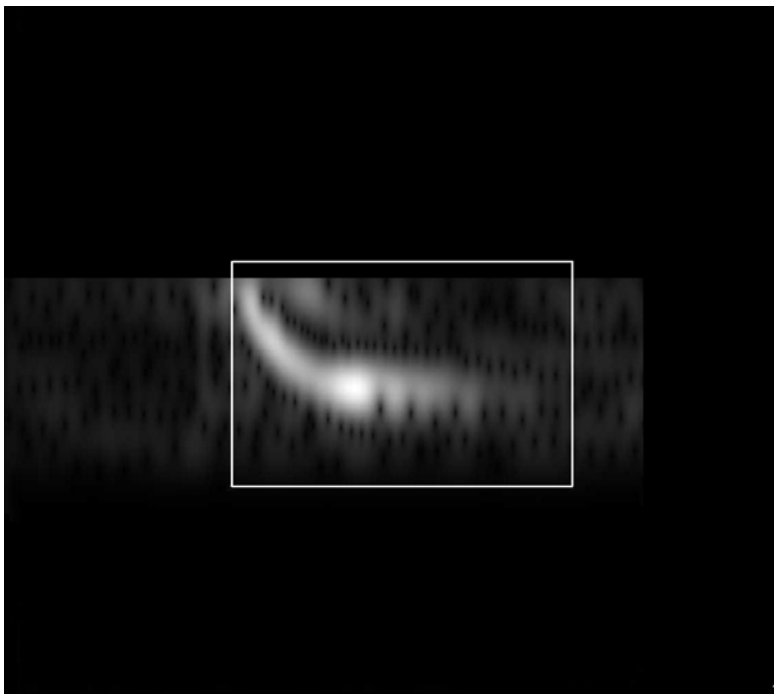

Fig. X.B.1_6: ***Sonogram of the calculated direct echo coming from a delta pulse. The axes are equal to those of Fig. X.B.1_5, ranging from 0 Hz to 5000 Hz on vertical axis and from 0 s to 0.2 s on horizontal axis.***

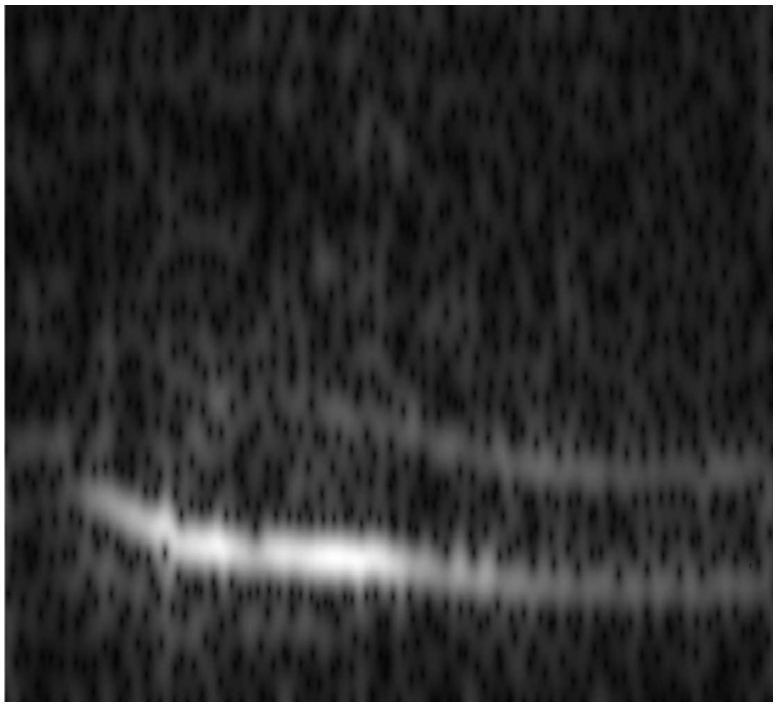

Fig. X.B.1_7: ***Sonogram of the recorded Quetzal bird chirp in the forest. The axes are equal to those of Fig. X.B.1_5, ranging from 0 Hz to 5000 Hz on vertical axis and from 0 s to 0.2 s on horizontal axis.***

However, the elevated amplitude patterns that do appear correspond more or less to the lines of Fig. X.B.1_5. Especially there is a strong appearance of the m=-4 or m=-5 back reflected sound. The fact that it is not simple to decide which order is actually determining the elevated amplitudes is probably due to the interference of several plane waves because the incident sound is spherical. This is slightly in contrast with the assumption of Lubman [5] that the Bragg-orders can be well seen in the sonogram of the recorded echo. In order to examine this contradiction, we have calculated the sonogram that actually corresponds to the recorded pyramid's echo of Fig. X.B.1_4. The result is shown in Fig. X.B.1_8.

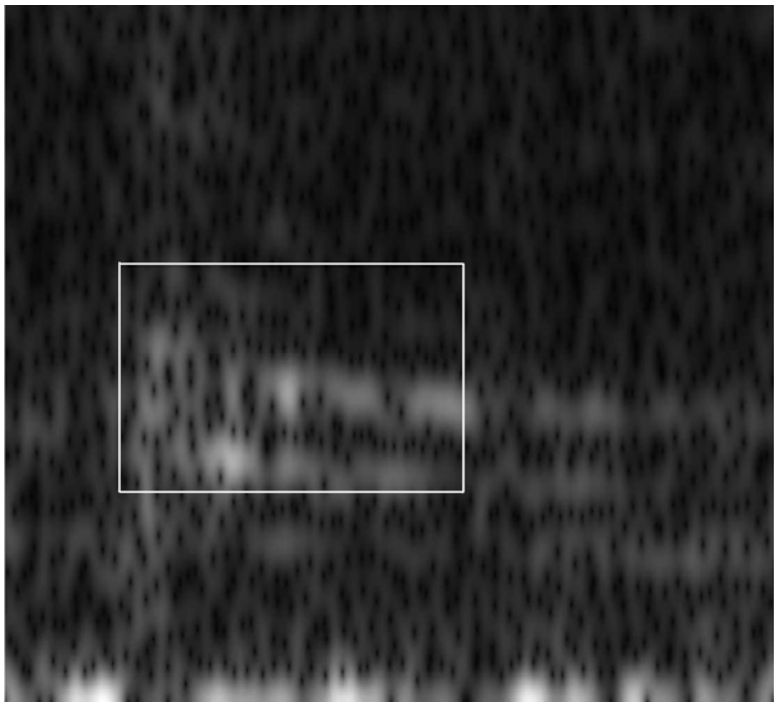

Fig. X.B.1_8: ***Sonogram of the recorded echo coming from the pyramid. The vertical axis is equal as in Fig. X.B.1_5, ranging from 0 Hz to 5000 Hz, the horizontal axis spans the same time interval length of 0.2 s. The reference window is situated at the same time/frequency values as in Fig. X.B.1_5.***

Within the reference time/frequency window, the same pattern can be found more or less (if you look through the noise) as in Fig. X.B.1_6. However, Fig. X.B.1_8 shows that it is absolutely not for certain that all patterns that are noticeable would correspond to the lines of Fig. X.B.1_5. There is even something more obscure, which is the presence of 'patterns' outside the reference window. If these were simply coming from Bragg diffraction, they would also appear in Fig. X.B.1_6, where not only the mathematical grating equation is taken into account, but also the continuity conditions. Since they do not appear in Fig. X.B.1_6 (or have an amplitude which is too small to be noticed), it can already be concluded that these patterns cannot simply be the result of pure Bragg diffraction and that an extra effect must be involved.

Direct echo coming from a handclap

The answer to the critical question as to what then actually causes these patterns can be revealed if one considers Fig. X.B.1_9.

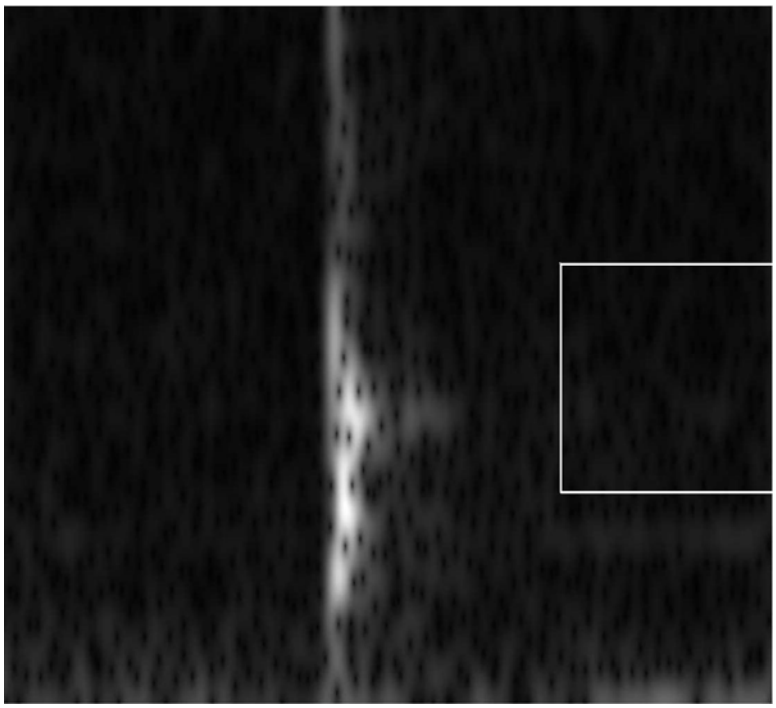

Fig. *X.B.1_9*: *Sonogram of the recorded (and mathematically isolated) handclap. Same comments on the axes as in Fig. X.B.1_8.*

The latter figure depicts the sonogram of the handclap taken from the recordings of Lubman [13] and being isolated from the echo of the same recording. A handclap is actually far from a delta function, because not all frequencies have the same amplitude. Actually, the handclap contains several frequency bands. For this purpose we have also simulated the echo resulting from a real handclap instead of a pulse. The handclap itself (as taken from Lubman [13]), which takes 0.02s and must be followed by 0.18s of silence in order to get a realistic time window of 0.2s, needs to be represented by 4096 frequencies in between 5 Hz and 25000Hz. Because of the amount of RAM memory needed and due to a limited CPU speed, taking into account all these frequencies in our diffraction procedure would result in a calculation time that exceeds the lifetime of our high speed computer.
This, together with the fact that the higher the frequencies, the more seriously Lipmann's conditions are violated, and a trade off between handclap reproducibility and calculation time, led to the decision to reduce the number of frequencies to 1968 in between 400 Hz and 10240 Hz. Taking into account higher frequencies would have violated Lipmann's conditions and would have taken us too much time. Consideration of only frequencies up to 5000 Hz led to an incident handclap that didn't sound right and led to an echo that did not at all correspond with reality. The reason of the latter effect is that a complicated handclap is much harder to deal with than the pulse of last section. Whereas a frequency chop for a pulse results in a new pulse that is quickly followed by a period of silence within the 2s time window of interest, a frequency chop for a

handclap results in unnegligible noise following the handclap, which is too strong if only frequencies up to 5000 Hz are considered. This noise, which is less important if frequencies up to 10240 Hz are taken into account, is also diffracted and due to time shifts may even overlap with neighboring time windows after diffraction. Therefore the numerical echo (as can be seen in Fig. X.B.1_10), corresponding with an incident numerical handclap with frequencies higher than 10240 Hz neglected, is, contrary to physical experiments, not limited in time.

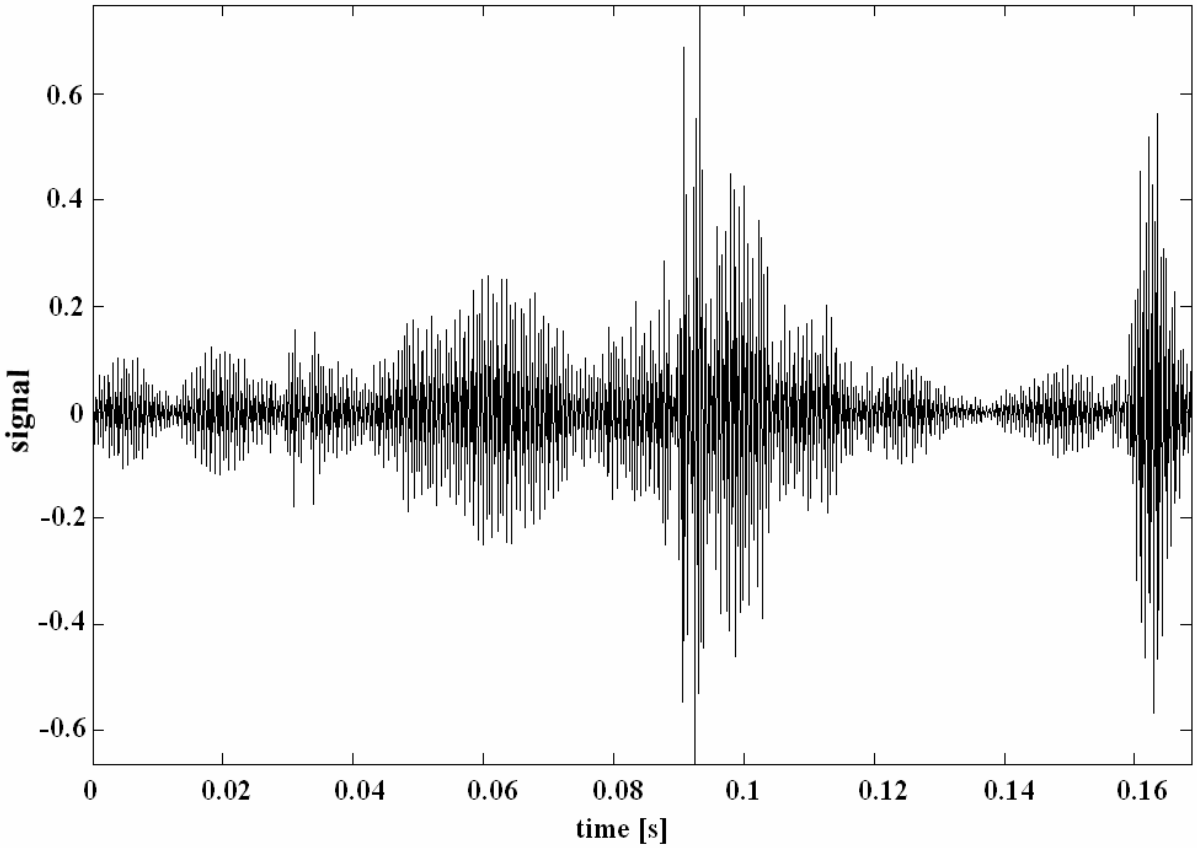

Fig X.B.1_10: ***calculated direct echo coming from a handclap***

In Fig. X.B.1_10, for reasons of calculation time limitations, we have, just as in the previous calculations, considered the results for all applied plane waves at all applied frequencies, but we have only taken into account 1024 positions of time within the interval of interest for reproducing the result. This means that a time limited Fourier transform cannot extract frequencies higher than the sampling frequency of 3034 Hz. However, if we take a look at the sonogram in Fig. X.B.1_11, which corresponds with the numerical signal in Fig. X.B.1_10 and is made just like all previous sonograms, we can see 4 frequency bands instead of only 2 in Fig X.B.1_6.
Even more important is that they coincide with the experimentally measured frequency bands of Fig. X.B.1_8. Therefore, even if, because of computer limitations, a true temporal description cannot be obtained, still what the frequencies are concerned the simulation reproduces the experimental result obtained by Lubman [13]. This proves that the lower two frequency bands in the experiments are mainly caused by the nature of the handclap and not as much by the diffraction process itself. In other words the echo is a function of the kind of incident sound.

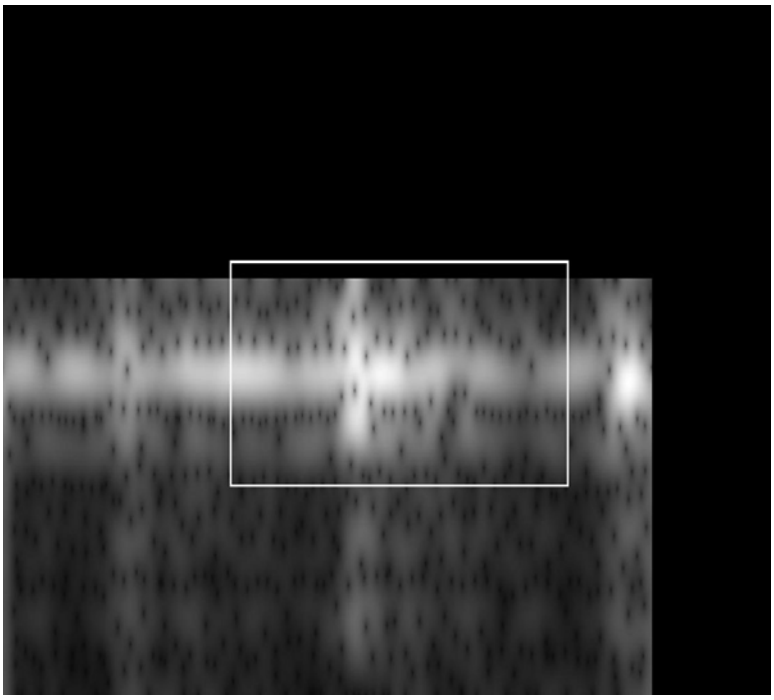

Fig X.B.1_11: ***spectrogram of the calculated direct echo coming from a handclap***

Direct and indirect echo coming from a handclap

In paragraph 3.1 we discussed the echo coming from a pulse and showed that the presence of 4 frequency bands in the reflected sound instead of 2 was probably due to the kind of incident sound. In paragraph 3.2 this statement was proved by simulating the echo coming from the handclap in the experiments [13]. Yet another important question that needs to be resolved is the influence of the ground in front of the stairs of the pyramid. Up until now we have neglected this effect. We now consider the extreme condition where the ground is a perfect reflector. Hence sound coming from the handclap is not only propagating straight to the pyramid, but is also reflected on the ground before propagating towards the pyramid. Furthermore sound reflected from the pyramid may be received after straight propagation from the stairs or may again be reflected by the ground before being received. Therefore the received signal *G* consists of 4 parts:
G_1: sound traveled directly to the pyramid and being received directly
G_2: sound traveled directly to the pyramid and being received after being reflected by the ground.
G_3: sound being reflected by the ground before having traveled to the pyramid and being received directly
G_4: sound being reflected by the ground before having traveled to the pyramid and being received after being reflected by the ground.
We call the person in front of the pyramid 'person' and his mirror image (see Fig. X.B.1_1) the 'mirror person'. The ground is replaced by a mathematical mirror plane. Mathematically G_1 is emitted by the person and again received by the person. G_2 is emitted by the person and received by the mirror person. G_3 is emitted by the mirror person and received by the person. G_4 is emitted

and received by the mirror person. By filling in the correct coordinates of the person $(\mathbf{d}+\mathbf{h})$ and the mirror person $(\mathbf{d}-\mathbf{h})$, simulation is again possible of each signal. Then

$$G = G_1 + G_2 + G_3 + G_4 \qquad \text{(X.B.1\_12)}$$

The result of G can be seen in Figs X.B.1_12-13. Again these figures cannot really tell anything about the temporal distribution of the frequencies, nevertheless it is seen that the ground has no influence on the presence or absence of the 4 frequency bands. In the future it would be great if someone would do some experiments at the pyramid by placing a reflector or an absorber in front of the staircase in order to see what effect it has on the received echo.

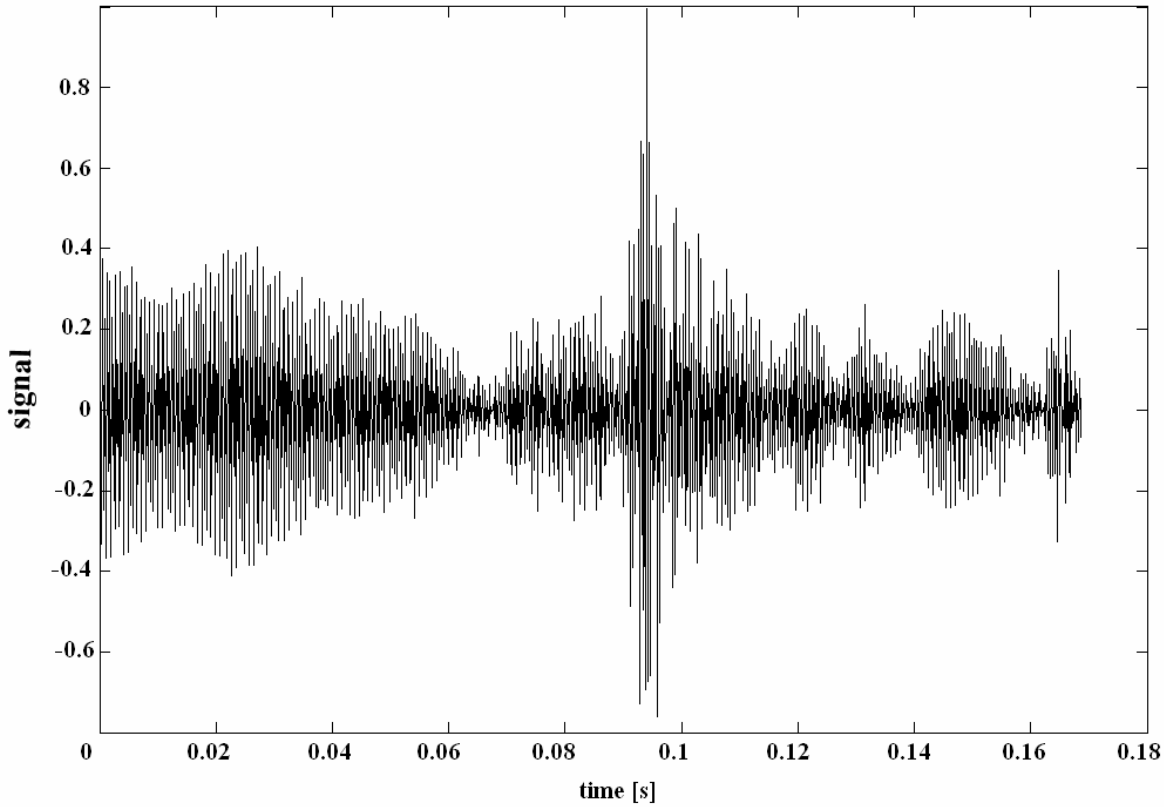

Fig X.B.1_12: ***calculated direct and indirect echo coming from a handclap***

EXPLANATION OF THE RAINDROP EFFECT

If people are climbing the pyramid, their shoes produce sound pulses containing all frequencies. Even though such pulses are more complicated, we model them here by means of a superposition of normally incident pure plane waves. Fig. X.B.1_14 shows the amplitude of the reflection coefficient of the zero order and the -1^{st} order as a function of the frequency.

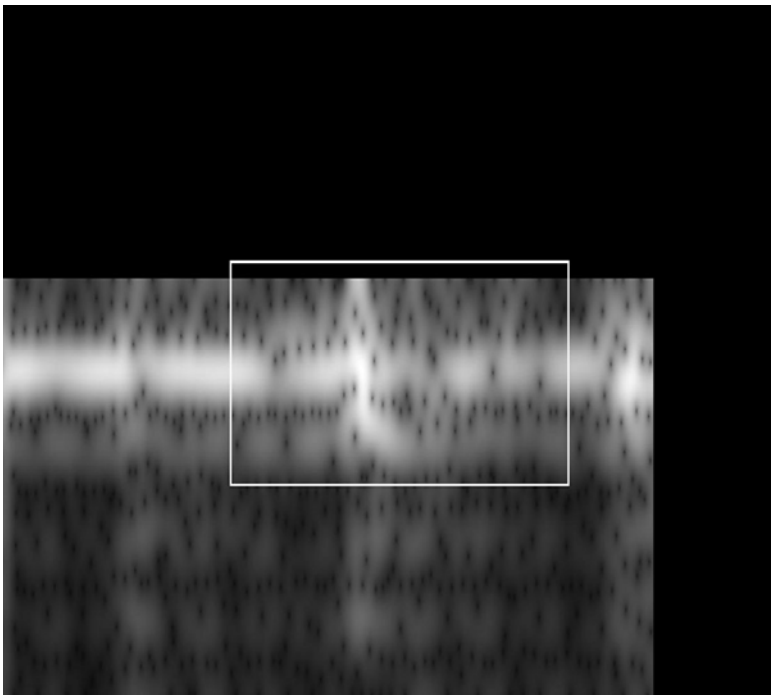

Fig X.B.1_13: ***spectrogram of the calculated direct and indirect echo coming from a handclap***

Since we are only interested in understanding the raindrop effect, we focus in Fig. X.B.1_15 on the frequency zone where the -1^{st} order reflected sound undergoes a transition from evanescent to bulk waves.

That happens at a frequency f given by

$$f = \frac{v}{\sqrt{2}q} = 919.57Hz \qquad \text{(X.B.1\_13)}$$

In addition it can be verified by what has been explained above that this transition zone fulfills the Lipmann conditions whence the validity of the numerical calculations cannot be cast doubt on.
On the right side of the transition frequency in Fig. X.B.1_15, the -1^{st} order reflected sound is as important, regarding its amplitude, as the zero order reflected sound. Furthermore, in Fig. X.B.1_16, the propagation direction (measured from the pyramid's surface) of the -1^{st} order reflected sound is depicted as a function of the frequency.

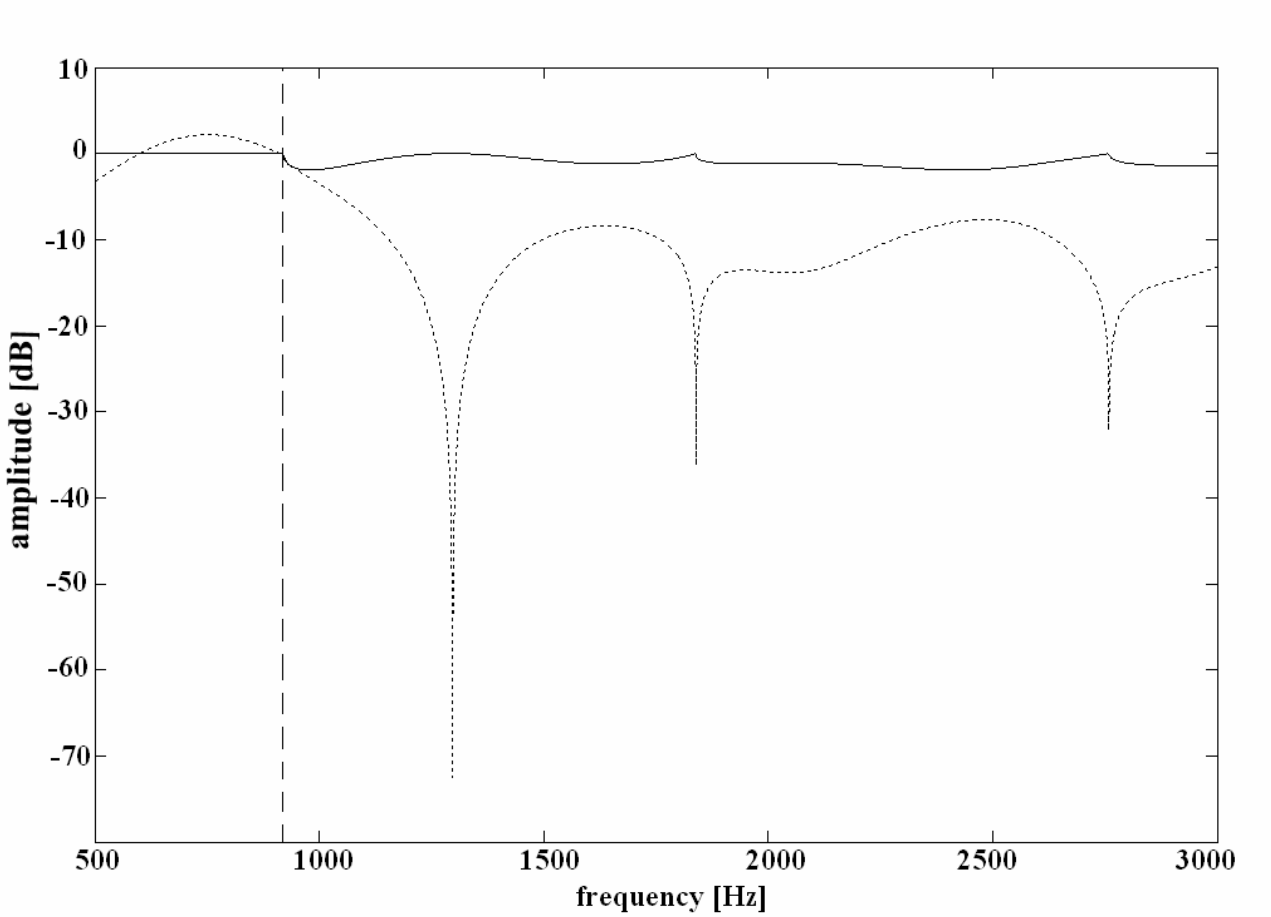

Fig. X.B.1_14: ***The zero order reflection coefficient (solid line) and the –1st order reflection coefficient (dotted line) as a function of the frequency, for normal incident sound on the pyramid. The left side of the dashed line corresponds to evanescent –1st order reflected waves, while the right side corresponds to bulk –1st order reflected waves.***

On the right of and close to the transition frequency, the –1st order diffracted sound travels almost parallel to the pyramid's surface. Now, since that sound is bulk in nature (not evanescent) and since it has a considerable amplitude (see Fig. X.B.1_15), it is actually hearable for the observer seated on the lowest stair step. The observed frequency range is limited since (see Fig. X.B.1_16) only a limited bunch of frequencies produce sound that can reach the observer's ear, which is situated at small angles from the pyramid's surface. Frequencies between 920Hz and 1000Hz indeed sound like the main frequency that is present in the bunch of frequencies generated by a raindrop falling in a bucket filled with water.

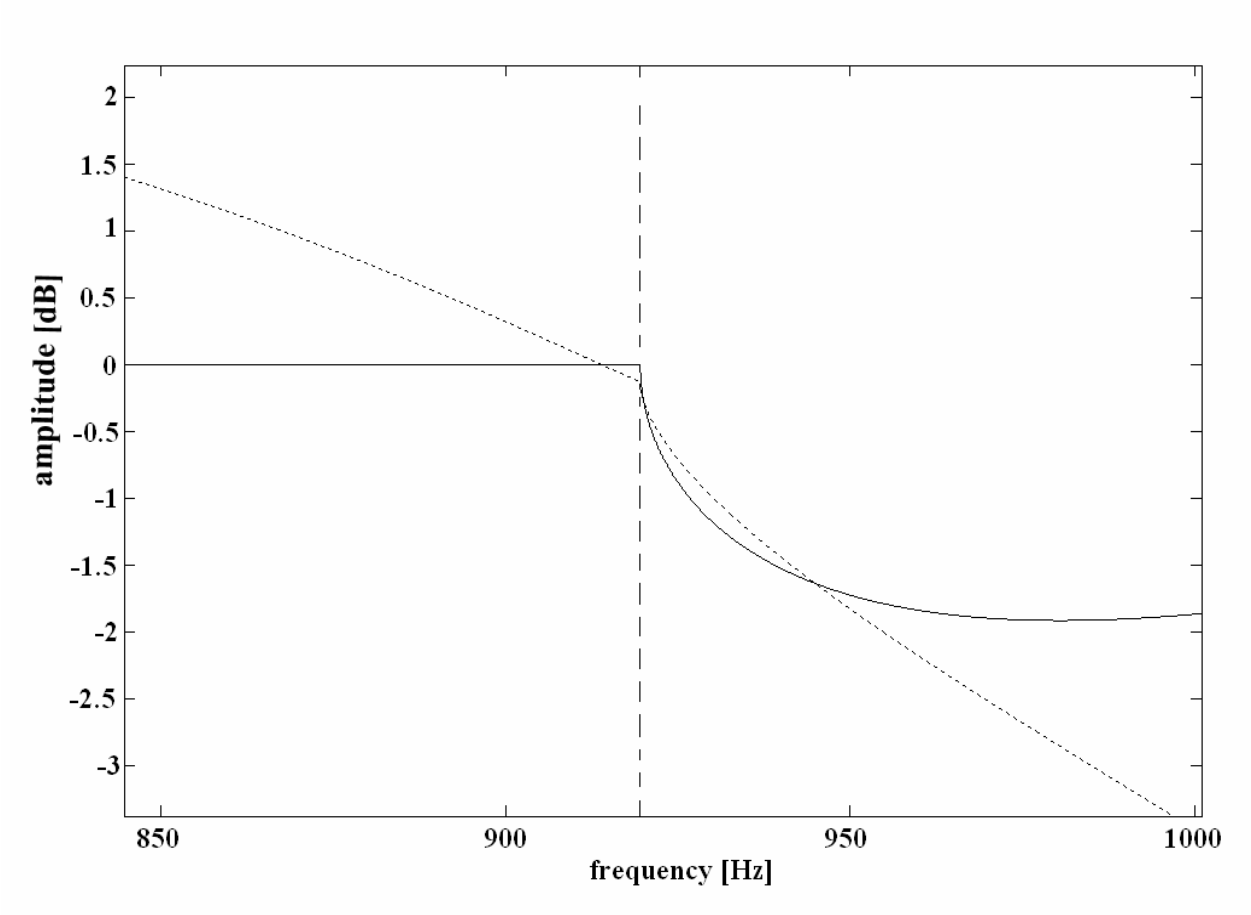

Fig. X.B.1_15: ***Close up of Fig. X.B.1_14.***

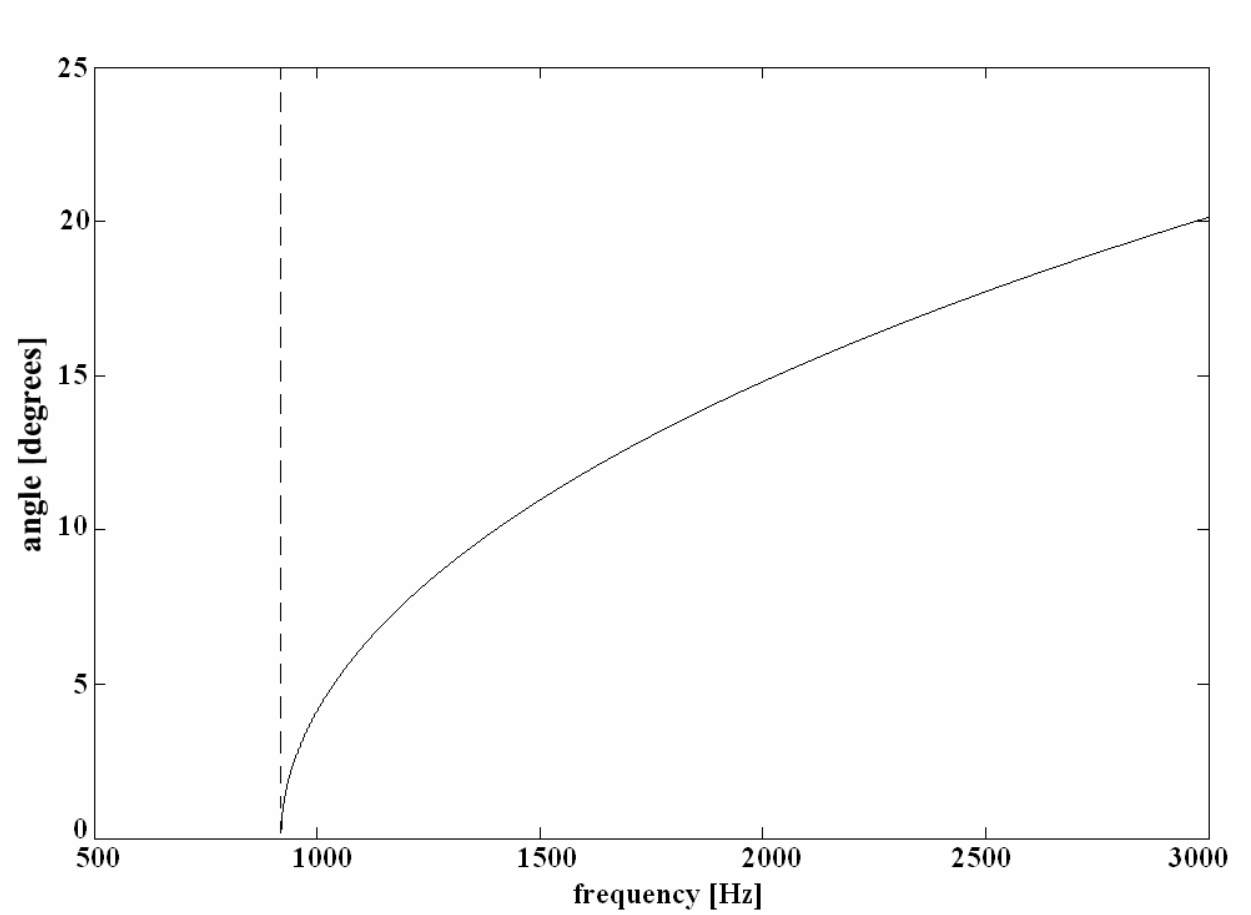

Fig. X.B.1_16. ***The propagation angle of the -1st order reflected sound as a function of the frequency, measured from the pyramid's surface.***

CONCLUDING REMARKS

It is shown that the echo that is produced by the pyramid consists of diffracted sound coming from the staircase. The echo is formed by a process which is connected with Bragg reflection, but more effects are as important as well, such as the continuity conditions on the stairs and the frequency pattern of the incident sound. Therefore some extended experiments in front of the pyramid, designed to measure the echo as a function of the incident sound, would be very enlightening. We would not be surprised if the use of drums or timber wood to produce sound pulses would result in a better echo. The model also showed that the ground in front of the pyramid has no influence on the reflected frequency bands. Nevertheless it could not be shown what the temporal effect is. It could elongate the echo or shorten it depending on the reflective properties of the ground. It would also be interesting to test the effect of the sound speed in air on the produced echo. This speed can vary in the dry season and wet season and can also vary with temperature. It is also explained how an observer seated on the lowest stair step may hear 'raindrops' falling in a water filled bucket when other people are climbing the upper stairs.

REFERENCES

[1] Wayne Van Kirk, “The accidental (acoustical) tourist”, J. Acoust. Soc. Am., 112(5), 2284, 2002

[2] David Lubman, “Acoustical features of two Mayan monuments a tChichen Itza: Accident or design”, J. Acoust. Soc. Am. 112(5), 2285, 2002

[3] David Lubman, “Singing Stairs”, Science news, 155, 44-45, 1999.

[4] David Lubman, “Mayan acoustics: Of rainbows and resplendent quetzals”, J. Acoust. Soc. Am., 106(4), 2228, 1999

[5] David Lubman, “Archaeological acoustic study of chirped echo from the Mayan pyramid at Chichén Itzá”, J. Acoust. Soc. Am., 104(3), 1763, 1998

[6] Bijal P. Trivedi, “Was Maya Pyramid Designed to Chirp Like a Bird?”, National Geographic Today, Dec. 6, 2002

[7] Fernando J. Elizondo-Garza, “Quetzal or not Quetzal, that is the question… on the stairs of the Castillo monument in Chichen Itza”, J. Acoust. Soc. Am., 112(5), 2285, 2002.

[8] Jorge Carrera, Sergio Beristain, “Theoretical interpretation of a case study: Acoustic resonance in an archeological site”, J. Acoust. Soc. Am. 112(5), 2285; paper 3aAA7 in proceedings of the first PanAmerican/Iberian meeting on acoustics, 2002.

[9] J.-M. Claeys, O. Leroy, “ Diffraction of plane waves by periodic surfaces”, Revue du Cethedec 72, 183-193 (1982)

[10] J. M. Claeys, Oswald Leroy, Alain Jungman, Laszlo Adler, “ Diffraction of ultrasonic waves from periodically rough liquid-solid surface”, J. Appl. Phys 54(10, 5657-5662 (1983)

[11] Nico F. Declercq, Joris Degrieck, Rudy Briers, Oswald Leroy, “A theoretical elucidation for the experimentally observed backward displacement of waves reflected from an interface having superimposed periodicity”, J. Acoust. Soc. Am. 112(5), 2414, 2002 ; paper 5aPA6 in Proceedings of the First PanAmerican/Iberian meeting on acoustics, 2002.

[12] Sergio Beristain, Cecilia Coss, Gabriela Aquino, Jose Negrete, “Tonal response on the stairway of the main pyramid at La Ciudela, Teotihuacan archeological site”, J. Acoust. Soc. Am., 112(5), 2285, 2002 ; paper 3aAA4 in Proceedings of the first PanAmerican/Iberian meeting on acoustics, 2002.

[13] David Lubman: http://www.ocasa.org/MayanPyramid.htm (site visited on 12/13/2002)

[14] Jacques R. Chamuel, Gary H. Brooke, “Transient Scholte wave transmission along rough liquid-solid interfaces”, J. Acoust. Soc. Am. 83(4), 1336-1344, 1988

[15] Leon Cohen, "Time-Frequency Analysis", Prentice Hall, 1995

Chapter XI Ultrasonic Polar Scans

In the aviation industry, the presence of ultrasonic testing techniques during maintenance, is indispensable. It is the high financial and human cost, when failing, that makes airplanes one of the outermost examined high-tech machines.

Nondestructive testing (NDT) of materials is costly. Therefore it is only used when it is cost-effective. This is the reason why NDT is widely applied at the beginning stages of the production process, in order to avoid very expensive product rejection at the end of the production process or even product withdrawals from the market afterwards. NDT techniques are also very popular during maintenance operations in situations where failure of a machine or a material is not allowed, such as in the aerospace industry, the nuclear and chemical industry, …

The application of sound for the purpose of NDT, is very popular. There are many reasons for this popularity. First of all, the technique is harmless to the operator, because there are no radio-active particles, or high energy particles involved. Secondly, sound investigates the mechanical properties of materials (not only the density, but also the stiffness) and penetrates into the bulk of the material under investigation. This makes it excellent for the investigation of materials that are exploited mechanically, like airplane wings, rotor blades, parts of mechanical constructions, …

Human beings and the evolution of the economy, commonly follow the path of lowest resistance. This is the reason why NDT techniques that are simple and easy to use, find their way into the modern world of technology much more quickly and massively. That's why classical C-scans and their necessary equipment, are most widespread in the world. C-scans are 'dummy' tools that enable the recording of echoes coming from the investigated material. They typically record delaminations inside layered structures, or the presence of voids and air bubbles.

This recording is very important, though the reason for the use of the word 'dummy', is that C-scans only employ a very small fraction of the extensive capabilities of sound in the investigation of materials.

The majority of the scientific literature about the interaction of sound with materials, is dealing with much more sophisticated phenomena and nondestructive techniques. Some of those –more complicated- techniques have found their way into 'the top of the top' in modern industry, such as the aviation industry, the military industry and the space travel industry.

Ultrasonic 'polar scans' are an example of less widespread techniques in modern industry that exploit a larger part of the capabilities of ultrasound to investigate materials. These scans form the topic of the current chapter. They will be extensively described further on.

At the end of the last century, Joris Degrieck has developed the machinery to perform ultrasonic polar scans and has shown, together with others, that the technique is excellent to 'show' the anisotropic stiffness of materials. That makes ultrasonic polar scans inviting for the investigation of fiber reinforced materials. Ultrasonic polar scans are also inviting for the investigation of other properties, such as the resin fraction, or the porosity,…

During the last two years, the ultrasonic polar scan apparatus has been modernized with the help of my colleague Geert Luyckx. The apparatus is now much more flexible, accurate and fast.

Nevertheless, the understanding of the formation of ultrasonic polar scans, and the simulations, have been limited to single-layered laminates of orthotropic symmetry. One of the purposes of my research the last years, was the development of models and computer programs to simulate and to understand the interaction of sound with multi-layered structures. My curiosity as a scientist elevated the expectations by extending the aims to materials of any kind of anisotropy. This would make the ultrasonic polar scan also applicable to investigate crystals and more complicated fiber reinforced composites. The results of this successful research are outlined in the current chapter.

This chapter consists of 4 sections. Section XI.A describes the principles of ultrasonic polar scans and what they are capable of.

Section XI. B explains how ultrasonic polar scans can be simulated. Simulations are shown for orthotropic materials, such as fiber reinforced composites, both for harmonic and for pulsed sound. In addition, it is shown that the simulations are also capable of handling more complicated structures of higher anisotropy, such as crystals. Unlike most composites, consisting of fibers that are distributed parallel to the plate surface and therefore make the normal to the surface an axis of symmetry of the material, crystals can be cut in any direction and therefore, ultrasonic polar scans must also be able to deal with any orientation. This capability is shown by means of some crystal examples, for single layers, for a multilayered system and for different orientations.

Fatigue damage is an interesting phenomenon in fiber reinforced composites. It is due to repeated deformation cycles. A famous example is the wing of an airplane. As a passenger, one can see the wingtips constantly moving upwards and downwards during the flight, especially when traversing clouds and at the moment of take off and landing. In metals, these deformations cause undetectable fatigue damage, leading to a certain, though unpredictable, failure at a specific instant in time, often followed by a crash or a serious moment of panic. Modern airplanes do not consist solely of metals, but also of fiber reinforced composites. In composites, fatigue damage consists of micro-cracks and results in a steady degradation that is detectable as a diminishing stiffness. In section XI.C, it will be shown numerically and experimentally that ultrasonic polar scans are capable of monitoring fatigue damage in composites.

In constructions, materials are almost always liable to applied and residual stress. The detection of stress inside a material is not an easy task, especially when, in a construction, the stress is slowly variable in time and depends on the position inside the construction. For that purpose, a study is presented in section XI.D that numerically shows to what extent ultrasonic polar scans are capable of detecting stress in laminates.

XI.A Ultrasonic Polar Scans as a possible means of nondestructive testing and characterization of composite plates

The ability of ultrasound to characterize fiber reinforced composites is well known [1-15]. Many techniques have been introduced of which 'time of flight' measurements are very famous [6-15]. The technique that is introduced here differs from 'time of flight' measurements in that it is based on amplitude measurements. A polar scan represents a fingerprint of the mechanical properties of a targeted spot on an investigated material. It is formed by registering the reflected or transmitted sound amplitude as a function of each possible angle of incidence. The present paper reports the ability of ultrasonic polar scans to determine the fiber orientation, the fiber volume fraction, the porosity and to monitor fatigue damage.
The contents of this section have been published as: Joris Degrieck, Nico F. Declercq, Oswald Leroy, "Ultrasonic Polar Scans as a possible means of nondestructive testing and characterization of composite plates", Insight - The Journal of The British Institute of Non-Destructive Testing, 45(3), 196-201, 2003. (Imp. Fact. 0.311; SCI-index, Materials Science – Characterization & Testing, rank:11/23)

INTRODUCTION

High quality fiber reinforced composite materials are often used because of their specifically tunable mechanical properties, embracing the principle of lowest possible mass for best suited stiffness. During manufacturing and service life, measurements of their local elastic properties are highly significant in order to examine deviations from the prescribed standards or due to degradation by damage. Since it is extremely time consuming and most often impossible to perform destructive measurements, the application of ultrasound to this end is probably most appropriate and its possibilities have been investigated for several years by various research groups [1-5]. The stiffness, strength and the specific mass of composites are highly influenced by the properties and the relative fractions of their constituents, by the processing parameters, by the physical structure of the composite (unidirectional, fabric,…) and by numerous kinds of defects and anomalies that may exist within these materials. Instant knowledge of the properties of composites is desirable during the development and designing of a new material or a new product, as the effect of using different constituents, different processing parameters or different volume fractions can be checked immediately without time consuming preparation of samples for destructive testing, as well as during the production process where deviations from a prescribed standard can be visualized immediately as to tune the production parameters without expensive time delay. Such knowledge is also inevitable in checking the degradation by damage and the remaining lifetime of composite products and constructions in service, and even in materials research [16-17] and the study of material mechanics in general, where information is necessary for the development and the verification of material models.

The usage of ultrasonic techniques in nondestructive testing and characterization of materials is widely accepted, the oldest of which is perhaps the classical C-scan to detect and

localize certain defects. Even though the classical C-scan has proved to be well suited for the task of detecting defects, an extension to more sophisticated means of measurements is needed especially if characterization of the stiffness is desirable. On fiber reinforced composite plates, the latter can only be performed if oblique incidence is considered as well.

Just like, for example, the well introduced time of flight measurements, a so called 'ultrasonic polar scan' is performed on a laminate, immersed in water and investigates anisotropic mechanical features of the laminate, exploiting its influence on obliquely incident sound. However, contrary to most established methods of ultrasonic nondestructive characterization methods for fiber reinforced composite plates, utilizing time of flight measurements [6-15], or even spectroscopy [5], the ultrasonic polar scan uses the amplitude of transmitted (or if necessary reflected) sound, which results from sound impinging the plate from every direction above the plate and is very easy to measure. Furthermore, a polar scan is able to measure sound amplitudes on a relatively small spot, whence it can present a local (though not a microscopic) fingerprint of the plate under investigation. The characteristic pattern of such a 'fingerprint' consists in fact of a set of rings, showing considerably less intensity than elsewhere on the registered polar scan. The rings are physically connected [18] to generated critical waves in the plate, such as leaky Rayleigh waves, leaky Lamb waves or even lateral waves [19-27]. Hence, they almost directly clarify the mechanical anisotropy and the stiffness of the investigated spot. The polar scan has already been shown to be a promising tool to determine the local fiber and resin fraction [29] and even the local porosity [28], whence anomalies in the production process can be revealed rapidly.

FEATURES AND CAPABILITIES OF THE POLAR SCAN

Ultrasonic polar scans have first been endeavored by van Dreumel and Speijer [1] who used them to determine the fiber orientation in composite laminates, and have been further developed by Degrieck et al. [2-4], who utilized them for additional applications such as the determination of the anisotropic (non-orthotropic) stiffness, fiber and resin fraction, porosity and fatigue damage.

Contrary to classical C-scans, in polar scans the transducer is not invariably directed perpendicular to the surface, scanning a whole area, but is constantly directed towards a particular targeted zone on the surface, occupying successively all possible incidence directions from the upper half space, and keeping a constant distance to the target, as shown in Fig. XI.A_1.

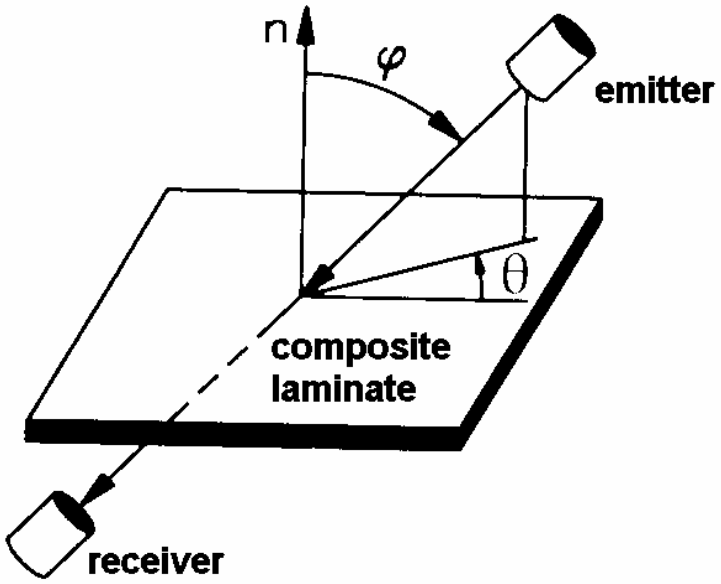

Fig. XI.A_1: ***In a polar scan, the target spot is impinged at constant distance form all possible angles*** (θ,φ)

A polar scan is the result of the complicated interaction of a pulsed directional bounded beam with a laminate possessing anisotropic elastic properties. When a bounded beam is incident on an orthotropic laminate, it is scattered [30] into longitudinal reflected sound and transmitted quasi-shear and quasi-longitudinal sound [31], which are in turn scattered and transmitted again successively until all energy is transformed into heat (because of damping [32-38] in the laminate), as depicted in Fig. XI.A_2.

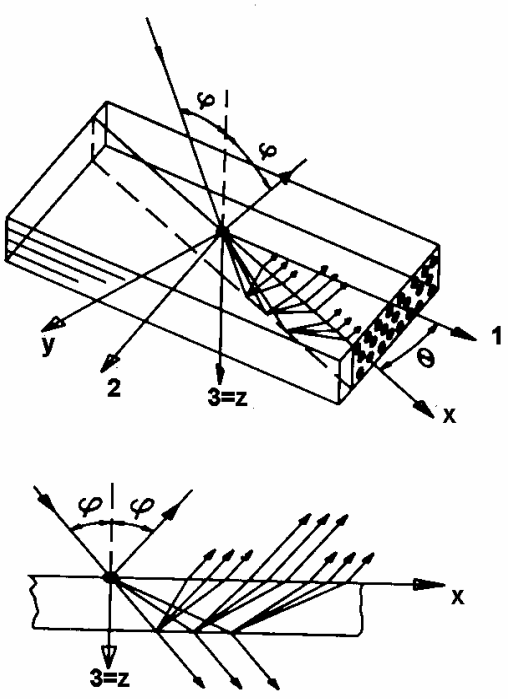

Fig. XI.A_2: ***Schematic of the interaction of one plane wave (i.e. one building block of a pulsed bounded beam) with a fiber reinforced plate (123: principle directions of orthotropy, XZ: plane of incidence), incident from an arbitrary angle*** (θ,φ)***. Upon incidence, one reflected longitudinal, 1 transmitted quasi longitudinal and 2 transmitted quasi shear waves are generated that by themselves interact again and again with the upper an lower boundaries of the plate until all energy is transformed into reflected and transmitted plane waves in the coupling liquid and heat (due to damping) in the solid.***

In Fig. XI.A_3, a polar scan is presented of a glass mat/epoxy composite. In this figure, each point corresponds to a direction (θ,φ) of incidence of the ultrasonic beam, with respect to the point of the material that is examined (cfr. Fig. XI.A_1). For clarity, the coordinate axes θ and φ have been depicted in Fig. XI.A_3. The grey level of each point is a measure of the amplitude of the transmitted ultrasonic beam for the corresponding angles of incidence. The value at $(\theta,\varphi)=(0,0)$ corresponds to the perpendicular position of the transducers and matches the value that would have been obtained in this point if a C-scan was performed.

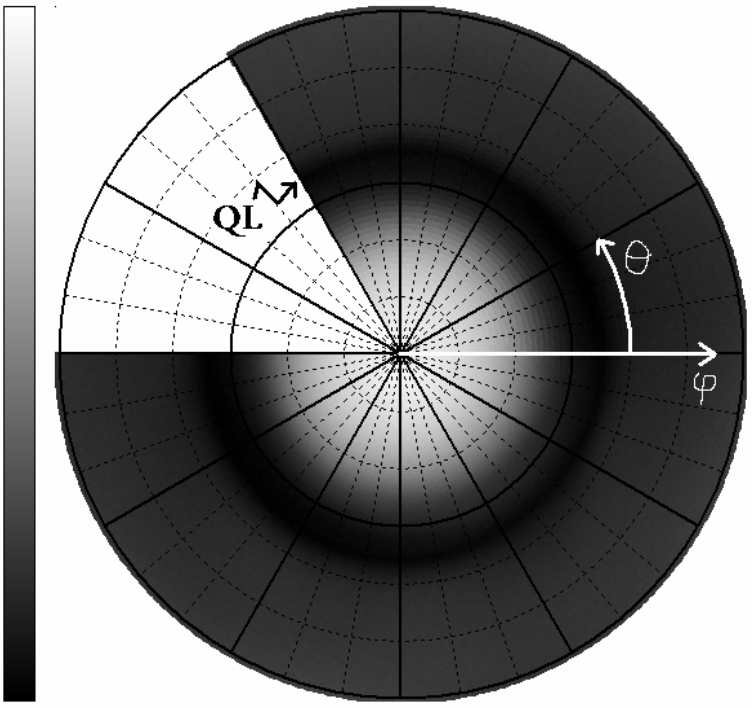

Fig. XI.A_3: ***Polar scan of a glass fabric/epoxy composite. A Polar Scan is obtained when the maximum amplitude of the transmitted ultrasonic beam is plotted in a polar diagram for all values of θ and φ. The scanning system prevents the transducer of moving around in full circles, which is the reason for the 'omitted' part in the Polar Scan. The appearance of perfect circles indicates isotropy. 'QL' means the ring that is caused by quasi longitudinal lateral waves.***

The experiments reported here are performed at a nominal frequency of 5MHz with a Krautkrämer H5M shock wave probe and a Krautkrämer USIP 20 ultrasonic apparatus, using a scanning system developed by WTCM (Research Center of the Belgian Metalworking Industries, Department of Pressure Equipment) and the authors' department of the Ghent University. For practicality, the receiver, intended to measure transmitted sound, is replaced by a metal reflector and one single ultrasonic transducer is used as emitter-receiver. Further, for reasons of mechanical simplicity, the transducer and reflector are mounted on the same fixture, which however prevents the transducer and reflector of moving along full circles $0<\theta<2\pi$ around the specimen and which explains why a part is 'omitted' in the reported polar scans.

It will be explained in the next section (XI.B) that the polar scans that are reported here, for a pulse, contain characteristic contours that are produced by 'lateral waves', i.e. sound traveling parallel to the interface having a bulk sound velocity. The use of harmonic waves

instead of a pulse, would have produced characteristic rings that result from the generation of plate waves (quasi Lamb waves).

Since there are three possible modes of lateral wave propagation inside a composite laminate [31], i.e. one quasi-longitudinal and two quasi-shear modes, three critical angles φ_{cr} can possibly exist for each angle θ, resulting in the expected appearance of three critical or characteristic contours of dropped intensity [18] in a polar scan. From Snell's law, we know that $\sin\varphi_{cr} = c_w/c$ in which c_w is the wave velocity of the coupling fluid and c is the velocity of the corresponding critical wave. The latter depends on θ, the specific mass of the composite laminate and of course its stiffness matrix C_{ij}. If, for a certain mode, the velocity is lower than the one in the coupling medium, no real φ_{cr} exists and hence the corresponding mode cannot be excited using impinging sound. The explanation of the different contours, i.e. due to quasi longitudinal lateral waves 'QL', due to quasi shear horizontal waves 'QSH' and due to quasi shear vertical waves 'QSV', is described in the sub-sections below and is schematically depicted in Fig. XI.A_4 for the isotropic case.

Determination of the fiber orientation

Because the stiffness of a fiber reinforced composite laminate depends on the direction with respect to the orientation of the fibers, it is possible to unveil this anisotropy by means of a polar scan. In the direction perpendicular to the fibers, the stiffness for longitudinal waves will be dominated by the resin, while along the direction of the fibers, the fibers will dominate the stiffness. The inner characteristic contour ('QL') of a polar scan corresponds to the generation of the quasi-longitudinal mode. The velocities of such waves, traveling along the in-plane axes of orthotropy of the material, are given by $\sqrt{C_{11}/\rho}$ and $\sqrt{C_{22}/\rho}$ respectively. Hence, recalling Snell's law, the directions θ corresponding to the lowest critical angle φ_{cr} correspond to angles of highest stiffness. For the case of a glass mat/epoxy composite, we recall Fig. XI.A_3, and we notice a perfect circle for 'QL', which unveils $C_{11} = C_{22}$ and hence shows in-plane isotropy, which is due to the random distribution of the fibers. This is not always the case for industrially produced SMC-laminates (G/P-SMC), as a consequence of the flow of the SMC material during the compression molding process. Examination using a polar scan indeed reveals unequal distribution of the fiber direction.

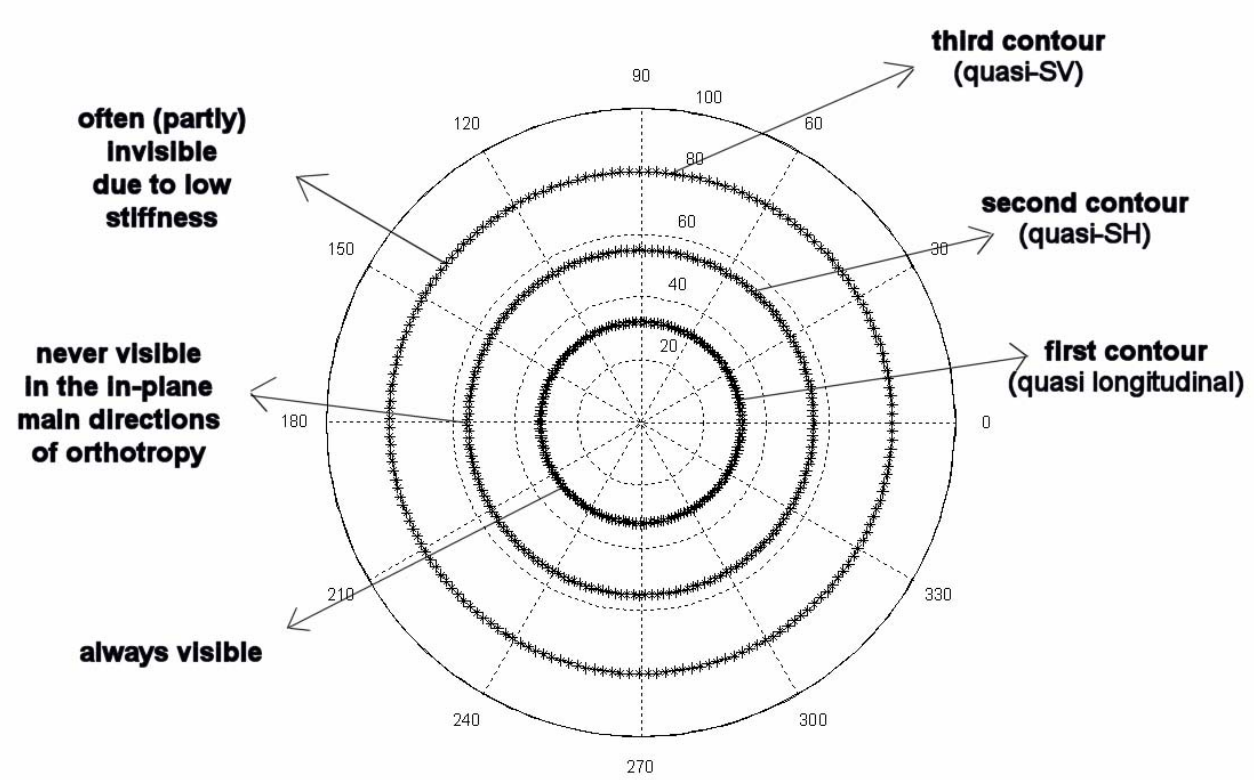

Fig. XI.A_4: ***Definition of the different contours that are possible in a polar scan. For simplicity, the exact shape of the contours has been chosen to be circular, which is most often not the case. Note that in practice, the third contour will coincide with the second contour in directions where shear vertical and horizontal stiffnesses are equal (e.g. in the fiber direction of unidirectional fiber reinforced composites).***

Fig. XI.A_5 presents a polar scan of unidirectional carbon fiber/epoxy composite. Here, anisotropy causes the inner ring ('QL') to be elliptical since the stiffness along the fibers differs much from the one perpendicular to them. The direction of the small axis of the inner ellipse ('QL') corresponds to the direction of highest stiffness, whence it is the fiber direction.

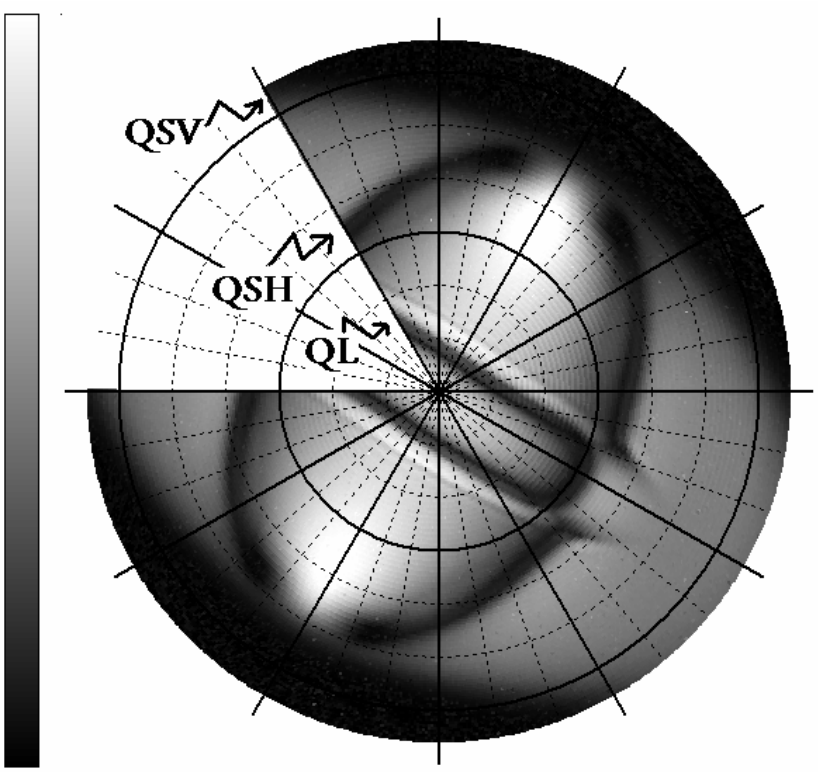

Fig. XI.A_5: ***Polar scan of a unidirectional carbon fiber/epoxy composite. The fibers lay along the smallest axis of the inner ellipse.***

The second contour ('QSH') is dominated by the in-plane shear properties of the material, because it is associated with the in-plane (or horizontally polarized) quasi-shear mode of wave propagation for which the particle displacement occurs parallel to the plane of the plate in the in-plane directions of orthotropy. The latter is the reason why, in these directions, the second contour ('QSH') cannot be 'closed', because pure horizontally polarized shear waves cannot be generated by impinging longitudinal waves. The latter can only induce vertical particle displacements in the in-plane directions of orthotropy. In isotropic and in-plane isotropic materials (cfr. Fig. XI.A_3), each direction corresponds to pure horizontally polarized shear waves, whence its characteristic contour ('QSH') does not appear in the polar scan for these materials.

The third contour ('QSV') is dominated by the out-of-plane (or vertically polarized) quasi-shear moduli of the material. Due to the low values of the vertical shear stiffness, the corresponding critical angles are frequently not real and are not present in the polar scan and if it is present, it is often not 'closed'.

For angles exceeding the third critical angle, all energy is totally reflected and there is no transmitted beam

Fig. XI.A_6 presents the polar scan of a carbon fiber fabric/epoxy composite. Comparison with Fig. XI.A_5 reveals the two perpendicular fiber directions of the used plain weave fabric.
Figs. XI.A_3-6 indicate how the symmetry or orthotropy of a fiber reinforced composite (or even each material showing orthotropic elasticity) is exposed by a polar scan.

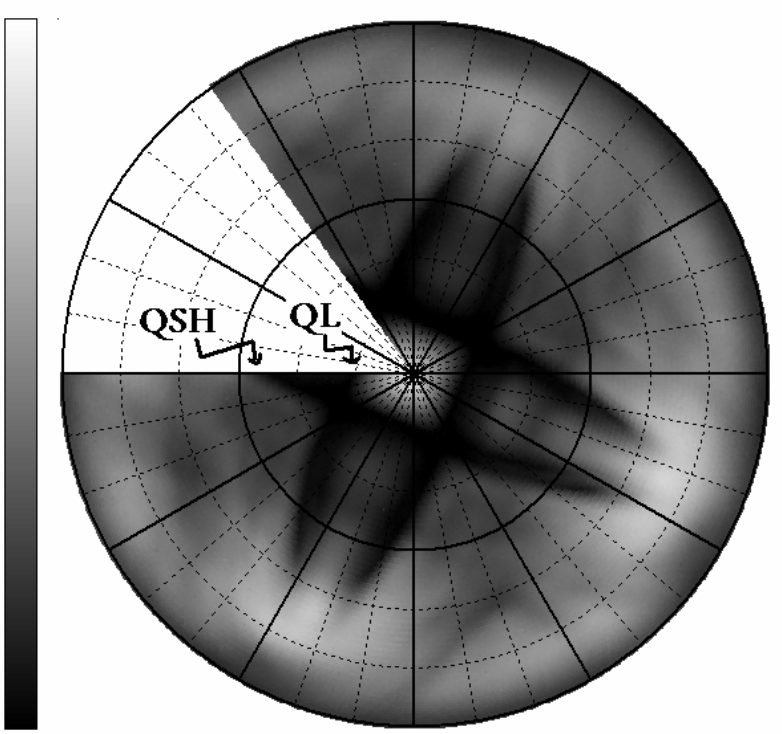

Fig. XI.A_6: ***Polar scan of carbon fiber fabric/epoxy. One notices additional fibers perpendicular to the ones of Fig. XI.A_4. The 'QL' contour is the 'square' in the middle, while the 'QSH' contour is the contour showing 4 branches.***

Determination of the fiber volume fraction

In Fig. XI.A_7, polar scans of a glass mat/ epoxy laminate are shown for different fiber volume fractions. Due to in-plane isotropy, (cfr. Fig. XI.A_3), one characteristic circle ('QL') is present. It is found that the amplitude of the scans decreases with increasing fiber volume fraction for low angles of incidence φ, which is due to elevated scattering of the beam on the fiber bundles. More important however is the outwards movement of the characteristic circle 'QL' with decreasing fiber volume fraction, which is due to a decrease of the ratio of in-plane stiffness to the specific mass.

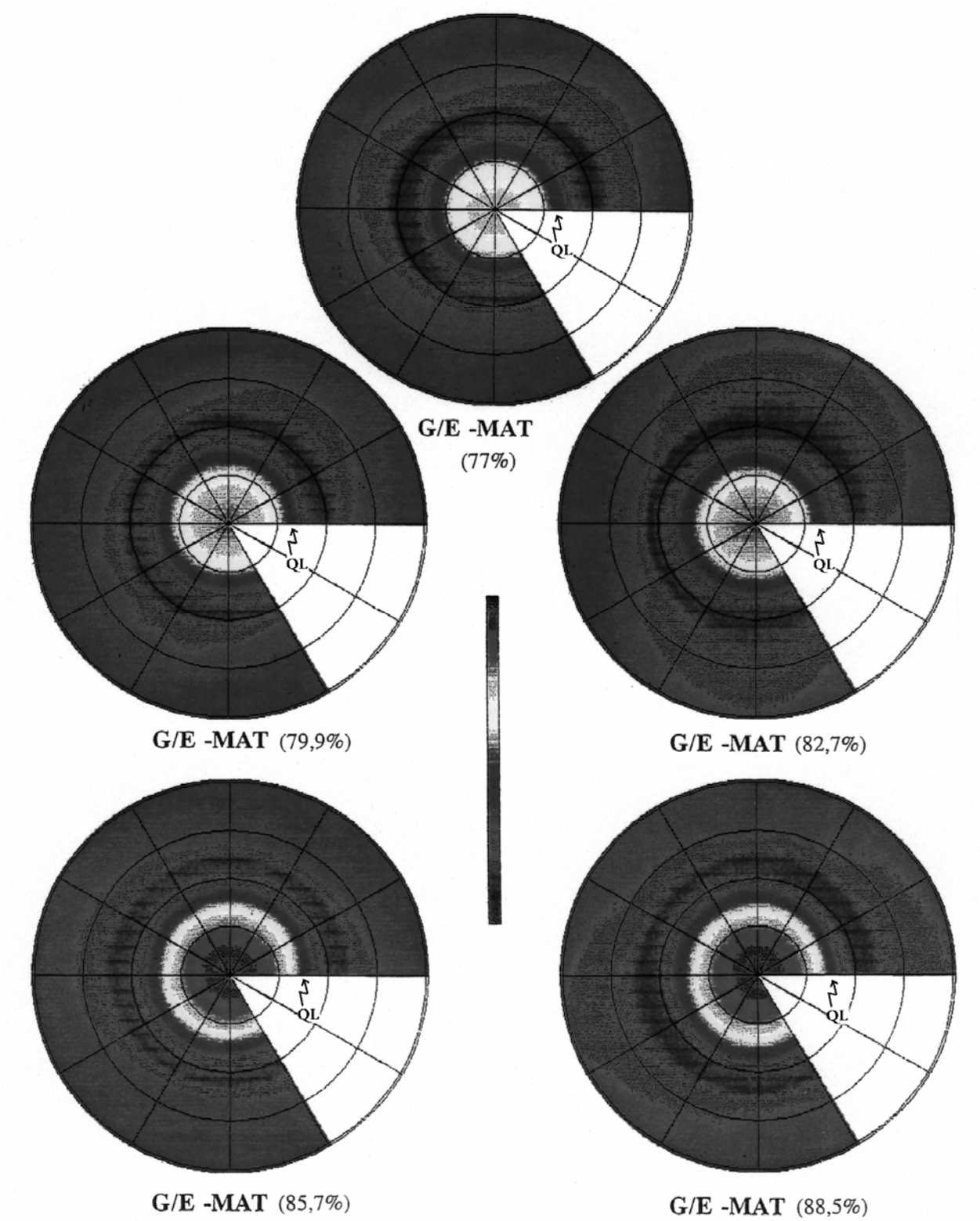

Fig. XI.A_7: ***Polar scans of chopped glass fiber mats in epoxy with resin volume fractions (in percent*****)**

Determination of the porosity

Fig. XI.A_8 presents polar scans of glass mat/epoxy composites containing different fractions of porosity. It is seen that there is a tendency in these polar scans which can be used in the future to determine non-destructively the fraction of porosity. Further research will have to unveil the exact theoretical correlation between porosity and the measured polar scan.

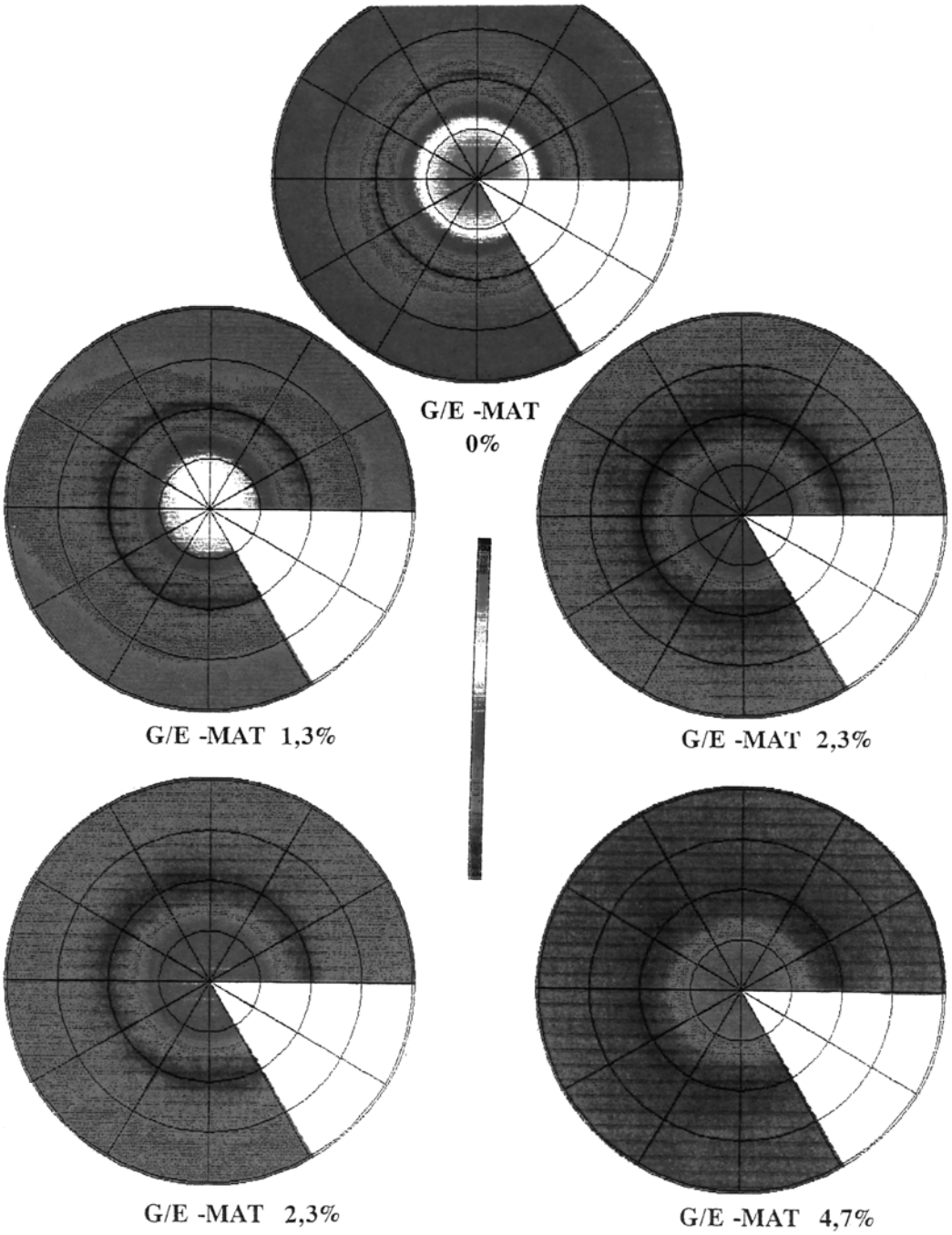

Fig. XI.A_8: ***Polar scans of chopped glass fiber mats in epoxy with different percentages of porosities.***

Determination of fatigue damage

In Fig. XI.A_9 respectively Fig. XI.A_10, a polar scan of a glass fabric/epoxy composite is presented before and after severe fatigue damage. The figures can be interpreted in terms of Snell's law. A higher stiffness involves higher velocities of lateral waves, which results in smaller critical angles. Hence, a larger ring of critical angles corresponds to slower lateral waves and to lower stiffness. The fatigue damage that is induced here is due to a repetitively applied force in one direction. The damage is limited to cracks in the matrix and does not involve fiber damage. Even though the force has been applied in only one direction, damage occurs in all directions. Due to this damage, the overall stiffness decreases whence the dark circle ('QL') of Fig. XI.A_9 tends to move outwards. Polar scans could therefore in the future ease fatigue monitoring in operating composite materials.

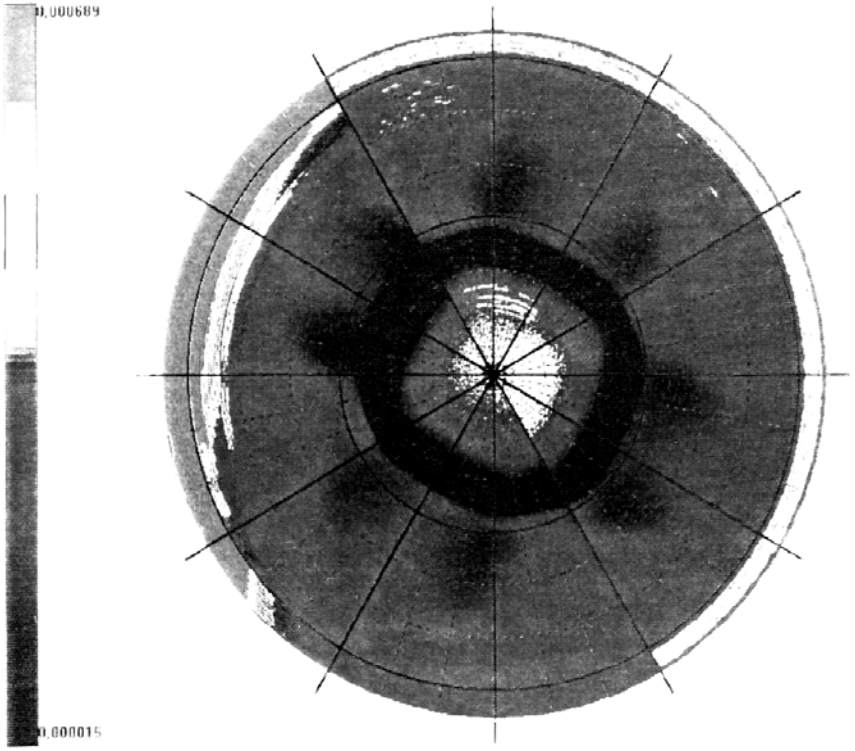

Fig. XI.A_9: ***Polar scan of glass fiber fabric /epoxy composite before fatigue damage.***

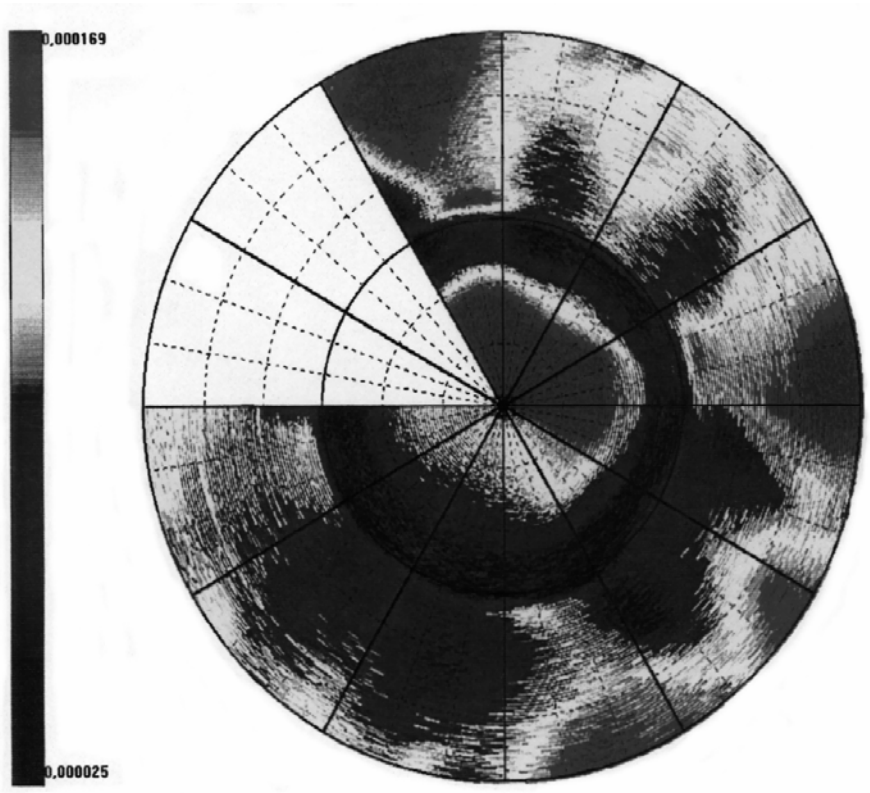

Fig. XI.A_10: ***Polar scan of glass fiber fabric /epoxy composite after fatigue damage. The dark circle of Fig. XI.A_9 is extended due to decreased stiffness as a consequence of the fatigue damage.***

CONCLUSIONS AND PROSPECTS

It is demonstrated that polar scans show promising abilities in the nondestructive characterization of fiber reinforced composite materials. Special attention is drawn to the determination of fiber orientation, fiber volume fraction, porosity and even monitoring of fatigue damage.

High performance simulations and inversion procedures with the goal to determine the elastic properties of composite materials are currently being developed as an improvement and as a sequel of earlier numerical methods that have been developed by Degrieck et al [2]. The polar scan apparatus is currently being modernized and further automated.

REFERENCES

[1] W. H. M. Van Dreumel, J. L. Speijer, "Nondestructive Composite Laminate Characterization by Means of Ultrasonic Polar Scan", Materials Evaluation, 39(10), 922-925, 1981

[2] J. Degrieck, D. Van Leeuwen, "Simulatie van een Ultrasone Polaire Scan van een Orthotrope Plaat", Proceedings of "The 3rd Belgian National Congres on Theoretical and Applied Mechanics", Liege University, 39-42, 1994 (in Dutch)

[3] J. Degrieck, "Some possibilities of nondestructive characterization of composite plates by means of ultrasonic polar scan", Non Destructive Testing, Van Hemelrijck & Anastassopoulos (eds), Balkema, Rotterdam, 225-236, 1996

[4] Nico F. Declercq, Joris Degrieck, Oswald Leroy, "Characterization of Layered Orthotropic Materials Using Ultrasonic Polar Scans", Proceedings of the 2nd FTW PhD symposium, Ghent University, 2001

[5] Anton I. Lavrentyev, Stanislav I. Rokhlin, "Determination of elastic moduli, density, attenuation, and thickness of a layer using ultrasonic spectroscopy at two angles", J. Acoust. Soc. Am. 102(6), 3467-3477, 1997
[6] Y. C. Chu, S. I. Rokhlin, "Comparative analysis of through-transmission ultrasonic bulk wave methods for phase velocity measurements in anisotropic materials", J. Acoust. Soc. Am. 95(6), 3204-3212, 1994
[7] David K. Hsu, Michael S; Hughes, "Simultaneous ultrasonic velocity and sample thickness measurement and application in composites", J. Acoust. Soc. Am. 92(2), 669-675 , 1992
[8] Y. Chu, S. I. Rokhlin, "A method for determination of elastic constants of a unidirectional lamina from ultrasonic bulk velocity measurements on [0/90] cross-ply composites", J. Acoust. Soc. Am. 96(1), 342-352, 1994
[9] S. I. Rokhlin, W. Huang, Y. C. Chu, "Ultrasonic scattering and velocity methods for characterization of fibre-matrix interphases", Ultrasonics 33(5), 351-364, 1995
[10] M. Deschamps, C. Bescond, "Numerical method to recover the elastic constants from ultrasonic group velocities", Ultrasonics 33(3), 205-211, 1995
[11] D. Degtyar, S. I. Rokhlin, "Comparison of elastic constant determination in anisotropic materials from ultrasonic group and phase velocity data", J. Acoust. Soc. Am. 102(6), 3458-3466, 1997
[12] Christophe Aristégui, Stéphane Baste, "optimal recovery of the elasticity tensor of general anisotropic materials from ultrasonic velocity data", J. Acoust. Soc. Am. 101(2), 813-833, 1997
[13] Christophe Aristégui, Stéphane Baste, "Optimal determination of the material symmetry axes and associated elasticity tensor from ultrasonic velocity data", J. Acoust. Soc. Am. 102(3), 1503-1521, 1997
[14] M. D. Enderby, A. R. Clarke, M. Patel, P. Ogden, A. A. Johnson, "An automated ultrasonic immersion technique for the determination of three-dimensional elastic constants of polymer composites", Ultrasonics 36, 245-249, 1998
[15] F. Reverdy, B. Audoin, "Elastic constants determination of anisotropic materials from phase velocities of acoustic waves generated and detected by lasers", J. Acoust. Soc. Am. 109(5), 1965-1972, 2001
[16] Y.C. Chu, S.I. Rokhlin, "Determination of macro- and micromechanical and interfacial elastic properties of composites from ultrasonic data", J. Acoust. Soc. Am. 92(2), 920-931, 1992
[17] W. Huang, S. I. Rokhlin, Y. J. Wang, "Effect of fibre-matrix interphase on wave propagation along, and scattering from, multilayered fibres in composites. Transfer matrix approach", Ultrasonics 33(5), 365-375, 1995
[18] D. E. Chimenti, S. I. Rokhlin, "Relationship between leaky Lamb modes and reflection coefficient zeroes for a fluid-coupled elastic layer", J. Acoust. Soc. Am. 88(3), 1603-1611, 1990
[19] V. T. Buchwald, "Rayleigh waves in anisotropic media", Quart. Journ. Mech. And Applied math., Vol XIV (4), 461-469, 1961
[20] V. T. Buchwald, A. Davis, "surface waves in Anisotropic Elastic Media", Nature 191, 899-900, 1961
[21] T. C. Lim, M. J. P. Musgrave, "Stoneley waves in anisotropic media", Nature 225, 372, 1970
[22] Adnan H. Nayfeh, D. E. Chimenti, "Propagation of guided waves in fluid-coupled plates of fiber-reinforced composite", J. Acoust. Soc. Am. 83(5), 1736-1743, 1988
[23] Vinay Dayal, Vikram K. Kinra, "Leaky lamb waves in an anisotropic plate. I: An exact solution and experiments", J. Acoust. Soc. Am. 85(6), 2268-2276, 1989
[24] D. E. Chimenti, R. W. Martin, "Nondestructive evaluation of composite laminates by leaky Lamb waves", Ultrasonics 29, 13-21, 1991
[25] T. C. T. Ting, D. M. Barnett, "Classifications of surface waves in anisotropic elastic materials", Wave Motion 26, 207-218, 1997
[26] M. Castaings, B. Hosten, "The use of electrostatic, ultrasonic, air-coupled transducers to generate and receive Lamb waves in anisotropic, viscoelastic plates", Ultrasonics 36, 361-365, 1998
[27] Eduardo Moreno, Pedro Acevedo, "Thickness measurement in composite materials using Lamb waves", Ultrasonics 35, 581-586, 1998
[28] H. Jeong, D. K. Hsu, "Experimental analysis of porosity-induced ultrasonic attenuation and velocity change in carbon composites", Ultrasonics 33(3), 195-203, 1995
[29] H. Jeong, "Multiple NDE Techniques for the Measurement of Constituent Volume Fractions in Metal matrix Composites", Res Nondestr Eval 9, 41-57 , Springer Verlag, 1997
[30] A. H. Nayfeh, D. E. Chimenti, "Ultrasonic Wave Reflection from liquid-coupled orthotropic plates with application to fibrous composites", J. Appl. Mechanics 55, 863-870, 1988
[31] L.P. Solie, B. A. Auld, "Elastic waves in free anisotropic plates", J. Acoust. Soc. Am. 54(1) , 50-65, 1973

[32] Marc Deschamps, Benard Hosten, "The effects of viscoelasticiy on the reflection and transmission of ultrasonic waves by an orthotropic plate", J. Acoust. Soc. Am. 91(4), 2007-2015, 1992
[33] Bernard Hosten, Michel Castaings, "Transfer matrix of multilayered absorbing and anisotropic media. Measurements and simulations of ultrasonic wave propagation through composite materials", J. Acoust. Soc. Am. 94(3), 1488-1495, 1993
[34] Martin L. Dunn, "Viscoelastic damping of particle and fiber reinforced composite materials", J. Acoust. Soc. Am. 98(6), 3360-3374, 1995
[35] Sandrine Baudouin, Bernard Hosten, "Immersion ultrasonic method to measure elastic constants and anisotropic attenuation in polymer-matrix and fiber-reinforced composite materials", Ultrasonics 34, 379-382, 1996
[36] B. Vandenbossche, R. D. Kriz, T. Oshima, "Stress-Wave displacement Polarizations and Attenuation in Unidirectional composites: theory and Experiment", Res. Nondestr. Eval. 8, 101-123, 1996
[37] Kendall R. Waters, Michael S. Hughes, Joel Mobley, Gary H. Brandenburger, James G. Miller, "On the applicability of Kramers-Krönig relations for ultrasonic attenuation obeying a frequency power law", J. Acoust. Soc. Am. 108(2), 556-563, 2000
[38] Eduardo Moreno, Pedro Acevedo, Martha Castillo, "Thickness measurement in composite materials using Lamb waves Viscoelastic effects", Ultrasonics 37, 595-599, 2000

XI.B Simulations of Harmonic and Pulsed Ultrasonic Polar Scans on Orthotropic Materials and More General Anisotropic Crystals.

Numerous experiments [1-5] have shown that ultrasonic polar scans are a promising tool for the non-destructive characterization of fiber reinforced composites. However, because of the requirement to invert experimental data for extracting quantitative information [5], numerical simulations are mandatory. Such simulations have been developed before for single layered fiber reinforced composites. Nevertheless, since the vast majority of composites are multi-layered, the development of extended numerical models is needed. Such model is presented, together with a presentation of numerical simulations of ultrasonic polar scans for multi-layered composites. It is also shown that the polar scan of a fabric reinforced composite is quite different from a polar scan of (0^0/90^0)-stacked unidirectional layers.

Furthermore, the difference between a polar scan for an incident harmonic wave and for an incident pulse is shown.

In addition, simulations of ultrasonic polar scans on crystals of any kind of anisotropy, of any orientation and of any number of layers, is possible. Some examples are shown as well.

Most of the contents of this section have been accepted for publication in NDT & E International (Imp. Fact. 0.752; SCI-index, Materials Science – Characterization & Testing, rank:3/23)

INTRODUCTION

The principle of lowest possible mass for best suited stiffness and strength is the driving force behind the tailoring of high quality composites and the manufacturing of composite structures. This objective can only be achieved if it comes together with characterization during manufacturing and service life. Because destructive measurements are expensive, time consuming and mostly impossible, the application of ultrasound to this end is appropriate and its possibilities have been investigated for several years by various research groups [6-18].

The strength, the stiffness, and the specific mass of composites are determined by the properties and the relative fractions of their constituents, by the physical structure of the composite (unidirectional, fabric,…), by the processing parameters, and by numerous sorts of defects and anomalies that can exist within these materials.

The use of ultrasonic techniques in nondestructive testing and the characterization of materials, is widely accepted, the oldest of which is perhaps the classical C-scan to detect and localize certain defects. Even though the classical C-scan has proved to be well suited for the task of detecting defects, an extension to more sophisticated means of measurements is necessary especially if characterization of the stiffness is requested. On fiber reinforced composite plates, this can only be performed if oblique incidence is considered as well.

An ‘ultrasonic polar scan’ is performed on a laminate immersed in water and investigates anisotropic mechanical features of the laminate exploiting its influence on obliquely incident sound. Nevertheless, contrary to most established methods of ultrasonic nondestructive characterization methods for fiber reinforced composite plates, utilizing time of flight measurements [9-16], or even spectroscopy [8], the ultrasonic polar scan uses the amplitude of transmitted (or if necessary reflected) sound, which results from sound impinging the plate from every direction above the plate and is relatively simple to measure.

Because a polar scan registers sound amplitudes on a small spot, it actually represents a local fingerprint of the plate under investigation. The characteristic pattern of such a ‘fingerprint’ consists in fact of a set of rings, showing considerably less intensity than elsewhere on the registered polar scan. The rings are physically connected [19] to generated critical waves in the plate, such as leaky Rayleigh waves, leaky Lamb waves or even lateral waves [20-32]. Hence, they almost directly clarify the mechanical anisotropy and the stiffness of the investigated spot.

It has been shown before [1-4, 33-34] that the ‘ultrasonic polar scan’ is a highly recommended and convenient to use technique for the characterization of the fiber direction, the orthotropic stiffness, and for the extraction of information about porosity, resin fraction, etcetera. Because fatigue damage induces stiffness reduction, it has been shown that polar scans are also excellent tools to monitor fatigue damage [35].

The present section (XI.B) focuses on the theoretical modeling of ultrasonic polar scans. The last part of the paper presents some numerical examples of ultrasonic polar scans, for incident harmonic waves as well as for an incident pulse. The numerical method outlined below, though not new by itself [39], but for the first time deployed for simulating ultrasonic polar scans, is based on the so called direct method and does not imply sophisticated matrix methods [36-37]. The technique is deterministic and is not built on the Floquet wave principle [38] for periodically layered systems.

THE EFFECT OF ORTHOTROPY ON ELASTICITY

In what follows, we apply the double suffix notation convention of Einstein. The dynamics of an anisotropic material is described [39] by

$$\frac{\partial \sigma_{ij}}{\partial r_j} = \rho \frac{\partial^2 u_i}{\partial t^2} \qquad \text{(XI.B\_1)}$$

while the generalized Hooke’s law, taking into account symmetry properties which are due to the analytical feature of the strain energy and the symmetric nature of the stress and strain tensors, is given by

$$\begin{bmatrix}\sigma_{11}\\ \sigma_{22}\\ \sigma_{33}\\ \sigma_{23}\\ \sigma_{13}\\ \sigma_{12}\end{bmatrix}=\begin{bmatrix}C_{11} & C_{12} & C_{13} & C_{14} & C_{15} & C_{16}\\ C_{12} & C_{22} & C_{23} & C_{24} & C_{25} & C_{26}\\ C_{13} & C_{23} & C_{33} & C_{34} & C_{35} & C_{36}\\ C_{14} & C_{24} & C_{34} & C_{44} & C_{45} & C_{46}\\ C_{15} & C_{25} & C_{35} & C_{45} & C_{55} & C_{56}\\ C_{16} & C_{26} & C_{36} & C_{46} & C_{56} & C_{66}\end{bmatrix}\begin{bmatrix}e_{11}\\ e_{22}\\ e_{33}\\ 2e_{23}\\ 2e_{13}\\ 2e_{12}\end{bmatrix} \qquad \text{(XI.B\_2)}$$

Further symmetry considerations [39] due to orthotropy result in

$$\begin{aligned}&C_{14}=C_{24}=C_{34}=C_{15}=C_{25}=C_{35}\\ &=C_{16}=C_{26}=C_{36}=C_{45}=C_{46}=C_{56}=0\end{aligned} \qquad \text{(XI.B\_3)}$$

In Engineering, orthotropic materials are often characterized by engineering constants, i.e. the Young's moduli E_{11}, E_{22} and E_{33}, the Poisson coefficients ν_{23}, ν_{13} and ν_{12}, and the shear moduli G_{23}, G_{13} and G_{12}.
Then

$$\begin{bmatrix}C_{11} & C_{12} & C_{13} & 0 & 0 & 0\\ C_{12} & C_{22} & C_{23} & 0 & 0 & 0\\ C_{13} & C_{23} & C_{33} & 0 & 0 & 0\\ 0 & 0 & 0 & C_{44} & 0 & 0\\ 0 & 0 & 0 & 0 & C_{55} & 0\\ 0 & 0 & 0 & 0 & 0 & C_{66}\end{bmatrix} \qquad \text{(XI.B\_4)}$$

$$=\begin{bmatrix}1/E_{11} & -\nu_{12}/E_{11} & -\nu_{13}/E_{11} & 0 & 0 & 0\\ -\nu_{21}/E_{22} & 1/E_{22} & -\nu_{23}/E_{22} & 0 & 0 & 0\\ -\nu_{31}/E_{33} & -\nu_{32}/E_{33} & 1/E_{33} & 0 & 0 & 0\\ 0 & 0 & 0 & 1/G_{23} & 0 & 0\\ 0 & 0 & 0 & 0 & 1/G_{31} & 0\\ 0 & 0 & 0 & 0 & 0 & 1/G_{12}\end{bmatrix}^{-1}$$

with

$$\nu_{32} = \nu_{23} \frac{E_{33}}{E_{22}} \tag{XI.B_5}$$

$$\nu_{31} = \nu_{13} \frac{E_{33}}{E_{11}} \tag{XI.B_6}$$

$$\nu_{21} = \nu_{12} \frac{E_{22}}{E_{11}} \tag{XI.B_7}$$

and

$$G_{ij} = G_{ji} \tag{XI.B_8}$$

THE PROPAGATION OF BULK PLANE WAVES

We represent the acoustic field inside and outside the composite as a superposition of all possible bulk modes given an incident bulk wave [40-41]. Therefore we are mainly interested in a resulting field and do not attempt to study sound rays and point sources in a composite [42-43]. The reverse Voigt procedure transforms the stiffness tensor C_{mn} of rank 2 to the stiffness tensor c_{ijkl} of rank 4 as $(1 \to 11)$, $(2 \to 22)$, $(3 \to 33)$, $(4 \to 23 = 32)$, $(5 \to 13 = 31)$ and $(6 \to 12 = 21)$. When necessary, the intrinsic stiffness constants $c_{ijkl} = c^{I}_{ijkl}$ can be transformed into stiffness constants $c_{ijkl} = c^{R}_{ijkl}$ in coordinates corresponding to a rotated (laboratory) system as follows:

$$c^{R}_{ijkl} = R_{im} R_{jn} R_{kp} R_{lq} c^{I}_{mnpq} \tag{XI.B_9}$$

where R_{ij} are the entries of the rotation matrix for a rotation from the intrinsic lattice coordinate system to the laboratory coordinate system.
Equation (XI.B_1) then becomes

$$\rho \frac{\partial^2 u_i}{\partial t^2} = c_{ijkl} \frac{\partial^2 u_l}{\partial x_j \partial x_k} \tag{XI.B_10}$$

A plane wave solution of (XI.B_10) is of the form

$$u_i = U_i \exp i\left(n_j r_j - \omega t \right) \tag{XI.B_11}$$

where **n** is the wave vector. If this is entered in (XI.B_10), straightforward calculations then result in

$$\left(\frac{1}{\rho}c_{ijkl}n_k n_j - \omega^2\delta_{il}\right)U_l = 0 \qquad \text{(XI.B\_12)}$$

The latter equation is called the Christoffel equation [39,44-47]. It relates the slowness n/ω and the polarization **U** to the propagation direction and is solved by demanding nontrivial solutions, followed by the determination of the corresponding eigenvectors.

THE SCATTERING OF PLANE WAVES

Snell's law

If sound inside the bulk of the composite laminate results from impinging plane waves (denoted by superscript 'inc'), Snell's law must be taken into account which, for interfaces perpendicular to n_3, states that

$$n_1 = n_1^{inc} \text{ and } n_2 = n_2^{inc} \qquad \text{(XI.B\_13)}$$

Then, requiring nontrivial solutions, (XI.B_12) leads to a sixth degree polynomial equation of the form

$$\beta^6 + B_5\beta^5 + A_4\beta^4 + B_3\beta^3 + A_2\beta^2 + B_1\beta + A_0 = 0 \qquad \text{(XI.B\_14)}$$

in which β represents n_3.
Furthermore, it can be shown [39] that the presence of symmetry higher than or equal to monoclinic symmetry (as is the case for orthotropy) results in

$$B_j = 0 \qquad \text{(XI.B\_15)}$$

whence 3 independent solutions

$$\beta_2 = -\beta_1 \quad \beta_4 = -\beta_3 \quad \beta_6 = -\beta_5 \qquad \text{(XI.B\_16)}$$

exist.

continuity of normal stress and displacement

For a plate immersed in water, two different continuity conditions are involved. The water/solid interface is determined by continuity of normal stress and normal displacement, hence along the interface,

$$u_3^{water} = u_3^{solid} \tag{XI.B_17}$$

and

$$\sigma_{i3}^{water} = \sigma_{i3}^{solid}, \quad i = 1,2,3 \tag{XI.B_18}$$

The solid/solid interface(s) are determined by the continuity of the displacement vector and continuity of normal stress, hence along the interface(s)

$$u_i^{solid} = u_i^{solid}, \quad i = 1,2,3 \tag{XI.B_19}$$

and

$$\sigma_{i3}^{solid} = \sigma_{i3}^{solid}, \quad i = 1,2,3 \tag{XI.B_20}$$

By taking into account the appropriate continuity conditions and by applying the discussion of the previous subsection, one is able to simulate a polar scan by building the continuity matrix and extract the amplitudes for the different bulk wave components in the composite and in the surrounding liquid. The procedure that we have developed, automatically builds the complete continuity matrix no matter how many layers are involved. Furthermore, we consider the composite plate as it is and do not use any simplification based on periodicity of the layers [38, 48].

THE PRINCIPLE OF A POLAR SCAN

A classical C-scan is formed by registering the reflected or transmitted signal in many spots on the laminate surface, by applying normal incidence. Most often, C-scans are used to detect material defects and eventually to find out the 3D locations of such defects. Lately, some attempts have been undertaken to unveil the fiber direction by means of C-scans. However, the reported methods can only be used if sufficient microscopic material defects exist on the fiber/matrix interface or if the fibers are not equally distributed within the matrix.

A polar scan differs from a classical C-scan in that the transducer is not constantly held perpendicular to the interface. On the contrary, a polar scan exploits oblique incidence and measures the reflected or transmitted specular sound resulting from sound that is subsequently incident from all possible directions from above the plate. As is seen in Fig. XI.B_1, the incidence direction is defined by (θ, φ).

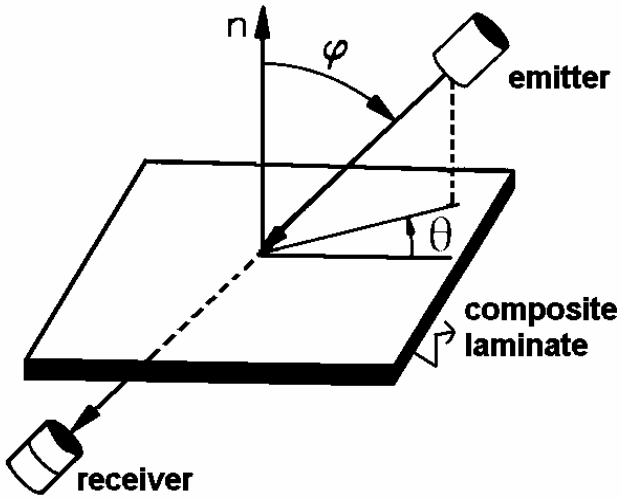

Fig. XI.B_1: ***The position of the transducers in a polar scan***

The reflected/transmitted amplitude is then registered in a polar diagram where each spot corresponds to a certain $(\theta + \pi, \varphi)$ and represents the amplitude for that direction. The radius in the registrations corresponds to φ, whereas the polar angle denotes θ. The grey scale is a measure for the received amplitude. Physically, the process of sound impinging the plate and traveling inside the plate, being scattered once and again by the different interfaces, is a very complicated phenomenon [42-43], cfr. Fig. XI.B_2.

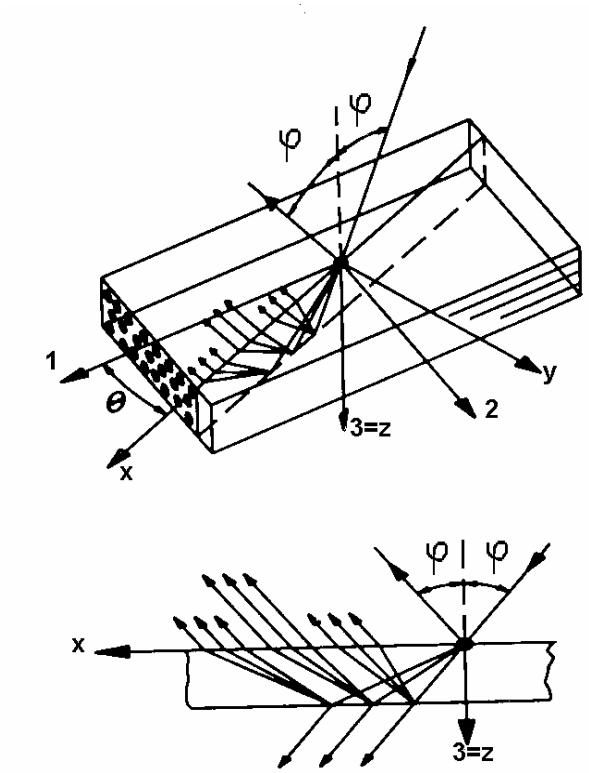

Fig. XI.B_2: ***The complicated interaction of an incident plane wave with a single layered composite plate. Each scattering generates 3 propagation modes in the plate and 1 in the liquid.***

However, for harmonic incident waves and for a pulse (we may always consider a pulse as a superposition of harmonic waves), a 'standing wave pattern (for the particle displacement as a function of the depth)' is formed inside the plate, which is modeled by demanding only 6 modes (the 6 coming from the Christoffel equation (XI.B_12)) propagating in each layer. This standing wave pattern may result in some kind of an eigen-vibration of the plate. If this occurs, this pattern is called a quasi Lamb wave. It is characterized by a reflection/transmission coefficient tending to zero. This results in 'dark regions' in the registered polar scan. The term 'quasi' is used in anisotropic materials and denotes the fact that these waves are a generalized form of Lamb waves that do exist in isotropic materials. Only along symmetry axes, the term 'quasi' could be replaced by 'pure'. A similar expression is later on used for 'quasi longitudinal' and 'quasi shear' waves. The quasi polarization only corresponds to a pure polarization as in isotropic materials, along axes of symmetry.

The position and the characteristics of these 'dark regions' are determined by the physical parameters of the plate, such as the thickness of the layers, the density, the stiffness coefficients and the damping. Ultrasonic polar scans form therefore an excellent tool for monitoring these physical properties. The interpretation of a polar scan is a difficult task. However, in the case of thick plates, the only patterns that do appear are due to bulk critical angles. For reasons of explanatory simplicity we solely focus on this case. Snell's law for critical waves is as follows

$$\sin\left(\varphi_{crit}\right)|_{\theta} = v_l / v_{crit}\left(\rho, C_{ij}, \theta\right) \tag{XI.B_21}$$

where v_l is the plane wave velocity in the liquid and v_{crit} is the velocity of the critical bulk wave. If a certain contour in one direction is wider than in other directions, this means that the velocity in the 'wider' direction is lower than in the other direction. For example the velocities of quasi longitudinal waves (corresponding to the inner contour of a polar scan) traveling along the in-plane axes of orthotropy are given by $\sqrt{C_{11}/\rho}$ and $\sqrt{C_{22}/\rho}$ respectively.
Hence, regarding equation (XI.B_21), the directions of highest stiffness produce the smallest critical angles for quasi longitudinal waves. Even though the contours of polar scans for thin plates are much more difficult to interpret, the basic idea remains unchanged. Furthermore, whenever a pulse is used instead of a harmonic wave, the remaining patterns of a polar scan correspond quite well to patterns that are caused by bulk lateral waves. That is because the dispersive nature of Lamb waves, i.e. a frequency dependent velocity, results in phase canceling for a pulse (because each plane wave component within the pulse, results in a largely different complex reflection coefficient), whereas bulk waves are not dispersive and their effects are not canceled out.

NUMERICAL EXAMPLES FOR HARMONIC WAVES

Hereafter, each polar scan is simulated for a 1mm thick fiber reinforced plate and an ultrasonic sound frequency of 5MHz. For multilayered systems, we consider layers of equal thickness. Furthermore the calculations are performed using realistic values for the materials properties. This involves the presence of damping and is determined by means of complex valued stiffness elements [49-55].

single-layered unidirectional carbon/epoxy fiber reinforced composites

The physical parameters of the carbon epoxy composite that are exploited here, can be found in Table XI.B_I. Fig. XI.B_3 presents the numerical simulation of an ultrasonic polar scan (in reflection) for a single layered unidirectional carbon/epoxy fiber reinforced composite.

Table XI.B_I: ***properties of one layer of***
- Carbon/Epoxy unidirectional fiber reinforced composites (Type A)
- Glass/Epoxy fabric fiber reinforced composites (Type B)
- FR4 (Type C)

parameter	Type A	Type B	Type C
$\rho \ \left[kg/m^3\right]$	1525	1750	1925
$E_{11} \ [MPa]$	$119130\times(1\text{-}0.0025\text{i})$	$20845\times(1\text{-}0.01\text{i})$	$20030(1-0.15i)$
$E_{22} \ [MPa]$	$8850\times(1\text{-}0.03\text{i})$	$20845\times(1\text{-}0.01\text{i})$	$22630(1-0.15i)$
$E_{33} \ [MPa]$	$10000\times(1\text{-}0.03\text{i})$	$8628\times(1\text{-}0.03\text{i})$	$8628(1-0.005i)$
ν_{23}	$0.475\times(1\text{-}0.015\text{i})$	$0.414\times(1\text{-}0.015\text{i})$	$0.5(1-0.005i)$
ν_{13}	$0.275\times(1\text{-}0.01\text{i})$	$0.414\times(1\text{-}0.01\text{i})$	$0.5(1-0.005i)$
ν_{12}	$0.306\times(1\text{-}0.01\text{i})$	$0.125\times(1\text{-}0.01\text{i})$	$0.1793(1-0.08i)$
$G_{23} \ [MPa]$	$3000\times(1\text{-}0.05\text{i})$	$2930\times(1\text{-}0.05\text{i})$	$3930(1-0.04i)$
$G_{13} \ [MPa]$	$5000\times(1\text{-}0.02\text{i})$	$2930\times(1\text{-}0.02\text{i})$	$3930(1-0.04i)$
$G_{12} \ [MPa]$	$5500\times(1\text{-}0.03\text{i})$	$3110\times(1\text{-}0.03\text{i})$	$4781(1-0.15i)$

The fibers are oriented along the 0^0 polar direction. In that direction, it is indeed verified that the inner contour (which corresponds to the quasi longitudinal plane wave critical angle) is smallest, which is caused by the elevated stiffness along the fiber direction. The other contours are a result of generated quasi-Lamb waves and a result of generated lateral quasi-shear waves. Fig. XI.B_4 is equivalent to Fig. XI.B_3, except that here the ultrasonic polar scan in transmission is plotted. Due to damping, the overall amplitude is smaller, but characteristic contours are still visible.

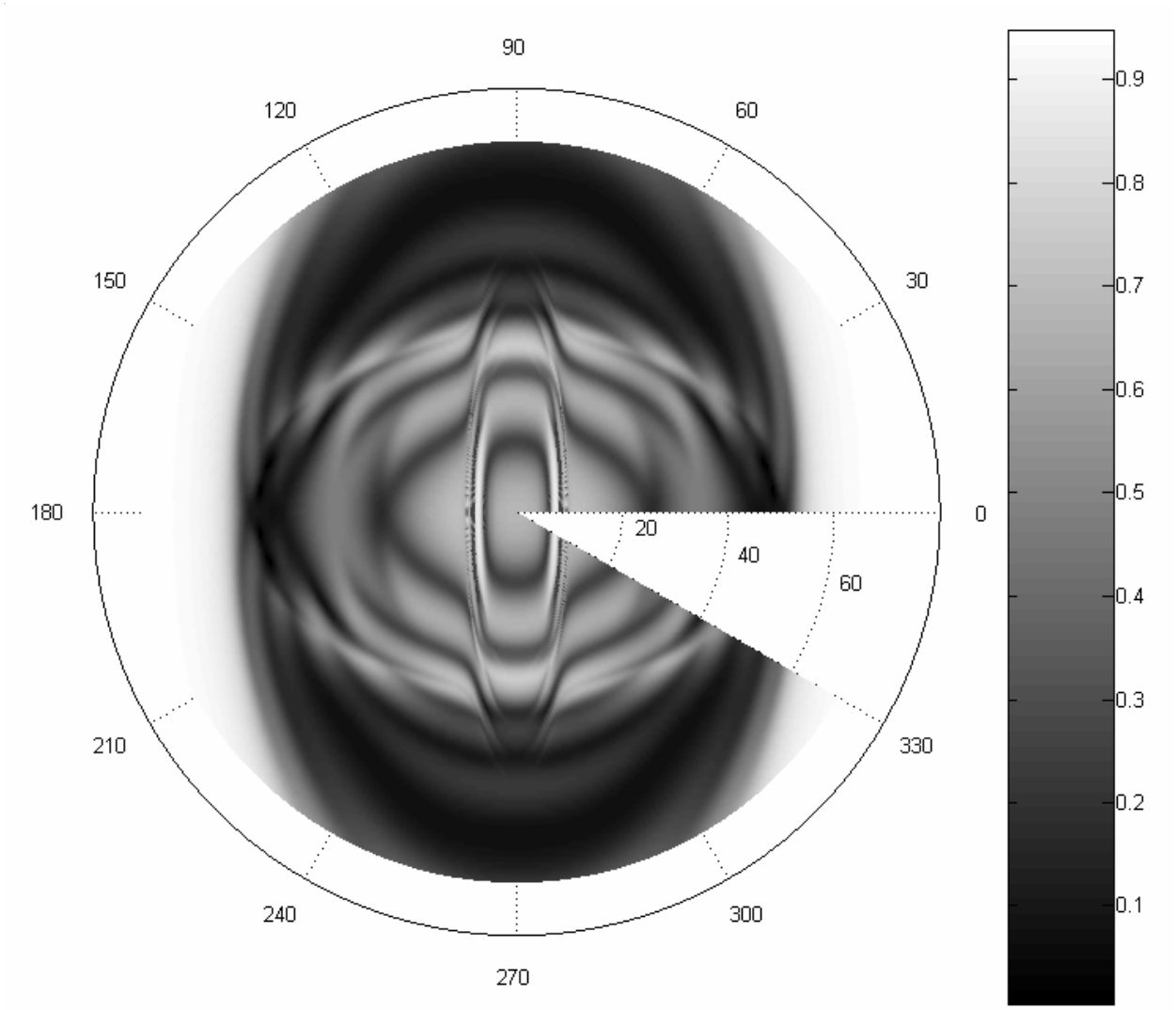

Fig. XI.B_3: ***Ultrasonic Polar Scan (harmonic, in reflection) of a single layered unidirectional fiber reinforced composite.***

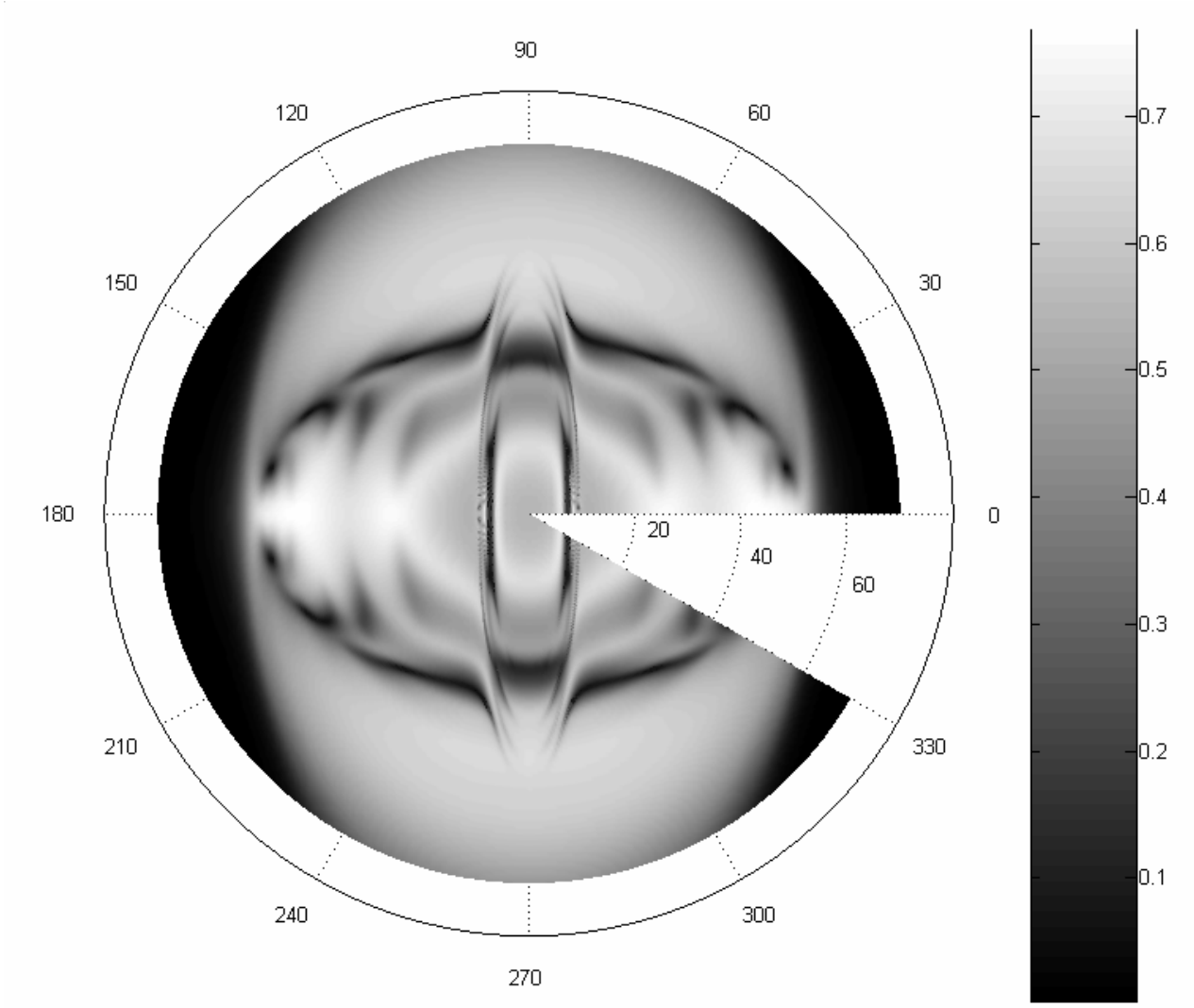

Fig. XI.B_4: ***Ultrasonic Polar Scan (harmonic, in transmission) of a single layered unidirectional fiber reinforced composite.***

double layered cross-ply carbon/epoxy laminate ($0^0/90^0$)

Each layer is characterized by physical parameters listed in Table XI.B_I (type A). Figs. XI.B_5 and XI.B_6 represent the numerical simulations of ultrasonic polar scans on a double layered carbon/epoxy fiber reinforced composite with the top layer consisting of fibers in the 0^0 direction and the bottom layer built up by fibers in the 90^0 direction. The presence of both symmetries (one on top of the other), is clearly visible in the characteristic contours if compared to Figs. XI.B_3 and XI.B_4. Moreover, it is seen that the reflected pattern in the 0^0 polar direction is not equivalent to the pattern in the 90^0 polar direction.

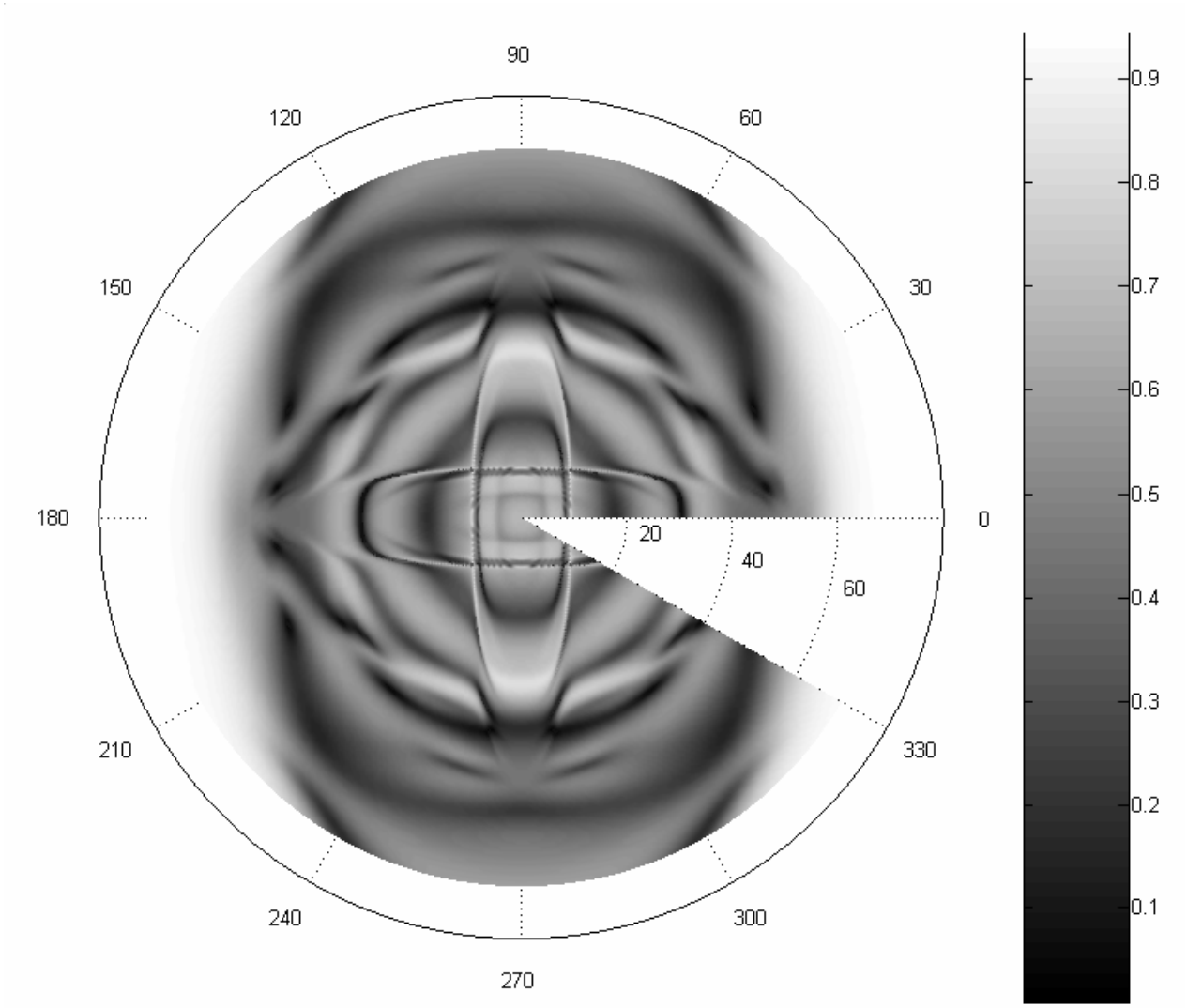

Fig. XI.B_5: ***Ultrasonic Polar Scan (harmonic, in reflection) of a double layered ($0^0/90^0$) cross-ply laminate.***

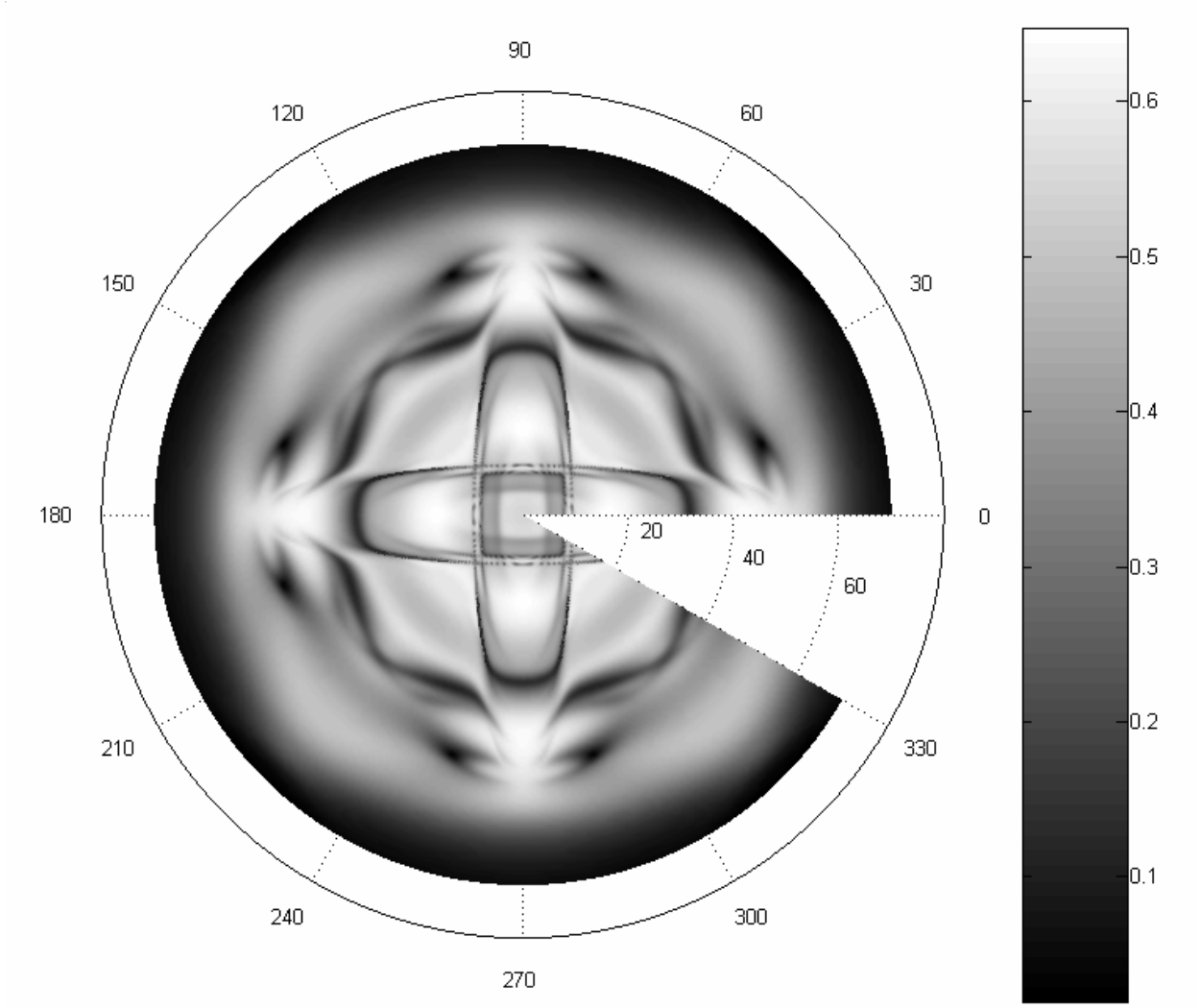

Fig. XI.B_6: ***Ultrasonic Polar Scan (harmonic, in transmission) of a double layered ($0^0/90^0$) cross-ply laminate.***

single layered fabric glass/epoxy reinforced composites

The physical properties of this composite are listed in Table XI.B_I (type B). Figs. XI.B_7 and XI.B_8 are the simulations of ultrasonic polar scans on a fabric glass/epoxy reinforced composite. Even though the laminate also consists of fibers in epoxy resin, the actual stiffness is different from the cross-ply composite described above. Hence only qualitative comparison is allowed. It is seen that the pattern in the 0^0 polar direction matches perfectly the pattern in the 90^0 polar direction. It is clear that the patterns qualitatively differ strongly form those of Figs. XI.B_5 and XI.B_6. Hence, a single layered fabric fiber reinforced composite is quite different from a ($0^0/90^0$) double layered fiber reinforced composite.

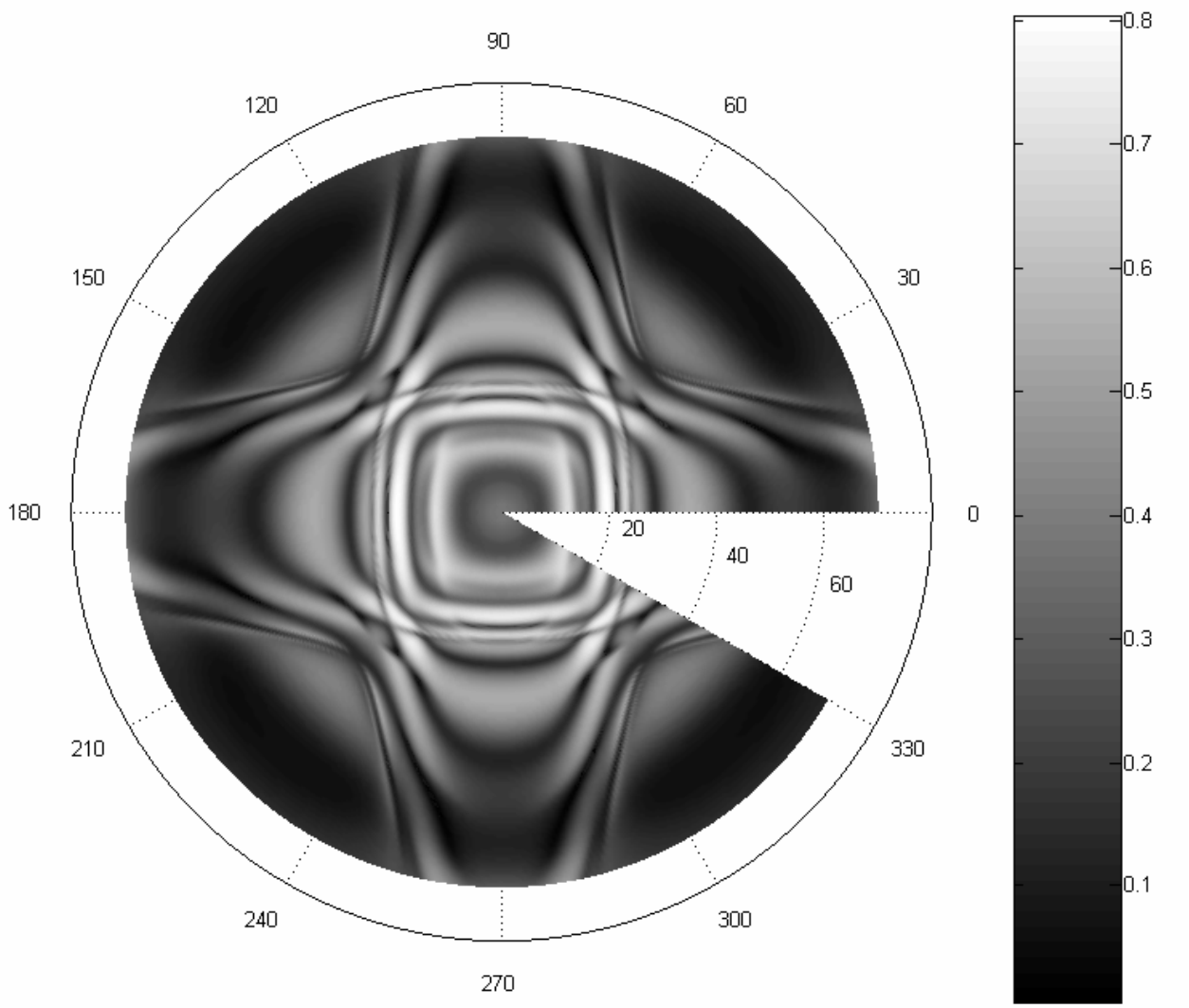

Fig. XI.B_7: ***Ultrasonic Polar Scan (harmonic, in reflection) of a single layered fabric reinforced composite.***

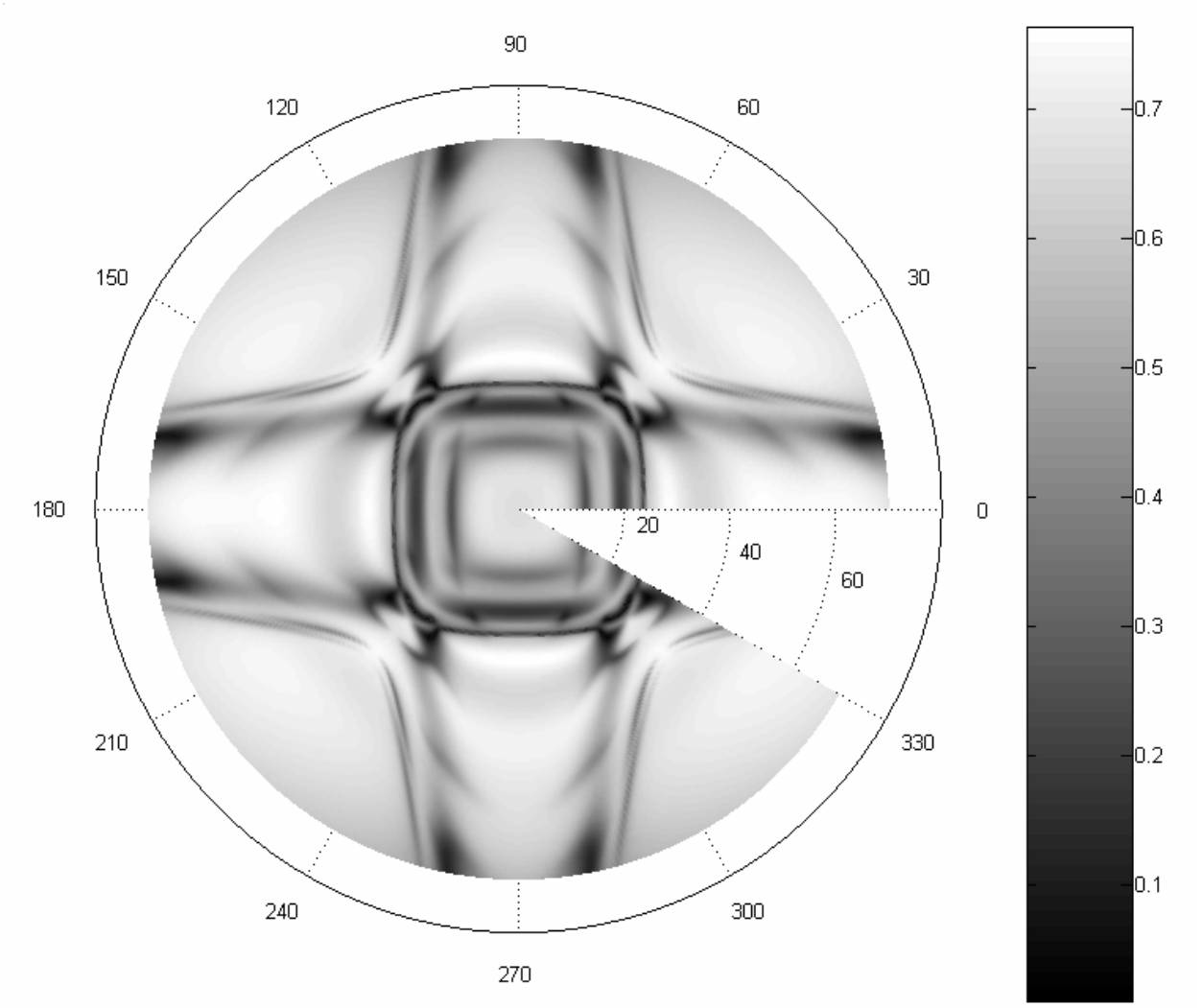

Fig. XI.B_8: ***Ultrasonic Polar Scan (harmonic, in transmission) of a single layered fabric reinforced composite.***

multi-layered cross-ply carbon/epoxy laminate ($0^0/90^0$)

Each layer is characterized by physical parameters listed in Table XI.B_I (type A). In order to check the relevancy of the above statement that a fabric fiber reinforced composite is different from a ($0^0/90^0$) stacked composite, we have decided to increase the number of layers to 10. The numerical result is seen in Figs. XI.B_9 and XI.B_10. Even though the number of layers is much larger, still there is a difference between the polar scans of Figs. XI.B_9 and XI.B_10 and the ones of Figs. XI.B_7 and XI.B_8. Even here, with a significantly increased number of stacked layers, the reflected pattern in the 0^0 polar direction still differs significantly from the pattern in the 90^0 polar direction.

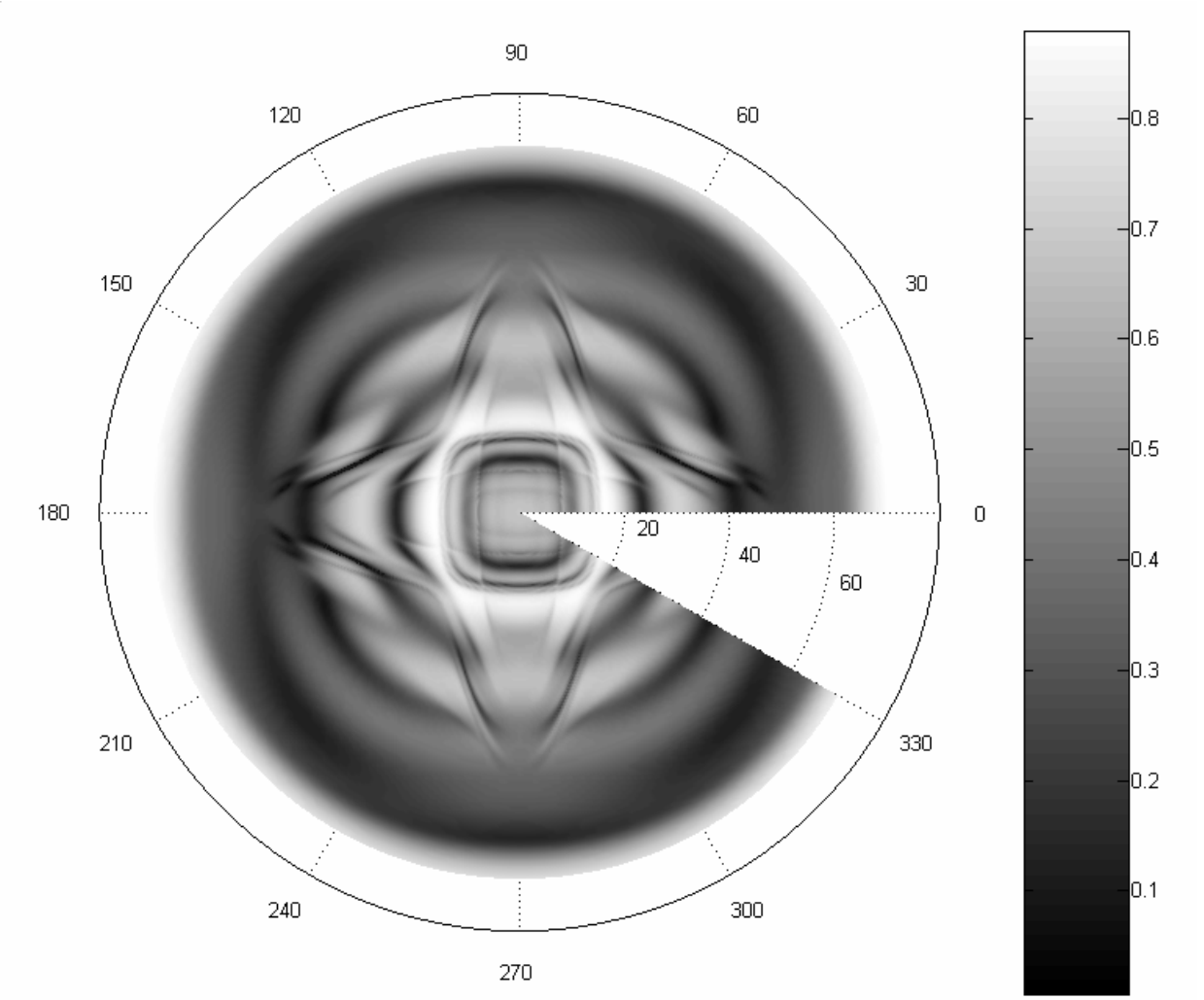

Fig. XI.B_9: ***Ultrasonic Polar Scan (harmonic, in reflection) of a cross-ply composite consisting of 10 ($0^0/90^0$) stacked layers of unidirectional fiber reinforced material.***

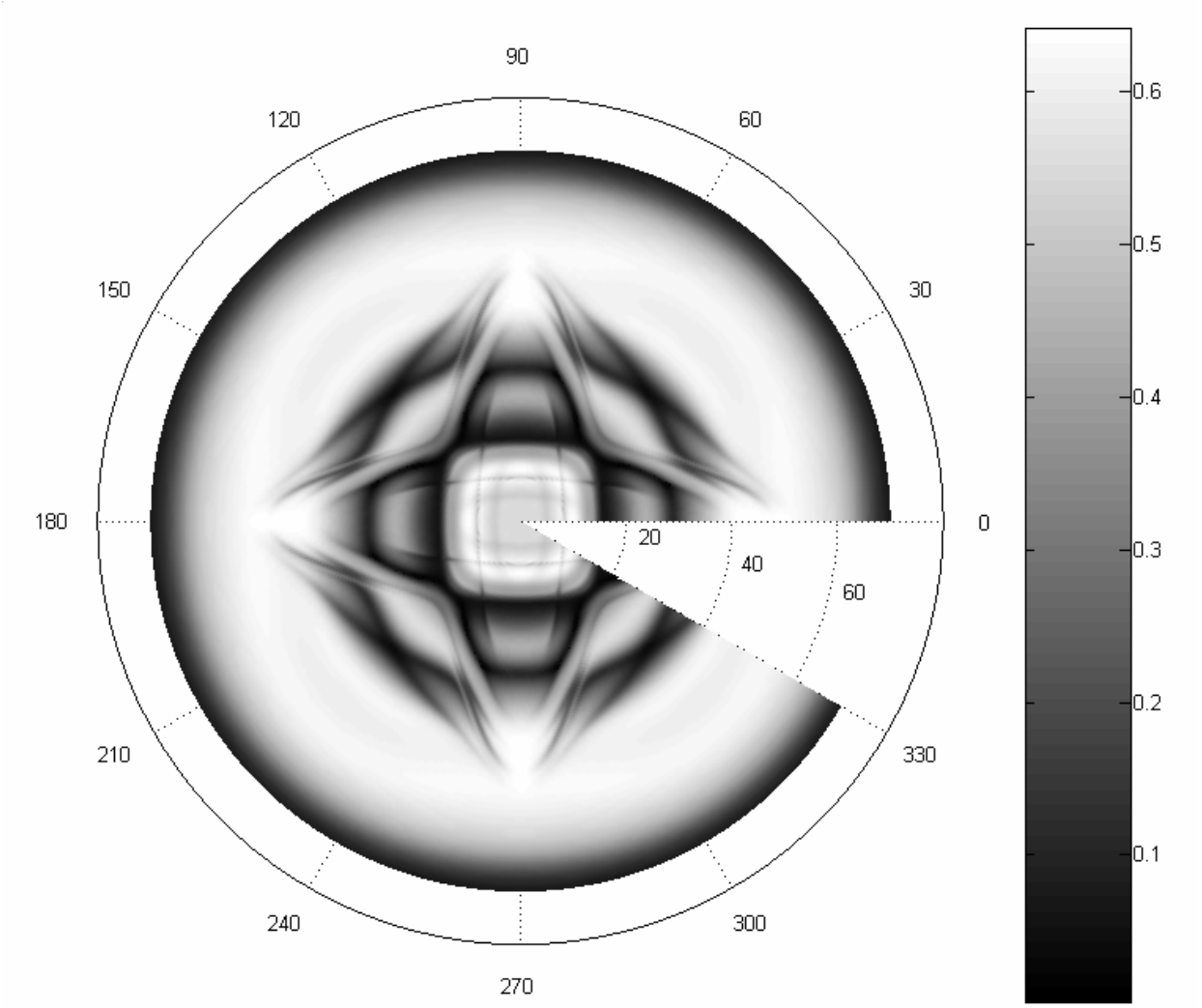

Fig. XI.B_10: ***Ultrasonic Polar Scan (harmonic, in transmission) of a cross-ply reinforced composite consisting of 10 ($0^0/90^0$) stacked layers of unidirectional fiber reinforced material.***

This finding is important since it is common for many researchers to model a fabric fiber reinforced composite as ($0^0/90^0$) stacked layers of unidirectional material. It is obvious from the given result that this should be avoided.

NUMERICAL EXAMPLE FOR A PULSE

A FR4 composite laminate is a fabric glass fiber reinforced epoxy composite and is frequently used in electronic devices. Table XI.B_I (type C) lists the material parameters of the FR4 laminate that is investigated here. We study the interaction of a pulse with the considered laminate. The considered pulse corresponds to a pulse that is generated by a Krautkrämer H5M shock wave probe [35] with a nominal frequency of 5MHz and is given by

$$\frac{ft}{M}\cos\left(2\pi ft\right)\exp\left(-\left(\frac{ft}{p}\right)^2\right) \qquad \text{(XI.B\_22)}$$

with $f = 5MHz$ and $p = 1.08$ and M a normalization constant. Expression (XI.B_22) is plotted in Fig. XI.B_11. This signal is simulated by means of the Fourier transformation whence it is written as a superposition of harmonic plane waves. Each of them is interacting with the composite as described earlier and the consequential field is again the summation of the resulting fields caused by each individual harmonic wave. The reflected amplitude is then defined as the maximum output as a function of time. The exact instant when that maximum is reached as well as the maximum value itself depend on the angle of incidence. In a polar scan for an incident pulse, the maximum reflected or transmitted value is plotted as a function of each angle of incidence. For the FR4 composite, here for a thickness of 1.2 mm, the polar scan in reflection is given in Fig. XI.B_12, whereas the one in transmission is given in Fig. XI.B_13. It is seen that no such complicated patterns appear as when an incident harmonic wave was considered (cfr. Fig. XI.B_8). As has been explained earlier, the reason for it is that the resulting patterns correspond to bulk critical angles and not to Lamb waves.

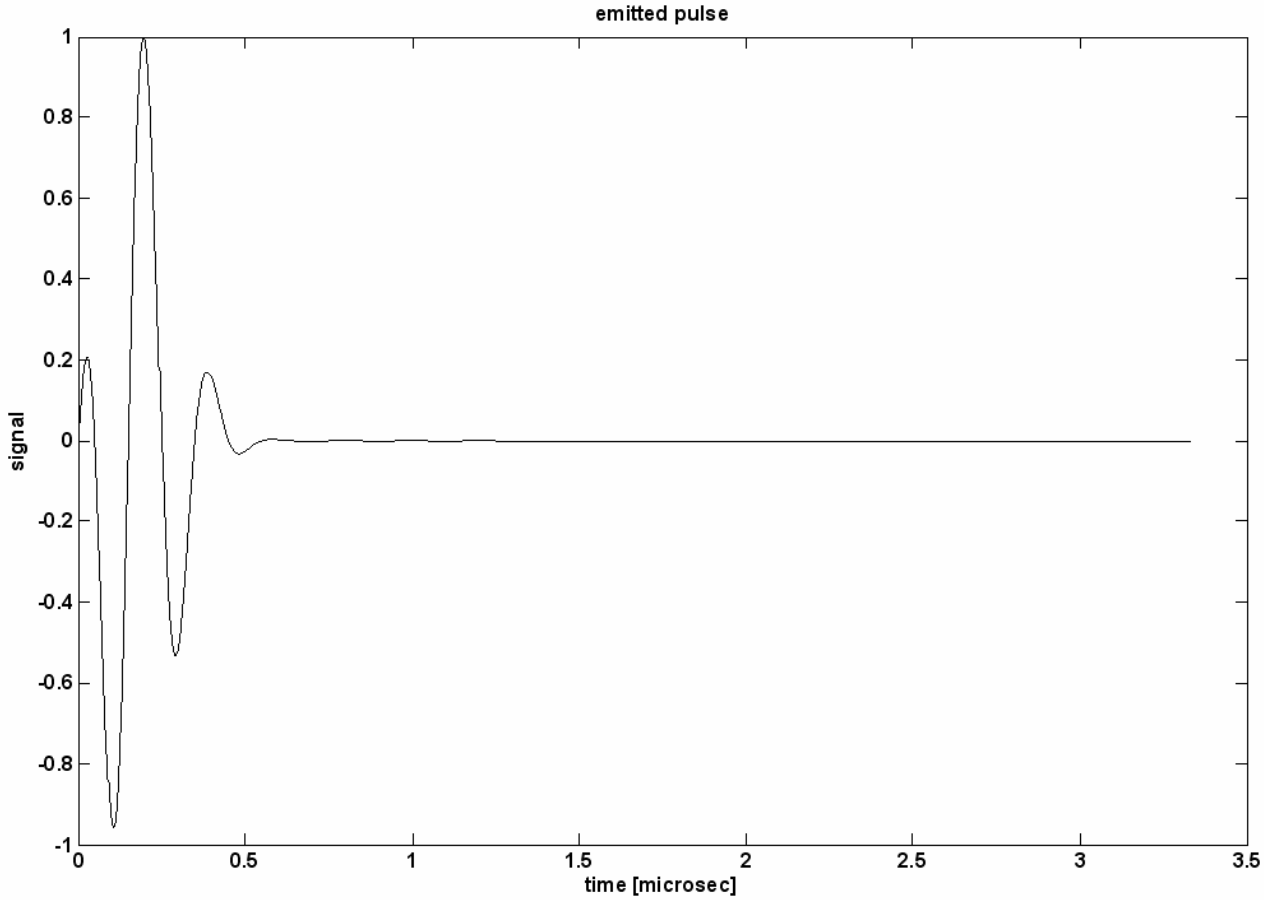

Fig. XI.B_11: ***The 'amplitude versus time'-profile of the impinging sound pulse.***

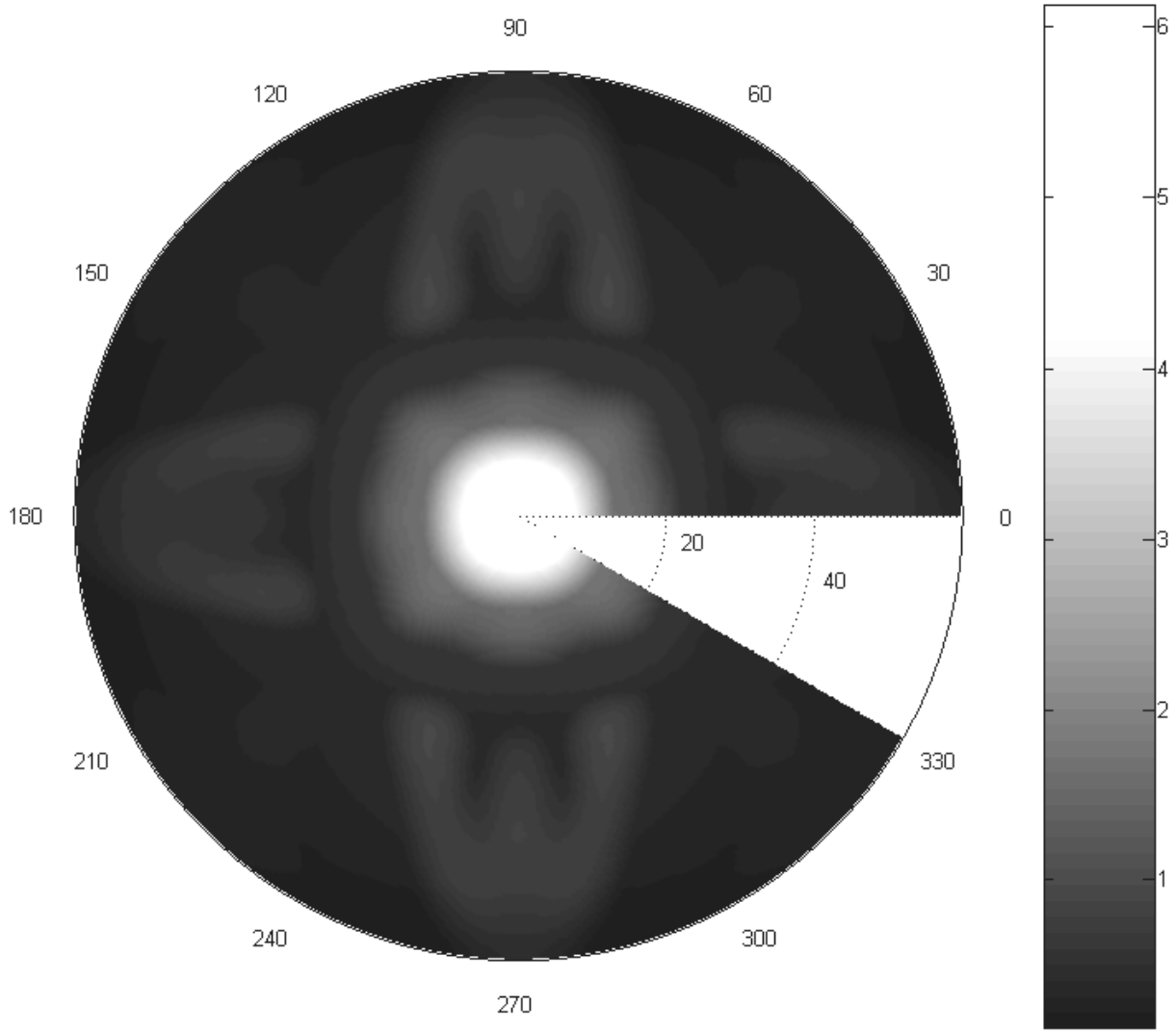

Fig. XI.B_12: ***simulation of the ultrasonic polar scan (pulsed, in reflection) on a FR4 plate***

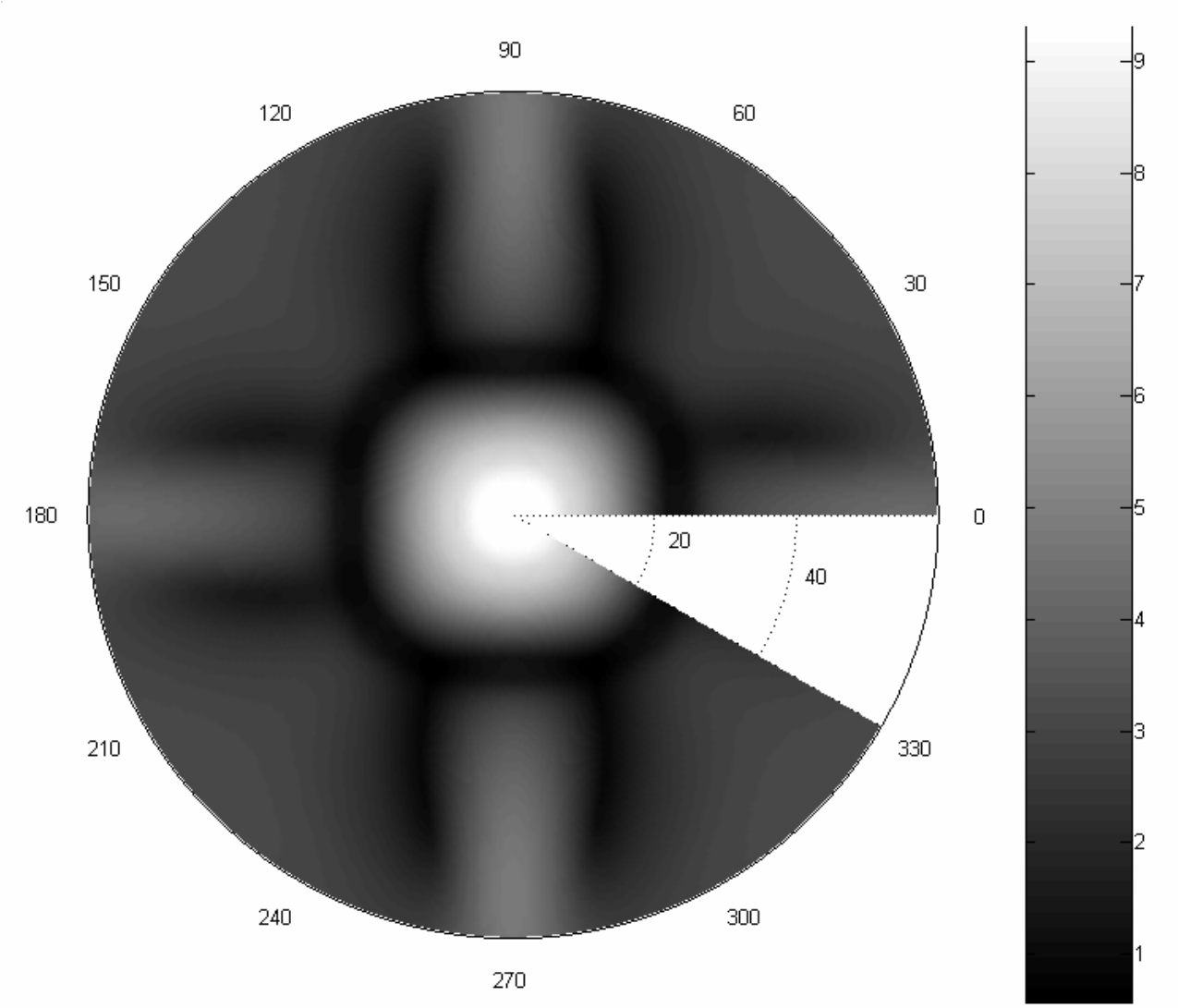

Fig. XI.B_13: ***simulation of the ultrasonic polar scan (pulsed, in transmission) on a FR4 plate***

POLAR SCANS ON CRYSTALS

Simulations of ultrasonic polar scans are not only developed for orthotropic materials, such as fiber reinforced composites, but also for crystals having any possible symmetry. Therefore, in what follows, some examples are shown for different kinds of crystals, having different orientations and also for the invented case of layered crystals. Note that relation (XI.B_3) is not applicable for symmetries that differ from orthotropy and that often, especially for rotated crystals, relations (XI.B_15-16) do not hold as well. Depending on the considered anisotropy, specific symmetry relations hold. They can be found in numerous works, e.g. the book by Nayfeh [39].

The rotation tensor $\left[R_{ij} \right]$ is given by

$$\left[R_{ij}^{..}\right]=\begin{bmatrix}1 & 0 & 0\\ 0 & C_\alpha & S_\alpha\\ 0 & -S_\alpha & C_\alpha\end{bmatrix}\times\begin{bmatrix}C_\beta & 0 & S_\beta\\ 0 & 1 & 0\\ -S_\beta & 0 & C_\beta\end{bmatrix}\times\begin{bmatrix}C_\gamma & S_\gamma & 0\\ -S_\gamma & C_\gamma & 0\\ 0 & 0 & 1\end{bmatrix} \tag{XI.B_23}$$

in which $C_\xi=\cos\xi$ and $S_\xi=\sin\xi$.

We have considered 4 orientations, of which 3 are labeled as X-cut, Y-cut or Z-cut and the 4rd is labeled as 'arbitrary':

orientation	α	β	γ
X-cut	0	$\pi/2$	0
Y-cut	$\pi/2$	0	0
Z-cut	0	0	0
'arbitrary'	$\pi/4$	$\pi/4$	$\pi/4$

(XI.B_24)

We consider a tetragonal 4mm crystal (Barium Titanate, $BaTiO_3$) and also a cubic $\bar{4}3m$ crystal (Gallium Arsenide, $GaAs$). For simplicity, we neglect piezoelectricity. The density of Barium Titanate is 6020 kgm^{-3}. The elastic constants $\left[\times10^{10}N/m^2\right]$ are

$$\begin{aligned}&C_{11}=27.5 \quad C_{12}=17.9 \quad C_{13}=15.1\\ &C_{33}=16.5 \quad C_{44}=5.43 \quad C_{66}=11.3\end{aligned} \tag{XI.B_25}$$

with

$$\begin{aligned}&C_{14}=C_{15}=C_{16}=C_{24}=C_{25}=C_{26}=C_{34}=C_{35}=C_{36}=0;\\ &C_{45}=C_{46}=C_{56}=0;\\ &C_{22}=C_{11};\quad C_{23}=C_{13};\quad C_{55}=C_{44}\end{aligned} \tag{XI.B_26}$$

The density of Gallium Arsenide is 5307 kgm^{-3}. The elastic constants $\left[\times10^{10}N/m^2\right]$ are

$$C_{11}=11.88 \quad C_{12}=5.38 \quad C_{44}=5.94 \tag{XI.B_27}$$

with

$$C_{14} = C_{15} = C_{16} = C_{24} = C_{25} = C_{26} = C_{34} = C_{35} = C_{36} = 0; \quad \text{(XI.B\_28)}$$
$$C_{45} = C_{46} = C_{56} = 0;$$
$$C_{13} = C_{12}; \quad C_{22} = C_{11}; \quad C_{23} = C_{12};$$
$$C_{33} = C_{11}; \quad C_{55} = C_{44}; \quad C_{66} = C_{44}$$

The crystals are immersed in water (density: 1000 kgm^{-3}, sound wave velocity: 1480 m/s)
Fig. XI.B_14 shows the simulated harmonic polar scan in reflection of a 3mm thick Z-cut Barium Titanate crystal. The corresponding polar scan in transmission is given in Fig. XI.B_15. The patterns are due to quasi Lamb waves and are determined by the symmetry properties of the crystal and by the physical properties, such as (thickness x frequency), density and elastic constants.
Figs. XI.B_15-22 show the harmonic polar scans in transmission for the different considered crystals and the considered orientations.

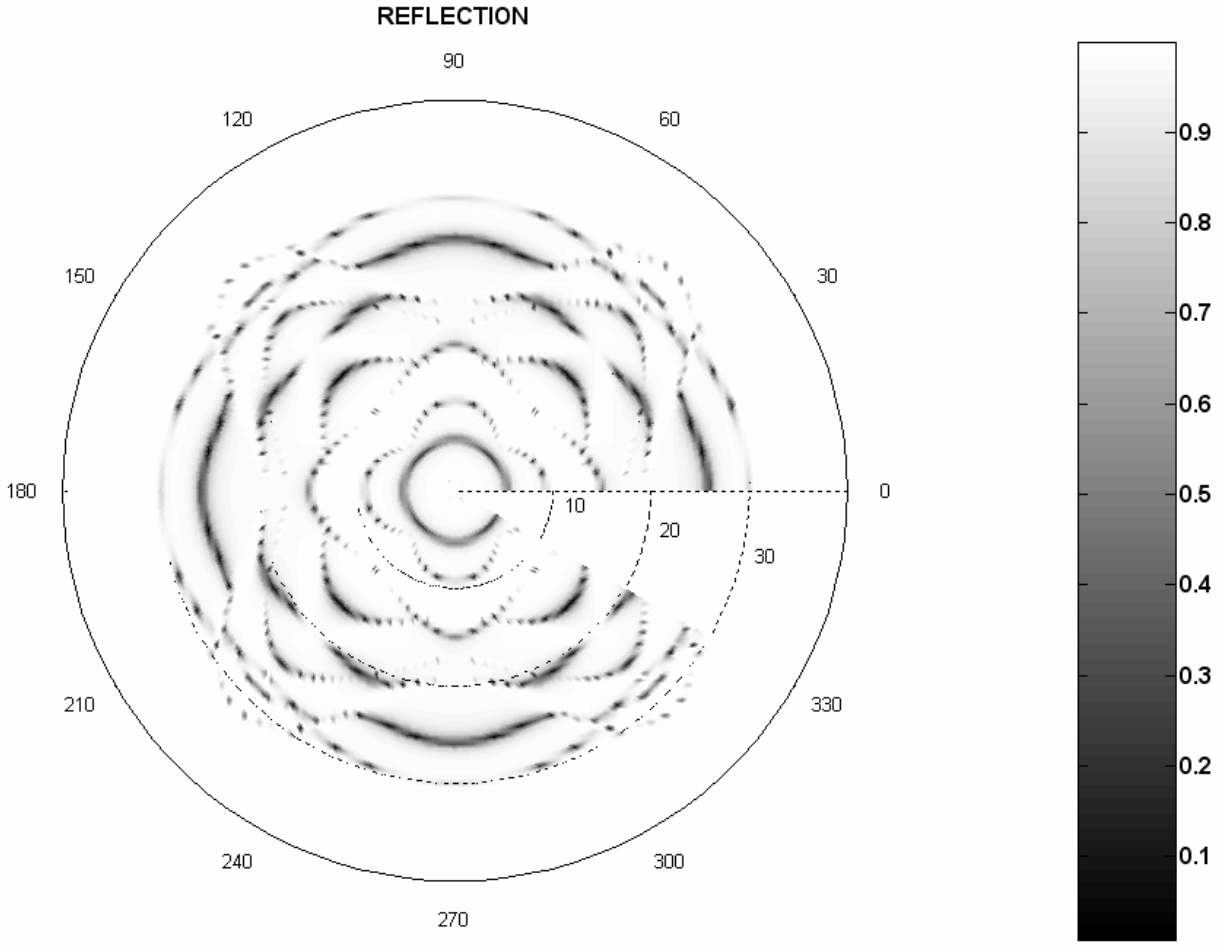

Fig. XI.B_14: ***simulated polar scan in reflection for a 3mm thick Z-cut Barium Titanate plate at 2 MHz***.

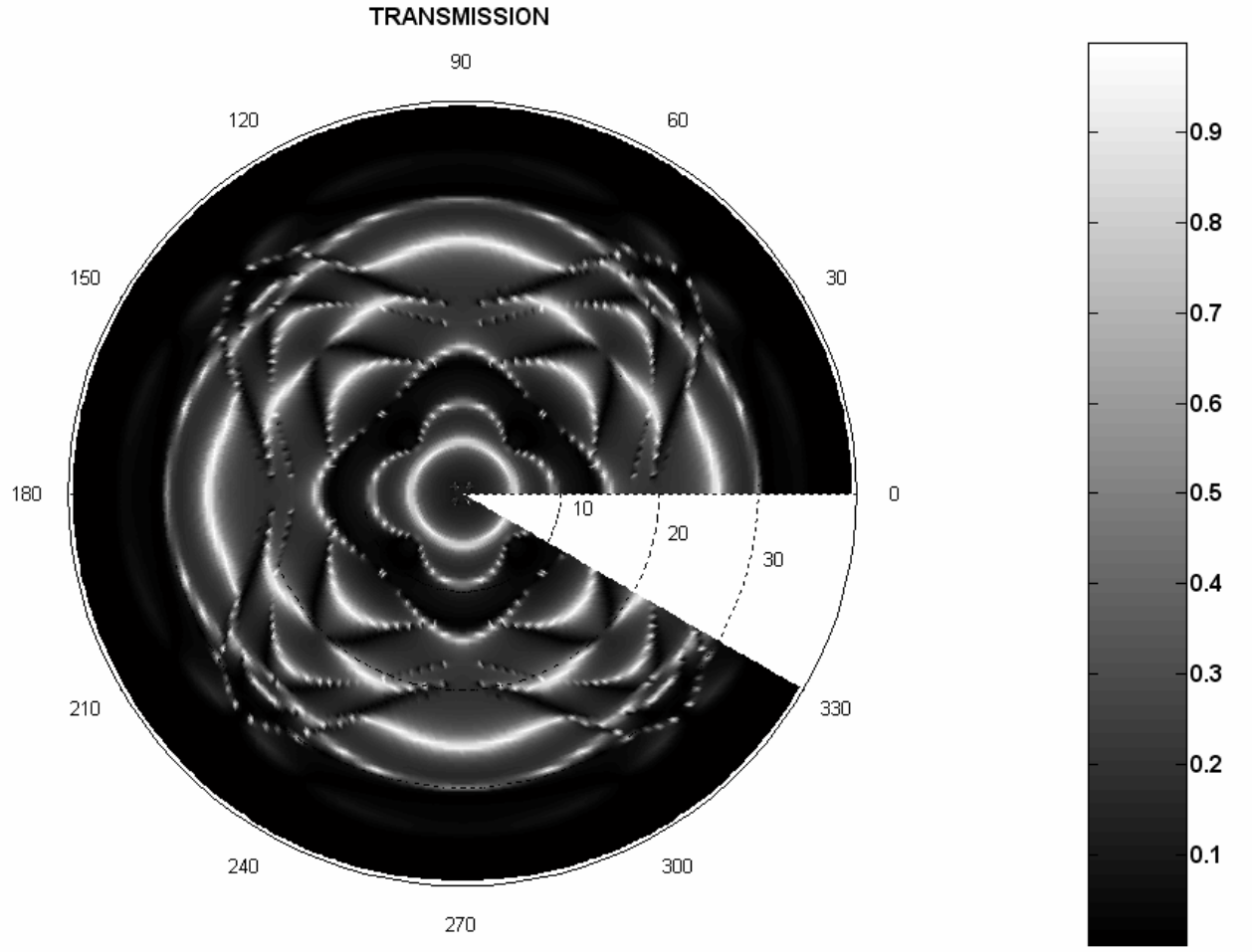

Fig. XI.B_15: ***simulated polar scan in transmission for a 3mm thick Z-cut Barium Titanate plate at 2 MHz.***

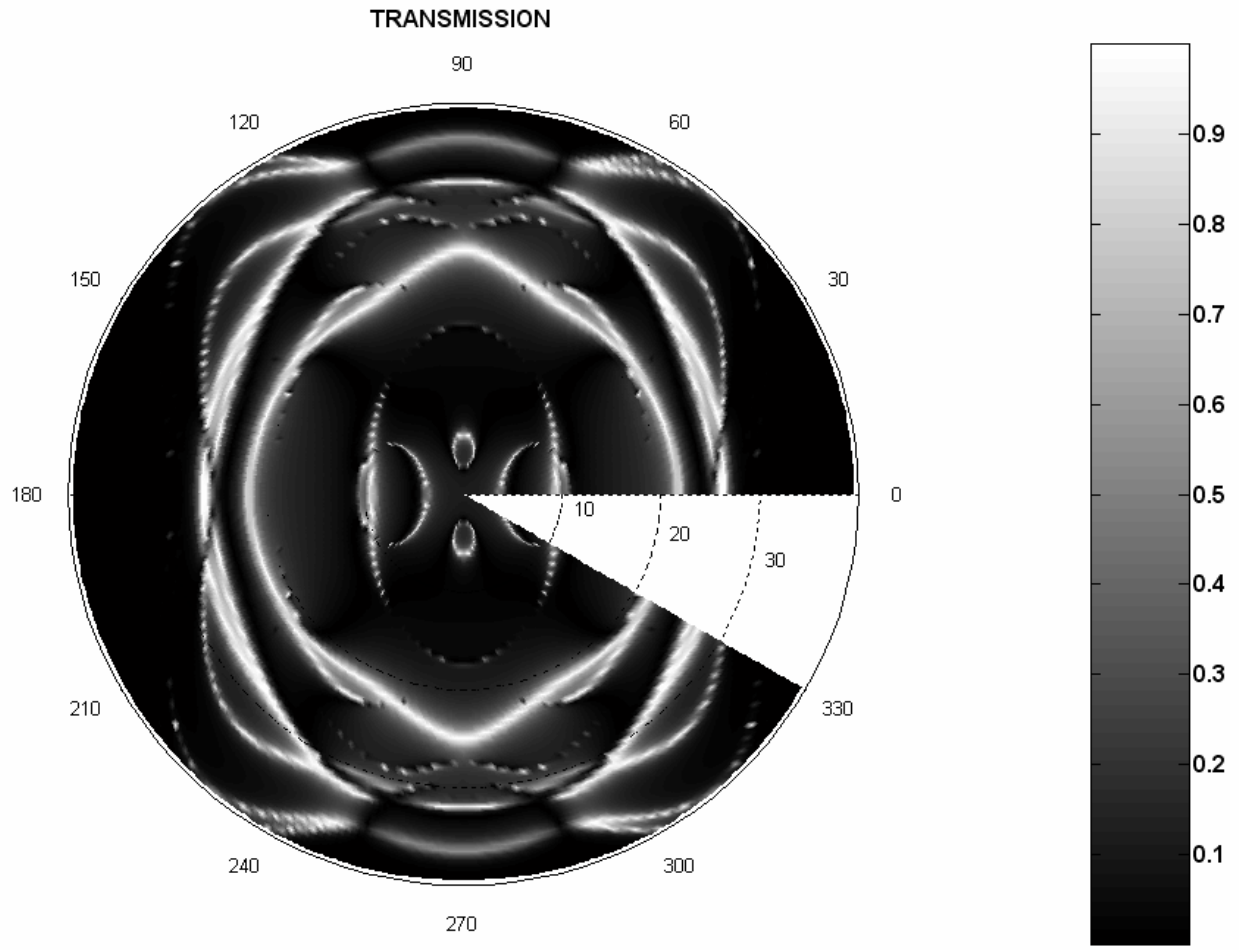

Fig. XI.B_16: ***simulated polar scan in transmission for a 3mm thick Y-cut Barium Titanate plate at 2 MHz.***

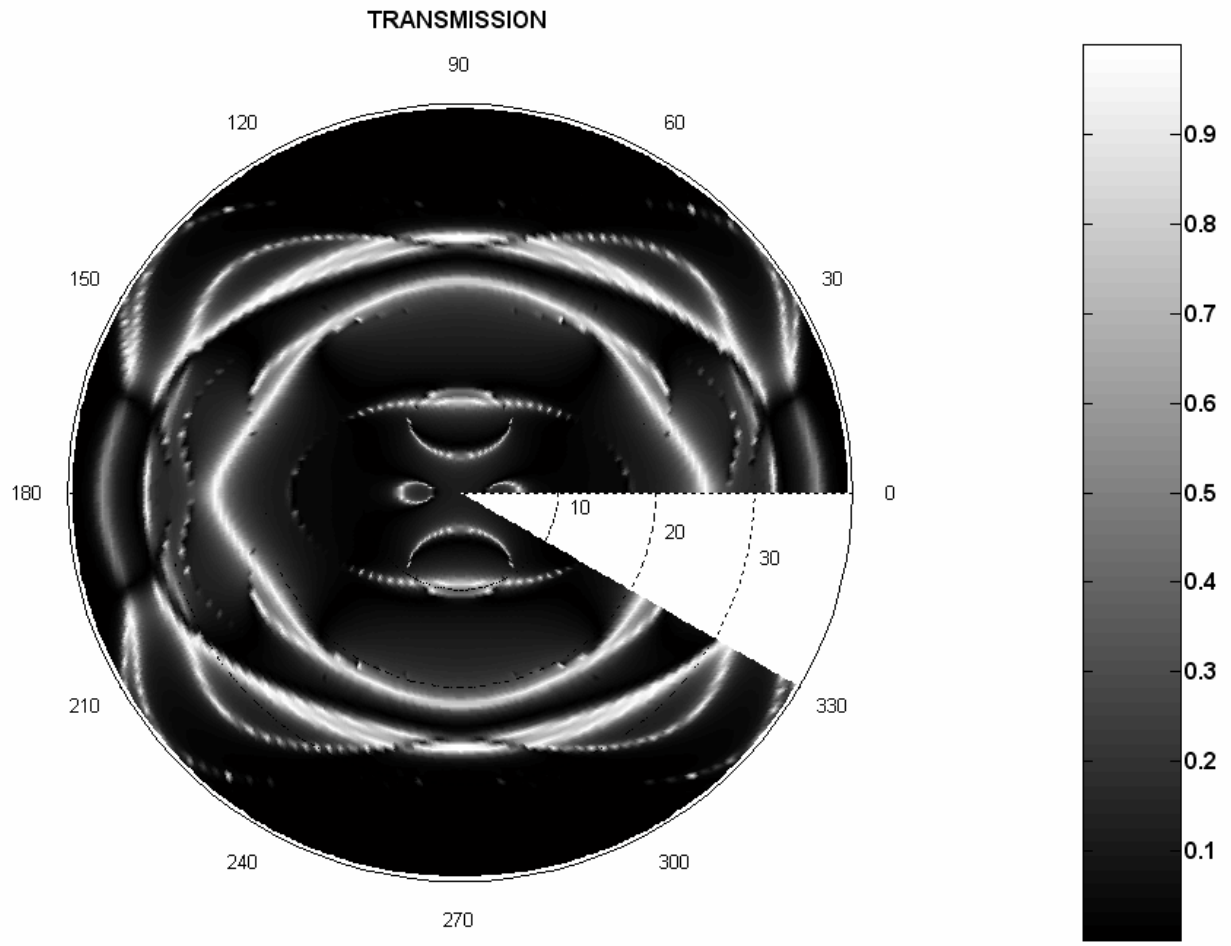

Fig. XI.B_17: ***simulated polar scan in transmission for a 3mm thick X-cut Barium Titanate plate at 2 MHz.***

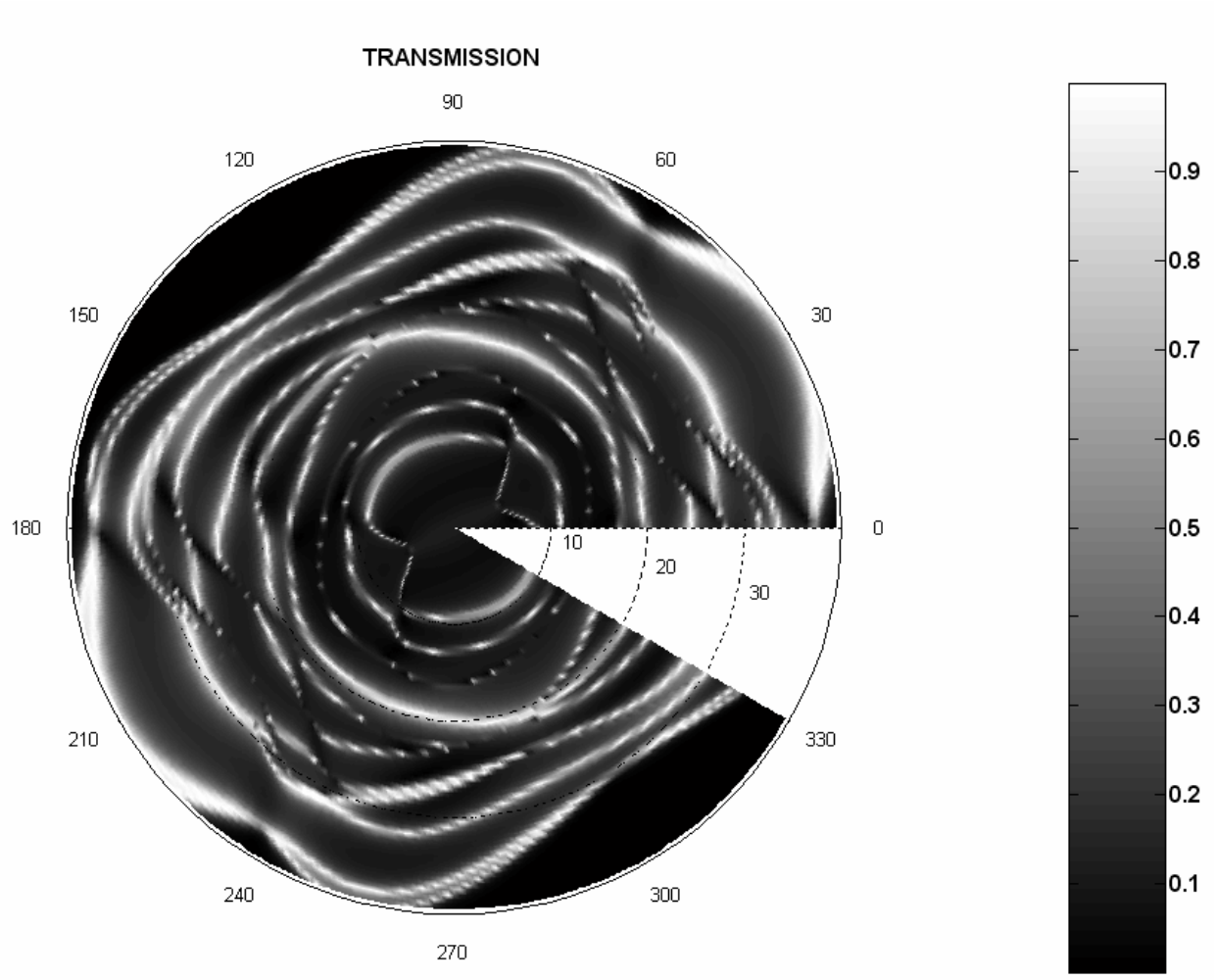

Fig. XI.B_18: ***simulated polar scan in transmission for a 3mm thick 'arbitrary'-cut Barium Titanate plate at 2 MHz.***

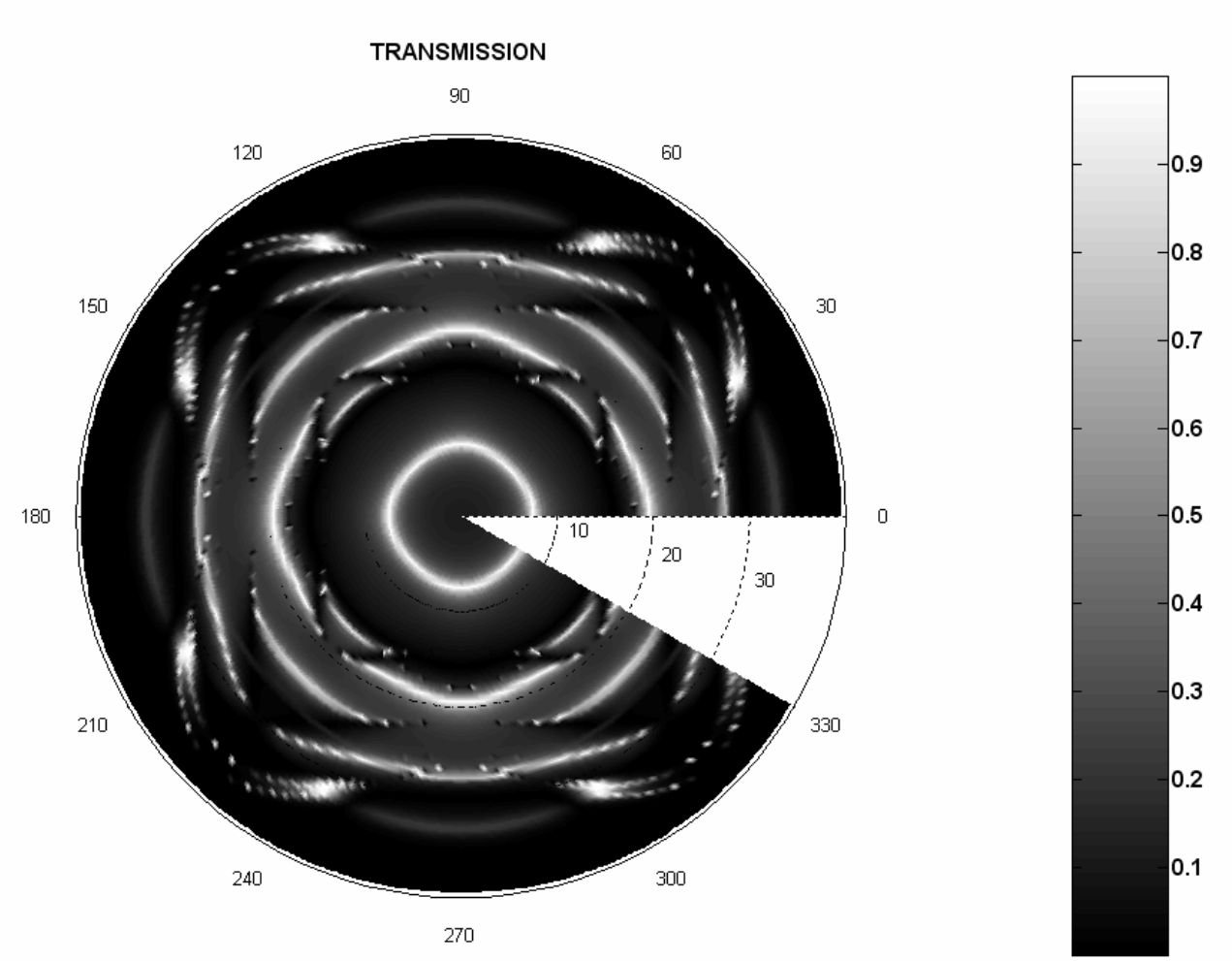

Fig. XI.B_19: ***simulated polar scan in transmission for a 3mm thick Z-cut Gallium Arsenide plate at 2 MHz.***

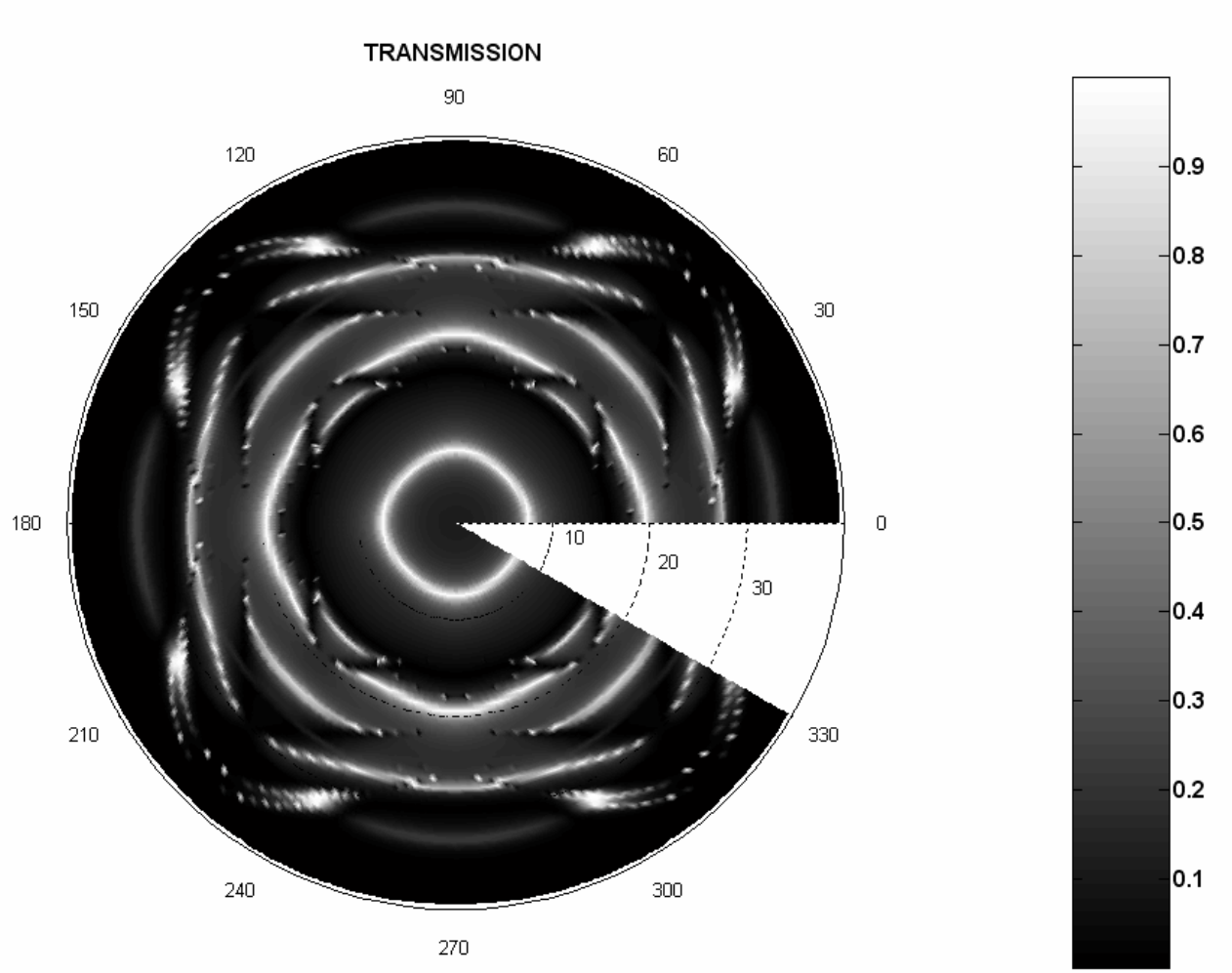

Fig. XI.B_20: ***simulated polar scan in transmission for a 3mm thick Y-cut Gallium Arsenide plate at 2 MHz***.

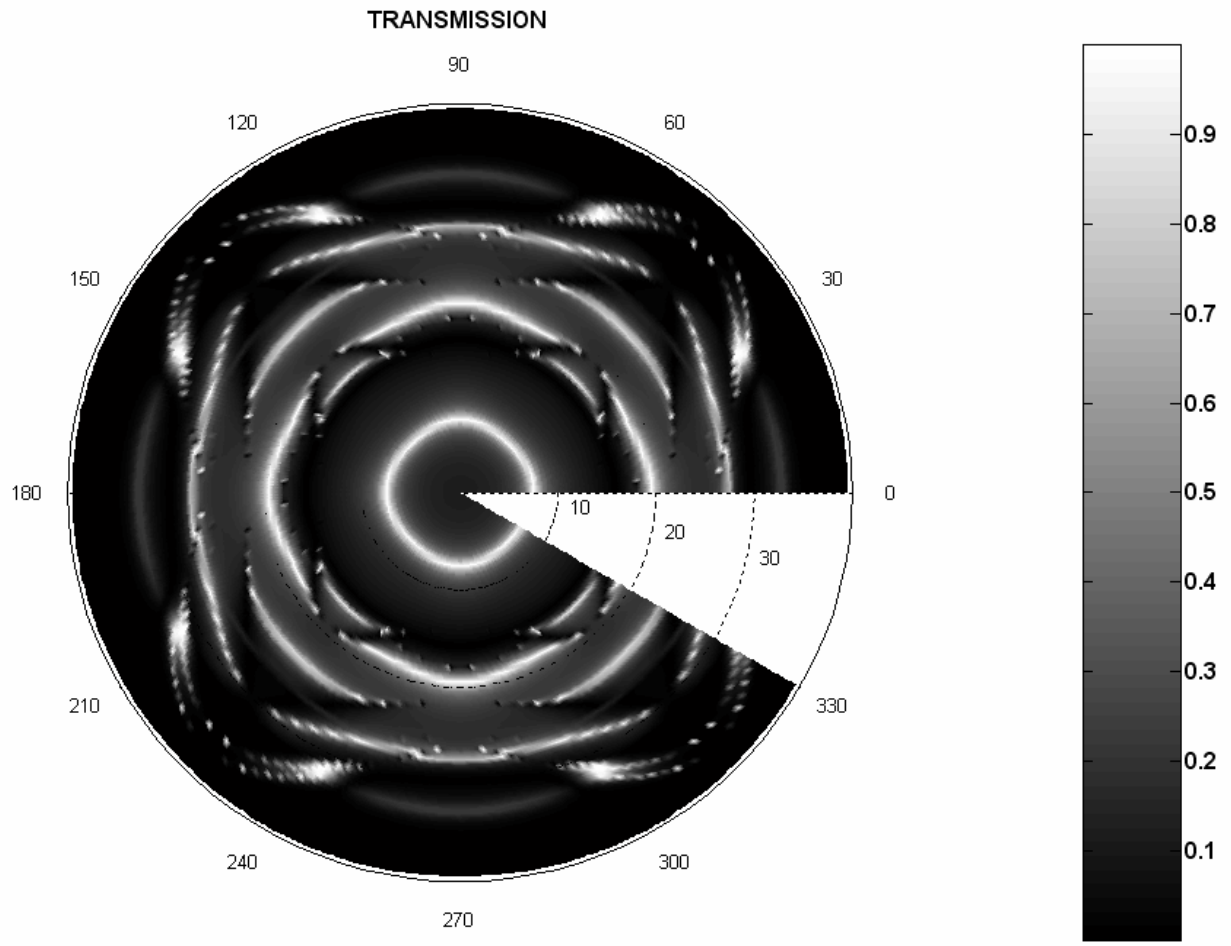

Fig. XI.B_21: ***simulated polar scan in transmission for a 3mm thick X-cut Gallium Arsenide plate at 2 MHz***

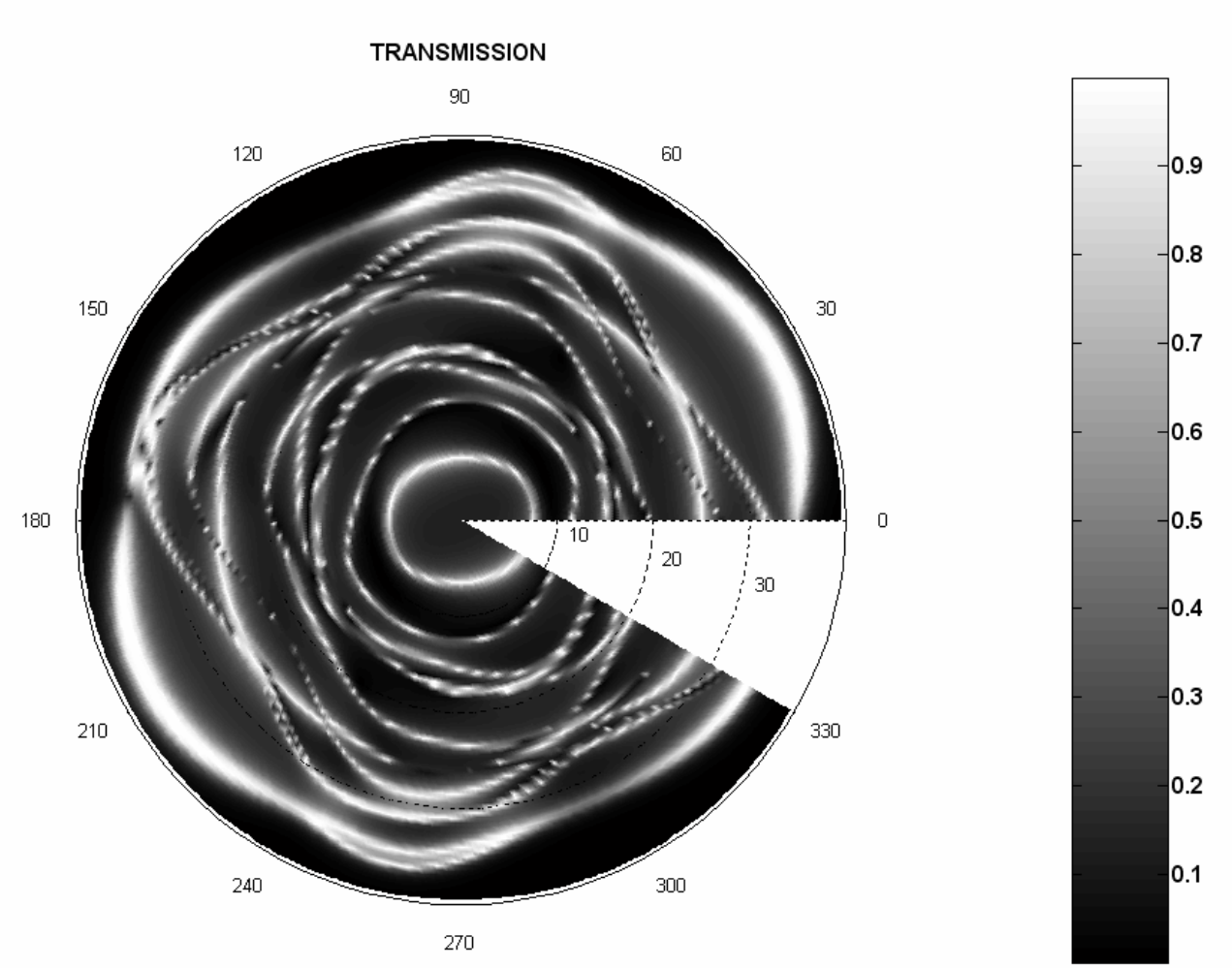

Fig. XI.B_22: ***simulated polar scan in transmission for a 3mm thick 'arbitrary'-cut Gallium Arsenide plate at 2 MHz.***

Figs. XI.B_23-26 show similar polar scans, but now for a layered system. The system consists of 2 layers of equal thickness. The total thickness is again 3 mm. The orientation of both layers is equal. The examples are given for Gallium Arsenide as upper layer and Barium Titanate as lower layer. The frequency is again 2 MHz.

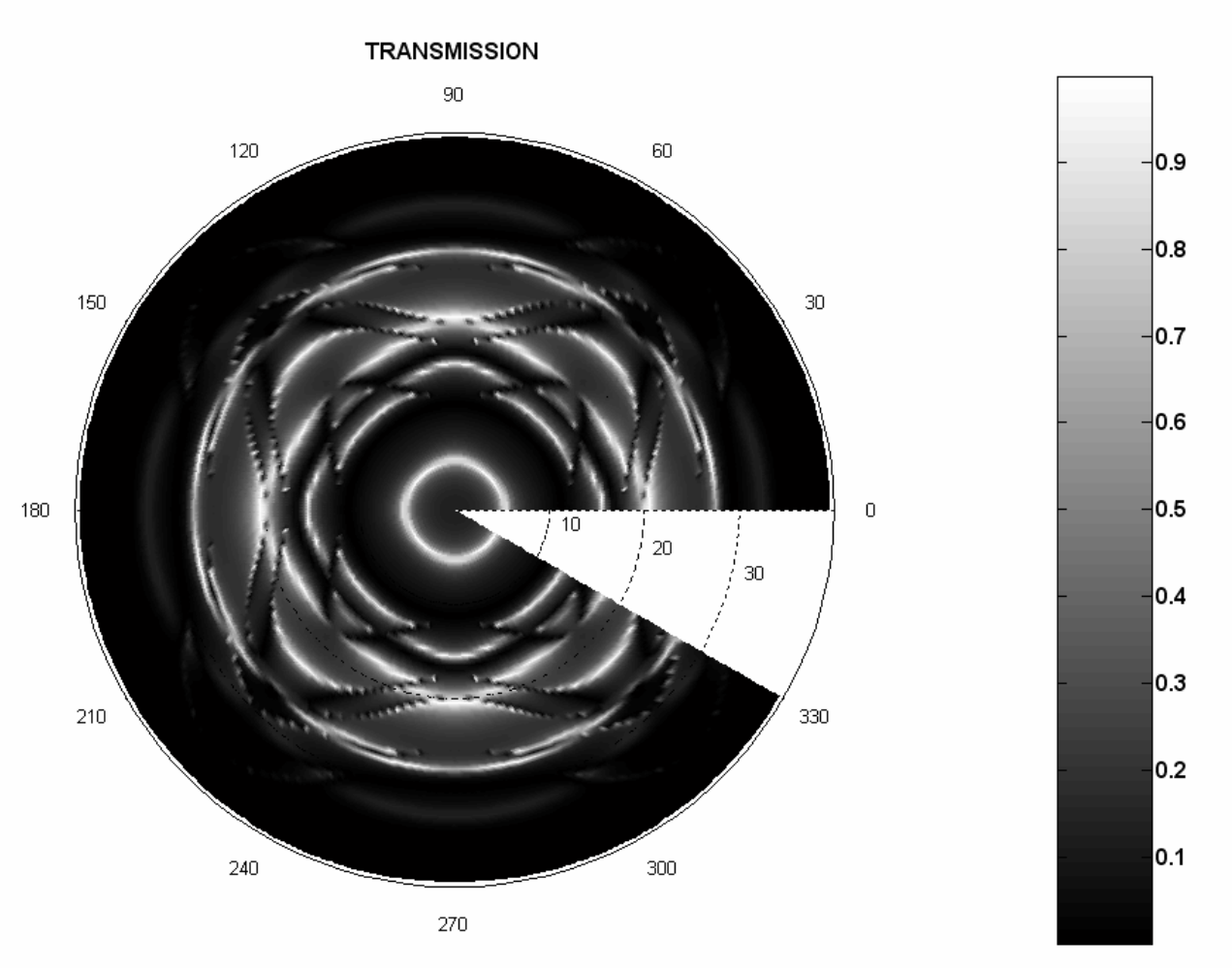

Fig. XI.B_23: ***simulated polar scan in transmission for a 3mm thick Z-cut layered plate at 2 MHz***.

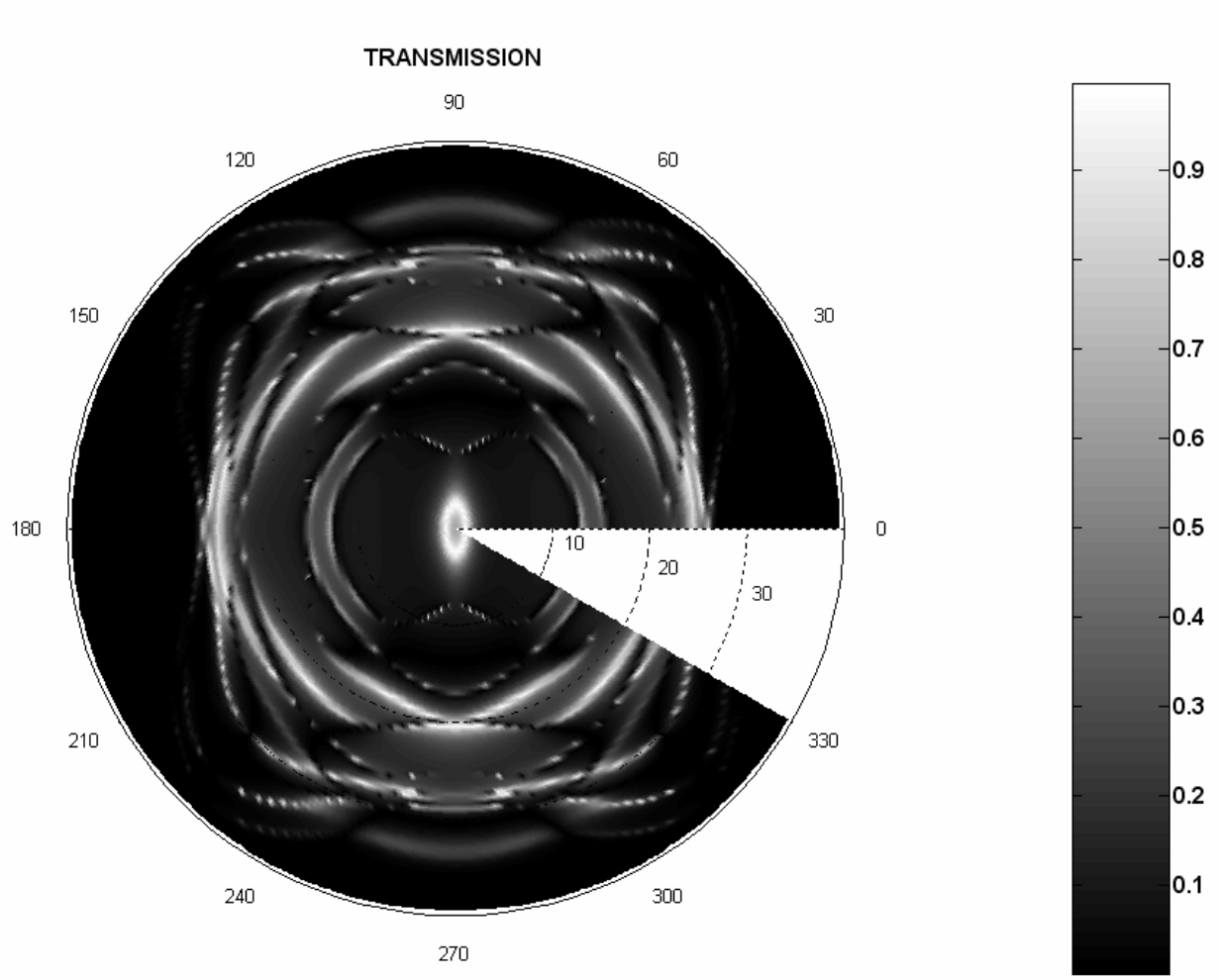

Fig. XI.B_24: ***simulated polar scan in transmission for a 3mm thick Y-cut layered plate at 2 MHz.***

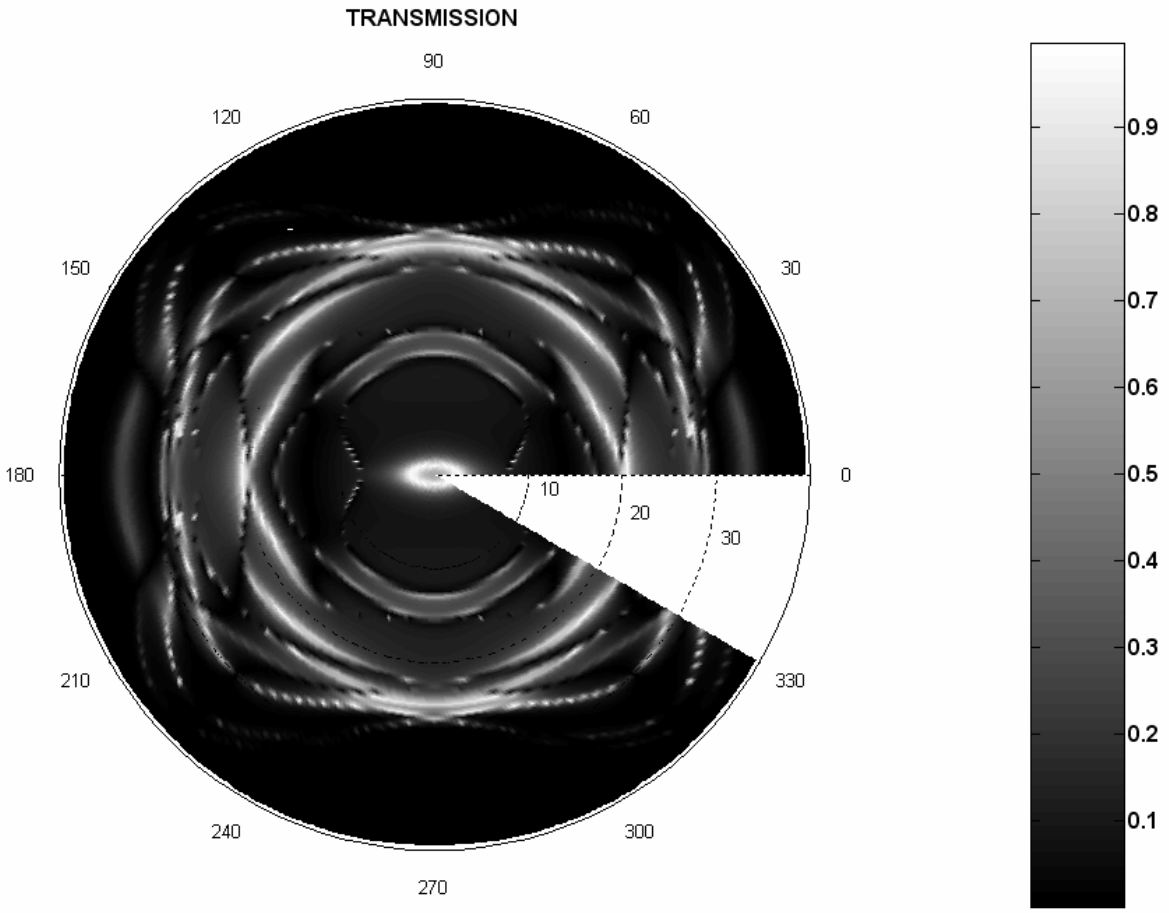

Fig. XI.B_25: ***simulated polar scan in transmission for a 3mm thick X-cut layered plate at 2 MHz***.

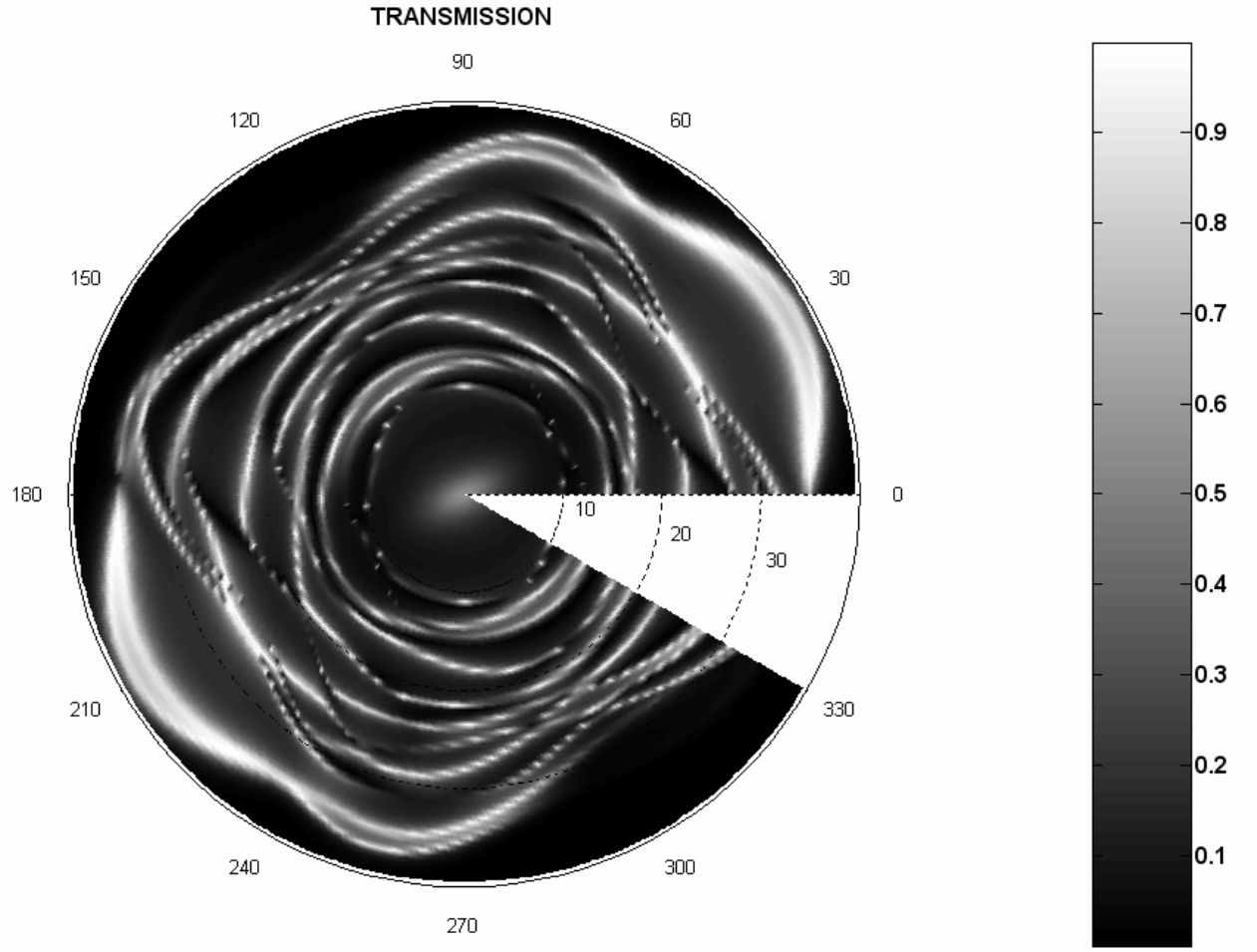

Fig. XI.B_26: ***simulated polar scan in transmission for a 3mm thick 'arbitrary'-cut layered plate at 2 MHz.***

CONCLUDING REMARKS

It is shown how numerical simulations of polar scans are performed, starting from simple principles of mechanics and wave motion. Even though simulations on single layered fiber reinforced composites already existed, the theoretical model has been extended to multi-layered composites and to crystals of any anisotropy. As an excellent example, it has been shown that fabric fiber reinforced composites cannot be modeled sufficiently accurate by means of a model in which unidirectional fiber reinforced layers are stacked in large numbers in the 0^0 polar direction and the 90^0 polar direction. We have discussed polar scans for incident harmonic waves and an incident pulse. These numerical simulations, together with the upgraded and highly modernized experimental set up may become a means of characterizing the stiffness of anisotropic plates. It is the author's purpose to develop an automated tool that applies a numerical/experimental inversion

technique and to rebuild the experimental apparatus to meet in-field requirements. Due to the strong connection to stiffness, the developed technique is intended to monitor fatigue damage on composites, porosity, and resin fractions. Furthermore, it will be used to verify micro-mechanical models.

REFERENCES

[1] Van Dreumel WHM.& Speijer JL. Nondestructive Composite Laminate Characterization by Means of Ultrasonic Polar Scan. Materials Evaluation 1981; 39(15): 922-925.

[2] Degrieck J, Van Leeuwen D. Simulatie van een Ultrasone Polaire Scan van een Orthotrope Plaat. In: Proceedings of the 3rd Belgian National Congres on Theoretical and Applied Mechanics, Belgium: Liege University, 1994; 39-42. (in dutch)

[3] Degrieck J. Some possibilities of nondestructive characterization of composite plates by means of ultrasonic polar scans. Non Destructive Testing,Van Hemelrijck & Anastassopoulos (eds). Rotterdam: Balkema 1996; 225-236.

[4] Declercq NF, Degrieck J, Leroy O. Characterization of Layered Orthotropic Materials Using Ultrasonic Polar Scans. In: Proceedings of the 2nd FTW PhD symposium, Belgium: Ghent University, 2001

[5] Degrieck J, Declercq NF, Leroy O. Ultrasonic Polar Scans as a possible means of nondestructive testing and characterization of composite plates. Insight – The Journal of the British Institute of Non-Destructive Testing 2003; 45(3): 196-201.

[6] Lavrentyev AI, Rokhlin SI. Determination of elastic moduli, density, attenuation, and thickness of a layer using ultrasonic spectroscopy at two angles. J. Acoust. Soc. Am. 1997; 102(11): 3467-3477

[7] Chu YC, Rokhlin SI. Comparative analysis of through-transmission ultrasonic bulk wave methods for phase velocity measurements in anisotropic materials. J. Acoust. Soc. Am. 1994; 95(11): 3204-3212

[8] Hsu DK, Hughes MS. Simultaneous ultrasonic velocity and sample thickness measurement and application in composites. J. Acoust. Soc. Am. 1992; 92(2): 669-675

[9] Chu Y, Rokhlin SI. A method for determination of elastic constants of a unidirectional lamina from ultrasonic bulk velocity measurements on [0/90] cross-ply composites. J. Acoust. Soc. Am. 1994; 96(1): 342-352

[10] Rokhlin SI, Huang W, Chu YC. Ultrasonic scattering and velocity methods for characterization of fibre-matrix interphases. Ultrasonics 1995; 33(10): 351-364

[11] Deschamps M, Bescond C. Numerical method to recover the elastic constants from ultrasonic group velocities. Ultrasonics 1995; 33(3): 205-211

[12] Degtyar AD, Rokhlin SI. Comparison of elastic constant determination in anisotropic materials from ultrasonic group and phase velocity data. J. Acoust. Soc. Am. 1997; 102(11): 3458-3466

[13] Aristégui C, Baste S. Optimal recovery of the elasticity tensor of general anisotropic materials from ultrasonic velocity data. J. Acoust. Soc. Am. 1997; 101(2): 813-833

[14] Aristégui C, Baste S. Optimal determination of the material symmetry axes and associated elasticity tensor from ultrasonic velocity data. J. Acoust. Soc. Am. 1997; 102(3): 1503-1521

[15] Enderby MD, Clarke AR, Patel M, Ogden P, Johnson AA. An automated ultrasonic immersion technique for the determination of three-dimensional elastic constants of polymer composites. Ultrasonics 1998; 36: 245-249

[16] Reverdy F, Audoin B. Elastic constants determination of anisotropic materials from phase velocities of acoustic waves generated and detected by lasers. J. Acoust. Soc. Am. 2001; 109(10): 1965-1972

[17] Pluta M, Every AG, Grill W, Kim TJ. Fourier inversion of acoustic wave fields in anisotropic solids. Phys. Rev. 2003; B 67 (14), Art. No. 094117

[18] Bescond C, Audoin B, Deschamps M, Qian M. Measurement by laser generated ultrasound of the stiffness tensor of an anisotropic material. Acta Acust United Ac 2002; 88 (1): 50-58

[19] Buchwald VT, Davis A. Surface waves in Anisotropic Elastic Media. Nature 1961; 191: 899-900

[20] Chimenti DE, Rokhlin SI. Relationship between leaky Lamb modes and reflection coefficient zeroes for a fluid-coupled elastic layer. J. Acoust. Soc. Am. 1990; 88(3): 1603-1611

[21] Buchwald VT. Rayleigh waves in anisotropic media. Quart. Journ. Mech. And Applied math. 1961; XIV (9): 461-469

[22] Lim TC, Musgrave MJP. Stoneley waves in anisotropic media. Nature 1970; 225: 372

[23] Nayfeh AH, Chimenti DE. Propagation of guided waves in fluid-coupled plates of fiber-reinforced composite. J. Acoust. Soc. Am. 1988; 83(10): 1736-1743

[24] Dayal V, Kinra VK. Leaky lamb waves in an anisotropic plate. I: An exact solution and experiments. J. Acoust. Soc. Am. 1989; 85(11): 2268-2276
[25] Chimenti DE, Martin RW. Nondestructive evaluation of composite laminates by leaky Lamb waves. Ultrasonics 1991; 29: 13-21
[26] Ting TCT, Barnett DM. Classifications of surface waves in anisotropic elastic materials. Wave Motion 1997; 26: 207-218
[27] Castaings M, Hosten B. The use of electrostatic, ultrasonic, air-coupled transducers to generate and receive Lamb waves in anisotropic, viscoelastic plates. Ultrasonics 1998; 36: 361-365
[28] Moreno E, Acevedo P. Thickness measurement in composite materials using Lamb waves. Ultrasonics 1998; 35: 581-586
[29] Jeong H, Hsu DK. Experimental analysis of porosity-induced ultrasonic attenuation and velocity change in carbon composites. Ultrasonics 1995; 33(3): 195-203
[30] Jeong H. Multiple NDE Techniques for the Measurement of Constituent Volume Fractions in Metal matrix Composites. Res Nondestr Eval 1997; 9: 41-57
[31] Zou W, Holland S, Kim KY, Sachse W. Wideband high-frequency line-focus PVDF transducer for materials characterization. Ultrasonics 2003; 41 (3): 157-161
[32] Ben Amor M, Ben Ghozlen MH, Lanceleur P. Modelling of elastic waves generated at the interface between anisotropic media. Acta Acust United Ac 2003; 89(9): 625-631
[33] Declercq NF., Degrieck J, Leroy O. Numerical simulations of ultrasonic polar scans on fiber reinforced composites. In Proceedings of the 29 Deutsche Jahrestagung für Akustik DAGA 2003, 18-20. March 2003, Aachen, Germany, 2003.
[34] Declercq NF, Degrieck J, Leroy O. Numerical simulations of ultrasonic polar scans. In Emerging Technologies in Nondestructive Testing, Van Hemelrijck, Anastasopoulos & Melanitis (eds); Lisse, 2004: Swets & Zeitlinger, p. 75-80
[35] Declercq NF, Degrieck J, Leroy O. On the influence of fatigue on ultrasonic polar scans of fiber reinforced composites. Ultrasonics 42, 173-177, 2004
[36] Wang L, Rokhlin SI. Ultrasonic wave interaction with multidirectional composites: Modeling and experiment. J. Acoust. Soc. Am. 2003; 114 (10): 2582-2595
[37] Hosten B, Castaings M. Surface impedance matrices to model the propagation in multilayered media. Ultrasonics 2003; 41(12): 501-507
[38] Potel C, Gatignol P, de Belleval JF. Energetic criterion for the radiation of Floquet waves in infinite anisotropic periodically multilayered media. Acta Acust united Ac 2001; 87 (3): 340-351
[39] Naefeh AH. Wave propagation in layered anisotropic media with applications to composites. North Holland series in Applied Mathematics and Mechanics, 1995
[40] Deschamps M, Hosten B. The effects of viscoelasticiy on the reflection and transmission of ultrasonic waves by an orthotropic plate. J. Acoust. Soc. Am. 1992; 91(9): 2007-2015
[41] Hosten B, Castaings M. Transfer matrix of multilayerd absorbing and anisotropic media. Measurements and simulations of ultrasonic wave propagation through composite materials. J. Acoust. Soc. Am. 1993; 94(3): 1488-1495
[42] Kim KY, Zou W, Sachse W. Wave propagation in a wavy fiber-epoxy composite material: Theory and experiment. J. Acoust. Soc. Am. 1998; 103 (10): 2296-2301
[43] Lu XR, Kim KY, Sachse W. In situ determination of elastic stiffness constants of thick composites. Comp Sc and Techn 1997 ;12: 753-762
[44] Pluta M, Schubert M, Jahny J, Grill W. Angular spectrum approach for the computation of group and phase velocity surfaces of acoustic waves in anisotropic materials. Ultrasonics 2000; 38(1-8): 232-236
[45] Bucur V, Lanceleur P, Roge B. Acoustic properties of wood in tridimensional representation of slowness surfaces. Ultrasonics 2002; 40(1-8): 537-541
[46] Bucur V. Techniques for high resolution imaging of wood structure: a review. Meas. Sc. & Techn. 2003; 14 (17): R91-R98
[47] Lanceleur P, de Belleval JF, Mercier N. Synthetic tridimensional representation of slowness surfaces of anisotropic materials. Acta Acust united Ac 1998; 84 (11): 1047-1054
[48] Maysenholder W. Sound transmission through periodically inhomogeneous anisotropic thin plates: Generalizations of Cremer's thin plate theory. Acta Acust united Ac 1998; 84(9): 668-680
[49] Carcione JM, Cavallini F, Helbig K. Anisotropic attenuation and material symmetry., Acta Acust united Ac 1998; 84 (3): 495-502
[50] Achenbach JD. Wave propagation in elastic solids. North Holland, 1975

[51] Dunn ML. Viscoelastic damping of particle and fiber reinforced composite materials. J. Acoust. Soc. Am. 1995; 98(11): 3360-3374
[52] Baudouin S, Hosten B. Immersion ultrasonic method to measure elastic constants and anisotropic attenuation in polymer-matrix and fiber-reinforced composite materials. Ultrasonics 1996; 34: 379-382
[53] Vandenbossche B, Kriz RD, Oshima T. Stress-Wave displacement Polarizations and Attenuation in Unidirectional composites: theory and Experiment. Res. Nondestr. Eval. 1996; 8: 101-123
[54] Kendall R. Waters, Michael S. Hughes, Joel Mobley, Gary H. Brandenburger, James G. Miller. On the applicability of Kramers-Krönig relations for ultrasonic attenuation obeying a frequency power law. J. Acoust. Soc. Am. 2000; 108(2): 556-563
[55] Moreno E, Acevedo P, Castillo M. Thickness measurement in composite materials using Lamb waves Viscoelastic effects. Ultrasonics 2000; 37: 595-599

XI.C On the Influence of Fatigue on Ultrasonic Polar Scans of Fiber Reinforced Composites

Ultrasonic Polar Scans have already proved to be well-suited as a practical means of characterizing fiber reinforced composite plates. The method consists of registering the reflected or transmitted sound amplitude as a function of each possible angle of incidence. It is hence an amplitude measurement by which it differs from more common 'time of flight' measurements. Ultrasonic Polar Scans are actually a fingerprint of a composite laminate. One of the many promising applications of the Ultrasonic Polar Scan is the monitoring of fiber reinforced composites in service. Especially the progress of fatigue damage can be monitored easily and nondestructively. This section presents numerical simulations of the influence of fatigue on Ultrasonic Polar Scans as well as some experimental results.

The contents of this section have been published as: Nico F. Declercq, Joris Degrieck, Oswald Leroy, " On the influence of fatigue on ultrasonic polar scans of fiber reinforced composites", Ultrasonics 42, 173-177, 2004. (Imp. Fact. 0.844; SCI-index, Acoustics, rank:11 /28)

EXPERIMENTAL PROCEDURE AND RESULTS

Causing Fatigue Damage

A FR4 composite laminate is a fabric glass fiber reinforced epoxy composite that is often used in electronic devices. The present paper reports experiments on such a FR4 sample. The use of the polar scan method to study the sample is discussed below. In between each polar scan, the sample has been subjected to applied dynamic (sinusoidal) strain in one direction. It is well known that this results in degradation of the material after a large number of cycles. This is called fatigue. Contrary to degradation in metals, in composites degradation always occurs in a relatively large zone (bulk degradation) and is accompanied by a diminishing stiffness in many directions. The dynamic strain is caused by clasping the sample in a system of two grabs that are connected to a machine that generates controlled displacements of the grabs relative to each other. The dimensions of the laminate inside the grabs system are shown in Fig. XI.C_1. The amplitude of the applied dynamic strain is 0.8% which for this material (E modulus is approximately 22GPa) corresponds to a maximal applied stress of 181 MPa, i.e. 60% of the strength of the laminate. The dynamic stress is applied at a pace of 2.5 Hz. Below, we will study the effect of this applied stress on an experimental polar scan before fatigue and after 39060 dynamic deformations.

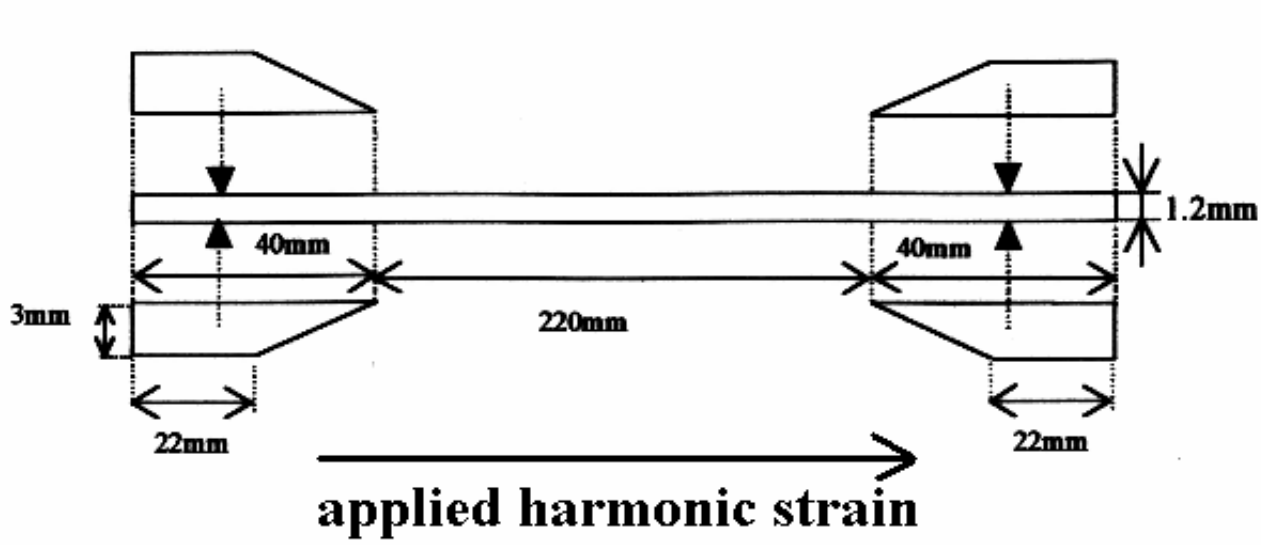

Fig. XI.C_1: ***A schematic view of the laminate inside the grabs during cyclic deformations. The dimensions of the sample are 300 mm (length) by 1.2 mm (thickness).***

The Principle of Ultrasonic Polar Scans in a Nutshell

Just like for example the well known time of flight techniques, an ultrasonic polar scan is performed on a plate immersed in water and investigates anisotropic mechanical properties of the laminate exploiting its influence on obliquely incident sound. Frequently in nondestructive characterization of fiber reinforced composite plates, time of flight measurements are used, which are relatively difficult to perform. The ultrasonic polar scan on the other hand applies the amplitude of transmitted (or if necessary reflected) sound, which results from sound impinging the plate from every direction above the plate and is relatively easy to measure. Furthermore, a polar scan is able to investigate sound amplitudes on a small area, whence it can present a local fingerprint of the laminate under investigation. The characteristic pattern of such a 'fingerprint' consists in fact of a set of rings, showing considerably less intensity than elsewhere on the registered polar scan. The rings are physically connected to generated critical waves in the plate, such as leaky Rayleigh waves, leaky Lamb waves or even lateral waves. Therefore, they almost directly elucidate the mechanical anisotropy and the stiffness of the investigated area.

Ultrasonic polar scans have first been developed by van Dreumel and Speijer [1] who used them to determine the fiber orientation in composite laminates, and have been further developed by Degrieck et al.[2-6], who utilized them for additional applications such as the determination of the anisotropic (non-orthotropic) stiffness, fiber and resin fraction and more.
Contrary to classical C-scans, in polar scans the transducer is not directed invariably normal to the surface, scanning a whole area, but is constantly directed towards a particular targeted zone on the surface, occupying successively all possible directions of incidence from the upper half space, and maintaining a constant distance to the target, as shown in Fig. XI.C_2. The measured amplitude is then plotted in a polar diagram where the radius corresponds to φ and the polar angle to θ.

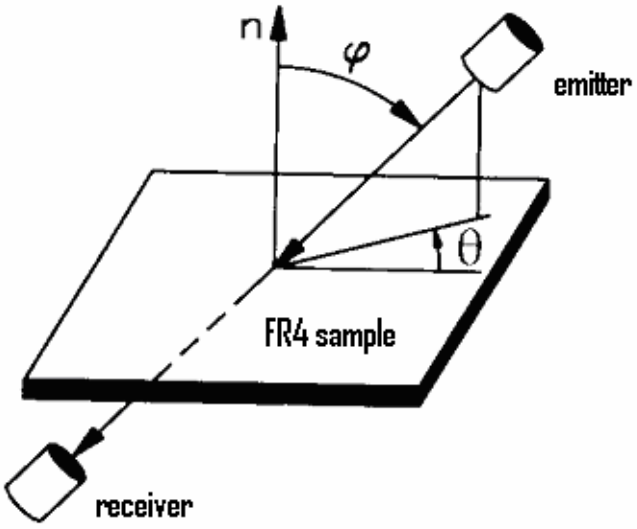

Fig. XI.C_2: ***In a polar scan, a spot is impinged at constant distance form all possible angles***

Experimental Results

The ultrasonic polar scans were experimentally performed using a Krautkrämer USIP20 ultrasonic apparatus and a Krautkrämer H5M shock wave probe with a nominal frequency of 5MHz. The pulse had a shape that is given in Fig. XI.C_3.

Since a shock wave probe generates sound that contains a large frequency range, the existence of Lamb wave angles is not directly visible in the overall reflected or transmitted amplitude. One would need to perform a frequency analysis of the received sound if the individual Lamb modes have to be detected. However the positive consequence of applying a shock wave transducer is that patterns appear at angles that almost coincide with bulk critical angles. That is because all frequency dependent Lamb modes phase-cancel each other, which is not the case for the effects at the frequency independent bulk critical angles. Therefore, the reflected sound, resulting from an impinging shock wave, will show maximum amplitude at bulk critical angles, while the corresponding transmitted sound will show a strong amplitude dip. Now, since bulk critical angles are relatively simply connected to the stiffness of the material through Snell's law and the Christoffel equation, they form an ideal fingerprint to visualize stiffness changes due to fatigue damage. In the experiments performed here, the maximum transmitted amplitude is measured for each angle of incidence, whence critical amplitude dip patterns will appear due to the bulk critical angles. The results for the ultrasonic polar scan in transmission is shown before fatigue (Fig. XI.C_4) and after fatigue caused by 39060 cycles of dynamic deformation as discussed above (Fig. XI.C_5).

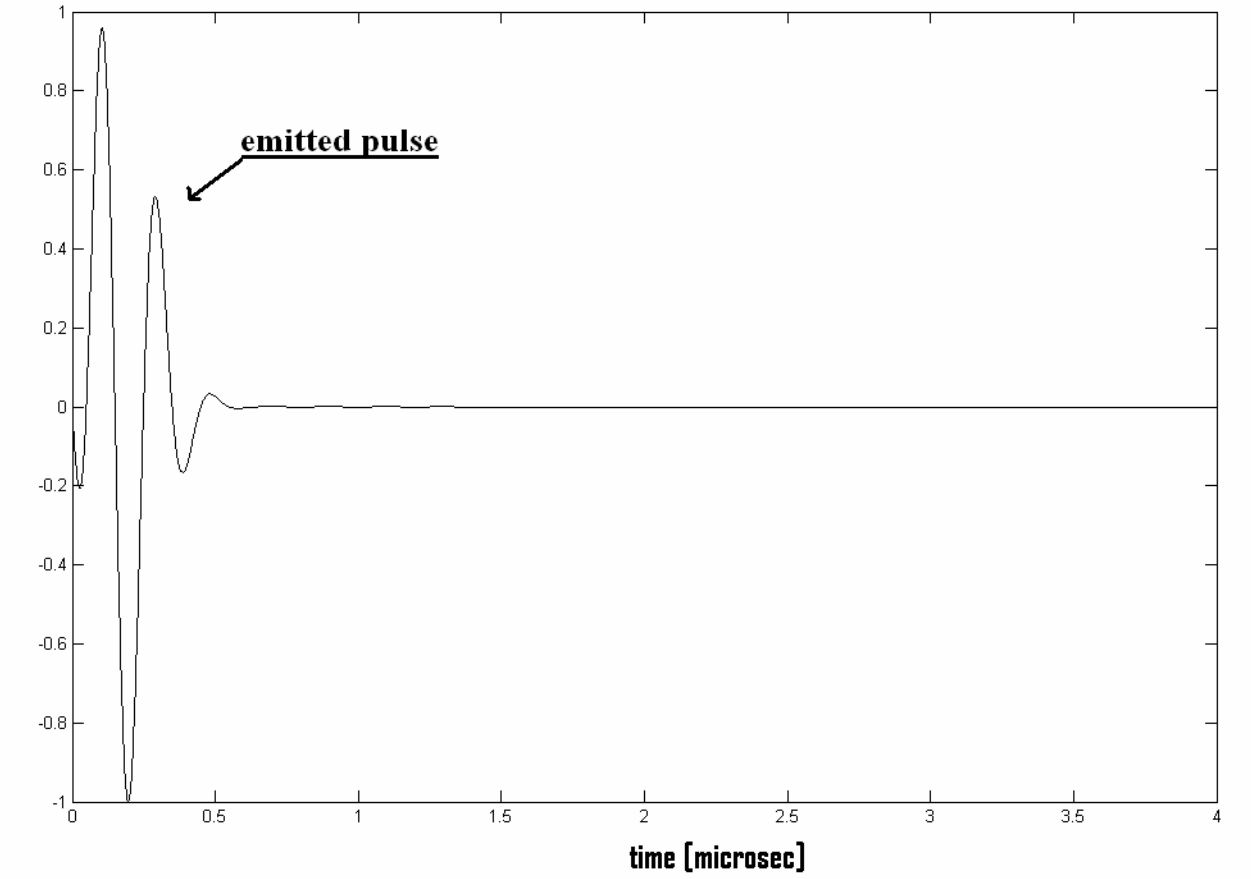

Fig. XI.C_3: ***The amplitude versus time profile of the impinging sound pulse.***

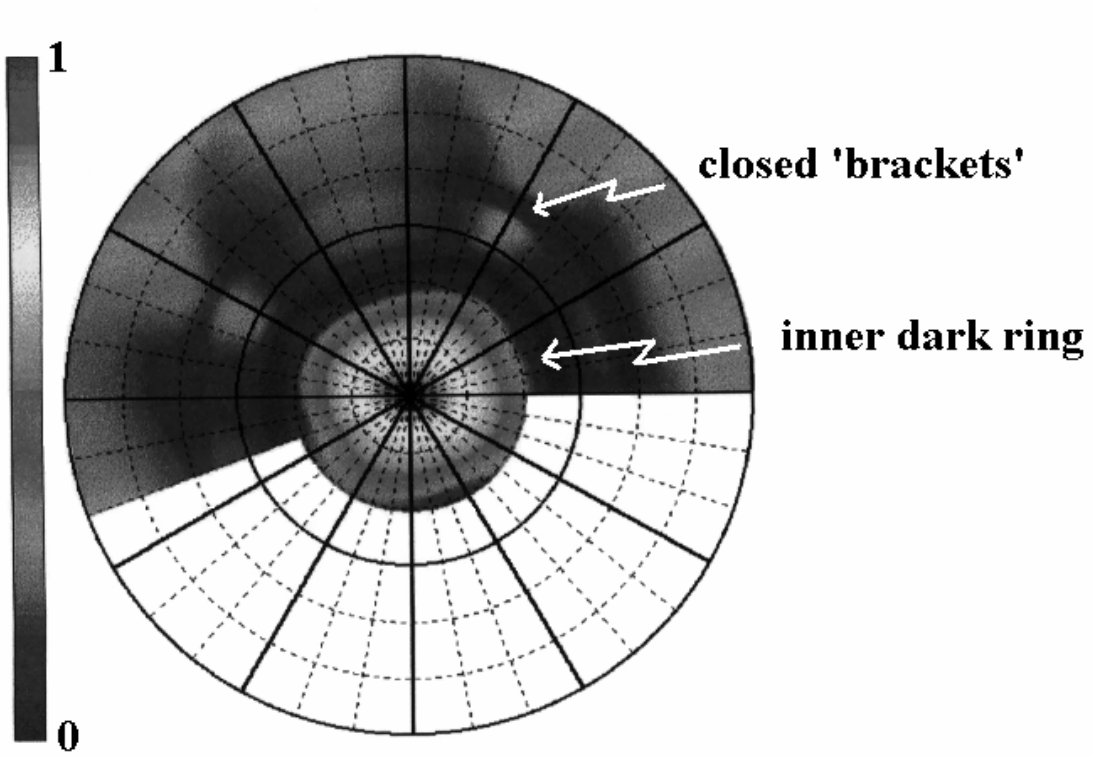

Fig. XI.C_4: ***Experimental ultrasonic polar scan on a FR4 plate before fatigue damage. The dotted circles of the diagram correspond to steps of 10^0. The amplitude is normalized.***

The 'omitted' parts in the polar scans of Figs XI.C_4-5 correspond to angles where no measurements have been performed. Since there are large areas where the amplitude changes very little, a plot where the brightness corresponds linearly to the intensity results in very ambiguous figures. Therefore we have opted to make plots in color and transform them to black and white pictures similar to a black and white copier. This results in figures where the brightness does not correspond one to one to a certain intensity. However, it is so that the dark center in the presented ultrasonic polar scans corresponds to maximum intensity. All other dark regions, exceeding $\varphi=10^0$, correspond to low intensities. The grey regions are more or less linearly related to medium intensities as can be noticed from the 'color bar' next to each polar scan. It is seen that the dark ring in between 20^0 and 30^0 has moved slightly (approximately 1^0 to 2^0) outwards after the fatigue damage has occurred. This ring is caused by the critical angle corresponding to quasi longitudinal waves. Hence, ultrasonic polar scans enable us to monitor fatigue damage.

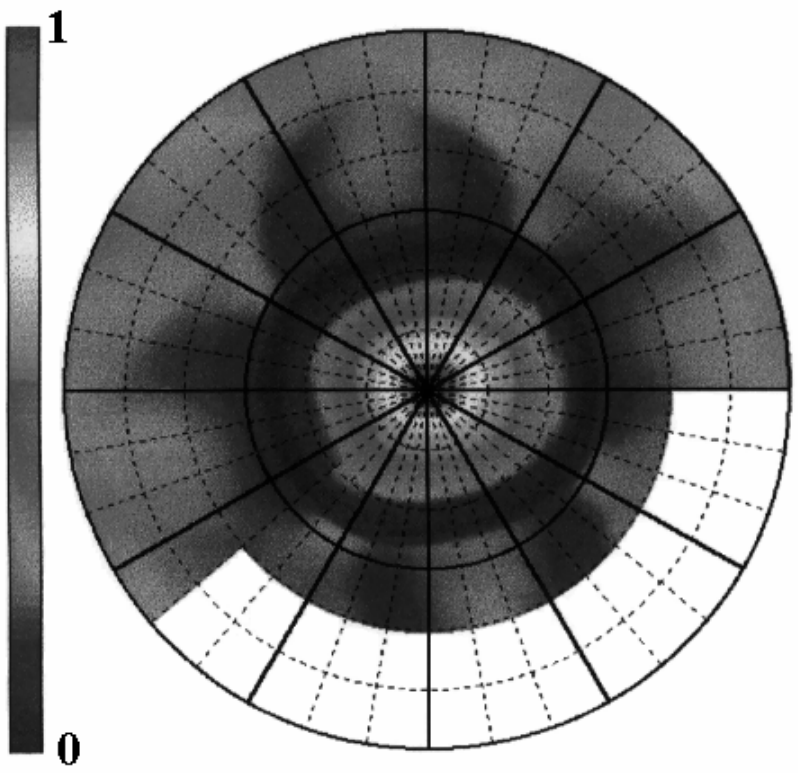

Fig. XI.C_5: ***Experimental ultrasonic polar scan on a FR4 plate after fatigue damage. Note that the inner dark ring has moved outward if compared with Fig. XI.C_ 4 and also that the closed brackets of Fig. XI.C_4 have opened. The amplitude is normalized.***

NUMERICAL SIMULATIONS

When sound is incident on a fiber reinforced laminate, there will be some scattering on the individual fibers. In some cases this is dramatic, especially when thick fibers or high frequencies are involved. For a FR4 composite, 5MHz is more or less the limit before this scattering becomes very important. At 5MHz, the scattering is not dramatic and does not change the influence of the overall stiffness parameters that determine the position of the 'dark rings' in polar scans. As can be seen in Ref [6], scattering on individual fibers mainly causes some deviations in the amplitude at normal incidence. These considerations result in a justification to apply an approach where the material properties are considered to be homogeneous throughout the plate. The theory that deals with this situation can be found for example to a large extent in the work of Nayfeh [7]. It is based on the plane wave solution of the equation of motion, the stress-strain relation for orthotropic materials, Snell's law combined with Christoffel's equation for revealing the possible values of the wave vector and the continuity conditions for normal stress and normal displacement along the water/solid interface. The sound field in the solid is then written as a linear combination of each possible plane wave inside the plate (6 in number), while the sound field in each liquid side is just one single plane wave solution. The continuity conditions are then represented by a linear matrix equation that can be solved by means of matrix inversion in order to find the complex amplitude of each plane wave that constitutes the sound field.

Besides the thickness, we do not know the exact values of the material parameters of the FR4 laminate that is investigated here. Therefore, we have applied numbers that are generally accepted as being reasonable numbers for this material. The values are found in Table XI.C_I, where symbols E denote Young's moduli, ν indicate the Poisson coefficients and G represent shear moduli.

Table XI.C_I: ***material properties used in the numerical simulations***

$\rho = 1925kg/m^3$		
$E_{11} = 20030(k-0.15i)MPa$	$E_{22} = 22630(k-0.15i)MPa$	$E_{33} = 8628(k-0.005i)MPa$
$\nu_{23} = 0.5(m-0.005i)$	$\nu_{13} = 0.5(m-0.005i)$	$\nu_{12} = 0.1793(m-0.08i)$
$G_{23} = 3930(k-0.04i)MPa$	$G_{13} = 3930(k-0.04i)MPa$	$G_{12} = 4781(k-0.15i)MPa$
before fatigue: k=1, m=1		
after fatigue: k=0.75, m=0.35		

The numerical simulation of an ultrasonic polar scan before fatigue damage is shown in Fig. XI.C_6.

There is of course no perfect similarity between Fig. XI.C_6 and Fig. XI.C_4, however the basic structure is the same and so is approximately the position of the dark ring that is caused by quasi longitudinal waves. In order to perform a simulation after fatigue damage, we have applied general features of fatigue damage that have recently been published [8-15]. These papers indicate that the E and G moduli tend to k=60% and that the Poisson coefficients tend to m=25% of their original values at the time that fracture occurs due to fatigue damage. Since the polar scan of Fig. XI.C_5 corresponds to severe fatigue damage, but not to the amount that causes fracture, we have entered k=75% and m=35% in the simulation that is shown in Fig. XI.C_7. Analysis of Figs XI.C_6-7 reveals that the dark ring moves form 23.25^0 to 24.88^0, which is in qualitative and more or less quantitative agreement with the experiments. It is also seen that the other patterns that are similar to brackets, tend to 'open' after fatigue damage. This is also in agreement with the experiments, where it is seen that before damage (Fig. XI.C_4), the 'brackets' are so closely situated to each other that they appear as closed circles, a phenomenon that disappears after fatigue damage (Fig. XI.C_5).

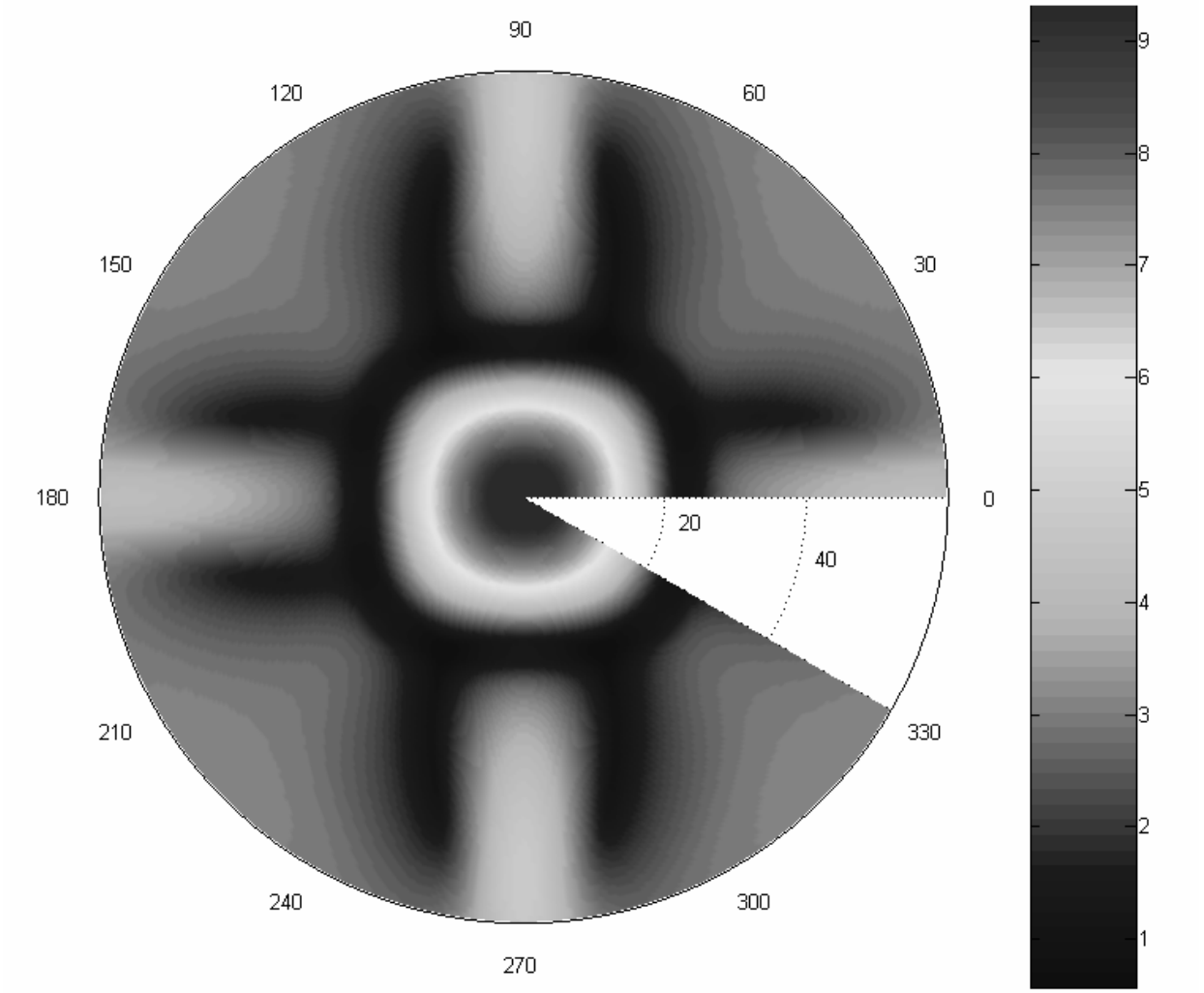

Fig. XI.C_6: ***simulation of ultrasonic polar scan on a FR4 plate before fatigue damage. The amplitude is given in exact numbers.***

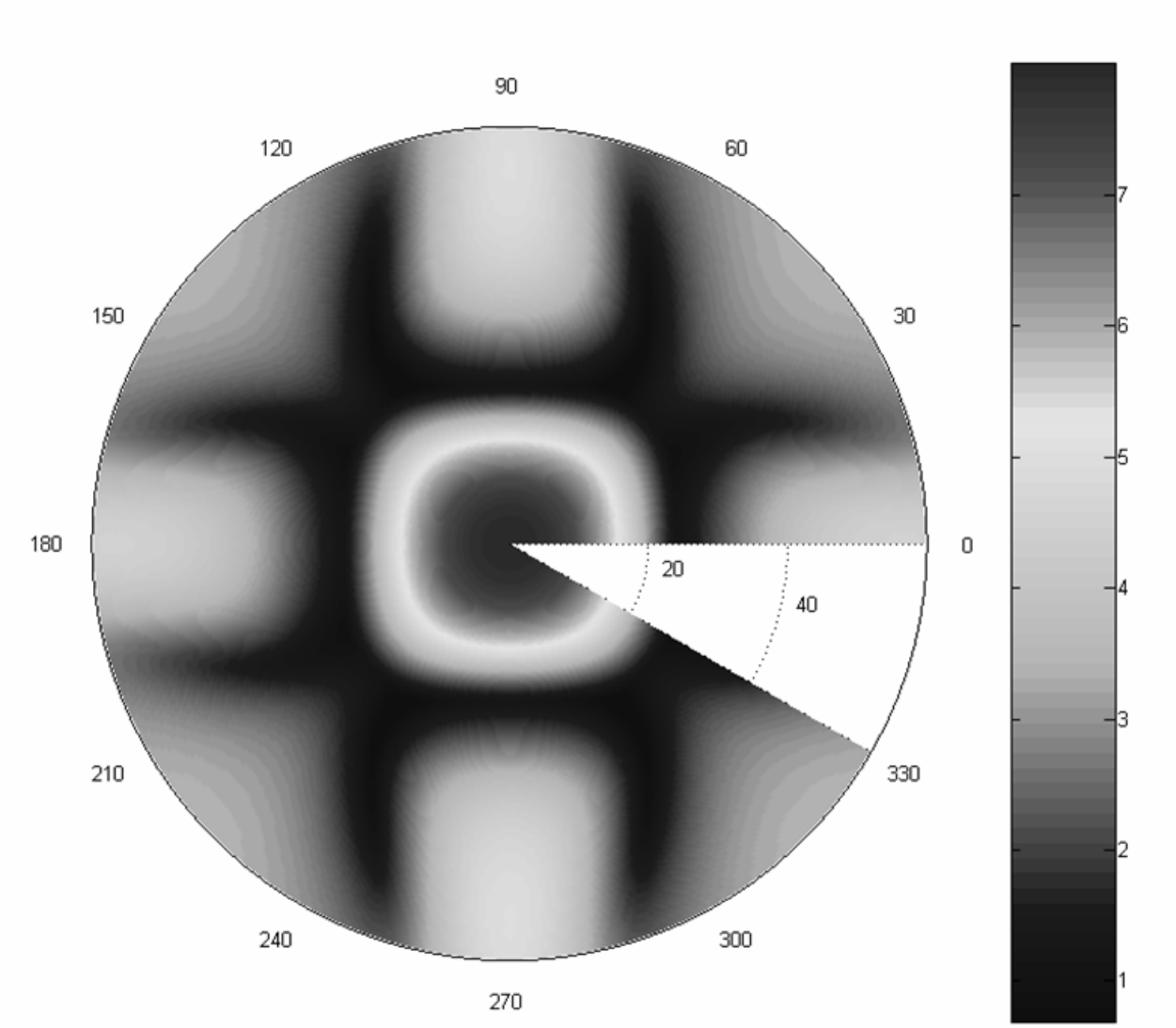

Fig. XI.C_7: ***simulation of ultrasonic polar scan on a FR4 plate after fatigue damage. The amplitude is given in exact numbers. It is seen that the inner dark ring has been shifted outward from 23.25^0 to 24.88^0 if compared with Fig. XI.C_6 and that the 'brackets-patterns' of Fig. XI.C_6 have opened more.***

CONCLUSIONS

It is shown by means of experiments and numerical simulations that ultrasonic polar scans are a possible tool to reveal fatigue damage. The simulations are in reasonable agreement with the experiments, and so is the evolution of the patterns in a polar scan due to fatigue damage. In the science and technology of composites, it is often desirable to measure the stiffness degradation of composites due to fatigue in order to verify physical micro-models for this phenomenon. Most often, destructive methods are used for that purpose, and frequently it is impossible to measure the out of plane properties. Ultrasonic polar scans may be an excellent tool for that purpose with the extra advantage that it is a nondestructive technique whence each measured sample (or part of a construction) might continue its life without destructive interruption.

REFERENCES

[1] W. H. M. Van Dreumel, J. L. Speijer, "Nondestructive Composite Laminate Characterization by Means of Ultrasonic Polar Scan", Materials Evaluation, 39(10), 922-925, 1981

[2] J. Degrieck, D. Van Leeuwen, "Simulatie van een Ultrasone Polaire Scan van een Orthotrope Plaat", Proceedings of "The 3rd Belgian National Congres on Theoretical and Applied Mechanics", Liege University, 39-42, 1994 (in Dutch)

[3] J. Degrieck, "Some possibilities of nondestructive characterization of composite plates by means of ultrasonic polar scan", Non Destructive Testing, Van Hemelrijck & Anastassopoulos (eds), Balkema, Rotterdam, 225-236, 1996

[4] Nico F. Declercq, Joris Degrieck, Oswald Leroy, "Characterization of Layered Orthotropic Materials Using Ultrasonic Polar Scans", Proceedings of the 2nd FTW PhD symposium, Ghent University, 2001

[5] Nico F. Declercq, Joris Degrieck, Oswald Leroy, "Numerical Simulations of Ultrasonic Polar Scans on Single Layered Fiber Reinforced Composites", proceedings of DAGA'03, 18-20 March 2003, Aachen, Germany.

[6] Joris Degrieck, Nico F. Declercq, Oswald Leroy, "Ultrasonic Polar Scans as a possible means of nondestructive testing and characterization of composite plates", Insight - The Journal of The British Institute of Non-Destructive Testing, 45(3), 2003.

[7] Adnan H. Nayfeh, *wave propagation in layered anisotropic media with applications to composites,* North-Holland, Elsevier, 1995

[8] Shun-ichi Bandoh, Kenji Matsumura, "On the Detection of Fatigue Damage in CFRP by measuring Poisson's Ratio", Hui, D. (ed.). Eighth International Conference on Composites Engineering (ICCE/8). Proceedings. Tenerife, Spain, 5-11 August 2001, pp. 55-56.

[9] Assa Rotem, "Stiffness Change of a Graphite Epoxy Laminate Under Reverse Fatigue Loading", Journal of Composites Technology & Research, 11(2), 59-64, 1989

[10] F. Gao, L. Boniface, S. L. Ogin, P.A. Smith, R.P. Greaves, "Damage accumulation in woven-fabric CFRP laminates under tensile loading: Part1. Observations of damage accumulation", Composites Science and Technology 59, 123-136, 1999

[11] F. Gao, L. Boniface, S. L. Ogin, P.A. Smith, R.P. Greaves, "Damage accumulation in woven-fabric CFRP laminates under tensile loading: 2. Modeling the effect of damage on macro-mechanical properties", Composites Science and Technology 59, 123-136, 1999

[12] R. Joffe, J. Varna, "Analytical modeling of stiffness reduction in symmetric and balanced laminates due to cracks in 90^0 layers", Composites Science and Technology 59, 1641-1652, 1999

[13] J. Varna, R. Joffe, N. V. Akshantala, R. Talreja, "Damage in composite laminates with off-axis plies", Composites Science and Technology 59, 2139-2147, 1999

[14] Ramesh Talreja, Selim Yalvac, Larry D. Yats, Derrick G. Wetters, "Transverse Cracking and Stiffness Reduction in Cross Ply Laminates of Different Matrix Toughness", Journal of Composite Materials, 26(11), 1644-1663, 1992

[15] R. J. Nuismer, S. C. Tan, "Constitutive Relations of a Cracked Composite Lamina", Journal of Composite Materials, 22, 306-321, 1988

XI.D A Numerical Study on the Feasibility of Visualization of Stress in Isotropic Plates by means of the Reflected Amplitude of Harmonic Ultrasonic Waves

It is well known that isotropic plates commonly possess residual stress which is frequently caused by manufacturing failures, which are often unavoidable. For some industries, it is highly important to be able to detect and characterize such unwanted effects. Furthermore, in engineering, it is often desirable to be able to measure the distribution of applied stress in structures. The present section describes a possible tool for that purpose. In advance of elaborated experiments that are possibly going to be performed at our lab the coming years, a numerical simulation is shown that reveals the influence of stress on the amplitude of sound reflected from plates that are isotropic in nature, but became anisotropic because of stress.

INTRODUCTION

During manufacturing, it often happens that residual stress enters the material. A famous example is the case of rolled steel plates. Also in processes where fast cooling occurs, due to the inhomogeneity of the materials and/or due to the difference in cooling rate at different spots in the material, residual stress is introduced. Of equal importance is the presence of applied stress in materials that are mounted in a construction. It is known that the presence of stress of any kind may have serious consequences on the behavior of that material and will certainly affect the remaining lifetime. It is therefore often of vital importance that the present stress can be detected or estimated by means of nondestructive testing. Several techniques exist to detect stress of which the use of ultrasound is very famous [1].

Because techniques that make use of a drilled hole [2-3] in the plate under investigation cannot be fully called nondestructive, we focus our survey on other techniques.

It is widely known that stress influences the stiffness of a material [4], whence it is reasonable that this stiffness change will affect results of vibration measurements [5-6]. The change in stiffness also influences the velocity of waves. However, if one needs to perform direct measurements of velocity changes, relatively large distances will be involved whence it is impossible to extract information on local stress variations. This problem can be resolved by applying phase measurements and can be found in the literature [7]. Nevertheless, most often, phase measurements are not very practical and require specialized equipment.

Perhaps the far most wonderful method to visualize stress in laminates has been introduced by Eva Drescher-Krasicka [8]. Her method consists of measuring amplitudes of reflected pulses originated from a focused normal incident pulse and separated from each other in time because of velocity differences of different bulk propagation modes (shear, longitudinal). Her method enables investigation of local stress variations in a microscopic manner. However,

separation of the pulses cannot occur if the thickness is too small or if one doesn't have the specialized microscopy apparatus. Besides, her method works best for large frequencies (>10MHz), whence the method becomes vulnerable to effects caused by small material inhomogeneities such as granula, micro cracks, …

Some reports [9-10] can be found that study the susceptibility of critical bulk waves for stress, but do not mention the situation for plates and do not mention the appearance of anisotropy due to stress.

Since the work of Cauchy [11], there have been many attempts to measure and to theoretically understand the influence of stress in the interaction of ultrasound with isotropic materials. Most of these attempts apply a more or less heuristic approach where the wave velocity is decomposed into its value in the unstressed case and an additional (positive or negative) number due to stress. The latter is then written as a linear combination of the components of the applied stress tensor. The linearity coefficients are then called acousto-elastic coefficients. The use of this approach is found in many papers [12-28], including the one of Ditri [10], where it is shown, using this heuristic approach, that the influence of stress can be visualized as very small changes in the bulk critical angles.

The present paper follows a more physical approach and focuses on the case of plates where Lamb waves play an important role.

Other authors describe methods based on critical phenomena such as Rayleigh waves. It is known that the velocity and the properties of Rayleigh waves is influenced by stress [29-30]. Nevertheless Rayleigh waves do not penetrate deep into the bulk of a material and can therefore only be applied in situations where surface stress needs to be determined. Furthermore, Rayleigh waves cannot be stimulated on relatively thin plates.

In the case of plates, it has been shown by several authors [31-32] that Lamb waves are also influenced by stress. A detailed study for very thin laminates can be found where it is shown that the lowest velocity Lamb waves are highly influenced by the presence of (very high) stress. In that study, the fact that isotropic materials become slightly anisotropic in the presence of stress is not studied and results for a more general kind of lamb waves for thicker plates are not mentioned. It is our aim to study the influence of stress on Lamb waves using a theoretical method that is more general than the one of ref [31]for very thin plates (foils). However, the latter paper mentions a technique which is contactless and is therefore very valuable for several applications.

In reference [33], a theoretical treatment is formulated in the case of incompressible materials. Though since all materials are actually compressible, we have opted for an approach which can be found in papers of Degtyar and Rokhlin [34-36]. They build a theory that describes the propagation of sound in stressed anisotropic materials, based on the approach of Man and Lu [37] that is valid for both residual stress and applied stress. Furthermore, Degtyar and Rokhlin show that, in order to describe the interaction of sound with stressed materials, the presence of stress must explicitly be considered in the continuity conditions at interfaces, which therefore differ from non-stressed systems [38]. The importance of their paper should not be underestimated. However, their study is limited to single interfaces and therefore does not explicitly span the interaction of sound with plates.

The current section XI.D applies the findings of Degtyar and Rokhlin [36] and studies the possibility of visualizing changes in material properties in the presence of stress by means of numerical simulations of the reflection of sound on stressed plates immersed in water. First, the theory of the propagation of plane waves in stressed materials is briefly described. Then the

continuity conditions are shown. Finally some numerical examples are shown for harmonic plane waves.

WAVES IN STRESSED ANISOTROPIC MATERIALS

For this situation, the constitutive equation relating stress and strain is given by [36]

$$\sigma_{ij} = \sigma_{ij}^0 + c_{ijkl}\varepsilon_{kl} + \frac{\partial u_i}{\partial r_k}\sigma_{kj}^0 \qquad \text{(XI.D\_1)}$$

where σ_{ij} is the first Piola-Kirchhoff stress tensor, σ_{ij}^0 is the initial static stress, ε_{kl} is the elastic deformation due to wave propagation, $\mathbf{u}$ is the particle displacement and c_{ijkl} is the fourth order stiffness tensor [36] which is dependent on the initial stress.
The linear equation of motion then becomes

$$\left(c_{ijkl} + \sigma_{jl}^0\delta_{ik}\right)\frac{\partial^2 u_k}{\partial r_j \partial r_l} = \rho\frac{\partial^2 u_i}{\partial t^2} \qquad \text{(XI.D\_2)}$$

Even the density ρ depends on the initial stress. However, this is taken into account in the stress dependent elastic constants. The calculation of these constants can be found in Degtyar and Rokhlin [34-36]. If plane waves

$$u_k = AP_k \exp iK\left(\mathbf{n}\bullet\mathbf{r} - V_p t\right) \qquad \text{(XI.D\_3)}$$

are a solution of (XI.D_2), the Christoffel equation is then given by [36]

$$\left[c_{ijkl}n_i n_l + \left(\sigma_{il}^0 n_i n_l - \rho V_p^2\right)\delta_{jk}\right]P_k = 0 \qquad \text{(XI.D\_4)}$$

where A is the amplitude, $\mathbf{P}$ is the unit displacement vector, $\mathbf{K} = K\mathbf{n} = \left(\omega / V_p\right)\mathbf{n}$ is the wave vector, V_p is the wave velocity, $\mathbf{n}$ is the wave normal, and $\mathbf{r}$ is the position vector. It can be shown that, just as in the case of unstressed anisotropic media, there are maximum 6 independent velocity solutions of equation (XI.D_4). In the case where the symmetry is not triclinic, but monoclinic or higher, there are actually only 3 independent solutions in the sense that the solutions can be split in two equivalent sets, i.e. a set of 3 up going waves and a set of 3 down going waves having equal velocity compared with the up going ones.

CONTINUITY CONDITIONS FOR A PLANE STRESSED INTERFACE

First of all, it is required that Snell's law holds at the interfaces. This means that the wave vector components along the interface remain constant which results in the fact that equation (XI.D_4) can be rewritten in a form where not just the velocities are found, but the wave vector components perpendicular to the interface, given the components along the interface.
Furthermore, for a liquid/solid interface, one demands continuity of normal displacement. In addition, continuity of normal stress must be invoked. The latter condition must also reckon with the initial stress. Hence one demands continuity of

$$\sigma_{i3} = c_{i3kl}\varepsilon_{kl} + \frac{\partial u_i}{\partial r_k}\sigma^0_{k3} \qquad \text{(XI.D\_5)}$$

It is shown by Degtyar and Rokhlin [34-36] that if the last term in (XI.D_5) is neglected, that the calculated results can only be approximations of the exact situation, especially around critical angles. The continuity conditions and the fact that the maximum number of independent solutions inside the stressed plate is 6 and 1 in each liquid medium, results in 8 equations and 8 unknown complex amplitudes. The 8 unknown amplitudes are then simply found from inversion of the continuity matrix.

NUMERICAL EXAMPLES

In what follows, ultrasound impinges a single layer of isotropic Titanium. The frequency is 6 MHz, the plate thickness is 1mm and is swamped in water of density 1000kg/m^3 and wave velocity of 1480m/s. The properties of Titanium [3] are 97 GPa for Young's modulus, 0.33 for Poisson's ratio and 4507 kg/m^3 for the density. The so called third order elastic constants that are needed in ref [36] to calculate the stress dependent elastic constants, are $C_{111} = -1358\,\text{GPa}$, $C_{112} = -1105$ Gpa and $C_{123} = -162\,\text{GPa}$. We apply different angles of incidence and we plot for each angle of incidence the reflected amplitude for plane waves. In these plots, the radius corresponds to the azimuthal angle in degrees, while the polar angle corresponds to the polar angle in degrees. Since residual stress can be present in many forms, we limit ourselves to two examples of (applied) stress in one direction at a time.

In Figs XI.D_1-3, the difference is shown for increasing stress in the x-direction, i.e. determined by a polar angle of 0^0.

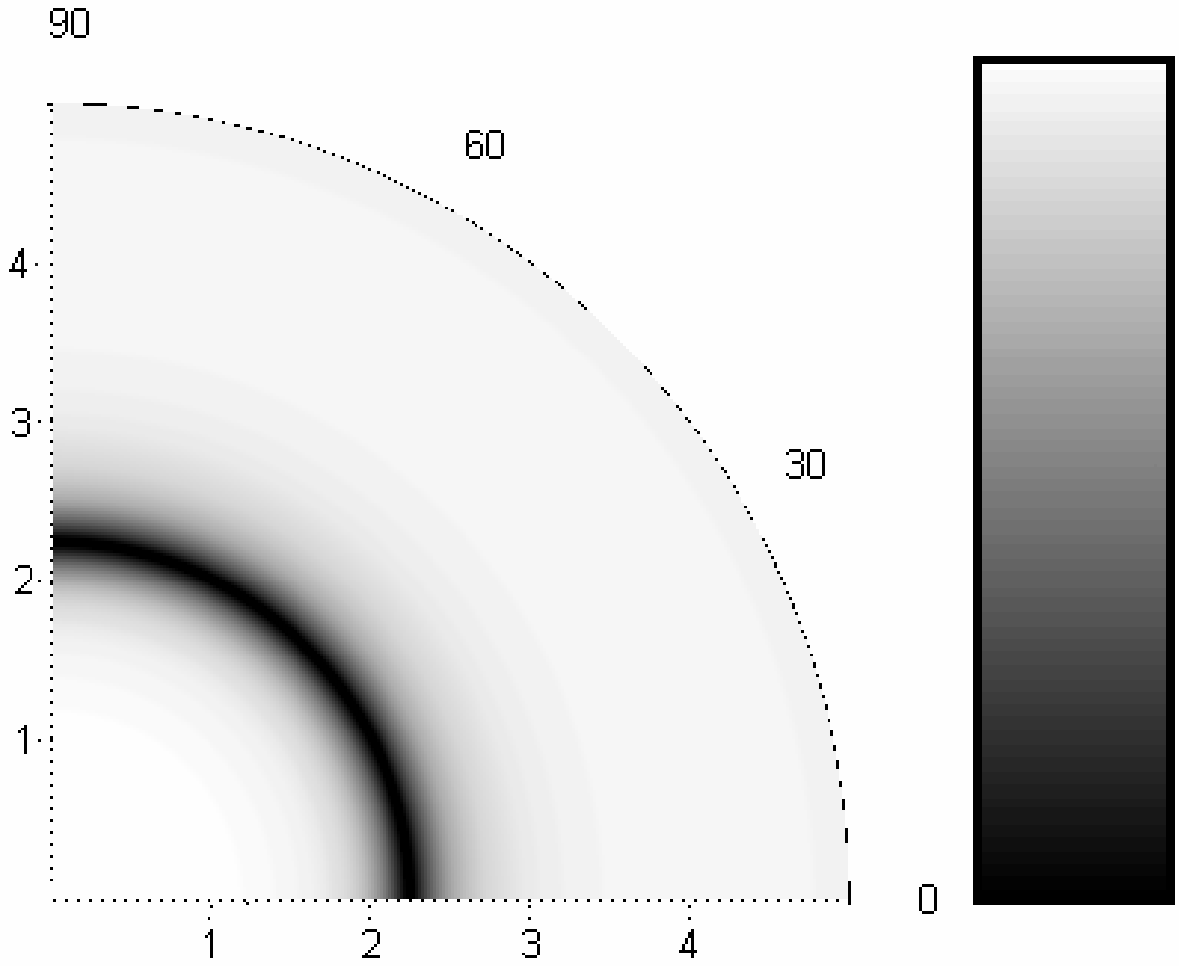

Fig. XI.D_1: ***Reflected amplitude for $\sigma_{11}=10^5$ Pa. The dark ring corresponds to the fastest Lamb wave for the given specimen.***

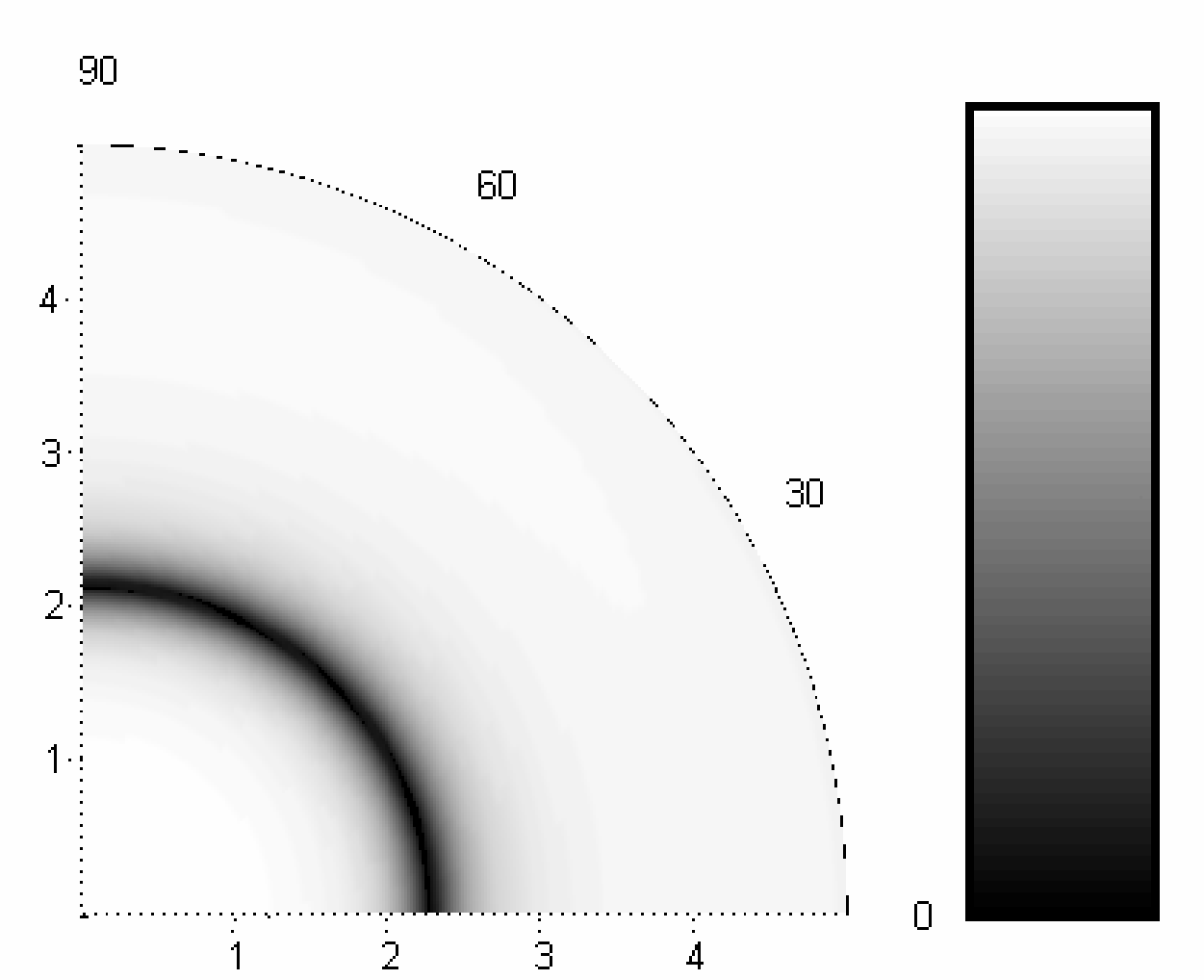

Fig. XI.D_2: ***Reflected amplitude for σ_{11}=10^8 Pa. The dark ring is now anisotropically deformed if compared with Fig. XI.D_1.***

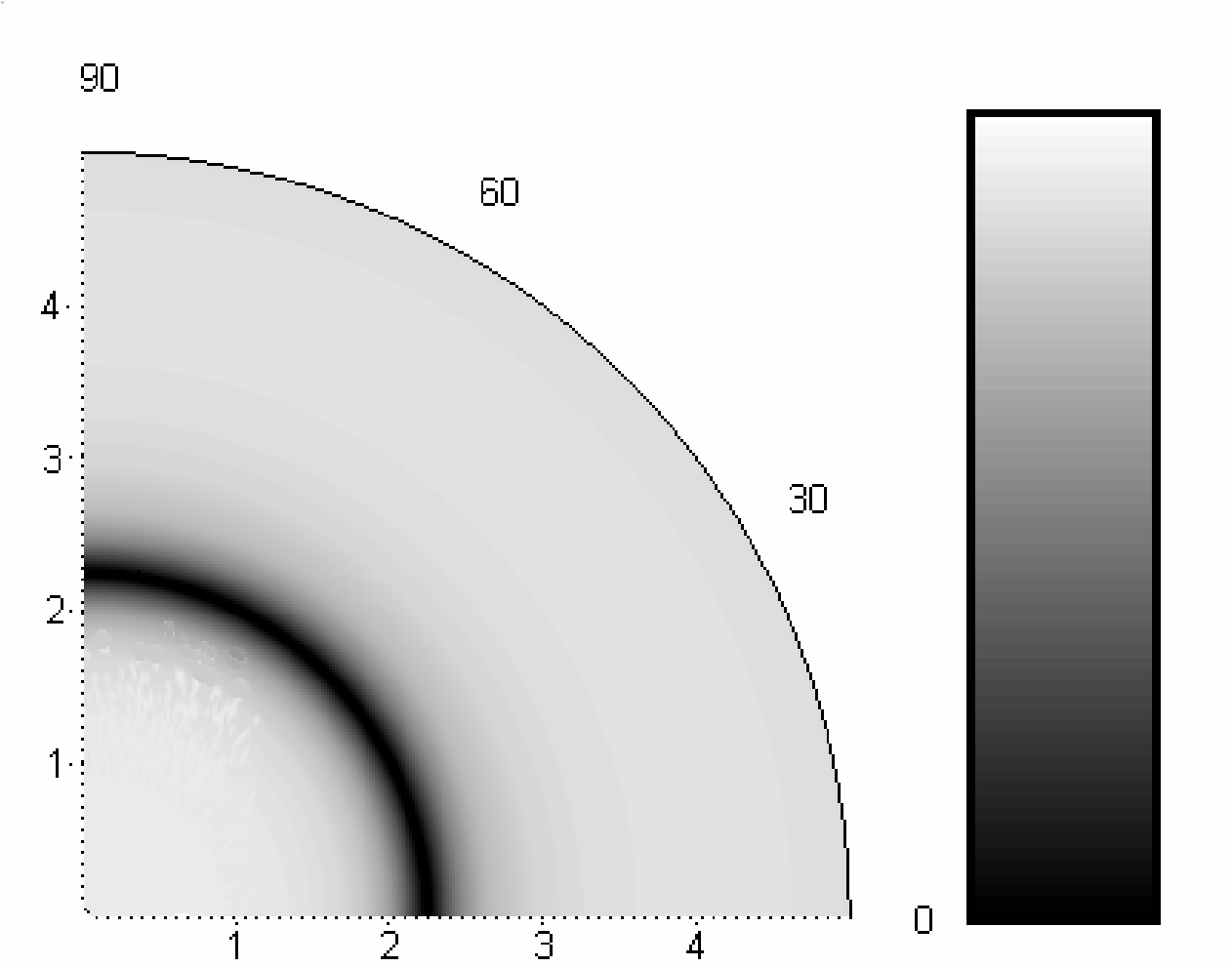

Fig XI.D_3: ***Reflected amplitude for σ_{33} =10^6 Pa. The dark ring is now isotropically deformed if compared with Fig. XI.D_1.***

It is noticed that for increasing stress, the fastest generated Lamb wave (corresponding to the smallest azimuthal angle, approx 2^0, which is the case that we wish to highlight) corresponds to a ring of amplitude dip, which obtains a larger radius in the direction of increased stress (x-direction) and a smaller radius in the perpendicular direction (y-direction). This already shows the appearance of anisotropy due to applied stress. It is for that reason that even in the case of isotropic materials, the theory for anisotropic materials must be considered.

The exact critical angle values of the fastest Lamb wave are listed in Table XI.D_I, together with the angle difference, for the case of σ_{11}=10^5 Pa and σ_{11}=10^8 Pa as in Figs XI.D_1-2.

In Figs XI.D_4-5, the normal stress (normal pressure) σ_{33} is increased. It is seen that the material remains isotropic and that the dark circle which corresponds to the fastest Lamb mode, becomes wider in radius for increased normal stress. The different values of the calculated lamb angles are tabulated in Table XI.D_II.

Table XI.D_I: ***Lamb angles of the fastest Lamb mode as a function of different values of applied stress in the x-direction***

	Lamb angle	
	x-direction	y-direction
$\sigma_{11}=10^5$ Pa	2.2326	2.2512
$\sigma_{11}=10^8$ Pa	2.2698	2.1581
difference	0.0372	-0.0931

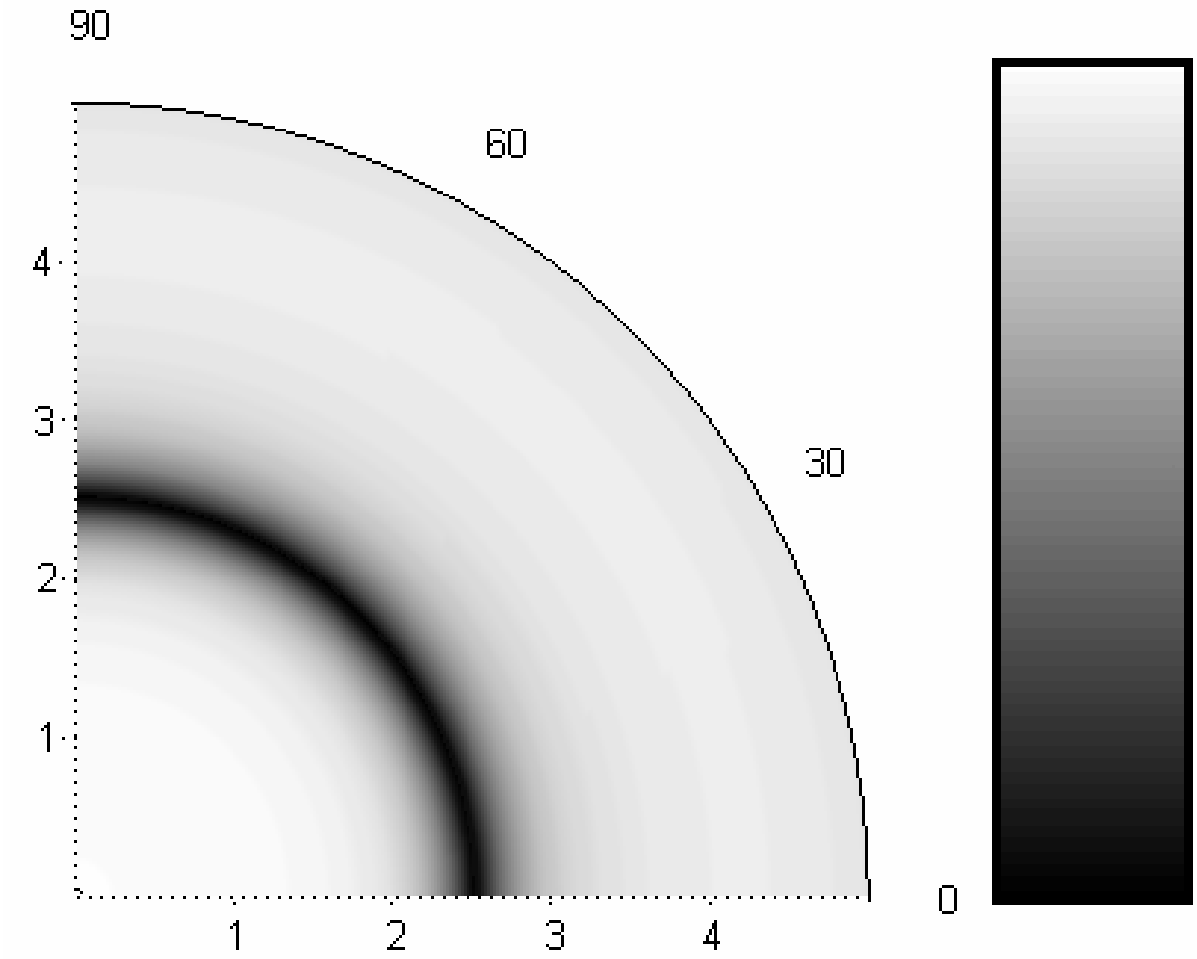

Fig XI.D_4: ***Reflected amplitude for $\sigma_{33}=10^8$ Pa. The isotropic deformation of the dark ring has increased compared to Fig. XI.D_3.***

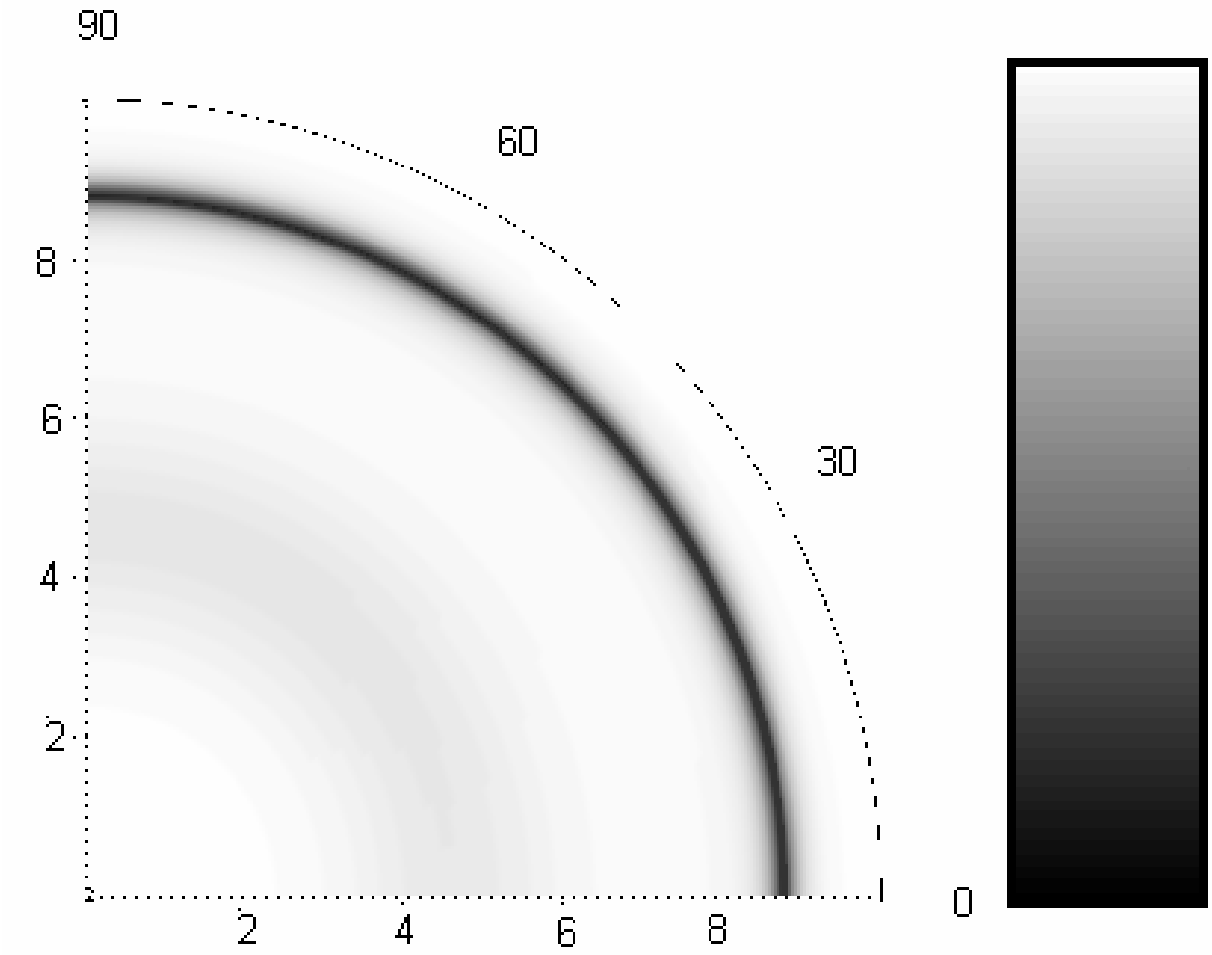

Fig XI.D_5: ***Reflected amplitude for σ_{33} =10^9 Pa. The isotropic deformation of the dark ring has increased compared to Figs XI.D_3-4.***

Table XI.D_II: ***Lamb angles of the fastest Lamb mode as a function of different values of applied stress in the z-direction***

	$\sigma_{33}=10^6$ Pa	$\sigma_{33}=10^8$ Pa	$\sigma_{33}=10^9$ Pa
Lamb angle	2.2326	2.5116	8.7950

It is noticed that the angles are much more susceptible to normal stress than to in-plane stress if compared with the values of Table XI.D_I. It is also noticed that the increase in angle is certainly not linearly related to the increase of pressure. Therefore it is shown that full simulations need to be performed (as is presented in this section) instead of heuristic modeling.

CONCLUDING REMARKS

It is shown, by means of exact numerical simulations, that multi-angle inspection of an isotropic titanium laminate reveals the presence of stress and also reveals anisotropy induced by stress. Therefore multi-angle incidence measurements may become a useful technique to characterize stress in isotropic laminates. In this section, the attention was focused on the fastest Lamb wave in order to show that not just the slowest Lamb mode is fairly sensible to stress as could be interpreted from [31]. It is also shown that the susceptibility of Lamb angles to stress, depends on the direction of the stress and is not linearly related to its magnitude.

REFERENCES

[1] Handbook on experimental Mechanics, edited by A. Kobayashi (SEM, New York, 1993)

[2] Method for characterizing residual stress in metals , Loren A. Jacobson, J. Acoust. Soc. Am. **113**, 2955 (2003)

[3] Measuring residual stresses in a steelpan, Andres Peekna and Thomas D. Rossing, J. Acoust. Soc. Am. **109**, 2483 (2001)

[4] R. Bruce Thompson, S. S. Lee, J. F. Smith, "Angular dependence of ultrasonic wave propagation in a stressed orthorhombic continuum: Theory and application to the measurement of stress and texture", J. Acoust. Soc. Am. 80(3),921-931 (1986)

[5] Vesna Damljanovic and Richard L. Weaver , "A vibration technique for measuring railroad rail stress", J. Acoust. Soc. Am. **112**, 2247 (2002)

[6] Vesna Damljanovic and Richard L. Weaver , "Towards a laser-vibrometry technique for measuring railroad rail stress", J. Acoust. Soc. Am. **113**, 2310 (2003)

[7] Masaru Kato, Takuso Sato, Keisuke Kameyama, and Hideyuki Ninoyu, "Estimation of the stress distribution in metal using nonlinear acoustoelasticity", J. Acoust. Soc. Am. 98(3), 1496-1504 (1995)

[8] Eva Drescher-Krasicka, "Scanning acoustic imaging of stress in the interior of solid materials", J. Acoust. Soc. Am. 94(1), 453-464 (1993)

[9] Stress measurement using critically refracted longitudinal waves, Don E. Bray, J. Acoust. Soc. Am. **108**, 2594 (2000)

[10] John j. Ditri, "On the measurement of residual stress through changes in critical angle", J. Acoust. Soc. Am. 102(2), 921-925 (1997)

[11] A. L. Cauchy, "De la pression ou tension dans un systeme de points materiels", Exer. Math. 3, 213 (1828)

[12] J. Deputat, "Application of the acoustoelastic effect in measurements of residual stresses", Arch. Acoust. 15(1-2), 69-92 (1990)

[13] J. J. Ditri and D. hongerholt, "Stress Distribution Determination in Isotropic Materials via Inversion of Ultrasonic Rayleigh Wave Dispersion Data", Int. J. Solids Struct. 33(17), 2437-2451 (1996)

[14] M. Hayes and R. S. Rivlin, "Propagation of a Plane Wave in an Isotropic elastic Material Subjected to Pure Homogeneous Deformation", Arch. Ration. Mech. Anal. 8(15), 15-22 (1961)

[15] M. Hayes and R. S. Rivlin, "Surface Waves in Deformed Elastic Materials", Arch. Ration. Mech. Anal. 8, 358-380 (1961)
[16] M. Hirao, H. Fukuoka, and K. Hori, "Acoustoelastic Effect of Rayleigh Surface Wave in Isotropic Material", J. Apll. Mech. 48, 119-124 (1981)
[17] M. Hirao, H. Fukuoka, Y. Murakami, "Resonance Acoustoelasticity Measurement of Stress in Thin Plates", Res. Nondestr. Eval. 4, 127-138 (1992)
[18] D. S. Hughes and J. L. Kelley, "Second-Order Elastic Deformation of Solids, "Phys. Rev. 92(5), 1145-1149 (1951)
[19] D. Husson and G. S. Kino, "A Perturbation Theory for Acoustoelastic Effects", J. Appl. Phys. 53(11)7250-7258 (1982)
[20] D. Husson, "A Perturbation Theory for the Acoustoelastic Effect of Surface Waves", J. Appl. Phys. 57(5), 1562-1568 (1985)
[21] T. D. Murnaghan, Finite Deformation of an Elastic Solid (Wiley, new York, 1951)
[22] R. W. Ogden and D. A. Sotiropoulos, "On Interfacial waves in Prestressed Layered Incompressible Elastic Solids, "Proc. R. Soc. London, Ser. A 450, 319-341 (1995)
[23] Y. H. Pao, W. Sachse and H. Fukuoka, "Acoustoelasticity and ultrasonic measurement of residual stress", in Physcial Acoustics, edited by W. P. Mason and R. N. Thurston (Academic, new york, 1984), Vol. 17, pp. 62-143
[24] D. A. Sotiropoulos and C. G. Sifiniotopoulos, "Interfacial Waves in Prestressed Incompressible Elastic Interlayers", J. mech. Phys. Solids 43(3), 365-387 (1995)
[25] T. Tokuoka and Y. Iwashimizu, "Acoustical Birefringence of ultrasonic Waves in Deformed Isotropic Elastic media", Int J. Solids Struct. 4, 383-389 (1968)
[26] R. A. Toupin and B. Bernstein, "Sound waves in deformed perfectly elastic materials. Acoustoelastic effect", J. Acoust. Soc. Am. 33, 216-225 (1961)
[27] A. Tverdokhlebov, "On the acoustoelastic effect," J. Acoust. Soc. Am. 73, 2006-2012 (1983)
[28] M. Obata, H. Shimada, and T. Mihara, "Stress Dependence of Leaky Surface Wave on PMMA by Line-focus-beam Acoustic Microscope", Exp. Mech. 34-39 (1990)
[29] B. G. Martin, "Theory of the effect of stress on ultrasonic plane-wave reflectivity from a water-metal interface", J. Acoust. Soc. Am. 65(6), 1380-1385 (1979)
[30] P. P. Delsanto, R. B. Mignogna, A.V. Clark, Jr, "Ultrasonic texture and stress measurements in anisotropic polycrystalline aggregates", J. Acoust. Soc. Am., 87(1), 215-224 (1990)
[31] C. Desmet, U. Kawald, A. Mourad, W. Lauriks, J. Thoen, "The behavior of Lamb waves in stressed polymer foils", J. Acoust. Soc. Am. 100(3), 1509-1513 (1996)
[32] Chi-Sing man, Wei-yang Lu, Qun Gu, Wenliang Tang, "Ultrasonic measurement of stress in weakly anisotropic thin sheets", J. Acoust. Soc. Am. 91(5), 2643-2653 (1992)
[33] J. L. Nowinski, "Reflection of acoustic waves at the interface of two highly stressed elastic half-space", J. Acoust. Soc. Am. 63(5), 1287-1291 (1978)
[34] A. D. Degtyar and S. I. Rokhlin, "Absolute stress determination in orthotropic materials from angular dependence of ultrasonic velocities", J. Appl. Phys, 78(3), 1547-1556 (1995)
[35] A. D. Degtyar, W. Huang, S. I. Rokhlin, "Wave propagation in stressed composites", J. Acoust. Soc. Am. 104(4), 2192-2199 (1998)
[36] A. D. Degtyar, S. I. Rokhlin, "Stress effect on boundary conditions and elastic wave propagation through and interface between anisotropic media", J. Acoust. Soc. Am. 104(4), 1992-2003 (1998)
[37] C.-S. Man and W. Y. Lu, "Towards an acoustoelastic theory for measurement of residual stress", J. Elast. 17, 159-182 (1987)
[38] Michel Castaings, Bernard Hosten, "Guided waves propagating in sandwich structures made of anisotropic, viscoelastic, composite materials", "J. Acoust. Soc. Am., 113(5), 2622-2634, 2003.

Chapter XII Sound in Piezoelectric Materials

A crystal is a solid material whose atoms are arranged in a definite pattern and whose surface regularity reflects its internal symmetry. Each of a crystal's millions of individual structural units contains all the substance's atoms, molecules, or ions in the same proportions as in its chemical formula. The cells are repeated in all directions to form a geometric pattern, manifested by the number and orientation of external planes (crystal faces). Crystals are classified into seven main crystallographic systems based on their symmetry: isotropic, trigonal, hexagonal, tetragonal, orthotropic, monoclinic, and triclinic. The picture on the left is a Quartz crystal. This crystal is one example of crystals whose mechanical behavior is connected to its electrical behavior and vice versa. The coupling effect is called 'the piezoelectric effect'. It was first observed by Paul-Jacques and Pierre Curie in 1880.

Just as any other student, during my education, I spent a major part of my valuable time on the study of algebra. A key fraction of this study was devoted to the group theory. It is a pity that somehow, one has never been able to explain to me what the significance of this theory was, besides a set of rules and axioms that suggested algebra being an intelligent 'game'. It was not until I intended to study the interaction of sound with composites, that I had to read a number of books dealing with point groups and symmetry operations and that I realized the importance of algebra and I started to enjoy the subject.

This is the reason why soon, I realized that I wanted to deal with crystals and examine more sophisticated properties of materials than solely their elasticity.

Piezoelectricity is one of the subjects that attracted me very quickly. It is the appearance of an electric field in certain nonconducting crystals as a result of the application of mechanical pressure. Pressure polarizes some crystals, such as quartz, by slightly separating the centers of positive and negative charge. The resultant electric field is detectable as a voltage. The converse effect also occurs: an applied electric field produces mechanical deformation in the crystal. Using this effect, a high-frequency alternating electric current can be converted to an ultrasonic wave of the same frequency, while a mechanical vibration, such as sound, can be converted into a corresponding electrical signal. Piezoelectricity is utilized in microphones, phonograph pickups, and telephone communications systems.

In ultrasonics, the device that transforms an electric signal into a sonic signal (and vice versa), is called 'a transducer'. Transducers were first applied for sonar systems, initially by the military, later by ocean liners, fishing vessels, cargo ships and submarines for underwater archeology.

Sonar, invented by Paul Langevin, was first used to detect submarines in 1916, this was 4 years too late for the Titanic and many other ships that sunk after encountering icebergs or other underwater obstacles. Nevertheless, the number of lives that have been saved by sonar after 1916 is overwhelming compared to the dramatic loss of the Titanic.

Anisotropy formed the core of Chapter XI. For sound waves, anisotropy of a certain media, means that its velocity and polarization depend on the direction of propagation. It also means that for most directions of propagation, the direction of phase propagation differs from that of energy propagation. To some extent, this is comparable to a sailing boat, steering in one direction, but being drifted in another course. Also, for a given direction in an anisotropic media, there are in general three sound velocities possible, comparable to the effect of birefringence in optics.

Section XII.A of this chapter describes the influence of piezoelectricity on the different modes of wave propagation. This section must be considered as an introductory section, because it describes the stiffening effect, which is well known. Nevertheless, the stiffening effect is presented graphically in a manner that I have not found in any book or paper dealing with piezoelectricity.

In Chapter IV, the concept of inhomogeneous waves was highlighted and further studied. So far, not a single researcher has ever studied the propagation of inhomogeneous waves in piezoelectric crystals. Therefore, in section XII.B.1, the concept of inhomogeneous waves is introduced in piezoelectric crystals.

Acousto-Optics is the interaction of light with sound. The Acousto-Optic effect was first observed in 1932 by Lucas, Biquard, Debije and Sears. The effect became extremely important after the invention of laser light by Theodore Maiman in 1960, and found its way in electronic communication systems and other fields of interest, very rapidly. Because of its importance in Acousto-Optics, the crystal of Paratellurite is central in section XII.B.2. This study is performed after fruitful discussions with Nataliya V. Polikarpova and Vitaly B. Voloshinov during a conference in Poland.

Robert Ballard and his research team discovered the wreck of the Titanic in 1986. Since then, submarines have frequently been used in underwater archaeology. For that purpose, the use of sonar systems is central. Because of the huge underwater pressure that is often encountered in underwater archaeology, the subject of the behavior of piezoelectric crystals under bias stress, is very important.

Special attention will be drawn on the behavior of inhomogeneous waves in this crystal.

In a television documentary in the second half of the 1980's, the discovery of the wreck of the Titanic by Robert Ballard, was shown. It was mentioned that the presence of extreme pressure at the depth of the wreck, was a difficult problem to deal with. Because I was still a child, my perception of the problem was rather simplistic and I thought that if the problem was just that the water wanted to enter the submarine, that it would probably be better to let it enter and obtain a stable situations instead of a vessel being crushed by that immense external pressure. Actually, this was not such a stupid idea, if only the electronic devices within the vessel would be submergible. Much later, when studying the effect of stress in plates on the propagation of sound (Chapter XI), I realized that the elimination of pressure by anti-pressure, was only realizable on a macroscopic scale. On a microscopic scale, it is not possible to let water enter metals and crystals in order to form this anti-pressure. This problem made me curious and made me realize that pressure does not only have a relative effect on vessels, but has an absolute influence on atomic lattices, such as piezoelectric crystals. Furthermore, submarines as they have been used by Robert Ballard to examine the seafloor, make use of sonar systems that consist of piezoelectric crystals. Therefore the study of the effect of pressure on such crystals, is not really unfounded.

In Chapter XI, the concept of stress in plates was introduced. It was based on a study by Degtyar and Rokhlin and involved an approach that was not immediately extendible to piezoelectric crystals. When screening the existing literature I could only find one paper dealing with piezoelectric crystals under pressure. However, only the effect on surface waves was examined and the paper showed some shortcomings that I wanted to avoid. Furthermore, the paper did not present the necessary symmetry relations of the higher order material constants and I could not find those relations anywhere else in the literature.

Therefore, I've chosen to deal with the problem from scratch. I decided to get in touch with Gérard A. Maugin. He recommended me to buy his book on Nonlinear Waves in Elastic Crystals. The book describes the basics of nonlinear effects in crystals and piezoelectric crystals and presents the basic expressions relating the energy of a crystal to field quantities. This book, together with the magnificent book by J. F. Nye (Physical Properties of Crystals) paved the way to build the necessary model to describe the propagation of sound in stressed piezoelectric crystals. I decided to follow the steps by Bertram A. Auld (for linear phenomena) in his famous book 'Acoustic Fields and Waves in Solids, Volumes I and II'. For reasons of completeness, I added to the theory an expression in the constitutive relation that was also used by Degtyar and Rokhlin (see section XI.D, for non-piezoelectric materials) in order to include plasticity as well. Nevertheless, this effect is only significant for extremely high pressures. It will be shown in section XII.C that the effect of stress on the slowness surfaces in piezoelectric crystals, results in graphical representations that sometimes look like an electron orbital in atoms. This is just a striking coincidence. Nevertheless, it is a reminder of the universality of the beauty of nature.

XII.A The effect of stiffening of crystals due to piezoelectricity

This section XII.A about 'stiffening' does not contain new results and is considered to be interesting background information. Nevertheless, in the literature, the stiffening effect itself, i.e. the change of the wave velocity due to the piezoelectric effect, has not been shown graphically. Also the representation of the change of polarization and the change of the energy flow due to the stiffening effect, cannot be found in any other published document. In what follows, changes of the slowness surface are represented by a new surface, whereas changes in the energy flow and in the polarization, are represented by arrows.

THEORETICAL DEVELOPMENT

For piezoelectric materials, the stress tensor [1-2] is given by

$$\sigma_{ij} = c_{ijkl} e_{kl} - \xi_{kij} E_k \tag{XII.A.1_1}$$

whereas the electrical displacement is given by

$$D_k = \varepsilon_{ki} E_i + \xi_{kij} e_{ij} \tag{XII.A.1_2}$$

where c_{ijkl} is the stiffness tensor, ξ_{kij} is the piezoelectric stress tensor, ε_{ij} is the dielectrical permittivity tensor, $\mathbf{E}$ is the electric field vector, $\mathbf{D}$ is the dielectric displacement vector and e_{kl} is the strain tensor.
For ultrasonic waves [1], the accompanying electric field is quasistatic and can be described by

$$\mathbf{E} = -\nabla\varphi \tag{XII.A.1_3}$$

with φ a scalar potential.
The acoustic wave equation for visco-elastic materials is given by

$$\frac{\partial \sigma_{ij}}{\partial r_j} = \rho \frac{\partial^2 u_i}{\partial t^2} \tag{XII.A.1_4}$$

whereas the electromagnetic field equations, in the absence of electric currents and electric loads are given by

$$\nabla \times \mathbf{E} = \mu_0 \frac{\partial \mathbf{H}}{\partial t} \tag{XII.A.1_5}$$

and

$$\nabla \times \mathbf{H} = \frac{\partial \mathbf{D}}{\partial t} \tag{XII.A.1_6}$$

Taking into account (XII.A.1_3), relations (XII.A.1_5-6) can be replaced by

$$\nabla \bullet \frac{\partial^2}{\partial t^2}\left(-\varepsilon_{ki} \frac{\partial \varphi}{\partial r_i} + \xi_{kij} \frac{\partial u_j}{\partial r_j} \right) = 0 \tag{XII.A.1_7}$$

If we consider plane waves, then

$$\mathbf{u} = A\mathbf{P} \exp i\left(k_x x + k_y y + k_z z - \omega t \right) \tag{XII.A.1_8}$$

and

$$\varphi = B \exp i\left(k_x x + k_y y + k_z z - \omega t \right) \tag{XII.A.1_9}$$

Then, relation (XII.A.1_7) immediately involves

$$B = \frac{k_r k_s \xi_{rsq} A P_q}{\varepsilon_{mn} k_m k_n} \tag{XII.A.1_10}$$

Furthermore, combining relations (XII.A.1_4) and (XII.A.1_7) delivers [1]

$$M_{ip} P_p = 0 \tag{XII.A.1_11}$$

Equation (XII.A.1_11) is the stiffened equation of Christoffel. Only nontrivial solutions $\mathbf{P} \neq 0$ are possible whenever

$$\det M = 0 \tag{XII.A.1_12}$$

The expressions of M_{ij} can be found in [1].
From [1] we know that the instantaneous Poynting vector, denoting the flow of energy, is given by

$$F_i = \frac{1}{2}\left[-\sigma_{ij} \frac{\partial u_j^+}{\partial t} + \varphi \frac{\partial D^+}{\partial t} \right] \qquad \text{(XII.A.1\_13)}$$

in which the superscript '+' means 'complex conjugate'. Relation (XII.A.1_13), becomes, for an amplitude equal to unity,

$$F_i = \frac{1}{2}\omega \left\{ \left(c_{ilkj} \right) k_k P_l^+ P_j + \left(B\left(\xi_{kij} k_k - \xi_{ijk}^+ k_k^+ \right) \right) P_j^+ + \varepsilon_{ij}^+ k_j^+ |B|^2 \right\} \qquad \text{(XII.A.1\_14)}$$

We begin the discourse with the slowness surface of the quasi shear horizontally polarized (QSH) mode in Lithium Niobate. The slowness value is the magnitude of the wave vector, divided by the angular frequency. The linear material properties of this crystal, can be found in ref [1]. First, we only consider the case where piezoelectricity is neglected. The slowness surface is formed by the slowness vectors for each possible direction of propagation. Therefore, each spot on the surface corresponds to a direction of propagation (measured from the origin position) and a slowness value (the length between the considered spot and the origin).

The different modes are celled after the sound polarization and are labeled as quasi longitudinal (QL), quasi shear horizontal (QSH) and quasi shear vertical (QSV). If it follows that the polarization is mainly directed along the propagation direction, the label QL is added. If the polarization is mainly shear and directed along the XY-plane, the label QSH is added. If the polarization is mainly shear and directed along the Z-axis, the label QSV is added.

Then, in Fig. XII.A_2, we consider the situation where piezoelectricity is involved. Comparison of Fig. XII.A_2 and Fig. XII.A_1 shows that there is a difference between the slowness surfaces and also between the polarization vectors. A similar conclusion holds for the vectors of energy flow and for the other two modes, i.e. the QSV (quasi shear vertical polarized) and the QL (quasi longitudinal polarized) modes.

In order to show the entire effect of stiffening, we therefore plot the difference between the considered values for the situation with piezoelectricity and the situation without piezoelectricity. The results are depicted in Figs XII.A_3-8 and show that stiffening effects depend on the direction and on the mode under consideration. Figs XII.A_3-5 show, by means of black arrows, the change of energy flow as a result of the presence of piezoelectricity, whereas Figs. XII.A_6-8 show the change of polarization due to piezoelectricity. Note that the polarization direction as well as the energy flow direction change under the influence of piezoelectricity. It is also important to put forward the fact that the arrows in the figures do not show the exact magnitudes of the changes they represent. They only show relative values per figure. Nevertheless, the direction is exact.

Furthermore, the effect on the slowness is far from negligible and is of the order of 1/10 of the slowness values. Note that the stiffening effect on the crystal, obeys the same symmetry laws as the ones of the crystal itself. In other words, piezoelectric stiffening does not change the symmetry of a crystal. In the section XII.C on the other hand, it will be seen that the effect of stress can change the symmetry of a crystal. This has also been shown in Chapter XI, section XI.D, where it was revealed that isotropic plates can become anisotropic when loaded by stress.

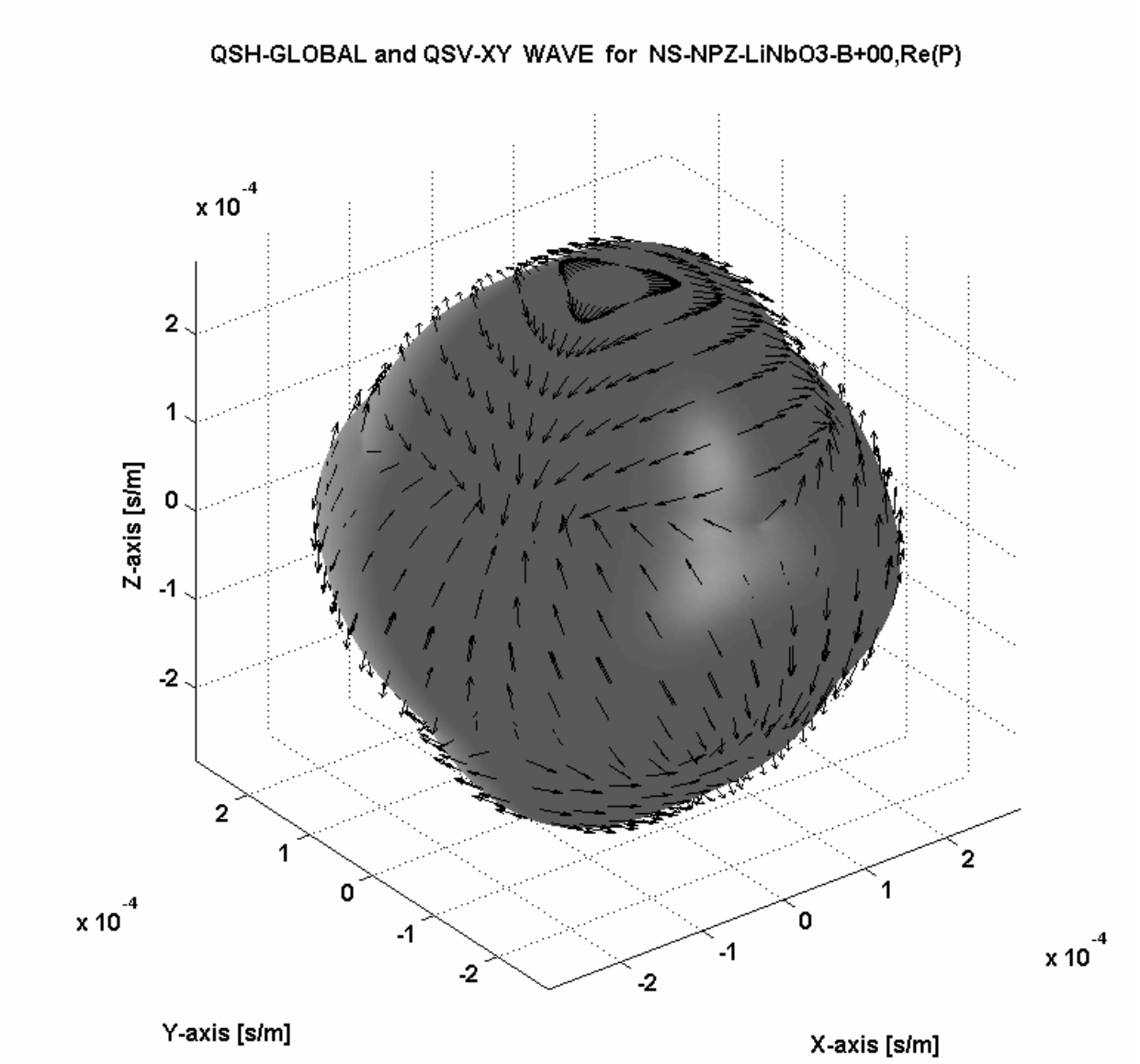

Fig. XII.A_1: ***The slowness surface for the QSH mode in Lithium Niobate, neglecting piezoelectricity. The black arrows denote the polarization for each spot.***

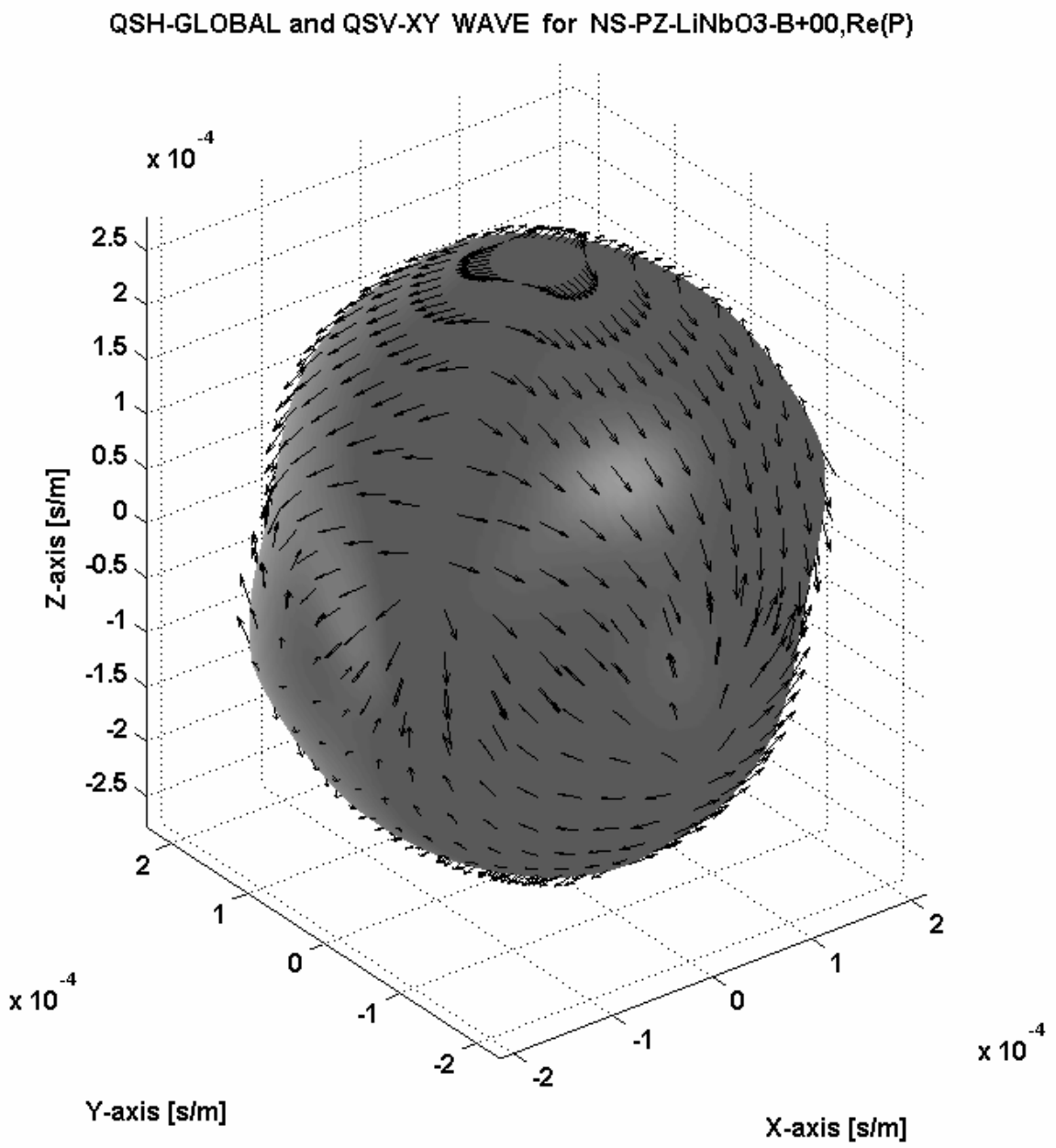

Fig. XII.A_2: ***The slowness surface for the QSH mode in Lithium Niobate, including piezoelectricity. The black arrows denote the polarization for each spot.***

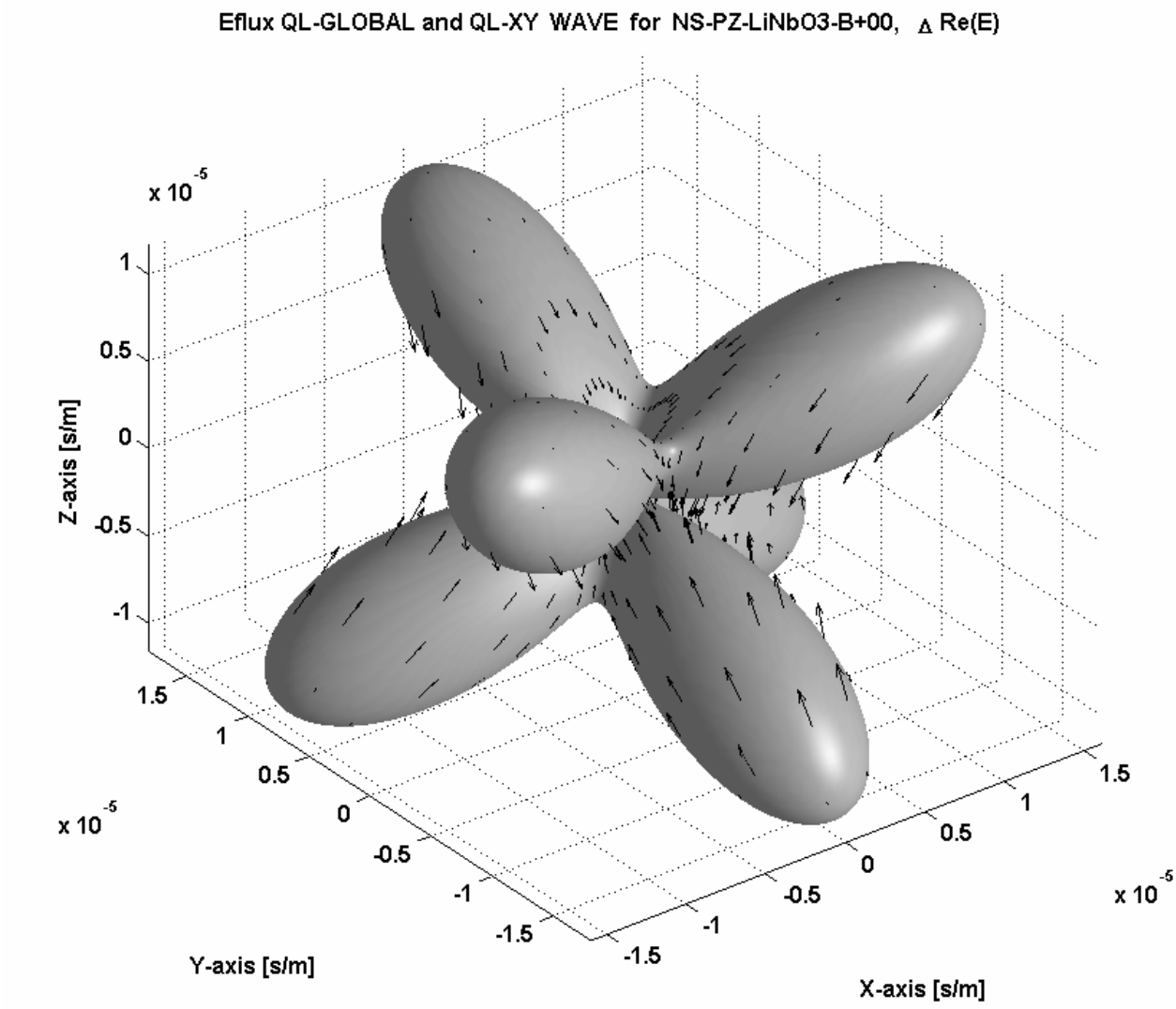

Fig. XII.A_3: ***The difference between the slowness surface for the QL mode in Lithium Niobate, including piezoelectricity, and neglecting piezoelectricity. The black arrows denote the difference of energy flow for each spot.***

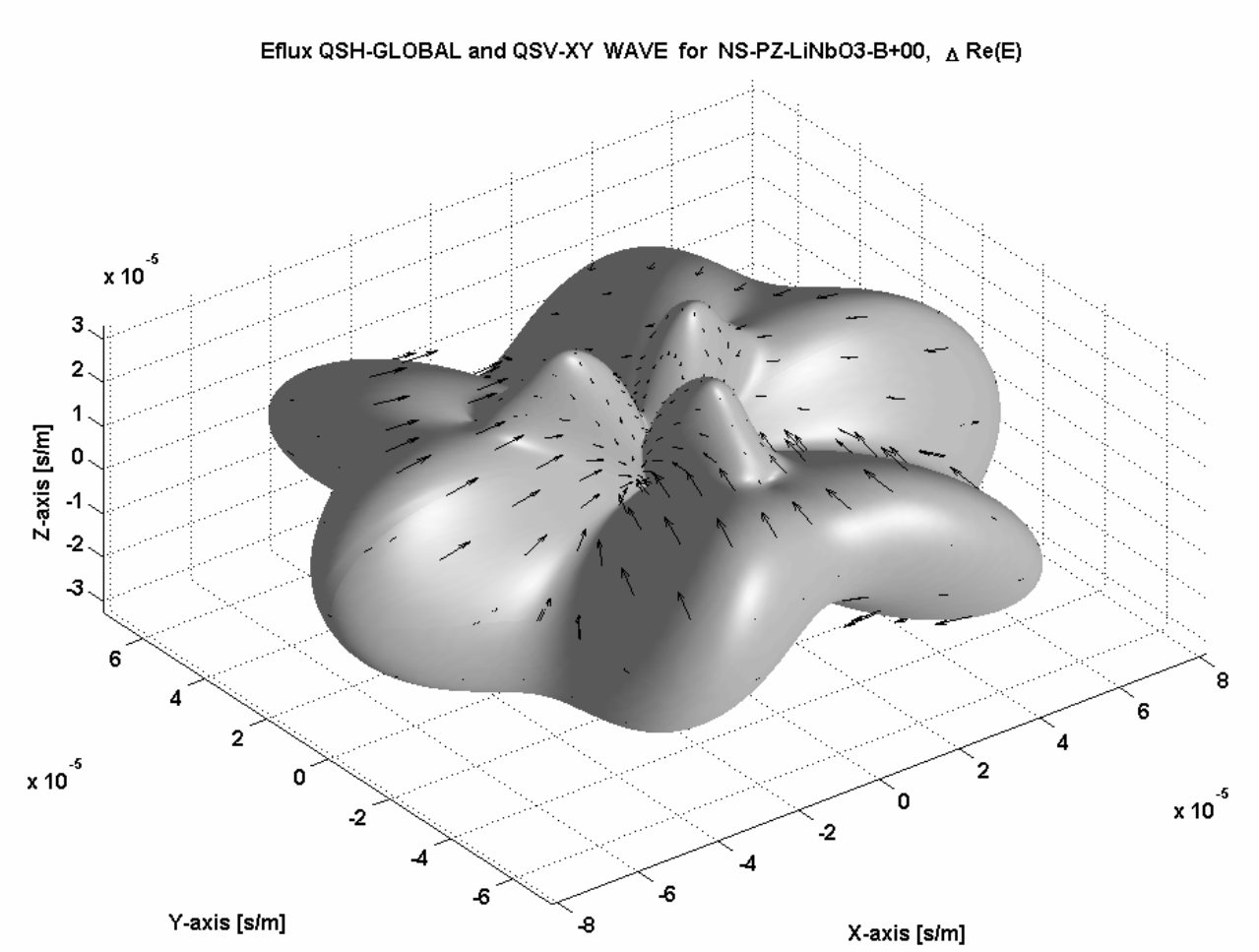

Fig. XII.A_4: ***The difference between the slowness surface for the QSH mode in Lithium Niobate, including piezoelectricity, and neglecting piezoelectricity. The black arrows denote the difference of energy flow for each spot.***

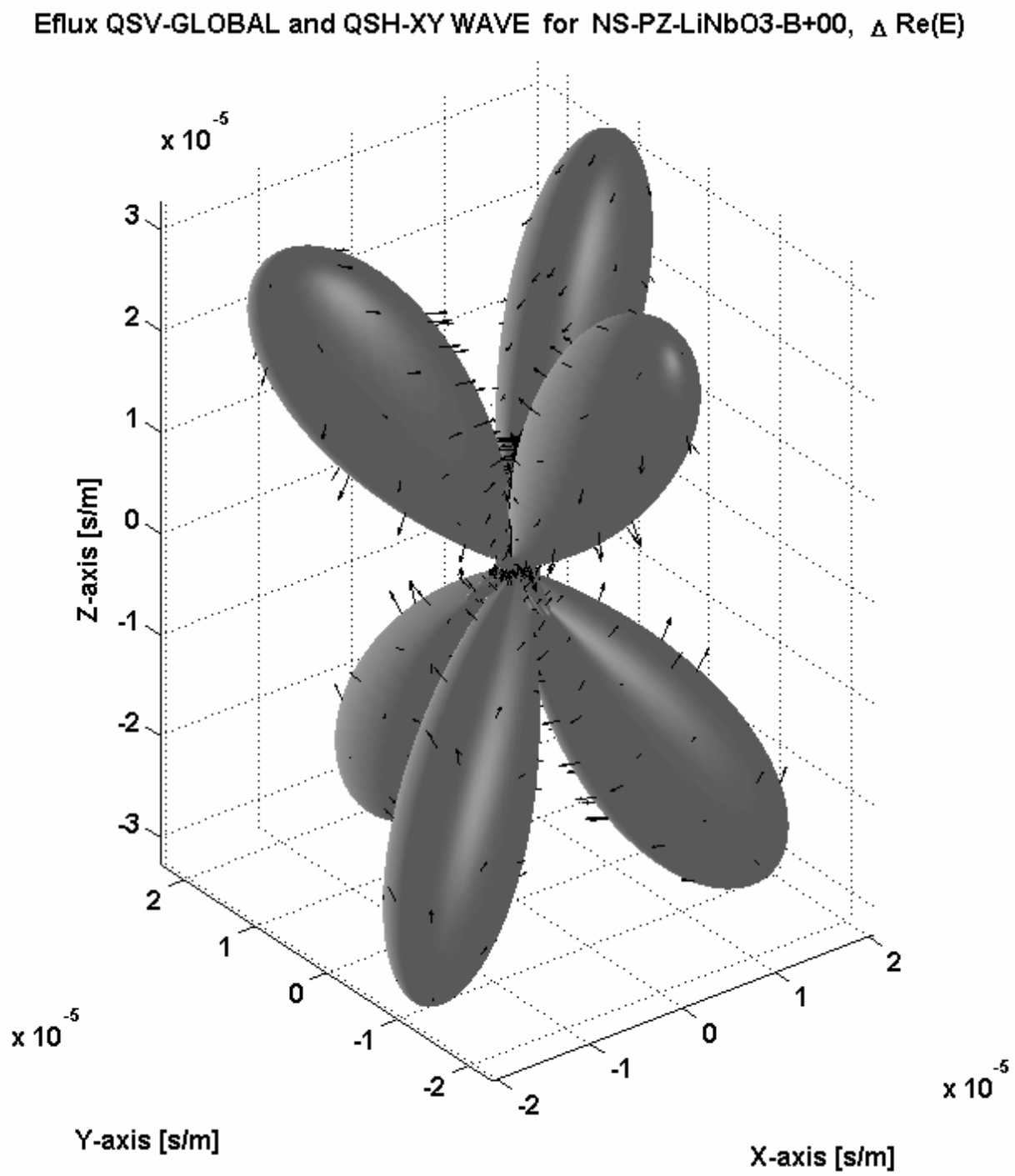

Fig. XII.A_5: ***The difference between the slowness surface for the QSV mode in Lithium Niobate, including piezoelectricity, and neglecting piezoelectricity. The black arrows denote the difference of energy flow for each spot.***

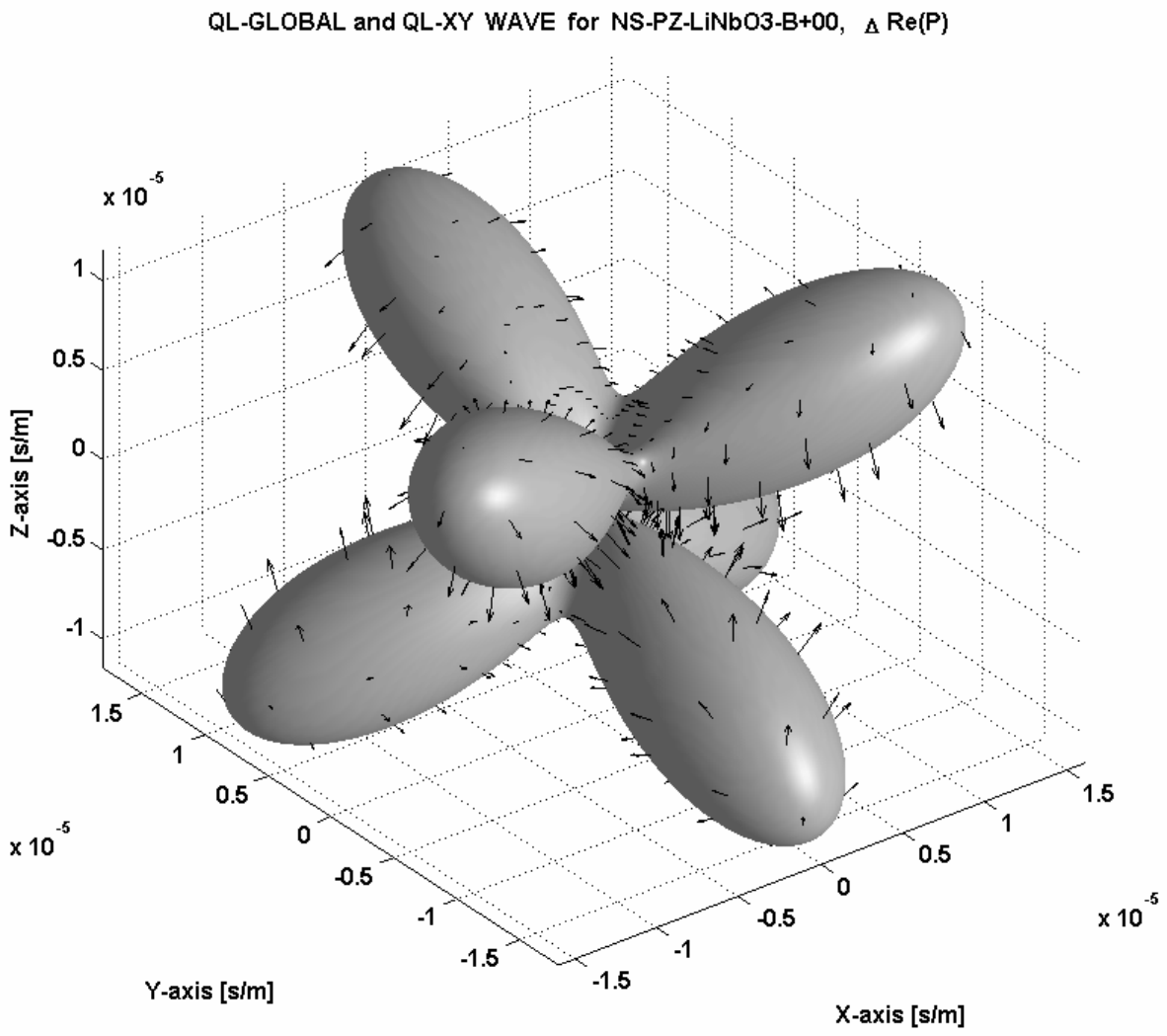

Fig. XII.A_6: ***The difference between the slowness surface for the QL mode in Lithium Niobate, including piezoelectricity, and neglecting piezoelectricity. The black arrows denote the difference in polarization vector for each spot.***

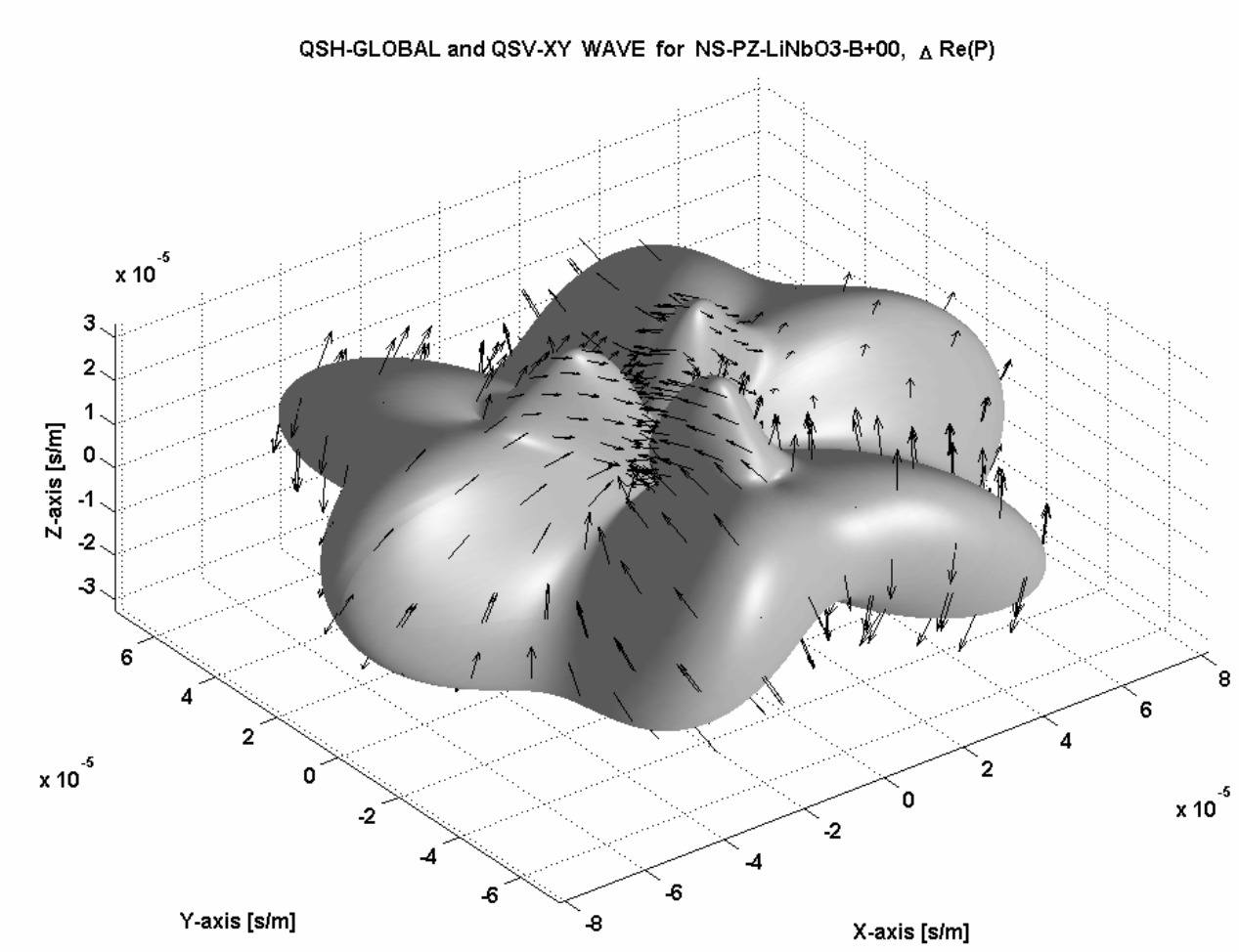

Fig. XII.A_7: ***The difference between the slowness surface for the QSH mode in Lithium Niobate, including piezoelectricity, and neglecting piezoelectricity. The black arrows denote the difference in polarization vector for each spot.***

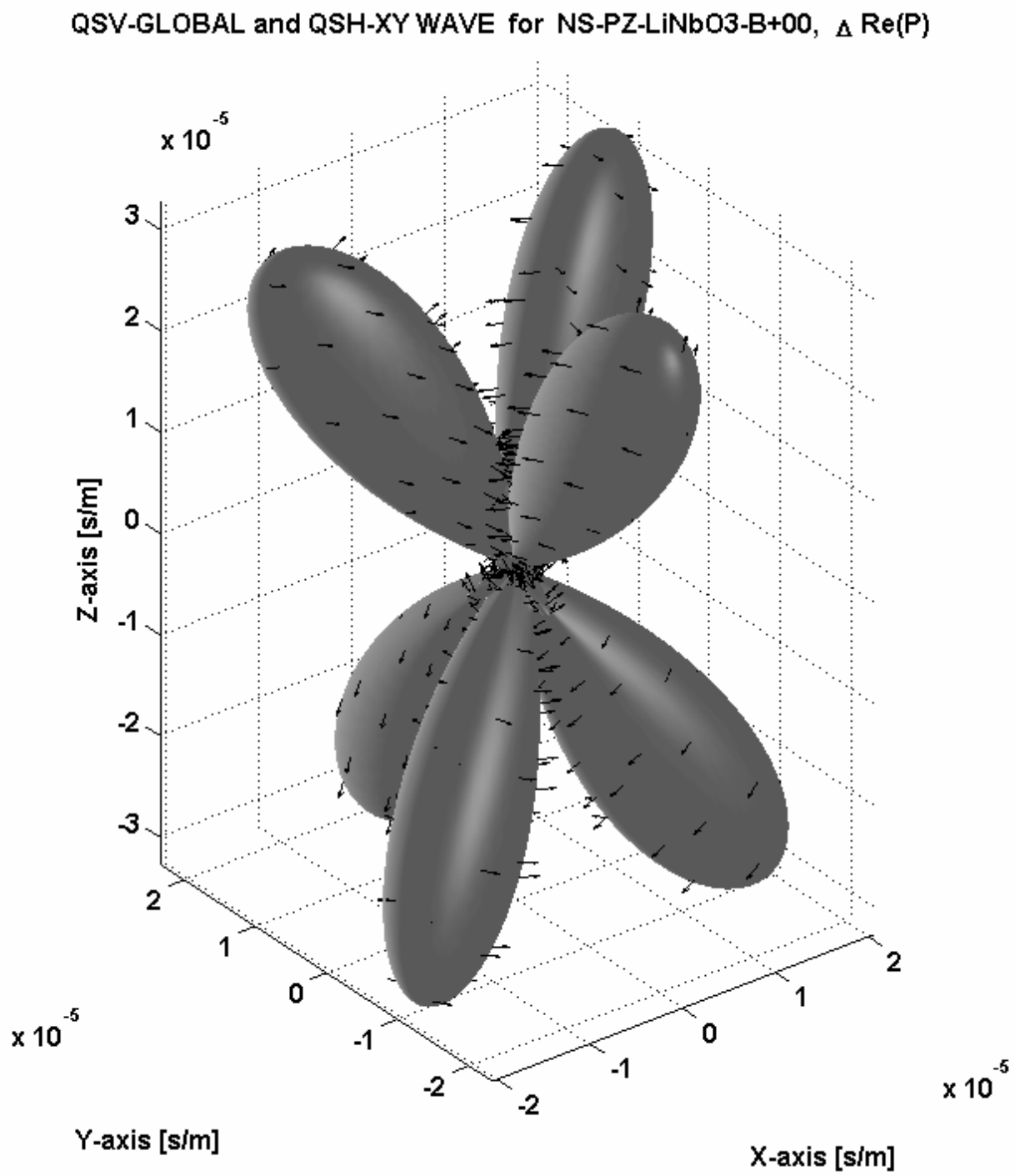

Fig. XII.A_8: ***The difference between the slowness surface for the QSV mode in Lithium Niobate, including piezoelectricity, and neglecting piezoelectricity. The black arrows denote the difference in polarization vector for each spot.***

REFERENCES

[1] B. A. Auld, *Acoustic fields and waves in solids, volume I, second edition*, Krieger, Florida, 1989
[2] Adnan H. Nayfeh, *wave propagation in layered anisotropic media*, north Holland, Elsevier, 1995

XII.B.1 Inhomogeneous waves in piezoelectric crystals

Inhomogeneous waves are described as pure homogeneous plane waves, except that the wave vector is complex valued. This results in an exponential decay of the amplitude along the wave front. The last 30 years, a lot of studies have been reported on the properties of inhomogeneous waves. It is, for example, known that their velocity depends on the inhomogeneity, in isotropic as well as in anisotropic media. Nevertheless, the influence of piezoelectricity, which is very important for a lot of crystals, has always been neglected in the reported studies. The present paper reports a study of the propagation of inhomogeneous waves in the bulk of piezoelectric crystals. Special attention is drawn on the susceptibility of inhomogeneous waves to the effect of piezoelectricity.

INTRODUCTION

From the very beginning, when inhomogeneous waves made their entry in acoustics, they have been either studied as side effects in scattering problems at interfaces between different media, or as independent physical entities, from a theoretical point of view as well as from an experimental point of view [1]. Most studies haven been undertaken for the case of isotropic media. Only a few studies have been reported of inhomogeneous waves in anisotropic media [2-11].
The present study extends the existing studies to the case where also piezoelectricity is involved. It is known that piezoelectricity results in a change (often called *stiffening effect*) of the elastic constants and this has effects on the propagation of homogeneous plane waves. More precisely, bulk homogeneous waves propagate at different velocities because of this stiffening. In the framework of the study of inhomogeneous waves, the question that needs to be resolved is the influence of the piezoelectric effect on inhomogeneous waves. Will this influence be different from the influence on homogeneous plane waves? It will be shown that inhomogeneous waves are more susceptible to the influence of piezoelectricity than homogeneous plane waves.

THEORETICAL DEVELOPMENT

For piezoelectric materials, the stress tensor [12-13] is given by

$$\sigma_{ij} = c_{ijkl} e_{kl} - \xi_{kij} E_k \qquad \text{(XII.B.1\_1)}$$

whereas the electrical displacement is given by

$$D_k = \varepsilon_{ki} E_i + \xi_{kij} e_{ij} \qquad \text{(XII.B.1\_2)}$$

where c_{ijkl} is the stiffness tensor, ξ_{kij} is the piezoelectric stress tensor, ε_{ij} is the dielectrical permittivity tensor, $\mathbf{E}$ is the electric field vector, $\mathbf{D}$ is the dielectric displacement vector and e_{kl} is the strain tensor.
For ultrasonic waves [12], the accompanying electric field is quasistatic and can be described by

$$\mathbf{E} = -\nabla\varphi \tag{XII.B.1_3}$$

with φ a scalar potential.
The acoustic wave equation for visco-elastic materials is given by

$$\frac{\partial\sigma_{ij}}{\partial r_j} = \rho\frac{\partial^2 u_i}{\partial t^2} \tag{XII.B.1_4}$$

whereas the electromagnetic field equations, in the absence of electric currents and electric loads are given by

$$\nabla\times\mathbf{E} = \mu_0\frac{\partial\mathbf{H}}{\partial t} \tag{XII.B.1_5}$$

and

$$\nabla\times\mathbf{H} = \frac{\partial\mathbf{D}}{\partial t} \tag{XII.B.1_6}$$

Taking into account (XII.B.1_3), relations (XII.B.1_5-6) can be replaced by

$$\nabla\bullet\frac{\partial^2}{\partial t^2}\left(-\varepsilon_{ki}\frac{\partial\varphi}{\partial r_i} + \xi_{kij}\frac{\partial u_j}{\partial r_j}\right) = 0 \tag{XII.B.1_7}$$

If we consider plane waves, then

$$\mathbf{u} = A\mathbf{P}\exp i\left(k_x x + k_y y + k_z z - \omega t\right) \tag{XII.B.1_8}$$

and

$$\varphi = B\exp i\left(k_x x + k_y y + k_z z - \omega t\right) \tag{XII.B.1_9}$$

Then, relation (XII.B.1_7) immediately involves

$$B = \frac{k_r k_s \xi_{rsq} A P_q}{\varepsilon_{mn} k_m k_n} \tag{XII.B.1_10}$$

Furthermore, combining relations (XII.B.1_4) and (XII.B.1_7) delivers [12]

$$M_{ip} P_p = 0 \tag{XII.B.1_11}$$

Equation (XII.B.1_11) is an extension of the Christoffel equation. Only nontrivial solutions $\mathbf{P} \neq 0$ are possible whenever

$$\det M = 0 \tag{XII.B.1_12}$$

The expressions of M_{ij} can be found in [12]. This 6th degree polynomial is the so called stiffened Christoffel equation.
From [12] we know that the instantaneous Poynting vector is given by

$$F_i = \frac{1}{2}\left[-\sigma_{ij} \frac{\partial u_j^+}{\partial t} + \varphi \frac{\partial D^+}{\partial t} \right] \tag{XII.B.1_13}$$

in which the superscript '+' means 'complex conjugate'. Without presuming the wave vector to be real or complex, it can be shown straightforwardly that (XII.B.1_13), becomes, for an amplitude equal to unity,

$$F_i = \frac{1}{2}\omega \left\{ \left(c_{ilkj} \right) k_k P_l^+ P_j + \left(B\left(\xi_{kij} k_k - \xi_{ijk}^+ k_k^+ \right) \right) P_j^+ + \varepsilon_{ij}^+ k_j^+ |B|^2 \right\} \tag{XII.B.1_14}$$

The average power then corresponds to the real part of F_i, whereas the peak reactive power corresponds to the imaginary part of F_i [12].

INHOMOGENEOUS WAVES

Whereas the behavior of inhomogeneous waves in anisotropic media is well described [2-11], the effect of piezoelectricity has not been considered so far. For piezoelectric materials, only homogeneous plane waves have, up until now, been studied [12]. A complete historical review of the theory of inhomogeneous waves, can be found in [1]. An inhomogeneous wave is defined as a plane wave, having a complex wave vector **k**. The notion of inhomogeneous waves inside the bulk of a piezoelectric crystal, is introduced through the concept of a complex direction. A real direction is then defined as a real vector $\mathbf{d}_1$, for which $\mathbf{d}_1 \cdot \mathbf{d}_1 = 1$. This is generalized to a complex direction $\mathbf{d} = \mathbf{d}_1 + i\mathbf{d}_2$, for which $\mathbf{d} \cdot \mathbf{d}^+ = 1$. Then, it is possible to determine the slowness value *l* from the following definition, given the angular frequency ω:

$$\mathbf{k} = l\omega\left(\mathbf{d}_1 + i\mathbf{d}_2\right) \tag{XII.B.1_15}$$

For every possible complex direction, it is possible to determine the slowness *l*. The number of combinations of $\mathbf{d}_1$ and $\mathbf{d}_2$ is reduced by introducing a complex direction that, for simplicity, contains no imaginary part along the z-axis.

$$\begin{aligned}&\mathbf{d}_1 + i\mathbf{d}_2 \\ &= \left\{\left(d_{1,x} - ib\sqrt{1-d_{1,y}^2}\right)\mathbf{e}_x + \left(d_{1,y} + ibd_{1,x}\right)\mathbf{e}_y + \left(d_{1,z}\right)\mathbf{e}_z\right\} / \sqrt{1+b^2\left(2d_{1,x}^2 + d_{1,z}^2\right)}\end{aligned} \tag{XII.B.1_16}$$

The parameter *b* (henceforth called *the inhomogeneity parameter*) is then a measure for the fraction of imaginariness of the complex direction.
When the direction (XII.B.1_16) is entered in the Christoffel equation (XII.B.1_12), the complex scalar $l = l_1 + il_2$ can be resolved. This value then determines the entire complex wave vector **k** as

$$\mathbf{k} = \left(\left(k_{1,x} + ik_{2,x}\right)\mathbf{e}_x + \left(k_{1,y} + ik_{2,y}\right)\mathbf{e}_y + \left(k_{1,z} + ik_{2,z}\right)\mathbf{e}_z\right) / N \tag{XII.B.1_17}$$

with

$$k_{1,x} = l_1 d_{1,x} + l_2 b\sqrt{1-d_{1,y}^2} \tag{XII.B.1_18}$$

$$k_{2,x} = -l_1 b\sqrt{1-d_{1,y}^2} + l_2 d_{1,x} \tag{XII.B.1_19}$$

$$k_{1,y} = l_1 d_{1,y} - l_2 b d_{1,x} \tag{XII.B.1_20}$$

$$k_{2,y} = l_1 b d_{1,x} + l_2 d_{1,y} \tag{XII.B.1_21}$$

$$k_{1,z} = l_1 d_{1,z} \tag{XII.B.1_22}$$

$$k_{2,z} = l_2 d_{1,z} \tag{XII.B.1_23}$$

and

$$N = \sqrt{1+b^2\left(2d_{1,x}^2 + d_{1,z}^2\right)} / \omega \tag{XII.B.1_24}$$

NUMERICAL RESULTS FOR LITHIUM NIOBATE

The physical parameters of Lithium Niobate are given in ref [12] and are summarized as:
The density is 4700 kgm^{-3} .
The elastic constants $\left[\times 10^{10} N/m^2\right]$ are

$$C_{33}=24.5 \quad C_{14}=0.9 \quad C_{44}=6.0 \qquad \text{(XII.B.1\_25)}$$
$$C_{11}=20.3 \quad C_{12}=5.3 \quad C_{13}=7.5$$

with

$$C_{15}=C_{16}=C_{25}=C_{26}=C_{35}=C_{36}=C_{45}=C_{46}=C_{34}=0; \qquad \text{(XII.B.1\_26)}$$
$$C_{56}=C_{14}; \quad C_{24}=-C_{14}; \qquad C_{55}=C_{44};$$
$$C_{23}=C_{13}; \quad C_{22}=C_{11}; \quad C_{66}=-C_{12}/2+C_{11}/2$$

The piezoelectric constants $\left[C/m^2\right]$ are

$$\xi_{31}=0.2 \quad \xi_{22}=2.5 \quad \xi_{15}=3.7 \quad \xi_{33}=1.3 \qquad \text{(XII.B.1\_27)}$$

with

$$\xi_{34}=\xi_{23}=\xi_{25}=\xi_{26}=\xi_{35}= \qquad \text{(XII.B.1\_28)}$$
$$\xi_{36}=\xi_{11}=\xi_{12}=\xi_{14}=\xi_{13}=0;$$
$$\xi_{32}=\xi_{31}; \quad \xi_{16}=-\xi_{22}; \quad \xi_{21}=-\xi_{22}; \quad \xi_{24}=\xi_{15}$$

The dielectric constants $\left[10^{-12} F/m\right]$ are

$$\varepsilon_1=389 \quad \varepsilon_3=257 \qquad \text{(XII.B.1\_29)}$$

with

$$\varepsilon_2=\varepsilon_1 \quad \varepsilon_4=\varepsilon_5=\varepsilon_6=0 \qquad \text{(XII.B.1\_30)}$$

Classically, taking into account Einstein's double suffix notation convention, the (real) wave vector **k** is replaced by $\mathbf{k}=l\omega\left(d_{1,g}\mathbf{e}_g\right)$ and entered into (XII.B.1_19). Then, for each (real) direction $\left(d_{1,x}, d_{1,y}, d_{1,z}\right)$, the eigenvalue *l* can be determined. This *l* is then the real slowness value. At the same time, the polarization vector **P** is determined as the eigenvector.

For the case of inhomogeneous waves, for each chosen real direction $\mathbf{d}_1$, and a parameter b, the value l is determined from (XII.B.1_15) and the Christoffel equation (XII.B.1_12). We have developed a program that is able to draw 3D slowness surfaces and, when necessary, adds arrows that represent the polarization or the energy flow (the real part of the Poynting vector). The modes are then named after the sound polarization and are labeled as quasi longitudinal (QL), quasi shear horizontal (QSH) and quasi shear vertical (QSV). If it follows that the polarization is mainly directed along the propagation direction, the label QL is added. If the polarization is mainly shear and directed along the XY-plane, the label QSH is added. If the polarization is mainly shear and directed along the Z-axis, the label QSV is added.

In Fig. XII.B.1_1, the slowness surface is depicted for the QSV-mode, in the case of homogeneous plane waves and neglecting piezoelectricity. In addition, arrows are added that correspond to the energy flux direction (the real part of the Poynting vector). If piezoelectricity is considered, a stiffening effect occurs whence the slowness changes, depending on the direction. This is seen in Fig. XII.B.1_2, where the slowness curve for the QSV-mode is considered, in the presence of piezoelectricity. Note the difference between Fig. XII.B.1_2 and Fig. XII.B.1_1. As a matter of fact, it is possible to plot the difference between Fig. XII.B.1_2 and Fig. XII.B.1_1.

This difference, corresponding to the difference between the case of piezoelectricity and the case of non-piezoelectricity, is shown in Fig. XII.B.1_3. The arrows correspond to the difference in real Poynting vectors (rescaled for visibility). Note that the crystal's symmetry is preserved in Fig. XII.B.1_3 and that some directions do not involve any stiffening effect, whereas others involve stiffening. The fact that the crystal's symmetry is preserved is worth noting. It means that the introduction of inhomogeneous waves by means of a complex direction, does not result in mathematical artifacts, giving results that do not reflect the physics of the crystal system under consideration.

A similar procedure, for the same QSV-mode, is followed for Figs XII.B.1_4-6, except that, now, each time, when drawing the arrows, the polarization vectors are considered and not the real Poynting vectors. Note that the piezoelectric effect, besides influencing the energy propagation direction, also has a strong influence on the polarization vectors. In what follows, in order to limit the number of presented figures, we only focus on the differences between the case with piezoelectricity and the case without piezoelectricity.

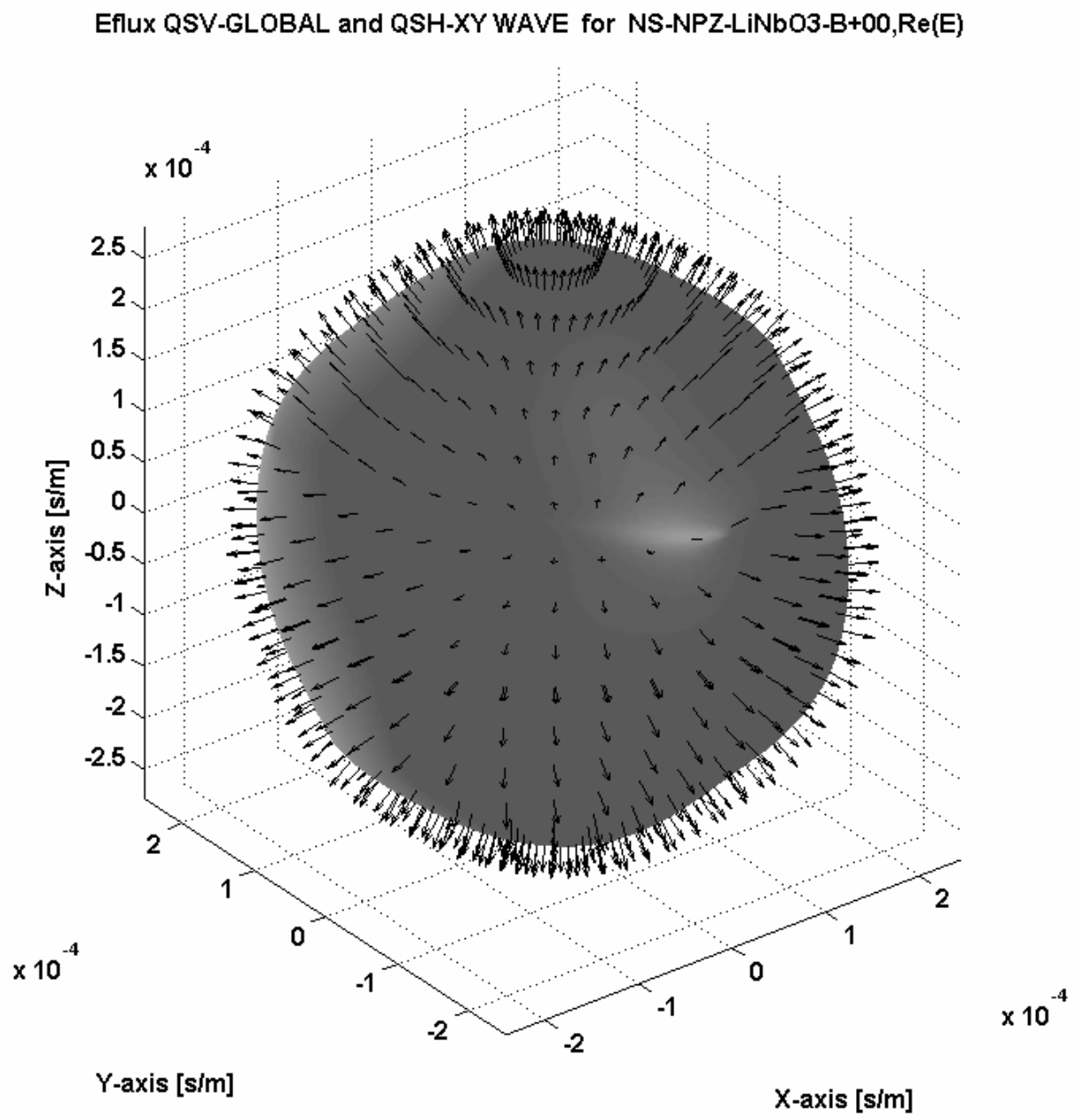

Fig. XII.B.1_1: ***The slowness surface for the QSV-mode, in the case of homogeneous plane waves, neglecting piezoelectricity. The associated arrows denote the energy propagation directions for each corresponding spot on the slowness surface.***

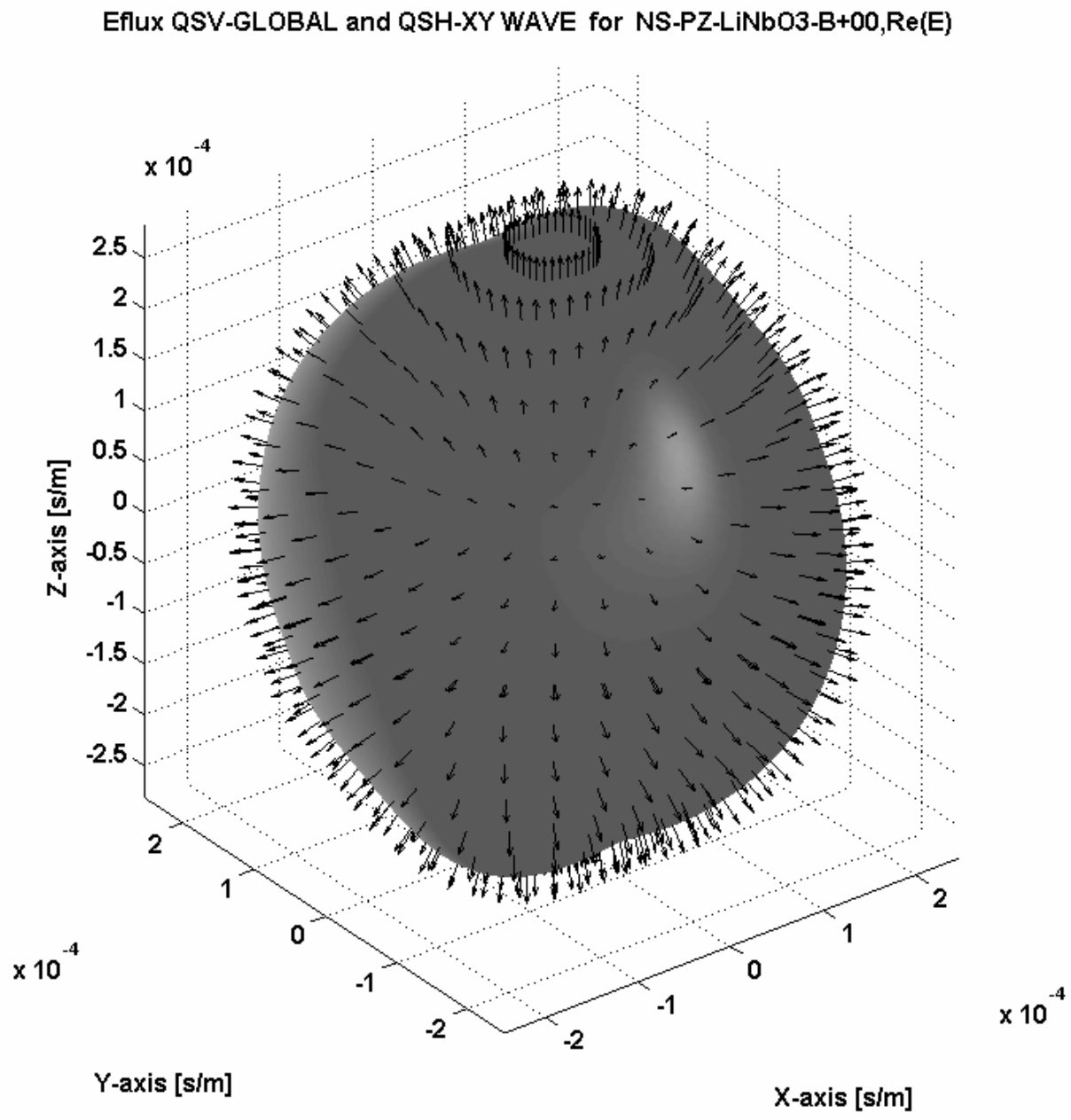

Fig. XII.B.1_2: ***The slowness surface for the QSV-mode, in the case of homogeneous plane waves, including piezoelectricity. The associated arrows denote the energy propagation directions for each corresponding spot on the slowness surface.***

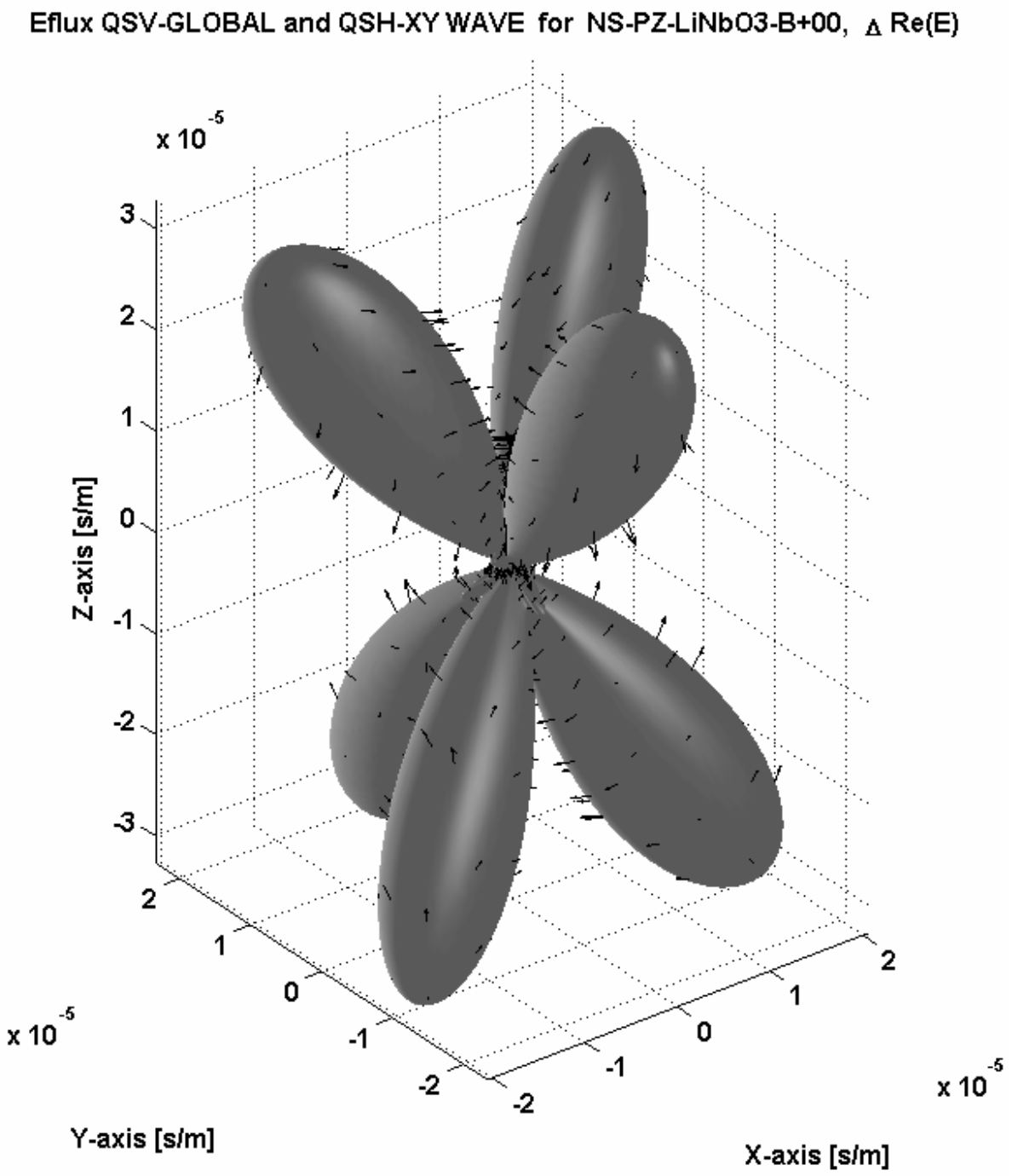

Fig. XII.B.1_3: ***The difference between the case when there is piezoelectricity involved and when the piezoelectric effect is neglected, for the QSV-mode. This figure physically corresponds to the difference between Fig. XII.B.1_2 and Fig. XII.B.1_1, i.e. Fig. XII.B.1_2 minus Fig. XII.B.1_1. The corresponding arrows denote the difference in energy propagation direction.***

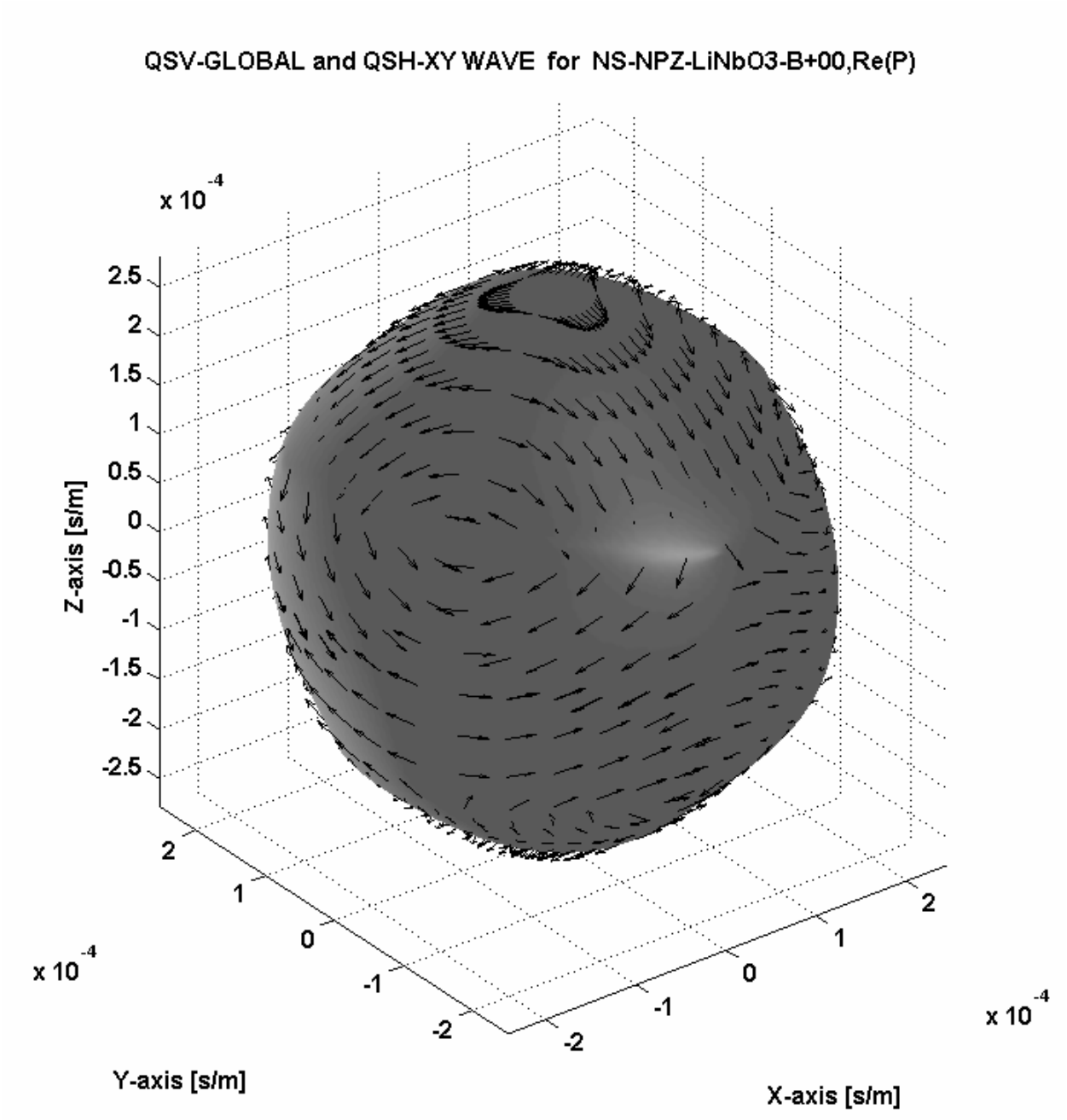

Fig. XII.B.1_4: ***This figure corresponds to Fig. XII.B.1_1, except that the arrows here denote the polarization.***

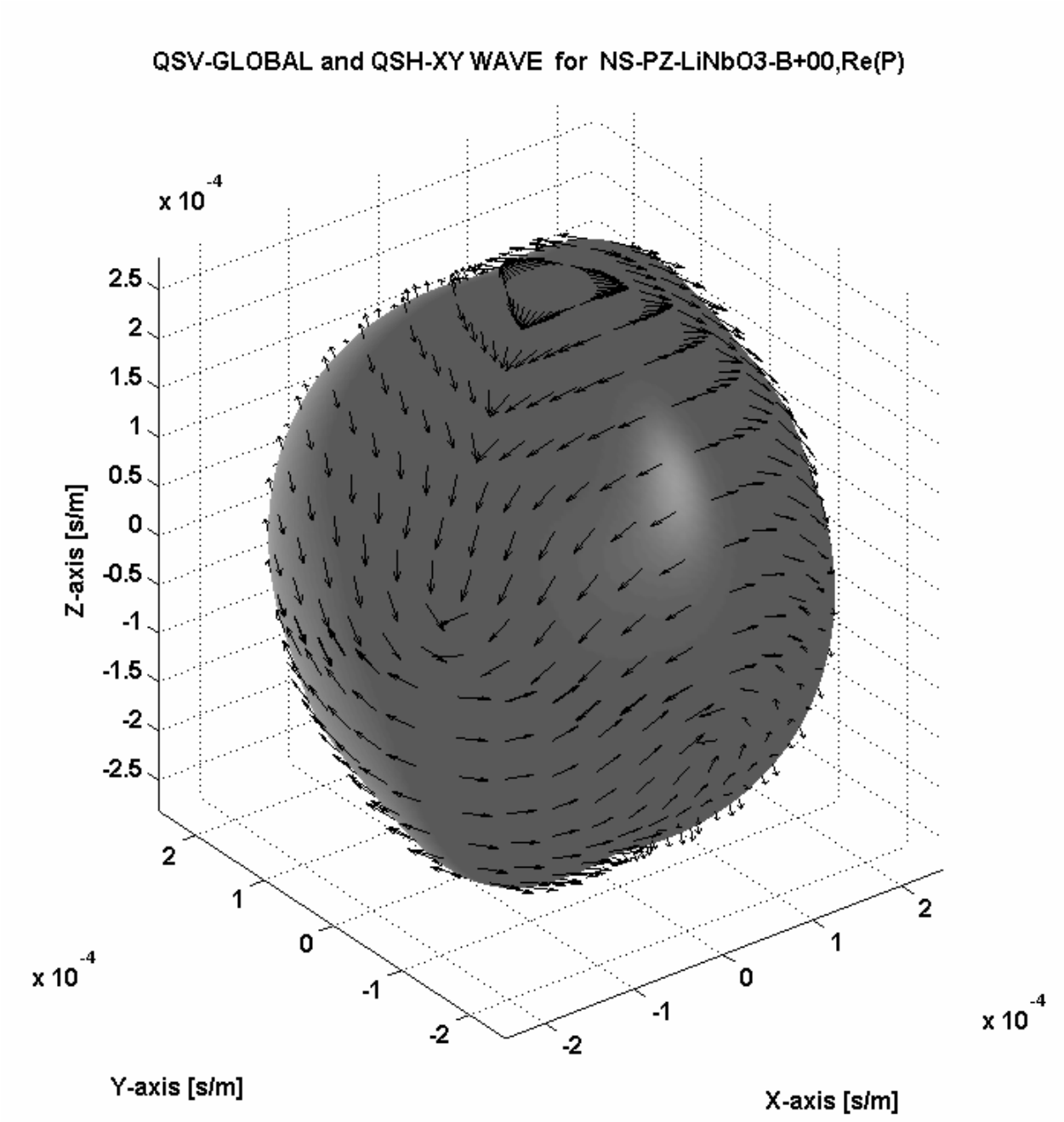

Fig. XII.B.1_5: ***This figure corresponds to Fig. XII.B.1_2, except that the arrows here denote the polarization.***

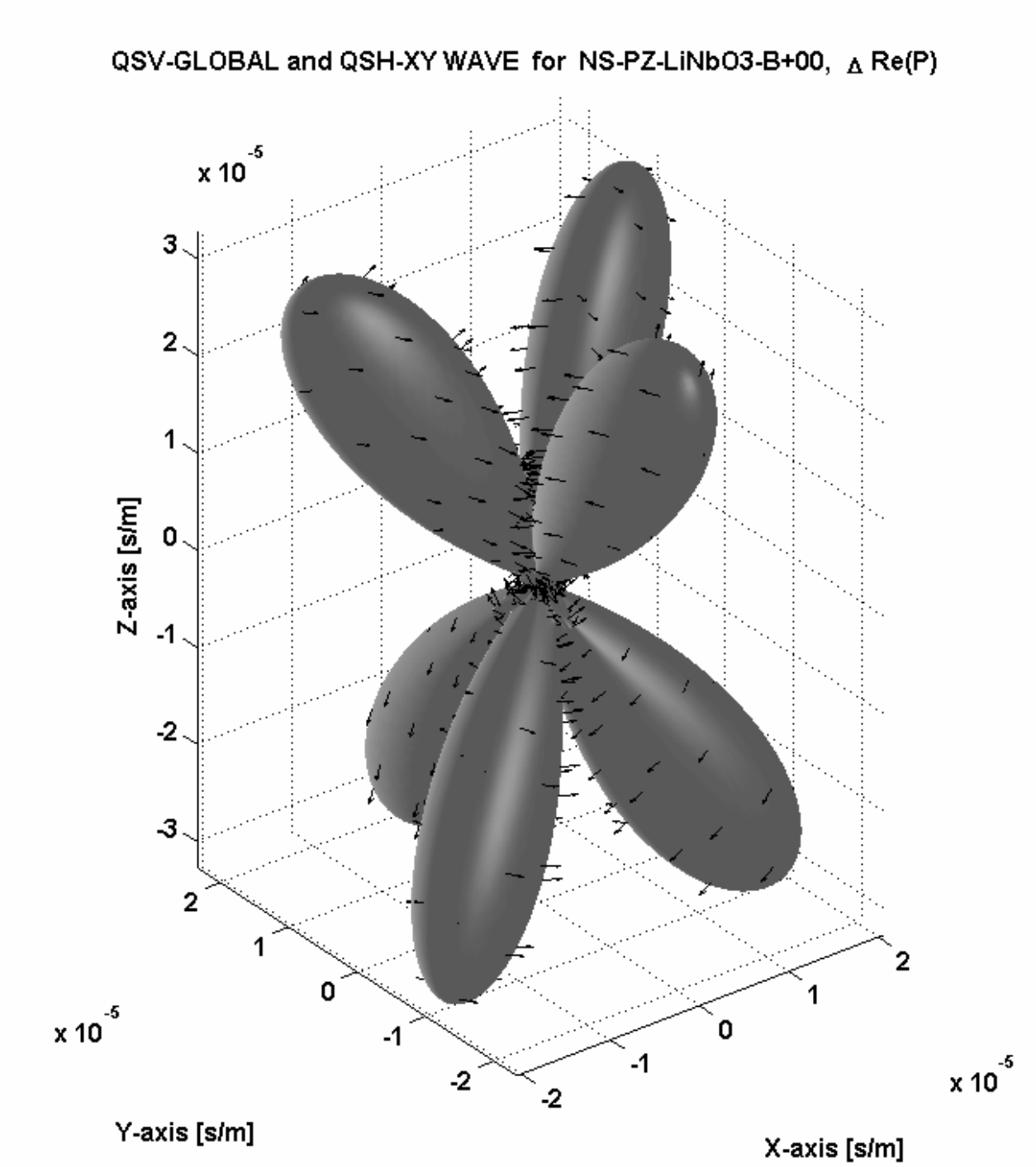

Fig. XII.B.1_6: ***The difference between the case when there is piezoelectricity involved and when the piezoelectric effect is neglected, for the QSV-mode. This figure physically corresponds to the difference between Fig. XII.B.1_5 and Fig. XII.B.1_4. The corresponding arrows denote the difference in polarization. In fact, this figure corresponds to Fig. XII.B.1_3, except that the arrows here denote the polarization.***

So far, only homogeneous plane waves have been considered, involving a parameter of imaginariness $b = 0$. Now we consider a parameter $b \neq 0$, resulting in inhomogeneous waves.

Fig. XII.B.1_7 shows the difference between the slowness surface for the QSV-mode, in the case of $b = 60/140$. The black arrows denote the difference between (the real part of) the Poynting vector for each considered direction.

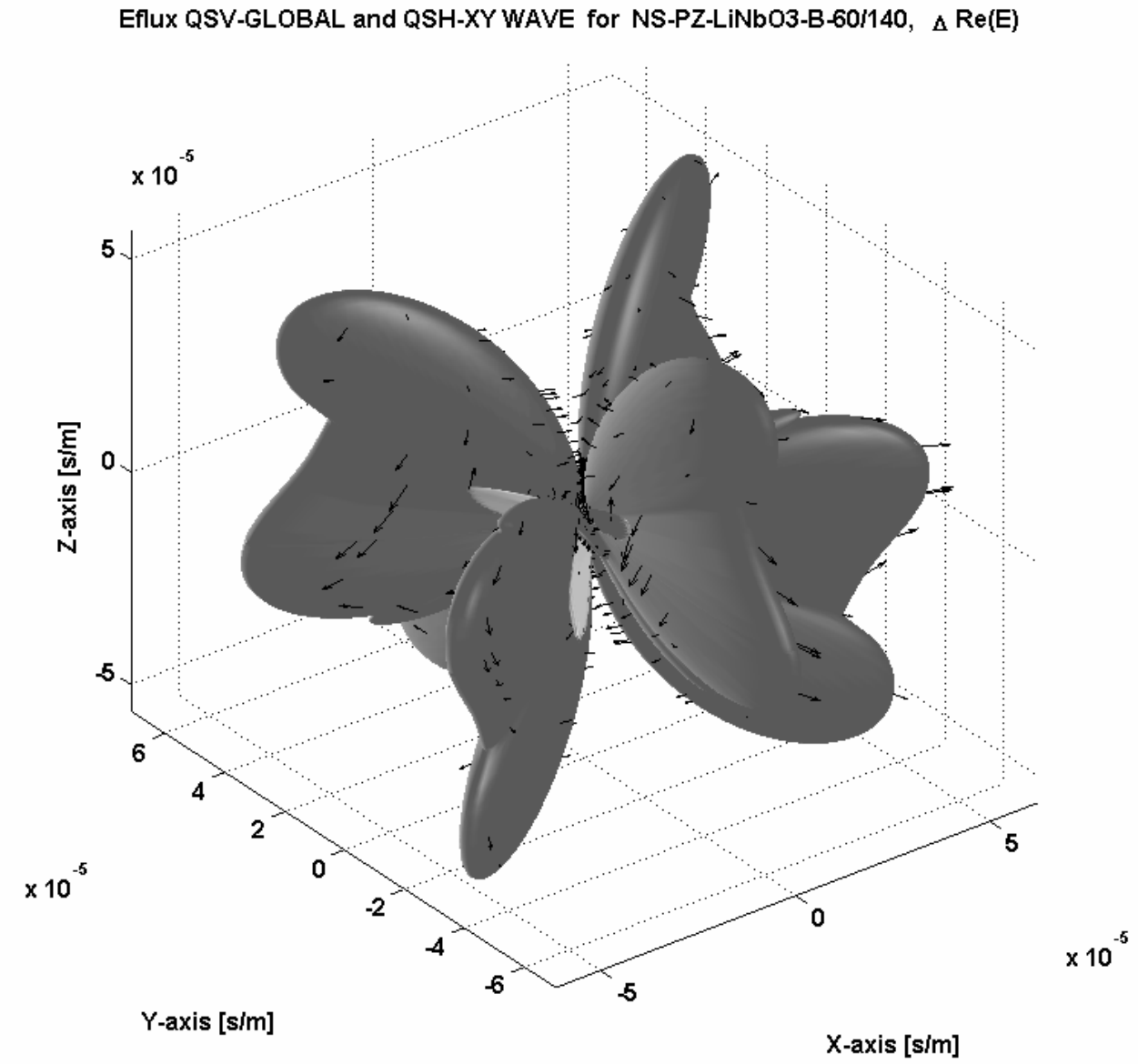

Fig. XII.B.1_7: ***The difference between the case when there is piezoelectricity involved and when the piezoelectric effect is neglected, for the QSV-mode, in the case on inhomogeneous waves. This figure corresponds to Fig. XII.B.1_3, except that inhomogeneous plane waves are considered here, characterized by a parameter of imaginariness b=60/140. The associated arrows denote the difference of the Poynting vector.***

Comparison between Fig. XII.B.1_7 and Fig. XII.B.1_3, shows that inhomogeneous waves are more susceptible for piezoelectricity than homogeneous plane waves. The reason is not clear, but it could be a result of the fact that for a considered mode, the presence of an inhomogeneity in the wave front, does not only influence the sound velocity, but also the

polarization (see previous section XII.A), whence the considered mode slightly changes its nature and becomes better influenced by the effect of piezoelectricity.
Fig. XII.B.1_8 corresponds to Fig. XII.B.1_7, except that, here, the difference of polarization is denoted by the black arrows.

If we take a look at the effect of piezoelectricity on the other modes, i.e. the QL-mode (Figs XII.B.1_9-10) and the QSH-mode (Figs. XII.B.1_11-12), then, it is noticed that also for these modes, the presence of inhomogeneity makes them more susceptible to the piezoelectric effect. Again, the reason is not certain, but it can be due to the change of polarization due to inhomogeneity.

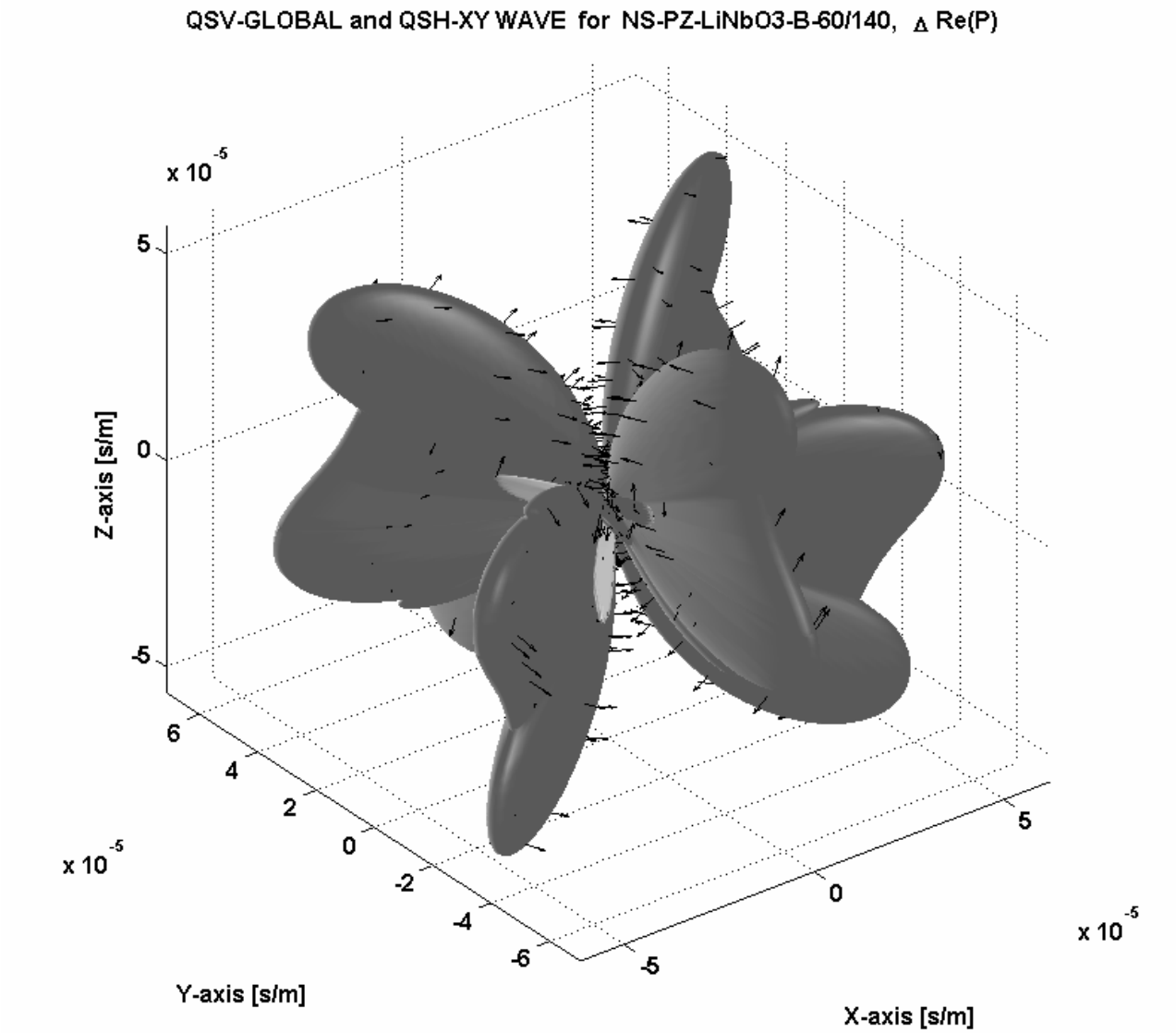

Fig. XII.B.1_8: ***The difference between the case when there is piezoelectricity involved and when the piezoelectric effect is neglected, in the situation of inhomogeneous waves. The corresponding arrows denote the difference in polarization. As a matter of fact, this figure corresponds to Fig. XII.B.1_6, except that inhomogeneous plane waves are considered here, characterized by a parameter of imaginariness b=60/140.***

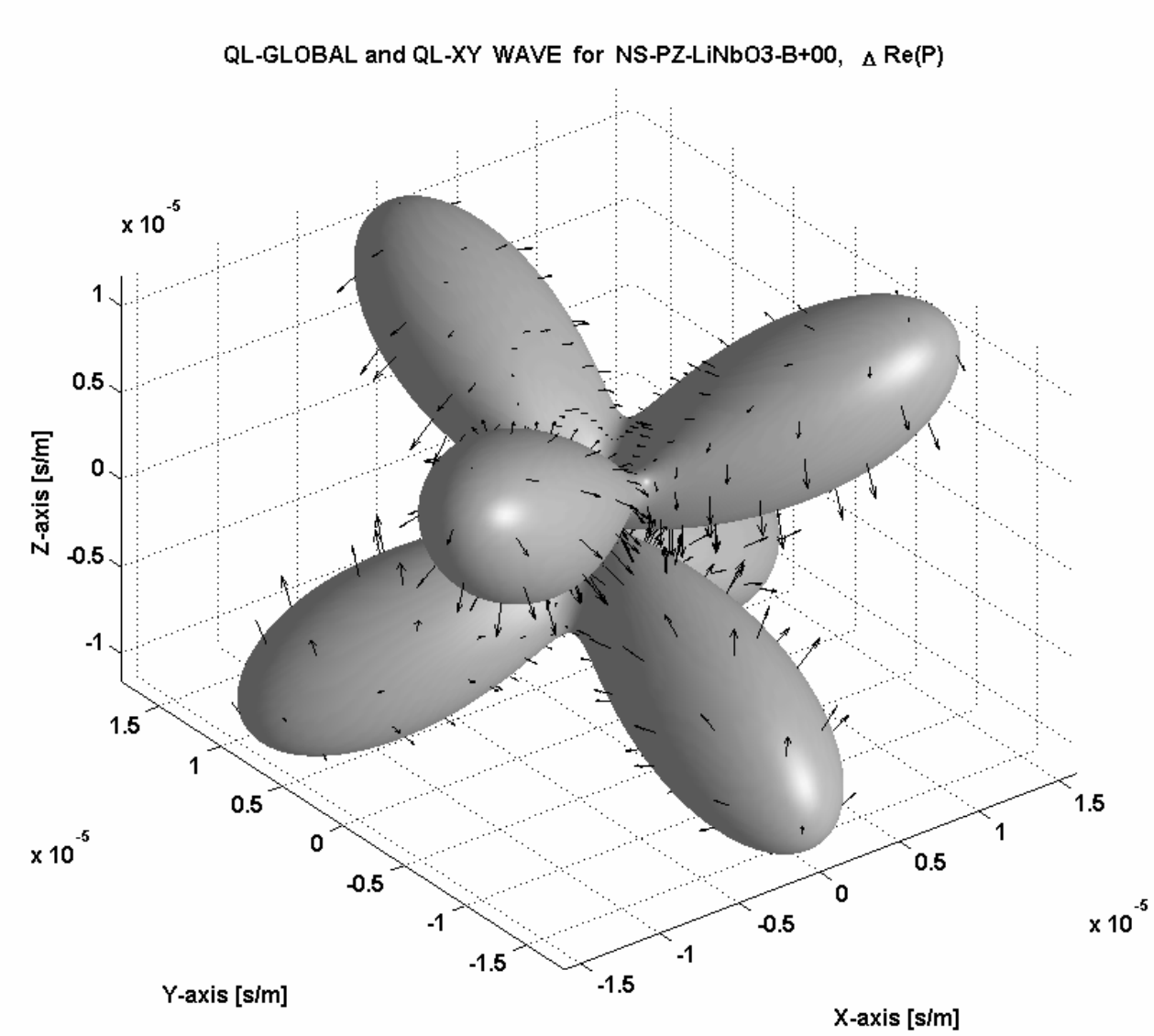

Fig. XII.B.1_9: ***This figure corresponds to Fig. XII.B.1_6, i.e. for the case of homogeneous plane waves, except that the QL-mode is considered here.***

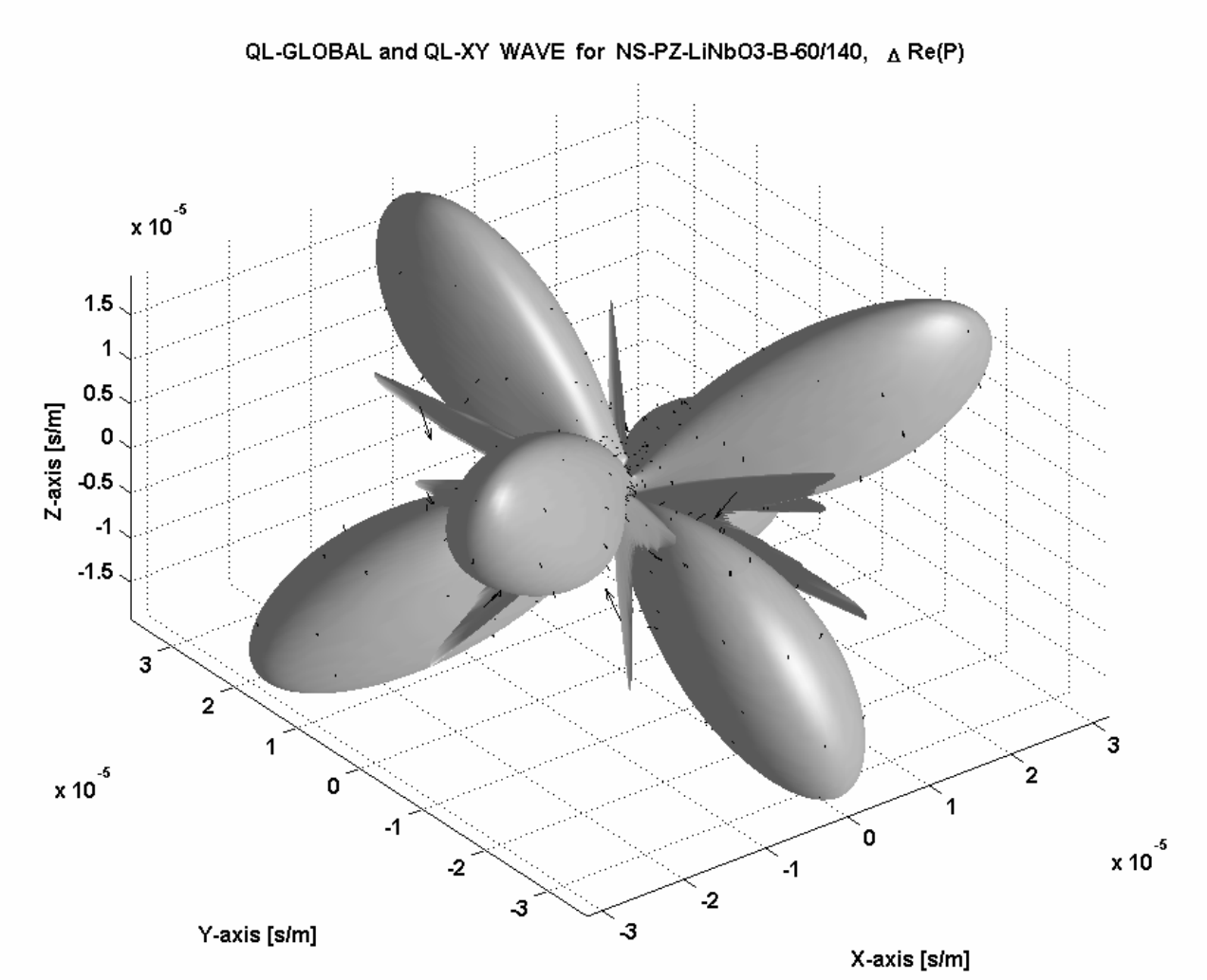

Fig. XII.B.1_10: ***This figure corresponds to Fig. XII.B.1_9, except that inhomogeneous plane waves are considered here, characterized by a parameter of imaginariness b=60/140.***

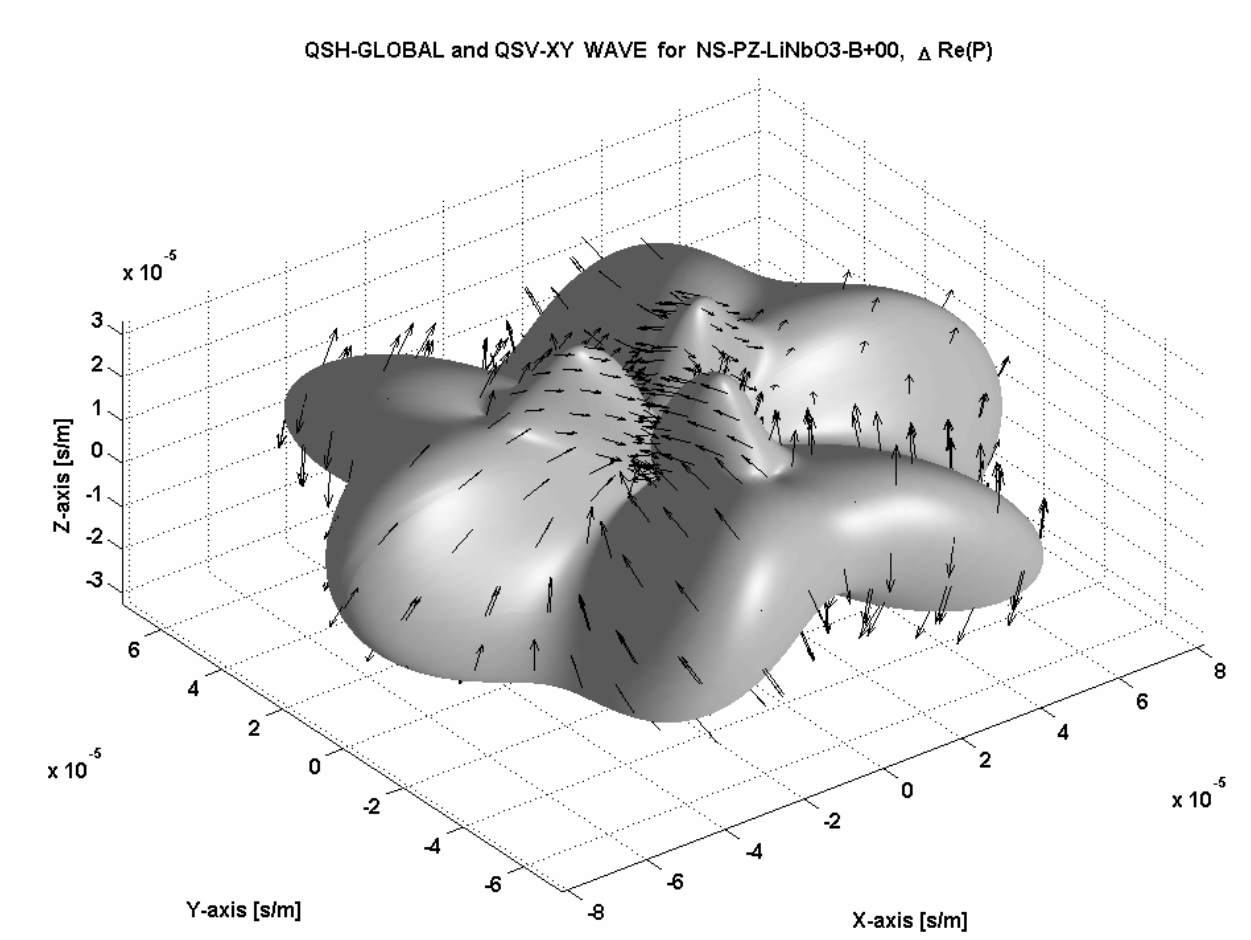

Fig. XII.B.1_11: ***This figure corresponds to Fig. XII.B.1_6, i.e. for the case of homogeneous plane waves, except that the QSH-mode is considered here.***

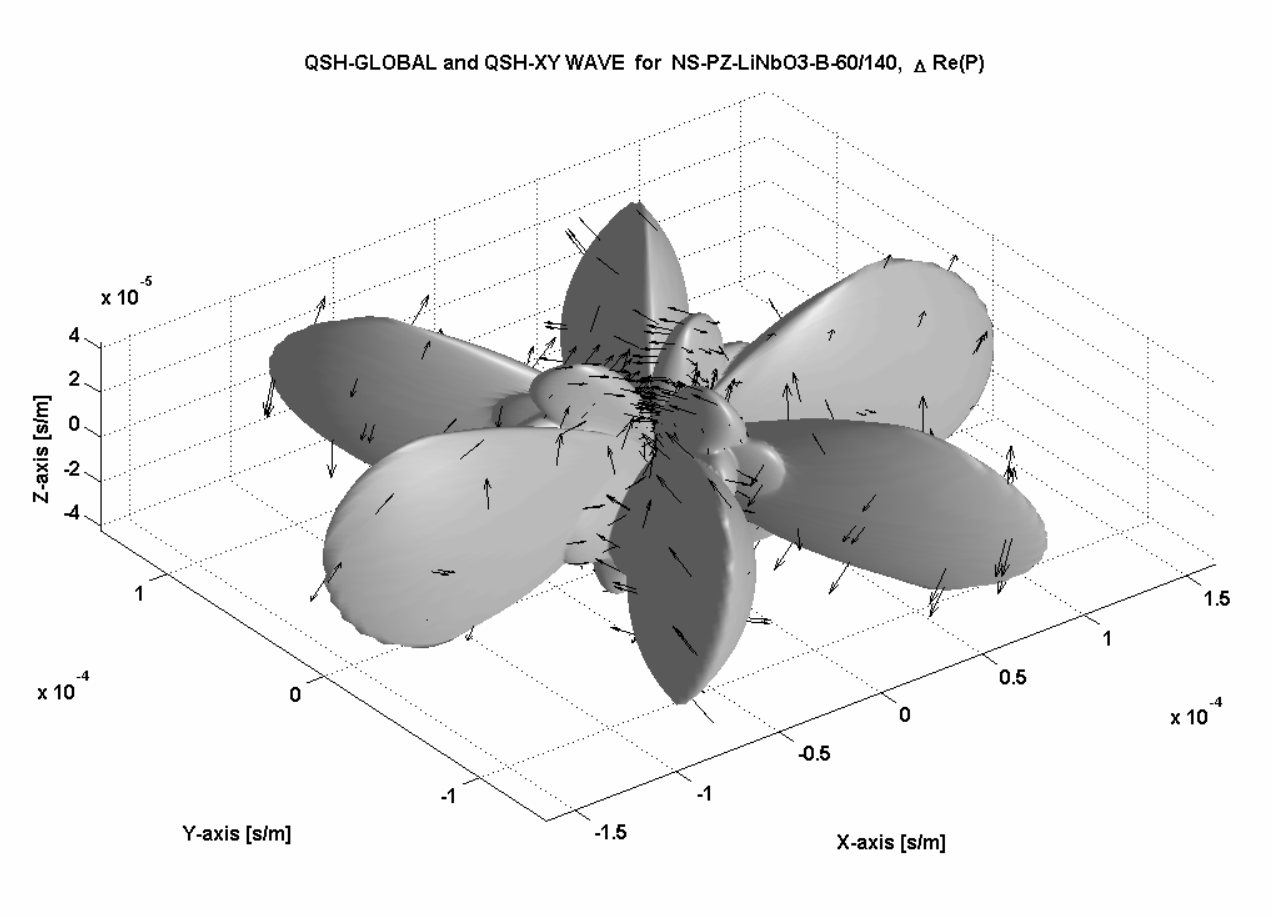

Fig. XII.B.1_12: ***This figure corresponds to Fig. XII.B.1_11, except that inhomogeneous plane waves are considered here, characterized by a parameter of imaginariness b=60/140.***

CONCLUSIONS

The study is valid for any piezoelectric crystal, though it has only been outlined for Lithium Niobate. It is shown that the effect of piezoelectricity is better felt by inhomogeneous plane waves than by homogeneous plane waves. This means that, even though piezoelectric effects are sometimes neglected when studying the interaction of sound with crystals, it is better not to neglect the effect if inhomogeneous waves are generated within the crystal or if the interaction of bounded inhomogeneous waves [14], with such crystals is considered.

REFERENCES

[3] Nico F. Declercq, Rudy Briers, Joris Degrieck, Oswald Leroy, "The History and Properties of Ultrasonic Inhomogeneous Waves", accepted for publication in IEEE-UFFC.

[4] Michael Hayes, "Inhomogeneous plane waves", Arch. Ration. Mech. Anal. 85, 41-79, 1984

[5] S. I. Rokhlin, T. K. Bolland, L. Adler, "Reflection and refraction of elastic waves on a plane interface between two generally anisotropic media", J. Acoust. Soc. Am. 79(4), 906-918, 1986

[6] B. Hosten, M. Deschamps, B. R. Tittmann, "Inhomogeneous wave generation and propagation in lossy anisotropic solids. Application to the characterization of viscoelastic composite materials", J. Acoust. Soc. Am. 82(5), 1763-1770, 1987

[7] B. Hosten, “Bulk heterogeneous plane waves propagation through viscoelastic plates and stratified media with large values of frequency domain”, Ultrasonics 29, 445-450, 1991
[8] Marc Deschamps, Bernard Hosten, “The effects of viscoelasticity on the reflection and transmission of ultrasonic waves by an orthotropic plate”, J. Acoust. Soc. Am. 91(4), 2007-2015, 1992
[9] Patrick Lanceleur, Helder Ribeiro, Jean-François De Belleval, “The use of inhomogeneous waves in the reflection-transmission problem at a plane interface between two anisotropic media”, J. Acoust. Soc. Am., 93(4), 1882-1892, 1993
[10] M. Deschamps, F. Assouline, “Attenuation Along the Poynting Vector Direction of Inhomogeneous Plane Waves in Absorbing and Anisotropic Solids”, Acustica – Acta Acustica, 86, 295-302, 2000
[11] Bruno Rogé, “Réflexion/transmission d’une onde plane inhomogene incidente sur une interface plane séparant deux milieux anisotropes", Thesis, Université de Technologie de Compiègne, France, 1999
[12] Boulanger P, Hayes M, “Special inhomogeneous waves in cubic elastic materials”, Zeitschrift fur angewandte mathematik und physik 51(6), 1031-1038, 2000.
[13] M. Deschamps, O. Poncelet, “Inhomogeneous plane wave and the most energetic complex ray”, Ultrasonics 40, 293-296, 2002
[14] B. A. Auld, *Acoustic fields and waves in solids, volume I, second edition*, Krieger, Florida, 1989
[15] Adnan H. Nayfeh, *wave propagation in layered anisotropic media*, north Holland, Elsevier, 1995
[16] Nico F. Declercq, Joris Degrieck, Oswald Leroy, "The Laplace transform to describe bounded inhomogeneous waves", J. Acoust. Soc. Am. 116(1), 51-60, 2004

XII.B.2 Enhanced anisotropy in Paratellurite for Inhomogeneous Waves and its Possible Importance in the Future Development of Acousto-Optic Devices

The anisotropic feature of most crystals, involves a direction dependent wave velocity for each of the possible modes. Paratellurite (Tellurium dioxide) is extraordinary because, for one of the propagation modes, i.e. the quasi shear horizontal (QSH) mode, the anisotropy is exceptional. This results, on the one hand in a very strong directional dependent sound velocity and on the other hand, in a low wave velocity in certain directions, resulting is a high figure of merit for the acousto-optical interaction. In the case of inhomogeneous waves, the slowness surfaces change their shape and magnitude, for all crystals. However, for paratellurite, this effect is again extraordinary. As soon as a relatively small inhomogeneity is considered, the sound velocity for the QSH mode becomes really exceptionally anisotropic, resulting in a slowness surface that is almost spherical, covered by pins. The velocity corresponding to those 'pins', is much lower than in the case of homogeneous plane waves, which is very promising for the future development of acousto-optic cells involving an even higher figure of merit.
This work is partly performed at the Department of Physics, M. V. Lomonosov Moscow State University, 119992 Moscow, Russia, in collaboration with Nataliya V. Polikarpova and Vitaly B. Voloshinov

INTRODUCTION

Because it is my intention to study the field of Acousto-Optics, apart from Schlieren photography, better in the future, a first step in this direction was taken by studying paratellurite. I have been introduced in the field of Acousto-Optics (apart from Schlieren photography) by Oswald Leroy, Mack A. Breazeale, Jacques Sapriel, Nataliya V. Polikarpova, Vitaly B. Voloshinov, Vladimir Kotov, Vladimir N. Molchanov, Sergey N. Antonov, Antoni Sliwinski, V. Petrov, J. Yamada, Raymond J. Besson, Ludmilla Kulakova, Gennady N. Shkerdin and lately, an extra and well appreciated stimulus also came from Robert Mertens. Also the fruitful discussions with other researchers and with fellow students during the "VII International Conference for Young Researchers on Wave Electronics and its Applications in Information and Telecommunication Systems, St Petersburg, Russia", organized by Sergei V. Kulakov and during the "9th School of Acousto-Optics and Applications , Gdansk, Poland", organized by Antoni Sliwinski, form a real impetus to study acousto-optics better in the future. The information about the Acousto-Optic background of paratellurite, as is outlined further on in this introduction, was partly obtained, after fruitful discussions, from Vitaly B. Voloshinov and Nataliya V. Polikarpova and also from the book of Xu and Stroud [1].

The subject of this section XII.B.2 is related to Acoustics and Acousto-Optics [1-7]. Acousto-Optics is the field of Physical Acoustics that investigates the phenomenon of the interaction of optic waves with diffraction gratings induced by acoustic waves in crystals. The investigations in Acousto-Optics, to a great extent, are stimulated by the wide applications of this physical phenomenon in science and technology for the control of parameters of optical beams. Dozens of modifications of acousto-optic modulators, deflectors, filters and optical information processing devices have been used in modern science and technology to regulate the amplitude, the frequency, the phase, the direction of polarization and other parameters of coherent and non-coherent beams [8-12].

Progress in Acousto-Optics during recent years was stimulated by the following reason. New crystalline materials have been grown by specialists in Crystal Technology, especially for the purposes of Acousto-Optics. These materials are characterized by a unique combination of physical properties, e.g. the optical, acoustic and acousto-optic properties. The new materials grown during the recent years are the crystals based on compounds of tellurium and mercury, e.g. paratellurite (TeO_2), calomel (Hg_2Cl_2), mercury bromide (Hg_2Br_2), mercury iodide (Hg_2I_2), etc. [8-13]. The single crystal of paratellurite (tellurium dioxide) is one of the most efficient materials known so far in Acousto-Optics. That is why the major amount (more than 90%!) of modern acousto-optic instruments used in science and technology utilize this crystalline material [12].

In acousto-optics, sound forms a diffraction grating on which light diffracts. The result of this interaction depends on the so called 'regime', which is determined by the parameter Q:

$$Q = \frac{2\pi\lambda L}{\Lambda^2 \cos\theta} \tag{XII.B.2_1}$$

where $L/\cos\theta$ is the length of interaction (the length of the light beam in the acousto-optic interaction area), λ is the optical wavelength within the medium, Λ is the acoustic wavelength and θ is the angle of light beam incidence (measured with respect to the acoustic wavefront).
Basically, there are three regimes [14], i.e. the Raman-Nath regime ($Q \ll 1$), the Bragg regime ($Q \geq 4\pi$) and an intermediate regime ($Q \approx 1$). In the Raman-Nath regime, several diffraction orders are stimulated, whereas in the Bragg regime, if light is incident at the Bragg angle, more than 85% of the light intensity is diffracted into the first diffraction order. Most acousto-optic devices operate in the Bragg regime and apply the acousto-optic effect for light deflection. The diffraction efficiency η in acousto-optics is the ratio of the intensity of the first order diffracted light and the zero order (un)diffracted light. If we consider the wavelength of light in free space, λ_0, the angle of light beam incidence (measured from the normal to the sound beam), θ, the length of interaction (the length of the light beam in the acousto-optic interaction area), L, the width of interaction (the length of the ultrasonic beam in the acousto-optic interaction area), H, the average energy flow of acoustic power, P_a , then, in the Bragg regime of diffraction, this diffraction efficiency is given by [1, 15-17]

$$\eta = \sin^2\left(\frac{\pi}{\lambda_0 \cos\theta}\left(\frac{M_2 L}{2H} P_a\right)^{1/2}\right) \tag{XII.B.2_2}$$

with

$$M_2 = \frac{n^6 p^2}{\rho V^3} \qquad \text{(XII.B.2\_3)}$$

for isotropic diffraction and

$$M_2 = \frac{n_i^3 n_d^3 p^2}{\rho V^3} \qquad \text{(XII.B.2\_4)}$$

for birefringent diffraction. The refractive index along the direction of incidence is given by n_i, whereas the one along the diffraction direction is n_d. The quantity M_2 is called the acousto-optic *figure of merit* and is completely determined by the properties of the considered media. The quantity p is the effective photoelastic coefficient, and depends on the elasto-optic properties of the considered media.

The basic advantage, characteristic feature and peculiarity of tellurium dioxide consist of the strong anisotropy of its elastic properties. The anisotropy contributes to the extremely high acousto-optic figure of merit of the material $M_2 = 1200 \cdot 10^{-18}\ \mathrm{s}^3/g$ that is about 1000 times higher than in the reference crystal of quartz [8-12]. The high figure of merit in paratellurite originates from the extremely low magnitude of the slow shear acoustic wave propagating along the [110] direction in the crystal (V = 616 m/s) that is only 2 times higher than the velocity of sound in air. On the other hand, the waves sent along the axes X ([100]) and Y ([010]) of the material are characterized by the velocity value V = 3050 *m/s* that is 5 times higher [11]. It should be noted that, in crystalline materials with a moderate elastic anisotropy, such as quartz, the ratio of the maximal and minimal phase velocity values is less than 2.5 [11, 18].

The strong dependence of the acoustic phase velocity on the direction of propagation automatically results in large walkoff angles ψ between the phase (V) and the group (V_g) velocities of ultrasound [11, 18, 19]. It was shown that the walkoff angle ψ between the acoustic wave vector and the Pointing vector in the crystal may exceed $\psi > 70^0$ [18, 19]. This characteristic feature of the waves is unique compared to the majority of other crystalline materials applied in Acoustics and Acousto-Optics. This peculiarity as well as the low phase velocity may give rise to many unusual and even new effects that can be observed during the propagation and the reflection of homogeneous bulk elastic waves in the materials [18]. It may also be expected that the elastic anisotropy influences not only the homogeneous bulk elastic wave propagation in paratellurite but also the propagation of inhomogeneous waves in the material. Therefore, one of the goals of the present research consists of the analysis of the propagation of inhomogeneous elastic waves in this extraordinary anisotropic material. Note that inhomogeneous waves [20] are not only important from a theoretical point of view, but they can also be generated experimentally in a bounded form [21].

THEORETICAL BACKGROUND

Field parameters

It is known [22-23] that for piezoelectric materials, the stress tensor is given by

$$\sigma_{ij} = c_{ijkl} e_{kl} - \xi_{kij} E_k \tag{XII.B.2_5}$$

whereas the electrical displacement is given by

$$D_k = \varepsilon_{ki} E_i + \xi_{kij} e_{ij} \tag{XII.B.2_6}$$

with

$$c_{ijkl} = \beta_{im}\beta_{jn}\beta_{kp}\beta_{lq} c'_{mnpq} \tag{XII.B.2_7}$$

$$\xi_{kij} = \beta_{kp}\beta_{iq}\beta_{jr}\xi'_{pqr} \tag{XII.B.2_8}$$

and

$$\varepsilon_{ki} = \beta_{kp}\beta_{iq}\varepsilon'_{pq} \tag{XII.B.2_9}$$

β_{ij} are the entries of the rotation matrix for a rotation from the intrinsic lattice coordinate system to the laboratory coordinate system whereas c_{ijkl} is the stiffness tensor, ξ_{kij} is the piezoelectric stress tensor, ε_{ij} is the dielectrical permittivity tensor, $\mathbf{E}$ is the electric field vector, $\mathbf{D}$ is the dielectric displacement vector and e_{kl} is the strain tensor. The quantities c_{ijkl}, ξ_{kij} and ε_{ij} are valid in the laboratory coordinate system, whereas c'_{ijkl}, ξ'_{kij} and ε'_{ij} are valid in the intrinsic lattice coordinate system.

From [22] we know that any field $\mathbf{E}$ can be described in a rotational field $\mathbf{E}^r$ with $\nabla \times \mathbf{E}^r \neq 0$ and an irrotational field $\mathbf{E}^{irr}$ with $\nabla \times \mathbf{E}^{irr} = 0$. For ultrasonic waves, the accompanying electric field is quasistatic and can be described by $\mathbf{E} = \mathbf{E}^{irr}$, whence

$$\mathbf{E} = -\nabla\varphi \tag{XII.B.2_10}$$

with φ a scalar potential.

the Christoffel equation

The acoustic wave equation for visco-elastic materials is given by

$$\frac{\partial \sigma_{ij}}{\partial r_j} = \rho \frac{\partial^2 u_i}{\partial t^2} \tag{XII.B.2_11}$$

whilst the electromagnetic field equations in the absence of electric currents and electric loads are given by

$$\nabla \times \mathbf{E} = \mu_0 \frac{\partial \mathbf{H}}{\partial t} \tag{XII.B.2_12}$$

and

$$\nabla \times \mathbf{H} = \frac{\partial \mathbf{D}}{\partial t} \tag{XII.B.2_13}$$

Taking into account (XII.B.2_10), relations (XII.B.2_12-13) can be replaced by

$$\nabla \bullet \frac{\partial^2}{\partial t^2} \left(-\varepsilon_{ki} \frac{\partial \varphi}{\partial r_i} + \xi_{kij} \frac{\partial u_j}{\partial r_j} \right) = 0 \tag{XII.B.2_14}$$

If we consider plane waves, then

$$\mathbf{u} = A\mathbf{P} \exp i\left(k_x x + k_x y + k_z z - \omega t \right) \tag{XII.B.2_15}$$

and

$$\varphi = B \exp i\left(k_x x + k_y y + k_z z - \omega t \right) \tag{XII.B.2_16}$$

Then, relation (XII.B.2_14) immediately involves

$$B = \frac{k_r k_s \xi_{rsq} A P_q}{\varepsilon_{mn} k_m k_n} \tag{XII.B.2_17}$$

Furthermore, combining relations (XII.B.2_11) and (XII.B.2_14) delivers [22]

$$M_{ip} P_p = 0 \tag{XII.B.2_18}$$

Equation (XII.B.2_18) is an extension of the Christoffel equation. Only nontrivial solutions $\mathbf{P} \neq 0$ are possible whenever

$$\det M = 0 \qquad \text{(XII.B.2\_19)}$$

The expressions of M_{ij} can be found in [22]. This 6th degree polynomial is the so called stiffened Christoffel equation.

energy flux

From [22] we know that the instantaneous Poynting vector is given by

$$F_i = \frac{1}{2}\left[-\sigma_{ij}\frac{\partial u_j^+}{\partial t} + \varphi\frac{\partial D^+}{\partial t}\right] \qquad \text{(XII.B.2\_20)}$$

in which the superscript '+' means 'complex conjugate'. Without presuming the wave vector to be real or complex, it can be shown straightforwardly that (XII.B.2_20), becomes, for an amplitude equal to unity,

$$F_i = \frac{1}{2}\omega\left\{\left(c_{ilkj}\right)k_k P_l^+ P_j + \left(B\left(\xi_{kij}k_k - \xi_{ijk}^+ k_k^+\right)\right)P_j^+ + \varepsilon_{ij}^+ k_j^+ |B|^2\right\} \qquad \text{(XII.B.2\_21)}$$

The average power then corresponds to the real part of F_i, whereas the peak reactive power corresponds to the imaginary part of F_i [22].

OVERVIEW OF CLASSICAL SLOWNESS SURFACES IN PARATELLURITE

Classically, taking into account Einstein's double suffix notation convention, the (real) wave vector **k** is replaced by $\mathbf{k} = l\omega\left(d_{1,g}\mathbf{e}_g\right)$ and entered into (XII.B.2_19). ω is the angular frequency. Then, for each (real) direction $\left(d_{1,x}, d_{1,y}, d_{1,z}\right)$, the eigenvalue l can be determined. This l is then the slowness value. At the same time, the polarization vector **P** is determined as the eigenvector. We have developed a program that is able to draw 3D slowness surfaces and, when necessary, adds arrows that represent the polarization or the energy flow. For paratellurite, the slowness surfaces form a complicated 3D structure, consisting of 3 layers that intersect one another. This means that, even though the combined set of three layers is unique, whenever the 3 surfaces are isolated from each other, the presence of an intersection makes that the solution is not unique. In what follows, the three slowness surfaces are isolated from each other through a procedure that classifies the slowness values for each direction, according to their magnitude.
The first mode then always has the largest slowness, the third mode the smallest, whereas the second mode has the intermediate value. The modes are then labeled according to the sound

polarization and are labeled as quasi longitudinal (QL), quasi shear horizontal (QSH) and quasi shear vertical (QSV). If it follows that the polarization is mainly directed along the propagation direction, the label QL is added. If the polarization is mainly shear and directed along the XY-plane, the label QSH is added. If the polarization is mainly shear and directed along the Z-axis, the label QSV is added. The exact physical parameters of paratellurite, that are used in the presented results, can be found in ref [22].

In Fig. XII.B.2_1, the slowness surface for the QL mode is depicted, together with black arrows that denote the polarization direction. Similar surfaces for the QSV and the QSH mode are depicted in Figs XII.B.2_2 and XII.B.2_3. As a demonstration, in Fig. XII.B.2_4, also arrows are added that correspond to the energy flow direction for the QSV mode. Note that the energy flow is directed almost perfectly perpendicular to the slowness surface. If piezoelectricity would have been neglected, the arrows would have been really perfectly normal to the slowness surface.

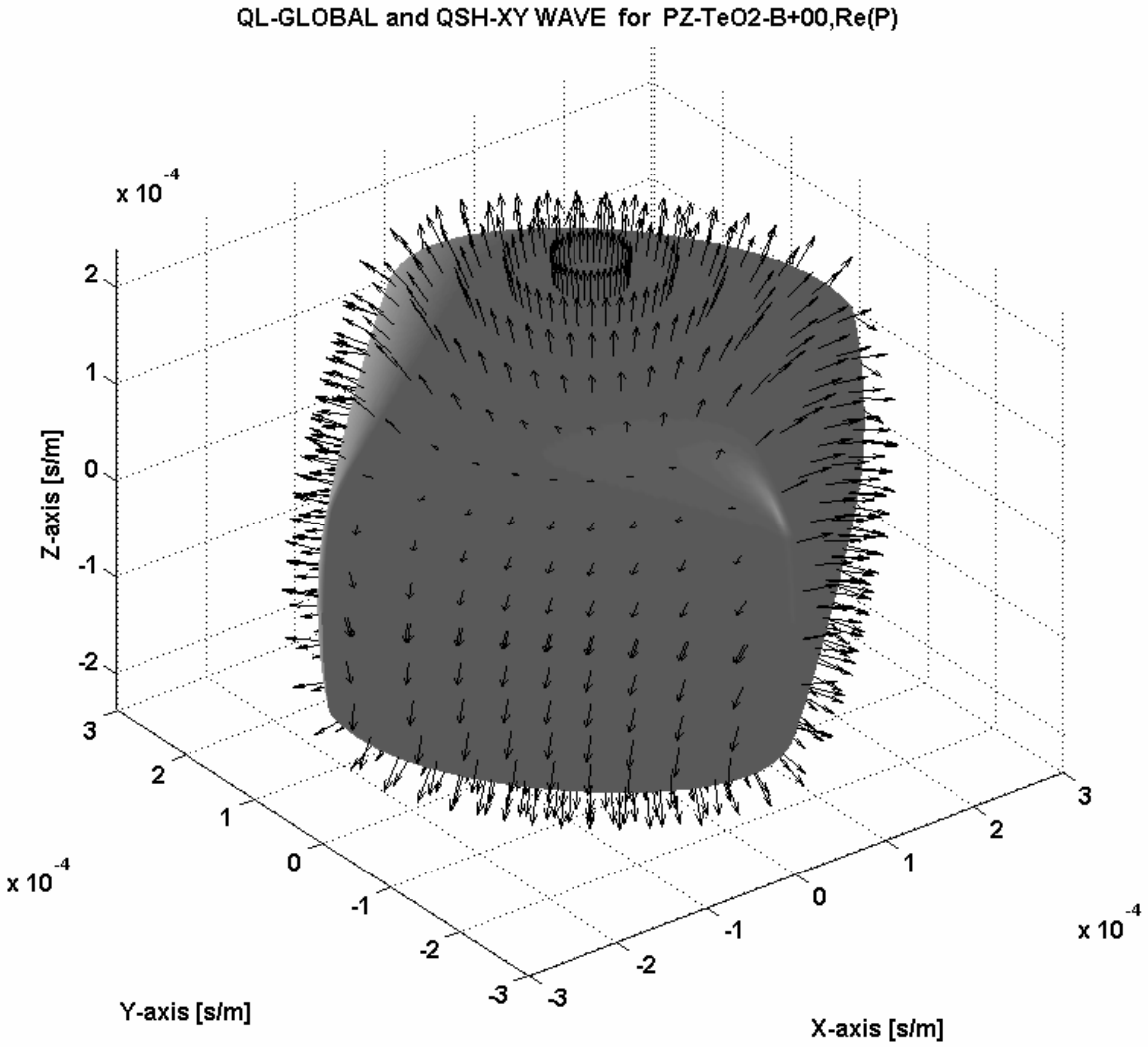

Fig. XII.B.2_1: ***Slowness surface of the QL mode in paratellurite for homogeneous plane waves. The black arrows denote the polarization vector at each point on the slowness surface.***

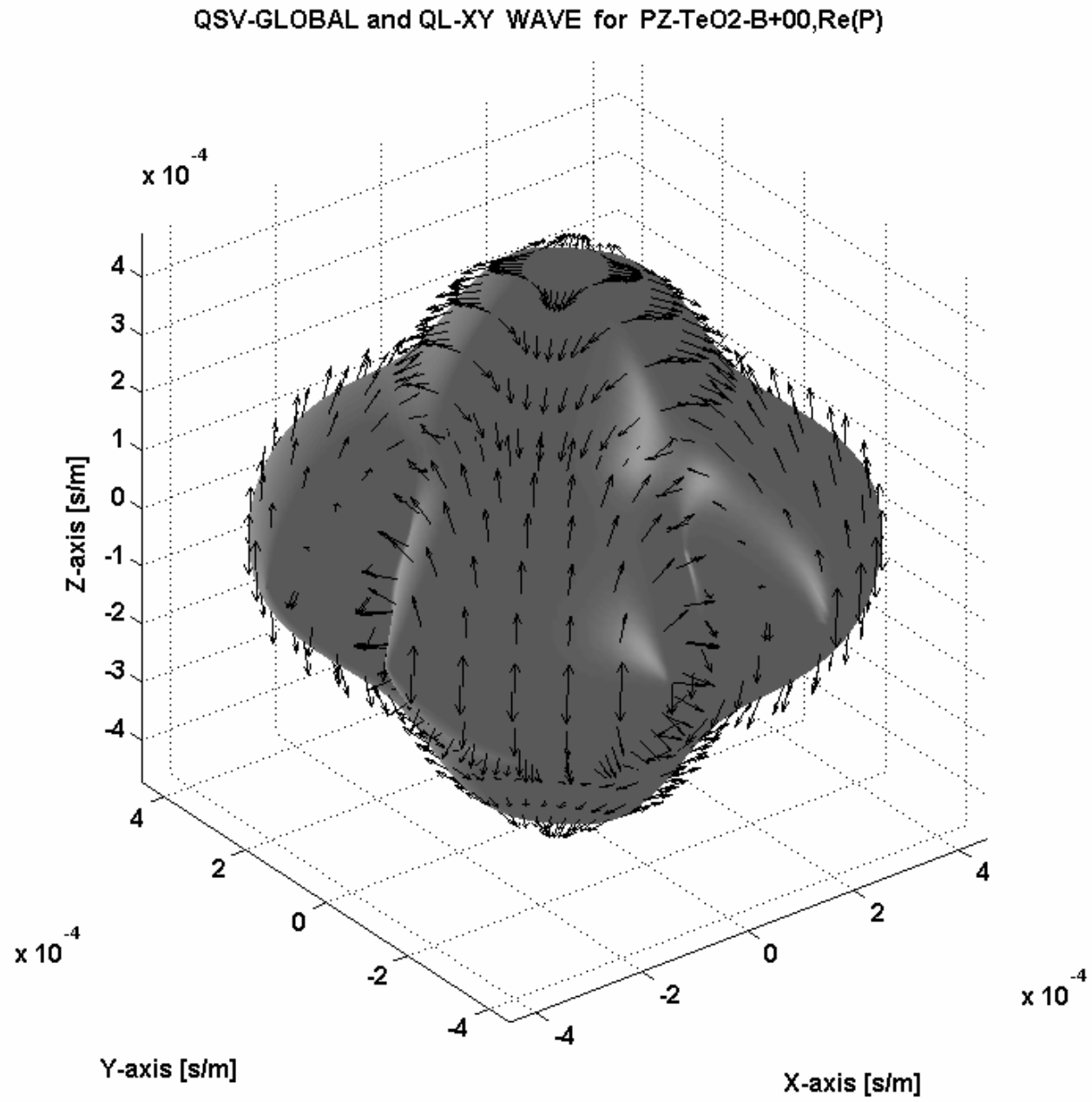

Fig. XII.B.2_2: ***Slowness surface of the QSV mode in paratellurite for homogeneous plane waves. The black arrows denote the polarization vector at each point on the slowness surface.***

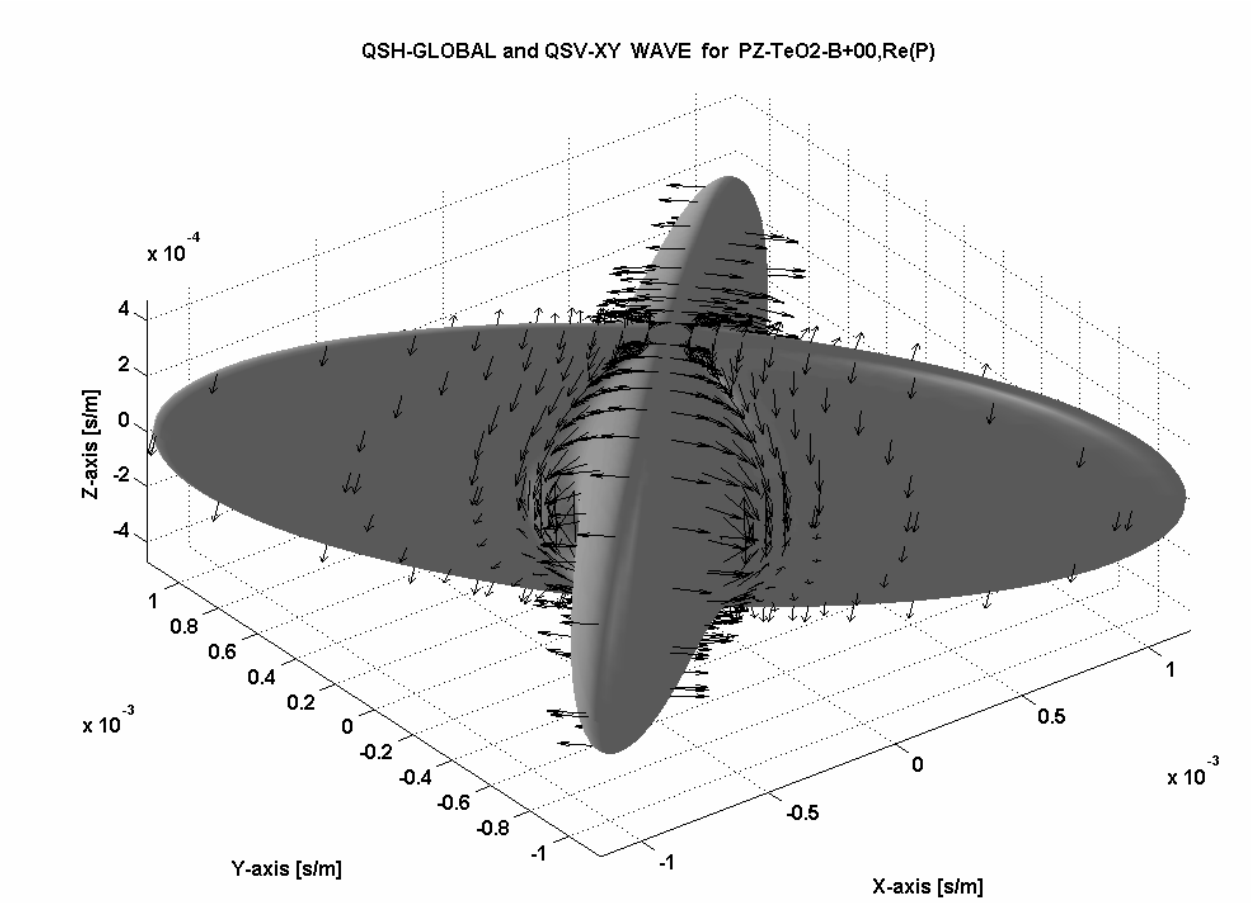

Fig. XII.B.2_3: ***Slowness surface of the QSH mode in paratellurite for homogeneous plane waves. The black arrows denote the polarization vector at each point on the slowness surface. Strong anisotropy is visible, resulting in 4 distinguishable lobes. This is a well known effect for this crystal.***

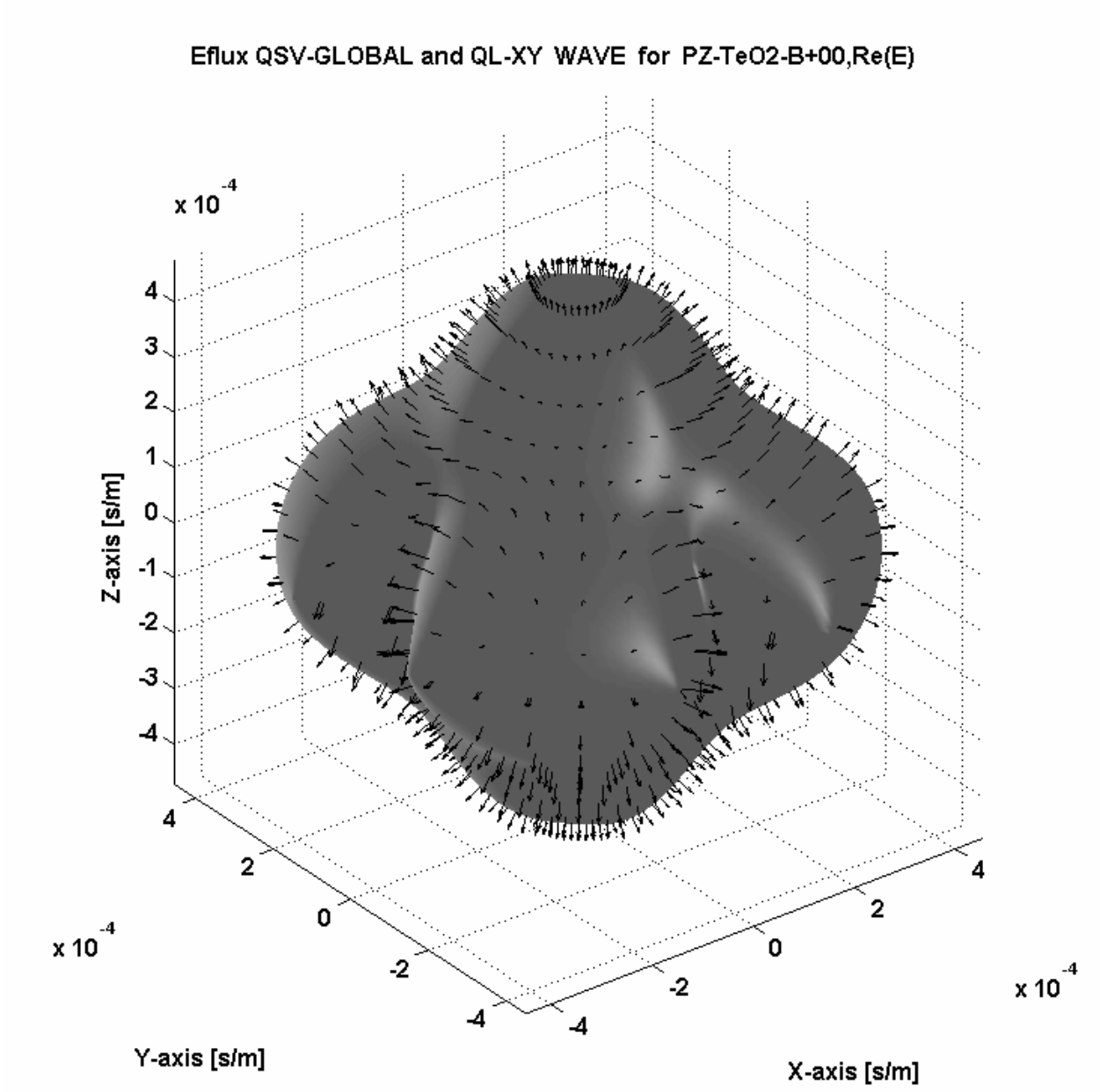

Fig. XII.B.2_4: ***Slowness surface of the QSV mode in paratellurite for homogeneous plane waves. The black arrows denote the Energy flow at each point on the slowness surface. Note that the energy flow is almost perfectly directed perpendicular to the slowness surface.***

INHOMOGENEOUS WAVES IN PARATELLURITE

The behavior of homogeneous plane waves in paratellurite is well described in many references (e.g. ref [1]). Nevertheless, it is also known that inhomogeneous waves can exist in anisotropic media [24-33]. A complete historical overview of the theory of inhomogeneous waves, can be found in [20]. An inhomogeneous wave is defined as a plane wave having a complex wave vector **k**. This results in an exponentially decaying amplitude along the wave front and in a phase velocity that differs from a pure plane wave. The notion of inhomogeneous waves,

inside the bulk of a piezoelectric crystal, is introduced through the concept of a complex direction. A real direction is then defined as a real vector $\mathbf{d}_1$, for which $\mathbf{d}_1 \cdot \mathbf{d}_1 = 1$. This is generalized to a complex direction $\mathbf{d} = \mathbf{d}_1 + i\mathbf{d}_2$, for which $\mathbf{d} \cdot \mathbf{d}^+ = 1$. Then, given the angular frequency ω, it is possible to determine the value *l* from the following definition of the complex wave vector:

$$\mathbf{k} = \mathbf{k}_1 + i\mathbf{k}_2 = l\omega\left(\mathbf{d}_1 + i\mathbf{d}_2\right) \tag{XII.B.2_22}$$

For every possible complex direction, it is possible to determine *l*. The number of combinations of $\mathbf{d}_1$ and $\mathbf{d}_2$ is reduced by introducing a complex direction that, for simplicity, contains no imaginary part along the z-axis.

$$\begin{aligned} &\mathbf{d}_1 + i\mathbf{d}_2 \\ &= \left\{\left(d_{1,x} - ib\sqrt{1-d_{1,y}^2}\right)\mathbf{e}_x + \left(d_{1,y} + ibd_{1,x}\right)\mathbf{e}_y + \left(d_{1,z}\right)\mathbf{e}_z\right\} / \sqrt{1 + b^2\left(2d_{1,x}^2 + d_{1,z}^2\right)} \end{aligned} \tag{XII.B.2_23}$$

The parameter *b* (henceforth called *the inhomogeneity parameter*) is then a measure for the fraction of imaginariness of the complex direction.
When the direction (XII.B.2_23) is entered in the Christoffel's equation (XII.B.2_19), the complex scalar $l = l_1 + il_2$ can be resolved. This value then determines the entire complex wave vector **k** as

$$\mathbf{k} = \left(\left(k_{1,x} + ik_{2,x}\right)\mathbf{e}_x + \left(k_{1,y} + ik_{2,y}\right)\mathbf{e}_y + \left(k_{1,z} + ik_{2,z}\right)\mathbf{e}_z\right) / N \tag{XII.B.2_24}$$

with

$$k_{1,x} / \omega = l_1 d_{1,x} + l_2 b\sqrt{1-d_{1,y}^2} \tag{XII.B.2_25}$$

$$k_{2,x} / \omega = -l_1 b\sqrt{1-d_{1,y}^2} + l_2 d_{1,x} \tag{XII.B.2_26}$$

$$k_{1,y} / \omega = l_1 d_{1,y} - l_2 b d_{1,x} \tag{XII.B.2_27}$$

$$k_{2,y} / \omega = l_1 b d_{1,x} + l_2 d_{1,y} \tag{XII.B.2_28}$$

$$k_{1,z} / \omega = l_1 d_{1,z} \tag{XII.B.2_29}$$

$$k_{2,z} / \omega = l_2 d_{1,z} \tag{XII.B.2_30}$$

and

$$N = \sqrt{1 + b^2 \left(2d_{1,x}^2 + d_{1,z}^2 \right)} \tag{XII.B.2_31}$$

From (XII.B.2_23-31) it is found that b influences directly the real and imaginary part of the wave vector. Furthermore, indirectly, i.e. numerically, the value b also influences the value l, whence $b = 0$ corresponds to a real value for l and $b \neq 0$ corresponds to a complex value for l. It is indeed found in (XII.B.2_23-31), that b and l, form $\mathbf{k}_2$.
Therefore, the inhomogeneity parameter b generates the inhomogeneous feature of sound and influences the sound velocity considerably. This will be shown for the different modes, respectively the QL-mode, the QSV-mode and the QSH-mode, in paratellurite. A similar effect occurs in other crystals. However, it will be shown that in paratellurite, in addition, something extraordinary happens to the slowness surface of the QSH mode.

In what follows, the slowness surfaces correspond, for each direction to the magnitude of the real part of the slowness vector $\mathbf{l} = \mathbf{k} / \omega$.

Inhomogeneous QL modes

The situation where the inhomogeneity parameter *b=0*, has already been given in Fig. XII.B.2_1. Fig. XII.B.2_5 and Fig. XII.B.2_6 show the situation when b is respectively 24/140 and 84/140. It is seen that the slowness surface changes significantly and that this change depends on the direction. Nevertheless, the values of the radius of the slowness surface, remains of the same order of magnitude and it is therefore mainly the shape of the surface that changes. This means that, for this mode, the use of inhomogeneous waves results in different characteristics, though spectacular changes are not observed. For demonstration purposes, in Fig. XII.B.2_6, the black arrows denote the (real part of the) polarization vectors.

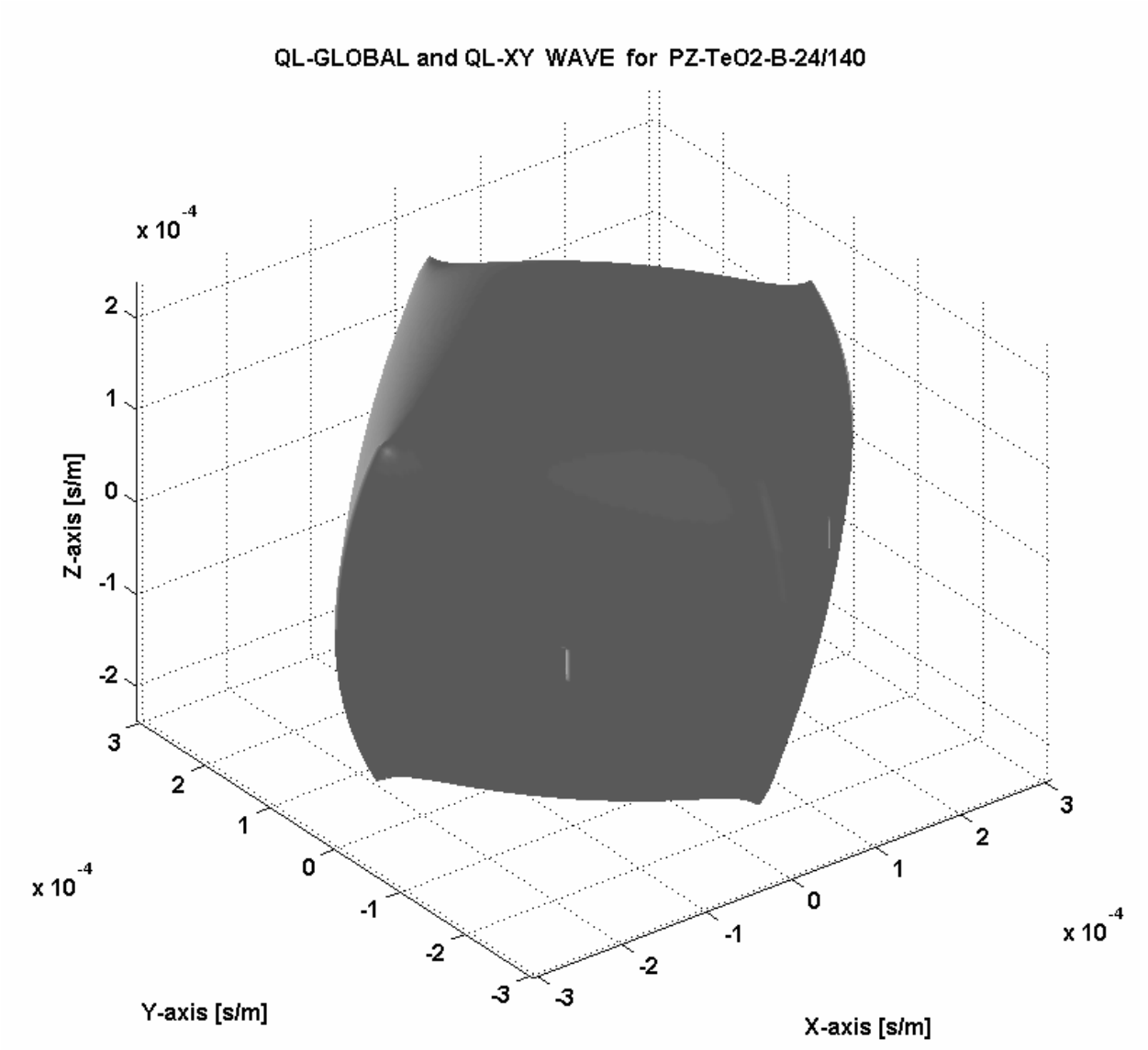

Fig. XII.B.2_5: ***Slowness surface of the QL mode in paratellurite for an inhomogeneity parameter b=24/140. The surface is a little bit less smooth that n in Fig.*** **XII.B.2_*1*.**

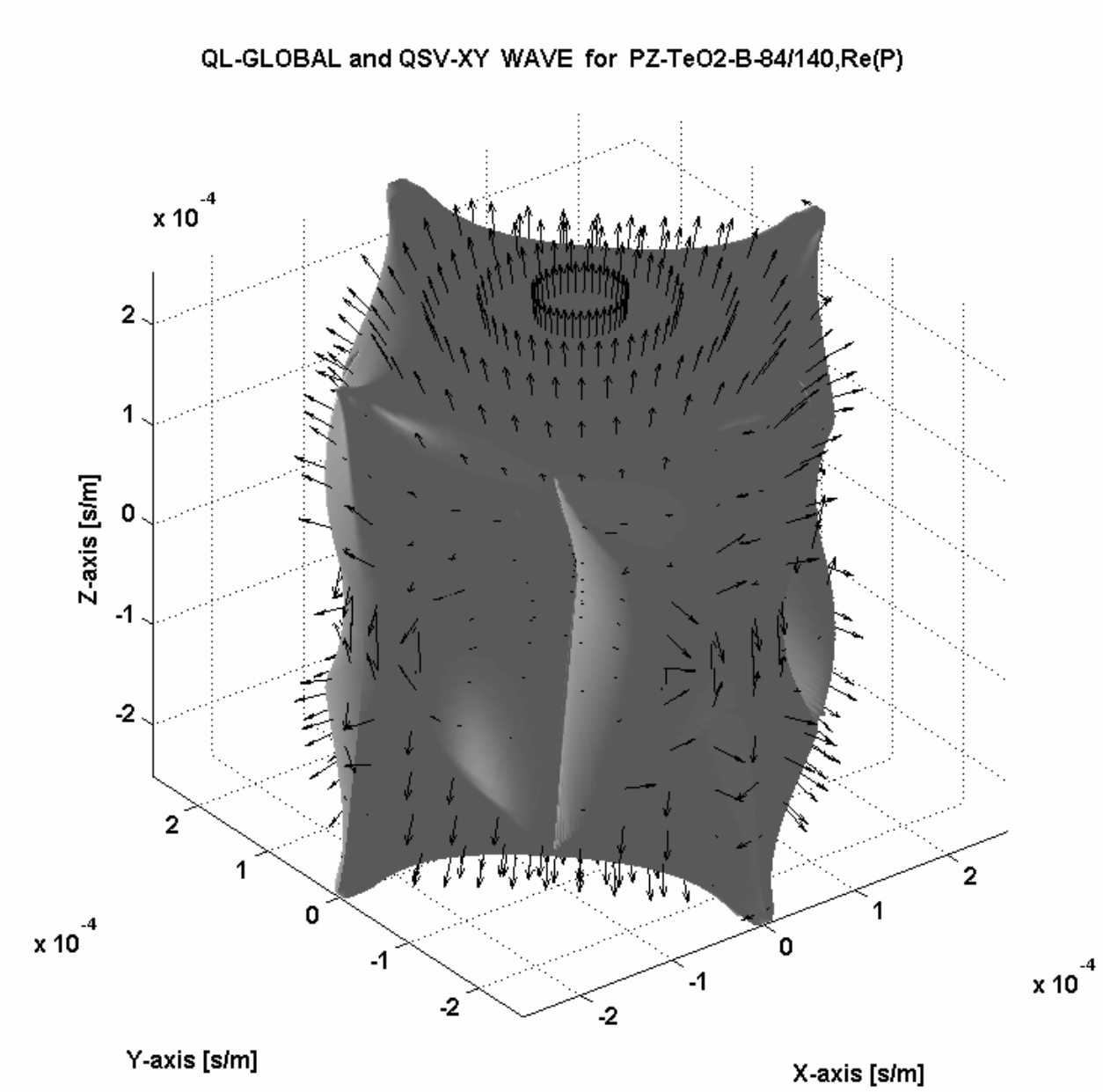

Fig. XII.B.2_6: ***Slowness surface of the QL mode in paratellurite for an inhomogeneity parameter b=84/140. The black arrows denote the polarization vector at each point on the slowness surface. A significant deformation is visible compared to Figs.*** **XII.B.2_*1* and XII.B.2_*5*.**

Inhomogeneous QSV modes

The situation where the inhomogeneity parameter *b=0*, has already been given in Fig. XII.B.2_2. Figs XII.B.2_7 and XII.B.2_8 show the situation when b is respectively 24/140 and 84/140. It is again seen that the slowness surface changes significantly and that the change depends on the direction. Besides the change of shape, the magnitude is also changed

considerably, whence the use of inhomogeneous waves, for this mode, will differ noticeably from the case of homogeneous plane waves. For demonstration purposes, in Fig. XII.B.2_8, the black arrows denote the (real part of the) polarization vectors.

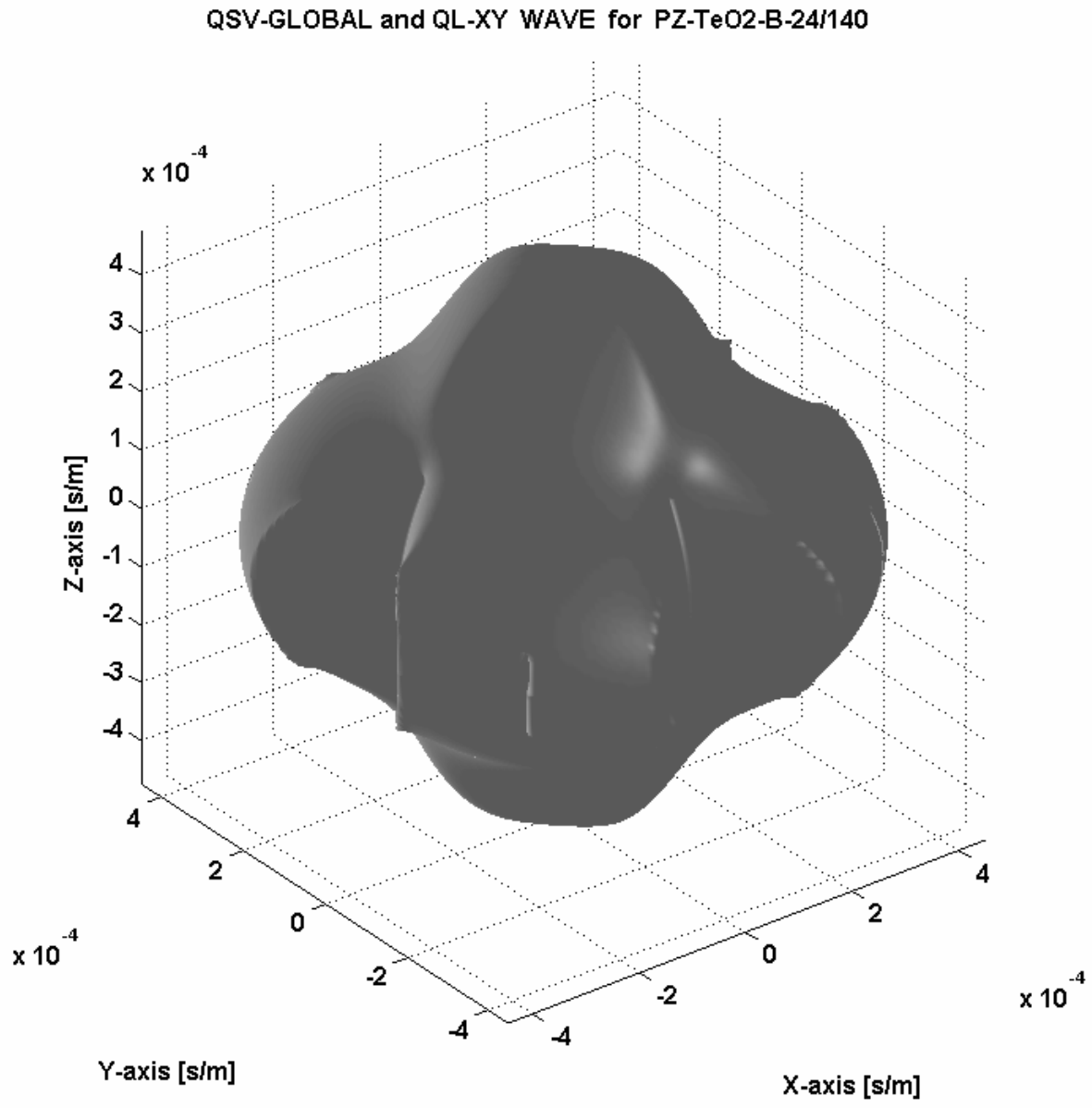

Fig. XII.B.2_7: ***Slowness surface of the QSV mode in paratellurite for an inhomogeneity parameter b=24/140. The surface is a little bit less smooth that n in Fig.*** **XII.B.2_*2*.**

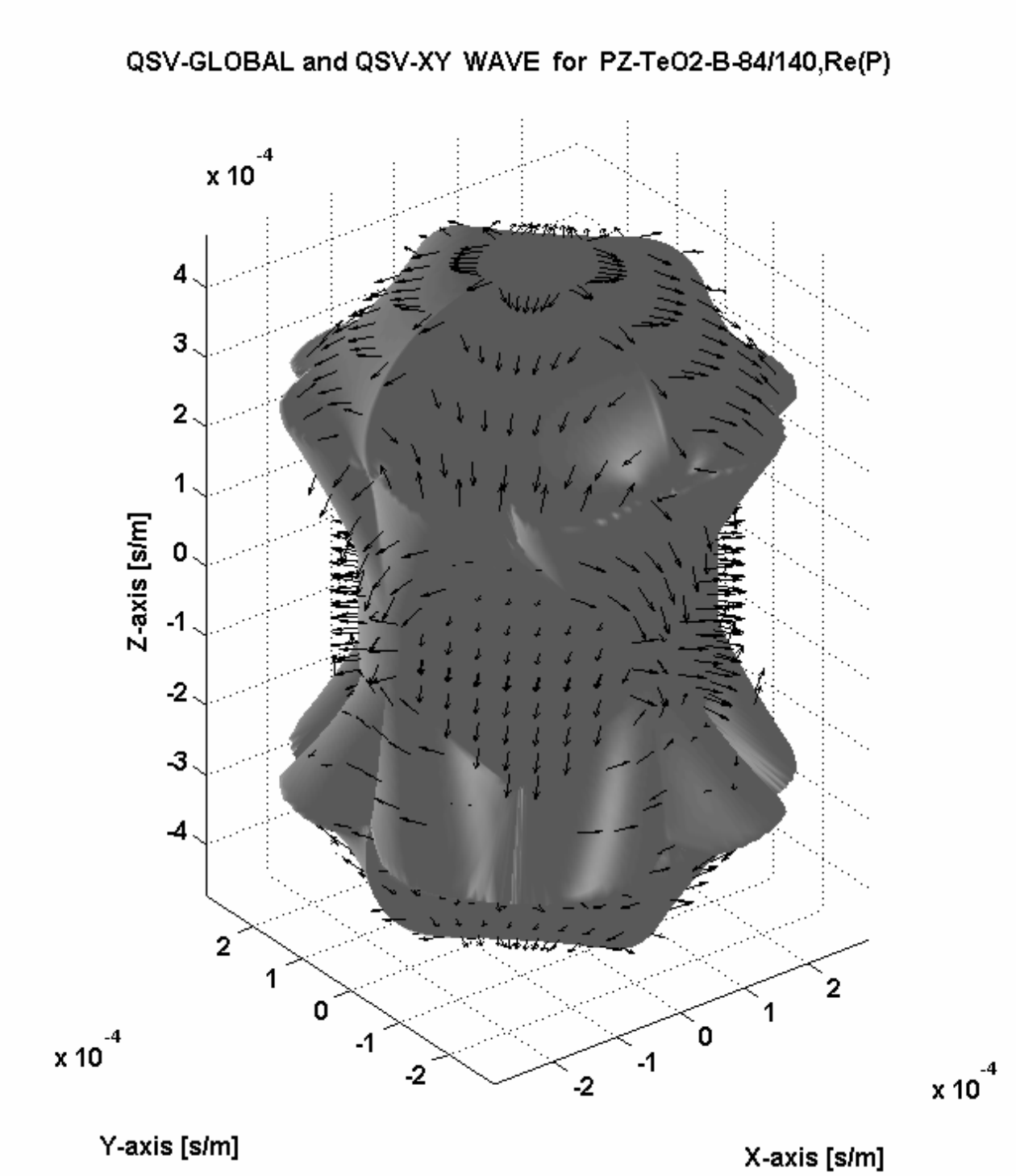

Fig. XII.B.2_8: ***Slowness surface of the QSV mode in paratellurite for an inhomogeneity parameter b=84/140. The black arrows denote the polarization vector at each point on the slowness surface. A significant deformation is visible compared to Figs.*** **XII.B.2_*2 and*** **XII.B.2_*7.***

Inhomogeneous QSH modes

Because we have noticed that something spectacularly happens to the QSH mode, when the inhomogeneity parameter b is increased, we first present the result for a small value of *b*, i.e. *b=12/140*, in Fig. XII.B.2_9. Comparison of Fig. XII.B.2_9 with Fig. XII.B.2_3 shows that the 'lobes' in this slowness surface, are more outspoken in Fig. XII.B.2_9 than in Fig. XII.B.2_3. This means that the anisotropy (or the dependence of the slowness on the direction) has increased. Further growth of the inhomogeneity parameter *b* to *b=24/140*, see Fig. XII.B.2_10, shows that a spectacular deformation of the lobes occurs, reflecting a spectacular increase of the anisotropy. The case of *b=84/140* is given in Fig. XII.B.2_11, where it is seen that the slowness curve has become almost like a sphere, covered by pins.

This means that the slowness is almost isotropic for most directions, and becomes extraordinary large (corresponding to an extraordinary low propagation velocity), for certain directions. For demonstration purposes, the black arrows denote the polarization vectors. This effect of extraordinary anisotropy occurs in any crystal, but only for very large values of *b*. The fact that the effect occurs for paratellurite even for small values such as *b=24/140,* is unique.

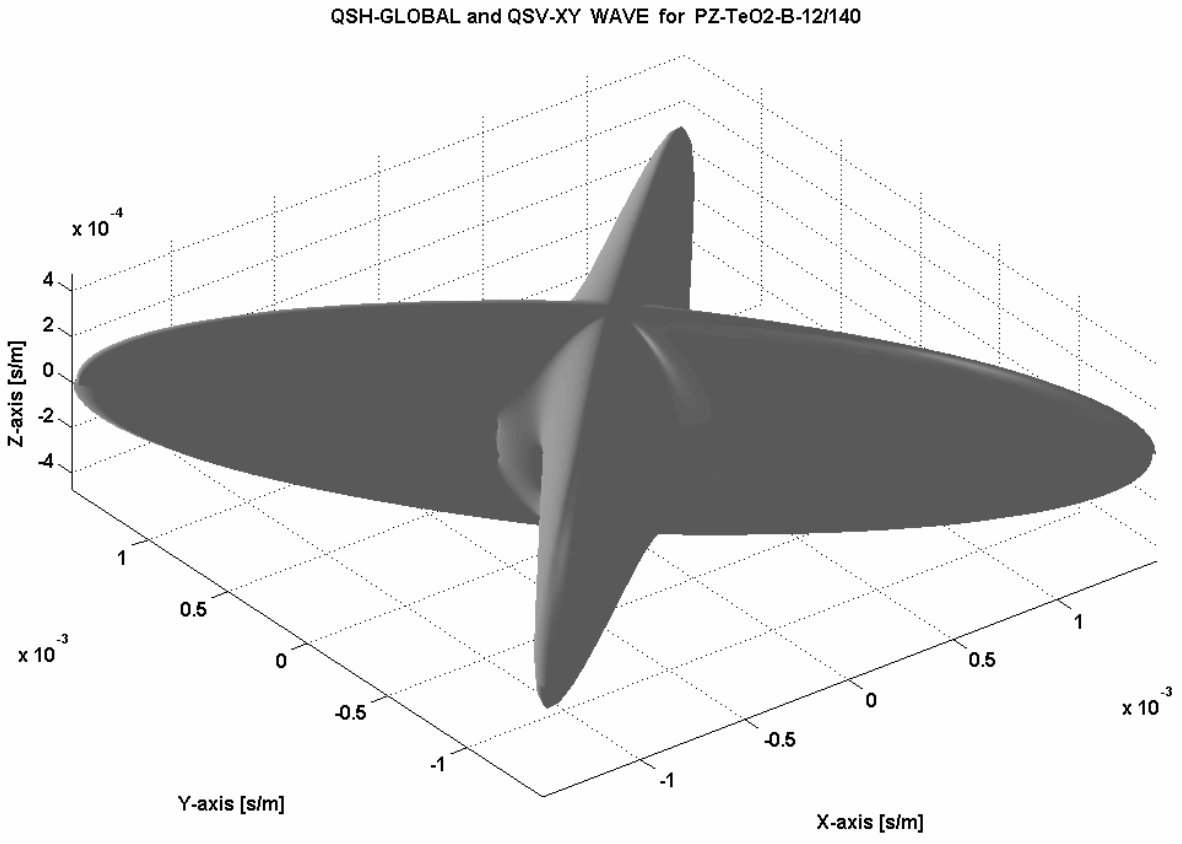

Fig. XII.B.2_9: ***Slowness surface of the QSH mode in paratellurite for an inhomogeneity parameter b=12/140. Compared to Fig.*** **XII.B.2_*3, a slightly increased anisotropy is visible.***

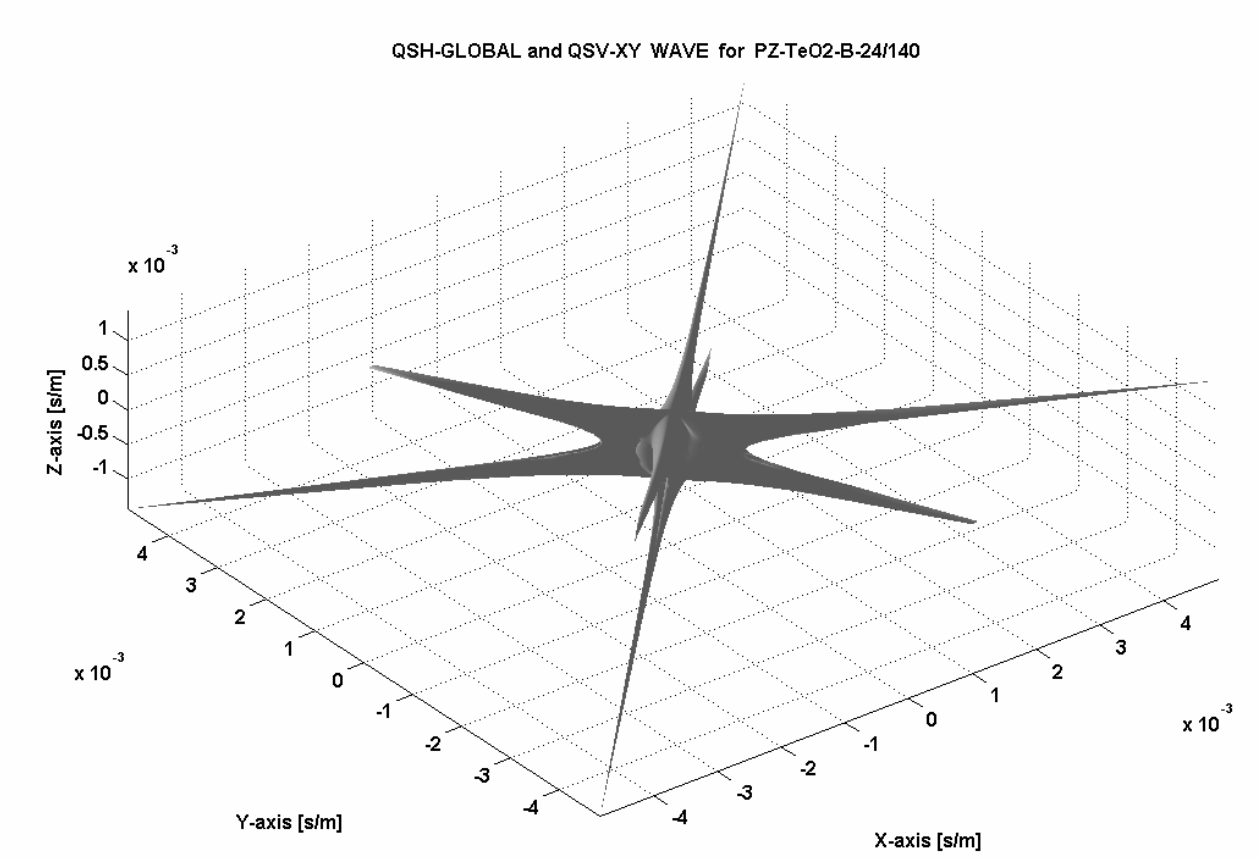

Fig. XII.B.2_10: ***Slowness surface of the QSH mode in paratellurite for an inhomogeneity parameter b=24/140. Compared to Fig.*** **XII.B.2_*9 and Fig.*** **XII.B.2_*3, the anisotropy is spectacularly increased. There is also a splitting effect visible of the 4 lobes.***

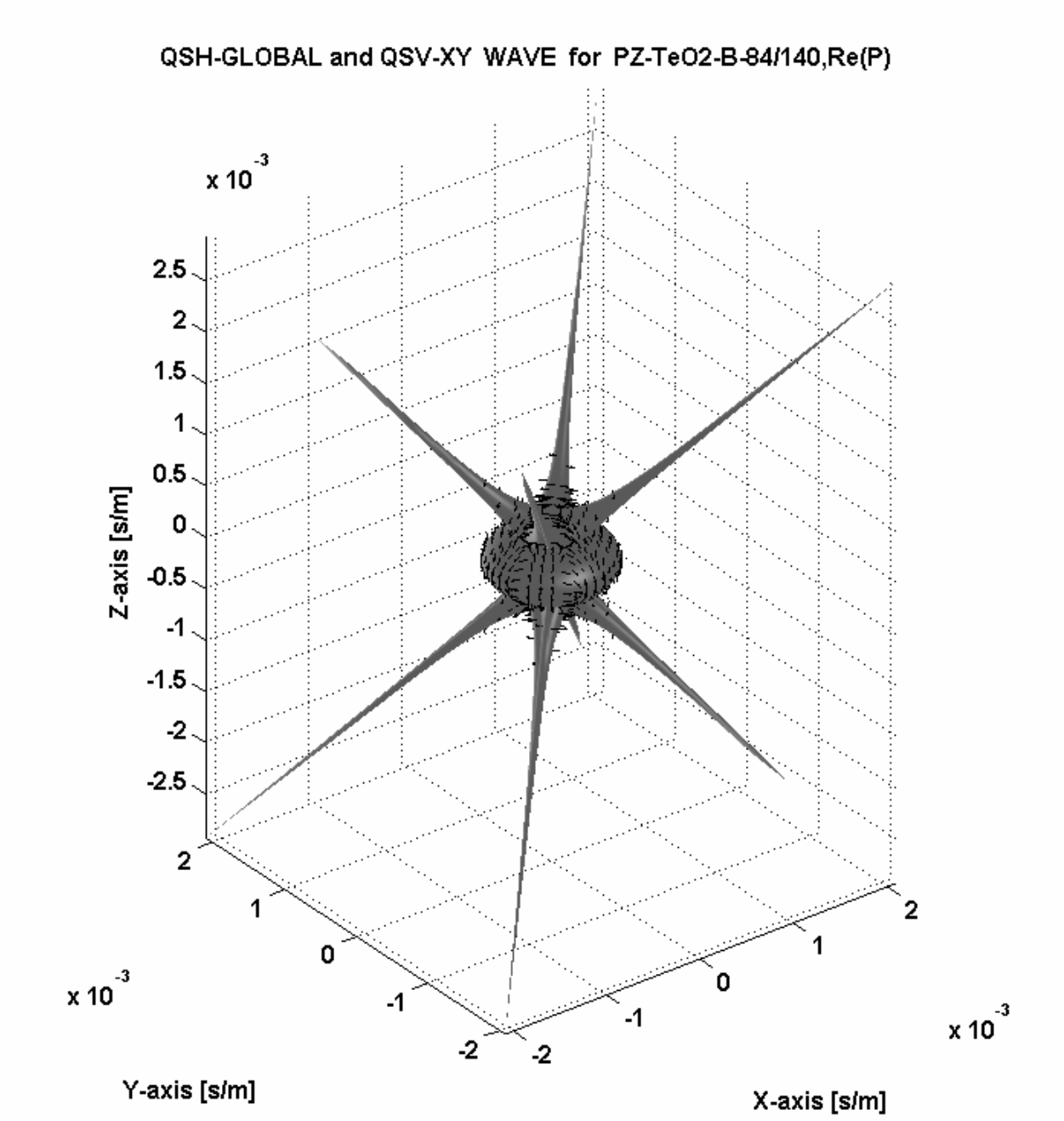

Fig. XII.B.2_11: ***Slowness surface of the QSH mode in paratellurite for an inhomogeneity parameter b=84/140. The black arrows denote the polarization vector at each point on the slowness surface. Compared to Fig.* XII.B.2*_10, the anisotropy is further increased resulting in an almost sphere, covered by 8 pins.***

POSSIBLE CONSEQUENCES IN ACOUSTO-OPTICS

It is known that one of the simplest ways to generate an inhomogeneous acoustic wave is to send a bulk elastic wave on a flat boundary separating two materials with unequal elastic properties or to organize incidence of the elastic energy on a free and flat surface separating a

crystal and the vacuum [11, 18, 34]. After reflection of the incident elastic energy form the boundary, it is quite likely to observe the inhomogeneous elastic wave propagating along the separating border. Consequently, the possibility of the inhomogeneous wave generation in an acousto-optic crystal tellurium dioxide should be considered each time a bulk acoustic wave is reflected from a free surface. Furthermore, acousto-optic devices could be manufactured in the future that produce bounded inhomogeneous bulk waves [21]. We would not be surprised that, especially in paratellurite, very interesting effects would be observable. This could generate new and modern acousto-optic devices.

It is known that the design of many classes of modern acousto-optic instruments using paratellurite as the medium of light and sound interaction, is based on the application of reflection of acoustic waves from optical facets separating the crystal and the air [9-12, 18, 34-39]. One of these classes is the class of tunable acousto-optic filters (AOTFs) using the collinear regime of acousto-optic interaction. These filters may be used in many modern systems intended for processing of optical signals in optics and spectroscopy, laser technology and optical information processing. For example, the filters have been used in modern optical WDM (wavelength division multiplexing) communication lines for selection of signals with different optical wavelengths propagating along the fiber waveguides [40, 35, 36, 38, 39]. The elastic reflection is applied in the acousto-optic cells with the purpose to organize, in the most simple and effective way, a collinear propagation of optic and elastic beams in the crystal. The acoustic reflection may also be used in acousto-optic devices based on paratellurite, such as deflectors, modulators and spectrum analyzers, to obtain transformation of a longitudinal acoustic wave into a slow shear acoustic wave propagating along the axis [110] or close to it [9, 10, 12, 18, 39]. In this way, matching of acoustic impedances of acousto-optic cells is obtained. It automatically results in the improvement of the basic operation parameters of the instruments. For example, the acoustic frequency bandwidth of diffraction and the diffracted light intensity may be sufficiently improved if one uses the transformation of the elastic modes [9, 10, 12].

It is evident that in all the described cases, the reflection of the acoustic waves may be accompanied by the generation of inhomogeneous waves, and the use of bounded inhomogeneous bulk waves is principally also possible. In some practical cases, the generation of inhomogeneous waves of the evanescent type, should be considered as a bad (parasitic) effect, because the efficiency of the elastic energy transformation is decreased. For this purpose, during the design of an acousto-optic instrument, it is necessary to know the laws and the conditions of the inhomogeneous waves generation and propagation in tellurium dioxide. This may result in the design of novel modifications of acousto-optic devices with improved parameters. On the other hand, if experiments would show that the use of bounded inhomogeneous bulk waves is favorable for some applications, additional studies will be required to predict the behavior of the considered inhomogeneous waves while propagating and while scattering, and to improve the design of the acousto-optic device and obtain better quality.

CONCLUSIONS AND PROSPECTS

In this section, the description and the laws of propagation of bulk inhomogeneous plane waves in the TeO_2 single crystal, are examined. The results of the investigation indicate that the efficiency of TeO_2 for the acousto-optic interaction, may be further enhanced, by using inhomogeneous waves instead of homogeneous plane waves. This is due to the increased velocity difference for certain directions, compared to the case when only homogeneous plane waves are taken into account. Acousto-optic modulators, deflectors and filters should be mentioned in this context. Furthermore, it must also be mentioned that the peculiarities of the inhomogeneous waves behavior are typical not only for the paratellurite single crystals but for many other materials, if they are characterized by a very strong elastic anisotropy. For example, the results of the analysis may be generalized to the entire family of crystals such as the mercury halides (calomel, mercury bromide and mercury iodide). At the moment, these materials, as well as paratellurite, are very promising for the application in modern acousto-optic devices.

The numerical study in this section shows that it is possible to predict the existence of new acoustic and acousto-optic phenomena in crystals such a paratellurite. The investigation of laws and regular trends of the propagation of waves in the new materials may be the basic direction of the future scientific research. Therefore, the study is not only interesting from a fundamental point of view, but also from the point of applications.

REFERENCES

[1] Jieping Xu, Robert Stroud, *Acousto-Optic Devices: Principles, Design and Applications*, John Wiley & Sons, Inc., 1992, New York

[2] J. Sapriel, *Acousto-Optics*, John Wiley & Sons, 1979

[3] Adrian Korpel, *Acousto-Optics : second edition*, Marcel Dekker, Inc, New York, 1997

[4] Adrian Korpel (editor), *Selected Papers on Acousto-Optics*, SPIE Milestone Series Volume MS 16, SPIE Optical Engineering Press, 1990

[5] Robert Mertens, "Sixty years of acousto-optics. Fifty years of scientific research at two Flemish universities (Gent and Leuven-Kortrijk), AWLSK, Klasse der Wetenschappen 57(3), 1995.

[6] W. Hereman, R. Mertens, F. Verheest, O. Leroy, J. M. Claeys, E. Blomme, "Interaction of light and ultrasound: acousto-optics", Physicalia Magazine 6(4), 213-245.

[7] Leroy Oswald, Declercq Nico F., Degrieck Joris, "The Acousto-Optic interaction from a fundamental point of view to its applications in non-destructive testing", ULT-Gen-002, Proceedings of Forum Acusticum (3rd EAA European Congress on Acoustics, XXXIII Spanish Congress, Tecniacustica 2002, 3rd Iberian Congress on Acoustics, European and Japanese Symposium - EAA - SEA - ASJ, Expoacustica 2002), Sevilla Spain, 16-20 Sepember 2002.

[8] A.Yariv, P.Yeh, *Optical Waves in Crystals*, Wiley and Sons, New York, USA (1984).

[9] J.Xu and R.Stroud, *Acousto-Optic Devices*, John Wiley & Sons, New York, USA (1992).

[10] A.Goutzoulis and D.Pape, *Design and Fabrication of Acousto-Optic Devices*, Marcel Dekker Inc., (1994).

[11] E.Dieulesint et D.Royer, *Ondes Elastiques dans les Solides,* Mason, Paris, France (1974).

[12] Willam L. Wolf, *Optical Engineer's Desk Reference*, Optical Society of America, Washington DC, USA (2003).

[13] M. Gottlieb, A. Goutzoulis and N. Singh, "High-performance acousto-optic materials: Hg_2Cl_2 and $PbBr_2$ ", *Opt. Eng*., 31, N 10, p. 2110-2117, 1992.

[14] W. R. Klein and B. D. Cook, "Unified approach to Ultrasonic Light Diffraction", IEEE Trans. Sonics and Ultrasonics, SU-14, 123-134, 1967

[15] G. A. Coquin, D. A. Pinnow, A. W. Warner, "Physical Properties of Lead Molybdate Relevant to Acousto-Optic Device Applications", J. Appl. Phys., 42, 2162-2168, 1971

[16] N. Uchida, Y. Ohmachi, "Elastic and Photoelastic Properties of TeO_2 Single Crystal", J. Appl. Phys, 40, 4692-4695, 1969
[17] T. Yano, A. Watanabe, "Acousto-Optic Figure of Merit of TeO_2 for Circularly Polarized Light", J. Appl. Phys. 45, 1243-1245, 1974
[18] N.V.Polikarpova and V.B.Voloshinov "Application of Acousto-Optic Interactions in Anisotropic Media for Control of Light Radiation", *Acustica-Acta Acustica*, v. 89, p. 930-935, 2003.
[19] V.B. Voloshinov, "Anisotropic Light Diffraction on Ultrasound in a Tellurium Dioxide Single Crystal", *Ultrasonics*, v.31, N 5, p.333-338, 1993.
[20] Nico F. Declercq, Rudy Briers, Joris Degrieck, Oswald Leroy, "The History and Properties of Ultrasonic Inhomogeneous Waves", accepted for publication in IEEE-UFFC.
[21] Nico F. Declercq, Joris Degrieck, Oswald Leroy, "The Laplace transform to describe bounded inhomogeneous waves", J. Acoust. Soc. Am. 116(1), 51-60, 2004
[22] B. A. Auld, *Acoustic fields and waves in solids, volume I, second edition*, Krieger, Florida, 1989
[23] Adnan H. Nayfeh, *wave propagation in layered anisotropic media*, North Holland, Elsevier, 1995
[24] Michael Hayes, "Inhomogeneous plane waves", Arch. Ration. Mech. Anal. 85, 41-79, 1984
[25] S. I. Rokhlin, T. K. Bolland, L. Adler, "Reflection and refraction of elastic waves on a plane interface between two generally anisotropic media", J. Acoust. Soc. Am. 79(4), 906-918, 1986
[26] B. Hosten, M. Deschamps, B. R. Tittmann, "Inhomogeneous wave generation and propagation in lossy anisotropic solids. Application to the characterization of viscoelastic composite materials", J. Acoust. Soc. Am. 82(5), 1763-1770, 1987
[27] B. Hosten, "Bulk heterogeneous plane waves propagation through viscoelastic plates and stratified media with large values of frequency domain", Ultrasonics 29, 445-450, 1991
[28] Marc Deschamps, Bernard Hosten, "The effects of viscoelasticity on the reflection and transmission of ultrasonic waves by an orthotropic plate", J. Acoust. Soc. Am. 91(4), 2007-2015, 1992
[29] Patrick Lanceleur, Helder Ribeiro, Jean-François De Belleval, "The use of inhomogeneous waves in the reflection-transmission problem at a plane interface between two anisotropic media", J. Acoust. Soc. Am., 93(4), 1882-1892, 1993
[30] M. Deschamps, F. Assouline, "Attenuation Along the Poynting Vector Direction of Inhomogeneous Plane Waves in Absorbing and Anisotropic Solids", Acustica – Acta Acustica, 86, 295-302, 2000
[31] Bruno Rogé, "Réflexion/transmission d'une onde plane inhomogene incidente sur une interface plane séparant deux milieux anisotropes", Thesis, Université de Technologie de Compiègne, France, 1999
[32] Boulanger P, Hayes M, "Special inhomogeneous waves in cubic elastic materials", Zeitschrift fur angewandte mathematik und physik 51(6), 1031-1038, 2000.
[33] M. Deschamps, O. Poncelet, "Inhomogeneous plane wave and the most energetic complex ray", Ultrasonics 40, 293-296, 2002
[34] B.A. Auld, *Acoustic Fields and Waves in Solids*, Robert Krieger Publ. Company, (1990).
[35] V.B.Voloshinov and V.N.Parygin, "Tunable Acousto-Optic Filters and Their Applications in Laser Technology, Optical Communications and Processing of Images", *Proc. SPIE*, v. 4353, p. 17-22, 2001.
[36] J. Sapriel, D. Charissoux, V. Voloshinov et al., "Tunable Acousto-Optic Filters and Equalizers for WDM Applications", *Journal of Lightwave Technology*, v.20, N5, p. 864-871, 2002.
[37] S.N. Antonov, A.V. Gerus and V.V. Proklov, "Effects at skimming incidence of sound on a boundary in TeO_2", *Sov. Phys. Tech. Phys*. 28, p. 984-987, 1983.
[38] J.C. Kastelik, M.G. Gazalet, C. Bruneel and E. Bridoux, "Acoustic shear wave propagation in paratellurite with reduced spreading", *J. Appl. Phys*., 74, N. 4, p. 2813-2817, 1993.
[39] C.D. Tran and G.-C. Huang, "Characterization of the collinear beam acousto-optic tunable filter", *Opt. Eng*., 38, N7, p.1143-1148, 1999.
[40] V.B.Voloshinov, "Close to Collinear Acousto-Optical Interaction in Paratellurite" *Opt. Eng.*, v. 31, N.10, p. 2089-2094, 1992.

XII.C Sound in Biased Piezoelectric Materials of General Anisotropy

A theoretical model is presented that describes the propagation of sound in biased piezoelectric crystals of any kind of symmetry. The symmetry relations for the higher order materials constants of trigonal 3m crystals, are calculated and listed in the appendix. The example of Lithium Niobate is highlighted, under influence of a bias pressure. The change of slowness, because of this pressure, is calculated for every direction. Also the influence of stress on the acoustic polarization and the energy flow is outlined. Furthermore, the difference between the case where piezoelectricity is included and the case where it is omitted, is discussed. The description of changing slowness surfaces, because of a bias field, is not limited to homogeneous plane waves, but also inhomogeneous plane waves are taken into account.

INTRODUCTION

In ultrasonics, a lot of studies have been published the last few decades about the interaction of ultrasound with commonly used materials, with the aim of nondestructive testing of materials. Therefore, most papers report results on isotropic media (stainless steel, brass,…) or orthotropic media [1-4] (mostly fiber reinforced composites). Modeling of materials of general (triclinic) anisotropy does not happen so frequently. Nevertheless, the basis principles of this modeling are given in standard books, such as the book by Nye [5], the book by Auld [6] or the book by Musgrave [7]. The reason is probably the difficulty to overcome the initial problems, when studying the propagation of sound in anisotropic media. With the existence of actuators and transducers, the need to understand the propagation of sound in piezoelectric crystals, has found entry in a number of research teams around the world. However, for the case of piezoelectric crystals, most attention went to the study of the propagation of surface waves.

On the other hand, in the field of nondestructive testing of materials, the presence of initial or residual stress in different materials, including anisotropic materials, has been taken into account [8-9] with the aim of evaluating residual stress in fresh materials or with the aim of evaluating applied stress in materials in civil constructions.

Lately, possibly with the purpose of measuring stress or with the purpose of controlling actuators [10-12] by means of stress, the propagation of surface waves on piezoelectric materials, has been studied [13]. This motivated us to study the propagation of bulk waves in the presence of a bias field and to find out whether the presence of piezoelectricity makes a crystal more or less susceptible to stress and also to find out how inhomogeneous waves behave in biased piezoelectric crystals.

This section is organized as follows: First of all, the acoustic field and the electric field are described and coupled to each other by means of the piezoelectric effect. The presence of a bias field, which can be an initial stress field or an initial electric field, is considered and entered in the constitutive relations, taking into account the fact that the linear material properties, characterizing the propagation of sound, are changed, compared to the unbiased state, because of the bias fields. Because of the possible large magnitudes of the bias fields, their influence on the materials is essentially nonlinear. Therefore, we consider sound, described in a linear regime, that

is propagating in a crystal whose properties are affected in a nonlinear way by the presence of a bias field. Expressions are obtained for the dependence of the material properties on the bias fields and these expressions are used to obtain a generalized form of the Christoffel equation for general anisotropic (triclinic) media. Furthermore, an expression is obtained for the energy flow of sound, in a piezoelectric crystal of any kind of anisotropy, in the presence of bias fields.

Finally, the concept of inhomogeneous waves is introduced by means of the concept of a complex direction. The purpose of considering inhomogeneous waves is not to find exact values of the velocity for a given inhomogeneity, but to find out whether such wave are more susceptible to stress, or in a different manner susceptible to stress, than homogeneous plane waves. This knowledge is important in order to find out whether it could be productive to apply inhomogeneous waves in the study of materials under stress. All calculations in this report are performed for Lithium Niobate [14, 15].

FOUNDATIONS OF THE MODEL

It is known [6, 16]] that for piezoelectric materials, in the absence of residual or applied stress, a linear regime holds and the stress tensor is given by

$$\sigma_{ij} = \sigma_{ij}^{M} - \xi_{kij} E_k \tag{XII.C_1}$$

whereas the electrical displacement is given by

$$D_k = \varepsilon_{ki} E_i + \xi_{kij} e_{ij} \tag{XII.C_2}$$

with the pure mechanically originating stress given by

$$\sigma_{ij}^{M} = c_{ijkl} e_{kl} \tag{XII.C_3}$$

and with

$$c_{ijkl} = \beta_{im} \beta_{jn} \beta_{kp} \beta_{lq} c'_{mnpq} \tag{XII.C_4}$$

$$\xi_{kij} = \beta_{kp} \beta_{iq} \beta_{jr} \xi'_{pqr} \tag{XII.C_5}$$

and

$$\varepsilon_{ki} = \beta_{kp} \beta_{iq} \varepsilon'_{pq} \tag{XII.C_6}$$

β_{ij} are the entries of the rotation matrix for a rotation from the intrinsic lattice coordinate system to the laboratory coordinate system while c_{ijkl} is the stiffness tensor, ξ_{kij} is the piezoelectric stress tensor, ε_{ij} is the dielectrical permittivity tensor, **E** is the electric field vector, **D** is the dielectric displacement vector and e_{kl} is the strain tensor. The quantities c_{ijkl}, ξ_{kij} and ε_{ij} are valid in the laboratory coordinate system, whereas c'_{ijkl}, ξ'_{kij} and ε'_{ij} are valid in the intrinsic lattice coordinate system. In what follows, a superscript '0' will denote initial quantities.

For biased piezoelectric materials, we consider a linear regime for the acoustic waves, but in a material that is biased by the pre-stressed state, whence the material parameters become stress dependent, i.e.

$$\sigma_{ij} - \sigma_{ij}^0 = c_{ijkl}^* e_{kl} - \xi_{kij}^* \left(E_k - E_k^0 \right) \tag{XII.C_7}$$

and

$$D_k - D_k^0 = \varepsilon_{ki}^* \left(E_i - E_i^0 \right) + \xi_{kij}^* e_{ij} \tag{XII.C_8}$$

where an asterisk denote a stress dependent parameter. It can be found in [17] that in the regime of quasi-electrostatics, the potential energy W can be expanded in a Taylor series as follows:

$$\begin{aligned} W = {} & W_0 + \frac{1}{2} c_{klmn} e_{kl} e_{mn} + \frac{1}{3!} c_{klmnpq} e_{kl} e_{mn} e_{pq} \\ & + \frac{1}{4!} c_{klmnpqrs} e_{kl} e_{mn} e_{pq} e_{rs} - \xi_{mkl} E_m e_{kl} - \frac{1}{2} \varepsilon_{kl} E_k E_l \\ & - \frac{1}{2} \xi_{mklpq} E_m e_{kl} e_{pq} - \frac{1}{6} \varepsilon_{klm} E_k E_l E_m - \frac{1}{2} \gamma_{mnkl} E_m E_n e_{kl} + h.o.t \end{aligned} \tag{XII.C_9}$$

with γ_{kijl} the electrostrictive tensor, ε_{kij} the higher order dielectric tensor and ξ_{kijml} the higher order piezoelectric tensor. The constants c_{ijklmn}, γ_{knij} and ε_{kij} describe the nonlinear behavior, which is caused by the initial stress and initial electric field. The expression 'h.o.t.' means 'higher order terms'.

Furthermore

$$\gamma_{kijl} = \beta_{km} \beta_{in} \beta_{jp} \beta_{lq} \gamma'_{mnpq} \tag{XII.C_10}$$

The quantity γ_{kijl} is valid in the laboratory coordinate system, while γ'_{mnpq} is valid in the intrinsic lattice coordinate system.

In addition, it is also known that, for the second symmetric fully contra-variant, material Piola-Kirchchoff stress tensor [17]

$$\sigma_{ij} = \frac{\partial W}{\partial e_{ij}} \tag{XII.C_11}$$

and

$$D_m = -\frac{\partial W}{\partial E_m} \tag{XII.C_12}$$

Whence, for the total field parameters

$$\begin{aligned} \sigma_{ij} &= c_{ijkl} e_{kl} + \frac{1}{2} c_{ijklmn} e_{kl} e_{mn} - \xi_{mij} E_m \\ &\quad - \xi_{mijkl} e_{kl} E_m - \frac{1}{2} \gamma_{mnij} E_m E_n + h.o.t. \end{aligned} \tag{XII.C_13}$$

$$\begin{aligned} D_m &= \xi_{mij} e_{ij} + \frac{1}{2} \xi_{mijkl} e_{ij} e_{kl} + \varepsilon_{mn} E_n \\ &\quad + \frac{1}{2} \varepsilon_{mnp} E_n E_p + \gamma_{mnij} E_n e_{ij} + h.o.t. \end{aligned} \tag{XII.C_14}$$

whilst for the initial field parameters

$$\begin{aligned} \sigma_{ij}^0 &= c_{ijkl} e_{kl}^0 + \frac{1}{2} c_{ijklmn} e_{kl}^0 e_{mn}^0 - \xi_{mij} E_m^0 \\ &\quad - \xi_{mijkl} e_{kl}^0 E_m^0 - \frac{1}{2} \gamma_{mnij} E_m^0 E_n^0 + h.o.t. \end{aligned} \tag{XII.C_15}$$

$$\begin{aligned} D_m^0 &= \xi_{mij} e_{ij}^0 + \frac{1}{2} \xi_{mijkl} e_{ij}^0 e_{kl}^0 + \varepsilon_{mn} E_n^0 \\ &\quad + \frac{1}{2} \varepsilon_{mnp} E_n^0 E_p^0 + \gamma_{mnij} E_n^0 e_{ij}^0 + h.o.t. \end{aligned} \tag{XII.C_16}$$

The acoustic field variables are then found by subtracting the initial fields from the total fields, applying the identity

$$ab - a^0 b^0 = b^0 \left(a - a^0 \right) + a^0 \left(b - b^0 \right) + \Delta \tag{XII.C_17}$$

with

$$\Delta = \left(a - a^0\right)\left(b - b^0\right) \approx 0 \tag{XII.C_18}$$

which then, after comparison with (XII.C_7) and (XII.C_8), results in

$$c^*_{ijkl} = c_{ijkl} + c_{ijklmn} e^0_{mn} - \xi_{mijkl} E^0_m \tag{XII.C_19}$$

$$\xi^*_{mij} = \xi_{mij} + \xi_{mijkl} e^0_{kl} + \gamma_{mnij} E^0_n \tag{XII.C_20}$$

$$\varepsilon^*_{mn} = \varepsilon_{mn} + \varepsilon_{mnp} E^0_p + \gamma_{mnij} e^0_{ij} \tag{XII.C_21}$$

The bias state is determined by the initial stress tensor $\left[\sigma^0_{ij}\right]$ and by the initial electric field vector $\mathbf{E}^0$. However, in expressions (XII.C_19-21), we need information about $\left[e^0_{kl}\right]$ instead of $\left[\sigma^0_{ij}\right]$. The values for $\left[e^0_{kl}\right]$ are found by first obtaining an initial ('guess') value

$$\left[e^{initial}_{kl}\right] = \left[c_{ijkl}\right]^{-1}\left[\sigma^0_{ij}\right] \tag{XII.C_22}$$

Then, the values in $\left[e^0_{kl}\right]$ are further optimized by a computer program until the values of $\left[\sigma^0_{ij}\right]$ in (XII.C_15) reach a value that differs less than δ from the exact bias stress. In the calculations described further on, we have chosen $\delta = 10^{-3}$ %, which is very small.
The difference Δ is calculated as follows:

$$\Delta = \sum_{i,j} \left| \sigma^0_{ij} - c_{ijkl} e^0_{kl} - \frac{1}{2} c_{ijklmn} e^0_{kl} e^0_{mn} + \xi_{mij} E^0_m + \xi_{mijkl} e^0_{kl} E^0_m + \frac{1}{2} \gamma_{mnij} E^0_m E^0_n \right| \tag{XII.C_23}$$

This optimization procedure is more accurate than the procedure of Liu et al [13], where, for the case of surface waves on biased piezoelectric crystals, in (XII.C_19-21), only the initial value $\left[e^{initial}_{kl}\right]$ obtained from (XII.C_22) is used, instead of the exact result $\left[e^0_{kl}\right]$.

Nevertheless, according to [18, 19] for stressed anisotropic materials (here extended to piezo-electric materials), one must add an extra term to (XII.C_7), i.e.

$$\sigma_{ij} - \sigma_{ij}^0 = c_{ijkl}^* e_{kl} - \xi_{kij}^* \left(E_k - E_k^0 \right) + \frac{\partial u_i}{\partial r_k} \sigma_{kj}^0 \tag{XII.C_24}$$

In the paper of Liu et al [13], the second term on the right side of (XII.C_24) is not explicitly taken into account, whilst according to Man and Lu [19] this term should be taken into account for generality (e.g for including plasticity due to the bias stress). Nevertheless, it will only be important for very high initial stress.

Consideration of (XII.C_7-8) and (XII.C_19-22) shows that there are two independent applied fields possible, i.e. a residual or applied stress and also an electric field.
Furthermore, from [5] we know that the following general symmetry relations hold:

$$\xi_{kij} = \xi_{kji} \tag{XII.C_25}$$

$$\varepsilon_{ki} = \varepsilon_{ik} \tag{XII.C_26}$$

and

$$\gamma_{kijl} = \gamma_{ikjl} = \gamma_{kilj} \tag{XII.C_27}$$

$$\varepsilon_{kij} = \varepsilon_{ikj} = \varepsilon_{kji} \tag{XII.C_28}$$

$$\xi_{kijml} = \xi_{kjiml} = \xi_{kijlm} = \xi_{kmlij} \tag{XII.C_29}$$

$$c_{ijklpn} = c_{jiklpn} = c_{ijlkpn} = c_{ijknp} = c_{klijpn} = c_{pnijkl} = c_{ijpnkl} \tag{XII.C_30}$$

Moreover, for any symmetry operation a_{ij} ,with 'a' a rotation or a reflection, on a crystal, the tensors describing the crystal must remain unchanged. This results in relationships between different elements of the tensors under consideration. In the appendix A, the calculated symmetry relations are shown for a trigonal 3m crystal.

Generally speaking, there are 5 different possible plane waves in a piezo-electric material, because the acoustic wave equation has three solutions and electromagnetism permits two more solutions. However these solutions are coupled in acousto-electromagnetic modes in piezo electric materials.

In addition, from [6] we know that any field $\mathbf{E}$ can be described in a rotational field $\mathbf{E}^r$ with $\nabla \times \mathbf{E}^r \neq 0$ and an irrotational field $\mathbf{E}^{irr}$ with $\nabla \times \mathbf{E}^{irr} = 0$. For ultrasonic waves, the accompanying electric field is quasistatic and can be described by $\mathbf{E} = \mathbf{E}^{irr}$, whence

$$\mathbf{E} = -\nabla\varphi \tag{XII.C_31}$$

with φ a scalar potential. It is shown in [20] that in the quasistatic approach, there are only 4 waves possible for each propagation direction.

A GENERALIZATION OF CHRISTOFFEL'S EQUATION

The acoustic wave equation for visco-elastic materials is given by

$$\frac{\partial \sigma_{ij}}{\partial r_j} = \rho^* \frac{\partial^2 u_i}{\partial t^2} \tag{XII.C_32}$$

with

$$\rho^* = \rho^0 \left(1 - e_{ii}\right) \tag{XII.C_33}$$

whereas the electromagnetic field equations in the absence of electric currents and electric loads are given by

$$\nabla \times \mathbf{E} = \mu_0 \frac{\partial \mathbf{H}}{\partial t} \tag{XII.C_34}$$

and

$$\nabla \times \mathbf{H} = \frac{\partial \mathbf{D}}{\partial t} \tag{XII.C_35}$$

Taking into account (XII.C_31), relations (XII.C_34-35) can be replaced by

$$\nabla \bullet \frac{\partial^2}{\partial t^2}\left(-\varepsilon^*_{ki}\frac{\partial \varphi}{\partial r_i} + \xi^*_{kij}\frac{\partial u_j}{\partial r_j}\right) = 0 \tag{XII.C_36}$$

We demand plane wave solutions, whence

$$\mathbf{u} = A\mathbf{P}\exp i\left(k_x x + k_y y + k_z z - \omega t\right) \tag{XII.C_37}$$

and

$$\varphi = B\exp i\left(k_x x + k_y y + k_z z - \omega t\right) \tag{XII.C_38}$$

Then, relation (XII.C_36) immediately involves

$$B = \frac{k_r k_s \xi^*_{rsq} A P_q}{\varepsilon^*_{mn} k_m k_n} \tag{XII.C_39}$$

For the purpose of what follows, we now prove that

$$\varepsilon^*_{ps} k_p k_s \neq 0 \tag{XII.C_40}$$

Well, from [5] it is found that

$$\varepsilon^*_{ps} E_p E_s = 2\Xi \tag{XII.C_41}$$

with Ξ the electric energy (which is always positive) and it can be shown straightforwardly that

$$\varepsilon^*_{ps} E_p E_s = Q \frac{|E|}{|k|} \tag{XII.C_42}$$

with

$$Q = \varepsilon^*_{ps} k_p k_s \tag{XII.C_43}$$

Therefore it is proved that condition (XII.C_40) holds.

Now, combining relations (XII.C_32) and (XII.C_36) delivers

$$M_{ip} P_p = 0 \tag{XII.C_44}$$

with

$$M_{ip} = k_m \left\{ \left(\varepsilon^*_{ms} k_s \right) \left(c^*_{ijpl} + \delta_{ip} \sigma^0_{lj} \right) k_j k_l + \xi^*_{lij} k_j k_l \xi^*_{mnp} k_n - \left(\varepsilon^*_{ms} k_s \right) \rho \omega^2 \delta_{ip} \right\} \tag{XII.C_45}$$

It can be shown straightforwardly that

$$M_{ip} = M_{pi} \tag{XII.C_46}$$

Equation (XII.C_44) is an extension of the Christoffel equation for the case of stressed piezoelectric materials. Only nontrivial solutions $\mathbf{P} \neq 0$ are possible whenever

$$\det M = 0 \tag{XII.C_47}$$

Then, if (XII.C_40) is taken into account several times, the polynomial equation (XII.C_47) ultimately becomes

$$\begin{aligned} & X_{npqrstvw} k_n k_p k_q k_r k_s k_t k_v k_w \\ & + Y_{npqrst} k_n k_p k_q k_r k_s k_t + Z_{npqr} k_n k_p k_q k_r \\ & + \Omega_{np} k_n k_p = 0 \end{aligned} \tag{XII.C_48}$$

The expressions for Ω_{np}, Z_{npqr}, Y_{npqrst} and $X_{npqrstvw}$ are given in the appendix B. Equation (XII.C_48) is the generalized form of the Christoffel equation expressed in the wave vector components.

In the case of scattering at an interface, the wave vector components k_1 and k_2 along the interface are known, because of Snell's law. Then, the polynomial (XII.C_48) can be transformed into an explicit polynomial in the unknown k_3, i.e.

$$\sum_{s=0}^{8} a_s k_3^s = 0 \tag{XII.C_49}$$

with

$$a_8 = X_{33333333} \tag{XII.C_50}$$

$$a_7 = \sum_{P(1)} X_{qrnpstxz} \tag{XII.C_51}$$

$$a_6 = Y_{333333} + \sum_{P(2)} X_{qrnpstxz} \tag{XII.C_52}$$

$$a_5 = \sum_{P(1)} Y_{npqrst} + \sum_{P(3)} X_{qrnpstxz} \tag{XII.C_53}$$

$$a_4 = Z_{3333} + \sum_{P(2)} Y_{npqrst} + \sum_{P(4)} X_{qrnpstxz} \tag{XII.C_54}$$

$$a_3 = \sum_{P(1)} Z_{npqr} + \sum_{P(3)} Y_{npqrst} + \sum_{P(5)} X_{qrnpstxz} \tag{XII.C_55}$$

$$a_2 = \Omega_{33} + \sum_{P(2)} Z_{npqr} + \sum_{P(4)} Y_{npqrst} + \sum_{P(6)} X_{qrnpstxz} \qquad \text{(XII.C\_56)}$$

$$a_1 = \sum_{P(1)} \Omega_{pn} + \sum_{P(3)} Z_{npqr} + \sum_{P(5)} Y_{npqrst} + \sum_{P(7)} X_{qrnpstxz} \qquad \text{(XII.C\_57)}$$

$$a_0 = \sum_{P(2)} \Omega_{pn} + \sum_{P(4)} Z_{npqr} + \sum_{P(6)} Y_{npqrst} + \sum_{P(8)} X_{qrnpstxz} \qquad \text{(XII.C\_58)}$$

in which $\sum_{P(n)}$ means summation over all the indices γ , e.g. $\gamma \in \{n, p, q, r, s, t\}$ that follow in the given quantity (for example *Y*) and multiplied by all corresponding k_γ and all the possible permutations of the indices γ given that always *n* of the indices γ are set different from '3' and the others equal to '3' and given the fact that k_γ is replaced by '1' whenever the corresponding γ is set equal to '3'.

Equation (XII.C_49) is an eight degree polynomial in the unknown k_3. It means that there are 8 solutions possible and therefore, for monoclinic materials, 4 modes are possible in the upward direction, accompanied by their 4 twin solutions in the downward direction. However, one of those modes is always [21] evanescent, is therefore only important along the interface and does not propagate into the bulk. This means that in the bulk of the crystal, only 6 types of propagating modes exist. Furthermore, for triclinic materials, these modes are two by two symmetric, whence only 3 physically different types of propagation modes exist. This reduction from 8 to 6 modes is also mathematically accomplished by consideration of a propagation direction **m**. Then, $k_i = km_i$ and the polynomial (XII.C_48) becomes

$$\begin{aligned} 0 = {} & X_{npqrstvw} m_n m_p m_q m_r m_s m_t m_v m_w k^6 \\ & + Y_{npqrst} m_n m_p m_q m_r m_s m_t k^4 + Z_{npqr} m_n m_p m_q m_r k^2 \\ & + H \end{aligned} \qquad \text{(XII.C\_59)}$$

with

$$\mathrm{H} = \Omega_{np} m_n m_p \qquad \text{(XII.C\_60)}$$

H being a nonzero constant number for a given media and given direction. The 6th degree polynomial (XII.C_59) corresponds to an extended form of what is generally known as the stiffened Christoffel equation, which is described by Auld [6] in the simpler case of unbiased materials and in section XII.A-B of the curent chapter XII. Therefore, the 3 types of solutions correspond to quasi acoustic bulk modes (one quasi longitudinal and 2 quasi shear).

Classically, taking into account Einstein's double suffix notation convention, the (real) wave vector **k** is replaced by $\mathbf{k} = l\omega\left(m_g \mathbf{e}_g \right)$ and is entered into (XII.C_59). ω is the angular frequency.

Then, for each (real) direction $\left(m_x, m_y, m_z \right)$, the eigenvalue l can be determined. This l is then the slowness value. At the same time, the polarization vector **P** is determined as the eigenvector. We have developed a program that is able to draw 3D slowness surfaces.

The modes are then labeled according to the sound polarization and are labeled as quasi longitudinal (QL), quasi shear horizontal (QSH) and quasi shear vertical (QSV). If it follows that the polarization is mainly directed along the propagation direction, the label QL is added. If the polarization is mainly shear and directed along the XY-plane, the label QSH is added. If the polarization is mainly shear and directed along the Z-axis, the label QSV is added.

THE ENERGY FLUX

From [6] and [22] we know that the instantaneous Poynting vector is given by

$$F_i = \frac{1}{2}\left[-\sigma_{ij} \frac{\partial u_j^+}{\partial t} + \varphi \frac{\partial D^+}{\partial t} \right] \qquad \text{(XII.C\_61)}$$

in which the superscript '+' means 'complex conjugate' . Without presuming the wave vector to be real or complex, it can be shown straightforwardly that (XII.C_61), in the presence of a bias field, becomes, for an amplitude equal to unity,

$$\begin{aligned} F_i = \frac{1}{2}\omega \Big\{ & \left(c_{ilkj} + \sigma_{kj}^0 \delta_{ij} \right) k_k P_l^+ P_j \\ & + \left(-i\sigma_{ij}^0 + B\left(\xi_{kij} k_k - \xi_{ijk}^+ k_k^+ \right) \right) P_j^+ + \varepsilon_{ij}^+ k_j^+ |B|^2 \Big\} \end{aligned} \qquad \text{(XII.C\_62)}$$

The average power then corresponds to the real part of F_i, whereas the peak reactive power corresponds to the imaginary part of F_i [6].

INHOMOGENEOUS WAVES

An inhomogeneous wave is defined as a plane wave having a complex wave vector **k**. The notion of inhomogeneous waves inside the bulk of a piezoelectric crystal, is introduced through the concept of a complex direction. A real direction is then defined as a real vector $\mathbf{d}_1$, for which $\mathbf{d}_1 \cdot \mathbf{d}_1 = 1$. This is generalized to a complex direction $\mathbf{d} = \mathbf{d}_1 + i\mathbf{d}_2$, for which $\mathbf{d} \cdot \mathbf{d}^+ = 1$. Then, it is possible to determine the value l from the following definition:

$$\mathbf{k} = l\omega\left(\mathbf{d}_1 + i\mathbf{d}_2\right) \tag{XII.C_63}$$

where ω is the angular frequency. For every possible complex direction, it is possible to determine *l*. The number of combinations of $\mathbf{d}_1$ and $\mathbf{d}_2$ is reduced by introducing a complex direction that, for simplicity, contains no imaginary part along the z-axis.

$$\begin{aligned}&\mathbf{d}_1 + i\mathbf{d}_2 \\ &= \left\{\left(d_{1,x} - ib\sqrt{1-d_{1,y}^2}\right)\mathbf{e}_x + \left(d_{1,y} + ibd_{1,x}\right)\mathbf{e}_y + \left(d_{1,z}\right)\mathbf{e}_z\right\} / \sqrt{1+b^2\left(2d_{1,x}^2 + d_{1,z}^2\right)}\end{aligned} \tag{XII.C_64}$$

The parameter *b* is then a measure for the fraction of imaginariness of the complex direction. When the direction (XII.C_64) is entered into the Christoffel equation, the complex scalar $l = l_1 + il_2$ can be resolved. This value then determines the entire complex wave vector **k** as

$$\mathbf{k} = \left(\left(k_{1,x} + ik_{2,x}\right)\mathbf{e}_x + \left(k_{1,y} + ik_{2,y}\right)\mathbf{e}_y + \left(k_{1,z} + ik_{2,z}\right)\mathbf{e}_z\right) / N \tag{XII.C_65}$$

with

$$k_{1,x} / \omega = l_1 d_{1,x} + l_2 b\sqrt{1-d_{1,y}^2} \tag{XII.C_66}$$

$$k_{2,x} / \omega = -l_1 b\sqrt{1-d_{1,y}^2} + l_2 d_{1,x} \tag{XII.C_67}$$

$$k_{1,y} / \omega = l_1 d_{1,y} - l_2 b d_{1,x} \tag{XII.C_68}$$

$$k_{2,y} / \omega = l_1 b d_{1,x} + l_2 d_{1,y} \tag{XII.C_69}$$

$$k_{1,z} / \omega = l_1 d_{1,z} \tag{XII.C_70}$$

$$k_{2,z} / \omega = l_2 d_{1,z} \tag{XII.C_71}$$

$$N = \sqrt{1+b^2\left(2d_{1,x}^2 + d_{1,z}^2\right)} \tag{XII.C_72}$$

NUMERICAL RESULTS

In this report, we limit the discourse to Lithium Niobate, because this is the only crystal of which all the necessary material constants are known to us. The material properties of Lithium

Niobate are given in Appendix A. The slowness of Lithium Niobate is of the order of magnitude of 1.8×10^{-4} sm^{-1}. Lithium Niobate is rather anisotropic, but not as extreme as for instance paratellurite [23, 24]. The slowness surfaces of Lithium Niobate are well known and can for example be found in section XII.A. As a result, in this report, only the changes are shown due to pressure (we do not consider an electric bias field). Consequently, the figures here show the difference between the slowness curves 'after pressure is applied' and 'before pressure is applied' (i.e. 'after' minus 'before'). The same holds for the added arrows, whether they represent the polarization or the energy flow. Furthermore, we only discuss real slowness surfaces, real energy flow and real polarization. The imaginary parts are mostly nil, and are only significant for inhomogeneous waves, as is known from other papers on inhomogeneous waves in isotropic and anisotropic media [25-36]. Whenever arrows are shown, their length must be regarded as a relative length. The exact values are calculated by means of our computer program, however during the plot procedure, they are enlarged or contracted automatically until their length fits best into the plot. Nevertheless, this contraction or enlargement, is the same for all arrows on the same plot. This is the reason why the overall presence of tiny arrows, if this is the case, is due to only a few larger arrows, that are sometimes hidden behind some of the lobes of the changed slowness curves. The computer program changes the values in order to make the largest arrows of reasonable size, resulting in the other arrows being very small. Furthermore, we mainly focus on the direction dependence of the described effects and not as much on their exact values.

The influence of stress in crystals – comparison between the piezoelectric case and the non-piezoelectric case

The purpose of this section is to show the influence of stress on the slowness curves and how the presence of piezoelectricity affects this influence. Fig. XII.C_1 shows the difference of the slowness curves, for the QL-mode, for a bias stress equal to a pressure of 90 MPa along the X-axis, without the presence of piezoelectricity.
Note that the slowness change is largest along the X-direction, but it is also significantly present along the [011] direction. This shows that a stress in one direction, not only changes the velocity of sound in that particular direction, but also in other directions. In Fig. XII.C_2, the same result is shown, except that piezoelectricity is included. Note that the main conclusions remain the same and that the magnitude of slowness change is of the same order. Nevertheless, the shape of the calculated lobes of Fig. XII.C_2, differs from the one in Fig. XII.C_1. This means that, for the QL-mode, piezoelectricity has no excessive impact on the influence of stress, but it has a significant impact on the details of the influence. Besides the slowness surfaces, also the change of polarization is shown in Fig. XII.C_1 and in Fig. XII.C_2 due to the presence of the pressure. Comparing Fig. XII.C_1 with Fig. XII.C_2 shows that the presence of piezoelectricity does not have a big influence on the change of polarization due to pressure. Note that the number of arrows in Fig. XII.C_2 and in Fig. XII.C_1 is the same, though the distribution density is different because the lobes in Fig. XII.C_2 are more 'swollen' than in Fig. XII.C_1.

In Fig. XII.C_3 and in Fig. XII.C_4, the same results are shown as, respectively, in Fig. XII.C_1 and in Fig. XII.C_2, but for the QSH mode. Here, the influence is again visible in all directions, though most outspoken along the [101] direction. The different behavior of the QSH-mode, compared to the QL-mode, is of course due to the difference in polarization between the two modes. Inasmuch as piezoelectricity had only a minor impact on the behavior of the QL-mode, Fig. XII.C_3 and Fig. XII.C_4 show that piezoelectricity has a major impact on the change

of the slowness surface of the QSH mode, not so much in the magnitude, but very much in the directional dependence of the effect.

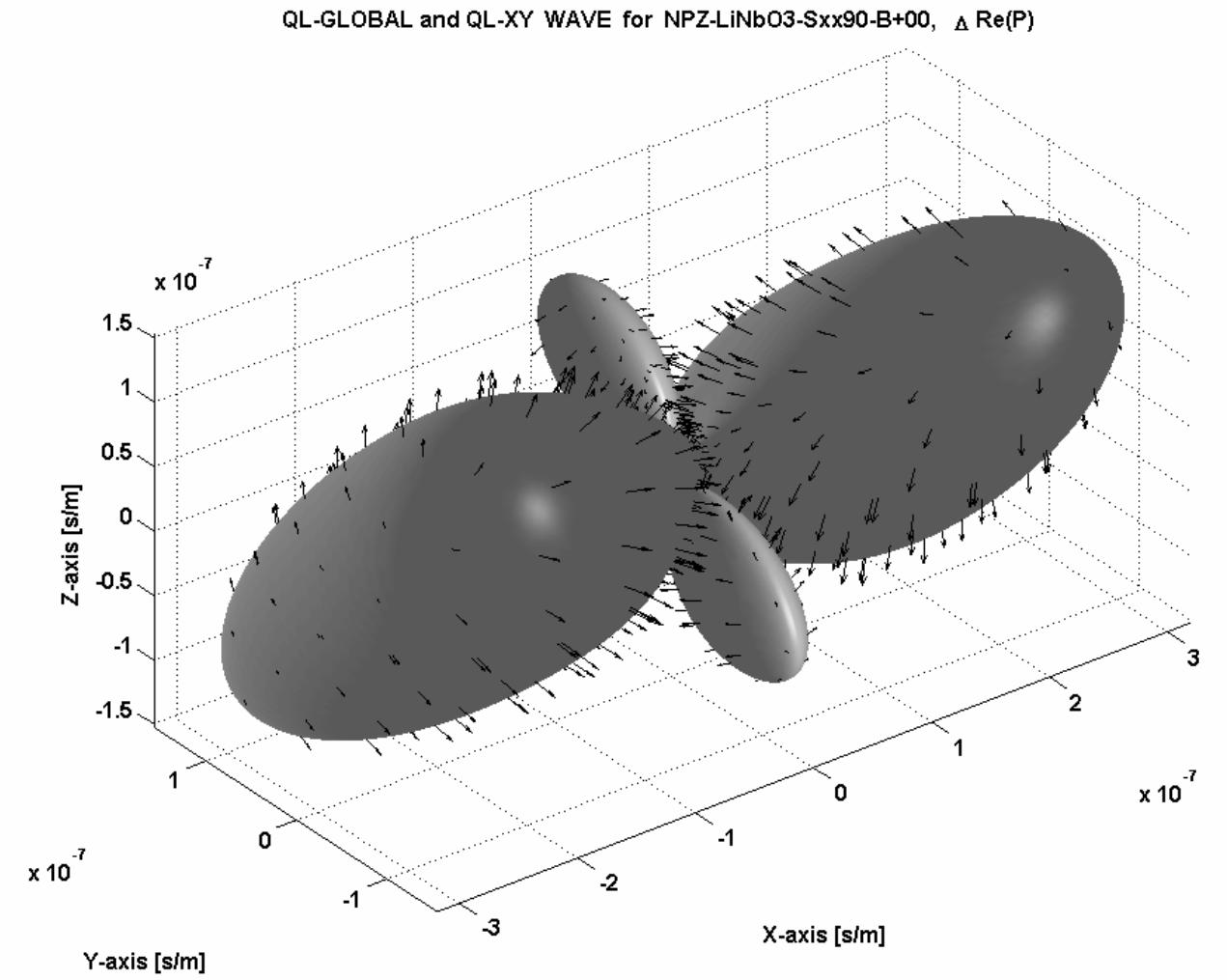

Fig. XII.C_1: ***The change of the slowness surface for the QL-mode, for a pressure of 90 MPa along the X-axis, in the case of homogeneous plane waves for non-piezoelectric Lithium Niobate. The arrows denote the change of polarization.***

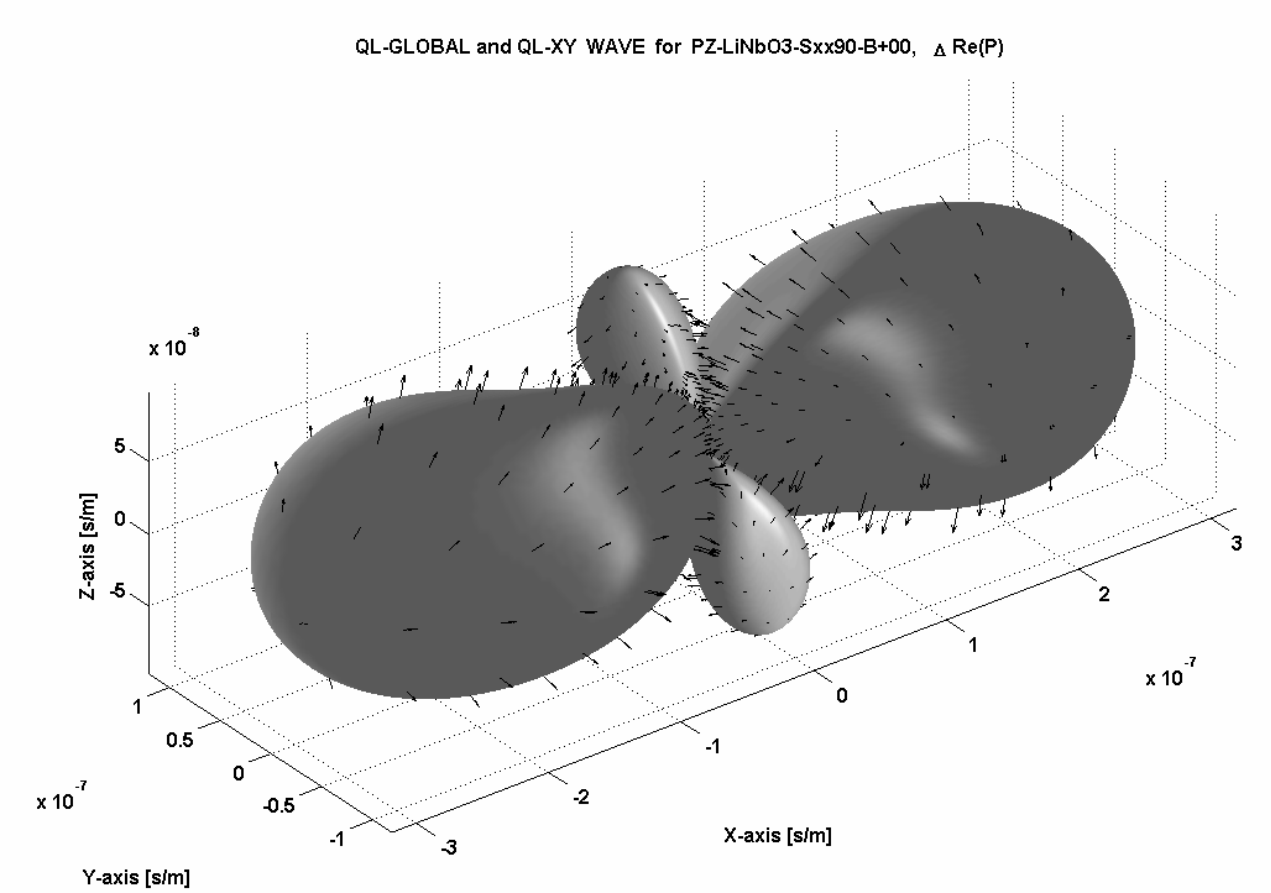

Fig. XII.C_2: ***The change of the slowness surface for the QL-mode, for a pressure of 90 MPa along the X-axis, in the case of homogeneous plane waves for piezoelectric Lithium Niobate. The arrows denote the change of polarization.***

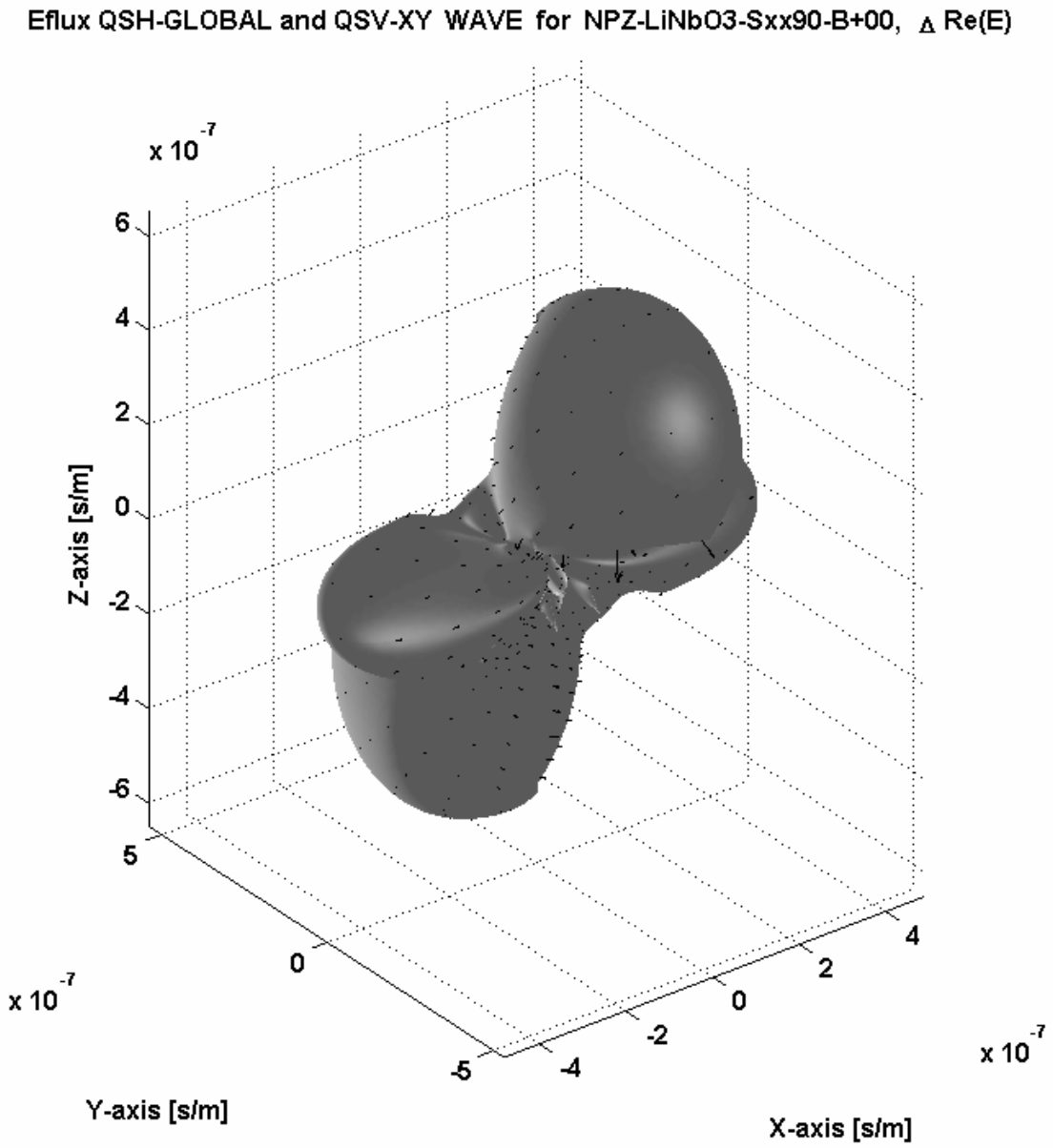

Fig. XII.C_3: ***The change of the slowness surface for the QSH-mode, for a pressure of 90 MPa along the X-axis, in the case of homogeneous plane waves for non-piezoelectric Lithium Niobate. The arrows denote the change of energy flux.***

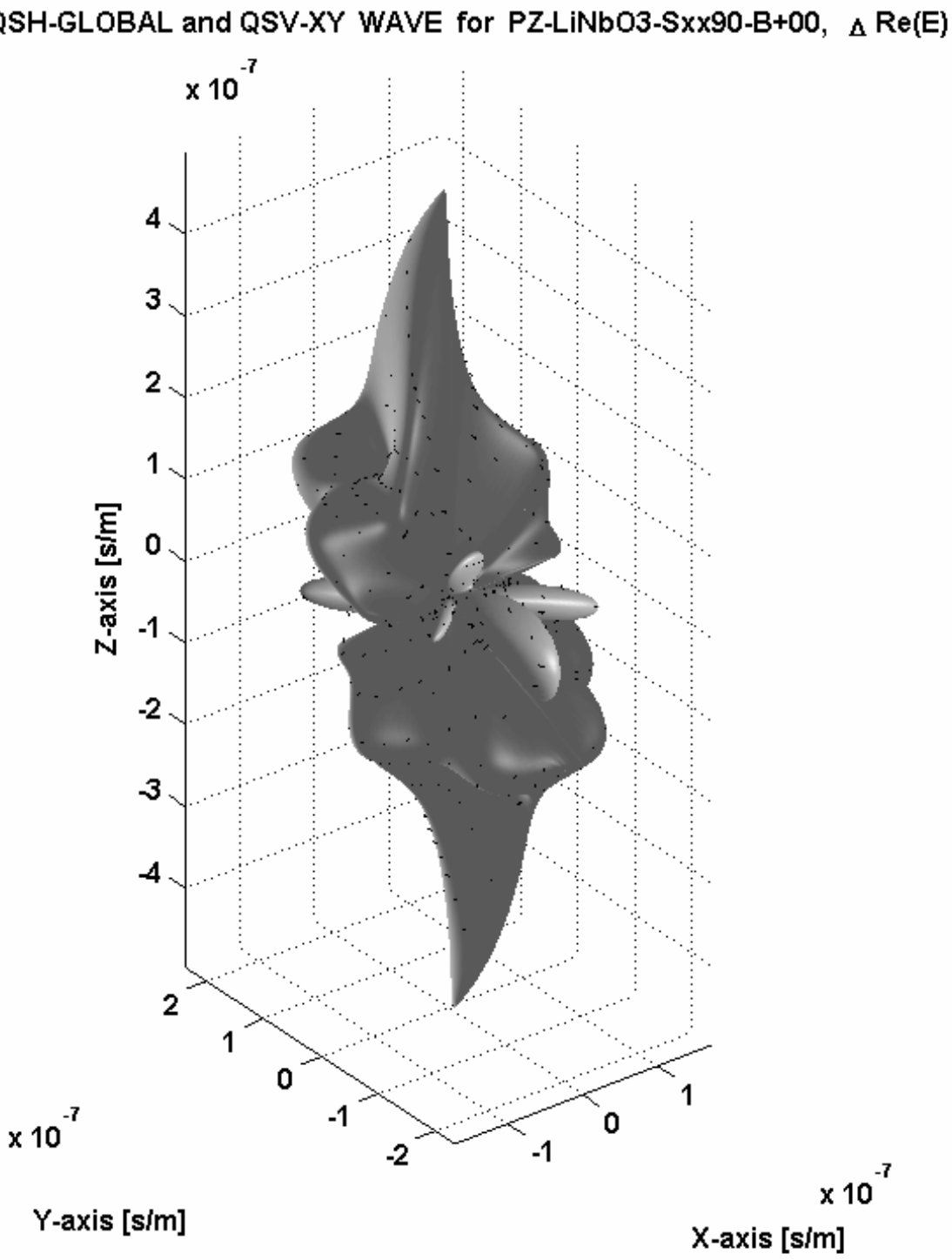

Fig. XII.C_4: ***The change of the slowness surface for the QSH-mode, for a pressure of 90 MPa along the X-axis, in the case of homogeneous plane waves for piezoelectric Lithium Niobate. The arrows denote the change of energy flux.***

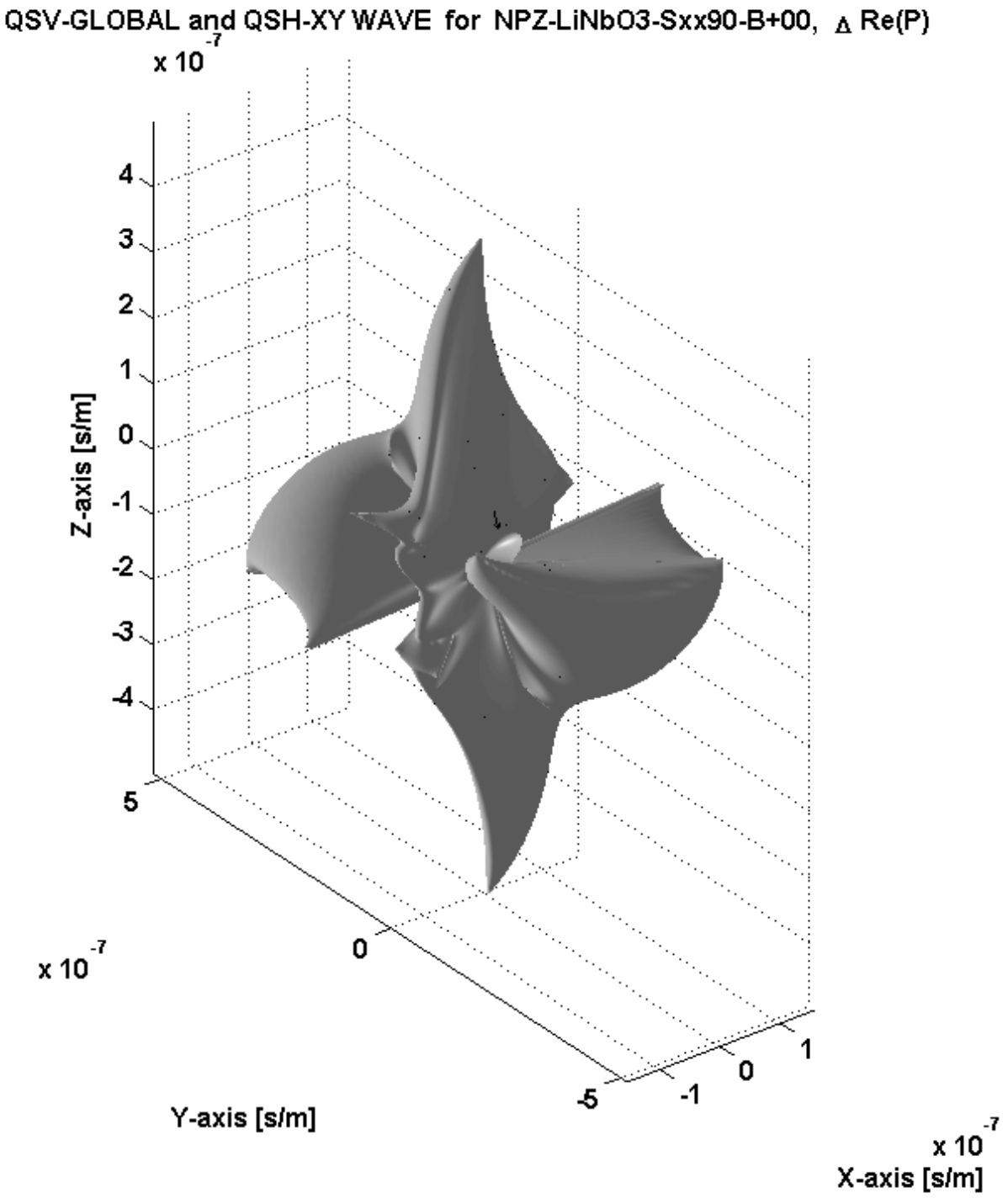

Fig. XII.C_5: ***The change of the slowness surface for the QSV-mode, for a pressure of 90 MPa along the X-axis, in the case of homogeneous plane waves for non-piezoelectric Lithium Niobate.***

Whereas the change of polarization was depicted as arrows in Fig. XII.C_1 and in Fig. XII.C_2, the change of the real part of the Poynting vector is depicted as arrows in Fig. XII.C_3 and in Fig. XII.C_4. Only in a few directions is the change of energy flow much larger than in the overall directions. This is the reason for the apparent very small arrows on the figures.

Fig. XII.C_5 and Fig. XII.C_6 again correspond to, respectively, Fig. XII.C_1 and Fig. XII.C_2, but for the QSV-mode. The influence of pressure is again very different for this mode. Furthermore, the effect of piezoelectricity is more outspoken in magnitude than for the other modes. The arrows denote the change of polarization, just as in Fig. XII.C_1 and in Fig. XII.C_2. Note again that only in a very few directions, the change is significantly larger than in the overall directions, which is once more the reason for the apparent very small arrows on the figures.
In the next sections, no arrows are depicted anymore on the slowness surfaces and only the slowness surfaces themselves are considered.

The influence of the inhomogeneity on the effect of stress in crystals for the piezoelectric case and the non-piezoelectric case

In this section, we are mainly interested in the cases of previous section, though in the presence of an inhomogeneity of the considered sound waves. For simplicity, we limit the discourse to a parameter of imaginariness $b = 60/140$. Fig. XII.C_7 corresponds to Fig. XII.C_1, i.e. the QL-mode, in the absence of piezoelectricity, though for $b = 60/140$. It is seen that the change of the slowness surface is again largest along the X direction and along the [011] direction. But the effect is much stronger along the [011] direction than in the case of homogeneous plane waves of Fig. XII.C_1. In Fig. XII.C_8, piezoelectricity is involved and the result is a very strong direction dependence of the slowness change.

In Fig. XII.C_9 and in Fig. XII.C_10, again inhomogeneous waves are considered with $b = 60/140$, for the QSH-mode and must be compared to Fig. XII.C_3, respectively Fig. XII.C_4. The overall effect is of the same order of magnitude as for homogeneous plane waves in Fig. XII.C_3 and Fig. XII.C_4, though in some directions, a much larger effect is visible. Also the shape of the surfaces without (Fig. XII.C_9) or with (Fig. XII.C_10) piezoelectricity involved, is very different. A significant difference between the slowness curves without or with piezoelectricity, was visible for the QSV-mode in Fig. XII.C_5, respectively Fig. XII.C_6. Again a significant difference is visible for inhomogeneous waves in Fig. XII.C_11, respectively Fig. XII.C_12.

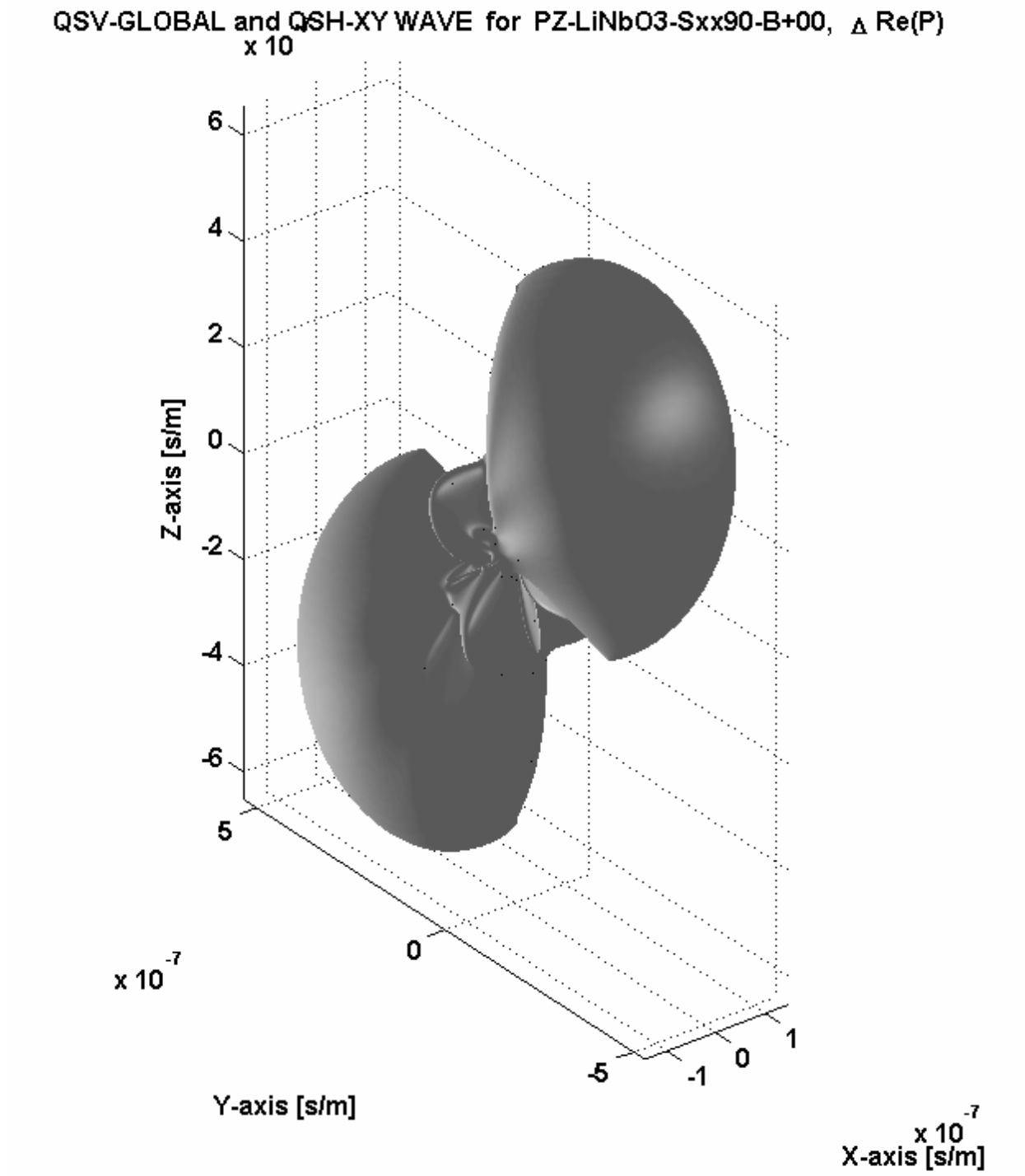

Fig. XII.C_6: ***The change of the slowness surface for the QSV-mode, for a pressure of 90 MPa along the X-axis, in the case of homogeneous plane waves for piezoelectric Lithium Niobate.***

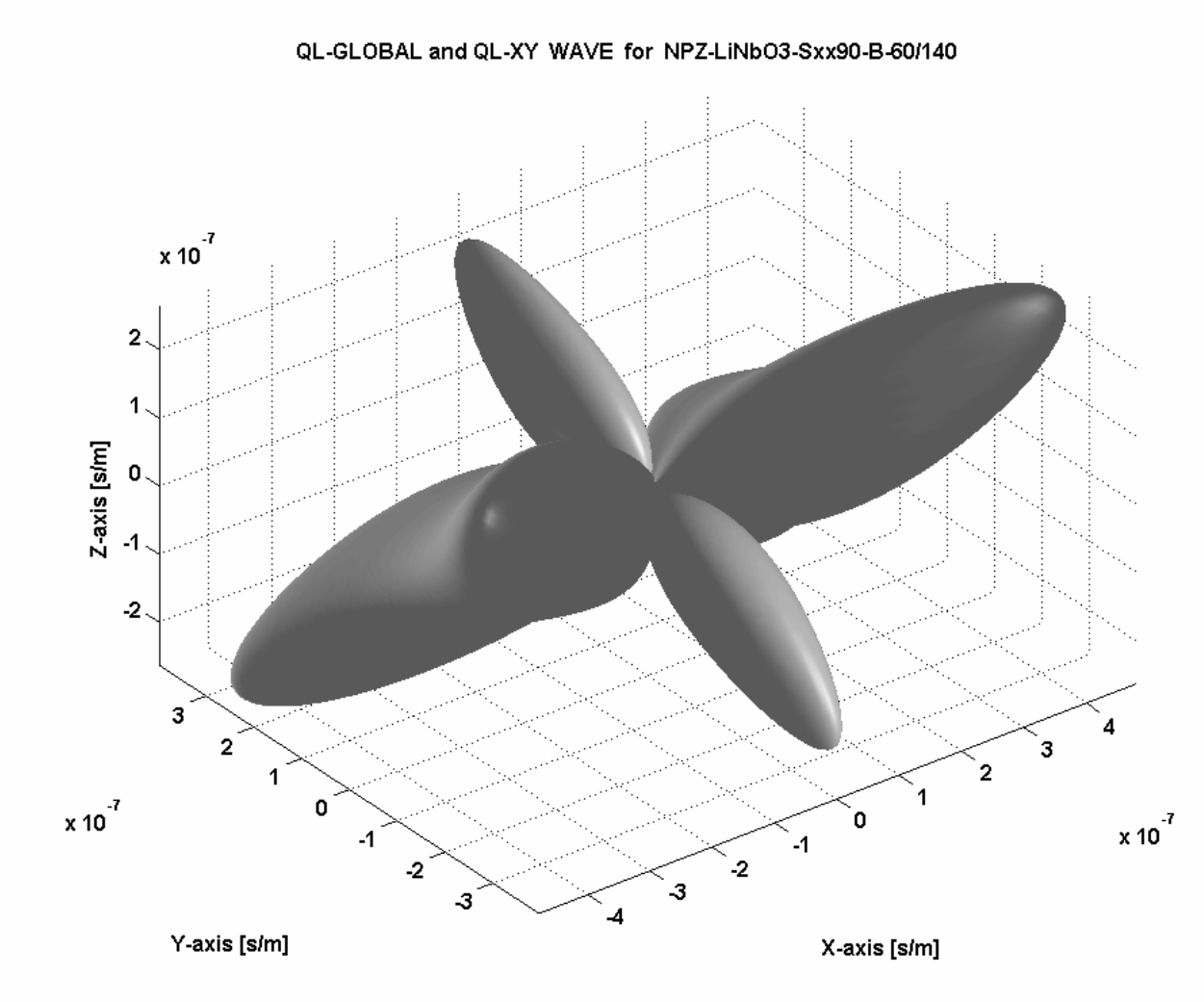

Fig. XII.C_7: ***The change of the slowness surface for the QL-mode, for a pressure of 90 MPa along the X-axis, in the case of inhomogeneous plane waves (b=60/140) for non-piezoelectric Lithium Niobate.***

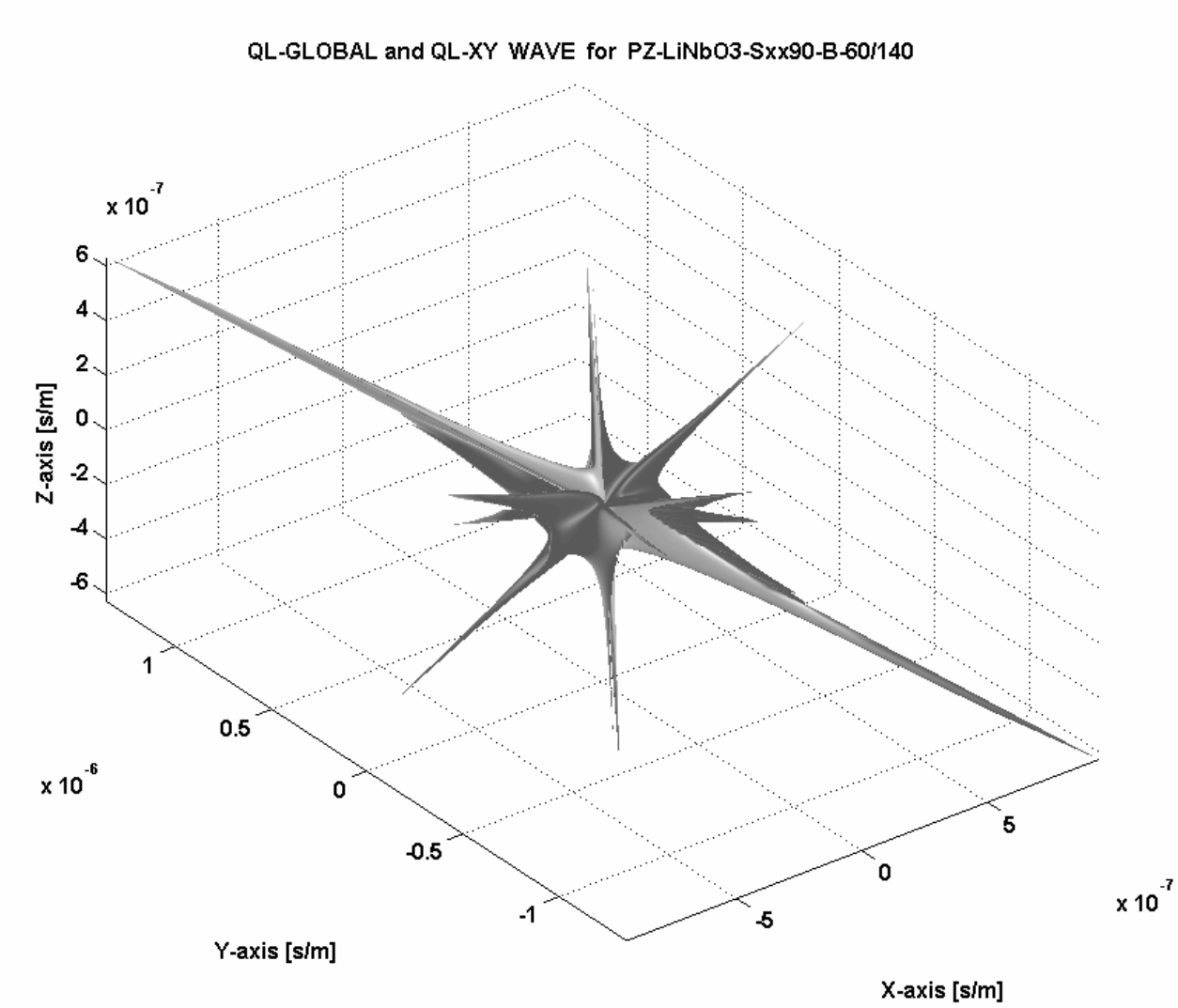

Fig. XII.C_8: ***The change of the slowness surface for the QL-mode, for a pressure of 90 MPa along the X-axis, in the case of inhomogeneous plane waves (b=60/140) for piezoelectric Lithium Niobate.***

The influence of the magnitude and the direction of stress in crystals

In this section, we limit the discourse to the case where piezoelectricity is involved. Contrary to the last two sections, here, different magnitudes of pressure are considered (instead of only 90 MPa), as well as different directions (instead of only the X-direction). In Figs XII.C_13-15, a pressure is considered along the X-direction, of 30 MPa. Fig. XII.C_13 corresponds to Fig. XII.C_2, Fig. XII.C_14 corresponds to Fig. XII.C_4, whereas Fig. XII.C_15 corresponds to Fig. XII.C_6. Note that the shape of the alteration of the slowness curves is essentially equal for the different magnitude of pressure, though the magnitude of the alteration is different. This means that the directional dependence of the effect of an applied pressure, is not influenced by the

magnitude of that pressure. Only the extent of the effect depends on the magnitude of the applied pressure.

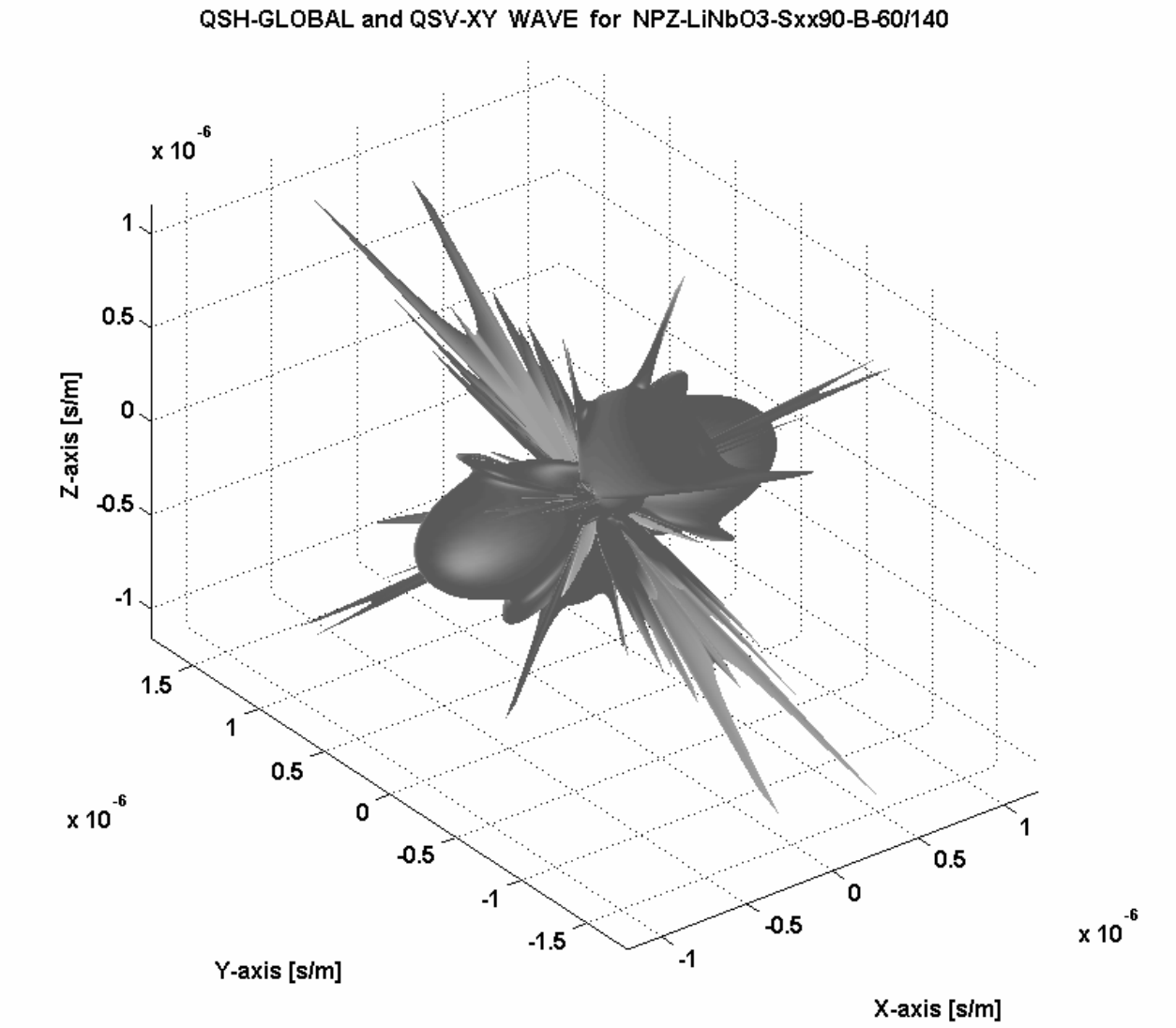

Fig. XII.C_9: ***The change of the slowness surface for the QL-mode, for a pressure of 90 MPa along the X-axis, in the case of inhomogeneous plane waves (b=60/140) for non-piezoelectric Lithium Niobate.***

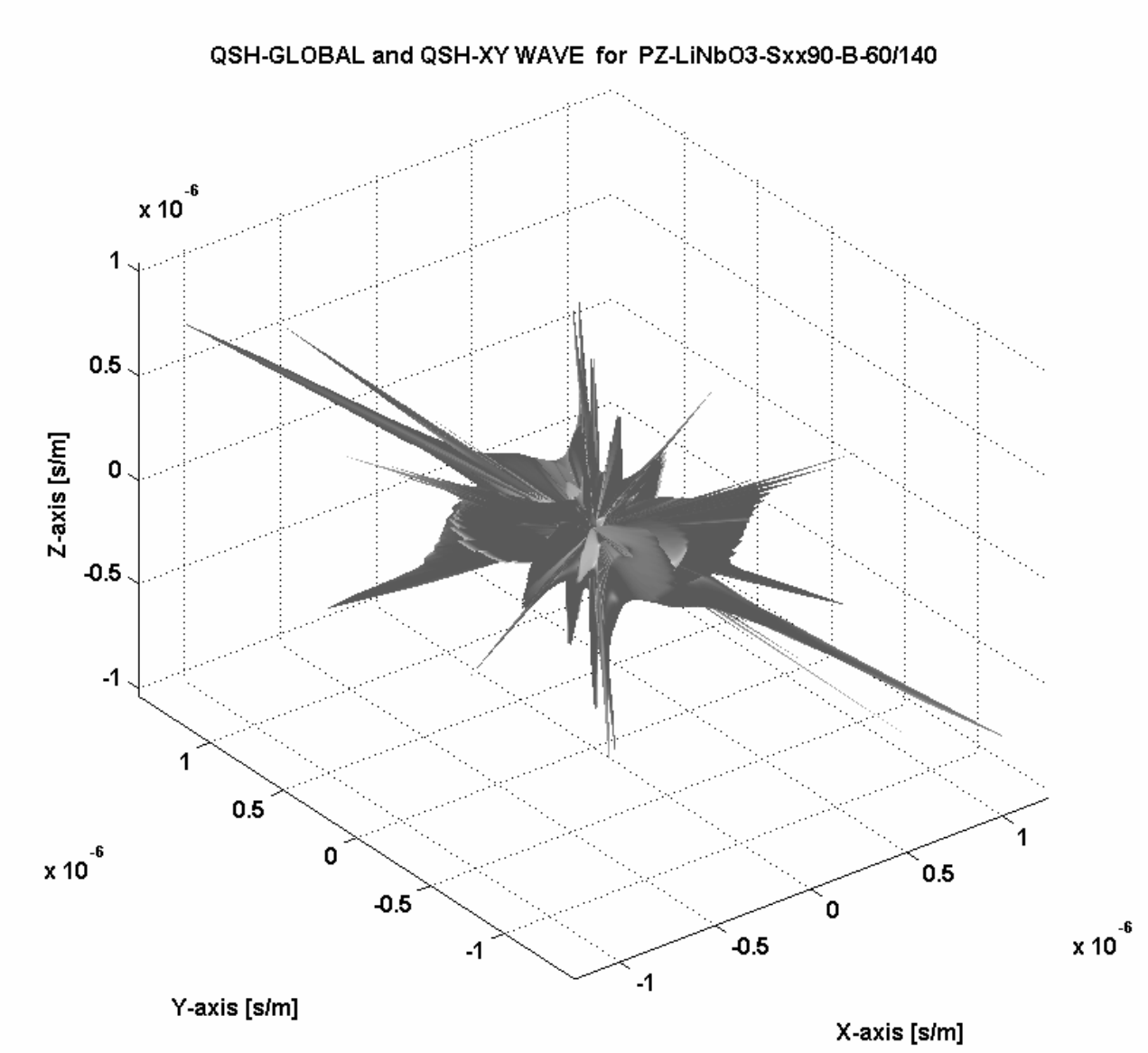

Fig. XII.C_10: ***The change of the slowness surface for the QL-mode, for a pressure of 90 MPa along the X-axis, in the case of inhomogeneous plane waves (b=60/140) for piezoelectric Lithium Niobate.***

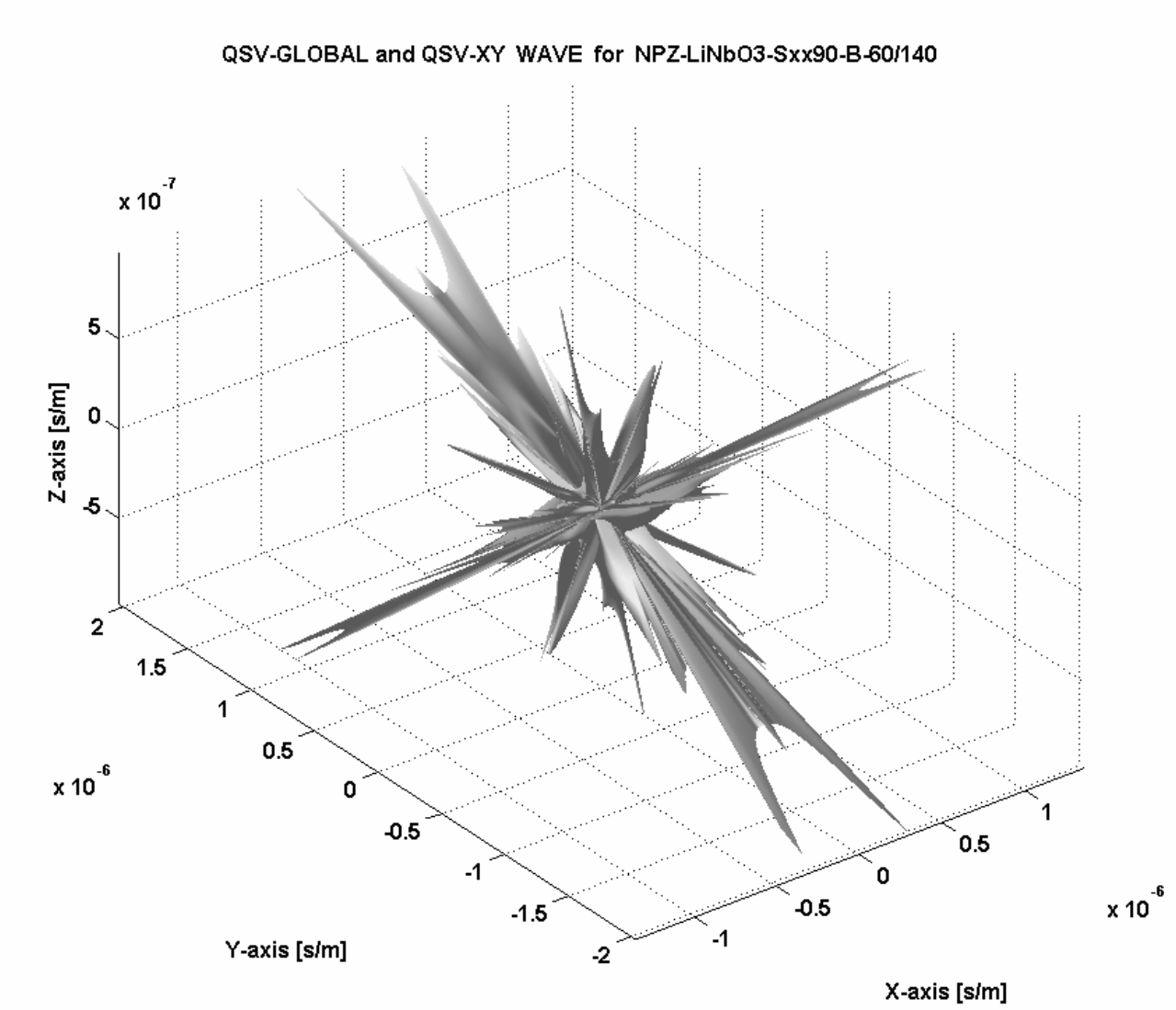

Fig. XII.C_11: ***The change of the slowness surface for the QL-mode, for a pressure of 90 MPa along the X-axis, in the case of inhomogeneous plane waves (b=60/140) for non-piezoelectric Lithium Niobate.***

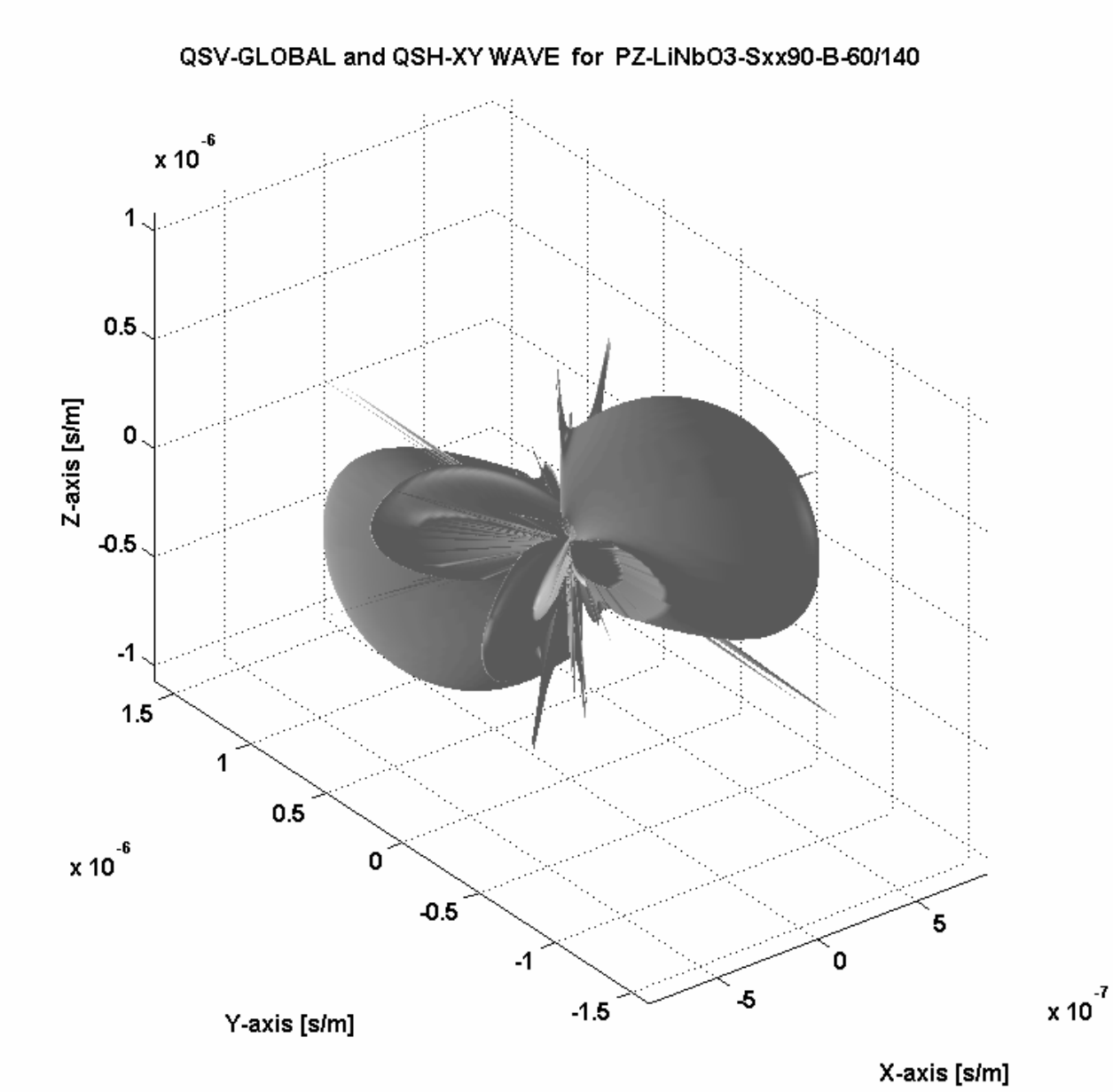

Fig. XII.C_12: ***The change of the slowness surface for the QL-mode, for a pressure of 90 MPa along the X-axis, in the case of inhomogeneous plane waves (b=60/140) for piezoelectric Lithium Niobate***.

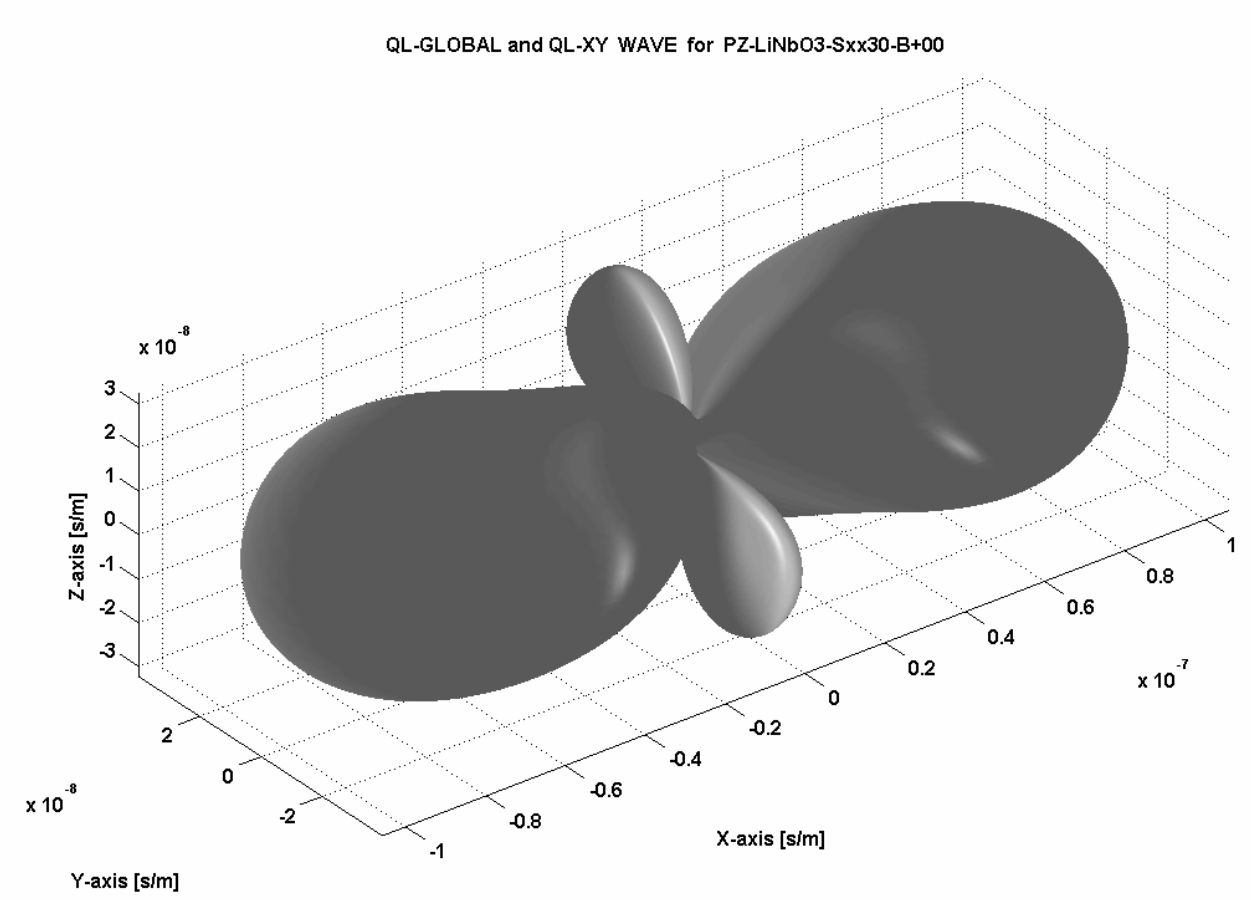

Fig. XII.C_13: ***The change of the slowness surface for the QL-mode, for a pressure of 30 MPa along the X-axis, in the case of homogeneous plane waves for piezoelectric Lithium Niobate.***

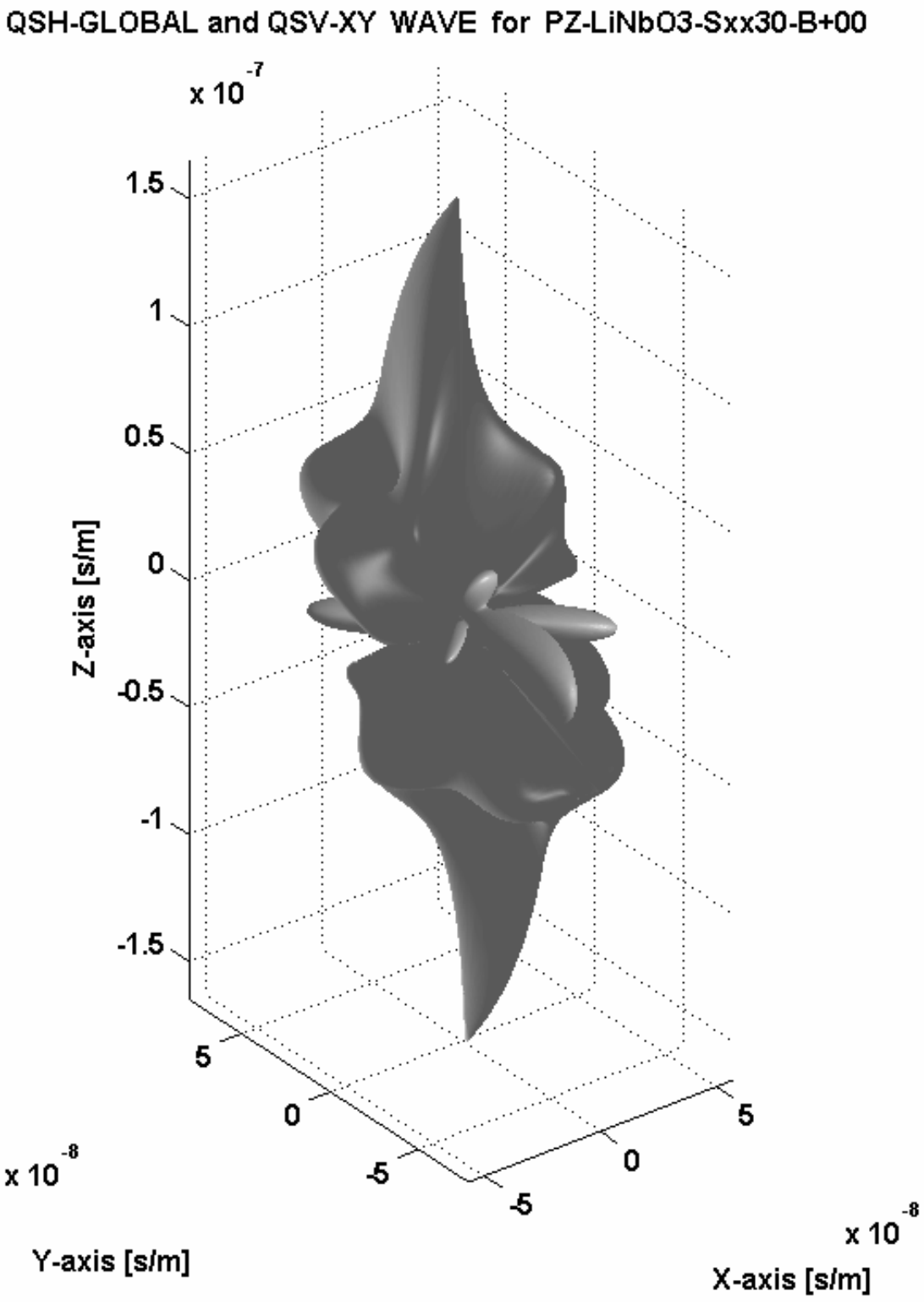

Fig. XII.C_14: ***The change of the slowness surface for the QSH-mode, for a pressure of 30 MPa along the X-axis, in the case of homogeneous plane waves for piezoelectric Lithium Niobate.***

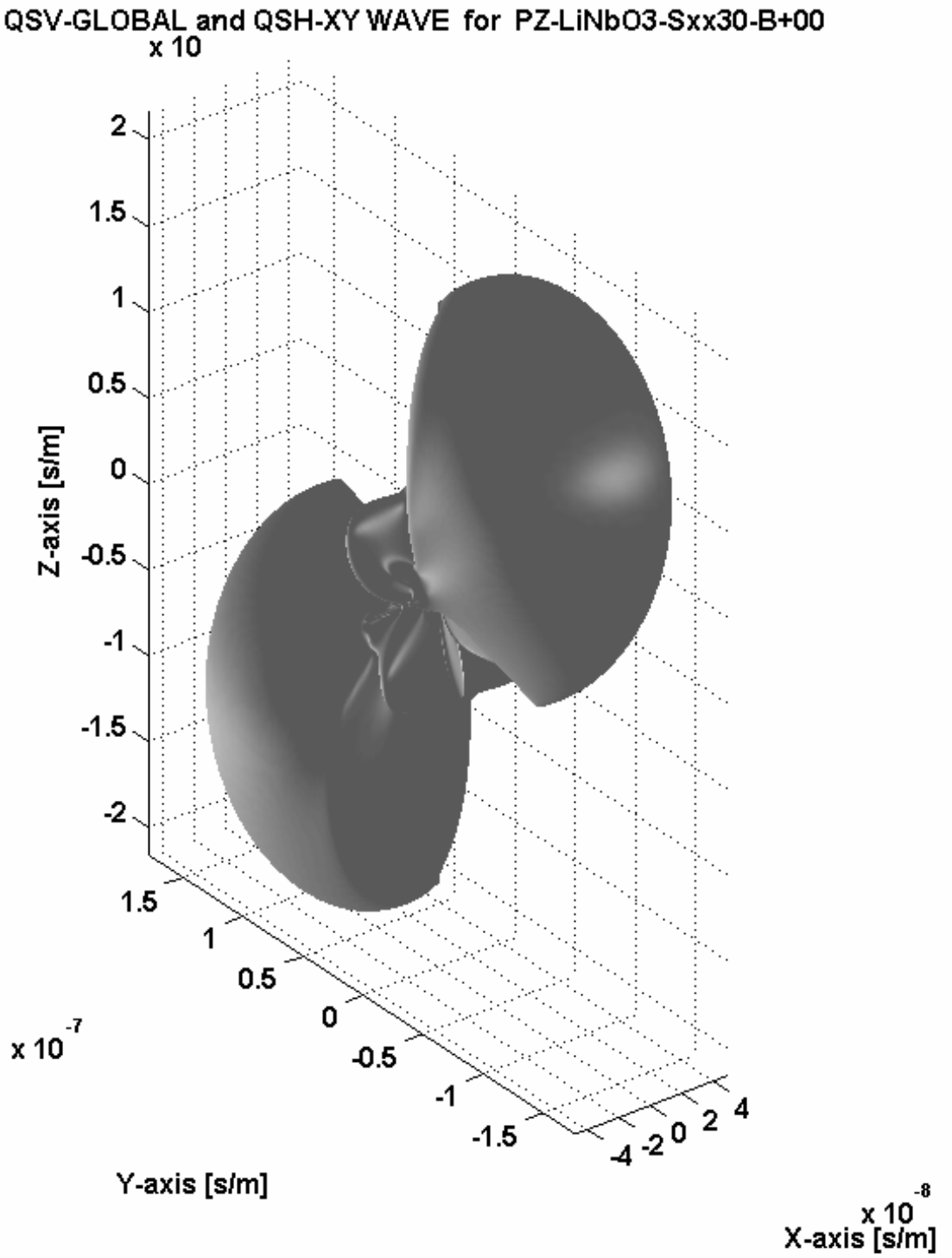

Fig. XII.C_15: ***The change of the slowness surface for the QSV-mode, for a pressure of 30 MPa along the X-axis, in the case of homogeneous plane waves for piezoelectric Lithium Niobate.***

Consequently, we consider a pressure of the same magnitude (60 MPa) as in the previous sections, though applied in another direction (along the Z-axis instead of the X-axis). The results

can be seen in Figs. XII.C_16-18. Fig. XII.C_16 corresponds to Fig. XII.C_2, Fig. XII.C_17 corresponds to Fig. XII.C_4, whereas Fig. XII.C_18 corresponds to Fig. XII.C_6. It is seen that the effect of a pressure severely depends on the direction of the pressure. This is, of course, due to the anisotropic nature of the considered crystal.

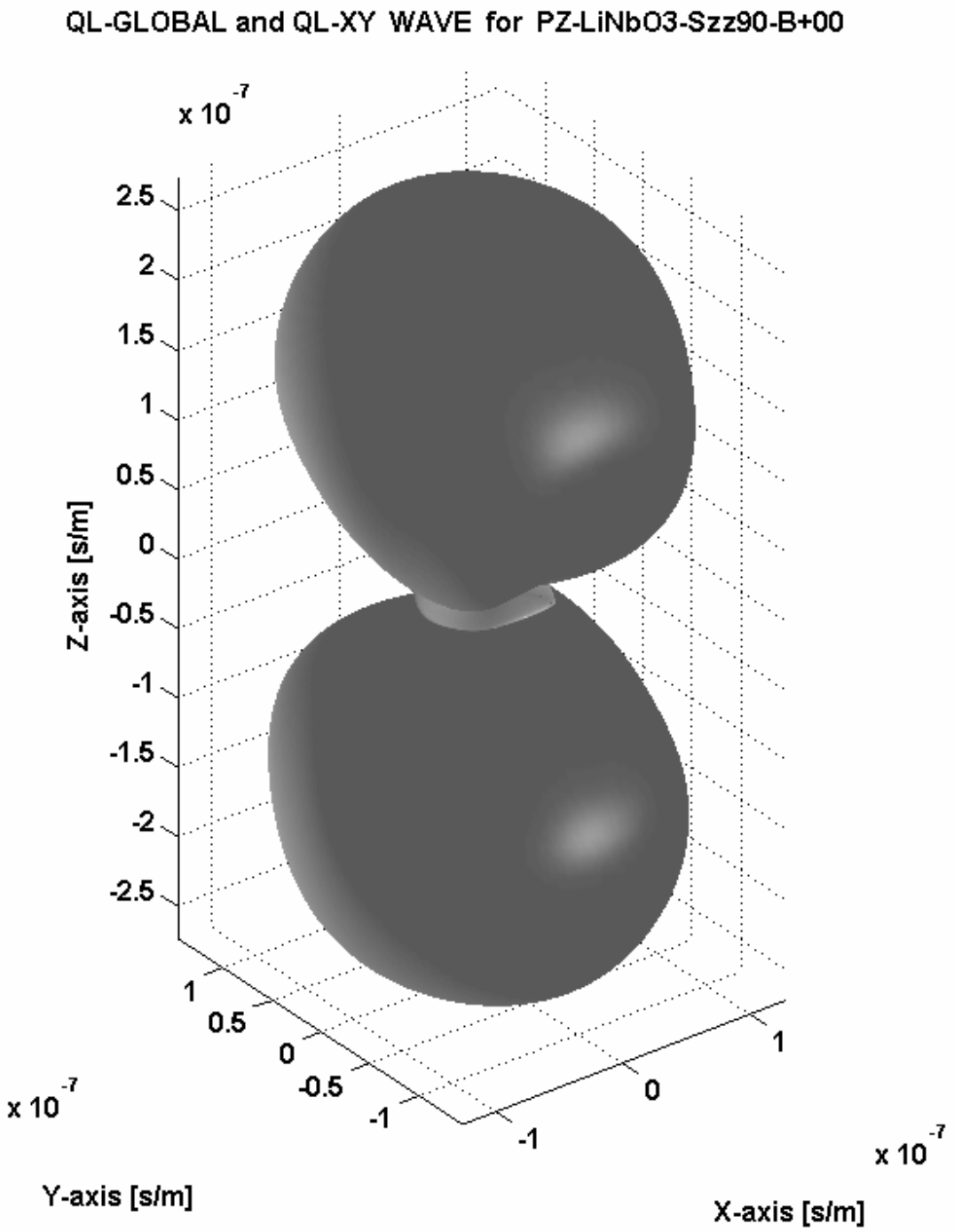

Fig. XII.C_16: ***The change of the slowness surface for the QL-mode, for a pressure of 90 MPa along the Z-axis, in the case of homogeneous plane waves for piezoelectric Lithium Niobate.***

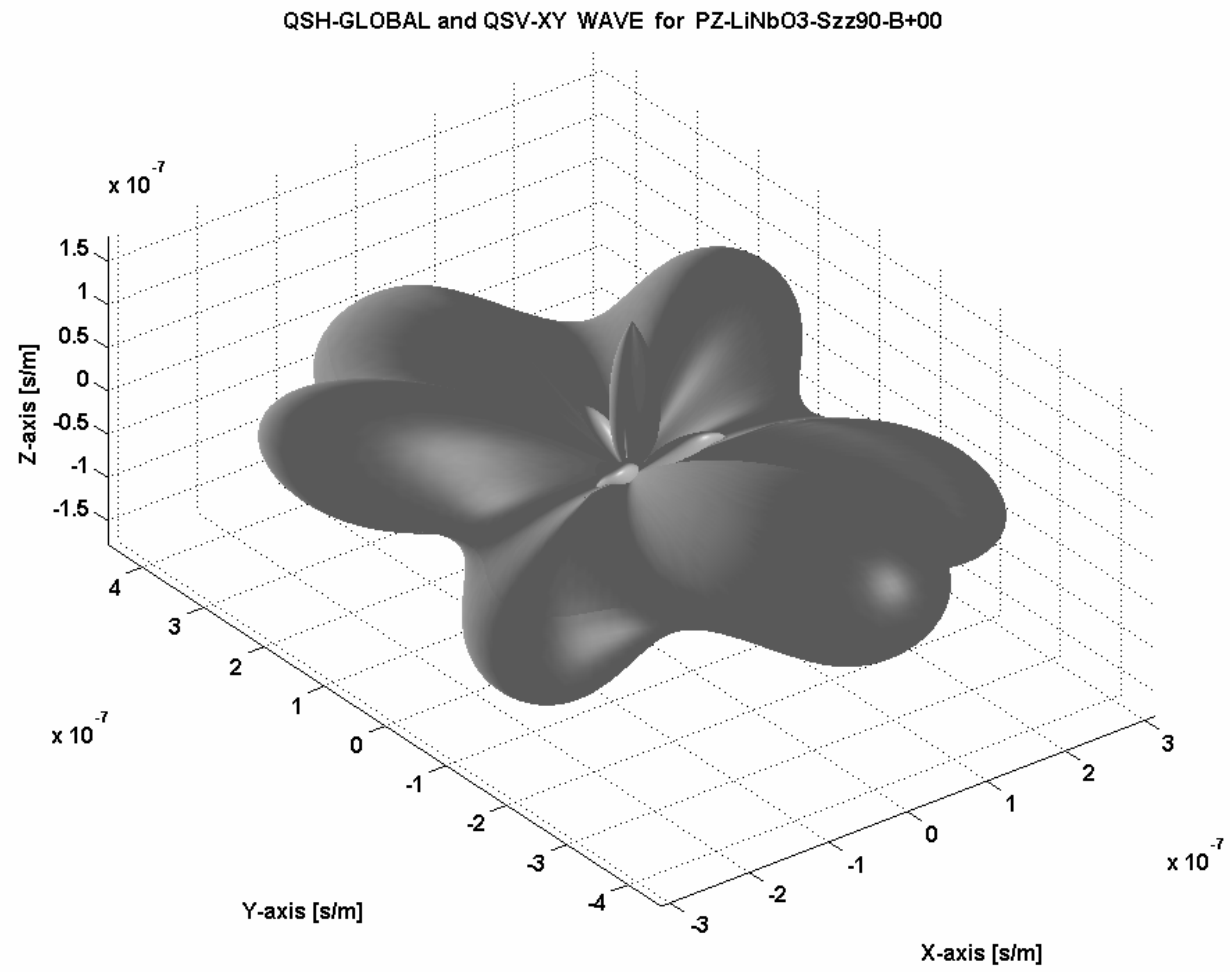

Fig. XII.C_17: ***The change of the slowness surface for the QSH-mode, for a pressure of 90 MPa along the Z-axis, in the case of homogeneous plane waves for piezoelectric Lithium Niobate.***

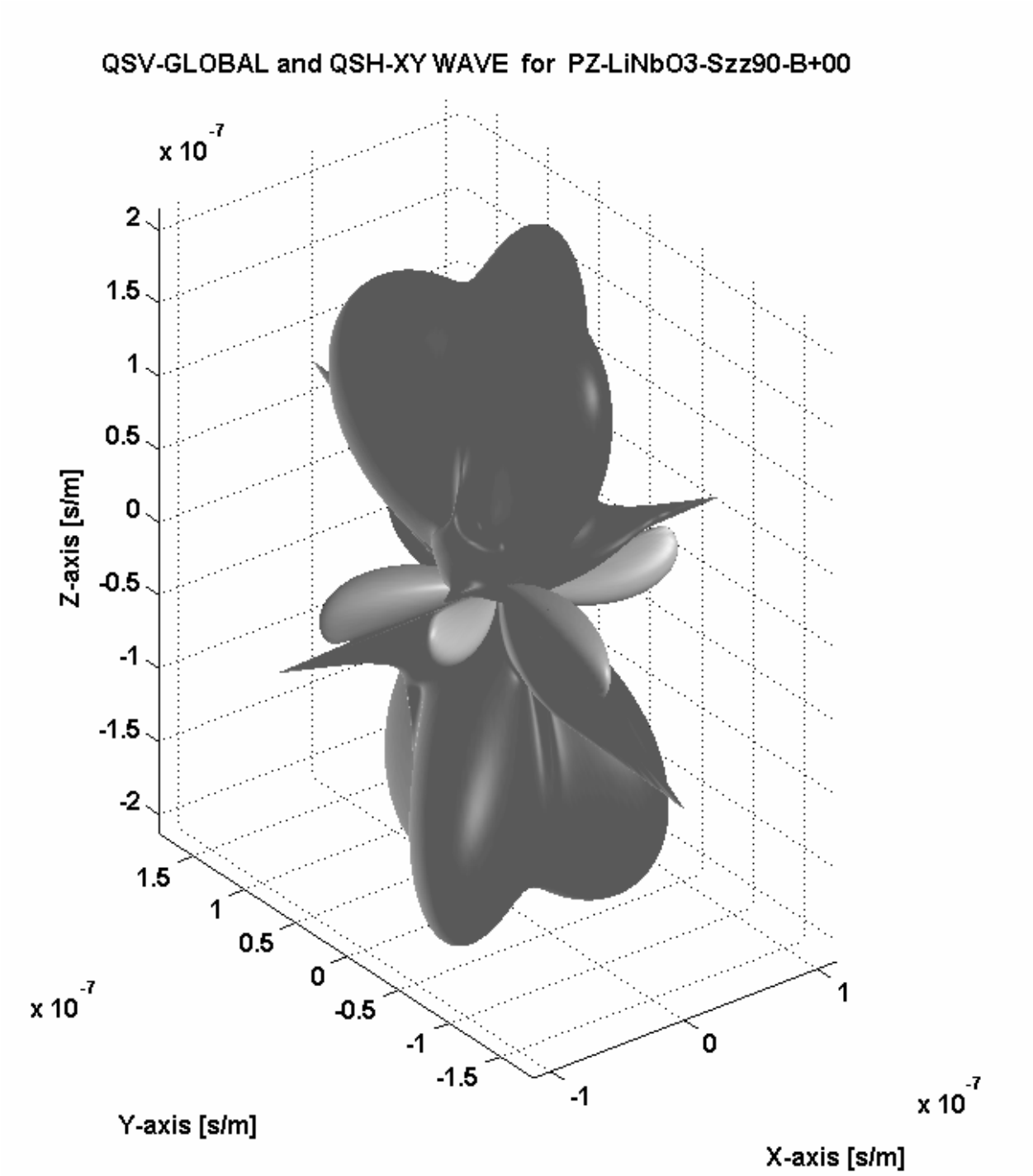

Fig. XII.C_18: ***The change of the slowness surface for the QSV-mode, for a pressure of 90 MPa along the Z-axis, in the case of homogeneous plane waves for piezoelectric Lithium Niobate.***

CONCLUSIONS

A generalized form of the Christoffel equation was formulated for biased piezoelectric crystals of general anisotropy. This is done by considering a linear acoustic regime in a crystal that is biased by nonlinear effects. An expression is given of the energy flux for the considered situation of biased piezoelectric crystals. Numerical results are reported for Lithium Niobate. The influence is calculated of an initial pressure, in the piezoelectric case and in the non-piezoelectric case, for homogeneous plane waves and also for inhomogeneous plane waves. Furthermore, the influence of the magnitude and the direction of the considered pressure, on the change in the acoustic wave velocity, was studied as well.

APPENDIX A

This appendix describes the symmetry relations between the different material property constants. The relations are calculated by a newly developed semi-automatic computer program that is able to handle any kind of symmetry relations and the results differ from the ones of [37, 38], where a trigonal $3\bar{m}$ crystal is considered, instead of the trigonal 3*m* crystal of the current report. The developed computer program uncovered one misprint in the material property tables in ref [13].

The different relationships for the trigonal 3m point group are determined by the generators of the group, these are:

$$a \in \left\{ \begin{bmatrix} -\frac{1}{2} & \frac{\sqrt{3}}{2} & 0 \\ -\frac{\sqrt{3}}{2} & -\frac{1}{2} & 0 \\ 0 & 0 & 1 \end{bmatrix}, \begin{bmatrix} -1 & 0 & 0 \\ 0 & 1 & 0 \\ 0 & 0 & 1 \end{bmatrix} \right\} \tag{XII.C_A1}$$

Any crystal having the trigonal 3m symmetry (for example Lithium Niobate) cannot have properties that alter when any of the generators (XII.C_A1) operate on it. Hence, all tensors describing the material properties of the crystal must remain unaffected by (XII.C_A1).

The transformations are performed as:

$$c_{ijkl} = a_{ip} a_{jq} a_{kr} a_{ls} c_{pqrs} \tag{XII.C_A2}$$

$$\varepsilon_{ij} = a_{ip} a_{jq} \varepsilon_{pq} \text{ with } \varepsilon_{ki} = \varepsilon_{ik} \tag{XII.C_A3}$$

$$\xi_{ijk} = a_{ip} a_{jq} a_{kr} \xi_{pqr} \text{ with } \xi_{kij} = \xi_{kji} \tag{XII.C_A4}$$

$$\gamma_{ijkl} E_j = a_{ip} a_{jq} a_{kr} a_{ls} \gamma_{pqrs} E_q \text{ with } \gamma_{kijl} = \gamma_{ikjl} = \gamma_{kilj} \tag{XII.C_A5}$$

$$\varepsilon_{ijk} = a_{ip} a_{jq} a_{kr} \varepsilon_{pqr} \text{ with } \varepsilon_{kij} = \varepsilon_{ikj} = \varepsilon_{kji} \tag{XII.C_A6}$$

$$\xi_{ijklm} = a_{ip} a_{jq} a_{kr} a_{ls} a_{mt} \xi_{pqrst} \text{ with } \xi_{kijml} = \xi_{kjiml} = \xi_{kijlm} = \xi_{kmlij} \tag{XII.C_A7}$$

$$c_{ijklmn} = a_{ip} a_{jq} a_{kr} a_{ls} a_{mt} a_{nv} c_{pqrstv} \text{ with} \tag{XII.C_A8}$$

$$c_{ijklmn} = c_{jiklmn} = c_{ijlkmn} = c_{ijknm} = c_{klijmn} = c_{mnijkl} = c_{ijmnkl}$$

On the one hand, if we demand that the transformations (XII.C_A2)-(XII.C_A8) for the operators (XII.C_A1) do not change the material constants, then we ultimately obtain, for Lithium Niobate the symmetry relations for the dependent materials constants, as listed below. On the other hand, the numerical values for the independent constants were obtained from [13].
The independent second order elastic constants $\left[\times 10^{10} N/m^2\right]$ are:

$$\begin{aligned} C_{33} &= 24.5 \quad C_{14} = 0.9 \quad C_{44} = 6.0 \\ C_{11} &= 20.3 \quad C_{12} = 5.3 \quad C_{13} = 7.5 \end{aligned} \tag{XII.C_A9}$$

The calculated symmetry relations between the dependent and independent second order elastic constants are:

$$\begin{aligned} &C_{15} = C_{16} = C_{25} = C_{26} = C_{35} = C_{36} = C_{45} = C_{46} = C_{34} = 0; \\ &C_{56} = C_{14}; \quad C_{24} = -C_{14}; \qquad C_{55} = C_{44}; \\ &C_{23} = C_{13}; \quad C_{22} = C_{11}; \quad C_{66} = -C_{12}/2 + C_{11}/2 \end{aligned} \tag{XII.C_A10}$$

The independent third order elastic constants $\left[\times 10^{11} N/m^2\right]$ are:

$$\begin{aligned} C_{333} &= -29.6 \quad C_{111} = -21.2 \quad C_{222} = -23.3 \quad C_{112} = -5.3 \\ C_{113} &= -5.7 \quad C_{114} = 2.0 \quad C_{123} = -2.5 \quad C_{124} = 0.4 \\ C_{133} &= -7.8 \quad C_{134} = 1.5 \quad C_{144} = -3.00 \quad C_{155} = -6.7 \\ &\qquad C_{344} = -6.8 \quad C_{444} = -0.3 \end{aligned} \tag{XII.C_A11}$$

The calculated symmetry relations between the dependent and independent third order elastic constants are:

$$\begin{aligned} &C_{236} = C_{336} = C_{334} = C_{115} = C_{116} = C_{566} = C_{666} = \\ &C_{346} = C_{345} = C_{445} = C_{446} = C_{226} = C_{335} = C_{145} = \\ &C_{135} = C_{245} = C_{136} = C_{246} = C_{225} = C_{146} = C_{235} = \\ &C_{125} = C_{126} = C_{556} = C_{555} = 0; \end{aligned} \tag{XII.C_A12}$$

$$C_{233} = C_{133}; \quad C_{255} = C_{144}; \quad C_{356} = C_{134}; \quad C_{234} = -C_{134}; \quad C_{223} = C_{113}$$
$$C_{244} = C_{155}; \quad C_{355} = C_{344}; \quad C_{455} = -C_{444}; \quad C_{466} = C_{124};$$
$$C_{266} = -C_{112}/4 + C_{111}/2 - C_{222}/4; \quad C_{456} = C_{155}/2 - C_{144}/2$$
$$C_{366} = -C_{123}/2 + C_{113}/2; \quad C_{224} = -2C_{124} - C_{114}$$
$$C_{156} = C_{114}/2 + 3C_{124}/2; \quad C_{256} = -C_{124}/2 + C_{114}/2$$
$$C_{166} = -C_{111}/2 - C_{112}/4 + 3C_{222}/4; \quad C_{122} = C_{111} + C_{112} - C_{222}$$

The independent second order piezoelectric constants $\left[C/m^2\right]$ are:

$$\xi_{31} = 0.2 \quad \xi_{22} = 2.5 \quad \xi_{15} = 3.7 \quad \xi_{33} = 1.3 \tag{XII.C_A13}$$

The calculated symmetry relations between the dependent and independent second order piezoelectric constants are:

$$\xi_{34} = \xi_{23} = \xi_{25} = \xi_{26} = \xi_{35} = \tag{XII.C_A14}$$
$$\xi_{36} = \xi_{11} = \xi_{12} = \xi_{14} = \xi_{13} = 0;$$
$$\xi_{32} = \xi_{31}; \quad \xi_{16} = -\xi_{22}; \quad \xi_{21} = -\xi_{22}; \quad \xi_{24} = \xi_{15}$$

The independent second order piezoelectric constants $\left[C/m^2\right]$ are:

$$\xi_{115} = 17.1; \quad \xi_{116} = -4.7; \quad \xi_{125} = 19.9; \tag{XII.C_A15}$$
$$\xi_{126} = 15.9; \quad \xi_{135} = 19.6; \quad \xi_{136} = -0.9;$$
$$\xi_{145} = 20.3; \quad \xi_{311} = 14.7; \quad \xi_{312} = 13.0;$$
$$\xi_{313} = -10.0; \quad \xi_{314} = 11.0; \quad \xi_{333} = -17.3;$$
$$\xi_{344} = -10.2;$$

The calculated symmetry relations between the dependent and independent third order piezoelectric constants are:

$$\xi_{346} = \xi_{245} = \xi_{246} = \xi_{334} = \xi_{122} = \xi_{233} = \xi_{134} = \xi_{235} = \tag{XII.C_A16}$$
$$\xi_{144} = \xi_{316} = \xi_{315} = \xi_{133} = \xi_{124} = \xi_{111} = \xi_{112} = \xi_{113} =$$
$$\xi_{114} = \xi_{326} = \xi_{216} = \xi_{215} = \xi_{345} = \xi_{155} = \xi_{336} = \xi_{123} =$$
$$\xi_{325} = \xi_{226} = \xi_{225} = \xi_{236} = \xi_{166} = \xi_{156} = \xi_{335} = 0$$

$$\xi_{255}=\xi_{145};\quad \xi_{214}=\xi_{125};\quad \xi_{244}=-\xi_{145};\quad \xi_{234}=\xi_{135}$$
$$\xi_{323}=\xi_{313};\quad \xi_{324}=-\xi_{314};\quad \xi_{356}=\xi_{314};\quad \xi_{213}=\xi_{136}$$
$$\xi_{223}=-\xi_{136};\quad \xi_{224}=\xi_{115};\quad \xi_{355}=\xi_{344};\quad \xi_{322}=\xi_{311}$$
$$\xi_{146}=\xi_{115}/2-\xi_{125}/2;\quad \xi_{366}=-\xi_{312}/2+\xi_{311}/2$$
$$\xi_{266}=-\xi_{126}/2+\xi_{116}/2;\quad \xi_{222}=-3\xi_{116}/2-\xi_{126}/2$$
$$\xi_{211}=3\xi_{126}/2+\xi_{116}/2;\quad \xi_{256}=\xi_{115}/2-\xi_{125}/2$$
$$\xi_{212}=-\xi_{126}/2+\xi_{116}/2$$

The second order independent dielectric constants $\left[10^{-12}F/m\right]$ are:

$$\varepsilon_1=389\quad \varepsilon_3=257 \tag{XII.C_A17}$$

The calculated symmetry relations between the dependent and independent second order independent dielectric constants are:

$$\varepsilon_2=\varepsilon_1\quad \varepsilon_4=\varepsilon_5=\varepsilon_6=0 \tag{XII.C_A18}$$

The third order independent dielectric constants $\left[10^{-19}F/m\right]$:

$$\varepsilon_{15}=-2.81\quad \varepsilon_{22}=-2.40\quad \varepsilon_{33}=-2.91 \tag{XII.C_A19}$$

The calculated symmetry relations between the dependent and independent third order independent dielectric constants :

$$\varepsilon_{11}=\varepsilon_{12}=\varepsilon_{13}=\varepsilon_{23}=\varepsilon_{14}=0 \tag{XII.C_A20}$$
$$\varepsilon_{24}=\varepsilon_{15};\quad \varepsilon_{16}=-\varepsilon_{22}$$

The electrostrictive constants $\left[10^{-9}F/m\right]$ are:

$$\gamma_{11}=1.11;\quad \gamma_{12}=2.19;\quad \gamma_{13}=2.32;\quad \gamma_{14}=1.51; \tag{XII.C_A21}$$
$$\gamma_{31}=0.19;\quad \gamma_{33}=-2.76;\quad \gamma_{41}=1.85;\quad \gamma_{44}=-1.83;$$

The calculated symmetry relations between the dependent and independent electrostrictive constants:

$$\gamma_{35} = \gamma_{36} = \gamma_{52} = \gamma_{25} = \gamma_{61} = \gamma_{16} = \gamma_{26} = \gamma_{34} = \gamma_{15} = \gamma_{53} = \gamma_{54} = \gamma_{51} = \gamma_{63} = \gamma_{64} = \gamma_{62} = \gamma_{43} = \gamma_{45} = \gamma_{46} = 0 \quad \text{(XII.C\_A22)}$$

$$\gamma_{32} = \gamma_{31} \quad \gamma_{65} = \gamma_{14} \quad \gamma_{42} = -\gamma_{41} \quad \gamma_{56} = \gamma_{41}$$

$$\gamma_{22} = \gamma_{11} \quad \gamma_{23} = \gamma_{13} \quad \gamma_{55} = \gamma_{44} \quad \gamma_{24} = -\gamma_{14}$$

$$\gamma_{21} = \gamma_{12}$$

$$\gamma_{66} = \gamma_{11}/2 - \gamma_{12}/2$$

APPENDIX B

This appendix presents the expressions for Ω_{np}, Z_{npqr}, Y_{npqrst} and $X_{npqrstvw}$ as a function of the stress dependent material constants c^*_{ijkl}, ξ^*_{mij} and ε^*_{mn} of (XII.C_19-21).

In the formulas below, for notational simplicity, the superscript '*' has been neglected in the material constants. Also the superscript '0' has been neglected in the stress tensor components.

$$
\begin{aligned}
X_{npstvwxz} &= \varepsilon_{vw}\sigma_{z,x}\left\{-c_{1n2p}c_{1s2t}-c_{1n3p}c_{1s3t}+c_{2s2t}c_{3p3n}\right. \\
&\left.+c_{1n1p}c_{2s2t}+c_{1n1p}c_{3t3s}-c_{2n3p}c_{2s3t}+\sigma_{pn}\left(c_{3t3s}+c_{2s2t}+c_{1t1s}\right)\right\} \\
&+\varepsilon_{vw}\left\{\sigma_{pn}\sigma_{ts}\sigma_{zx}+2c_{1n2p}c_{1s3t}c_{2x3z}-c_{2n3p}c_{2s3t}c_{1x1z}-c_{1n3p}c_{1s3t}c_{2x2z}\right. \\
&\left.+c_{1n1p}c_{2s2t}c_{3x3z}-c_{1n2p}c_{1s2t}c_{3x3z}\right\} \\
&+2c_{1n2p}c_{1s3t}\xi_{z2x}\xi_{vw3}-c_{1n3p}\xi_{t1s}\xi_{vw3}c_{2x2z}+2c_{1n2p}\xi_{t1s}\xi_{vw3}c_{2x3z} \\
&-c_{2n3p}\xi_{t2s}\xi_{vw3}c_{1x1z}-c_{2n3p}c_{2s3t}\xi_{z1x}\xi_{vw1}-c_{1n2p}c_{1s2t}\xi_{z3x}\xi_{vw3} \\
&+c_{1n1p}c_{2s2t}\xi_{z3x}\xi_{vw3}-c_{1n3p}c_{1s3t}\xi_{z2x}\xi_{vw2}+c_{1n1p}\xi_{t2s}\xi_{vw2}c_{3x3z} \\
&-c_{1n2p}\xi_{t1s}\xi_{vw2}c_{3x3z}+2\xi_{p1n}\xi_{vw2}c_{1s3t}c_{2x3z}-\xi_{p1n}\xi_{vw2}c_{1s2t}c_{3x3z} \\
&+\xi_{p1n}\xi_{vw1}c_{2s2t}c_{3x3z}-\xi_{p1n}\xi_{vw3}c_{1s3t}c_{2x2z}-\xi_{p2n}\xi_{vw3}c_{2s3t}c_{1x1z} \\
&+\sigma_{pn}\sigma_{ts}\xi_{z3x}\xi_{vw3}+\sigma_{pn}\xi_{t2s}\xi_{vw2}\sigma_{zx}+\xi_{p1n}\xi_{vw1}\sigma_{ts}\sigma_{zx} \\
&+\sigma_{pn}c_{2s2t}\xi_{z3x}\xi_{vw3}+c_{1n1p}\sigma_{ts}\xi_{z3x}\xi_{vw3}+\sigma_{pn}\xi_{t2s}\xi_{vw2}c_{3x3z}-c_{1n3p}\xi_{t1s}\xi_{vw3}\sigma_{zx} \\
&+c_{1n1p}\xi_{t2s}\xi_{vw2}\sigma_{zx}-c_{1n2p}\xi_{t1s}\xi_{vw2}\sigma_{zx}-c_{2n3p}\xi_{t2s}\xi_{vw3}\sigma_{zx}-\xi_{p1n}\xi_{vw3}c_{1s3t}\sigma_{zx} \\
&-\xi_{p1n}\xi_{vw2}c_{1s2t}\sigma_{zx}+\xi_{p1n}\xi_{vw1}c_{2s2t}\sigma_{zx}-\xi_{p2n}\xi_{vw3}c_{2s3t}\sigma_{zx}+\xi_{p1n}\xi_{vw1}\sigma_{ts}c_{3x3z}
\end{aligned}
\tag{XII.C_B1}
$$

$$
\begin{aligned}
Y_{npstvw} &= -\rho\omega^2\varepsilon_{vw}\left\{2\sigma_{pn}c_{3s3t}+\sigma_{pn}c_{2s2t}+c_{2n2p}\sigma_{ts}+2c_{1n1p}\sigma_{t,s}+c_{2n2p}c_{3s3t}\right. \\
&\left.+c_{1n1p}c_{3s3t}+c_{1n1p}c_{2s2t}-c_{1n3p}c_{1s3t}-c_{1n2p}c_{1s2t}-c_{2n3p}c_{2s3t}+3\sigma_{pn}\sigma_{ts}\right\} \\
&-\rho\omega^2\left\{2\sigma_{pn}\xi_{t3s}\xi_{vw3}+\sigma_{pn}\xi_{t2s}\xi_{vw2}+\xi_{p2n}\xi_{vw2}\sigma_{ts}+2\xi_{p1n}\xi_{vw1}\sigma_{ts}\right. \\
&+c_{1n1p}\xi_{t3s}\xi_{vw3}+c_{2n2p}\xi_{t3s}\xi_{vw3}-c_{1n3p}\xi_{t1s}\xi_{vw3}+c_{1n1p}\xi_{t2s}\xi_{vw2}-c_{1n2p}\xi_{t1s}\xi_{vw2} \\
&-c_{2n3p}\xi_{t2s}\xi_{vw3}+\xi_{p2n}\xi_{vw2}c_{3s3t}+\xi_{p1n}\xi_{vw1}c_{3s3t}-\xi_{p1n}\xi_{vw3}c_{1s3t}-\xi_{p1n}\xi_{vw2}c_{1s2t} \\
&\left.-\xi_{p2n}\xi_{vw3}c_{2s3t}+\xi_{p1n}\xi_{vw1}c_{2s2t}\right\}
\end{aligned}
\tag{XII.C_B2}
$$

$$
\begin{aligned}
Z_{npst} &= \rho^2\omega^4\varepsilon_{st}\left(c_{1n1p}+3\sigma_{pn}+c_{2n2p}+c_{3n3p}\right) \\
&+\rho^2\omega^4\left(\xi_{p1n}\xi_{st1}+\xi_{p2n}\xi_{st2}+\xi_{p3n}\xi_{st3}\right)
\end{aligned}
\tag{XII.C_B3}
$$

$$
\Omega_{vw} = -\varepsilon_{vw}\rho^3\omega^6 \tag{XII.C_B4}
$$

REFERENCES

[1] M. Pluta, A. G. Every, W. Grill, “Inversion of acoustic diffraction fields in anisotropic solids”, Ultrasonics 42(1-9), 243-248, 2004

[2] Joris Degrieck, Nico F. Declercq, Oswald Leroy, "Ultrasonic Polar Scans as a possible means of nondestructive testing and characterization of composite plates", Insight - The Journal of The British Institute of Non-Destructive Testing, 45(3), 196-201, 2003.

[3] Nico F. Declercq, Joris Degrieck, Oswald Leroy, " On the influence of fatigue on ultrasonic polar scans of fiber reinforced composites", Ultrasonics 42, 173-177, 2004.

[4] Nico F. Declercq, Joris Degrieck, Oswald Leroy, "Simulations of Harmonic and Pulsed Ultrasonic Polar Scans", accepted for publication in NDT & E International

[5] J. F. Nye, *Physical Properties of Crystals - Their Representation by Tensors and Matrices*, Oxford Science Publications, 1985

[6] B. A. Auld, *Acoustic fields and waves in solids, volume I, second edition*, Krieger, Florida, 1989

[7] M. J. P. Musgrave, *Crystal acoustics: Introduction to the study of elastic waves and vibrations in crystals*, Holden-Day, California, 1970

[8] A. D. Degtyar, W. Huang, S. I. Rokhlin, “Wave propagation in stressed composites”, J. Acoust. Soc. Am. 104(4), 2192-2003, 1998

[9] A. D. Degtyar, S. I. Rokhlin, “Stress effect on boundary conditions and elastic wave propagation through an interface between anisotropic media”, J. Acoust. Soc. Am. 104(4), 1992-2003, 1998

[10] J. Friend, K. Nakamura, “A piezoelectric micromotor using in-plane shearing of PZT elements”, IEEE-ASME Trans. on Mechatronics 9(3), 467-473, 2004

[11] Yun C. H., T. Hasegawa, K. Nakamura, S. Ueha, “An ultrasonic suction pump with no physically moving parts”, Jap. J. Appl. Phys. Part 1, 43(5B), 2864-2868, 2004

[12] J. Friend, K. nakamura, S. Ueha, “Acoustic waveguides for actuators”, Jap. J. Appl. Phys. Part 1, 43(5B), 3040-3044, 2004

[13] H. Liu, Z. B. Kuang, Z. M. Cai, “Propagation of Bluestein – Gulyaev waves in a prestressed layered piezoelectric structure”, Ultrasonics 41, 397-405, 2003

[14] M. A. Breazeale, I. V. Ostrovskii, M. S. McPherson, “Thermal hysteresis of nonlinear ultrasonic attenuation in Lithium Niobate”, J. Appl. Phys. 96(5), 2990-2994, 2004

[15] M. S. McPherson, I. Ostrovskii, M. A. Breazeale, “Observation of acoustical memory in LiNbO3”, Phys. Rev. Let. 89(11), art no 115506, 2002

[16] Adnan H. Nayfeh, *wave propagation in layered anisotropic media*, north Holland, elsevier, 1995

[17] Gerard Maugin, Nonlinear Waves in Elastic Crystals, Oxford Science Publications,1999

[18] A. D. Degtyar, S. I. Rokhlin, “Absolute stress determination in orthotropic materials from angular dependences of ultrasonic velocities”, J. Appl. Phys. 78(3), 1547-1556, 1995

[19] A. S. Man and W. Y. Lu, “Towards an acoustelastic theory for measurement of residual stress”, J. Elast. 17, 159-182, 1987

[20] B. A. Auld, *Acoustic fields and waves in solids, volume II, second edition*, Krieger, Florida, 1989

[21] Private communication with Alexandre Darinskii, Institute of Crystallography, Russian Academy of Sicences, Leninsky pr. 59, Moscow, 119333, Russia.

[22] Boris D. Zaitsev, Iren E. Kuznetsova, “The Energy Density and Power Flow of Acoustic Waves Propagating in Piezoelectic Materials”, IEEE trans. on UFFC 50(12), 1762-1765, 2003

[23] V.B. Voloshinov, "Anisotropic Light Diffraction on Ultrasound in a Tellurium Dioxide Single Crystal", *Ultrasonics*, v.31, N 5, p.333-338, 1993

[24] N.V.Polikarpova and V.B.Voloshinov “Application of Acousto-Optic Interactions in Anisotropic Media for Control of Light Radiation”, *Acustica-Acta Acustica*, v. 89, p. 930-935, 2003

[25] Nico F. Declercq, Rudy Briers, Joris Degrieck, Oswald Leroy, “The History and Properties of Ultrasonic Inhomogeneous Waves”, accepted for publication in IEEE-UFFC.

[26] Nico F. Declercq, Joris Degrieck, Oswald Leroy, "The Laplace transform to describe bounded inhomogeneous waves", J. Acoust. Soc. Am. 116(1), 51-60, 2004

[27] Michael Hayes, “Inhomogeneous plane waves”, Arch. Ration. Mech. Anal. 85, 41-79, 1984

[28] S. I. Rokhlin, T. K. Bolland, L. Adler, “Reflection and refraction of elastic waves on a plane interface between two generally anisotropic media”, J. Acoust. Soc. Am. 79(4), 906-918, 1986

[29] B. Hosten, M. Deschamps, B. R. Tittmann, “Inhomogeneous wave generation and propagation in lossy anisotropic solids. Application to the characterization of viscoelastic composite materials”, J. Acoust. Soc. Am. 82(5), 1763-1770, 1987
[30] B. Hosten, “Bulk heterogeneous plane waves propagation through viscoelastic plates and stratified media with large values of frequency domain”, Ultrasonics 29, 445-450, 1991
[31] Marc Deschamps, Bernard Hosten, “The effects of viscoelasticity on the reflection and transmission of ultrasonic waves by an orthotropic plate”, J. Acoust. Soc. Am. 91(4), 2007-2015, 1992
[32] Patrick Lanceleur, Helder Ribeiro, Jean-François De Belleval, “The use of inhomogeneous waves in the reflection-transmission problem at a plane interface between two anisotropic media”, J. Acoust. Soc. Am., 93(4), 1882-1892, 1993
[33] M. Deschamps, F. Assouline, “Attenuation Along the Poynting Vector Direction of Inhomogeneous Plane Waves in Absorbing and Anisotropic Solids”, Acustica – Acta Acustica, 86, 295-302, 2000
[34] Bruno Rogé, “Réflexion/transmission d’une onde plane inhomogene incidente sur une interface plane séparant deux milieux anisotropes", Thesis, Université de Technologie de Compiègne, France, 1999
[35] Boulanger P, Hayes M, “Special inhomogeneous waves in cubic elastic materials”, Zeitschrift fur angewandte mathematik und physik 51(6), 1031-1038, 2000.
[36] M. Deschamps, O. Poncelet, “Inhomogeneous plane wave and the most energetic complex ray”, Ultrasonics 40, 293-296, 2002
[37] R. F. S. Hearmon, “Third-order Elastic Coefficients”, Acta Cryst. 6, 331-340, 1953
[38] R. F. S. Hearmon, “Equations for Transforming Elastic and Piezoelectric Constants of Crystals”, Acta Cryst. 10, 121-124, 1957

Chapter XIII Acoustic Microscopy

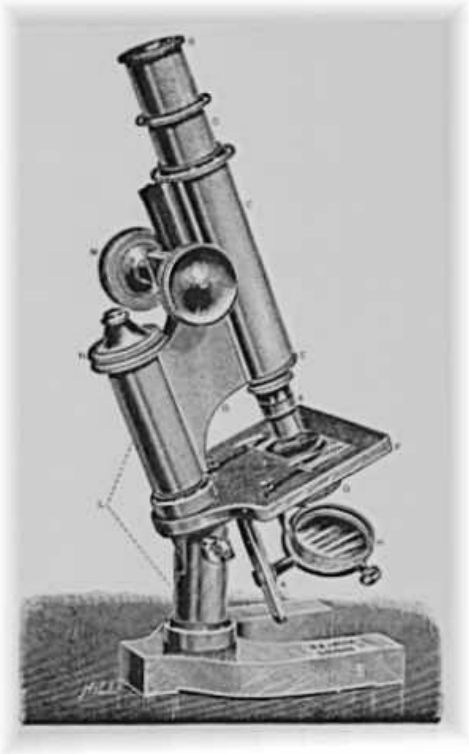

According to the Britannica encyclopedia, a microscope is an instrument that produces enlarged images of small objects, allowing them to be viewed at a scale convenient for examination and analysis. The optical microscope and the electron microscope are, of course, well known. The acoustic microscope is less known to the wide public. An acoustic microscope examines the mechanical properties of a material at a microscopic scale. Because the mechanical properties of a material contain information that is not detectable by means of any other microscope, the acoustic microscope is complementary equipment in the investigation of materials, in materials science as well as for the purpose of nondestructive testing.

Traditionally, acoustic microscopes mainly investigate the surface properties of materials or at the most the near surface regions. Even though this information is very important, it is perhaps not satisfactory for people who would like to investigate the interior regions. In the field of ultrasonics, there are also so called C-scans, that enable inspection of the interior (the bulk) of materials. C-scans are typically formed by means of relatively low frequency ultrasound, in the interval between 0.5 MHZ and 15 MHz. These frequencies allow deep penetration and are generated by transducers of types that are very robust and well known. Nevertheless, for the investigation of thin laminates or for the investigation of thin layers within a layered structure, those C-scan transducers are not satisfactory, because they produce wave lengths well over the characteristic dimensions of the material under investigation. Especially for the study of the microscopic structure of fiber reinforced composites, they are not suitable.

When I was in Delft, on the occasion of the congress “Ultrasonics International 2001”, I met Yulia S. Petronyuk and Vadim M. Levin of the Institute of Biochemical Physics, of the Russian Academy of Sciences, in Moscow. They were working on the development of a new type of acoustic microscope, being able to perform C-scans on a microscopic scale.

With their equipment, they were able to produce low aperture focused beams at higher frequencies than is used in classical C-scans, still lower than the GHz frequencies that are sometimes used in classical acoustic microscopy. After long discussions with them, I discovered that the core of their invention, besides the spatial shape of their bounded beam, was the (temporal) shortness of the produced pulse. This shortness produced very high in-depth accuracy within a layered structure. Because I then had the intention to investigate fiber reinforced composites by means of Polar Scans, I could not withstand the urge to collaborate with them and to visit their lab in order to investigate composites. Due of the fact that their equipment was still under development and because I realized at that point that the road ahead for my own study of the interaction of ultrasound with composites, was still very long, we decided to postpone our collaboration. Finally, in the late summer of 2004, I have been able to go to Moscow and to perform the necessary investigations together with them, on fiber reinforced composites. These investigations followed long term scientific communications by E-mail and by standard post. It will be seen in this chapter that the technique can be used to 'visualize' the interior structure of fiber reinforced composites. Therefore the sole section of the chapter deals with so called 'bulk imaging' of composites. In the future, it is my aim to study this bulk imaging further and to be able to investigate the phenomenon of fatigue damage and impact damage inside composites. This study is very inviting, because fatigue damage and impact damage are two important fields of investigation in our department in Gent.

XIII.A Microscopic Bulk Imaging of Fabric Fiber Reinforced Composites

Microscopic bulk imaging combines a newly developed C-scan apparatus and sophisticated data acquisition technology, with high quality ultrasonic microscopy technology. The system generates ultra short ultrasonic pulses (less than two wavelengths long) having a nominal frequency of 50 MHz. The technique is also applicable at higher frequencies. The ultrasonic beam is focused, having a relatively small aperture. Layer-by-layer imaging of the internal microstructure of carbon fiber reinforced composites (CFRC) and glass fiber reinforced composites (GFRC) is achievable. The method provides a spatial lateral resolution in the order of 50 microns and an in-depth resolution in the order of 80 microns. Echo signals reflected from structural units, such as plies, fiber bundles and micro-flaws form acoustic images of the microstructure at different depths inside the samples. The images make it possible to see ply arrays, the stacking of bundles within plies and the binding material distribution within the bulk of the composite. They reveal failures of interply adhesion, buckling of single plies and fiber bundles, internal defoliations, disbonds and voids. The series of successive images offer outstanding possibilities to reconstruct the bulk structure, to estimate local variations of the properties, and the topological and geometrical characteristics of the structural components. The imaging technique has been applied to study different types of fiber packing – unidirectional, cross-ply and fabric laminates. In addition, high-resolution (one micron) acoustic images are also presented at higher frequencies, for larger aperture, that allow the investigation of the fiber distribution within a single bundle. The images also allow the visualization of the structure of fiber bundle crossovers and disbondings at interfaces and the evaluation of the interaction of a single fiber with the resin or even elastic characteristics of individual fibers.

This work was performed at the Acoustic Microscopy Laboratory, Institute of Biochemical Physics, Russian Academy of Sciences, Moscow, in collaboration with Yulia S. Petronyuk, Vadim M. Levin and Liu Songping

INTRODUCTION

Perhaps the most famous technique for nondestructive testing of materials, is the classical C-scan [1]. The technique applies relatively low frequency sound beams, typically 0.5 MHz to 15 MHz, having a small aperture. Such C-scans are mostly used to detect large internal flaws in laminates. However, to characterize local properties ultrasonically, such as the microstructure and microscopic defects in CFRC and GFRC composite laminates (if statements hold for both, we will simply call them FRC laminates), very high spatial resolution is needed. The size of a probing ultrasonic beam is required to be at least in the range of the structural-element characteristic sizes. In classical C-scans [1], this is not the case because the size of the applied bounded beam and the applied wavelength are to big. Such beams are therefore not suitable for extracting local information of FRC materials, only for global or integral information of materials. The spot (size) of the beam in the focal (waist) area can be made very small by using a high frequency focused beam. Contrary to classical C-scans, classical acoustic microscopy

applies high frequency sound beams, typically 20 MHz to several GHz, that have a very large aperture θ_m.

Though, for high-aperture beams ($\theta_m \sim 30^0$ - 60^0), the major part of the incident radiation reflects at the upper interface of a solid plate. Only a small part penetrates into the plate. Furthermore, the penetrating beam dramatically changes its structure because of refraction phenomena. Therefore, only a minute portion of the incident energy participates in the formation of signals reflected from the lower interface of the plate and obstacles situated within the bulk. In fact, the signal to noise level of the relevant echo signals is far too small to be detectable. Therefore, high-aperture focusing systems are applied only for studying the surface and near subsurface regions.

Employment of large aperture, high frequency ultrasound (0.25 – 2.0 GHz) makes it possible to achieve a resolution of 0.5 μm to 100 μm. An overview of the technique and applications of acoustic microscopy, can be found in refs [2-10] and also to some extent in the 32nd volume (2nd issue) of the IEEE-UFFC Journal in 1985. Classical acoustic microscopy has always been used to study surface or near surface characteristics [11, 12] or coatings [13-17]. In classical acoustic microscopy, often a so called *V(z)* curve is measured and studied [18-33] for harmonic waves, and reveals the surface structure [21, 29, 34] and properties [29]. There is a firm relationship between classical acoustic microscopy and surface wave properties. These surface waves are generated because of the very high aperture and their properties reveal specific local surface quality [35-37].

Classical acoustic microscopy is also commonly used to extract the local elastic features of materials [38-45] and is therefore also applicable to extract stress properties [46] such as in the case of the acousto-elastic effect [47]. If classical acoustic microscopy is applied in transmission instead of reflection, the averaged through thickness properties are studied at a very high lateral resolution [48].

Besides measuring V(z) curves, it is also possible to measure the time of flight in the case of pulses. The technique has for example been applied to extract local stiffness properties in composites [49-50, 34].

The experimental equipment described in the current paper is able to perform time-of-flight measurements in a combination of relatively low aperture and high frequencies, typically between 50 MHZ and 300 MHz. It can be used in a C-scan mode and results in a very high in-depth resolution because of (contrary to other established systems) the generation of extremely short acoustic pulses. Some astonishing results have been obtained in the characterization of fullerene ceramics [51]**.** Nevertheless, the topic of this paper is imaging of the bulk of the materials by using this 'very short pulse' acoustic microscopy equipment. The difference between measuring and imaging can be found in [52].

Imaging in acoustic microscopy has always been limited to imaging surfaces [21, 11, 36, 53, 12, 54] in the case of very high frequencies, or, to imaging of the bulk of a material in the case of relatively low frequencies [52, 54-58]. This is an important drawback that is overcome with the equipment applied in this Chapter XIII. Actually, the reason for the fact that high frequency ultrasound is not so popular for bulk imaging is the fact that, formerly, transducers were relatively narrow banded, and due to damping within the material, this narrowness is further enhanced, resulting in a diminished resolution in the depth of the material. This effect is less outspoken for lower frequencies. If however broad bandwidth, high frequency, transducers are used, which is the case in our equipment, after damping within the bulk of the plate, the bandwidth is still large enough to preserve fairly good in depth resolution.

For completeness, it is important to note that there also exists the imaging technique of scanning tomographic acoustic microscopy [59-61], where high frequency plane waves are applied, in combination with a laser. However, the technique is not really suitable for highly complex materials such as multilayered multidirectional carbon fiber reinforced materials.

This section XIII.A is structured as follows: First, a short theoretical background will be presented on how an incident focused sound pulse is transformed into a reflected pulse after interaction with an isotropic homogeneous solid plate, immersed in water. This information is important, because the pulse shape plays an important role in the interpretation of A-scans, B-scans and C-scans. Even though the presented microscopy equipment can also be applied for extraction of quantitative properties, such as time of flight and hence also the stiffness, the goal of this report is to explain the imaging technique and to show how it is able to visualize the internal structure of FRC laminates with a resolution comparable to the size of the minuscule fiber bundles inside. Therefore, a short description of the equipment and its capabilities will be given, followed by a thorough study of images of the internal structure of different FRC laminates.

The importance of imaging the internal structure of FRC laminates is diverse. Through contacts with different FRC manufacturers, we were asked to develop a technique to 'see' the internal structure in order to detect bad contacts between fibers and resin, in order to detect initial micro cracks due to inhomogeneous shrinking during the fabrication and much more. On the other hand, the technique is really important for materials scientists as well, for obvious reasons. Our department is also on the leading edge in fatigue testing and its respective modeling through finite element methods. Unlike macroscopic elasticity changes, as was reported in [1, 62], knowledge of the initial microscopic aspects, during the first cycles of fatigue testing, is indispensable.

THEORETICAL BACKGROUND

Specific features of the interaction of ultrasound with a layered structure of fiber reinforced laminates and possible mechanisms of acoustical contrast, are discussed in this section.

Acoustic images are formed by means of echo signals reflected at both faces of a plate and at internal interfaces within the interior. In order to visualize the bulk microstructure, and in order to understand the formation of acoustic contrast, it is necessary to know what structural elements are able to generate reflected or backscattered echo signals, it is indispensable to know whether these signals can be resolved by the receiving microacoustical system (acoustic microscope) and it is essential to know what structural parameters establish the level of the ultrasonic echoes.

The interaction of ultrasound with layered fiber reinforced media critically depends on the relationship between the wavelength of the probe radiation and the characteristic sizes of the structural elements of the material. A material is perceived by low-frequency (long-wave) ultrasound as a homogeneous medium. Such an object may be characterized by a set of elastic moduli that are expressed through the densities of the composed material and ultrasonic velocities. The presence of the microstructure directly not only results in background scattering, but also determines indirectly the overall elastic and viscoelastic properties of the composite. Therefore, low frequencies (10 MHz to 15 MHz) are commonly used to visualize large-scale defects inside the laminate, or to measure the overall elastic properties of fiber reinforced composites [1].

Contrary to low frequency ultrasound, high-frequency ultrasound is essentially susceptible to inhomogeneities within the bulk of the material and effectively reflects and refracts at interfaces between structural elements having different mechanical properties.
The frequency range of 25 MHz up to 100 MHz, which has been employed in our experiments, provides a sensibility in the range of 100 μm up to 150 μm for the visualization of the bulk structure elements.

Perhaps the most important aspect of fiber reinforced composites, that is accessible for high frequency imaging, is the set of individual lamina. Microscopic imperfections and anomalies of the lamina stacking, can be resolved. The interface between the immersion liquid and the solid, the interfaces between different plies, the interfaces between lamina and separate resin and the boundaries between defects and plies, are outstanding examples of what is accessible by the presented technique.

In Fig. XIII.A_1, the possible origins of ultrasonic pulse reflection, inside a fiber reinforced laminate structure, are illustrated. The upper face and the bottom of a plate are the most outspoken sources of echo signals (Fig. XIII.A_1.a). Furthermore, each ply-ply interface on itself (Fig. XIII.A_1.b) is an independent source of echo pulses. Ultra-short probe pulses, having a temporal width of approximately 30 ns to 40 ns, provide sufficient time resolution that enables one to distinct between echoes reflected from interfaces of neighboring plies, because the characteristic delay time between such echoes is typically between 70 ns and 100 ns. In addition, locally, within a fiber reinforced composite, the ply stacking produces sufficiently thick (150 μm to 300 μm) intermediate resin layers (Fig. XIII.A_1.c). Then, each boundary of the intermediate layer is again a source of a reflected echo pulse.

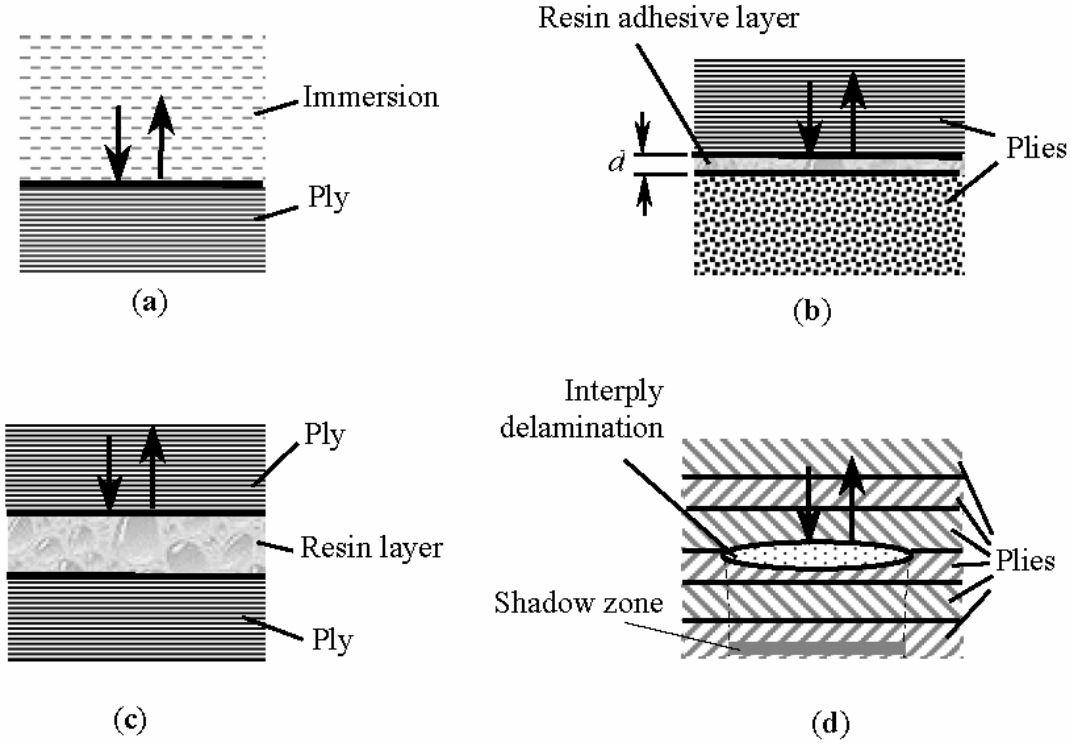

Fig. XIII.A_1: ***Feasible types of ultrasonic reflection in FRC laminates: a) – reflection at immersion /carbon fiber ply interface; b) – reflection at ply/ply interface; c) – reflection at carbon fiber ply/resin layer interface; d) – reflection at defect boundary.***

Besides, it also occurs that the resin matrix, in between layers, contains particular elements of fiber reinforcement, such as individual threads or large locks of fibers, isolated from a bundle. Also these structural components generate echo signals, again, due to reflection of the ultrasonic probe pulse at their interfaces with the resin. Because the mechanical characteristics of these components are close to the ones of a prepreg ply, their resulting echoes are mixed with the information coming from the neighboring ply–resin interface.

Apart from the lamina structure containing an arrangement of fiber reinforcing elements, fiber reinforced laminates may also contain common imperfections such as faults and inclusions. Most of these imperfections are caused by failure of the material integrity, resulting in delaminations at the interply interfaces, cracks of various orientations with respect to the direction of ply stacking, and voids. The significant difference in acoustic properties between the faults and the surrounding matter, provides total reflection of the probe beam from the imperfection boundaries and results in the formation of so called shadow zones underneath the defects (Fig. XIII.A_1.d). Yet another type of frequently present elements are inclusions of alien material, such as glass or polymer threads in stitched composite materials. Whenever the difference in acoustic properties of the inclusions and the overall laminate is significant, high efficiency of reflection (sometimes close to unity) and the formation of shadow effects arise, that are similar to the effect of extensive imperfections such as voids and delaminations.

The mechanisms of contrast formation in acoustic imaging will be explained further on in more detail for different types of fiber reinforced composites, while presenting the experimental results.

EXPERIMENTAL EQUIPMENT

Fig. XIII.A_2 is the schematic diagram of the experimental setup. The system mainly consists of four parts: the electronic unit, the mechanical scanning unit, the acoustic focusing system and the host computer. Ultra-short repetitive probing focused pulses, of 30 ns to 40 ns width, are generated by a high frequency (HF) transducer, attached to an acoustic lens. The combination is called the acoustic head. The acoustic head is constructed as a rod of melted quartz with a flat transducer on the one end and a spherical surface on the other end. In our experiments, the length of the rod is 30 mm and the diameter is 10 mm. The transducer is a Y-cut Lithium Niobate crystal, 6 mm in diameter.

The thickness of the transducer provides an operation frequency of 50 MHz. In order to generate extremely short pulses, a special backing on the ‘free side’ of the transducer, that critically damps vibrations of the transducer, is applied. So, the quality of this backing is mainly responsible for the high quality of the experimental setup. As a consequence, the resulting bandwidth is highly increased and spans approximately 30% to 50% of the central frequency for a 25 MHz to 100 MHz transducers. To be precise, as a result of the backing characteristics, the frequency band is a little bit asymmetric and spans further in the low frequency range than in the high frequency range. For a 50 MHz transducer, the pulse length is 35 ns, which is slightly longer than would have been in the case of a perfectly symmetric frequency band. The acoustic lens consists of a spherical surface with a diameter of 5 mm, which is less than the diameter of the rod. The radius of the spherical curvature is 10 mm. The aperture angle θ_M is 11^0 and provides a focal distance in water of 13.3 mm.

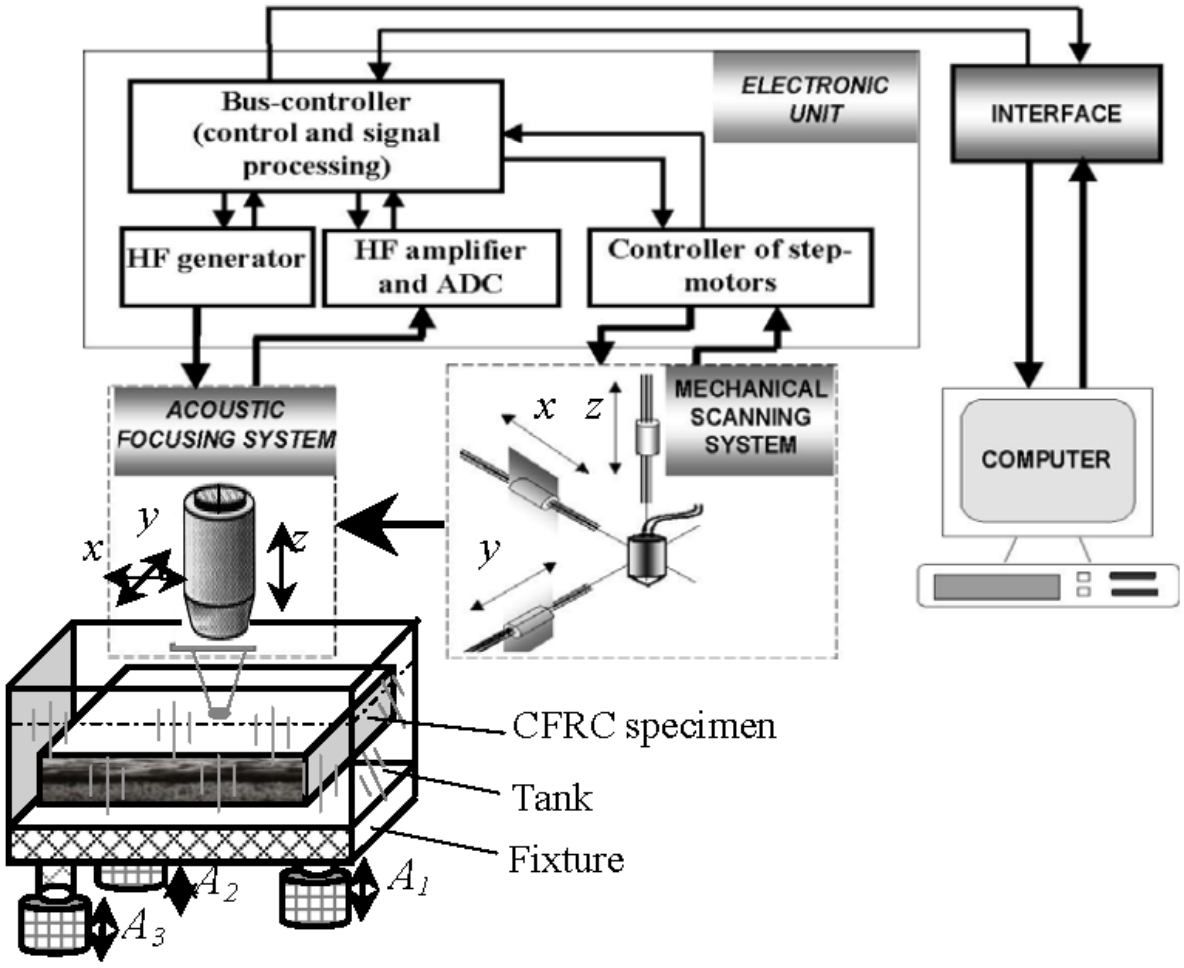

Fig. XIII.A_2: ***Schematic diagram of the experimental set-up.***

In our experiments, the reflection mode of operation is used. In this case, the signal, reflected from the specimen, is received by the same acoustic lens. Then, the outgoing signal is fed to the HF amplifier and ADC in the electronic unit for amplifying and digitizing. Its sampling rate is 200 MHz. The digitized echo signals are sent to the host computer via the interface for processing, displaying and imaging. The specimens are immersed in a fluid. Distilled water is used in the reported experiments. The scanning motions are driven by step-motors, which are controlled by the electronic unit. In the experiments, the motor step is 0.05 mm. The scanning parameters and signal processing parameters, such as the size of the scanned area, the signal gain, the time-scale, etc., are stored as part of the header in the data structure for post-processing and image reconstruction when the specimen is scanned along a raster.

Different imaging (B- and C-scan imaging) can be performed by 1D or 2D motion of the acoustic lens over the specimen. The 3D imaging technique is based on layer-by-layer scanning at different depths. A successive series of C-scans has been employed to characterize the bulk microstructure of fiber reinforced materials. The B-scans have been applied to visualize cross sections.

DESCRIPTION OF THE ACQUISITION METHOD

Characteristics of the ultrasonic focused beam and the influence of the aperture

A high spatial resolution, focused beam can be obtained from parallel plane waves by designing a proper lens, as sketched in Fig. XIII.A_3. The parallel plane waves can be excited from a plane transducer.

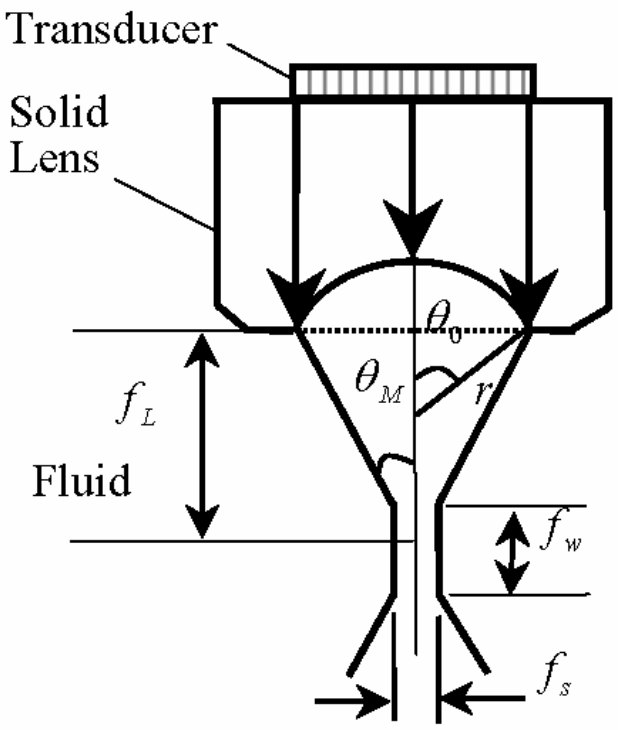

Fig. XIII.A_3: ***Schematic illustration of the focusing of a beam***

A convergent beam is generated when the parallel ultrasonic beam passes through the spherical surface of the lens because of refraction of the acoustic rays. Such a focusing transducer, formed by a spherical acoustic lens, produces sound, characterized by a focal distance, depending on the 'lens-immersion acoustic property ratio $\frac{c}{\upsilon}$' and the aperture angle of the lens θ_M, given by [6]

$$f_L = \frac{r}{1-\frac{c}{\upsilon}}, \qquad \text{(XIII.A\_1)}$$

where υ is the sound velocity in the lens (solid buffer rod), c is the sound velocity in the immersion fluid, and r is the radius of the spherical surface (curvature) of the lens. This expression (XIII.A_1) is obtained from ray-considerations and application of Snell's law. The aperture θ_M of the lens is expressed by [6]

$$\tan\theta_M = \frac{\sin\theta_0}{\cos\theta_0 - \frac{c}{\upsilon - c}} \qquad \text{(XIII.A\_2)}$$

where θ_0 and θ_M are defined in Fig. XIII.A_3. Of course, the real structure of a focused beam also depends on the wavelength of the applied ultrasonic radiation. The length of the focal waist f_w and the diameter of the focal spot f_s are the main parameters that characterize a focused ultrasonic beam. They can be expressed in terms of the wavelength λ as [6]

$$f_w = \frac{2\lambda}{1-\cos\theta_M} \qquad \text{(XIII.A\_3)}$$

$$f_s = \frac{0.61\lambda}{\sin\theta_M} \qquad \text{(XIII.A\_4)}$$

Depending on the application, the aperture angle θ_M and the wavelength λ can be adapted in order to reach optimum conditions. A lens with larger aperture results in a smaller focal spot and therefore an increased lateral resolution. It provides high resolution acoustic imaging and local measurement, though only in the region of the surface or the near-subsurface. This is due to a short focal waist, which is dramatically distorted inside the body of the investigated specimen. The correlation between the aperture θ_M and the length of the focal waist f_w as well as the diameter of the focal spot f_s are shown in Fig. XIII.A_4. The latter figure shows the relative size of the focal spot and the focal waist, for a small and a large aperture θ_M. For example, for an aperture $\theta_M \in \left[5^0, 11^0\right]$, the focal spot size is $f_s \in \left[2\lambda, 7\lambda\right]$ and the focal waist is $f_w \in \left[58\lambda, 109\lambda\right]$. On the other hand, for an aperture $\theta_M \in \left[30^0, 50^0\right]$, the focal spot size is $f_s \approx \lambda$, whereas the focal waist is $f_w \in \left[5\lambda, 15\lambda\right]$. So, in the case of a low-aperture, the lateral resolution (size of the focal spot) decreases in comparison with the high-aperture case, though this increase is not as dramatic as the increase of the penetration depth (the focal waist). Therefore, a convergent ultrasonic beam with a long focal waist is suitable to extract information about bulk elasticity, as well as for bulk imaging.

The aberration effect

When a convergent ultrasonic beam propagates towards a fluid/solid interface (plane-parallel), aberration of the convergent beam will arise from refraction of wave rays at the fluid/solid interface, as is schematically illustrated in Fig. XIII.A_5. The focal distance f_L in the solid will become shorter than in the fluid f_v due to refraction of the convergent beam at the fluid/solid interface.

In addition, the length of the focal waist f_w will also decrease compared to the case when there is only fluid

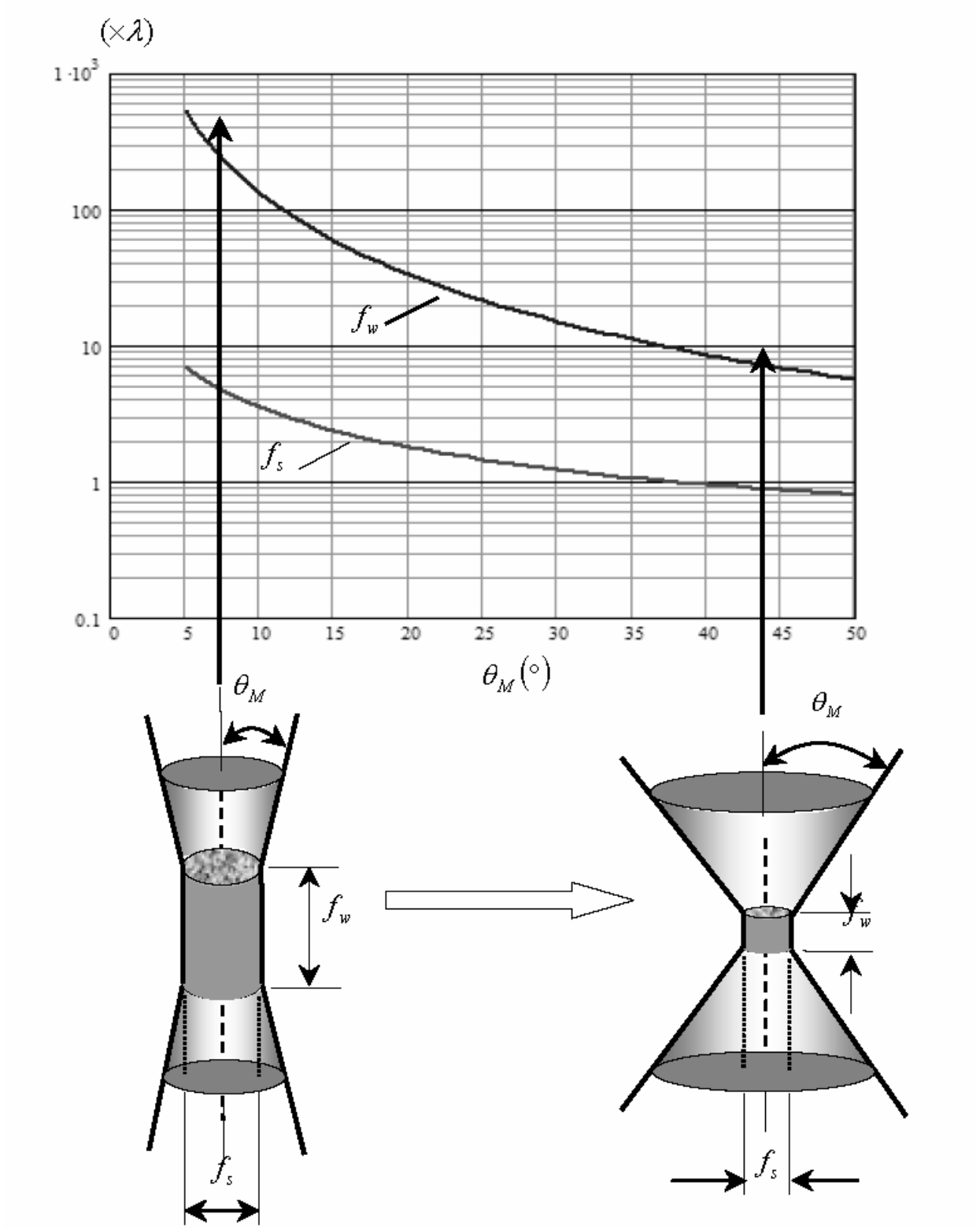

Fig XIII.A_4: ***Illustration of focusing systems with different apertures. Left: low aperture focusing system, right: high aperture focusing system***

The size of the focal spot in the solid f_s^{solid} will increase due to refraction and aberration at the fluid/solid interface, and it can be expressed approximately by [6]

$$f_s^{solid} = \left\{ \left[\frac{\left(c/v - 1 \right)^2}{4 f_a^{\,2}} h^3 \right]^2 + \left(\frac{0.61 \lambda_s f_b^{\,2}}{h} \right)^2 \right\}^{\frac{1}{2}} \qquad \text{(XIII.A\_5)}$$

where the parameters f_a, f_b and h are shown in Fig. XIII.A_5, and λ_s is the wavelength in the solid. Thus, the in-depth resolution will decrease with the lens moving down towards the specimen.

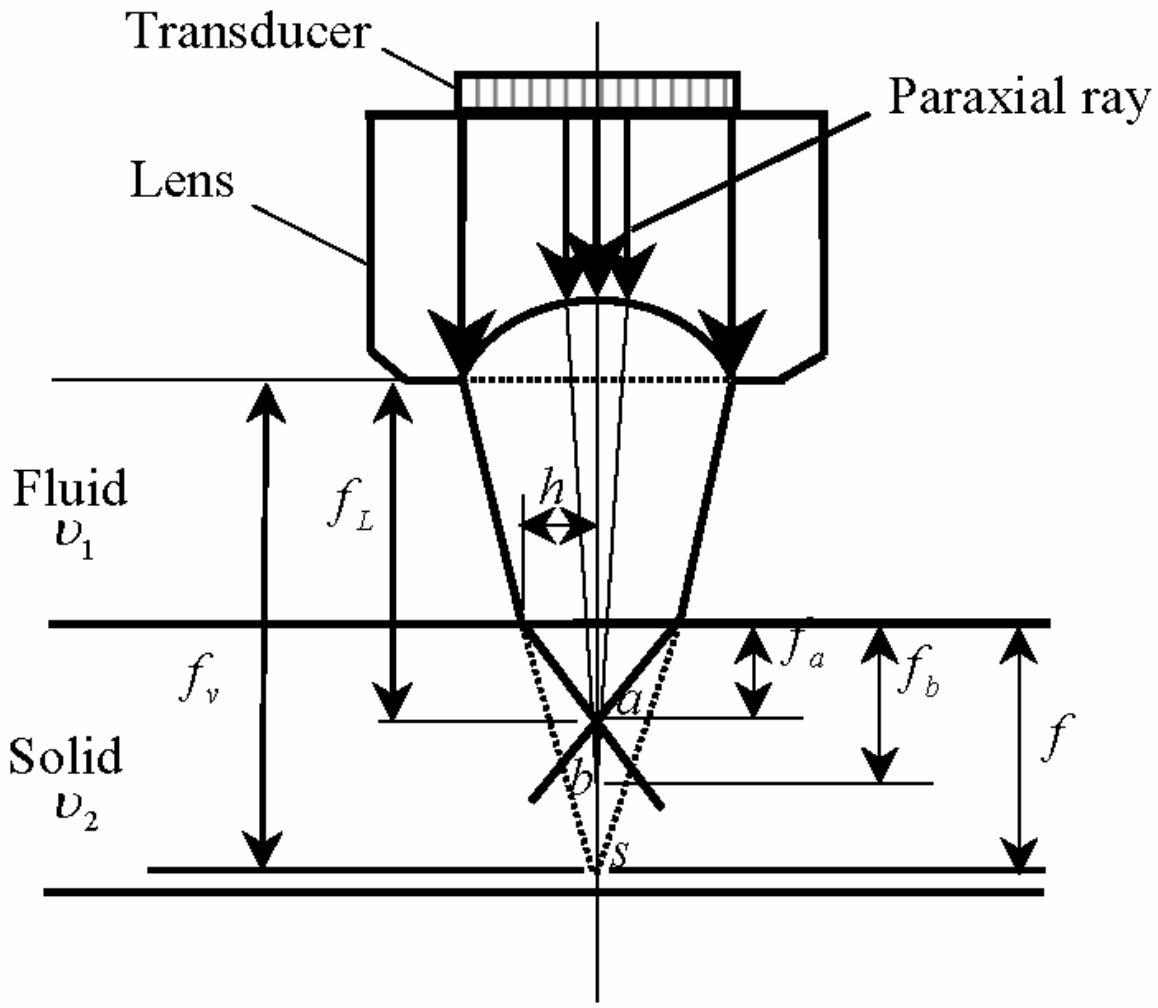

Fig. XIII.A_5: ***Aberration of a convergent beam at a fluid/solid interface.***

Received pulse characteristics

The pulse signal, which is received by an acoustic lens after reflection from the solid plate, can be expressed by [3]

$$V(t,z) = 2\pi \int B_\omega \iint f(k_x,k_y) R\left(k_x,k_y\right) \exp\left(2iz\sqrt{k^2-k_x^2-k_y^2}\right) dk_x dk_y e^{-i\omega t} d\omega \qquad \text{(XIII.A\_6)}$$

z is the ray distance from the transducer to the surface of the specimen;
ω is the angular frequencies;
B_ω is the mean efficiency of the transducer at the frequency ω;
$\vec{k}\ (k_x,k_y,\sqrt{k^2-k_x^2-k_y^2})$ is the wave vector of the beam spatial spectrum components;
$R\left(k_x,k_y\right)$ is the partial reflection coefficient from the plate;
$f\left(k_x,k_y\right) = P^{\langle in\rangle}\left(k_x,k_y\right)\cdot P^{\langle out\rangle}\left(k_x,k_y\right)$ is the aperture function, where $P^{\langle out\rangle}(k_x,k_y)$ is the angular spectrum of the output from the plate, and $P^{\langle in\rangle}\left(k_x,k_y\right)$ is the angular spectrum of the input coming from the acoustic lens.

As is seen from expression (XIII.A_6), the properties of the specimen are incorporated in the reflection coefficient $R\left(k_x,k_y\right)$, which is, from a mathematical point of view, real valued, because the employed low aperture does not involve critical angles. The partial reflection coefficient $R\left(k_x,k_y\right)$ can be expressed as [3]:

$$\begin{aligned} \mathrm{R}\left(k_x,k_y\right) &= \mathrm{R}_S\left(k_x,k_y\right) + \mathrm{R}_{L1}\left(k_x,k_y\right)\cdot\exp\left(i\cdot 2d_1\cdot\sqrt{\frac{\omega^2}{c_{L1}^2}-k_x^2-k_y^2}\right) \\ &+\mathrm{R}_{L2}\left(k_x,k_y\right)\cdot\exp\left(2i\left(d_1\cdot\sqrt{\frac{\omega^2}{c_{L1}^2}-k_x^2-k_y^2}+d_2\cdot\sqrt{\frac{\omega^2}{c_{L2}^2}-k_x^2-k_y^2}\right)\right)+\ldots \end{aligned} \qquad \text{(XIII.A\_7)}$$

where $\mathrm{R}_{L1}\left(k_x,k_y\right)$ is the reflection coefficient of longitudinal waves from the first interface (measured from the upper face of the specimen), where $\mathrm{R}_{L2}\left(k_x,k_y\right)$ is the reflection coefficient of longitudinal waves from the consequent interface, and so on. The value d_M is the distance between interface *M* and interface *M-1*. The value c_{LM} is the longitudinal wave velocity between interface *M* and interface *M-1*.

The harmonic functions in (XIII.A_7) describe the time of flight for the longitudinal waves in each composite layer. If the duration of the probe pulse is short enough, the echo pulses from each individual interface can be resolved, and can be employed for layer-by-layer imaging. The contrast of the ultrasonic imaging of the composite layers is then determined by the

reflection coefficients $R_S(k_x,k_y)$, $R_{L1}(k_x,k_y)$, $R_{L2}(k_x,k_y)$ and so on. Because of the long focal waist and the low aperture, and because longitudinal waves propagate faster than shear waves, the obtained echo is primarily determined by the reflection coefficient of longitudinal waves. For the applied case of normal incidence, the reflection coefficient R_{LM} at the interface M, is given by [63]

$$R_{LM} = \frac{Z_{M+\delta} - Z_{M-\delta}}{Z_{M+\delta} + Z_{M-\delta}} \qquad \text{(XIII.A\_8)}$$

where Z_J is the acoustical impedance in the layer above the interface M ($J = M - \delta$) or the acoustical impedance in the layer underneath the interface M ($J = M + \delta$). Then, the transmission coefficient T_{LM} is given by [63] $T_{LM} = 1 + R_{LM}$.
For the task of measuring the amplitude of the ultrasonic reflection in composite media, for different types of interfaces, our experimental setup can be applied.

acoustic imaging method for CFRC laminates

The study of the bulk microstructure of fiber reinforced composites is conducted by employing a micro-acoustic system, which is schematically presented in Fig. XIII.A_2. The reflected signal is received by the same focusing lens in a pulse-echo mode. The signal is digitized and stored in the equipment's memory together with the coordinates of the point where the measurement has been performed. The measurement is repeated for each subsequent point of the scanning field. It is possible to represent the stored data on the computer display in different ways, such as A-scan, B-scan and C-scan.
In the A-scan, besides the echo reflected at the upper surface of the plate (signal **F**), the received pulse series also involves signals reflected from the bottom of the plate (**B**) as well as from the internal microstructure and defects or elastic irregularities inside the bulk ($\mathbf{D_i}$). Contrary to long pulses, when short probe pulses are employed (Fig. XIII.A_6), echo signals resulting from reflection at different depths within the bulk, are resolved in time (Fig. XIII.A_7). The echoes **B** and $\mathbf{D_i}$ are formed by a round-trip phenomenon of the longitudinal elastic wave pulse inside the specimen to a reflector (e.g. a defect) and back.

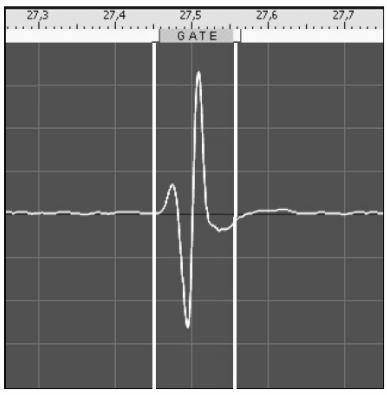

Fig. XIII.A_6: ***Probe pulse generated by the low-aperture acoustic microscope (of the Acoustic Microscopy Lab., RAS; operation frequency of 50 MHz***

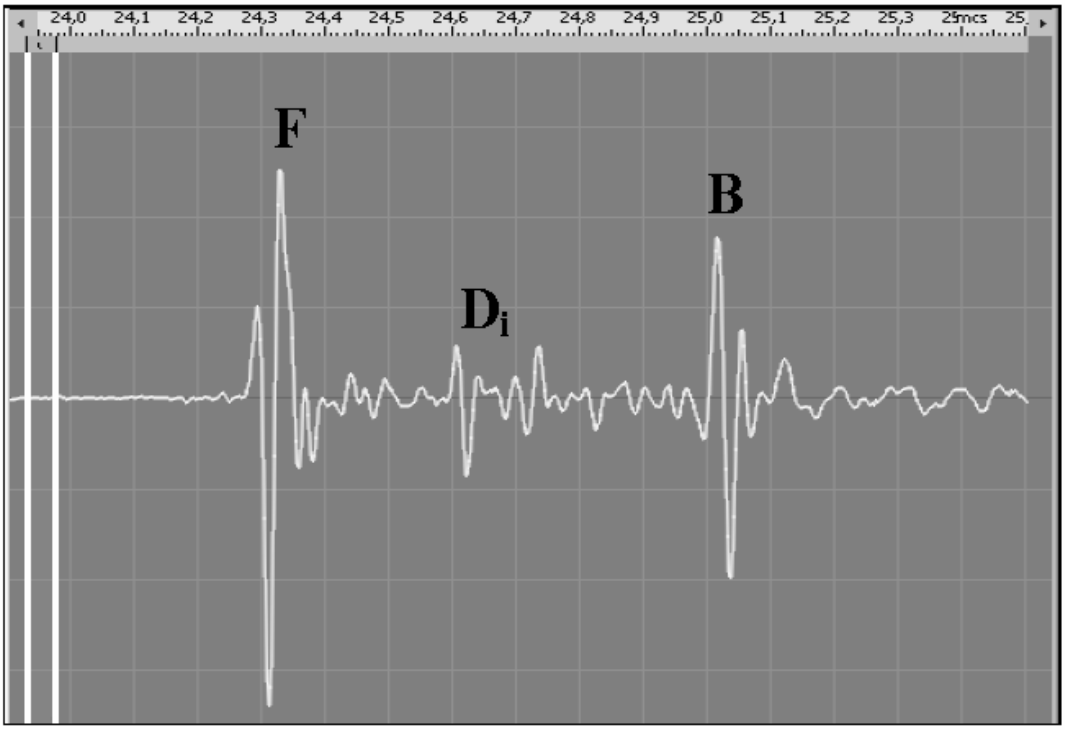

Fig. XIII.A_7: ***Received signal in the low-aperture acoustic microscope (of the Acoustic Microscopy Lab., RAS; operation frequency of 50 MHz). The echo pattern: F; the signal from the face: B; the pulse from the bottom: D_i; the echo from elements of the bulk microstructure (unidirectional CFRC composite 1.21 mm thick with intermediate resin layer of 210 μm).***

The time intervals (delay times) τ_i between the reference pulse **F** and other echo pulses, define the depth position d_i of the *i*-th internal reflector: $d_i = \frac{1}{2} \cdot c_L \cdot \tau_i$, where c_L is the velocity of longitudinal elastic waves in the object material. Measuring delay times allows one to find depth positions for respective elements of the bulk microstructure.

The recorded signal at each point of the scanning area (A-scan) is saved and used to form acoustic images. There are two main ways of image formation. In both cases, the imaging is controlled by a system of electronic switches, called the electronic gate (see Fig. XIII.A_8). The gate makes it possible to choose a delay time interval and to work with signals only within the chosen interval. *B*-scans (Fig. XIII.A_9) are formed by recording the entire signal within the electronic gate for each spot along a strait position scanning line. The scanning position corresponds then to the *x*-axis; whereas the delay time (transformed depth position) is plotted as ordinate. The time-dependent magnitude of the echo signal is represented by a grey scale. Usually, *B*-scans consist of straight and curved lines and spots and they display the in-depth distribution of internal interfaces. A *B*-scan can be treated as a cross-section image of the specimen's elastic microstructure.

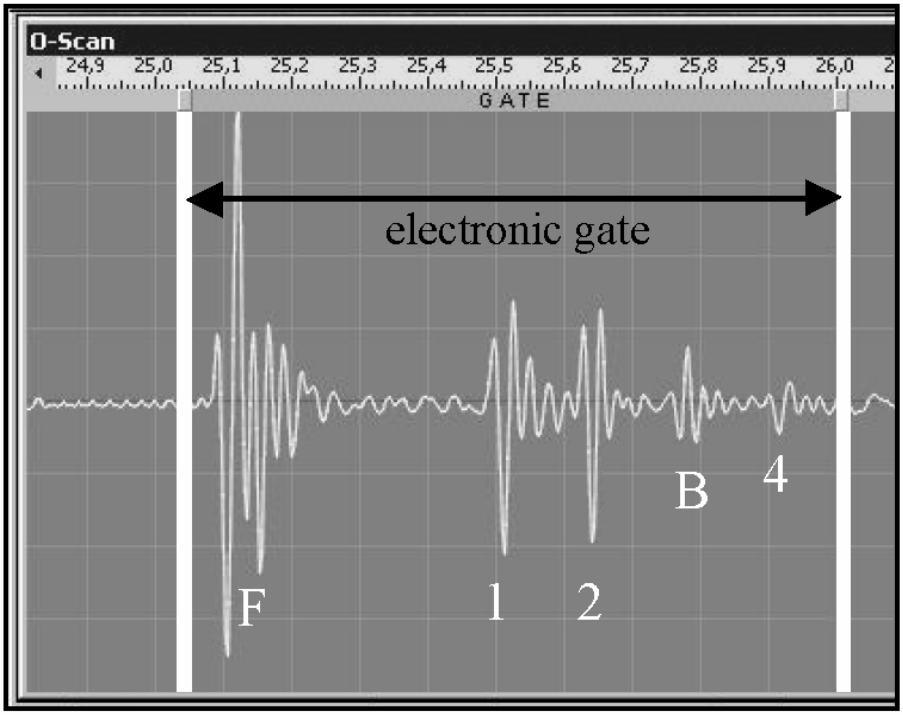

Fig. XIII.A_8: ***Formation of B-scans: structure of the echo signal and electronic gate position (CFRC composite with intermediate resin layer: 1, 2 – resin layer top and bottom.***

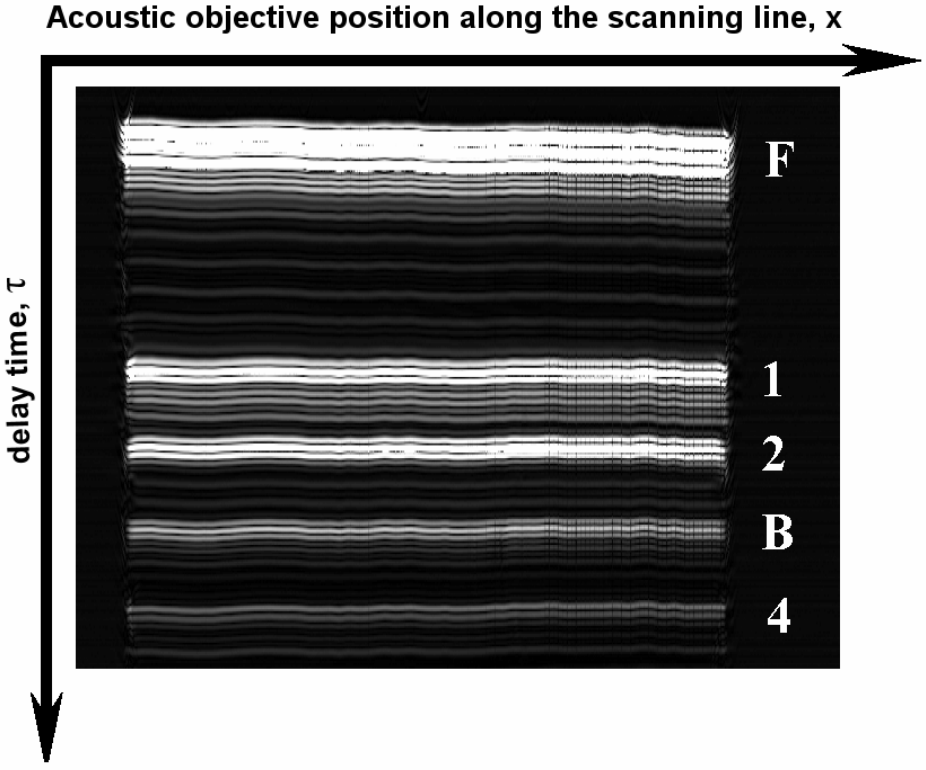

Fig. XIII.A_9: ***Formation of B-scans: respective B-scan (CFRC composite with intermediate resin layer: 1, 2 – resin layer top and bottom.***

Whereas B-scans are formed by 1D scanning (along a straight line), C-scans (Fig. XIII.A_10) are formed by 2D scanning on a chosen surface, and are formed as grey-scale images displaying the maximum of the echo-signal amplitude within a short time interval defined by the electronic gate. *C*-scans reproduce the internal microstructure within a certain layer at a definite depth inside a plate. The gate position and its width are tuned; therefore the object structure may be displayed at any depth inside the bulk of the plate by changing the electronic gate position. A series of acoustic images in parallel sections (*B*- and *C*-scans) can be obtained for the visualization of the bulk microstructure of the entire plate. The series of planes makes it possible to restore the 3*D* microstructure of the interior of an object. This formation can be called the *pseudo-tomographic mode* of acoustic imaging and differs from actual *tomography* [59-61] in that only the normal incidence direction is considered.

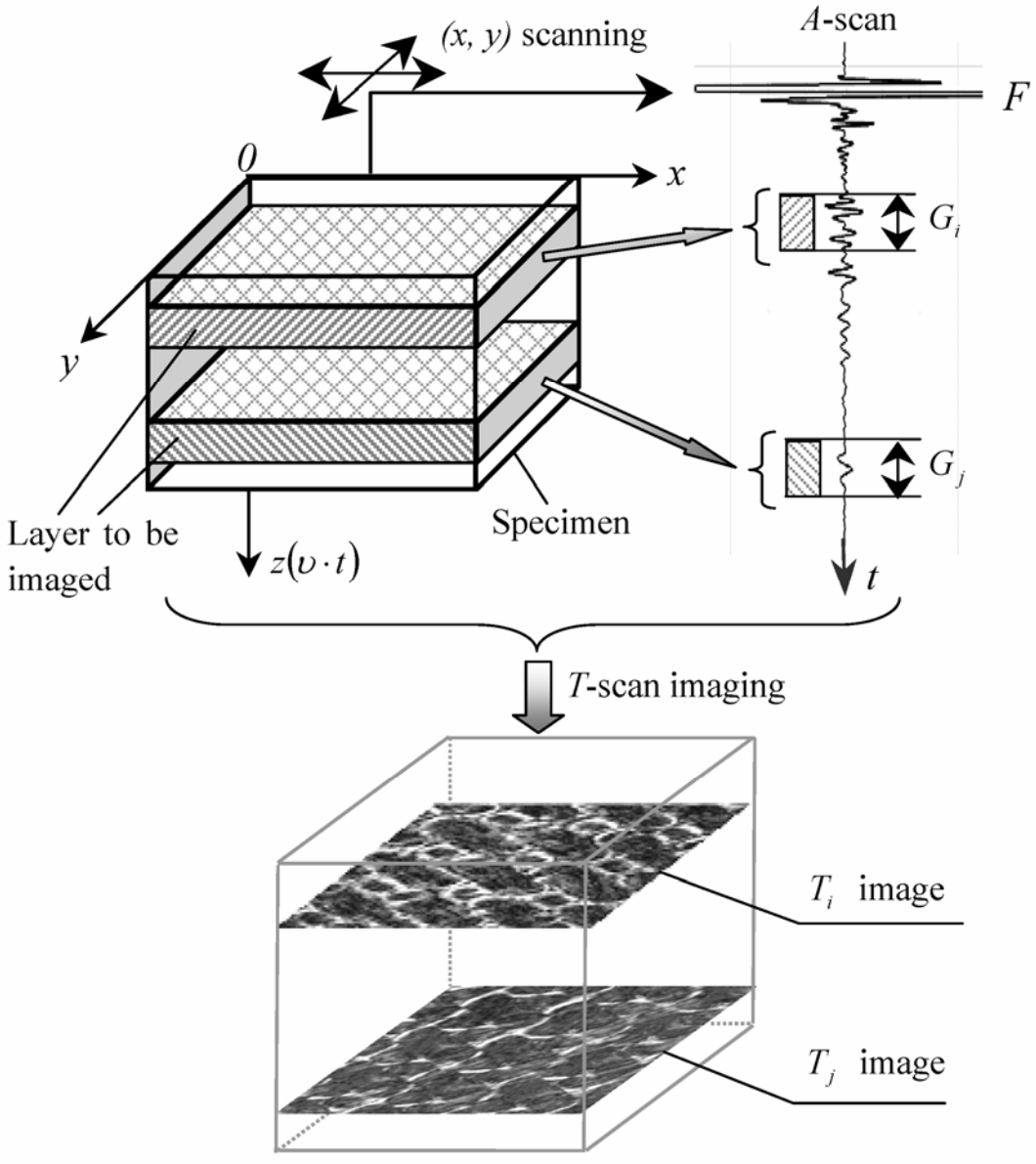

Fig. XIII.A_10: ***Formation of successive series of C-scan acoustic images.***

The earlier described experimental setup enables one to obtain a resolution, both lateral and in depth, that makes the structural elements of CFRC laminates and their possible flaws and anomalies, resolvable. Furthermore, the penetration depth is of the order of 2 mm to 4 mm, whence, for most applications, the plates are examinable through their complete bulk.
Time-of-flight measurements of ultrasonic ultra short pulses uncover the depth of reflectors and the amplitude of the pulses depends on the nature of the encountered structural elements.
If we consider a C-scan of a certain depth, then differences in the recorded amplitude within the corresponding electronic gate, produce contrast. This contrast is the key feature of the 'imaging' process.

All *A*-scan signals are digitized and stored in the storage medium for post-reconstruction of the bulk microstructure of the specimen in *B*-scan imaging. Local RF echo signal patterns can be obtained exactly corresponding to a position in the *B*- and *C*-scan images by dragging the mouse cursor to the position of interest if necessary. Then, the transducer is moved automatically to the corresponding location in the specimen under the control of the host computer. Therefore, the combination of successive series of *C*-scans and *B*-scans provides three-dimensional scanning acoustic imaging to study and observe the bulk microstructure of CFRC laminates.

DESCRIPTION OF THE SAMPLES

In this report, we consider 4 FRC specimens:

Pure unidirectional carbon fibers in Bismaleinide resin

The laminate consists of a stacking of unidirectional prepreg layers as $[0^0/0^0/0^0/0^0/\text{adhesive film}]_{2s}$ with an adhesive layer in the middle. The resin is of the Bismaleimide resin QY8911 family, whereas the carbon fibers are of the T300 style. Each prepreg layer is 0.125mm thick, whereas the complete thickness after curing is 1.17 mm

unidirectional and cross-ply fabric carbon fibers in Poly Phenyl Sulphide

The laminate consists of layers of carbon fibers of the type 3K HT JB, arranged as a 5-harness satin weave fabric, in Poly Phenyl Sulphide (PPS) resin. Each layer has a thickness of about 0.3 mm. The layers are stacked as $[0°]_8$ for the unidirectional sample and as $[0°/90°]_{2s}$ for the cross-ply specimen. The total thickness of the laminate is 2.38mm. Furthermore, the number of fiber bundles is 70 per 10cm.

unidirectional fabric glass fibers in epoxy

The laminate consists of layers of glass fibers of the type Roviglass R17/475, arranged as a 3-harness satin weave fabric, in epoxy resin. Each layer has a thickness of about 0.375 mm. The layers are stacked as $[0°]_8$.

RESULTS

The main elements of the regular microstructure of FRC laminates to be visualized are interfaces between individual components of the internal microstructure, i.e. plies, fiber bundles

and threads, large locks of fibers integrated into bundles. Surfaces of all these elements are irregular and rough, therefore contacts between them is never perfect. Actually, contacts are provided by interspaces filled by resin, see Fig. XIII.A_11.

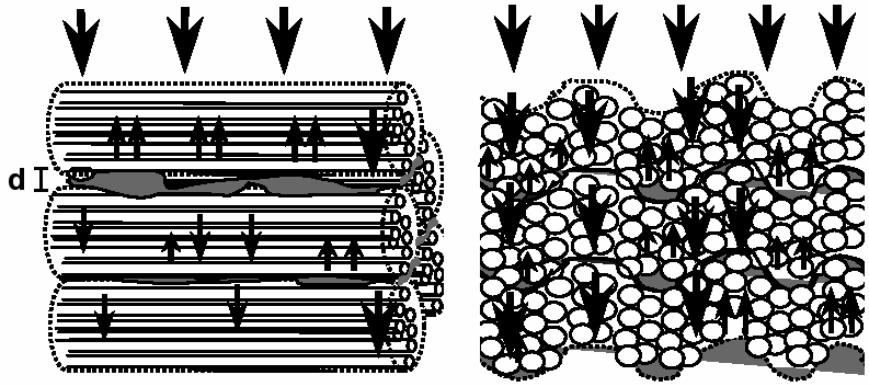

Fig. XIII.A_11: ***Mechanism of contrast for regular microstructure in FRC laminates: There is echo formation at resin interspaces.***

Ultrasound of high frequency is susceptible to such microscopic interfaces. The efficiency of the reflection critically depends on the resin interspace thickness *d*. The reflection coefficient varies from 0 for tight contact up to 0.4 for an interspaced thickness of ≈ 13 μm. Because the plies are always rough, the resin thickness between plies has a spatially varying thickness. Imaging will therefore result in varying grey scale within a fixed layer depth. Therefore, the micro-relief of the ply-ply interface, caused by thickness modulation as a result of particular fiber locks and bundles, makes it possible to see the packing of plies, the fiber bundle configuration in individual plies within each ply, the fiber orientation in an individual bundle and variations in the distribution of adhesive resin thickness between neighboring plies. This phenomenon provides the mechanism of acoustic contrast for the display of topological peculiarities of the bundle arrangement as well as for imaging defects of ply and fiber bundle stacking, buckling, lamina folds and corrugations, pleats ruptured bundles and locks. Acoustic images excellently display failures of material integrity, such as voids, interply delaminations, defects of adhesion for individual bundles, cracks, porosity and also inclusions.

In the examples discussed further on, the width of the electronic gate that controls the imaging of individual layers, has been taken minimal (20 ns to 40 ns, resulting in a spatial interval of 60 μm to 120 μm) in order to optimize visualization of the transition from one ply to another.

Pure unidirectional carbon fibers in bismaleinide resin

The sample characteristics are described in previous section. The series of C-scan images in Fig. XIII.A_12 gives the internal structure of a composite system composed of two 4-ply unidirectional CFRC plates with intermediate resin layer (Fig. XIII.A_12a). The series represents the 3D specimen microstructure from its polished face (image #0) up to its unpolished bottom (#7). Images # 1-2 of the upper part of the compound plate display small variations of bundle orientation in different plies of stacking and the occurrence of buckling in the ply packing. Images #3-6 include transition zones nearby the upper (#3-5) and the lower (#4-6) boundaries of the resin layer. Both interfaces include extended voids that are absolute reflectors for ultrasonic

radiation. We see these voids as bright areas in pictures #3-6 and their shadows in the image #7 of the specimen's bottom.

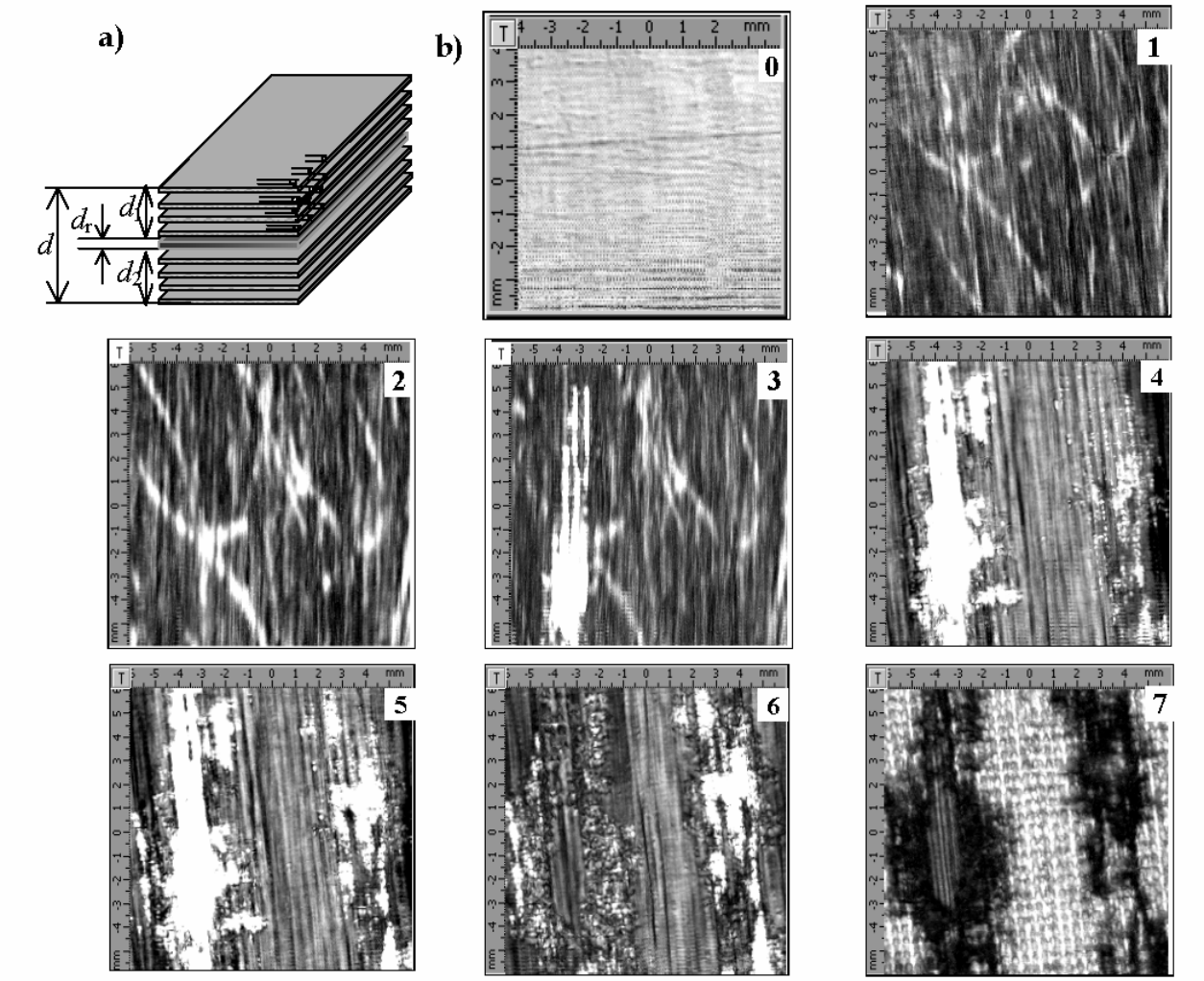

Fig. XIII.A_12: ***Bulk microstructure of a unidirectional CFRC laminate compound. a) –sample structure - upper and lower parts of 4 prepreg plies (d_1= d_2= 0.48 mm) separated by the resin ribbon (dr= 0.21 mm); b) –series of acoustic images of the bulk microstructure at progressively increasing depth from the specimen face (0) to the bottom (7).***

unidirectional and cross-ply fabric carbon fibers in Poly Phenylene Sulfide

The characteristics of the samples are given earlier. Fig. XIII.A_13 corresponds to the unidirectional case, whereas Fig. XIII.A_14 corresponds to the cross-ply case. Each of those figures are composed of C-scan images at different depths, beginning with the upper surface (#1) and ending with an image of the bottom (#12).

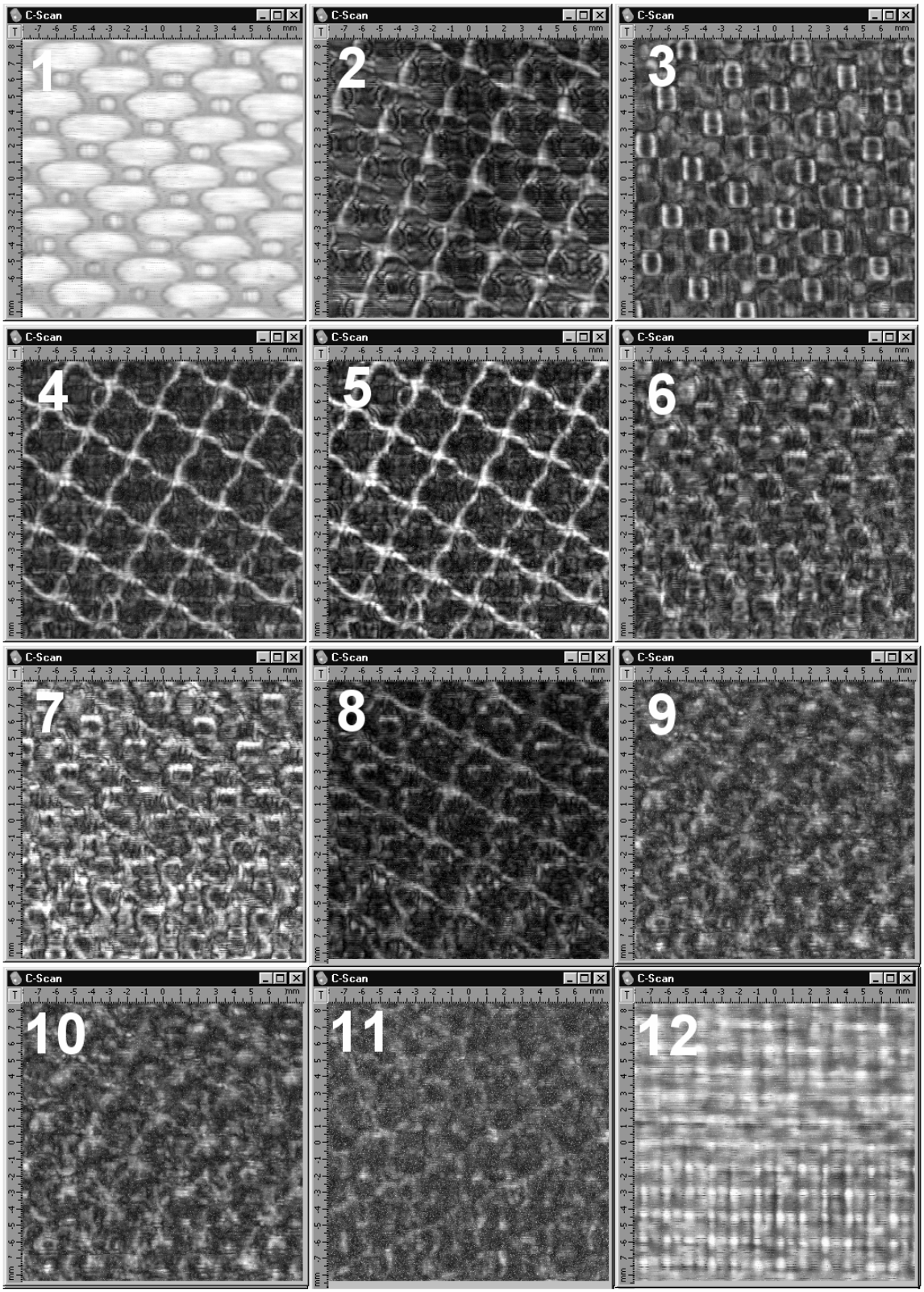

Fig. XIII.A_13: ***C-scan images at different depths, beginning with the upper surface (#1) and ending with an image of the bottom (#12), for unidirectional fabric carbon fibers in Poly Phenylene Sulfide (PPS).***

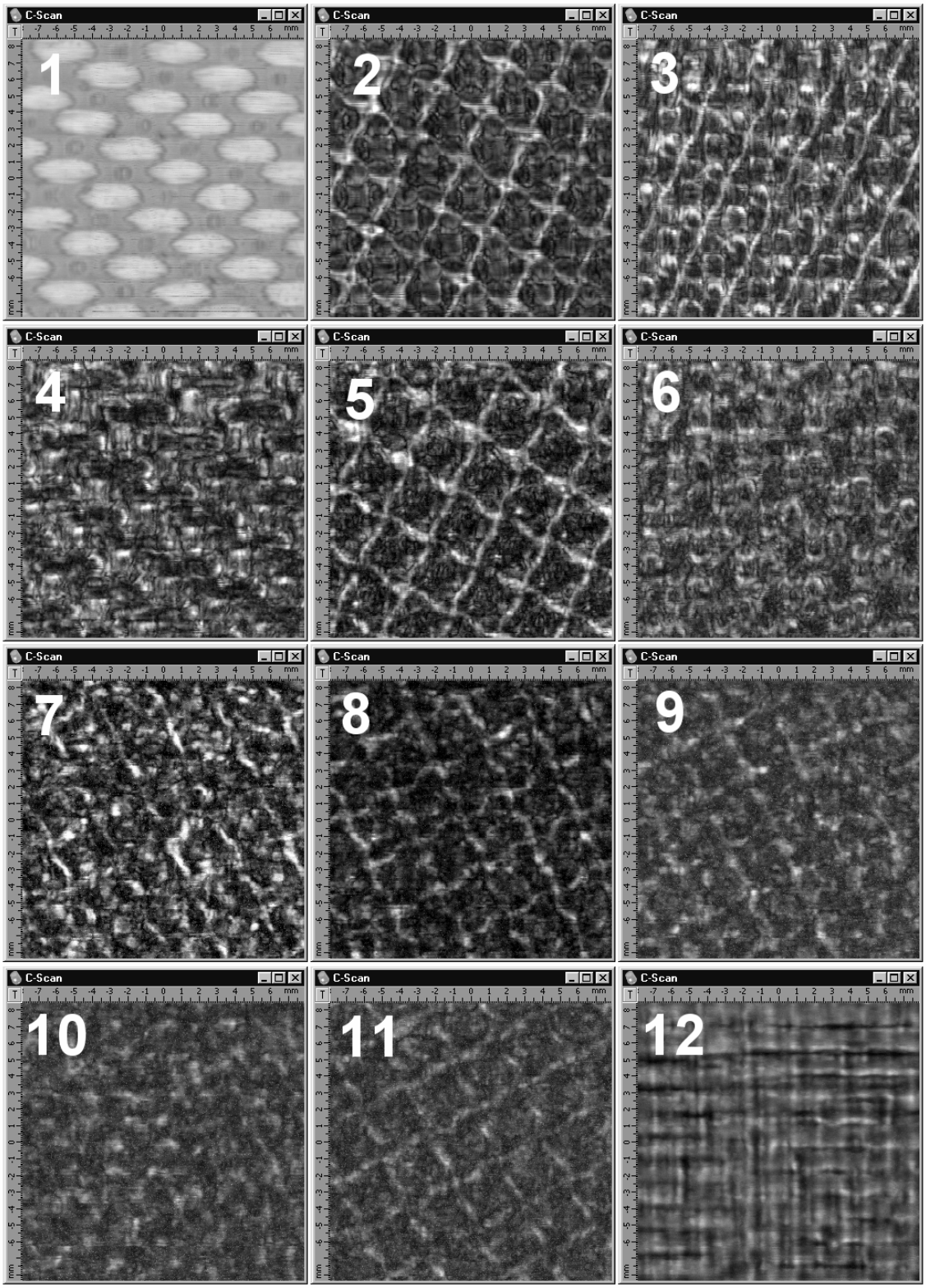

Fig. XIII.A_14: ***C-scan images at different depths, beginning with the upper surface (#1) and ending with an image of the bottom (#12), for cross-ply fabric carbon fibers in Poly Phenylene Sulfide (PPS).***

The main contrast originates from the inhomogeneous distribution of matrix material because of the non-flat topology of fiber bundle weaving. Bending of weft and warp bundles within an individual fabric ply results in the formation of thick interspaces filled by polymer binding, i.e. resin pockets. Enlarged thickness of the pockets provides an elevated level of ultrasonic reflection from these areas. So, acoustic images of woven composites reflect a regular distribution of resin pockets that are different at various depths inside the specimen.
Note that the symmetry is visible for the different layers and that it is easy to distinguish between the unidirectional system and the cross-ply system. Because of the relatively small difference between acoustic impedance of the resin and the fibers, a very deep penetration depth is realized with preservation of contrast during imaging. Therefore, high quality images are obtainable up to the lower layers.

unidirectional fabric glass fibers in epoxy

The characteristics of the sample are given earlier. Fig. XIII.A_15 is composed of three C-scans. The upper part corresponds to the upper interface, the middle corresponds to a position within the bulk, whereas the lower part corresponds to an image of the lower interface. It is clear that the images miss contrast. The reason is the strong difference in acoustical impedance between glass fibers and the resin. This results in fairly high reflectivity on the upper fibers and a lack of energy penetrating deep into the specimen. Therefore, even though the lower surface is possibly visualized, the technique does not work as excellent for this kind of material as in the case of carbon fibers in PPS.

To demonstrate potentialities of high-resolution acoustic microscopy, optical and acoustic images of the fine structure of a carbon fiber bundle crossover in zones of interweaving of bundles are given in Fig. XIII.A_16.
The acoustic images have been made with the wide-aperture acoustic microscope *Elsam* (*Leica*, Germany; frequency range of 100 MHz – 2000 MHz); for operation frequencies of 100 and 400 MHz. As it is seen from the pictures, acoustic images make it possible to see details of the bundle intersection.

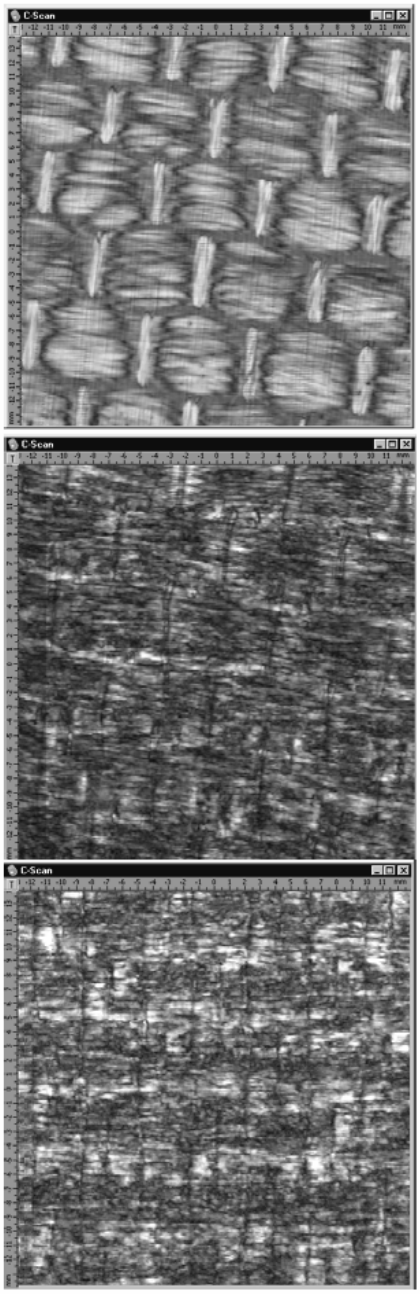

Fig. XIII.A_15: ***C-scan images at different depths for unidirectional fabric glass fibers in epoxy. The upper part corresponds to the upper interface, the middle corresponds to a position within the bulk, whereas the lower part corresponds to an image of the lower interface.***

Additional experiments for fabric carbon fibers in Poly Phenylene Sulfide

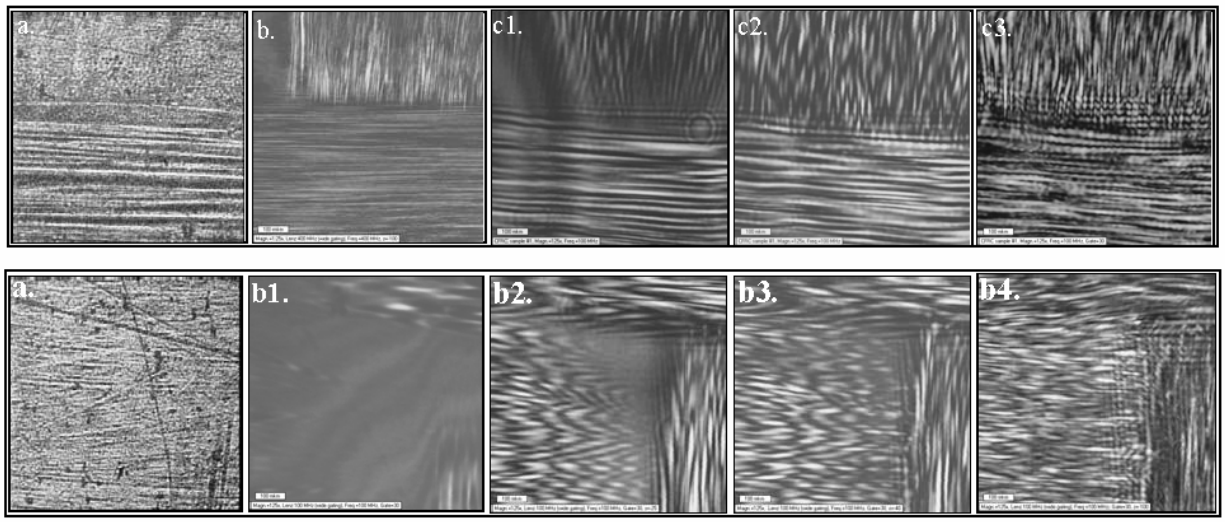

Fig. XIII.A_16: ***Fine structure of a bundle crossover: upper row – crossing two bundles (a.-optical image; b.-high-resolution acoustic image of the surface structure, f = 400 MHz; c1.–c3. - acoustic images of the surface and the subsurface microstructure of a bundle interweaving at increasing depth inside the subsurface zone), f = 100 MHz; lower row – crossing of three bundles (a.-optical image; b1.–b4. - acoustic images at an increasing depth in the subsurface zone, f = 100 MHz).***

CONCLUSIONS AND PROSPECTS

A short overview of the existing literature on this subject, has been given. We have described what possible causes of internal reflections are possible. The main physical properties of focused beams are given, together with a short description of the aberration effect. The experimental equipment is described, as well as the data acquisition method for A-scans, B-scans and C-scans. Results are shown for different samples. We have shown that the method is much more fruitful for CFRC laminates than for GFRC laminates. For reasons of completeness, we have also shown the capability of classical acoustic microscopy in a pulse-echo mode, to image the surface structure of fiber reinforced composites.

In the future, the technique of micro-acoustic bulk imaging will be further developed. Additional studies on laminates containing fatigue damage and impact damage, are also planned.

REFERENCES

[1] Joris Degrieck, Nico F. Declercq, Oswald Leroy, "Ultrasonic Polar Scans as a possible means of nondestructive testing and characterization of composite plates", Insight - The Journal of The British Institute of Non-Destructive Testing, 45(3), 196-201, 2003.
[2] Calvin F. Quate, “Acoustic microscopy”, Physics Today, August, 34-42, 1985
[3] Joie Jones, “A short history of acoustical microscopy”, J. Acoust. Soc. Am. 112(5), 2208-2208, 2002
[4] Andrew Biggs, Acoustic Microscopy, Clarendon Press, Oxford, 1992
[5] S. Boseck, “Akustische Microskopie”, Phys. Bl. 49(6), 497-502, 1993 (In German)
[6] Briggs, A. *Acoustic Microscopy Clarendon Press*, Oxford, 1992.
[7] Briggs, A. *Advances in Acoustic Microscopy*, Plenum Press, New York, 1995.

[8] Briggs, A, and W. Arnold, *Advances in Acoustic Microscopy*, Plenum Press, New York, 1996.
[9] Lemons,R. A. and C. F. Quate. Acoustic Microscopy, in *Physical Acoustics*, Mason, W. P. and Thurston, R. N. Academic Press., London, 1979, pp. 1-92.
[10] Sokolov, S. , The ultrasonic microscope, *Doklady Akademia Nauk SSSR* (in Russian) 64, 333-336, 1949.
[11] Paul A. Reinholdtsen, Butrus T. Khuri-Yakub, "Image Procesing for a Scanning Acoustic Microscope That Measures Amplitude and Phase", IEEE Trans. on UFFC 38(2), 141-147, 1991
[12] Manika Prasad, " Mapping impedance microstructures in rocks with acoustic microscopy", The Leading Edge , Februari 2001, 172-179, 2001
[13] J. Kushibiki, H. Ishiji, T. Kobayashi, N. Chubachi, I. Sahashi, T. Sasamata, "Characterization of 36^0YX-$LiTaO_3$ Wafers by Line-Focus-beam Acoustic Microscopy", IEEE Trans. on UFFC 42(1), 83-90, 1995
[14] Lugen Wang, "The contrast mechanism of bond defects with the scanning acoustic microscope", J. Acoust. Soc. Am. 104(5), 2750-2755, 1998
[15] Pavel Zinin, Odile Lefeuvre, Andrew Briggs, Brent D. Zeller, Peter Cawley, Anthony Kinloch, Xiaorong Zhou, George Thompson, "Determination of density and elastic constants of a thin phosphoric acid-anodized oxide film by acoustic microscopy", J. Acoust. Soc. Am. 106(5), 2560-2567, 1999
[16] Y.-C. Lee, J. D. Achenbach, M. J. Nystrom, S. R. Gilbert, B. A. Block, B. W. Wessels, "Line-Focus Acoustic Microscopy Measurements of Nb_2O_5/MgO and $BaTiO_3$/$LaAlO_3$ Thin-Film/substrate Configurations", IEEE Trans. on UFFC 42(3), 376-380, 1995
[17] Zhiqi Guo, J. D. Achenbach, Anita Madan, Keith Martin, M. E. Graham, "Integration of modeling and acoustic microscopy measurements for thin films", J. Acoust. Soc. Am. 107(5), 2462-2471, 2000
[18] Andrew Briggs, "Acoustic microscopy – a summary", Rep. Prog. Phys. 55, 851-909, 1992
[19] G. Every, K. Hillmann, K. U. Wurz, H. Hasselmann, W. Grill, "Phase singularities in scanning acoustical microscopy", J. Acoust. Soc. Am. 98(6), 3375-3382, 1995
[20] Andrew Madeyski, Lawrence W. Kessler, "Initial Experiments in the Application of Acoustic Microscopy to the Characterization of Steel and to the Study of Fracture Phenomena", Trans. on Sonics and Ultrasonics, Vol 23(5), 363-357, 1976
[21] E. Forgber, G. Heygster, S. Boseck, "Modeling the imaging properties of SAM", Optik 87(4), 170-178, 1991
[22] H. L. Bertoni, "Ray-Optical Evaluation of V(z) in the Reflection Acoustic Microscope", Trans. Son. Ultras. 31(2), 105-116, 1984
[23] Isao Ishikawa, Kageyoshi Katakura, Yukio Ogura, "Full-circular Surface Acoustic Wave Escitation for High Resolution Acoustic Microscopy using Spherical lens and Time gate technology", IEEE Trans on UFFC 46(1), 41-46, 1999
[24] Jun-ichi Kushibiki, Mototaka Arakawa, "A Method for Calibrating the Line-Focus-Beam Acoustic Microscopy System", IEEE Trans. on UFFC 45(2), 421-430, 1998
[25] Kai Hong Chan, Henry L. Bertoni, "Ray Representation of Longitudinal Lateral Waves in Acoustic Microscopy", IEEE Trans. on UFFC 38(1), 27-34, 1991
[26] Klaus Kosbi, Wieland Weise, Ulla Scheer, Uwe Laun, Siegfried Boseck, "Measurement of surface wave velocity and anisotropy at edges using point-focus acoustic microscopy", P. Tortoli, L. Masotti (eds.), *Acoustical Imaging, Vol. 22*, Plenum press, new York, 1995, pp. 677-682
[27] M. K. Kuo, G. Y. Liu, H. K. Chung, "Wavenumber formulation for V(z) curves of line-focus acoustic microscopy", Ultrasonics 34, 327-329, 1996
[28] M. K. Kuo, G. Y. Liu, H. K. Chung, "Wavenumber formulation for V(z) curves of line-focus acoustic microscopy", Ultrasonics 34, 327-329, 1996
[29] P. B. Nagy, L. Adler, "Guided interface waves and their roles in acoustic microscopy", Colloque de Physique, Colloque C2(51), 1273-1276, 1990
[30] S. Hirsekorn, W. Arnold, "High-resolution materials characterization by conventional and near-field acoustic microscopy", Ultrasonics 36, 491-498, 1998
[31] T. Ghosh, K. I. Maslov, T. Kundu, "A new method for measuring surface acoustic wave speeds by acoustic microscopes and its application in characterizing laterally inhomogeneous materials", Ultrasonics 35, 357-366, 1997
[32] T. Kindu, C. S. Jørgensen, "Measuring elastic properties of bones and silicon from V(z) curve generated by multiply reflected signals", ultrasonics 39, 515-524, 2002
[33] Yuu Ono, Jun-ichi Kushibiki, "Experimental Study of Construction Mechanism of V(z) Curves Obtained by Line-Focus-Beam Acoustic Microscopy", IEEE Trans. on UFFC 47(4), 1042-1050, 2000

[34] V. Eyraud, M.-H. Nadal, C. Gondard, "Texture measurement of shaped material by impulse acoustic microscopy", Ultrasonics 38, 438-442, 2000
[35] Claudio Pecorari, G. Andrew D. Briggs, "Acoustic Microscopy and Dispersion of Leaky Rayleigh Waves on Randomly Rough Surfaces: A Theoretical Study", IEEE Trans. on UFFC 43(3), 428-433, 1996
[36] Matthew Clark, Steve D. Sharples, Michael G. Somekh, "Fast, All-Optical Rayleigh Wave Microscope: Imaging on Isotropic and Anisotropic Materials", IEEE Trans on UFFC 47(1), 65-74, 2000
[37] Shamachary Sathish, Richard W. Martin, "Quantitative Imaging of Rayleigh Wave Velocity with a Scanning Acoustic Microscope", IEEE Trans. on UFFC 49(5), 550-557, 2002
[38] J. Ndop, T. J. Kim, W. Grill, "Spatially resolved characterization of materials by scanning nonfocal surface focused transmission acoustic microscopy with phase contrast", Ultrasonics 36, 461-466, 1998
[39] M. Deschamps, A. Som, "Acoustic signature of dispersive and orthotropic composites using a focused microscope", J. Acoust. Soc. Am. 93(3), 1374-1384, 1993
[40] Motohiro Okade, Koichiro Kawashima, "Local stress measurement on polycrystalline aluminum by an acoustic microscope", Ultrasonics 36, 933-939, 1998
[41] Noritaka Nakaso, Yusuke Tsukahara, Noriyoshi Chubachi, "Evaluation of Spatial Resolution of Spherical-Planar-Pair Lenses for Elasticity Measurement with Microscopic Resolution", IEEE Trans. on UFFC 43(3), 422-427, 1996
[42] Shamachary Sathish, Richard W. Martin, Thomas J. Moran, "Local surface skimming longitudinal wave velocity and residual stress mapping", J. Acoust. Soc. Am. 115(1), 165-171, 2004
[43] Wei Li, Jan D. Achenbach, "Determination of Elastic Constants by Time-Resolved Line-Focus Acoustic Microscopy", IEEE Trans. on UFFC 44(3), 681-687, 1997
[44] Yung-Chun Lee, Jin O. Kim, Jan. D. Achenbach, "Acoustic Microscopy Measurement of Elastic Constants and Mass Density", IEEE Trans. on UFFC 42(2), 253-264, 1995
[45] Z. Yu, S. Boseck, "Inversion of V(z) data in the scanning acoustic microscope to determine material properties of a layered solid", Optik 88(2), 73-79, 1991
[46] Drescherkrasicka, E. and J. R. Willis. Mapping stress with ultrasound. *Nature* 384(6604): 52-55, 1996.
[47] T. Berruti, M. M. Gola, G. A. D. Briggs, "Acoustoelastic measurements on aluminum alloy by means of a contact and a non-contact (LFB acoustic microscopy) technique", J. Acoust. Soc. Am. 103(3), 1370-1376, 1998
[48] Roman G. Maev, Vadim M. Levin, "Principles of Local Sound Velocity and Attenuation Measurements Using Transmission Acoustic Microscope", IEEE Trans. on UFFC 44(6), 1224-1231, 1997
[49] Lugen Wang, Stanislav I. Rokhlin, "Time-Resolved Line Focus Acoustic Microscopy of Layered Anisotropic Media: Application to Composites", IEEE Trans. on UFFC 49(9), 1231-1244, 2002
[50] Lugen Wang, "Determination of elastic constants of composites by time-resolved acoustic microscopy", Ultrasonics 37, 283-289, 1999
[51] Sofia Berezina, Vladimir Blank, Vadim levin, Vyacheslav Prokhorov, "Observation of ultrasound velocity gradient in fullerene ceramics by acoustic microscopy", Ultrasonics 38, 327-330, 2000
[52] R. S. Gilmore, "Industrial ultrasonic imaging and microscopy", J. Phys. D: Appl. Phys. 29, 1389-1417, 1996
[53] W. Ngwa, R. Wannemacher, W. Grill, "Phase-sensitive acoustic microscopy of polymer thin films", Ultrasonics 42, 983-987, 2004
[54] J. B. Liu, J. N. Peterson, F. Forsberg, M. D. Jaeger, D. B. Kynor, R. J. Kline-Schoder, "Acoustic microscopy system: design and preliminary results", Ultrasonics 42, 337-341, 2004
[55] J. Ndop, T. J. Kim, W. Grill, M. Pluta, "Synthetic aperture imaging by scanning acoustic microscopy with vector contrast", Ultrasonics 38, 166-170, 2000
[56] K. I. Maslov, T. Kundu, O. I. Lobkis, "Acoustic microscopy for spherical inclusion characterization", J. Acoust. Soc. Am. 100(1), 80-85, 1996
[57] Lobkis, O. I., T, Kundu, and P. V. Zinin. A theoretical analysis of acoustic microscopy of spherical cavities, *Wave Motion* **21**(2), 183-201, 1995.
[58] P. Zinin, W. Weise, O. Lobkis, and S. Boseck, The theory of three-dimensional imaging of strong scatterers in scanning acoustic microscopy, *Wave Motion*, **25**(3), 213-236, 1997.
[59] Daesik Ko, A. Meyyappan, "Scanning Tomographic Acoustic Microscopy Using Shear Waves", IEEE Trans. on UFFC 44(2), 425-430, 1997
[60] S. Davis Kent, Hua Lee, "Quantization Bit Rate Reduction in Scanning Tomographic Acoustic Microscopy", IEEE Trans. on UFFC 42(3), 464-477, 1995

[61] Zse-Chering Lin, Hua Lee, Glen Wade, “Scanning Tomographic Acoustic Microscope: A Review”, IEEE Trans. on Sonics and Ultrasonics 32(2), 168-180, 1985
[62] Nico F. Declercq, Joris Degrieck, Oswald Leroy, " On the influence of fatigue on ultrasonic polar scans of fiber reinforced composites", Ultrasonics 42, 173-177, 2004
[63] L. M. Brekhovskikh, O. A. Godin, *Acoustics of Layered Media I*, Springer Berlin, 1990

Chapter XIV Exotic Topics

According to Webster's dictionary, the word 'exotic' means 'attractively strange'. I believe that this is the exact reason why the subjects in this chapter caught my attention.

In the field of ultrasonics, the Schoch effect is very well known. The effect consists of the splitting of a bounded beam, reflected from a solid plate. When performing Schlieren experiments, suddenly I noticed that one of my glass samples resulted in a strange counterpart of the Schoch effect, never described before. I saw a reflected beam, split in three parts instead of two. Furthermore, the position of the three parts was such that one was forward displaced, another one was backward displaced and the third one was situated in-between. This remarkable phenomenon is now well known as the double sided bounded beam displacement. It is described in section XIV.A of this chapter

XIV.A The double sided ultrasonic beam displacement

It is a well established idea in optics as well as in ultrasonics that a bounded Gaussian beam, when reflected from an interface, can be displaced in the forward or in the backward direction, depending on the propagation direction of leaky waves that are generated by the incident beam. Such a displacement is often accompanied by the so called Schoch effect characterized by a null strip in between a specular and a nonspecular reflected beam, and a trailing field that is much further displaced. The current paper shows experimentally and numerically that a simultaneous forward and backward displacement is possible accompanied by two null strips and being only the result of forward propagating Lamb waves.
The contents of this section have been published as: Nico F. Declercq, Joris Degrieck, Oswald Leroy, "The Double Sided Ultrasonic Beam Displacement", Appl. Phys. Let. 85(18), 4234-4236, 2004 (Imp. Fact. 4.207; SCI-index, Physics-Applied, rank:3/76)

In optics, the Goos-Hänchen theory predicts a lateral displacement of a light beam that is internally reflected from a dielectric interface [1]. This phenomenon appears when incident from an optically denser medium at an angle close to the critical angle, resulting in the transfer of a portion of the energy into the rarer medium by means of excitation of an electromagnetic field that travels along the interfae. This energy leaks back into the denser medium and becomes part of the reflected beam exhibiting a lateral displacement that appears as a forward beam shift. This was studied by Tamir and Bertoni [2]. The early experiments of Schoch [3-5] applying the acoustic analog of the Goos-Hänchen effect for an acoustic beam reflected from a liquid-solid interface showed a forward lateral displacement of the reflected ultrasonic beam. It has been shown before [6-8] that a backward displacement of an ultrasonic beam is also possible when backward propagating surface waves are stimulated on periodically rough surfaces. The expression ‘null strip’ was mentioned in Neubauer and Dragonet [9]. The effect consisting of both a forward and a backward displacement on a smooth interface, accompanied by two null strips, has never been observed and has certainly never been published before. The experiments in this paper are performed by means of a Schlieren experimental setup [10] and the liquid/solid interfaces are smooth.

There is an unwritten law that whenever leaky Rayleigh waves or leaky Lamb waves are generated by means of an incident bounded beam, the Schoch effect occurs and vice versa. As an example, a typical Schoch effect is shown in Fig. XIV.A_1, where sound is incident on a thin aluminum plate under a Lamb wave angle. It is seen that there is no backward displacement of the reflected beam. What is visible, is a forward displaced (nonspecular) sound lobe separated from the main (specular) reflected sound beam by a null strip. This is because the nonspecular lobe is out of phase with the specular sound beam. The null strip is the result of phase canceling. A trailing field at larger distances is also visible.

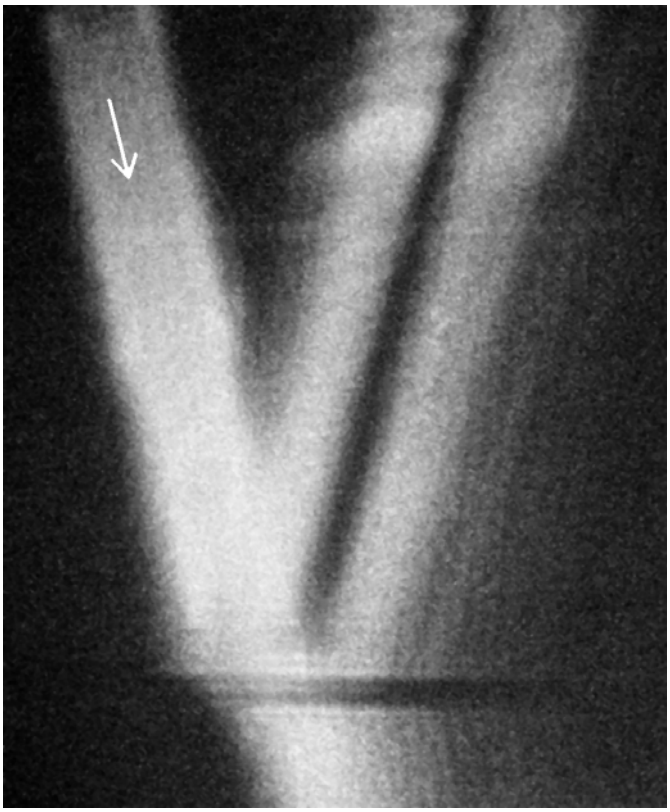

Fig. XIV.A_1: ***The typical Schoch effect of a bounded ultrasonic beam on a thin aluminum plate. Only a forward displacement is visible accompanied by a trailing field.***

We have performed experiments on glass plates. The longitudinal sound velocity in glass is 5660 m/s, whereas the transversal sound velocity is 3520 m/s. The density is 2500 kg/m^3. Water is characterized by a longitudinal sound velocity of 1480 m/s and a density of 1000 kg/m^3. The well expected Schoch phenomenon was visible at certain angles depending on the frequency that was used and depending on the thickness of the plate. Nevertheless, for the combination of a plate thickness of 1.23 mm and a frequency of 3 MHz, a completely unexpected phenomenon appeared. The physical beam width was 1 cm. The result can be seen in Fig. XIV.A_2.
The glass plate is indicated by means of white dashed lines. The white arrow denotes the direction of incidence. There is a forward displaced lobe and also a backward displaced lobe. Both lobes are separated from the specular lobe by means of a null strip. If the left lobe was not backward displaced and was hence the specular lobe, the effect could have been regarded as a very strong trailing field. However it is clear that the first lobe is not a specular lobe but is indeed backward displaced. In order to make sure that the effect was not caused by edge effects of the plate that was used, we have studied different positions of incidence and we have also studied the effect of smooth edges and rough edges. No difference was visible except when incidence occurred so close to the edge that the forward displaced sound beam ‘touched’ or even surpassed the edge.

Simulations were performed by means of a decomposition of the incident bounded beam into plane waves in accordance with the Fourier transform. Continuity of normal stress and normal particle displacement was considered [11] along the water-glass interfaces of the plate. The reflected profile was studied along the interface water/upper side of the plate.

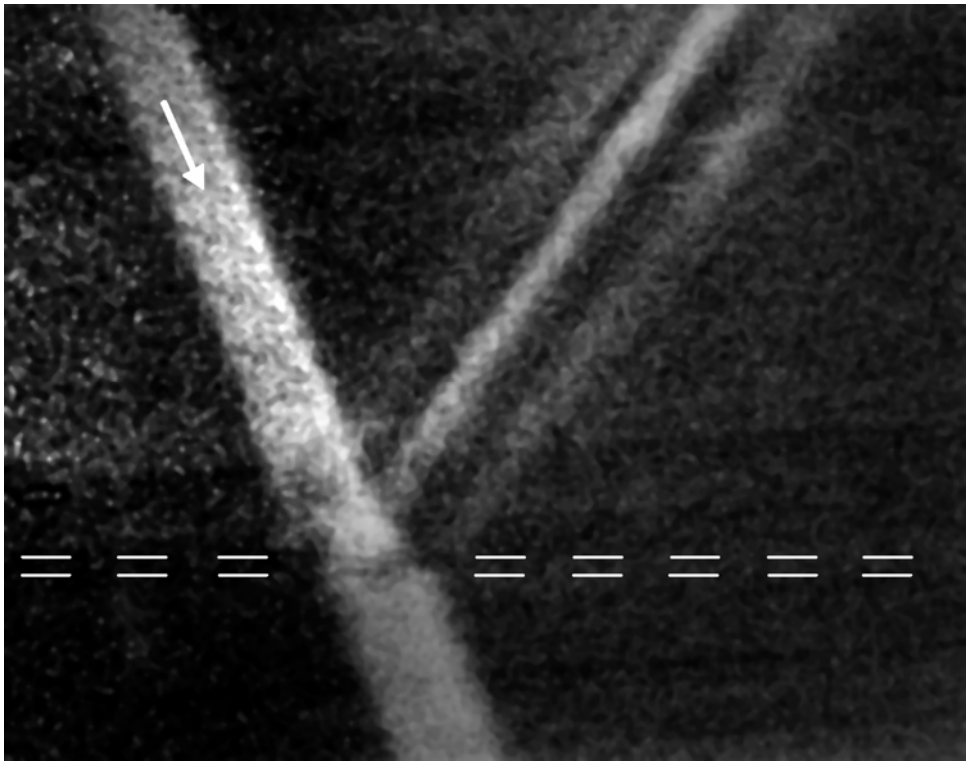

Fig. XIV.A_2: ***The double sided beam deformation. A backward and a forward displaced beam are visible together with the central specular reflected beam.***

The same parameters were used as in the experiments. The reflected beam profile as a function of the angle of incidence can be seen in Fig. XIV.A_3. It is seen that at 18.29^0 and at 13.91^0 there is a regular Schoch effect. Nevertheless, at 28.35^0 there are two null zones separating three reflected beams. This is the double sided beam deformation that corresponds with Fig. XIV.A_2.

The mentioned angles correspond with the dispersion curves of Fig. XIV.A_4, denoting the pole position of the reflection coefficient for pure harmonic plane waves. It is seen that the double beam deformation effect occurs at the angle that stimulates the A_0 Lamb mode. The Schoch effect is not visible for the S_0 stimulating angle. The calculated profile in amplitude and in phase corresponding to the angle of incidence of 28.35^0 is shown in Fig. XIV.A_5, where it is seen hat the left and the right lobe are out of phase with the central specular reflected lobe. A backward propagating sound field could be characterized by a negative group velocity. However, according to the dispersion curves in Fig. XIV.A_4 and according to knowledge obtained from ref 12, this is never the case and hence there is no backward propagating sound field present. Therefore the effect is the result of a (complicated) interaction between the amplitudes and phases of the plane waves that are the building blocks of the incident bounded beam and the generated Lamb waves. As a conclusion, it is shown experimentally and numerically that double beam deformations are possible on smooth plates swamped in water. It is also shown that this effect, in the example studied here, is not caused by backward propagating sound in the plate.

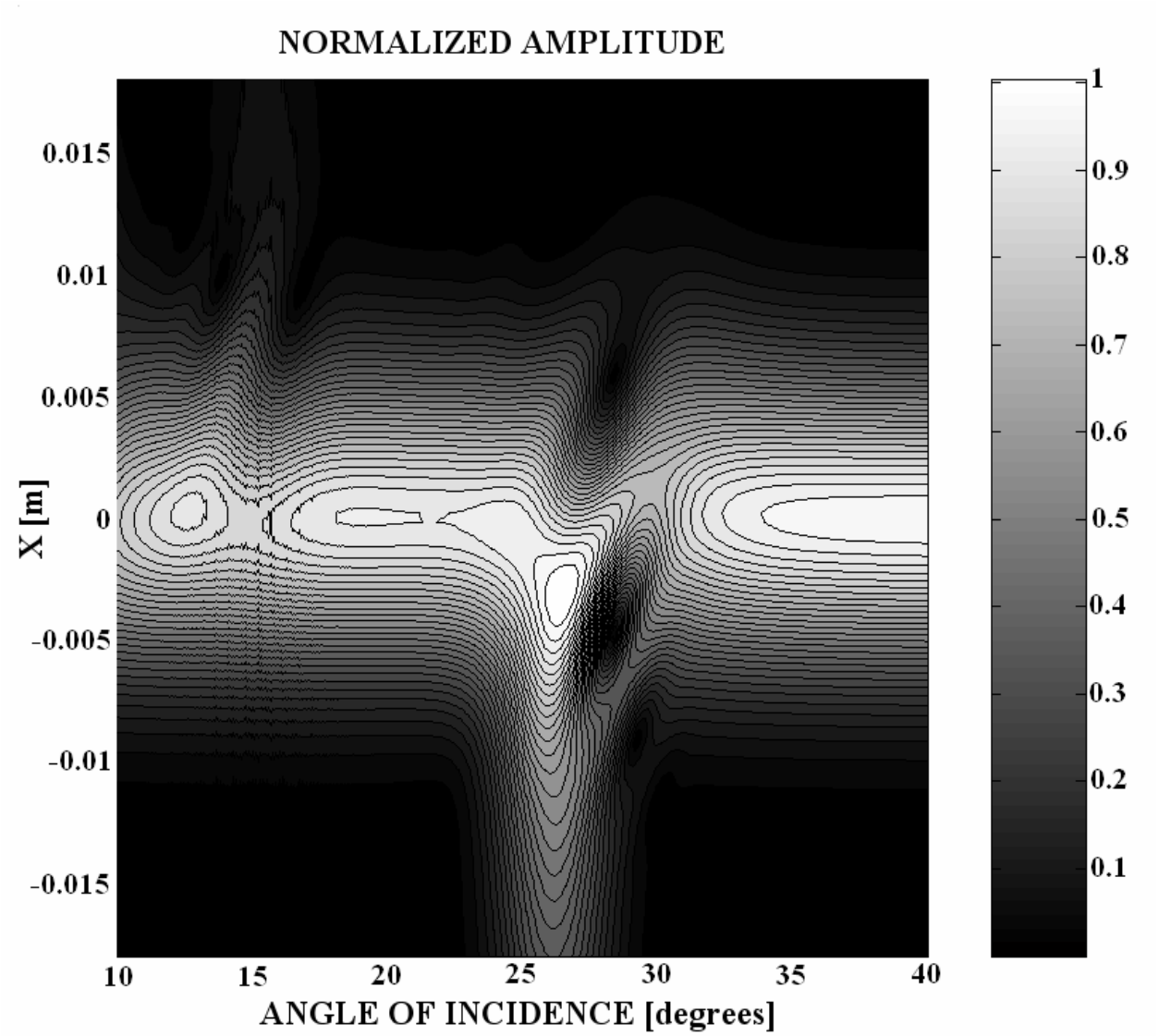

Fig. XIV.A_3: ***Simulation (filled contour plot) of the reflected beam profile as a function of the angle of incidence. Negative positions correspond with backward positions. At 28.35^0 the situation of Fig.*** **XIV.A_*2 can be seen.***

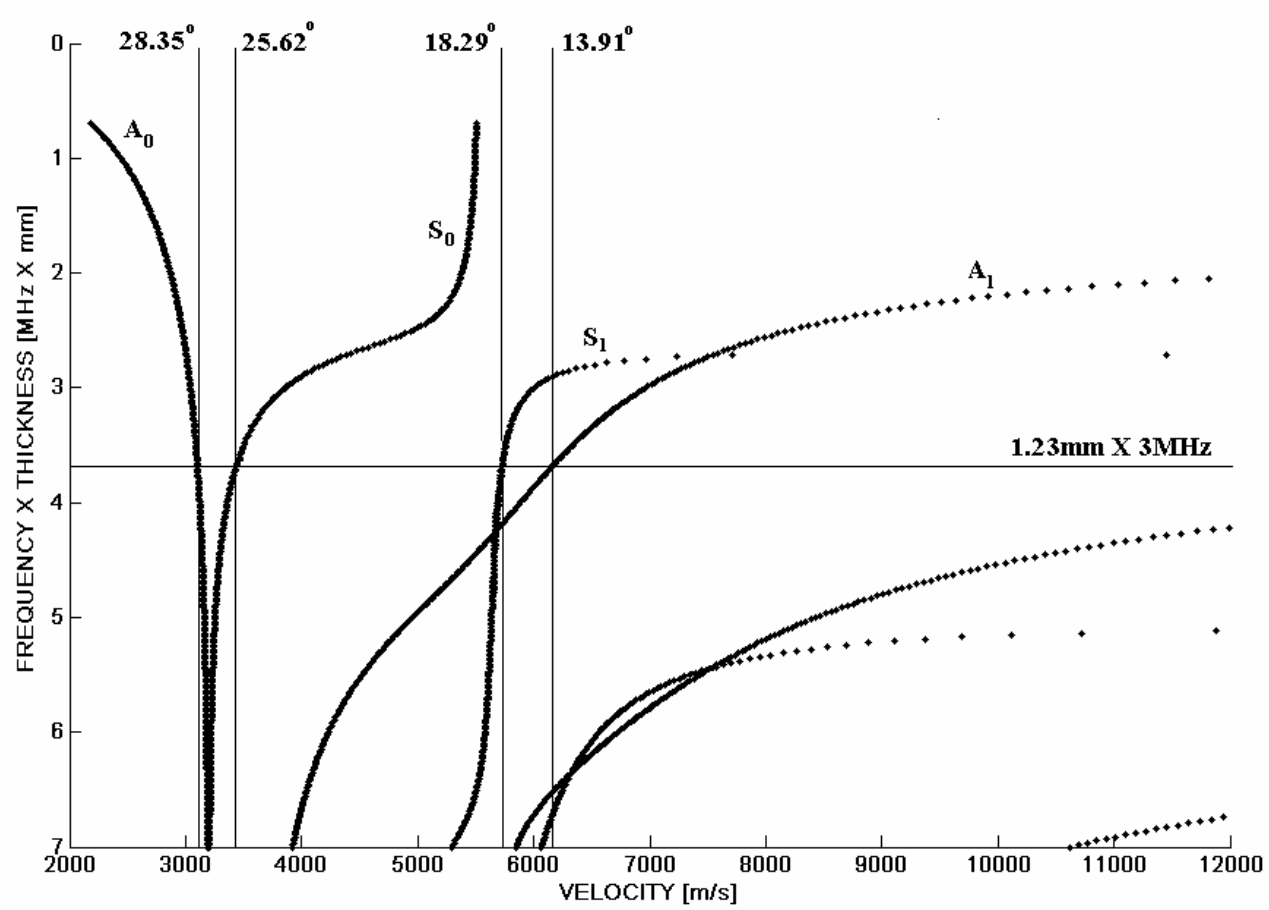

Fig. XIV.A_4: ***The dispersion curves of a glass plate. The horizontal line corresponds to the experiments reported here. The vertical lines correspond to the angles of incidence of 28.38^0, 25.62^0, 18.29^0 and 13.91^0***

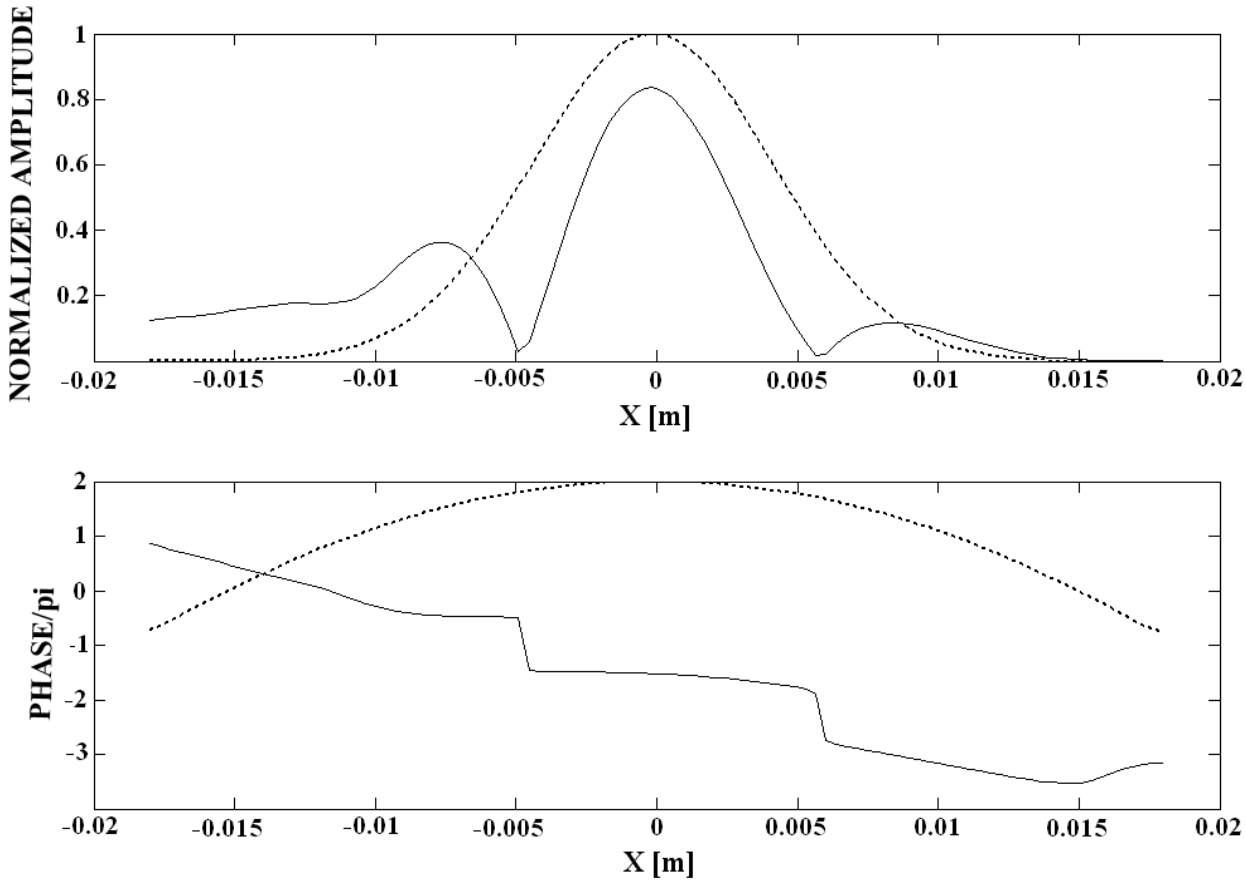

Fig. XIV.A_5: ***Simulation of Fig.* XIV.A_*2, i.e. incidence at 28.35^0. Dotted curve: incident beam profile, solid curve: reflected beam profile. Note that the forward and the backward displaced beams are out of phase with the specular central lobe.***

REFERENCES

[1] Von F. Goos and H. Hänchen, Annalen der Physik., vol. **6**. No. 1, 333-64 (1947)

[2] T. Tamir and H. L. Bertoni, J. Acoust. Soc. Am. **61**, 1397-1413 (1971)

[3] A. Schoch, Nuovo Cimento (Suppl.) **7**, (9), 302 (1950)

[4] Schoch, "Der Schalldurchgang durch plate", Acustica 2, 1-17, 1952

[5] Schoch, "Seitliche Versetzung eines total-reflektierten Strahls bei Ultraschallwellen", Acustica 2, 18-19, 1952

[6] M. A. Breazeale, Michael Torbett, "Backward displacement of waves reflected from an interface having superimposed periodicity", Appl. Phys. Let., 29(8), 456-458, 1976.

[7] Nico F. Declercq, Joris Degrieck, Rudy Briers, Oswald Leroy, "A Theoretical elucidation for the experimentally observed backward displacement of waves reflected from an interface having superimposed periodicity", J. Acoust. Soc. Am. 112(5), 2414, 2002

[8] Nico F. Declercq, Joris Degrieck, Rudy Briers, Oswald Leroy, "Theoretical verification of the backward displacement of waves reflected from an interface having superimposed periodicity", Appl. Phys. Let. 82(15), 2533-2534, 2003

[9] Neubauer W. G., Dragonet L. R., "Measurement of Rayleigh phase velocity and estimates of shear speed by Schlieren visualization", J. Appl. Phys. 45(2), 618-622, 1974

[10] M. A. Breazeale, "From monochromatic light diffraction to colour schlieren photography", J. Opt. A: Pure Appl. Opt. 3, S1-S7, 2001

[11] Adnan H. Naefeh, *Wave propagaton in layered anisotropic media with applications to composites*, North-Holland, Amsterdam, 1995

[12] M. F. Werby, H. Überall, “The analysis and interpretation of some special properties of higher order symmetric Lamb waves: The case for plates”, J. Acoust. Soc. Am. 111(6), 2686-2691, 2002.

Chapter XIV Exotic Topics

According to Webster's dictionary, the word 'exotic' means 'attractively strange'. I believe that this is the exact reason why the subjects in this chapter caught my attention.

In the field of ultrasonics, the Schoch effect is very well known. The effect consists of the splitting of a bounded beam, reflected from a solid plate. When performing Schlieren experiments, suddenly I noticed that one of my glass samples resulted in a strange counterpart of the Schoch effect, never described before. I saw a reflected beam, split in three parts instead of two. Furthermore, the position of the three parts was such that one was forward displaced, another one was backward displaced and the third one was situated in-between. This remarkable phenomenon is now well known as the double sided bounded beam displacement. It is described in section XIV.A of this chapter

XIV.A The double sided ultrasonic beam displacement

It is a well established idea in optics as well as in ultrasonics that a bounded Gaussian beam, when reflected from an interface, can be displaced in the forward or in the backward direction, depending on the propagation direction of leaky waves that are generated by the incident beam. Such a displacement is often accompanied by the so called Schoch effect characterized by a null strip in between a specular and a nonspecular reflected beam, and a trailing field that is much further displaced. The current paper shows experimentally and numerically that a simultaneous forward and backward displacement is possible accompanied by two null strips and being only the result of forward propagating Lamb waves.
The contents of this section have been published as: Nico F. Declercq, Joris Degrieck, Oswald Leroy, "The Double Sided Ultrasonic Beam Displacement", Appl. Phys. Let. 85(18), 4234-4236, 2004 (Imp. Fact. 4.207; SCI-index, Physics-Applied, rank:3/76)

In optics, the Goos-Hänchen theory predicts a lateral displacement of a light beam that is internally reflected from a dielectric interface [1]. This phenomenon appears when incident from an optically denser medium at an angle close to the critical angle, resulting in the transfer of a portion of the energy into the rarer medium by means of excitation of an electromagnetic field that travels along the interfae. This energy leaks back into the denser medium and becomes part of the reflected beam exhibiting a lateral displacement that appears as a forward beam shift. This was studied by Tamir and Bertoni [2]. The early experiments of Schoch [3-5] applying the acoustic analog of the Goos-Hänchen effect for an acoustic beam reflected from a liquid-solid interface showed a forward lateral displacement of the reflected ultrasonic beam. It has been shown before [6-8] that a backward displacement of an ultrasonic beam is also possible when backward propagating surface waves are stimulated on periodically rough surfaces. The expression ‘null strip’ was mentioned in Neubauer and Dragonet [9]. The effect consisting of both a forward and a backward displacement on a smooth interface, accompanied by two null strips, has never been observed and has certainly never been published before. The experiments in this paper are performed by means of a Schlieren experimental setup [10] and the liquid/solid interfaces are smooth.

There is an unwritten law that whenever leaky Rayleigh waves or leaky Lamb waves are generated by means of an incident bounded beam, the Schoch effect occurs and vice versa. As an example, a typical Schoch effect is shown in Fig. XIV.A_1, where sound is incident on a thin aluminum plate under a Lamb wave angle. It is seen that there is no backward displacement of the reflected beam. What is visible, is a forward displaced (nonspecular) sound lobe separated from the main (specular) reflected sound beam by a null strip. This is because the nonspecular lobe is out of phase with the specular sound beam. The null strip is the result of phase canceling. A trailing field at larger distances is also visible.

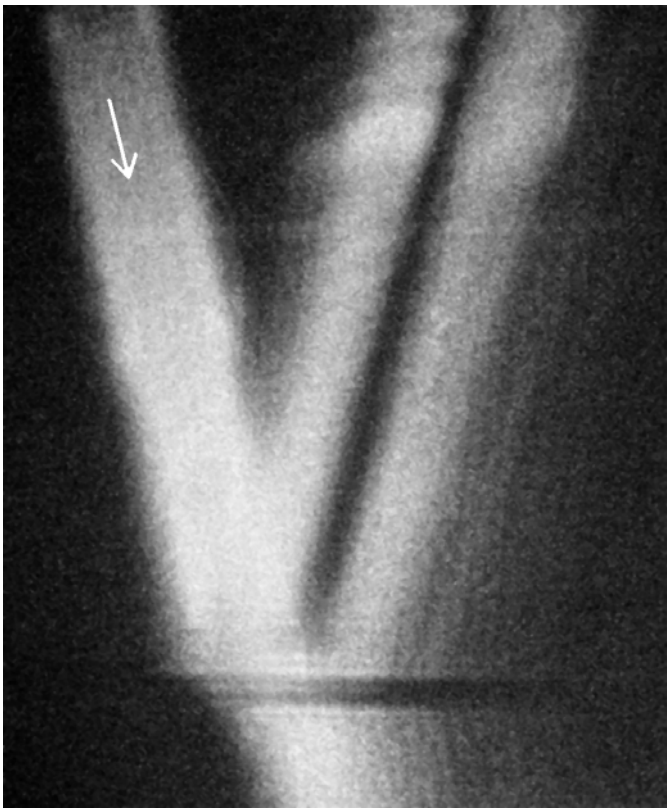

Fig. XIV.A_1: ***The typical Schoch effect of a bounded ultrasonic beam on a thin aluminum plate. Only a forward displacement is visible accompanied by a trailing field.***

We have performed experiments on glass plates. The longitudinal sound velocity in glass is 5660 m/s, whereas the transversal sound velocity is 3520 m/s. The density is 2500 kg/m^3. Water is characterized by a longitudinal sound velocity of 1480 m/s and a density of 1000 kg/m^3. The well expected Schoch phenomenon was visible at certain angles depending on the frequency that was used and depending on the thickness of the plate. Nevertheless, for the combination of a plate thickness of 1.23 mm and a frequency of 3 MHz, a completely unexpected phenomenon appeared. The physical beam width was 1 cm. The result can be seen in Fig. XIV.A_2.
The glass plate is indicated by means of white dashed lines. The white arrow denotes the direction of incidence. There is a forward displaced lobe and also a backward displaced lobe. Both lobes are separated from the specular lobe by means of a null strip. If the left lobe was not backward displaced and was hence the specular lobe, the effect could have been regarded as a very strong trailing field. However it is clear that the first lobe is not a specular lobe but is indeed backward displaced. In order to make sure that the effect was not caused by edge effects of the plate that was used, we have studied different positions of incidence and we have also studied the effect of smooth edges and rough edges. No difference was visible except when incidence occurred so close to the edge that the forward displaced sound beam ‘touched’ or even surpassed the edge.

Simulations were performed by means of a decomposition of the incident bounded beam into plane waves in accordance with the Fourier transform. Continuity of normal stress and normal particle displacement was considered [11] along the water-glass interfaces of the plate. The reflected profile was studied along the interface water/upper side of the plate.

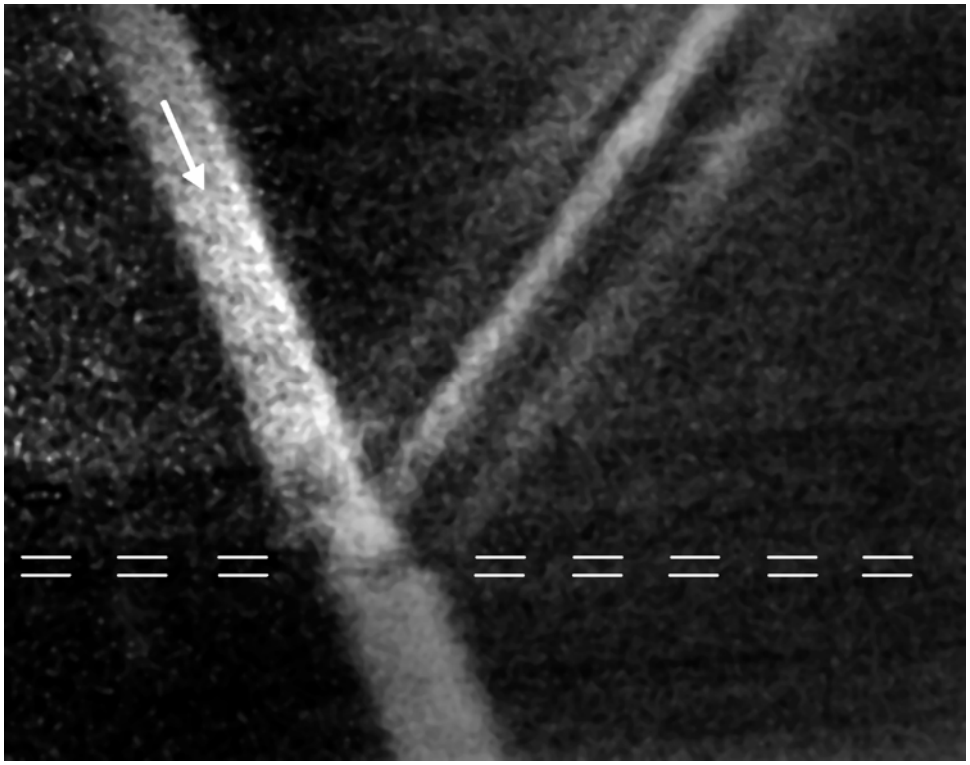

Fig. XIV.A_2: ***The double sided beam deformation. A backward and a forward displaced beam are visible together with the central specular reflected beam.***

The same parameters were used as in the experiments. The reflected beam profile as a function of the angle of incidence can be seen in Fig. XIV.A_3. It is seen that at 18.29^0 and at 13.91^0 there is a regular Schoch effect. Nevertheless, at 28.35^0 there are two null zones separating three reflected beams. This is the double sided beam deformation that corresponds with Fig. XIV.A_2.

The mentioned angles correspond with the dispersion curves of Fig. XIV.A_4, denoting the pole position of the reflection coefficient for pure harmonic plane waves. It is seen that the double beam deformation effect occurs at the angle that stimulates the A_0 Lamb mode. The Schoch effect is not visible for the S_0 stimulating angle. The calculated profile in amplitude and in phase corresponding to the angle of incidence of 28.35^0 is shown in Fig. XIV.A_5, where it is seen hat the left and the right lobe are out of phase with the central specular reflected lobe. A backward propagating sound field could be characterized by a negative group velocity. However, according to the dispersion curves in Fig. XIV.A_4 and according to knowledge obtained from ref 12, this is never the case and hence there is no backward propagating sound field present. Therefore the effect is the result of a (complicated) interaction between the amplitudes and phases of the plane waves that are the building blocks of the incident bounded beam and the generated Lamb waves. As a conclusion, it is shown experimentally and numerically that double beam deformations are possible on smooth plates swamped in water. It is also shown that this effect, in the example studied here, is not caused by backward propagating sound in the plate.

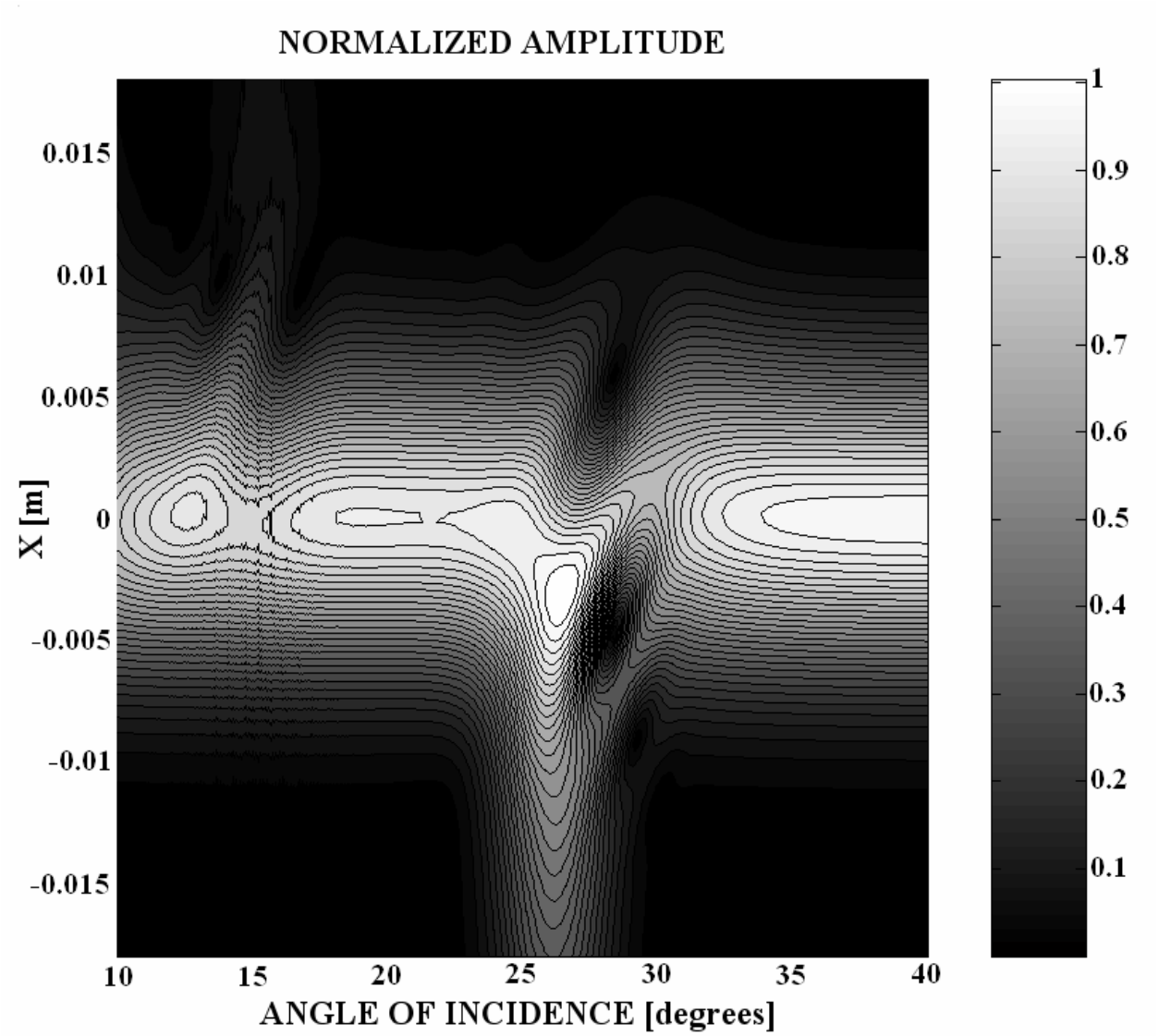

Fig. XIV.A_3: ***Simulation (filled contour plot) of the reflected beam profile as a function of the angle of incidence. Negative positions correspond with backward positions. At 28.35^0 the situation of Fig.*** **XIV.A_*2 can be seen.***

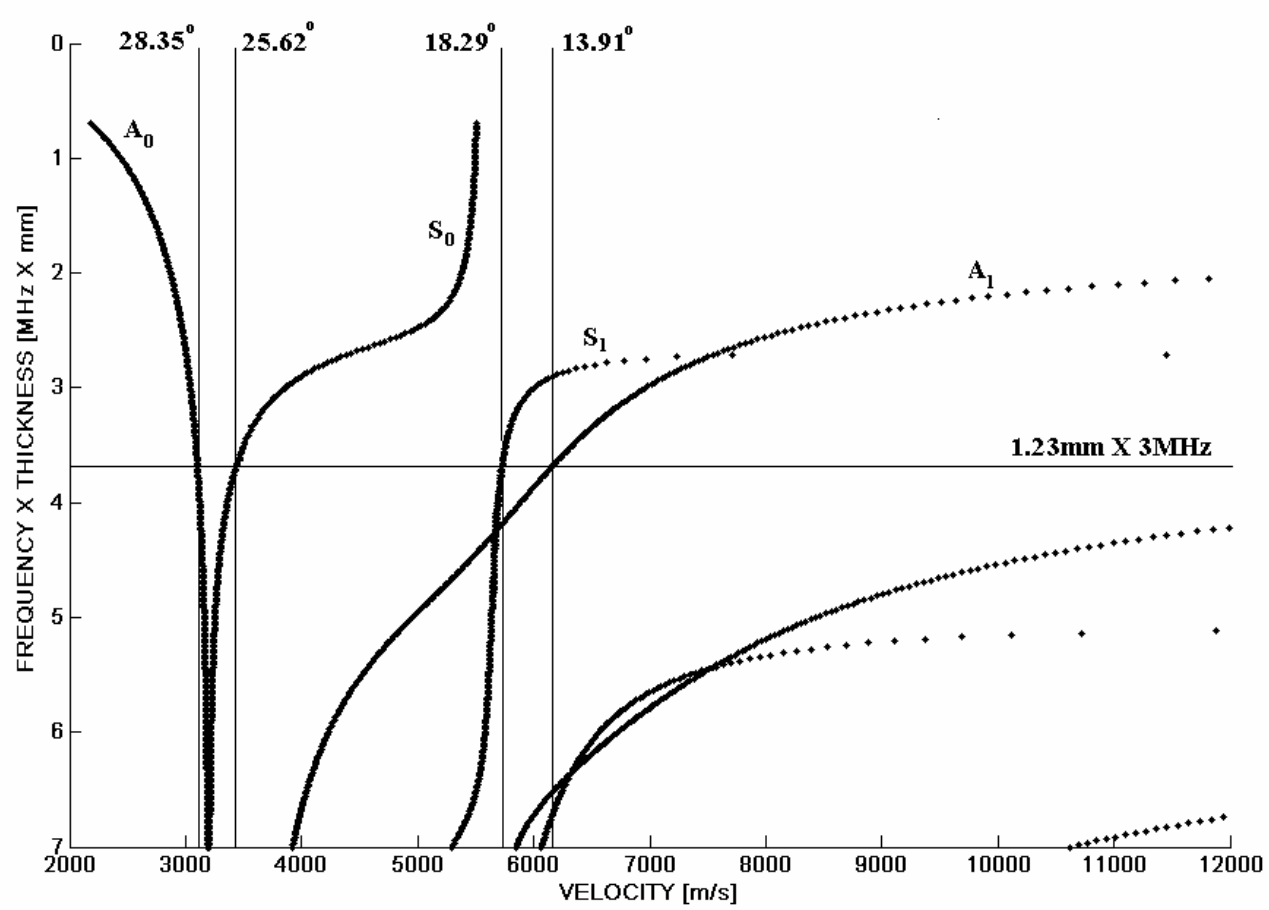

Fig. XIV.A_4: ***The dispersion curves of a glass plate. The horizontal line corresponds to the experiments reported here. The vertical lines correspond to the angles of incidence of 28.38^0, 25.62^0, 18.29^0 and 13.91^0***

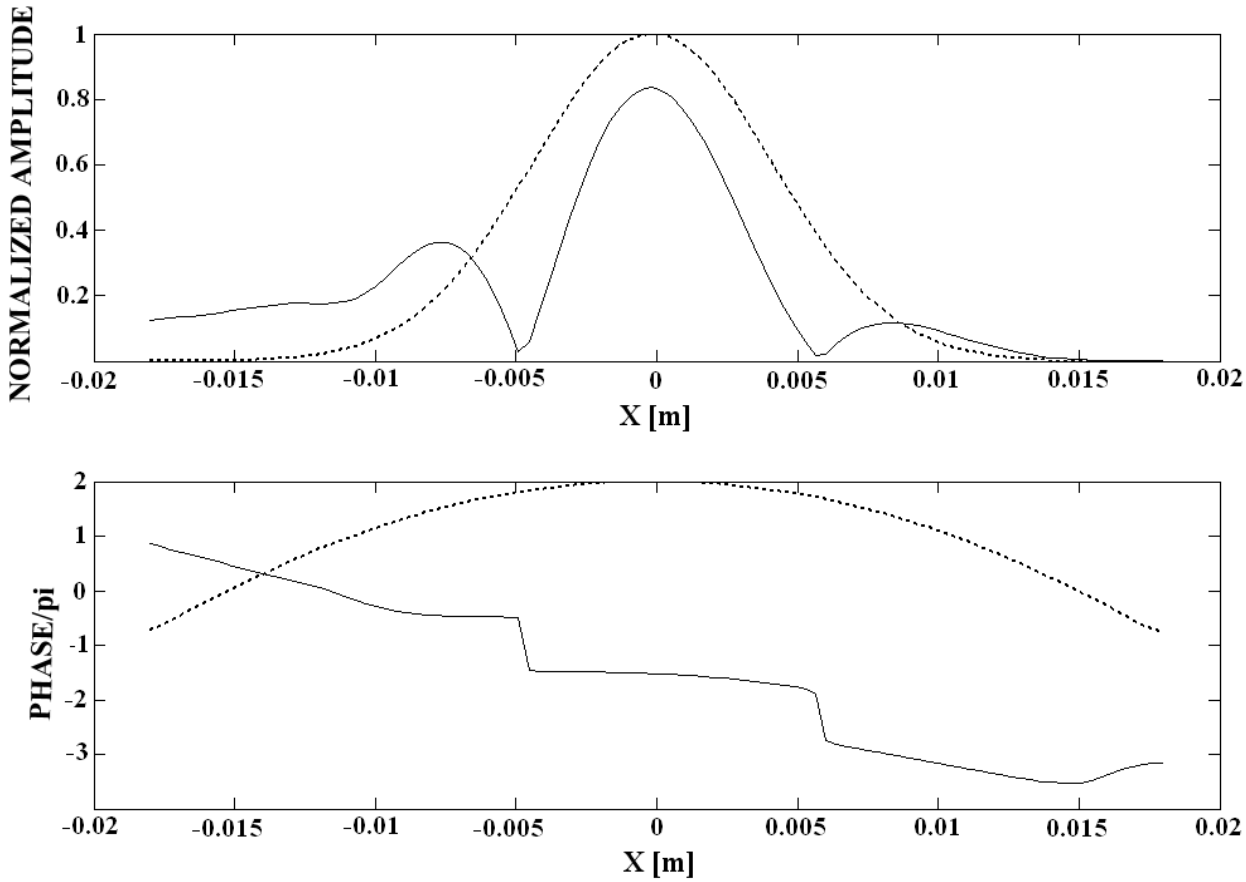

Fig. XIV.A_5: ***Simulation of Fig.* XIV.A_*2, i.e. incidence at 28.35^0. Dotted curve: incident beam profile, solid curve: reflected beam profile. Note that the forward and the backward displaced beams are out of phase with the specular central lobe.***

REFERENCES

[1] Von F. Goos and H. Hänchen, Annalen der Physik., vol. **6**. No. 1, 333-64 (1947)

[2] T. Tamir and H. L. Bertoni, J. Acoust. Soc. Am. **61**, 1397-1413 (1971)

[3] A. Schoch, Nuovo Cimento (Suppl.) **7**, (9), 302 (1950)

[4] Schoch, "Der Schalldurchgang durch plate", Acustica 2, 1-17, 1952

[5] Schoch, "Seitliche Versetzung eines total-reflektierten Strahls bei Ultraschallwellen", Acustica 2, 18-19, 1952

[6] M. A. Breazeale, Michael Torbett, "Backward displacement of waves reflected from an interface having superimposed periodicity", Appl. Phys. Let., 29(8), 456-458, 1976.

[7] Nico F. Declercq, Joris Degrieck, Rudy Briers, Oswald Leroy, "A Theoretical elucidation for the experimentally observed backward displacement of waves reflected from an interface having superimposed periodicity", J. Acoust. Soc. Am. 112(5), 2414, 2002

[8] Nico F. Declercq, Joris Degrieck, Rudy Briers, Oswald Leroy, "Theoretical verification of the backward displacement of waves reflected from an interface having superimposed periodicity", Appl. Phys. Let. 82(15), 2533-2534, 2003

[9] Neubauer W. G., Dragonet L. R., "Measurement of Rayleigh phase velocity and estimates of shear speed by Schlieren visualization", J. Appl. Phys. 45(2), 618-622, 1974

[10] M. A. Breazeale, "From monochromatic light diffraction to colour schlieren photography", J. Opt. A: Pure Appl. Opt. 3, S1-S7, 2001

[11] Adnan H. Naefeh, *Wave propagaton in layered anisotropic media with applications to composites*, North-Holland, Amsterdam, 1995

[12] M. F. Werby, H. Überall, “The analysis and interpretation of some special properties of higher order symmetric Lamb waves: The case for plates”, J. Acoust. Soc. Am. 111(6), 2686-2691, 2002.

Chapter XV Conclusions and Prospects

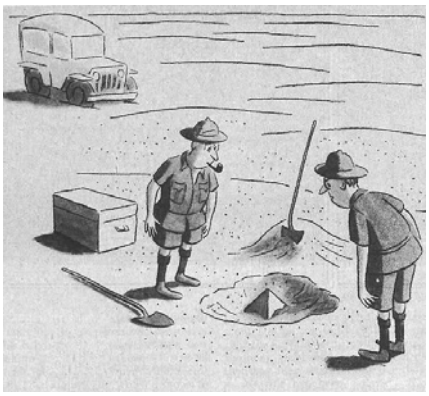

Three years ago, I started to dig. I found my rock and described it in this dissertation. It is my desire to keep digging and find out how deep this rock is buried underneath the desert sand.

When I graduated, neither did I believe that I was a scientist, nor did I believe that any of my student colleagues were scientists. We simply all had proved that we were able to reproduce books. As a matter of fact, it is unfortunate that the circumstances during one's education often favor memorization and prohibit imagination. In addition, when a person graduates, he obtains not only his degree, but he also carries heavy luggage, filled by problems and a self- and socially conditioned, often unrealistic, image of his capabilities and shortcomings.

When I started this research, I have simply 'deleted' the past and have started from scratch, supported by my wife, son and family. I had the fortune to join the pleasant research team of Joris Degrieck and keep in touch with Oswald Leroy and Rudy Briers. These three people possess three common characteristics : they are genuine scientists, they are correct and they are human. It has been my pleasure to learn from them different aspects of life and science and it will be an honor to preserve their qualities in what I do during my future life.

It has never been my aim to write a dissertation. I just wanted to do science and to discover the world. Nevertheless, I have tried to make this dissertation enjoyable and I hope that the reader got pleasure from reading it.

A chapter entitled 'Conclusions and Prospects' also requires some considerations about the future. I would like to continue my life as a researcher, but simultaneously, I realize that one's future is sometimes determined by external aspects. Because I cannot manipulate these external aspects, it is not allowed to dream about the future, though dreams are tempting…

Nico F. Declercq